

N72-22250-312

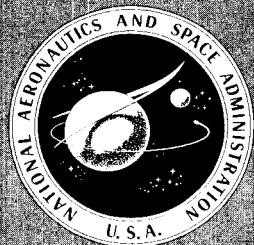
NASA SP-298

SPACE SIMULATION

CALL FILE COPY

A symposium held in
NEW YORK CITY, NEW YORK

May 1-3, 1972



NATIONAL AERONAUTICS AND SPACE ADMINISTRATION

SPACE SIMULATION

The proceedings of a symposium held May 1-3, 1972,
at the Americana Hotel, New York City, New York

Sponsored by

Institute of Environmental Sciences
The American Institute of Aeronautics and Astronautics
The American Society for Testing and Materials
and the National Aeronautics and Space Administration

Prepared at Goddard Space Flight Center



Scientific and Technical Information Office
NATIONAL AERONAUTICS AND SPACE ADMINISTRATION
Washington, D.C. 1972

FOREWORD

The National Aeronautics and Space Administration served as a co-sponsor of the Sixth Space Simulation Symposium. These proceedings were published as a NASA Special Publication in order to give the participants and attendees of the conference a permanent record of the material presented and to make the technology of space simulation available to others who may find in this technology solutions to problems extant in their respective fields.

Space exploration has posed the most challenging technical difficulties man has yet faced and solved. The technology evolved by the space program has relevance to many other fields, especially to the area of environment control and modification. This latter field promises to be one of extreme importance in this decade. The technology of space simulation has evolved many solutions to problems of a similar nature to those now affecting our environment.

NASA is pleased to cooperate with the Institute of Environmental Sciences, the American Institute of Aeronautics and Astronautics, and the American Society for Testing and Materials in advancing the frontiers of knowledge in the important area of space simulation and to make these proceedings available to other areas of science and technology.



John F. Clark
Director
Goddard Space Flight Center

PREFACE

These Proceedings are the sixth of a series of conferences jointly sponsored by the Institute of Environmental Sciences (IES), American Institute of Aeronautics and Astronautics (AIAA), and the American Society for Testing and Materials (ASTM). Also, the National Bureau of Standards (NBS) was a co-sponsor for the fifth conference in this series and the National Aeronautics and Space Administration was a co-sponsor for the sixth conference of the series. Each of the above societies assumes, in turn, the responsibility for organizing and conducting the conferences. These societies joined in this cooperative effort for several reasons. One, to reduce the number of conferences in this field with the resultant economies to both participants and societies; two, to provide a mechanism by which a majority of the papers in this field could be published in a single volume; and three, to provide a forum for presentation of **results** from this field to a larger audience than would otherwise be possible.

The Technical Committees of the sponsoring societies which are involved in space simulation assist in organizing the technical program of the conferences. These committees are:

IES - Solar Radiation Committee
AIAA - Ground Testing and Simulation Committee
ASTM - Committee E-21 on Space Simulation

The technical program committee is formed of members from each of the above committees.

The three societies have a Permanent Policy Committee, made up of two members from each society, to formulate general policy for the organization and conduct of the conferences. In this manner, the rules and regulations of each society for the conduct of meetings are adhered to as much as possible.

A General Committee is appointed for each conference which has the responsibility for arranging and conducting the meeting and publishing the Proceedings. The Sixth Space Simulation Conference, for which

the Institute of Environmental Sciences was the host society, was held concurrently with the Annual Meeting of the IES. The facilities, publicity, and outside program for this meeting were arranged by the respective representatives of the IES Annual Meeting Management Committee. For this meeting, the General Committee consisted of the General Chairman, John D. Campbell, the Technical Program Chairman, and the IES Publications Vice-President, R. T. Hollingsworth.

The Sixth Space Simulation Conference was held in New York City at the Americana Hotel on May 1-3, 1972. These proceedings were published by the NASA which was a co-sponsor for the meeting. Members of the Technical Program Committee performed the function of editor for papers presented in sessions which they organized.

Charles H. Duncan
Chairman, Technical
Program Committee

COMMITTEES FOR SIXTH SPACE SIMULATION CONFERENCE

GENERAL COMMITTEE

General Chairman - John D. Campbell, Perkin-Elmer Corp.
Publications Chairman - R. T. Hollingsworth, NASA/GSFC
Program Chairman - Charles H. Duncan, NASA/GSFC

PROGRAM COMMITTEE

Fritz N. Benning - Spectrolab Division of Textron
Eugene N. Borson - The Aerospace Corporation
George J. Frankel - Grumman Aerospace Corporation
John E. Gilligan - IIT Research Institute
Terry L. Hershey - Spectrolab Division of Textron
R. E. "Zeke" King - McDonnell Douglas Astronautics
J. M. Krafft - U. S. Naval Research Laboratory
Malcolm A. Lillywhite - Martin Marietta Corporation
Emile S. J. Wang - McDonnell Aircraft Company
James J. Webb - NASA/GSFC
George F. Wright - Sandia Laboratories

JOINT POLICY COMMITTEE

IES

John D. Campbell - Perkin-Elmer Corporation
R. T. Hollingsworth - NASA/GSFC

AIAA

Aleck C. Bond - NASA/MSC
R. E. Covey - Jet Propulsion Laboratory

ASTM

Joseph C. Richmond - National Bureau of Standards
Rodney W. Johnson - NASA Headquarters

TABLE OF CONTENTS

SESSION I

HIGH ENERGY LIGHT SOURCES

- Session Organizer - Terry L. Hershey
Spectrolab, Division of Textron, Inc.
- Session Chairman: - Terry L. Hershey
Spectrolab, Division of Textron, Inc.
- Session Co-Chairman - Donald Male
Arnold Engineering Development
Center

<u>Paper No.</u>		<u>Page</u>
1	Operation of Southwest Research Institute's High-Intensity Arc-Image Facility, E. Jack Baker, Jr., Southwest Research Institute	1
2	High Intensity Lamps, Len Reed, ILC, Inc.	11
3	Time, Peak Power, and Spectral Advantages Over Continuous Discharge Lamps and A Margin of Safety Standards for Flash Tube Design, Louis R. Panico and Gene Magna, Xenon Corp.	13
4	Development of A High Power, High Reliability Short-Arc Xenon Radiation Source, J. J. Malloy, International Telephone & Telegraph, Electron Tube Division and Clifton S. Fox, Night Vision Laboratory	15
5	A 400 kW Arc Lamp for Solar Simulation, Arthur J. Decker and John Pollack, NASA, Lewis	17
6	Development of a High Irradiance Source, Albert R. Lunde, The Boeing Company	19

7	Design and Performance of the RASTA High Power Laser, George W. Sutton and Arne C. J. Mattsson, Avco Everett Research Laboratory	39
---	--	----

SESSION 2

MANNED EFFECTS: WEIGHTLESSNESS - I

Session Organizer	- George J. Frankel Grumman Aerospace Corp.
Session Chairman	- George J. Frankel Grumman Aerospace Corp.
Session Co-Chairman	- Paul R. Gauthier The Boeing Company

<u>Paper No.</u>		<u>Page</u>
8	Experiments with the Skylab Fire Detectors in Zero Gravity, Dr. R. M. F. Linford, McDonnell Aircraft Co.	41
9	Training & Certification Program of the Operating Staff for a 90-Day Test of a Regenerative Life Support System, W. P. Waters, McDonnell Douglas Astronautics Co.	57
10	Facilities & Support Systems for a 90-day Test of a Regenerative Life Support System, Robert L. Malin, McDonnell Douglas Astronautics Co.	69
11	Safety Aspects of a 90-day Manned Test of a Regenerative Life Support System, J. P. Valinsky, McDonnell Douglas Astronautics Co.	79
12	G. E. Underwater Test Facility Studies in Zero G Simulation, Ruth H. Fry, General Electric Space Div. Underwater Test Facility	89
13	A Man-Rated Altitude Chamber for Education and Research-in a High School, Robert A. G. Montgomery, Jr., Project SPARC-NE High School, Philadelphia, Pa.	103

SESSION 3 CONTAMINATION - I

Session Organizer - Eugene N. Borson
 The Aerospace Corporation

Session Chairman - Eugene N. Borson
 The Aerospace Corporation

Session Co-Chairman - Raymond Kruger
 NASA, Goddard Space Flight
 Center

<u>Paper No.</u>		<u>Page</u>
14	Vacuum Stability Testing of Apollo 15 Scientific Instrument Module (SIM) Non-Metallic Materials and Reversion of Silicone Rubber in a Motor Switch, H. M. Clancy, North American Rockwell.	107
15	Some New Techniques in Passive Contaminant Analysis of Space Environment Simulation Chambers, Calvin M. Wolff, Brown and Root-Northrop	151
16	Photoluminescence and Optical Transmission of Diffusion Pump Oil, Roger L. Kroes, NASA, Marshall Space Flight Center	171
17	Radiation Effects on Contaminants From the Outgassing of Silastic 140 RTV, Peter F. Jones, The Aerospace Corporation	173
18	Integrated Real-Time Contamination Monitor: Optical Module, Gary M. Arnett and Roger C. Linton, NASA, Marshall Space Flight Center	179
19	Experimental Determination of Sticking Coefficients, E. E. Klingman, NASA, Marshall Space Flight Center.	181

SESSION 4

THERMAL TECHNIQUES, SOLAR SIMULATION AND RADIATION

Session Organizer - James J. Webb, NASA,
Goddard Space Flight Center

Session Chairman - James J. Webb, NASA,
Goddard Space Flight Center

Session Co-Chairman - Robert G. Fink
Perkin-Elmer Corporation

<u>Paper No.</u>		<u>Page</u>
20	Environmental Simulation from 0.01 to 100 Solar Constants, John R. Jack and Ernie W. Spisz, NASA, Lewis Research Center	193
21	Variable Geometry Total Radiation Detector System, Jerry G. Greyerbiehl, NASA, Goddard Space Flight Center	195
22	The Design and Application of an Infrared Simulator for Thermal Vacuum Testing, Steven P. Wallin, NASA, Manned Spacecraft Center; Calvin Wolff and Douglas J. Skinner, Brown & Root-Northrop	197
23	Control of an Artificial Infrared Environment to Simulate Complex, Time-Varying Orbital Conditions, Ray L. Dewey, NASA, Manned Spacecraft Center	217
24	Predicting and Analyzing the Thermal Flux Incident on Test Articles in a Simulated Space Environment, Steven P. Wallin, NASA, Manned Spacecraft Center; D. W. Halstead, James H. Stuart and C. L. Smithson, Jr., The Boeing Company	231
25	An Automated System for the Alignment of Large Area Modular Solar Simulators, James P. Vincent, NASA, Manned Spacecraft Center; Leo F. Polak and P. S. Fisher, Electro-Optical-Systems, Xerox	251

SESSION 5

MANNED EFFECTS: WEIGHTLESSNESS - II

- Session Organizer - George J. Frankel
Grumman Aerospace Corp.
- Session Chairman - George J. Frankel
Grumman Aerospace Corp.
- Session Co-Chairman - Paul R. Gauthier
The Boeing Company

<u>Paper No.</u>		<u>Page</u>
26	A Comparison of Simulated Reduced Gravity Flight with Actual Orbital Flight Conditions, Donn Eisele, NASA, Langley Research Center; Scott MacLeod, Grumman Aerospace Corporation	269
27	Full-Scale Skylab Apollo Telescope Mount Deployment Tests, G. F. Fricker, McDonnell Aircraft Company.	281
28	Manned Thermal-Vacuum Test Operations: Its Development from Experimental to Routine, Paul R. Gauthier, The Boeing Company; Herbert G. Sherwin, Brown Root-Northrop; Marion M. Lusk, NASA, Manned Spacecraft Center	291
29	Zero "G" Manual Cargo Handling, Amos A. Spady, Jr. and Gary P. Beasley, NASA, Langley Research Center	313
30	Habitable Atmospheres which Do Not Support Combustion, Dr. Edward T. McHale, Atlantic Research Corporation	331
31	Low-G Simulation Testing of Propellant Systems Using Neutral Buoyancy, D. L. Balzer and R. J. Lake, Jr., RCA Astro Electronics Division	337

SESSION 6

CONTAMINATION - II

Session Organizer - Eugene N. Borson
The Aerospace Corp.

Session Chairman - Eugene N. Borson,
The Aerospace Corp.

Session Co-Chairman - Raymond Kruger, NASA,
Goddard Space Flight Center

<u>Paper No.</u>		<u>Page</u>
32	Predicting Spacecraft Self-Contamination in Space and in a Test Chamber, Dr. John J. Scialdone, NASA, Goddard Space Flight Center	349
33	Preparation, Verification, and Operational Control of a Large Space-Environment-Simulation Chamber for Contamination Sensitive Tests, James T. Visentine and John W. Ogden, NASA, Manned Spacecraft Center; Melvin L. Ritter, Brown & Root- Northrop; Charles F. Smith, NASA, Marshall Space Flight Center	361
34	V-3 Contamination Test in the Manned Spacecraft Center's Vacuum Chamber-A, Philip W. Tashbar, Daniel B. Nisen, and W. Walding Moore, Jr., NASA, Marshall Space Flight Center	389
35	Dynamics of Spacecraft Contamination, Robert J. Naumann, NASA, Marshall Space Flight Center	405
36	Holographic Analysis of Particle Size Distribution and Particle Velocities for Skylab Contamination Ground Test, John R. Williams and Dr. Robert L. Kurtz, NASA, Marshall Space Flight Center	407

SESSION 7

THERMAL CONTROL MATERIALS – SIMULATION AND PERFORMANCE

Session Organizer - Jack E. Gilligan
 Illinois Institute
 of Technology

Session Chairman - Jack E. Gilligan,
 Illinois Institute
 of Technology

Session Co-Chairman - Dennis Farnsworth
 Martin Marietta Corporation

<u>Paper No.</u>		<u>Page</u>
37	The Determination and Optimization of (RUTILE) Pigment Particle Size Distributions, L. Willard Richards, National Research Corp.	409
38	Satellite Temperature Correlation of Predicted, Test, and Flight Data, Harry Apoian, The Aerospace Corp.	425
39	Effects of Surface Bubbles on Heat-Transfer Characteristics of Spacecraft Paints, Reagan S. Redman, NASA, Manned Spacecraft Center	445
40	Space Simulation and Rate Dependent Radiation Testing, H. E. Pollard and D. C. Briggs, Philco Ford Corporation	453

SESSION 8

CONTAMINATION III: EFFECTS AND INSTRUMENTATION

- Session Organizer - Fritz Benning
Spectrolab, Division of Textron
- Session Chairman - Fritz Benning
Spectrolab, Division of Textron
- Session Co-Chairman - Calvin Wolff
Brown & Root-Northrop/NASA,
Manned Spacecraft Center

<u>Paper No.</u>		<u>Page</u>
41	Environmental Simulation Testing of Solar Cell Contamination by Hydrazine, W. Walding Moore, Jr., NASA, Marshall Space Flight Center	461
42	A Contamination Experiment Investigating the Failure of the Nimbus IV Filter Wedge Spectrometer, Raymond Kruger, NASA, Goddard Space Flight Center	469
43	Contaminant Removal from Optical Surfaces, Theodore Baurer, Harold W. Goldstein, and Irwin M. Pikus, G. E. Space Division	487
44	Effects of Surface Contamination on the Infrared Emissivity and Visible-Light Scattering of Highly Reflective Surfaces at Cryogenic Temperatures, Walter Viehmann and Alfred G. Eubanks, NASA, Goddard Space Flight Center	489
45	An Instrument for Real-Time Detection of Contamination in Space Environmental Test Chambers, Robert G. Richmond, NASA, Manned Spacecraft Center; Henry N. Harmon, The Boeing Company	503
46	The Use of a Quartz Crystal Micro-Balance and an Optical Reflectometer to Determine Contaminant Material Optical Constants, D. A. Wallace and R. L. Chuan, Atlantic Research	521

47	A Space Simulation Test Chamber Development for the Investigation of Radiometric Properties of Materials, David L. Enlow, General Electric Co.	523
----	--	-----

SESSION 9

SPACECRAFT TESTS AND FACILITIES

Session Organizer	- R. E. "Zeke" King McDonnell Douglas Astronautics Co.
Session Chairman	- R. E. "Zeke" King McDonnell Douglas Astronautics Co.
Session Co-Chairman	- H. Allgauer Hughes Aircraft Company

<u>Paper No.</u>		<u>Page</u>
48	Thermal Vacuum Chamber Shroud Performance with Gaseous Nitrogen Cooling, Richard A. Farmer, Martin Marietta Corporation	535
49	Advantages of Cryopumping with Liquid Hydrogen Instead of Helium Refrigerators, John W. Anderson and J. E. Tueller, Lockheed Missiles and Space Company.	549
50	Development of a Carbon Cloth Heat Post Module for Thermal Vacuum Testing of a Spinning Spacecraft, M. B. Levine and L. A. Nelson, Hughes Aircraft Company.	555
51	The Design and Operation of a Planet Emitted and Albedo Radiation Simulator, George E. Sweet, John T. Taylor and Ira H. A. Abbot, NASA, Langley Research Center	565
52	Spacecraft Thermal Vacuum Testing, B. F. Elam and L. D. Lancaster, Martin Marietta Corp.	593
53	Some Contamination Problems in the European TD Satellite, J. Dauphin, G. Schamle and A. Zwaal, European Space Research Organization	613

54	Martian Gravity Simulator for Full-Scale Viking Landing Tests, Ulysse J. Blanchard and Sandy M. Stubbs, NASA, Langley Research Center	629
----	---	-----

SESSION 10

NOVEL AND UNIQUE FACILITIES UTILIZATION

Session Organizer	- Malcolm A. Lillywhite Martin Marietta Corporation
Session Chairman	- Malcolm A. Lillywhite Martin Marietta Corporation
Session Co-Chairman	- Cassandra Martin University of Denver Department of Biology Deborah Strange Bower Martin Marietta

<u>Paper No.</u>		<u>Page</u>
55	Utilization of Aerospace and Military Technology in Solving Man's Terrestrial Problems, Malcolm Lillywhite, Martin Marietta Corp.	647
56	Simulation of Wind Effects on Buildings by Means of Wind Tunnels, J. E. Cermak, Fluid Mechanics Programs, Colorado State University, Ft. Collins, Colorado	649
57	Aerospace Technology for Medicine and Biology, Jerry U. Mayeux, Department of Manned Experiments and Life Sciences, Martin Marietta Corporation . . .	651

58	Water Conservation Through Advanced Technology, J. F. Baxter and L. O. Williams, Martin Marietta Corporation, Denver, Colorado	653
59	Application of Thermodynamic Modeling Techniques to Environmental Pollution, L. D. Lancaster and B. F. Elam, Thermophysics Section, Martin Marietta Corporation, Denver, Colorado	655
60	Technology of Planetary Extreme Environment Simulation, M. E. Wakefield, L. E. Apodaca, C. A. Hall, Martin Marietta Corporation, Denver, Colorado	657
61	Determination of Trace Impurities or Pollutants in Ambient Gas Samples Using a Combination of Gas Chromatographic and Infrared Techniques, Jack Smith, Martin Marietta Corporation, Denver, Colorado	673

SESSION 11

ABLATIVE REENTRY MATERIALS

Session Organizer - George F. Wright, Jr.
Sandia Laboratories

Session Chairman - George F. Wright, Jr.
Sandia Laboratories

Session Co-Chairman - R. B. Pope
Sandia Laboratories

<u>Paper No.</u>		<u>Page</u>
62	Operating Characteristics of the Air Force Flight Dynamics Laboratory 50 Mega Watt Hypersonic Test Leg, John C. Beachler and Werner A. Kachel, Air Force Flight Dynamics Laboratory	675
63	Molecular Beam Simulation of Planetary Atmospheric Entry--Some Recent Results, J. B. French and Dr. Neil M. Reid, University of Toronto; A. O. Nier and J. L. Hayden, University of Minnesota	687
64	Superalloy Material Tests in a Plasma Arc Tunnel, Donald W. Land, McDonnell Douglas Research Laboratories	703
65	Ablative Materials Evaluation for High Performance Lifting Entry Vehicles, Don L. David, K. R. Carnahan, Convair Division of General Dynamics; Richard N. Mueller, Wright-Patterson Air Force Base.	723
66	Development of a Silicone Ablator for High-Heat-Flux and High-Shear-Rate Conditions, Richard A. Campbell, James A. Ramseyer, and Arnold Huntress, Dow Corning Corporation	725
67	An Evaluation of Flight Data for the Apollo Thermal Protection System, Eugene P. Bartlett, Aerotherm Division of Acurex Corporation; Donald M. Curry, NASA, Manned Spacecraft Center	749

SESSION 12

MASS SPECTROMETRY AND VACUUM MEASUREMENTS

- Session Organizer - Emile S. J. Wang
McDonnell Douglas Corp.
- Session Chairman - Emile S. J. Wang
McDonnell Douglas Corp.
- Session Co-Chairman - James O. Ballance, NASA,
Marshall Space Flight Center

<u>Paper No.</u>		<u>Page</u>
68	Spacecraft Applications of Quadrupole Mass Spectrometry, Matthew P. Thekaekara, NASA, Goddard Space Flight Center	769
69	Integrated Real Time Contamination Monitor - Residual Gas Analyzer Module, Thomas R. Edwards, NASA, Marshall Space Flight Center	787
70	Directional Molecular Flow Analysis and Leak Detection with a Rotable Gas Analyzer in a Large Space Simulation Chamber, Horst K. F. Ehlers, NASA, Manned Spacecraft Center	789
71	Residual Gas Analyzer Calibration, R. H. Lilienkamp, McDonnell Aircraft Company	803
72	A Comparison of Quartz Crystal Microbalance Measurements with Mass Spectrometer Determinations, Raymond Kruger, Dr. John J. Scialdone and Harold Shapiro, NASA, Goddard Space Flight Center	815
73	A Vacuum Thermogravimetric Method for Outgassing Evaluations of Silicone-Coated Fiberglass Cloth, Lawrence B. Jensen, Gerald B. McCauley, and Mike Honma, Lockheed Palo Alto Research Laboratory; Arnold E. Hultquist, Lockheed Missiles and Space Company	831

SESSION 13

SPECIAL TOPICS

Session Organizer	- Charles H. Duncan, NASA, Goddard Space Flight Center
Session Chairman	- Donald L. Anderson, NASA, Ames Research Center
Session Co-Chairman	- Dewey E. Wornom, NASA, Langley Research Center

<u>Paper No.</u>		<u>Page</u>
74	Prediction of the Mechanical Properties of a Filled Elastomer in Vacuum, Gerald L. Gregory, NASA, Langley Research Center	843
75	Accelerated Testing of a Filled Elastomer in Vacuum, Morris L. Evans and Dr. Thomas C. Ward, Virginia Polytechnic Institute and State University; Gerald L. Gregory, NASA, Langley Research Center	859
76	Changes in Some Physical Properties Induced by Vacuum Heat Treatment, Arnold E. Hultquist, Lockheed Missiles and Space Company	875
77	Thermal Testing Techniques for Space Shuttle Thermal Protection System Panels, B. G. Cox, McDonnell Aircraft Company	881
78	STADAN and Data Relay Satellite Simulation (Emphasis on the Scheduler), Barry Kerne and Norman Shusterman, Operations Research, Inc.; P. Pease, NASA, Goddard Space Flight Center	899
79	SAS Attitude Support System, John L. Snyder, Computer Sciences Corp; Gary F. Meyers, NASA, Goddard Space Flight Center	909
80	Techniques Associated with Thermal-Vacuum Testing of the OAO-C Heat Pipes, James P. Marshburn, NASA, Goddard Space Flight Center	933

SESSION 14

SOLAR CONSTANT AND SOLAR SIMULATION TESTING

Session Organizer - Charles H. Duncan, NASA,
Goddard Space Flight Center

Session Chairman - Charles H. Duncan, NASA,
Goddard Space Flight Center

Session Co-Chairman - Robert P. Parrish, Jr.
Martin Marietta Corporation

<u>Paper No.</u>		<u>Page</u>
81	Radiation Scales on which Standard Values of the Solar Constant and Solar Spectral Irradiance are Based, Matthew P. Thekaekara, NASA, Goddard Space Flight Center	947
82	Proposed Specification for the Solar Constant and Air Mass Zero Solar Spectral Irradiance, IES Solar Radiation Committee and ASTM Space Simulation Committee E-21	955
83	Recommended Practice for Solar Simulation for Thermal Balance Testing of Spacecraft, IES Solar Radiation Committee and ASTM Space Simulation Committee E-21	969
84	Mechanisms for the Adhesion of Silver to Glow Discharge Sensitized Perfluorinated Ethylene Propylene (FEP), John B. Schutt, William H. Gilchrist, Robert N. Sheehy, Frank N. Paczkowski, NASA, Goddard Space Flight Center	1059

SPACE SIMULATION

ABSTRACT

This volume contains either the final draft or the abstract of all the papers presented at the Sixth Space Simulation Conference held in New York City at the Americana Hotel on 1, 2, 3 May 1972. The general scope of the conference was the area of space simulation: facilities, effects, measurements, and applications. The range of topics covered is indicated by the session titles which included:

High Energy Light Sources

Contamination

Thermal Techniques: Solar Simulation and Radiation

Thermal Control Materials

Spacecraft Tests and Facilities

Novel and Unique Facility Utilization

Ablative Reentry Materials

Special Topics (Predictive Testing, Physical and Mechanical Properties, Computer Simulation)

Mass Spectrometry and Vacuum Measurements

Solar Constant and Solar Simulation Testing

Three sessions were held on contamination and two on manned effects and weightlessness. The remainder of the topics were covered in a single session. Included in these proceedings are two items produced by the IES Solar Radiation Committee and the ASTM E21.70 Subcommittee on Solar Simulation. These are: Recommended Practice for Solar Simulation for Thermal Balance Testing of Spacecraft; and Engineering Standard for the Solar Constant and Air Mass Zero Solar Spectral Irradiance.

Key Words: ablation, contamination, computer simulations, mass spectrometry, vacuum measurements, solar simulation, facilities, spacecraft tests, manned effects, weightlessness, high energy light sources, radiometry, thermal techniques, heat transfer, thermal control materials.

INTRODUCTION

The purpose of this conference, as stated in the Call for Papers, was to provide a meaningful exchange of information on advances in the space simulation field with major emphasis placed on ingenuity and new techniques. This technology encompasses all aspects of simulating the space environment and the effects of this environment upon man and matter. Much of this technology is applicable to ecological studies and to the development of methods to control pollution of the environment. The conference was held concurrently with the IES Annual Meeting which was primarily concerned with these matters. This provided a mechanism for an interaction between those working in aerospace technology and environmental control which would not otherwise have been possible.

The papers accepted for presentation were separated into fourteen sessions and are grouped by session in the order presented at the meeting. The final drafts of these papers were not reviewed by the session organizers for possible changes before the volume went to press. Therefore, each author must assume full responsibility for the content of his paper.

OPERATION OF SOUTHWEST RESEARCH INSTITUTE'S HIGH-INTENSITY ARC-IMAGE FACILITY

E. Jack Baker, Jr., *Southwest Research Institute, San Antonio, Texas*

ABSTRACT

The arc-image furnace was primarily designed as a high-intensity pure thermal radiation test facility.

INTRODUCTION

The high-intensity, pressurized, arc-image facility, located at Southwest Research Institute (SwRI), is capable of delivering pure radiant thermal flux in excess of 4.5×10^7 watts/m² to the face of a 1.6-cm diameter specimen. The facility was designed, built and tested in 1958 under the sponsorship of the National Aeronautics and Space Administration. During the last 13 years, SwRI has made many changes in the design and operation of the facility which have improved its performance.

Originally the facility was intended for use in the evaluation of candidate materials for ablative heat shields on NASA's Mercury, Gemini and Apollo programs. It has continued to be an evaluation tool for NASA over the last decade, and a great deal of valuable information has been generated in the field of high-temperature ablation.

Several additional uses have developed during this period. These include the simulation of nuclear weapon effects and the general field of high-temperature physics. To our knowledge, this facility has the highest pure thermal flux capability of any laboratory tool of its type in the world. This paper describes its operation, characteristics and potentialities.

DESIGN PRINCIPLES AND GENERAL DESCRIPTION

The SwRI arc-imaging furnace utilizes twin parabolic searchlight mirrors to collect thermal radiation from a direct-current arc and to focus it upon a test specimen held in a controlled environment remote from the arc. It was designed to provide pure thermal radiation at the highest possible flux density for at least 15 sec on material specimens of the largest practical size. In accord with these design objectives, the mirror system has a magnification of unity so that the region of

high thermal flux at the specimen location is about equal in volume to the volume of the "anode ball" (the region of gas just beyond the anode which has the highest temperature in the electric arc). The optical system is normally focused upon the center of the anode ball, which is near the plane containing the rim of the anode crater.

The arc (and, incidentally, the whole optical system) is operated in a pressurized environment of from 2 to 10 atm, in order to increase the density and voltage drop of the arc and to decrease its size. Tests have been made at SwRI comparing arc outputs at different pressures, which indicate that radiation output does increase with pressure, in this "convection stabilized" arc as it does in "wall stabilized" arcs. Air is the only medium which has been used for arc pressurization.

During operation, the arc is continuously "blown" with converging streams of high velocity air. Approximately 450 grams of air per second are injected at sonic velocity around the arc in a converging cone which is coaxial with the anode. The air blast serves to oxidize and cool ionized matter, thus removing flame and ionized gas layers so that the collecting mirror receives radiation directly from the "anode ball" portion of the arc, which is therefore not obscured by absorbing matter at lower temperature. In addition, the air blast apparently "convection stabilizes" the arc and greatly increases the voltage drop across it.

The resulting arc, as seen through filters by means of periscopes and windows installed in the pressure vessel, is a blue-white brush about 1 in. long and 7/8 in. in diameter. It produces a rushing sound audible above the subdued roar of the enclosed air blast. At current settings of 2500 to 3000 amperes, more than 1 megawatt of electrical power is dissipated in the arc and electrodes, of which about 350 kW are unaccounted for by electrode resistances and are probably dissipated in the arc. The corresponding thermal radiation power delivered to the target region totals about 16 kW, with an average flux density up to 1000 gram-calories/cm² sec or 3700 BTU/sq ft sec, at the present time.

MAJOR COMPONENTS

Arc-Imaging Optics

Figure 1 shows a simplified schematic diagram of the arc-imaging system enclosed in the pressure vessel. It consists of two 37-1/4-in. diameter, 15-in. focal length parabolic mirrors (from searchlights) facing one another, with the arc positioned at the focus of one paraboloid and the target, or specimen, at the focus of the other. There are 6-in. holes cut in the center of each mirror. Figure 2 shows the physical arrangement of

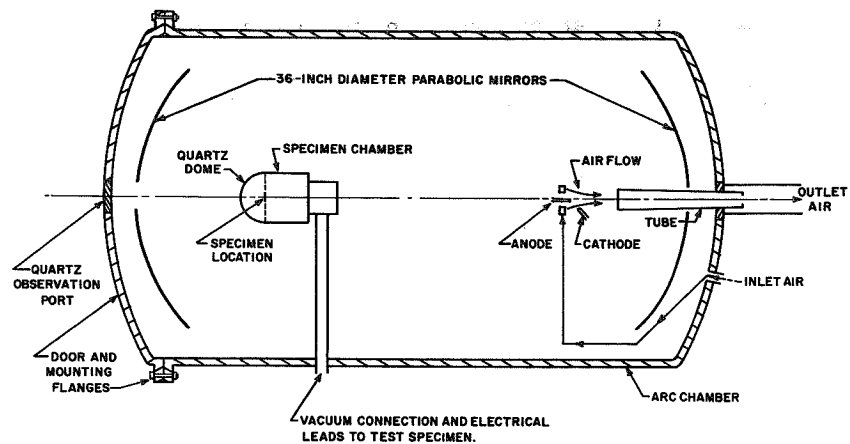


Fig. 1—Schematic diagram of arc-imaging system

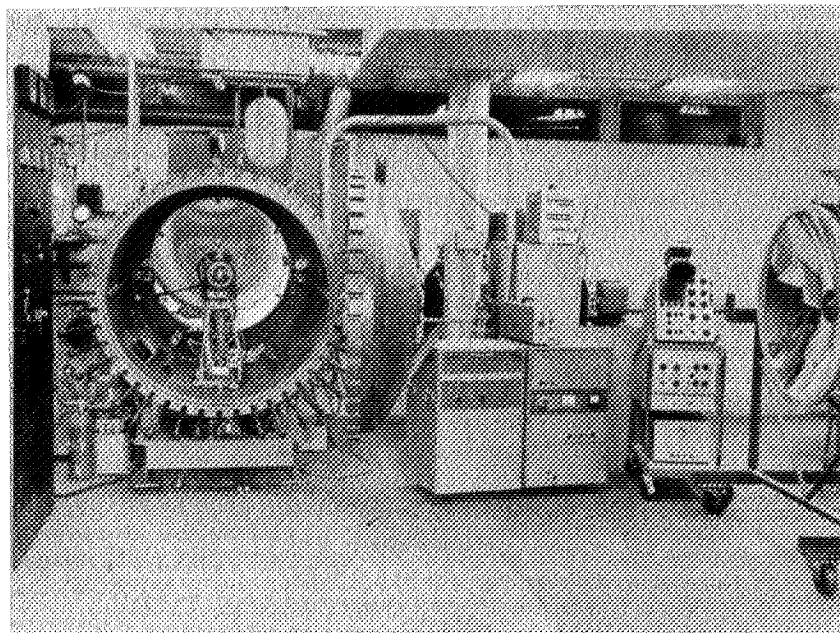


Fig. 2—Physical arrangement of various components

various components; one mirror is shown at the right on the rolling stand used to remove it from the tank. Accurate alignment of both mirrors, the arc, and the specimen on a common axis is essential to prevent coma in the image. Both stellite and back-silvered glass mirrors have been used. Because they are heavier and thinner, the stellite mirrors require some warping adjustment, by means of shimming the clamps in the steel support frames, to reduce coma. With both types, "good" images (1/16 in. in diameter) have been produced from a "point" test source at the arc position.

The diameter of the image of the anode ball, or "hot spot", is approximately 7/8 inch. Consequently, the limiting diameter of a disc specimen is 3/4 in. if fairly uniform irradiation is required. Defocusing the specimen by moving it toward the arc-imaging mirror permits an increase in specimen diameter while maintaining uniformity of radiation flux density; however, the flux density falls off sharply because the 130-deg angle subtended at the focal spot by the imaging mirror produces a limited depth of field.

Specimen Environment

The specimen is contained in a pressure-and-vacuum-tight steel housing and is irradiated with thermal energy through an optical-glass dome. The steel specimen housing is provided with connections to the outside of the arc furnace pressure vessel such that the housing can be evacuated or pressurized. The glass dome, sealed with an O-ring, can support somewhat more than 5 atm of internal pressure in the vessel; hence, the present upper limit of specimen pressure environment is approximately 15 atm. A usual low pressure value is of the order of 0.05 mm Hg, at the present time.

The specimen housing is so designed that it can contain alternatively a circulating-water, black body cavity calorimeter for the measurement of thermal flux under experimental conditions. Within the housing, immediately under the glass dome, are high-speed, rotary-solenoid-operated, clam-shell shutters which permit the duration of specimen exposure to be controlled.

Electrodes, Holders and Controls

The arc stand and electrodes originally used were taken from an Army surplus 60-in. searchlight. However, at operating currents above 500 amperes, it was found that electrode erosion was too rapid for the available motor drive to handle it and that toothed-wheel electrode drivers were unreliable. A series of modifications finally produced electrode holders operable up to 3000 amperes.

The anode holder is of brass, assembled with bolts, having

a Rhodium plated brass faceplate, graphite nozzle and graphite radiation-shield ring. The current contacts are four copper filled graphite generator brushes, cooled and pressed with a force of about 15 lb each against the anode by air pressure from the nozzle feed chamber. The anode itself forms the inside of the inner annular nozzle; hence, it is air-cooled. Furthermore, the portion between the brushes and the crater end is only 1 in. long, so that, during active feeding, the resistive heating and spalling should be reduced.

The anode is rotated at about 200 rpm by a small motor to insure symmetrical erosion and crater development. It is retracted or fed into the arc by the hydraulic cylinder. This cylinder is controlled by a two-way electrical valve operated either manually or automatically by a photocell located in the arc chamber and connected in a bridge circuit, viewing a leading edge of the anode. By these means, the anode ball is customarily maintained within 5 mm of the focus of the collecting mirror, despite consumption of the anode at rates up to 2 cm/sec.

As anodes, National Carbon Company "Ultrex" electrodes 16 mm in diameter, having a 12-mm misch-metal core, rated at 325 amperes, are customarily used. It was found that solid graphite anodes produce much less radiation. Copper and aluminum-cored anodes unfortunately spray molten drops which adhere to the arc mirror. However, a 16-mm anode machined from solid misch metal (rare-earth oxides) has given an excellent radiation output without any spalling on prolonged runs at 3000 amperes, and has no more electrical resistance than "Ultrex" or graphite anodes. With all anodes, the combined (cold) resistance through the anode holder, from cable to anode tip (measured by a four-probe method) is only $0.012\ \Omega$, and the electrical power losses and resistive heating in this part of the circuit (presumably up to 100 kW) are considered relatively minor at this time.

As cathodes, 11-mm solid "H-I Projection" carbons, from National Carbon Company, have been used almost exclusively. These small, hard rods have a relatively high cold resistance ($0.015\ \Omega/\text{in.}$), and they glow brilliantly, erode rapidly, spall and curl somewhat at currents above 2000 amperes, but they have the advantage of casting a relatively narrow shadow on the arc mirror.

The cathode holder employs a reliable chain drive with an insulated setscrew clamp. The angle between the cathode and the anode axis is adjustable, but 47° gives good cathode sculpturing and reasonably small mirror shadowing without as much tendency for the arc to blow out as is found at larger angles with present values of current and air-jet flow. It has been found necessary for the cathode tip to extend completely through the annular air stream into the "anode brush" to avoid

frequent blowing out of the arc.

Current to the cathode is carried as close to the arc as possible without excessive mirror shadowing by means of twelve cantilever-spring contacts of 0.1-in. tungsten rods. These are protected from overheating and oxidation by a replaceable graphite cap which is continuously filled and flushed with argon or dry nitrogen during operation. Unfortunately, the (cold) contact resistance is $0.020\ \Omega$ or higher, despite reasonably high contact pressures (2 lb per spring) and a large total (3 sq cm) ground and lapped contact area. Further improvement is probably needed to reduce what appear to be excessive power losses (up to 250 kW) in the present cathode and cathode holder.

Cathode erosion rates range up to about 2 cm/sec. The position of the cathode tip is controlled automatically by a variable-speed electric gearhead motor with an electric clutch. Upon application of the arc voltage, this mechanism advances the cathode until current begins to flow. When the electrodes burn away until the voltage drops to a predetermined level, the mechanism advances the cathode further in short bursts in an attempt to maintain the arc voltage within 5% of this value. At present, the automatic feed can maintain the arc voltage within this range. The current is maintained by setting the firing level of the power supply. Therefore, we have complete control of the current and voltage, and thus the power dissipation across the arc.

Rectifier

The rectifier which supplies d-c power to the arc is a three-phase, full vane type using six GE type GL5564/507 ignitrons. The continuous rating of the unit is 500 kVA corresponding approximately to the theoretical maximum d-c line voltage of 560 volts and an arc current of 900 amperes. For 1 min, an overload of 2400 amperes is permissible. For an arc duration of 1.4 sec, overload currents up to 9000 amperes are permissible. The firing times of the ignitrons can be adjusted by means of a small, "synchro" three-phase transformer, whose outputs are clipped and differentiated to provide six trigger pulses in a definite phase relationship. By adjusting the angle between the rotor and stator of this synchro, the arc voltage and current can be continuously varied from zero to the maximum permitted by circuit resistance (about 3000 amperes at this time).

Because of the high power requirements for operating the arc, a separate substation was constructed to service the facility. The substation is powered by a 13,800-volt primary transmission line.

Compressed Air System

A three-stage air-and-water-cooled compressor system with an average capacity of 26 SCFM and a discharge pressure of 1000 psig is used to charge a 52-cu ft accumulator. A fast-acting pressure regulator on the discharge of the accumulator is used to reduce inlet pressure to the arc nozzles to a constant value which may be adjusted up to about 250 psig. Two fast-acting solenoid-controlled pneumatic valves operate simultaneously to turn on the air blast at the arc and to open the tank exhaust, which is metered with an appropriately sized orifice. It has been found to be very important to maintain a constant pressure in the arc chamber so that a cloud of water vapor is not formed due to sudden decompression. This is true even though the air used to charge the vessel is passed through a drier.

The pressure vessel housing the imaging furnace has been tested to 250 psi, but is operated at half that pressure. It is equipped with two 8-in. access portholes opposite the arc and the specimen region, three 3-in. windows, and a hinged access door held by forty-four 1-in. bolts.

When the facility was first put into operation, a great deal of difficulty was encountered because the tank gases become heavily contaminated with brown nitrogen oxides and grey smoke consisting mostly of lanthanum and cerium carbonates coming from the anode core. These combustion products reduced the radiation flux available at the target to 30% of its initial value after 4 sec of operation. This restriction was overcome by re-designing the exhaust and scavenging system.

FACILITY CALIBRATION

The amount of energy incident on any diameter focal point in the specimen chamber, where the front surface of the specimen would be installed, can be measured during calibration tests using a water flow, black body, spherical cavity calorimeter. This calorimeter has been used for a number of years in conjunction with the arc-image facility, with very good repeatability and accuracy.

The basic design of the calorimeter is simple and straightforward. A 1-1/2-in. diameter spherical, thin shell, brass cavity is chemically blackened. Copper tubes are soldered to the outside of the brass cavity, assuring good thermal contact. During a run, water is circulated through the copper tubing, and the temperature differential of the water entering and leaving the calorimeter is continuously recorded by using a differential Thermopile. The total water that flows through the calorimeter is collected and recorded along with the time lapse. From these data, the average flow is calculated.

The calorimeter is designed so that any aperture up to 1 in. in diameter may be used in conjunction with it. This is done by machining a hole the diameter of the desired aperture in a 3/8-in. -thick graphite disk. A 130-deg included angle taper from the front to the back of the disk is then machined. With this geometry, none of the energy that should reach the calorimeter is blocked. This leaves a razor edge on the back surface of the disk which is the diameter of the desired aperture. For this program, the aperture was 4/8 in. in diameter, the same as the specimen diameter. The aperture disk is thermally isolated from the rest of the calorimeter so that only the energy passing through the aperture is absorbed by the calorimeter.

During a calibration run, the arc is allowed to run long enough to allow the calorimeter to reach equilibrium. Since the water flow and aperture are constant during a given run, the indication of equilibrium is a constant temperature differential. From the aperture area, water flow rate and the equilibrium temperature differential, the energy per unit area and the unit time entering the calorimeter are easily calculated.

A correlation is made of the flux measured during calibration runs between the water flow calorimeter and the signal from an asymptotic calorimeter (HyCal #C-1135) located in the collimated beam between the two parabolic mirrors. The signal from the asymptotic calorimeter is then used to determine the incident flux on the face of a specimen during an actual test run. The output from the asymptotic calorimeter is thus recorded, along with the thermocouple records during a test, to give the incident flux level.

TEST INSTRUMENTATION

The results of the test conducted in the SwRI arc-image facility are measured and recorded during the course of experiments. Some of the measurements that have been made are surface time-temperature and internal time-temperature histories, strain-gage measurements, ion emission and naturally thermal degradation which is visually observed. In order to record the effects of the intense thermal flux, we must use high-speed recording equipment such as oscillographs, oscilloscopes and motion picture cameras.

An example of a thermocouple-instrumented specimen installation and a typical oscillograph record obtained for a specimen is shown in Figures 3 and 4.

We have designed a special three-color pyrometer for use in this facility. Its design and location are shown in Figure 5. It can be seen from this schematic that we may simultaneously measure the surface temperature, take motion pictures of the

test exposure and view the test in real time.

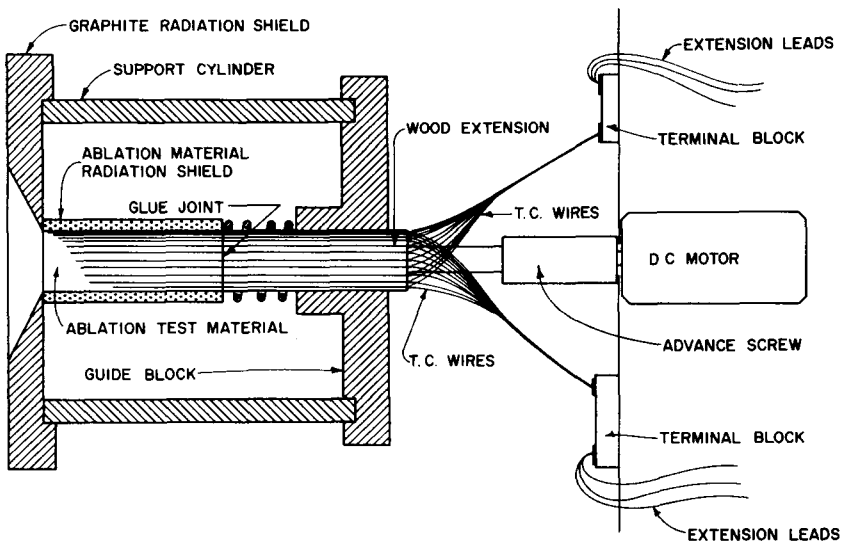


Fig. 3—Thermocouple-instrumented specimen installation

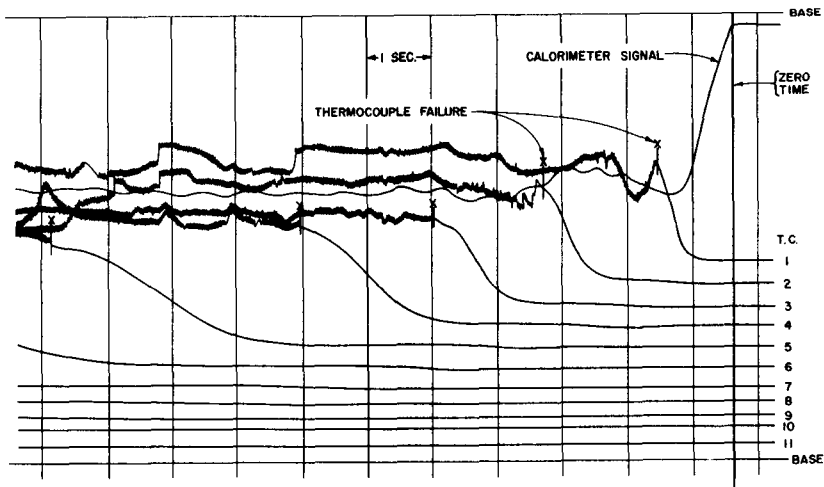


Fig. 4—Typical oscillograph record

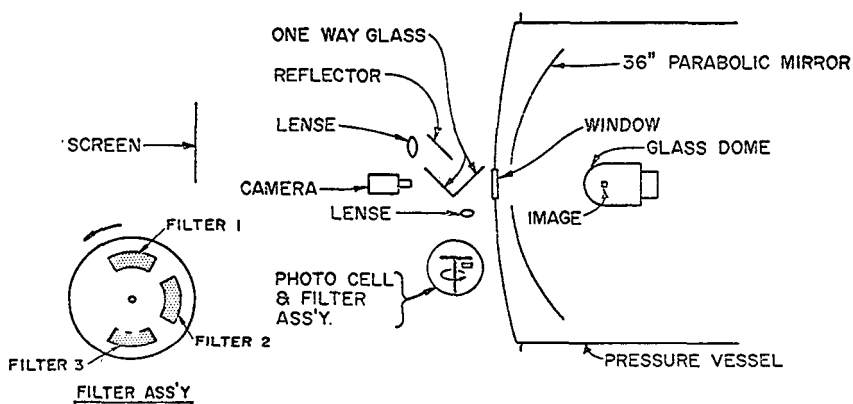


Fig. 5—Design and location of three-color pyrometer

SUMMARY AND CONCLUSIONS

This paper has described an enclosed, air-blown, arc-imaging furnace operating at up to 10 atm of arc pressure, dissipating on the order of 1 MW of electric power, and delivering thermal radiation to a 5/8-in. diameter disc or rod specimen held in a controlled environment, at an average flux intensity up to 1000 gram-calories/cm² sec. Details of its construction and operation have been given. Several associated measuring instrument systems and a few examples of typical test results have also been described.

It is suggested that this extremely versatile facility is presently or potentially suitable for the following types of scientific work:

- (1) Studies of the properties of materials at high temperatures.
- (2) Development of new high-temperature materials through controlled melting and freezing, by vapor deposition of refractory substances, and by high-temperature chemical reactions.
- (3) Laser and other optical studies requiring an intense source of prolonged illumination.

It is anticipated that the versatility and available radiation intensity of this facility will continue to be improved as it is used for present and future research programs.

HIGH INTENSITY LAMPS

Len Reed, *ILC, Inc.*

ABSTRACT

The spectral tailoring of gas discharge lamps has been practiced since the turn of the century, and more recently the use of new materials of construction such as sapphire, niobium and active metal brazes has resulted in a wider range of metal gas vapors being used.

Often a noble gas such as argon or mercury or both, are "doped" with an active metal or metal halide vapor, which since it possesses lower excitation energy levels will be predominately present in the emission spectra of the lamp. Thus, for example, indium and gallium additions are used for blueprint lamps, bismuth and thallium for underwater sources, high pressure sodium for visible illumination, potassium-rubidium mixtures for Nd:YAG laser pumping and cesium for covert illumination.

The principles underlying the selection of a source for a particular application is outlined. The considerations involved in the construction of typical C. W. and pulse long arc and short arc sources are given.

Finally, a review of the various categories of sources presently in use will be made and the direction for future efforts to produce yet more efficient and long life lamps will be charted.

TIME, PEAK POWER, AND SPECTRAL ADVANTAGES OVER CONTINUOUS DISCHARGE LAMPS AND A MARGIN OF SAFETY STANDARDS FOR FLASHTUBE DESIGN

Louis R. Panico and Gene Magna, *Xenon Corp.*

ABSTRACT

Shorter pulse durations at fixed energy levels produce higher peak powers and higher current densities. The increased current densities generate hotter color temperatures resulting in a spectral shift towards the Ultra-Violet. The Ultra-Violet output of the flashtube is increased with shorter pulse durations at fixed energy levels. Flashtube designs requiring both short pulse and infra-red are limited by this characteristic. The pulse duration is a function of the wavelength being observed; the pulse rise time is heaviest in the Ultra-Violet with the pulse fall time shifting towards the infra-red.

Design standards for reliable flashtube operation based upon starting characteristics can be determined from the anode voltage/trigger voltage curve. As the anode voltage is increased the trigger voltage required can be reduced. However, the curve can vary from tube to tube and a margin of safety must be determined for each lamp design.

DEVELOPMENT OF A HIGH POWER, HIGH RELIABILITY SHORT-ARC XENON RADIATION SOURCE

J. J. Malloy, *International Telephone & Telegraph, Electron Tube Division*,
and Clifton S. Fox, *Night Vision Laboratory*

ABSTRACT

The objective of the work covered by this paper was to increase the power handling capability, efficiency, and reliability of the liquid cooled short-arc xenon lamp for military searchlights and solar simulation radiation sources.

The work involved the application of new techniques to increase power handling, efficiency, and reliability. This included use of new fabrication and inspection techniques not used before, such as electron beam welding and ultrasonic braze inspection procedures to provide reliability and consistency of the lamps. The work also covered the problems of anode dissipation, cooling efficiency, cathode design, and quartz problems which have caused reliability problems in solar simulation applications in the past. A new method of seal assembly was also investigated. A unique mechanically designed depressurization system was developed to be used with a fully sealed liquid cooled lamp to provide safety during storage and handling, which should provide a retrofit design for existing simulators with little system modification.

A 400 KW ARC LAMP FOR SOLAR SIMULATION

Arthur J. Decker and John Pollack, *NASA, Lewis Research Center*

ABSTRACT

At Lewis Research Center, an arc lamp has been operated at 400 kW in argon. The arc lamp has radiated 80 kW of directed radiation. The optical train of the lamp consists of a parabolic collector of 4 feet aperture and an optical integrator made from two lenticular arrays of 124 lenses each. The arc lamp has been designed for use in a vacuum chamber with a collimator 100 feet away. The design allows a uniform irradiance over a 15 foot by 30 foot rectangular beam. The nominal beam size is 580 feet.² This paper summarizes the design, operation, and evaluation of the performance, of the arc lamp.

DEVELOPMENT OF A HIGH IRRADIANCE SOURCE

A. R. Lunde, *The Boeing Company, Seattle, Washington*

ABSTRACT

Irradiance levels up to $17.27 \text{ BTU/in}^2\text{-sec.}$ with a non-uniformity ratio of 1.07 have been developed to simulate high heat flux loads on the surface of different materials. This has been achieved by an arc image furnace utilizing a 50 kw xenon short arc lamp mounted within an elliptical collector.

INTRODUCTION

Structural integrity of materials subjected to extreme heating rates ($15 \text{ BTU/in}^2\text{-sec.}$ and above) is presently a prime problem in the development of turbine blades, rocket nozzles, and reactors. Transpiration cooling, i.e., the use of gaseous fluid to assist in the transfer of these energies through the material presents an attractive approach to the solutions of these problems. Porous materials with very uniform continuous porosity have been developed. These materials offer a means of utilizing the transpiration cooling technique. Tests have been conducted at high heating rates to obtain insight into heat transfer and fluid flow mechanics in systems of this type. A 50 kw xenon short arc lamp provides the known radiant source which is free of problems associated with convection such as found in high temperature flows.

The original requirement specified peak irradiance levels to $25 \text{ BTU/in}^2\text{-sec.}$ over a 0.75 inch diameter target; but after achieving this, it was determined that the uniformity was not acceptable. This required additional modification to the optical path of the light rays by some type of energy condenser. A schematic of the final system setup is illustrated in Figure 1 and the system operational schematic in Figure 2.

This facility was developed under a joint effort of NASA-Lewis Research Center, Tamarack Scientific Company, Inc., and The Boeing Company for use on contract NAS3-12012, Fundamental Study of Transpiration Cooling.

The numbers in parenthesis refer to references listed at the end of this paper.

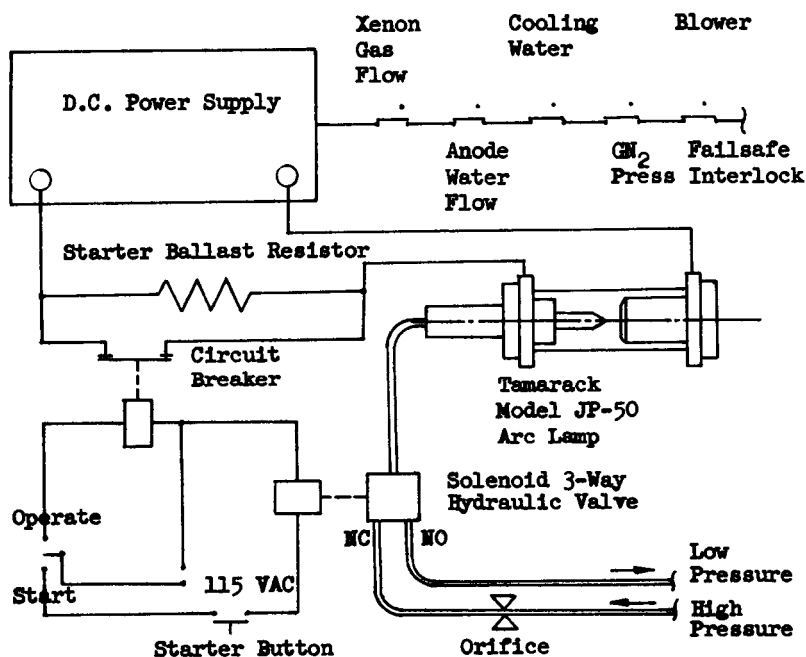


FIG. 2 - SYSTEM OPERATIONAL SCHEMATIC

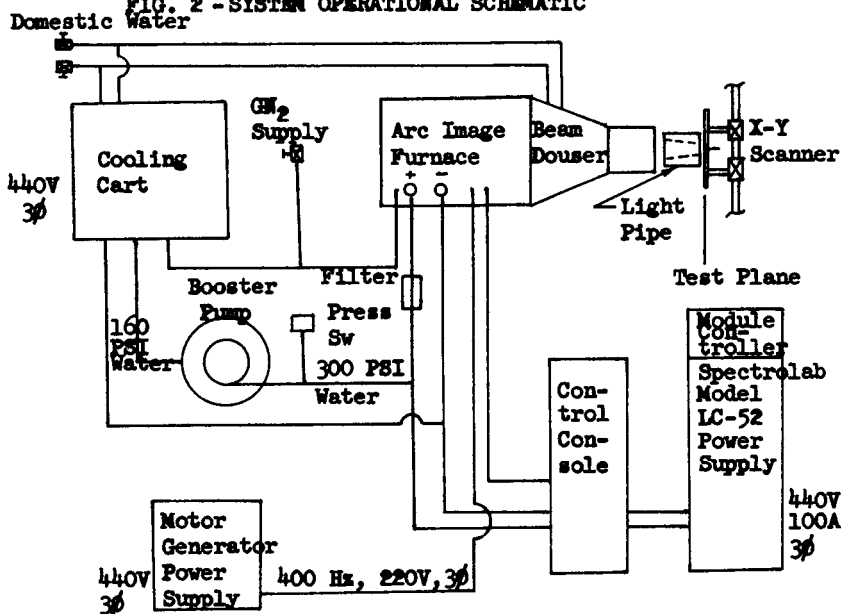


FIG. 1 - TEST SET-UP AND EQUIPMENT

This paper describes the facility that was developed to produce high and uniform irradiance levels. It is presented in four sections: 1) arc image furnace description and capability, 2) calibration techniques and instrumentation, 3) approach to uniformity improvement of the arc image furnace performance by use of energy condensers, and 4) final system performance using the hexagonal light pipe.

Arc Image Furnace

A model HTF-50 arc image furnace was procured from Tamarack Scientific Company for the high energy source. It consists of a high radiance lamp and collector. The lamp is tungsten tip copper electrodes within a double tubular quartz envelope as shown in Figure 3a. The special feature of the lamp is its 6 millimeter arc gap (see Figure 3b). This small gap provides the high radiance and small source required to produce a high irradiance and small image at the target from the 22.0 inch diameter collector. The arc is jet-pinchd by high velocity xenon gas passing around it from cathode to anode. The collector is a water cooled cast aluminum, nickel coated, aluminized reflector. Figure 4 is a photograph of the arc image furnace system.

The arc image furnace was operated at different power levels, lamp/collector focal distances, and collector to target distances. The different values were selected experimentally to optimize irradiance levels and uniformity at the target plane. These measurements were made by recording the irradiance level versus radial distance at the target plane with a Hy-Cal Model C-1312-A calorimeter mounted on an X-Y scanner. The distance from the collector to the target plane is 18.5 inches. A reference plane was established 3.0 inches in front of the target plane for ease of locating the calorimeter and scanner mechanism. This reference plane will be identified by the reference dimension of $Z = 3.0$ for a collector to target plane distance of 18.5 inches. Throughout the remainder of this paper, the target plane will be measured from the reference plane.

The test results from the arc image furnace are tabulated in Table 1. The term "Non-Uniformity Ratio" (NUR) is introduced and defined as follows for simplicity of data presentation:

$$NUR = \frac{PI}{EI} \quad \text{where } PI = \text{peak irradiance normally at the center of the beam}$$

and $EI = \text{edge irradiance or the lowest irradiance level within a radius of 0.375 inches from the center of the beam}$

Two typical energy distribution scans are shown in Figure 5. Scan number 24 exemplifies maximum irradiance and large center to edge non-uniformity ratio while scan number 3 exemplifies low irradiance and small non-uniformity ratio.

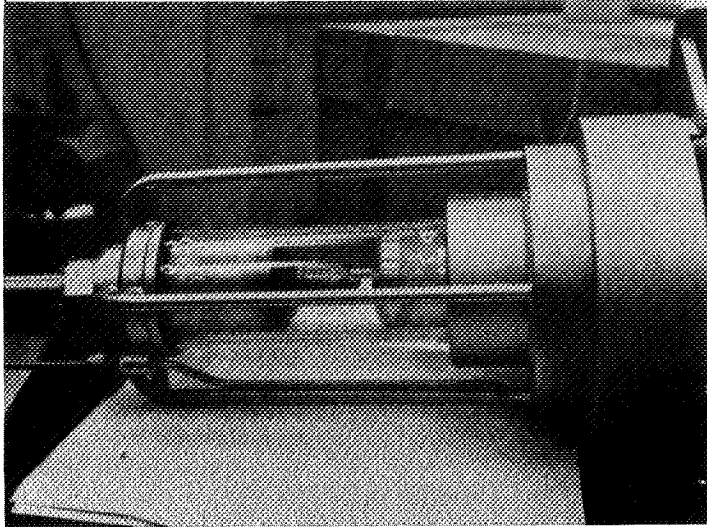


FIG. 3a-50KW XENON ARC LAMP

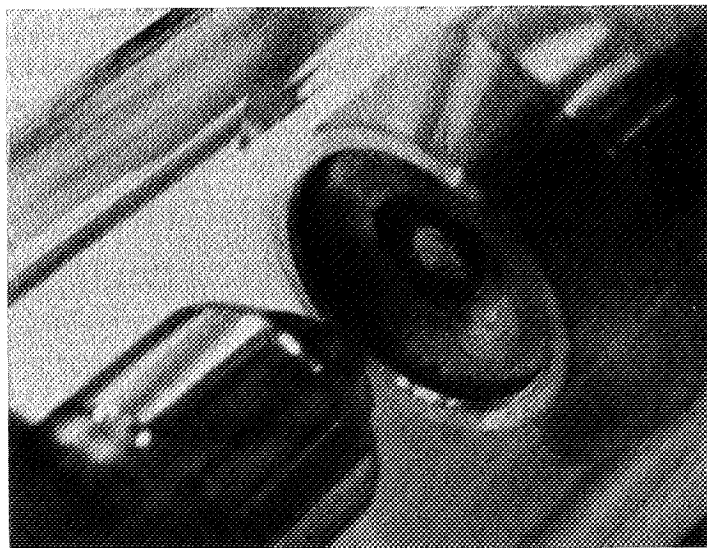


FIG. 3b-ARC LAMP ELECTRODES

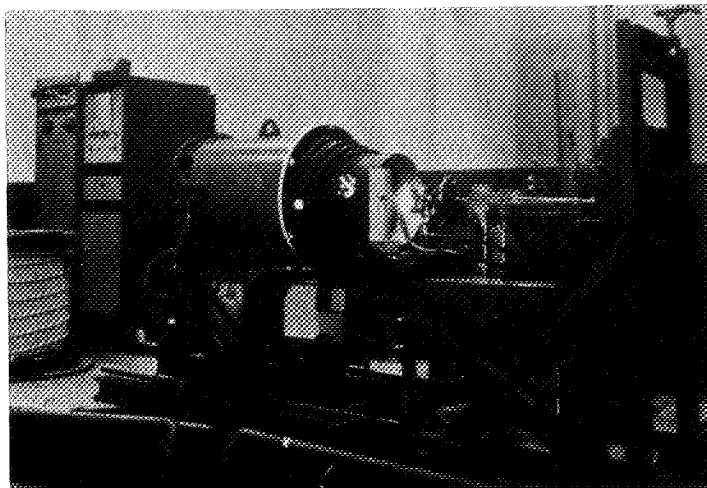


FIG. 4-ARC IMAGE FURNACE SYSTEM

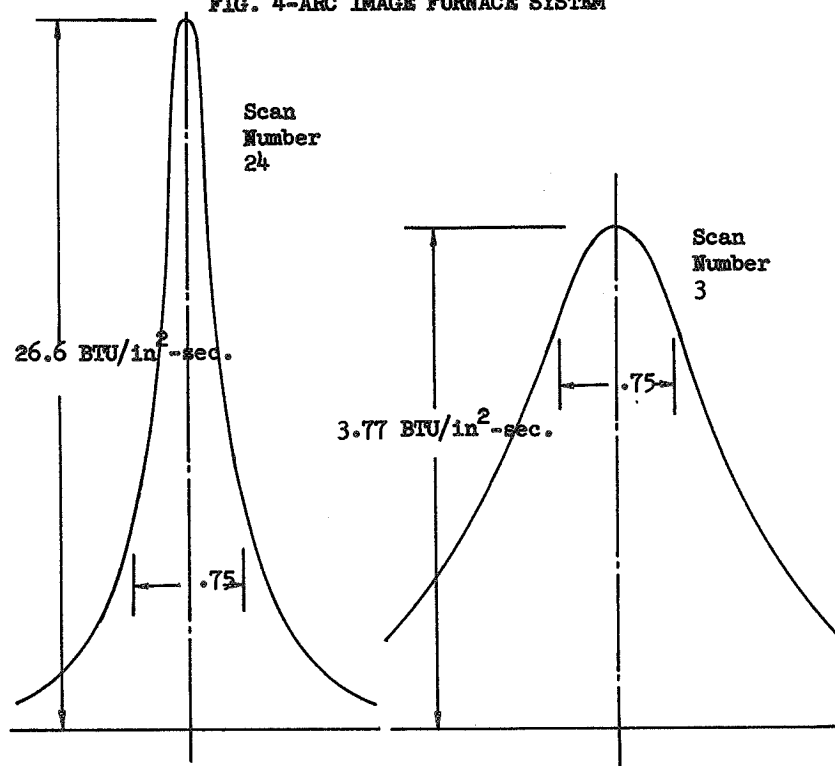


FIG. 5-TYPICAL IRRADIANCE SCANS

TABLE 1
ARC IMAGE FURNACE TEST RESULTS

<u>Scan Number</u>	<u>Target Distance (Z) (Inches)</u>	<u>Focal Length (Inches)</u>	<u>System Power (KW)</u>	<u>PI BTU in²-sec.</u>	<u>NUR</u>
1	5.0	1.40	23.4	1.47	1.35
2			35.5	2.30	1.22
3			53.9	3.77	1.22
4		1.52	23.6	3.33	1.71
5			36.0	5.06	1.60
6			53.9	7.88	1.46
7		1.62	23.8	6.00	2.33
8			35.8	8.97	2.12
9			54.2	13.5	1.76
10	4.0	1.40	23.6	4.83	1.92
11			35.8	7.59	1.78
12			54.2	11.7	1.70
13		1.52	23.4	8.62	3.74
14			35.8	12.7	2.39
15			54.2	18.4	2.12
16		1.62	23.4	9.90	3.58
17			35.8	14.4	3.17
18			54.2	22.7	2.77
19	3.0	1.40	23.4	10.8	3.48
20			35.5	15.5	3.07
21			53.9	21.7	2.74
22		1.52	23.2	13.5	4.87
23			35.5	19.1	4.15
24			53.9	26.6	3.30
25		1.62	23.4	11.2	3.46
26			35.5	14.7	2.85
27			53.9	20.1	2.50
28	2.0	1.40	23.4	10.7	4.04
29			35.5	14.7	3.24
30			53.9	20.1	2.92
31		1.52	23.4	6.50	2.40
32			35.5	9.15	2.09
33			53.9	13.4	1.93
34		1.62	23.4	5.17	2.25
35			35.5	7.01	1.95
36			53.9	9.90	1.81

A typical system power versus peak irradiance curve is shown in Figure 6. This curve represents data taken at a reference plane to target distance (Z) of 3.0 inches and a reference focal adjustment screw length of 1.52 inches, which was found to be the point of maximum peak irradiance. The focal adjustment screw length represents a reference dimension that relates the change of the lamp position within the fixed collector. This reference dimension will be identified throughout the remainder of this paper as the focal length (F.L.).

System voltage versus current is plotted in Figure 7. The spectral energy distribution from the lamp and collector is plotted in Figure 8.

The maximum performance of the arc image furnace provides a peak heat flux at the center of the target of $26.6 \text{ BTU/in}^2\text{-sec.}$ with a non-uniformity ratio of 3.30 over a 0.75 inch diameter target at a lamp power of 50.8 kw as shown in Figure 5, scan number 24. The uniformity of the energy distribution over the 0.75 inch disk target can be improved by defocussing the lamp at a loss of peak irradiance while keeping the input lamp power constant. For example, at 50.8 kw input lamp power, the non-uniformity ratio is improved from 3.30 to 1.76 by defocussing while the peak irradiance at the beam center is decreased from 26.6 to $13.5 \text{ BTU/in}^2\text{-sec.}$ as tabulated in Table 1, scan number 9.

Calibration and Instrumentation

The calorimeters used to measure the high heat flux are Hy-Cal Model C-1312. The calorimeters were initially calibrated by the manufacturer against a gray body to approximately $400 \text{ BTU/ft}^2\text{-sec.}$ ($2.78 \text{ BTU/in}^2\text{-sec.}$) and then linearly extrapolated to 2000 or $4000 \text{ BTU/ft}^2\text{-sec.}$ (13.89 or $27.78 \text{ BTU/in}^2\text{-sec.}$ respectively), depending upon the specific operational range of the calorimeter. The face of the calorimeter was coated with a special coating of known absorptivity. However, after a short period of time exposed to the high irradiance, it was visually evident that the absorptivity of the coating was changing.

It was therefore necessary to re-calibrate the calorimeters at higher irradiance levels. The sensitivity of the calorimeters was then determined with the use of an electron beam heater and the coating removed from the sensor surface leaving the bare material as the exposed surface. This heater is a modified commercial electron beam welder used as the basis of a system which functions as a simulator of total heat flux for development, test and calibration of heat rate instruments used in advanced aerospace programs. (1) This equipment has been used for the above purposes over a range of a few $\text{BTU/ft}^2\text{-sec.}$ to greater than $4500 \text{ BTU/ft}^2\text{-sec.}$ ($31.25 \text{ BTU/in}^2\text{-sec.}$). In the use of the electron beam heater all of the incident energy from the heater is absorbed since it is known that surface characteristics have no effect on the electron beam. Incorporated within the electron beam heater is a slug calorimeter. Attached to this calorimeter

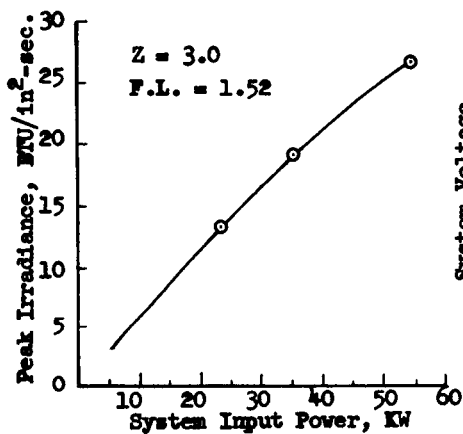


FIG. 6-PEAK IRRADIANCE

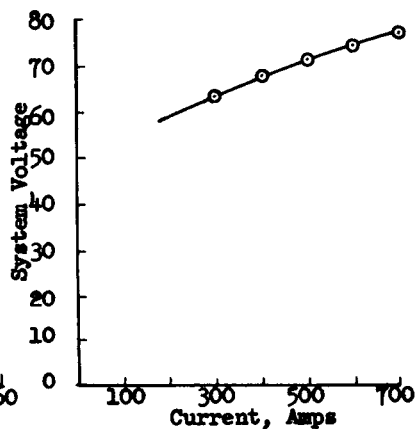


FIG. 7-VOLTAGE CHARACTERISTICS

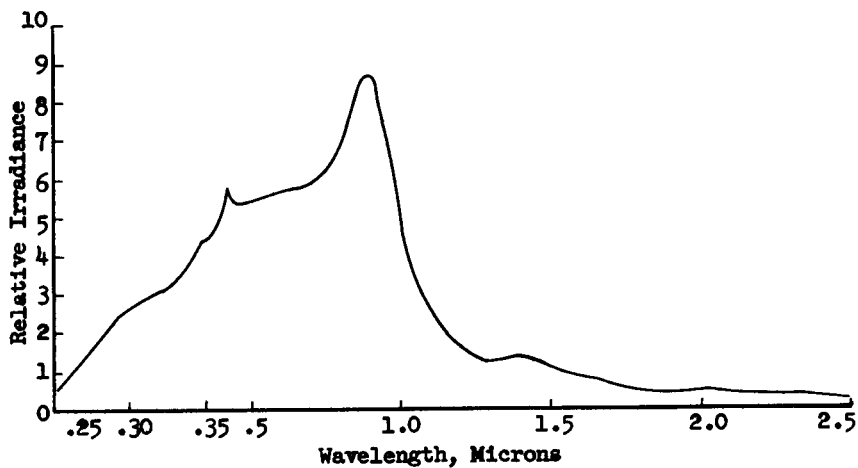


FIG. 8-SPECTRAL ENERGY DISTRIBUTION

is an absolute thermocouple traceable to the NBS. The rate of change in temperature of the slug calorimeter provides an absolute irradiance level. In the calibration procedure the slug calorimeter and the calorimeter to be calibrated are mounted on a rotary mount. The electron beam is started and adjusted at different flux levels and the two calorimeters are alternately intercompared and output readings recorded. This provides an absorbed sensitivity for the calorimeter. Figure 9 is a plot of the sensitivity of calorimeter serial number 36008. It shows the manufacturer's provided sensitivity, the absorbed sensitivity from the electron beam, and the actual arc image furnace irradiance level with an absorptivity of 0.785.

The next step in calibration of the calorimeter was to determine the surface absorptivity as a function of the energy distribution from the arc image furnace. Absorptivity measurements were made by first placing the calorimeter with a clean and bare detection face at the test plane and obtaining an output signal at some fixed irradiance level. Then, utilizing the beam douser without interrupting the beam operation, the calorimeter was coated with a 0.95 absorptivity material and replaced exactly at the same test plane location. The output signal was again obtained. With this data the bare surface absorptivity was calculated. The bare absorptivity is equal to 0.95 times the ratio of the bare signal to the coated signal. For example, the absorptivity was observed to increase after initial exposure from about 0.50 to 0.785 on calorimeter serial number 36008. This was due to oxidation of the sensor surface under the high heat load. After initial exposure and during the scans taken for determining the operating characteristics of the arc image furnace the absorptivity remained constant and was measured to be 0.785 with a maximum deviation of ± 2 percent. This value was confirmed by a post run absorptivity measurement. Figure 10 shows the change in absorptivity with exposure time. Because of this effect on the calorimeter at the high irradiance levels, a pre-test and post-test measurement of the absorptivity was determined each time the calorimeter was used. The calibration results of the calorimeters used are tabulated in Table 2.

Performance Improvement

Analysis of the specimen configuration to be used for tests on the Transpiration Cooling Program indicates that the non-uniformity ratio of 3.3 at 26.6 BTU/in²-sec. from the arc image furnace is unacceptable. A non-uniformity ratio of 1.5 was analytically determined to be the maximum tolerable for the test samples. Seven possible approaches were considered to determine the best method for improvement of the uniformity. They were: 1) refractive wedge blocks near the collector, 2) dispersion lens near the target plane, 3) oscillation of the arc image furnace to obtain a rastered output, 4) new contour collector and improved optical quality of the lamp quartz envelope,

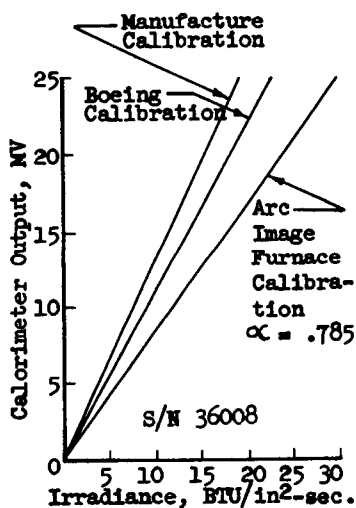


FIG. 9-CALORIMETER
SENSITIVITY

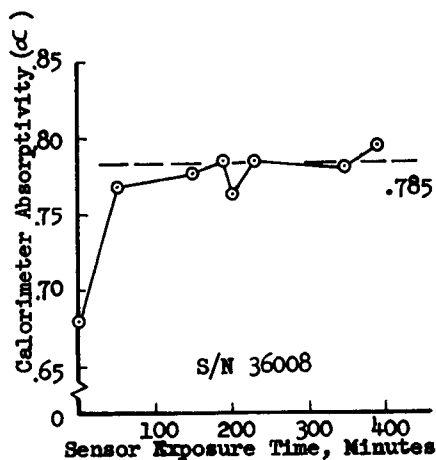


FIG. 10-CALORIMETER
ABSORPTIVITY

TABLE 2
CALORIMETER CALIBRATION

<u>Calorimeter Identification</u>	<u>Sensitivity</u> <u>mv/BTU/in²-sec.</u>	<u>Absorptivity</u>
C-1312-1500 S/N 36008	1.11	0.785
C-1312-2000 S/N 41745	0.649	0.795
C-1312-4000 S/N 38169	0.458	0.803

5) uniformity filter, 6) single bounce pyramidal reflector, and 7) rectangular light pipe. After considerable analysis and discussion, approaches 6) and 7) appeared to hold the best promise as energy condensers from a conservation of energy outlook and for this particular application. It was estimated that as many as five iterative configurations would be required to establish a final configuration. Two configurations from each of the two methods would be constructed and its performance measured. A final configuration would be chosen from the results obtained. Tamarack Scientific Company, the manufacturer of the arc image furnace, would build each energy condenser and Boeing would test it using the arc image furnace. Then the results would be analyzed and discussed between Tamarack and Boeing and the next iterative configuration generated.

The principle of the energy condenser is to accept a maximum amount of energy available at the entrance, reflect it through the condenser with a high efficiency and uniformly redistribute the energy at the exit. This can be accomplished by either one of the two methods chosen. The first method considered is a single reflection of the rays from a highly reflective contoured surface that redirects the energy that would normally fall outside the target area to fill in the edge of the target circle. This concept is referred to as the flux trap. The contour is established by a ray trace process. A model of the arc of the lamp is established and different rays weighted according to the radiance of the arc and collector magnification. Through the ray trace process a contour is established that will reflect the maximum amount of energy that falls outside the target towards the edge of the target. This energy would raise the existing irradiance at the edge of the target without contributing any more to the center of the target. The result would be improved uniformity at high irradiance levels.

The second and final method considered in this study is a multiple reflection of the rays from highly reflective surfaces that produce a mixing effect of the energy at the exit. This concept is referred to as the straight taper light pipe. Determination of the light pipe configuration is based on the desired beam diameter and the subtense angle of the energy from the source. (2) The light pipe theory indicates the more reflections that a light pipe generates before reaching the target plane, the more uniform will be the energy distribution. Further mixing is accomplished by making the cross section of the pipe a polygon. (3) It can be seen that the light rays from a concentric beam which strike the centerline of one of the flat surfaces will be directed toward the center of the target. In a similar manner, the light rays that strike off the centerline will be directed away from the target center.

A total of five energy condensers were built and evaluated on the basis of non-uniformity of irradiance and maximum irradiance. A summary of the description for the five energy condensers is tabulated in Table 3. Photographs of four of the








energy condensers are shown in Figures 11 through 14. The first energy condenser was similar to the fourth except for the entrance diameter. The reflective surface of the condensers consisted of a nickel substrate with vapor deposited aluminum and MgF_2 overcoating.

The equipment used originally to calibrate the arc image furnace was used to evaluate the energy condensers. The primary difference was the placement of the energy condenser entrance at the target plane. This established a new target plane at the exit of the condenser. The calorimeter was aligned with the exit surface of the condenser with approximately 0.025 inches clearance to prevent any damage to the calorimeter detector surface. In order to insure traceability to the original calibration data, repeatability of condenser evaluation and eliminate any possible errors that result from the calorimeter, a scan was made with the energy condenser removed at the end of each condenser evaluation. This information allowed for uniformity and irradiance comparison.

A summary of the energy condenser performance for the five energy condensers is tabulated in Table 4. The arc image furnace was operated at a nominal 19 kw for all conditions of each condenser evaluation. This power level was high enough to maintain a stable arc and yet low enough to not significantly affect the lamp life. Also included in Table 4 is an estimation of the maximum irradiance obtainable while operating the arc image furnace at maximum power. This assumes that the peak performance is linear with system power. This appears to be a good approximation based on the arc image furnace performance data presented earlier in this paper. The energy distribution for the five condensers is shown in Figure 15. The effects of the energy condensers are quite apparent by the redistribution of energy from the arc image furnace.

It is important to note that the energy distribution from the second energy condenser is not typical of this type as illustrated by the fifth energy condenser performance. Analysis of the total energy delivered by the second energy condenser revealed that only 57 percent of the energy that entered the condenser was delivered to the target with an estimated surface reflectance of 0.83. The surface reflectance is calculated by estimating an average number of reflections each light ray will have as it passes through the light pipe. This is accomplished by directing a laser beam at different positions and angles to the condenser entrance and counting the number of reflections the laser beam encounters. The average surface reflectance is then equal to the decimal efficiency raised to the power of the average number of laser beam reflections. An important development resulting from the study of this problem was the improved optical quality and high reflectance surfaces of condensers 3, 4, and 5. This is shown by comparing the efficiency of the third condenser of 80 percent and a surface reflectance of 0.93 to the second condenser of 57 percent and surface reflectance of





TABLE 3
ENERGY CONDENSER DESCRIPTION-SUMMARY


<u>Number</u>	<u>Description</u>	<u>Entrance Diameter (in)</u>	<u>Exit Diameter (in)</u>	<u>Length (in)</u>
1	Flux Trap No. 1	2.75	0.80	1.90
2	Hexagonal Light Pipe No. 1	1.35 	0.80 	2.88
3	Square Light Pipe	1.35 	0.75 	3.45
4	Flux Trap No. 2	3.90	0.87 	2.40
5	Hexagonal Light Pipe No. 2	1.35 	0.75 	4.28

 Across flats


 Across flats of an octagon

TABLE 4
ENERGY CONDENSER PERFORMANCE

<u>Number</u>	<u>Description</u>	<u>Peak  Irradiance BTU in²-sec.</u>	<u>NUR</u>	<u>Peak  Irradiance BTU in²-sec.</u>	<u>NUR</u>
1	Flux Trap No. 1	12.0	4.76	34.2	4.23
2	Hexagonal Light Pipe No. 1	4.05	1.63	11.5	1.45
3	Square Light Pipe	5.66	1.05	16.1	1.01
4	Flux Trap No. 2	20.2	7.80	57.5	5.10
5	Hexagonal Light Pipe No. 2	5.71	1.01	17.3 	1.07 

 Performance at lamp power of 19 kw

 Estimated performance at lamp power of 50 kw

 Actual performance

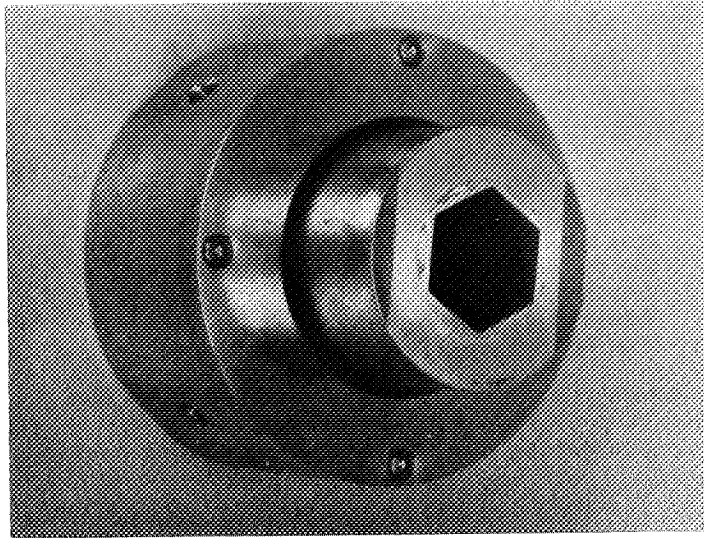


FIG. 11-HEXAGONAL LIGHT PIPE NO. 1

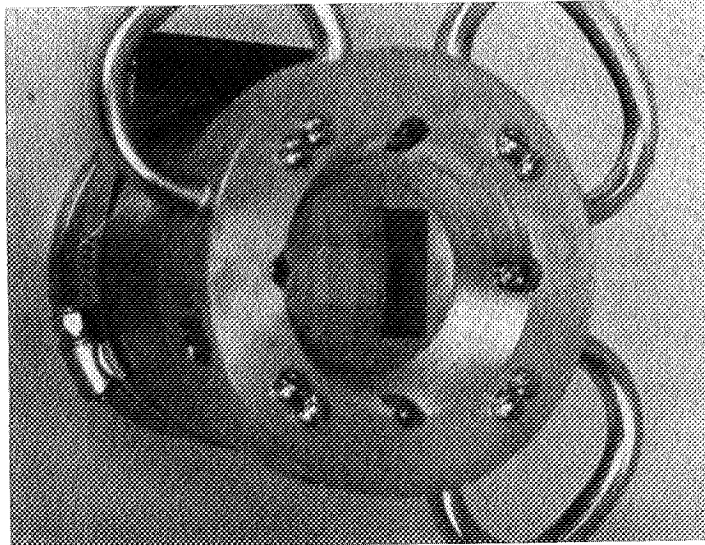


FIG. 12-SQUARE LIGHT PIPE

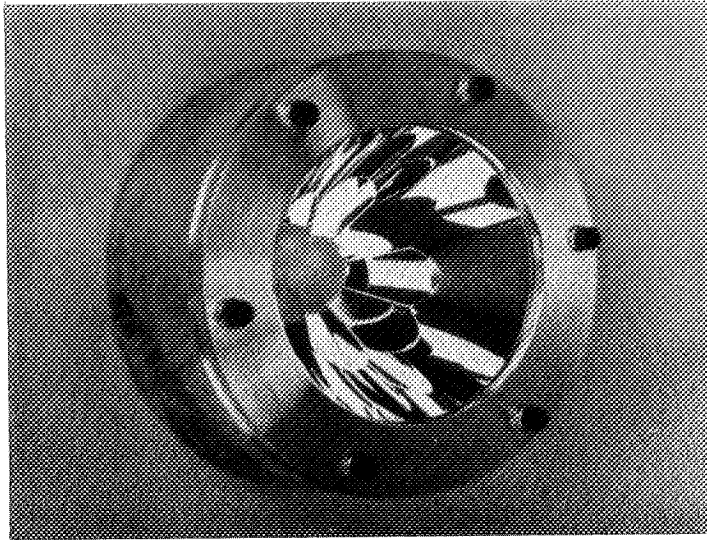


FIG. 13-FLUX TRAP NO. 2

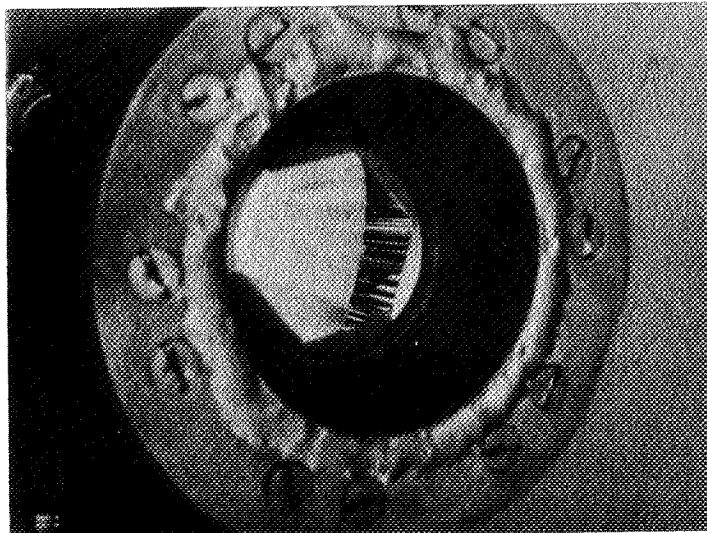


FIG. 14-HEXAGONAL LIGHT PIPE NO. 2

ESTIMATED PERFORMANCE
AT LAMP POWER OF 50 KW

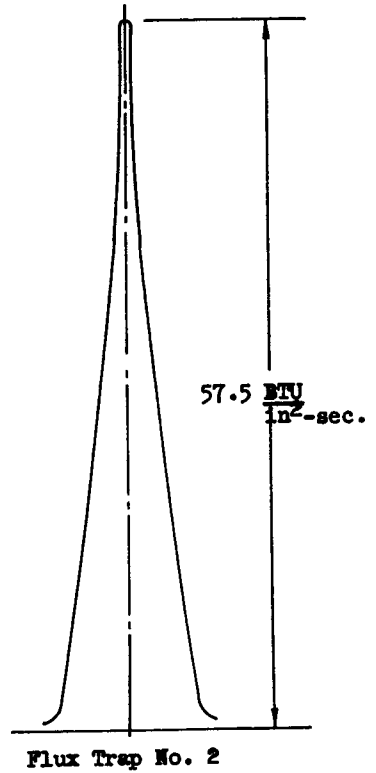
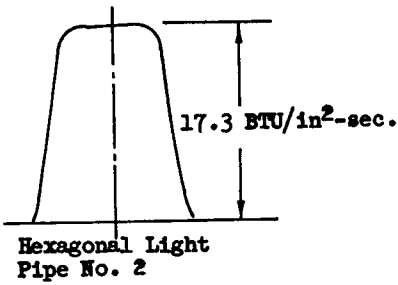
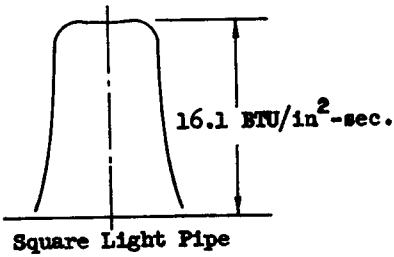
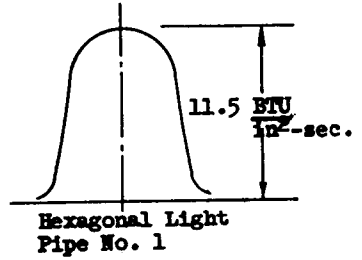
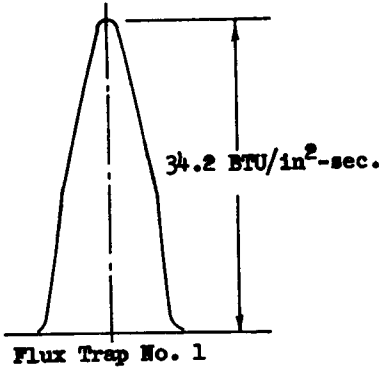


FIG. 15-ENERGY CONDENSER
DISTRIBUTIONS

0.83. This is seen in Figure 16 where the percent of total energy available from the arc image furnace versus beam radius is plotted and compared to energy condensers number 2 and 3. Of the 65 percent of the total energy available 20 percent is absorbed by the reflecting surfaces or 80 percent of the collected energy is measured at the target. This means that only 52 percent of the total energy available from the arc furnace is delivered to the target by the square light pipe. It is concluded that the energy distribution of the fifth condenser was greatly enhanced by the improved surface reflectance.

It seems possible that more energy could be delivered to the target by simply increasing the light pipe entrance dimension. However, the entrance opening is limited for the light pipe configuration by having a fixed exit diameter and convergent angle from the arc image furnace. In fact, if the entrance is enlarged it can be easily demonstrated by ray trace that this additional energy will be reflected back out the entrance.

Evaluation of the first four energy condensers was made in an attempt to choose a final configuration. The original requirements specified an improvement in the non-uniformity ratio with a design goal of 1.5. Therefore, the flux trap configuration (condenser numbers 1 and 4) was eliminated because of the energy distribution as seen in Figure 15. However, it is apparent that the peak irradiance from the flux trap was increased significantly and that a greater percent of the total energy available was delivered to the target.

Based on the performance of the second and third light pipes, the hexagonal light pipe was chosen as the final configuration. It was felt that the same distribution would be provided but that the maximum irradiance would increase due to improved surface reflectance. The low non-uniformity ratio for the square light pipe of 1.05 would provide a lower peak irradiance than the hexagonal light pipe as indicated in Figure 17. Comparison of the energy distribution curves, Figure 15, the percent total energy available versus beam radius, Figure 16, and the percent total energy available versus non-uniformity ratio, Figure 17, indicates that a maximum peak irradiance and specified non-uniformity ratio would be obtained with the hexagonal light pipe.

System Performance with Hexagonal Light Pipe

An evaluation of the final configuration energy condenser was performed to determine the maximum operational characteristics of the arc image furnace with the hexagonal light pipe. Optimum performance was established by varying the lamp power, lamp focal position, and target plane distance. The test setup was similar to all previous discussed systems.

The light pipe configuration is hexagonal in cross section with dimensions of 1.35 inches across the flats and 1.55 inches from point to point at the entrance. The exit dimensions are

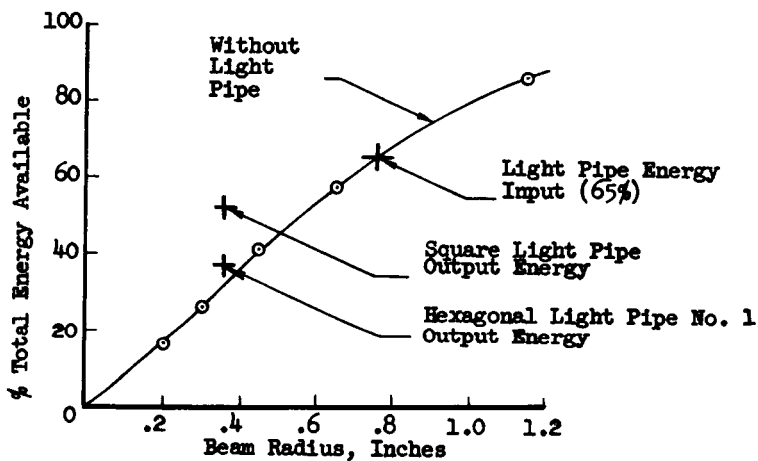


FIG. 16-PERCENT ENERGY AVAILABLE VS. BEAM SIZE

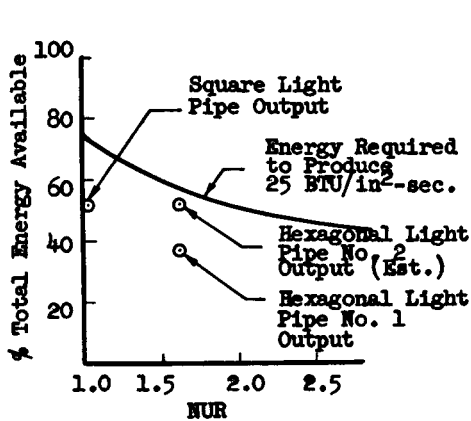


FIG. 17-NON-UNIFORMITY RATIO VS. AVAILABLE ENERGY

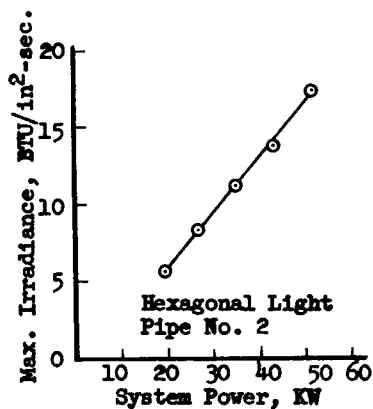


FIG. 18-MAXIMUM IRRADIANCE CAPABILITY

0.75 inches across the flats and 0.86 inches point to point. The overall length is 4.28 inches. The reflecting surface is a nickel substrate with vapor deposited aluminum and MgF_2 overcoating. The light pipe entrance was located at the target plane of the arc image furnace. All scans of the energy distribution were taken across the flats of the light pipe.

The test results of the hexagonal light pipe are tabulated in Table 5. A plot of system power versus maximum irradiance is shown in Figure 18.

The test results from the second hexagonal light pipe revealed an unexpected energy distribution. The energy distribution was identical to that of the square light pipe. Re-evaluation of the ray traces and the data obtained with the laser beam in determining the number of reflections relative to centerline displacement and incident angle revealed that more reflections occurred for the rays that exit the light pipe near the edge. The poor reflectance of the first hexagonal light pipe could then account for the energy drop off at the edge of the exit beam. Improved reflectance of the light pipe merely increased the irradiance level at the edge with only a slight increase in the overall irradiance, as indicated in Table 4.

Conclusion

The maximum irradiance obtainable from the Tamarack Model HTF-50 arc image furnace with the hexagonal light pipe is $17.27 \text{ BTU/in}^2\text{-sec.}$ with a non-uniformity ratio of 1.07. The energy condenser had to be designed to be compatible with the dimensional constraints of the arc image furnace because it was developed first. It is felt that a new system could be designed and fabricated that would be more efficient and deliver a greater percent of the energy on the target from the furnace. This is obvious from Figure 16 because 35 percent of the energy from the arc image furnace is lost at the entrance of the light pipe. For example, only 75 percent of the total energy available is required to produce $25.0 \text{ BTU/in}^2\text{-sec.}$ with a non-uniformity ratio of 1.00 on a 0.75 inch diameter target with an overall light pipe efficiency of 80 percent. It is conceivable that the performance could be further improved by using even higher power lamps such as 70 or 100 kw and designing the system for optimum performance. Important aspects to be considered in the specifications would be irradiance level, non-uniformity ratio, target diameter, and target plane to arc furnace distance.

TABLE 5
FINAL CONFIGURATION-HEXAGONAL LIGHT PIPE
TEST RESULTS

<u>Scan Number</u>	<u>Target Distance (Z Inches)</u>	<u>Focal Length (Inches)</u>	<u>System Power (KW)</u>	<u>PI BTU in²-sec.</u>	<u>NUR</u>
1	3.0	1.52	18.7	5.38	1.09
2	4.0	1.72	18.7	5.71	1.01
3	4.0	1.72	26.6	8.27	1.02
4	4.0	1.72	34.8	11.15	1.04
5	4.0	1.72	42.9	13.76	1.07
6	4.0	1.82	51.1	14.19	1.06
7	4.0	1.62	51.1	16.31	1.10
8	5.0	1.62	51.1	13.27	1.10
9	5.0	1.72	51.1	16.18	1.08
10	5.0	1.82	51.1	15.50	1.05
11	4.0	1.72	51.1	17.27	1.07

Calorimeter S/N 38169

Acknowledgment

The author wishes to express his gratitude to Ron Sheets of Tamarack Scientific Company, Anthony Fortini and Donald Buchele of NASA-Lewis Research Center for their technical support in making this development successful.

References

1. Electron Beam Simulation of Aerospace Vehicles Heating Rates, W. W. Woods, and D. L. Martin, Electron and Laser Beams Symposium, April 1, 1965.
2. Cone Channel Condenser Optics, Don E. Williamson, Journal of the Optical Society of America, Volume 42, Number 10, October, 1952.
3. The Use of a Kaleidoscope to Obtain Uniform Flux Over a Large Area in a Solar or Arc Imaging Furnace, M. M. Chen, J. B. Berkowitz-Mattuck, and P. E. Glaser, Applied Optics, Volume 2, Number 3, March, 1963.

DESIGN AND PERFORMANCE OF THE RASTA HIGH POWER LASER

George W. Sutton and Arne C. J. Mattsson, *Avco Everett Research
Laboratory*

ABSTRACT

The RASTA (Radiation Augmented Special Test Apparatus) laser, the first to exceed 100 kW, was designed to supply radiation energy to determine material effects in a high flux environment. This paper describes the design concept and initial testing. Basically it is a CO₂ gas dynamic laser, which uses the combustion of cyanogen and oxygen at 15-20 atm., diluted with nitrogen cyanogen, to form the lasing media. Population inversion is achieved with quick-freeze (0.7 mm throat) nozzles and expansion to Mach 4, reducing the temperature to about 300°K. The cavity is 80 cm wide, 20 cm high, and about 20 cm in the flow direction, and operates at about 0.1 atm. static pressure. A split supersonic diffuser is used to recover the pressure to exhaust directly to the atmosphere. Although this laser was later operated both as a MOPA and single mode, for the purposes of providing a heating source, multimode operation was selected.

EXPERIMENTS WITH THE SKYLAB FIRE DETECTORS IN ZERO GRAVITY*

R. M. F. Linford, *McDonnell Douglas Corporation, St. Louis, Missouri 63166*

ABSTRACT

The Skylab Fire Detector is the first known device for alerting the crewmen of a manned space vehicle to the presence of an on-board fire. The detector is extremely sensitive to the low-level ultraviolet radiation emitted by burning materials. To evaluate the sensitivity of the detection system, it was necessary to record the detector output while viewing typical spacecraft materials burning in the appropriate environment. The zero-gravity environment of space flight eliminates the convection associated with an earthbound fire, and therefore, it was essential that the experiments be conducted under weightless conditions.

To conduct the test, small samples of spacecraft materials were ignited in a 5 psi oxygen-rich atmosphere inside a combustion chamber. The chamber free-floated in the cabin of a C-135 aircraft, as the aircraft executed a Keplerian parabola. Up to 10 seconds of zero-gravity combustion were achieved. The Skylab fire-detector tubes viewed the flames from a simulated distance of 3m, and color movies were taken to record the nature of the fire.

The experiments established the unique form of zero-gravity fires for a wide range of materials. From the tube-output data, the alarm threshold and detector time constant were verified for the Skylab Fire Detection System.

INTRODUCTION

An ultraviolet detector has been selected as the basic sensor for the NASA Skylab Fire Detection System. The detector package has been developed by McDonnell Douglas Corporation and Honeywell, Inc. around a detector tube manufactured by the latter company.

This device is extremely sensitive, responding to picowatts (10^{-12}W) of radiation in the 185 to 270 nm wavelength band. With such a sensitive detector, extensive investigation and exacting design has been necessary to exclude all possible sources of false alarms.¹ From the results of the analyses, the alarm-threshold has been set to preclude such false alarms, due either to weak ultraviolet sources in the Skylab or the proton fluxes encountered in near-earth orbit. The alarm threshold, as dictated by the false alarm studies, determines the sensitivity of the fire sensor, or, more importantly, the size to which a flame must grow before it is detected.

*This paper reports work performed under NASA Contract NAS9-6555.

A prediction of the detection capability from the known spectral calibration curve of the detector-tube is rendered impossible by a complete lack of spectral radiance data of fires at applicable wavelengths. Further, any such data obtained in the laboratory under normal gravitational conditions would inadequately represent a fire burning in the low-pressure, oxygen-rich, zero-gravity environment of the Skylab. Convection currents are established around earth-bound fires maintaining supplies of fresh oxygen to the flames but in the weightless condition there will be no such convection. As the fire burns a cloud of undisturbed combustion products will surround the flame and may lead to eventual extinction. In addition to their self-extinguishing action, these particulate and gaseous combustion products will be in the optical viewing path of the detectors. Small particles will scatter the short wavelength ultraviolet radiation, and some radiation may be absorbed by the gases produced. Both mechanisms will reduce the output of the fire-detector tube.

Knowledge of the size of fire that would trigger the Skylab Emergency Alarm was important in determining crew procedures in the event of such an alarm. An incipient fire might be extinguished while a larger fire might necessitate an immediate evacuation of the vehicle. Therefore, to evaluate the capabilities of the Skylab detector, a series of experiments was conducted in an aircraft flying zero-gravity parabolas in an attempt to simulate the type of fire a detector must sense. In this paper we shall describe these experiments and briefly summarize some of the results which demonstrated the performance of the device, and confirmed that the threshold and time-constant settings had been optimized.

FIRE SENSOR

The basic element of the sensor used in the Skylab fire-detection system is an ultraviolet-sensitive tube manufactured by the Research Division of Honeywell, Inc., Minneapolis. This tube has been incorporated into the Skylab sensor through the cooperative efforts of McDonnell Douglas Corporation and the Honeywell Aerospace Division, also in Minneapolis. A diagram of the tube is shown in Figure 1. The principle of operation is similar to that of a Geiger-Mueller counter: Photo-electrons, liberated from the cathode by incoming ultraviolet radiation, initiate an avalanche ionization of the gas in the tube, the driving capacitor discharges and a voltage pulse is generated at the output. As the pulse-rate is roughly proportional to the intensity of the incident ultraviolet radiation this rate is used to indicate the presence of a fire.

The spectral sensitivity of the detector is shown in Figure 2. Short-wavelength response is limited by atmospheric absorption of radiation, and the work function of the photocathode material sets the upper limit. With the cathode used in the Skylab sensor the tube is insensitive to all radiation at wavelengths longer than 270 nm. Thus, the tube is "blind" to most sources of background ultraviolet radiation such as the spacecraft lighting and the filtered solar energy penetrating the spacecraft windows. As the curve in Figure 2 indicates, the device will generate approximately 60 counts per second in response to 1 pW cm^{-2} of radiation.

Extensive investigation of the Spacecraft environment, to determine the risk of false-alarms, resulted in the selection of a 35-count-per-second alarm-threshold. Thus, a fire which results in approximately 1 pW cm^{-2} of radiation (in the 185 to

270 nm wavelength band) at the fire detector, will initiate an alarm in the Skylab Caution and Warning System.

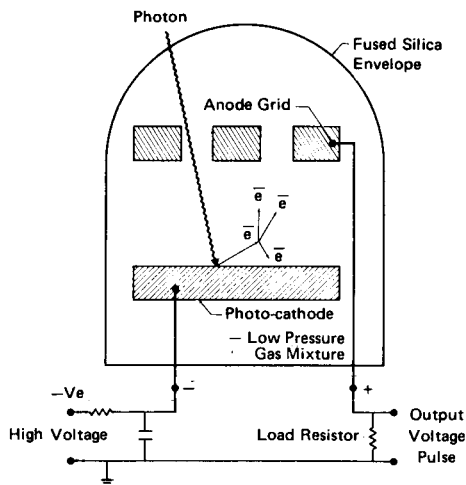


FIGURE 1 BASIC OPERATION OF THE HONEYWELL ULTRAVIOLET FIRE-DETECTOR TUBE

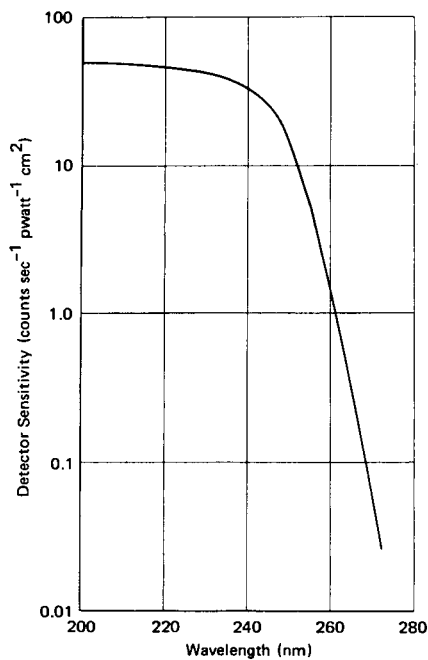


FIGURE 2 SPECTRAL CALIBRATION OF TYPICAL HONEYWELL ULTRAVIOLET FIRE-DETECTOR TUBE

ZERO-GRAVITY SIMULATION

The USAF zero-gravity aircraft was selected as providing the longest and best-controlled period of weightlessness. The aircraft, a C-135, flies the trajectory illustrated in Figure 3. During an ideal maneuver, up to 30 seconds of zero-gravity is available, but, in reality, the limitations of the weather and pilot skill reduce this period to as little as 20 seconds, and minor perturbations from zero-gravity often will occur during that period. To eliminate some of the effects of these small g-forces, the combustion chamber was released to free-float in the cabin, until it collided with the walls, floor or ceiling, or until the 2 g's occurred at the pull-out of the maneuver.

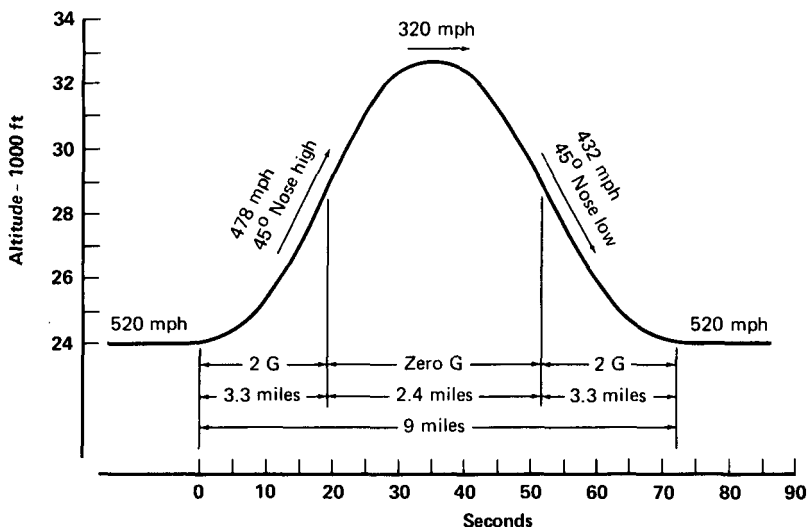


FIGURE 3 TRAJECTORY OF C-135 DURING ZERO-GRAVITY MANEUVER

The average combustion period lasted 10 seconds, the rest of the time being used for getting into position, the decision-time on the potential for free-floating, and the delay before ignition of the sample. However, this was adequate time for the fire-detection experiment in which the first 5 seconds after ignition were of particular interest.

A photograph of a chamber during such a free-float is included as Figure 4.

EXPERIMENTAL TECHNIQUE

The equipment was designed so that a small fire could be ignited in a 5 psi atmosphere under zero-gravity conditions and be monitored both by the fire detectors and a movie camera.

Eight zero-g combustion chambers were available at MSC-Houston² and these were modified to provide an optical viewing window, detector optics and a camera mount. An over-all picture of the chamber is shown in Figure 5. Both the detector

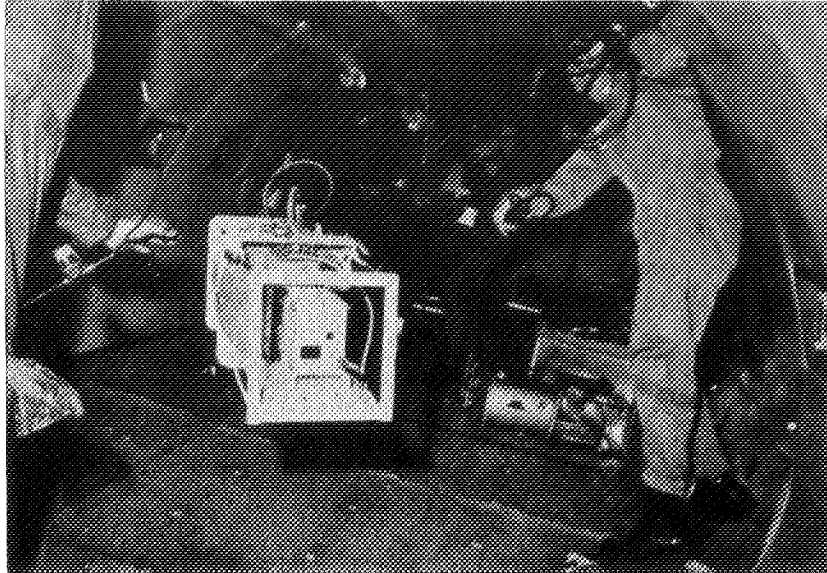
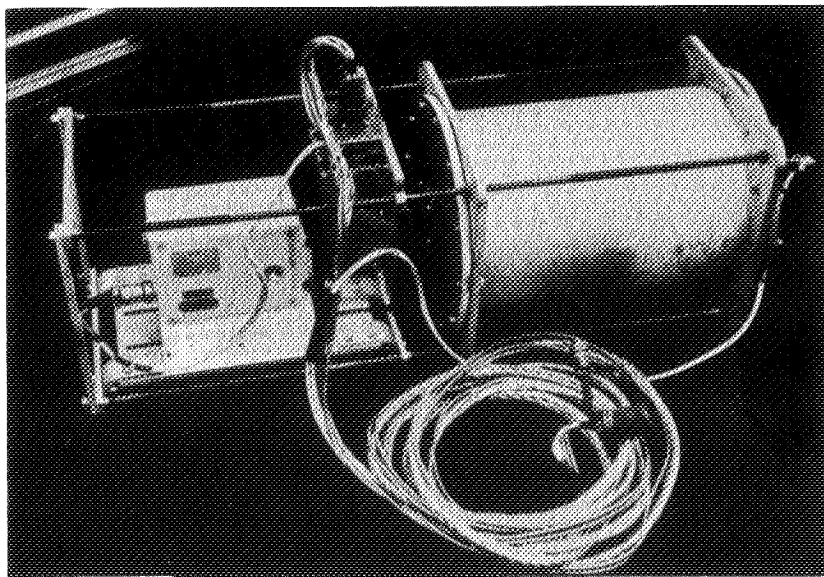


FIGURE 4 FREE-FLOAT EXPERIMENT



**FIGURE 5 ASSEMBLED COMBUSTION CHAMBER, DETECTOR MOUNT
MOVIE CAMERA AND UMBILICAL CORD**

and the camera were mounted so they could be easily removed for transfer between chambers after each zero-g burn. All of the controls were mounted on an instrument package bolted to the aircraft and connected to the chamber by a 20-foot "umbilical cord". Ground support equipment was also assembled for reduction of the data between flights.

Combustion Chambers

The aluminum combustion chambers were of 25 cm internal diameter, and 37.5 cm long, with a volume of approximately 15 liters. One of the end-plates was fitted with a 7 cm diameter, 6 mm-thick Suprasil 2* window through which the ultraviolet radiation was monitored. The other end-plate supported the sample holder and ignition coil. A 6-inch length of 18-gage nichrome wire provided both support for the sample and the source of ignition. Large samples were slipped inside the turns of the coil, and small samples were mounted on a third wire support in contact with the igniter.

Prior to each flight the eight chambers were loaded with a sample, evacuated and backfilled to 5 psi with premixed 75% N₂/25% O₂ gas.

Ignition of Samples

As the aircraft entered the zero-gravity phase of the maneuver, and the chamber floated up from the floor, a judgment was made as to the stability of the free-float and the decision was taken whether or not to ignite the sample. Approximately 30 amps was passed through the igniter coil from the aircraft 28 volt d.c. supply, until the detector output, as monitored on an oscilloscope, indicated ignition of the sample. The current was then switched off to prevent failure of the coil and the resultant perturbation of the environment of the flame. All the samples used in these experiments ignited within 3 seconds of the closure of the igniter switch.

To ensure that the igniter coil could not excite the fire-detector tubes, several tests were run in which the coil alone was heated until it burned out. Only in those instances in which an arc was drawn by the failing wire, did the detectors respond. However, in most of the flight experiments the igniter coil was not burned out and therefore could not have affected the data in any way. In the few cases in which the wire did separate, the data was rejected.

Detector-Tube Optics

When installed in the Skylab, the fire sensors must detect flames at distances up to, and sometimes in excess of 3 meters (10 feet). All specifications and previous experiments utilized this distance as a standard, and ideally the detector would have been placed 3 m from the fire in these studies. Because of the need to free-float the apparatus a 3 m fire-to-detector separation was impractical and had to be simulated optically. A diagram of the optical arrangement is shown in Figure 6 and a photograph of the detector mount is included in Figure 7.

*Trademark of Amersil, Inc. for their synthetic fused silica.

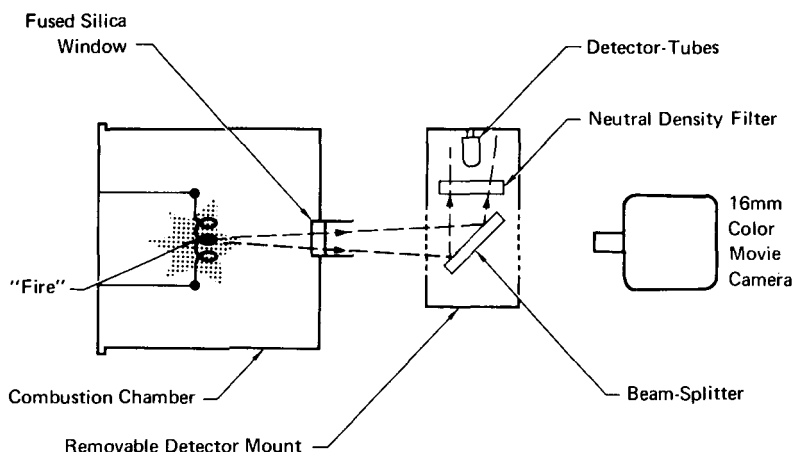
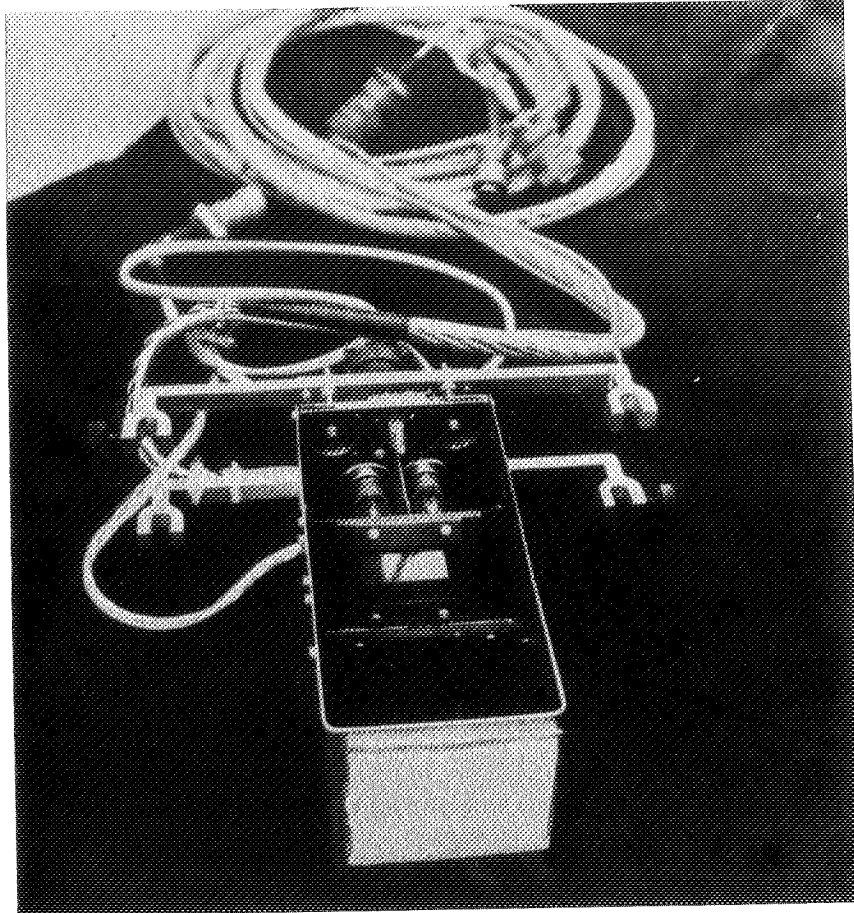


FIGURE 6 OPTICAL TRANSFER SYSTEM

Radiation emitted by the flame, emerging through the fused silica window was incident upon the beamsplitter. This component was designed to reflect 10% of the ultraviolet radiation. A thin aluminum film was deposited on a soda-lime glass substrate and, as this glass is opaque at the wavelengths of interest (185-270 nm), it acted as a front-surface reflector only. Ninety percent of the visible radiation was transmitted and was recorded on the color-film in the 16 mm movie camera. The reflected ultraviolet radiation was then further attenuated by the neutral density filter which had a density of 1.0, i.e., a transmittance of approximately 10%. Each of the three optical elements was measured and their properties are summarized in Figure 8. The net transmission of the system was close to 1% throughout the bandwidth of the detectors. As the actual separation between the detector and the fire was about 30 cm the effective range was ten times this, or 3 m, on the basis of the inverse-square law. An experimental check of this distance simulation showed that the arrangement was equivalent to a separation of about 2.9 m.

Two detectors were used in the experiments to provide reliability in the event of breakage and also to determine the performance of tubes of different sensitivity. As calibrated by Honeywell, their response to the "standard flame"* at 3 m was 62 counts/second and 85 counts/second. A low range tube will register a minimum of 50 counts/second. A high range tube will register a maximum of 100 counts/second; thus, the tubes used in the experiments were representative of those to be used in the Skylab. They were installed side-by-side, symmetrically about the axis of the optical system, but carefully shielded from each other to eliminate "cross-talk" and errors due to reflections from neighboring surfaces. A cylindrical shield was installed around the window to prevent the detectors' viewing the flames by reflection from the inner wall of the chamber.

*The standard flame is a methane diffusion flame with an ionization current of $50\mu\text{A}$.



**FIGURE 7 DETECTOR MOUNT SHOWING DETECTORS,
TEST LAMP AND OPTICAL COMPONENTS**

Each combustion chamber was equipped with a permanently installed silica window, but all the other optical components were mounted in the detachable detector mount, which was moved to the next chamber after each test run. This optical assembly was shock-mounted to protect the fragile glass components.

Detector and Data Recording Circuits

All the electrical and data recording circuits were controlled from an instrument package bolted to the deck of the aircraft (Figure 9). Twenty feet of umbilical cord provided a nonrestricting link between the controls and the chamber.

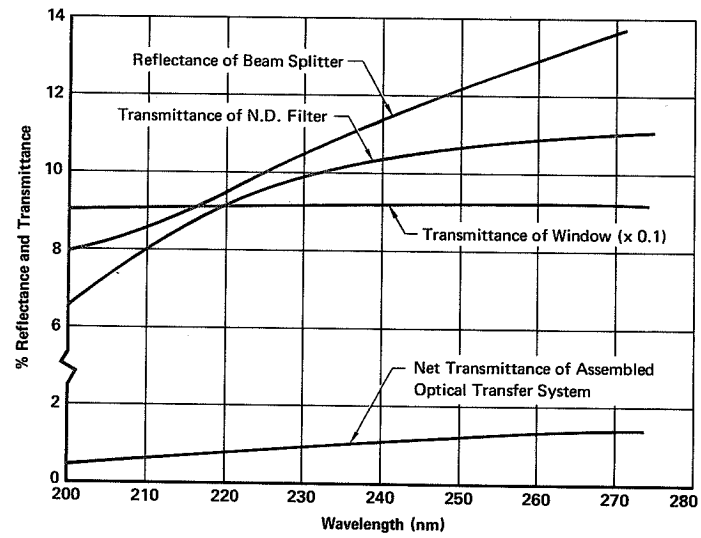


FIGURE 8 REFLECTANCE AND TRANSMITTANCE OF OPTICAL TRANSFER SYSTEM COMPONENTS

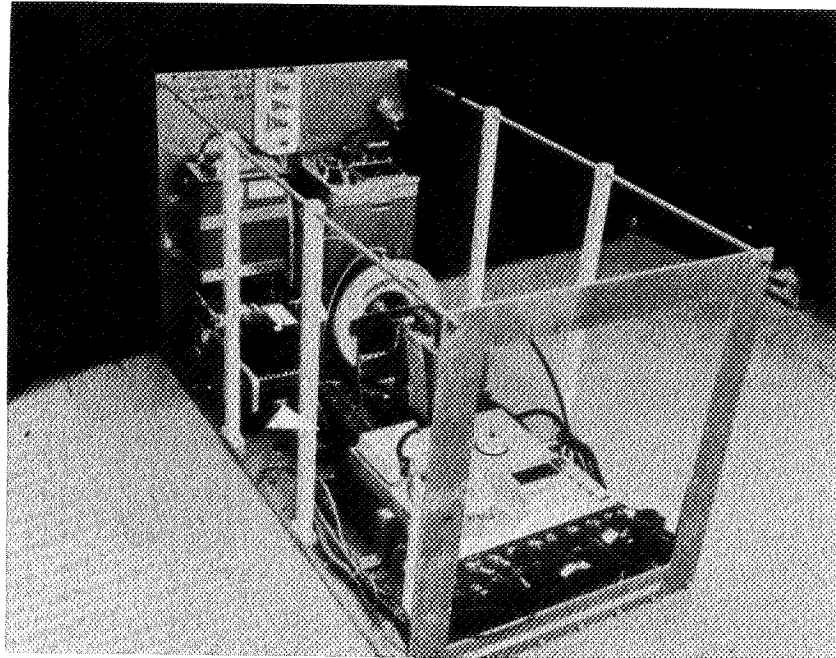


FIGURE 9 INSTRUMENT PACKAGE AND CONTROLS

Each of the detector-tubes was connected to an independent power supply which was carefully shielded to prevent electrical interference between the two circuits. The electrical circuits are illustrated in Figure 10. Data was recorded on an FM tape recorder and was monitored on an oscilloscope and frequency counter. One track on the tape was used to maintain a verbal record of the experiment. The operator of the experiment maintained a running commentary on the salient features of each float, including details of collisions with the interior of the aircraft.

A pulse generator was included to provide a series of 0.1 second timing pulses to the timing lights in the movie camera. This timer was switched on as the igniter switch was closed, and the pulses were recorded on the film throughout the duration of the burn.

For in-flight testing of the system, a small Honeywell neon source-tube was installed in the detector mount. This source could be activated by a switch on the instrument control package and provided a means of checking the operation of the complete detector control and recording systems.

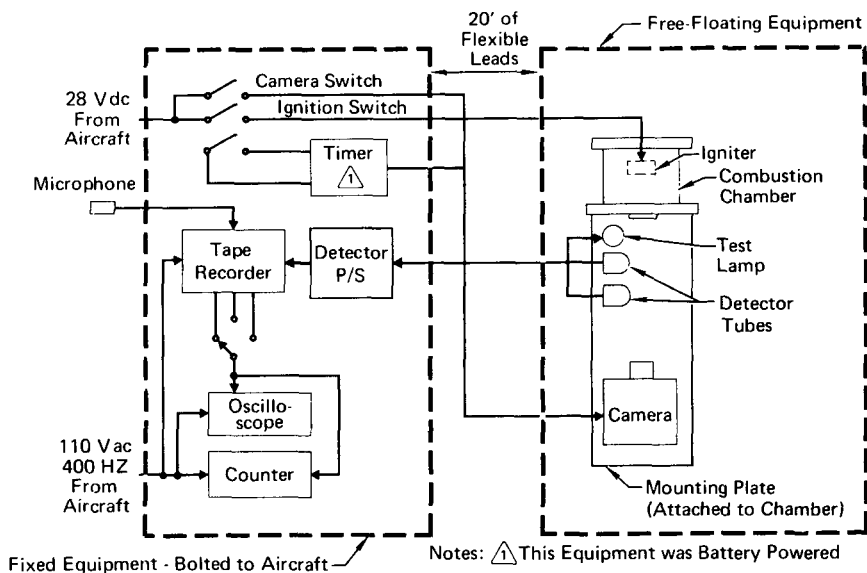


FIGURE 10 ELECTRICAL CIRCUITS

Photographic Recording

A Milliken DBM 4C 16 mm movie camera installed on the chamber frame was used to photograph the burning samples. Pictures were taken at 24 frames/second on Kodak Ektachrome EF Type 7241 daylight film. The lens of the camera was approximately 35 cm from the flame.

Data Reduction

After each flight the data tapes were reduced to a form in which they could be analyzed. Ground-support equipment assembled for this purpose included a frequency counter and a digital recorder with a monitoring oscilloscope. The tapes were played back into the counter, which was set to gate for 0.1 seconds, 4 times per second. To ensure that data were not lost in the dead-time of the counter-printer combination, this play-back procedure was repeated five times. The counter was started at a different point in the tape each time and the average of the five readings for each period was calculated.

MATERIALS TESTED

Selection of the materials to be burned was made on the basis of flammability and the quantity of the materials used in the Skylab, and with the advice of fire-protection personnel at NASA and McDonnell Douglas Corporation. The materials are listed in Table I. Sample configurations were determined by the form of the available material, and the combustion time and intensity of trial burns during laboratory tests. Sufficient material was required to maintain combustion through the 10 to 15 seconds of the zero-gravity expected but not much beyond the return to normal gravity. Ground-based experiments were run with each of the materials and, following these tests, the sample sizes listed in Table I were selected.

TABLE I SAMPLE CONFIGURATIONS

Material	Use	Sample Dimensions
Constant Wear Garment Cloth	Astronaut Underwear	- 5 x 1 cm - loosely rolled
Teleprinter Paper		- 20 x 1 cm - loosely rolled
Mosite Sponge (1062)	Insulation for Coolant Lines	- 4 x 0.5 x 0.5 cm
Coolanol-soaked Mosite Sponge	Heat-transfer Fluid	- 4 x 0.5 x 0.5 cm
Polyurethane Foam	OWS Insulation	- 1 x 1 x 1 cm
Photographic Film (Estar Base)		- 10 cm x 16 mm - loosely rolled
Epoxy Potting Compound (Stycast 1090)	OWS Electrical Wiring	- 0.5 x 0.5 x 0.5 cm
Silicone Potting Compound (EC1663)	AM Electrical Wiring	- 1 x 1 x 0.5 cm
Epoxy-Polyurethane (EMS 369)	AM Water Bottles	- 0.5 x 0.5 x 0.5 cm
Silicone Rubber (RTV 90)	Adhesive	- 1 x 1 x 1 cm
PBI Cloth	Sleeping Bags	- 10 x 1 cm - loosely Rolled
Durette Cloth	Sleeping Bags	- 10 x 1 cm - loosely rolled

SUMMARY OF EXPERIMENTS

The statistics of the experiment are given in Table II. A large number of parabolas were flown to achieve stable conditions for 22 free-floats. This number of burns was dictated by the need to get at least one good set of data for each material. Although some of the free-floats were marred by collisions with the walls of the vehicle, sufficient data was obtained within the first few seconds after ignition to demonstrate the capabilities of the detector tubes.

TABLE II STATISTICS OF THE ZERO-GRAVITY EXPERIMENTS

• 8 Combustion Chambers	• 22 Successful Burns	• 146 Parabolas
• 3 Flights	• 12 Materials	• 2 Detectors

RESULTS OF THE EXPERIMENTS

It would be inappropriate to discuss all the results of the experiments in this paper but data from two successful burns is included to demonstrate the nature of the results. Figures 11 and 13 show two series of photographs from individual frames of the movie film. These indicate the unique nature of zero-g combustion, the spherical flame growth and the starvation of the fire by the combustion gases. The self-extinguishing phenomenon is emphasized by the detector output curves (Figures 12 and 14) generated by the fires shown in Figures 11 and 13. Compared with the one-gravity fires the zero-g flames diminish quickly after the initial flare-up and might have extinguished completely if the free-floats had not been perturbed. The curves also show that the fire detector would have detected the ignition of the fires within a second or two from a distance of 3 m. A complete analysis of all this experimental data has shown that all the materials studied will emit sufficient ultraviolet radiation when ignited such that this will be readily detected from across the spacecraft. Alarm-threshold and time-constant settings for the Skylab Fire Sensors were thus confirmed and calibrated units are now being installed in the flight vehicles.

ACKNOWLEDGEMENTS

An experiment of this kind required the assistance of divers personnel. The author was fortunate to have the skilled assistance of his colleagues: Robert Kohl and John Sneed during the preparations for the flight, Robert Renfro during the zero-gravity flights, and John Jachmann with the data reduction. Both Dayton Walker and Dr. Robert Johnson of Honeywell, Inc. are gratefully recognized for their advice and the loan of equipment for the test. Don Griggs and Captain Jim Lackey of the "Zero-G Crew" at Wright-Patterson AFB deserve mention for their tolerance of amateur free-floaters. Finally, Howard Kimzey of the NASA Manned Spacecraft Center and Bob Cretcher of Wright-Patterson AFB were extremely helpful in providing the combustion chambers which were modified for this experiment.

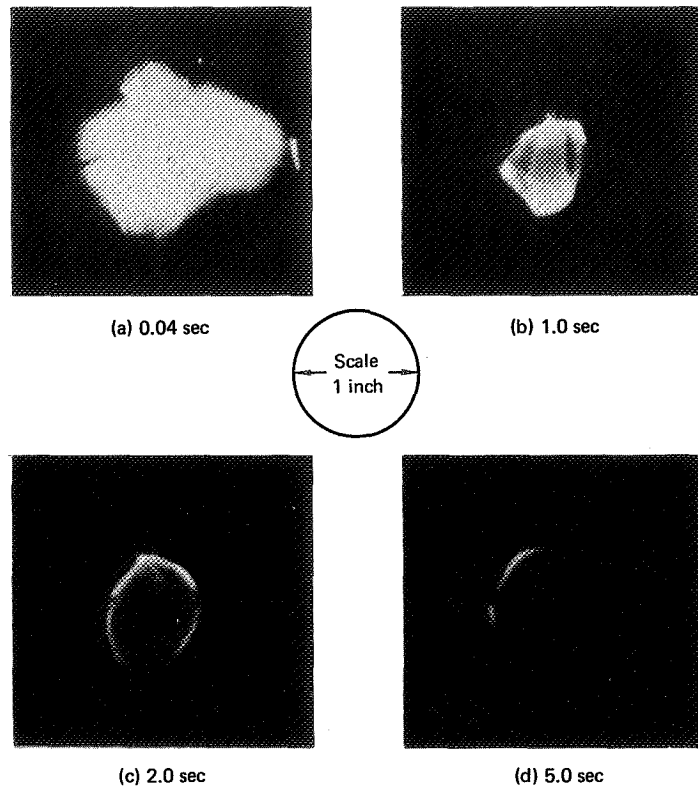


FIGURE 11 COMBUSTION OF PHOTOGRAPHIC FILM IN ZERO-G-FREE FLOAT I

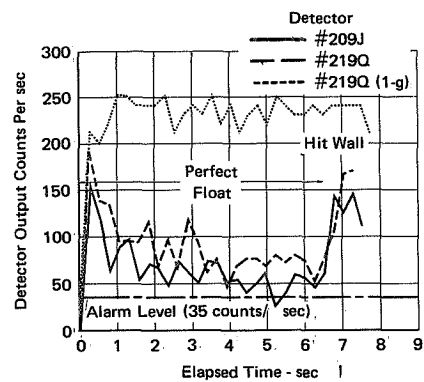


FIGURE 12 DETECTOR OUTPUTS DURING ZERO GRAVITY COMBUSTION OF PHOTOGRAPHIC FILM

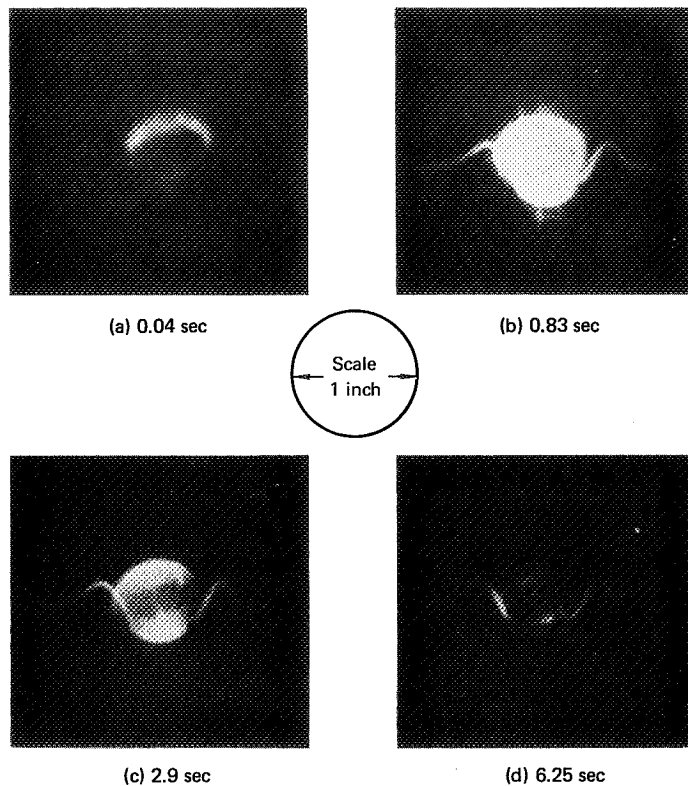


FIGURE 13 COMBUSTION OF CONSTANT-WEAR GARMENT CLOTH IN ZERO-G

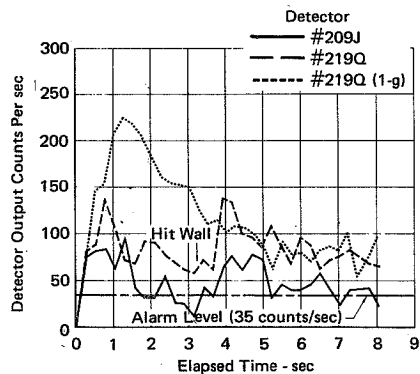


FIGURE 14 DETECTOR OUTPUTS DURING ZERO GRAVITY COMBUSTION OF CONSTANT WEAR GARMENT CLOTH

REFERENCES

1. R. M. F. Linford, "Application of an Ultraviolet-Sensitive Fire Detector in a Manned Space Vehicle", a paper presented to the Fall Meeting of the Optical Society of America, Ottawa, October 1971.
2. Chambers previously used, as reported by J. H. Kimzey et al in "Flammability in the Zero-Gravity Environment", NASA TR R-246, October 1966.

TRAINING AND CERTIFICATION PROGRAM OF THE OPERATING STAFF FOR A 90-DAY TEST OF A REGENERATIVE LIFE SUPPORT SYSTEM

W. P. Waters, McDonnell Douglas Astronautics Co., Huntington Beach, California

ABSTRACT

Prior to beginning a 90-day test of a regenerative life support system, a need was identified for a training and certification program to qualify an operating staff for conducting the test. The staff was responsible for operating and maintaining the test facility, monitoring and ensuring crew safety, and implementing procedures to ensure effective mission performance with good data collection and analysis. The training program was designed to ensure that each operating staff member was capable of performing his assigned function and was sufficiently cross-trained to serve at certain other positions on a contingency basis. Complicating the training program were budget and schedule limitations, the high level of sophistication of test systems, and the fact that the individuals preparing for the test were required to take time from their duties to spend in the classroom. These complications tended to present a dilemma of having either a well-trained crew or holding to the test schedule.

INTRODUCTION

The operational 90-day manned test of a regenerative life support system was conducted to provide data on crewmen and equipment performance in a closed ecology approximating that of an orbiting spacecraft.¹ The test began on June 13, 1970, when four crewmen entered the McDonnell Douglas Astronautics Company (MDAC) Space Station Simulator (SSS), and was successfully completed 90 days later.

As indicated in Reference 1, the 90-day test was preceded by tests of complete, manned life support systems conducted by MDAC for a period of 60 days, by the National Aeronautics and Space Administration (NASA) for 28 days, and by other tests of short duration. A team of representatives from Governmental agencies, industrial organizations, and universities was formed for planning and participating in the program. Government agency representatives were drawn from five NASA Centers; the Navy, Army, and Air Force; the Atomic Energy Commission; the Department of Transportation; and the committees of the National Academy of Science. They were joined by representatives of more than 30 industrial contributors and 7 universities. Close coordination among these representatives enhanced the exchange of valuable scientific and technical data. The SSS and its facilities and support systems are described elsewhere.²

Successful Major Milestones

At the moment the simulator hatch closed for the start of the test, the following major milestones were successfully realized.

Internal Crew Selection—From an original pool of approximately 50 graduate students, a primary 4-man crew and backup 3-man crew were selected based upon the results of questionnaires, personal interviews, medical examinations, and psychological evaluations.³

System and Subsystem Readiness and Checkout—A representative, but not exhaustive, list of systems and subsystems installed and functionally evaluated prior to test start included (1) the life support system,⁴ (2) oxygen recovery subsystem,⁵ (3) waste management subsystem,⁶ (4) water management subsystem,⁷ and (5) trace contaminant analysis.⁸

Development of Normal, Contingency, and Emergency Procedures—These procedures and their integration with the personnel protective system are discussed in Reference 9.

Selection, Training, and Certification of the Operating Staff—These aspects are discussed herein.

OPERATING STAFF

The operating staff consisted of four teams of five men each which were responsible for operating and maintaining the test facility, monitoring and ensuring crew safety, and implementing procedures to ensure effective mission performance with good data collection and analyses. The staff of 20 men comprised four rotating shifts of 5 men per shift to provide continual coverage during the test. Four of the five positions for each shift were filled by MDAC employees, while the fifth position was held by a contract physician who acted as medical monitor.

Staff Positions and Duties

The staff positions and staff member duties are described in the following paragraphs.

Test Conductor—The test conductor was responsible for the operation of the SSS and the overall function of the operating staff. He was required to man the test conductor's console which controlled the normal and emergency operational functions of the SSS. He was required to man his station at all times, except for short periods of time when he was relieved by the engineering monitor.

Communications Monitor—The communications monitor, who reported to the test conductor, manned a communications console continually throughout the test, except for short periods of time when he was relieved by the engineering monitor. He was responsible for the audio-visual operations of the communications console and for all SSS crew communications. His responsibility also encompassed day-to-day monitoring of behavioral aspects of the test.

Engineering Monitor—The engineering monitor, who also reported to the test conductor, was responsible for the operation of all SSS controls, monitoring of the life support system, and the acquisition of all pertinent engineering data. In addition to these duties, he was trained and certified to act as a temporary operator at the test conductor and communications monitor consoles.

Technician—A mechanical or electrical technician supported the operating staff members and provided maintenance of the test facility and supporting equipment. The technician reported to the engineering monitor.

Medical Monitor—The medical monitor was a qualified physician licensed to practice medicine in California and was responsible for monitoring the health of the SSS crew.

OPERATING STAFF TRAINING PROGRAM

The objective of the training program was to produce four qualified and certifiable teams with one individual trained as backup for each position. In addition, varying degrees of cross-training among staff members was required. For certain general operations, the test conductor, the communications monitor, and the engineering monitor had to be capable of interchanging positions with no loss of effectiveness. The engineering monitor also was required to substitute for either the test conductor or the communications monitor when they left their stations.

Complicating the training program was the high level of sophistication of the test systems and subsystems, and the fact that the individuals designing, evaluating, and installing them also were required to participate in the training program. Further, their participation was dual. For some portions of the program, a given individual may have been the instructor while for others he was the student. These complications tended to present the dilemma of having either a well-trained operating staff or holding to the test schedule. It was clear that a disproportionate amount of classroom time would inhibit realization of other test objectives.

Tending to resolve this dilemma, however, was the fact that a considerable pool of experienced personnel was available from which to select operating staff members. Many individuals had participated in previous extended manned tests in the SSS. Thus, a significant contribution to the production of a certifiable operating staff was achieved through management personnel coordination in identifying knowledgeable individuals. The goal of the selection process was to minimize training requirements and to produce autonomous operating staffs. Especially important to the training program was the test management's insight in cutting across various scientific and intracompany disciplines in its selection process.

Staff roles and requirements were analyzed early in the selection process. Five men were then selected for each of the staff positions. (Medical monitors were supplied from a contract pool of licensed physicians and did not participate in the training and certification program.) The communications monitors were given screening tests identical to those used for initial onboard crew screening since their task was central to all inside-outside communications and, thus, necessitated a compatible individual for the role. Attempts were made to match characteristics of the communications monitors with those of the onboard crew to minimize personality-biased incidents of intercrew hostility.

The test conductors and engineering monitors were selected by the test program manager on the basis of experience, system knowledge, and specialty area. Shift assignments were made to equalize distribution of areas of specialty across every shift.

The electrical or mechanical technicians were selected on the basis of their familiarity with the facility and previous experience in manned simulator tests.

With selection of the proposed staff members complete, specialists in the appropriate disciplines were assigned to develop curricula, lectures, and tests and to direct practice sessions until appropriate proficiency levels were realized.

There were varying degrees of cross-training required among the staff members so that the test conductor, the communications monitor, and the engineering monitor would be adequately trained to interchange positions with equal effectiveness. Emergency training required cross-training to assure high reliability in the execution of various modes of test operations.

Training Courses

There were nine specific training courses developed. Each course consisted of classroom sessions and practical, on-the-job instruction. The courses, their duration, and the required operating staff attendance are indicated in Table 1. A synopsis of each of the courses is given in the following paragraphs.

Table 1—Operating Staff Training Plan

Course	Operating Staff Position				Course Duration*
	Test Conductor	Com Monitor	Engr Monitor	Tech	
SSS Familiarization	X	X	X	X	4(1)
Communications Control Console	X	X	X		8(7)
Life Support Monitor Console	X		X		8(4)
Gas Analysis Console	X		X		12(8)
Test Conductor's Console (Chamber Operations)	X		X		8(8)
Lock Control Console (Lock Operations)	X		X	X	2(1)
Data Systems Operations	X	X	X		12(8)
Maintenance Procedures	X		X	X	8(6)
Operating Procedures	X	X	X	X	12(8)

**The numerals in parentheses represent the number of hours of practical instruction per course.*

Space Station Simulation Familiarization—This course provided familiarization with test objectives and conditions, operating staff functions in the various operating modes, and overall facility and support equipment orientation. It is beyond the scope of this paper to discuss the complexity and sophistication of the test which is discussed more fully in Reference 1. However, some inferences may be drawn by referring to Figures 1 through 9, which represent handouts presented, and some of the materials discussed, during the familiarization course.

Communications Control Console Operation—This course provided familiarization with the closed circuit TV system, the audio-video tape, and special effects systems. It provided an opportunity for each potential staff member to operate the console under the supervision of the instructor.

Life Support Monitor Console Operation—This course defined the console's monitoring capabilities while emphasizing critical parameters, limits, and special operating procedures.

Gas Analysis Console Operation—This course enabled potential staff members to operate and calibrate the gas analysis console and to gain experience in its operation.

Test Conductor's Console Operation—This course provided class and practical instruction in vacuum and pneumatic systems operation, and normal and emergency abort functions.

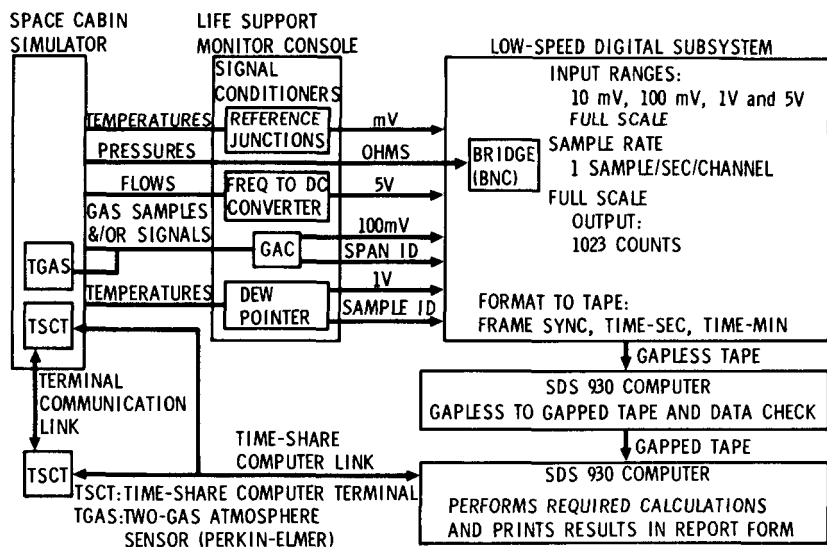
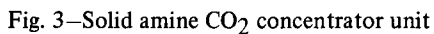
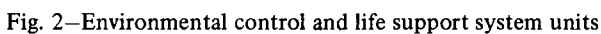


Fig. 1—Life support instrumentation data management subsystem



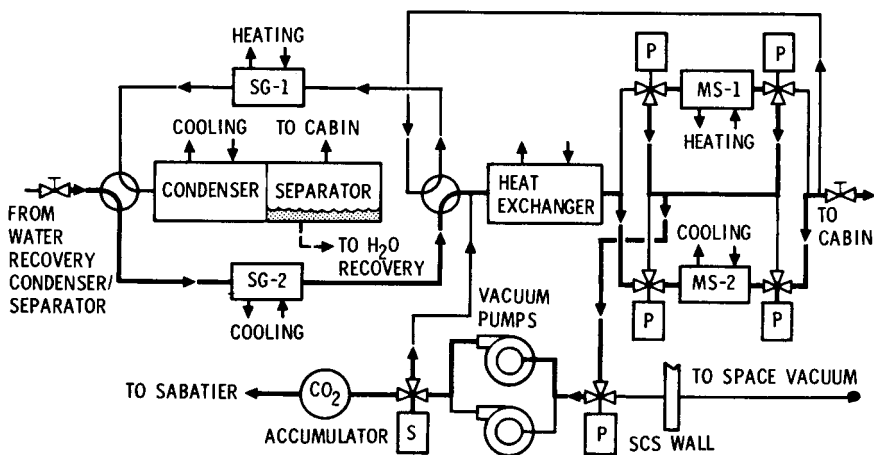


Fig. 4—CO₂ concentrator subsystem

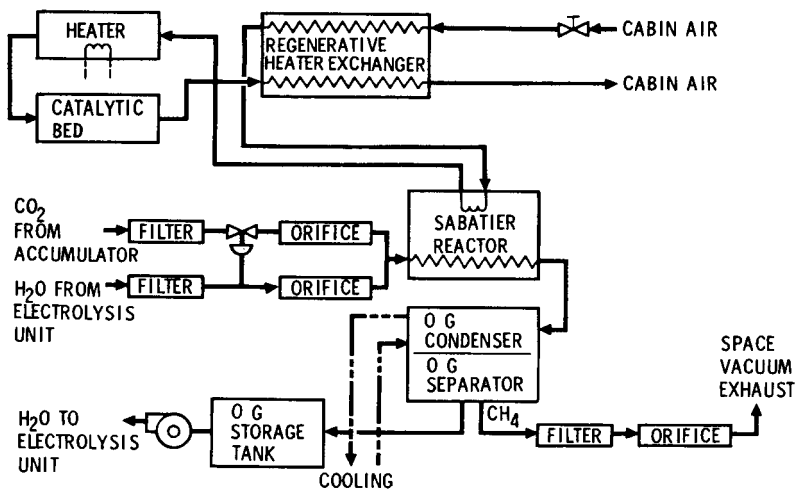


Fig. 5—Integrated sabatier and toxin control

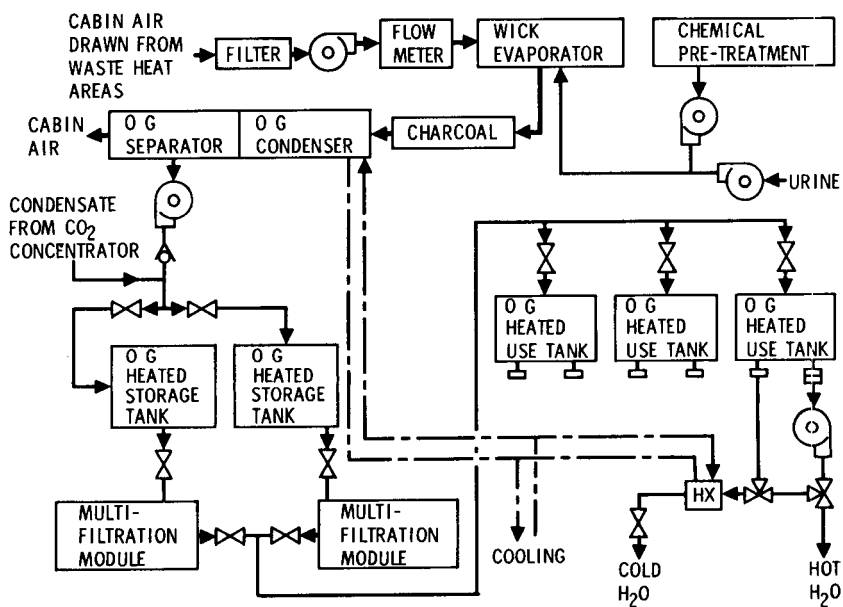


Fig. 6—Potable water recovery and humidity control unit

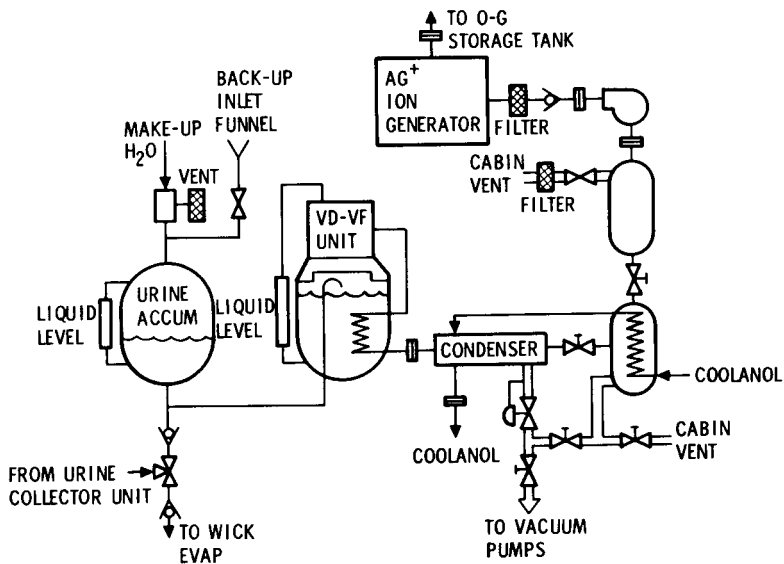


Fig. 7—Vacuum distillation—vapor filtration (VD-VF) water recovery unit

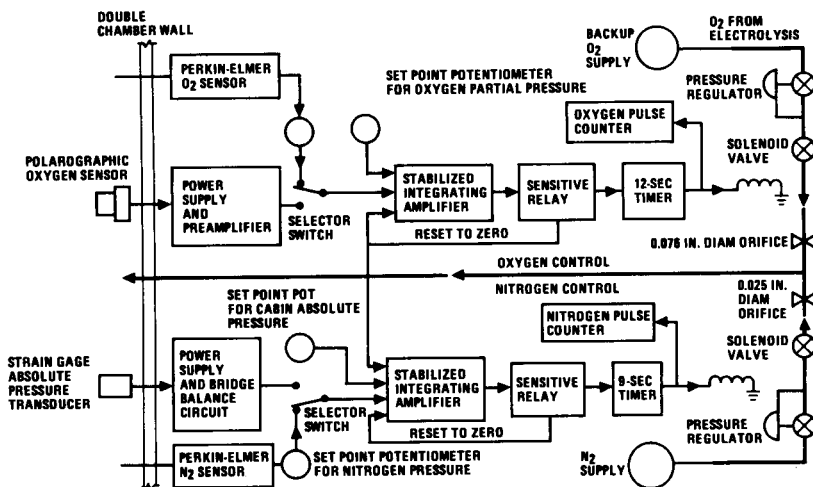


Fig. 8—Atmosphere supply control subsystem

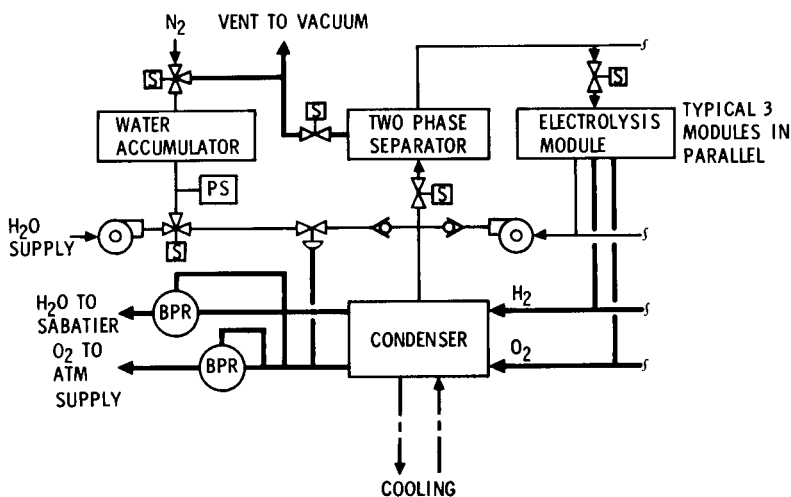


Fig. 9—Electrolysis unit

Lock Control Console Operation—This course familiarized potential staff members with lock operations for introducing and removing the crew from the SSS while maintaining it at reduced pressure.

Data Systems Operation—This course provided familiarization with acoustical data link, analog measurement system, physiological data system, low speed data system, data logger, and strip chart recorder. Each potential staff member was required to operate and troubleshoot the data system.

Maintenance Procedures—This course was oriented toward the daily, routine maintenance tasks required in support of long-term facility operation.

Operating Procedures—This course instructed the potential operating staff members in the procedure appropriate for each of three operating modes and each individual's responsibility in program protocol. It was intended that each member be exposed to the procedures to such an extent that he was able to act instinctively, but rationally.

CERTIFICATION

Upon successful completion of the training program, a dry-run was conducted in which the members of the operating staff demonstrated proficiency during simulated normal, contingency, and emergency operations. Satisfaction of test management resulted in the formal certification of each staff member for a particular staff position. The formal record maintained for each certified staff member is shown in Figure 10.

DISCUSSION

The operating staff training and certification program was considered adequate. The practical or on-the-job portions appeared to be more valuable than the class room sessions. This may have been because the on-the-job portions were conducted when all systems were completely or nearly completely finalized, while the classroom portions occurred much earlier in the program. Handout material, prepared by each instructor for his particular course, proved of great value. This material was used not only as a training aid, but, after assembly into appropriate notebook form, as a reference manual for use throughout the test.

Significantly aiding the training and certification program was the test management's early and continuing interest in it. In addition, an Operational Readiness Inspection Committee (ORIC), constituted according to NASA guidelines, had been formed during the planning stages of the test. Timely review of the proposed training program by ORIC, its recommendations for training program improvement, and its continued interest throughout the conduct of the program resulted in a well-trained and certified operating staff.

REFERENCES

1. J. K. Jackson. *A 90-Day Operational Test of an Advanced Life Support System*. McDonnell Douglas Paper WD 1580. Presented to Aerospace Medical Association Annual Meeting, Houston, Texas, April 26-29, 1971.
2. R. L. Malin. *Facilities and Support Systems for a 90-Day Test of a Regenerative Life Support System*. McDonnell Douglas Paper WD 1535, November, 1971.

SSS FACILITIES OPERATION TRAINING AND CERTIFICATION RECORD

Name: _____ Loc/Dept: _____ Emp No.: _____

I (we) attest that the individual named above has successfully satisfied the criteria established for the following course(s):

Course	Instructor	Date
SSS Familiarization	_____	_____
Comm Control Console	_____	_____
LSM Console	_____	_____
Gas Analysis Console	_____	_____
Test Conductor Console	_____	_____
Lock Control Console	_____	_____
Data System Operations	_____	_____
Maintenance Procedures	_____	_____
Operating Procedures	_____	_____

In view of the above, I hereby recommend certification of this individual for the following operating staff position(s).

_____	_____
Date	Training Coordinator

I hereby certify this individual is qualified to perform the function of the aforementioned position(s).

_____	_____
Date	Branch Chief, Space Simulation Lab

Endorsed by: _____
Training Director
Space Station Simulator Program

Program Manager
Space Station Simulator
Program

Chief Engineer
Advance Biotechnology
& Power Sys

Medical Director
Space Sta Sim
Program

Fig. 10—Space Station Simulator facilities operation training and certification record

3. Test Report, *Test Results, Operational Ninety-Day Manned Test of a Regenerative Life Support System*. NASA CR 111881, May 1971.
4. M. S. Bonura and L. G. Barr. *Life Support System Operational and Maintenance Data for the 90-Day Space Station Simulator Test*. McDonnell Douglas Paper WD 1581. Presented to SAE-ASME-AIAA Intersociety EC/LS Conference, San Francisco, California, July 12-14, 1971.
5. E. S. Mills, T. J. Linzey, and J. F. Harkee. *Oxygen Recovery for the 90-Day Space Station Simulator Test*. McDonnell Douglas Paper WD 1596. Presented to SAE-ASME-AIAA Intersociety EC/LS Conference, San Francisco, California, July 12-14, 1971.
6. R. E. Shook and G. W. Wells. *Waste Management for the 90-Day Space Station Simulator Test*. McDonnell Douglas Paper WD 1608. Presented to SAE-ASME-AIAA Intersociety EC/LS Conference, San Francisco, California, July 12-14, 1971.
7. D. F. Putnam, E. C. Thomas, and G. V. Colombo. *Water Management Results for the 90-Day Space Station Simulator Test*. McDonnell Douglas Paper WD 1582. Presented to SAE-ASME-AIAA Intersociety EC/LS Conference, San Francisco, California, July 12-14, 1971.
8. P. P. Mader, A. S. Lucero, and E. P. Honorof. *Analysis of Trace Contaminants*. McDonnell Douglas Paper WD 1595. Presented to SAE-ASME-AIAA Intersociety EC/LS Conference, San Francisco, California, July 12-14, 1971.
9. J. P. Valinsky. *Safety Aspects of a 90-Day Manned Test of a Regenerative Life Support System*. McDonnell Douglas Paper WD 1748, November 1971.

FACILITIES AND SUPPORT SYSTEMS FOR A 90-DAY TEST OF A REGENERATIVE LIFE SUPPORT SYSTEM

Robert L. Malin, *McDonnell Douglas Astronautics Co., Huntington Beach, California*

ABSTRACT

Rigid reliability and safety requirements were imposed on the facilities and support systems to assure successful completion of a manned 90-day test of a regenerative life support system.

INTRODUCTION

A 90-day test of a regenerative life support system was recently completed by McDonnell Douglas Astronautics Company (MDAC) in a Space Station Simulator (SSS). The long duration of the test and the fact that it was manned, combined to impose rigid reliability and safety requirements on the facility systems as well as the regenerative life support systems. Consequently, where adequate reliability could not be built into essential facility systems, either backup systems or components were provided.

The SSS had been used for similar tests of 60 and 28 days, and other shorter tests. However, these earlier tests were conducted in a facility essentially dedicated to the single aspect of conducting a manned test within the SSS. For the 90-day test, the SSS was relocated from the MDAC Santa Monica location to Huntington Beach, and integrated into the existing Space Simulation Laboratory facilities.

Consequently, in addition to the normal personnel protection systems¹ present for crew safety and the training of the operating crew² required for the safe and efficient conduct of any manned test, additional problems were encountered in integrating the test and facility. These problems were basically ones of creating a continuing awareness among all the personnel in the building that all activities had to be planned and executed in regard to their possible impact on the 90-day test.

Awareness was intensified by (1) placing signs on every piece of equipment whose operation could directly or indirectly affect the 90-day test, (2) painting switches on all breaker panels a bright contrasting color when they serviced the facility directly or indirectly, (3) restricting access to the test control area to the maximum extent possible, and (4) holding frequent meetings with personnel in the building other than those directly in support of the test to inform them of these warnings and their significance.

The procedures proved to be effective and during the 90-day test, no ongoing operation of the Space Simulation Laboratory occurred which could have compromised the 90-day test objectives in any way.

Basic facility improvements from previous test runs included a substantially upgraded communications system, the addition of an autoclave sterilization system, new cold traps for backing the waste management system, and an upgraded

vacuum capability. Because of a life support unit in the chamber utilizing radioactive isotopes, access to the test area was restricted. This restricted access requirement was new to the facility but proved to be beneficial in promoting an essential test procedure of having the test conductor aware at all times of the personnel within the test area and of their functions.

FACILITY ORIENTATION

The SSS is a chamber 40 feet long by 12 feet in diameter, double-walled, and covered with thermal insulation. Its double wall construction permits a pressure to be maintained in the annulus which is lower than that in the test volume even though it is maintained at an equivalent altitude of 10,000 feet. This setup permitted the more realistic situation of having the leakage outboard. The SSS is shown in Figure 1.

The SSS contains an airlock and two pass-through ports which allow for the ingress and egress of personnel and equipment while the chamber is maintained at altitude. The interior configuration of the SSS has been described in other papers³ dealing with the aspects of the test and will not be discussed herein.

The primary facility controls were centered in the test conductor's console (Figure 2) and were under the direct control and observation of the test conductor. Secondary control of each facility item was located at its site. The test control area layout is shown in Figure 3.

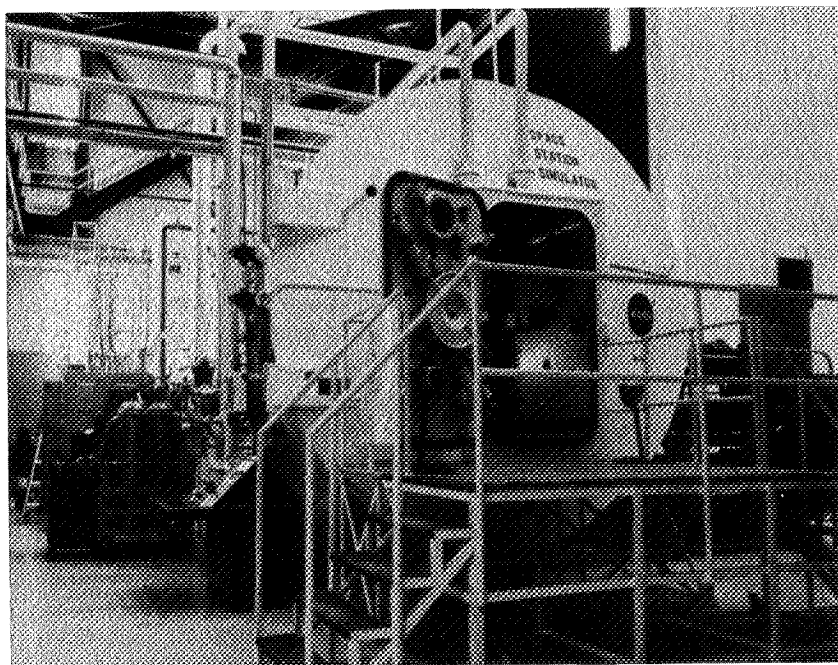


Fig. 1—Space Station Simulator

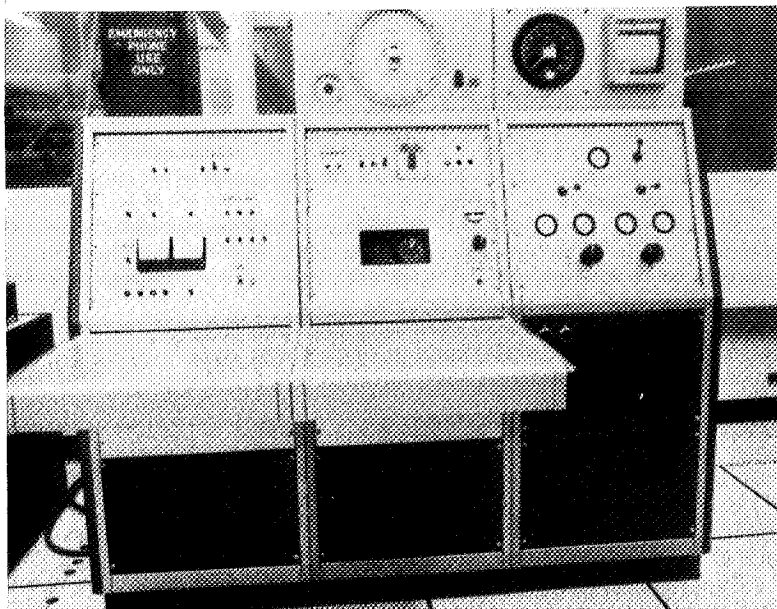


Fig. 2—Test conductor's console

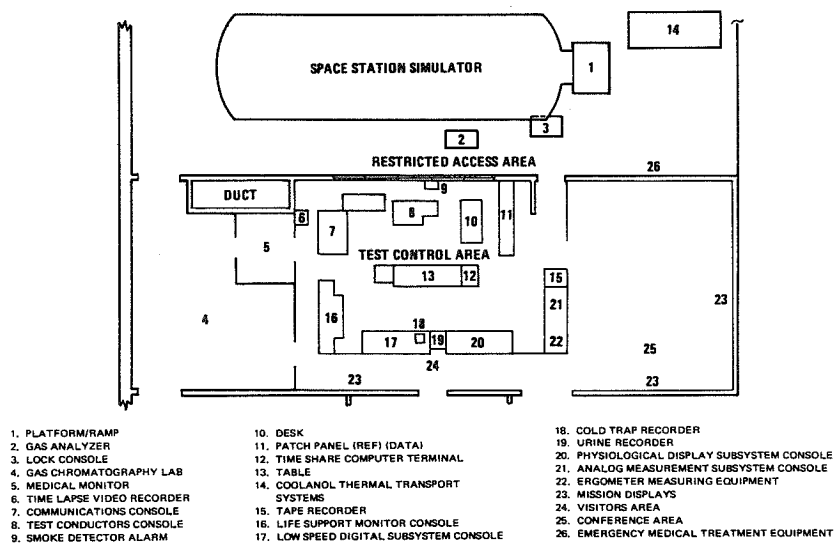


Fig. 3—Space Station Simulator test control area

ELECTRICAL POWER SUPPLY AND DISTRIBUTION SYSTEM

Electrical power supplied to the SSS consisted of 400-cycle, 120/208-volt, three-phase; 60-cycle, 115-volt, single phase; and 28 vdc.

The 400-cycle power was supplied by two motor-generator units, one serving as a backup for the other. In case of a failure of the primary unit, the switchover to and startup of the backup unit was to be accomplished manually. The five minutes it would take to accomplish the switchover were easily allowable, thus, an automatic system was not required.

During the course of the test, the primary unit wore out several drive belts necessitating switchover to the backup unit. However, these switchovers, due to the maintenance inspection procedures, were anticipated and accomplished without significant interruptions in the power supply.

The 28-vdc supply was provided by a 300-ampere capacity rectifier with a 200-ampere capacity rectifier as a backup. These power supplies were powered by the building's 440 vac system, a failure of which would prevent any 28 vdc being supplied to the SSS. Since 28 vdc was critical for the continued operation of essential facility functions, a third backup was provided in the form of wet cell batteries. The batteries provided sufficient power to continue operation for approximately 10 hours.

Failure of either of the rectifiers automatically put the batteries on line, and restoration of supply by either rectifier automatically put the batteries back in a trickle charge mode which maintained them at full capacity.

The 115-vac was supplied through normal facility circuits. The primary problem to be solved was to properly size fuses to prevent circuit overloads which could act as ignition sources and yet permit operation without numerous blown fuses.

Several power failures occurred during the test resulting in interruptions of 3 to 8 seconds in length. These power failures occurred outside the building and were not associated with the testing activities. During the interruptions, the batteries provided essential power which prevented possible premature test terminations.

In addition, 440-vac was used, but only for support equipment exterior to the SSS. This power was used for various pumps and chillers and was not provided with a backup system.

VACUUM SYSTEM

The vacuum system was composed of a primary system and two auxiliary systems. The primary system was used to establish the initial vacuum level in the SSS and to maintain the desired pressure level, and for elevator operations in the airlock. Auxiliary vacuum systems were used for (1) operation of the pass-through ports and (2) a utility vacuum system servicing various onboard life support units.

Primary Vacuum System

The primary vacuum system was pumped by two Stokes 300 CFM Microvac pumps and Roots blowers and a Gast 39 CFM roughing pump. The Gast pump ran continuously to maintain the chamber at the desired pressure level. The two Stokes pumps were used for all other primary operations and also ran continuously during the test. All pumps ran continuously to provide a means of evacuating the SSS quickly to extinguish a fire and for performance of emergency

lock operations if necessary. Since the pumps required nearly 1/2 hour to start, it was better to run them continuously rather than to risk getting them started quickly in case of an emergency.

The primary vacuum system was controlled by manual and electro-pneumatic gate valves. The electro-pneumatic valves were operated by switches in the test conductor's console. Lights installed next to each switch indicated whether the valves were opened or closed.

Fisher pneumatic valves were used to control cabin and annulus evacuation rates. The cabin vacuum control valve was operated manually by a hand loader. Two ΔP control valves were operated manually in unison by the hand loader, or automatically by a ΔP controller. The large ΔP control valve was used for coarse adjustments and the small ΔP control valve was used to maintain the set differential pressure. The ΔP valves controlled the amount of ambient air bleeding into the annulus vent line. The Gast pump then pumped the ambient bleed plus the cabin leakage to achieve the desired annulus pressure level. The ΔP controller operated from a signal manually selected from one of two ΔP transmitters which measured the cabin-to-annulus ΔP .

Operation of the lock vacuum system was entirely manual. One-inch valves located in the lock control console permitted fine control of the lock pressure through adjustments in the evacuation rate and in the ambient bleed. An altimeter and rate-of-climb meter and an absolute pressure gauge provided the lock status to the console operator.

The inner and outer airlock doors each contain seal guard vacuums which were evacuated by a small mechanical roughing pump. Controls in the lock control console were used to vent each void to ambient, to the lock, or to the cabin as appropriate for lock operations.

Two electro-pneumatic valves operated from the test conductor's console permitted equalization of the cabin and lock pressures, or the annulus and lock pressures. A manual override valve was provided in case of a failure of the electrical circuit on these valves. Operation of the manual override valve opened the cabin/annulus equalization valve and closed the lock/annulus equalization valve, notwithstanding the position of the switches on the test conductor's console and the possibility that electrical power may not be available. Thus, the inside crew members were assured access to the lock and to safety regardless of the nature of any emergency situation taking place. As a further safety measure, all of the electro-pneumatic valves in the vacuum systems were on the emergency power bus supplied by the wet cell battery pack previously described.

Auxiliary Vacuum Systems

The two auxiliary vacuum systems are described in the following paragraphs.

Pass-Through Ports—Two pass-through ports, each 18 inches in diameter and 24 inches long, permitted passing material and equipment in or out of the SSS cabin while the cabin was evacuated. Both ports were equipped with inner and outer doors sealed with two O-ring seals and a guard vacuum between the O-rings.

One of the two ports was equipped with an autoclave. The sterilization system included the autoclave, its boiler, and controls and provided the capability for sterilizing equipment passed into or out of the cabin or for sterilizing itself to allow a sterile interface between the cabin interior and the outside.

Utility Vacuum System—The utility vacuum system consisted of two 15 cfm roughing pumps, two cold traps, interconnecting tubes and valves, pressure and temperature gauges, and the cold trap temperature control network. One vacuum pump was operated continuously to back the cold traps and the other was held as a backup. The traps were operated at -40° to -80°F to trap the water vapor. Operation was cycled between the two traps so that one was being thawed and drained when the other was in use. Gaseous nitrogen at 80° to 120°F was flowed through to thaw the traps and the resultant water was manually drained from the bottom of the trap.

PNEUMATIC SUPPLY SYSTEM

The pneumatic supply system was used to provide 100 psi air to operate the pneumatic valves on the vacuum systems. The primary supply was the normal plant air system of compressed air at 115 psi. A standby compressor was provided to start automatically and provide compressed air if the plant air supply fell below 80 psi. An audio alarm was provided to warn personnel when the plant air supply fell below 85 psi. The horn could not be silenced manually but would stop automatically when the standby compressor had built the system pressure above 85 psi.

HOT AND COLD COOLANOL SYSTEM

Thermal transport for SSS interior systems was provided by two Coolanol systems. The hot Coolanol system delivered Coolanol 35 at 350°F to provide thermal energy for the silica gel and molecular sieve beds during desorption cycles of the carbon dioxide concentrator unit. The cold Coolanol system supplied Coolanol 35 to the SSS at 37°F for numerous life support units.

In operation, the Coolanol 35 was heated in a reservoir to the desired set point temperature, normally 350°F , by a 440-volt immersion heater, and was then pumped into the SSS by a circulation pump. The circulated fluid returned to the reservoir, where a nitrogen blanket was maintained to prevent contact with oxygen.

Several failures of the circulation pump seal occurred during the test which necessitated removal and repair of the pump. A second pump was available as a backup and since the hot Coolanol system could be shut down for several hours without risking the test objectives, the backup pump was not permanently installed but was held on-the-shelf. When a seal failure occurred, the primary pump was removed from the system, the backup pump installed and the primary pump was then repaired and held as the backup unit.

The cold Coolanol was chilled by two refrigeration units and held in a 90 gallon insulated storage tank. The two chillers could be operated individually to provide a standby capability for reliability or together to provide additional capacity. Both units had their own pumps and controls and both used water as a heat sink.

Two identical circulation pumps were provided for reliability and were operated singly to deliver the cold Coolanol to the chamber. Since cold Coolanol was more essential to the life support units, both circulation pumps were permanently installed. No failures occurred on this system during the entire test.

Isolation valves were provided on both systems to permit removal and/or repair of the major components without draining the entire system.

All lines and major components were insulated to reduce thermal leaks.

ELECTROLYZER SYSTEM

A Stuart electrolytic hydrogen plant was used as a backup to the two flight type electrolyzers. The plant is capable of producing up to 12 cubic feet of hydrogen and 6 cubic feet of oxygen per hour. The unit operated continuously and switchover to it was accomplished automatically by the onboard two-gas pneumatics control system. Numerous failures of the flight units necessitated frequent reliance on this system. This plant consists of an air-cooled transformer and rectifier, three Stuart electrolytic cells connected electrically in series, a water seal, and, for each gas, a low pressure gas-holder, an air-cooled electrically driven compressor, a purification system, and storage and reserve tanks. In addition, interconnecting piping, various protective devices, and controls for automatic operation were provided.

GAS SUPPLY SYSTEM

The gas supply system consisted of an oxygen and nitrogen supply and distribution network. The gases were used to backfill the cabin with the specified partial pressure of each gas and as a backup for the onboard atmospheric gas generation and supply system. In addition, the nitrogen was used as a pneumatic pressure source to operate pneumatic valves and to pressurize bladders in several onboard units.

The oxygen system consisted of a supply of four K bottles of aviator breathing oxygen manifolded through pigtails and valves to a regulator where the system pressure was adjusted to 50 psig. A sample port below the regulator allowed samples to be taken for purity testing. The supply line was then divided into two lines. One line entered the chamber through a solenoid valve which was controlled by the onboard two-gas control system. The other line passed through a hand valve and was vented into the cabin for use to establish the initial partial pressure level of oxygen.

The nitrogen supply system consisted of two supply lines and one return line. The cabin backfill line was supplied from a liquid nitrogen boil-off. The second nitrogen supply was identical to that described for the oxygen system.

To preserve the mass balance of the interior atmosphere, a return nitrogen line was provided to carry the vented nitrogen gas from the pneumatic valves and regulators to the annulus where it was removed by the Gast pump.

COMMUNICATIONS SYSTEM

The communications system was an audio-video monitoring and recording system. A block diagram schematic of the system is provided in Figure 4. Control of the entire system was centered in the communications console (Figure 5). This system included remote camera/microphone units, video monitors, a special effects unit, standard and time lapse video tape recorders (VTR's), an audio recorder, an intercom, and a public address (PA) system.

The remote camera/microphone units consisted of a closed circuit television (CCTV) camera mounted with a nondirectional microphone attached below it. Six of these units were placed in various parts of the SSS. Each camera was connected to its own video monitor in the control console and to several video switchers. The microphones were wired to an amplifier system and to several of the switchers. A seventh TV camera remained outside the cabin.

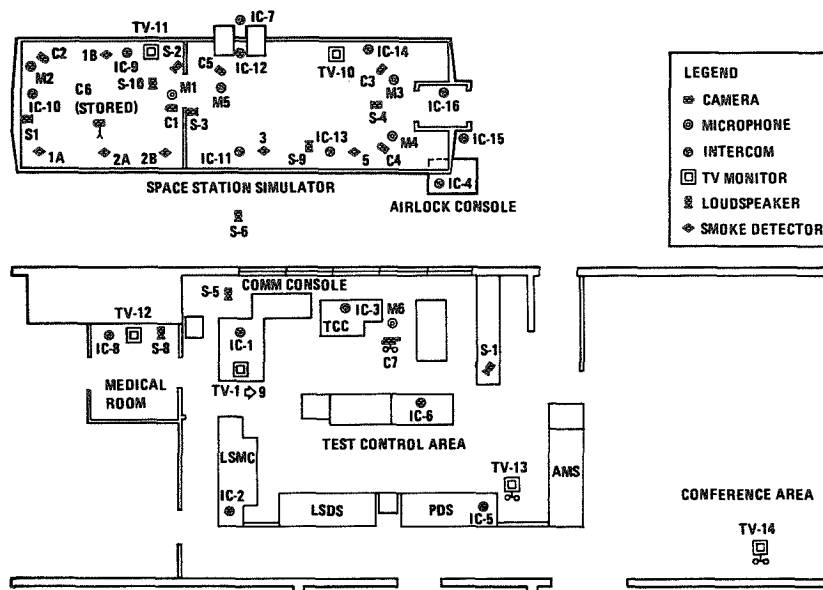


Fig. 4—Space Station Simulator communication system block diagram



Fig. 5—Communications console

Eight small screen monitors and one large screen monitor/receiver were mounted in the control console. Seven of the small monitors were used with the seven cameras in the system and the remaining small monitor showed the output of VTR No. 2. The large screen receiver/monitor supplied Off-the-Air signal monitor for VTR No. 1. Two small screen monitors were located inside the cabin and could be connected to any standard broadcast TV channel or to any of the closed circuit cameras.

Two standard VTR's were included in the system to provide a record of the visual and audio data gathered by the console. VTR No. 1 was used to record any significant portions of the experiment. VTR No. 2 was used to record reactions of the subjects during an emergency condition. Two time lapse recorders were provided to allow time study comparisons.

The intercom permitted up to 16 stations to have up to 3 independent simultaneous conversations. Also, it permitted any entertainment source to be fed to the subjects via earphones or on the PA. Any of the three intercom channels could be recorded by the audio tape recorder or connected to an outside telephone line, and calls could be originated or received. A standby battery power supply provided power to the intercom.

The PA system did four jobs (1) the operator of the console could page via loudspeaker into the SSS, (2) any station in the SSS or the control room could page to the control room, (3) any intercom station outside the SSS or any conversation on the intercom busses could be fed to the SSS PA system by the operator, and (4) the audio channel of VTR No. 1 could be fed to a speaker in the SSS.

A smoke detection system interfaced the communication system. Six smoke detection units located in the cabin were interconnected with three annunciator panels and the video system. When a smoke detector unit was actuated, the following functions were performed (1) an identifying light illuminated on each panel, (2) two buzzer alarms sounded in the cabin, (3) a bell alarm sounded in the test control area, (4) the appropriate camera for viewing the suspect area was selected and its output sent to VTR No. 2 and to the large monitor screen, and (5) a signal was sent to the plant security center which automatically dispatched the plant fire department.

CONCLUSIONS AND RECOMMENDATIONS

The successful completion of the planned 90-day test, without significant interruption in essential facility services, warrants an overall conclusion that the basic facility is satisfactory for conducting long-duration manned tests.

Another conclusion is that a manned chamber test may be successfully integrated into an existing, multi-faceted laboratory without compromising the safety of the manned test or the efficiency and operation of the other laboratory activities. This conclusion is based on the fact that during the 90-day test, numerous other tests were conducted in the MDAC Space Simulation Laboratory without any loss of efficiency or flexibility. Some of these tests, which were of a classified nature, were conducted in a 39 foot space simulation chamber which shared its pumping system with the SSS. Successful completion of these simultaneous operations required only a minimum of coordination and planning.

Notwithstanding the conclusions noted above, several recommendations can be made to improve the facility for future tests.

The biggest single improvement would be to integrate all the monitor and alarm functions into a single operation. As used for this test, each facility unit

which utilized alarms had them localized at the unit. Despite the fact that each alarm was selected so that it could be distinguished from all the others, and that extensive training of the operating staff was accomplished prior to the test, when an alarm sounded, it was time-consuming and nerve-wracking to identify the source of the problem. It would have been much better to place all the monitor functions in a computer and have one centralized CRT for displaying the alarm and its cause. In addition, such a computer would permit real-time display of data from the life support units as well.

Another recommendation would be to change the Coolanol 35 thermal transport system to one utilizing water as a transport medium. Leakage of Coolanol into the chamber would seriously jeopardize the continuance of a run, whereas the leakage of water, even in significant quantities, probably would not.

REFERENCES

1. J. P. Valinsky. *Safety Aspects of a 90-Day Manned Test of a Regenerative Life Support System*. McDonnell Douglas Paper No. WD-1748, November 1971.
2. W. P. Waters. *Training and Certification Program of the Operating Staff for a 90-Day Test of a Regenerative Life Support System*. McDonnell Douglas Paper No. WD-1533, November 1971.
3. *Preliminary Results From an Operational 90-Day Manned Test of a Regenerative Life Support System*. NASA SP-261, November 1970.

SAFETY ASPECTS OF A 90-DAY MANNED TEST OF A REGENERATIVE LIFE SUPPORT SYSTEM

J. P. Valinsky, *McDonnell Douglas Astronautics Co., Huntington Beach, Calif.*

ABSTRACT

A system of operational readiness reviews and pretest activities was directly responsible for identifying many hazards and potentially unsafe conditions which could have made the successful 90-day manned test a catastrophe.

INTRODUCTION

The operational 90-day manned test of a regenerative life support system was planned to provide data on the performance of equipment and crewmen in the closed ecology approximating that of an orbiting spacecraft.¹ In order to meet this general goal, several objectives were established. These objectives were (1) operate a regenerative life support system for 90 days without resupply, (2) evaluate advanced life support equipment and processes, (3) determine the ability of the crew to operate, maintain, and repair equipment, (4) reach a microbial and chemical equilibrium in a closed environment, (5) obtain data on physiological and psychological effects of long-duration confinement on the crew, (6) determine the precise role of man in performing in-flight experiment, and (7) obtain a material balance, a thermal balance, and power requirements.

The Space Station Simulator (SSS) in which the test was performed is a double-walled horizontal cylinder, 12 feet in diameter and 40 feet in length (Figure 1). The 4,100-cubic foot chamber is designed for operation at reduced atmospheric pressure to duplicate proposed space vehicle cabin atmosphere composition. An annular space between the inner and outer walls normally is operated about 5 inches of water below cabin pressure, ensuring that all leakage is outboard, to provide realistic testing and evaluation of environmental control and life support equipment. The chamber is provided with 4 inches of insulation to minimize thermal and acoustic transmission.²

An airlock is provided at one end of the chamber, with a volume of 160 cubic feet for entrance and egress of the crew. A pass-through port containing an autoclave was used weekly for passout of samples for analysis. The autoclave was sterilized before each use to ensure microbial isolation of the test chamber. A second pass-through port is installed in the chamber but was not used during the 90-day test. The airlock and pass-through ports are normally held at annulus pressure (slightly below cabin pressure) when not in use.

The intent of this paper is to identify the safety aspects of the manned SSS test, the methods used to satisfy safety requirements, and to evaluate the safety systems and procedures in light of the test results.

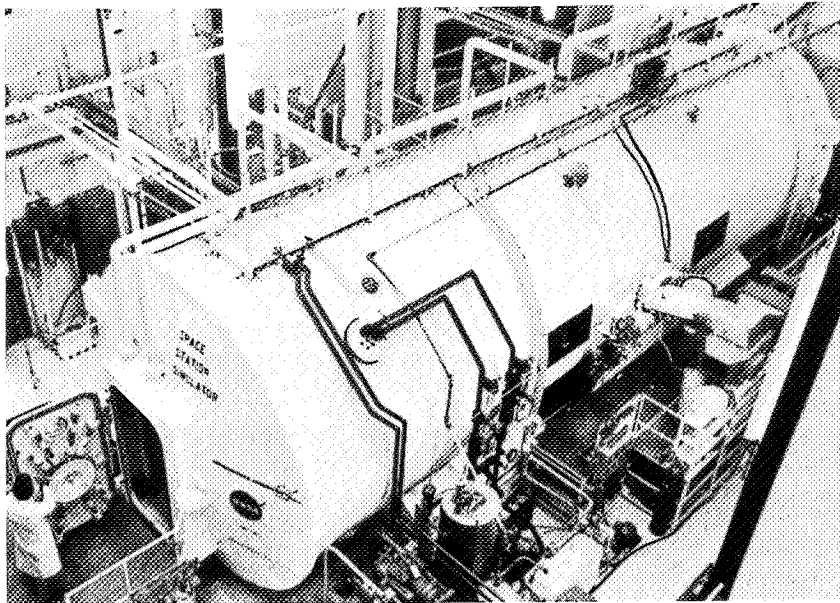


Fig. 1—Space Station Simulator

SAFETY ASPECTS

It was felt that the most critical hazard to which the onboard crew would be exposed during the test was an uncontrollable fire. The Apollo fire clearly indicated that emergency systems, procedures, and careful planning specifically aimed at eliminating a possible fire are mandatory for manned testing in simulated spacecraft environments. The two main objectives to prevent potential fires were to eliminate combustibles and ignition sources. Both of these objectives are idealistic and impossible to achieve in a Research and Development (R&D) manned testing situation. To approach them, however, a system of documentation, quality control, and safety reviews was initiated.

Two initial primary documents were (1) a Test Plan and Procedure which detailed the test plan, objectives, and procedures, and (2) a Design Requirements Drawing, which included material, cleanliness, inspection, and performance requirements.

The two documents were drafted early in the program to allow management and safety reviews before systems and procedures were finalized. Upon approval, these documents were used by system and quality control engineers as guides in accomplishing their respective tasks.

Since it is generally known that a test system composed of R&D hardware does not always satisfy the ideal of absolute safety, potential problems were identified and emergency systems, procedures, and training were incorporated into the test system to satisfy the goal that no single point failure could cause a catastrophic incident.

In addition to the recognition of fire as a serious potential incident, also identified were atmospheric contaminants, radiation hazards (isotopes were used in the Life Support System), electrical power failures, space cabin pressure changes, pressurized system rupture, electric shock, and crew medical problems.

FAILURE MODE, EFFECT, AND CRITICALITY ANALYSIS

The failure mode, effect, and critically analysis (FMECA) is a technique for determining the qualitative and quantitative effects of each failure mode of each component in all subsystems and their effect, in turn, on mission operations. Use of FMECA permitted the classification of each failure mode according to a safety/reliability index which, in turn, identified undesirable single point failures. Further, the FMECA permitted a quantitative evaluation of each failure mode as a function of its probability of failure and its importance or criticality in the subsystem.³

Results of the analysis indicated that there was no evidence of the existence of a potential single point failure which could cause a crew member fatality or immediate test abort.

However, mission rules were established which demanded a test abort if (1) an uncontrollable fire occurred and/or (2) if all means of communication, both audio and visual, were lost simultaneously.

Although it was recognized that an uncontrollable fire was unlikely due to the control of allowed combustibles in the SSS and the elimination of potential ignition sources, extensive training of a rescue crew, the installation of a fire detection and suppression system (water spray system), and the capability of a rapid rate of SSS repressurization were additional factors in ensuring crew safety.

With the redundancy of the audio and visual systems, plus the line-of-sight capability to view the crew through the SSS view ports, the possibility of simultaneous loss of all communication was very remote. Any external malfunction of the intercom or television systems could, in most cases, be repaired by the operating staff.

QUALITY ASSURANCE PLAN

The purpose of the 90-day mission quality assurance plan was to ensure (1) documentation of material and configuration control, (2) control of workmanship, quality, and safety, (3) verification of installation and operation of equipment, components, systems, and instrumentation, (4) certification of all checkout operations including both preruns and postruns, (5) inventory control, (6) resolution of all Operation Readiness Inspection Committee (ORIC) discrepancies, and (7) equipment certification control.

SAFETY REQUIREMENTS

The 90-day manned test was conducted according to the policy and procedures as specified in the National Aeronautics and Space Administration (NASA) Management Manual Instructions 1710.2 and 1710.3, dated November 17, 1969, from the Langley Research Center (LRC). These documents replaced the NASA, Manned Spacecraft Center documents (MSC1 8825.2 and MSC Safety Manual, Part 7) by a contract change on March 9, 1970. The requirements of the McDonnell Douglas Astronautics Company (MDAC) policy (Company Policy CP 5.061-C) for manned tests were also satisfied.⁴

All test procedures, plans, operating manuals, and electrical/mechanical installation drawings were reviewed by the Operational Readiness Inspection Committee (ORIC) which had been constituted according to NASA requirements and whose members represented the disciplines of engineering, safety, quality

assurance, aerospace medicine, employe relations, and legal. The training and certification plans for the operating staff and onboard crew members also were reviewed by the committee. Crew and staff proficiency was observed during dry-run and system checkout tests.

Meetings of the ORIC during the design phase were held monthly and, after installation and prior to system checkout, the committee met weekly. Many potential safety problems were corrected without major hardware rework or procedural changes as a result of early recommendations made by the ORIC. A total of 21 meetings were held.

A series of pretest activities and readiness reviews were held to establish that the entire test system was ready for the 90-day manned test. This series of events is shown in Figure 2.

TEST OPERATIONS

Test operations were classified as normal test operations, contingency test operations, or emergency test operations.

Normal test operations included all the preplanned activities associated with accomplishing the test objectives.

Contingency test operations were initiated in the event of abnormal test conditions that did not activate emergency test operations, such as a system/partial system malfunction, medical problem, smoke alarm, abnormal trace contaminant buildup, or the inability of the test to meet major program objectives. The contingency test operations mode could be initiated only by the test conductor. This mode of test operation provided for the use of ad hoc procedures to correct any unforeseen situations that could affect crew health and safety or test objectives.

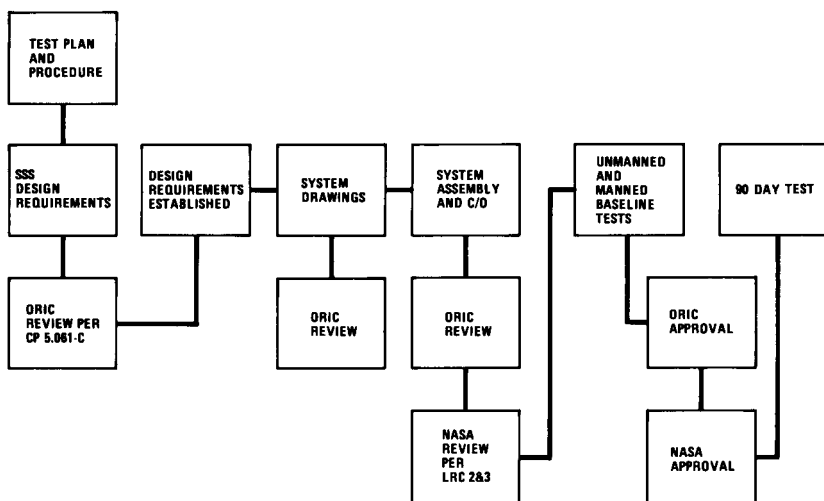


Fig. 2—Safety review flow chart

Emergency test operations (ETO) were divided into three categories — test conductor's ETO, medical ETO, and fire abort ETO. The test conductor's and medical ETO were time-phased procedures utilizing emergency and supporting equipment as required to provide maximum safety for the crew consistent with varying conditions. The fire abort ETO was an automatic operation used only in the event of a fire when it was anticipated that conditions would not allow for planned staff/crew reaction time.

RESULTS

A need for thorough unmanned checkout test prior to the manned tests was clearly identified by events which occurred during unmanned baseline preliminary tests.

During one such test, a quick-disconnect failed and sprayed 20 gallons of 350°F heat transfer fluid in the simulator. This failure was caused by the incompatibility of the heat transfer fluid with an esoteric aluminum alloy used in the quick-disconnect.

Another incident occurred when a failure in the electrolysis unit allowed hydrogen to leak into an oxygen line causing the oxygen purifier to overheat and ignite. This resulted in an intense, but localized fire outside the simulator.

Both of these incidents were caused by interactions that were not identifiable by the previously discussed failure and safety reviews. Thus, these incidents serve to indicate that it is virtually impossible to predicate all undesirable possibilities by analysis alone.

During the 90-day test, 55 contingencies occurred. Of these, 49 were alarms triggered by smoke detectors and were found to be false alarms, 2 were short-duration electrical power failures and the emergency systems functioned as planned without loss of control of primary functions, and 4 were caused by atmospheric contaminants in the form of high hydrocarbon and carbon dioxide levels,⁵ however, in all four instances the situation was quickly rectified by the life support systems.

Because of the number of false smoke alarms, it became increasingly difficult for the operating staff to respond effectively to them. Moreover, they were unreliable. During the 5-day manned checkout run, an air pump motor overheated and produced a small amount of smoke in the cabin. The crew smelled the smoke and identified the problem, yet the detectors failed to detect the smoke. This was one of the factors which led to a procedure that only two of the four onboard crewmen would be allowed to sleep at any given time.

EMERGENCY SYSTEMS

The emergency systems used for the 90-day test were developed during the past seven years of manned testing in the SSS. These systems have been upgraded over the years and also modified to meet the individual test requirements. The primary systems and equipment used are listed in Tables 1 and 2. The arrangement of the test system is shown in Figure 3.

SUMMARY

Previous manned testing at MDAC indicated a deficiency in documentation and change control. These deficiencies hindered both safety reviews and fault isolation activities.

Table 1
EMERGENCY SYSTEMS AND EQUIPMENT INSIDE
THE SPACE STATION SIMULATOR

Unit/Purpose	Description	Quantity/Location
Survivair Sac-Pac Air Packs to provide protection from smoke inhalation.	Packs contain a quick-donning, lightweight, full-face mask, and approximately 15 minutes air supply.	5 units inside cabin, 4 at air pack stations and 1 under bunk.
CO ₂ Hand-Held Fire Extinguishers for fire fighting.	Units contain five pounds of CO ₂ .	4 units in cabin adjacent to air pack stations.
Water Spray Nozzles for crew protection from heat and flames in event of major fire.	Nozzles supplied from regular sprinkler system water supply for the building and energized from the main control console by the test conductor.	11 nozzles near cabin ceiling, above air pack stations, and along central aisle of cabin and bunk area.
Two Fire Hoses for fighting small fires.	Two 1-inch diameter water hoses equipped with an adjustable nozzle.	2 hoses, one near command area and one near airlock area.
Smoke Detectors to detect and notify of smoke within the cabin.	Smoke detectors coupled with an inside/outside alarm and video recording system.	6 detectors in area near electrical equipment and potential fire hazards.
Toxic Gas Level System to detect levels of atmospheric contamination and immediately notify the crew and test conductor.	System in operation continually for detection of carbon dioxide, carbon monoxide, total hydrocarbons, oxygen, methane, and hydrogen. Periodic analyses prepared for other trace contaminants.	1 system, adjacent to SSS.
Emergency Lighting System for backup system during power failure or abort procedures.	Battery-operated lights illuminated automatically upon loss of primary 110-vac lighting circuit power. Four cabin lights are 28-vdc, 25-watt sealed-beam lamps.	4 lights in cabin over main aisle.

Unit/Purpose	Description	Quantity/Location
Alpha Survey Meter for radiation detection.	Portable count-rate meter with alpha-detecting scintillation probe.	1 meter stored inside SSS.
Air Sampler for radiation detection.	Constant volume air sample with lower and upper limit alarms.	1 sampler installed inside SSS.
Personnel dosimeters for radiation detection.	One tissue equivalent and one neutron insensitive, 0 to 200 mrad.	1 set maintained on each crewman's person.

Table 2
ADDITIONAL EMERGENCY SYSTEMS AND EQUIPMENT USED

Unit/Purpose	Description	Quantity/Location
Emergency Power Supply; 28-vdc Battery for power source for emergency systems during power failure.	Standby battery 28-vdc power source.	1 battery and charger outside and under the SSS.
Emergency Lighting System for backup system during power failure.	Battery-operated 6-vdc, 25-watt sealed-beam lamps energized automatically upon loss of primary power.	Various lamps located to illuminate all critical operating areas.
Cabin Repressurization System to rapidly repressurize the cabin.	Actuated from the test conductor's console. System pressurizes the cabin from 10 psia to sea level within 55 seconds.	1 system on SSS.
Cabin Pressure Relief Valves to relieve cabin over-pressure.	Relief valves to relieve any sudden over-pressure condition.	2 valves on cabin vent line.
Cabin Power Emergency Shutoff Switch to terminate all electrical sources to SSS.	Switch actuation terminates all electrical power to cabin interior, except power for intercom and television cameras.	1 switch on test conductor's main control console.

Unit/Purpose	Description	Quantity/Location
Emergency Abort Switch to initiate emergency abort procedures with various cabin simulator systems.	<p>Lifting lever guard and placing switch to ON position accomplishes:</p> <ul style="list-style-type: none"> ● All inside power, except to the intercom and television cameras, shuts off. ● The inside, battery-operated emergency lights illuminate. ● Power to the outside Coolanol-35 pumps shuts off, and valves in supply and return lines close. ● The water spray system is actuated. ● The Lock-Annulus Equalization valve closes. ● The Lock-Cabin Equalization valve opens. ● The hydrogen and oxygen accumulators are vented. 	1 switch on test conductor's main control console.
Hot Line Emergency Telephone to obtain immediate support from the MDAC Fire Department and Dispensary.	Telephone connected to MDAC Main Security Desk; if removed from hook, an immediate alert is established at MDAC Fire Department and Dispensary. Fire trucks and an ambulance crew are dispatched without necessity of conversation.	1 telephone on test conductor's main control console.

Unit/Purpose	Description	Quantity/Location
Fire and Smoke Protective Equipment for protection for the rescue crew during fire abort procedures.	Coats, hats, boots, gloves, fabricated with Gentex (rayon/mylar); air packs, consisting of a full face mask and an approximate 15-minute air supply.	2 sets at outer airlock door, outside SSS.
CO ₂ Extinguisher for fire fighting.	CO ₂ nozzle connected to a 75-lb CO ₂ supply by means of a 50-foot hose on a reel.	1 extinguisher at outer airlock door, outside SSS.
Emergency Medical Treatment Facilities for on-site medical treatment of injured or incapacitated crew members.	Facility equipped with an internal/external defibrillator, a heart-pacer, an EKG machine, therapeutic O ₂ , a manual resuscitator, a stretcher, and resuscitative drugs. Also available nearby is the MDAC Dispensary and ambulance.	1 facility in immediate area of SSS.

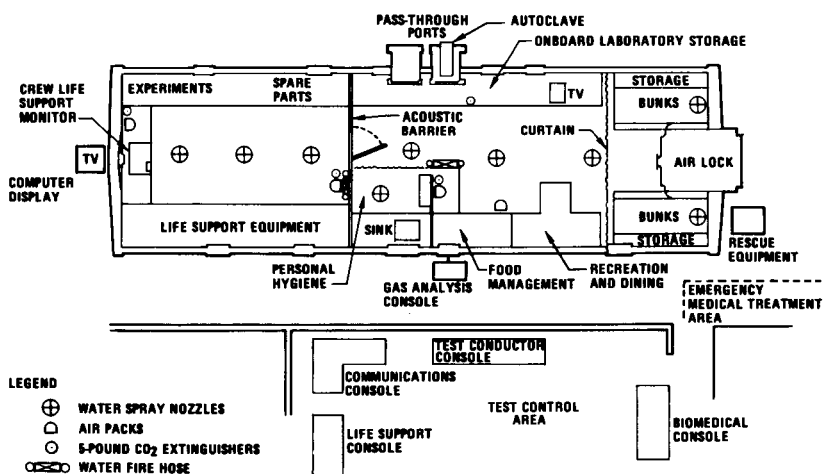


Fig. 3—Space Station Simulator arrangement

Considerable effort was expended early in this program to improve the noted deficiencies and satisfy the more stringent safety and program requirements.

The contractual safety requirements stipulated documentation, training, facility, quality control, systems analysis, medical surveillance, material control, and checkout operations. The design requirements drawing was initiated to integrate the safety and program requirements into a single document that would be useful to the design and testing engineers, and also to provide visibility for quality control and safety reviews. A drawing section list also was created to maintain a current list of all the latest drawing changes to preclude the use of obsolete documentation.

The efforts stated in the previous paragraph were successful in fulfilling both the safety and program requirements.

CONCLUSION

Based upon the experience of the 90-day manned test and previous manned testing at MDAC, the importance of the selection of competent personnel to serve on safety review committees cannot be over emphasized. The ORIC members for the 90-day test were a definite asset to the program. Their technical competence allowed excellent communication and cooperation which was essential in completing the program within the budget and schedule constraints.

The design requirements drawing has resulted in a basic manned testing document which is presently being upgraded for future manned tests at MDAC.

REFERENCES

1. J. K. Jackson. *A 90-Day Operational Test of an Advanced Life Support System*. McDonnell Douglas Paper WD 1580, July 1971.
2. R. L. Malin. *Facilities and Support Systems for a 90-Day Test of a Regenerative Life Support System*. McDonnell Douglas Paper WD 1535, November 1971.
3. Test Report. *Final Test Plan and Procedure, Operational Ninety Day Manned Test of a Regenerative Life Support System*. NASA CR-111882, May 1971.
4. R. E. King. *Operational Readiness Inspection Committee Report for Operational Ninety Day Manned Test of a Regenerative Life Support System*. McDonnell Douglas Report MDC G1037, July 1970.
5. P. P. Mader, A. S. Lucero, and E. P. Honorof. *Analysis of Trace Contaminants*. McDonnell Douglas Paper WD 1595, April 1971.

GE UNDERWATER TEST FACILITY STUDIES IN ZERO G SIMULATION

Ruth H. Fry, *General Electric Company, Space Division, Valley Forge, Pennsylvania*

ABSTRACT

The Underwater Test Facility is an indoor controlled environment test facility designed specifically for zero G simulation, hydrospace manned and unmanned equipment development, and personnel training for both space and underwater exploration.

INTRODUCTION

The General Electric Underwater Test Facility is unique in the nation in that its capabilities range from controlled buoyancy experimentation to the development of Closed Cycle Rebreathing units which are operable to 1500 feet underwater for a maximum duration of 8 hours, to zero G simulation blood transfusions underwater. All of these programs are conducted in an indoor controlled environment.

UTF Capabilities

Before describing some of the programs in zero G simulation which have been performed at the UTF, a brief explanation of the Facility itself is in order to give a better understanding of the type of simulation projects conducted there and of the general environment in which the projects were completed (see Figure 1). The Underwater Test Facility (constructed in 1968 and operational in January 1969) was built specifically for the testing and evaluation of astronaut subjects and to provide information for the design and development of crew procedures, the design and development of spacecraft subsystems and equipment that interfaces with the crew, and the checkout and evaluation of unmanned spacecraft and manned spacecraft equipment in a zero G or controlled buoyancy state underwater. The main test tank is capable of docking three S-4B's simultaneously and of containing two or three different projects at any one time, depending of course on the area required for each program in the tank. The main tank contains 315,000 gallons of chlorinated, purified and filtered water. The diatomaceous earth filtration system requires a 24-hour period for complete turnover of the main tank capacity. The surface environment of the UTF main

and secondary tank areas is controllable from approximately 45 to 98°F dependent upon the type of requirements of the individual program. During normal operating conditions the air temperature is maintained at 90°F.

The main test tank is 25 feet deep by 60 feet long by 28 feet wide, with water temperature controllable from ambient (about 60°F) to 110°F. Adjacent to the main tank is a smaller circular tank 12 feet in diameter by 8 feet deep, temperature controllable from 34 to 212°F, which is affectionately called the "wine vat" (Figure 1A).

Built into the main test tank is a water manifold pressurization system, i.e., a self-contained water supply for water pressurizing space suits. Above this system is an air manifold pressurization system (bottle or tube trailer supplied) extending 60 feet along one wall of the tank which is used for hookah breathing, air pressurization of Apollo suits, or in performing shirt-sleeve zero G tests.

Basically, most of the programs conducted at the UTF since 1969 have been in the water pressurization mode of zero G simulation (Figure 2). However, the UTF is equipped to perform in the air-pressurized zero G mode. This mode was used on the M-508 Astronaut Performance Program and also on Experiment A & B which were air-pressurized Apollo suit programs (Figure 3).

To supplement the air-pressurized mode and to meet NASA specifications, a 4-man recompression chamber is available with fully certified Navy trained chamber operators (Figure 4).

In order to meet safety regulations and to further document and enable topside personnel to observe a project being conducted underwater, a closed circuit TV system is available which includes audio communication with a videotape recorder for surface and underwater use simultaneously. The system comprises two underwater cameras, one mobile and one stationary unit, one topside camera, and three surface monitors; each one can be independently connected to the video recorder if desired. The audio system for underwater useage is a "snoopy" type helmet with a bone knocker and a mouthpiece communicator in the second stage of the regulator. The air supply is hookah, for ease of operation by the TV cameraman while underwater. All topside monitors and electronic equipment are located in a 70°F Test Control Room with a 10 foot by 4 foot viewport overlooking the main tank test area. This enables topside personnel to work more efficiently and safely in a cooler temperature-controlled area separate from the main tank area. Also available is an inhouse underwater photographer who specializes in underwater motion picture photography but who also does slide photography. The major problem encountered in an indoor underwater test facility relative to quality photography is adequate lighting. To alleviate this problem, a movable cross bar of 6 Colortran quartz lights with three underwater quartz lights is used throughout both test tanks. To date, no serious problems have been encountered relative to

underwater lighting at the UTF. However, we have found that for such projects as thermal pollution and underwater telemetry studies, a Milliken camera mounted on the highbay area catwalk over the main tank is a most efficient method of obtaining accurate data (Figure 4A).

To further explain UTF Safety Regulations, a medical staff is on hand at all times when a program is in progress underwater, with a fully equipped medical dispensary immediately adjacent the UTF briefing room.

Other auxiliary systems and surface test support areas include:

- Available underwater support systems and surface preparation areas in addition to the ones already mentioned.
- Scuba support equipment and a fully equipped pressure suit and Scuba maintenance area.
- A staff of engineers, designers, technicians and certified divers, including Navy and NASA qualified underwater safety personnel and a Professional Associated of Diving Instructors (PADI) Certified Scuba Instructor.

For equipment preparation such as unmanned spacecraft testing (docking and maneuvering), deep sea submersibles, or underwater cockpit escape tests from a jet, there is a highbay area 61 feet by 25 feet by 20 feet high leading from the exterior of the building in the UTF area to the edge of the main tank area for equipment transportation and preparation. Supplementary to these areas there is an overhead trolley crane rated at 4000 pounds which is movable the length and width of the main and secondary tank areas. There is also a 10-ton cherry picker mobile throughout the Facility, available for placing equipment in the main and secondary tank areas.

Additional areas include Fabrication and Assembly Areas, a Briefing Room where personnel can relax and discuss problems or have lunch in the comfort of bathing suits and work clothes, an office area, and Men's and Women's Locker and Shower Rooms.

The entire Underwater Test Facility is a Closed Area which is secure for all classified and proprietary testing.

A few of the programs conducted at the UTF and some of the problems encountered therein are presented next.

HEMAR

The HEMAR Program, i. e. , Human Engineering Criteria for Maintenance and Repairs of Space Stations, in particular Experiment B, required that EVA and IVA activities be simulated in which a subject removed and replaced modules representing equivalent earth weights of 25, 50, 118 and 228 pounds. Package sizes ranged from 0.3 feet to 7 feet 3 inches. The entire experiment was conducted in zero G in the water-pressurized mode under 3.5 psi (gage) with the subject in a Gemini space suit (Figure 5). The value of the module replacements of HEMAR

lies primarily in being able to state with authority the mass that was simulated and the force required to overcome the hydrodynamic drag problems. After conducting HEMAR Phases I and II, including Experiment B, all of which were performed in zero G in the water-pressurization mode, it was found that the subject appeared to be in a state closer to zero G than he would be in the air-pressurized mode. This is because the subject is effectively flating inside the suit under water-pressurization, not as in air pressurization "hanging from his armpits in the Apollo suit." Depressurization in the water mode is also easier and quicker to accomplish than air depressurization and there is a greater degree of safety, as the safety diver can get air to the subject in approximately 8 seconds as compared to the apparent hazards of air depressurization underwater. This is discussed further below.

M-508

Another program conducted in zero G but in an air-pressurized mode with the subject in an Apollo suit was the M-508 Astronaut Performance Program. The pressurization system for the neutral buoyancy simulation consisted of an air bank, 2 stage regulator, backpack, surface flowmeter, and pressure gage. The backpack was originally designed and developed by the General Electric Company as a water pressurization device to be used in conjunction with a specially designed quick-disconnect helmet. This system proved to be safe, reliable, and efficient as used in previous tests (reference the HEMAR, NAS 8-21429, 15 June 1969). The backpack was easily modified to be used as an air pressurization device without destroying its capability for water pressurization. The backpack compensates for pressure differentials as the subject descends to working depth, i. e., 15 to 20 feet. However, the pressure could also be controlled manually by the safety diver to assist the subject's ingress and egress. The air flow rate and pressure were maintained at 10 cfm and 3.5 psi (gage) respectively and continually monitored on the surface to ensure the safety of the subject (Figure 5A). The M-508 Program (NAS 9-8640) or Astronaut Zero Gravity Performance Evaluation Program was designed to fill a gap in our knowledge of man's capabilities to perform complex tasks in the zero-gravity environment. The resultant experimental program involved an evaluation of the major facets of astronaut performance while restricted to a limited work-site area. The program was performed during the period July 1968 through February 1970 and encompassed: (1) the definition and preliminary design of Experiment M-508, an experiment concerned with astronaut worksite performance evaluation; (2) the fabrication of prototype hardware and collection of simulated astronaut worksite performance data using various ground based zero-gravity simulation modes; (3) the collection of additional data on man's force emission

capability to establish 1-G and zero-G baselines; and (4) the preparation and publication of a Handbook of Human Engineering Design Data for Reduced Gravity Conditions.

Helmet Distortion

The use of water buoyancy or underwater zero G testing for reduced gravity simulation necessitates the employment of means to restore natural vision to the subject in the underwater environment. During the zero G simulation tests conducted underwater, certain visual differences between the space flight situation and the underwater simulation have been detected. In order to alleviate this problem, the UTF staff instituted a program entitled "Space Suit Helmet Development for Neutral Buoyancy Simulation." The primary objective was to analyze and describe the optical distortion that results from use of an air-filled Apollo pressure helmet underwater. The second objective was to develop and evaluate a molded, form-fitting spinoff of a Scuba faceplate for use with a water-filled pressure suit and for utilization during underwater simulation of shirt sleeve testing. The third objective was to test air-filled scleral contact lenses for underwater simulation. Test results revealed that peripheral vision was less than anticipated and that the lenses expose the subject's eyes to water with the risk of physical, chemical, or biological damage.

Underwater Telemetry Studies

With regard to the field of underwater equipment testing, a series of underwater tests of the GE Pressure Transducer and Telemetry System which was developed in 1965 have been conducted at the UTF to measure the base/drag characteristics of water entry models during descent. A sealed transducer and telemetry system have transmitted an unmodulated FM signal during descent to a 25-foot depth of water. The pressure sensor and telemetry system in a sealed vessel has been subjected to an oscillating pressure, has successfully transmitted an intelligible pressure-modulated FM signal, and has sensed underwater sounds in the sealed vessel while submerged. The ultimate goal is to develop a pressure transducer and telemetry package capable of withstanding launch loadings of several thousand G's from the NOL gun launch facility and to broadcast use base pressure data from 25 to 50 foot depths of water during the model descent to the bottom of the tank. The telemetry system is presently capable of withstanding launch loads; however, the studies are to demonstrate the feasibility of transmitting a signal from a 25-foot depth of water.

Tektite II

Further examples of other types of programs conducted at the UTF have been the Tektite II 40-hour Scuba Training Course conducted for GE Ocean Systems personnel who were scheduled to participate in the Tektite II Underwater Habitat Program. This program was conducted on St. John Island in the Caribbean in 1970. A majority of the students in the GE Underwater Test Facility Scuba Certification course went on to receive their PADI internationally recognized Scuba Certification.

Thermal Pollution

The Lake Michigan Thermal Pollution Test Program, which involved applying the thermal effluent modeling techniques to the prediction of a specific power plant's operating conditions, concentrated on the examination of the thermal effects due to the operation of a single unit with a vertical discharge. These tests were simulated in the UTF main and secondary tanks by introducing heated water with a 20° gradient from the secondary tank (110 to 112°F) into the main tank (90°F) through PVC piping and a flow meter, thus over the thermocouples at specific locations around the outlet pipe (see Figure 1A).

Blood Transfusions in Zero G

With regard to the zero G simulated underwater blood transfusions, this particular project was part of the Integrated Medical and Behavioral Laboratory Measurement System (IMBLMS) nicknamed "the chicken machine." In effect, the subject was strapped into a chair (Figure 6) (which had a bottled supply of compressed air connected) and was then given simulated blood transfusions by injecting colored fluid into a chicken breast strapped to the subject's arm. Other medical tests such as electrocardiograms were given to determine the feasibility of performing such operations in space. Additional equipment tests were conducted utilizing microscopes, blood cultures on slides, using vacuum suction to anchor syringes and medical supplies to consoles during the underwater tests, and developing a new system of rubber foot restraints for the subject's utilization while in zero G.

Mark 10 Closed Cycle Rebreather

The UTF has been used extensively since January 1969 for the development and checkout of hardware for the GE Ocean Systems Programs Department, Re-Entry and Environmental Systems Division. The Mark 10 UBA Program has utilized the Facility during development testing of new hardware concepts and for the checkout of all hardware prior to delivery to GE customers (Figure 7).

The Controlled Oxidation Heater Program has utilized the main and secondary cold tank Facilities for development and proof testing of heater components. Other types of equipment which have been evaluated in the Facility include diver communications and diver physiological monitoring hardware, as well as customer utilization of the Mark 10 units in the UTF main tank.

The Mark 10 Mods 0 and Mod 3 are an example of UTF capability to evaluate aquanauts and aquanaut equipment under controlled conditions simulating either tropical or cold environments such as 80 to 110°F air and water temperatures or 34°F water and 45°F air temperatures.

Supplemental utilization of the UTF has been by TV networks, such as for an educational show in Japan explaining the Mark 10 Closed Cycle Rebreather Unit. The Nipon Japanese TV Network filmed a 1-hour show in both the UTF Briefing Room and the Main Tank Area. The Gene Crane show, a local TV station, filmed an interview with GE and U.S. Navy personnel utilizing the Mark 10 unit and a National Geographic Special, later filmed in Alaska, was partially prepared at the UTF.

Thus, the excellent visibility and photographic qualities of the tank areas create an ideal setting for not only testing of personnel and equipment but also for documenting various projects and experiments (Figure 7A). Additional information on programs conducted at the UTF or information about the Facility itself may be obtained from GE UTF personnel or the Marketing Department, Space Division, Valley Forge, Pa.

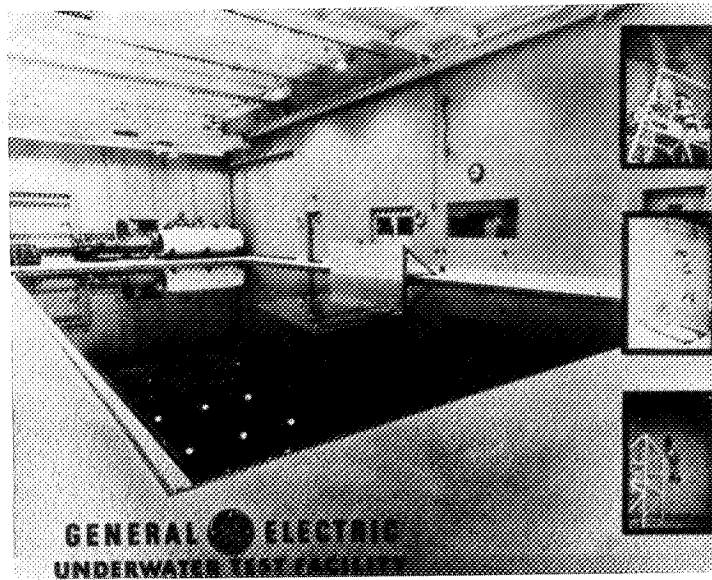


Figure 1

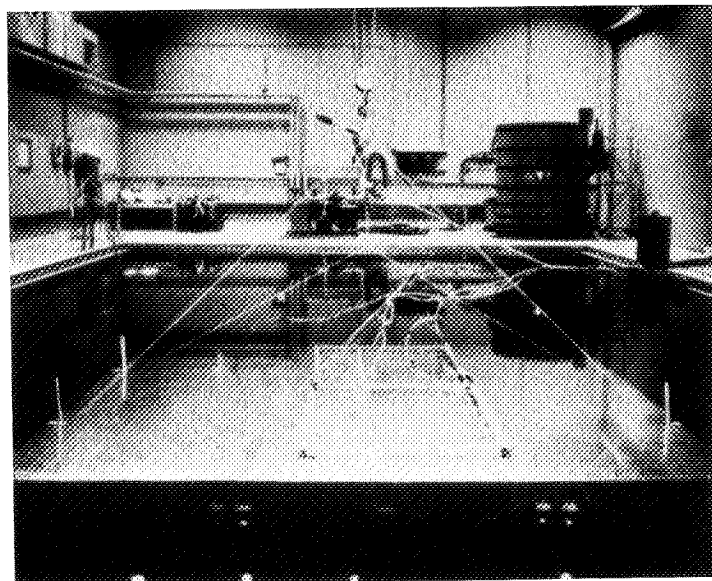


Figure 1A

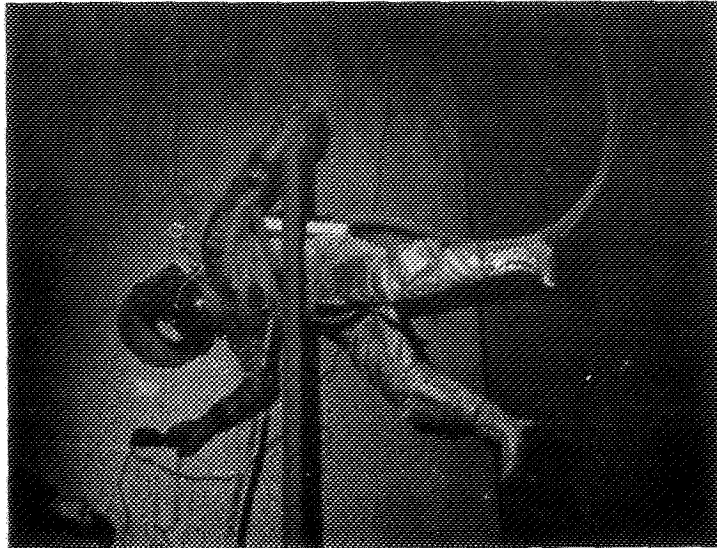


Figure 2

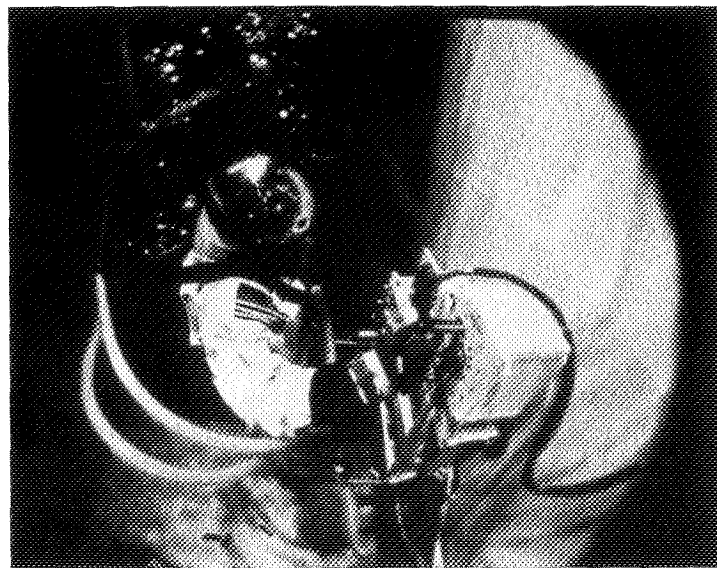


Figure 3

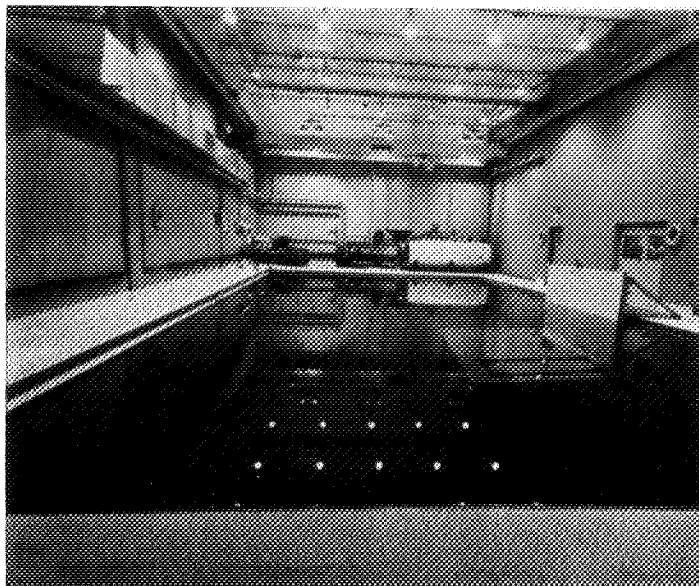


Figure 4



Figure 4A

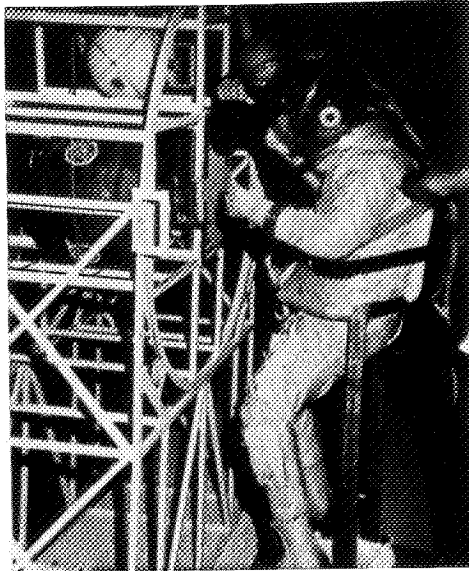


Figure 5

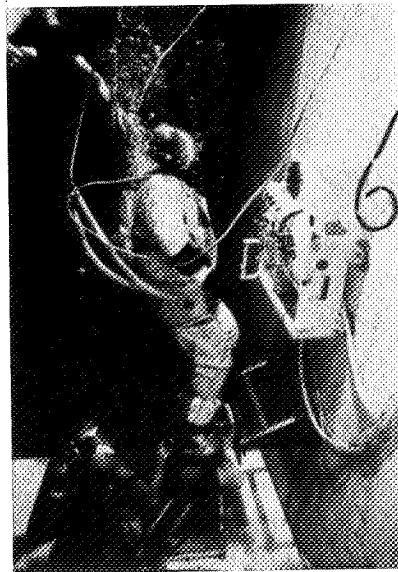


Figure 5A

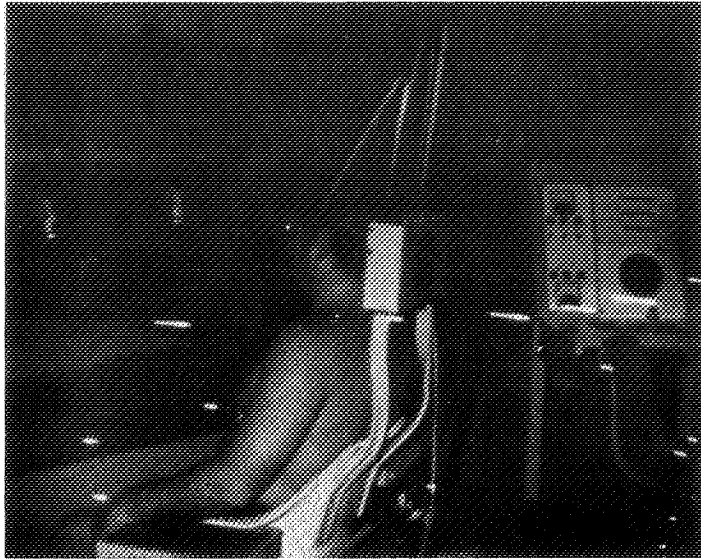


Figure 6

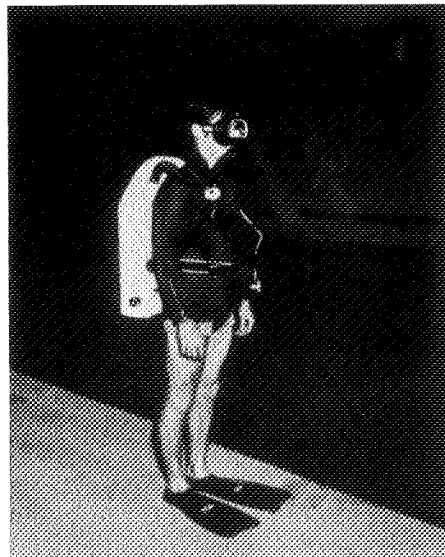


Figure 7

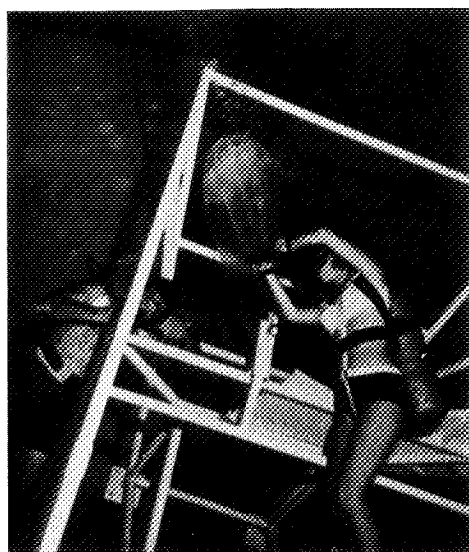


Figure 7A

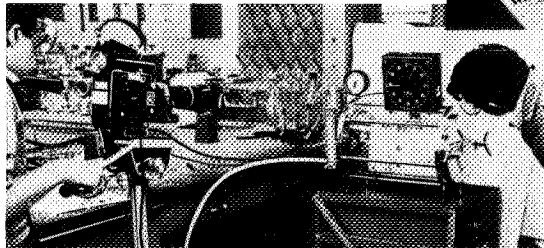
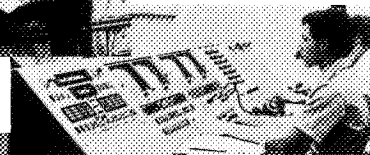
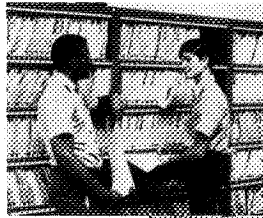
A MAN-RATED ALTITUDE CHAMBER FOR EDUCATION AND RESEARCH — IN A HIGH SCHOOL

Robert A. G. Montgomery, Jr., *Project SPARC Coordinator, Aero-Space Activity Manager, Project SPARC — NEHS, School District of Philadelphia, Cottman and Algon Avenues, Philadelphia, Pennsylvania 19111*

Space simulation technology is now being introduced in both theory and experiment to the high school level of education. A unique program, Project SPARC (SPAcE Research Capsule), has been operating in the Philadelphia School District for eight years. Specific design requirements have been established for a man-rated altitude chamber to be occupied and operated by high school students. The chamber will be used for research as well as educational purposes. The configuration of this simulator matches the Apollo Command Module. Criteria for safety and program implementation will be discussed for such an unusual application.

Problems of environmental control functions, oxygen enriched atmospheres, pressure suit operation, medical monitoring, three-axis motion, life support, and flight simulation are all approached in this facility. A brief introduction to the philosophy of operation will set the stage for a discussion of the chamber design and capability. The state-of-the-art now permits more serious application of space simulation technology to a wider market in the areas of education and research.

"The paper work and background research are sometimes staggering. You never appreciate them until a full flight test is running."

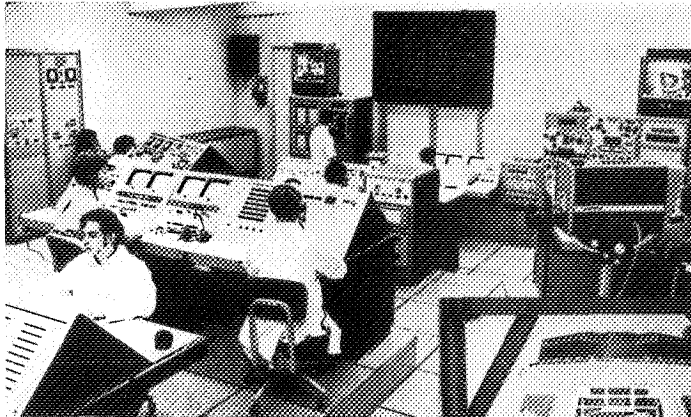


Flammability tests under varying altitude environments qualify materials. A seemingly endless number of checking procedures are part of the quality control system.

Project SPARC, Northeast High School, Cottman and Algon Avenues, Philadelphia, Pa. 19111

Interim Pictorial Report 1970

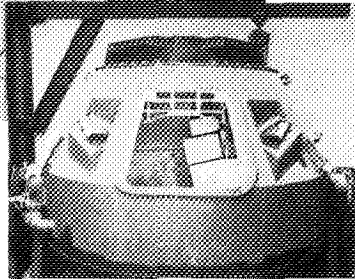




Those who are familiar with the original Systems Evaluation Facility will be amazed at this growth.

"High school was never like this."

Control room facilities are undergoing operational checkout while the Apollo (Command Module) attitude chamber is under construction. The Apollo simulator will also provide three axis motion. Control stations include: Master Control, Observation Board, Environmental Control, Medical Monitor, Flight Simulation and Data Acquisition.



Spin table tests on the Student Astronauts provide valuable medical detail for the continuing studies with Jeanes Hospital. Careful design and planning are paramount to any research activity.



VACUUM STABILITY TESTING OF APOLLO 15 SCIENTIFIC INSTRUMENT MODULE (SIM) NON-METALLIC MATERIALS AND REVERSION OF SILICONE RUBBER IN A MOTOR SWITCH

H. M. Clancy, *North American Rockwell, Downey, California*

ABSTRACT

Vacuum stability screening tests were performed on the Apollo 15 Scientific Instrument Module (SIM) bay non-metallic materials in accordance with the NASA document SP-R-0022. The testing was necessary to support the evaluation to determine the effect material outgassing contamination would have on the SIM bay optical lenses and sensing devices. The Apollo 15 SIM experiments were reported to be highly successful, therefore, it is assumed that contamination due to the outgassing of non-metallic materials did not affect equipment operation. A related problem, the reversion of a silicone rubber grommet which affected a electrical motor switch operation is also reported.

1. INTRODUCTION

The concern for materials outgassing under space conditions and the subsequent contamination of windows or critical instruments was expressed from the beginning of the space program. It took the problems of Gemini, Apollo and the work of JPL to demonstrate that optical surface contamination was real. Gemini showed the "gross" contamination potential of rocket engine exhaust (See Figure 1) and convinced the Apollo designers that a boost cover was necessary to protect the windows and thermal control coating from the plume of the launch escape tower when jettisoned.

Now that this gross contamination potential had been resolved, more subtle problems arose. This was dramatically illustrated when Apollo 8 orbited the moon for the first time but was unable to take photographs or television pictures through the large window as the result of contamination from silicone rubber seals. The pictures were then taken from a less contaminated but smaller window. Meanwhile, a test was developed by JPL to demonstrate the materials contamination potential for the unmanned spacecraft since it would be more sensitive to operational problems not having the man present to provide the correction factor.

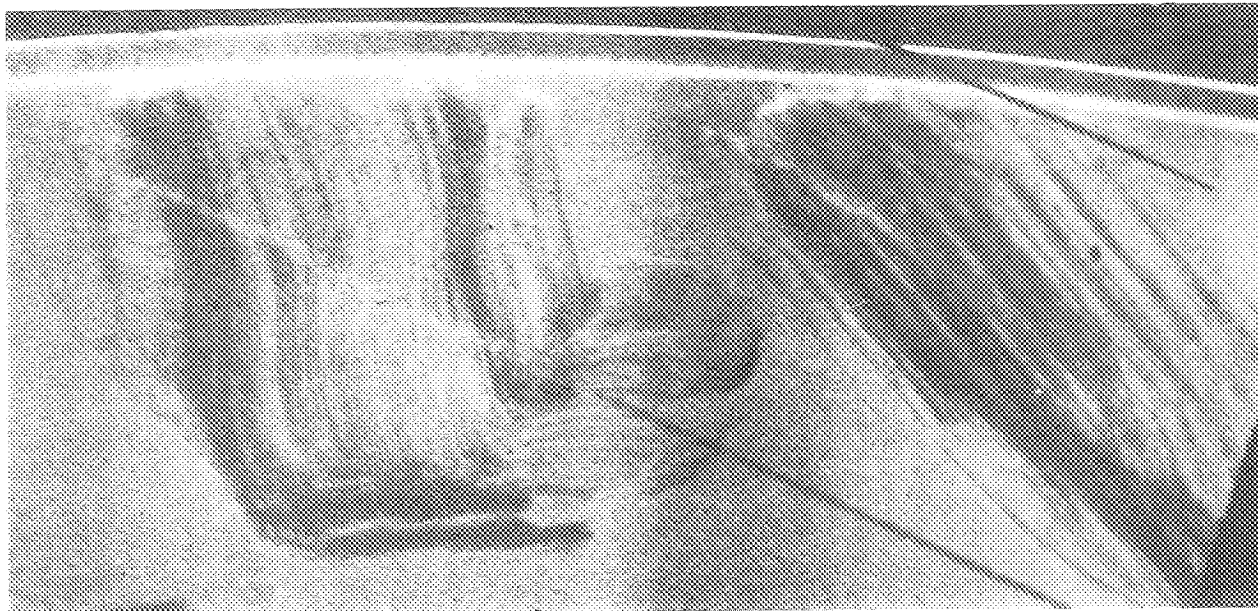


FIGURE 1 SPACECRAFT WINDOW CONTAMINATION

With this test came a new space age acronym, "VCM" meaning volatile condensable material which describes the contaminant deposited on the critical surface. While JPL provided the impetus and set the course for materials testing, it remained for a large program like Apollo to broadly implement the requirement for all nonmetallic materials used in the SIM (Scientific Instrument Module) (See Figure 2) on Apollo 15, 16 and 17. The first such flight of Apollo 15 became fantastically successful when for the first time the discoveries from the orbiting spacecraft rivaled those made on the lunar surface. However, as with the broad application of any principle, many problems arose and deficiencies in the VCM testing concept were identified. This paper describes the control of materials within the SIM and the successful contribution of this effort to the Apollo program.

The VCM problem was not limited to optics as shown when Apollo 14 had a mysterious failure of a hermetically sealed motor switch during flight. Another such failure occurred while Apollo 15 was undergoing check out. The motor switch was in general use throughout the spacecraft. Examination of early supplier tests found several other such mysterious motor failures wherein the switch would not transfer. An in-depth investigation was initiated and showed contaminants which were the petroleum based lubricant used on the motor bearings and a silicone oil similar to that found on Apollo 8 windows. The silicone oil contaminant was traced to a tiny wire grommet smaller than a pea which had been cut from a sheet of cast RTV. The RTV had received only a room temperature cure and under the heat of the motor operation reverted, giving a low molecular weight gas phase silicone which condensed on all internal surfaces. Test motors were run with the petroleum based lubrication intentionally applied to the motor armature. Similar tests were conducted with the oil from reverted RTV. The operation was normal if not slightly improved with lubricant but erratic with the silicone oil and a varnish like track deposited on the armature surface underneath the brushes, similar to that seen on failed motors.

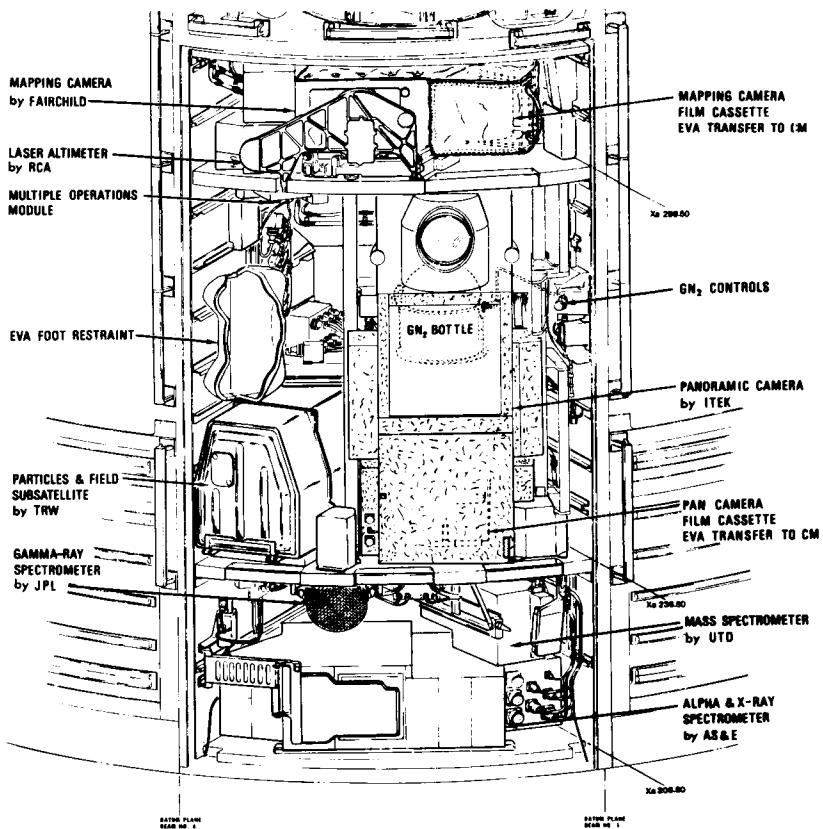


FIGURE 2 APOLLO 15 SCIENTIFIC INSTRUMENT MODULE

This report is divided into the following phases:

Phase I. Outgassing Properties of SIM Bay Nonmetallic Materials

- A. Obtaining outgassing data on the Apollo SIM Bay nonmetallic materials in accordance with the requirements specified in the Reference (a) NASA document.
- B. Establishing groundrules for certain small quantities of materials that could not meet the outgassing requirements, but would not present any contamination problem during flight.
- C. Establishing preconditioning procedures for relative large amounts of material that did not meet the outgassing requirements.

Phase II. Motor Switch Problem - Silicone Rubber Reversion

- A. Investigation of the failure of motor switch.
- B. Development of a test to duplicate silicone effect in erratic motor switch operation.

2. Phase I - Outgassing Properties of SIM Bay Nonmetallic Materials

2.1 Testing Scope

Early in the plan to add a SIM to Apollo, NASA wrote a specification, (Reference a) for the testing and acceptance of materials. The test, patterned after the JPL test, consisted of exposing a material sample to 250F under vacuum for 24 hours while collecting outgassed products on a plate at 70F. The acceptance criteria was 1% weight loss and 0.1% VCM. Early in the material test program three elements of the test were found to be critical. One was the development of a simple, low cost technique wherein a large number of materials could be gang tested. The second consideration was test accuracy providing for minimal handling of the samples and the third was sample configuration. A test technique satisfying these requirements was devised and consisted of using split test tubes with lapped surfaces. The upper section of the test tube (See Figure 3) was used as the VCM collector surface, the

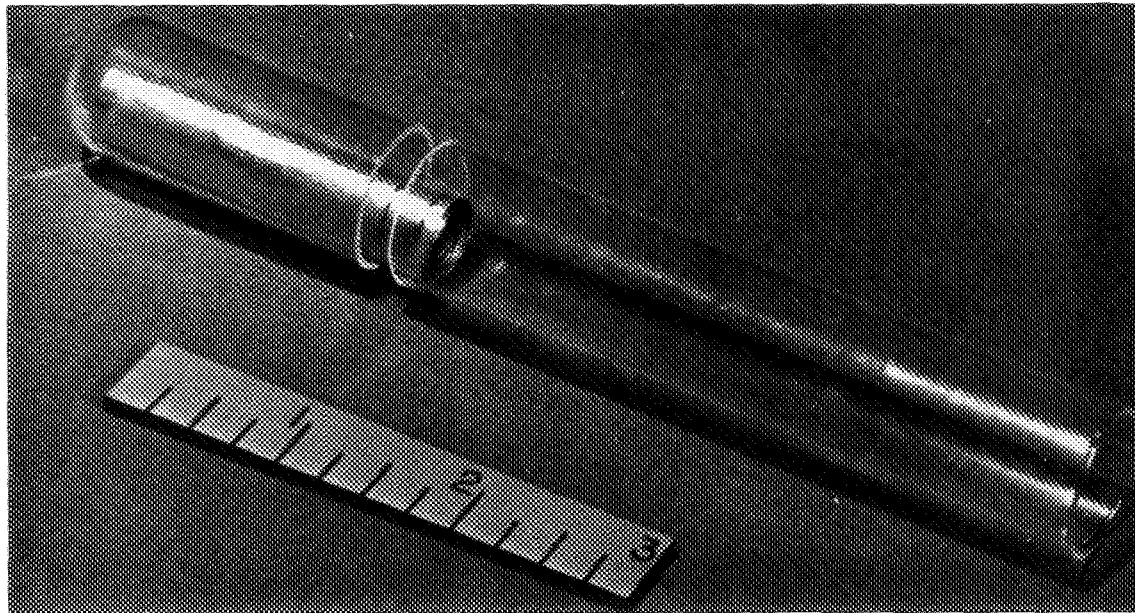


FIGURE 3 SPLIT TEST TUBE WITH ALUMINUM FOIL TEST SAMPLE

lower half of the test tube as a liner for the heating block containing the samples. At the conclusion of the test, the block was allowed to cool under vacuum and the system then back filled to 1 atmosphere with dry nitrogen. Sample tubes and VCM tubes were dessicated after test until the final weighings were made. Specimen configuration was found to be particularly critical on coating materials which had been applied to a screen, according to the original procedure. The coating was usually too thick, trapping thinners and giving high VCM results. This problem was corrected by applying the coating to an aluminum foil substrate per the applicable production specification and then placing the coiled specimen in the test tube. Samples like tapes were tested in their use configuration with the sticky side down on an aluminum strip.

2.2 Special Considerations

Early in the material control program it became apparent that many materials in wide use by both NR and its subcontractors could not meet the VCM requirements. Most of these materials were in limited use and constituted more of a nuisance than a contamination potential. Typical of these materials was marking ink which by the nature of its solvent would not meet weight loss or VCM and yet whose total quantity was negligible. As the result, the so-called "area rules" were generated by NR and NASA for the disposition of applicable cases:

These rules are:

1. The material application is under 2 inches of surface area; the material has less than 3% weight loss and 1% VCM and is not in line of sight of critical surfaces or
2. The material application is under 0.25 square inches and not in line of sight of critical surfaces. In this case there is no limit on weight loss or VCM.

Materials which exceed the basic criteria and area rule are the subject of a program deviation.

2.3 Special Tests

It is difficult to accept the restriction and narrow scope of the standard VCM criteria as discussed above. Consider the designer or program manager who says, "Yes, I know its a standard test that run at 250F but this material never gets over 130F", or who asks, "What amount of condensate can I expect on my optics operating at 40F?" The area rule was the first attempt to add some realism to the acceptance criteria. NR's next solution, although on a limited scale, was to test four selected materials at the sample temperature of 130F and with the collector at 40F and measure the degree of contamination with a nephelometer. These optic tests were conducted for NR by Ball Brothers. Both organizations, NR and Ball Brothers, conducted vacuum stability tests on duplicate samples that were prepared by NR for comparative purposes.

2.4 Standard VCM Equipment Operation and Description (Reference b)

Vacuum system components consisted of an Ultek 400 liter per second pump and a 15CFM Welch rough pump. The vacuum chamber was an 18-inch diameter bell jar of 113 liters internal volume. Base plate and collar were an integral unit from Ultek. Cooling water, electrical power, thermocouples, and vacuum gauge were led into the bell jar through vacuum feedthroughs at the collar. A Phillips vacuum gauge was used for monitoring chamber pressure. Chamber pressure for all tests was less than 10^{-7} mm.

The heating and cooling blocks were fabricated from copper with positions drilled for eleven sample tubes. The hot block was heated by two 115 VAC Cal Rod heaters. Temperature control was accomplished with a 115 VAC Variac. Prior to beginning of testing, the Variac input setting was calibrated for $125 \pm 1^\circ\text{C}$ under simulated test conditions: pressure less than 10^{-7} mm, sample tubes placed in all heating block positions. The Variac setting providing 125°C was obtained by measuring temperatures from the thermocouples suspended into sample tubes at depths simulating test specimens.

Cooling was accomplished with non-recycled plant cooling water. The water temperature of this system was usually

22-24C, but by restricting flow on the outlet side the cooling block temperature was consistently maintained at $25 \pm 1\text{C}$ with the chamber of test pressure and the heating block at test temperature. Cooling block temperature was verified in the same manner as the heating block, by two thermocouples suspended into the centers of two sample tubes in the area of cooling.

During the test, the heating block was monitored for average temperature with iron-constantan thermocouples mounted at the midpoint of the block face and equally spaced along its length. The cooling block temperature was monitored in a similar fashion. A two pen recorder was used to monitor temperature continuously during test. A test system schematic is presented in Figure 4 and the heating and cooling block is shown in Figure 5.

2.5 Sample Preparation

Test sample preparation was carried out per Reference (a) except for those cases in which a configurational test was required. Solid materials were usually tested without further processing, the sample being cut into approximately 1/16-inch pieces. Coatings and related materials were processed per applicable specification, applied by dipping to a cylinder fabricated from 100 mesh stainless steel screen, and then cured as required by the specification. Cylinder dimensions were 1.5-inches in length by 0.5-inches in diameter. The cylinders were vapor degrease and oven dried prior to coating. Test sample weight was maintained between 100 to 200 mg in all cases except configurational tests. The method used for processing each of the materials tested is presented, for convenience, with the discussion of results in Tables I thru VII.

Configurational tests refer to samples prepared and/or tested in a manner reflecting their usage on the spacecraft. The following examples are typical of configuration tests: Some of the configurations are shown in Figure '6.

1. Adhesives bonded between aluminum foil rectangles.
2. Double-back tape sandwiched between aluminum foil.
3. Half to one inch sections of elastomers and sealants.

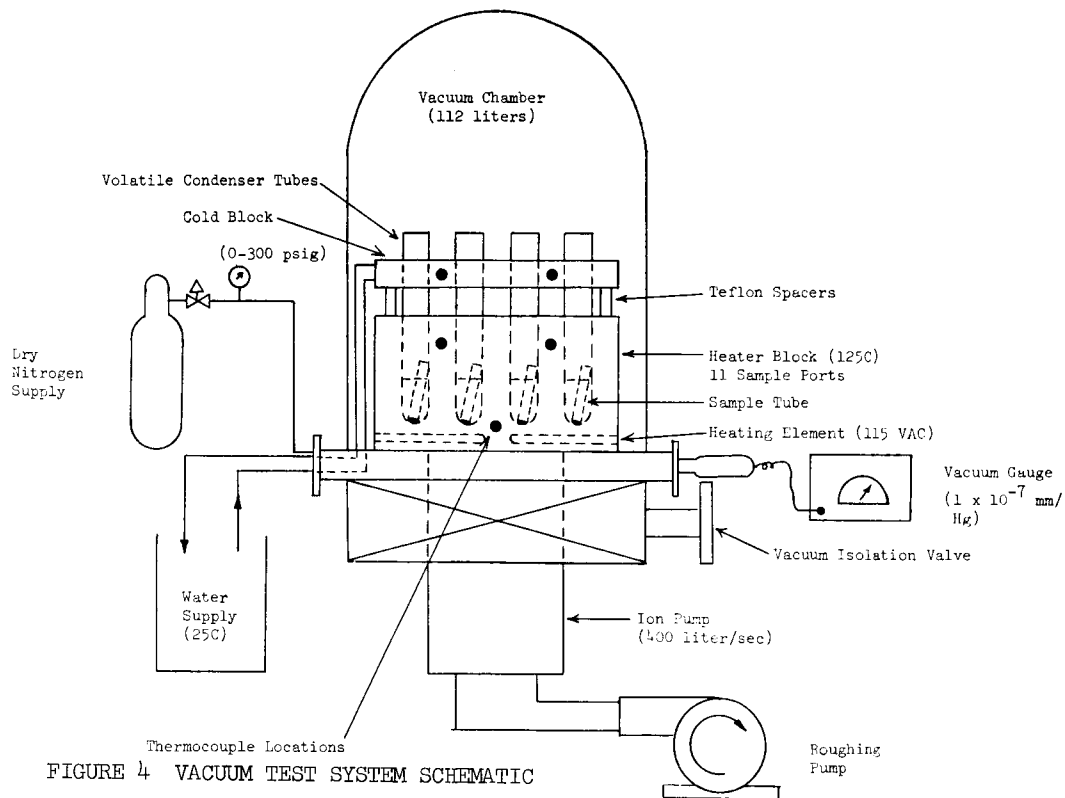


FIGURE 4 VACUUM TEST SYSTEM SCHEMATIC

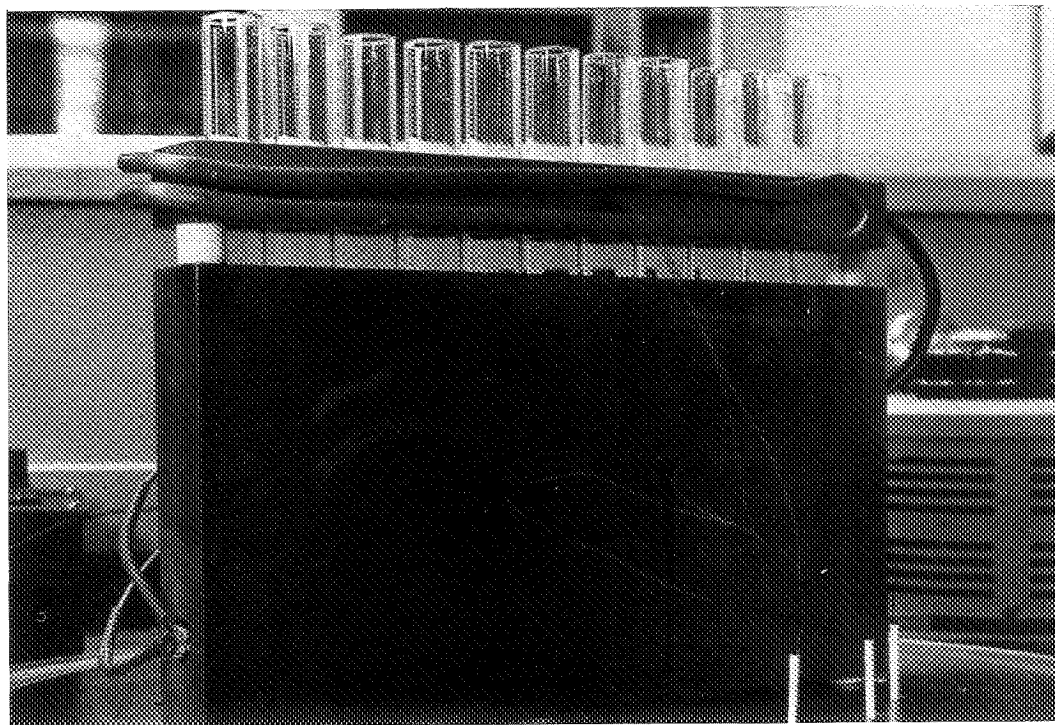


FIGURE 5 SPLIT TEST TUBE IN HEATING AND COOLING COPPER BLOCK

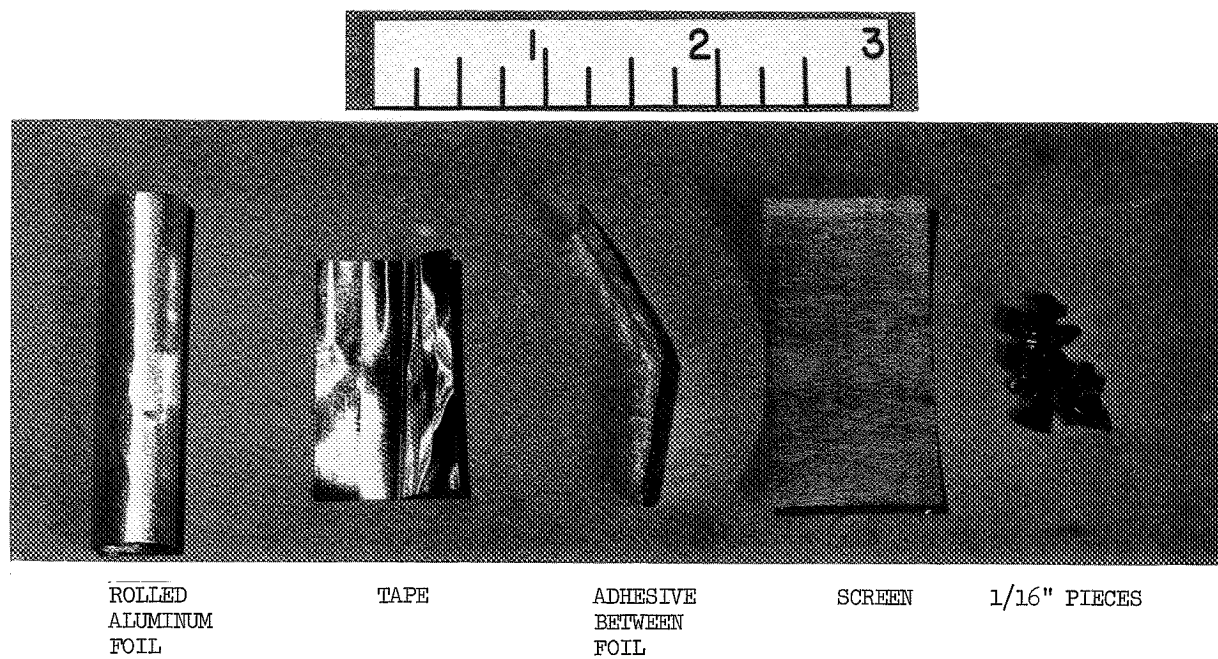


FIGURE 6 TEST SAMPLE CONFIGURATIONS

4. Silicone rubber wrapped with low VCM tape.
5. Tape bonded to aluminum foil.
6. Coatings applied to aluminum foil.

2.6 Test Methods

In the early part of the test program the samples were suspended by a thin wire in a test tube. Cahn balance pans were used for holding the small pieces of solid samples. The samples were suspended from rigid aluminum rods screwed into aluminum caps which had been machined to fit loosely in the tops of the lipless test tubes. The length of the support rods and the thin wires were such that the samples were well within the area of the heating block. Tare weights for the pans and screens and sample weights were obtained on a Mettler Microbalance. The VCM collector tubes were weighed on a 0.1 mg Sartorius balance. The weight of the collector tubes was greater than the 20 gm maximum capacity of the microbalance.

In order to reduce the VCM tube weights to values weighable on the microbalance, the test technique was modified. The original VCM tubes were cut into two sections (See Figure 3). One section of 4-inches in length was used as the VCM collector tube. The remaining 2-inch section was used as a liner for the heating block. The position of the interface between the two sections was one inch below the top of the heating block. The liners and VCM tubes were numbered with respect to each other and their position in the heating block. Lapping the two tubes together and maintaining position relative to each other yielded a good butt joint seal. The VCM tubes were covered loosely during test with a small piece of aluminum foil. A record of VCM tube weights was also kept for the remainder of the test program as a means of eliminating random weighing errors. Percent weight loss and percent VCM were calculated in the usual manner. The test period, 24 hours, was considered to begin when heating block temperature reached 125C at a chamber

pressure less than 10^{-7} mm. At the conclusion of test, the block was allowed to cool to 50C under vacuum and the system then back filled to 1 atmosphere with dry nitrogen gas. Sample tubes and VCM tubes were dessicated after test until the final weighings were made.

2.7 Discussion of Results

Test results are presented in Tables I thru VII. For ease in data comparison, the materials were organized in tables based on one of the following generic types:

<u>Table</u>	<u>Generic Type</u>
I	Adhesive and Potting Compounds
II	Elastomers
III	Foams
IV	Lubricant
V	Plastics
VI	Primers, Coatings and Ink
VII	Tapes and Films

A silicone rubber that serves as a clamp cushion is used to secure wire bundles in the spacecraft was tested in various configurations 1/16" pieces, one piece (1.5 inches long) and one piece covered with a pressure sensitive tape coat has low outgassing properties (See Table II).

Sample configuration was not a factor that decided if one silicone rubber failed or passed the outgassing requirement, but the particular piece of silicone rubber that was tested. Both the 1/16" pieces and one piece samples passed and failed the 1% weight loss and 0.1% VCM. Since a large number of these clamps were used in the SIM Bay, they were preconditioned at 275°F for 48 hours at a vacuum of 10^{-4} in order that they would consistently meet the outgassing requirements. This preconditioning was also necessary with a urethane door seal and silicone rubber mount material (See Table III). Table IV lists different types of lubricants that were tested, dry film and greases. With only one exception, one dry film coating meets the outgassing requirements provided they were baked between 300-400°F. The greases did not meet the outgassing

requirements. The epoxy-amine coating meets the outgassing requirement by using an aluminum foil as a substrate in place of a screen (See Table VI). Data variations in duplicate runs were most pronounced with coatings and related materials that required processing. Even though support screens were identical in surface area, the two samples were from the same coating mix, uniform coating thickness could not be achieved when meeting the sample weight requirement of 100 to 200 mg.

Besides non-uniformity, the coating thickness on the screen is many times that specified for spacecraft usage. The Andrew Brown coating (Table VI) at the 1 mil maximum thickness allowed for the spacecraft, had an approximate weight of 4 mg on a support screen.

With materials such as the Andrew Brown (Table VI) with specified 24 hour air dry cures, the overly thick coating can result in a material being tested which is neither completely cured nor free of higher boiling solvents such as amyl acetate or cellosolve acetate. Differential Thermal Analysis (DTA) studies done in the Physical Chemistry Lab on several thick air dry ablative coatings has shown this to be the rule rather than the exception. After one month, one of the coatings still had two high boiling solvents present.

TABLE I
ADHESIVES AND POTTING COMPOUNDS
OUTGASSING TEST RESULTS
TESTED PER NASA SPEC. SP-R-0022

TRADE NAME AND NUMBER	MANUFACTURER	TYPE OF ADHESIVE OR POTTING COMPOUND	SAMPLE PREPARATION	PERCENT ⁽¹⁾	
				WEIGHT LOSS	VCM
Epoxylite 203	Epoxylite	Epoxy	Screen	1.76	0.28
Epon 828/Versamide 115	Shell/General Mills	Epoxy/Polyamide	Screen	1.00	0.05
APCO 320/CORFIL 615	Bloomingtondale	Epoxy	Sandwiched between aluminum foil	1.19	0
APCO 320/CORFIL 615	Bloomingtondale	Epoxy	1/16" pieces cut from production part	0.47	0.
6-1015 Adhesive	Organocerams	Neoprene	Screen	2.91	1.32
DPS-142	Deutsch	RTV Silicone	Screen	0.20	0.07
DPS-181	Deutsch	RTV Silicone	Screen	0.17	0
PR 1710 Adhesive	Products Research	Viton	Sandwiched between two pieces of aluminum foil	19.1	0

TABLE I (CONTINUED)

TRADE NAME AND NUMBER	MANUFACTURER	TYPE OF ADHESIVE OF POTTING COMPOUND	SAMPLE PREPARATION	PERCENT(1)	
				WEIGHT LOSS	VCM
Corfil 615/DTA Adhesive	Bloomingtondale	Epoxy	Sandwich between 2 pieces of aluminum foil	0.80	0
HT 424 Adhesive	Bloomingtondale	Epoxy/Phenolic	Sandwich between 2 pieces of aluminum foil	0.25	0
Epon 954 Adhesive	Shell Co.	Epoxy	Sandwich between 2 pieces of aluminum foil	0.35	.04
RTV-560	General Electric	Silicone Rubber, RTV	Screen	1.20	0.44
DC92-018	Dow Corning	Silicone Rubber	Screen	1.15	0.81

(1) Average of two specimens.

TABLE II
ELASTOMERS
OUTGASSING TEST RESULTS
TESTED PER NASA SPEC SP-R-0022

TRADE NAME AND NUMBER	MANUFACTURER	TYPE OF RUBBER	SAMPLE PREPARATION	PERCENT(1)	
				WEIGHT LOSS	VCM
B612-70 Rubber	Parker Seal Co.	Butyl	1/16" pieces	0.76	0.35
MIL-R3065 Rubber	Adel	Silicone	1/16" pieces	0.92	0.58
MIL-R-3065 Rubber	Adel	Silicone	1/16" pieces	0.34	0.05
MIL-R-3065 Rubber	Adel	Silicone	1.5" length of clamp cushion	0.55	0.28
MIL-R-3065 Rubber	Adel	Silicone	1.5" length of clamp cushion	0.40	0.07
MIL-R-3065 Rubber Mystik Tape 7455	Adel	Silicone	1.5" length of clamp cushion wrapped with mystik tape	0.64	0
G-2072-4 Rubber	L. A. Standard	Silicone	1/16" pieces	0.67	0.12

TABLE II (CONTINUED)

TRADE NAME	MANUFACTURER	TYPE OF RUBBER	SAMPLE PREPARATION	PERCENT(1) WEIGHT LOSS	VCM
R-10470 Sponge AMS-3195	Connecticut	Silicone	1/16" pieces	0.06	0.03
SM3500-41	Cannon	Silicone	1/16" pieces	0.32	0.03
DPS-118	Deutsch Co.	Silicone	1/16" pieces	0.11	0.02
DMSI-123-05	Deutsch Co.	Silicone	1/16" pieces	0.22	0.04
DC6-1104	Dow Corning	Silicone	1/16" pieces	0.10	0.02
DC-651	Dow Corning	Silicone	1/16" pieces	0.04	0
Fluorel RL-2060	Raybestos Manhattan	Fluorocarbon	1/16" pieces	1.40	0.75
Florel RL-3603	Raybestos Manhattan	Fluorocarbon	1/16" pieces	0.30	-

(1) Results are an average of two specimens.

TABLE III
FOAMS
OUTGASSING TEST RESULTS
TESTED PER NASA SPEC SP-R-0022

TRADE NAME AND NUMBER	MANUFACTURER	TYPE OF FOAM	SAMPLE PREPARATION	PERCENT(1)	
				WEIGHT LOSS	VCM
9811-25	CPR Division Upjohn	Urethane	1/16" pieces	5.86	3.96
9811-25	CPR Division Upjohn	Urethane	1/16" pieces, vacuum baked at 125°C for 48 hours at 1×10^{-6} mm/hg	0.56	0
Barry Shock Mount	Barry Controls	Silicone Rubber	1/16" pieces	1.52	.35
Barry Shock Mount	Barry Controls	Silicone Rubber	1/16" pieces, vacuum baked for 24 hours at 125°C and 1×10^{-6} mm/hg	0.30	0.16
Barry Shock Mount	Barry Controls	Silicone Rubber	1/16" pieces, vacuum baked for 48 hours at 125°C and 1×10^{-6} mm/hg	0	0

(1) Average of a minimum of 3 samples.

TABLE IV
LUBRICANTS
OUTGASSING TEST RESULTS
MATERIALS APPLIED TO 1" x 2" STAINLESS STEEL SCREEN
TESTED PER NASA SPEC. SP-R-0022

TRADE NAME AND NUMBER	MANUFACTURER	TYPE OF LUBRICANT	SAMPLE PREPARATION	PERCENT(1)	
				WEIGHT LOSS	VCM
Molykote 321	Dow Corning	MoS ₂ Inorganic Binder	RT - 72 hour	2.54	2.15
Lubeco 905	Lubeco	MoS ₂ Inorganic Binder	260°F-3.5 hour	2.04	0
Lubeco N35UA	Lubeco	MoS ₂ Organic Binder	240°F - 3 hour	1.12	.19
Emralon 312	Acheson	MoS ₂ -Organic Binder	300°F - 0.5 hour	0.65	0
Molykote 106	Dow Corning	MoS ₂ -Organic Binder	300°F - 1 hour	1.23	.29
Electrofilm 5896	Electrofilm	MoS ₂ -Organic Binder	400°F- 1 hour	0.32	0

TABLE IV (CONTINUED)

TRADE NAME AND NUMBER	MANUFACTURER	TYPE OF LUBRICANT	SAMPLE PREPARATION	PERCENT (1)	
				WEIGHT LOSS	VCM
Everlube 620	Everlube	MoS ₂ -Organic Binder	400°F - 1 hour 400°F - 1 hour	0.18	0
DAG 244	Acheson	Graphite	300°F - 1 hour	0.67	0
Krytox 240 AC	Dupont	Fluorinated Grease	None	7.68	6.01
DC20-057	Dow Corning	Silicone Grease	None	2.28	.64
DC 55 Pneumatic	Dow Corning	Silicone	None	17.9	5.97

(1) Average of 2 test samples.

TABLE V
PLASTICS
OUTGASSING TEST RESULTS
TESTED PER NASA SPEC. SP-R-0022

TRADE NAME AND NUMBER	MANUFACTURER	TYPE OF PLASTIC	SAMPLE PREPARATION	PERCENT (1)	
				WEIGHT LOSS	VCM
Laminate - MIL-P-79, Type FBG, Grade CE	Synthane - Taylor	Cotton Base - Phenolic	1/16" pieces	0.41	0.06
Thermofit RNF 100 Heat Shrink Tubing	Rayclad	Irradiated	1/16" pieces	0.56	0.24

TABLE VI
PRIMERS, COATINGS AND INK
OUTGASSING TEST RESULTS
TESTED PER NASA SPEC. SP-R-0022

TRADE NAME AND NUMBER	MANUFACTURER	TYPE OF PRIMER, COATING OR INK	SAMPLE PREPARATION	PERCENT (1) WEIGHT LOSS	VCM
A423/T252 Coating	Andrew Brown	Epoxy - Amine	Screen	9.46	0.25
A423/T252	Andrew Brown	Epoxy - Amine	Aluminum Foil	1.00	0.02
X73 Marking Ink	Independent Ink Co.	-	Screen	5.52	1.45
X73 Marking Ink	Independent Ink Co.	-	Aluminum	6.8	0.7
Fluorel, CTGL 3202-6	Raybestos Manhattan	Fluorocarbon	Screen	1.67	0.09
Velvet Coat	3M	Polyester	Aluminum Foil	4.25	0.08
Torque Stripe	Semco	Polyester	Aluminum Foil	2.17	0.09

TABLE VI (CONTINUED)

TRADE NAME AND NUMBER	MANUFACTURER	TYPE OF PRIMER, COATING OR INK	SAMPLE PREPARATION	PERCENT(1) WEIGHT LOSS	VCM
DC92-007 Thermal Coating	Finch		Aluminum Foil Pre-conditioned 24 hours at 125°C, 10 ⁻⁶ vacuum	.25	0.3
M-602 Bondmaster Primer	Pittsburg Plate Glass		Screen	0.84	.04
Chemlock 205	Hughson Chemical		Screen	5.29	1.72

(1) Average of at least two specimens

TABLE VII
TAPES AND FILM
OUTGASSING TEST RESULTS
TESTED PER NASA SPEC. SP-R-0022

TRADE NAME AND NUMBER	MANUFACTURER	TYPE OF TAPE OR FILM	SAMPLE PREPARATION	PERCENT (1)	
				WEIGHT LOSS	VCM
Velcro, Hook, No. 65	American Velcro	Nylon Polyamide	1/16" pieces	1.33	0.30
Velcro, Pile Standard	American Velcro	Nylon Polyamide	1/16" pieces	1.96	0
Velcro, 80 Hook	American Velcro	Polyester/Urethane Binder	1/16" pieces	0.44	0.23
Velcro, 1000 Loop	American Velcro	Polyester/Urethane Binder	1/16" pieces	0.47	0.28
Mylar, Type A	Dupont	Polyester	1/16" pieces	0.20	0
Mystik Tape 7455	Borden Chem. Co.		Two pieces mated together at adhesive side	0.74	0

TABLE VII (CONTINUED)

TRADE NAME AND NUMBER	MANUFACTURER	TYPE OF TAPE OR FILM	SAMPLE PREPARATION	PERCENT (1)	
				WEIGHT LOSS	VCM
Mystik Tape 7361	Borden Chem. Co	Teflon	Two pieces mated together at adhesive side	0.45	0
467 Adhesive Transfer Tape	3M		Tape placed between 2 pieces of aluminum foil	0.96	0
Mystik Tape No. 7503	Borden Chem. Co.		Two pieces mated together at adhesive side	0.10	0
Nomex Tape TIE HT-30LOC-B	Bentley - Harris		1/16" pieces	0.56	0

(1) Results are the average of two samples.

2.8 Comparative Study with Ball Brothers Research Co.

In order to determine the agreement or differences that exist between data generated by NR and a recognized testing agency such as Ball Brothers, both facilities conducted vacuum stability tests on duplicate samples that were prepared by NR. The program conducted by both facilities included testing their samples at temperatures that simulate the environment; the nonmetallic materials will be exposed to in the Apollo Scientific Instrument Module (SIM). During space flight, the SIM materials will be exposed to a maximum temperature of 130°F with critical optical surface temperature of 40°F. As a result of the flight temperatures being lower than the standard test temperatures, four typical SIM nonmetallic materials were tested to obtain the following information:

1. The effect of the lower material outgassing temperature (130°F) on sample weight loss.
2. The effect of the lower collector temperature (40°F) on VCM.
3. Determine the effects of forward light scatter caused by outgassing products condensing on the collector (optical surface). The Ball Brothers Research Corporation (BBRC) has developed a nephelometer to measure the amount of forward light scatter caused by outgassing products condensed on the collector. Results obtained with the nephelometer are used in addition to VCM data obtained by the standard test to determine if a material is suitable for space application. It was requested that nephelometer data be obtained on NR test samples to determine how they compared with BBRC material acceptance guidelines.

There is a considerable difference between the NR equipment (see Section 2.4) and the Ball Brothers vacuum testing equipment. A schematic of the Ball Brothers vacuum exposure chamber is shown in Figure 7. The NR sample is placed in the bottom part of a split test tube and the VCM is collected in the upper half of the test tube. The Ball Brothers sample is placed in a cup that is heated and the VCM deposits on a collector disk that is in sight of the heated material.

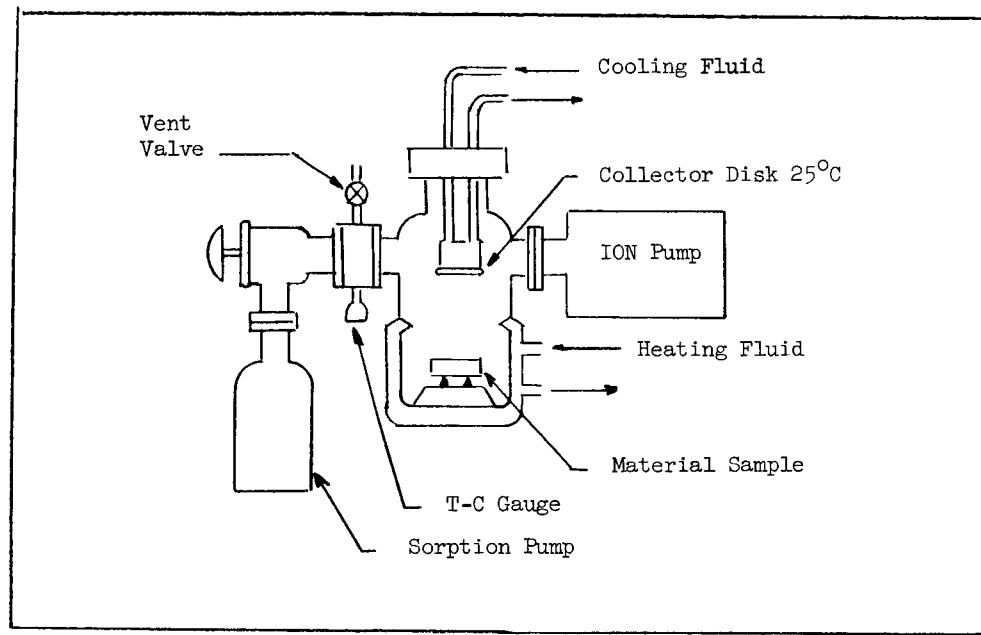


FIGURE 7 SCHEMATIC OF VACUUM EXPOSURE CHAMBER

Test results were obtained on Velcro, epoxy coating, neoprene adhesive and silicone rubber. The lower flight material temperature of 130 F significantly decreased the epoxy coating and neoprene adhesive percent weight loss and the VCM test results (see Table VIII). Both of these materials would have a higher weight loss at the higher standard test temperature of 275°F since they contain residual solvents.

The lower critical surface (collector)flight temperature of 40°F did not affect the VCM results for all the materials tested. The 77°F and 40°F collector temperature VCM results were similar for materials heated at 130°F. This is important data since the VCM is that portion of the material weight loss that contaminates an optical lens during flight.

Both Ball Brothers and NR tested the same four materials at simulated flight temperatures. Ball Brothers verified NR results since data were comparable at both testing laboratories (See Table IX) for the silicone rubber and Velcro material. The nephelometer data (See Table X) indicates that there is a greater amount of light scattering at the lower 5°C (40°F) flight than the higher 25°C (77°F) test condensing temperatures for only the Velcro and silicone rubber. Ball Brothers reported in Reference (c) that the nephelometer data indicates that the silicone rubber and Velcro did not meet their nephelometer requirements, therefore, both materials should be baked prior to installation in the spacecraft.

TABLE VIII

VACUUM STABILITY TESTS - NR DATA (1)

MATERIAL (1)	°F HEATING/COLLECTOR TEMPERATURES					
	% Weight Loss			% VCM		
	257/77	130/77	130/40	257/77	130/77	130/140
Velcro, Hook, Nylon No. 65	1.95	1.83	1.89	0	0.07	0.09
Epoxy Coating, MB0125-033	9.46	1.89	1.46	0.25	0.03	(2)
Neoprene Adhesive, MB0120-028	2.89	0.72	0.75	2.09	0.05	(2)
MB0120-028 Silicone Rubber, ZZ-R-765	0.20	0.20	0.18	0.01	0.03	0.04

(1) Data - Based on the average of two test samples.

(2) Loss of temperature control during test.

TABLE IX

NR AND BALL BROS. DATA VACUUM STABILITY TEST RESULTS

MATERIAL	% WGT. LOSS HEATING TEMP.		% VCM CONDENSING TEMP.			
	130°F		+40°F		+77°F	
	BALL	NR(1)	BALL	NR(1)	BALL	NR(1)
Velcro, Hook, Nylon No. 65	2.10	1.86	0.07	0.09	0.04	0.07
Epoxy Coating, MB0125-033	4.63 ⁽³⁾	1.68 ⁽³⁾	0.02	(2)	0	0.03
Neoprene Adhesive, MB0120-028	2.81 ⁽³⁾	0.74 ⁽³⁾	0.04	(2)	0	0.05
Silicone Rubber, ZZ-R-765	0.25	0.19	0.02	0.04	0.04	0.03

- (1) The NR weight losses are the average of test results obtained on 4 samples. The NR VCM values are the average of test results obtained on 2 samples.
- (2) Loss of temperature control during test.
- (3) Sample configurations were different at both laboratories. The Ball Brothers 1" x 2", 100 mesh stainless steel screen samples were flat and the NR samples were a 1/2" diameter x 2" tube made from the 1" x 2", 100 mesh stainless steel screen. Apparently this is the reason for the wide difference in weight loss values for the epoxy coating and neoprene adhesive at both testing facilities.

TABLE X
BALL BROTHERS NEPHELOMETER DATA (1)

MATERIAL	Condensing Temp Millivolts	
	77°F	40°F
Velcro, Hook, Nylon No. 65	32.9	52.4
Epoxy Coating, MB0125-033	0.015	0.105
Neoprene Adhesive, MB0128-028	0.020	0.050
Silicone Rubber, ZZ-R-765	0.975	59.9

- (1) The VCM products were collected on a glass lens at Ball Brothers. The lens were placed in a nephelometer to measure the light scatter caused by the deposit of VCM products and the light scatter is measured in millivolts (MV).

2. Conclusions

2.9.1 The test equipment, methods, and sample preparations used to test in accordance with Reference (a) furnish reliable data that was useful to evaluate nonmetallic materials used in the Apollo SIM bay.

2.9.2 The following conclusions pertain to the comparative studies conducted by Ball Brothers and NR.

2.9.2.1 Lowering the material temperature from 250°F (standard) to 130°F (flight) decreased the percent weight loss results on the epoxy coating and neoprene adhesive. Similar percent weight loss results were obtained on the Velcro and silicone rubber tested at both temperatures.

2.9.2.2 The flight (40°F) and standard (77°F) test collector temperature VCM results are comparable. The lower collector temperature did not increase the VCM.

2.9.2.3 Ball Brothers test data compared closely with NR test results.

2.9.2.4 Nephelometer tests did show significant contamination for Velcro and silicone rubber whereas the VCM test did not.

3. PART II - REVERSION OF SILICONE RUBBER (Reference (d))

3.1 Motor Switch Problem

It was observed that motors which fail the qualification (See Fig tests have a thicker than normal brush track on their commutators. The brush track composition was determined to be a mixture of the motor's silver-graphite brush dust, bearing lubricant, and "silicone oil" from reverted RTV O-rings. It was hypothesized that the mode of motor failure is a buildup on the commutator of the above mixture which, being a poor conductor, results in decreased current to the armature, and, in turn, decreased motor torque.

Comparative analyses of motor brush tracks indicated that failure was not due to any contaminant that was unique between normal and failed motors, but that contaminant quantity was the

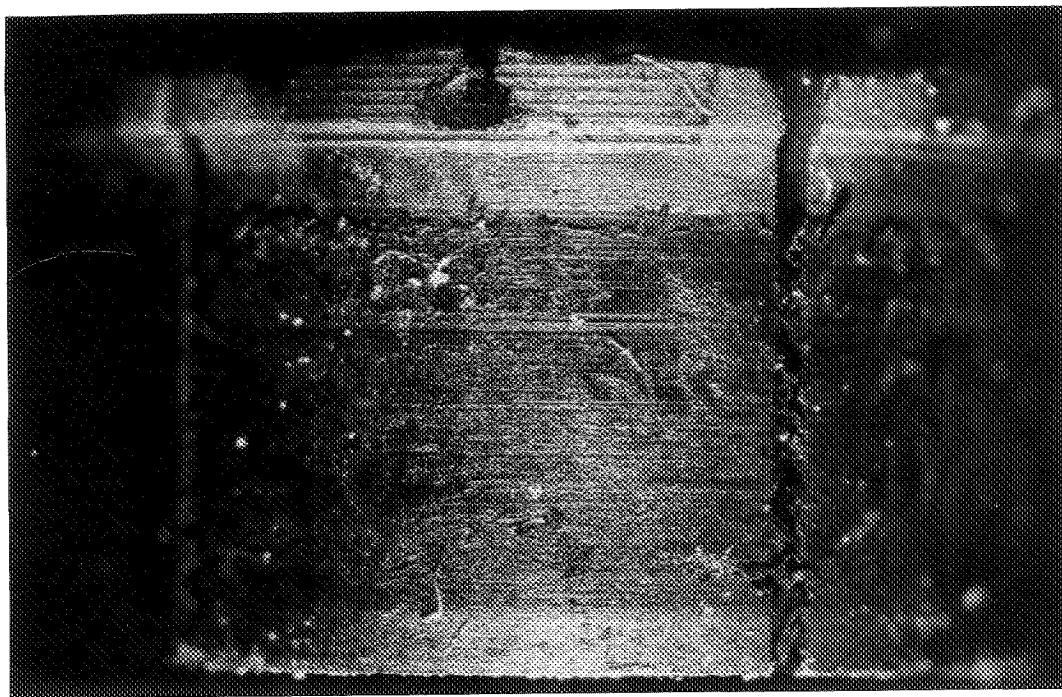


FIGURE 8 CONTAMINATED MOTOR SWITCH

key factor. Tests directed toward producing the brush track and/or erratic current traces observed in the failed motors were conducted at the suppliers with normal motors. The motor lubricant, when brushed on the commutator of a normal motor, did not produce any of the failure characteristics, but the reverted RTV silicone "oil" did produce an erratic current trace and apparent initial stages of track buildup.

In Reference (e) it was reported that a silicone rubber which contains acid or base catalyst, if heated for 24 hours at 480°F in a sealed tube, deteriorates and becomes soft and weak. This reversion is similar to the motor switch silicone rubber reversion.

Tests were performed to determine if the reverted O-ring Eccosil 4850 silicone can be repolymerized by itself or in combination with the American Oil Co. #160 lubricant under conditions of electrical arcing which occur in the switch motors. The designated conditions were 20,000 arcs at 60 arcs/second between copper and graphite-silver electrodes with a maximum current of 7 amperes in a 14.7 psia nitrogen atmosphere. Repolymerization and/or viscosity increase of the "silicone oil" and/or lubricant would present a feasible mechanism for the brush track buildup observed on the failed motors' commutators.

3.2 Tests to Simulate Problem

3.2.1 Preparation of Reverted O-Ring Type Silicone Rubber

Eccosil 4850 silicone resin procured from Emerson-Cuming, Inc. was catalyzed with 1% W of the supplied Catalyst 25, deaerated and allowed to cure overnight under ambient conditions. Strips of the cured rubber were suspended in test tubes and subjected to $400 \pm 25^\circ\text{F}$ at $< 10^{-4}$ Torr for 24-48 hours in the VCM apparatus. The reverted rubber and other volatile condensable material (VCM) that collected on the test tubes' wells was rinsed out with carbon tetrachloride (CCl_4) and combined into one portion. After the CCl_4 was allowed to evaporate, an infrared spectrophotometric analysis was conducted on the residue to verify that it was identical to the reverted silicone rubber previously found on the motor parts.

100-200 mg of the following samples were placed in the copper cup electrode of the Paragraph 2.3 arcing apparatus and subjected to 20,000 arcs of 2.5 amps to determine if there was a visible increase in viscosity:

- (a) 100% No. 160 Lubricant, American Oil Co.
- (b) 100% Reverted Eccosil 4850 from Paragraph 3.2.1.
- (c) 25-75 No. 160 - Reverted Silicone.
- (d) 75-25 No. 160 - Reverted Silicone.
- (e) 50-50 No. 160 - Reverted Silicone.
- (f) Dow Corning 200 Fluid (Dimethylpolysiloxane), 50 cs at 25°C.

3.2.2 Arcing Apparatus

An electromechanical circuit interrupter was made by modifying one pole of a two-pole single throw relay to hold the carbon brush. The relay was then hooked up in the test circuit as shown in the schematic (Figure 9).

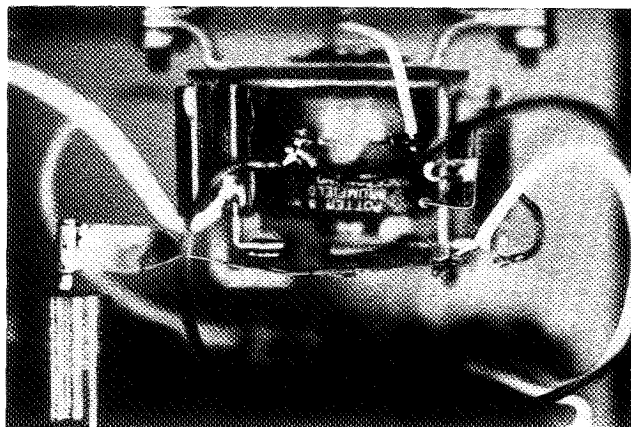
Shunting the 24 vdc relay coil with the 500 mfd capacitor resulted in a cycling rate of approximately 3 cps. Thus the 20,000 cycle test run required somewhat less than two hours for completion. The actual number of cycles was monitored with a 6 digit 28 vdc counter utilizing the unmodified contact in the test circuit. A 10 ohm resistance in the test circuit limited the current to about 2.5 amps at 28 vdc and simplified pulse current measurement with the oscilloscope, a 10 volt indication representing a current of 1 amp.

The assembly was placed in a 3 cu.ft. test chamber which was purged with nitrogen before commencing the test. The relay coil was energized and the test circuit power supply adjusted to give a current of 2.5 amps.

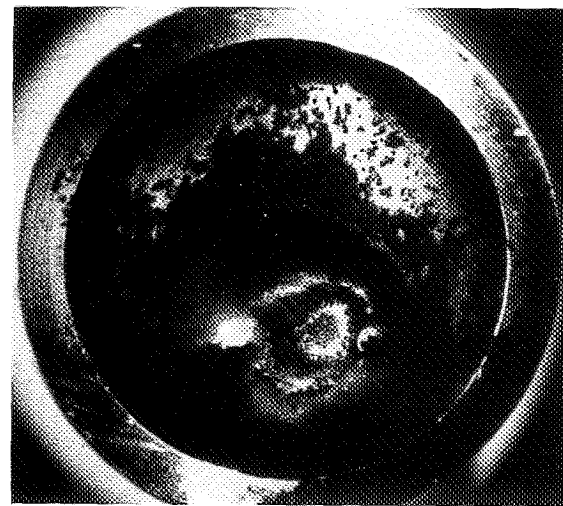
3.3 Results and Discussion:

3.3.1 100% No. 160 Lubricant

At the conclusion of arcing, there appeared to be a fine dispersion of carbon in the oil at the point of arcing surrounded by clear oil in the copper cup. There was no discernible repolymerization or viscosity increase noted by probing the oil with a needle point.



Closeup of electrical arcing mechanism - note copper cup in bottom left corner that holds liquid with graphite brush touching.



Photomicrograph (8X Mag.) of arced DC-200 fluid.

FIGURE 9 ARCING MECHANISM AND ARCED DC-200 FLUID

3.3.2 100% Reverted O-Ring Silicone "Oil"

Arcing results were the same as noted above for the lubricant.

3.3.3 25% Lubricant - 75% Reverted Silicone

The arcing produced a viscous gelatinous mass as shown in the top photo of Figure 12. Microscopic examination indicated it was a mucous-like substance (middle photo, Figure 10), filled with very fine carbon particles. It could be picked up on the needle point and possessed some elasticity as shown in the Figure 10.

3.3.4 75% Lubricant - 25% Reverted Silicone

Needle probing indicated the dispersion was a little more viscous than the original oil mixture.

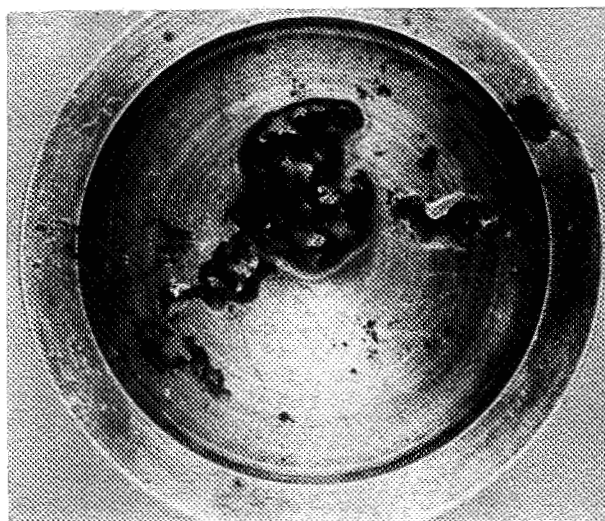
3.3.5 50% Lubricant - 50% Reverted Silicone

There was very little liquid remaining in the cup at the conclusion of the arcing, but there was a mound of carbon particles in the cup with the motor brush imprint in the center. The carbon material had the consistency of wet sand.

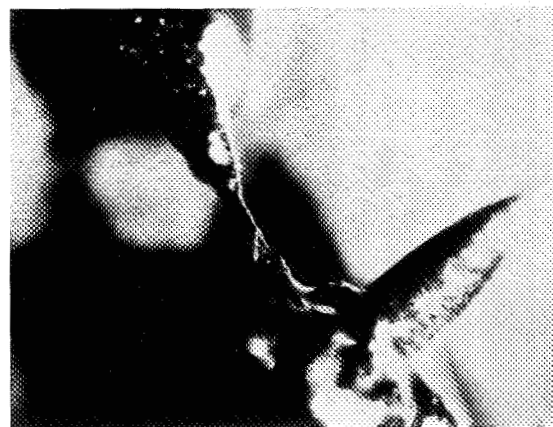
3.3.6 Dow Corning 200 Fluid (Dimethylpolysiloxane)

The investigator was curious whether a carbon dispersion would result from arcing of a commercial silicone oil, such as DC-200. In other words, was there something unique about reverted RTV or would any silicone fluid do the same thing. In test, the DC-200 produced a dispersion similar to that of the reverted RTV.

3.3.7 It was noted during the preceding tests upon microscopic examination that the carbon brushes had very little erosion, not nearly enough to account for the amount of carbon particles in the copper cups. It was suspected then that the carbon in the dispersions was not predominantly from the brushes



Photomicrograph (8X Mag.) of
arced 25-75 Lubricant-Reverted
silicone mixture.



Photomicrograph (40X Mag.) of
globule being stretched between
pin points.

FIGURE 10 DISPERSION GLOBULES PRODUCED BY ARCING

as originally assumed, but from decomposition of the liquid oils by the arcing. This was subsequently proved when a typical carbon dispersion was obtained by arcing with a copper instead of a graphite electrode (Figure 9).

4. CONCLUSION

It seems logical that this same "carbonization" of the lubricant-reverted silicone is occurring in the motors from arcing to increase the brush track.

4. ACKNOWLEDGEMENTS - Appreciation is extended to Mr. D. W. Houston, Jr. and Mr. G. J. DeMatteo of NR for the design and development of the vacuum stability equipment and conducting the tests on the SIM Bay nonmetallic materials, and to S. M. Mitchell of NR for developing a test that simulated the reverted silicone rubber that existed in the failed motor switches. Appreciation is also extended for the excellent lab reports prepared by these gentlemen which made this paper possible.

5. REFERENCES:

- Reference: (a) NASA Specification SP-R-0027, "Vacuum Stability Requirements of Polymeric Materials for Spacecraft Application"
- (b) NR Report LR 7059-4427, "Apollo Product Support - Preparation of Non-Metallic Materials for NASA/MSD Vacuum Stability Tests - Apollo "J" Missions
- (c) Ball Brothers Report. "Report on Thermal-Vacuum Contamination Tests of North American Rockwell Materials"
- (d) "NR Report LR9245-4409, "Investigation of Apollo CSM Kinetics Switch Motor Failure", dated September 29, 1971.
- (e) "Reinhold Plastics Applications Series on Silicones", by Meals and Lewis

SOME NEW TECHNIQUES IN PASSIVE CONTAMINANT ANALYSIS OF SPACE ENVIRONMENT SIMULATION CHAMBERS

C. M. Wolff, Brown & Root-Northrop, Houston, Texas

ABSTRACT

A technique in surface sampling has been developed and evaluated, the KBr pelletizing technique has been extended to include heavy oils for infrared analysis, and transmittance and specular reflectance measurements at 2000 Å wavelength have been found very sensitive to contamination.

INTRODUCTION

Passive contamination analysis involves measurement of the change in the amount of contamination, the contamination identity, and the contamination effects that occurred in a vacuum chamber during a given period, the beginning and end of which were at ambient conditions (1). Some methods of sampling for passive analysis are (a) the insertion of plates in the chamber, the faces of the plates are rinsed and the rinsings concentrated and analyzed to determine the identity and quantity of contaminants; (b) the insertion of optical surfaces in the chamber, the optical properties of the surfaces are measured before insertion and after removal; and (c) the sampling of chamber surfaces directly by swabbing. Some improvements in technique and new ideas in interpretation of data have been developed and evaluated for these three methods of passive sampling.

POTASSIUM BROMIDE PELLETIZING OF HEAVY OILS

The technique of mixing powdered solid samples with dry potassium bromide powder (KBr) and subsequent formation of a transparent or translucent pellet under high pressure has been a routine procedure for many years (2). This technique has been used primarily as a tool for qualitative analysis because the KBr material does not have absorption bands in the infrared region of the spectrum (transmittance range 0.21 to 28 microns (μ)), whereas solvents do absorb in that region.

Quantitative analysis has not been very successful with pelletized samples because of the problem of getting the sample uniformly dispersed in the medium, except when considerable time is expended in hypersonically vibrating or lyophilizing (freeze drying) the KBr-sample mixture (3). The problems in quantitative analysis are to have a technique with good repeatability of absorbance (log of inverse of transmittance) for a given quantity of sample and to have good adherence to Beer's Law (linear relationship between quantity of sample in pellet and absorbance of pellet). The latter necessity can be circumvented if calibration curves are provided, which should be done in any case to determine the performance of the technique.

The KBr pelletizing technique has been extended to include heavy oils (molecular weight of several hundred or greater, i.e., of vapor pressure below $10\ \mu$). This technique permits qualitative and quantitative analysis of volatile condensible materials deposited in vacuum chambers, such as space environment simulation chambers, being those with low enough volatility not to evaporate at ambient temperature and pressure (due to containment by collision with air molecules) but of sufficient volatility to migrate under vacuum. Liquids of greater volatility are susceptible to loss during evacuation of the KBr-contaminant mixture, which is necessary to remove air, moisture, and solvent from the pellet that would otherwise cause the pellet to become opaque or shatter upon decompression. The technique is as follows:

- a. Add from 0.3 to 0.5 milliliter (ml) of carbon tetrachloride (CCl_4) solution containing the contaminant to 250 milligrams of predried KBr powder, 200 to 350 mesh, in a small agate mortar.

- b. Grind slurry with agate pestle until solvent has evaporated (visibly), and continue to grind for several minutes.

- c. Transfer mixture to 1/2-inch evacuable pellet die; tamper and circulate die plunger to achieve a flat surface of the mixture in the die.

- d. Evacuate, using rough pump (mechanical) outfitted with exhaust vent or exhaust vapor trap and a cryogenically cooled cold finger in the vacuum line (to prevent pump oil's backstreaming into mixture) for 60 seconds (maximum).

e. Slowly apply force to the die to a maximum of 20 000 pounds, maintaining that force while pumping on the die for 60 seconds.

This technique has been found acceptable for typical contaminants in vacuum chambers, including refined petroleum oils (found in rough pump oils, greases, lubricants, paints, atmospheric pollution), dioctyl phthalate and dibutyl phthalate (common to alkyd paints, softeners in polymers, some diffusion pump oils), polydialkylsiloxane type silicones (outgassed by silicone rubbers, greases, and oils), and DC-705 methylphenyltrisiloxane diffusion pump oil. These compounds have characteristic infrared spectra which are fully displayed through the KBr pellet (see Figures 1a through 1d), making the technique ideal for contaminant identification by chemical classification (hydrocarbon, phthalate ester, polydialkylsiloxane) and even for specific identification of DC-705. None of these compounds, however, have shown acceptable adherence to Beer's Law when analyzed by this technique. Calibration data demonstrate necessity of referral to the nonlinear calibration curves for quantitative analysis. Calibration curves for these compounds are presented in Figures 2a through 2d. The calibration data are not only specific to the materials (or classes of materials) tested, but to some extent depend on the personnel and equipment; thus, each laboratory endeavoring this type of analysis should prepare its own calibration curves. On a weight basis, the data for a typical petroleum hydrocarbon and polydialkylsiloxane should be fairly consistent for all similar compounds of molecular weight of several hundred or greater, since petroleum hydrocarbons contain mainly CH_2 , CH_3 , and C-C bonds, and the polydialkylsilox-

anes are repetitions of the monomer
$$\begin{array}{c} \text{R} \\ | \\ -\text{Si}-\text{O}- \\ | \\ \text{R} \end{array}$$
, where R is mostly

methyl (in some instances ethyl) and rarely of higher carbon content. Concerning hydrocarbons and polymers, infrared analysis has an advantage over gas chromatographic-mass spectrometric analysis in that, in the latter, individual data are given for each hydrocarbon fraction and for each member of a polymeric series present; this information being virtually of no value except the data must be summed for the classes of compounds to determine the quantity of each class of compounds present. Relative quantities of fractions or polymers are of little value in identifying the sources of contamination because of the uncertainty in the ratio of outgassing of contaminants containing these

fractions and the confusion added by the possibility of having several sources emitting the same contaminants in different ratios. Infrared analysis, however, looks at petroleum hydrocarbons, or more precisely, methyl and methylene groups as a composite to give a single value indicating the mass of methyl and methylene groups present; likewise, total silicones (polydialkylsiloxanes) can be determined from one of several absorption bands. One additional step must be taken in calculation of the quantities of contaminants in multicomponent systems; that step is to correct the data for compounds that have absorption bands at the same wavelength, usually because of the same chemical group (methyl, silicon-oxygen, etc.) being present in the several constituents present. Examples of compounds with similar peaks are given in Table 1. The problem is relatively simple, as exemplified by the following case in which four types of contaminants are present: petroleum hydrocarbons, phthalate esters, polydialkylsiloxanes, and DC-705.

- a. Determine DC-705 present by the absorbance of its unique bands at 7.0 and 10.0 μ .

- b. Determine polydialkylsiloxane present by ascertaining the 8.0 or 12.5 μ absorbance of the DC-705 present (step a), and subtract those values from the 8.0 or 12.5 μ absorbance of the spectrum of the KBr pellet in consideration.

- c. Determine the phthalate ester present by the absorbance of its unique band at 5.8 μ .

- d. Determine the absorbances of the DC-705, polydialkylsiloxanes and ester found in the previous three steps at 3.4 μ , add the absorbances, and subtract the total from the 3.4 μ absorbance of the KBr pellet in question to determine the hydrocarbon absorbance at 3.4 μ . For a given mass of contaminant, polydialkylsiloxanes and DC-705 have very weak absorption at 3.4 μ , such that only the contribution of the ester at that wavelength will need consideration, unless, of course, the silicones are present in quantities much greater than the petroleum hydrocarbons.

For other contaminants present, quantitative calibration curves must be prepared after the contaminants have been identified. After testing in the large Chamber A at the NASA Manned Spacecraft Center (MSC) for several years with the chamber empty and also with a variety of test articles in the chamber, the infrared spectra indicate that the four varieties of contaminants

mentioned (petroleum hydrocarbons, phthalate esters, polydialkylsiloxane silicones, and DC-705) have been the only contaminants found, except for three or four out of over a hundred samplings, and, in those cases, the exceptional contaminants were present in amounts much less than the hydrocarbons or esters. Generally, in the Chamber A at MSC, petroleum type hydrocarbons have been the most persistent contaminant, with phthalate esters being somewhat less, polydialkylsiloxanes much less, and DC-705 occurring infrequently and only at very low levels. (The typical average contamination level for the Chamber A, all volatile condensible materials, has been on the order of 2×10^{-7} g/cm² (approximately two monomolecular layers) for test periods of about 1 week.)

One important limitation of the KBr pelletizing technique is that the sample mass should not exceed 0.5 percent of the pellet mass. For the case of a 250-mg pellet, this corresponds to 1.25 mg, or for a 1-square-foot surface, roughly 12 monolayers of contaminant. (The estimation of 10^{-7} g/cm² being one monolayer is derived from the thickness of one molecular layer of oil of molecular weight 300, density of 1 g/cm³.) The maximum is a suggested limit to maintain the mechanical integrity of the pellet. Higher concentrations can be achieved, provided the pellets do not crumble and calibration points are provided. It is important to point out that the quantity of KBr in the pellet is not critical, as long as the diameter is the same, since the transmittance of the pellet is proportional to mass per unit area and is independent of thickness (and thus of KBr mass) within limits of at least 10 percent and likely much more.

The precision of measurement at a given mass is somewhat better than the adherence of the absorbance and mass to Beer's Law, as demonstrated in Table 2. The nonadherence to Beer's Law is not a significant source of error when the calibration curves are used; however, the uncertainty in reproducing pellets of consistent absorbance for a given mass cannot be discounted. For ordinary analyses, this uncertainty is very poor; but it must be remembered, if 1 square foot of area is analyzed, the uncertainty is on the order of 0.1 to 0.2 monolayers, which is quite respectable for surface contamination analysis.

One rule of thumb observed in the pelletizing of liquid samples is that the smaller the sample, the clearer the pellet. For heavy samples, pellets may appear opaque but still yield easily interpretable spectra in the range 2.5 to 15 μ . This is because scattering of light, the cause of opacity in this case, decreases exponentially with increasing wavelength, and this

phenomenon is dramatically displayed with (visibly) opaque pellets, the transmittance of which at $2.5\ \mu$ may be 50 percent but approach 100 percent at $15\ \mu$. In measuring opaque pellets, it is advisable to use a reference beam attenuator in the reference beam of the infrared spectrophotometer and to adjust the transmittance at $2.5\ \mu$ to about 50 percent, and, if the spectrum ordinate goes off scale, the reference beam attenuator should be used to bring the ordinate down (by transmitting more reference energy). Such changes in the spectrum do not affect the data if the changes are made where no critical absorption bands occur. The trace of the spectrum is extrapolated through the absorption band being evaluated, and the absorbance of the band at its minimum wavelength is the negative logarithm of the transmittance at the minimum divided by the transmittance indicated by the extrapolated line at the same wavelength, as depicted in Figure 3.

OPTICAL PROPERTIES AT 2000 Å

The nature of most organic and inorganic compounds is to tend to absorb light very strongly in the region of 2000 angstroms (Å), the boundary between the near and the vacuum ultraviolet. This tendency is due to absorption of quanta of light by electrons wherein they are energetically elevated to distinct higher energy states from their distinct ground states. For inorganic compounds, or salts, the absorption is a result mainly from transitions of electrons of the anionic atoms (halogen, oxygen family). In organic compounds, there is absorption due to transitions of electrons involved in the interatomic multiple bonds, such as double bonds (ethylene, propylene, etc.), triple bonds (acetylene, propyne, etc.), and aromatic compounds (benzene, toluene, naphthalene, etc.), in increasing order. Single bonds (C-C, C-H, C-O), that is, the electrons comprising them, do not usually absorb energy significantly at wavelengths above 1900 Å. Nonbonding electrons (electrons not involved in a bond but present on an atom in the molecule) on oxygen and halogen family atoms do strongly absorb at 2000 Å. Inner shell electrons of atoms in the first two rows of the periodic table do not absorb at wavelengths above 1000 Å. As a rule, then, most compounds absorb light at 2000 Å stronger than at any longer wavelength. Most commercial ultraviolet-visible spectrophotometers are capable of measurement at 2000 Å, beyond which (at shorter wavelengths) atmospheric oxygen and the quartz optics of the instrument (and also mirrored surfaces) begin to absorb light extensively, prohibiting further measurement. Thus, the 2000 Å wavelength is the most suitable wavelength for the observation of contaminants via their optical effects.

The extent of absorption of a chemical compound at any wavelength is expressed by its extinction coefficient, and if Beer's Law is applicable to the conditions of dispersion of the compound in its matrix and the optical configuration, the transmittance (T) of the compound is determined from the relationship

$$T = 10^{-\mathcal{E}lc}$$

where \mathcal{E} is the molar extinction coefficient, l is the optical path through the compound (in centimeters) or the matrix containing the compound, and c is the concentration of the compound per unit volume, expressed in moles per liter. The units of the extinction coefficient are liter mole⁻¹ centimeter⁻¹. The expression presented is the most common one employed; however, extinction coefficient may be expressed in other units and may apply to the base e (2.718...). For use in surface contamination measurement, to describe the mass per unit area, another form of extinction coefficient (hereafter called extinction coefficient $\bar{\mathcal{E}}$) is more appropriate, being given in terms of cm² g⁻¹. Inspection of the transmittance-path-concentration relationship makes it evident that optical absorption is a function of mass per unit area; thus, the negative log of transmittance should be a function of the type of contaminant, the wavelength, and the mass per unit area of the contaminant; that is, the extent of surface contamination. Further, since the net transmittance of a system is the product of the transmittances of its parts, the negative log of the transmittance (absorbance) is the sum of the products of the extinction coefficient of each component and the surface contamination level of that component.

With the theoretical apparatus available, it might be thought possible to obtain close correlation with identified and measured surface contaminants and transmittance at a given wavelength; however, such is not the case. The nature of electronic absorption in a given molecular bond, as is the case in the ultraviolet, is such as to be disturbingly dependent on the electronic structure of the rest of the molecule and the physical state (solvent if in solution, or pure). Unlike changes in vibrational energy, which are measured in the infrared portion of the spectrum and are fairly consistent for similar bonds among different molecules, the extinction coefficient may differ by orders of magnitude because of the difference in two otherwise identical molecules of only one double bond. Another unfortunate feature of ultraviolet spectra is that they are lacking in detail; that is, compounds usually have one or two broad, rather shapeless transmittance

minima. However, infrared spectra have numerous narrow and distinctly shaped bands, making identification of the absorbing species quite simple.

In spite of the fact that the transmittance changes cannot be used to determine the level or identity of contamination present, this parameter can be used to determine the presence of contamination and to crudely determine the relative amounts and directionality of contamination about a chamber. The effort is worthwhile mainly because very little effort is involved. The procedure is as follows:

- a. Clean several ultraviolet grade quartz disks, 1-inch diameter, 1 millimeter (mm) thick.
- b. Place the disks at various chamber locations that are to be investigated before the chamber is to be employed. One side of each disk may be masked with foil to obtain information on the direction of contaminant propagation.
- c. After work in the chamber is concluded, remove the disks and catalog them according to their location and orientation.
- d. Tune the spectrophotometer to 2000 Å; do not use nitrogen purge.
- e. Measure the transmittance of each disk, moving the carriage holding the disk out of the sample beam to obtain a tare reading for the spectrophotometer.
- f. Clean the disks (200-proof ethyl alcohol is a good solvent, with low lint tissue paper).
- g. Measure the transmittance of each disk again as in step e.

Extinction coefficients vary widely among chemical species and are tabulated in Table 3 for the common contaminants in vacuum chambers. Of these values, that for SunVis 706 is the least meaningful because petroleum hydrocarbons consist of predominantly aliphatic hydrocarbons yet contain olefinic hydrocarbons in large amounts with aromatics in lesser amounts; since the relative amounts and sizes of these constituent molecules differ, the extinction coefficient is highly variable among petroleum products. Dioctyl phthalate is a common contaminant that is a unique chemical species, as is DC-705. The extinction coefficient for DC-200 is meaningful, although the substance is a mixture of species each containing a different number of the

same building block (monomer), the absorbing species

$$\begin{array}{c} \text{CH}_3 \\ | \\ \text{-Si-O-} \\ | \\ \text{CH}_3 \end{array}$$

Molar extinction coefficients are not quoted for DC-200 and SunVis 706 because they are not unique species, but are mixtures of molecules of varying molecular weights.

The sensitivities of the quartz disks to the contaminants is dependent on the type of contaminant and the quantity thereof. Approximating one monomolecular layer of contaminant to be 10^{-7} g/cm², the transmittance losses to be expected for 10^{-7} g/cm² of the materials listed in Table 3 are presented in Table 4. The applicability of these values are subject to the limitations on the corresponding extinction coefficients, described previously. Another interesting and advantageous datum is that pure water is virtually transparent at 2000 Å since a monolayer of water can be expected on any clean surface exposed to the atmosphere.

Other factors, however, affect transmittance at 2000 Å. These factors include the scattering of light by particulate contaminants. Also, if volatile fluorine-containing organic compounds were present in the chamber and ultraviolet light were also present, as in solar simulation, there is a chance that the fluorocarbons could decompose, forming fluorine-containing free radicals in the chamber which etch silicated surfaces, such as glass and quartz. The 2000 Å wavelength is very susceptible to scattering effects, being according to Rayleigh's scattering principle that scattering is inversely proportional to wavelength, and 2000 Å is the shortest wavelength that can be practically measured.

Transmittance is not the only property that can be monitored to detect contamination. Specular reflectance is also readily measurable and is, in general, more sensitive to contamination than transmittance. Reflection from a single surface required the light to pass through the contaminant layer twice. If the mirrored surface is overcoated, for example, with magnesium fluoride or silicon monoxide, the contamination could also exhibit an effect on the interference behavior of the overcoated mirror, either to increase specular reflectance or to decrease it. Specular reflectance attachments are available for some commercial spectrophotometers. Since absolute values are not required, no standardization procedures are necessary, only measurement of the mirrors before insertion in the chamber or measurement afterward, followed by cleaning and remeasurement. As mirrored surfaces are very susceptible to changes in reflectance due to handling, it is recommended that mirrors be measured before insertion in the chamber and after removal, rather than post-test measurement, cleaning, and remeasurement.

Optical property measurement is not restricted to 2000 Å. The entire ultraviolet spectrum may be run if optical contamination is critical for a given chamber operation. Actually, that wavelength range of concern for an optical surface should be measured for optical samples. If a laboratory has a vacuum ultraviolet spectrophotometer, it is possible to measure changes in the optical properties in that range (1150 to 2000 Å) if the sample compartment is not evacuated. Evacuation of the contaminant-containing crystal would otherwise cause loss of contaminant, since the contaminant was also transmitted to the surface in a vacuum. Vacuum ultraviolet radiation is transmitted through nitrogen in the range 2200 to 1150 Å. Oxygen, and especially water vapor, absorb heavily in that region. The vacuum ultraviolet spectrometer must be outfitted with a sample compartment (the atmosphere of which is independent from the rest of the instrument), permitting reloading of the sample compartment and consequent nitrogen filling of the small sample compartment volume while leaving the rest of the optical path under vacuum. The optical path in the compartment should be minimized, being no more than a few millimeters. Extinction coefficient, expressed as a function of partial pressure and optical path, are quoted for atmospheric gases at 1216 Å in Table 5.

Chemical compounds do, as a rule, have higher absorption in the vacuum ultraviolet region of the spectrum than at around 2000 Å. They absorb especially strongly near 1600 Å (4), making this region more sensitive to contamination than 2000 Å. It is interesting to note, however, that investigations at the MSC Chamber A, the Naval Research Laboratories in Washington, D. C. (5), and at NASA Marshall Space Flight Center (6) indicate that contamination affects transmittance and reflectance more at 2000 Å than at the hydrogen Lyman-alpha line, 1216 Å.

WIPE SAMPLING

The contamination present on surfaces in the vacuum chamber can be determined by wipe sampling. This procedure is as follows:

- a. Rinse a glass wool swab in spectroquality carbon tetrachloride.
- b. Place the swab at the mouth of a glass vial half filled with spectroquality CCl_4 , and cap the vial (with Teflon lined cap).
- c. At the location in the chamber to be sampled, open the vial and grasp the glass wool swab with "triceps" type (three pronged) forceps, and immerse it in the CCl_4 at the bottom of the vial.

d. Wipe 1 square foot of area with the swab, using upward strokes to avoid streaming of the CCl_4 from the wipe area.

e. Replace the swab in the vial, cap the vial, and label the vial according to the location sampled.

f. Wipe sampled area and vicinity with water-dampened cloth, such as a diaper, to remove particulate contamination left behind by the swab.

g. In the laboratory, transfer the swab and CCl_4 to a 150-ml beaker, boil down to about 10 ml total volume (in a fume hood).

h. Pass the solution through a $0.20\ \mu$ glass fiber filter mounted in a Swinny type adapter for a hypodermic syringe, the adapter being mounted on a 30-cc syringe. Deliver solution into a graduated 17-ml centrifuge tube (to remove glass particles in the solution).

i. Evaporate the solution to about 0.5 ml total volume.

j. Proceed with pelletizing process described previously in this paper.

k. Rinse centrifuge tube with additional 0.5 ml CCl_4 and add to KBr mixture (to retrieve any remaining contaminant).

l. Measure infrared spectrum of KBr pellet in the region 2.5 to 15 μ .

NOTES: Prepare a control sample and process simultaneously with other samples, except, of course, do not sample with it. This provides tare values, if extraneous material is found. Spectroquality CCl_4 is sufficiently free from contamination that would give spurious results (such as hydrocarbons) as not to require further processing.

If the sample is also to be examined by gas chromatography (see following), transfer 30 microliters (μl) of the solution resulting from step i to a capillary melting point tube and seal off the open end of the tube with a soft flame.

Carbon tetrachloride is a very toxic substance and should be handled in a fume hood or only when wearing appropriate protective respirator mask.

In spite of the problem with particulate material from the glass wool swabs, they are still the most preferable. Investigations of several types of natural and synthetic cloths (including nylon and dacron) indicate, that after repeated boilings in solvent, the background contaminant level (as hydrocarbons) was

still too high. And although carbon tetrachloride is quite toxic, it has a real advantage in that it has no carbon-hydrogen bonds which otherwise may show up in the infrared spectrum as hydrocarbon if all of the CCl_4 were not removed from the KBr pellet, and since it is very poorly combustible, it is weakly detected by the sensitive hydrogen flame ionization detectors in gas chromatographs, and thus the solvent tailing present in gas chromatograms is much smaller with CCl_4 than with other solvents.

Freons would also be acceptable, except that they are not obtainable in spectroquality grades and would require further processing to make them acceptable for infrared spectral work.

Direct quantitative interpretation of the KBr spectra is not possible with wipe sampling because the efficiency of recovery varies with the amount of sample and the type of contaminant. This efficiency reflects that of recovery from the sampled area and also recovery of the sample from the swab. Recovery efficiency will increase with increasing contaminant levels, since there is sufficient material to significantly overshadow that retained due to surface phenomena (adsorption). Likewise, more surface active materials (such as silicones) will have poorer recovery efficiencies than less active materials (such as hydrocarbons). For example, the recovery efficiency for hydrocarbons at the $3 \times 10^{-7} \text{ g/cm}^2$ level is about 50 percent whereas the efficiency is only about 20 percent for silicones present at the same level. Like KBr pelletizing quantitative calibration curves, the recovery efficiencies for wipe sampling should be run independently by each laboratory that endeavors this technique, and the quantities of material detected in the pellets must be corrected according to these efficiencies.

One important application of wipe sampling is to measure the contamination on a given surface or surfaces in a chamber before the chamber is used and to repeat the measurement after use, for the exact same locations. This yields information on the volatile condensible materials accrued on the chamber surfaces during use. Chamber surfaces sampled may also include solar simulator mirrors (only those that are overcoated, however). The technique is most frequently used to identify and measure contaminants visibly present on a surface, such as a grease smear, a splotch fluorescing under black light, or a persistently damp location.

Misleading interpretations of accurate wipe sample results may often be encountered when the materials measured and identified are of too low vapor pressure to be a significant source of

contamination to the vacuum environment. Vaporization rate is a function of vapor pressure of the contaminant and the surface area occupied by the contaminant, according to the relationship

$$\phi = 0.0584 \left(\frac{M}{T} \right)^{1/2} P$$

where ϕ = evaporation rate, $\text{g/cm}^{-1}\text{sec}^{-1}$

M = molecular weight

T = contaminant temperature, $^{\circ}\text{K}$

P = contaminant vapor pressure, torr

Thus, if the vapor pressure of a contaminant were 10^{-10} torr, its molecular weight 300, and its temperature in the chamber 80°F , its evaporation rate would be $5.0 \times 10^{-7} \text{ g/cm}^2/\text{day}$. Further, if the area of chamber surface covered by this contaminant were 1 percent of the total area of the chamber inner walls, the average rate of contamination buildup on a surface in the chamber would be roughly one-twentieth of a monomolecular layer per day, assuming a monolayer is 10^{-7} g/cm^2 . A more accurate method of determining mass transferred from one surface to another is as follows:

$$Z = \frac{\phi \Omega}{\pi} \frac{A_s}{A_t} \cos \theta \cos \xi$$

where Z is the mass deposition per unit area on the target

Ω is the solid angle of the target viewed by the contamination source

A_s is the surface area occupied by the contaminant source

A_t is the surface area of the target

θ is the angle subtended by a line from the center of the contaminant to the center of the target and the perpendicular line through the center of the contaminant plane

ξ is the angle subtended by a line from the center of the contaminant to the center of the target and the perpendicular line through the center of the target plane

Examination of this relationship shows that a large quantity of a low vapor pressure contaminant located over a small surface

area is not as detrimental as a small quantity of the same contaminant (a few monolayers) coating the entire chamber inner wall.

A simple method is available for examining the volatility of the wipe sampled material. This is to inject some of the material into a gas chromatograph equipped with a nonpolar column, such as SE-30, with column temperature of 275° C. If the retention time for the material, or any component thereof, is less than five times the retention time of DC-705 under the same column and conditions, then the material may be a potentially serious contaminant. If the total mass of material injected is known and the gas chromatograph is outfitted with a flame ionization detector the sensitivity of which is approximately linear with mass for organic compounds, then the fraction of each constituent detected can be estimated, providing the system is calibrated with a known mass of organic material. For the case of solid impurities dissolved in the CCl_4 during wipe sampling, which would show up under infrared analysis, no indication for these impurities would be seen on gas chromatographic investigation, and neither would the nonvolatile greases and liquids. Gas chromatographic analysis also provides a backup for the infrared analysis (via pellets) of the materials collected by wipe sampling. DC-705, for example, is detectable with gas chromatography at levels corresponding to a few thousandths of a monolayer over 1 square foot of surface.

ACKNOWLEDGMENTS

The author wishes to acknowledge the diligent laboratory work of B. B. Curtis, G. E. Seach, F. P. Veitch, and F. Wilson of Brown & Root-Northrop Space Environment Simulation Laboratory in developing and calibrating the KBr pelletizing and wipe sampling techniques.

REFERENCES

1. Wolff, C. M., and M. L. Ritter: National Bureau of Standards Special Publication No. 336, 1971, pp 25-49.
2. White, R. G.: Handbook of Industrial Infrared Analysis. Plenum Press, New York, 1964, pp 116-169.
3. Mason, W. B. "Infrared Microsampling in Bio-Medical Investigations," paper presented at Pittsburg Conference on Analytical Chemistry and Applied Spectroscopy, March 1958.
4. Pickett, L. W., M. Muntz, and E. M. McPherson. Journal of the American Chemical Society, Vol. 73, 1951, p 4862.
5. Angel, D., Naval Research Laboratories, Washington, D. C. Private Communication, October 7, 1971.
6. Smith, C., Marshall Space Flight Center, Huntsville, Alabama. Private Communication, October 7, 1971.

TABLE 1
COMMON INFRARED ABSORPTION BANDS USED FOR
QUANTITATIVE ANALYSIS

Wavelength	Compounds with common bands	Absorbing chemical group
3.42 μ	Petroleum hydrocarbons	methyl C-H
	Esters (phthalate)	methyl C-H
	Polydialkylsiloxanes (very slight)	methyl C-H
	DC-705 (very slight)	methyl C-H
8.0 μ	Polydialkylsiloxanes	Si-CH ₃
	DC-705	Si-CH ₃
	Esters (so broad that the sharp silicone band appears superimposed on it)	C-O
12.5 μ	Polydialkylsiloxanes	Si-CH ₃
	DC-705	Si-CH ₃

TABLE 2
PRECISION AND BEER'S LAW ADHERENCE OF KBr PELLETIZING TECHNIQUE

Compound	Mass, mg	Precision, % [†]	Absorbance/mass (A/M), mg ⁻¹	A/M standard deviation
SunVis 706 Oil (hydrocarbon)	0.03	40	1.56	30
	3.42 μ			
	.10	20	2.22	
	.30	10	1.50	
Diocetyl phthalate (ester)	1.0	9	.99	19.5
	.03	25	1.19	
	5.8 μ			
	.10	3	1.71	
DC-200 (polydimethyl siloxane)	.30	7	1.83	21.8
	1.0	4	2.11	
	.03	4	3.33	
	8.0 μ			
DC-705 Oil (methylphenyl trisiloxane)	.10	6	2.40	14.4
	.30	11	2.00	
	.03	13	.818	
	7.0 μ			
	.10	18	.780	
	.30	7	.580	

[†] Standard deviation

TABLE 3
EXTINCTION COEFFICIENTS AT 2000 ÅNGSTROMS FOR
COMMON VACUUM CHAMBER CONTAMINANTS

Contaminant	Extinction coefficient	Molar extinction coefficient
Petroleum hydrocarbon (SunVis 706)	$1.32 \times 10^4 \text{ cm}^2 \text{ g}^{-1}$	$3.24 \times 10^4 \text{ l}^\dagger \text{ mole}^{-1} \text{ cm}^{-1}$
Ester (dioctyl phthalate)	$1.22 \times 10^5 \text{ cm}^2 \text{ g}^{-1}$	
DC-200 (polydimethylsiloxane)	$4.13 \times 10^3 \text{ cm}^2 \text{ g}^{-1}$	
DC-705 (1, 2, 3 trimethyl 1, 1, 2, 3, 3-pentaphenyl trisiloxane)	$2.25 \times 10^5 \text{ cm}^2 \text{ g}^{-1}$	$1.22 \times 10^5 \text{ l}^\dagger \text{ mole}^{-1} \text{ cm}^{-1}$

[†] Liter

TABLE 4
TRANSMITTANCE LOSS AT 2000 ÅNGSTROMS CAUSED BY A $1 \times 10^{-7} \text{ g/cm}^2$
LAYER OF COMMON CHAMBER CONTAMINANTS

Contaminant	Transmittance loss at 2000 Å, %
Petroleum hydrocarbon (SunVis 706)	0.3
Ester (dioctyl phthalate)	2.8
DC-200 (polydimethylsiloxane)	.1
DC-705 (1, 2, 3 trimethyl 1, 1, 2, 3, 3 pentaphenyl trisiloxane)	5.0

TABLE 5
EXTINCTION COEFFICIENTS OF ATMOSPHERIC GASES
AT 1216 ÅNGSTROMS (LYMAN-ALPHA)

Gas	Extinction coefficient, $\text{atm}^{-1} \text{ cm}^{-1}$
Nitrogen	0.005
Oxygen	.3
Water vapor	396.

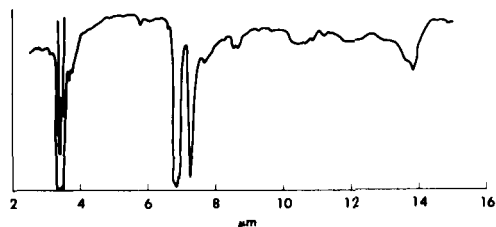


Fig. 1a—Infrared spectrum petroleum oil or grease (hydrocarbon)

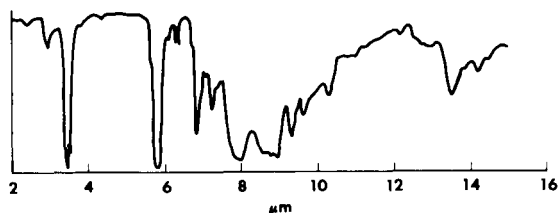


Fig. 1b—Infrared spectrum of tall oil alkyd - used in paints, out-gassed from 3M Nextel paints (Spectrum is characteristic of phthalate esters.)

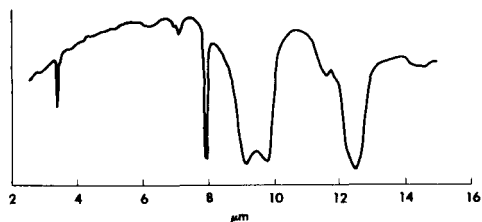


Fig. 1c—Infrared spectrum of polydimethyl siloxane - common to most silicone oils, grease, and rubbers

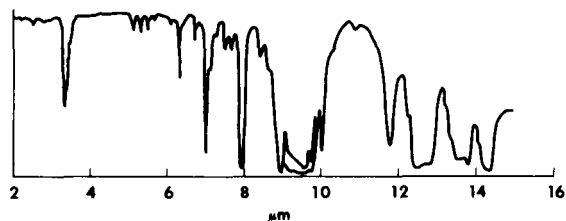


Fig. 1d—Infrared spectrum of DC-700 series oils (methyl-phenyl trisiloxanes)

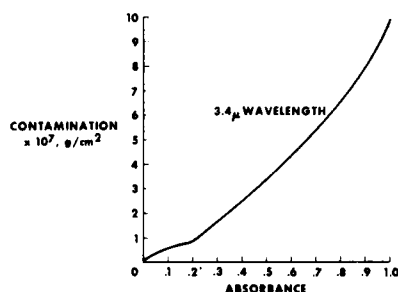


Fig. 2a—SunVis 706 (typical hydrocarbon) - absorbance of 13 mm KBr pellet versus contamination level of 12 in. by 12 in. contamination collection unit

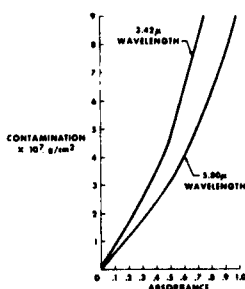


Fig. 2b—Diocetyl phthalate (ester) - absorbance of 13 mm KBr pellet versus contamination level on 12 in. by 12 in. contamination collection unit

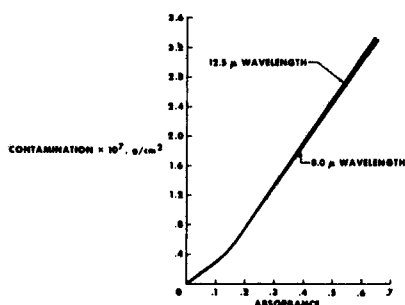


Fig. 2c—DC-200 oil (polydimethyl siloxane, as from silicone grease and rubber outgassings) - absorbance of 13 mm KBr pellet versus contamination level on 12 in. by 12 in. contamination collection unit

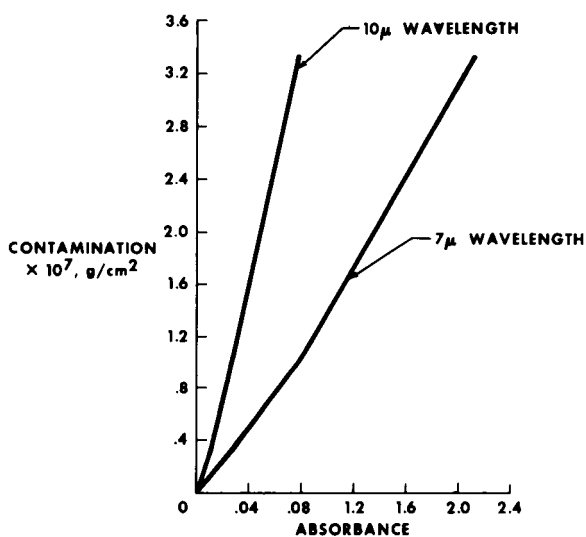


Fig. 2d—DC-705 oil - absorbance of 13 mm KBr pellet versus contamination level on 12 in. by 12 in. contamination collection unit

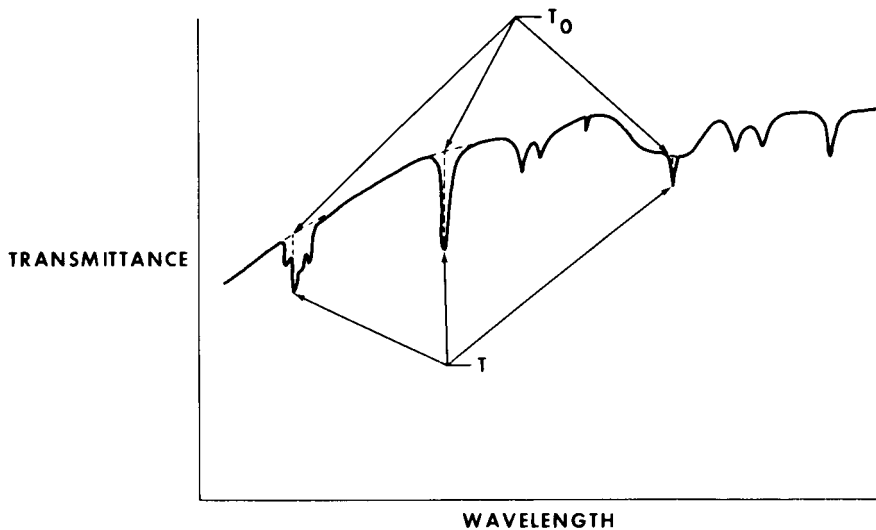


Fig. 3—Extrapolation of base line to determine transmittance of base line, T_0 , at the wavelength of the transmittance minimum

PHOTOLUMINESCENCE AND OPTICAL TRANSMISSION OF DIFFUSION PUMP OIL

Roger L. Kroes, *NASA, Marshall Space Flight Center*

ABSTRACT

The photoluminescence and optical transmission of four widely used diffusion pump oils DC705, DC704, convalex 10 and convoil 20 were measured. Each of the oils was found to be transparent throughout the visible region, showed some absorption in the near uv region, and became very opaque below approximately 320 nm. Both convalex 10 and convoil 20 turned yellow after exposure to uv light. No such change was noted in DC705 and DC704. Photoluminescence was produced in each of the four different oils when irradiated with uv light. Various wavelengths of monochromatic light from 250 nm up to the visible region were used for excitation. The luminescence spectra were measured by scanning the light output of the samples perpendicular to the excitation light direction with a grating monochromator. Both DC705 and DC704 showed an identical luminescence peak at 350 nm. The spectra of convalex 10 and convoil 20 were fairly complex with several peaks in the region from 350 nm to 480 nm.

RADIATION EFFECTS ON CONTAMINANTS FROM THE OUTGASSING OF SILASTIC 140 RTV

Peter F. Jones, *The Aerospace Corporation, El Segundo, California*

ABSTRACT

Exposure of the volatile condensable material (VCM) from Silastic 140 RTV adhesive sealant to 147.0-nm radiation, simulating the space radiation environment in synchronous earth orbits, induces absorption of visible light by the VCM. This results in an increase in the absorptance of coated optical elements, such as solar-cell cover glasses and second-surface mirrors for thermal control. A contaminant thickness of 0.1 μm or more could result in a change in solar absorptance of the second-surface mirrors from 0.06 to ~ 0.16 in a period of about 1.5 yr in space. Calculations indicated that the VCM thickness would have to be less than $\sim 0.005 \mu\text{m}$ to keep the change in solar absorptance < 0.01 for a 3-yr mission.

INTRODUCTION

Although it is generally recognized that the outgassing of polymeric materials can degrade satellite system performance by contamination of satellite optical components, not enough attention has been given to the subsequent effects of the space radiation on the contaminant. In some cases (such as for the system studied in this report), the satellite system degradation may be entirely due to the radiation-induced darkening of the contaminant. This report reviews our studies on the effects of irradiation in space on the volatile condensable material (VCM) from Silastic 140 RTV adhesive sealant (a methylsiloxane manufactured by the Dow Corning Corporation).

Silastic 140 was selected by a contractor to seal openings of a Titan IIC payload fairing. Previously reported experiments have shown that Silastic 140 outgasses volatile condensable material (VCM) when heated (Ref. 1). The VCM could condense on a payload that is at a lower temperature than the fairing. Therefore, the contractor performed several thermal-vacuum mass loss measurements and collected VCM from the Silastic 140 RTV on a quartz plate. No change in transmittance due to the deposit was noted, but the VCM is transparent to radiation in

the wavelength band from $<0.20\ \mu\text{m}$ to $>3.0\ \mu\text{m}$. However, even transparent depositions on coated optics can affect the transmission. Solar-cell cover glasses, which have a magnesium fluoride antireflection coating, could show as much as a 3% loss in transmission for a thick deposit ($>1\ \mu\text{m}$). This was not a major problem, however, because a $1\text{-}\mu\text{m}$ thickness was not likely and a 3% loss in power was not considered critical.

Our previous laboratory work has shown that the uv visible absorption of polysiloxanes and other polymeric materials increases when subjected to far uv irradiation (Ref. 2). This poses a potential problem for VCM deposits on optical materials exposed to solar uv and trapped particle radiation in space.

Specimens of the Silastic 140 VCM supplied by the contractor were irradiated with far uv at a wavelength of $147.0\ \text{nm}$ from a low-pressure xenon lamp. This irradiation resulted in large increases in absorption, which would increase the solar absorptance of second-surface mirrors used for thermal control and decrease the transmittance of the solar-cell cover glasses.

VACUUM ULTRAVIOLET IRRADIATION

The optical transmission of polymeric films can be degraded significantly by the solar uv and trapped particle radiation environment in space. The effects of the uv radiation are usually evaluated by means of high-pressure xenon lamps because the spectral distribution of their radiation is approximately the same as the sun's spectrum for wavelengths (λ) greater than $\sim 190\ \text{nm}$ (the cutoff of the quartz window). These lamps were not appropriate for the present study because pure methylsiloxane films do not absorb for wavelengths greater than $\sim 175\ \text{nm}$ (Ref. 3). We chose to use a low-pressure xenon lamp with a sapphire window that was constructed in our laboratory. The low-pressure lamp provided a monochromatic irradiation source at $147.0\ \text{nm}$, with no other emission lines (intensity less than 0.1% of that at $147.0\ \text{nm}$) for $\lambda < 450\ \text{nm}$ (Ref. 4).

The lamp we used had a photon flux at $147.0\ \text{nm}$ of $4.0 \times 10^{14}\ \text{photons cm}^{-2}\ \text{s}^{-1}$, as determined by conversion of CO_2 to CO (Ref. 5). For comparison, the solar photon flux for $\lambda < 175\ \text{nm}$ is $3.0 \times 10^{12}\ \text{photons cm}^{-2}\ \text{s}^{-1}$ (Refs. 6 and 7). Thus, for an optically thick sample, 1 hr of irradiation in the laboratory is equivalent to 133 hr of exposure to solar uv radiation (assuming that all photons with $\lambda < 175\ \text{nm}$ are equally effective in producing damage). For 147.0-nm irradiation of a methylsiloxane $>90\%$ of the photons are absorbed for thicknesses $>0.1\ \mu\text{m}$. It was assumed that the absorption in this spectral region is the same as that of polyethylene, which also has an absorption threshold of $175\ \text{nm}$ (Ref. 8).¹ For our experiments,

¹Unfortunately, there are no data available for the far uv absorption of polymethylsiloxanes. Most organic polymers, however, have similar absorption coefficients in the far uv (Ref. 8).

we used films of the Silastic 140 outgassing products, several micrometers thick and deposited on Suprasil quartz plates. The optically thick samples were used so that we could be certain that all of the incident photons would be absorbed and also because our original estimates indicated the film thickness could be as much as 1 μm . The sample was irradiated in a vacuum (pressure $<10^{-5}$ torr), but it was removed from the vacuum periodically for measurement of its optical transmission spectrum. We have previously found that the spectrum for other siloxane films is not affected by exposure of the sample to air after irradiation (Ref. 2).

The uv-visible transmission spectra of the film after various irradiation times are shown in Figure 1. Although the infrared spectrum was not monitored, our previous investigation of polymethylsiloxane and other polymers had shown no change in the infrared spectrum, even after significant changes in the uv spectrum (Ref. 2). The spectra shown in Figure 1 have not been corrected for scattering. In Figure 2, we have plotted the change in the absorbance (optical density) at 300 nm vs the time of irradiation. This figure shows that the radiation-induced absorption is starting to level off or saturate. We also observed that the viscous oil deposit on the quartz plate had solidified, presumably as a result of crosslinking of the siloxane.

CALCULATION OF SILOXANE DEGRADATION EFFECTS ON SECOND-SURFACE MIRROR AND SOLAR CELL PERFORMANCE

From the spectra in Figure 1, we calculated that the solar absorptance (α_s) of a siloxane-contaminated second-surface mirror (made with Ag deposited on quartz) would increase from 0.060 to 0.067 after an exposure equivalent to the 2-hr laboratory irradiation. For the 51-hr laboratory irradiation, α_s would increase to 0.159. This would result in a temperature increase of ~ 60 K for a flat plate normal to the sun's rays and with the rear surface insulated. Although the effects produced by the 2-hr irradiation were considered acceptable for this mission, the damage after 51 hr would most likely lead to overheating of satellite components. In addition, for the long-time irradiation, the power generated by the solar cells would be decreased because of absorption by the irradiation-colored siloxane film. For the 27-hr irradiation, the solar cell current would be degraded by 2.4%; for the 51-hr exposure, the solar cell current would decrease by 4.5%.

With an optically thick siloxane film ($>0.1 \mu\text{m}$), our 51-hr irradiation was equivalent to 1.53 yr in space (assuming the film was exposed to the sun 12 hr per day). Because of the significant degradation observed for thick films, it becomes important to better characterize the expected thickness of the siloxane film. With the vacuum uv absorption spectrum of polyethylene (Ref. 8) as a model for the siloxane film, we

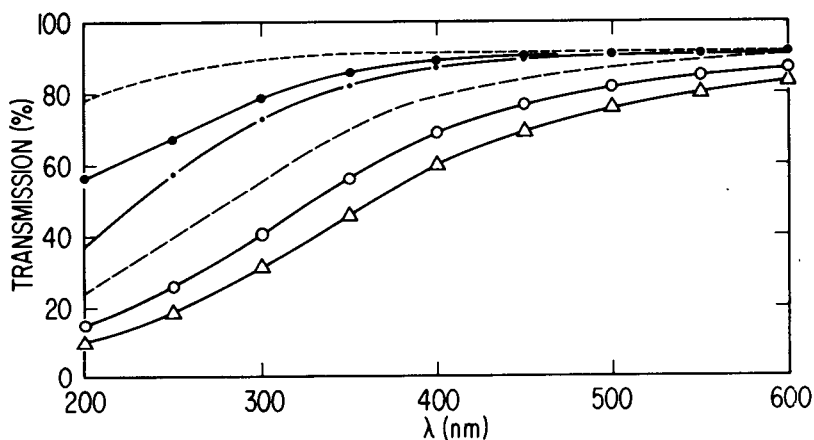


Fig. 1. Transmission spectra of Silastic 140 outgassing deposit for various irradiation times: -- before irradiation, • after 2 hr, •—• after 4 hr, — after 12 hr, O—O after 32.5 hr, and Δ—Δ after 51 hr.

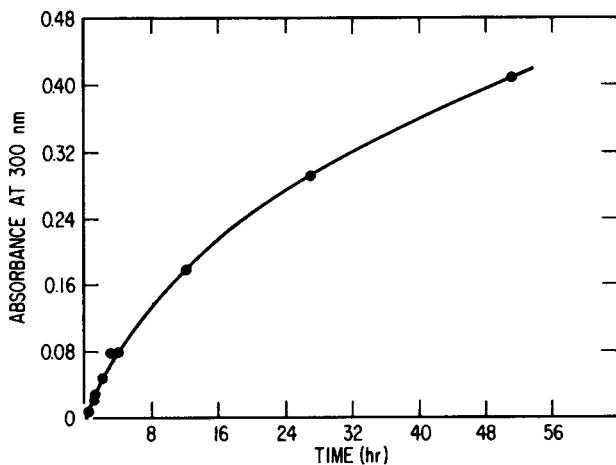


Fig. 2. Variance of absorbance at 300 nm of Silastic 140 outgassing deposit vs time of irradiation.

calculated that the film thickness must be less than $\sim 0.005 \mu\text{m}$ if the space radiation damage for a 3-yr mission in synchronous orbit is to be less than that observed for the 2-hr laboratory irradiation ($\Delta\alpha_g = 0.007$).

We did not investigate the possibility that absorption in the uv induced by the far uv irradiation leads to additional degradation. Also, we did not include the possible damage by the charged particles trapped in the earth's magnetic field. For a synchronous orbit, however, the energy deposited by these particles in the thin siloxane film is only 1/100th the energy deposited by the far uv radiation. Experiments are currently under way in our laboratory to determine the wavelength dependence of the photodegradation and to evaluate the importance of synergism between the far uv and the visible-near uv spectral ranges.

REFERENCES

1. A. Fisher and B. Mermelstein, "Outgassing Studies on Some Polymer Systems for GSFC Cognizant Spacecraft," Preprint No. X-735-70-73, Goddard Space Flight Center, Greenbelt, Maryland (February 1970).
2. P. F. Jones and A. R. Calloway, unpublished data.
3. G. Rausa, "Ultraviolet Radiation Induced Effects in Some Optical Materials," Proceedings of AIAA Thermophysics Specialist Conference, AIAA No. 67-344 (17-20 April 1967).
4. H. Okabe, "Intense Resonance Line Sources for Photochemical Work in the Vacuum Ultraviolet Region," J. Opt. Soc. Am. **54**, 478 (1964).
5. J. Y. Yang and F. M. Servedio, "Far Ultraviolet Photolysis of Carbon Dioxide," Can. J. Chem. **46**, 338 (1968).
6. K. G. Widing, J. D. Purcell, and G. D. Sandlin, "The UV Continuum 1450-2100 Å and the Problem of the Solar Temperature Minimum," Solar Phys. **12**, 52 (1970).
7. H. E. Hinteregger, "The Extreme Ultraviolet Solar Spectrum and Its Variation During a Solar Cycle," Ann. Geophys. **26**, 547 (1970).
8. R. H. Partridge, "Vacuum-Ultraviolet Absorption Spectrum of Polyethylene," J. Chem. Phys. **45**, 1685 (1966).

INTEGRATED REAL-TIME CONTAMINATION MONITOR: OPTICAL MODULE

Gary M. Arnett and Roger C. Linton, *NASA, Marshall Space Flight Center*

ABSTRACT

The optical module of an Integrated Real-Time Contamination Monitor is being developed for evaluating the effects of both ground-based and spaceflight contamination environments. A laboratory version of the IRTCM has been built and tested under conditions simulating a serious gaseous contaminant environment. The optical properties of selected surfaces including mirrors, windows, and the crystals of operating quartz-crystal microbalances were monitored at two wavelengths in the vacuum ultraviolet before, during, and after the introduction of various contaminants in gaseous form. The results show the effects of contamination, particularly for certain vacuum pump oils, to be dependent on the optical element material, the thickness deposited, and most strikingly, the type of contaminant. The optical constants of the contaminants at the monitoring wavelengths were determined and a comparison made for the calculated versus the measured changes in optical properties. Design features of the IRTCM will be reviewed as they affect this type of data and their interpretation, and those features of the advanced IRTCM now being developed which improve on its applicability will be discussed.

1-1-10

1-1-10

EXPERIMENTAL DETERMINATION OF STICKING COEFFICIENTS

E. E. Klingman, *Marshall Space Flight Center, Huntsville, Alabama*

ABSTRACT

A Monte Carlo computer program is used in conjunction with experimental data to determine the sticking coefficient for RTV-501 on silver.

INTRODUCTION TO THE PROBLEM

On many experimental satellites, and particularly on the Skylab, there is concern about contamination effects degrading the performance of the primary scientific experiments. For this reason a great amount of effort has been spent attempting to assess the seriousness of this problem and to minimize such degradation. The problem can be divided into three main categories as follows:

1. Source of contamination; outgassing, waste dumps, RCS, etc.
2. Mass transport; contaminant cloud, collisions with surfaces
3. Effect of contaminants; deposition on UV irradiated surfaces, etc.

The relationship of these three areas is shown schematically in Figure 1.

It is easily seen from Figure 1 that the sticking coefficient which measures the probability of a particle sticking to a surface enters into two of the major areas of the contamination analysis program. This, then, is the motivation for experimental and theoretical efforts to determine such coefficients. In this report the preliminary experimental results are described. Such preliminary results were needed rather quickly as input to the mass transport program. They were obtained as rapidly and as simply as possible. More elaborate

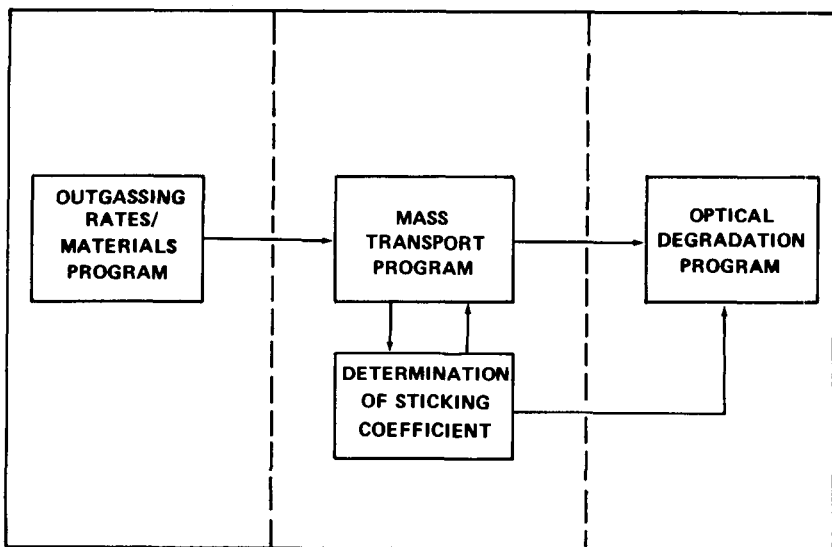


Fig. 1. Subprogram in the Contamination Program

and accurate experimental work is proceeding and will be the subject of a following report.

Mass Transport Tools

Prior to any experimental work, the mass transport problem was analyzed, and it was decided to adopt a Monte Carlo approach. This decision was based on the mean free path of the particles which generally exceeded the container dimensions. Thus, only particle-wall collisions were considered. Since the sticking coefficients were not known, it was uncertain whether the particle would make enough collisions with the walls to be randomized and susceptible to a kinetic gas treatment.

Subsequent work in this area compared a two-dimensional Monte Carlo treatment with a two-dimensional analytic solution [1] in order to gain confidence in the Monte Carlo and some feel for the technique. The following work has been strictly Monte Carlo and has resulted in a program for calculating mass flow in a cylindrical container and another program for

three-dimensional rectilinear enclosures with sources and sinks. Both three-dimensional programs have the capability of analyzing either a point source or an extended source. A schematic drawing of the cylinder Monte Carlo program is illustrated in Figure 2.

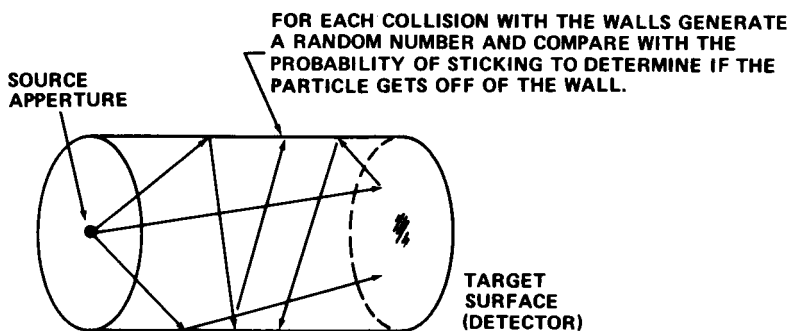


Fig. 2. Simplified representation of Monte Carlo cylinder model

In the Monte Carlo work to date it has been assumed that the particles leave the wall with a cosine distribution which has both theoretical and experimental backing. Most of this work, however, is based on atomic particles. Recent work done in Germany by Becker [2] used "cluster" molecules. As these are the types most relevant to spacecraft contamination, this factor is being studied; and it is possible that the Monte Carlo computer programs will be modified to take such collisions into account.

The results of a given Monte Carlo run are a function of source rate, type of source, target area, container dimensions, and sticking coefficient. The results of greatest interest are those in which only the sticking coefficient, γ , is free to vary. In this case, runs will be made for several values of γ , and the percentage, β , of all emitted particles which strike the target area (and are assumed to stick) is plotted versus γ . Figure 3 shows a typical graph from a series of Monte Carlo runs.

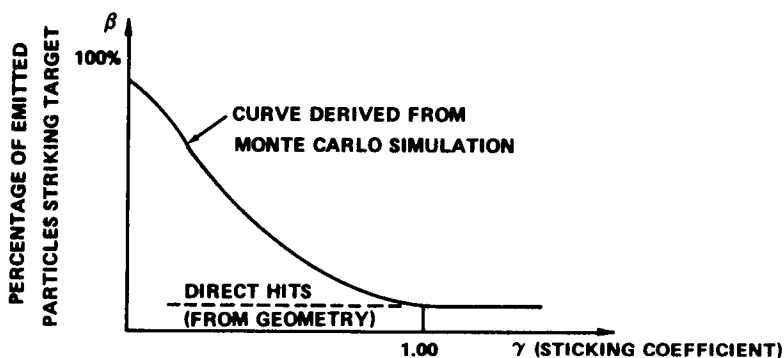


Fig. 3. Particle reaching target as a function of sticking coefficient

From Figure 3 it is seen that an asymptote which the curve must approach is the percentage of direct hits, i.e., those particles which leave the source and travel directly to the target without encountering any walls on the way. The particular value is a function only of geometry and is, therefore, a most important value since it can serve as a reference point and as a tie between the Monte Carlo model and a physical model. It will be seen in a later section that the use of this reference allows one to disregard the efficiency of the detector, i.e., it does not require knowledge of the sticking coefficient on the target surface (assumed non-zero).

Experimental Setup

The actual physical situation approximates the Monte Carlo model as closely as possible. A cylinder is used to contain the particles emitted from a source. The source used was a sample of RTV-501 seated tightly in a heater and placed in close proximity to an input aperture. The source temperature was held at 100°C. The cylinder surface was silver plated.

The detector used was an ARC quartz crystal microbalance (QCM) with silvered quartz detecting (target) surface. The general experimental setup is as shown in Figure 4.

The experimental setup was designed to obtain engineering data by a deadline. RTV-501 was chosen as a fairly dirty source

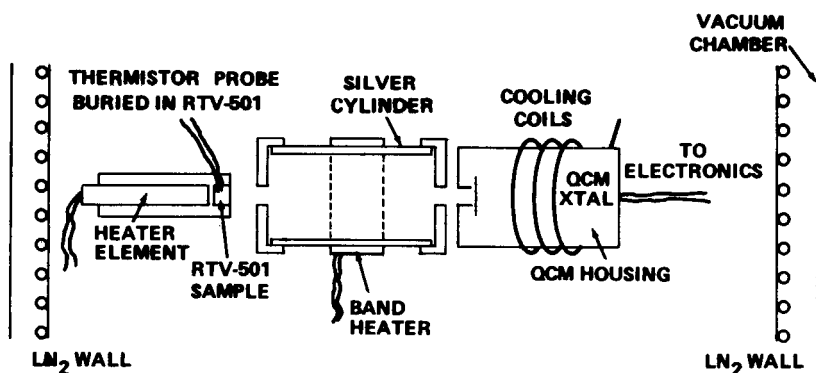


Fig. 4. Experimental setup

typical of that flown on Skylab. The silver cylinder was chosen to be representative of several Skylab surfaces, as well as to obtain data on the QCM surface coating. The weakest feature of the system from the viewpoint of physics is the inability to obtain really clean surfaces. From the engineering data viewpoint, this is not a great disadvantage and, to some degree, is almost desirable.

Experimental Procedure

The first readings taken were background readings with and without the cylinder present. The high background noise of early runs was eliminated by enclosing the system in an LN_2 cold wall. As a simple check on the system, the sample (RTV-501) was placed at the source location, the cylinder was removed, and the direct hits were measured for various source-to-target distances. The change in particle count, i.e., frequency shift of the QCM, could be calculated from geometrical considerations assuming a cosine distribution from the source. The outgassing was found to be given by the cosine law to within a few percent. The target was then repositioned at the distance corresponding to the length of the cylinder, and the direct hits were measured. The cylinder was then installed in place, and the total hits were measured. These two measurements, with and without the cylinder in place, yield the sticking coefficient. It

should be noted that stay times are assumed to be approximately zero if the particle re-evolves, and approximately infinite otherwise.

Calculation of the Sticking Coefficient

For comparison purposes, it is worth calculating the direct hits expected from geometry with those obtained from a Monte Carlo calculation. If the source is considered to be emitting particles into a hemisphere of radius equal to the distance of the target from the source, then the probability of a particle striking element ds of the total surface S is ds/S for isotropic emission. If the emission of particles follows the cosine law, then the probability is $ds(\cos \theta)/S$. Noting that $ds = r^2 d\theta d\phi \sin \theta$, the ratio of the particle striking the target at a distance R from the source is

$$\text{Direct hits} = \frac{2\pi R^2 \int_0^{\pi/2} \sin \theta \cos \theta d\theta}{2\pi R^2 \int_0^{\pi/2} \sin \theta \cos \theta d\theta} \frac{\text{target surface}}{\text{surface}}$$

For a target surface with radius 0.33 cm at a distance of 5.6 cm from the source, the direct hits can be calculated to be:

Geometric: direct hits = 0.346% of total flux

Monte Carlo: direct hits = 0.373% of total flux

The Monte Carlo figure was obtained as an average of eight runs of 10,000 particles each. Continuing with the calculation of the sticking coefficient, it is necessary to define certain terms.

$$R = \text{source rate} = \frac{N_{\text{emitted}}}{\text{-unit time}}$$

α = efficiency of QCM, i.e., percent of particles sticking to QCM

$$\beta = \frac{N_{\text{rec}}}{N_{\text{emitted}}}; \text{ theoretical Monte Carlo calculation in which } \alpha = 100\% \text{ (independent of source rate)}$$

Ψ = geometric form factor, including cosine distribution; applies only to direct hits, determined from Monte Carlo calculations

N_{QCM} = number of particles seen by QCM

Certain relations follow immediately from the above definitions:

$$N_{\text{REC}} = \Psi R \Delta t \quad (\text{a})$$

$$N_{\text{QCM}} = \alpha N_{\text{REC}} \quad (\text{b})$$

For the following calculations it is necessary to realize that the number of particles received is a function of the sticking coefficient, γ , and the distance, x , from source to target, i.e.,

$$N_{\text{REC}} = N_{\text{REC}}(\gamma, x)$$

whereas the geometric form factor $\Psi = \Psi(x)$ is a function of the distance only (for given target and source dimensions) but only has meaning for $\gamma = 1$. Thus, in the relation

$$N_{\text{QCM}}(1, x) = \alpha R \Psi(x) \Delta t$$

the known values are $N_{\text{QCM}}(1, x)$ and $\Psi(x)$. The value of $N_{\text{QCM}}(1, x)$ is the experimental reading of the QCM with no cylinder present, i.e., the measurement of direct hits. The value of $\Psi(x)$ is the Monte Carlo form factor (0.00373 for this experiment). The source rate and the value of α (actually the sticking coefficient for the QCM is unknown. Thus, it is seen that the relation between the theoretical number received per unit time and the experimental number emitted per unit time is

$$N_{\text{emitted}}(1, x) = \frac{N_{\text{QCM}}(1, x)}{\alpha \Psi(x)}$$

It is assumed that number emitted is relatively independent of the sticking coefficient, i.e., the vapor pressure of the material exceeds the vacuum pressure. With the cylinder in place, the number of particles measured by the QCM is assumed related to the theoretical value $N_{\text{REC}}(\gamma)$ through relation (b).

Thus, experimental determination of β is found by

$$\beta = \frac{N_{\text{REC}}(\gamma, x)}{N_{\text{emitted}}} = \frac{\left(\frac{1}{\alpha}\right) N_{\text{QCM}}(\gamma, x)}{\left(\frac{1}{\alpha}\right) \frac{N_{\text{QCM}}(1, x)}{\Psi(x)}}$$

It is seen that the efficiency of the QCM cancels out of the equation, leaving β expressed in terms of three quantities, all of which are known. It is then possible to go to Figure 3 and determine where on the β -versus- γ curve the measurements occur. This is shown in Figure 5.

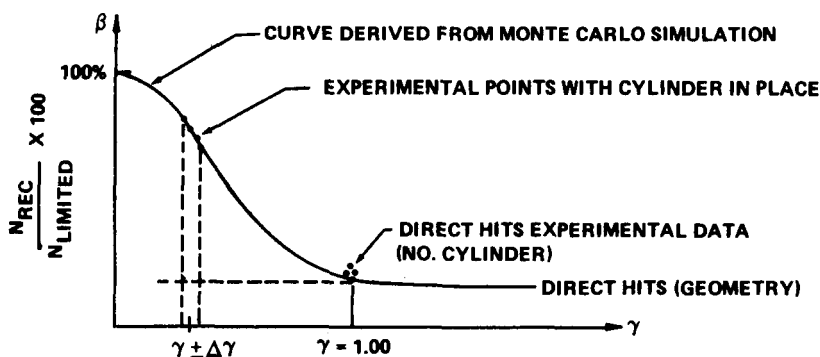


Fig. 5. Experimental determination of γ .

Experimental Results

Measurements were made of the background count by operating the system in its normal mode, with the exception of the absence of the RTV sample. For convenience of representation, the mass flux will be given in units of $\Delta f/5$ min. Some of the measurements were made at one-second intervals, and some were made at ten-second intervals and averaged about several points. Figure 6 is presented as an example of the time scale of the experiment. The system is seen to require about one-half hour to stabilize such that vacuum, LN_2 walls, and heater elements come to their equilibrium conditions. Measurements of background count were made both in the direct hits configuration and in the cylinder configuration. The background for direct hits was 0.45714 Hz/5 min, with a standard deviation of 0.35887.

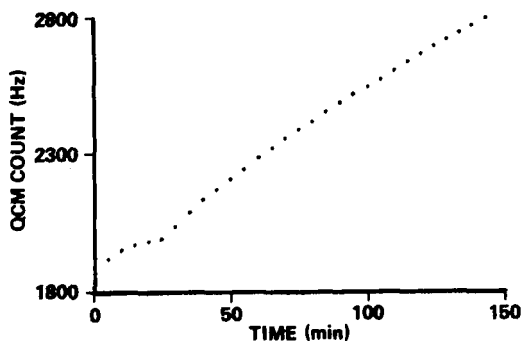


Fig. 6. Illustrating time for system to stabilize.

This measurement was made without a cold (LN_2) collimator in place, which was present for all data runs, and so represents a worst-case noise figure. With the cylinder in place, the background averaged 5.5 Hz/5 min over a range of temperatures with a worst case of 9.33 Hz/5 min. The direct hits configuration is shown in Figure 7. Two runs in this configuration, over one-hour periods, yielded 9.871 Hz/5 min with standard devia-

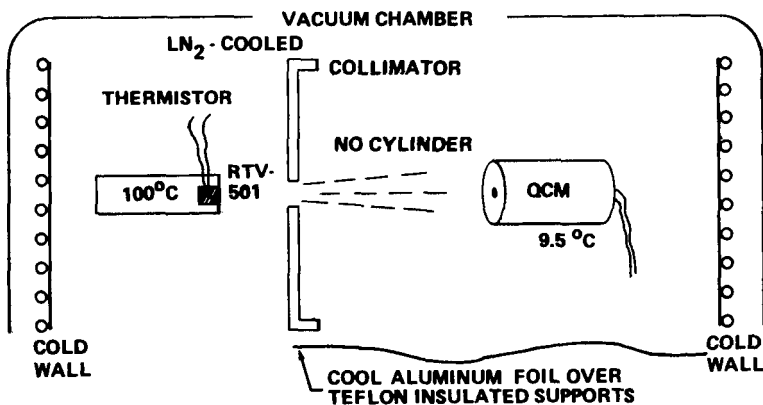


Fig. 7. Direct hits configuration.

tion 1.89, and 9.960 Hz/5 min with standard deviation 1.437. The figure 9.92 Hz/5 min is taken to be the direct-hit rate.

Since the experiment was run on engineering-type surfaces, the silver cylinder was cleaned and baked out before each run.

This procedure did not fully compensate for the history of the cylinder; and each run, though qualitatively the same, varied slightly in actual counts. The sticking coefficient-versus-temperature curves are all nearly identical but displaced by a constant small amount. The data used in the following calculations represent a typical run and differ by less than 10 percent from any other cylinder run. The procedure for each cylinder run was as follows:

1. Bake out cylinder (previous night)
2. Pump and cool down system to 10^{-6} and LN_2 temperature
3. Monitor background count
4. Heat cylinder to approximately 33°C and let stabilize
5. Monitor background count
6. Heat RTV-501 to 100°C and let stabilize
7. Cut power off cylinder heater, allowing cylinder to radiate to LN_2 walls and drop in temperature
8. Monitor cylinder temperature, QCM count, time, and $\Delta f/\Delta t$ simultaneously

The background count at 33°C was 15.3 Hz/5 min with standard deviation of 5.6 based on 42 data points. Data available from two runs in which the cylinder was at the same temperature yield mass fluxes with the cylinder in place of 126.0 Hz/5 min and 173.1 Hz/5 min, which correspond to values of β of 0.04738 and 0.06509, respectively. By considering the plot of points of the Monte Carlo data in Figure 8, it is seen that this is in the region of the three data points at $\gamma = 0.05, 0.1$, and 0.2 . A curve fit to these points yields the equation

$$\beta = 0.0900 e^{-7.810 \gamma}$$

with a correlation coefficient of -0.98981. Using this curve, one obtains the relation

$$\gamma = \frac{1}{-7.810} \ln \left(\frac{\beta}{0.0900} \right)$$

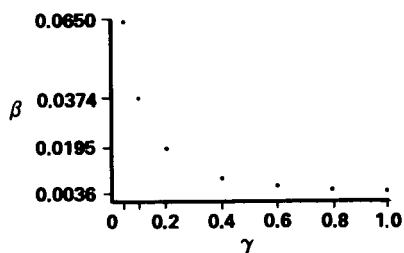


Fig. 8. Monte Carlo computer calculation of sticking coefficient.

which can be used to obtain values of γ for the experimentally measured β . This has been done, and the values are shown schematically in Figure 9. The range of values for the silver at 20.5°C is from .0415 to .0822.

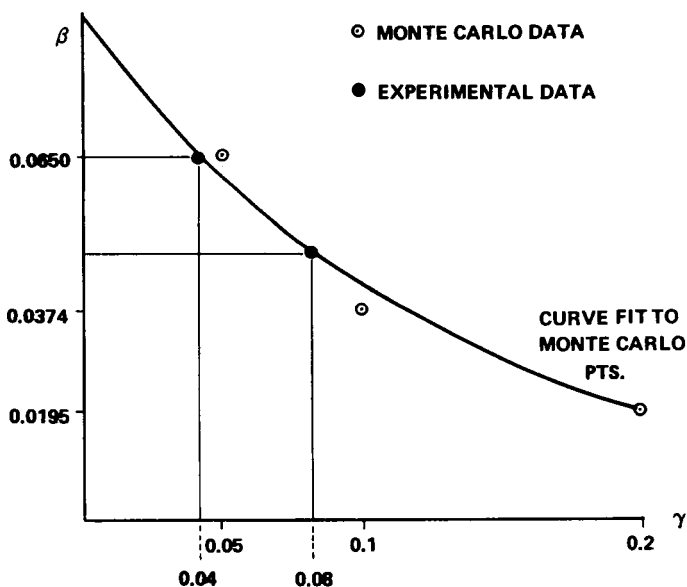


Fig. 9. Determination of sticking coefficient using Monte Carlo generated curve.

REFERENCES

1. Klingman, Edwin: Analysis of a Two-Dimensional Mass Transport Problem in Contamination of Space Flight Experiments, NASA TM X-64581, February 18, 1971.
2. Becker, E. W.; Klingelhofer, R.; and Meyer, H.: Rarified Gas Dynamics, (L. Trilling and H. Y. Wachman, eds.). 6th Inter. Sym., Cambridge, Mass., p. 1349 (Academic Press, New York, 1969).

ENVIRONMENTAL SIMULATION FROM 0.01 TO 100 SOLAR CONSTANTS

John R. Jack and Ernie W. Spisz, *NASA, Lewis Research Center*

ABSTRACT

The requirement to obtain thermal radiative property data for solar intensity levels ranging from 0.01 to 100 solar constants has led to the development of two environmental simulators at the Lewis Research Center. One simulator has the capability of operating from 0.01 to 20 solar constants with a control system which will maintain a constant intensity output or perturb the intensity in a sinusoidal fashion. The other simulator is capable of providing a solar radiation intensity of 100 solar constants which simulates the space environment at 0.1 AU.

The 20 solar constant simulator consists of a 12 KW carbon arc with associated optics. Its output as measured in the test plane is a beam 5 inches in diameter at the maximum intensity level of 2800 mW/cm² (or 20 solar constants). The intensity can be continuously varied by the moveable zoom lens. Low intensity levels are achieved by using apertures and/or fine wire mesh screens that act as neutral density filters. Programmed intensity perturbations are also obtainable by automatic control of the zoom lens.

The 100 solar constant simulator uses as its basic radiation source a 20 kW xenon compact arc lamp located at the focus of an ellipsoidal collector. The beam passes from the collector through the lenticular lens system to produce a final test plan beam approximately 5 inches in diameter having an intensity of approximately 14 W/cm² (100 solar constants).

A challenging problem encountered in the development of the two simulators was the radiometers required to accurately measure and map the absolute radiation intensity distribution in the test plane. The radiometer used for the 20 solar constant simulator was a conventional silicon solar cell that was operated photoconductively (rather than photovoltaically). By operating the cell in a photoconductive mode, the relationship between radiant intensity and measured current is linear.

It is the intent of this paper to discuss completely the characteristics of both simulators in terms of spectral content, intensity level, beam uniformity, stability and control characteristics.

In addition the radiometer problems encountered in both simulators and the unique photoconductive utilization of a silicon solar cell as the radiometer for intensities up to 20 SC will be discussed in detail. Radiation property data obtained on metals and coatings utilizing the 20 SC simulator will also be presented.

VARIABLE GEOMETRY TOTAL RADIATION DETECTOR SYSTEM

Jerry G. Greyerbiehl, *NASA, Goddard Space Flight Center*

ABSTRACT

A system of instrumented grooved black plate detectors has been designed which directly determines chamber solar simulation intensity data. When coupled with a variable geometry structure configured to simulate spacecraft thermal nodal areas, solar and chamber radiation inputs for predictive testing are obtained for inclusion in the analytical model.

Intensity data is obtained from calibrated resistance wire thermometers mounted on each detector assembly. Detector coatings can be varied to duplicate flight spacecraft coatings in order to determine coating thermal properties in the chamber environment. The detector operating principle is one of electrical substitution wherein the unknown thermal input is compared to a known electrical power input.

The development program consisted of a prototype and an advanced detector system. The prototype assembly consisted of single sensor detectors. The advanced system employs a double heater/sensor arrangement which eliminates the unknown variable heat loss evident during the early work with the prototype unit.

Although minor problems were encountered, recent operation during chamber calibration for spacecraft solar simulation testing indicates agreement with the existing solar cell radiometer technique on the order of 10%.

This method of intensity determination is particularly applicable to large area solar simulators of poor uniformity. A unique and important application of this detector assembly involves the determination of direct and extraneous chamber thermal energy and its effect on the thermal balance of the spacecraft configuration to be tested. Once developed, the detector assembly enables an accurate measurement of the thermal fluxes over all areas of a spacecraft.

THE DESIGN AND APPLICATION OF AN INFRARED SIMULATOR FOR THERMAL VACUUM TESTING

Douglas J. Skinner,^a Steven P. Wallin,^b and Calvin M. Wolff^a

ABSTRACT

An infrared simulator was developed and installed in Chamber A in support of the Apollo lunar-exploration mission thermal vacuum testing. The simulator was designed to provide thermal simulation of the radiation emitted and reflected by the lunar surface incident on the Apollo service module in a 60-mile-altitude lunar orbit. The infrared simulator comprises 18 individually controlled zones that provide the irradiance profiles over a 180° arc around the spacecraft, simulating the flux levels of equatorial, polar, and 45° lunar orbits.

INTRODUCTION

An extensive design and development program was initiated to provide a large infrared (IR) simulator for the thermal vacuum testing of the Apollo scientific instrument module (SIM). The primary design requirements are as follows.

1. Isotropic (diffuse) IR flux must be provided over a 180° arc around the Apollo service module to simulate the directionality of lunar thermal emission. The isotropicity is necessary because some critical components recessed in the (SIM) reflective cavity are sensitive to directionality and because many of the critical surfaces are not diffuse absorbers.

2. The flux must be controllable independently in 18 evenly spaced heater zones parallel to the axis of the service module to achieve the various orbital flux profiles.

3. The color temperature must not exceed 600° F and should match that portion of the lunar surface corresponding to each heater zone; that is, the product of the vehicle-to-simulator view factor and the hemispherical emittance should be as close to

^aBrown & Root-Northrop, Houston, Texas.

^bNASA Manned Spacecraft Center, Houston, Texas.

unity as possible because of numerous critical heat-transfer surfaces having varying IR absorption spectra.

4. The thermal response time must be minimized to allow controllability for each heater zone to simulate transient flux conditions.

5. The flux range at the spacecraft surface must be controllable from 140 to 440 Btu/ft²-hr for each heater zone.

6. The system must be compatible with the existing 6-bit binary input, 12-kilowatt, and 117- or 208-volt proportional power controllers.

The final configuration of the IR simulator is a retractable, semicylindrical envelope located opposite the solar simulation array. The power to each heater zone was controlled to a predetermined profile to provide a transient circumferential flux profile equivalent to that experienced in a 60-mile-altitude lunar orbit. For lunar darkside simulation, the simulator was retracted so that the spacecraft could view the liquid-nitrogen-cooled chamber paneling.

The mechanical design, the thermal design (including the special preparation of the heater strips), the control system, and the calibration of the IR simulator are described.

MECHANICAL DESIGN

Cage Structure

The IR simulator is a semicylindrical envelope with 18 heater zones positioned 18 inches from the spacecraft at a diameter of 16 feet with an overall height of 18 feet (Figs. 1 and 2). These heater zones are mounted in a cage structure, which is composed of an inner support frame and a concentric outer structural member. The four equally spaced support and structural members are connected by self-adjusting cross braces. The outer structural member with the slotted cross braces provides for the expansion and contraction of the cage while providing structural rigidity. The inner and outer sections are 17 feet 4 inches and 21 feet 4 inches in diameter, respectively. The entire structure was fabricated from 2-inch o.d., 0.188-inch wall, 6061-T6 aluminum tubing. The total weight of the structure, including heater zones and power cabling, is 1900 pounds.

Because of the high operating temperature of the heater strips and the exposure of the cage structure to the liquid-nitrogen-cooled cryogenic panels, the inner and outer frame would experience large temperature gradients (approximately 460° F at the center of the simulator). This condition necessitated a thermal stress analysis of the entire structure. The

digital computer program, "STRAN," was used to calculate the forces, bending moments, and deflections caused by the expected temperature gradients. The maximum compressive and tensile stresses were calculated to be 13 220 psi and 12 780 psi, respectively, and provided a safety factor in excess of 3.0.

Support Structure

The support structure comprises a vertical truss and support arm structure, double-hinged upper lifting booms, and cross-braced stabilizer booms (Figs. 1 and 2). The vertical truss support arm and upper lifting booms were fabricated from 6-inch-wide flange H-beams of 6061-T6 aluminum. Two-inch o.d., 0.125-inch wall aluminum tubing was used for the stabilizer booms. All bearings and pivot pins were 300 series stainless steel. The structural analysis of the IR simulator support system indicated stresses <10 000 psi, which provided a safety factor of 3.5 for the stainless steel components and slightly >3.0 for the aluminum members.

Infrared Simulator Heater Zone

A typical IR simulator heater zone is presented in Figure 3. The zone is composed of four 208-inch-long high-purity 80-percent nickel, 20-percent chromium strips 3.75 inches wide and 0.006 inch thick. The strips were connected in series with a copper bus at the top and bottom; and the zone temperature was controlled by the average of 6 to 12 thermocouple readings, depending on zone location. Several thermocouples were installed on the back side of the heater strips to provide control and the temperature gradient over the entire length of the strip. The special high-response copper-constantan thermocouple installation is shown in Figure 4. This attachment provided good thermal contact and fast response time with the heater but was electrically isolated from the strip. The electrical-mechanical details are illustrated in Figure 5. As shown, the four heater strips were spaced 1/4 inch apart with glass-filled Teflon spacers, which were bolted on the back side of the heater strips by self-locking stainless steel nuts and bolts. A 1/16-inch copper strip was installed between the heater strip and the Teflon spacer to decrease the possibility of localized hot spots. The glass-filled Teflon spacers were selected after several candidate materials were evaluated for mechanical integrity under temperature extremes of -320° to +450° F. The 1/8-inch-thick copper bus sections also were bolted to the heater strips with stainless steel self-locking nuts and bolts. Again, this assembly was selected

after several techniques (silver soldering, brazing, etc.) had been evaluated. Two 4-inch-long stainless steel springs were installed at the bottom of the heater-zone assembly and were adjusted to provide a 100-pound tension preload at ambient temperatures. This assembly ensured a flat heater zone under temperature extremes from full power (320° F) to cold-soak (-150° F) temperatures.

Chamber A Installation

The installation of the IR simulator in Chamber A at the NASA Manned Spacecraft Center (MSC) is shown in Figures 1 and 2. The IR cage structure is supported by a 1/2-inch-diameter stainless steel lift cable and the vertical truss structure. The cage is cantilevered on two 264-inch-long lifting booms. A box-section hinge system was designed for the cage end of the booms, which were spring loaded to provide positive positioning of the cage during retraction and redeployment.

To achieve the near-zero flux levels corresponding to the dark side of the moon, the simulator had to be lifted above the SIM bay to allow the spacecraft to view the liquid-nitrogen-cooled cryogenic panels. After a thorough review of several mechanisms, a parallelogram lift system was selected. This system provides excellent repeatability of precise positioning of the IR simulator around the spacecraft. A plan view of the IR simulator deployed at a distance of 18 inches around the spacecraft is shown in Figure 1.

Lift Mechanism

The IR simulator cage structure was automatically retracted by a 1/2-inch cable and winch-motor assembly, which was installed at an elevation of approximately 65 feet. (See Fig. 1.) The drive system comprises a 1.5-horsepower, 3-phase, 208-volt motor connected to an 80:1-ratio gearbox. The entire drive system, including the magnetic brake, was enclosed in a vacuum-tight housing. The housing is pressurized to 30 psia with dry nitrogen. Controlled heaters are installed to maintain the components at essentially ambient temperature. The output shaft of the gearbox is connected to the drum through a vacuum feedthrough. The lift mechanism was designed to fully retract the IR simulator in less than 1 minute. In addition to the magnetic brake, the support-arm pads also provided a positive stop during the lowering of the IR simulator.

THERMAL DESIGN

Heat Source

Three types of flux-generating systems were investigated:

1. Quartz-tungsten IR lamps with reflectors
2. Film heaters embedded in Kapton and mounted on 1/16-inch-thick, black-painted aluminum sheet
3. Directly excited, very thin nickel-chromium alloy sheets

The IR lamps were rejected because of their inability to meet the isotropicity requirement and also because of their very high color temperature ($>1000^{\circ}$ F, and variable, depending on the power input). The film heater on an aluminum sheet was rejected, after laboratory testing, because of the slow thermal response (300° to 0° F in 15 minutes, 0° to 300° F plateau in 10 minutes) and the danger of outgassing (of heater and adhesive) of condensable materials upon heater failure. Also, because of the large area of the simulator required (approximately 500 ft^2), the heater cost was high, approximately $\$50/\text{ft}^2$. The directly excited, thin nickel-chromium strips met the requirements when painted with a high-emissivity coating. This material proved to be ideal because its high mechanical strength permitted physical integrity of very thin strips and because its relatively high resistance permitted high-voltage, low-current operation. The thin strips have a very large surface-to-thermal-mass ratio, which provides the fast thermal response.

For compatibility with the existing 6-bit binary input, 12-kilowatt, 117- or 208-volt proportional controllers and for provision of the optimum view factor from the test article, each simulator zone consisted of four parallel vertical strips 17 feet long, 3-3/4 inches wide, and 0.006 inch thick. The strips were connected electrically in series. To minimize arcing (corona), the 120-volt mode of the power controllers was employed. Use of this mode required a resistance of 1.5 ohms, which corresponded to a maximum power input of 8×10^3 watts/zone. Several material and fabrication problems had to be solved prior to the final design of the system. The final selection of materials and fabrication techniques are discussed in some detail herein.

Heater-Strip Material

The material selected was a high-purity "Tophet A" alloy, 80-percent nickel, 20-percent chromium, and essentially iron free. The resistivity of this material is 510 ohms/mil foot at 20° C, with deviation ranging from -0.7 to +6 percent in the range -60° to +400° F.

Thermocouples

Copper-constantan thermocouples embedded in Kapton film were selected to provide fast thermal response and electrical isolation from the heater strips. The embedded thermocouples were applied with Minnesota Mining and Manufacturing Company (3M) no. 467 adhesive transfer tape. (See Fig. 4.) The Kapton film has been shown to be unaffected by operation at temperatures up to 500° F. The thin thermocouple foil and thin (approximately 1 mil) Kapton film caused negligible temperature differential between the thermocouple and the heater strip. The thin material also has a very small thermal mass and, thus, permits the thermocouple to closely follow the variation in the heater-strip temperatures.

Heater-Strip Insulation

The electrical insulation and heater-strip spacers were Teflon with 25-percent-glass filler. Wherever Teflon was to be placed over the heater strip, copper was attached first to the strip to create an electrical short over the covered area and, thereby, to prevent excessive temperatures caused by inhibition of heat dissipation by the Teflon.

Heater-Strip Coating

An extensive evaluation of several materials was made before the 3M Nextel 401C-10 black velvet paint was selected. Some of the coatings that were tested and rejected are the following.

1. Potassium silicate black - This coating, developed at the NASA Goddard Space Flight Center by Schutt, was the most promising because it was of higher emittance than any other coating evaluated; because it is electrically insulating; and because it is inorganic, which is highly desirable from a contamination standpoint. Unfortunately, the material did not adhere well enough to the nickel-chromium alloy to be acceptable. The problem areas were around nonmetallic parts (insulators, spacers, thermocouples), which seemed to be centers about which the

coating would blister and eventually flake off. The alloy was degreased and given a final bath in hot 3-percent hydrogen peroxide to 1-percent ammonia solution to provide as clean a surface as possible. The surface was also "broken," before cleaning, with fine grit emery cloth. This paint, however, adhered very well to aluminum and to sandblasted nickel-chromium alloy. The 6-mil-thick alloy, however, was so thin that it severely warped upon sandblasting; therefore, such pretreatment was unacceptable.

2. Magna X-500 - This is a low-outgassing urethane, flat-black material that is electrically conductive. The material adhered well to the nickel-chromium alloy, but its emittance was approximately 6 percent less than that of the 3M black velvet paint. The electrical conductivity was not desirable because of the danger of shorting between the strips, which were only 1/4 inch apart.

3. Plasma-jet-applied ceramic coatings - Emittances of these coatings were lower than emittances of coatings mentioned previously, and all ceramic coatings required sandblasting for adherence.

The method developed for applying the 3M paint to the nickel-chromium strip is as follows.

1. Surface preparation

a. Place full-length heater strips on workbench covered with clean polyethylene film.

b. Clean strips with precision-grade Freon, using paper wipes. Clean gloves (polyethylene or other plastic) are to be worn for this and following operations.

c. Prepare a solution of two parts of water and one part of Dupont 57175 metal conditioner. Apply the solution to the strips with a brush or sponge, and scrub surfaces with 220- to 280-grit sandpaper or steel wool until the glaze is removed. Keep the surface wet with the solution during the deglazing operation.

d. Wipe off all the solution from the surface, using a clean, dry cloth; and let the surface dry for 10 minutes.

e. Assemble heater strips with other parts to form individual IR simulator heater zone. (See Fig. 3.) Mount the entire assembly in a special handling fixture.

f. Apply thermocouples (copper-constantan embedded in Kapton film), using 3M no. 467 adhesive transfer tape as a bonding material. Using a lamp, heat the thermocouples to 160° F for 5 minutes. While heating, press the thermocouple to remove all air bubbles.

g. Wipe off heater surfaces with methyl ethyl ketone.

2. Priming

a. Prime the heater surfaces with 3M Nextel 901C primer, and air flash for 3 to 5 minutes. Priming and coating are to be done along the long dimension. Use a spray gun for the operation.

b. Air dry for 5 to 7 minutes before proceeding to the next step.

3. Coating and drying

a. Prepare 3M 401C-10 Nextel black velvet paint according to the manufacturer's specifications.

b. Spray a thin coat, followed immediately by a thick coat, of 3M black velvet paint such that a total coating thickness of 0.002 to 0.003 inch is achieved.

c. After 2 hours of air drying, cover the coated surface with a polyethylene film to prevent the collection of dust particles on the surface.

4. Outgassing - Outgas the fully assembled IR simulator heater zone for a minimum of 4 hours at 250° F at a pressure below 1×10^{-3} torr.

Infrared Simulator Heater-Zone Performance

Several thermal vacuum tests were conducted on full-scale prototype IR simulator heater zones. The coatings previously mentioned were evaluated, using different surface preparation and coating techniques. In addition, several types of controllers, thermocouples, and electrical connections were evaluated. The heatup and cooldown responses of the preproduction IR simulator heater zone are presented in Figure 6. The data are for an isolated heater zone that is not exposed to an external radiation source. The view factor from the spacecraft to the complete 18-zone IR simulator with the 18-inch space between the heater strips and the spacecraft skin is 0.92. The hemispherical emittance of the 3M black velvet paint is between 0.85 and 0.90. Because of the high view factor, the heater strips also were heated by radiation emitted by the spacecraft skin. This effect required that the zones be controlled by temperature instead of by power output. Heating of the heater strips by the spacecraft also caused slower cooling response. However, this effect did not cause any problem of maintaining transient flux conditions during the hot portions of lunar orbit.

The final installation had the disadvantage that the low flux levels required to accommodate the orbital profile of transcending to the dark side of the moon could not be achieved with the simulator in the deployed position. Because the simulator had

to be retracted to facilitate the installation and removal of the calibration fixture and the actual test vehicle, the retraction system was designed for cryogenic vacuum service. The results from the full-scale system show that the cooldown response was similar to the prototype data when the simulator was in the retracted position. The flux level at the test article decreased from a maximum of $440 \text{ Btu/ft}^2\text{-hr}$ to $5 \text{ Btu/ft}^2\text{-hr}$ in approximately 90 seconds.

CONTROL SYSTEM

The IR simulator was controlled by the acceptance checkout equipment (ACE) computers that are part of the data acquisition and recording system in the MSC Space Environment Simulation Laboratory (SESL). A software computer program was developed to permit either open- or closed-loop control of the 18 power zones to a predefined temperature profile and to provide automated control of the IR simulator lift mechanism for positioning the IR simulator. The computer program generated a 6-bit power signal for each of the 18 power controllers. The details of this program and the general approach to the use of the computer for this application are described in a paper by Dewey (1). The power controllers were silicon-controlled rectifiers capable of producing 12-kilowatt, 117-volt rectified alternating current. The software package provided for considerable flexibility through real-time C-start input of options, including the following.

1. Selection of up to 99 different desired temperature profiles
2. Selection of the time interval between power control signal updates
3. Selection of parameters that regulated the "look-ahead" feature to allow for the thermal response of the heaters to a power change
4. Use of multipliers to modify the desired input-temperature profile for each control zone
5. Definition of thermocouples to be averaged for closed-loop temperature control
6. Definition of lift-mechanism-control parameters
7. Selection of control, timing, and cathode-ray-tube display modes

The IR simulator control sensors were copper-constantan thermocouples mounted on, and electrically isolated from, the heater strips. The thermocouples were arranged in a pattern that provided six thermocouples per heater control zone near the edge of the IR simulator and 12 thermocouples per heater zone

near the center of the IR simulator over the open SIM bay on the test article. Any combination of the thermocouples on a given control zone could be averaged and used as the closed-loop control signal for that zone.

The control program read the desired temperature profile recorded on magnetic tape and compared the desired temperature for the current update interval to the measured temperature for each heater control zone. The program then corrected the command to the power controllers to cause the measured temperature to approximate the desired temperature at the end of the update interval. The computer program used a look-ahead feature - based on the difference between the actual and desired temperatures, the length of the update interval, and the physical properties of the heater system - to determine the correction to the power command for each update. At a prescribed time in the profile, the IR simulator could be lowered or raised automatically to provide a step heat input to the test article or to provide a large view of the chamber liquid-nitrogen-cooled cryogenic panels for a low-flux environment.

To provide the data required for the desired-temperature-profile tape, a thermal model of the IR simulator/test-article system was developed. The data required for the profile tape consisted of a set of a desired temperature for each heater control zone for a given update interval that corresponded to a given location in a simulated orbit. The determination of the temperature distribution on the IR simulator heater zones was based on a known flux distribution incident upon the Apollo service module in lunar orbit. The model consisted of 18 planar heater nodes, and 18 corresponding strip nodes on the spacecraft were defined. After determining all of the necessary "script F" radiation exchange factors by using a computerized Monte Carlo technique, a system of 18 simultaneous equations was defined by equating the desired flux for each spacecraft node to the summation of the flux contribution from all heaters. The system of simultaneous equations was solved to determine the required temperature distribution for each update interval. To simulate the equatorial and 45° lunar-orbital environments required for the testing program, the update interval used was 100 seconds, or one update every 5° during the lunar orbit of 2 hours. The starting point for the simulated orbits was defined as the subsolar point, or the center of the dark side of lunar orbit. Approximately 30 minutes after the start of a simulated orbit, the IR simulator was lowered to the proximity of the spacecraft; and, approximately 1 hour later, the IR simulator was raised to simulate the spacecraft passing the terminator to the dark side of the moon.

The simultaneous-equation technique of determining the desired temperature profile was used as a first approximation to be later verified and adjusted during the planned calibration test. The computer program used to solve the simultaneous-equation network also was used to punch cards formatted as required for direct input to the ACE software package. The only significant problem encountered when using this modeling technique was that, during certain portions of lunar orbit, particularly during the 45° inclination orbits, large variations in the required circumferential flux distribution caused the unique network solution to include several temperatures below 0° R. A trial-and-error adjustment of the desired flux distribution was required to correct the network solution to yield a meaningful temperature distribution without significantly altering the resulting flux distribution.

The calibration test data showed that the fluxes incident to the spacecraft both for the equatorial and 45° orbits were approximately 10 to 15 percent higher than those predicted by using the simultaneous-equation network. Because the solution technique did not include reflected and re-emitted energy, this result was expected. Corrections were made in real time during the test by using a C-start input of a multiplying factor for each heater zone, which reduced the desired temperature values by 5 percent. A comparison of the desired flux distribution and the actual flux obtained during the calibration test on a node near the center of the spacecraft for the equatorial orbit is shown in Figure 7, and the same comparison for the 45° inclination orbit for a node near the solar side of the spacecraft is shown in Figure 8.

INFRARED SIMULATOR CALIBRATION

Because the heater strips of the IR simulator are affected by heat emanating from the test article and because, in some locations on the test article, the net flux received at a surface resulted from reflections from several surfaces on the test article itself, the simulator was calibrated with a mockup of the 2TV-2 service module (known as the "boilerplate"), which was outfitted with radiometers. (See Fig. 9.) The radiometer-laden spacecraft scanned the flux profile of the IR simulator, and also of the solar simulation system, as it was rotated 350° about its vertical axis. Details of the calibration phase and the resulting computer direction for programmed operation of the system in actual testing were discussed in the previous section. The radiometers employed are of two types. One is the Boelter-type heat-flux transducer, coated with high-emissivity, 3M black velvet paint, mounted directly on the boilerplate spacecraft skin with a continuous-type

adhesive (epoxy). The second radiometer is the same type of sensor mounted on a water-cooled (and heated) aluminum block. The water permitted the radiometer to be maintained at constant temperature and was the eventual source of sink of transferred radiation.

The calibration of these radiometers was simple and direct. The technique provided, in a single measurement, an accurate determination of the radiometer sensitivity to incident IR hemispherical radiation in vacuum without the need for an irradiance reference. The radiometers were simply placed in a vacuum chamber, their temperatures were controlled by water flow, and their environments were configured so as to view only black, cryogenically cooled (77° K) surfaces. Because of the radiometer sensing-element design (2), the response is equal in magnitude but opposite in sign for emitted irradiance as compared to absorbed irradiance. Because, according to Kirchoff's law of radiation, hemispherical emittance for a gray body over a given wavelength interval is equal to the hemispherical absorptance for the same interval, the sensitivity of the radiometers for incident hemispherical IR radiation is calculated according to

$$S = \frac{\sigma(T^4 - T_w^4)}{V}$$

where S = radiometer output, Btu/ft²-hr-mv

σ = Stefan-Boltzmann constant, 0.173×10^{-8} Btu/ft²-hr-°R⁴

T = temperature of the radiometer in the calibration chamber, °R

T_w = temperature of calibration chamber walls, °R

V = radiometer output at temperature T in calibration chamber, mv

It is seen that the flux used for the calibration is that emitted by the radiometer itself to the cold environment, and the only intrinsic parameter that must be accurately known is the radiometer temperature.

The exact value of radiometer emittance is not necessary, provided that the surface is gray in the IR region and is approximately a Lambertian (diffuse) surface in the IR region, as explained in the following.

If the emittance ϵ were known, a calibration factor for absorbed irradiance would be calculated from

$$S^1 = \epsilon S \quad (2)$$

When irradiance is measured, the absorbed irradiance would be determined by

$$\alpha \dot{Q} - \epsilon \sigma T^4 = S^1 \cdot V \quad (3)$$

where V = millivolt output in measurement

α = radiometer absorptivity

\dot{Q} = incident irradiance

ϵ = radiometer emissivity

Because, according to Kirchoff, $\alpha = \epsilon$, the value of \dot{Q} is determined by

$$\dot{Q} = \frac{S^1 \cdot V + \epsilon \sigma T^4}{\alpha} = \frac{\epsilon SV + \epsilon \sigma T^4}{\alpha = \epsilon} = SV + \sigma T^4 \quad (4)$$

and, thus, the value of ϵ disappears in the determination. For the particular type of radiometer employed, the temperature differential between the front face and the rear (reference) face of the slab is much less than 1° F. Therefore, errors caused by differences in measured (body) temperature and sensing-surface temperature are negligible. It has been found that the most accurate temperature measurement is made by silver soldering the measuring thermocouple to the radiometer water line as close to the radiometer as possible, then by wrapping the water line with reflective insulating film. Of course, this procedure requires sufficient water flow. A flow of 0.2 gal/min through 1/4-inch-o. d. line is sufficient.

The radiometers mounted directly on the spacecraft (without water lines) were calibrated in the same manner by mounting them on a plate, the temperature of which was controlled by circulating water. These radiometers had thermocouples embedded in the sensor for temperature measurement. Although this type of thermally nonstabilized radiometer performed as expected during calibration (where heat was supplied by a constant-temperature stream of water), the radiometers gave very spurious data when mounted on the thin spacecraft skin, whereupon

the radiometers had to use internal heat content as heat sources and sinks. It is believed that this perturbation of radiometer heat content caused severe thermal gradients within the sensor, which in turn gave the erroneous data, because the sensor measures heat transfer by measuring the temperature differential created by heat traversing its narrow conductive thickness. Such radiometers have been used with success if they are mounted on thick copper blocks, the thermal mass of which essentially dampens the temperature excursions in the radiometer and, thereby, permits it to function properly.

An important factor in the use of the radiometers is that the normal solar absorptance of the 3M black velvet paint is approximately 10 percent higher than the hemispherical IR emittance; and, when radiometers calibrated as described herein are used to measure solar simulation, this difference must be considered in interpreting the data.

CONCLUSION

This IR simulation system also was used successfully to provide the total flux profile incident on the earth-viewing portions of the service module when in earth orbit. It is believed that the techniques described herein may provide solutions to many problems of thermal irradiance simulation in testing articles with varied thermal control surfaces, where diffuse radiation and spectral match is necessary.

ACKNOWLEDGMENTS

The authors wish to acknowledge the contributions of the following SESL Brown & Root-Northrop (BRN) engineering groups, NASA MSC Technical Services Division (TSD), and NASA MSC Space Environment Test Division (SETD) personnel for their assistance in the successful development and implementation of the IR simulator.

BRN Electrical Engineering Group - Electrical and controller system design

BRN Design Group - Lift mechanism and mechanical design

BRN Environmental Measurements Group - Thermal stress analyses, thermal design and development

NASA TSD - Evaluation and development of coating techniques and heater-zone fabrication

NASA SETD - Design and development of the computer operations controlling the simulation system

REFERENCES

1. Dewey, R. L. : Control of an Artificial Infrared Environment to Simulate Complex, Time-Varying Orbital Conditions. Paper presented at The Sixth IES-AIAA-ASTM Space Simulation Conference, New York City, Apr. 30, 1972.
2. Boelter, L. M. K. ; Poppendiek, H. F. ; and Gier, J. T. : An Investigation of Aircraft Heaters XVII - Experimental Inquiry into Steady State Unidirectional Heat-Meter Corrections. Report to the National Advisory Committee for Aeronautics, Washington, D. C. (Aug. 1944).

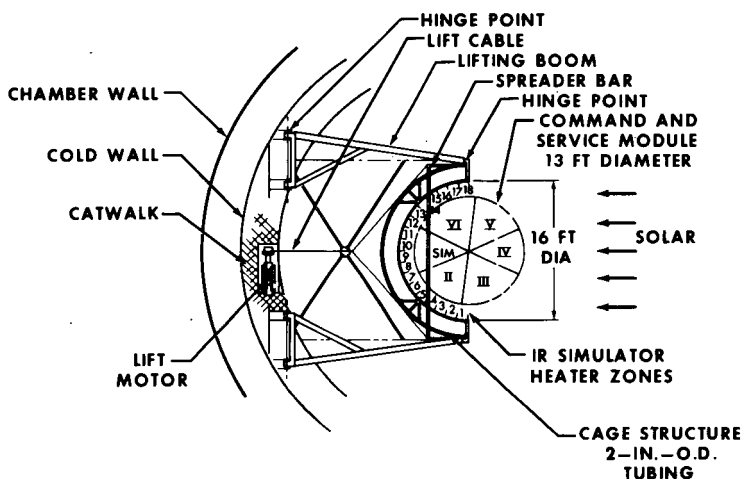


Fig. 1—Infrared simulator lift mechanism

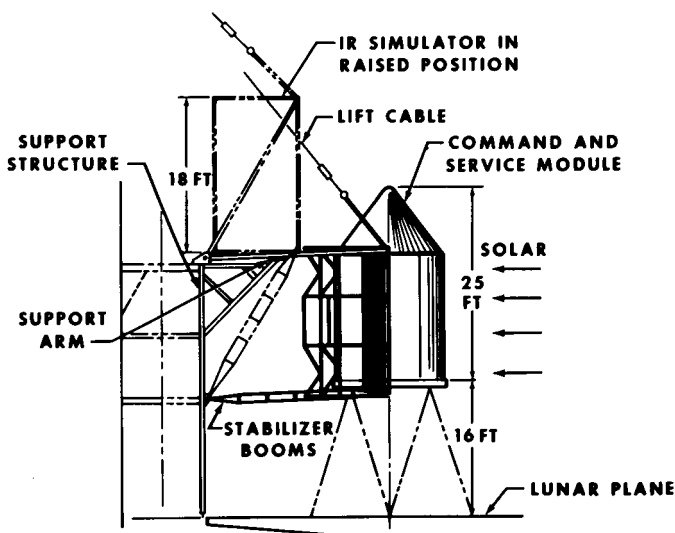


Fig. 2—In-chamber installation of the IR simulator

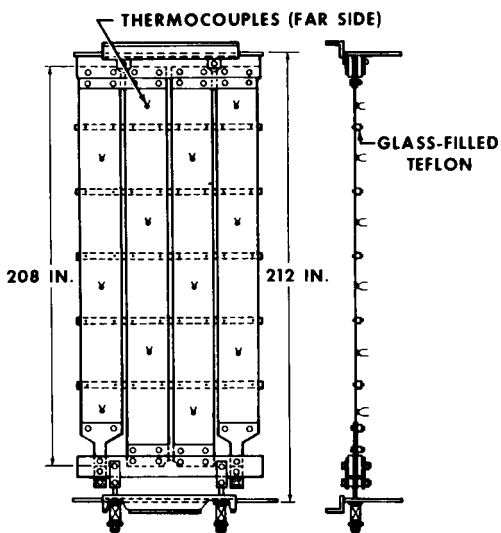


Fig. 3—Typical simulator heater zone with thermocouple installation

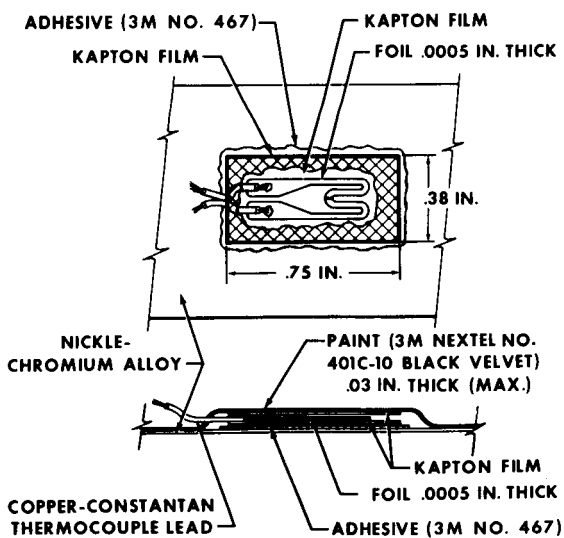


Fig. 4—Thermocouple installation detail

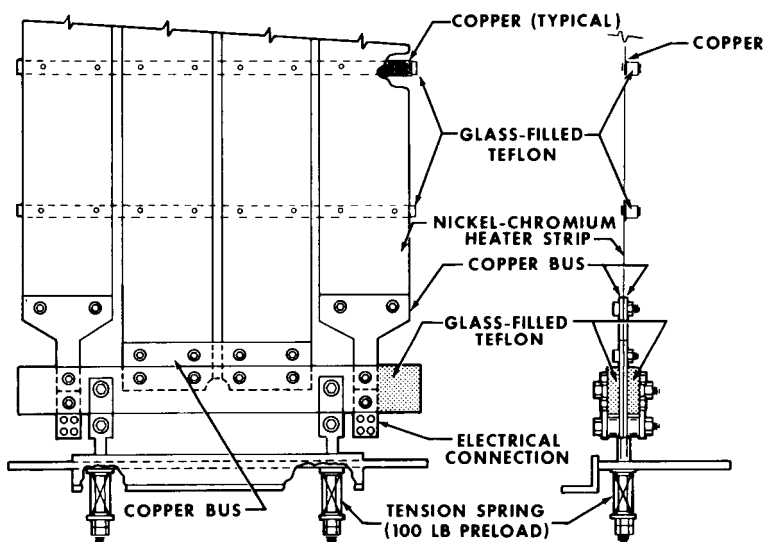


Fig. 5—Infrared simulator heater-zone electrical connection detail

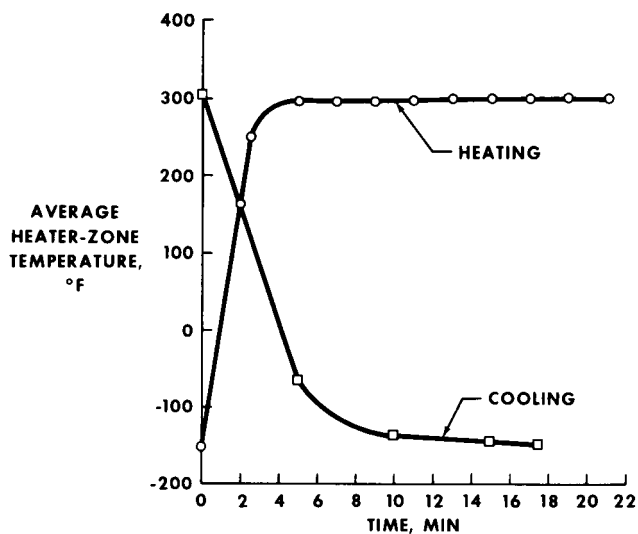


Fig. 6—Thermal response of full-scale proto-type IR simulator heater zone

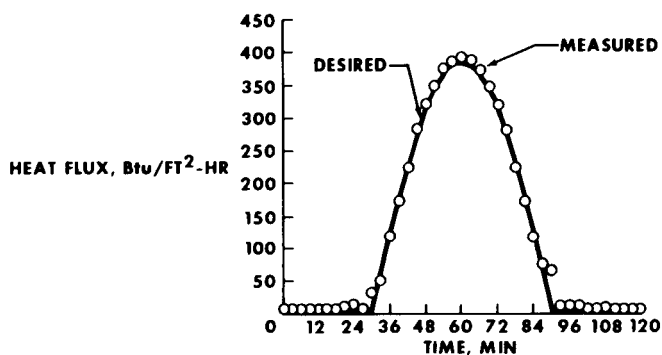


Fig. 7—Comparison of desired and measured flux (0° orbit, center of spacecraft)

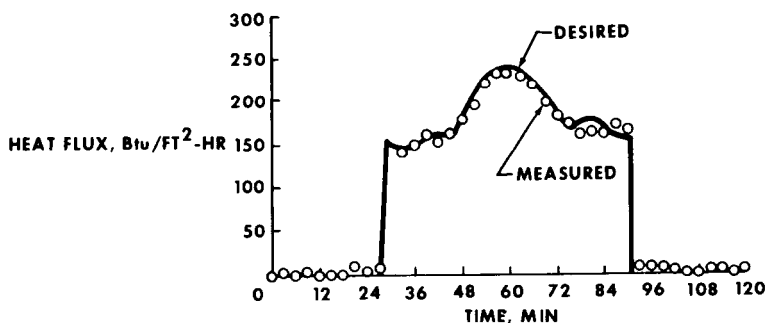


Fig. 8—Comparison of desired and measured flux (45° orbit, hot side of spacecraft)

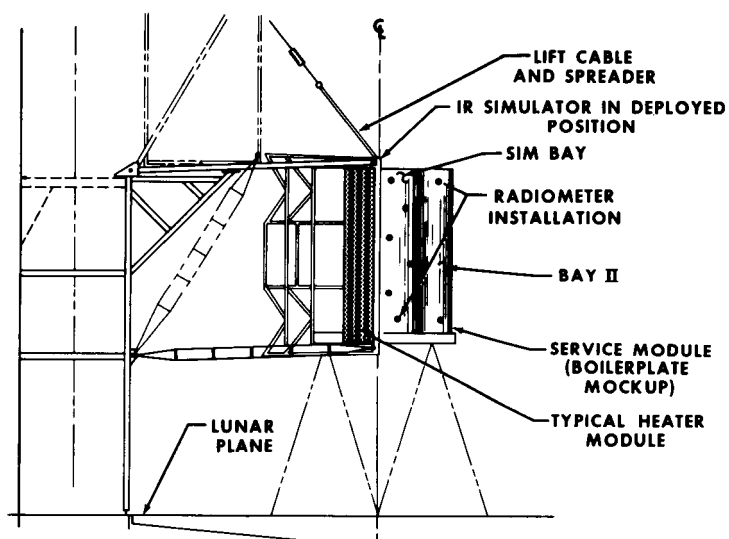


Fig. 9—Calibration system for IR simulator

CONTROL OF AN ARTIFICIAL INFRARED ENVIRONMENT TO SIMULATE COMPLEX, TIME-VARYING ORBITAL CONDITIONS

Ray L. Dewey, *NASA Manned Spacecraft Center, Houston, Texas*

ABSTRACT

A computer-controlled infrared simulation system has recently been developed for thermal vacuum ground testing of spacecraft in the Space Environment Simulation Laboratory of the NASA Manned Spacecraft Center. The system can simultaneously follow as many as 30 separate time-varying intensity profiles for irradiation of different areas of a test spacecraft, producing an environment that more closely resembles the changing conditions experienced by an orbiting spacecraft than has heretofore been possible.

This paper includes a description of the hardware employed, but emphasis is placed upon computer techniques that have been developed to maximize the capabilities of the control system within the constraints imposed by a limited computer capability. Among the topics discussed are open-loop control, closed-loop control, manual alteration of profiles, compensation for slow response of the radiation source, and compensation for interacting control zones. Examples of typical results obtained using the control system are also presented.

INTRODUCTION

For two of its recent thermal vacuum test programs, the Space Environment Simulation Laboratory at the NASA Manned Spacecraft Center (MSC) at Houston, Texas, has found it necessary to reproduce the diffuse infrared (IR) radiation that emanates from the earth and the moon. Therefore, two separate IR simulators were developed, each especially designed to meet the requirements of its associated test article, plus a single computerized control system adaptable to both.

The first simulator — for use with the Skylab Apollo Telescope Mount (ATM) — was developed by the NASA Marshall Space Flight Center (MSFC) at Huntsville, Alabama. The MSFC engineers chose tubular quartz lamps as their IR source, chiefly to permit the flexibility of adjustment that they required for uniform illumination of the irregular ATM surface. The spectral characteristics of these lamps, however, do not match the characteristics of the IR radiation encountered in orbit, so that uncertainties could occur in the test data. To avoid this problem, the lamps are controlled to produce desired levels of absorbed heat flux rather than desired levels of incident heat flux. The absorbed heat flux is measured in each of 25 control zones by means of slab radiometers coated with the same paint as the test article and mounted on its surface.

In contrast to the ATM, the Apollo Service Module has a variety of surface coatings exposed to the IR environment, each of which reacts differently to any error in the spectral characteristics of the incident radiation. Thus, the major requirement that the MSC engineers faced in their development of the service model IR simulator was to obtain the best possible spectral simulation. For this reason, relatively low-temperature heater strips were selected in preference to high-temperature quartz lamps. These heater strips are arranged in the form of a half cylinder around the test article and are divided into 18 control zones. Electrically insulated thermocouples are attached to the strips to monitor the zone temperatures. Although heater strips are the best choice for meeting the overriding spectral requirements, other characteristics of the strips are less than ideal. Because of their large area, the strips cause considerable blockage between the test article and the cold walls of the vacuum chamber, requiring that the simulator be retracted during low flux portions of each orbit. Also, the relatively large mass of the strips makes their response to changes in input power very sluggish, requiring that the control system be more sophisticated.

In the interest of economy, it was decided to use the existing Acceptance Checkout Equipment (ACE) computer system for control of both IR simulators. However, because of the already heavy usage of ACE for acquisition and display of test data, as well as for sending commands to the test article, the addition of this substantial new task had to be accomplished without requiring undue amounts of computer memory or of computation time. How this was successfully accomplished is the subject of this paper.

CONTROL SYSTEM DESCRIPTION

In the operation of the control system, time profiles of desired output values for each control zone are supplied to the computer from digital magnetic tape. Using the profile information, together with feedback data and manual inputs, as applicable, the computer calculates six-bit binary commands for each zone and transmits them to numerical-input power controllers. The power controllers accept the binary commands from the computer and adjust their outputs accordingly, holding these new power levels until again commanded by the computer during the next command update. At the same time, pertinent data are displayed on a character-display cathode-ray tube (fig. 1) or on event lights (fig. 2), and also are filed on digital magnetic tape for a permanent record.

For long periods of time during test operations, the control system can be left alone to operate automatically. However, a considerable number of real-time options are available to the operator: (1) to select the set of profiles to be followed, (2) to start and stop the control program, (3) to adjust the gain of each zone control loop, (4) to choose either of two redundant feedback sensors for each zone (if applicable), (5) to select either open-loop or closed-loop control for each zone, (6) to multiply the profile for any zone (or zones) by a factor of 0.10 to 10.00, (7) to override the profile with a manual input for any zone (or zones), and (8) to change the interval between command updates to any value from 10.0 to 409.5 seconds.

This control program was designed for maximum flexibility in order to be adaptable to many varied test situations. For example, the profile tape may have on it as many as 99 files containing separate sets of zone profiles. Each of these profiles is made up of a series of number pairs that define for each update both a desired output (e.g., temperature or heat flux) for use in the closed-loop control mode and a six-bit binary command level for use in the open-loop control mode. A profile may have as few as two updates or as many as thousands of updates, depending upon the duration of the profile and the time interval between updates.

One of the options of the control program — to automatically repeat a file on the profile tape until stopped by the operator — is particularly useful for simulating the cyclic thermal conditions encountered by an orbiting spacecraft. Synchronization of other test operations with these simulated orbits is made possible through the use of a flag word in the computer memory that is set by the control program each time

the profile begins anew. The flag word is monitored by other computer programs as their signal to begin operations. This method is used, for example, to synchronize the automatic retraction of the service module IR simulator during the low-flux portion of each orbit.

The primary function of the computer in this system is to select the proper command levels for the various zones. In order to accomplish this function, the computer must know how much output to expect from each of the zones for all of the 64 possible command levels. Because storage of this information within the computer would ordinarily consume a large portion of the computer memory, a simplifying assumption has been made that the output-versus-input relationships for all zones can be normalized to a single curve. If normalizing factors for each of the separate zones are chosen properly, the resulting common curve represents the percentage of each zone's maximum output that each command level would produce. (Hereinafter, when percentage is mentioned it should be understood to mean percentage of maximum output.) Memory storage requirements are then reduced to a single table of 64 percentage values (one for each possible command level) plus the normalizing factor for each zone.

OPEN-LOOP CONTROL

A conceptual block diagram of the control system is shown in Figure 3. For open-loop control, the command level from the profile tape is sent out unchanged unless the operator intervenes to alter it. If the operator considers that the output of a zone is consistently too high or too low, he can input a multiplying factor to correct it. In order that this factor's effect will be linear upon the zone's output, the profile command level must be converted into percentage output before multiplication and, afterward, the result must be converted back into a command level. The conversion in both cases is accomplished by locating the command (or percentage) in the calibration table to find its associated percentage (or command). If instead the operator wishes to override the tape input altogether, he may specify the output that he desires in terms of temperature (or heat flux). The computer first translates this request into an equivalent percentage output through multiplication by the normalizing factor for the zone and then finds the associated command level in the calibration table.

CLOSED-LOOP CONTROL

For closed-loop control, the calibration table is not considered to be an absolute relationship of output to command, but its validity for relating changes in output to changes in command is unquestioned. Two commands per zone are calculated at the time of each update: (1) the command that will cause the output to change from its present value to the desired value in the time allowed between updates and (2) the command that will maintain this desired output when it has been reached. The first "output-changing" command is sent out immediately. If, at the time of the next update the desired output has actually been reached, then sending of the "output-holding" command will result in no change of the output during the following update interval. It follows, then, that if any change is required at this time, it must be made relative to this output-holding command, or, more specifically, it must be made relative to the percentage value associated with this command in the calibration table. This percentage value is called the "basis" because it is carried over from the previous update as the basis from which the next change will be made.

Although thus far in this explanation it has been postulated that the desired output has been reached at the time of the next update, the same method can be used even if the output is higher or lower than desired. In this case, the assumption is made that the relationship of equilibrium output values to command levels has shifted in such a manner that whatever value the output has attained is the value that will be maintained by the output-holding command.

The different characteristics of the two simulators require that the above principles of closed-loop control be applied in a different manner for each. The ATM control loop is the simpler one because the zones reach equilibrium (or nearly so) within the 60-second update interval. Thus, the output-changing command and the output-holding command are the same. Because the calibration table is based upon equilibrium values, the new command to be sent in each update is found by simply moving within the table a distance from the basis equal to the required change in output. That is, the desired change — converted to percentage output through multiplication by the normalizing factor — is added to the basis, then the command level in the table is found whose percentage value is most nearly equal to the sum. The basis for the next update is the exact percentage associated with this new command and thus may differ slightly from the sum used to locate it.

The service module IR simulator does not reach equilibrium conditions within its 100-second update interval. Thus, if the command to be sent in each update were calculated in the same way as for the ATM simulator, the desired change in output would not be accomplished in the 100 seconds allowed. In order to force the output to change the required amount, a command must be chosen whose expected equilibrium output is farther away from the basis than is actually desired. This can be done by exaggerating the amount of desired output change before using it to find a new command. The amount of exaggeration required, however, has been found to vary as a function of (1) the value of the basis and (2) the resulting command level chosen. (This would seem to indicate that the basic dependence is upon the temperature from which the change is to be made and the equilibrium temperature toward which the zone is driven.)

The family of 64 curves indicated in Figure 4 was developed from zone response data, but to have stored them in computer memory would again have exceeded the available space. A study of the curves, however, revealed that their spacing from each other is related to the percentage values in the calibration curve (fig. 5). This relationship allows the re-creation of the 64 curves from any one of them by the use of the calibration curve. As was done with the calibration curve, then, one of the multiplier curves is stored as a table of 64 values in the computer memory.

Computation of commands is as follows. A tentative output-changing command is determined by choosing a trial command — thus establishing a multiplier value — and then using this multiplier to exaggerate the desired change. If the command defined by this exaggerated change value is other than the trial command, another trial command is chosen and the process is repeated. This procedure continues until the correct command is found. In contrast, the output-holding command is found in exactly the same manner as before. This is because the command necessary to maintain an output value is independent of how this output value may have been attained.

In closed-loop operation, as in open-loop operation, the operator may either modify or completely override the profile. If the operator chooses to modify the profile, he inputs a factor for direct multiplication of the profile desired values. Should he wish to override the profile, he simply inputs his own desired value to replace the profile desired value.

SENSOR FAULT DETECTION

Additional computations are made to aid the operator in detecting a sensor fault and in identifying which sensor, primary or secondary, has failed. For detection of a fault, the two redundant sensor outputs are compared. If the difference exceeds a specified fraction of the primary sensor value, a "high" or "low" indicator light is illuminated. To determine which of the sensors has failed, the power into each zone is monitored and compared to the expected power. If the difference exceeds a specified fraction of the expected power, a high or low light is illuminated. The faulty sensor is identified from the combination of lights, as shown in Table I.

Because the expected power is different for each zone and changes from update to update, it would be logical to include it on the profile tape. This would, however, require a larger tape input buffer area in the computer memory and would complicate generation of the tape. A better method is to use the direct relationship between the command levels on the profile tape and the expected power, requiring only that additional calibration information be available within the computer to relate the two. This calibration information is supplied to the computer as another single table of 64 percentages common to all zones (one for each command level), plus a value unique to each zone, which, when multiplied by a percentage from the table, results in the expected power for that zone.

CONTROL ZONE INTERACTION

A computational technique to compensate for interaction between zones was developed for use in ATM testing, but use of this technique later became unnecessary when baffles were installed to block spillover of IR radiation between zones. Before the hardware was modified, though, a change in the intensity of one zone affected as many as three of the adjacent zones.

The standard method of solving this problem would have been to express it as a series of simultaneous equations, whose solution could then be found using matrix techniques; however, because such complex calculations — repeated at one-minute intervals — are not practical on the ACE computers, an iterative technique was substituted.

In the first iteration, preliminary commands are calculated for each zone in a fixed sequential order, taking into account the expected spillover from only those adjacent zones which precede the affected zone in the sequence. (Contributions from each zone to adjacent zones preceding it are stored for use in

the next iteration.) In subsequent iterations, commands are recalculated for each zone in the same sequential order as before, with contributions both from preceding zones and from succeeding zones. The contributions from the preceding zones are as recalculated in the current iteration, while the contributions from the succeeding zones are as calculated in the previous iteration. The computation is terminated when an iteration has been completed in which no change was made in command levels or when a specified time limit has been exceeded.

This process of solution can best be understood by considering a system having only two zones. First, a command for Zone 1 is calculated without regard to any spillover from Zone 2. Next, a Zone 2 command is determined that will add the proper intensity to that already present due to spillover from Zone 1. But because of spillover back to Zone 1 from Zone 2, the intensity of the Zone 1 lamps must now be reduced. This, however, reduces the spillover to Zone 2, requiring that its lamp intensity be increased. When the amount of correction needed for both zones diminishes to less than half of the difference between the command selected and the next adjacent command in the calibration table, the optimum set of commands has been found. Note that this method takes advantage of the incremental nature of the system to avoid needless computational refinement while still obtaining the proper result.

RESULTS OF USING THE CONTROL SYSTEM

The automatic operation of the IR simulators during both series of test operations has been highly satisfactory. Examples of the infrared environment actually produced versus the profile that was desired are presented in Figure 6 for the ATM and in Figure 7 for the service module.

CONCLUSIONS

The use of a computer for automatic control of changing infrared environments has proved to be a very practical means of obtaining accurate simulations over long periods of time with minimum manpower requirements.

REFERENCES

Apollo Telescope Mount

Bachtel, F. D., and Loose, J. D.: Design and Control of an Orbital Heating Simulator. Paper No. 71-432, AIAA 6th Thermophysics Conference, Tullahoma, Tennessee, April 26, 1971.

Service Module

Wallin, S. P., Wolff, C. M., and Skinner, D. J.: The Design and Application of an Infrared Simulator for Thermal Vacuum Testing. Paper prepared for the IES/AIAA/ASTM Space Simulation Conference, New York City, April 30, 1972.

TABLE I. - SENSOR FAULT DETECTION

Alternate sensor (compared to sensor in control loop)	High	Low	High	Low	OK	OK	High	Low	OK
Actual power (compared to expected power)	High	Low	Low	High	High	Low	OK	OK	OK
Action required	Place the alternate sensor in the control loop	Place the alternate sensor in the control loop	Change to open loop control	Change to open loop control	Try placing the al- ternate sensor in the control loop	Try placing the al- ternate sensor in the control loop	None	None	None

0002 RUN 04 01/36/01 ORBIT 02 00/02/03

	ZONE 01	ZONE 02	ZONE 03
DESIRED H/F	123.8	101.6	076.2 BTUH
H/F ERROR	-003.8	002.4	000.0 BTUH
ALT-CONTROL	001.0	000.7	-000.2 BTUH
LOOP ADJUST	01.00	01.01	01.00 XFAC
EXPECTED PWR	03.90	03.72	02.94 KW
POWER ERROR	-00.03	00.06	00.00 KW
	ZONE 04	ZONE 05	ZONE 06
DESIRED H/F	095.8	098.4	073.0 BTUH
H/F ERROR	-001.6	001.6	-002.0 BTUH
ALT-CONTROL	000.5	-000.9	001.1 BTUH
LOOP ADJUST	01.00	01.00	00.96 XFAC
EXPECTED PWR	03.60	03.66	02.85 KW
POWER ERROR	-00.09	00.04	-00.01 KW
	ZONE 07	ZONE 08	ZONE 09
DESIRED H/F	130.2	095.2	119.8 BTUH
H/F ERROR	000.2	-002.8	003.1 BTUH
ALT-CONTROL	000.6	-001.0	000.0 BTUH
LOOP ADJUST	01.04	01.00	01.00 XFAC
EXPECTED PWR	04.08	03.59	00.22 KW
POWER ERROR	00.06	00.02	00.01 KW

Fig. 1—Typical cathode-ray tube display

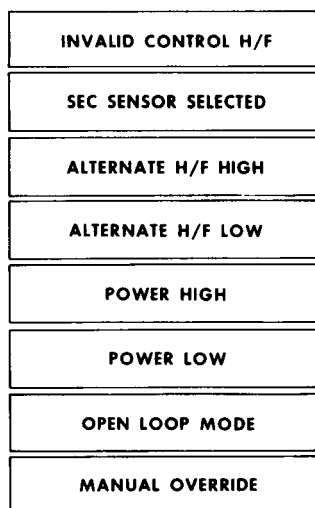


Fig. 2—Event lights (typical for each zone)

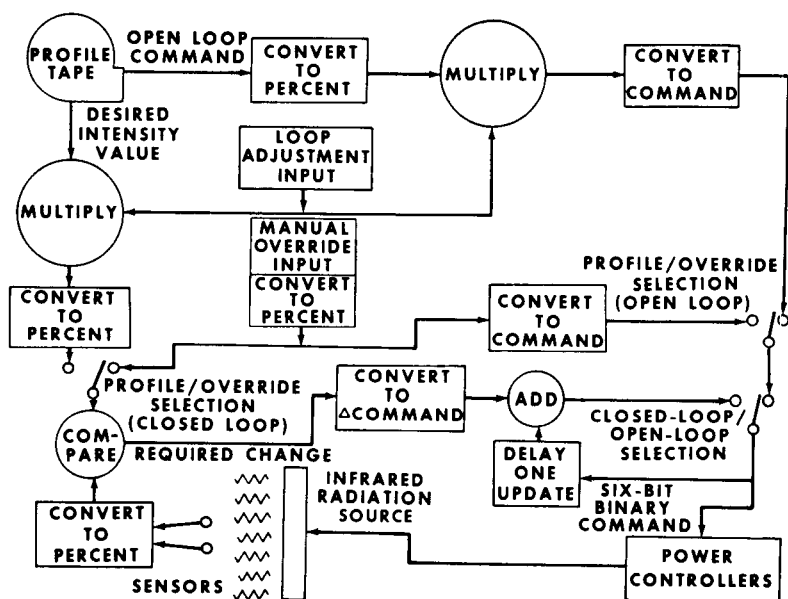


Fig. 3—Control system conceptual block diagram

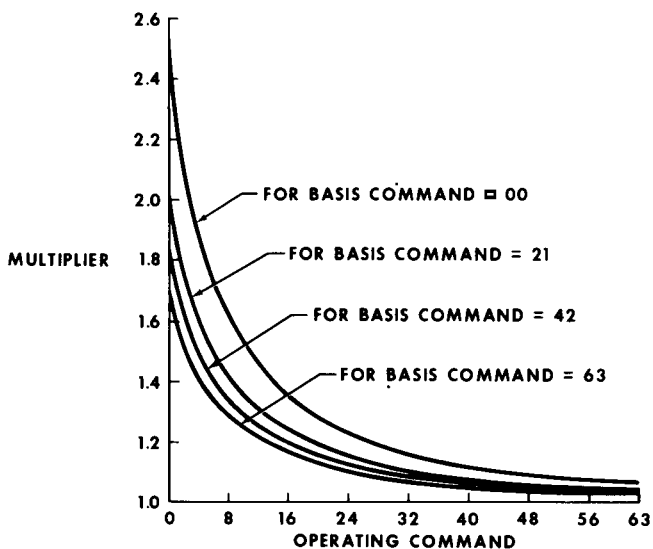


Fig. 4—Multipliers for the service module test series

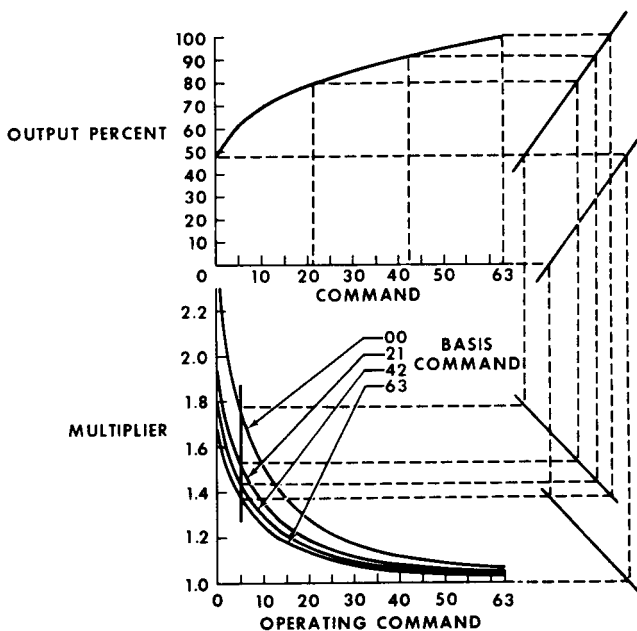


Fig. 5—Relationship of multipliers to the calibration curve

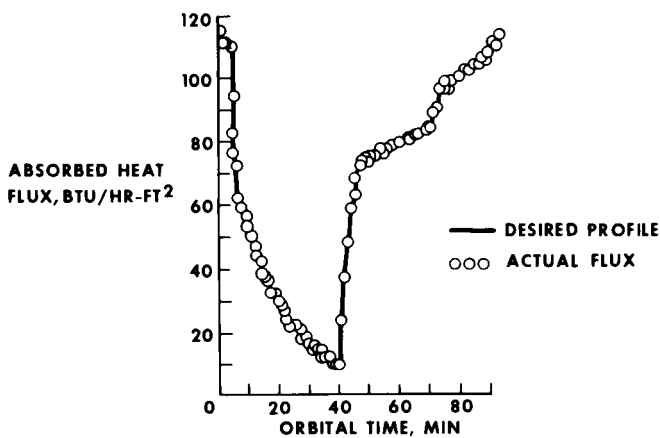


Fig. 6—ATM thermal environment

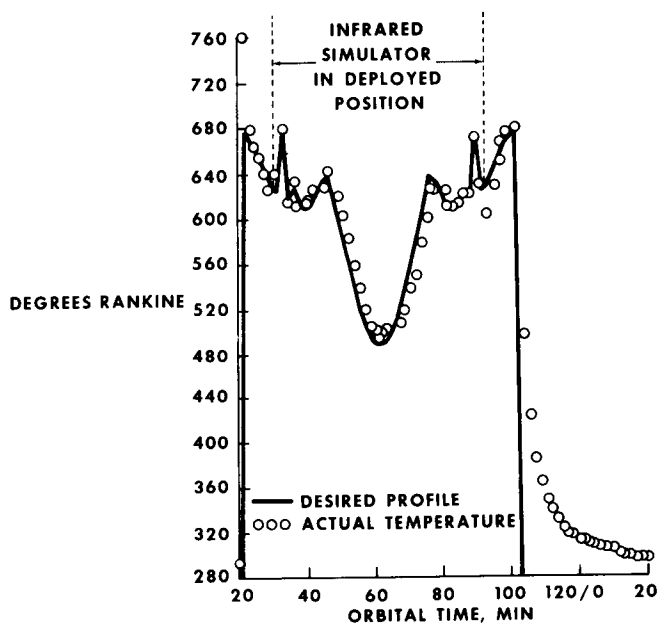


Fig. 7—Service module thermal environment

PREDICTING AND ANALYZING THE THERMAL FLUX INCIDENT ON TEST ARTICLES IN A SIMULATED SPACE ENVIRONMENT

Steven P. Wallin (*NASA*), D. W. Halstead, J. H. Stuart, and C. L. Smithson, Jr. (*Boeing Company*), Manned Spacecraft Center, Houston, Texas

ABSTRACT

The increase in importance and sophistication of thermal-vacuum testing has accentuated the problem of defining the environment to which the test article was subjected. An adequate definition of the test environment is essential to the verification of test-article thermal models. The technique used for defining the test environment at the NASA Manned Spacecraft Center Space Environment Simulation Laboratory and its application during a recent major thermal-vacuum testing program is discussed.

INTRODUCTION

Underlying the ability to verify spacecraft thermal models as a primary benefit of thermal-vacuum testing is the necessity to obtain an adequate description of the actual test environment. The two basic requirements in describing a test environment are adequate instrumentation and data handling facilities to provide the necessary test data and an analytical technique to translate the measured parameters into thermal fluxes incident on the test article. The purpose of this report is to describe the analytical technique used at the Space Environment Simulation Laboratory (SESL) to obtain the required test-environment description and to discuss the application of this technique during a major thermal-vacuum testing program.

BACKGROUND

At the SESL, two separate organizations are involved in conducting thermal-vacuum tests. The permanent laboratory staff prepares and operates the facility and most of the special

test equipment and obtains test data describing the test conditions and spacecraft performance. A transient "user" organization operates the spacecraft being tested and performs the analyses of spacecraft performance.

Until recently, user organizations analyzed and processed facility test data required to define the test environment as part of the spacecraft performance analysis. This procedure had a number of disadvantages. The test environment was defined by personnel who were not familiar with the test facility, and the techniques were redeveloped for each testing program. The resulting inefficiencies detracted from timely spacecraft performance analysis.

As a solution to the problems caused by the user analyzing test-environment data, a staff of thermal engineers was established at the SESL. The staff of facility-oriented thermal engineers performs the analysis of test data to define the test environment and provides the data to the user. The staff also provides continuity between testing programs so that continuous improvements can be made in analysis techniques and instrumentation application.

Because of the wide variety of thermal-vacuum testing programs conducted in the test chambers operated by the SESL, a generalized computer program was developed to be used in the analysis and processing of test-environment data. The program identified as the Space Chamber Analyzer-Thermal Environment (SCATE) program, was developed by The Boeing Company under contract to the NASA Manned Spacecraft Center (MSC).

THE SCATE PROGRAM

In a space-chamber test, the thermal environment is described best by specifying the thermal fluxes incident on the test-article surface nodes. This program calculates these thermal fluxes from chamber and test-article temperatures and from solar-simulator data. Thermal fluxes calculated by SCATE may be compared with measured thermal fluxes to confirm the SCATE model.

Basic Program Features

The program is a thermal-modeling program that can accommodate a wide variety of test configurations. To minimize the data handling by the analyst, the program accepts test data recorded on magnetic tape. The program was developed with capabilities to handle test-article rotation, large arrays of

solar-simulator irradiance values, chamber lighting, and extraneous sources of thermal radiation.

The chamber and the test-article surfaces are defined by geometrical input data using five basic surface types: parallel-ograms, discs, cylinders, spheres, and cones. Thermal nodes are defined on these surfaces to represent the chamber and spacecraft geometry, and the solar simulation system is defined as a set of hexagons.

The program calculates thermal fluxes originating from three types of sources.

1. Infrared (IR) radiation from test-article, test-chamber, and thermal-simulator surfaces
2. Solar radiation from the solar simulation system
3. Thermal radiation from chamber lights

Thermal radiation from chamber lights is included because a survey of the thermal-vacuum facility at the MSC has shown the lights to be a significant thermal source in a "cold soak" environment. For IR radiation, both total and reflected fluxes are determined; and for solar radiation, direct and reflected fluxes are found. Only direct thermal radiation from the chamber lights is calculated because the reflected energy is considered negligible.

At MSC, the test facility data are collected on magnetic compressed-data tapes (CDT). Solar-simulator irradiance values, solar-module on-off data, chamber temperatures, and test-article temperatures can be read from these tapes by a computer program and reformatted and recorded on a new tape that is used as input to SCATE.

The solar simulation systems in the thermal-vacuum chambers are composed of arrays of hexagonal modules. The irradiance data are collected by a radiant intensity measuring system (RIMS). Each solar simulation system has a similar RIMS that consists of a bar that traverses the solar beam output by the solar simulators. The bar is instrumented with radiometers on 10-inch centers and with a position-indicator system. During a scan of the solar simulation system, the radiometer data and the position information are recorded continuously on the CDT. These data values are used by SCATE as an array of irradiance values because solar-flux densities vary from point to point. A position on a test-article surface is related to a position in this array, and a four-way interpolation establishes the direct solar irradiance to a surface normal. The cosine is found for the test-article surface-normal vector and the negative solar vector. The product of this cosine and the direct solar-irradiance value defines the flux to the test-article surface at the desired position.

Radiation-exchange factors and surface temperature are used to determine the IR fluxes. Radiation-exchange factors and average solar-flux densities are used to determine the reflected solar fluxes. These radiation-exchange factors may be supplied as input data to SCATE or can be calculated by a SCATE sub-routine that uses a Monte Carlo technique.

The flux from chamber lights is considered to be inversely proportional to the square of the distance and to be a function of the angle between the light axis and the direction vector from the light to the test-article surface. At desired positions on the test-article surfaces, the sums of the thermal fluxes from all the lights are calculated.

An additional program feature of SCATE is the calculation of fluxes to a rotating test article. This calculation can be accomplished for an axisymmetric test article located with its axis on the chamber axis. For a rotated test article, direct solar and direct light fluxes are calculated to the surfaces in the same manner as for a nonrotated test article; however, the IR fluxes and the reflected solar fluxes are found by an interpolation procedure. The fluxes to nonrotated surfaces act as an array that is interpolated to establish fluxes to rotated positions.

The program limitations are the number of nodes, 150 maximum; the number of solar modules, 75 maximum; the top sun compared with side sun, only one sun at a time; the number of lights, 200 maximum; and the rotation, only an axisymmetric test article lined up on the chamber axis.

The SCATE Application

The program was used to analyze the test environment for the testing of an Apollo service module (SM), 2TV-2, which was conducted in chamber A of the SESL. The 2TV-2 test vehicle was configured to represent both Skylab and the Apollo J-mission series. Apollo 15, which was flown in July 1971, was the first of the Apollo J-mission series.

The test program was designed to determine the effect of the open scientific instrument module (SIM) bay on the J-mission SM and to demonstrate, evaluate, and verify the functional capabilities, performance, and design adequacy of the new and modified thermal control components as integrated in a Skylab SM. The required test environment included simulation of earth-orbit and lunar-orbit heating rates as well as simulation of solar and "deep space" environments.

To provide simulation of the earth-orbit and lunar-orbit heating, an IR simulator was designed and built. For simulation of the deep space and the cold portion of lunar orbit, the IR simulator was retracted from the vicinity of the test article. To simulate the hot portion of lunar or earth orbit, the IR simulator was lowered to the proximity of the spacecraft with the heaters approximately 18 inches from the vehicle surface. The IR simulator in its lowered position around the 2TV-2 vehicle is shown in Figure 1. The heaters were configured in 18 control zones and were controlled by a closed-loop computerized control system to a specified temperature profile for each control zone. The heaters were arranged in a semicylindrical configuration enveloping 180° of the SM and extending approximately 18 inches beyond each end of the SM. For the 2TV-2 test-data analysis, a special-purpose SCATE routine was developed to handle the IR simulator without reducing the total number of thermal nodes available for the 2TV-2 test model.

Before testing the 2TV-2 SM, a thermal-vacuum calibration of the entire test setup was performed using a boilerplate SM instrumented with radiometers and thermocouples. During this test, the performance of the IR simulator was verified and the desired temperature profiles were corrected to yield the desired flux profiles. The SCATE thermal models were developed for both the 2TV-2 calibration and SM tests. The calibration test model was used for model correlation, and the 2TV-2 SM test model was used for analysis to provide test-environment data.

Calibration/Correlation Test on the 2TV-2

The 2TV-2 calibration test was performed to prepare the chamber facility for the 2TV-2 Apollo SM test. The 2TV-2 calibration test article (SM boilerplate) was a cylindrical vehicle, 13 feet in diameter and 15 feet in height, and was used to simulate the 2TV-2 test vehicle. For the 2TV-2 configuration, the SM SIM bay was open, thus exposing equipment to be used in lunar-orbit experiments to the test environment. The boilerplate included a mockup of the open SIM bay as well as paint patterns similar to the 2TV-2 SM. The boilerplate was exposed to several environments, including an equatorial lunar orbit, a 45° lunar orbit, and a transearth coast period (rotation of the vehicle about its center line with the sun perpendicular to the center line), using the same equipment and techniques as planned for the 2TV-2 vehicle test.

The primary purpose of the calibration test was to calibrate and adjust the IR simulator and "background" test environment. A secondary objective was to calibrate the thermal mathematical model of the test setup, including the solar simulator, IR simulator, and chamber background.

The SCATE model of the calibration test setup consisted of the following.

1. A cylinder represented the chamber walls.
2. A disc represented the chamber floor (lunar plane).
3. A frustum section and disc represented the top of the chamber and the IR contribution from the top solar simulator.
4. A parallelogram, divided into three thermal nodes, represented the IR contribution from the side solar simulator and the uncooled area above and below the side sun.
5. A half cylinder, divided into 18 nodes, represented the IR simulator in the down position and the same for the IR simulator in the raised position.
6. A cylinder for the boilerplate vehicle with large nodes represented the vehicle surface, and small nodes represented the radiometers mounted on the vehicle.
7. Surface properties for all nodes were included.

Radiation-exchange factors for the radiometer nodes were calculated based on the previous information. Calculation of transient IR fluxes for the lunar-orbit profiles was accomplished by inputting transient node temperatures to the program. Twenty-four radiometers provided data to be correlated with the SCATE model calculations of flux incident on the radiometer nodes. A typical comparison of the correlated mathematical model output with test data for the lunar-orbit simulations is shown in Figure 2. The step functions at each end of the plots are caused by the IR simulator being lowered and raised, respectively.

Correlation of solar flux incident on the rotating vehicle was accomplished by the use of the RIMS data and the SCATE-rotation option. A typical comparison of radiometer data with SCATE-calculated flux for one revolution is shown in Figure 3. The short-duration spikes could not be duplicated because a RIMS scan of the solar simulator required approximately 8 minutes. Also, the RIMS radiometers are 10 inches apart, and SCATE performs a linear interpolation for flux between the radiometers. Therefore, nonlinear variations in solar irradiance between radiometers would not be indicated.

A comparison of radiometer output with SCATE calculations for one revolution of the vehicle with the solar and IR simulators off is shown in Figure 4. The purpose of the scan was to measure background stray radiation in the chamber. The rise

to approximately $15 \text{ Btu/ft}^2 \text{ hr}$ was caused by IR from the solar-simulator mirrors and the uncooled wall above and below the side sun.

As a result of correlating these test data, the 2TV-2 test was begun with a calibrated model of the chamber, the solar simulator, and the IR simulator. Furthermore, the accuracy of a computerized thermal model to define the thermal test environment was demonstrated.

Spacecraft Test on the 2TV-2

An important objective of the 2TV-2 test was to obtain test environment and spacecraft data for the user organization for use with the Apollo spacecraft thermal analytical model (TAM). The TAM had the capability to predict spacecraft thermal response to an input environment. The use of SCATE to calculate the incident energy on each spacecraft surface node during the test simplified the task of applying the test-environment data to the spacecraft TAM. The same technique can be used for analyzing spacecraft test performance with SCATE data and for predicting spacecraft flight performance.

To use properly the capabilities of SCATE, it was necessary to define an acceptable interface between the SCATE environment model and the user spacecraft TAM. The SCATE environment model of the spacecraft consisted of 73 basic surface nodes corresponding to the surface nodes in the spacecraft TAM and six pseudosurface nodes over the open SIM bay to facilitate projection of the post-test analysis to flight analysis. The SCATE has a limitation that the spacecraft must be axisymmetric to enable calculation of IR flux during spacecraft rotation. Because the mapping camera in the SIM bay (Fig. 5) was extended during the test, as shown in Figure 6, an additional 25 pseudonodes were added to the environment model to make the model axisymmetric. An additional 48 nodes were required to define the basic thermal-vacuum chamber, IR simulator, and spacecraft support structure.

Following a detailed checkout of the SCATE model, pretest environment calculations were completed for representative sections of test-phases A to K (Fig. 7). Nominal chamber conditions were assumed for all pretest environment calculations. These data were provided to enable calculation of pretest temperature predictions. In addition, post-test calculations to define the test environment were required for the entire test time line. The task was reduced greatly by use of SCATE, which has the

capability to use magnetic-tape input of temperature and solar-simulator irradiance data. The use of tape input also reduces the possibility of input errors and allows much greater flexibility in selecting calculation intervals because required data values are available for any calculation time selected. The SCATE data-input tapes were derived directly from parameters recorded during the test on the facility CDT.

Card input to the basic SCATE model primarily consists of control data such as spacecraft orientation and rotation rates, the time interval at which thermal flux calculations are required, and on-off status of each solar-simulator module.

Plots of selected parameters from the CDT were examined before each computer run of the model to determine the calculation interval as determined by a parameter change of sufficient magnitude to change significantly the induced spacecraft environment, that the measurements recorded on the SCATE input data tape were recorded continuously without intermittent loss of data, the times at which any solar simulator module in the solar array inadvertently went off and was brought back on, and the orientation of the spacecraft (lunar plane angle) for the time period under consideration.

The IR flux data curves generated by the SCATE model for a pseudosurface node on the SIM bay during a cold-soak test phase (phase D) and a lunar-equatorial-orbit test phase (phase H) are shown in Figures 8 and 9. A solar-flux data curve produced by the SCATE model for a surface node exposed to the solar simulator during the test is shown in Figure 10. These plots are typical of those produced by SCATE and were transmitted to the user along with the data recorded on magnetic tape. The flux data plots proved to be the best method of checking the environment data produced before the data is released for use in the spacecraft TAM because the trends and values were known. The basic SCATE model remained constant throughout the test, and most time-varying input data were input by magnetic tape; therefore, input errors were located quite easily and eliminated.

The environment data delivered to the user is being presently used as input data to large integrated spacecraft TAM. Preliminary TAM results are available for components located in the SIM bay during the last 6 hours of test phase D, cooldown stabilization, and the last 12 hours of test phase H (lunar orbit, equatorial hot case). The solar simulator was operating during test phase H, but the spacecraft orientation prevented solar impingement on components located in the SIM bay. Post-test TAM data are not available presently using the solar-environment data produced by the SCATE environment model.

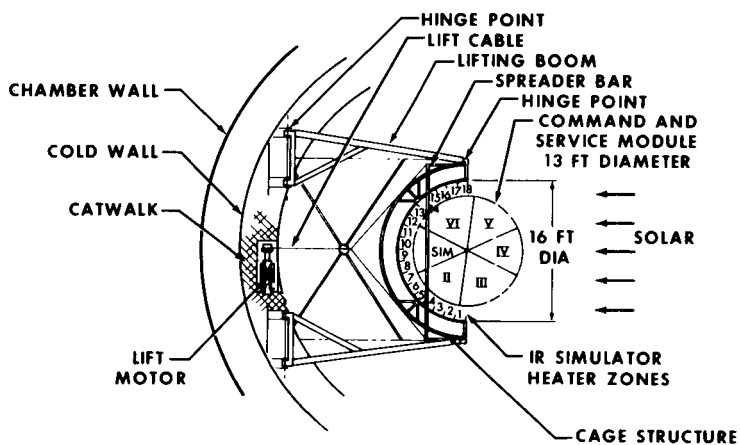
Typical results obtained during the post-test analysis using SCATE data as input to the user spacecraft TAM are compared with thermocouple data recorded during the test in Figures 11 to 16. Figure 5 is a sketch of the spacecraft SIM bay illustrating the location of the components. A description of the figures presenting the post-test analysis results follows.

1. The results for two cover nodes (1453 and 1454) on the X-ray/alpha spectrometer are shown in Figure 11. The location of the X-ray/alpha spectrometer is illustrated in Figure 5. The post-test analysis data presented is for the last 6 hours of test phase D.
2. The post-test TAM results for a node representing the front cover of the subsatellite package are presented in Figure 12, along with sketches illustrating the TAM nodal representation.
3. The size of the buffer-amplifiers housing, along with the TAM results for the last 6 hours of test phase D and the last 12 hours of test phase H, are presented in Figures 13 and 14. The location of buffer amplifier in the SIM bay is shown in Figure 6. The complete housing for the buffer-amplifier cover was represented as one node in the TAM.
4. The post-test analysis results for one of the cover nodes of the multiple operation module (MOM) are shown in Figures 15 and 16. The nodal pattern for the MOM cover is shown in Figure 17. The MOM is located on the underside of the top shelf in the SIM bay as shown in Figure 5.

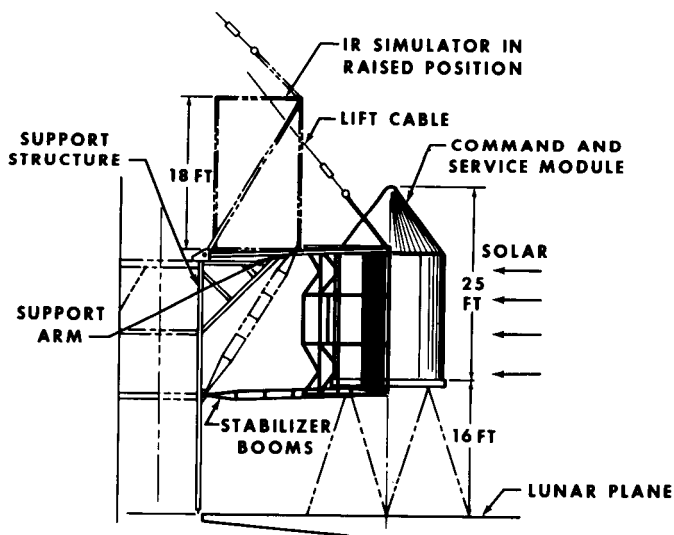
The preliminary post-test analysis shows good correlation between the analytically calculated temperatures and the thermocouple data recorded during the test. The smoothed step function effect of the thermocouple curves is a result of the band pass data process used to record the data. The nodal mesh used in the analysis of the 2TV-2 test data was as coarse as possible to reduce the complexity of the models. This nodalizing technique may cause problems when temperatures for a large thermal node predicted using average incident fluxes are correlated to temperatures measured by a single thermocouple during periods of transient thermal environment. This effect can be detected in the data presented; however, the good overall correlation achieved is indicative of the fact that a thermal model in which a coarse nodal mesh is used can yield good data correlation with only slight variations during transient periods.

CONCLUSIONS

Correlation between measured and predicted thermal fluxes from the 2TV-2 calibration test definitely demonstrated the feasibility of using a generalized computer program to provide a description of the thermal environment of sufficient accuracy and reliability for post-test spacecraft thermal-model verification. The use of SCATE with automated test data input by facility-oriented personnel greatly increased the efficiency and the reliability with which extremely large quantities of test data from the 2TV-2 vehicle test were handled as compared to long post-test analysis efforts required previously in similar test programs at the Space Environment Simulation Laboratory. Correlation of the measured and predicted test-article temperatures during the 2TV-2 vehicle test is indicative that the analysis of the environment data using SCATE was sufficiently thorough and accurate to provide good test-article thermal-model verification.



(a) Plan view



(b) Elevation view

Fig. 1—Test setup for the 2TV-2

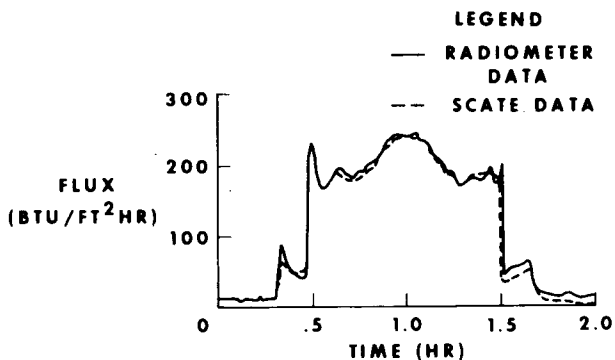


Fig. 2—Comparison of a radiometer time history with SCATE data for an orbital simulation

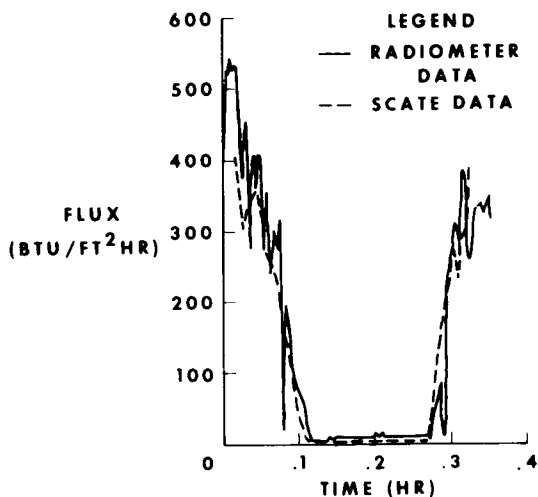


Fig. 3—Comparison of a radiometer time history with SCATE data for one revolution of the test article with solar simulation

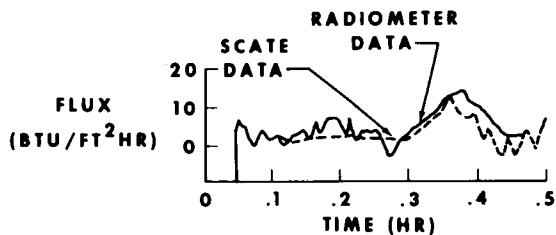


Fig. 4—Background radiation

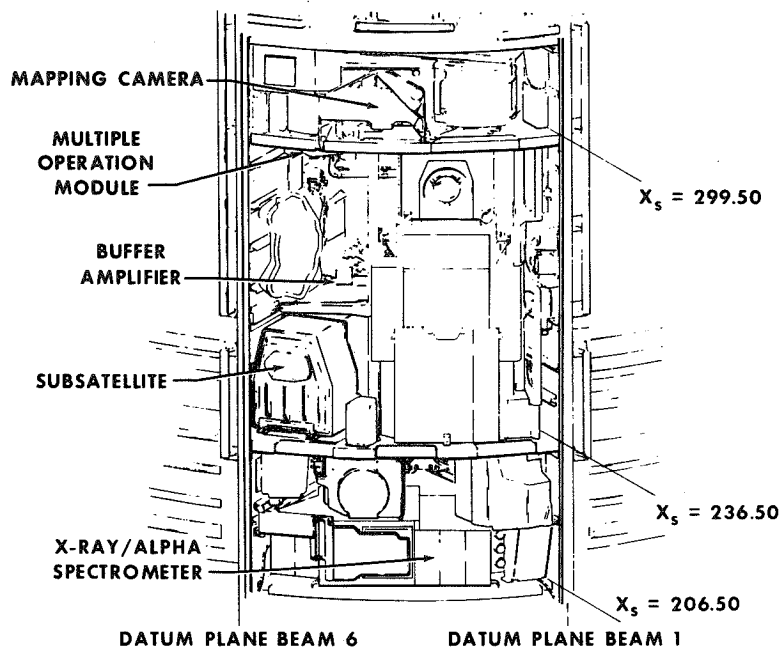


Fig. 5—The 2TV-2 spacecraft SIM bay

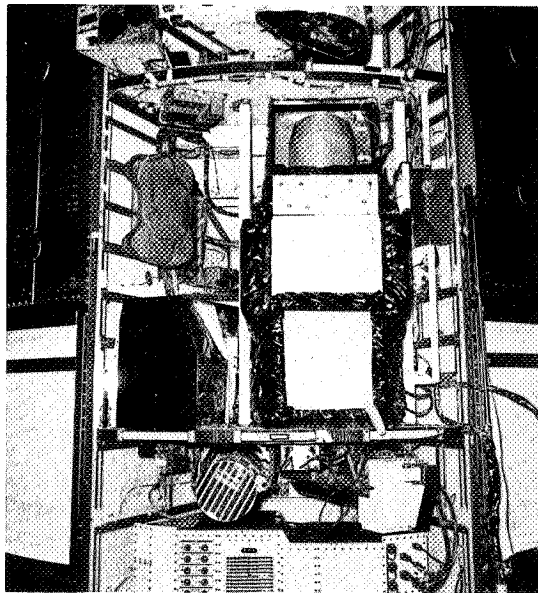


Fig. 6—The 2TV-2 spacecraft SIM bay test photo

TEST PHASE - DESCRIPTION	SCHEDULED TEST TIME (HR)	SOLAR SIMULATOR INTENSITY SOLAR CONSTANTS	IR SIMULATOR OPERATION	SPACECRAFT REFERENCE ANGLE TO CHAMBER NORTH
A - SKYLAB LOW-ORBIT INCLINATION	48	.7	DOWN-ON LEVEL, 20 DEGREE ORBIT FLUX PROFILE	55 DEGREE
B - SKYLAB HIGH-ORBIT INCLINATION	36	1	DOWN-ON LEVEL, 73.5 DEGREE ORBIT FLUX PROFILE	55 DEGREE
C - REACTION CONTROL SYSTEM QUAD C COOLDOWN RESPONSE	20	.5	UP-OFF	270 DEGREE
D - STABILIZATION FOR J-MISSION	24	0	OPERATE AS REQUIRED FOR STABILIZATION	128 DEGREE
E - LUNAR ORBIT, 45 DEGREE INCLINATION COLD CASE	24	0	CYCLIC UP-DOWN, 45 DEGREE ORBIT FLUX PROFILE	128 DEGREE
F - LUNAR ORBIT, 45 DEGREE INCLINATION COLD CONTINGENCY	6	0	UP-OFF	128 DEGREE
G - LUNAR ORBIT, 45 DEGREE INCLINATION COLD CONTINGENCY	6	.7	CYCLIC UP-DOWN, 45 DEGREE ORBIT FLUX PROFILE	128 DEGREE
H - LUNAR ORBIT EQUATORIAL HOT CASE	24	.7	CYCLIC UP-DOWN, 0 DEGREE ORBIT FLUX PROFILE	128 DEGREE
I - LUNAR ORBIT EQUATORIAL HOT CONTINGENCY	6	.7	CYCLIC UP-DOWN, 0 DEGREE ORBIT FLUX PROFILE	253 DEGREE
J - TRANSEARTH COAST PASSIVE THERMAL CONTROL	12	1	UP-OFF	3 RPH
K - SERVICE PROPULSION SYSTEM OXIDIZER TANK AND QUAD B THERMAL RESPONSE, TANK FULL	24	1/0	UP-OFF	0 DEGREE/ 100 DEGREE
L - PASSIVE THERMAL CONTROL AND STABILIZATION SERVICE PROPULSION SYSTEM OXIDIZER TANK DRAINED	12	1	UP-OFF	3 RPH
M - SERVICE PROPULSION SYSTEM OXIDIZER TANK AND QUAD B THERMAL RESPONSE, TANK EMPTY	24	1/0	UP-OFF	0 DEGREE/ 180 DEGREE
N - ENVIRONMENTAL CONTROL SYSTEM RADIATOR TEST	20	0	CYCLIC UP-DOWN, EARTH ORBIT FLUX PROFILE	180 DEGREE

Fig. 7—The 2TV-2 test-phase outline

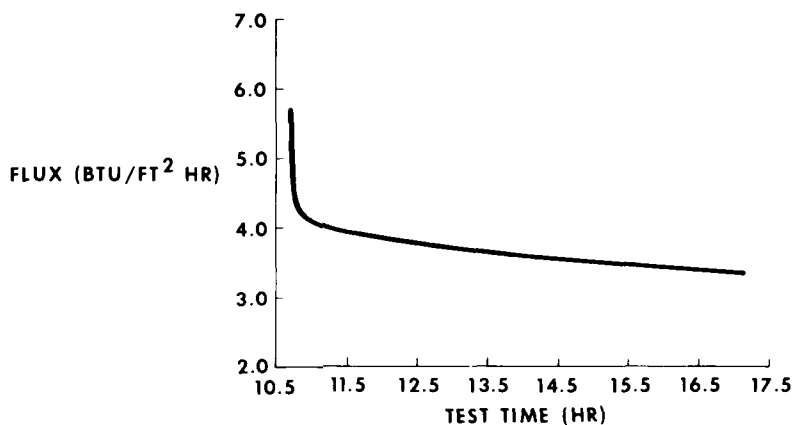


Fig. 8—The 2TV-2 test-phase D total IR flux for SCATE node 15

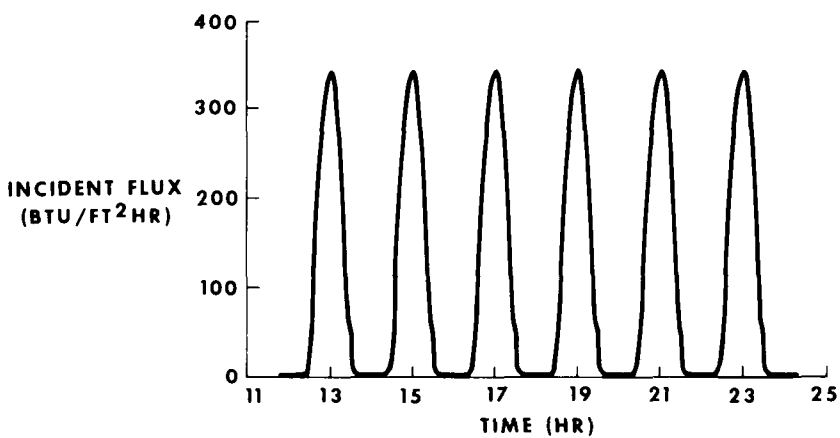


Fig. 9—Incident IR flux data for SCATE node 15 — test phase H

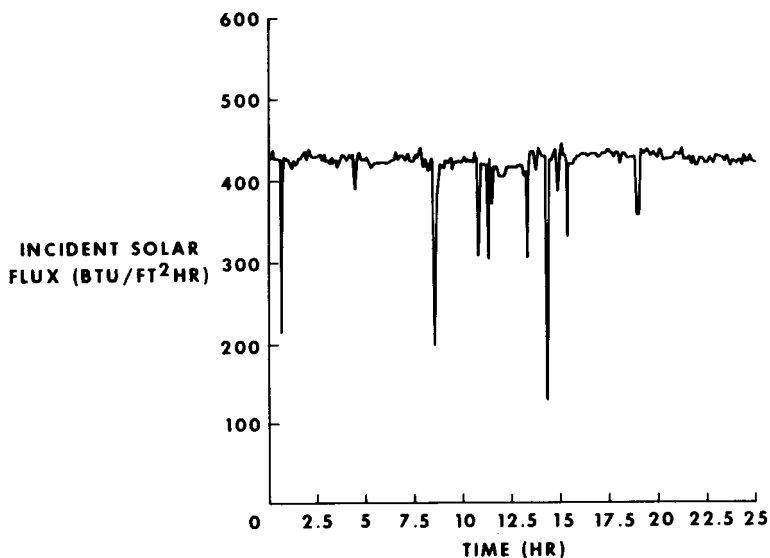


Fig. 10—Incident solar flux data for SCATE node 9 — test phase B

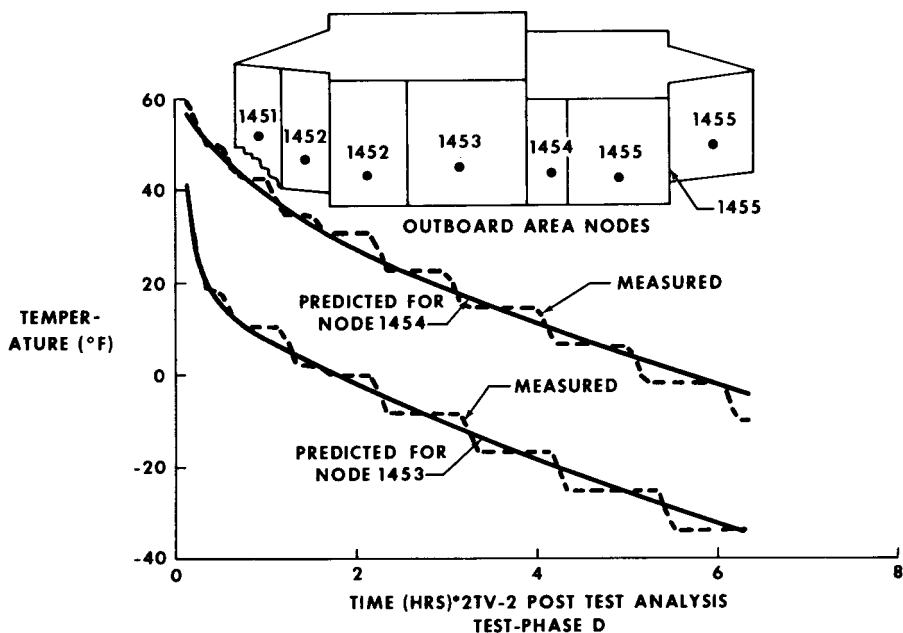


Fig. 11—X-ray/alpha spectrometer

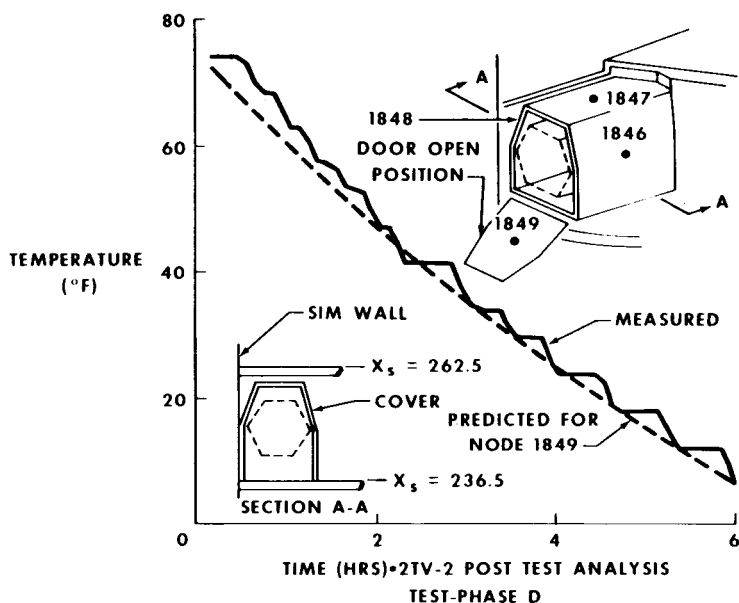


Fig. 12—Front subsatellite cover

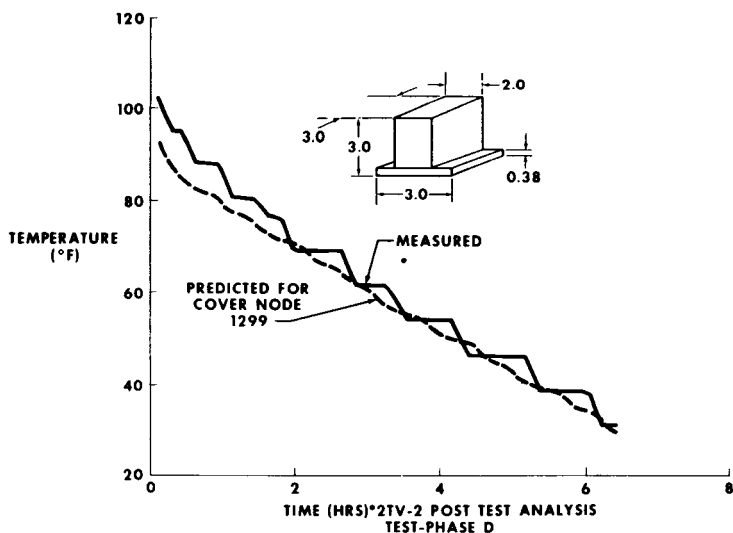


Fig. 13—Buffer amplifier cover

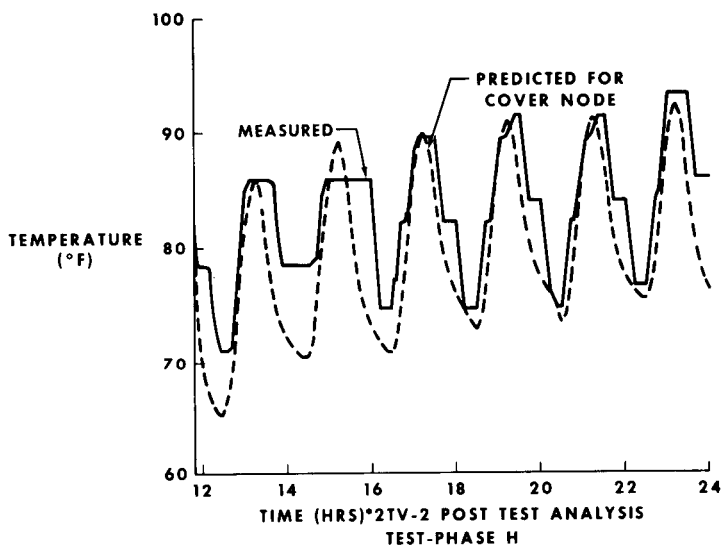


Fig. 14—Buffer amplifier cover

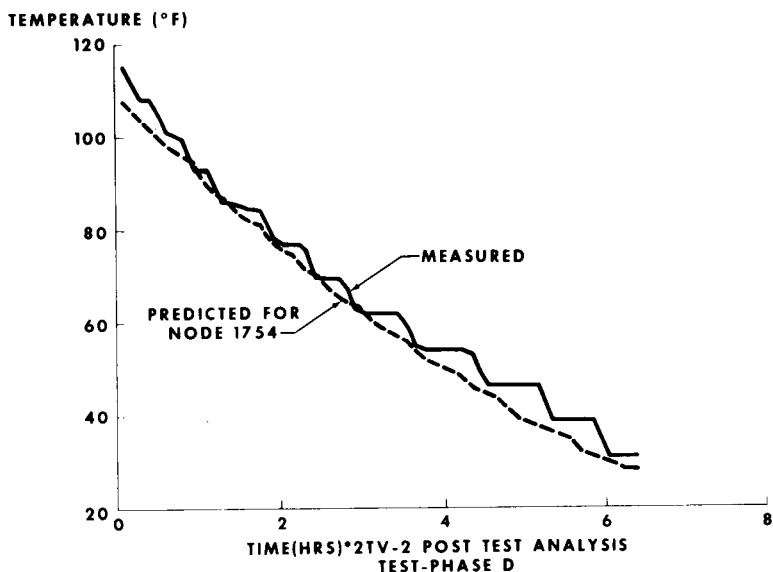


Fig. 15—Multiple operation module

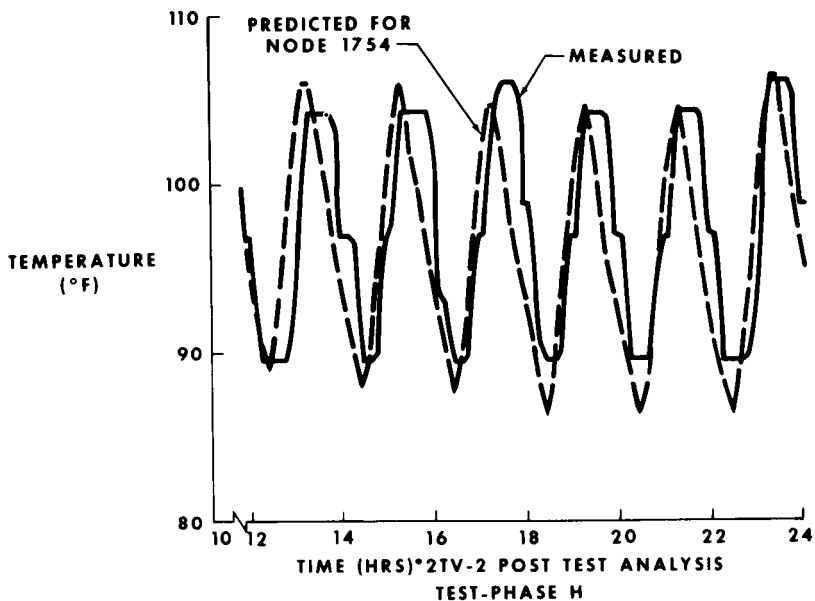


Fig. 16—Multiple operational module

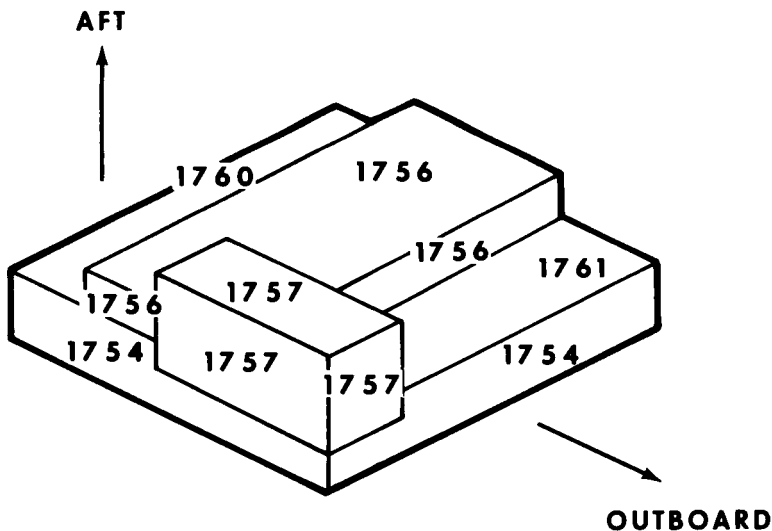


Fig. 17—Multiple operation module node identification

AN AUTOMATED SYSTEM FOR THE ALINEMENT OF LARGE AREA MODULAR SOLAR SIMULATORS

James P. Vincent, *NASA, Manned Spacecraft Center*; Leo F. Polak and
P. S. Fisher, *Electro-Optical-Systems, Xerox*

ABSTRACT

A real-time optical alinement and diagnostic system is being assembled for installation at the Space Environment Simulation Laboratory at the NASA Manned Spacecraft Center. This system will be used to measure and analyze the performance of optical components, assemblies, and full modules. This information, in turn, is used to aline assemblies and modules. The system capability includes such functions as the generation and updating of a catalog, which serves as permanent record in addition to providing the capability to predict in-chamber performance of optics combinations before they are mounted in the chamber.

The system consists of four major portions: (1) scanner, (2) alinement and diagnostic display console, (3) data acquisition, processing, and output system, and (4) data handling and display system. The scanner is preprogramed for four modes or scanning patterns and two sensor configurations. The alinement and diagnostic display console includes a cathode-ray tube, a C-START module, and the scanner control panel. The data acquisition, processing, and output system includes the execution of preprogramed algorithms for the calculation and display of uniformity, asymmetry, maximum, minimum, figures of merit, and other pertinent data. From the time the operator presses the start button to start the scanner until the results are displayed, 4 minutes are required.

This paper describes the development of the system and the planned method of use. Available preliminary test results also are discussed.

INTRODUCTION

The optical alinement of large area solar simulators usually is accomplished by several techniques, all of which are extremely complex and time consuming. The degree of complexity and the time required for alinement increase almost exponentially with the number of optical components because, after each optical component is repositioned, various data are taken and analyzed to determine whether improvement by additional alinement is possible. This effort usually involves an iterative process, with data analysis and repositioning of the optics depending primarily on manual techniques.

The modular solar simulation system, which is an integral part of the Space Environment Simulation Laboratory (SESL) at the NASA Manned Spacecraft Center (MSC), currently is alined by using manual techniques and conventional equipment such as lasers, optical telescopes, and micrometers with grid patterns and radiometer data. Each of the 100 solar simulator modules has four refractive and four reflective components and irradiates approximately 10 square feet. Alinement requires an average of 24 man-hours per module, and optimum uniformity of irradiance is seldom achieved.

To achieve optimum alinement and reduce the man-hours, a computerized real-time optical alinement and diagnostic system (ROADS) is being developed for use with the SESL solar simulator modules. This system will assimilate the module data and automatically analyze the data for optimum performance criteria. The displayed data will provide alinement instructions to the operator. Actual repositioning of the components will be a manual, not an automatic, process. This automated alinement system, ROADS, will have four major subsystems: (1) a sensor panel and controller, (2) an alinement and diagnostic display console (ADDC), (3) a data acquisition subsystem, and (4) a data handling and display subsystem (DHDS). The ROADS will be integrated with the SESL computer complex, or acceptance checkout equipment (ACE). In this paper, the ROADS is described in detail, the current alinement techniques are compared with the automated techniques, and the advantages and planned application of ROADS are identified.

THE ROADS CONCEPT

The ROADS will be a computer-centered system for facilitating the alinement of the modular solar simulation system of the SESL. The ROADS will use computer facilities within the SESL as a data acquisition subsystem and as a DHDS. These

subsystems will process and store or display (or both) the data received from the sensor panel and controller, which will be located in the alinement area. The data will be displayed on a cathode-ray tube (CRT) in the ADDC located in the alinement area or on a line printer located in the computer room. The ROADS will compare the performance from a burner/collector subassembly or a collimator subassembly with the optimum performance as predicted by computer analysis. The ROADS then will provide alinement guides for use in improving alinement of a given subassembly. The ROADS interface with the SESL computer facilities and the ROADS subsystems are described in detail in the following sections.

THE ROADS INTERFACE WITH ACE AND SESL

The ROADS will use the computers within the ACE, which is an integral part of the SESL. The ACE is a computer-controlled system used for spacecraft checkout and operation in either of the two space environment simulation chambers. Two ACE stations are located in the SESL. Each station consists of an uplink computer, a downlink (D/L) computer, and associated peripheral equipment such as CRT's, C-START modules, data acquisition adapters, recorders, and line printers. When ROADS is in operation, a complete ACE station will be used. The ACE station will be programed to collect data from the ROADS ADDC and from the ROADS sensor panel and controller. The collected data will be processed, displayed, and retained by ACE.

MAJOR SUBSYSTEMS

The ROADS will be divided into four major subsystems:

1. A sensor panel and controller subsystem
2. An ADDC
3. A data acquisition subsystem
4. A DHDS

The sensor panel and controller subsystem will direct the movement of the sensors. The ADDC will contain status indicators, controls for the sensor panel controller, a CRT, and a C-START module. Both the sensor panel and the ADDC will be integrated with the data acquisition subsystem, which will acquire the sensor reading, positional data, and status information from the sensor panel and from the ADDC and will transmit the data to the DHDS. This subsystem will provide for all processing and displaying of the data. Figure 1 is a block diagram that includes information flow.

Sensor Panel and Controller

The sensor panel will be a multiple-purpose, electro-mechanical scanner, complete with radiometric detectors as shown in Figure 2. The scanner will be designed to operate with each of the three alignment stands shown in Figure 3, as well as in each of the space environment simulation chambers in the SESL. The scanner will include a preprogramed scanning detector bar using four water-cooled Hy-Cal model P-8410 detectors. The detectors will be positioned manually in either the coarse configuration or the fine configuration. In the coarse configuration, the detectors will be mounted vertically abreast on 4-inch centers. The detectors will be mounted vertically abreast on 1.5-inch centers in the fine configuration. The sensor panel will operate in one of four automatic modes.

1. Limited mode for alining the collector subassembly
2. Intermediate mode for alining the refractive optics of the collimator subassembly
3. Full mode for alining the reflective and full optics of the collimator subassembly and testing of the entire module for the 50-foot throw

4. Expanded mode for use with the 65-foot throw

The expanded, full, intermediate, and limited modes will cover areas of approximately 70 by 64 inches, 54 by 48 inches, 30 inches square, and 12 inches square, respectively. The four modes will be selected manually, and the movement of the sensors in each mode will follow a preprogramed pattern. The sensor panel and controller will be designed to scan rectangular areas of various sizes within the maximum dimensions of 70 by 64 inches.

The speed of the detector bar will be selected by the operator to be 1, 2, 3, or 4 inches per second (IPS). With the 2-IPS speed and the fine detector configuration, the entire 54- by 48-inch test area will be scanned in less than 4 minutes. The smallest test area (12 inches square) will be scanned in approximately 90 seconds.

The sensor panel also will operate in a manual mode. In this mode, the operator can position the detector bar in any location within the 70- by 64-inch scan area. The movement of the detector bar will be controlled in the horizontal (X) and vertical (Y) direction by a momentary 4-way switch on the scanner control panel.

The scanner control panel will contain controls for selecting manual or automatic operation, X-Y position control for manual operation, a speed selector, a power switch, and START and RESET buttons. Controls on the scanner will provide selection

of detector configuration and automatic scanner mode. Indicator lights will be provided for scanner mode, configuration, scanner ready, and scanning in progress. The scanner panel is shown in Figure 4.

While the major application of ROADS will occur in the alinement area, the system also can be used in either of the two space environment simulation chambers at ambient pressures only. When used in one of the two chambers, the target plane and scanner mechanism will be removed from the scanner base and integrated with an existing transport mechanism. This interface will allow the scanner to be positioned in the chamber to cover any desired area of the test volume.

Alinement and Diagnostic Display Console

The ADDC will consist of an electronics rack containing the ROADS scanner control panel, a C-START module, and a CRT. The C-START module will contain switches for communicating a 10-character word to the DHDS. Each character will represent the digits 0 to 9 and the characters + and -. Included in the module are lights for indicating confirmation of word receipt or completion of resultant action. The CRT will provide the capability for display of up to 20 pages of alphanumeric information. The operator can selectively call up, for display, any of the 20 pages of data.

Data Acquisition Subsystem

The data acquisition subsystem will include several ACE systems, which take the output of the ROADS scanner panel and the ROADS ADDC to the digital test measurement system (DTMS). At the DTMS, the information will be conditioned, converted to digital form, and transmitted in a serial pulse code modulated (PCM) data train to the data acquisition and decommutation equipment (DADE), which synchronizes to the incoming serial PCM bit stream, decommutates the data, and presents them to the data processing system. A block diagram of this subsystem is shown in Figure 5.

The required outputs of the ROADS scanner panel and controller will be transmitted by using twisted shielded-wire pairs, which are standard for the ACE. Two-level (0 volt or 5 volts) digital data will be used to indicate the speed setting, the mode, the detector configuration, a run status, and the X and Y position of the center of the top detector. The detector output, which will be continuous analog data, ranges from 0 to 10 millivolts. The

analog data will be sampled 50 times per second, whereas the digital data, read as switch closures, will be sampled 10 times per second.

The accuracy of the data from the detectors collected by the data acquisition subsystem will be a limitation of ROADS. Since the detectors have an exponential step-response function with a time constant of 250 milliseconds, the accuracy of each measurement will be a function of the speed at which the sensors are moved. During the initial stages of alinement of a subassembly, the requirements for accuracy of the sensor data will be less stringent than during the final stages of alinement. Thus, during the initial stages of alinement, the higher scanner speeds probably will be used with the lower speeds reserved for the final stages of alinement.

Data Handling and Display Subsystem

The DHDS will consist of the ACE data processing system, a symbol generation and storage (SGS) unit, a C-START module, and a CRT. The ACE data processing system includes the digital computers and associated peripheral equipment. The SGS unit will generate output for the CRT display units. The C-START module and the CRT will be part of the ROADS ADDC, which normally will be located in the alinement area.

Operation of the DHDS will be divided into a number of tasks, and each major function will be a task. Table 1 is a list of these tasks. The initiation of a particular task and input to the DHDS will be controlled by using the C-START module in the ROADS ADDC. There will be two different types of C-START commands: input commands and action commands. Input commands will provide parameters (such as unit identification and partition-character set information) to the D/L computer. An input command will not disrupt D/L operation. The purpose of the action command will be to initiate a D/L task.

The first major task of the DHDS will be the collection of output data from the ROADS scanner panel and controller. After the data are collected for the entire scan area, pictorial representations of the collected data, statistics, and indications of misalinement will be presented on the CRT. (See Fig. 6.)

Task 2 will provide broad flexibility in the generation of CRT flux-uniformity displays of irradiance data such as those collected by task 1. The CRT displays may use as many as six pages.

Task 3 will provide for printing information similar to that described previously under task 2. This task will provide hard-copy documentation of the final performance of a collector subassembly, collimator subassembly, or complete module.

An important function of the DHDS will be the generation and maintenance of an MDF on magnetic tape. This file will contain performance data for each of the subassemblies alined by using ROADS as well as modules tested by ROADS.

Tasks 4 to 8 are concerned directly with the MDF. Task 4 will provide the initialization of the MDF. Stored information representing the final performance data for a particular subassembly or module will be added to the MDF by using task 5. Data retrieval from the MDF is accomplished by task 6.

The deletion from the MDF of the performance data for a particular unit will be accomplished by task 7. This task will be used only to make minor deletions to the file. Major deletions can be made by using task 4.

A summary of the contents of the MDF will be generated by task 8. A digit in the C-START command word serves to designate whether the summary will appear on the CRT, be printed on the line printer, or be punched with the card punch. The summary will consist of a tabular output with one line representing each unit: collector, collimator, or complete module.

This summary of the MDF will provide several things: (1) a means to determine which units have been alined, (2) a means of reviewing the performance of each of the alined assemblies, and (3) when all the assemblies have been alined, a listing of performance parameters for each assembly. This last listing will be used to optimally place the assemblies in the side or top sun, to optimally replace a burner/collector subassembly, and to predict the combined performance of particular collector/collimator pairs.

Task 9 will generate magnetic tape output for use in generating isointensity plots. This task will suitably process the data in the performance data buffer and generate a properly formatted magnetic tape. This magnetic tape will be taken to the data reduction center at MSC for final processing.

Task 10 will predict the combined performance of three adjacent modules. The task will consist of retrieving the performance data for each of the modules from the MDF, predicting the combined performance by summing the data in overlapping areas, and displaying the data along with appropriate qualitative and quantitative performance measures on the CRT. The predicted combined-performance data will be stored in the performance data buffer for use with other tasks.

CURRENT PROCEDURES

At present, the burner/collector subassemblies are alined by manual techniques, using many iterative steps. An autocollimating alinement rod is inserted in the burner, and components

within the burner are alined mechanically to the rod as shown in Figure 7. The collector mounting points are alined manually by using a specially designed fixture to orient the points relative to the alinement rod.

A collector subassembly is mounted to the burner, and the optical axis is established by autocollimating a laser beam from a mirror mounted in the jaw as shown in Figure 8. The two mirrors are centered on the laser beam by adjusting the radial position of the mirrors until the reticles attached to the mirrors are coincident with the laser beam. The collector lens is centered on the optical axis by adjusting the radial position until the reticles (etched on both surfaces of the lens) are on the laser beam and autocollimation from both surfaces of the lens occurs.

A point source is inserted in the jaw of the burner, and the mirror tilt and axial spacings are adjusted until the projected image is focused and centered on the projection screen located in front of the collector. If the image is symmetrical about the optical axis and focused on the screen, the collector is considered alined. The image is photographed to provide a record of alinement, and the distances between the various components are recorded.

Collimator subassemblies also are alined by manual techniques, in accordance with the collimator alinement setup shown in Figure 9. A field lens mirror fixture is installed in the collimator alinement stand, and the optical axis is established by using a laser beam. A collimator subassembly is installed, and the field lens mirror fixture is replaced with a small xenon lamp. The large collimator (no. 4) mirror is centered on the optical axis and positioned accurately relative to the field lens plane by adjusting kinematic-type mirror mounts. (See Fig. 10.)

The smaller negative lens then is centered on the optical axis by adjusting the lens until its reticles are coincident with the laser beam and the laser beam is autocollimated from both surfaces of the lens. The lens is positioned axially such that the front surface of the lens is positioned precisely relative to the field lens plane.

The smaller (no. 3) mirror is installed and centered on the optical axis by adjusting the radial displacement of the mirror. The mirror tilt is adjusted until the reflected pattern from the xenon lamp is centered on the circular pattern of the target screen. The dimension between the mirror and the field lens plane is positioned precisely.

The large positive lens is installed and centered on the optical axis by adjusting the optical mounts until the reticles on

the surfaces of the lens are coincident with the laser beam. The tilt of the lens is corrected by autocollimating the laser beam from both surfaces of the lens. Finally, the distance between the positive and negative lenses is positioned precisely.

The collimator is considered properly alined if the projected pattern is symmetrical about the optical axis. The projected pattern is photographed to provide a record of the alinement, and the distances between components are recorded.

THE ROADS PROCEDURES AND CAPABILITIES

Two types of collector/lamp units are used in the SESL solar simulators. One is a carbon arc burner/collector assembly. The other is a recently developed deep collector/reflector used with a xenon lamp. With ROADS, the carbon arc burner/collector assembly will be alined by first alining the reflective system with a douser in place over the collector lens. Then, the collector lens will be alined with a douser in place over one of the reflectors. For repeatability, ease of operation, and a well-defined test beam, the collector will be alined with a halogen-quartz lamp as a source instead of a carbon arc. Each subsystem, reflective and refractive, will be alined by positioning components to match as closely as possible a previously established nominal distribution. All measurements will be made with the ROADS scanner, with which each scan will take less than 1 minute. The complete collector subassembly output will be compared to a nominal curve and displayed as deviation from the nominal, vertical symmetry, horizontal, asymmetry, axial alinement, minimum and maximum intensity, and other pertinent data. The test-plane area (plane of the field lens) will be divided into quadrants, and each is evaluated and assigned a figure of merit (FOM) according to the average irradiance in that quadrant. The use of the FOM will be discussed later. Only the CRT displays and the Alinement Instructions will be needed by the operator to complete an alinement.

The xenon lamp collector/reflector will be alined similarly. Because this system consists of only one optical component, the alinement procedure will be accomplished much more quickly than with the three-component carbon arc system.

The collimator subassembly consists of two lenses and two reflectors. As with the collector subassembly, each of these subsystems, reflective and refractive, will be alined and components will be positioned to match the corresponding nominal curve as closely as possible. Each scan will be followed by CRT displays similar to those of the collector, including the FOM.

Module performance will be measured on an alinement bench consisting of a carbon arc source, a previously alined collector subassembly, a throat (as used at the penetration of the chamber), and a previously alined collimator subassembly. The module then will be scanned and evaluated by ROADS, and a flux-uniformity display as shown in Figure 6 will be presented.

The performance of a module will be predicted by averaging each quadrant FOM of the collector and collimator subassemblies. This capability will be extremely important when, during a vehicle test, a burner/collector assembly must be replaced for one reason or another. The FOM's for previously alined collector subassemblies will be listed from the MDF and compared to the FOM of the collimator subassembly in the chamber. Averaging the FOM for each quadrant of the collector and collimator subassemblies will result in a module FOM which indicates a range of uniformity that can be expected in the chamber.

MULTIMODULAR PREDICTION

The procedure for predicting the multimodular performance will be straightforward. The data for the three modules will be called for from the MDF by task 10 and, thereby, a CRT display will be produced at the intersection of the three modules. Two intersections are typical of all intersections: two on top with one on the bottom and one on top with two on the bottom. (See Figs. 11 and 12.) It will be possible to input the data for one module in two or all three positions for analytical purposes. Multimodular testing will be possible only in the chamber at ambient pressure because no test bench capable of accommodating three modules is available. For this test, the center point of the scanner will be positioned at a point corresponding to the intersection to be examined.

DATA STORAGE AND RETRIEVAL

The DHDS will generate and maintain a record of the final performance of subassemblies alined by ROADS and modules tested by ROADS. This record will be called the MDF and will be stored on magnetic tape. The information contained on the MDF for each unit will consist of the collected performance data, the determined qualitative and quantitative measures of performance, the date the data were taken, and other identifying information.

CONCLUSIONS

Several advantages to using ROADS for alinement of solar simulator modules are anticipated. The ROADS will review the alinement data and provide the operator with instructions for use in further alinement. The ROADS should greatly reduce the iterative process of repositioning optics and analyzing data. The optics will be positioned by the operator, the data will be accumulated and processed by the computer, and corrective guides will be provided for the operator. This process will hopefully shorten the time required to aline the various optical subassemblies and reduce the manpower required for alinement. The major advantage of ROADS should be improved performance of the solar simulation system. The ROADS should provide for more precise alinement than previously possible. Therefore, the maximum uniformity attributable to alinement should be obtained.

**TABLE 1. - DATA HANDLING AND
DISPLAY SUBSYSTEM TASKS**

Task	Function
1	Collect data from ROADS scanner and generate CRT displays
2	Generate special CRT displays of stored performance data
3	Generate printed display of stored performance data
4	Initialize master data file (MDF)
5	Add stored performance data to MDF
6	Retrieve data from MDF
7	Delete unit from MDF
8	List summary of the MDF
9	Generate plot tape for isointensity plotting
10	Predict multimodular performance data

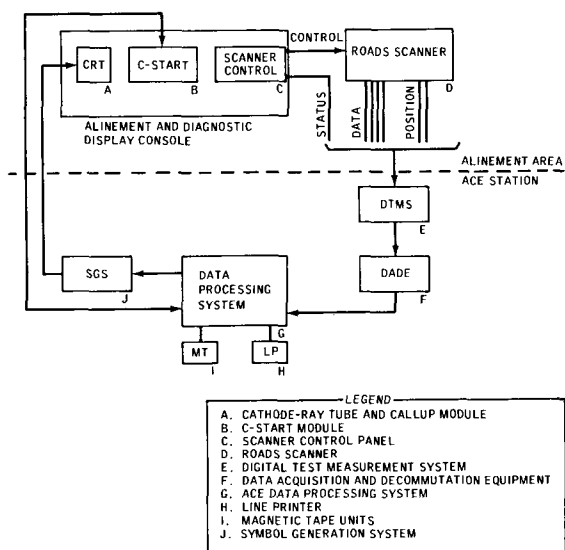


Fig. 1—Block diagram of ROADS

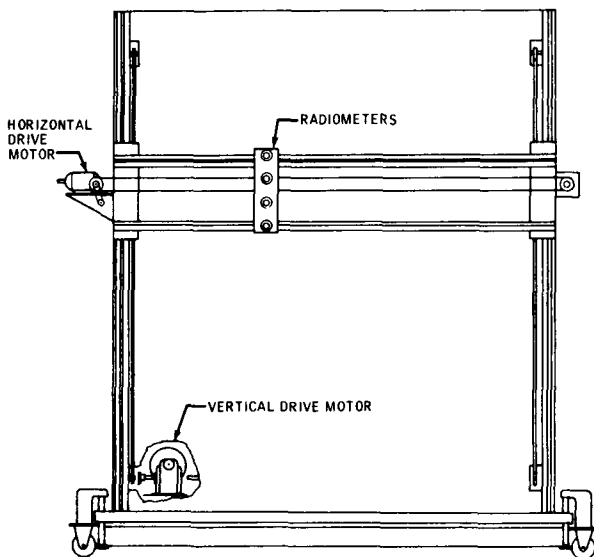


Fig. 2—Sensor panel of ROADS

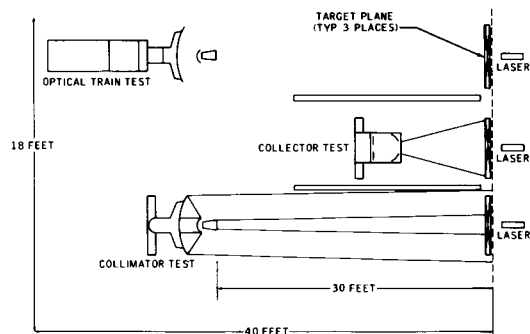


Fig. 3—Scanner alignment stands

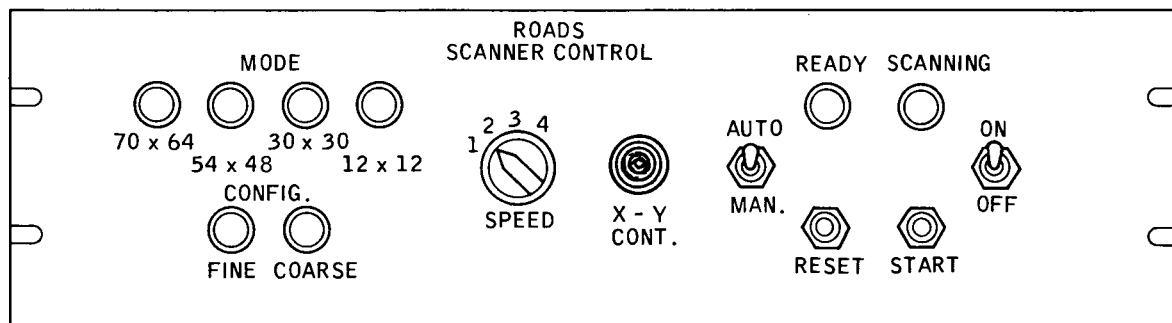


Fig. 4—Scanner control panel

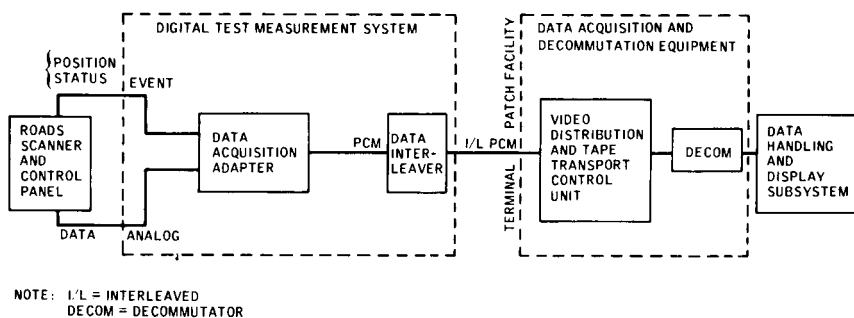


Fig. 5—Block diagram of data acquisition subsystem

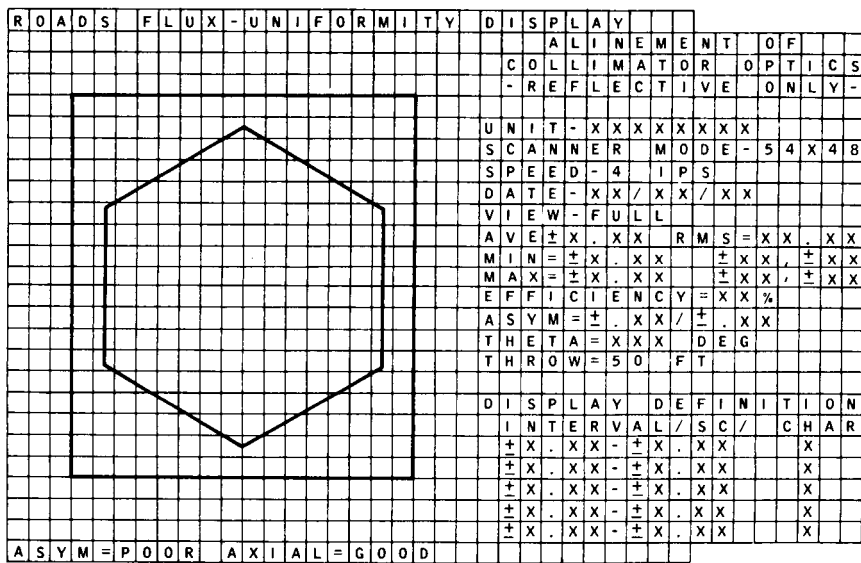


Fig. 6—Flux-uniformity display-alinement of collimator optics

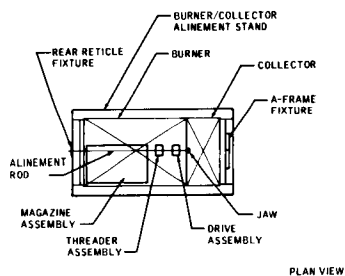


Fig. 7—Collector alinement setup

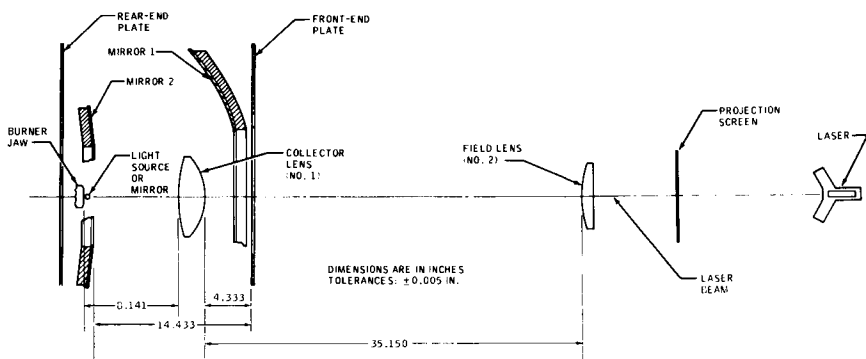


Fig. 8—Collector optical layout

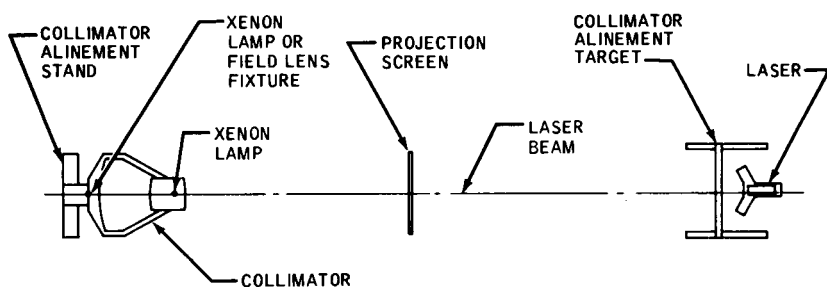
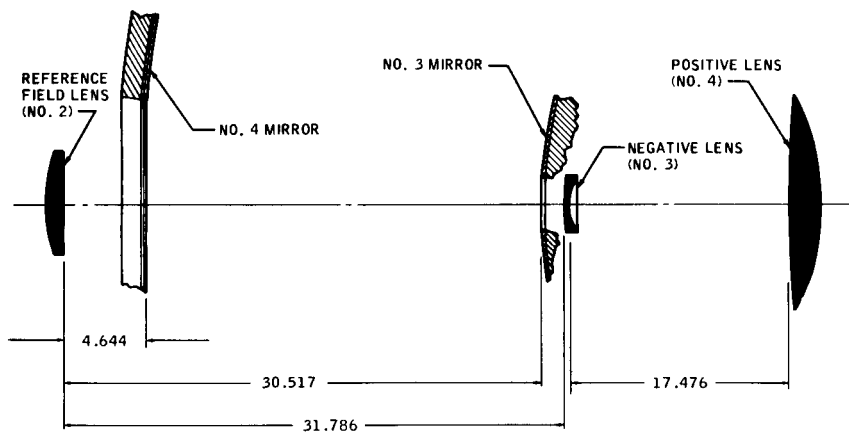


Fig. 9—Collimator alinement setup



DIMENSIONS ARE IN INCHES
TOLERANCES: ± 0.005 IN.

Fig. 10—Collimator optical layout

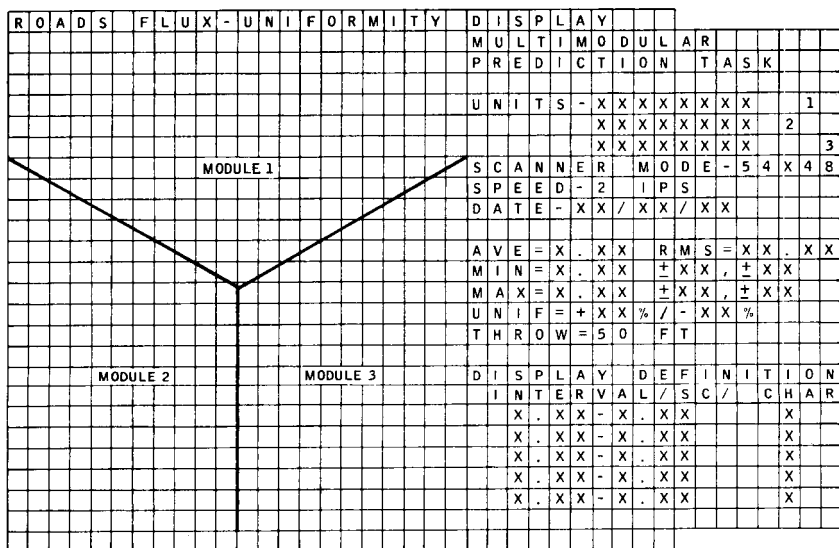


Fig. 11—Flux-uniformity display-multimodular prediction task (one module above)

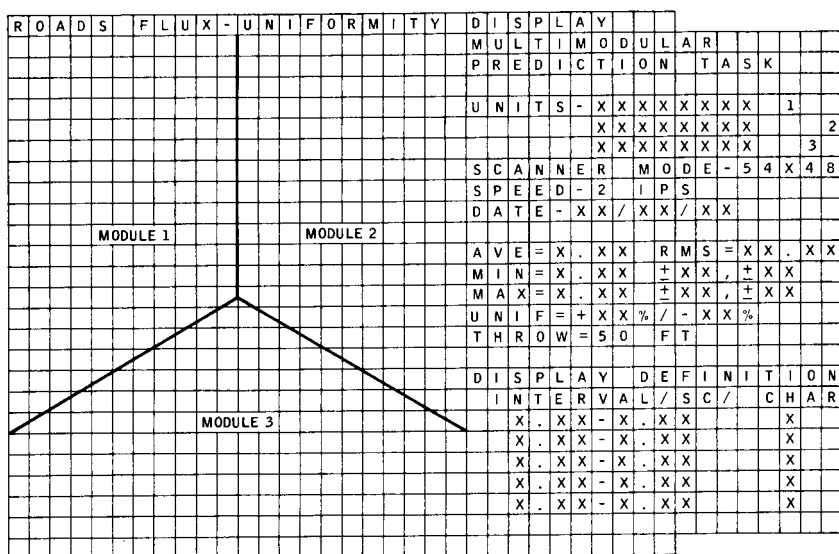


Fig. 12—Flux-uniformity display-multimodular prediction task (two modules above)

A COMPARISON OF SIMULATED REDUCED GRAVITY FLIGHT WITH ACTUAL ORBITAL FLIGHT CONDITIONS

Donn Eisele, *NASA Langley Research Center, Hampton, Virginia*; Scott MacLeod, *Grumman Aerospace Corporation, Bethpage, New York*

ABSTRACT

Five basic techniques used to simulate reduced gravity are compared. Some representative, Apollo 7 experiences are cited for comparison.

INTRODUCTION

Space itself is not inherently dangerous but it is unremittingly demanding of precision and unforgiving of error. The high costs of space flight in terms of risk, time and money have dictated that each flight be exercised in minute detail prior to launch in order to efficiently utilize the flight time and to avoid surprises. Numerous simulation techniques, developed over the years, permit the astronaut to experience conditions that are anticipated for portions of his space flight. These techniques also permit the spacecraft and the mission operational procedures to be optimized prior to launch. The temperatures and pressures experienced in space are easily simulated under controlled conditions in earthbound facilities. Acceleration forces greater than $\pm 1\text{-g}$ can also be simulated very closely by a number of well proven techniques. The challenge which confronted the innovative design engineer at the beginning of the manned space program was to reproduce the conditions of reduced gravity in the controlled environment of a simulator.

The weightlessness, or zero-g, experienced in orbital flight is actually a state of balanced forces rather than weightlessness. The earth's gravitational pull is balanced by the centrifugal force resulting from the object's orbital velocity. It must be remembered that the object considered here is the spacecraft, the astronaut, and everything in his immediate area of activity. It is this totality that presents one of the more difficult problems of simulating reduced gravity.

This paper offers a description of five basic techniques used to simulate reduced gravity along with a discussion of the relative merits of each. Major emphasis has been placed on the complementary techniques of water immersion and parabolic flight because of their capability to more nearly simulate the total environment.

A few representative examples from Apollo 7 experiences are presented in order to offer a better understanding of actual orbital flight conditions.

SIMULATION TECHNIQUES

The purpose in simulating the conditions produced by reduced gravity is to permit scientists to more accurately predict the performance of man and vehicle under such conditions. The answers sought from such simulations include psychological, physiological, and physical responses to a long term reduced gravity environment.

Each of the simulators presently used to evaluate performance in a reduced gravity environment possesses certain advantages and disadvantages relative to actual orbital space flight.

Air Bearings - (Figure - 1)

Reduced gravity is simulated by using air-lubricated thrust bearings to provide almost frictionless contact surfaces that are suspended on a cushion of air. The air bearing method offers the advantages of long duration test times, the ability to accommodate large masses, five degrees of freedom, and repeatable data. The major disadvantages of this method include body motion restrictions and the subject's awareness that the operation is being conducted in a one-g environment.

Cable Suspension - (Figure - 2)

The test subject is suspended by long cables attached to the major segments of his body. Counterweights, attached to the other ends of the suspended cables support the desired amount of his weight. This also permits the degree of reduced gravity to be varied by replacing the counterweights. This system offers limited six degrees of freedom and is very useful in evaluating surface traverses made under simulated, reduced gravity conditions.

Inclined Plane - (Figure - 3)

The inclined plane has been utilized almost exclusively for the purpose of simulating the anticipated problems of man walking on the lunar surface. The test subject is suspended by long cables attached to the major segments of his body and perpendicular to the body axis. The floor plane is inclined 9.5° from the vertical so that the resultant force of the subject against the plane is equal to $1/6$ his normal weight. Normal walking movements of the body appendages are perpendicular to the suspension cables. This results in minimal restriction to the arms and legs during a traverse. The subject is not free to move sideways or to turn around. The usefulness of this technique is therefore confined to activities not requiring such motions.

Water Immersion - (Figure - 4)

In the water immersion facility, reduced gravity is simulated by totally submerging the weighted subject in the water. Breathing air can be provided through the normal pressure suit loop or by use of standard scuba equipment when a pressure suit is not required for the simulation.

This technique permits a subject to function in six degrees of freedom for long periods of time, free of any constraining attachments.

Since it also provides total support of the body appendages, it is particularly adaptable to force application tasks where body movements and position do not change rapidly. Reasonably slow movements are required during simulation because of the damping effects resulting from hydrodynamic drag. There is, of course, no simulation of the internal physiological effects of weightlessness. Task selection should consider this aspect.

Water immersion facilities have been used extensively as zero-g simulators for purposes similar to the KC-135's. The principal advantage of the neutral buoyancy technique is that one can function indefinitely and continuously in a more-or-less weightless state.

Although one may be neutrally buoyant, he is not truly weightless. Gravity still acts on the body's organs, and one retains a strong sense of "up and down". There is some difficulty in achieving the perfect neutral condition, and even when there is no perceptible drift toward the surface or the tank floor, the body tends to assume some preferred orientation: feet high or low, and some body roll bias. These effects can be eliminated to the necessary degree of precision through judicious attachments of small blocks of foam or lead weights. Tools and equipment generally are not neutrally buoyant and will sink or float unless held or tethered. The adverse effects of water drag on test results, and the like, tend to be exaggerated by persons unacquainted with weightlessness and neutral buoyancy. In zero-g, tasks and movements are slow and measured; thus, viscous effects are of little consequence.

Water immersion facilities have been employed extensively in crew training for space flight, especially for EVA work. For example, on Gemini 12, the most ambitious earth orbital EVA flight to date, the flight crew and engineers worked out procedures and timelines in great detail using the neutral buoyancy technique. The smooth and successful accomplishment of all EVA objectives on Gemini 12 attests to the efficacy of the water tank as a training device and zero-g simulator. Extensive exercises under neutral buoyancy conditions have contributed materially to preliminary training, engineering evaluation, and have been instrumental in solving some EVA difficulties associated with the forthcoming Skylab missions.

The neutral buoyancy technique has been used to study intra-vehicular manual cargo transfer without the use of mechanical devices or special handling equipment. Simulated cargo modules

of greater than 1500 lbs mass and 100 cubic feet volume were handled with ease, using only one or two simple, fixed hand rails as mobility aids. The study concluded that the internal dimensions and geometry of space ships, rather than any inherent human limitation, would constrain the size and mass of cargo modules for weightless flight.

Parabolic Flight (KC-135 Aircraft) - (Figure - 5)

Reduced gravity can be simulated by flying a Keplerian trajectory. By varying the trajectory parameters, a variety of gravity levels can be obtained. The reduced gravity, parabolic flight maneuver is the best presently available technique for approximating all of the sensations of orbital flight.

The sensation of falling and its attendant physiological and psychological responses are present during the parabolic maneuver. Six degrees of freedom and rapid motions are available to the subject with no perceptible drag effects and with no constraining attachment.

This technique's major disadvantage is the very short duration of reduced gravity available during each trajectory. The KC-135 aircraft offers approximately 30 seconds of zero-g test time from each maneuver. As many as 50 or 60 trajectories might be required to satisfy the data requirements. Many tasks cannot be performed in a series of 30 second increments and therefore are not adaptable to this technique. Each reduced gravity period is followed immediately by a high gravity pull-up that must be considered in the design of the experiment and the task to be performed. Two additional problems associated with this technique are the aircraft's limited volume and the high incidence of nausea among the test personnel.

The KC-135 has proven to be a useful zero-g simulator in many respects. As a test bed for scientific experiments, it has been used extensively to investigate various physical phenomena of weightlessness. In support of manned space flight, the "K-bird" has flown hundreds of hours for general crew training and familiarity; training for specific zero-g tasks; and assessment and evaluation of zero-g hardware in its design environment.

Both zero-g aircraft and water immersion facilities have proved to be highly useful devices for crew training, engineering evaluations, and human factor studies pertaining to zero-g flight. Each has its own unique advantages and drawbacks. The two devices tend to complement each other and will continue to be invaluable in assessing and investigating a variety of phenomena associated with manned space flight.

Only one zero-g flight was conducted in preparation for Apollo 7. The aircraft was equipped with a full-scale mockup of the command module. Not every task called for in the flight plan was performed. Those which promised to cause some difficulty in orbital flight or that were hard to accomplish in one-g were emphasized. These included pressure suit donning, crew couch operation, and changing environmental system canisters. When all

the tasks were easily accomplished, further zero-g training was deemed unnecessary. Subsequent experience on Apollo 7 bore out the correctness of that judgement. The manual tasks were easier in actual orbital flight than they were on board the KC 135.

Some Actual Orbital Flight Conditions

Adapting to weightlessness on Apollo 7 was both easy and rapid. The initial reaction once the lap restraint was unbuckled, was a vague sense of uneasiness or insecurity, and a feeling of fullness in the head. The uneasiness disappeared in a matter of minutes; the feeling of fullness persisted throughout the flight, and was aggravated, perhaps, by a persistent head cold after the first two days.

At no time during the flight did any one suffer nausea, dizziness, disorientation, or other adverse effects - despite the fact that the spacecraft was in a slow random tumble most of the time. In fact, a number of body motion and acrobatic maneuvers were performed for the television "Wally, Walt, and Donn Show" broadcasts which were intended to entertain viewers and to demonstrate to earthbound counterparts how easy it was.

The United States manned space program has been remarkably free of adverse zero-g effects on crewmen. The sole exception occurred on an early Apollo flight when one crewman experienced nausea during the first day. Even this condition did not materially affect his performance or the orderly progress of the flight. The Russian cosmonauts experienced difficulty on some flights, but the ones who were the sickest were the non-pilots. All U.S. space crewman to date have been either practicing test pilots, or experienced jet fighter pilots, or both. This observation suggests that repeated exposure over a period of years to unusual attitudes, high-g forces and rapid rotation in aerial flight may render one insensitive to the peculiar motions and body sensations of weightlessness. Thus the common airplane may persist as a useful training device for space flight candidates - especially those with little or no flying experience.

Mobility, restraint, and body control come quite easily with only a little practice. The Apollo 7 crew was able to move about and position themselves with great precision. Any protuberances of hard structure served, if they could be grasped with feet or fingers. Most of the time the crew floated free with only occasional soft random contact with the ship's structure. Firm restraint was needed only during launch, entry, and during main rocket thrusting. These thrusts produced an abrupt jolt to the body if one were not firmly strapped in the couch.

The spacecraft's tumbling motion and the unique arrangement of its viewing windows produced unusual kaleidoscopic views of earth. The crew soon learned to anticipate the sequence of window views. By using the feet to grasp a couch strut, they were able to control their bodies and to position their faces at the appropriate window. This procedure also left both hands free to manipulate the cameras and accessories.

Operating the optical navigation equipment proved quite simple. Small hand holds were mounted adjacent to the small, pencil-like control sticks. The technique used was to actuate the controllers with thumb and forefinger and wrap the other fingers around the handhold. No other restraint was necessary.

Small, half-inch squares of Velcro, located judiciously throughout the spacecraft, were effective as temporary restraints for small articles such as food bags, pens, data books, hand tools, and the like. The Velcro was not suitable as permanent stowage because small objects would dislodge easily and float about the cabin.

Defecation proved to be the only really difficult and unpleasant task. Numerous small items had to be used, and one had to plan ahead and proceed carefully to be sure that all necessary articles were secured temporarily, yet within easy reach when needed. The principal problem was entrapping and retaining the fecal matter, while completing the procedure, until the containment bag could be sealed. The whole ungainly process made a major endeavor out of what is normally a routine function.

Although urination was not difficult, it did entail a tedious and time-consuming procedure involving the turning of valves, the attaching of fittings, etc. - all of which had to be done in the correct sequence. Otherwise, spillage, cabin gas leakage, or possibly urine dump line freezing could result.

Donning and doffing pressure garments was accomplished with ease, and was normally done, one crewman at a time, owing to the close confines of the cabin. Simultaneous suit donning was demonstrated on one occasion. A modest amount of mutual assistance was necessary.

Sleeping was easy, once one became accustomed to the absence of a mattress pressing against his back. At first, the individuals attempted to wedge an arm or elbow or even his head against some part of the structure, as a substitute for mattress pressure, but after two or three days its need was no longer felt. The crew experimented with sleeping unrestrained and found that to be the sublime sleep experience.

The crews which landed on the moon report no problem with the reduced gravity there. As is well documented by television and motion picture film, they adapted readily the moon's unique gravity field. Whatever fatigue they did experience was ascribed to the general level of activity, long hours between rest periods, and work against the pressure suits which are somewhat stiff when pressurized.

The challenge of simulating reduced gravity in a controlled environment and at minimum cost has been approached from five basic paths. Each solution offers unique advantages and disadvantages relative to the others, but no individual reduced gravity simulator can duplicate the totality of orbital flight conditions.

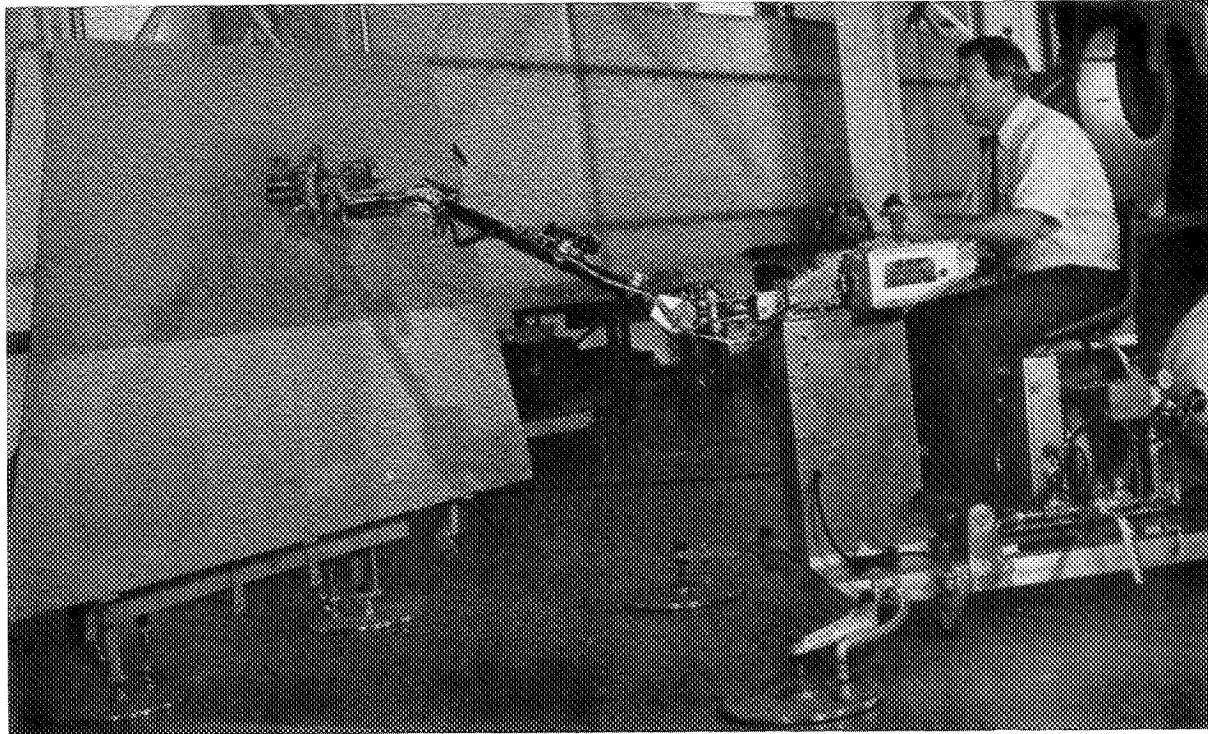


FIGURE 1 - Air Bearings

Subject removing article from test board with manipulator in simulated zero-g.



FIGURE 2 - Cable Suspension - Test subject simulating traverse under reduced gravity conditions.

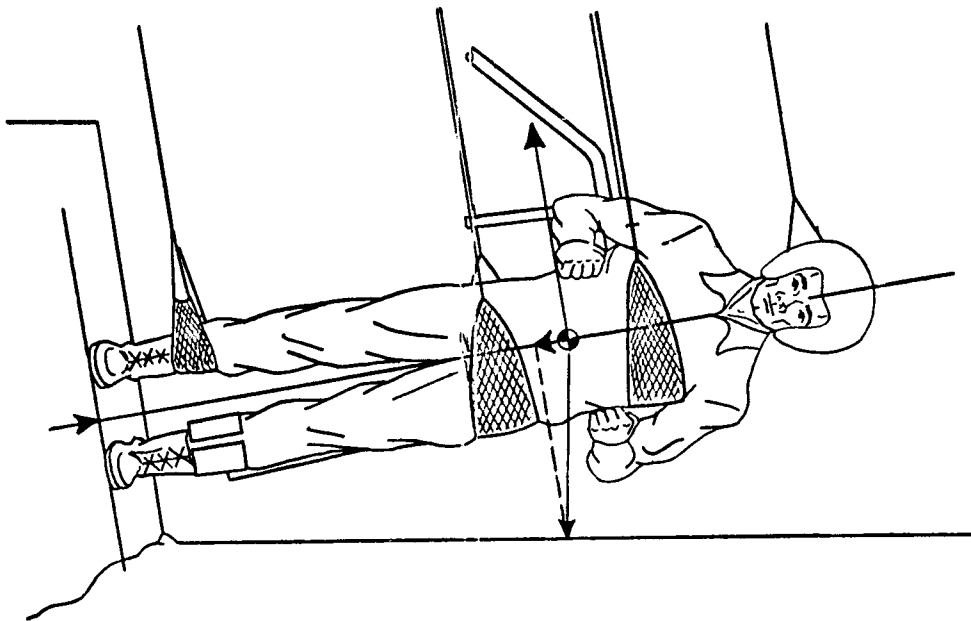


FIGURE 3 - Inclined Plane - Subject simulating traverse under $1/6g$ conditions.

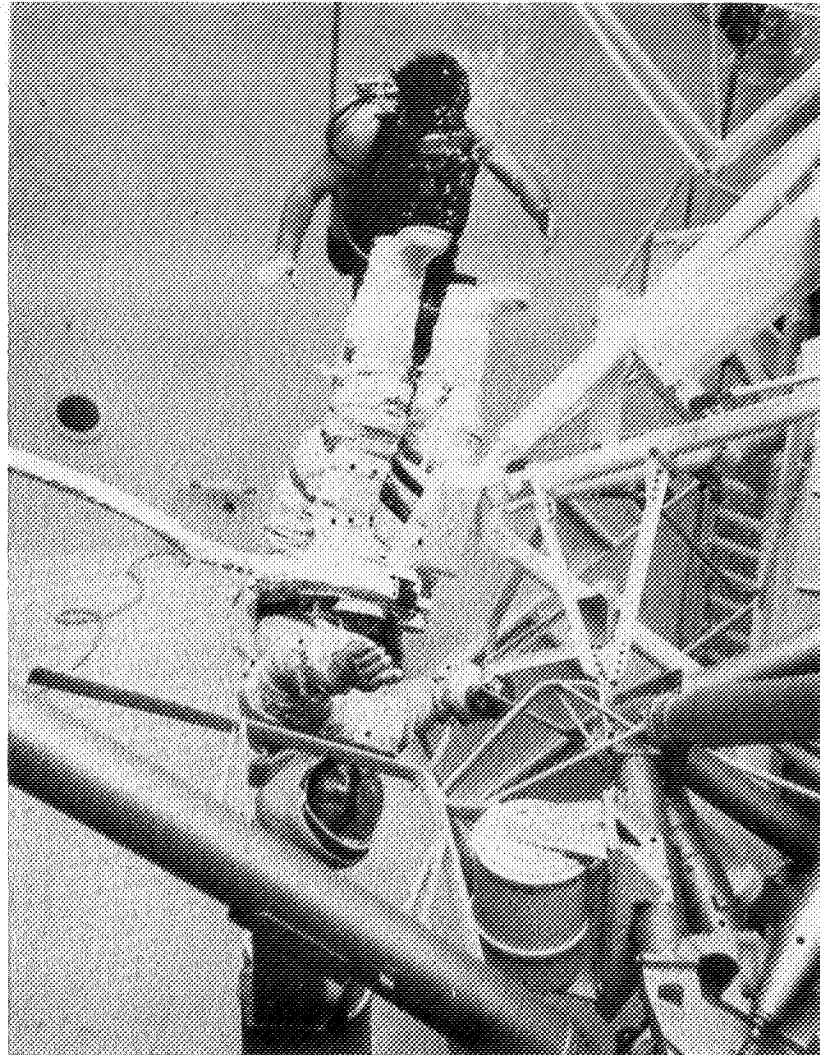


FIGURE 4 - Water Immersion

Simulated zero-g EVA task -(Note Safety Diver)

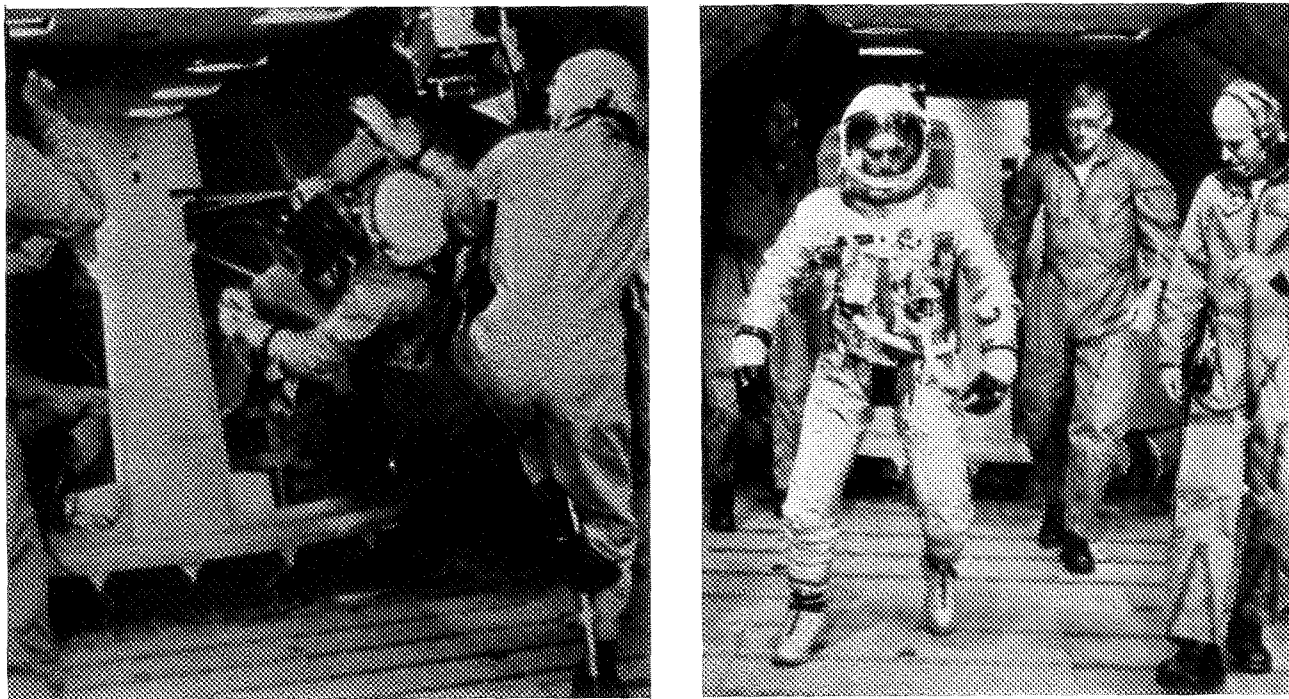


FIGURE 5 - Parabolic Flight - Simulation in the KC-135 of egress at zero-g and a traverse at $1/6$ g.

FULL-SCALE SKYLAB APOLLO TELESCOPE MOUNT DEPLOYMENT TESTS*

G. F. Fricker, *McDonnell Aircraft Company, St. Louis, Missouri 63166*

ABSTRACT

During the initial stages of the NASA Skylab orbit, the Apollo Telescope Mount (ATM) is deployed by the Deployment Assembly (DA) which clears the Multiple Docking Adapter (MDA) axial docking port. This is an essential prerequisite to docking the Command Service Module (CSM) with the orbital workshop and subsequent occupancy of the workshop by the Apollo three-man crew.

The objectives of the full-scale NASA Skylab ATM deployment test program were (1) to evaluate the design concept of the DA and deployment mechanisms while functioning in a zero-g environment with simulated ATM mass properties and (2) to evaluate the effects of handling, transporting, and deployment with respect to the structural geometry and stability of the DA.

A steel prototype DA, simulating geometry and spring rate, was used for the design concept phase of the test program, while a flight-configuration aluminum DA was used for acceptance and qualification phases. The zero-g environment was simulated by positioning the DA with its launch axis horizontal and counterbalancing its weight. The mass moment of inertia of the 25,000 pound ATM was simulated by a ballasted swing arm which was supported independently from the floor and coupled to the movable upper DA at the theoretical center-of-gravity (c.g.) of the ATM.

The deployment rate and deployment reel voltages, currents, cable forces, and reel-in rates were monitored for a wide range of DA test conditions. Pyrotechnic release mechanisms, and deployment latch performance were evaluated. ATM look-axis alignment and critical DA geometry were ascertained through the use of extensive optical tooling.

Test results indicated that the DA is functionally adequate to deploy the ATM mass in a zero-g environment, even during induced marginal conditions, and that the structural stability of the DA is adequate to meet the stringent alignment requirements.

INTRODUCTION

An important piece of hardware for the NASA Skylab program is the Deployment Assembly (DA) for which the McDonnell Douglas Astronautics Company - Eastern Division (MDAC-E) received a contract for design, manufacture, and demonstration of satisfactory performance. The DA, during the initial stages of

*This paper is related to work performed under NASA Contract NAS9-6555.

the Skylab orbital mission, rotates the Apollo Telescope Mount (ATM) ninety degrees from its original launched position to provide a clear passage to the Multiple Docking Adapter (MDA) axial docking port as shown in Figure 1. This is an essential procedure which must be accomplished before docking the Command Service Module (CSM) with the MDA/Skylab cluster.

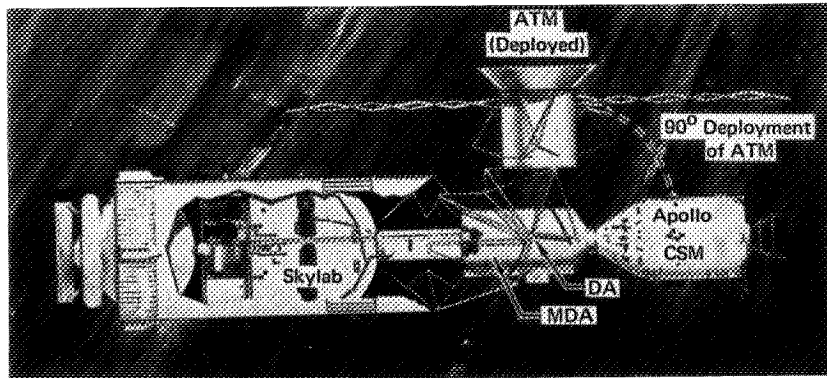


FIGURE 1 NASA SKYLAB CLUSTER

The objectives of this particular test program, full-scale NASA Skylab ATM deployment, were (1) to demonstrate that the DA was capable of absorbing orbital docking, maneuvering, and deployment loads while maintaining its structural geometry and stability, (2) to demonstrate, under both normal and adverse conditions, that the deployment and latching mechanisms would rotate the DA/ATM through a ninety degree arc and hold it securely in a deployed attitude, (3) to demonstrate that every circuit of a 2000 strand wire bundle assembly would remain operational through its anticipated life and (4) to demonstrate that the DA transportation vehicles and handling devices would function properly while maintaining the structural geometry and stability of the DA.

The test program was performed in two phases – development and qualification. A DA constructed of steel tubes representing the production configuration was employed for the development tests, while a flight configuration DA fabricated of aluminum tubing was employed for the qualification tests (Figure 2). After the MDAC-E testing, the flight-configured DA was shipped to the NASA Marshall Space Flight Center for further testing.

DESCRIPTION OF TEST ARTICLES

The DA is a hinged truss assembly made up of two structurally independent trusses. The lower or stationary truss, at its lower extremity, attaches to the Fixed Airlock Shroud (FAS) at five places. The FAS, being very stiff as compared to the DA, assumes the role of a “fixed” base or foundation.

Two trunnions at the upper extremities of the lower DA form the hinge about which deployment occurs. The upper or movable truss repositions or deploys the

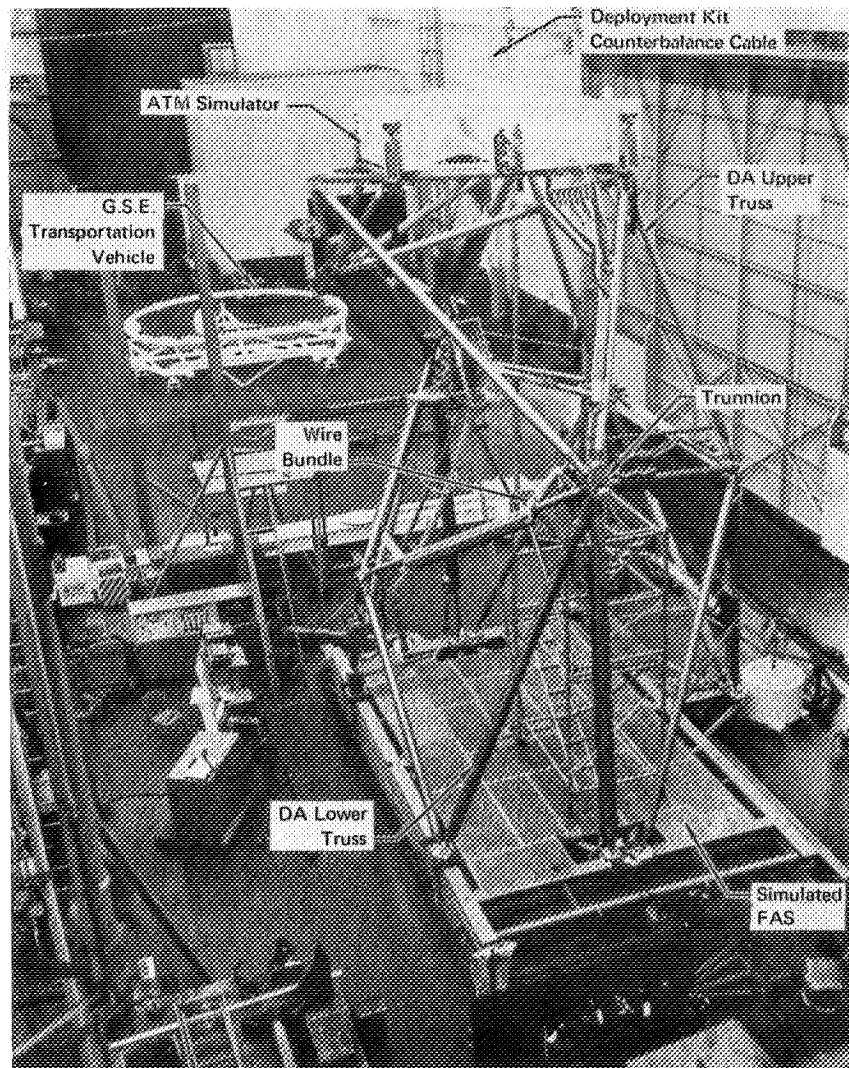


**FIGURE 2 TEST SETUP ALUMINUM (FLIGHT CONFIGURATION)
DA - LAUNCH POSITION**

ATM when in orbit. Deployment begins when a release system consisting of pyrotechnic pin-pullers unlocks the upper truss from a launch attitude to permit it to be rotated to the deployed position. A negator spring at each trunnion applies a constant restraining torque of 1800 inch-pounds on each half of the hinge to offer resistance to the deployment reel cables and thereby eliminate jerking movements.

Two deployment reels (Figure 3), one on the upper truss and one on the lower truss, take up parallel cables on their drums to reposition the DA/ATM assembly and engage the deployment latch. These reels have Harmonic Drive gear reducers with a final ratio of 4912 to 1. This ratio enables either reel to be capable of deploying

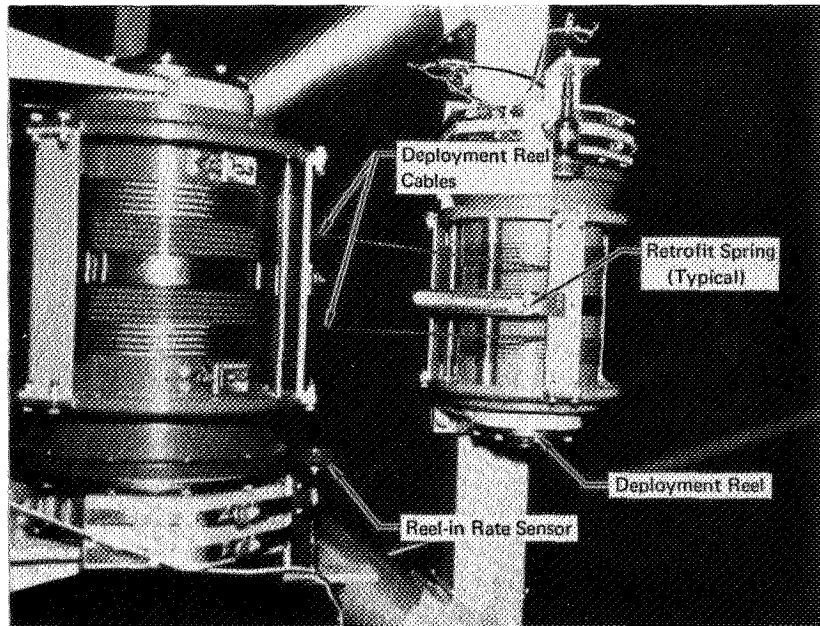
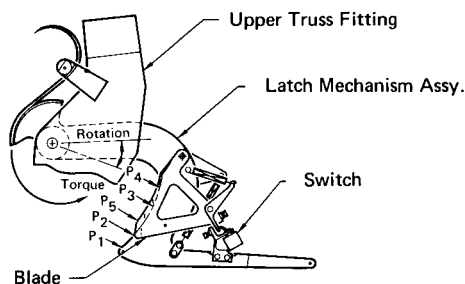
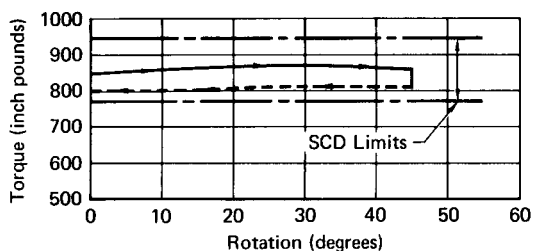


FIGURE 3 DEPLOYMENT REEL INSTALLATION (DA DEPLOYED)

the upper DA even though the reel drive motor produces only 21 inch-ounces of torque. At the conclusion of the maneuver the deployment latch mechanism is forced open and engaged by tension in the deployment reel cables. The latch, which is equipped with a negator spring, first resists opening by the seating ramp and then latches after it has been driven over the seating ramp. The latch is also equipped with a ratchet mechanism which positively prevents it from reopening after latching. The deployment latch characteristics are shown in Figure 4. When the latch is closed, a stud on the upper DA protrudes into a conical hole on the lower DA to prevent any further movement of the two trusses in relation to each other.

The DA also supports two large wire bundles, one passing across each trunnion. These must flex each time the DA is deployed. The bundles extend from the ATM atop the upper truss down the entire length of the DA and across the DA/FAS interface.

The DA used for development testing (Figure 5) was fabricated primarily from steel tubing with production-type fittings employed at critical areas. Production wire bundles were attached not only to demonstrate their flexibility and reliability but also to produce their representative effects on the deployment process. The



The load required to depress the ratchet teeth were measured and found to be as follows:

- P₁ = 4.3 pounds
- P₂ = 5.2 pounds
- P₃ = 6.5 pounds
- P₄ = 8.9 pounds

The load required to depress the blade assembly to operate the switches was found to be:

$$P_5 = 16 \text{ pounds}$$

The load required to depress the blades until they were flush with the latch surface was found to be:

$$P_5 = 47 \text{ pounds}$$

**FIGURE 4 DEPLOYMENT ASSEMBLY LATCH CHARACTERISTICS
TORQUE vs ROTATION OPERATING FORCES**

steel tube trusses were designed to approximate the spring rates of the production trusses. This full-scale prototype DA was twenty-eight feet tall with its pentagonal base being inscribed by a circle approximately 20 feet in diameter.

The DA used for qualification testing was a flight-configured aluminum structure incorporating all hardware deemed necessary for the successful conclusion of the qualification phase.

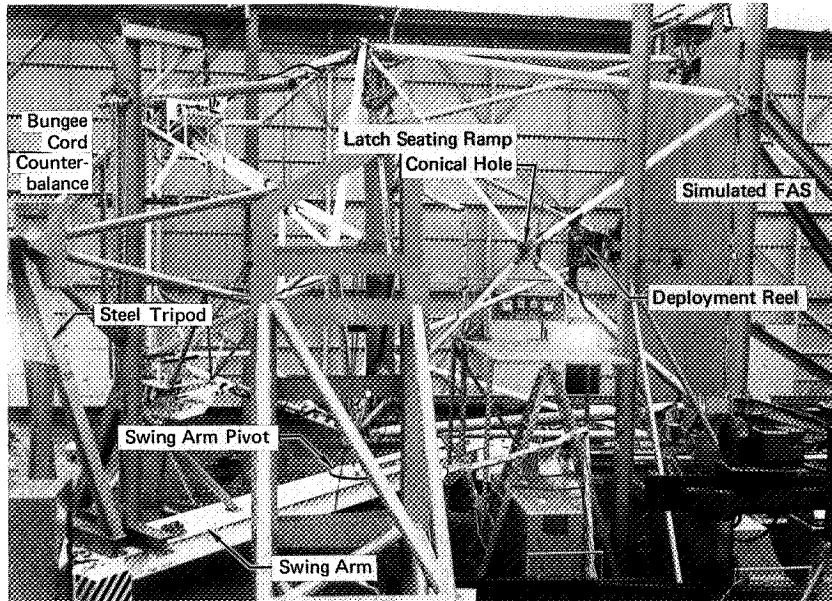


**FIGURE 5 TEST SETUP STEEL (DEVELOPMENT CONFIGURATION)
DA - ZERO-G TEST**

The simulated FAS was a three-tiered steel structure designed to provide a rigid base for the DA. The bottom tier was anchored to the laboratory floor, while the center tier was adjustable in relation to the bottom tier for alignment purposes. The upper tier was attached to the base of the DA and rotated about one end to a vertical position to place the DA longitudinal axis in a horizontal position for the zero-g deployment tests.

The simulated ATM mass, commonly referred to as the "swing arm" was a lead-ballasted steel beam weighing 47,000 pounds. The swing arm was pivoted on a two-inch diameter steel ball which enabled the arm to be balanced prior to deployment and to travel with the upper DA during deployment. The swing arm simulated a 25,000 pound ATM mass with a mass moment of inertia of 254,880 slug-ft² measured about the DA trunnions. The swing arm was attached by a steel tripod to the upper DA at the theoretical center-of-gravity (c.g.) of the ATM. This arrangement imposed the inertia of the ATM on the DA without imposing the weight, a simulation of the zero-g orbital condition.

A counterbalance system was constructed to offset the weight of the DA. The unique feature of the counterbalance system was a soft-spring bungee-cord member which negated the weight of the rotating upper DA while retaining its freedom to respond to inertial loads.

TEST PROCEDURES

Development Tests

The prototype steel DA used for the development tests was assembled and aligned on the simulated FAS using optical tooling. The top tier of the FAS was then rotated 90 degrees to a vertical position (see Figure 5) placing the DA launch axis in a horizontal position over the swing arm. Diagonal braces were then installed between the top and middle tiers of the FAS to form a firm support for the DA base. Lead filled counterbalance trays were attached to the DA lower truss via cables suspended from an overhead structure. The swing arm was attached to the DA upper truss at the theoretical center-of-gravity of the ATM by a ball and slotted plate arrangement which allowed only vertical movement of the DA with respect to the swing arm. The bungee-cord counterbalance system was then anchored to the swing arm and connected to the upper DA to support its weight. This arrangement allowed the swing arm, upper DA, and counterbalance to rotate together in a horizontal plane.

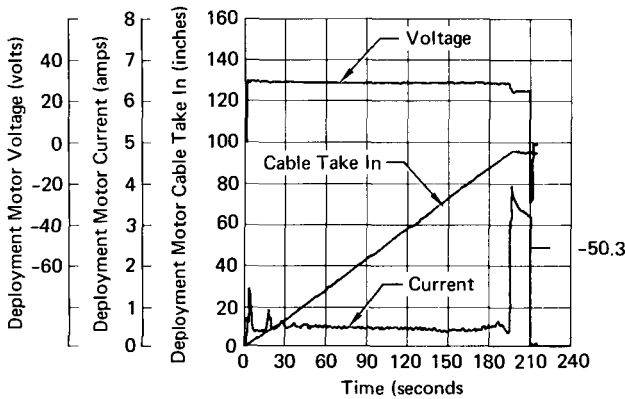


FIGURE 6 DEPLOYMENT REEL CHARACTERISTICS (RUN 14)

With the DA in the launch position, the pin-pullers were retracted, the deployment reels were energized and the upper DA was pulled to the deployed position where latching occurred. A time history of the deployment reel cable tension, rate of cable take-up, reel motor voltage and amperage was recorded for each deployment maneuver. The data from Run 14 (Figures 6 and 7) provide a typical time history.

After latching, loads were induced in the latch by applying simulated maneuvering (75 pounds) and docking (5000 pounds) loads at the ATM theoretical c.g. No misalignment or latch failure occurred.

Tests were then conducted to simulate partial malfunctionings of the system such as: low reel motor voltage, cable fouling, one missing cable, one reel motor inoperative, and latch misalignment up to three quarters of an inch in all directions. The pyrotechnic pin-pullers were also tested to see if they would retract under a 500-pound load applied at the ATM theoretical c.g. A total of thirty-six deployments were performed with no serious anomalies.

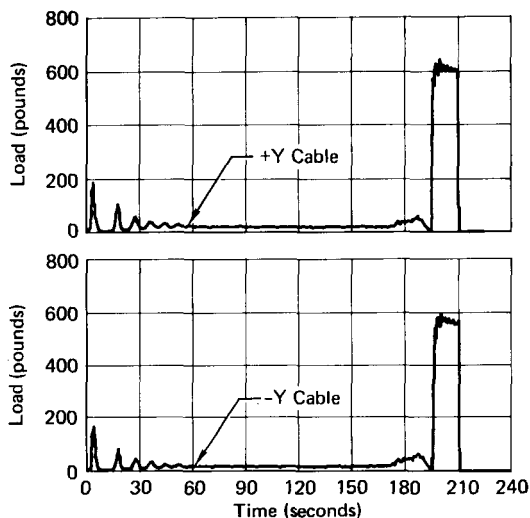


FIGURE 7 DEPLOYMENT REEL CABLE LOADS (RUN 14)

Qualification Tests

The flight-configured aluminum DA was assembled by manufacturing personnel and aligned on a production prototype FAS using optical tooling. This DA was then carefully removed from the FAS and placed aboard a transporting vehicle. Special Ground Support Equipment structures were attached to the DA prior to its being disconnected from the FAS to ensure that the alignment of the DA did not deteriorate. The transporting vehicle was then towed over the road to the test laboratory.

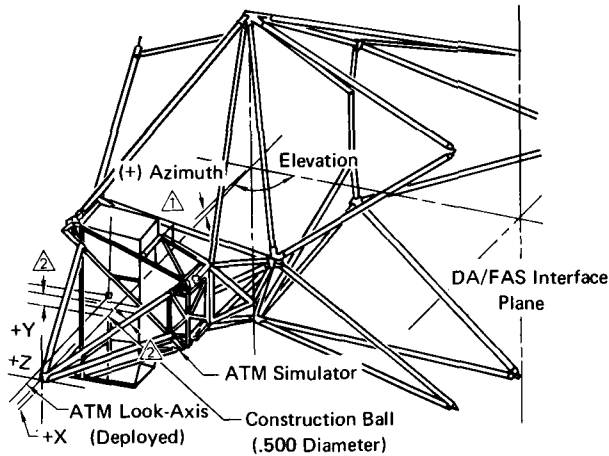
Once inside the test laboratory the DA was removed from the vehicle and placed atop the simulated FAS (see Figure 2). The attach fittings of the simulated FAS had been aligned, by optical tooling, to positions identical to those on the production prototype FAS from which the DA had been removed.

When the DA was attached to the simulated FAS it was necessary to verify that the alignment had not deteriorated. Table I is an example of the alignment data and how it was obtained. A special Ground Support Equipment counterbalance system was rigged from the ceiling of the laboratory building (Figure 8) to overcome the weight of the upper DA while it was being rotated from the launch position to the deployed position to verify alignment. The alignment in elevation and azimuth had to be maintained with ± 15 minutes of their nominal positions. An optical theodolite was used to measure these small angle variations in look-axis alignment.

Upon completion of the alignment verification the DA/FAS assembly was rotated 90 degrees to place the DA in the horizontal position over the swing arm. The DA was counterbalanced, and a second alignment verification was performed.

A zero-g, powered deployment was performed using production DA systems to satisfy the DA qualification test requirements.

TABLE I ALIGNMENT DATA



- 1 The following sign convention was adopted for azimuth readings. Positive azimuth is clockwise rotation when looking forward from the DA/FAS interface. This also coincides with the "right-hand-rule" where the vectored positive azimuth reading points toward +Z.
- 2 These dimensions were recorded with the DA Upper Truss in the launch attitude (not deployed) relative to the DA/FAS interface plane and referenced to a .500 diameter construction ball located on the ATM Simulator at Y-.5.000 and Z 0.000.
- 3 Readings were taken 3 times and results were identical within .001 inch.

Test Phase	Test or Operation Being Performed	Alignment and Look-Axis Data				Latch Alignment	
		DA in Launch Attitude 2		DA Deployed		Gap at Ratchet Tooth (inches)	Stud/Cone Gap (inches)
		Pitch (inches)	Yaw (inches)	Elevation (degrees-minutes-seconds)	Azimuth 1 (degrees-minutes-seconds)		
Assembly and Alignment in Building 66	Pitch & Yaw Reading	.027	-Y 5.057	—	—	—	—
	Manual Deployment	—	—	89° 59' 15"	0° 1' 1"	.050	.142
	Power Deployment	—	—	89° 57' 1"	0° 0' 11"	.049	.142
Transport to Building 102	GSE Transporter and Related Hardware	—	—	—	—	—	—
Acceptance Testing Building 102	Pitch & Yaw Reading	.135	-Y 5.053	—	—	—	—
	Manual Deployment	—	—	89° 57' 38"	0° 2' 16"	.058	.140
	Power Deployment	—	—	89° 56' 37"	0° 0' 36"	.056	.140
Setup	Reposition DA/FAS so Launch Axis is Horizontal	—	—	—	—	—	—
Qualification Testing	Manual Deployment	—	—	90° 3' 27"	0° 0' 1"	.044	.147
	Pyro Release & Deploy	—	—	90° 3' 44"	0° 0' 9"	.058	.140
	Simulated Inertia Load	—	—	89° 58' 30"	0° 1' 1"	.057	.140
Setup	Reposition DA/FAS so Launch Axis is Vertical	—	—	—	—	—	—
Acceptance Testing Building 102	Powered Deployment	—	—	89° 57' 37"	0° 1' 35"	.056	.140
Latch Alignment Tool Trial Fit	DA Upper Latch 3	—	—	—	—	.136	.140
	DA Lower Latch 3	—	—	—	—	.128	.136

Following this test the DA was rotated to the vertical position where a third alignment verification was performed. With Special Ground Support Equipment handling devices installed, the DA was removed from the FAS and placed aboard its transporting vehicle and prepared for delivery to the customer.

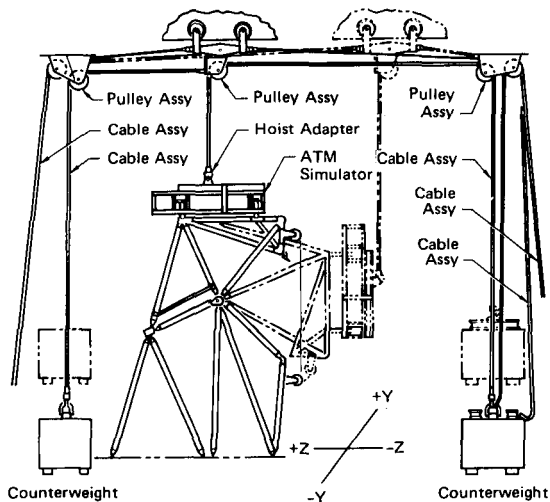


FIGURE 8 GROUND SUPPORT EQUIPMENT SPECIAL COUNTERBALANCE

TEST RESULTS

The results of the development test indicated that the steel prototype DA did exhibit structural characteristics such as strength, stiffness and alignment maintainability similar to those of the flight-configuration aluminum DA.

The pyrotechnic pin-pullers retracted properly under a 500 pound load applied at the ATM theoretical c.g.

A single deployment reel was capable of deploying the DA when operating with reduced voltage (26 volts versus 30 volts normal). One reel cable had sufficient strength to deploy the DA and absorb the 600 pound final stall load required to ensure latch capture.

The latch would capture and hold the DA trusses in the deployed position while absorbing the inertia load imposed by the moving 25,000 pound ATM. The latch remained closed while being subjected to the 5000 pound simulated docking loads. The latch would close and latch while misaligned up to three-quarters of an inch in a radial direction.

The wire bundle continuity did not deteriorate after 36 deployments.

The results of the qualification test indicated that the production prototype DA with proper handling will maintain its alignment while being transported and that its special handling devices will function to keep the DA aligned through the manufacturing and final assembly phases of the NASA Skylab Program.

MANNED THERMAL-VACUUM TEST OPERATIONS: ITS DEVELOPMENT FROM EXPERIMENTAL TO ROUTINE

Paul R. Gauthier (*Boeing Co.*), Herbert G. Sherwin (*Brown and Root-Northrup*), and Marion M. Lusk (*NASA, Manned Spacecraft Center, Houston, Texas*)

ABSTRACT

Manned operations have been a significant part of Gemini and Apollo thermal-vacuum test programs. The development of test techniques and equipment at the Space Environment Simulation Laboratory is discussed relative to these programs.

INTRODUCTION

Since the advent of the United States space program, many large space-simulation facilities have been constructed to subject spacecraft to the mission environments. The NASA Manned Spacecraft Center (MSC) was involved particularly in spacecraft and associated systems that were designed to be operated in space by men; thus, it was apparent that the major space-simulation facilities at the MSC would have to be designed to permit men to perform tasks safely in a thermal-vacuum test environment.

Experience with altitude-chamber operations for aircraft personnel provided a basis for approaching some of the problems associated with manned operations in a space simulator. However, to a large extent, many of these problems were being faced for the first time. Laboratory managers, engineers, and medical personnel were involved jointly in defining the requirements for man rating space-simulation facilities at the MSC (ref. 1). The task was complicated further by the large size of the MSC chambers.

Because these requirements were based on the "best available" knowledge and theory of the early 1960's, it was natural that initial chamber-shakedown tests and early manned tests would result in confirmation of the adequacy of some systems as well as demonstrating the need for improvement of other systems. Because the advancement in complexity of flight systems required more advanced test techniques as well as

increased reliability for long-duration tests, this upgrading of chamber equipment and operating techniques became a continuous process.

Although extensive engineering had gone into the design of systems directly associated with manned operations, performance and reliability under test conditions could only be verified completely by actual test experience. Therefore, early test programs could be considered "experimental."

The development of significant aspects of test equipment and test techniques, from initial design to maturity as manned systems, is discussed in this report. The contributions to the national space program made by manned testing will be evident in the descriptions of the major test programs that have been successfully conducted in the MSC facilities.

BASIC REQUIREMENTS

Manned testing influences the design and operation of almost all systems in a space-simulation facility because failures or malfunctions in many systems affect the crewmen. However, the emphasis in this report will be placed on systems that are associated directly with the crewman and that are of primary importance to his ability to perform tasks safely in the thermal-vacuum environment. The following eight elements are involved in the basic requirements.

1. A protective enclosure (a spacecraft or a space suit) capable of containing a physiologically acceptable environment at all times
2. A life support system, to provide the required environment under normal and off-normal conditions
3. Instrumentation to monitor the gaseous environment and the medical condition of the crewmen
4. Verbal and visual communication with the crewmen at all times
5. A means of rapid repressurization of the vacuum chamber in event of crewmen incapacitation
6. The capability for prompt rescue and medical treatment
7. A fire protection system for the chamber, the manlocks, and the test spacecraft
8. A competent, well-trained test organization

The methods used to fulfill these requirements have varied during the development of manned testing at the NASA Space Environment Simulation Laboratory (SESL). The following sections are descriptions of the incorporation of these elements into the major test programs.

INGRESS/EGRESS TECHNIQUES

The manned test programs conducted at the SESL since 1965 have been characterized by various techniques for crewmen ingress and egress. The mode used for any given test was dependent upon the objectives of the test, the reliability of the prime life support system, and the mobility aspects of the required test operations. Likewise, the biomedical instrumentation, communications, and degree of redundant capability varied from test to test as necessary to support the chosen test mode.

The test modes may be grouped into four major categories.

1. Use of facility umbilicals for life support, communications, and physiological monitoring
2. Use of flight-type portable life support systems with facility gas, communication, and instrumentation umbilicals
3. Use of flight-type portable life support systems only, with radio-frequency communications and telemetry
4. Use of portable oxygen ventilators for transfer to spacecraft or extravehicular life support systems

FIRST-GENERATION TECHNIQUES

The initial test to "man rate" the facility occurred in October 1965 after a series of shakedown tests of the SESL chambers and a thorough checkout of manned operations systems. A crewman, who was wearing a Gemini-type space suit modified for chamber usage, entered chamber B while it was in a thermal-vacuum condition. Life support was provided by a closed-loop environmental control system (ECS) by means of gas umbilicals.

Voice communications and biomedical data were transmitted by means of an electrical umbilical. Total test time in the chamber was approximately 10 minutes. This brief but significant test was the beginning of the "first generation" of testing in the SESL.

Gemini Program Tests

The first use of the facility for manned testing of space-flight hardware occurred shortly thereafter. In January 1966, a thermal-vacuum evaluation of the astronaut maneuvering unit (AMU), planned for use on certain Gemini flights, was conducted in chamber B (fig. 1). In this test, the Gemini extravehicular life support system (ELSS) was the primary

means of life support. Because the ELSS normally was started at a pressure of 280 torr, the facility ECS was used during manlock evacuation to that pressure; then, the facility ECS was disconnected.

Although the crewman was free of the facility ECS umbilicals, the high-pressure oxygen-supply line to the ELSS was still necessary, as were electrical cables for communications and biomedical instrumentation. Once the crewman was in the workstand, a transfer of oxygen and communications lines from the ELSS to the AMU was made and a connection was made for the oxygen outflow from the ELSS. These tasks were repeated in reverse order during egress.

The crew-equipment tests for the Gemini X and XI missions involved a somewhat different technique for ingress because leakage problems developed with the facility closed-loop ECS. The portable oxygen ventilators, which the crewmen used during transfer to the manlock, also were used as a means of life support to a pressure of 280 torr, where the ELSS was started and the ventilator disconnected. During egress, the manlock was repressurized to 380 torr, and the ventilator was reconnected before ELSS deactivation.

Although the method was satisfactory from a suit-flow and pressure standpoint, there were some drawbacks. Each ventilator had a relatively short use time (20 to 30 minutes); therefore, any time-consuming problems occurring during manlock checkout and pumpdown required ventilator changes.

Apollo Program Tests

The initial design-verification testing of the Apollo extra-vehicular mobility unit (EMU) was performed in chamber B using a lunar-crater thermal simulator and solar simulation to provide lunar-surface environmental conditions. This new portable life support system (PLSS) necessitated modification of the previous ingress/egress techniques. The suit was pressurized to 950 torr (3.8 psid) before pumpdown to verify accessibility of the PLSS controls. Because the facility ECS could not be used to perform this function, an oxygen ventilator was used. After completion of the accessibility check, the suit was depressurized and the facility ECS connected. After the manlock was evacuated and the manlock pressure was equalized with the chamber pressure, the PLSS was activated by the crewman. The ECS umbilicals were disconnected and an emergency oxygen-purge valve/relief valve was installed. Then, the crewman opened the inner manlock door and proceeded to the workstand within the lunar crater (fig. 2).

During egress, when the pressure was 140 torr, the ECS was reconnected and the PLSS was deactivated.

A similar test program to qualify the EMU was conducted in chamber A. The most significant change was the addition of an emergency oxygen umbilical that was carried into the chamber with the communications and instrumentation cables.

Discussion

The initial tests resulted in the establishment of operational procedures for conducting manned tests in the SESL and the verification of the satisfactory operation of most of the facility systems. Certain aspects, however, required improvement.

The inherent awkwardness of the early space suits often complicated even simple tasks. Operation of the PLSS controls was troublesome because the controls were located behind and out of sight of the crewman. It was possible to shutoff the oxygen supply valve inadvertently, and, in fact, this potentially dangerous situation occurred in the manlock on two separate occasions. Rapid repressurization of the manlock prevented any serious consequences. These experiences resulted in changes to flight hardware in order to eliminate the occurrence of similar problems in future tests and on space flights.

The lack of space-suit mobility affected the relatively simple act of opening and closing the manlock inner door. It was a tiring and time-consuming exercise, particularly at the conclusion of a strenuous test, to close and latch the door so that the manlock could be repressurized. To remedy this situation, development of a remotely controlled opening/closing/latching mechanism for one of the chamber B manlock inner doors was planned.

Crewmen carried emergency oxygen systems that could only be actuated by the crewmen. Rapidly changing off-normal conditions experienced during some of these tests were indicative of the need for an emergency oxygen system under the control of outside personnel. This requirement was incorporated into the design of a new facility ECS. For this and other operational reasons, the closed-loop ECS was unsatisfactory for SESL operations and was replaced with an open-loop system in preparation for the second-generation test programs.

SECOND-GENERATION TECHNIQUES

Although the experience gained from chamber, space-suit, and spacecraft tests in 1966 had resulted in the basic

techniques for conducting manned operations and in an appreciation of the effort required to prepare and maintain a fully manned facility, 1967 was the year of change. The Apollo spacecraft tragedy at the NASA John F. Kennedy Space Center in January focused attention on manned spacecraft operations and vacuum-chamber testing. The MSC Safety Manual was revised extensively and imposed stringent requirements on the design, testing, and configuration control of systems associated with manned testing. When these safety standards were adopted, the SESL was immersed deeply in preparing for major Apollo lunar module (LM) and Apollo command and service module test programs.

The most far reaching of the new safety policies concerned oxygen compatibility and flammability. The materials criteria established for spacecraft systems, space suits, life support systems, rescue-personnel clothing, and instrumentation eliminated many commercial products because of the lack of definitive test data and material certification. The comprehensive materials test program instituted by the NASA provided valuable guidance to the SESL equipment designers for choice of materials to be used in man-rated systems.

The protection of the crewmen and the spacecraft from the hazards of oxygen-fed fires required the selection of an effective fire-suppression system. After evaluation of several fire extinguishing methods, a water-spray system was designed and installed in both chambers A and B. The system is divided into various control zones and can be actuated only at chamber (or manlock) pressures greater than 300 torr.

This method of fire suppression has been demonstrated under the 300 torr, cold (200° K) conditions, after an emergency repressurization, with no significant effects on chamber systems or rescue modes.

Lunar Module Tests

The first manned spacecraft test run in the SESL after incorporation of several significant improvements to manned operations equipment was the most complex test attempted. The LM (test article LTA-8) thermal-vacuum test program in chamber B was planned to simulate orbital- and lunar-mission time lines under varying thermal conditions. This test program required several 12-hour periods of manned occupancy of the spacecraft. Therefore, crewmen had to ingress and egress the LM while it was in a thermal-vacuum condition.

The ingress/egress technique was developed using the concept of umbilical transfers, with the three modules of the new

facility ECS, through the flow-distribution panel, providing life support to two crewmen in the manlock, chamber, or spacecraft. Basically, the sequence of events was as follows.

1. The two crewmen entered one of the chamber B manlocks and were connected to facility gas and electrical umbilicals.

2. The crewmen manlock was evacuated and manlock pressure was equalized with the chamber, which was at test-environment conditions, so that the manlock-to-chamber door could be opened remotely.

3. The crewman entered the chamber and transferred to another set of gas and electrical umbilicals stowed in the chamber.

4. The crewmen climbed a ladder to a platform in front of the spacecraft hatch and entered the LM (fig. 3).

5. The crewmen transferred to the spacecraft gas and electrical umbilicals, stowed the chamber umbilicals on the platform, and closed the hatch.

During egress, the procedure was repeated in reverse. The total time for ingress was 1-1/2 to 2 hours; for egress, the total time was 1 hour. More detailed information on the LTA-8 program is available in reference 2.

Command And Service Module Tests

The testing of the command and service module 2TV-1 test vehicle in chamber A during 1968 involved the simplest technique for ingress and egress. The three crewmen entered the spacecraft (fig. 4) at atmospheric pressure before chamber pumpdown and remained in the spacecraft throughout the test until atmospheric conditions were reestablished. Except for a short period to verify spacecraft performance with an open hatch and depressurized cabin, the crewmen were exposed primarily to a 250 torr (5 psia) oxygen cabin environment.

Access to the spacecraft was by means of a "clamshell" ramp, which was retracted against the chamber wall during the test phases and swung in to surround the command module for normal or emergency entrance.

Apollo Extravehicular Mobility Unit Qualification

In 1968, the Apollo EMU was modified to incorporate the latest fire-retardant materials and to upgrade the basic performance capabilities. These changes required requalification of the EMU in a thermal-vacuum environment during February 1969 (ref. 3).

A lunar-surface thermal simulator (LSTS), in the form of a circular infrared-heater array, was used in conjunction with the normal facility vacuum, cryogenic, and solar-simulation systems to provide the various cold and hot environments required for the test program.

The ingress/egress technique was based on the need to relieve 45.4 kilograms (100 pounds) of the 54.6-kilogram (120 pound) "earth weight" of the PLSS during test operations in both the chamber and the manlock. A trolley/monorail system (fig. 5), with an integral falling-restraint mechanism, was designed by SESL personnel. The monorail was split at the manlock inner door to allow the door to be opened for ingress and closed on egress. Latching and unlatching of the monorail sections was performed pneumatically.

Upon arrival at the manlock, the crewman was transferred to the facility ECS umbilicals and disconnected from the portable-oxygen ventilator. The crewman then donned the PLSS. All biomedical and test instrumentation was connected and verified, the manlock was evacuated to 250 torr (5 psia), the PLSS was activated, and the ECS was placed in a "bypass" mode. However, the gas umbilicals were left connected to the suit for use in the event of PLSS malfunction or depletion.

After manlock evacuation and equalization with the chamber, the inner door was opened and the manlock portion of the monorail was moved into place by the crewman. The crewman then entered the chamber (fig. 5) pulling the gas, electrical, and instrumentation umbilicals behind in a trough designed for this purpose. When the crewman reached the center of the LSTS, the LSTS door was closed so that the proper lunar-surface conditions could be simulated. Similar sequences were repeated, in reverse during egress, with the facility ECS placed in "flow" mode at 250 torr (5 psia).

Discussion

During 1968 and 1969, approximately 600 hours of manned operations were conducted on the LTA-8, 2TV-1, and EMU test programs. Spacecraft, space suits, life support systems, and facility systems were subjected to a wide range of environmental conditions and were proved to have a high degree of reliability. The complexity of test preparation and test operations imposed many demands on the NASA/contractor test teams. The completion of these programs established a major advance in the status of manned testing.

Certain changes were made to manned-operations systems before these test programs. Most of these modifications were

acceptable. Other modifications were improved (as required) during the test programs. The initial design of the monorail system required certain monorail latching and unlatching functions to be performed by the crewman. This was awkward and time consuming, and the system was modified to incorporate a pneumatic latching mechanism controlled by the manlock operator. The misalignment of the manlock and chamber monorails, caused by thermally induced movement, required some redesign.

The growth of confidence in manned thermal-vacuum operations was demonstrated during the LTA-8 program. During the first series of tests, two egresses were performed at 300 torr (6 psia), warm-chamber conditions, to reduce the risk factor. Egress while in a thermal-vacuum condition became the preferred method by the last series of tests.

THIRD-GENERATION TECHNIQUES

The SESL had demonstrated a capability to conduct a wide variety of manned operations by May 1969. The space suits and portable life support systems had been qualified fully through many hours of use while in severe thermal-vacuum environments. Test programs, therefore, became more diversified and involved the use of the normal and emergency capabilities of the flight equipment.

Apollo Flight Crew Training

The flight and backup crewmen for the Apollo 9, 11, 12, 13, and 14 missions participated in lunar-surface-simulation tests in the SESL chambers (primarily chamber B) as part of their mission training. These 3- to 4-hour tests were planned to familiarize the crewmen with the operation of the Apollo EMU in a thermal-vacuum environment while working with lunar scientific experiments.

From a manned operations viewpoint, the most significant aspect of these tests was the use of the PLSS without facility gas and electrical umbilicals for backup oxygen and physiological monitoring. This test mode was justified by the flight qualification of the EMU in previous tests and by the desire to perform crew training in flight configuration.

The facility ECS was used only at pressures greater than 250 torr (5 psia) and was disconnected once the PLSS was started. The flight oxygen purge system (OPS), mounted on top of the PLSS, provided an emergency 30-minute oxygen supply. Communications, biomedical data (electrocardiogram only), and PLSS operating parameters were transmitted by means of telemetry.

By freeing the crewmen from the constraints of the umbilicals, a great mobility increase was achieved, which enabled test operations with the scientific equipment that would not have been possible otherwise (fig. 6). However, the combined earth weight of the PLSS/OPS, 54.6 kilograms (120 pounds), required the use of the SESL monorail system to relieve 45.4 kilograms (100 pounds) of this load from the crewman. A chamber work area, 3.05 by 3.66 meters (10 by 12 feet), was provided by the design and installation of a two-dimensional extension of the monorail in a "bridge crane" configuration.

Lunar-Surface Scientific and Engineering Tests

Several tests of scientific equipment requiring deployment by a crewman have been conducted on a rapid-response basis. This response has been possible because of the SESL policy of maintaining manned test capability on a continuous basis. Tests in this category have included the Apollo lunar aseptic sampler, the modular equipment transporter, and the lunar rover fender deployment programs.

Apollo 15 Extravehicular Mobility Unit Tests

The 1969 tests had resulted in the qualification of the EMU for the early lunar missions (Apollo 11 to 14). Changes to the PLSS and OPS to increase the usable amount of oxygen, water, and electrical power, as well as modifications to the space suit to increase mobility, required requalification of the Apollo 15 EMU configuration. These tests were conducted during April 1971 with essentially the same chamber configuration used for the 1969 tests.

During June 1971, a test program was performed to evaluate the effect of the strenuous Apollo 15 lunar-surface time line on the physiological condition of a crewman. Three 6- to 7-hour tests were run in a 2-day period using the PLSS/OPS as the only life support systems below 250 torr (5 psia). These tests were similar to the technique used for the crew-training tests.

Discussion

During this "generation" of testing, the basic test techniques changed very little. The primary emphasis was on using a man-rated facility for training astronauts and for evaluating scientific equipment. Although the risks inherent in a thermal-vacuum environment were still present, the probability that equipment

failure could occur had been demonstrated to be low. In addition, experience with preparation of the facility made it possible to conduct manned tests with lead times primarily based on the availability of test articles and special test equipment.

MANNED TEST SYSTEMS

Certain systems and types of equipment have been involved in all manned tests. Performance capabilities of these items greatly influenced the test techniques previously described. Improvements in these systems made possible the development of manned test operations to the present capability. The emphasis in the following discussion will be on the effect of actual test experience on system modifications.

Facility Environmental Control System

A facility system to provide the proper gaseous environment for crewmen wearing space suits is one of the obvious requirements for a man-rated facility. However, the actual performance specifications are not as apparent because test techniques play a significant role in the design of such a system. Also, often a facility ECS is quite different from the ECS used on board a spacecraft. The SESL staff has had experience with both closed- and open-loop environmental systems, and has used this experience to develop a highly reliable, flexible system that has supported major test programs.

The initial construction of the SESL facility included a multimodule ECS system for chambers A and B. Based on the existing spacecraft technology, the ECS was of a closed-loop, recirculating design (fig. 7). This system was used for the early tests, including the Gemini space suits and first Apollo EMU, in the chambers.

This complex system was less than desirable from a maintainability and reliability standpoint. Problems with the operation of the circulation blower, the carbon dioxide removal canister, and the water condenser often caused degradation of the desired gas composition. Oxygen and carbon dioxide partial-pressure sensors were required for constant monitoring of the gas flow, which introduced the problems of instrument maintenance and calibration. However, the most significant problem was elimination of air leaks, which diluted the oxygen content, into the system.

New LTA-8 program requirements for test operations plus the inadequacy of the old ECS modules led to the decision to design, fabricate, and install an ECS with broad capabilities

for normal and off-normal operations. The design specifications were based on actual test experience and on particular plans for the LTA-8 test.

The new design (fig. 8) was an open-loop system that minimized leakage, contamination, and thermal-control problems common to closed-loop systems. The gas (oxygen or air) was supplied to the ECS modules from high-pressure tube trailers and exhausted by facility vacuum pumps. Although this mode of operation uses considerable amounts of gas, the great increase in system operating performance and reliability offsets this disadvantage.

The most significant test operation advantages of this system were as follows.

1. The capability to use the ECS (with clean dry air) to conduct dry runs with pressurized space suits

2. The capability to adjust suit pressure on an absolute and differential basis

3. The availability of an alternate vacuum-pumping source

4. The incorporation of relief valves and safety interlocks to minimize the effect of system malfunctions and operator errors

5. The capability of switching a crewman from one ECS module to another by means of the flow-distribution panel

6. With large suit leaks, the flow capability to maintain space-suit pressure at normal levels

Test operations with this configuration of three ECS modules, interconnected by a flow-distribution panel, over the 180 hours of manned operations associated with the LTA-8 program, were excellent. The systems proved to be very reliable in maintaining suit pressure and flow under a wide range of environmental conditions in the manlock, chamber, and spacecraft. The only deficiency was in the area of thermal control, in which long umbilicals negated close-tolerance temperature conditioning.

All manned testing in chamber B since the testing of LTA-8 has involved a single crewman. These tests have been supported by the ECS configuration shown in Figure 9. Depending on the test technique, the ECS has been used as both a primary and backup life support system. This configuration provides the following capabilities.

1. Full capability for normal and off-normal operations associated with tests requiring life support by means of gas umbilicals

2. Capability to operate in a "flow" or "bypass" mode for tests of flight life-support equipment

3. A backup life-support means for emergency situations

The SESL staff has found, based on 3-1/2 years of test operations with this ECS, that the open-loop design is superior to the closed-loop configuration for manned activities and is more adaptable to changing test techniques.

Biomedical Instrumentation

The risks involved in performing manned operations in a vacuum chamber require that suit environmental conditions and crewman physiological status be monitored continuously. The SESL personnel developed two groups of sensors to perform these functions (table I). Power and signal lines for this instrumentation are routed through an electrical umbilical. A fuse box at the chamber/umbilical interface provides protection against current overloads.

Test experiences over the past 5 years using this equipment have been good and the basic design remains unchanged. Improvements in sensor application techniques and types of materials used for harnesses have been the most significant changes. However, the relative fragility of sensors, cables, and electrical connectors has been the cause of test holds resulting from loss of mandatory biomedical data.

These problems have been overcome by incorporating biomedical checkout sequences into the space suit donning procedures at several intermediate points. Electrical cables in the biomedical-sensor room and in the suit-donning area are connected to the medical display consoles in the control room. Thus, satisfactory final checkout of the instrumentation in the suit room usually results in satisfactory operation of the system in the manlock and chamber.

Normally, crewmen entering the chambers with facility gas umbilicals have worn the full set of instrumentation. When portable life support systems were used, biomedical data were limited to heart-rate information because the radiofrequency telemetry link was equipped only for this measurement.

Repressurization Systems

The initial design of the emergency repressurization system was based on the use of dry gas stored in sufficient quantity to return the chamber to a pressure of approximately 300 torr (6 psia) within 30 seconds. The original concept was to use nitrogen during the first 5 seconds of repressurization, then to use 100-percent oxygen during the remainder of the cycle so that the oxygen partial pressure would be sufficient to sustain

life at the final pressure of 300 torr (6 psia). This concept was changed before it was implemented to include a 20-percent oxygen/80-percent nitrogen mix to avoid the problems of handling large amounts of 100 percent oxygen. This system was demonstrated successfully; however, severe fogging in the chamber occurred when ambient air was used to continue the repressurization to a pressure of 760 torr (14.7 psia). The fogging was eliminated by increasing the storage-tank capacity so that sufficient gas was available to repressurize the chamber to ambient pressure.

The manlock emergency-repressurization capability is similar to that of the chamber. However, the manlocks do not have any low-temperature panels or temperature-control devices. This allows the manlocks to be repressurized with ambient air without concern for fogging caused by condensation of water vapor.

Originally, the manlock repressurization criteria were selected to match the chamber criteria with regard to time to repressurize to a safe pressure. The original performance requirement was 30 seconds to 300 torr (6 psia). Minor equipment modifications made it possible to decrease the repressurization time to 15 seconds.

The means for activating the emergency-repressurization system are redundant because both manual and automatic means are provided. The medical officer and the test director can initiate chamber emergency repressurization manually. The automatic initiation of manlock or chamber repressurization is controlled by pressure switches located within the space suit. These pressure switches are set to initiate repressurization if the suit pressure drops to 102 torr.

Originally, the circuitry of the automatic repressurization system was set up to provide repressurization of the volume (chamber or manlock) based on whether the crewman was connected to a manlock or chamber electrical umbilical. The plan was based on the assumption that the electrical umbilicals would be connected and disconnected by the crewman while moving about in the vacuum.

Providing the crewman with enough manlock electrical umbilical to allow full mobility in the chamber became more desirable than changing umbilicals. A selection circuit was provided so that either the manlock or chamber emergency-repressurization system was selected based upon the position of the crewman or the chamber-door configuration.

Rescue Operations

Rescue of the crewmen from the chamber after an emergency involved unique problems. After an emergency repressurization, the chamber had a total pressure of approximately 300 torr (6 psia) and a gas temperature of approximately 200° K. Special clothing for the rescue personnel was developed to cope with these environmental conditions. A coverall garment (fig. 10) was fabricated with integrated helmet, boots, and gloves. The helmet had a built-in oxygen mask and regulator.

This equipment was impractical. The bulkiness and complexity of the clothing made a rescue operation extremely difficult. Subsequently, the life-support equipment was changed to standard U. S. Air Force-type masks, helmets, regulators, and walk-around bottles. A cold-weather garment (fig. 11) was evaluated for protection from the 200° K chamber temperatures.

After several trial rescues in the chamber after emergency repressurizations, it was determined that ordinary street clothes could be worn by the rescue personnel for 5 to 10 minutes without discomfort. This time was adequate for rescue operations. The clothing now being used consists of waffle-weave long-john underwear, a Beta-cloth flying-type coverall, and safety-type boots (fig. 12).

The oxygen equipment has changed very little. One change involved the design and fabrication of a special backpack containing two emergency high-pressure oxygen cylinders. Normal-use oxygen is supplied through a flexible hose from the chamber supply. An oxygen transfer is accomplished by simply uncoupling the flexible hose quick-disconnect fitting, which allows the backpack source to supply the breathing regulator.

The communications equipment worn by the rescue personnel had several changes. The first problem discovered was that the wire insulation used on the communication lines became brittle and cracked during cold exposure. This problem, along with tangling of communication lines, made the use of hard-line communications a questionable means of operation. Then, a two-way radio link was tried and was fairly successful. These radios had only 100 milliwatts of power, and it was possible to have dead spots within the chamber. Now, a 5-watt radio system is in use; the problem is eliminated.

Rescue personnel are now independent workers who have completely portable oxygen and communication systems. This freedom of movement has resulted in the capability to rescue crewmen from the chamber or spacecraft at a pressure of 300 torr (6 psia) in medically acceptable time (table II). These times vary significantly with the test configuration and are based on getting oxygen

to the crewmen as quickly as possible. Then, the crewmen would be moved from the chamber or spacecraft to the manlock, which would be repressurized to ambient pressure.

TEST-TEAM ORGANIZATION

A significant factor in the conduct of the manned test operations has been the manner in which the SESL test personnel have worked together. The organization of the personnel who deal directly with the systems that affect the crewmen is shown in Figure 13.

The NASA test director has the overall responsibility for the test and usually directs test-team leaders and the crewmen in the performance of test sequences. The NASA medical officer (MO) primarily is concerned with physical examination of the crewmen and monitoring their physiological condition during test. Unless an off-normal situation arises, the MO usually does not perform an active role in the test procedure.

Pretest-preparation activity is primarily the responsibility of the contractor crew support conductor (CSC). The CSC, the suit room conductor (SRC), and the contractor technicians are associated with biomedical sensing, suit-room support, rescue-equipment checkout, and facility ECS operation and manlock preparation. Once the crewman arrives at the manlock, most of the activities before entrance into the test chamber are directed by the CSC. Contractor technicians operate the ECS and manlocks and are stationed in one of the two manlocks at an intermediate pressure, 380 torr (7.3 psia), to assist the crewman in normal and off-normal situations.

Engineers and technicians associated with portable life support systems, telemetry ground stations, and test articles are included in the test team as required.

This basic organization has worked well for a variety of manned tests. In addition to the test-team functions during tests, the test-team personnel normally are associated closely with the preparation of facility systems and special test equipment before a test. This familiarity with the test equipment supplements the normal training that is required of all manned test personnel.

Originally, the laboratory operating policies governing manned test programs were issued as part of the overall Apollo Program procedures for ground tests. To make the policies more responsive to particular test programs, the SESL staff has incorporated the policies into its own set of general operating procedures for the facility.

Test Readiness Review Boards have been the major management tool used to ensure that the facility, test article, and test team are prepared sufficiently to conduct the desired test program. These boards consist of senior supervisory personnel from all organizations involved in the program, including the Safety Office and Quality Assurance Office. Although major inadequacies have been uncovered only rarely by these reviews, many significant problem areas have been identified and corrected before the start of testing.

CONCLUSION

The test techniques used by the SESL staff over the past 6 years have undergone continuous development in response to test-article requirements and growing experience with actual manned operations. This development has resulted in the confidence that both simple and complex manned tasks can be performed safely in a thermal-vacuum environment. This confidence is based on the demonstrated performance and reliability of facility systems during 1100 hours of manned testing, as well as on the professional competence of the test organization.

REFERENCES

1. Chappee, J. H. ; and Smith, G. B. , Jr. : Man-Rating Considerations in the Design and Operation of Hard Vacuum Chambers. Proceedings of the AIAA Space Simulation Testing Conference, 1964, pp. 60-64.
2. Gauthier, P. R. ; and Pearson, O. L. : Manned Test Operations for the Apollo Lunar Module in a Simulated Space Environment. NASA TN D-5760, June 1970.
3. Sanders, R. E. ; Vincent, J. P. ; and Maples, H. E. : Engineering and Operational Experiences Related to Lunar Surface Thermal-Vacuum Qualification of the Apollo Extravehicular Mobility Unit. AIAA/ASTM/IES 4th Space Simulation Conference (AIAA paper 69-992), 1969.

TABLE I - SPACE SUIT INSTRUMENTATION

Sensor	Range
Safety instrumentation package	
Oxygen partial pressure	0 to 1040 torr (0 to 20 psia)
Carbon dioxide partial pressure	0 to 40 mm Hg
Suit pressure	0 to 1040 torr (0 to 20 psia)
Baroswitches	Switch closure
	102 ± 12 torr (2.0 ± 0.25 psia)
Biomedical	
Two electrocardiograms	0 to 5 volts
Impedance pneumograph	0 to 5 volts
Body temperature	32° to 40° C (90° to 105° F)

TABLE II - TYPICAL CREWMEN RESCUE TIMES^a

Test configuration	Time to administer oxygen to the crew, min:sec	Total time to the manlock, min:sec
Flight crewman in chamber	0:25	1:00
Three crewmen in 2TV-1 spacecraft	0:55	3:00
Two crewmen in LTA-8 spacecraft	1:36	4:12

^aThe times listed do not include the initial 30 seconds required for chamber repressurization.

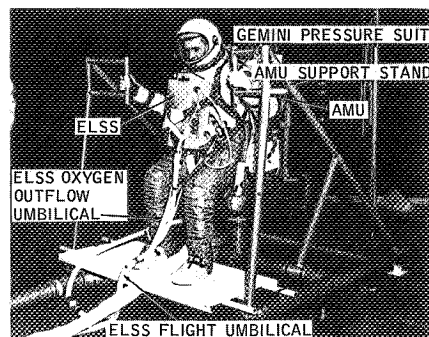


Fig. 1—The AMU test

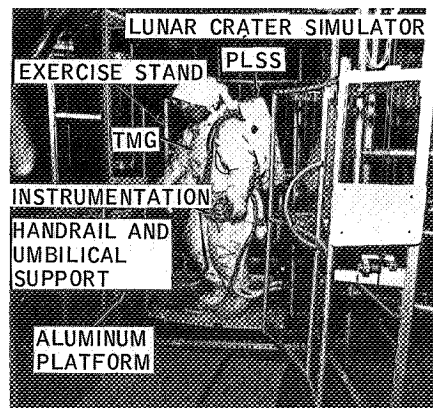


Fig. 2—The EMU test

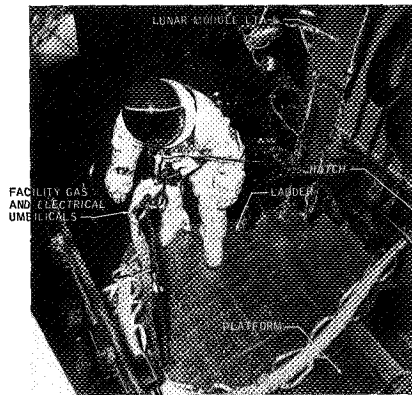


Fig. 3—Lunar module ingress

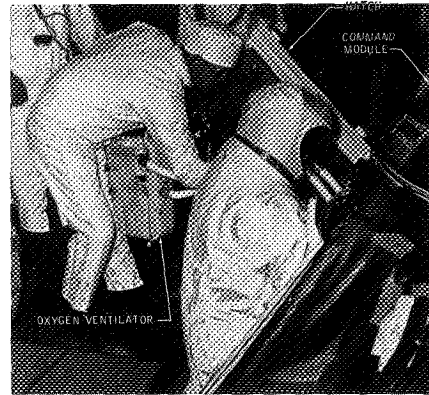


Fig. 4—Command module ingress

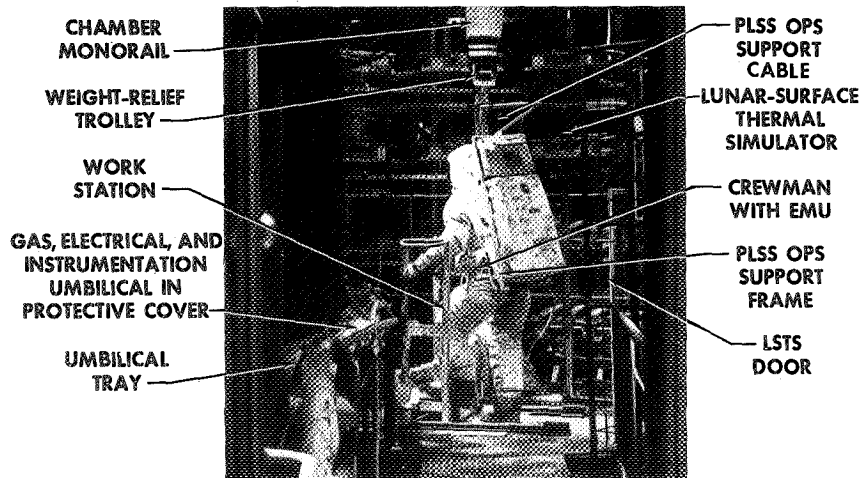


Fig. 5—Crewman exercising in lunar-surface thermal simulator (door open)

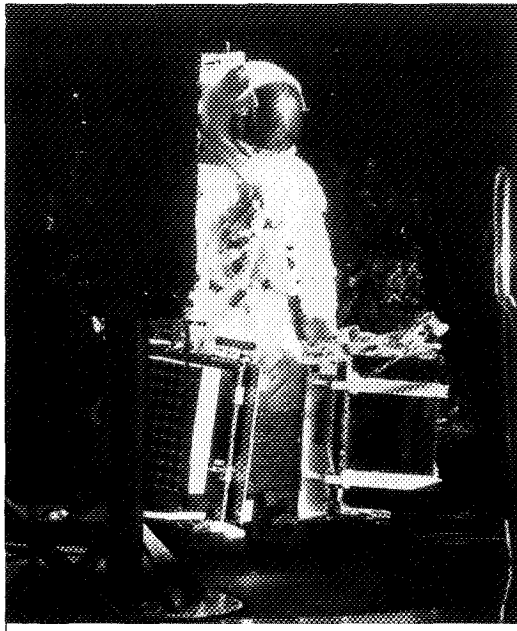


Fig. 6—Apollo 11 crewman carrying scientific package

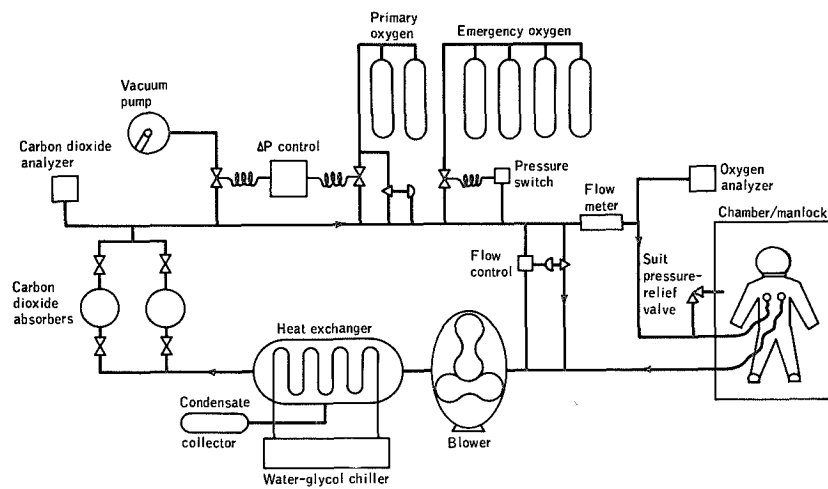


Fig. 7—Closed loop environmental control system (simplified)

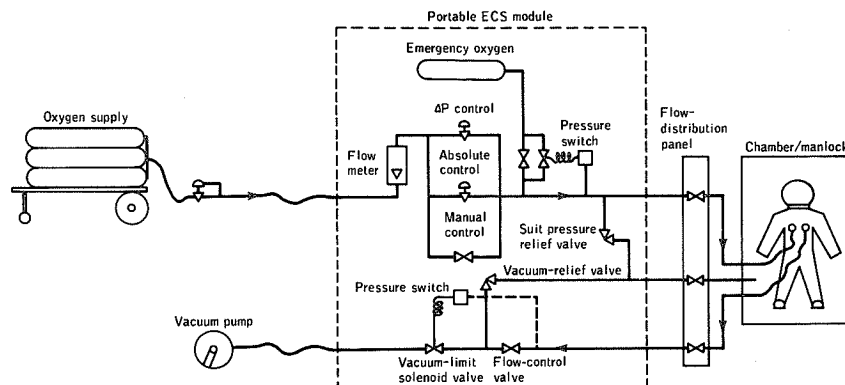


Fig. 8—Open loop environmental control system (simplified)

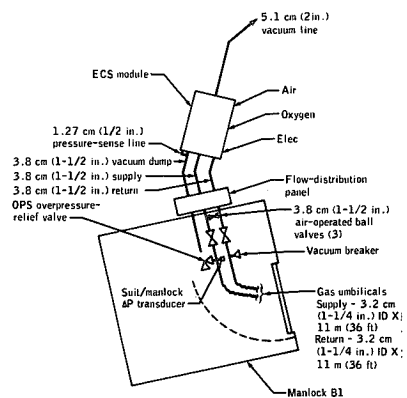


Fig. 9—Schematic of the facility ECS

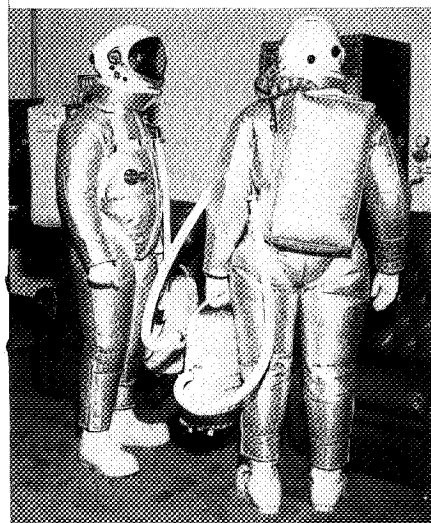
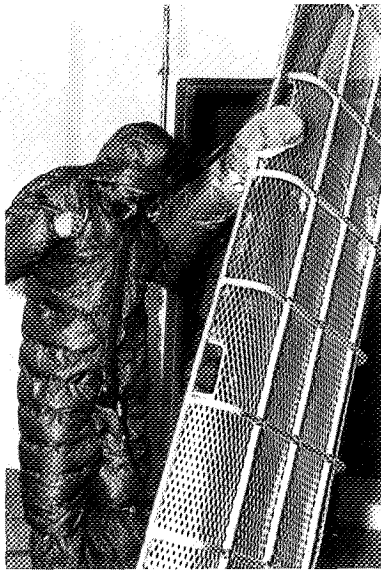


Fig. 10—First evaluation rescue gear



**Fig. 11—Second evaluation
rescue gear**



**Fig. 12—Final configuration
rescue gear**

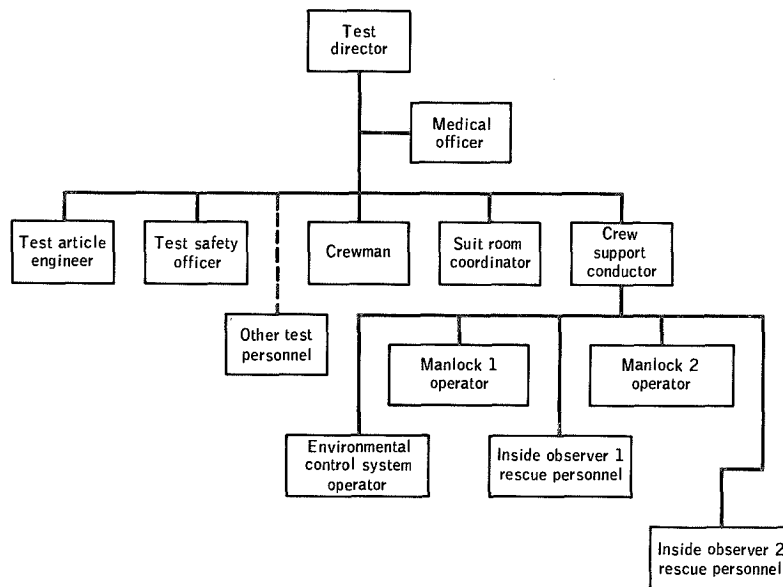


Fig. 13—Test-team organization

ZERO "G" MANUAL CARGO HANDLING

Amos A. Spady, Jr., and Gary P. Beasley, *NASA Langley Research Center, Hampton, Virginia*

INTRODUCTION

One of the prime goals of the shuttle program is the safe delivery and in-orbit handling of large amounts of cargo. In order to assure the safe, efficient handling of the cargo during all of the proposed shuttle missions and to determine man's role in cargo handling, extensive analysis and simulation is required.

In response to this need, a series of studies has been conducted at NASA Langley utilizing its Water-Immersion Simulator facility to better define the cargo that can realistically be handled by man. The initial phase of the program was a parametric study to define man's intravehicular (IV) cargo transfer capabilities, and its results are reported in Reference 1. Additional phases of the study, covered in this report, deal with: (1) man's ability to perform extravehicular (EV) cargo transfer, (2) the ability to transfer cargo through a 1.5-m (5-foot) diameter tunnel (IV), and (3) the utilization of electroadhesive/electromagnetic mobility aids for both IV and EV self-locomotion and cargo transfer.

SYMBOLS

I	moment of inertia, kg-m^2
M	mass of the package, kg
V	volume, m^3
x,y,z	reference axis

Subscripts

c.m.	moment of inertia about center of mass
1,2,3	moment of inertia axes as defined by sketches in Tables I and II

FACILITIES

All tests were conducted in Langley's Water-Immersion Simulator (WIS) facility. The WIS is 6.1 m (20 feet) deep and 12.2 m (40 feet) in diameter. The facility has three large windows for observation and photographic purposes. It is equipped with three closed-circuit television cameras which can be remotely controlled to track the subject - this allows all tests to be

recorded on video tape for data purposes. In addition, for selected tests, motion pictures and still photographs were taken.

TESTS AND RESULTS

The overall results of the study will be discussed in three phases: (1) man's ability to perform extravehicular (EV) cargo transfer, (2) man's ability to transfer cargo through a tunnel (IV), and (3) the use of electromagnetic/electroadhesive mobility aids for both IV and EV activities. The mass, volume, and moments of inertia of the packages (simulated cargo) used for these studies are given in Tables I and II. The packages, subjects, and subject-pressure suit combination were made neutrally buoyant for all tests in order to simulate zero-g conditions. It should be noted that the subjects could transfer all the packages tested; therefore, no manual cargo transfer limits were established.

One factor which must be considered in any water-immersion study is the effect of hydrodynamic drag and, as it is relevant to all phases of the study, it will be covered first. Drag is a function primarily of package frontal area and velocity (Ref. 2). The method used for package construction (pipes and spheres) (Fig. 1) was chosen to minimize the package frontal area in all attitudes. The average velocity used by the subjects was less than 0.77 km/hr (0.7 ft/sec) for all tests. While the package drag was not eliminated, its low values are considered to be such that it should not appreciably affect the trends noted in the results.

Man's Ability to Perform Extravehicular Cargo Transfer

The motion aids provided for this study consisted of nominal 1-inch (2.5-cm) galvanized pipe (rails). The pipe rails formed a rectangular course 6 by 6 m (20 by 20 feet) (Fig. 1). The spacing between the rails could be varied from approximately 25.4 cm (10 inches) to 76.2 cm (30 inches). The subjects wore a Manned Orbital Laboratory (MOL) suit pressurized to 0.259 km/cm² (3.7 psi) above ambient. The suit was made neutrally buoyant by using up to 68 kg (150 pounds) of lead.

The subjects were initially instructed to transfer each package around the motion aid course, first using a single rail, then using two rails. It became apparent in tests of the first package (package 1, Table I) that the use of a single-rail mobility aid was possible but impractical as the subjects could not grip the rail with their legs due to leg mobility limitations imposed by the pressure suit. The inability to use the legs prevented adequate control of the subject-suit combination and the package without overexertion. The overexertion, according to subjects' comments, was a function of the forces required to provide rotational control of the subject-suit combination while using only one hand on the rail. Consequently, EV tests using a single rail were discontinued.

After completing each transfer task, using the various packages and the two-rail mobility aid, the subjects were asked to rate the task in terms of: (1) translational maneuverability, (2) rotational maneuverability, (3) visibility, and (4) task effort using the rating scale shown in Table III. They were also asked to comment on the effect of rail width. After each test period, the subjects were questioned to determine the reason each task was given a particular rating and to ascertain the interrelation of the factors rated.

Translational Maneuverability - The subjects' translational maneuverability ratings (the ability to start and stop linear motion) versus package mass are shown in Figure 2. In general, the subjects commented that package mass was not a significant factor.

Rotational Maneuverability - The rotational maneuverability (the ability to start, stop, and control rotational motions) is primarily a function of package moment of inertia. The subjects' rotational maneuverability ratings versus package moment of inertia about the center of mass are given in Figure 3. As can be noted from the figure, the data contain a fair amount of scatter. According to subject comments, this was caused by difficulty in judging the force required to move the suit (shoulder, elbow, wrist, etc.) which is greater than the force required to rotate the packages having small moments of inertia; therefore, small corrections are difficult to apply. For the large moment of inertia packages, the force required to rotate the packages is generally equal to or greater than forces required to move the suit; therefore, fairly precise inputs to the package can be made. The trade off between the difficulties associated with controlling the small moment of inertia packages and the effort required for controlling the large moment of inertia packages caused the subjects' ratings to be in the same relative range for all packages.

Visibility - The subjects were instructed to pretend that the boxes were solid; consequently, they attempted to look over, around, or under the packages in order to determine their position with respect to the motion aid course. The larger packages decreased the subjects' ability to "see around" the cargo. The larger size boxes and the restricted visibility of the suit required that the subject periodically change his position on the motion aids in order to observe his progress. The frequent body positioning caused a general increase in the overall workload and resulted in a degrading of the visibility ratings as package size increased. This is shown in Figure 4, which gives subjects' visibility ratings versus package volume for all packages tested.

Task Effort - The task effort parameter was used as a means of determining the test subjects' opinion concerning the degree of

difficulty of the transfer task considering all factors. All of the subjects commented that the major effort required was not a function of the packages but was a function of the difficulties associated with the encumbrances of the pressure suit itself. In general, the subject had to plan each move so that adequate contact with the mobility aids could be maintained. At the corners the subjects tended to anchor themselves to the rails using their legs, rotate the packages using both hands, then push the package away from them and use both hands to turn themselves around the corner. They then proceeded to catch up with and establish control over the package.

The subjects' ratings of task effort are shown versus package moment of inertia in Figure 5. As the encumbrance of the suit was the major contributor to task effort, the ratings were fairly consistent over the entire range. The slight downgrading of the rating for the largest package, according to subjects' comments, is primarily a function of visibility as previously described.

Effect of Rail Width - Rail separation distances of 25.4, 30.5, 35.6, 40.6, 45.7, and 76.2 cm (10, 12, 14, 16, 18, and 30 inches) were evaluated. The subjects commented that the 25.4- and 30.5-cm (10- and 12-inch) rails were too narrow. The 35.6-, 40.6-, and 45.7-cm (14-, 16-, and 18-inch) rail separation distances were usable with the 40.6-cm (16-inch) being preferred. These spacings allowed a subject to either place his legs outside the rails and squeeze or put his legs between the rails and press outward. These separations worked equally well for shirt-sleeve (Ref. 1) and pressure-suited applications. The 76.2-cm (30-inch) rail separation was found to be too great. The subjects commented that it was comparable to a one-rail system.

Tunnel Cargo Transfer

This phase of the study to determine man's cargo transfer capabilities was directed at defining the problems associated with moving cargo in a confined area. A 4.6-m (15-foot) diameter by 9.1-m (30-foot) long mockup of a shuttle cargo container was utilized. The mockup had a center tunnel made up of 1.5-m (5-foot) diameter 2.5-cm (1-inch) pipe rings (stringers) on 1.5-m (5-foot) centers. The shuttle cargo container will not have a smooth wall passageway. The passageway will be defined by a series of dividers (stringers) with the space between the stringers providing access to the toroidal storage compartments. Two 2.5-cm (1-inch) pipes spaced 40.6 cm (16 inches) apart, set approximately 15.2 cm (6 inches) in from the tunnel wall, were provided as mobility aids (Fig. 6). The subjects for the IV portions of the study were dressed in wet suits as described in Reference 1. In this study, the subjects were required to remove the packages from a storage area into the tunnel, transfer the package the length of the tunnel and return, then replace the package in the storage area. Packages 1 through 5 of Table I were used.

The test subjects stated that packages 1, 2, and 5 could be taken out of storage, transferred, and put back in storage without difficulty. The ease of the task was such that the subjects agreed that a rating (Table III) of 1 or 2 would apply for task effort. The subjects also commented that package 5 was, in general, a little easier to manage than packages 1 and 2. This was attributed to the fact that the forces required to maneuver package 5 were more in line with the force levels the subjects preferred to use for control, while for packages 1 and 2 the subjects had to be cautious to keep from overcontrolling.

Packages 3 and 4 (Table I) were found to be impractical due to size. The approximate 2.5-cm (1-inch) clearance between the packages and the stringers was not sufficient to allow the subject to transfer the package without bumping or catching on the stringers, which would define the shuttle cargo container passageway.

The subjects could transfer packages 1, 2, and 5 without using the mobility aids; that is, they could pull themselves along using the stringers. However, both subjects strongly preferred the use of the two-rail mobility aid because of the better body and package control available. The subjects commented that a break in the motion aids (for instance, their absence in a hatchway or airlock) would not present any difficulties. They felt that the walls or stringers in those sections would be adequate substitutes.

The subjects tried pulling the packages behind them but found that they did not have sufficient command of the package to keep from striking the tunnel walls because they could not observe package position.

Electromagnet Motion Aid Study

As part of the Langley I/EV studies, a potentially usable phenomenon called electroadhesion has been investigated. This phenomenon, which utilizes electrostatic attractive forces between conductive surfaces, looks particularly attractive in the extravehicular environment. If electroadhesion proves practical, it will provide a flexible, multipurpose mobility and restraint aid which can be used on any conductive surface; for example, the skin of a spacecraft. The initial development of electroadhesives is covered in Reference 3, and the additional development needs and possible applications are covered in Reference 4. The purpose of this study was to evaluate the potential applications and attachment forces needed for such a system. Electromagnets were used to simulate electroadhesives because electroadhesives will not operate underwater.

The study was very preliminary in nature and used one subject for all phases of the study. However, various parts of the study were tried by three other subjects and their observations and comments, while not included, are in agreement with those of the principal subject.

Two possible areas of electroadhesive/electromagnet utilization were investigated. The first area covered the use of electromagnets as a self-locomotion transfer device, and the second area evaluated the electromagnets as a cargo transfer aid. As a self-locomotion transfer aid, both foot magnets and hand-held magnets were evaluated, Figure 7. In the cargo transfer study the hand-held magnets and a combination of foot/hand magnets were utilized. The self-locomotion and cargo transfer portions of the study were performed under both IV and EV conditions.

Self-Locomotion Transfer - In the self-locomotion transfer phase of the study, the subject was required to move himself along a steel plate 0.46 m (1.5 feet) wide by 6.1 m (20 feet) long. The initial effort utilized electromagnetic shoes attached securely to the feet, with the soles of the feet parallel to the face of the magnets. Each subject was able to move successfully in a "walking" manner. However, after 2 to 3 minutes of effort the subjects complained of discomfort due to pain developing in the lower leg region (the tibialis anterior muscles). This pain was apparently caused by the difference in technique required to "walk" in zero-g as compared to a one-g environment. Walking in one-g is essentially a process of falling and catching oneself; however, in a zero-g environment the ability to fall is absent. The subject must compensate for the lack of ability to generate forward motion from falling by using the muscles of his lower leg (primarily the tibialis anterior) to position his center of mass forward of his pushing foot. In order to accomplish this a body lean angle on the order of 35° to 45° is required. As the average flexion of the ankle is limited to approximately 35° (Ref. 5), the ankle is maintained at its maximum flexion position causing the tibialis anterior muscle to be in constant tension, which results in the discomfort noted. In an attempt to alleviate the discomfort, the sole of the shoe was canted with respect to the face of the magnets so that near normal flexion and extension angles of the ankle could be used. Cant angles of 20° , 30° , and 45° were evaluated. The subjects could "walk" equally well at all three cant angles without discomfort; however, the subjects preferred the 20° or 30° (Fig. 8) cant angles for executing turns. "Walking" was also successfully accomplished by a pressure-suited subject (EV). The same conclusions found with the shirt-sleeve conditions also applied to the pressure suit concerning foot cant angles.

The subjects found they could "walk" at all magnetic force levels between 222 and 448 newtons (50-100 pounds) but preferred a minimum force of approximately 356 newtons (80 pounds) because of the "feeling of security" it provided. The subjects found that they could, by torquing the foot, easily break the magnetic contact with the surface and preferred to do so rather than use the switches provided to turn off the electromagnetic field.

A second means of self-locomotion transfer utilized hand-held electromagnets under both IV and EV conditions. Transfer

was accomplished by maneuvering in a hand-over-hand fashion. Force levels of between 222 and 356 newtons (50-80 pounds) were used with equal success, and the subjects again preferred torquing the magnets to break the magnetic contact. The subjects commented that they preferred to use either the hand-held electromagnets or the pipe-rail mobility aids for self-locomotion, rather than the "walking" method for both IV and EV situations.

Cargo Transfer - For cargo transfer, the use of a hand-held magnet as a multipurpose package handle was studied. The subject was required to transfer the package by using a one-hand magnet as a mobility aid and the second as a package handle. This means of cargo transfer is analogous to a one-rail mobility aid in that the majority of the subject and package rotational control is provided by one hand. For the IV situation the task can be accomplished but a two-rail mobility was preferred (Ref. 1), and for the EV situation the task was possible but impractical due to overexertion (see basic EV study contained previously in this report).

Cargo transfer using a combination of foot magnets for "walking" and a hand-held magnet for package control was evaluated (Fig. 9). The fact that the subject could use the inertia of the packages, particularly the large inertia packages, to assist him in walking (he used it to help pull himself along) made this mode of package transfer attractive. In several instances during an EV task, the package was used by the subject to return himself to the steel plate after having inadvertently lost contact. In the opinion of the subjects, the task effort for EV cargo transfer is less than for the two-rail mobility aid discussed previously. The foot magnets allow the subject to operate in an upright position rather than a prone position. The upright position affords greater visibility and allows the package to be handled farther from the spacecraft surface. This enhances the capability of an astronaut to maneuver cargo over or around any protuberances present on the outside of the spacecraft.

GENERAL COMMENTS

The time available to conduct the programs covered in this report was limited. Therefore, the results are based primarily on the comments obtained from the subjects after completing each task one time. The fact that the subjects could accomplish the various tasks the first time they were tried is significant in that any task should become easier to accomplish with training and experience.

The use of pressure suits in a water-immersion simulation creates a number of problems that would not be present in an actual zero-g situation. The two primary problems are: (1) the subject is still in one-g within the suit, and (2) the additional mass and moment of inertia caused by the necessary ballast.

For the first case, the fact that the subject is still affected by gravity within his suit causes a number of pressure points to be present, which would not exist in zero-g. The pressure points are painful in certain situations and consequently cause the subject to limit his mobility. Also, it means that as the subject moves within the suit he causes small changes in the man-suit neutral balance for which he must compensate.

For the second case, the additional mass which is added to the suit to make it neutrally buoyant (between 59 to 68 kg (130 to 150 pounds)) adds to the overall inertia of the man-suit combination. While the added mass does not present a problem for linear motion, the increase in the overall moment of inertia is significant when the subject is required to rotate the man-suit combination using only one hand. The anomalies produce physiological problems which should not be present in an actual zero-g situation. Therefore, the data presented herein are considered to be conservative.

RESUME

The general results of the three phases of the study reported in this paper can be summarized as follows:

Extravehicular Cargo Transfer

1. The largest package tested, with a mass of 754 kg (51 slugs), moment of inertia about its center of mass of 304 kg-m^2 (285 slug-ft^2), and a volume of 4 m^3 (143 ft^3), was within the subjects' cargo transfer capabilities; therefore, no manual cargo transfer limits were established.
2. The subjects could successfully transfer all cargo using a two-rail mobility aid. They stated that it was not practical to attempt to transfer cargo using a one-rail mobility aid.
3. Based on subjects' comments, the two-rail mobility aid should have a separation distance of between 40.6 and 45.7 cm (16 and 18 inches) for both IV and EV application.
4. The major factor affecting the subjects' ability to perform cargo transfer tasks was the encumbrances of the pressure suit rather than of any of the package parameters.

Tunnel Cargo Transfer

1. The 1.5-m (5-foot) diameter tunnel limited the size of a package which could be transferred, rather than package mass, moment of inertia, or man's capability.
2. The subjects could transfer the cargo using the stringers (pipes) which defined the tunnel walls; however, they strongly preferred the use of a two-rail mobility aid.

Electromagnetic/Electroadhesive Mobility Aids

1. Electroadhesive/electromagnetic devices can be used as both mobility and cargo transfer aids; therefore, additional development is suggested.

2. The hand-held electromagnets (simulated electroadhesors) appear to provide a practical means for moving about in a zero-g environment for both IV/EV situations.

3. With a 20° to 30° cant angle between the sole of the subject's feet and the face of the electromagnet, the subjects could walk with relative ease. With the sole of the foot parallel with the face of the electromagnets, the subject developed pain in his lower legs (tibialis anterior muscles).

4. Walking for either IVA or EVA is more difficult than moving about in a hand-over-hand manner, except for the case of EV cargo transfer.

The results of the studies indicate that man can perform a variety of cargo transfer tasks. However, most of the work reported herein is of a preliminary nature and additional research is needed to extend these results to assure that complete design data are available.

REFERENCES

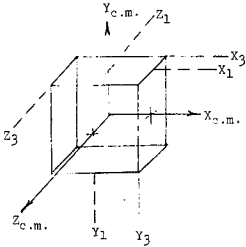
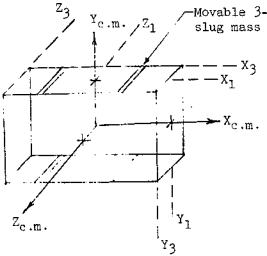
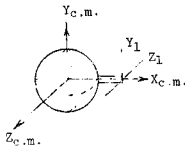
1. Spady, Amos A., Jr.; Beasley, Gary P.; and Yenni, Kenneth R.: Preliminary Results of Manned Cargo Transfer Studies Under Simulated Zero-g Conditions. Presented at the AIAA/ASMA Weightlessness and Artificial Gravity Meeting, Williamsburg, Va., Aug. 9-11, 1971. AIAA Paper 71-851.

2. Goldstein, Sidney E.; and Alvarado, U. R.: A Method of Obtaining High Fidelity Underwater Simulation on Manned Space Activities. Presented at the AIAA Fourth Annual Meeting and Technical Display, Anaheim, Calif., Oct. 23-27, 1967. AIAA Paper 67-925.

3. Krape, Richard P.: Applications Study of Electro-adhesive Devices. NASA CR-1211. Chrysler Corp. Space Div., New Orleans, La., October 1968.

4. Beasley, Gary P.; and Hankins, Walter W.: Development of Electroadhesive Devices for Zero-g Intra/Extravehicular Activities. Presented at the AIAA/ASMA Weightlessness and Artificial Gravity Meeting, Williamsburg, Va., Aug. 9-11, 1971. AIAA Paper 71-853.

5. Webb, P., ed.: Bioastronautics Data Book. NASA SP-3006, 1964.

PACKAGE NUMBER	APPROXIMATE DIMENSIONS, m			APPRX VOLUME, m ³	MASS, kg	EARTH WEIGHT, LBS	MOMENT OF INERTIA, kg - m ²									
	ΔX	ΔY	ΔZ				$X_{c.m.}$	X_1	X_3	$Y_{c.m.}$	Y_{1-2}	Y_3	$Z_{c.m.}$	Z_{1-2}	Z_3	
	1	.61	.61	.61	.23	49	108	7.2	11.3	15.5	7.2	11.3	15.5	7.2	11.3	15.5
	2	.61	.61	.61	.23	91	210	12.8	20.4	28	12.8	20.4	28	12.8	20.4	28
	3	1.1	1.1	1.1	1.2	73	163	19.6	35	51	19.6	35	51	19.6	35	51
	4	1.1	1.1	1.1	1.2	136	300	50	86	122	50	86	122	50	86	122
	5	1.2	.76	.76	.71	244	540	41 to 53	73 to 97	107 to 130	23 to 105	107 to 189	127 to 223	41 to 101	124 to 185	158 to 219
	6	17" diameter			.042	46	101	.3	-	-	.3	4.7	-	.3	4.7	-

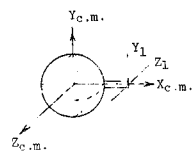
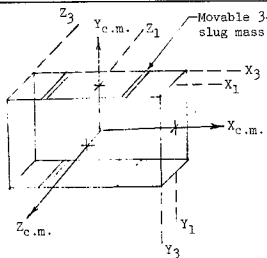
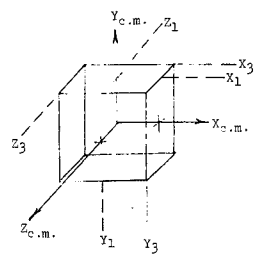


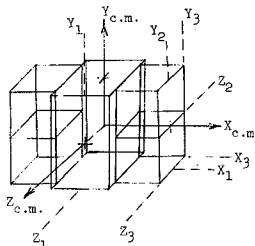
TABLE I.- BASIC PACKAGES

BASIC PACKAGES USED AND POSITION	APPROXIMATE DIMENSIONS, m			APPROXIMATE VOLUME, m ³	MASS, kg	EARTH WEIGHT, LBS	MOMENT OF INERTIA, kg - m ²											
	ΔX	ΔY	ΔZ				$X_{c.m.}$	X_1	X_2	$Y_{c.m.}$	Y_1	Y_2	Y_3	$Z_{c.m.}$	Z_1	Z_2	Z_3	
<div>1 1</div>	1.2	.61	.61	.45	98	216	14.3	23	32	23	31	57	65	23	31	57	65	
<div>1 2</div>	1.2	.61	.61	.45	144	318	20.2	32	44	31	45	66	77	31	45	66	77	
<div>2 2</div>	1.2	.61	.61	.45	190	470	26	41	56	42	57	103	117	42	57	103	117	
<div>3 4</div>	2.1	1.1	1.1	2.43	210	463	70	122	173	113	174	250	301	113	174	250	301	

<div>1 1 2 2</div>	1.2	1.2	.61	.91	287	636	65	158	182	62	89	131	154	86	113	155	178
<div>3 1 1 1</div>	1.4	1.2	.76	1.16	343	756	46	173	204	85	146	298	331	93	231	306	435
<div>3 2 2 2</div>	1.4	1.2	.76	1.16	435	960	65	225	266	111	176	305	346	124	315	351	498

TABLE II. - PACKAGES CONSTRUCTED USING BASIC PACKAGES AS
BUILDING BLOCKS

BASIC PACKAGES USED AND POSITION	APPROXIMATE DIMENSIONS, m			APPROXIMATE VOLUME, m ³	MASS, kg	EARTH WEIGHT, LBS	MOMENT OF INERTIA, kg - m ²											
	ΔX	ΔY	ΔZ				$X_{c.m.}$	X_1	X_3	$Y_{c.m.}$	Y_1	Y_2	Y_3	$Z_{c.m.}$	Z_1	Z_2	Z_3	

	<table border="1"><tr><td>1</td><td>3</td><td>2</td></tr><tr><td>1</td><td>2</td><td></td></tr></table>	1	3	2	1	2		2.0	1.2	.76	1.61	533	1,116	88	285	334	193	270	595	645	216	413	632	844
1	3	2																						
1	2																							

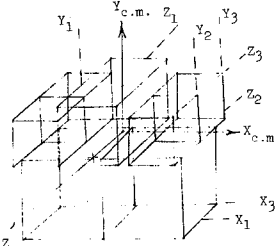
	<table border="1"><tr><td>1</td><td>5</td><td>2</td></tr><tr><td>4</td><td>3</td><td></td></tr></table>	1	5	2	4	3		2.1	1.8	1.2	4.05	744	1,640	290	1228	1512	385	660	1228	1504	497	821	1341	1392
1	5	2																						
4	3																							

TABLE II.- PACKAGES CONSTRUCTED USING BASIC PACKAGES AS
BUILDING BLOCKS - Concluded

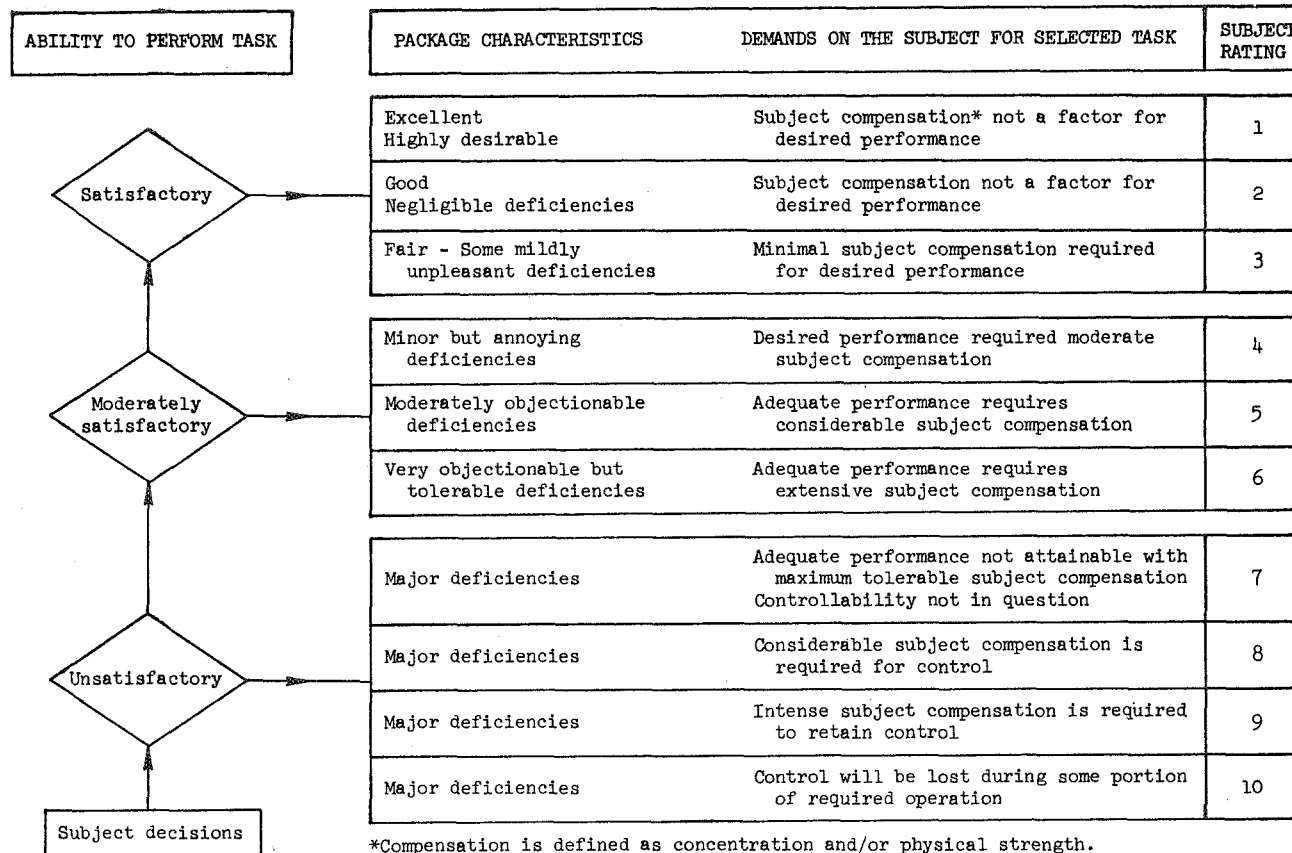


TABLE III.- SUBJECT RATING SCALE

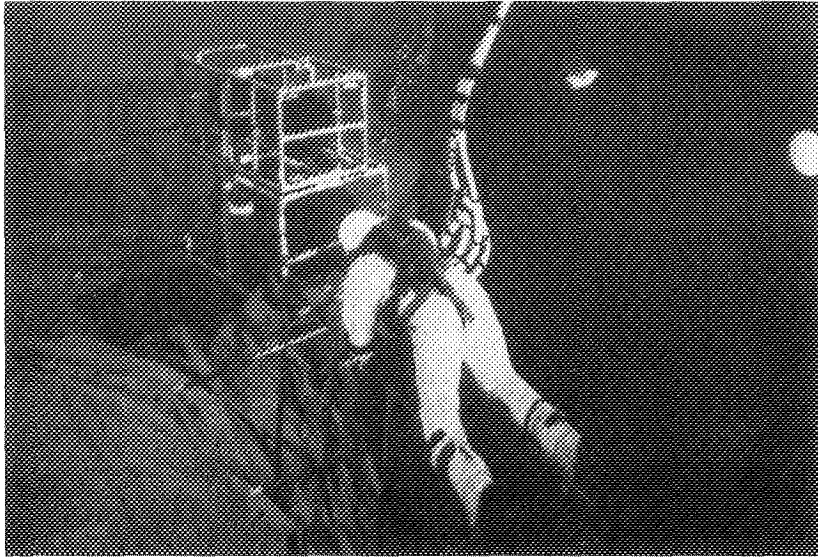


Figure 1.- Subject, in a MOL suit, transferring 343 kg (23.5 slugs) package using a two-rail motion aid.

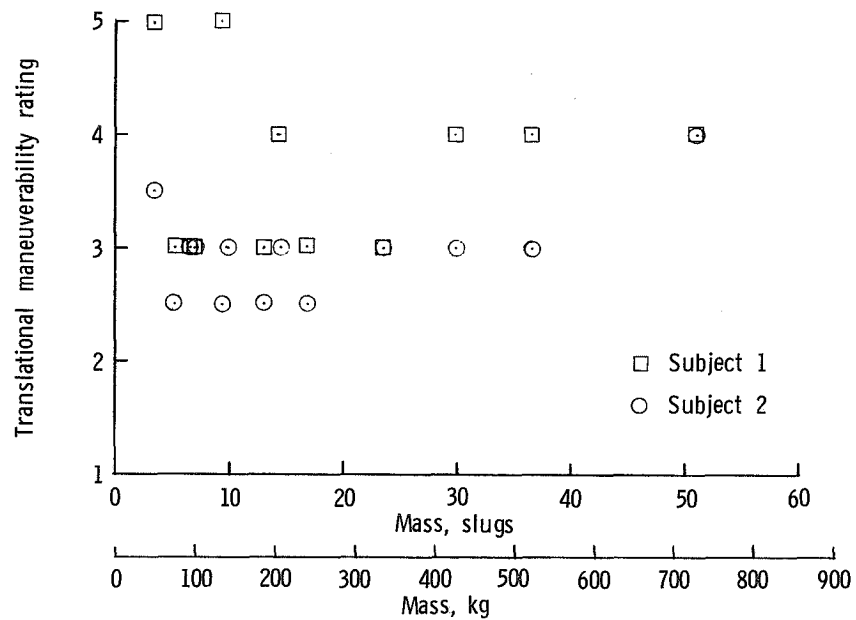


Figure 2.- Subject's translational maneuverability ratings as a function of package mass.

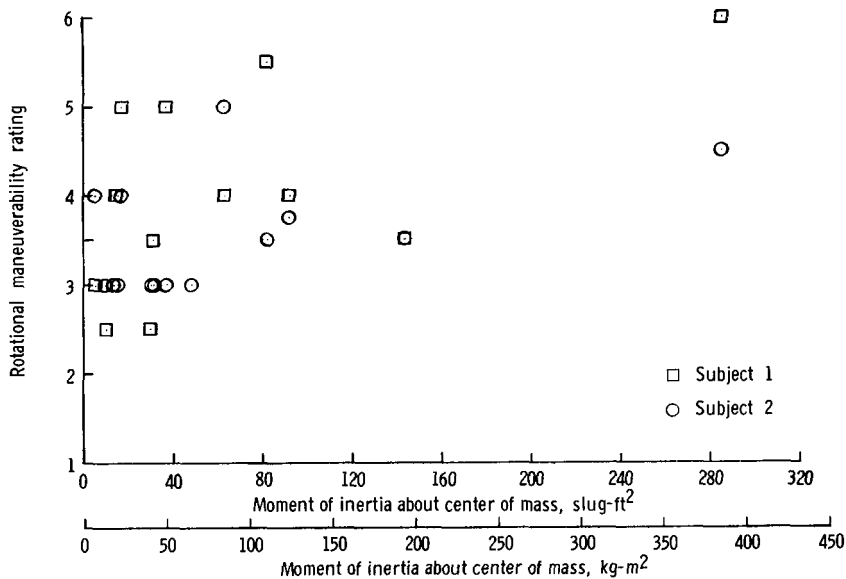


Figure 3.- Subject's rotational maneuverability ratings as a function of package moment of inertia about its center of mass.

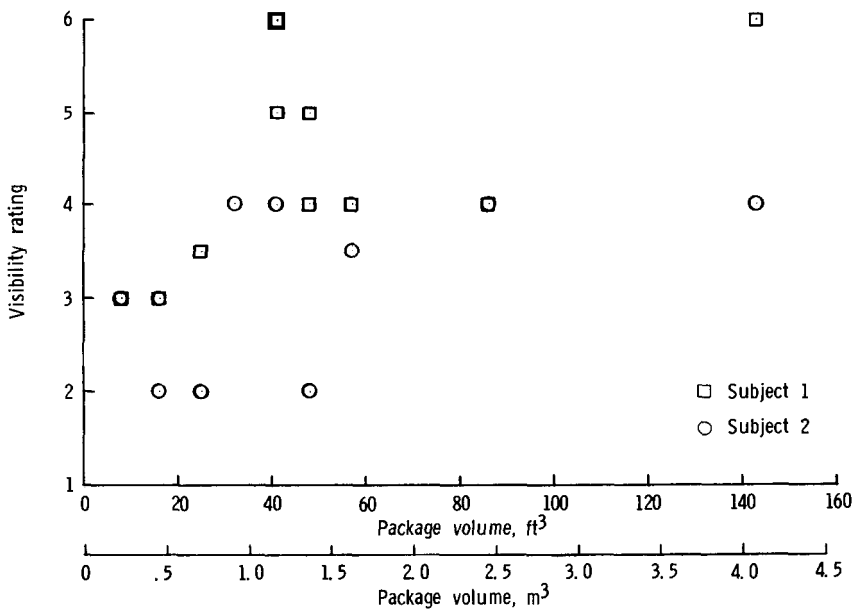


Figure 4.- Subject's visibility ratings as a function of package volume.

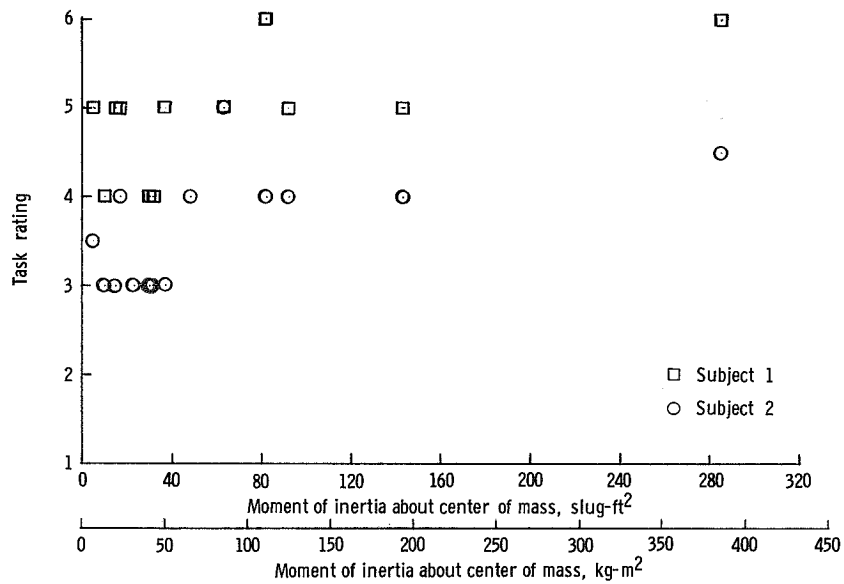


Figure 5.- Subject's task effort ratings as a function of package moment of inertia about its center of mass.

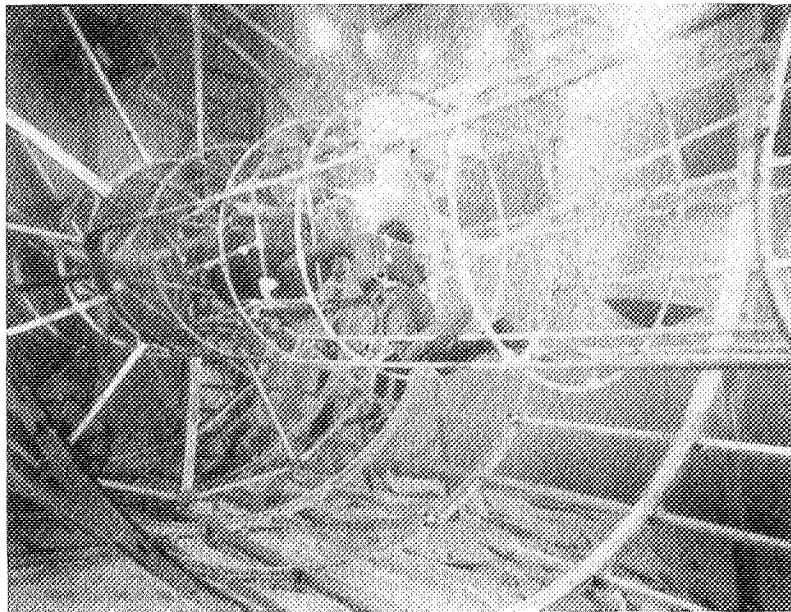


Figure 6. Subject transferring 244 kg (16.75 slugs) along a 1.5-m (5-ft) diameter tunnel.

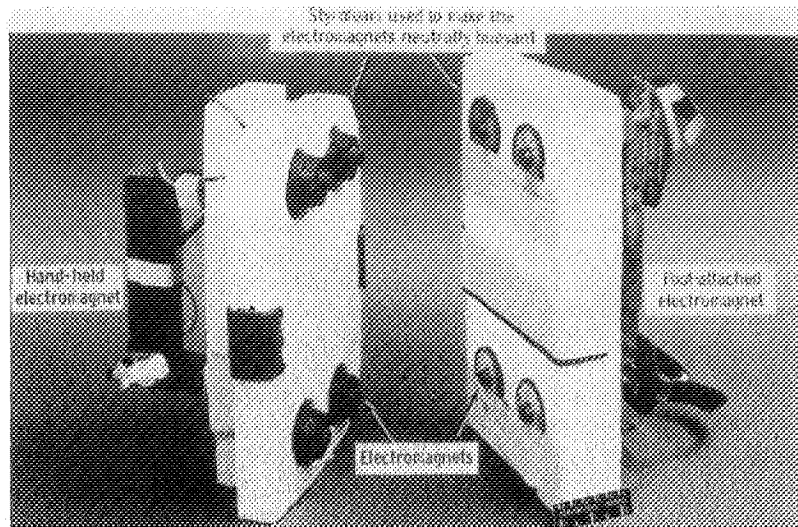


Figure 7.- Neutrally buoyant hand-held and foot-attached electromagnets.

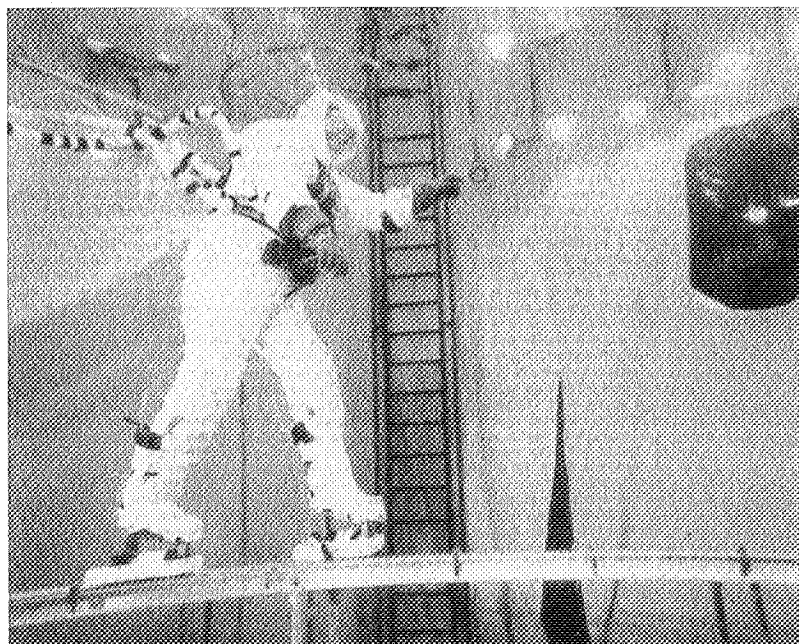


Figure 8.- Subject in a MOL suit using electromagnetic shoes, with a 30° cant, for self-locomotion.

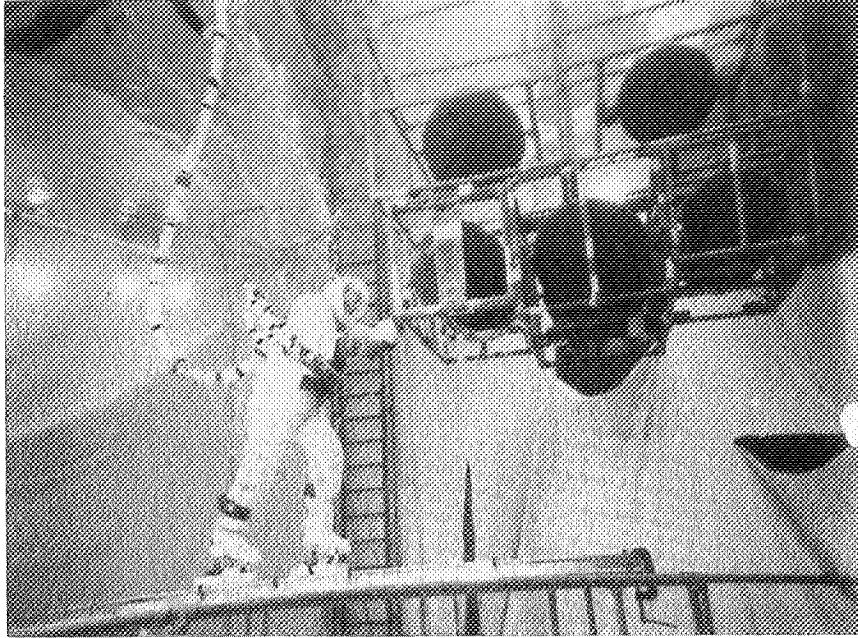


Figure 9.- Subject in a MOL suit transferring a 744-kg
(51 slugs) package.

HABITABLE ATMOSPHERES WHICH DO NOT SUPPORT COMBUSTION

Edward T. McHale, *Atlantic Research, a Division of the Susquehanna Corporation, Alexandria, Virginia*

ABSTRACT

A concept has emerged in our laboratories which promises to represent a major advance in fire protection systems for confined spaces. It appears that habitable atmospheres can be developed in which humans will be able to live and function normally for extended periods of time with no physiological harm, but which at the same time will not support combustion of ordinary materials such as paper, cloth, gasoline, etc. These atmospheres might contain 3 psia partial pressure of oxygen as does ordinary air; or oxygen-enriched atmospheres as used in aerospace environments could be employed. In addition, certain inert polyatomic gases, namely, CF_4 , C_2F_6 or C_3F_8 , are incorporated into the atmosphere. These impart the property of completely suppressing flammability, while retaining the life support capability. These perfluorinated agents are not to be confused with other halogenated compounds that contain elements other than carbon and fluorine in the molecule. Some of the other compounds, notably CF_3Br (Halon 1301), are effective fire suppressants but are not physiologically inert.

At the present time a major program is being conducted under sponsorship of the U. S. Army, Office of the Chief of Research and Development (Contract DAHC19-71-C0026) to evaluate the validity of the concept. The program involves measurement of materials flammability in the atmospheres, determination of the stability of the atmospheres under fire conditions, and an animal toxicology study which will include cardiac sensitization tests. Program results to date, while favorable, are too incomplete to form the basis of a conclusive report. The study will be completed in March, 1972, and at that time a full manuscript will be prepared for distribution at the Sixth IES/AIAA/ASTM Space Simulation Conference in May. In the following discussion of the present abstract, a summary of the background of the concept is presented, together with some technical data from various laboratories, and an outline of the research investigation that is being conducted.

As a result of applied research programs that were carried out at Atlantic Research and elsewhere, (1-3) it became known that the rate of flame spread over burning material was a strong inverse function of the heat capacity per mole of oxygen of the

oxidizing atmosphere. Thus, for example, cotton fabric burns in a 21/79, O₂/He atmosphere ($C_p=27$ cal/°C mole O₂) at roughly three times the rate it burns in air ($C_p=33$ cal/°C mole O₂). It was discovered that if the heat capacity of the atmosphere could be raised to ~50 cal/°C mole O₂, the atmospheres would not support combustion of any ordinary material. Many properties of the environment determine the rate of flame spread, and the simple correlation with heat capacity obtains because the agents being considered are inert and only act physically to suppress combustion; they exhibit no chemical inhibiting action as many flame suppressants do (4). Combustion depends on the feedback of energy from the flame zone to the unburned fuel in order to bring it to the combustion temperature. Inert gas diluents act as heat sinks for the combustion energy, cooling the flame and interfering with this feedback process and, at sufficiently high concentrations, quenching combustion.

However, the atmosphere plays a different role in sustaining life than in supporting combustion. The life support function requires a partial pressure (~2.5 psi or greater) of oxygen sufficient to maintain the necessary oxygen tension in the blood. Diluent gases, if they are physiologically inert, have only a minor effect on this process. Hence, by the selection of a proper additive it should be possible to prepare an atmosphere of high heat capacity that is also physiologically inert. This would comprise a habitable atmosphere that would not support combustion.

After a literature search and an in-house experimental program, it was found that the completely-fluorinated lower hydrocarbons comprised a class of compounds which apparently fulfilled all the requirements of the concept. At present the candidate agents which appear most promising are CF₄, C₂F₆ and C₃F₈. The amounts of these materials that must be added to air to completely suppress the ignition and flame propagation of four selected materials were found to be:

<u>Material</u>	<u>Volume % Fluoro-carbon Added to Air</u>	<u>Heat Capacity (cal/°C mole O₂)</u>
Cotton Flannel	18.7% CF ₄	49
	11.0% C ₂ F ₆	48
	9.4% C ₃ F ₈	51
Tissue Paper	12.0% C ₂ F ₆	49
Foam Plastic	3.1% C ₂ F ₆	37
Kerosine	7.3% C ₂ F ₆	43

Listed in the last column of the above table are the heat capacities of the air/fluorocarbon atmospheres. The addition of agent to air, of course, reduces the O₂ concentration, but even

in the worst case above (18.7%) the O_2 content is 17.0%. This corresponds to the O_2 partial pressure that is present at an altitude of approximately 5000 feet; hence, no serious physiological effect will occur.

Materials have also been found to be non-flammable in oxygen-enriched atmospheres containing $> 40\%$ O_2 provided sufficient fluorocarbon is present. In the current testing program, the flammability of numerous materials including cellulose, plastics, solvents, etc., will be measured for a range of fluorocarbon/air mixtures.

The effectiveness of the agents as fire suppressants is well established by the experimental program of which the above examples represent a sampling of the results. It is equally important to determine whether these agents are physiologically inert. This latter aspect of the concept could not be settled as conclusively as the combustion aspect because of the paucity of toxicological data on these agents. However, the results of the limited studies that have been conducted are entirely favorable and indicate a complete lack of physiological activity for these compounds. Before citing specific examples of the physiological inertness of the agents, it should be mentioned again that the completely fluorinated compounds being discussed here are not to be classed with other Halons which contain elements other than fluorine in the molecules (Br, Cl, H). Other halocarbons do exhibit pharmacological or neurological effects and would not be suitable for use as habitable atmospheres.

The most extensive toxicological study involving any compounds of the perfluorocarbon class is that of Clayton et al. on octafluorocyclobutane (5). Mice, rats, rabbits and dogs were exposed to a 10% concentration of the fluorocarbon in air six hours a day for a total of 90 exposures. Detailed studies during and after the exposure program showed no observable physiological effects. As a result of these studies, octafluorocyclobutane has received FDA approval for use in food aerosols.

Toxicity data on the straight chain fluorocarbons are much more limited. However, because of their much greater stability, they might be expected to be even more inactive than the cyclic compound. Clayton (6) reports single four hour exposures of mice or rats to atmospheres containing 80% CF_4 , C_2F_6 , or C_4F_{10} and 20% oxygen without evidence of anesthetic effects or physiological damage. There is thus substantial reason to believe that mammals, and presumably humans, could live for extended periods of time in atmospheres containing certain fully saturated fluorocarbons in concentrations sufficient to suppress combustion without impairment of faculties or permanent harm. Much more data must be accumulated, however, including human exposure data, before the safety and effectiveness of this approach to fire safety can be fully assessed.

The present program is designed to develop these necessary toxicology data in animal studies, but will not include human exposures at present. Three types of animal studies are under-way: 1) acute inhalation; 2) ten-day inhalation; and 3) cardiac sensitization. In the first of these, LC₅₀ levels (if any) for male rats will be measured for the three candidate fluorocarbons. In the second study, continuous exposure of rats and guinea pigs for 10 days will be conducted at the usage concentration of the agents. The animals will be subjected to clinical observations, hematological and biochemical studies. Following terminal sacrifice, gross pathologic and histopathologic examinations will be performed. The cardiac sensitization studies will involve subjecting dogs to the usage concentrations of the agents. EKG patterns will be monitored with and without exogenously delivered epinephrine.

It is envisioned that the habitable atmospheres will be employed in two types of modes. The first type will be as a continuously present atmosphere which will prevent combustion from initiating. In the second mode, the agents will be dispersed into a confined chamber to extinguish a fire after it starts. Occupants of the chamber would then not have to evacuate afterwards. The second mode of application requires that the stability of the agents to fire conditions be known, and also that the toxicity of any decomposition products be determined. Scaled fire tests are being conducted to investigate both of these problems. Chemical analyses of decomposition products are being made for a range of conditions, and animal exposures to the pre- and post-fire atmospheres are planned. Complete post-exposure examinations of the animals as described for the 10-day inhalation study will be made.

REFERENCES

- 1) "The Effects of 100% Oxygen at Reduced Pressure on the Ignitability and Combustibility of Materials," Huggett, C., von Elbe, G., Haggerty, W., and Grossman, J., USAF School of Aerospace Medicine, SAM-TR-65-78, December, 1965.
- 2) "The Combustibility of Materials in Oxygen-Helium and Oxygen-Nitrogen Atmospheres," Huggett, C., von Elbe, G., and Haggerty, W., USAF School of Aerospace Medicine, SAM-TR-66-85, December, 1966.
- 3) "Region of Noncombustion in Nitrogen-Oxygen and Helium-Oxygen Diving Atmospheres," Cook, G. A., Dorr, V. A., and Shields, B. M., I and EC Process Design and Development 7, 308 (1968).
- 4) "Survey of Vapor Phase Chemical Agents for Combustion Suppression," McHale, E. T., Fire Research Abstracts and Reviews 11, 90 (1969).

- 5) "Toxicity Studies with Octafluorocyclobutane," Clayton, J.W., Delaplane, M.A., and Hood, D.B., Industrial Hygiene Journal 21, (5), 382 (1960).
- 6) "Fluorocarbon Toxicity and Biological Action," Clayton, J. W., Fluorine Chemistry Reviews 1, 197 (1967).

LOW-G SIMULATION TESTING OF PROPELLANT SYSTEMS USING NEUTRAL BUOYANCY

D. L. Balzer and R. J. Lake, Jr., *RCA, Astro-Electronics Division, Princeton, New Jersey*

ABSTRACT

At the RCA Astro-Electronics Division a two liquid, neutral buoyancy technique is being used to simulate propellant behavior in a weightless environment. By equalizing the density of two immiscible liquids within a container (propellant tank), the effect of gravity at the liquid interface is balanced. Therefore the surface-tension forces dominate to control the liquid/liquid system configuration in a fashion analogous to a liquid/gas system in a zero gravity environment.

INTRODUCTION

A major problem in the acceptance of many surface tension propellant management system designs for weightless spacecraft applications is the inability to conduct demonstration tests in a sea-level force field. Extensive mathematical analysis can be performed to verify the integrity of the surface-tension system but any one-g testing can at best be accomplished through similarity principles and/or dimensional analysis. This problem not only makes design and development testing extremely difficult and uncertain but completely precludes any full-scale earth-based performance verification tests. There are several low-g test methods available, as will be described later, but each has shortcomings and limitations such that no one technique is entirely satisfactory.

RCA has developed a technique of simulating propellant orientations within weightless systems, such as on-orbit spacecraft. By balancing the densities of two immiscible liquids within a container, a neutral buoyant condition is achieved, negating the effect of gravity at the fluid interface. This neutral buoyancy technique is neither expensive nor complicated and can demonstrate an exact static zero-gravity simulation for full-sized systems.

LOW-g SIMULATION TECHNIQUES

Among the types of test techniques used to simulate low-gravity environments to study fluid behavior are:

- Scale Models
- Free Fall
- Ballistic Trajectories
- Electric Force Fields
- Magnetic Fields
- Neutral Buoyancy Fluid Mixtures.

In general, for investigation of system phenomena no one technique is sufficiently adequate. Only by use of several is it possible to sufficiently characterize the system to develop successful hardware operational confidence.

For low-gravity simulations the problem is physically one of designing the experiment to reduce the effects of gravity to the degree that the other forces of interest acting on the system will not be overshadowed. For fluid systems the behavior can be defined by the magnitude of various dimensionless groups of variables. References 1 through 3 are representative of the use of dimensionless groups for evaluating liquid behavior.

An obvious approach to reducing the effect of gravity is to scale the characteristics of the system to maintain a constant value of the model-to-prototype dimensionless group. This scaling commonly involves geometry and liquid model-to-prototype physical properties. For simulation of very small accelerations, e.g., $<10^{-3}g$'s, the physical properties of liquids are not sufficiently different to be of great benefit and the primary working variable is the physical dimensions of the models. For example, when scaling the Bond number (see page 6) of a 10-foot diameter system in a $10^{-4}g$ environment to one g , a model of 0.1-inch diameter results. For models this small, scaling of complex geometries becomes extremely difficult, fluid behavior cannot be readily observed, and the magnification of fluid viscous effects cannot be accurately evaluated.

One helpful test technique for the study of hydrostatic configuration of liquids in specialized geometry, axisymmetric tanks that avoids the small model problem is two-dimensional testing. By placing the liquid between two closely spaced plates, the surface-tension force of the liquid across the narrow gap is sufficiently strong to hold the liquid against the force of gravity. With the model horizontal, the gas/liquid interface along the length of the plate is

then configured by the surface-tension force of the liquid. By tilting the plate, the effective gravity (earth g 's) acting on the "two-dimensional interface" is equal to the sine of the angle of inclination. In this manner various acceleration environments can be simulated. An obvious limitation of this technique is that the model results only have application to three-dimensional revolutions of the two-dimensional geometry.

Perhaps the most common test technique that permits simulation of the low- g environment is free-fall testing. As the name implies, free-fall testing consists of dropping the test article from a predetermined height and allowing it to fall undisturbed to earth. Since all elements of the system are being accelerated at the same rate in an unrestrained manner, the relative gravity-induced forces between the liquid, gas and container are zero. This approach is applicable to both static and dynamic testing. An additional capability of free-fall testing is the ability to obtain controlled low- g test environments by imposing small accelerations on the tankage system during the free-fall period. The primary constraint is the limited test time available within practical free-fall heights. A height of 100 feet yields a free-fall time of only 2.6 seconds. The time required for liquid reorientation from its initial one- g configuration to a low- g condition of interest limits model sizes to a maximum of about one foot.

Airplanes flying zero- g ballistic trajectories and sounding rockets have been used as alternate approaches to achieve longer test times (up to several minutes) but the acceleration environments are difficult to control. In addition, the liquids often receive unpredictable induced motions during entry into the zero- g condition that may destroy results and the flight costs are high.

Several techniques have been attempted that use electric, magnetic, or a combination of electric and magnetic fields to cancel the gravitationally induced body force. The most promising of these appears to be the use of a magnetizable fluid in the presence of a directed magnetic field (Reference 4). The advantage of this technique is that, with a properly designed magnet, a true zero-gravity simulation can be achieved for extended time periods. The disadvantages are that the largest available magnet has a core diameter of only about three inches and there will be some variation in magnetic field across the core diameter which will distort the test results.

Another approach to cancelling the effect of gravity on the system is to focus attention at the interface and use two immiscible liquids of equal densities to simulate the gas/liquid prototype system. This neutral buoyancy technique has the advantage of demonstrating reasonably exact static (equilibrium) interface zero-g equilibrium conditions by controlled density mismatches and showing certain types of low-g dynamic characteristics of the system.

The idea is not new; Plateau published reports of a similar technique in 1861, although not for the same purpose (Reference 5). The development of neutral buoyancy as a controlled test procedure for hardware design verification testing appears to have received little attention, with the only known reported effort being a demonstration test for the Centaur vehicle (Reference 6). The technique is being developed for this purpose at the Astro-Electronics Division of RCA and has proven to be a valuable tool to test the performance of surface-tension expulsion devices.

TECHNIQUE DEVELOPMENT

In order to develop a viable technique to demonstrate low-g liquid equilibrium propellant location, RCA initiated an investigation of neutral buoyancy testing. The goal was to conduct full-size hardware tests in transparent containers. Initial efforts were centered around finding two immiscible liquids compatible with plastic models, primarily because of low cost and ease of fabrication of complex plastic models by conventional machining and gluing techniques.

Many likely candidates were screened, with the most promising being acetophenone and water sucrose solutions. Although immiscible mixtures with matched densities could be formulated, unacceptable and inconsistent contact angles were encountered and in some cases, unexplained multiple layer stratification of the solutions resulted.

It was decided to abandon the plastic model restriction and consider glass models with metal internal structures. The physical properties of these materials permitted consideration of a much wider range of fluids. Liquid candidates of interest scheduled for evaluation were water with chlorinated hydrocarbon mixtures.

Discussions with the Jet Propulsion Laboratory revealed that they were also employing the neutral buoyancy technique with all-glass models and had achieved good simulations with a chloroform/hexane mixture and water. For this system, both fluids wet

the surfaces and proper action relies on the preferential surface wetting of the water. This combination was tried with moderate success. Under closely controlled conditions, with clean surfaces, the two fluid system reacted as predicted by analysis. The primary difficulty is the sensitivity of the system to contamination. Any organic impurities as greases, oils, etc. are non-wetting with water and anomalous interfaces result. Also the metal surfaces were not consistently selectively wetted by the water and, in fact, the converse was usually the situation.

Based on the results, it appeared that a desirable situation would be to treat the surfaces such that one liquid would be wetting and the other non-wetting. This condition was achieved by applying a thin film of teflon on the model interior surfaces. The chloroform/hexane mixture wets the teflon while the water does not. This combination showed a near-zero-degree contact angle at the interface and yielded consistent and repeatable results with a minimum of care. The film of teflon is sufficiently transparent to permit visual and photographic data recording.

OPERATING THEORY

List of Symbols

Bo	Dimensionless Bond Number $\left(\frac{\rho g r^2}{\sigma} \right)$
g	Gravity (ft/sec ²)
h	Liquid Height (ft)
r	Tube Radius (ft)
r ₁ , r ₂	Meniscus Principal Radii of Curvature (ft)
P _{atm}	Atmospheric Pressure (psf)
P _l	Liquid Static Pressure (psf)
p	Density (slug/ft ³)
σ	Surface Tension (lb _f /ft)
θ	Contact Angle (degrees)

A dimensional analysis to define the static behavior of a fluid system under low-g conditions was developed. A determination of the interface configuration for this environment requires the consideration of four physical parameters: contact angle, surface tension, fluid density and characteristic length. Following are simplified definitions of each parameter and its function in the physical system.

The contact angle is a measure of the wettability of the solid structure by the liquid propellant. A force diagram of a liquid drop in contact with a solid and a gas is shown in Figure 1. The angle of primary importance in determining the liquid configuration is the solid-liquid contact angle, θ . Most common propellants are wetting (i.e. $\theta < 90^\circ$) on the surfaces of metallic tanks with a near-zero-degree contact angle. The test fluids are chosen such that the interface between the liquid simulating the prototype pressurant and propellant forms a zero-degree contact angle with the tank wall measured through the propellant simulant.

The second parameter of interest, surface tension (σ), is an intermolecular force that occurs between two substances and/or two phases of the same substance. The surface tension of a liquid acts as though there were a thin contractible membrane of uniform tension covering its surface. In this discussion, surface tension will refer to the surface tension of the liquid/liquid interface which contacts the tank wall.

The density of both the propellant and pressurant fluids must be considered in the theoretical and experimental analysis. In order to simplify the mathematical analysis, the densities of the individual liquids will be treated as a density gradient ($\Delta\rho$) across the fluid interface. It will later be shown that the density gradient is directly proportional to the simulated g-level.

The remaining parameter of primary importance is the system characteristic dimension (r). The physical dimension of the system in which the capillary force is to act must be known or estimated in order to make predictions about the interface. One finds this dimension either intuitively from the system geometry, (e.g. tank radius) or calculates an equivalent dimension (e.g. radius of liquid fillet expected in an open capillary structure).

In the neutral buoyancy technique, by exactly matching the liquid densities of two immiscible liquids, the fluid interface is acted upon only by surface tension forces simulating the force condition of a space environment. A simple analysis (Reference 7)

develops a figure-of-merit, Bond Number, as a useful criteria for determining the predominance of either capillary or body forces. Consider the liquid column height in the tube of Figure 2. Considering a force balance on the system, the pressure differential associated with the rise height is:

$$P_{\text{atm}} - P_1 = \Delta P = \Delta \rho gh \quad (1)$$

While the corresponding force holding the liquid in the tube is the liquid surface tension acting around the tube circumference:

$$\Delta P = \frac{2\pi r \sigma}{\pi r^2} \quad (2)$$

Equating equations (1) and (2)

$$\frac{2\pi r \sigma}{\pi r^2} = \Delta \rho gh \quad (3)$$

Dividing the right side by the left and considering the limiting condition as $h \rightarrow r$; the resulting non-dimensional ratio of surface tension forces to body forces is:

$$\frac{\Delta \rho g r^2}{\sigma} \quad (4)$$

This group of parameters forms the well known Bond Number ($B_0 = gr^2/\sigma$) which is used as a determination of capillary-dominated or gravity-dominated hydrostatic regimes. For Bond Numbers less than one, it is found that capillary forces predominate and thus the liquid column would rise with a curved meniscus as defined by the Laplace equation.

$$\Delta \rho gh = \sigma \cos \theta \left(\frac{1}{r_1} + \frac{1}{r_2} \right) \quad (5)$$

Conversely for $B_0 \gg 1$ the column would not rise and the interface would be flat at a level with the external liquid. This analysis shows how the Bond Number is used to describe the static interface shape of a two fluid system with respect to the forces acting on it. Figure 3 shows liquid/vapor interfaces in a cylindrical container for various Bond Numbers.

Applying the foregoing analysis to our system we see that the more exact the density balance between the liquids the lower the Bond Number (as $\Delta \rho \rightarrow 0$, $B_0 \rightarrow 0$). A zero density gradient yields a Bond Number of zero and a complete domination of surface tension. This shows that even though the tests are designed to demonstrate surface tension controlled behavior the absolute value of surface tension is not critical for zero-g simulation. When the densities are not exactly

balanced, it can be seen from the Bond Number that the physical dimensions of the container become important; i.e., small containers maintain capillary domination even with slight density mismatch. Therefore, for larger systems it becomes important to match the liquids as closely as possible to achieve acceptable results.

TEST PROCEDURE AND RESULTS

The test models are either full-size or scaled prototype glass tankage with either glass or metallic liquid orientation structure. After fabrication, all internal surfaces are sprayed with a thin teflon film and the model is assembled. A chloroform/hexane mixture of unit density is used to simulate the liquid propellant and distilled water to simulate the gas phase pressurant.

The chloroform/hexane solution is mixed to have a density near that of the water and the two fluids are placed in the model to the desired fill ratio. The final density of the system is trimmed by adding drops of either the more dense chloroform or less dense hexane until neither liquid constituent exhibits a tendency to rise. In this condition an interface will be observed in the model, invariant of its orientation in space. This condition represents a state of zero-g and a Bond Number of zero. A typical neutral buoyancy test result of the zero-g configuration of propellant in a tank with a surface tension orientation structure is shown in Figure 4.

Once the neutral buoyancy system has been balanced, results are consistently repeatable. However, since the two liquids have different density-temperature relationships, thermal gradients in the system environment cause density imbalances and interface distortion. An environment controlled within a few degrees such as most room-temperature environments is acceptable for low-g demonstration purposes.

Although often annoying for zero-g simulations, the thermal density shift can be used to advantage. We are now in the process of developing a technique using a thermally controlled chamber to simulate low-g environments such as those created during spacecraft engine thrust periods. By raising or lowering the temperature, the hydrostatic head gradient across the interface can be controlled to theoretically simulate force-field levels from zero to fractional g's. The effective g-level being simulated in the model can be calibrated by using a reference interface of the same liquids in the straight section of a cylinder. Both

are placed in a thermally controlled chamber and the chamber temperature is adjusted to different values. By comparing the meniscus shape in the standard cylinder with a known Bond Number curve, similar to Figure 3, the effective g-level is determined for the model results. Thus the neutral buoyancy technique can also demonstrate static interfaces occurring during thrusting and other perturbation periods during a spacecraft mission.

To compare the results between neutral buoyancy experiments and both drop-tower tests and computer simulations, a four-inch diameter spherical glass container with a one-inch long standpipe was fabricated and tested. The results for various fill conditions closely matched the drop-tower tests and analytical data from Reference 8. Figure 5 shows a 40-percent propellant-fill condition for the model and computer simulation. This comparison provides an excellent verification of the validity of the neutral buoyancy low-g interface shapes.

Dynamic simulations using neutral buoyancy are not applicable as exact models because the viscous shear between two liquids is much higher than that between gas and propellant, and the inertia force of the ullage gas is insignificant compared to the liquid simulant. However, under low flow-rate conditions where these are only secondary effects, dynamic simulations are excellent demonstrations of outflow sequence and expulsion efficiency. A 16-mm movie has been produced to demonstrate the zero-g expulsion of the capillary propellant management system shown in Figure 4.

CONCLUSIONS

The neutral buoyancy technique is a simple method of analyzing fluid systems under zero-gravity conditions. Inexpensive testing can be conducted for concept development, performance tradeoffs, and verification of system performance as a pre-qualification or flight test program. The simple and inexpensive apparatus required make this method a viable technique for small-scale laboratory experiments as well as large-scale system simulation.

REFERENCES

1. W. C. Reynolds, "Hydrodynamic Considerations for the Design of Systems for Very Low Gravity Environments", Technical Report LG-1, Department of Mechanical Engineering, Stanford University, 1 September 1961.
2. D. L. Balzer, "Advanced Propellant Management System for Spacecraft Propulsion Systems", Summary Report NASA-CR-102181, September 1969.
3. S. C. DeBrock, D. L. Balzer, et al, "A Survey of Current Developments in Surface Tension Devices for Propellant Acquisition", Journal of Spacecraft and Rockets, Vol. 8, No. 2, February 1971, pp. 83 - 98.
4. F. T. Dodge, L. R. Garza, "Magnetic Fluid Simulation of Liquid Sloshing in Low Gravity", NASA-CR-102862, August 1970.
5. J. Plateau, "Experimental and Theoretical Research into the Equilibrium Shapes of a Fluid Mass without Weight", Annaler der Physique, 1861.
6. G. B. Wood, "Zero-G Report Liquid/Liquid Models", Convair Astronautics Report No. 55D859-9, 28 May 1962.
7. H. Abramson, "The Dynamic Behavior of Liquids in Moving Containers", NASA SP-106, 1966.
8. H. Paynter, "Investigation of Space Storable Propellant Acquisition Devices", Vol. II, NASA CR-111343, August 1970.

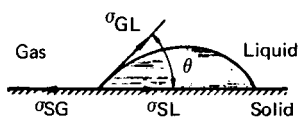


Figure 1. Surface Tension Contact Angles

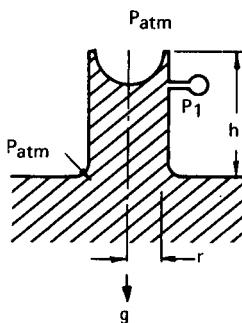


Figure 2. Capillary Force in a Tube

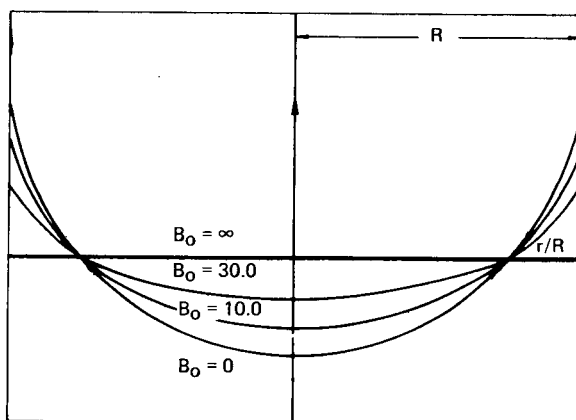


Figure 3. Liquid-Vapor Interface Equilibria in Cylindrical Containers

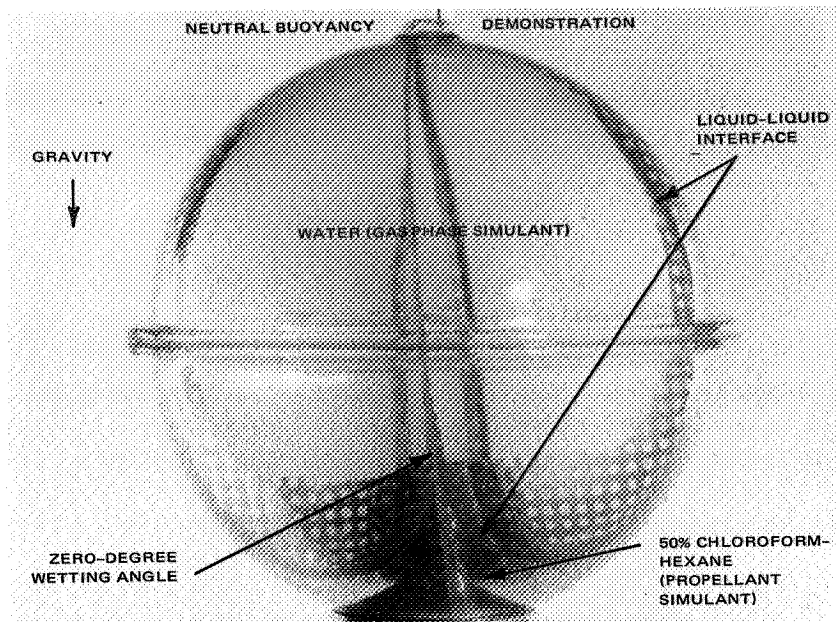


Figure 4. Surface Tension Model

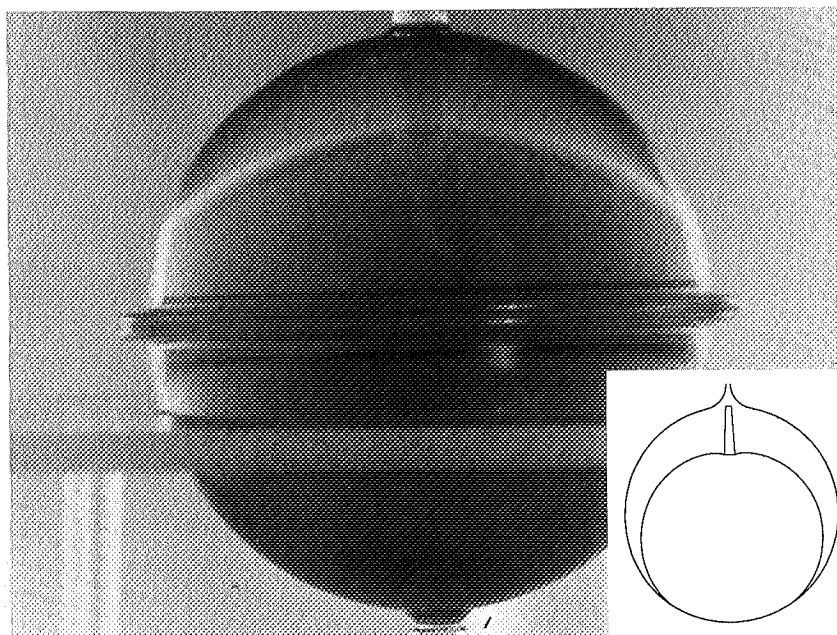


Figure 5. Standpipe Design 40% propellant

PREDICTING SPACECRAFT SELF-CONTAMINATION IN SPACE AND IN A TEST CHAMBER

John J. Scialdone, *Goddard Space Flight Center, Greenbelt, Maryland*

ABSTRACT

The self-contamination of a spacecraft, defined as the return and deposition of outgassed molecules on its critical surfaces, was investigated. Theoretical relations for the flux, density, and pressure of the emitted gas as a function of altitude, radius, and distance from the spacecraft surface were developed. The flux of these outgassed molecules which return to the emitting surface was also obtained and shown to be dependent on altitude, dimensions, and on the magnitude of outgassing. The rate of condensation and the time for the formation of a monolayer of the returning molecules can be calculated.

The self-contamination of a spacecraft undergoing vacuum chamber test was also analyzed and compared to the equivalent parameters for the orbital conditions.

INTRODUCTION

The accumulation of molecules on surfaces may change the surface optical properties. In general, this contamination consists of water vapor and medium to high molecular weight organic materials having low vapor pressures. Low molecular weight organic materials which have a very high vapor pressure (volatile) at room temperature do not remain on surfaces unless these surfaces are at temperatures lower than -60°C . These do not present a problem since spacecraft surface temperatures are generally above that value. However, recent experiments on spacecraft have been flown utilizing detectors cooled to a temperature of 175K or lower. At these temperatures, most of the gases will condense and lower the efficiency of optical surfaces.

In space, a satellite can become self-contaminated and deterioration of optical, thermal and electrical systems may occur. The self-contamination in space, when not produced by direct internal impingement of desorbed molecules on critical surfaces, has been thought of as being produced by a cloud consisting of satellite emitted gases and particulate matter surrounding the craft. Various theories have been suggested to confirm the existence and to evaluate this so-called cloud. Radiation

pressure, aerodynamic drag, solar wind, charge drag, Lorentz forces have been invoked to retain the cloud of emitted gas around the spacecraft. Meanwhile, flight experiments have been few and their results inadequate for characterization or establishment of this cloud. In the following pages, an atmosphere produced by the spacecraft outgassing is described, and the fraction of the outgassed molecules which return to the spacecraft surface as a result of their collisions with the ambient neutral particles is calculated. Curves have been prepared showing the dependence of the "cloud" and the fraction of returning molecules on the altitude and size of the spacecraft.

In addition, the spacecraft self-contamination during testing in a space chamber is examined. This contamination is produced by the return flux of desorbed molecules reflected by the chamber walls. This return flux is dictated by the space chamber wall surface capture coefficient and the geometry of the spacecraft and chamber.

In this paper, the two conditions are evaluated and an attempt is made to predict and model the tests so that the real and surrogate space environment for the spacecraft are similar. Correlation for the time required to form a monolayer on a cold surface in space and in the test chamber is made. The correlation indicates, within the limits of the idealized analysis, the length of testing necessary to reproduce the space contamination. It is expected that this analysis will be beneficial in predicting alterations of thermal and optical surfaces.

ORBITING SATELLITE

Concentration of Outgassing Around the Satellite

For the assumption that the density around a spherical satellite of radius R is such that the radially desorbed molecules in their large majority do not collide with each other and their trajectory is straight up to the collision with ambient molecules, the density as shown in Ref. (1) is

$$n_D = \frac{N_D e^{-x/\lambda_D}}{4 \pi (R + x)^2 v_D} \quad (\text{cm}^{-3}) \quad (1)$$

where:

N_D is the number of molecules per second coming from the spacecraft which can be obtained from any of the commonly used measures of the outgassing, for example, Q (torr ℓ s^{-1}), or \dot{m} (g s^{-1})

x is the radial distance in the direction of motion from the satellite

v_D is the mean thermal velocity of the desorbed molecules

λ_D is the mean free path (MFP) of the desorbed molecules in the condensation region of the orbiting spacecraft.

The MFP for a molecule emitted parallel or perpendicular to the orbit velocity vector is approximated respectively by

$$\lambda_D = \frac{v_D}{v_0 + v_D} \lambda_0 \quad \text{and} \quad \lambda_D = \frac{v_D}{(v_0^2 + v_D^2)^{1/2}} \lambda_0 \quad (2)$$

where λ_0 and v_0 are the ambient MFP and the orbiting velocity.

Expressing Equation (1) in terms of flux, and substituting λ_D for the parallel emitted molecules, (λ_D for parallel and perpendicular molecules practically coincide for near earth orbits, where $v_D \ll v_0$) one gets for the emitted flux,

$$\phi_D = \frac{N_D e^{-\frac{v_D + v_0}{v_D} \frac{x}{\lambda_0}}}{4 \pi (R + x)^2} \quad (\text{cm}^{-2} \text{ s}^{-1}) \quad (3)$$

The outgassing concentration given by Equation (1) has been plotted parametrically in Figure 1 as a function of the distance, spacecraft radius and orbit altitudes. The value of the thermal velocity employed for the calculations was taken as .4 kms⁻¹. Figure 1 shows also an equivalent pressure at various locations. This is obtained from $P = n K T$ substituted in Equation 1.

Flux and Density of Molecules Returning to the Satellite Surface

The difference between the molecules which reach distance x and $x + \Delta x$, represents the molecules which have collided with the ambient molecules within the distance Δx . If this number is divided by the shell area $4 \pi (R + x)^2$, one gets the collisions Δn occurring at distance x in a volume having a unit base and Δx as thickness (Ref. 1).

If further, these Δn are summed for $0 \leq x \leq \infty$, the total number of the molecules which will have collided in the unit semi-infinite column in front of the spacecraft per unit time is the flux

$$\phi'' = \int_0^\infty \frac{N_D e^{-x/\lambda_D} dx}{4 \pi (R + x)^2 \lambda_D} = \frac{N_D}{4 \pi \lambda_D R} \quad (\text{cm}^{-2} \text{ s}^{-1}) \quad (4)$$

for $\lambda \gg R$.

After collision, these molecules' velocities become less than the

satellite velocity and are reacquired by the satellite. If the velocity of approach is on the average v_n , the apparent density of the returning molecules at the spacecraft surface will be

$$n'' = \frac{N_D}{4\pi\lambda_D v_n R} \quad (\text{cm}^{-3}) \quad (5)$$

Knowing the gas temperature, an equivalent pressure can also be obtained using the perfect gas law.

Ratio of Emitted to Returned Molecules

The fraction of the desorbed flux which finds its way back to the spacecraft surface in the region of condensation is given by the ratio of Equation (3) taken for $x = 0$ and Equation (4) i.e.

$$\frac{\phi''}{\phi_D} = \frac{R}{\lambda_0} \left(\frac{v_D + v_0}{v_D} \right) \quad (6)$$

The ratio of the apparent pressures and densities between emitted and returned molecules can be obtained similarly from Equations (5) and (1).

Figure 2 is a plot of the ratio of the returning flux to the emitted flux as a function of the altitude. The ratio decreases rapidly with altitude reaching a practically constant value beyond 1000 km, and increases with the radius of the satellite. The apparent pressures and density which decay in the same manner as the flux, have been plotted on the same figure for an estimated returning velocity equal to one-half the orbital velocity (Ref. 1).

An important consideration is the effect of the return flux on the total pressure at the surface of the satellite. The total pressure P_t produced by the outgassing will be given by the sum of the emitted molecules pressure P_D and the pressure of the returned molecules P'' . In normalized form, this is given by

$$\frac{P_t}{P_D} = \left(1 + \frac{\phi''}{\phi_D} \sqrt{\frac{T_n}{T_D}} \right) = \left(1 + \frac{R}{\lambda_D} \frac{v_n}{v_D} \right) \quad (7)$$

which is obtained by substituting

$$\frac{P''}{P_D} = \frac{\phi''}{\phi_D} \frac{v_n}{v_D},$$

given by the previous equations. It is readily seen that the effect of the return molecules is undetectable if one attempts to measure the pres-

sure. The total pressure is almost entirely produced by the desorbed pressure and a pressure measurement would be insensitive to the returned molecules because of the relative dimensions of R and λ at the altitudes under consideration ($\lambda \gg R$).

Contamination Caused by the Returning Flux and Time for Monolayer Formation

The returning molecules may enter an opening or impinge on surfaces on which they may deposit as adsorbate or condensate. If the pressure exerted by the contaminant gas on the surface is less than the saturation vapor pressure of the same contaminant on the surface a few monolayers or fraction of one may form. An equilibrium between molecules arriving and leaving the surface will be established. The number of adsorbed molecules per unit area will be given by $\sigma = \alpha_s \phi'' \tau$ where α_s is the sticking coefficient and τ is the average residence time for the molecule on the surface. This last parameter according to Frenkel's relation is a function of the heat of adsorption of the gas and of the surface temperature. The adsorption will decrease exponentially with the temperature and increases also exponentially with the heat of adsorption. For condensation to occur, the partial pressure of the contaminant P'' must be higher than the saturated vapor pressure P_s of the contaminant corresponding to temperature T_s of the surface. The saturation pressure is given by the Clapeyron relation. The rate of condensation will be given by the difference between the impinging flux and the evaporating flux as dictated by the saturation pressure. If P_s is an order of magnitude or lower than P'' the evaporation can be disregarded and the rate of condensation will be,

$$\nu = \alpha \phi'' = \alpha \frac{P''}{K T_n} \frac{v_n}{4} = \frac{\alpha}{4} \frac{P_D}{K T_D} v_D \left(\frac{\phi''}{\phi_D} \right) \quad (\text{cm}^{-2} \text{s}^{-1}) \quad (8)$$

where α is the coefficient of condensation.

The last expression was obtained by multiplying the expression for the rate of condensation by ϕ''/ϕ_D and then dividing by

$$\frac{\phi''}{\phi_D} = \frac{P''}{P_D} \frac{v_D}{v_n}$$

which is given by the previous relations.

The time required for the accumulation of a monolayer of molecules on a surface will be given by the following relation:

$$t = \frac{N_m}{\nu} = \frac{4 K T_D}{\alpha v_D} \frac{N_m}{\left(\frac{\phi''}{\phi_D} \right) P_D} \quad (\text{s}) \quad (9)$$

where N_m is the number of molecules in a monolayer per cm^2 , P_D is the desorbed pressure at the surface given as per Equation (1) by

$$P_D = n_D K T_D = \frac{N_D K T_D}{4 \pi R^2 v_D}.$$

Figure 3 has been plotted to show the time of monolayer formation as a function of the contamination parameter ϕ''/ϕ_D , and P_D which is a measure of the spacecraft outgassing.

VACUUM CHAMBER TESTING — SPACECRAFT SELF-CONTAMINATION

Vacuum chambers have been designed to minimize the return of molecules to the spacecraft by having walls capable of absorbing almost all molecules emitted from the spacecraft. This is based on the expectation that in space there is a negligible probability of collision of an emitted molecule with another to cause its return. Accordingly, it is expected that only those surfaces which can "see" each other and thus have a probability of direct molecular encounter may become contaminated. Based on this, the surface walls of the chambers have been designed to act as molecular traps in the same manner as they do for radiation.

The molecular self-contamination in a chamber bears no direct dependence on the chamber pressure or the mean free path of the gas in the chamber. The pressure, however, as a measure of density is significant for gas conduction and radiation heat transfer effect and for voltage breakdown. The mean free path parameter which is so important for space contamination, has no comparable significance in a space chamber since for a relatively low gas pressure or density, the MFP of the molecules will exceed the dimensions of the chamber. In a chamber test the molecules emitted from the spacecraft will collide with the walls and some of them will be reflected back if the walls are not a perfect sink. These return molecules constitute the contaminating molecules and may provide an "additional contamination not present in space". For a test chamber where gas is removed only by pumps, the probability that a molecule is removed is roughly the ratio of the pumping port area and that of the entire projected chamber wall. This ratio generally is no more than .01 for large chambers. For cryopumped chambers with a refrigerated but nonpumping shield, the capture probability is not higher than about .3 and for an unshielded cryopump surface is about .8 (Ref. 2 and 3). The molecules not captured on the first encounter with the wall will leave the walls randomly, some intercept the spacecraft and others — other parts of the walls. A quasi-equilibrium condition is established

when molecules are removed from the chamber after a number of collisions with the walls and spacecraft. Chuan (Ref. 2) derives for this condition of equilibrium a self-contamination coefficient C_s . This is defined as the ratio of the molecules returning to the test object after collision with the chamber wall to those emitted from the test object. The derivation, involving form factors and properties of surfaces, is based on the assumption that the chamber and spacecraft are concentric spheres and the gas emission from the spacecraft and the pumping walls is uniformly distributed. This coefficient C_s is given by

$$C_s = \frac{1}{1 + \frac{\eta_c}{1 - \eta_c} \frac{1}{\eta_m} \frac{A_c}{A_m}} \quad (10)$$

where

- η_c is the chamber wall capture probability
- η_m is the spacecraft surface capture probability
- A_c, A_m the surface areas of the chamber and spacecraft respectively.

It is apparent from its definition that the above coefficient corresponds to the flux ratio ϕ''/ϕ_D (Eq. 6) which was derived for the self-contamination in space.

A plot of the coefficient C_s is reproduced in Figure 4. It is shown as a function of the spacecraft chamber diameter ratios and for various values of the wall capture coefficients η_c . The value of η_m will depend on the spacecraft surface properties, and the contaminating molecules. The figure has been plotted for $\eta_m = .5$.

The equivalent in chamber-pressure consisting of molecules coming directly from the spacecraft and those returning from the walls was also derived. The equation normalized by the surface pressure produced by the effusion rate, which is

$$P_D = \frac{\dot{m}}{4 \pi R^2} \left(\frac{2 \pi K T_m}{M} \right)^{1/2},$$

is given by

$$\frac{P_c}{P_D} = \frac{1}{2} \left[1 + C_s \left(\frac{1 + \left(\frac{T_c}{T_m} \right)^{1/2}}{\eta_m} - 1 \right) \right] \quad (11)$$

It is seen that measurement of pressure (density) is insensitive to changes in C_s for values less than .2. Therefore, the pressure is not a

meaningful parameter for evaluation of self-contamination in a chamber. The same was even more true for space conditions.

COMPARISON OF SELF-CONTAMINATION IN SPACE AND TEST CHAMBER

On the previous pages, the various relations which apply to the space and chamber self-contamination were indicated. For both operations, it has been pointed out that pressure at the surface is not sufficiently indicative of the degree of self-contamination. It was also pointed out that the simulation of the space density does not reproduce the MFP of space, because the MFP is limited to the largest dimension of the chamber. On the other hand, in space the "reduced" ambient mean free path determines the number of returning molecules. In the space chamber, the return is dictated mainly by the chamber interior surface. However, in both cases, the flux ratio between the molecules returned to the surface and those emitted can provide a meaningful contamination parameter. If equal self-contamination occurs in a test chamber and in space, the coefficient C_s must be equal to the ϕ''/ϕ_D . In that case, with the appropriate substitution from Equations (10) and (6) the required wall capture coefficient must be

$$\eta_c = \frac{1 - \frac{R}{\lambda_D}}{1 + \frac{R}{\lambda_D} \left(\frac{A_c}{\eta_m A_m} - 1 \right)} \approx \frac{1}{1 + \frac{R}{\lambda_D} \frac{A_c}{A_m \eta_m}} \quad (12)$$

This indicates that, to reproduce a 200 km orbit whose expected contamination ratio is $\phi''/\phi_D = 10^{-1}$ (Figure 2), the capture coefficient for $D_c/D_m \approx 3.16$ and spacecraft surface coefficient $\eta_m = .5$, must be about .31 (see also Figure 4). As mentioned, this value is available with cryo-pumped chambers with a refrigerated but non-pumping shield. If the self-contamination is 10^{-3} as for an orbit of 400 km, η_c must be .98. This capture is not generally available and more contamination is to be expected in the chamber than in orbit. According to Reference 4, the molesink chamber at JPL has a self-contamination of 4×10^{-4} for a diameter ratio of 10. This self-contamination corresponding to a 500 km altitude as per Figure 2, requires a wall capture coefficient of about .95.

In view of the above, the contamination produced in a test chamber could be similar to that in space if the wall capture coefficient can be adjusted, in relation to the chamber and spacecraft diameter ratio. Obviously, this is not practical or possible for the simulation of high altitude orbits. Consequently, in many cases, the contamination in space

cannot be reproduced in a chamber and must be inferred from chamber results.

For a chamber test the spacecraft self-contamination can be calculated if the capture coefficient and the ratio of diameters is known. Alternatively, the average ratio of the emitted and returned flux obtained using quartz crystal microbalances or tubulated ion gages will give directly the self-contamination. With this known parameter, any other measurement such as the emitted pressure, the outgassed quantity per unit time, the number of monolayers of contaminants, and the time of monolayer formation in the chamber test can be determined by simple ratio to the same quantities which will be obtained in space. For example, with known C_s and ϕ''/ϕ_D and the time for the formation of a certain contamination thickness during test, t_c , the time, t_s , which will be required in space for the same accumulation assuming the same condition of temperature and outgassing, will be

$$t_s = t_c \frac{C_s}{\frac{\phi''}{\phi_D}} \quad (13)$$

Alternatively, the rate of condensation, ν_c , on a cold surface on the spacecraft is established during test, then the equivalent rate in space is

$$\nu_s = \nu_c \frac{\frac{\phi''}{\phi_D}}{C_s} \quad (14)$$

Other parameters such as total contaminant deposition and outgassing rates can be estimated. However, comparisons of ground test results and expected space results will have to take into account the effect of spacecraft rotation and the fact that the estimated contamination in space is applicable to the frontal area of the spacecraft only, i.e., the condensation region.

CONCLUSION

In the direction of the velocity vector, the molecules outgassed from the spacecraft produce a concentration which diminishes with distance from the surface. The decrease is a function of the altitude and the spacecraft radius. For a 100 km orbit, the outgassing concentration at a distance of 10 cm from the surface has diminished one order of magnitude. At 500 km the one order of magnitude decrease occurs at about 2 meters from the surface.

The spacecraft self-contamination decreases rapidly with orbit altitude. The ratio of the returned to the emitted molecular flux varies from one half at 160-170 km down to one millionth or less at 1000 km and higher. On the other hand, self-contamination during vacuum chamber tests may be larger or less than that in space depending on chamber-spacecraft dimensions and chamber wall capture coefficient. Tests conducted in conventional vacuum chambers can provide returning contaminating fluxes comparable to those expected in space up to an altitude of about 400 km. For higher altitudes involving return fluxes less than 10^{-3} of those emitted, the chamber tests can produce larger contamination than that in space. Ground and space self-contamination can be related. The condensation rates and time of monolayer formation can be established, provided the chamber capture coefficient is known or better still the return to the emitted flux is measured in the chamber. For both space and ground, the self-contamination can be established by the measurement of the emitted and return flux. Pressure measurements are not sensitive to the addition of returning molecules and cannot indicate self-contamination.

REFERENCES

1. Scialdone, J. J., "Self-contamination and Environment of an Orbiting Satellite", NASA Technical Note (Goddard Space Flight Center, Greenbelt, Maryland) [in preparation].
2. Chuan, R. L., "Molecular Flux and Equivalent Pressure in a Space Environment Chamber", Agard Specialists' Meeting on "Fluid Dynamic Aspects of Space Flight", Marseilles, France, April 1964.
3. Dawson, J. P., "Prediction of Cryopumping Speeds in Space Simulation Chambers", AIAA Space Simulation Testing Conference, Pasadena, California, November 1964.
4. Stephens, J. B., and Wallace, D. A., "Space Molecular Sink Facility Design", AIAA Space Simulation Testing Conference, Pasadena, California, November 1964.

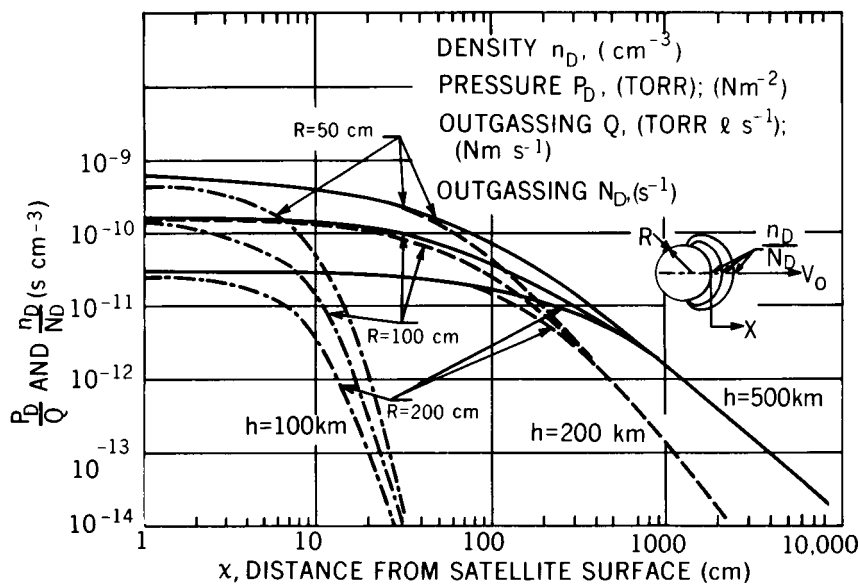


Figure 1. Concentration and Pressure of Outgassing Versus Distance

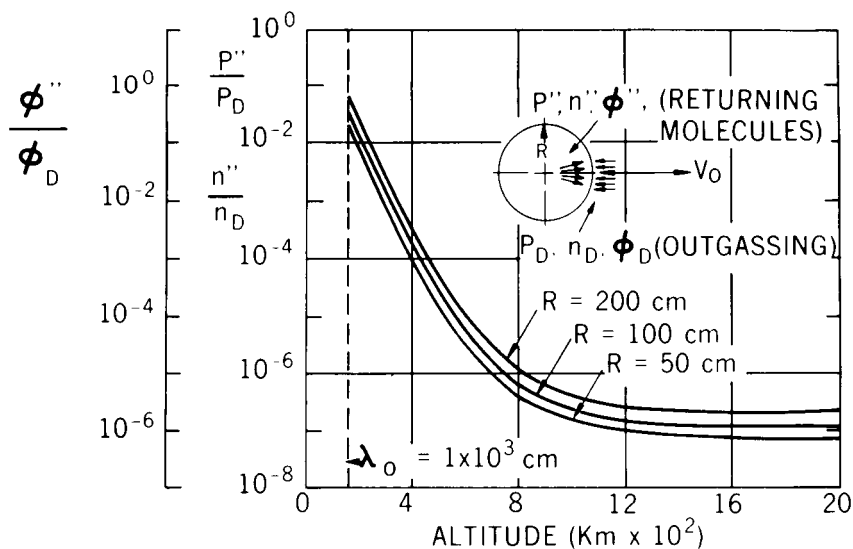


Figure 2. Returning Flux Versus Altitude

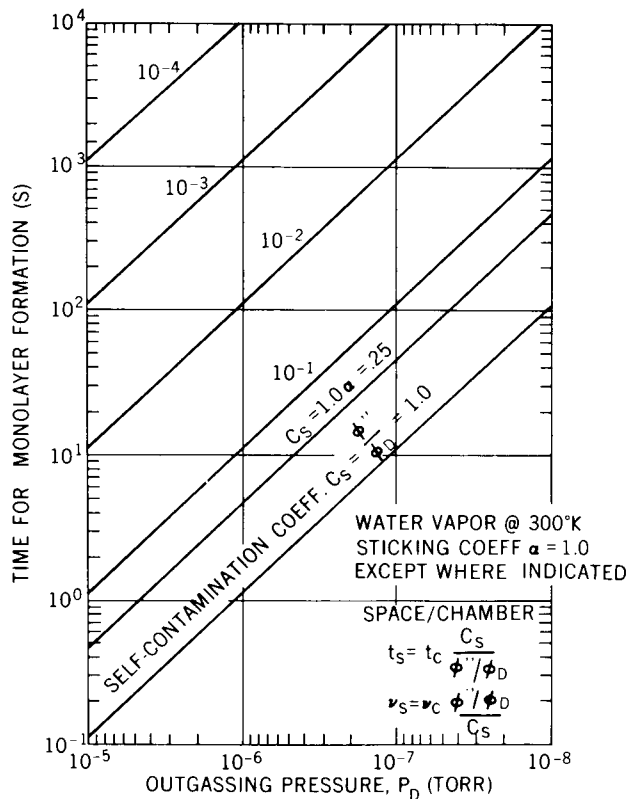


Figure 3. Time for Monolayer Formation Versus Outgassing Pressure and Self-Contamination Coefficient

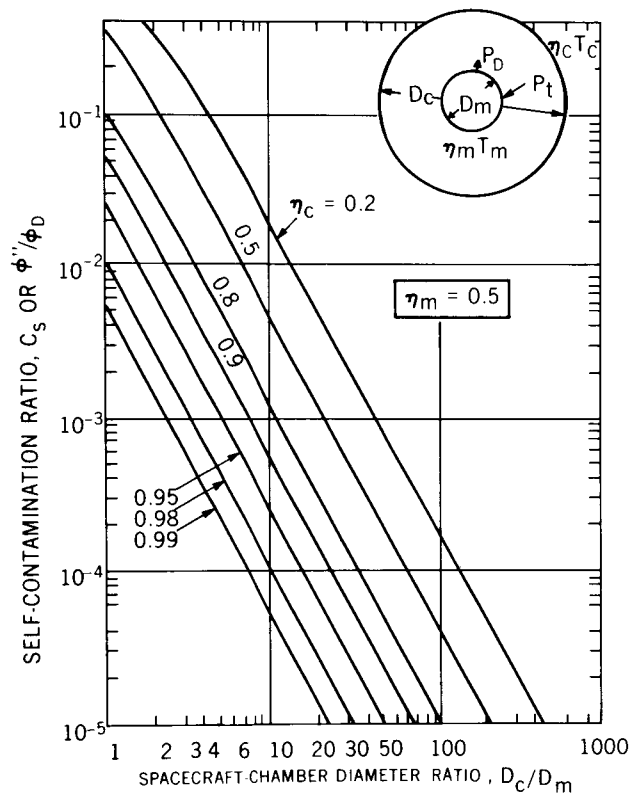


Figure 4. Self-Contamination Coefficient Versus Spacecraft-Chamber Diameter Ratio

PREPARATION, VERIFICATION, AND OPERATIONAL CONTROL OF A LARGE SPACE-ENVIRONMENT-SIMULATION CHAMBER FOR CONTAM- INATION SENSITIVE TESTS

James T. Visentine (NASA), John W. Ogden (NASA), Melvin L. Ritter (*Brown and Root-Northrop*), Manned Spacecraft Center, Houston, Texas, and Charles F. Smith (NASA), Marshall Space Flight Center, Huntsville, Alabama

ABSTRACT

Thermal-vacuum testing of spacecraft carrying sensitive optical instruments poses special problems to the test facility with regard to contamination control during both preparation and test activities. A 2-year program to prepare chamber A at the NASA Manned Spacecraft Center for Apollo telescope mount thermal-vacuum tests is discussed. This program covers modification to existing chamber systems, the development of facility and chamber operating procedures, the selection of chamber cleaning and control methods, and the development and evaluation of diagnostic instrumentation. Specific details are included to illustrate the extensive efforts made to ensure a minimum contamination environment for the Apollo telescope mount test series. Recent thermal-vacuum tests of this chamber at progressive stages of cleanliness have demonstrated the success achieved in reducing the particulate and molecular contamination levels of the basic chamber interior. Data are presented that compare these "base line" contamination results.

INTRODUCTION

Contaminants may be introduced into a space-environment-simulation chamber during initial construction phases and during preparation and testing activities on spacecraft carrying sensitive optical instruments. Once introduced, these contaminants can cause severe detrimental effects on the instruments, such as a reduction in the reflectivity of mirrors and gratings of high-resolution vacuum ultraviolet (UV) spectrometers.

In relation to space-environment-simulation testing, contaminants are subdivided into two categories. The first category is particulate contamination that consists generally of dust particles, lint, rust, chafed particles from thermal and electrical insulator materials, and human epidermal cells. This form of contamination can present serious problems if it is not discovered and removed because particulates can degrade delicate electronic contacts, miniature mechanical systems, and block slits of spectrometers. Particulate contamination normally is experienced only during times when the chamber pressure is high enough to allow airborne transport; that is, during spacecraft preparation and checkout activities, during the initial chamber-pumpdown phase, and during the final phases of re-pressurization. The presence of particulates under high-vacuum (test) conditions seldom is experienced because there is no external source of particles and no matrix for the mobility of particles other than spacecraft waste dumps and the gravitational field.

The other category is molecular contamination. This form of contamination presents a more serious problem during high-vacuum conditions than particulate contamination. Molecular contamination consists of chemical substances and compounds that migrate and deposit in the chamber test volume as individual molecules or as clusters of molecules (ref. 1). When these substances condense on optical elements, they usually form two main types of contaminating surface layers: smooth and continuous layers of light absorbing and nonabsorbing materials, and surface condensations in the form of droplets that cause light scattering. The degradation caused by these contaminating surface layers normally is not permanent. When the source of contamination is removed, complete recovery usually occurs if the vacuum system is reasonably clean. However, it has been shown that restoration does not occur if a contaminated optical surface is irradiated with UV or other molecule-decomposing particles, such as electrons or protons (ref. 2). On the contrary, irradiation of contaminated mirrors with UV energy enhances the reflectance decrease and makes it permanent because the residue formed during the irradiation does not evaporate.

Materials that produce contaminating surface layers in a space-simulation chamber are derived from a myriad of sources. The most common sources, however, are backstreaming from mechanical pumps and oil-diffusion pumps; evaporation and sublimation of substances from warm chamber walls; desorption and outgassing products from paints, epoxies, and insulating

materials; and thermal decomposition of high-molecular-weight materials resulting in the release of light, volatile fractions.

The purpose of this report is to describe the overall program developed for chamber A at the NASA Manned Spacecraft Center (MSC) to reduce the particulate and molecular contamination levels during preparation and checkout activities for the Apollo telescope mount (ATM) and to maintain these levels within the test-environment requirements. This program covers modification to existing chamber systems, development of facility and chamber-operating procedures, selection of chamber cleaning and control methods, and development and evaluation of diagnostic instrumentation. Test results are presented that list principle contaminants and levels of concentration for three previous "base line" contamination-measurement tests. Conclusions and recommendations also are presented that review the present program in relation to future thermal-vacuum tests at the MSC.

FACILITY DESCRIPTION

Chamber A is a stainless-steel vessel 19.8 m in diameter and 36.6 m high. A side-hinged door, which provides a 12.2-m-diameter clear opening for vehicle loading, is located in the cylindrical section. The chamber is equipped with a rotating platform (lunar plane) for supporting test vehicles weighing up to 68 100 kg. Personnel access is provided from four manlocks and one chamber door. Double manlocks are provided at the lunar-plane level and the midchamber level. The access door is located at the upper chamber level.

The chamber interior is lined with black, liquid-nitrogen-cooled heat-sink panels that operate at approximately 90° K. The chamber vacuum system consists of a mechanical roughing system, eighteen 81-cm-diameter oil-diffusion pumps, and gaseous-helium-cooled cryopumping surfaces that operate at a temperature of approximately 17° K. Chamber pressure normally is maintained below 1×10^{-6} torr by the use of the helium cryopanel that produce pumping speeds for gases condensable on their surfaces in excess of 10 000 000 l/sec.

The chamber also is equipped with a top solar simulator system that consists of external carbon-arc light sources and internal collimating optics. The target area for the top sun system is 4 m in diameter. Within this area, the radiant energy intensity can be controlled in the range of 622 to 1353 w/m².

A larger "side" solar simulator is not used in ATM testing, and the penetration area for the light sources has been

covered temporarily by a liquid-nitrogen-cooled shroud that shields the ATM from the warm chamber wall.

Test-Vehicle Description

The ATM is an optical experiment payload consisting of six experiments designed specifically to study solar phenomena.

Experiment SO52 - White-Light Coronagraph--This experiment uses an externally occulted coronagraph to monitor, in the 4000 to 6000 Å wavelength range, the brightness, form, and polarization of the solar corona from 1.5 to 6 solar radii. It is used to study the evolution of coronal activity and to correlate this activity with events on the surface of the sun.

Experiment SO54 - X-Ray Spectrographic Telescope--This experiment records spectra of the solar flare X-ray emission in the 2- to 10-Å wavelength range with a resolution of 0.5 Å. It is used to follow the evolution of the spatial image and the spectrum of a flare throughout its lifetime and to observe the evolution of nonflaring active regions on the surface of the sun.

Experiment SO55A - UV Scanning Polychromator/Spectroheliometer--This experiment photoelectrically records high-resolution solar images in six spectral lines simultaneously and operates in the 300- to 1350-Å wavelength range. It is used to observe the solar atmosphere near or above active regions on the solar disk.

Experiment SO56 - Dual X-ray Telescope--This experiment obtains high-resolution (5 arc sec) photographs of the coronal X-ray emission of the sun in the 3- to 60-Å wavelength range. It is used to monitor active solar regions during both active and quiescent periods and to record total solar X-ray flux measurements.

Experiment SO82A - Extreme UV Coronal Spectroheliograph--This experiment obtains high resolution (5 arc sec) spectroheliograms of the solar atmosphere in the 150- to 650-Å wavelength range. It is used to provide an increased understanding of solar physics with possible practical application in the research of nuclear production.

Experiment SO82B - Extreme UV Spectrograph--This experiment records spectra of the solar disk in the 900- to 3900-Å wavelength range with a 0.08 to 0.16 Å spectral resolution. It

is used to record spectra from discrete areas of activity in the chromosphere of the sun.

The ATM provides a mounting structure, electrical power, fine pointing system, and environmental control for these experiments. It weighs 11 200 kg and is 4.39 m in length and 4.37 m in diameter. The ATM test configuration is shown in Figure 1.

Cleanliness Requirements

Tests on the ATM thermal systems unit and prototype vehicle were performed in chamber A during July and August of 1970 and October and November of 1971, respectively. Tests on the ATM flight vehicle presently are scheduled to be conducted during June and July of 1972. To protect the sensitive optical experiments on these vehicles from particulate and molecular contamination, the following rigid set of cleanliness specifications have been established by the NASA.

1. The chamber environment surrounding the ATM vehicle during preparation and checkout activities must approach the requirements of a conventional class 10 000 clean room (ref. 3). A class 10 000 clean-room environment is defined as an environment that has no more than 10 000 particles per 28.3 l of air larger than 0.5μ in size and not more than 65 particles per 28.3 l of air greater than 5μ in size.

2. Under thermal-vacuum test conditions, optical degradation for a first-surface aluminized mirror maintained at 20°C and irradiated with the Lyman Alpha hydrogen line (1216 \AA radiation) shall be less than 5 percent for the solar irradiation test phase (40-hr duration) and less than 10 percent for the entire test (70-hr duration).

To meet these requirements, extensive modifications had to be made to the chamber systems and operating procedures.

CHAMBER PREPARATION

Hardware and Procedural Modifications

Oil-Diffusion Pumps--It has been assumed previously that the most probable source for molecular contamination in vacuum chambers is oil-diffusion pumps (ref. 4). When a diffusion pump is fitted with an optically dense baffle, visible films of condensed oil above the baffle usually are prevented but contamination of the system by molecular film still can occur (ref. 5). The causes of such contamination may be summarized as

reevaporation of oil condensed on the baffle, direct penetration of the baffle after intermolecular collisions, and migration along warm boundary walls with subsequent reevaporation into the system.

To limit the quantity of molecular contamination introduced into the chamber by the oil-diffusion pumps, three corrective actions were used. The first action was to operate only four of the 18 pumps on the chamber and to use these four pumps for removing the noncondensable gas-leak loads. Calculations revealed that the combined pumping speed of these diffusion pumps would be satisfactory for removing the small "noncondensable" ATM gas load from the chamber. The second corrective action was to install liquid-nitrogen-cooled baffles between these four pumps and the angle valves that connect the pumps to the chambers. The baffles used are designed to provide optimum protection against the causes for diffusion-pump oil contamination. Each baffle is equipped with an anti-oil migration barrier and uses a double-bounce, optically tight chevron configuration. As a final corrective action, a procedural change was made to restrict operation of the oil-diffusion pumps to chamber pressures below 5×10^{-3} torr rather than the previous procedural upper limit of 5×10^{-2} torr to minimize direct penetration of the baffle by high-temperature oil molecules following intermolecular collisions.

After the liquid-nitrogen baffles were installed, tests were performed on one diffusion pump to measure the backstreaming rate under normal operating conditions. The average backstreaming rate was determined to be 5.17×10^{-9} g/cm²/day, or approximately 0.04 monolayers/day (ref. 6). As a result of these tests, it was decided that the diffusion pumps would not degrade the cleanliness levels inside the chamber because the backstreaming rates were low. Moreover, liquid-nitrogen heat-sink panels directly in front of the port openings, which were not considered in the backstreaming measurements, would be cooled to cryogenic temperatures before the diffusion pumps were opened to the chamber, providing additional assurance that oil would not reach the test volume.

Mechanical Pumping System--Corrective actions also were employed to limit the quantity of contamination introduced into the chamber by the mechanical (roughing) pumping system. These actions included installation of a liquid-nitrogen baffle in the roughing duct between the chamber isolation valve and the mechanical pumps and blowers, and a procedural change to close

the chamber isolation valve between the mechanical pumps and the chamber at a pressure of 1×10^{-3} torr, rather than at 5×10^{-4} torr as was done previously. To minimize back-streaming from the mechanical pumping system, cooldown of the baffle during pumpdown is initiated at a chamber pressure of 1 torr.

Air Locks and Chamber-Air-Recirculation System-- Facility modifications also were required to limit the quantity of particulate contamination introduced into the chamber. A cleanliness requirement established by the NASA was to approach a conventional class 10 000 clean-room environment inside the chamber during ATM preparation and checkout activities. To meet these limitations, the following corrective actions were used.

1. Double door air locks were installed at all laboratory entrances and maintained at a slightly positive pressure (0.4 torr) to limit the amount of particulate contamination introduced into the laboratory high-bay area.

2. Air showers were installed at all chamber personnel entrances to limit the quantity of contamination introduced into the chamber by test-team personnel.

3. All test-team personnel were required to dress in lint-free clothing before entering the chamber through the manlocks and upper level door.

4. The chamber-air-recirculation system was upgraded substantially to remove particulate contamination by providing a 99.97-percent effective filtration capability for particles 0.3μ in size or larger. This capability was established by adding prefilters that were 85 percent effective in removing particles 5μ in size or larger and high efficiency particulate air filters that trapped particles not removed by the prefilters. A mechanical blower was used to maintain the chamber pressure slightly above ambient pressure (0.4 torr) to limit the quantity of particulate contamination introduced into the chamber through the personnel entrances. The volumetric flow of air through the chamber when the recirculation system was in operation was 5.6×10^5 l/min. The recirculation system also was used to maintain the relative humidity inside the chamber below 50 percent when the vehicle loading door was closed. A schematic showing the chamber A air-recirculation system is included in Figure 2.

Chamber Cleaning and Preparation

Particulate contamination levels were controlled during ambient conditions by modifying the chamber-air-recirculation system to maintain a conventional class 10 000 clean-room environment inside the chamber. Molecular contamination, however, is more difficult to control and adheres to surfaces more tenaciously than particulate contamination. Two main types of molecular contaminants generally are observed in relation to the way these materials adhere to surfaces: those that exhibit a random molecular arrangement in the monolayer adjacent to the surface and those that show a definite preferred molecular orientation in the final monolayer (ref. 7).

The first class of materials, such as paraffin waxes and mineral oils, do not possess strong dipole moments and are retained on surfaces by weak Van der Waal forces and unsaturated metal forces. These materials are removed easily from substrates such as metals and optical elements by flushing the surfaces with reagents such as trichloroethylene and carbon tetrachloride. Molecular contaminants that exhibit a definite preferred orientation on surfaces such as diffusion- and mechanical-pump oils, greases, and residues of various cutting, lubricating, and cooling formulations possess strong dipole moments, and monolayers become tightly bonded to the substrates. If a sufficient amount of these materials is absorbed, the molecules in the final monolayer will align with one portion standing fairly erect. As the thickness of the film is increased beyond a monolayer, the orientation of the molecules becomes increasingly random. Molecules that exhibit preferred orientation in the final monolayer do so because such an arrangement is more stable than a randomly oriented system.

A program was implemented to select a detergent solution best suited to remove both kinds of molecular contaminants from the interior chamber surfaces. A total of four detergent solutions were tested. The detergent selected was found to be the most efficient in removing such tightly bonded substances as silicone oils, hydrocarbons, and phosphate ester fluids from surfaces, leaving behind a minimum of residue after the surfaces were rinsed with deionized water. These tests, the results of which are listed in Table I, consisted of contaminating quartz disks with 2×10^{-5} g/cm² of sample and washing the disks with 50 ml of detergent solution. The disks were allowed to drain dry and were rinsed with 50 ml of boiling deionized water. The quantity of contamination remaining on the surfaces was determined by measuring the transmittance losses of the quartz disks in the near UV wavelength region.

The chamber-cleaning operation consisted of directing the detergent solution (one part detergent to 200 parts deionized water) onto the interior chamber surfaces using high-pressure hoses. The chamber was cleaned from the top down. A total of 18 900 l of detergent solution was used to clean the chamber. The chamber surfaces were then rinsed using 189 000 l of deionized water.

After the chamber was cleaned and outgassed to remove traces of moisture, particulate measurements were made and wipe samples were obtained from representative locations throughout the chamber and were analyzed to verify that only minute traces of contaminants and detergent residue remained. The results of the particulate measurements under various operating conditions, before and after chamber cleaning, are shown in Table II. Before cleaning the chamber, a conventional class 10 000 clean-room environment could not be maintained with 12 or more persons in the chamber with the recirculation blower on and the vehicle loading door closed (Tab. II). However, subsequent to chamber cleaning, the ambient environment was maintained well within the specifications for a conventional class 10 000 clean room. The results of the wipe-sample analysis are summarized in Table III. The molecular-contamination levels were reduced significantly as a result of chamber cleaning (Tab. III). These results revealed that the cleanliness level of the chamber interior now was satisfactory for proceeding with the contamination-verification test program.

To remove any contaminants introduced during preparation and checkout activities, it has become common practice to perform a pretest bakeout of the chamber. This is accomplished by increasing the lunar plane and liquid-nitrogen shrouds to a temperature of 40° C and operating the chamber at a pressure less than 5×10^{-3} torr for a minimum period of 72 hr. The temperature and pressure parameters were selected because they were within the operational limitations of the chamber. The increased temperature and reduced pressure increased the outgassing rates of materials in the chamber interior. The time duration was selected because it has been shown that the outgassing rates for many polymers and metal surfaces decrease exponentially with time (ref. 8), and that at the end of the period, the outgassing rates would be reduced to a level that would not be detrimental to the ATM optical experiments.

Material Selection and Control

Before chamber cleaning was accomplished, a material selection and control program was implemented to minimize recontamination of the interior chamber walls and cryopanel surfaces by introduction of polymeric materials that have high outgassing rates at elevated (125°C or greater) temperatures. The criterion used at the MSC for material selection is based on the quantity of volatile condensable material and weight loss of a material sample maintained under controlled conditions (ref. 9). A material sample is rated as acceptable if it has a maximum volatile condensable material of 0.1 percent and a total weight loss of 1.0 percent when tested under a pressure of 10^{-6} torr or less, a specimen temperature of $+125^{\circ} \pm 1^{\circ}\text{C}$, a condensable plates temperature of $+25^{\circ} \pm 1^{\circ}\text{C}$, and a vacuum exposure time of 24 hr.

As part of a continuing program to refine and extend the material-selection criteria, an additional technique for material evaluation is being considered by the MSC. This technique would require material specimens to be tested under conditions similar to those previously mentioned and irradiated with UV energy. Materials otherwise acceptable would be disapproved for vacuum-chamber application if UV irradiation caused unacceptable increases in weight loss and quantity of volatile condensable materials. Acceptance criteria for this technique has not been established at the present time.

A material-usage-control board has been established by the MSC that has jurisdiction over all materials to be installed in the test chambers. Materials that have been tested but failed to meet the requirements just mentioned may be used if the performing organization can provide rationale for its use that is approved by this board. Usually, materials are approved that fail to meet the selection requirements if the material is the best available for the particular application; the quantity and surface area of the material is small, and not in the immediate vicinity of an optical element; and the material may be vacuum cured before use.

As a final safeguard against contamination introduction, all polymeric materials used in chamber A for the first time must be preprocessed by exposure to a room-temperature environment and maintained at a pressure less than 1×10^{-5} torr for at least 4 hr. All materials (including polymeric materials and metal assemblies) must be cleaned thoroughly with either

Freon TF or ethyl alcohol, inspected using the black-light technique, and wrapped in clean-room bags for handling before installation in the test chamber.

DIAGNOSTIC INSTRUMENTATION

Three basic objectives for contamination measurement in space-simulation chambers are to determine the effects of contamination in relation to sensitive experiments on the test vehicle, to identify the contaminants and determine their concentrations (qualitative and quantitative analysis), and to determine the sources of contamination. Several groups of instruments are used by the MSC and the NASA George C. Marshall Space Flight Center (MSFC) in the ATM program for accomplishing these objectives.

Vacuum Ultraviolet Reflectometers

An in situ reflectometer, or real-time contamination monitor (RTCM), was developed to monitor the degree of optical degradation resulting from the formation of surface films during thermal-vacuum tests. This instrument consists of a radiation source, detectors, and a first-surface (Al + MgF_2) mirror mounted on an optical bench. The system essentially is monochromatic and monitors reflectance changes on the mirror using the 1216-Å line (Lyman Alpha) emitted by the radiation source. A detailed description of this instrument is found in reference 2. Locations and operating environments for this instrument are shown in Figure 3 and Table IV. One of the reflectometers is shown in Figure 4.

Residual Gas Analyzers and Ionization Gages

Three systems are used for qualitative analysis of gaseous contaminants in the chamber-vacuum environment: monopole residual-gas analyzers, quadrupole residual gas analyzers and direction gas flow measurement (DGFM) systems. Locations and operating environments for these instruments are shown in Figure 3 and Table IV.

The monopole and quadrupole residual gas analyzers are standard instruments modified for use in large space-simulation chambers. Modifications to the quadrupole residual-gas analyzers included lengthening the electric cables between the analyzer head and control console to approximately 17 m, installing a special low-noise preamplifier at the analyzer head, and

changing mass coils for the radio frequency rf/dc generator inside the control unit. Modification to the monopole residual-gas analyzer (RGA) included lengthening the electric cables between the analyzer head and control unit and modifying the electronics within the radio frequency tank circuit. One of the quadrupole residual-gas analyzers is shown in Figure 4.

The DGFM System--The DGFM system is used to identify chamber leak sources and residual gases in the chamber environment. It also is used to determine locations of contaminant sources within the chamber. This system consists of two units. The first unit includes two pairs of ionization gages (one pair of redundancy) and a quadrupole RGA mounted on a rotatable platform within the chamber. The second system is identical to the first except that two millitorr gages are used in place of the quadrupole RGA and are used to locate chamber leak sources at higher chamber pressures (10^{-2} torr to 10^{-4} torr). The pressure gages and quadrupole RGA are equipped with tubulations to provide more accurate angular definition of a directional gas flow source. A detailed description of the DGFM is found in reference 10.

Quartz Crystal Microbalances

Two kinds of quartz-crystal microbalances are used to measure the quantity of molecular contamination that condenses on the reflectometer mirrors to produce reflectance changes. The first unit is a deposit thickness monitor (DTM) and the second unit is a quartz-crystal microbalance contamination monitor (QCM/CM). Locations and operating environments for these instruments are listed in Figure 3 and Table IV.

Both quartz-crystal microbalances basically consist of a sensing crystal, a reference crystal, and electronics for driving the crystals and producing an audio-beat frequency by mixing the fundamental crystal frequencies. The DTM has a sensing crystal located on the oscillator unit inside the chamber and a reference crystal located in the control unit outside the chamber. The QCM/CM has both crystals located in the oscillator unit inside the chamber.

The sensing crystal for both quartz-crystal microbalances is tuned initially below the reference crystal. As contamination condenses on the sensing crystal, it lowers its resonant frequency and, in turn, causes the frequency difference, or beat frequency, to increase. Changes in beat frequency are recorded because they are directly proportional to changes in mass on the sensing-crystal surface.

Analytical-Test Specimens

Three kinds of analytical specimens are used to obtain quantitative and qualitative information concerning condensable chamber contaminants: contamination-collection units, stainless-steel disks, and aluminum disks. Locations and operating environments for these specimens are listed in Figure 3 and Table IV.

Contamination-Collection Units--The contamination-collection units (CCU) are passive-sampling devices and are used to collect condensable contaminants from the chamber environment for post-test analysis. These specimens consist of a 30 by 30 by 0.5-cm Pyrex glass plate mounted in an aluminum frame. Fifteen contamination-collection units were used during recent tests. Three of the contamination-collection units are mounted in a temperature controlled ($5^{\circ} \pm 1^{\circ}$ C) test bed and are exposed individually during chamber pumpdown, test, and repressurization. The remaining contamination-collection units are not temperature controlled and are allowed to cool until they reach thermal equilibrium with the chamber-heat-sink panels. After the test is completed, the contamination-collection units are removed from the chamber, and contaminants are collected, identified, and concentrated for infrared- and gas-chromatographic analysis. A detailed description of contamination-collection unit analysis techniques is found in reference 11.

Stainless-Steel and Aluminum Disks--These test specimens also are passive-sampling devices and consist of two types that are exposed to the chamber environment at two temperatures. One group of specimens is mounted on two temperature controlled ($5^{\circ} \pm 1^{\circ}$ C) test beds. One test bed exposed the specimens to the chamber environment for the duration of the test. The other test bed is equipped with a four-section shutter arrangement and is controlled remotely to expose four different sets of specimens sequentially to the chamber environment for specific test phases (pumpdown, high vacuum, solar, and repressurization). The other group of specimens is placed in special holders or mounted individually at various locations within the chamber such as roughing lines and pump ports. These specimens are not temperature controlled. The deposits collected on both groups of disks are analyzed with infrared spectrophotometers and residual-gas analyzers after the test is completed.

Optical Test Specimens

These test specimens also are passive-sampling devices and consist of four types: quartz disks, Al + MgF₂ mirrors, platinum mirrors, and gold mirrors. These specimens are mounted on the temperature controlled test beds and also in the special holders that are not temperature controlled. The quartz disks and Al + MgF₂ mirrors also are mounted on selected contamination-collection units within the chamber. These specimens are removed from the chamber after the test is completed. Transmittance and reflectance measurements are made on the quartz disks and mirrors, respectively, to determine the degree of optical degradation subsequent to exposure to the test environment. An optical test bed is shown in Figure 5.

Test Results

Three contamination-verification tests, identified as tests V-1, V-2, and V-3, were conducted in chamber A at progressive stages of cleanliness to determine molecular-contamination levels present during test conditions. These conditions were defined as a chamber pressure of 1×10^{-5} torr or less and a liquid-nitrogen heat-sink panel temperature of 100° K or less. During these tests, the top solar simulator system was operated both intermittently and continuously at an intensity level of one-solar constant. The duration of the test phase, including solar-simulator operation, is listed for each test in Table V.

Test V-1 was conducted in December 1969 and was a base line test of the empty chamber to evaluate the contamination levels after system and procedural modifications previously discussed were incorporated. Test V-2 was performed during May 1970 to verify that the corrective actions required, subsequent to the V-1 test, had reduced the contamination levels for the chamber. Test V-3 was performed during July 1971, to verify that the chamber was still at the level of cleanliness obtained during the V-2 test and that the addition of such ATM support equipment as the infrared simulator and UV calibration sources did not degrade the clean environment.

Test V-1 - Contamination Verification

The molecular-contamination levels measured during this test were higher than for subsequent tests, although the test environment did meet the cleanliness requirements established

by the NASA. The test results are summarized in Table V. The average reflectance loss for the MSFC aluminized mirrors at a wavelength of 1216 Å was 7 percent. The maximum reflectance loss for these mirrors occurred at a wavelength of 2000 Å and was 15 percent. There was good correlation between this value and the reflectance losses recorded at this wavelength for the MSC aluminized mirrors that was 16 percent. A comparison between these data and the real-time reflectometer measurements could not be made because the reflectometers became inoperative early in the test. In addition to loss of the reflectometer data, no data were obtained from the residual-gas analyzers because these instruments also became inoperative early in the test.

The correlation obtained between the QCM real-time measurements and the CCU post-test analysis results were good also. The quartz-crystal microbalances were maintained at approximately 0° C during the test, whereas, the temperature of the contamination-collection units was uncontrolled. The quartz-crystal microbalances recorded an overall contamination level of $8 \times 10^{-7} \text{ g/cm}^2$. The CCU analysis results indicated an average contamination level of $6 \times 10^{-7} \text{ g/cm}^2$.

The dominant contaminants, as determined from analysis of the contamination-collection units, consisted of paraffinic hydrocarbons and alkyl phthalate esters. Silicones also were present on the contamination-collection units in trace amounts. The paraffinic hydrocarbons have saturated or slightly unsaturated long-carbon atom chains and are similar in many respects to mineral oil. The sources for these contaminants include human-skin oils, lubricant used on the diffusion-pump angle-valve shafts, various cutting oils and cooling formulations, and outgassing products from epoxy paints. The alkyl phthalate esters are typical components of tall oil alkyd resin-based paints. Heavy esters, alkyd resins, drying oils, and alcoholic ethers (cellosolves) are used as matrices for these paints and are the major outgassed materials (ref. 12). The most likely source for this contaminant is the black epoxy paint used on the chamber-heat-sink panels and lunar plane. The silicones are of the polydialkylsiloxane type and are similar to polymers of dimethylsiloxane. These silicones are different in chemical structure from silicone diffusion-pump oil that is a methyl-phenyltrisiloxane compound. Sources for the dimethylsiloxane include silicone oils, greases used on "O"-ring seals, rubbers, and sealants.

Analysis results of the analytical specimens indicated that mechanical-(roughing) pump fluids also were present in the test volume. Diffusion-pump oil was not found on the

contamination-collection units or analytical specimens in the test volume. This fluid was, however, found on the contamination-collection units placed behind the chamber heat-sink panels directly in front of the diffusion-pump ports. Trace amounts of this fluid were present in addition to the hydrocarbon lubricant used on the angle-valve shafts. The average contamination level for the contamination-collection units at this location was $10 \times 10^{-7} \text{ g/cm}^2$.

Corrective Actions

To reduce the contamination levels measured during the V-1 test and to maintain these levels below the acceptable limits for the ATM test program, several corrective actions were employed. First, unused mechanical fluid lines and electrical conduits inside the chamber were either removed or capped to limit contamination resulting from evaporation of oil films inside the fluid lines and outgassing of electrical wiring insulation inside the conduit. Second, materials inside the chamber such as electrical cables, wiring harnesses, cable ties, and tape were reviewed for outgassing properties. Materials that were unacceptable were either removed or replaced. Third, the common practice of lubricating O-ring seals with silicone oil or grease was discontinued. A new procedure was established that required these seals to be installed dry. Subsequent tests revealed this procedure did not adversely affect seal reliability. Finally, traces of grease and oil deposited on interior chamber surfaces during leak-checking operations were discovered and removed. A second contamination-verification test was performed after these corrective actions were implemented.

Test V-2 - Contamination Verification

The molecular-contamination levels measured during this test were lower than for the previous test and were within the cleanliness requirements established by the NASA for the ATM test program. The test results are summarized in Table V. The maximum reflectance loss was recorded for the MSC aluminized mirrors and was 14 percent. The reflectance loss recorded for the real-time reflectometer during the high-vacuum phase was 10 percent. However, these measurements are not representative of the cleanliness level of the chamber because reflectance losses for the MSC aluminized mirrors were not recorded at a wavelength of 1216 Å, and the real-time reflectometer was not maintained at a temperature near 20° C

as required by the acceptance criteria. Reflectance losses for the MSC mirrors were recorded at a wavelength of 2000 Å. The reflectometer showed a loss in reflectance when its mirror was cold and an increase in reflectance when it was warmed by radiation from the top solar simulator system.

The least reflectance losses were recorded for the MSFC aluminized mirrors on the test beds and are representative of the cleanliness levels of the chamber because reflectance measurements were made at wavelengths that included 1216 Å, and the mirrors were maintained at a temperature near 20° C during the test. The average reflectance loss recorded for the test bed mirrors exposed for the duration of the test was 4.9 percent. The average reflectance loss recorded for the test bed mirrors exposed during the solar phase and high-vacuum phase was 2.3 and 4.1 percent, respectively.

During this test, real-time gas-analysis data were recorded with the MSFC monopole RGA. The other residual-gas analyzers either became inoperative or malfunctioned, and presentable data were not obtained from them. Mass scans recorded with the monopole RGA primarily indicated an air leak, and occasionally higher molecular-weight peaks appeared that indicated the presence of alcohol. This compound probably was released when the helium cryopanel inadvertently warmed during the test. These peaks persisted for only a few hours. The presence of alcohol was attributed to cleaning agents used in the chamber before the test.

The correlation obtained between the QCM real-time measurements and the CCU post-test analysis results was again in good agreement. The quartz-crystal microbalances recorded an overall contamination level of 4×10^{-7} g/cm². The CCU analysis results indicated an average contamination level of 3×10^{-7} g/cm² for passive and temperature controlled contamination-collection units.

The dominant contaminant as determined from analysis of the contamination-collection units was a paraffinic hydrocarbon. Trace amounts of organic esters also were present; however, these substances were unidentifiable because of low concentrations. Evidence of mechanical-pump oils, silicone oils, and greases also were found on the contamination-collection units in extremely small concentrations. The temperature controlled contamination-collection units indicated the greatest quantity of contamination was deposited during chamber repressurization.

Approximately 4.5×10^{-7} g/cm² was collected during this phase, whereas, 1.83×10^{-7} and 0.14×10^{-7} g/cm² were deposited during pumpdown and test phases, respectively. Diffusion-pump

oil did not appear on any of the contamination-collection units in the chamber. The contaminants on the contamination-collection units facing the diffusion-pump ports were predominately hydrocarbons. The average contamination level at this location was approximately 4.3×10^{-7} g/cm².

Trace amounts of contaminants also were found on the analytical specimens located in the test volume. Only one specimen showed a significant amount of contamination. This particular sample was located between the chamber wall and heat-sink panels and collected approximately 3.4 mg of hydrocarbons.

Test V-3 - Contamination Verification

The molecular-contamination levels measured during this test were lower than for the two previous tests. These results indicated the cleanliness levels for the chamber were not degraded by the addition of the ATM support equipment. The test results are summarized in Table V. The real-time reflectometer showed a slight reflectance loss during the solar phase but gradually recovered during the remainder of the high-vacuum phase. This recovery is attributed to sublimation or evaporation of surface contaminants that condensed on the reflectometer mirror during the solar phase.

Optical data for the MSFC test bed specimens yielded reflectance values that were within the limits of the test criteria for all samples, except those under shutter no. 2 (high vacuum), which yielded marginal data. This was consistent with the results obtained in the V-2 test in that samples under shutter no. 2 showed the largest loss in reflectance. The reflectance losses for these samples were measured at 1600 Å because this is the strongest line in the hydrogen spectrum. Reflectance losses for the MSC samples were measured at 2000 Å and compared favorably with the losses for the samples placed under shutter no. 2 (12 percent and 11 percent, respectively). Again, these values do not relate directly to cleanliness acceptance criteria, inasmuch as the reflectance measurements were not recorded at a wavelength of 1216 Å.

The residual gas analyzers operated satisfactorily during this test, and data obtained with these instruments indicated that most molecular activity occurred during the solar phase when shutter no. 3 on the test bed was open. The activity began approximately 1 hr after initiation of the continuous solar burn and terminated 30 min after this phase was completed. These data are consistent with reflectance losses recorded with the real-time reflectometer that indicated maximum degradation occurred during the solar phase of the test cycle. These losses are attributed to the formation of surface films that occurred

when molecular contaminants were released from chamber surfaces warmed by the solar energy.

The correlation between the QCM real-time measurements and the CCU post-test analysis results was again in good agreement. The data listed in Table V for the temperature controlled contamination collection units indicated that maximum contamination occurred during pumpdown. Approximately

$0.32 \times 10^{-7} \text{ g/cm}^2$ was collected during this phase, whereas, an insignificant amount was deposited on the contamination-collection units during the high-vacuum phase and repressurization. The quartz-crystal microbalances also measured contamination during pumpdown. Contaminants that deposited on these instruments during this time began to slowly evolve once test conditions were achieved. The quartz-crystal microbalances continued to recover throughout the high-vacuum phase.

The CCU analysis results revealed that the contaminants in the test volume were predominantly hydrocarbons. Trace amounts of esters and silicones (including diffusion-pump oil) also were present on the CCU. The contamination-collection units facing the diffusion-pump ports collected the greatest quantity of contamination. Traces of diffusion-pump oil also were found on these contamination collection units. The average quantity of contamination for the CCU at this location was

$2.75 \times 10^{-7} \text{ g/cm}^2$, whereas, the test volume average was $0.84 \times 10^{-7} \text{ g/cm}^2$.

The CCU near the real-time reflectometers indicated a contamination level that was much greater than the average throughout the chamber. A quantity of $1.3 \times 10^{-7} \text{ g/cm}^2$ was measured at this location. The quartz disk on this unit indicated severe optical degradation (-49 percent). The predominant contaminant was found to be tape residue. A severe reflectance loss was observed for the MSC real-time reflectometer during chamber repressurization. During this time, the mirror reflectance fell from approximately 71 percent to 35 percent. These losses were attributed to condensation of tape residue that was released under high temperatures when electrical power cables for the ATM infrared simulator began to inadvertently arc or short circuit during repressurization.

Summary and Conclusions

The results of the last two contamination-verification tests revealed that a large thermal-vacuum test chamber can be

operated to produce a minimum contamination environment suitable for testing advanced spacecraft carrying sensitive optical experiments. With the measurement techniques used, it has been possible to identify partially and to measure accurately contaminants present under high-vacuum conditions during any specific test. Several general observations may be made as a result of these tests.

1. Contamination traceable to the four oil-diffusion pumps was not detected in the shrouded chamber volume during the first two tests. Only slight traces were detected during the last test.

2. Measurements obtained from the optical samples and real-time reflectometer indicate that chamber A is acceptable for Apollo telescope mount use according to the established test criteria.

3. Residual-gas-analyzer data detected gaseous molecular contaminants within the shrouded chamber volume at various phases during the test cycle. Most molecular activity occurred during the continuous solar burn. The optical samples exposed during this time experienced minor reflectance losses. The contaminants present are either transparent to the wavelengths being scanned or are not condensing on the $\text{Al} + \text{MgF}_2$ surfaces.

Future spacecraft may require more stringent contamination requirements and functional testing much longer than experienced at the present time. This will impose a severe constraint on environmental test engineers in selection of chamber materials and development of new diagnostic instrumentation. Future tests will require assurance that the test facility is clean and that the test environment presents a minimum contamination hazard.

REFERENCES

1. Wolff, C. M.; and Ritter, M. L.: Contamination Measurement in Space Environment Simulation Chambers, NBS Special Publication 336, U.S. Government Printing Office, Washington, D.C., 1970.
2. Hass, G.; and Hunter, W. R.: Laboratory Experiments to Study Surface Contamination and Degradation of Optical Coatings and Materials in Simulated Space Environments. Applied Optics, vol. 9, no. 9, Sept. 1970, pp. 2101-2110.
3. NASA MSC Standard C-4: Clean Rooms and Work Stations. Oct. 1966.
4. Bergquist, L. E.: Measurement of Contamination in Vacuum Chambers. Paper presented at the ASTM/IES/AIAA 2nd Space Simulation Conference, Sept. 1967.

5. Oswald, R. D.; and Crawley, D. J.: A Method of Measuring Back Migration of Oil Through a Baffle. *Vacuum*, vol. 16, no. 11, pp. 623-624.
6. BRN/SESL Technical Report: Diffusion Pump A-1 Backstreaming Test. Rept. 169-06-21, Feb. 1970.
7. Feder, D. O.; and Koontz, D. E.: Detection, Removal and Control of Organic Contaminants in the Production of Electron Devices. Paper presented at ASTM Symposium on Cleaning of Electronic Device Components and Materials, STP 246, 1959, pp. 40-63.
8. Santeler, D. J.; Holkeboer, D. H.; Jones, D. N.; and Pagano, F.: Vacuum Technology and Space Simulation. NASA SP-105, 1966.
9. NASA Specification: Vacuum Stability Requirements of Polymeric Material for Spacecraft Application. SP-R-022, Dec. 1969.
10. Ehlers, H. K. F.: Directional Molecular Flow Analysis and Leak Detection with a Rotatable Gas Analyzer in a Large Space Simulation Chamber. Paper presented at the 6th IES/AIAA/ASTM Space Simulation Conference, 1972.
11. Wolff, C. M.: Some New Techniques in Passive Contaminant Analysis of Space Environment Simulation Chambers. Paper presented at the 6th IES/AIAA/ASTM Space Simulation Conference, 1972.
12. Hummel, D. O.: Infrared Spectra of Polymers. *Inter-science*, 1966.

TABLE I. - EVALUATION OF DETERGENT SOLUTIONS FOR CHAMBER A CLEANING APPLICATION^a

Detergent	Test fluid				
	Houghto-Safe 1055 ^b	Houghto-Safe 1120 ^b	SunVis 706 ^c	DC 705 ^d	DC 11 ^e
No. 1 (boiling) percent remaining weight, g/cm ²	0.89 percent 1.7×10^{-7}	0.79 percent 1.6×10^{-7}	5.0 percent 0.1×10^{-6}	0.07 percent 0.1×10^{-7}	116 percent 2.3×10^{-5}
No. 2 (boiling) percent remaining weight, g/cm ²	0.66 percent 1.3×10^{-7}	0.86 percent 1.7×10^{-7}	5.8 percent 1.2×10^{-6}	0.47 percent 1.0×10^{-7}	67.7 percent 1.4×10^{-5}
No. 3 (boiling) percent remaining weight, g/cm ²	0.53 percent 1.0×10^{-7}	0.69 percent 1.4×10^{-7}	4.3 percent 9.0×10^{-7}	0.22 percent 0.4×10^{-7}	6.4 percent 1.3×10^{-6}
No. 4 (room temp.) percent remaining weight, g/cm ²	0.66 percent 1.3×10^{-7}	0.40 percent 0.8×10^{-7}	4.3 percent 9.0×10^{-7}	0.17 percent 0.3×10^{-7}	6.4 percent 1.3×10^{-6}

^aQuartz disks contaminated with 2×10^{-5} g/cm² of sample.

^bHoughto-Safe 1055 and 1120 are phosphate ester fluids used as mechanical-pump oil.

^cSunVis 706 is a hydrocarbon used as hydraulic fluid for the diffusion-pump angle valves.

^dDC 705 is a silicone diffusion-pump oil.

^eDC 11 is a silicone grease used as an O-ring sealant.

^fMass increase is a result of soap residue remaining on contaminated disk.

**TABLE II. - CHAMBER A PARTICULATE CONTAMINATION
LEVELS FOR AMBIENT ENVIRONMENTS**

Chamber status	Before cleaning		After cleaning	
	Particles/28.3 l			
	>0.5μ	>5.0μ	>0.5μ	>5.0μ
Access doors closed - recirculation blower on - one man in the chamber	9 000	80	800	14
Access doors closed - recirculation blower on - 12 men in the chamber	17 960	231	1 400	12

TABLE III. - WIPE-SAMPLE ANALYSIS RESULTS FOR REPRESENTATIVE CHAMBER A
INTERIOR LOCATIONS

Wipe-sample location	Contamination (10^{-7} g/cm ²)							
	Before cleaning				After cleaning			
	H/C ^a	Ester ^b	Silicone ^c	D/P fluid ^d	H/C ^a	Ester ^b	Silicone ^c	D/P fluid ^d
Backside of liquid nitrogen panel, facing diffusion-pump port	20.0	6.0		18.0	1.4			3.0
Front side of liquid nitrogen panel midchamber level, southeast side	3.6	1.3						
Front side of liquid nitrogen panel midchamber level, southwest side	5.5	2.4			5.6	0.82		
Roughing duct entrance	34.0	23.0	1.9	2.5	8.9	17.0	trace	
Chamber wall, below lunar plane	11.0	5.4	9.3		1.0			

^aH/C - paraffinic hydrocarbon.

^bEster - alkyl phthalate ester.

^cSilicone - polydialkylsiloxanes.

^dD/P fluid - diffusion-pump fluid.

TABLE IV. - CHAMBER A CONTAMINATION-MEASUREMENT SYSTEMS

System	Instrument	Quantity		Operating conditions		Purpose
		MSC	MSFC	Pressure	Temperature	
Reflectometer	RTCM	1	3	$<10^{-3}$ torr (P, T) ^{a, c} <600 torr (R) ^b $<10^{-3}$ torr	20° C 20° C (I) Uncontrolled (2)	Optical effects measurement
Total and partial pressure analyzers	DGFM	2		$<10^{-2}$ torr	N/A	Directional gas flow analysis
	Monopole RGA		1	$<10^{-4}$ torr	N/A	Qualitative measurement
	Quadrupole RGA	1	2	$<10^{-4}$ torr	N/A	
	Ionization gages		3	$<10^{-4}$ torr	N/A	Total pressure measurement
Quartz-crystal microbalance	DTM		2	≤ 760 torr	5° C	Quantitative measurement
	QCM/CM	2	1	≤ 760 torr ≤ 760 torr	20° C Uncontrolled	
Analytical and optical test specimens	Passive contamination-collection units and analytical specimens	12	24	≤ 760 torr	Uncontrolled	Quantitative, qualitative, and effects measurement (post-test)
	Passive optical samples	8	24	≤ 760 torr	Uncontrolled	
	Temperature controlled contamination-collection units	1		$>10^{-5}$ torr (P) ^a	5° C	
		1		$<10^{-5}$ torr (T) ^c	5° C	
		1		$>10^{-5}$ torr (R)	5° C	
	Temperature controlled contamination-collection units optical samples	6		$>10^{-5}$ torr (R)	5° C	
		8	24	≤ 760 torr	5° C	
	Open test bed optical samples and analytical specimens	8	24	≤ 760 torr	5° C	
	Shuttered test bed optical samples and analytical specimens	2	8	$>10^{-5}$ torr (P) ^a	5° C	
		2	8	$<10^{-5}$ torr (T) ^c	5° C	
		2	8	$<10^{-5}$ torr (S) ^d	5° C	
		2	8	$>10^{-5}$ torr (R) ^b	5° C	

^a(P) = Pumpdown.^b(R) = Repressurization.^c(T) = Test phase.^d(S) = Solar phase.

TABLE V. - CHAMBER A CONTAMINATION-VERIFICATION-TEST SUMMARY

Instrument	Chamber A ATM contamination-measurement tests representative data			
	H/C> Ester>>Silicone ^a		H/C> Ester>>Silicone ^a	
	ATM V-3 (July 1971)	ATM V-2 (May 1970)		ATM V-1 (Dec. 1969)
I. RTCM - $\Delta R/R$ at 1216 Å Solar phase High-vacuum phase	-1.41 percent +0.70 percent	+4.1 percent -10.0 percent		(e)
II. MSC aluminum mirrors - $\Delta R/R$ at 2000 Å ^b Test volume average Passive CCU average	-12.2 percent -11.0 percent	-14.0 percent (f)		-16.0 percent (f)
III. MSFC aluminum mirrors - $\Delta R/R$, average ^b Shuttered test bed Shutter no. 1 (roughing) Shutter no. 2 (high vacuum) Shutter no. 3 (solar) Shutter no. 4 (repressurization) Test bed at 1.5-m elevation Test bed at 5.8-m elevation	1600 Å -2.5 percent -11.0 percent -2.0 percent -1.0 percent -0.6 percent (f)	1150 Å -1.9 percent -11.5 percent -7.9 percent -7.5 percent -7.8 percent -11.2 percent	1216 Å -2.4 percent -4.1 percent -2.3 percent -3.45 percent -4.25 percent -5.55 percent	(f) 1216 Å 1600 Å 2000 Å -7 percent -5 percent -15 percent (f)
IV. QCM/CM - 10^{-7} g/cm ² Solar phase High-vacuum phase	-0.75 -0.25	+1.1 +4.0		+3.1 +8.0
V. MSC CCU analysis - 10^{-7} g/cm ² Test volume average Diffusion pump average CCU 1-3 (roughing) CCU 1-4 (high vacuum) CCU 1-5 (repressurization)	0.84 2.75 0.32 0.00 0.04	3.0 4.3 1.83 0.14 4.47		6.0 10.0 (f) (f) (f)
VI. MSC quartz disks - $\Delta T/T$ at 2000 Å ^c Test volume average Passive CCU average MSFC test bed average	-6.0 percent -5.7 percent -12.8 percent	-2.8 percent -2.7 percent -6.1 percent		-4.5 percent -4.5 percent -3.9 percent
VII. Test time, hr ^d	82 (40)	120 (31)		61 (31)

^aDominant contaminants are listed for each test in decreasing order of concentration; H/C represents paraffinic hydrocarbons; ester-alkyl phthalate esters; and silicone-polydialkylsiloxanes.

^b $\Delta R/R$ is percent change in optical (specular) reflectance.

^c $\Delta T/T$ is percent change in optical transmittance.

^dFirst value is for time at high vacuum; second value is for time of solar operation.

^eInstrument inoperative during test.

^fInstrument/samples not used for test.

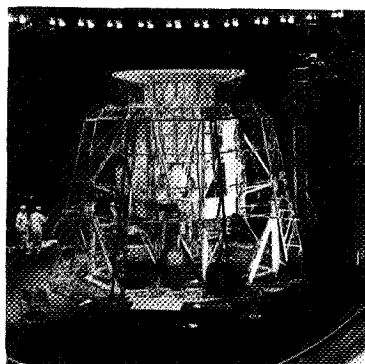


Fig. 1—Chamber A ATM test configuration

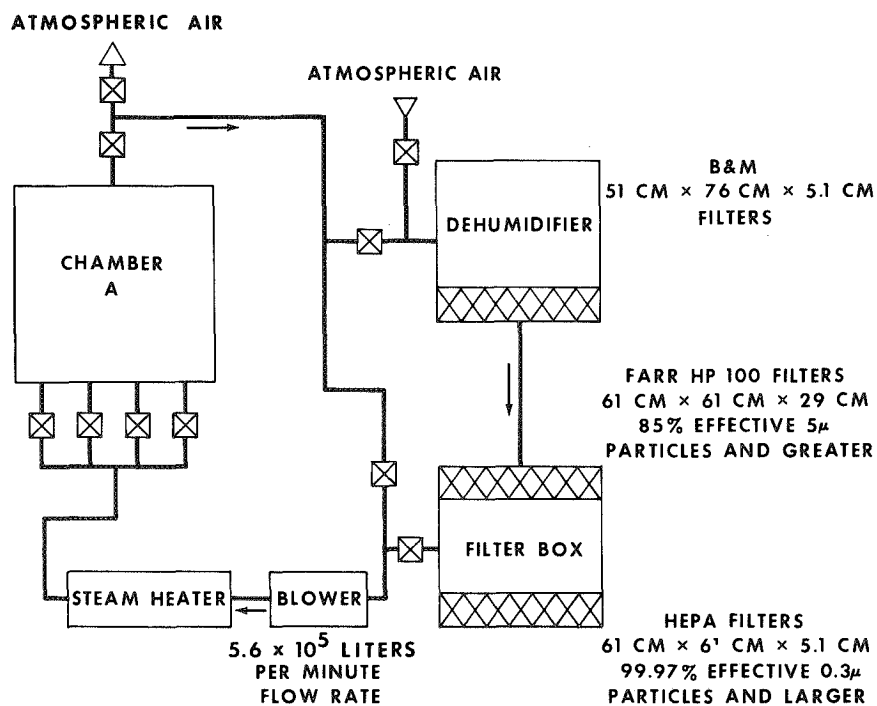


Fig. 2—Chamber A air recirculation system

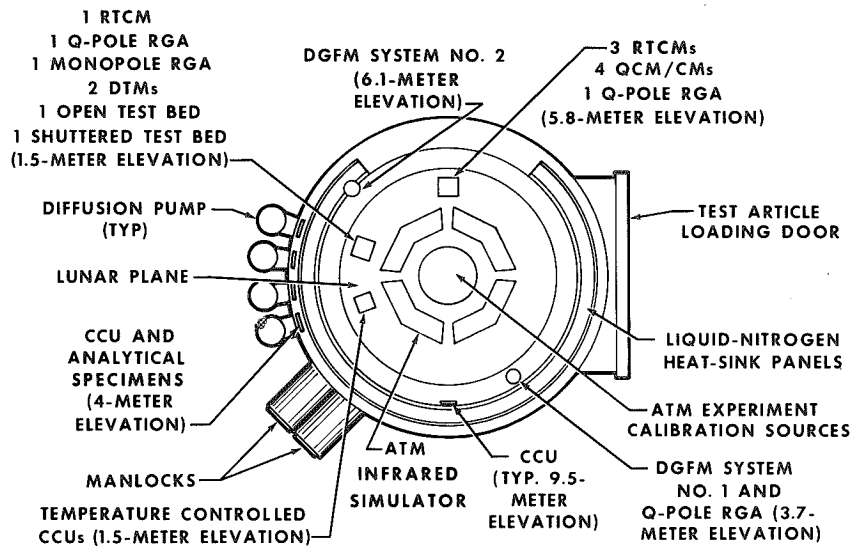


Fig. 3—Plan view for A contamination measurement systems location for V-3 verification test

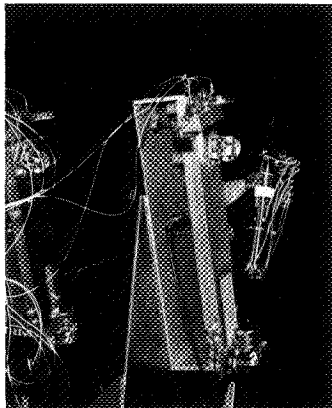


Fig. 4—MSFC RTCM and quadrupole RGA

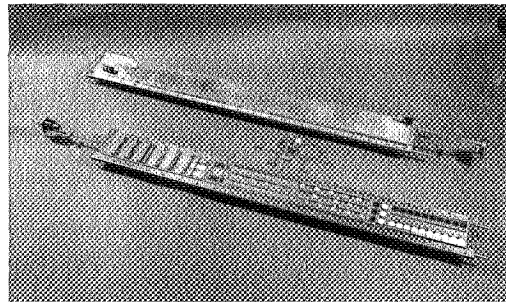


Fig. 5—MSFC open test bed

V-3 CONTAMINATION TEST IN THE MANNED SPACECRAFT CENTER'S VACUUM CHAMBER-A

Philip W. Tashbar, Daniel B. Nisen, and W. Walding Moore, Jr., *Marshall Space Flight Center, Huntsville, Alabama*

ABSTRACT

During the summer of 1971, an operational checkout test of the Manned Spacecraft Center's Chamber-A vacuum facility was performed. The V-3 Contamination Test was designed to measure the degree to which the vacuum facility might be a source of contamination. This report details one test measurement subsystem consisting of a quadrupole residual gas analyzer (RGA), a quartz crystal microbalance (QCM), and an ion gauge, and the test measurements made.

INTRODUCTION

The Apollo Telescope Mount (ATM) is a manned solar observatory that is to be placed above the earth's atmosphere. The ATM is capable of observing, monitoring, and recording the structure and behavior of the sun. The ATM instruments will provide data in the white-light, the ultraviolet, and the X-ray regions of the spectrum. Observations will be conducted both within and near the solar disc. The ATM is a part of NASA's Skylab and orbital workshop (Fig. 1) and is interfaced onto the Skylab's Multiple Docking Adapter (MDA). The attitude of the orbital workshop and the ATM will be in the solar inertial mode, with the solar panels maintained perpendicular to the sun for experiment operations. The ATM experiments are housed in a cylindrical canister which is compartmented by a cruciform-shaped longitudinal spar structure dividing the cylinder into four equal quadrants.

Since early orbital flight experiments, it has been recognized that there is a contamination threat from spacecraft effluences which could degrade optical experiments through scattering of signals and deposition onto critical surfaces, i.e., the ATM optical environment may be contaminated. Contamination sources from large space stations, such as Skylab,

include outgassing of materials, fuel-cell purging, Reaction Control System (RCS) engine firings, waste disposal, and space station gaseous leaks. A more impending threat is the ATM internal contamination and contamination of the ATM optics from vacuum chamber contaminants during ground testing. Since in orbit and in some cases from vacuum chamber solar suns (depending on wavelength cut-off) the ultraviolet component of the solar spectrum possesses sufficient energy per quantum to ionize and dissociate contaminants, a polymerized contaminant film can be formed on the ATM optics. This crosslinked deposit can have entirely new optical properties that would not be expected from any of the individual contaminants depositing in the absence of UV radiation.

The V-3 Contamination Test was performed in vacuum Chamber-A of the Space Environment Test Division at the Manned Spacecraft Center (MSC) in Houston, Texas. The objective of the test was to verify that Chamber-A and its associated systems and vehicle support equipment would not be a source of contamination to the ATM optical instruments. The ATM is scheduled to be tested at MSC later this year.

Chamber-A

Chamber-A is a stainless steel vacuum chamber 19.81 meters in diameter and 36.58 meters high. The chamber is housed in the high-bay structure of building 32 at the Manned Spacecraft Center. The pumping system for the chamber includes mechanical and diffusion pumps and a 20°K cryopump employing gaseous helium. Black, heat sink, nitrogen-cooled panels line the interior of the chamber and operate at approximately 90°K. The chamber is also equipped for solar simulation from the top and from one side. Chamber-A is equipped with eighteen diffusion pumps, but only four were used for this test.

The cleaning procedure for the interior of the chamber, prior to the test, included cleaning the side and top sun with Freon. The chamber was cleaned with deionized water and Penn-6 from the 2.44-meter level to the bottom of the plenum, and all chamber surfaces were cleaned with deionized water. In addition, chamber surfaces exhibiting 3×10^{-6} kg/m² of contamination were cleaned with Freon.

Test Requirements

One test requirement specified that the chamber pressure

was to be held at 1.333×10^{-4} N/m² (1×10^{-6} Torr) for a period of 2.52×10^5 seconds (70 hours) minimum. This was amended during the test to 2.666×10^{-4} N/m² (2×10^{-6} Torr) due to leaks from the chamber exterior. All the liquid nitrogen panels, as well as the lunar plane, were to be cooled by LN₂ to 100°K or lower. A minimum of five gaseous helium panels were to be cooled to approximately 20°K. Gaseous nitrogen was used for the repressurization cycle of the test.

The top sun and an IR cage provided the solar simulation for this test. They were operated for 7.2×10^4 seconds (20 hours) in cyclic operation of 3.6×10^3 seconds (1 hour) on and 1.8×10^3 seconds (1/2 hour) off, 7.2×10^4 seconds (20 hours) of continuous burn, and 1.08×10^5 seconds (30 hours) of IR cage on with top sun off. The contamination limits for this test specified that during the 1.44×10^5 seconds (40 hours) of solar operation, the Naval Research Laboratory's Real Time Contamination Monitor (RTCM) was to show no more than 5 percent reflectance loss when monitoring a light source of the Lyman-alpha wavelength of hydrogen. For the total test of 2.52×10^5 seconds (70 hours), this RTCM was not to exceed 10 percent total reflectance loss.

Test Configuration

The contamination monitoring instrumentation was located on a 5.79-meter high platform inside Chamber-A on the north axis just outside the IR cage. Figure 2 shows the IR cage encircling the square ring. The square ring is the support stand for the ATM. In the left background is the platform that supports the contamination detectors. The detectors included a quartz crystal microbalance (QCM), a quadrupole residual gas analyzer (RGA), and an ion gauge. The RGA (Fig. 3) was used in conjunction with the Naval Research Laboratory's RTCM. The RGA was mounted so that its ion source could view any contaminants re-evolving from the RTCM mirrors when the mirrors are heated. The RTCM measures the changes in reflectance of a mirror surface at 121.6 nanometers (1216 \AA), the Lyman-alpha line of hydrogen. The RTCM was designed and built by William R. Hunter of NRL. Figure 4 shows the two-piece QCM and ion gauge mounted on the stand and viewing the center of the chamber. Figure 5 is a view of the FI-4 chamber penetration that carried through the electrical, water, and gas lines to the contamination detectors. The data acquisition equipment (Fig. 6), from right to left, consisted of a Hewlett Packard X-Y recorder, an ATEC frequency counter, a Hewlett Packard 2010 data acquisition

system, a Pace thermocouple reference junction for copper-constantan referenced to 3.389×10^2 °K, and the quadrupole electronics console. On the extreme left of Figure 6 is NRL's RTCM electronics rack and an IBM card reader.

Quartz Crystal Microbalance (QCM)

The purpose of the QCM is to detect and measure mass deposition of contaminants on a real-time basis. The two-piece QCM (Fig. 7) used in the V-3 Contamination Test is a qualification unit for the QCM flight unit that is to fly on the T-027 sample array. This sample array will be deployed through the Scientific Airlock of the Skylab. Also, there will be two and four one-piece QCM's on the ATM sunshield and near the EREP, respectively.

The Atlantic Research Corporation of Costa Mesa, California, under the supervision of Robert J. Naumann and Philip W. Tashbar, designed and built the QCM quality and flight units. Testing of these QCM units was performed in the Atmospheric Laboratory of the Space Sciences Laboratory of Marshall Space Flight Center.

The sensor for the QCM is made up of two identical AT-cut quartz crystals, each operating at approximately 10 MHz. The pair of crystals is mounted in a sandwich between a metal ring to minimize the temperature gradient between them. The sensing crystal operates with its sensing area exposed to the contaminants to be monitored. The reference crystal is shielded from the contaminants. A thermistor, located on the reference side of the metal ring, monitors the crystal temperature. The resonant frequencies of the reference and sensing crystal are subtracted, yielding an audio signal that shifts upward in frequency as mass accumulates. Since thermal tracking between the sensing and reference crystal is not precise for the large temperature excursions found in orbit, a temperature-versus-frequency curve is provided to correct the frequency for mass deposition calculations.

The QCM electronics is hermetically sealed in a stainless steel container to prevent self-contamination of the quartz crystals. Argon is injected and sealed in the container at 1.515×10^5 N/m². The quartz crystals in the QCM have the following specifications:

Frequency	10 MHz
Angle of Cut	$0.6165 \text{ radians} \pm 3.0 \times 10^{-4}$
Thickness	$1.27 \times 10^{-4} \text{ meters}$
Diameter	$1.236 \times 10^{-2} \text{ meters} \pm 2.54 \times 10^{-4}$

Quadrupole Residual Gas Analyzer

The quadrupole RGA (Fig. 8) is an Electronic Associates, Inc. (EAI) Model Number 250A nude head that has a normal operating distance of 1.8288 meters from its electronics console. For this test the quadrupole head was operated at 42.67 meters from its electronics console. This was accomplished by designing an RF link between the RF-DC generator and the quadrupole head.

The EAI quadrupole RGA uses a group of four cylindrical rod-shaped electrodes that have superimposed on them DC and RF voltages balanced about ground. These DC and RF potentials provide the filtering action, and only ions with a specific mass-to-charge ratio reach the detector. Ions of heavier and lighter masses are deflected away from the quadrupole's axis and hit the rods.

The ionization source for the quadrupole head was EAI's 353 single-filament axial cross-beam ionizer. This was later changed for the ATM prototype thermal vacuum test. The ion source change consisted of modifying the quadrupole head to accept EAI's dual filament 1330 axial cross-beam ionizer. Both types of ionizers required modification of the filament cables for operation at 43 meters due to the increase of cable resistance. EAI's ion sources are current regulated.

The detector for the quadrupole head is a 14-stage beryllium-copper electron multiplier. The output signal from the electron multiplier was carried over 42.67 meters of 50-ohm coaxial cable and fed into an ESA-75 solid state electrometer. This electrometer is capable of measuring input currents ranging from 10^{-4} to 10^{-12} amps. The increased cable length required that the scan rate for the quadrupole be set at slow speeds. This was due to the increased RC time constant created by the additional capacitance of the coaxial cables and the one-megohm input resistance required by the electron multiplier. Scan rates above some threshold speed rates distorted the shape of the mass peaks.

Pressure Gauge

The pressure gauge used in the test was Varian Associates' dual-filament nude ionization gauge. This gauge will measure pressures from 1.333×10^{-2} N/m² (10^{-4} Torr) to 1.333×10^{-8} N/m² (10^{-10} Torr). For operation at 42.67 meters, larger wires were used for the filament cables to reduce resistance, and two resistors in the filament circuit were removed.

RF Link

The RF-DC generator supplies the proper voltage to the quadrupole rods. The DC/RF voltage ratio determines both the resolution and sensitivity of the quadrupole. As the DC and RF voltages are swept, ions pass through the quadrupole in order of increasing mass. The quadrupole's RF-DC generator was set for the mass range 10-250 AMU at a frequency of 3.3 MHz. Modifications, to be detailed at a later time, made the adjustment of the RF-DC generator independent of cable length. These included coupling coils at each end of the coaxial line such that their reactance at 3.3 MHz becomes equal to the characteristic line impedance. Overall, the instrument's operation in the laboratory provided acceptable mass spectra scans; and with additional designing and precise workmanship, the instrument should perform on an equal basis with standard cable length systems.

Test Results

The pumpdown of the chamber began at 1200 hours on July 12, 1971. Figures 9 through 13 are graphs of the QCM frequency, the thermistor temperature of the reference crystal, and the pressure of the chamber versus time of the test. At approximately 1944 hours (Fig. 9), cryopumping in the chamber began. At 1947 hours diffusion pump number 2 was brought on line.

On July 13, 1971, at 0151 hours (Fig. 10), three additional diffusion pumps were brought on line. At 0250 hours the heaters were activated on the nitrogen purge line that attaches to the ATM canister. The QCM detected this latter event by recording 10^{-6} kilograms of contaminants which had a stay time of 1.08×10^4 seconds (3 hours). Since the QCM's operation was saturated for this event and later returned to its normal operating frequency, water is thought to be the contaminant. This was later confirmed by one of the authors (WWMJ) using the QCM

and exposing it to water, nitrogen, and argon dumps while under the same vacuum conditions. The water dumps gave positive results. At 0600 hours the IR cage in the chamber and the top sun were turned on for the 7.2×10^4 -second (20-hour) cyclic operation of 3.6×10^3 seconds (one hour) on and 1.8×10^3 seconds (1/2 hour) off. At this time, the water vapor evolved from the QCM's crystal surface. This 7.2×10^4 -second (20-hour) solar cycling operation ended at 0130 hours on July 14, 1971. (Note, in Figure 9, the tracking of the QCM frequency with the change in thermistor temperature due to the solar cycling.) At this time, the quadrupole RGA was inoperative due to a shorted filament in the ion source.

On July 14, 1971, at 0200 hours (Fig. 11), the IR cage and the top sun were switched on for a 7.2×10^4 -second (20-hour) continuous burn. Beginning at approximately 1200 hours, the QCM detected, in a span of 7.2×10^3 seconds (2 hours), contaminants of 4.6×10^{-9} kg, 5.5×10^{-9} kg, and 5.8×10^{-9} kg, respectively. The average stay time for these contaminants was 1.8×10^3 seconds (1/2 hour). Note that the thermistor temperature was stable for this period of the test. No correlation with chamber events has been made at this time. At 2200 hours the cold-soak phase of the test began.

At 0030 hours on July 15, 1971 (Fig. 12), 3×10^{-9} kg of contaminants deposited on the QCM and had a stay time of 1.8×10^3 seconds (1/2 hour). The spikes on the pressure curve are due to inert gases being purged through an ultraviolet source that is being calibrated on the inside of the chamber. These gases included helium and a helium-neon mixture.

On July 16, 1971, at 0400 hours (Fig. 13), the diffusion pumps were turned off and the chamber warmup sequence began. At 0420 hours heating of the lunar plane was initiated. In-bleed of warm nitrogen was started at 0612 hours to bring the chamber pressure up to around 5.332×10^2 N/m² (4 Torr). At this time, the QCM became saturated and stopped oscillating for 2.16×10^4 seconds (6 hours). The IR cage was turned on to one-third maximum at 0603 hours, and at 0725 hours the lunar plane reached a temperature of 280°K. At 1750 hours the nitrogen in-bleed was increased. Note the spike on the QCM frequency curve for this event.

Conclusions

There were no long-time effects from the contaminants

detected by the QCM. Whether these contaminants would degrade the ATM optics is now being determined by processing in correlation with NRL's RTCM data analysis. A comprehensive picture of whether these or any other type of contaminants mentioned will degrade the ATM optics can only be assessed after laboratory optical contamination experiments are performed in the presence of ultraviolet radiation.

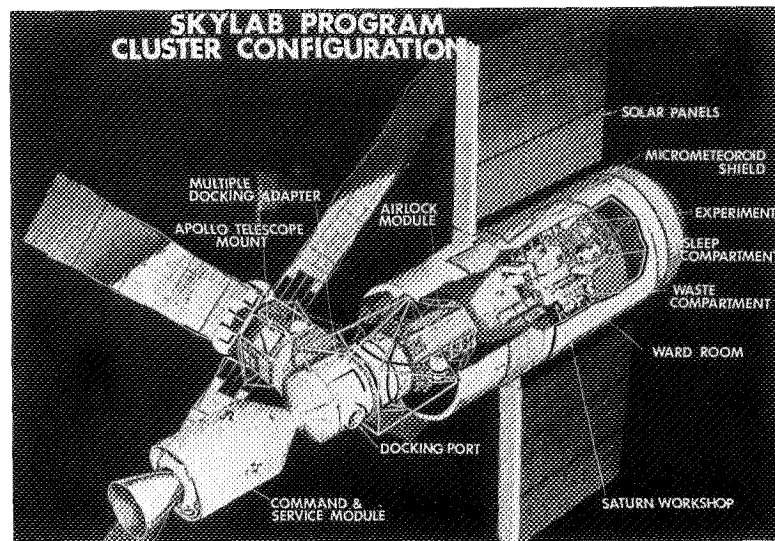


Fig. 1. Skylab Program cluster configuration.

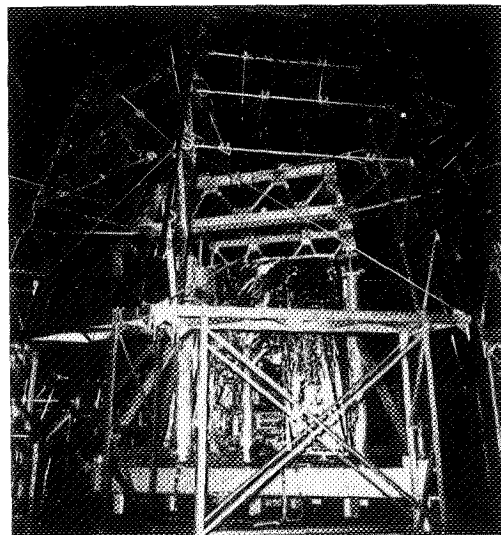


Fig. 2. The IR cage encircling the square ring inside Chamber-A.

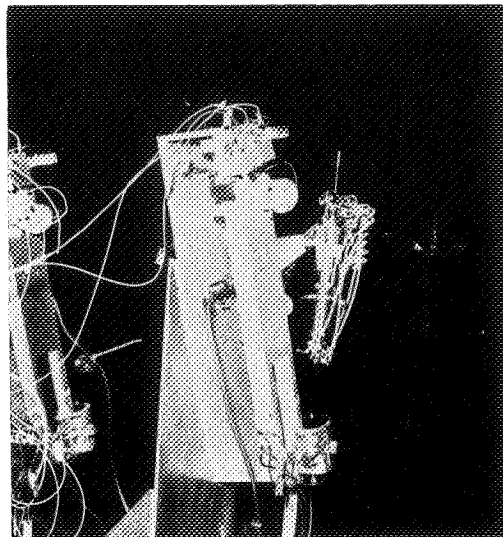


Fig. 3. The quadrupole RGA viewing the RTCM mirror.

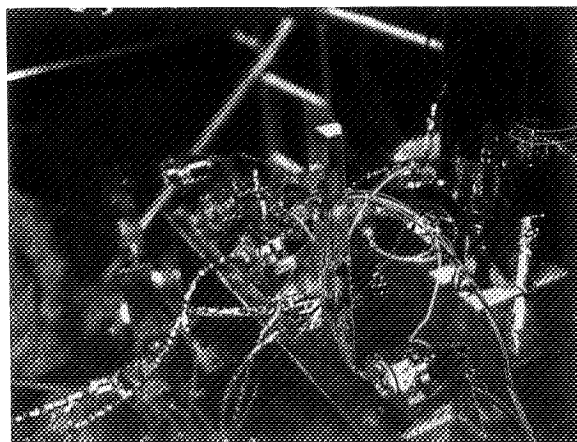


Fig. 4. The QCM and ion gauge viewing the center of Chamber-A.

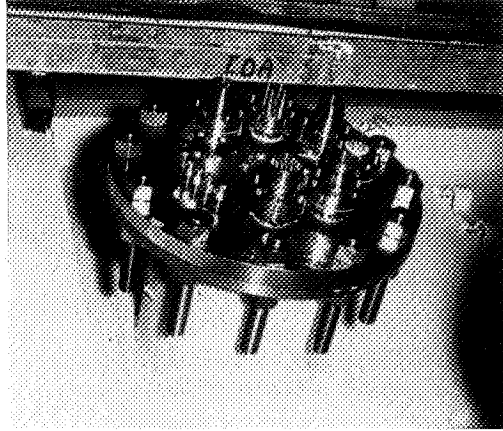


Fig. 5. FI-4 Chamber-A penetration that carried through the electrical, water, and gas lines to the contamination detector.

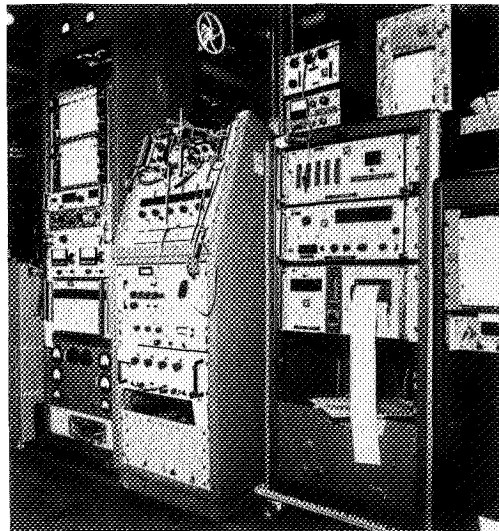


Fig. 6. Contamination detector data acquisition equipment.

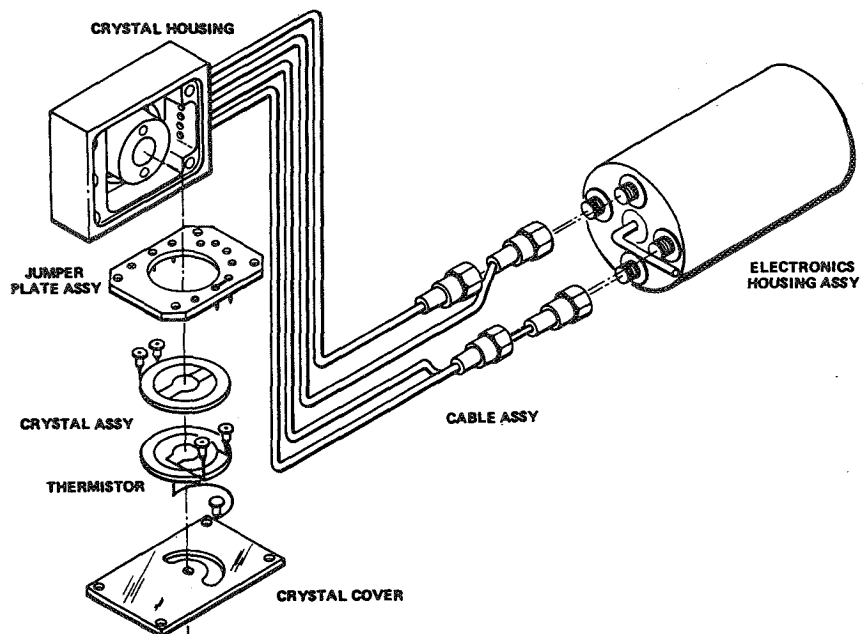


Fig. 7. Exploded view of the two-piece QCM.

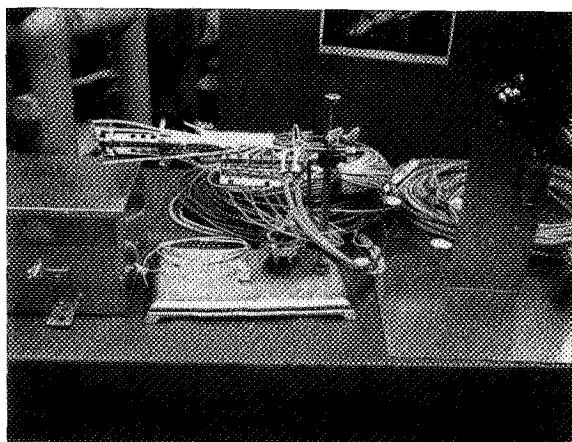


Fig. 8. Nude quadrupole detector head in mounting configuration plus ion gauge and QCM.

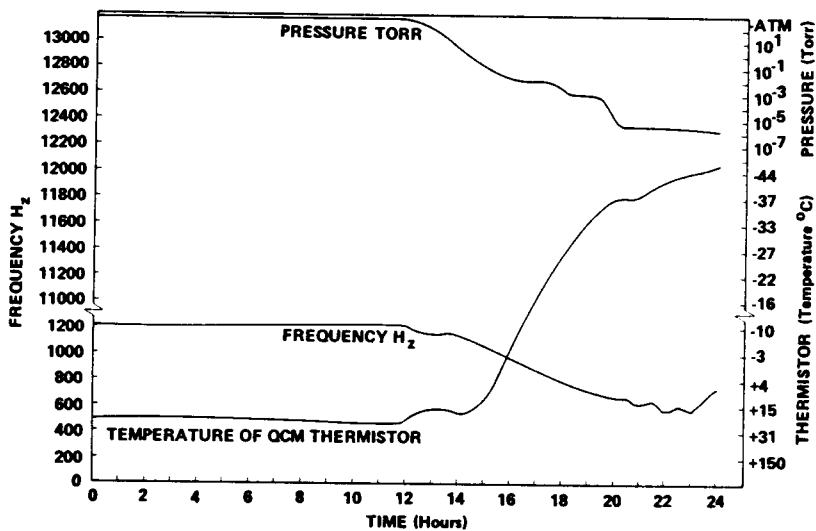


Fig. 9. QCM data, V-3 Contamination Test, July 12, 1971.

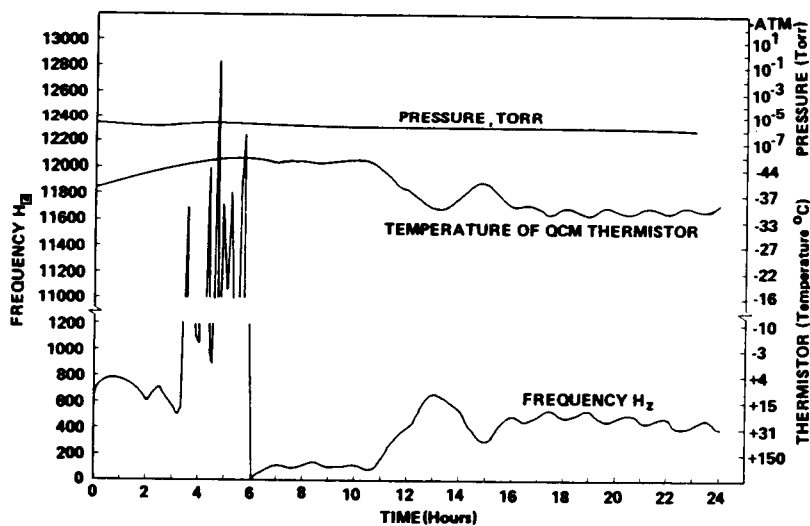


Fig. 10. QCM data, V-3 Contamination Test, July 13, 1971.

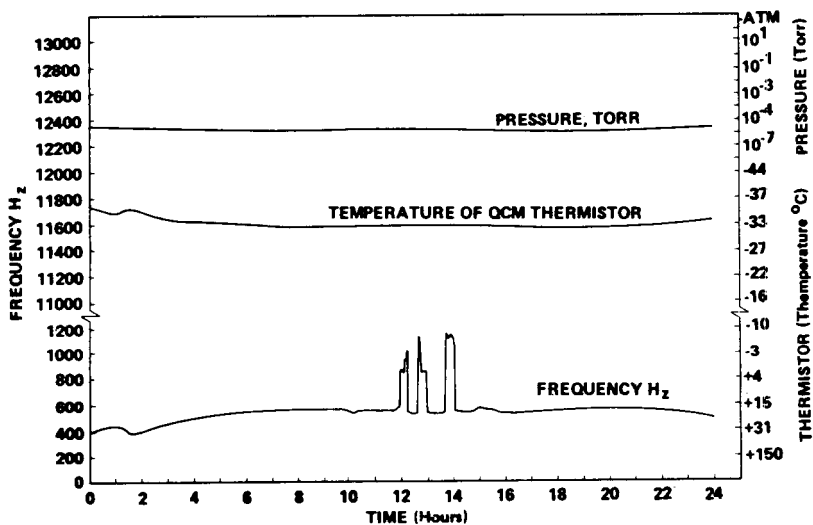


Fig. 11. QCM data, V-3 Contamination Test, July 14, 1971.

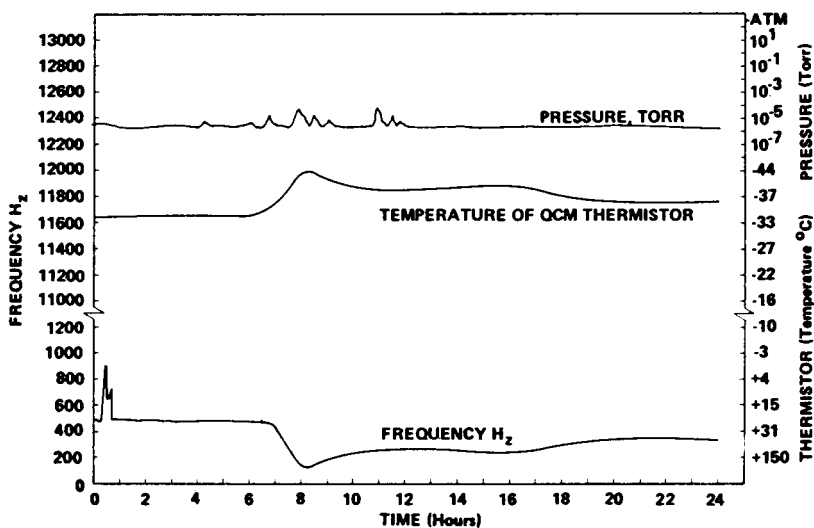


Fig. 12. QCM data, V-3 Contamination Test, July 15, 1971.

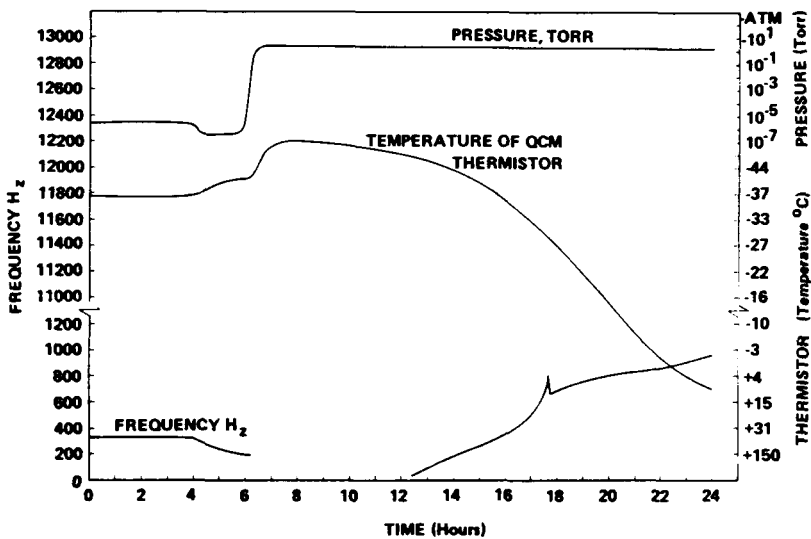


Fig. 13. QCM data, V-3 Contamination Test, July 16, 1971.

DYNAMICS OF SPACECRAFT CONTAMINATION

Robert J. Naumann, *NASA, Marshall Space Flight Center*

ABSTRACT

The problem of deposition of contaminants on critical optical surfaces of spacecraft is considered from a fundamental point of view which includes the source function, transport phenomena, and adsorption on a surface. Particular attention is paid to the problem of molecules being scattered back to the spacecraft by the contamination cloud around the spacecraft. It is shown that except for unusual circumstances the greatest contamination threat to critical optical surfaces is from sources within the experiment rather than those external. The dynamic equilibrium of the surface in question with the contaminating atmosphere is considered and it is shown that chemisorption is required to produce any significant degradation. The theoretical results predicted in this study are compared with contamination measurements made on the ATM during thermal vacuum testing at the MSC Chamber A.

HOLOGRAPHIC ANALYSIS OF PARTICLE SIZE DISTRIBUTION AND PARTICLE VELOCITIES FOR SKYLAB CONTAMINATION GROUND TEST

John R. Williams and Robert L. Kurtz, *NASA, Marshall Space Flight Center, Huntsville, Alabama*

ABSTRACT

The Skylab design includes several overboard vent systems which constitute potential experiment contamination sources. These include the waste tank nonpropulsive vents (NPVS), contingency condensate system, molecular sieve, and various experiment vents.

The Skylab Contamination Ground Test Program (SCGTP) has been designed to analyze and test the major vents in a simulated vacuum environment. The molecular sieve, contingency condensate system, and waste tank volume with nonpropulsive vents will be simulated and their resultant effluents analyzed in relation to their effect upon Skylab mission objectives.

The SCGTP is a million dollar plus test encompassing a total of three months. It is being conducted to provide basic contamination data, under simulated space environment, to supplement analysis in developing a Skylab operational control program. The SCGTP results will provide quantitative data which could be extrapolated using the Skylab contamination analytical mathematical model to predict contamination environments during Skylab operations.

Present estimates of the particle size distribution and velocities encompass several orders of magnitude; therefore, analytical predictions are inherently uncertain. The objectives of the test program, described in this paper, are to determine the particle size distribution and particle velocity vectors for actual Skylab contamination sources such as condensate dumps, molecular sieve dumps, waste tank/fecal dryer dumps, and waste tank/biocide dumps. The test program designed to produce the type of data mentioned above consists of small scale in-house simulations, large scale contracted tests with actual Skylab hardware.

The basic method used to obtain the needed data is in-line "Gabor type" holography. A collimated beam of light from a double pulse ruby laser is passed through the test chamber by using normal vacuum windows. The collimated beam ranges from 2" to 4" in diameter and passes across the particle flow. After passing through the particle field and

exiting the test chamber, the light is collected by a lens system which images the particle field on high resolution film. A hologram of the imaged particle field is produced on the film since the light undiffracted by the particles serves as the reference beam and interferes with the light diffracted by the particles. Thus, the entire particle field is stored in the form of a hologram. When the holograms are illuminated with a continuous wave laser, the entire particle field is reconstructed. The reconstruction can now be viewed with a high resolution TV system and analyzed plane by plane. The total particle size distribution can be determined. By double pulsing the laser and noting the particle travel between pulses, the velocity vectors can be obtained.

This paper presents data obtained in this test program using the above technique.

THE DETERMINATION AND OPTIMIZATION OF (RUTILE) PIGMENT PARTICLE SIZE DISTRIBUTIONS

L. Willard Richards, *National Research Corp. (A Subsidiary of Cabot Corp.), Cambridge, Massachusetts 02142*

ABSTRACT

A light scattering particle size test which can be used with materials having a broad particle size distribution is described. This test is particularly useful for pigments. The relation between the particle size distribution of a rutile pigment and its optical performance in a gray tint test at low pigment concentration is calculated and compared with experimental data.

INTRODUCTION

The problem of understanding and describing the factors which determine the optical performance of a pigmented material, such as a paint film, can be divided into two parts:

1. The determination of the average light scattering and absorbing properties of the composite material which makes up the dried paint film. This information can be specified by giving the scattering and absorbing properties of a layer of infinitesimal thickness. In more technical language, it can be specified by the phase function and extinction coefficient (or the scattering function and absorption coefficient) of the material.

2. The use of this information to determine the optical properties, such as reflectance and transmittance, of a piece of the material of specified size and shape under given illumination conditions and in known surroundings.

Satisfactory solutions to the second part of this problem have recently become available^{1,2,3} so it is the first part which is in need of additional work. At low pigment volume concentrations (PVC), the pigment particles are well enough separated from each other that they scatter independently. In this case the average light scattering properties of the

material can be obtained by averaging the light scattering properties of the individual particles. Therefore, the first part of the problem is solved at low PVC by providing a simple method for characterizing the light scattering properties of pigments.

It is well known that when the volume concentration of a rutile pigment is above 10 or 15%, its scattering efficiency depends rather strongly on the PVC⁴. These effects become particularly dramatic above the critical PVC, where the pigment concentration is so high that the binder can not fill all of the remaining space.⁵ Therefore the present work is restricted to low pigment concentrations.

The range of concentrations over which the performance of a pigment is independent of its concentration depends rather strongly on the system being studied. For example, it has been shown that the scattering efficiency of polystyrene latex particles suspended in water remains constant at concentrations which can go as high as 30% by volume⁶. On the other hand, the efficiency of rutile pigments begins to fall off at about 9% PVC.⁷

This paper describes a light scattering particle size test which is quite useful in characterizing pigments and shows how the information obtained from the test can be used to predict the relative optical performance of several pigment samples at low PVC.

PARTICLE SIZE DETERMINATION

The particle size of a pigment has a marked influence on its optical properties, and this is especially true when its major function is scattering light. With rutile (titanium dioxide) pigments the particle size is important enough that an experienced observer can visually detect a change of only 2 or 3% in the mean particle diameter by observing the resulting change in color of a gray paint. Therefore any successful study of the optics of pigmented materials must include an accurate characterization of the particle size distribution of the pigments.

The need to know the particle size distribution accurately arises from the sensitivity of the light scattering properties of pigments to particle size, and this strong dependence can be turned to advantage in a particle size test which is based on light scattering techniques. This section of the paper

describes an experimentally simple procedure which has been used for rutile pigments, and which produces an excellent characterization of the particle size distribution of a pigment sample in about 20 minutes of an operator's time.

Nearly all light scattering particle size tests known to the author are performed in much the same way: Some kind of light scattering measurement is made, and then the results are compared with theoretical calculations until a fit is found^{8a}. This technique requires either a large file of calculated results for the possible indices of refraction and particle size distributions, or the ability to do new calculations as needed. The former procedure is used in this work. Here a dilute suspension of the pigment is prepared and placed in a recording spectrophotometer. Then an extinction spectrum (turbidity spectrum) is recorded and compared with transparent overlays containing the results of theoretical calculations.

Experimental Procedure

This particle size test was designed to be experimentally simple⁹, and then the theory was fit to the procedure. Therefore the experiment is described first.

The choice of techniques and materials used in preparing the dilute dispersion of the pigment is rather arbitrary. In this work an aqueous dispersion is prepared as follows: A few grams of pigment and some plastic balls are placed in a small bottle or vial and shaken on some such device as a Spex mill (R) for 10 or 15 minutes. This breaks up the agglomerates, and tends to reduce the apparent change in particle size when the pigment is calcined. Then 0.200 g of pigment are weighed into 100 ml of water containing 0.002% potassium tripolyphosphate and 1.5 milliequivalents per liter of sodium hydroxide. This suspension is sonified for 2 min at a power level of 100 watts, an aliquot taken and diluted by a factor of 100, sonified, and used to fill a 1 cm spectrophotometer cell. This procedure is reasonably successful at producing disperions with optical properties which are not changed by additional attempts to improve the dispersion.

A Bausch and Lomb Spectronic 505 was used in this work, but any recording spectrophotometer should be satisfactory. Since the spectrum is quite smooth, it can be recorded rather rapidly. The instrument measures

the amount of light which is either absorbed or scattered through a large enough angle by the pigment dispersion that it does not fall on the detector.

Theoretical Analysis

The extinction of a collimated light beam passing through a dilute suspension containing n particles per unit volume is given by the expression:

$$I/I_0 = \exp (-n \bar{C}_{\text{ext}} X) \quad (1)$$

where I_0 is the incident intensity, I is the transmitted intensity of the collimated beam, \bar{C}_{ext} is the average extinction cross section of the particles, and X is the path length of the beam in the suspension. Here the extinction includes both absorption and scattering, but a small correction is made to account for the light which is scattered through a small enough angle that it still reaches the detector of the spectrophotometer. This expression assumes that the particles are well enough separated that they scatter as individuals (dependent or cooperative scattering can be neglected) and that a negligible amount of light reaching the detector has been scattered more than once (multiple scattering can be neglected).

The particle size distribution function used in the theoretical calculations is a log-normal function

$$f(D) = \frac{1}{\sqrt{2\pi} D \sigma} \exp \left[-\frac{1}{2} \left(\frac{\ln D/D_g}{\sigma} \right)^2 \right] \quad (2)$$

where $f(D)$ is the fraction of the number of particles with diameters between D and $D+dD$, D_g is the geometric mean diameter, and σ is the standard deviation of the normal distribution which is obtained in a plot of number frequency as a function of $\ln D$. It has been found from experience with electron micrograph particle counts that this function can fit the observed histograms about as well as any. Perhaps more importantly, it has been found that the rather restricted families of light scattering curves which can be generated from this distribution function nearly always provide an excellent fit to the experimental results. This distribution function was chosen quite early in the work. If the choice were to be made again, the zeroth order logarithmic distribution would also be considered.¹⁰

As has already been mentioned, it is necessary to correct the calculated intensity of scattering because of the finite acceptance angle of the detector of the spectrophotometer. We obtained the necessary information about the geometry of the detector optics by making some small, hollow prisms from microscope coverslip glass, filling them with water, measuring the angular deflection produced by each prism in a beam of sunlight, and then observing the effect of each prism on the spectrophotometer response. Essentially all of the light deflected through angles up to 4° reaches the detector of the Spectronic 505, and the fraction detected at larger angles falls approximately linearly to zero at 12° .

The scattering cross sections for the individual pigment particles were calculated from the Mie equations. Of course, these equations are not entirely appropriate for commercial pigments, but it appears that the approximations involved in using them do not lead to significant problems. The equations describe the light scattering properties of homogeneous, isotropic spheres, whereas rutile particles are birefringent and often angular. The deviations from spherical shape are assumed to be small enough compared to the wavelength of light that they can be satisfactorily neglected, and the actual particle replaced by a sphere of the same volume. The work of Felder shows that this is a reasonable approximation.¹¹

In the early exploratory phases of this work it was arbitrarily decided to use an index of refraction half way between the values for the ordinary and extraordinary ray as reported by deVorel¹², and that original choice has not been changed. Most other workers have made the more reasonable approximation that the average should weight the ordinary index of refraction twice as much as the extraordinary index.^{13,14} Rutile absorbs in the blue end of the spectrum, and data for the strength of the absorption were obtained from Cronemeyer.¹⁵ The index of refraction of water was obtained from the International Critical Tables.¹⁶

A file of the results obtained from the Mie equations was prepared for particle diameters from 0.005 to 1.4 μm in steps of 0.005 μm , and for wavelengths in vacuum from 300 to 800 nm in steps of 25 nm. The quantity calculated was the corrected efficiency factor for extinction

$$Q_{\text{corr}} = Q_{\text{ext}} - \frac{2\lambda_m}{\pi^2 D^2} \int_0^\pi g \frac{i_1 + i_2}{2} \sin\theta d\theta \quad (3)$$

where Q_{ext} , i_1 and i_2 are dimensionless parameters obtained from the Mie equations^{8b} and λ_m is the wavelength of light in the water. The factor g has a value of unity between 0° and 4° , and decreases linearly to zero at 12° . The term with the integral accounts for the forward scattered light which reaches the detector, and it is adequate to evaluate it by calculating $(i_1 + i_2)/2$ at only 4° and 8° and using the expression

$$\begin{aligned} & \int_0^\pi g \frac{i_1 + i_2}{2} \sin\theta d\theta \\ & \approx \frac{4.3\pi}{180} \left[\left(\frac{i_1 + i_2}{2} \right)_{4^\circ} \sin 4^\circ + \left(\frac{i_1 + i_2}{2} \right)_{8^\circ} \sin 8^\circ \right]. \end{aligned} \quad (4)$$

The average scattering cross section was calculated for each particle size distribution at each wavelength from

$$\bar{C}_{\text{ext}} = \frac{\pi}{4} \int_0^\infty D^2 Q_{\text{corr}} f(D) dD. \quad (5)$$

In order to determine the number of particles present, it is also necessary to calculate the average volume per particle \bar{v} in a similar manner. Since most chemical spectrophotometers record absorbance A , and the volume concentration $n\bar{v}$ rather than the number concentration n is known, it is convenient to convert Eq. 1 into the form

$$A = \frac{1}{2.303} n\bar{v} \frac{\bar{C}_{\text{ext}}}{\bar{v}} X = (2.05 \times 10^{-2} \mu\text{m}) \frac{\bar{C}_{\text{ext}}}{\bar{v}}. \quad (6)$$

Here the right hand side of the equation has been evaluated for a titania concentration of 2.00×10^{-5} g/cc or $n\bar{v} = 4.73 \times 10^{-6}$ and a cell path length $X = 1$ cm.

The calculations were done at each of the 21 wavelengths for all combinations of D_g in the range from $0.12 \mu\text{m}$ to $0.3 \mu\text{m}$ in steps of $0.01 \mu\text{m}$ and the log-normal σ in the range from 0.2 to 0.5 in steps of 0.02. Sample results are shown in Fig. 1, where it is easy to see the effects of small changes in D_g or σ on the calculated results. Smooth curves were

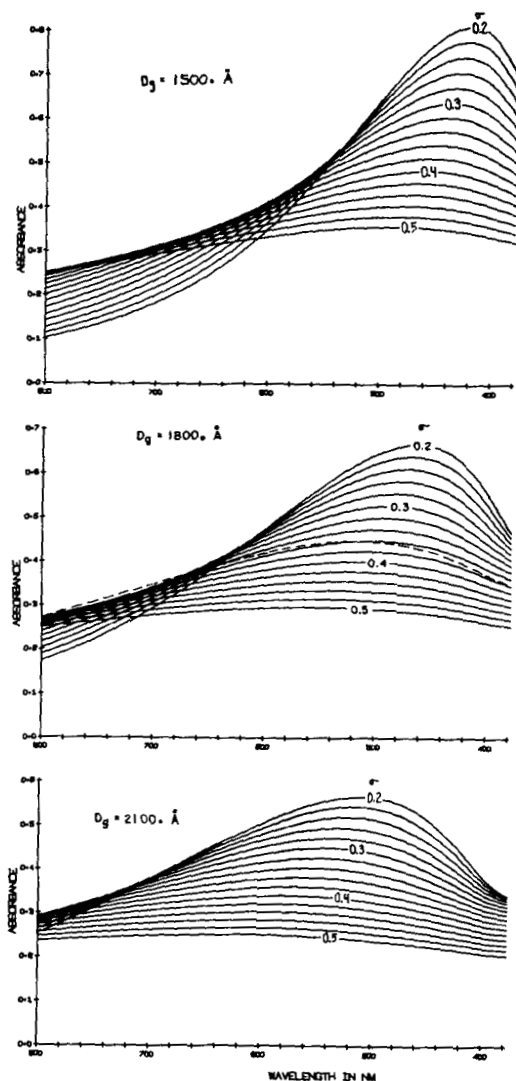


Fig. 1. Samples of the curves used for determining the particle size distribution of rutile pigments. The effect of a 100 Å change in the geometric mean diameter is shown by the dotted line for $D_g = 1900$ and $\sigma = 0.34$ in the middle plot.

drawn through the calculated points to the same scale as the spectrophotometer trace, and then they were copied onto Mylar (R) using the Ozalid (R) process. This makes it a simple matter to place various families of calculated curves over the experimental spectrum, and to determine the log-normal particle size distribution which scatters light most nearly in the same manner as the pigment sample.

Results

Reference data were obtained by counting 1000 particles on electron micrographs using the Zeiss Particle Size Analyzer TGZ3. The size of the circle was adjusted by eye to have the same area as the image of the pigment particle. Small aggregates were counted as separate particles unless the particles appeared to be fused together, in which case they were treated as one particle. Occasional large aggregates were ignored.

At the time this test was being evaluated, 26 rather similar pigment samples with duplicate particle counts were available. Values for D_g and the log-normal σ were calculated from the histograms, and were in the range $0.135 < D_g < 0.165 \mu\text{m}$ and $0.32 < \sigma < 0.40$. Duplicate light scattering tests were performed. The precision of each test method could be determined from the replication, and the standard errors in Table I describe the uncertainty of a single determination due to its lack of precision. More recent checks have always given better values for the precision of the light scattering test.

Table I
Standard Errors Describing the Precision of the Methods

Test Method	Log-normal σ	D_g
Particle Count	0.03	0.01 μm
Light Scattering	0.015	0.004 μm

A comparison between the two test methods showed that on the average the light scattering test gave a D_g larger by 0.004 μm and a σ larger by 0.037. The range of values obtained from the tests was only slightly larger than would be expected if all tests had been run on the same pigment, so these data can not be used to determine how the light scattering test results change when the pigment particle size distribution is altered. The absolute comparison between experiment and theory in Fig. 2 shows that the

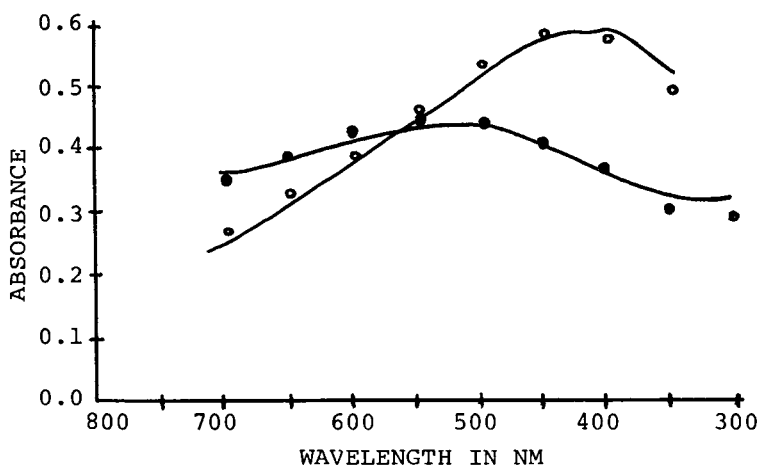


Fig. 2. A comparison between observed extinction spectra (lines) and values calculated using the Mie equations and histograms from electron micrograph particle counts (points) for two rutile pigment samples.

test does respond to differences in pigments.

Two other descriptions of light scattering particle size tests for rutile have recently appeared in the literature.^{13,14} Barnett and Simon obtained agreement between light scattering and particle count results comparable to that reported here, but used a much more cumbersome procedure to analyze the experimental spectra. It is not understood why Slepety's obtained much greater differences between the results of the two test methods.

Summary

The light scattering test is a rapid and reliable method of characterizing the particle size distribution of a pigment. In addition, it has the advantage of directly measuring the light scattering ability of the pigment, which is the property that provides the motivation for wanting to know the particle size distribution.

PARTICLE SIZE OPTIMIZATION

Pigments are used under conditions where multiple scattering is important, so any attempt to calculate an optimum particle size distribution should include

the effects of multiple scattering. Although the literature abounds with calculations or estimates of the optimum particle size for pigments, it is believed that this is the first report to describe the optimization of particle size distributions in a multiple scattering situation.

The optimization is carried out using the same general procedure as is used in the particle size tests. Enough calculations are done to characterize the pigment performance throughout the range of particle size distributions which are believed to be close to optimum distribution, and then the most desirable distributions are selected. Usually this choice involves some compromises.

One example, the optimization of rutile pigments in gray tints, is presented here to show the kind of results that can be obtained. This example was chosen because the tint test is perhaps the most common one for evaluating the relative optical efficiencies of competitive white pigments. These same techniques could have been used to calculate the hiding power of incompletely hiding white paints, or the appearance of materials when viewed by transmitted light, to name some examples.

The steps in the calculation are as follows:

1. Do the Mie calculations for all particle sizes and wavelengths. In this case the Mie calculations were done in the same way as for the particle size test, except that an index of refraction of 1.54 was used for the medium surrounding the pigment particles and no correction was required for the light scattered through a small angle. In addition, the angular dependence of the scattering was calculated through the full 180° range in steps of 10° .

2. Set up families of particle size distributions and use the results of the Mie calculations to obtain the scattering and absorbing properties of each distribution at each wavelength. The log-normal distribution was used here.

3. Do the multiple scattering calculations for each particle size distribution at each wavelength to determine the reflectance spectrum of the paints. In this work the two-flux equations were used to determine the reflectance of a very thick paint film. The scattering coefficients were determined from the results of the Mie calculations using Eqs. 22 and 77 of reference 2, and the constant absorption coefficient

was chosen so that the reflectances were approximately 0.5. Surface reflection coefficients (Saunderson corrections¹⁷) were used. The fraction 0.0976 of the diffuse illumination is reflected at the first surface and is not included in the final calculated reflectance. The internal reflection coefficient r was obtained from the formula

$$r \pm 0.0014 = 0.5683 + (0.0643 \pm 0.0068)/R_{\infty} - (0.0126 \pm 0.0023)/R_{\infty}^2, \quad (7)$$

where R_{∞} is the reflectance calculated without the surface reflection corrections. This relation was obtained from a regression analysis of 46 values of r and R_{∞} obtained from the many-flux calculation using phase functions A, B, C, and D and $10^{-6} < k/s < 4 \times 10^{-2}$ as described in the text accompanying Table V of reference 2. The values after each \pm sign give the standard error to be associated with the quantity ahead of the sign, and they are reported here to show how well the regression line fits the data.

4. Use the tristimulus theory of vision to convert these spectra into the visual appearance of the paint film. This part of the calculation is not discussed here because an excellent description of it is already available.¹⁸ The CIE functions and data for illuminant C were taken from this reference.

The results are given in Fig. 3. Here the vertical axis gives the visual brightness of the gray paint in units of Y CIE. The undertone is measured by the quantity $(Z-X)/Y$, and some lines of constant undertone are shown along with their numerical values. The figure is an isometric plot rather than a perspective drawing. The advantage of this representation is that the scale of the coordinates is not distorted, so that the data can be read from any place on the plot using the scales on the axes. Also, if it is viewed from a distance, it is very nearly in perspective.

Two approaches can be used to demonstrate the reliability of these calculations. One is to substantiate the accuracy of each step. It has been shown by Richards¹⁹ and also by Fig. 2 of this paper that Mie calculations give a good description of the optical properties of commercial rutile pigments at very low pigment concentrations. At low concentrations the scattering properties of collections of particles are reliably obtained by adding the contributions of the individual particles.^{8c} A reflectance of 0.5 is a bit low for the two-flux multiple scattering calculations

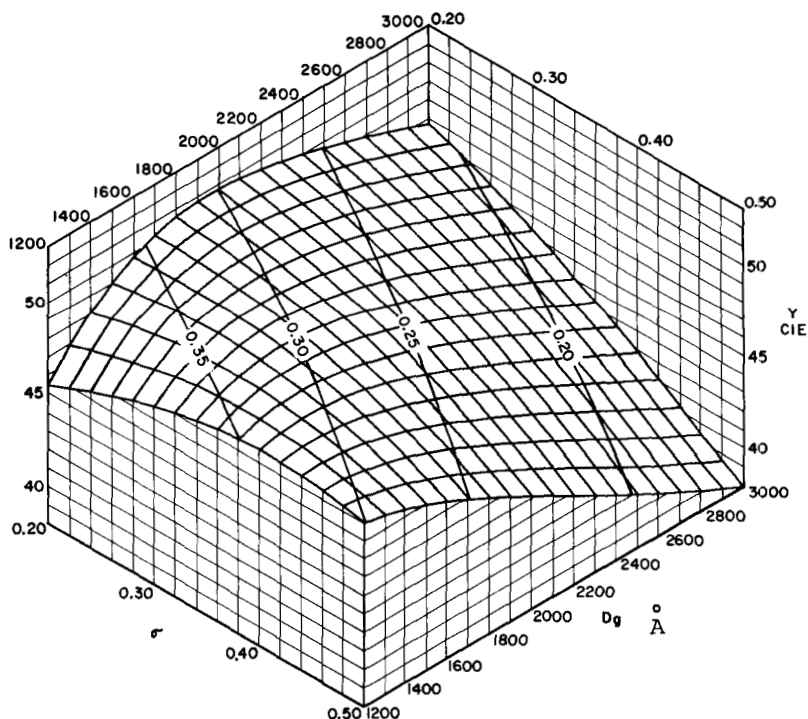


Fig. 3. The dependence of the optical performance of rutile pigments in a gray tint test on their particle size distribution. Lines of constant $YF=(Z-X)/Y$ are also shown on the surface.

to have excellent accuracy², but it is believed that the relative values of the reflectances are entirely adequate for the present purposes. Finally, the reliability of the tristimulus calculation is well documented.¹⁸

It should be emphasized again that the assumptions used in the calculations are valid only at low pigment concentrations. It is well known that the performance of rutile pigments depends on the PVC and that even the relative performance of several pigments can change when the PVC at which they are compared changes⁴. One way of showing that the scattering

efficiency of rutile pigments must decrease at high PVC is to note that the scattering cross section per particle is larger than the geometrical cross section. Therefore, it is possible to pack the pigment particles so closely that each particle can not scatter independently of its neighbors. (If the particles did scatter independently, the cross sections would overlap.) The results of Mie calculations show that the scattering efficiency of rutile pigments must begin to fall off before the PVC becomes as high as 15%.

Another method of demonstrating the usefulness of the calculations is to compare them directly with experimental data.²⁰ Gray paint films were prepared from each of 14 different pigments with D_g in the range from 0.17 to 0.21 μm and σ in the range from 0.35 to 0.40 as determined by the light scattering particle size test. A Color Eye (R) filter photometer was used to characterize the reflectance of each paint in terms of the CIE X, Y, and Z. A calibrated white Vitrolite (R) was used as a reference standard and the specular reflectance was excluded. The observed Y and $YF = (Z-X)/Y$ were divided by the Y and YF of a reference pigment and the results expressed as %Y and %YF. A linear regression analysis was done to determine how the observed %Y and %YF depends on D_g and σ . In Table II the experimental regression coefficients are compared with the slope of the surface in Fig. 3 and with the calculated data for YF evaluated in the range of values for D_g and σ which contain most of the experimental points.

The data used here were obtained in connection with other projects, and nearly enough fit the present needs so that it did not seem necessary to repeat the experiments. Their major disadvantage in the present comparison is that the gray paints had a PVC of 15%, which is high enough that the theoretical calculations are not strictly applicable. Even so, the agreement between the experimental results and the theoretical calculations is rather good.

The limitation of this optimization calculation to low PVC's means that it does not apply to such important end uses as medium or high PVC latex paints. More to the point of this conference, it does not apply to the high PVC paints often used for thermal control of space vehicles. This limitation is caused by only one problem: the light scattering properties of a closely spaced collection of particles can not be predicted from the scattering by the same particles when they are well separated from each other.

Table II
A Comparison Between Experiment and Theory

	Experimental regression coefficient and its standard error	Theoretical value from Fig. 3
$\left(\frac{\partial Y}{\partial \sigma}\right)_{D_g}$	-32 ± 11	-41
$\left(\frac{\partial Y}{\partial D_g}\right)_{\sigma}$	$10 \pm 11 \mu\text{m}^{-1}$	$-60 \mu\text{m}^{-1}$
$\left(\frac{\partial YF}{\partial \sigma}\right)_{D_g}$	-93 ± 16	-106
$\left(\frac{\partial YF}{\partial D_g}\right)_{\sigma}$	$-260 \pm 20 \mu\text{m}^{-1}$	$-390 \mu\text{m}^{-1}$

The light scattering particle size test does not suffer from this limitation, and is of rather general applicability. It can be used for any particles of known index of refraction which have a size comparable to the wavelength of the radiation used and which can be suspended in a medium with an appreciably different index of refraction. Pigments are one class of materials for which this test is ideally suited.

ACKNOWLEDGEMENTS

This work was done at the Billerica Research Center of the Cabot Corporation. It is a pleasure to thank T. F. Swank and L. J. Petrovic for the use of their unpublished work^{9,20} and P.S. Mudgett for calculating and plotting the results shown in Figs. 1 and 3. A less complete account of some of this material was accepted in February 1971 for inclusion in the Pigment Handbook²¹.

REFERENCES

1. H.C. Hottel, A. F. Sarofim, L.B. Evans, and I. A. Vasalos, J. Heat Transfer, Trans. ASME, Series C 90, 56 (1968).
2. P. S. Mudgett and L. W. Richards, Appl. Optics 10, 1485 (1971).
3. P. S. Mudgett and L. W. Richards, submitted to J. Colloid and Interface Sci.
4. R. J. Bruehlman, L. W. Thomas and E. Gonick Official Digest (Fed. of Soc. for Paint Tech.) 33, 252 (1961).

5. See, for example, F. B. Steig, Jr., J. Paint Technol. 39, 703 (1967).
6. I. A. Vasalos, Effect of Separation Distance on the Optical Properties of Dense Dielectric Particle Suspensions (Ph.D. thesis, M.I.T., August, 1969).
7. R. J. Bruehlman and W. D. Ross, J. Paint Technol. 41, 584 (1969).
8. M. Kerker, The Scattering of Light and Other Electromagnetic Radiation (Academic Press, New York, 1969), a. See Chapter 7 for a review, b. pp. 47 and 50, c. p. 312.
9. The experimental procedure was developed by T. F. Swank.
10. W. F. Espenscheid, M. Kerker, and E. Matijevic J. Phys. Chem. 68, 3093 (1964).
11. B. Felder Helv. Chim. Acta 51, 1224 (1968).
12. J. R. DeVore, J. Opt. Soc. Am., 41, 416 (1951).
13. C. E. Barnett and G. G. Simon, J. Colloid and Interface Sci. 34, 580 (1970).
14. R. A. Slepety's, J. Paint Technol. to be published.
15. D. C. Cronmeyer, Phys. Rev. 87, 876 (1952).
16. E. W. Washburn, Ed., International Critical Tables (McGraw-Hill, New York, 1930), Vol. 7, p. 13.
17. J. L. Saunderson, J. Opt. Soc. Am. 32, 727 (1942).
18. D. B. Judd and G. Wyszecski, Color in Business, Science and Industry, 2nd Ed. (John Wiley and Sons, New York, 1963).
19. L. W. Richards, J. Paint Technol. 42, 276 (1970).
20. L. J. Petrovic, unpublished data.
21. T. C. Patton, Ed., Pigment Handbook (Wiley-Interscience, New York, 1972).

SATELLITE TEMPERATURE CORRELATION OF PREDICTED, TEST, AND FLIGHT DATA

H. Apoian, *The Aerospace Corporation, El Segundo, California*

ABSTRACT

This study compares satellite temperature predictions with thermal vacuum test results and shows the improvement from testing. Orbital data were compared with prediction/test results to determine quantitatively an expected error criteria.

INTRODUCTION

This paper reports on the development of the thermal design for a communications satellite. Thermal vacuum test results are reviewed and tabulated, and indicate the chronological improvement in test models and testing techniques. Comparisons of the mathematical model predictions with (a) thermal development model test results, (b) engineering development model test results, and (c) qualification model test results, demonstrate how analytical methods and testing techniques are improved by using experimental data resulting from the thermal vacuum test program. A final correlation with orbital telemetry data indicates the degree of accuracy obtainable in the development program and gives some indication of the individual contributions of the analytical and experimental aspects.

There are continuing requests for information on the efficacy of thermal vacuum testing in the thermal design of satellites and in the predictions of orbital temperatures. Adequacy of thermal control can be verified or altered as testing progresses and as the satellite acquires new or additional components. The necessity for iteration during design requires that testing be initiated early in the program in order to optimize thermal design. Additionally, only through testing will some of the less obvious deficiencies be detected. A thermal development program involves iteration and reconciliation of analytical and experimental information to reinforce predictions and enhance the confidence level. These data show thermal vacuum testing effectiveness and the accuracy to be expected from current temperature prediction methods.

Usually the necessity for thermal vacuum testing is questioned and budgetary limitations demand justification for tests and the expected return from expenditures. The experience

gained from exposure to the various contractors' test facilities and testing techniques provides a unique background for evaluating the merits of testing. Without case histories to support the utility of testing, it is very difficult to determine the benefits to be derived from thermal vacuum tests. In this respect, the availability of flight data presents a unique opportunity to make a comparison with comprehensive and well-documented thermal vacuum test data.

PROPOSAL THERMAL ANALYSIS

Orbital Thermal Control

The discussion of thermal design analysis and thermal vacuum testing of the communications satellite ranges from the original concept which established design philosophy, through testing, to a comparison with flight data. The evolution of the thermal design stems from a simple 2-node and 4-node mathematical model to a coarse model of 25 nodes which was expanded and modified to a final 223-node model. The spacecraft temperatures were then predicted with the mathematical model and were used to establish test requirements and model instrumentation.

The spacecraft used for the study is a communications satellite, currently stationed in synchronous orbit. It was launched into a 20,019 n mi near-synchronous equatorial orbit from the ETR in 1969, using a Thor-Delta (DSV-3L) booster and a solid-rocket apogee boost motor to establish final orbit. The current orbit weight is 285 lb with a life expectancy of five years. Thermal requirements are based on a nominal 90-rpm spin rate and a sun angle variation of ± 23.5 deg. The cylindrical solar array was designed to accommodate a normal power requirement of 86 w, at summer solstice, after degradation effects due to exposure to the space environment during the five-year mission lifetime. Sixty-eight watts of power are supplied by rechargeable nickel-cadmium batteries during the eclipsing phases (about 70 minutes max.). Figure 1 shows the general configuration and the major spacecraft components.

Thermal analysis in support of an RFP (Request for Proposal) for the satellite consisted of an initial 2-node model to establish the basic thermal design concept. It was assumed that internal energy could be dissipated through the solar array panels; however, due to a ± 23.5 deg variation in sun angle¹, the central node temperature fluctuations were excessive. To reduce the sun angle effect, the design was modified by insulating the ends of the cylindrical satellite to maintain equipment

¹Sun angle, θ , is the angle between the normal to the spin axis and the solar incidence; positive is toward the antenna.

temperature within prescribed allowable limits. This configuration established the philosophy for the basic thermal control concept.

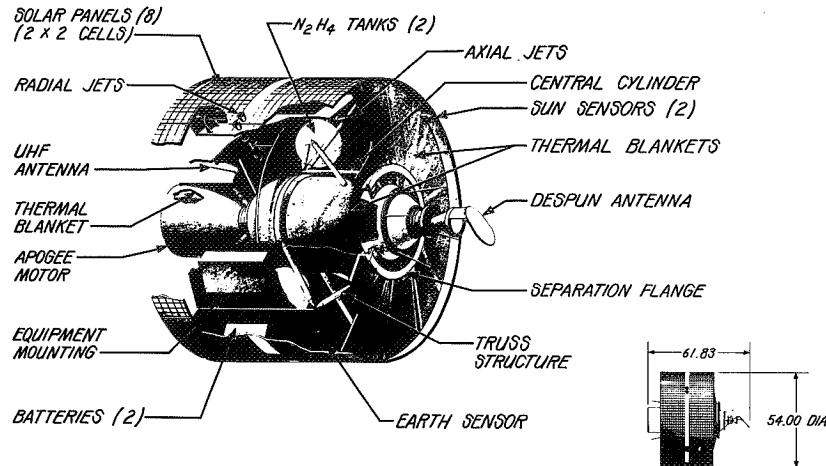


Fig. 1—Satellite configuration

Thermal Environments

The spacecraft environment for thermal design was defined by temperature limits for prelaunch through orbital operation at synchronous altitude. Thermal control prior to launch (transport and on-pad conditions) was maintained between minimum/maximum limits by conditioned air flow into the spacecraft at required rates. During ascent, and before fairing separation, the spacecraft is heated by radiation from the fairing due to external aerodynamic heating. Heat transfer within the fairing must be limited to low enough rates to prevent deterioration of thermal control coatings or damage to multi-foil insulation. After fairing jettison, free molecular heating must also be maintained within appropriate limits. If satellite components are subjected to solar radiation before spin-up, excessive localized heating may affect the thermal balance. Exposure to heat loads during the transfer orbit also requires consideration in thermal design since high sun angles (above 30 deg) may be encountered prior to transfer from the elliptical orbit to the synchronous orbit. Of special concern are isolation of the apogee boost motor during firing and the effect on the thermal balance resulting from the thermophysical properties of the spent boost motor casing and nozzle. Finally, on-orbit thermal control requirements for a five-year spacecraft life necessitate special consideration of, for example, the despun antenna, batteries, reaction control equipment, and electronic components.

THERMAL DESIGN AND ANALYTICAL MODELING

Coarse Analytical Model

Once the philosophy for thermal control was established by the simple thermal model, a 25-node model was generated to define primary thermal requirements. The principle components and spacecraft subsystems were included to determine thermal loads and temperatures for prelaunch, ascent, orbit transfer, and on-orbit environmental conditions. This coarse model was subsequently revised when power studies indicated excessive loads for operation of the electronically despun antenna in addition to unsatisfactory thermal control. As a result of studying the 25-node model, thermal design changes were incorporated in the subsequent multi-node thermal network that formed the basis for the detailed mathematical model.

Analysis of Critical Components

Investigation of thermal requirements for environmental conditions encountered by the satellite indicated that modification of the thermal design was necessary to prevent the apogee boost motor from exceeding the 40°F to 100°F allowable limits. To assure that this limit is not exceeded, the sun angle must remain between ± 30 deg during the transfer orbit.

Verification of this effect through the use of the coarse model resulted in changes that were incorporated into the initial detailed model. The detailed model was eventually expanded to include all thermally sensitive components and subsystems as well as all radiative interactions with the surrounding environment.

Detailed Analytical Model

Prior to generating a detailed analytical model, a preliminary 49-node model was used to define heat transfer paths, insulation requirements, thermal control coatings, and isolation requirements for the various components. The preliminary model also determined critical components and checked the adequacy of a passive thermal control system. Subsequent analyses resulted in a final detailed model having 223 nodes with 326 conduction resistors and 1091 radiation resistors. These analytical models were also instrumental in preparing for thermal vacuum testing by defining materials, thermal control coatings, and component thermal mass simulation. Studies with the analytical model implemented test plans and procedures by defining spacecraft thermal characteristics, coatings requirements, thermocouple locations, and distribution of anticipated heat loads. Thermophysical properties of the spacecraft, such as materials, weights, specific heats, thermal conductivity, and thermal control surface optical properties were defined in

the detailed mathematical model. In the anticipated range of variation of sun angle, solar intensity, and eclipses encountered in orbit, the effect of fluctuations of equipment power dissipation on satellite thermal control was determined with the multi-node model. In addition to being tested at minimum (65 w) and maximum (90 w) power loads, the model was analyzed for solar fluxes at sun angles of 0, ± 30 , and ± 70 deg in order to include all likely critical thermal environmental conditions.

THERMAL DEVELOPMENT MODEL TESTS

Test Model Configuration

The primary objective of the thermal development test program using the development model was to verify the detailed analytical thermal model. A full-scale flight type structure was instrumented for temperature, heat flux, and power dissipation in order to determine effectiveness of insulation, coatings, and thermal paths. Simulated thermal masses were used for subsystem components, solar panels, reaction control equipment, and the despun antenna. Secondary objectives were (a) to determine performance during "worst case" mission phases, (b) to determine subsystem component performance and (c) to verify simulation capability of the vacuum chamber solar beam, infrared heaters, and associated hardware. Additionally, thermal development tests will verify functional capability of the vacuum chamber, solar flux simulation, infrared heater operation, adequacy of test instrumentation, and operation of miscellaneous associated hardware.

The satellite model utilized simulated thermal masses (within ± 10 percent) to represent subsystem components when flight hardware was unavailable or impractical to use during tests. Modelling error as a result of using simulated components was not quantitatively established since, for initial tests, the error is secondary to the goal of establishing thermal design feasibility.² The appropriate capacity, base mounting, geometry, and heat dissipation were simulated as closely as practicable. The location and size of the apogee boost motor (with 250 lb of solid propellant) posed a potential thermal control problem due to (a) propellant temperature constraints prior to ignition (i.e., minimum 40°F, maximum 100°F), (b) heat transfer during motor burn, (c) gradients and peak temperatures resulting from soak-back, and (d) heat transfer across the empty casing and the nozzle after burn. Solar arrays were simulated to provide optical properties approximating the actual solar cells (xenon absorptivity of 0.75 and infrared emissivity of 0.89 versus solar absorptivity of 0.75 and emissivity of 0.80).

² The incident solar flux is more than 10 times the internal power dissipation.

The model set-up inside the thermal vacuum test chamber is illustrated in Fig. 2. The mechanically despun antenna end of the model is attached to the spin fixture which is mounted on a support frame. At the apogee motor end, the drive motor is attached to an empty casing to rotate the model. Instrument readings are picked up at a slip ring and transferred through hardlines onto a data recorder. Model instrumentation measured temperatures, heat fluxes, and power dissipations for the various testing conditions. The model used five infrared heaters to supplement the solar beam and one heater to simulate the apogee boost motor firing. There were 150 thermistors, 45 thermopiles, and 8 calorimeters on the test model.

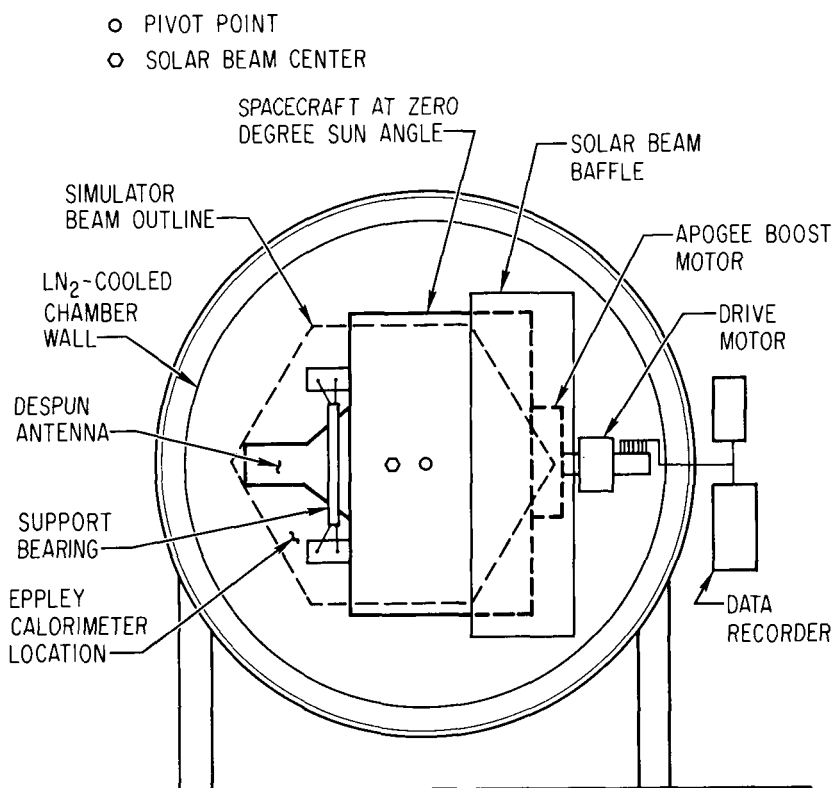


Fig. 2—Solar beam/model geometry (10-ft x 20-ft Philco-Ford thermal vacuum chamber, simulator beam displaced 8 in.)

Chamber Configuration

All thermal vacuum testing was done in a 10-ft by 20-ft chamber in compliance with test methods and requirements listed in Ref. 1. The test chamber had liquid-nitrogen-cooled walls and was capable of pressures in the range of from 10^{-7} to 10^{-8} mmHg, using a diffusion pump and titanium sublimator. A bank of 5 kw unfiltered xenon lamps provided the solar simulator beam source. Infrared heaters were used to supplement the solar beam for heating the thermal model surfaces. Heat fluxes on the model were monitored with eight radiation balance calorimeters (± 8.5 percent uncertainty) with coatings identical to the surfaces being monitored. An Eppley reference calorimeter (± 3 percent uncertainty) which was stationary with respect to the chamber walls was used to monitor flux intensity. The flux distribution of the xenon array at the model was measured with a rake consisting of 29 solar cells calibrated with an Optical Coating Laboratories, Inc., solar simulator.

The thermal vacuum chamber xenon lamp bank was located external to the chamber in a hexagonal array of 10 lamps (5 kw per lamp). An integrating lens unit directs the beam onto the collimating mirror through a window in the chamber wall. The simulated solar flux at the model can be varied from 95 to 510 Btu/hr-ft² with ± 3 percent root mean square (RMS) uniformity.

A spin fixture supported the test model at the apogee boost motor nozzle and at the separation ring. The drive motor was attached to the spin fixture at the nozzle, and rotated the development model from 3 to 10 rpm (At 3 rpm the solar array temperature fluctuation is about 2°F.). In addition to rotation about the spin axis, the model can be pivoted ± 70 deg about the geometric center to simulate orbital variations in sun angle. The infrared heater power leads and instrumentation leads were fed through the chamber wall to the slip rings and stepper switch.

Since the 10-lamp hexagonal array did not completely cover the full size thermal model (see Fig. 2), the solar simulator was offset 5 deg toward the despun antenna regions. As shown in Fig. 2, a solar beam baffle was used to block extraneous radiation on the aft region of the satellite. To properly simulate heat loads in the area blocked by the baffle, quartz jacketed tungsten filament infrared lamps with polished aluminum reflectors were used. With the solar beam on, the infrared lamps were adjusted until all radiation balance calorimeters indicated the correct flux on the model. Due to the difference between optical properties of the actual solar arrays and those of the simulated arrays, a one "sun" simulation required an incident flux of 462 Btu/hr-ft². Similarly, with the white thermatrol surfaces of the despun antenna, one "sun" is defined as 522 Btu/hr-ft². To satisfy the despun antenna requirements, the xenon lamps were set for 522 Btu/hr-ft²; however, due to the

limited beam area of the xenon lamps, the solar panels are only partially illuminated. Even with the beam intensity set at 522 Btu/hr-ft², the solar panels received only 452 Btu/hr-ft². The difference between 452 and 492 Btu/hr-ft² was made up by the infrared arrays.

Test Conditions and Experimental Data

A total of eleven tests were performed to investigate effects of sun angle variation, orbit transfer, orbit eclipse, apogee boost motor firing, and minimum and maximum operational power levels. Seven of the tests were performed at a 0-deg sun angle to determine effects at maximum spacecraft power conditions (90 w) during synchronous orbit, at minimum power conditions (65 w) during eclipse periods, and for apogee boost motor firing during orbit transfer. The remaining four tests simulated a transfer orbit maneuver at a -70 deg sun angle and at ± 30 deg sun angles, and a cold case environment with minimum power at a -30 deg sun angle. For these various conditions, only the 0-deg and +30-deg sun angle tests were compared with predicted data and tabulated to establish test effectiveness for the development, engineering, and qualification thermal models.

During thermal development testing, uncertainties and problems were encountered with both the model and the chamber. Examination of the test data revealed the following problem areas relative to thermal design and testing:

1. Excessive heat leak through the spin fixture resulted in low temperatures for the mechanical despun antenna and central cylinder.
2. Shadowing of the mechanically despun antenna by the spin fixture and low simulated power dissipation resulted in low test temperatures.
3. Inadvertent solar beam misalignment and over-age lamps caused a 40 percent error in flux intensity.
4. The solar beam baffle was at an average temperature of -40°F. To minimize heating effects from the solar baffle, liquid nitrogen cooling was later installed.
5. Low effectiveness of end radiation shields required the addition of five layers of aluminized mylar.
6. Reaction control solenoid valve temperature was low due to the insulation being shorted by a strap holder.

Test Results

In general, the objectives of the development tests were accomplished, indicating that the spacecraft thermal design was adequate for the anticipated worst case conditions. Taking into account the anomalies associated with the tests, the detailed analytical model was verified as capable of satisfactorily predicting spacecraft temperatures. Also, functional capability of the vacuum chamber and associated hardware was verified and proved adequate for engineering and qualification model thermal tests.

As a result of development tests, the spacecraft thermal design was modified to improve thermal control. Specific modifications included: (1) the mechanically despun antenna surface emittance was reduced; (2) additional insulation was added to the antenna and it was isolated from the communications horn; (3) silver-filled silicone was used to improve interface thermal conductance; (4) insulation of RCE solenoid valves was improved; (5) radiative coupling between the battery and solar panels was reduced; (6) the duration and/or extent of the transfer orbit maneuver was limited; and (7) the radiation shield performance was improved with the addition of aluminized mylar.

To improve simulated orbital conditions imposed on the model within the vacuum chamber, the following modifications were made: (1) the spin fixture forward support was removed to eliminate heat leaks and shadowing, (2) the solar baffle was cooled with liquid nitrogen to simulate space sink temperature, (3) unsatisfactory xenon lamps were replaced, and (4) recalibration of some of the instrumentation was made. Test data acquired during testing in conjunction with test procedures were the primary basis for these modifications.

Although temperatures of some components show a 30°F to 40°F difference between test and prediction, the average spacecraft temperatures were approximately 10°F lower than those that had been predicted. This however is attributed primarily to low simulated solar fluxes during testing. The mechanically despun antenna (M/DA) had excessive heat leakage and insufficient internal power dissipation. The low sun sensor assembly temperature is attributed to the low xenon absorptance of the gold surfaces, $\alpha_{\text{xenon}} = 0.14$ versus a solar absorptance of 0.28.

Table I lists the components used for the comparative study for 0-deg and 30-deg sun angles. The 20 components listed in Column 1 correspond to the spacecraft components for which telemetry sensor data were available. Column 2 shows minimum/maximum acceptable temperature limits for which these units are designed. Component temperature margins can be determined from the difference between these allowables and the test and predicted temperatures that are shown in Columns 3

Table 1-Thermal development test results

1	2	3	4	5	6	7	8
Components	Min./Max. Qual. Temp Limits, °F	0° Sun Angle			30° Sun Angle		
		Test, °F	Predicted Temp, °F	ΔT, °F	Test Temp, °F	Predicted Temp, °F	ΔT, °F
<u>Communication</u>							
L.F. Amplifier #1	-10/122	54	68	-14	57	60	-3
Loc. Oscillator #1	0/110	53	68	-15	68	61	+7
L.F. Amplifier #2	-10/122	89	79	+10	91	60	+31
Loc. Oscillator #2	0/110	70	76	- 6	78	69	+9
Filter Coupler Detector	-20/150	--	(DNA) ^o	---	--	(DNA)	--
<u>Spacecraft</u>							
Equipment Panel 6	-10/122	66	81	-15	72	75	-3
Equipment Panel 7	-10/122	58	72	-14	61	65	-4
Central Cylinder	30/100	51	71	-20	49	61	-12
Motor/Drive, Flange	-10/135	36	54	-18	--	(DNA)	---
Solar Array, Center High	-130/120	--	(DNA)	---	--	(DNA)	---
<u>Power</u>							
PCU Shunt Regulator	0/120	69	80	-11	64	73	-9
Battery #1 Internal	30/105	62	70	- 8	57	61	-4
Battery #2 Internal	30/105	50	74	-24	66	66	0
<u>Thrusters</u>							
Forward Axial Valve #1	40/140	56	73	-17	66	73	-7
Forward Axial Thruster #1	-20/1500	32	18	-14	128	95	+33
Aft Axial Valve #2	40/140	54	73	-19	84	66	+18
Aft Axial Thruster #2	-20/1500	28	16	+12	22	7	+15
Radial Valve #1	40/140	51	80	-29	66	74	-8
Radial Thruster #1	-20/1500	76	71	+ 5	65	60	+5
Propellant Tank #2	40/140	65	69	- 4	66	70	-4
RMS (TEST) = 15.6°F					RMS (TEST) = 13.6°F		

^o DNA signifies that component temperatures were not analytically predicted or test results were not available.

and 4. The temperature differences, ΔT in Column 5, are used to calculate the RMS differences between test and analytical prediction.

The difference in RMS value between 0-deg and 30-deg sun angles does not imply that one can more accurately predict and/or simulate conditions at a 30-deg sun angle than at a 0-deg sun angle. The variation is probably an indication of the scatter of data.

In order to sufficiently define the error between test and analysis with a single parameter, the RMS of the temperature difference between test and prediction was used as an error criterion. Although it is possible to characterize the error by other methods (e.g., arithmetic average, mean and standard deviation, etc.), the RMS value is a more sensitive indicator if large temperature differences exist. Chronologically, the RMS temperature difference should decrease as spacecraft test and analysis progresses. Subsequent sections of the report show how much the RMS value decreases as testing and analytical refinements evolve. The final comparison with flight data shows the agreement that is achievable after a comprehensive thermal vacuum test program.

The RMS is defined by the expression

$$\text{RMS} = \sqrt{\frac{\sum \Delta T^2}{n}}, \text{ } ^\circ\text{F}$$

where ΔT is the difference between predicted values and thermal vacuum test temperatures. As shown in Table I, the RMS (TEST) temperature differences are 15.6°F for 0-deg sun angles and 13.6°F for 30-deg sun angles. Maximum temperature differences as high as 33°F were observed during these tests.

ENGINEERING DEVELOPMENT TESTS

Test Model Configuration

The primary purpose of engineering development tests was to verify subsystem interface compatibility and to operate subsystems over the temperature range anticipated in orbital operation. As a secondary objective, temperatures of components and assemblies were monitored in order to determine thermal design performance. The thermal model consisted of flight type subsystem components, structure, thermal components, thermal paths, and finishes (simulated components included reaction control equipment, solar panels, mechanically despun antenna bearings, and apogee boost motor).

Five thermal vacuum tests, simulating synchronous orbit conditions, were performed on the engineering model. Three tests were conducted at a 0-deg sun angle which simulated a maximum solar heating condition, a maximum power level during an eclipsed orbit, and a minimum power level during an eclipsed orbit. Two tests at a 30-deg sun angle simulated minimum solar heating (-30-deg sun angle) and maximum solar heating (+30-deg sun angle). The spacecraft model was assumed to be in thermal equilibrium when component temperature changes were 1°F or less per hour.

Thermal Vacuum Test Chamber

Test simulation for the engineering test model was considerably improved over the thermal development model tests. A new solar beam baffle with a liquid-nitrogen-cooled surface replaced the original baffle in order to better simulate space temperatures. Except for minor changes, the test chamber was essentially the same as for the thermal development tests.

Correlation of Test Results

In general, engineering development test results show the sun sensor, reaction control hydrazine tubing, and propellant valves exceeded the minimum allowable temperature limits during and following eclipse.³ The mechanically despun antenna temperature was lower than predicted due to the influence of the separation ring and central cylinder. The analytical model predicted higher temperatures and did not show a temperature gradient along the central cylinder. The thermal model was therefore modified to reflect this effect. Also, the power conditioning unit exceeded predicted temperatures subsequent to failure of the boost regulator (resulting from momentary shorting of main power bus).

Overall, test temperatures indicated good agreement with predicted levels. To better represent the spacecraft thermal design, the analytical thermal model had been revised to incorporate changes as a result of the preceding thermal vacuum testing. Equipment temperatures at thermal equilibrium were generally within 5°F to 10°F of predictions.

Table II lists the test and predicted temperatures for the components shown for the 0-deg and 30-deg sun angles. The RMS (TEST) temperature difference has improved from 15.6°F for the thermal development test to 13°F for the engineering

³ A thermal mockup of the reaction control equipment (RCE) was used. The propellant tanks were filled with 60:40 ratio of ethylene glycol and distilled water. The tubing and solenoid valves were not filled with simulated hydrazine liquid.

Table 2-Engineering development test results

1	2	3	4	5	6	7	8
Components	Min./Max. Qual. Temp Limits, °F	0° Sun Angle			30° Sun Angle		
		Test Temp, °F	Predicted Temp, °F	ΔT, °F	Test Temp, °F	Predicted Temp, °F	ΔT, °F
<u>Communication</u>							
L.F. Amplifier #1	-10/122	72	72	0	58	64	-6
Loc. Oscillator #1	0/110	74	73	+1	59	65	-6
L.F. Amplifier #2	-10/122	82	84	-2	70	76	-6
Loc. Oscillator #2	0/110	83	82	+1	69	74	-5
Filter Coupler Detector	-20/150	--	(DNA)	--	--	(DNA)	---
<u>Spacecraft</u>							
Equipment Panel 6	-10/122	--	(DNA)	--	--	(DNA)	---
Equipment Panel 7	-10/122	--	(DNA)	--	--	(DNA)	---
Central Cylinder	30/100	65	77	-12	76	79	-3
Motor/Drive, Flange	-10/135	55	69	-14	81	74	+7
Solar Array, Center High	-130/120	--	(DNA)	--	--	(DNA)	---
<u>Power</u>							
PCU Shunt Regulator	0/120	114	89	+25	91	101	-10
Battery #1 Internal	30/105	78	74	+ 4	59	79	-20
Battery #2 Internal	30/105	76	80	- 4	61	79	-18
<u>Thrusters</u>							
Forward Axial Valve #1	40/140	72	78	- 6	63	76	-13
Forward Axial Thruster #1	-20/1500	57	31	+26	104	91	+13
Aft Axial Valve #2	40/140	73	78	- 5	58	74	-16
Aft Axial Thruster #2	-20/1500	47	25	+22	26	16	+10
Radial Valve #1	40/140	82	82	0	66	78	-12
Radial Thruster #1	-20/1500	81	72	+ 9	65	77	-12
Propellant Tank #2	40/140	83	72	+11	63	70	-7
RMS (TEST) = 13.0°F					RMS (TEST) = 11.3°F		

development test at a 0-deg sun angle and from 13.6°F to 11.3°F at a 30-deg sun angle. Also, the maximum temperature difference for the series of tests was improved from 33°F to 26°F as a result of improved testing techniques and better correlation of analytical predictions.

QUALIFICATION MODEL TESTS

Test Model Configuration

The final series of tests used a qualification model to verify interface compatibility and to operate the subsystems using flight hardware in a vacuum environment over a temperature range more severe than that predicted for orbital operation. In addition, temperatures of selected components and assemblies of the spacecraft were monitored in order to determine thermal design performance. A series of six space simulation tests were performed on the qualification spacecraft. There were four tests at a 0-deg sun angle which included environmental conditions for maximum solar heating, for worst cold case, and for eclipse operation at both minimum and maximum equipment power levels. The remaining two tests were at a -30-deg sun angle at minimum solar heating and at a +30-deg sun angle at maximum solar heating conditions.

The qualification model was equipped with flight subsystem components, structure, thermal components, thermal paths, and finishes. Simulated components included 60:40 ratio (by weight) of ethylene glycol and distilled water to thermally simulate hydrazine. The apogee boost motor casing was titanium with a 10-mil stainless steel nozzle in place of the silica-phenolic Thiokol nozzle.

Correlation of Test Results

The spacecraft satisfactorily completed simulated tests with no major problems.

The results of tests on the qualification model indicated that all measured components remained within their allowable temperature limits at all times during the six tests. Good agreement was obtained between the test and predicted temperatures. Of the 243 measured temperatures, 88 percent were within 15°F of comparable predicted temperatures. All components were within their qualification test temperature limits during all tests. The analytical model was slightly revised on the basis of the qualification test results.

Table III lists the test and predicted temperatures of the components shown for 0-deg and 30-deg sun angles. The RMS (TEST) temperature difference was again improved over the engineering development test from 13.0°F to 10.5°F at a 0-deg

Table 3- Qualification model test results

1	2	3	4	5	6	7	8
Components	Min./Max. Qual. Temp Limits, °F	0° Sun Angle			30° Sun Angle		
		Test Temp, °F	Predicted Temp, °F	ΔT, °F	Test Temp, °F	Predicted Temp, °F	ΔT, °F
<u>Communication</u>							
I. F. Amplifier	-10/122	64	70	-6	69	61	+8
Loc. Oscillator #1	0/110	60	71	-11	66	62	+4
I. F. Amplifier #2	-10/122	76	79	-3	72	71	+1
Loc. Oscillator #2	0/110	72	77	-5	68	70	-2
Filter Coupler Detector	-20/150	70	(DNA)	---	74	74	0
<u>Spacecraft</u>							
Equipment Panel 6	-10/122	71	78	-7	72	76	-4
Equipment Panel 7	-10/122	74	73	+1	75	69	+6
Central Cylinder	30/100	63	73	-10	73	71	+2
Motor/Drive, Flange	-10/135	46	61	-15	78	74	+4
Solar Array, Center High	-130/120	73	69	+4	56	56	0
<u>Power</u>							
PCU Shunt Regulator	0/120	85	87	-2	88	87	-1
Battery #1 Internal	30/105	86	65	+11	62	73	-11
Battery #2 Internal	30/105	67	(DNA)	---	65	73	-8
<u>Thrusters</u>							
Forward Axial Valve #1	40/140	71	74	-3	72	73	-1
Forward Axial Thruster #1	-20/1500	28	28	0	83	81	+2
Aft Axial Valve #2	40/140	61	74	-13	46	71	-25
Aft Thruster #2	-20/1500	19	21	-2	65	62	+3
Radial Valve #1	40/140	73	77	-4	73	74	-1
Radial Thruster #1	-20/1500	66	(DNA)	---	72	75	-3
Propellant Tank #2	40/140	107	76	+31	99	73	+26
				RMS (TEST) = 10.5 °F		RMS (TEST) = 9.1 °F	

sun angle and from 11.3°F to 9.1°F at a 30-deg sun angle. However, maximum test/prediction differences of 31°F and 26°F were observed for 0-deg and 30-deg sun angles, respectively.

SUMMARY TABLE AND FLIGHT DATA

The thermal vacuum testing summary, Table IV, compares the results of the space simulation tests. The table indicates the trend in RMS temperature improvement as a result of testing and of revising the analytical model. In addition to reducing the RMS temperatures, thermal control was improved, potential failures were determined, and testing techniques were refined.

Table IV Thermal vacuum testing summary

<u>Prediction</u>	<u>Type Test</u>	<u>RMS</u>		<u>T, max</u>	
		<u>$\theta=0^\circ$</u>	<u>$\theta=30^\circ$</u>	<u>$\theta=0^\circ$</u>	<u>$\theta=30^\circ$</u>
Initial Model	Thermal Development	15.6°F	13.6°F	29°F	33°F
Revised Model	Engineering Development	13.0°F	11.3°F	26°F	20°F
Prequalification	Qualification Testing	10.5°F	9.1°F	31°F	26°F

The results on Table V, post-qualification test predictions, compares the spacecraft orbital telemetry data (TLM) with analytical predictions based on the final (post-qualification test) revised model. The temperature difference (ΔT), Column 6, was determined from the difference between flight data, Column 3, and 30-deg sun angle predicted values corrected for the 24.05-deg actual sun angle, Column 5. This correction was made in Column 4 using the following relation:

$$T_{\text{CORR}, \text{ } ^\circ\text{R}} = T_{\text{PRED}} \times \left(\frac{\cos 24.05^\circ}{\cos 30^\circ} \right)^{1/4}, \text{ } ^\circ\text{R}$$

The RMS (TLM) temperatures, for which sensor data was available, result in a value of 10.2°F. Examination of individual components shows substantial reduction in temperature differences as a result of refining thermal vacuum testing and iteration of the mathematical model after each test. It must be pointed out that temperature differences as great as 20°F still occur between flight temperatures and predictions even after testing. This is significant in that improvement in thermal design, after a series of thermal vacuum tests, does not imply that the ultimate in controlling spacecraft temperatures will be achieved.

Table 5.— Post-qualification test predictions, 24.05° sun angle

1	2	3	4	5	6
Components	Min./Max. Qual. Temp Limits, °F	Telemetry Sensor, °F	Pred. Temp, °F	Corr. Pred, °F	ΔT, °F
<u>Communication</u>					
I. F. Amplifier	-10/122	61	61	68	-7
Loc. Oscillator #1	0/110	58	62	69	-11
I. F. Amplifier #2	-10/122	74	71	78	-4
Loc. Oscillator #2	0/110	72	70	77	-5
Filter Coupler Detector	-20/150	72	74	81	-9
<u>Spacecraft</u>					
Equipment Panel 6	-10/122	70	76	83	-13
Equipment Panel 7	-10/122	69	69	76	-7
Central Cylinder	30/100	66	71	78	-12
Motor/Drive, Flange	-10/135	78	74	81	-3
Solar Array, Center High	-130/120	61	56	63	-2
<u>Power</u>					
PCU Shunt Regulator	0/120	95	87	94	+1
Battery #1 Internal	30/105	80	73	80	0
Battery #2 Internal	30/105	79	73	80	-1
<u>Thrusters</u>					
Forward Axial Valve #1	40/140	66	73	80	-14
Forward Axial Thruster #1	-20/1500	86	81	88	-2
Aft Axial Valve #2	40/140	58	71	78	-20
Aft Axial Thruster #2	-20/1500	49	62	69	-20
Radial Valve #1	40/140	66	74	81	-15
Radial Thruster #1	-20/1500	82	75	82	0
Propellant Tank #2	40/140	68	73	80	-12
RMS (TLM) = 10.2°F					

CONCLUSIONS

As a result of the series of thermal vacuum tests, the accuracy of temperature predictions of spacecraft components was significantly improved. The RMS temperature difference between predicted and measured values for critical components was reduced from about 15°F initially, to about 10°F after test and mathematical model improvements. Maximum component temperature differences between prediction and test were about 30°F for each test and about 20°F between prediction and orbital data. Based on the resultant correlation of these data, one can reasonably expect about a 15°F RMS error between prediction and test or orbital conditions, for an uncorrected thermal model, with a maximum component temperature difference of roughly 30°F. After thermal tests and adjustments to the analytical model, one may expect an improvement of roughly 30 percent in RMS error and corresponding improvements in maximum component temperature differences from predicted values.

Thermal vacuum tests are valuable in identifying deficiencies in spacecraft thermal design. Potential flight failures of components may be avoided by improving thermal performance and by design modification as a result of testing. Also, evolution of the thermal design, through thermal vacuum testing, increases confidence in and reliability of the spacecraft. The effectiveness of testing was indicated by the reduction of the RMS temperature difference. In addition to improving the thermal model accuracy, these results were useful in establishing test requirements and test techniques for new spacecraft programs.

ACKNOWLEDGMENTS

The author wishes to express his appreciation to the personnel of the Philco-Ford Corporation, Space Reentry Systems Division for their support and thorough documentation. Their work in formulating a comprehensive test program, conducting successful thermal vacuum tests, and recording data in sufficient detail made the correlation of results feasible. W. F. Schmidt of Philco-Ford Corporation was especially helpful in making suggestions and providing information necessary for meaningful documentation.

The contributions of members of the Fluid Mechanics Department of The Aerospace Corporation in the preparation of this report are also gratefully acknowledged.

REFERENCES

1. Space Simulation, Environmental Test Methods, MIL-STD-810B.

2. "Engineering Development Thermal Test Results," Report No. RN-DA 1894, Philco-Ford Corp., Space and Reentry Systems Division, Palo Alto, Calif.
3. "Qualification Model Space Simulation Test Temperatures," Report No. RN-DA 2105, Philco-Ford Corp., Space and Reentry Systems Division, Palo Alto, Calif. (15 Oct. 1969).

EFFECTS OF SURFACE BUBBLES ON HEAT-TRANSFER CHARACTERISTICS OF SPACECRAFT PAINTS

Reagan S. Redman, *NASA Manned Spacecraft Center, Houston, Texas*

ABSTRACT

An analytical investigation was conducted to determine the effect of surface bubbles on the heat-transfer characteristics of thermal-control coatings. The characteristics are affected by bubbles, and changes in these characteristics are functions of bubble size and configuration and internal and external bubble environments. Under certain internal bubble environmental conditions, the changes in the heat-transfer characteristics were calculated, were significant, and should be considered.

INTRODUCTION

As a part of the posttest evaluation of the 2TV-2 command and service module thermal-vacuum tests at the NASA Manned Spacecraft Center Space Environment Simulation Laboratory, an empirical investigation to determine the hemispherical emissivity of the spacecraft thermal-control paint was conducted with coated radiometers exposed under vacuum to a black surface at liquid-nitrogen temperatures. During this investigation, an unanticipated increase in the sensitivity of a radiometer with a bubble in its coating was observed. Postflight photographs (Fig. 1) of the Apollo 15 lunar-landing mission revealed that bubbles existed in one service module thermal-control coating. As a result of these two significant observations, an analytical investigation was begun to determine the effects of surface bubbles on the heat-transfer characteristics of thermal-control coatings. The investigation was conducted by means of the development of a mathematical model of the heat-transfer characteristics of the bubble.

MODEL DEVELOPMENT AND DESCRIPTION

The mathematical model was designed for parametric analysis of the effect of bubbles on the transfer of heat into and out of the coating substrate. The model contained a flat substrate covered with a thermal-control coating in which a bubble was defined. Provisions were included in the model for variation of the predominant coating thermal characteristics and the internal and external bubble environments. Bubble conditions and parameters that were considered to provide only second-order effects on the transfer of heat were not incorporated in the model.

The model was divided into a series of thermal nodes (Figs. 2 and 3) to provide analysis of heat flow into and out of the various model surfaces. Geometric radiation-exchange factors were computed between the model thermal nodes with the Boeing 2110 Program (Ref. 1). After computing the geometric radiation exchange factors, the bubble model was analyzed with the Systems Improved Numerical Differencing Analyzer (SINDA) thermal analyzer program (Ref. 2). The SINDA program is extremely flexible and permits easy manipulation of model parameters to allow for analysis of various bubble configurations and thermal-control coating properties over a wide range of external and internal bubble environments. The model provided for definition of the surface properties of each nodal surface, allowing considerable latitude in defining the thermal coating being investigated. Provisions were made for impressing heat loads on the model to enable analysis of bubbled surfaces exposed to combinations of deep-space and solar-flux environments.

Internal bubble environments were defined by the generation of "coupling factors" that combined the convective and conductive heat-transfer modes into equivalent singular conductors between each of the appropriate nodes in the model. By means of variation of the coupling factors, analysis was made of bubbles with internal environments ranging from any gas species at atmospheric pressure to a total absence of gas within the bubble.

ANALYSIS TECHNIQUES

The bubble-model configuration for this investigation consisted of a single bubble in the center of the model surface (Figs. 2 and 3). To approximate an assumed average bubble shape, the bubble was defined by a hemispherical segment with the distance from the top of the bubble to the substrate equal to one-half of the radius of the sphere. For the purpose of this investigation, it was assumed that the coating separated cleanly

from the substrate, thereby simplifying the definition of the interior bubble and substrate surfaces.

The effect of the bubble on the heat-transfer characteristics of the thermal-control coating was determined by comparing the net heat flux through the substrate directly beneath the bubble with the net heat flux through the remainder of the thermal-control coating. The substrate area directly beneath the bubble, node 6, and the remainder of the thermal-control surface, node 5, were made constant-temperature boundary nodes to facilitate the analysis of the net heat flux through the nodes (Fig. 2). By use of this approach, the variations in heat flux through the nodes became functions of the absorptivity (α) and emissivity (ϵ) of the surfaces and the incident heat flux. A hemispherical surface, node 7, was placed over the coating and bubble to simulate the deep-space heat sink. The node also was maintained as a constant-temperature boundary node for the same reason.

The α and ϵ of the thermal-control coating were varied over a range of values of 0.1 to 0.9. This range of values represents the α and ϵ values for most thermal-control coatings. A value of 1.0 was used for the α/ϵ ratio for all cases to provide a base line for analysis of thermal-control coatings with α/ϵ values other than 1.0. The substrate area directly beneath the bubble was given an α and ϵ value of 0.9, which is representative of a metallic or organic material that is used commonly as a substrate for thermal-control coatings.

The coupling factors were given values to represent bubble internal environments ranging from one atmosphere of air to a total vacuum. Thermal heat loads of zero and 1380 W/m^2 were imposed on the model to simulate exposure of the bubble to deep space and to one earth solar constant, respectively. These ranges of coupling factors and thermal loads represent the full range of realistic thermal-vacuum test and space-flight conditions.

ANALYSIS DISCUSSION

Two basic findings have resulted from this investigation. First, the heat-transfer characteristics of a thermal-control coating are affected significantly when bubbles occur in the coating. Second, these changes in heat-transfer characteristics are functions of the size and configuration of the bubble, the internal environment of the bubble, and the environment to which the bubble is exposed.

The ratio of the net heat flux through node 6 (the area directly beneath the bubble) to the net heat flux through a corresponding flat unbubbled surface is plotted in Figures 4 and 5. These ratios were calculated over a range of bubble internal environments and surface properties with and without exposure to solar flux.

For the case with no impressed heat load, the ratio of the heat flux through the bubble to that through a flat unbubbled surface was found to range from 1.32 (for a bubble with an α and ϵ of 0.1 and a coupling factor of 3×10^{-4} W/°F) to 0.48 (for a bubble with an α and ϵ of 0.9 and a coupling factor of 3×10^{-9} W/°F). The ratio value 1.32 represents a condition in which the bubble contains a sufficient mass of air so that the bubble temperature approaches the temperature of the substrate surface directly beneath the bubble. Under such a condition, there is an increase in heat leaked out of the thermal-control surface because the surface area of the bubble is larger than its projected area. This heat-leak increase is approximately proportional to the ratio of surface area of the bubble to its projected area. The heat-leak increase is not exactly proportional to the area increase because the bubble has a small view of the surrounding flat surface and receives energy emitted from that surface with the result that the net heat loss from the bubble decreases.

The case of an impressed heat load on a bubble containing a substantial mass of air presents a situation in which a slight increase in heat is leaked into the thermal-control surface. The raised surface of the bubble receives reflected energy from the surrounding surface and, thereby, effectively increases its projected area. The ratio of net heat fluxes is 1.07 with an impressed heat load of 1380 W/m^2 (Fig. 4).

The heat-transfer characteristics are changed drastically for the bubble configuration with an internal vacuum. For this condition, the bubble acts as an insulator for the substrate beneath it, and the net heat flux into or out of the substrate is reduced significantly. The heat-transfer characteristic is illustrated by the net heat-flux ratios of 0.48 for zero impressed heat load and 0.39 for an impressed heat load of 1380 W/m^2 (Fig. 4).

The analysis in this investigation was conducted for a single bubble; therefore, the total effect on a thermal-control system would be related to the percentage of the thermal-control coating that contains bubbles.

CONCLUSIONS

Although the model used in this investigation was relatively simple, because second-order effects were not considered, the model is indicative that the occurrence of bubbles in a thermal-control coating may affect significantly the heat-transfer characteristics of the coating. Therefore, the effect will be proportional to the percentage of the surface that contains bubbles. The most significant factor encountered in predicting the effects of bubbles on thermal-control coatings was the internal atmosphere of the bubble.

REFERENCES

1. Don A. Davis and Raleigh L. Drake: AS-2110, "Monte-Carlo Direct View Factor Program and Generalized Radiative Heat Transfer Program." The Boeing Company, 1966.
2. James P. Smith: "Systems Improved Numerical Differencing Analyzer (SINDA) User's Manual," TRW Systems Group, Houston, Texas, NASA Contract 9-10435, 1971.

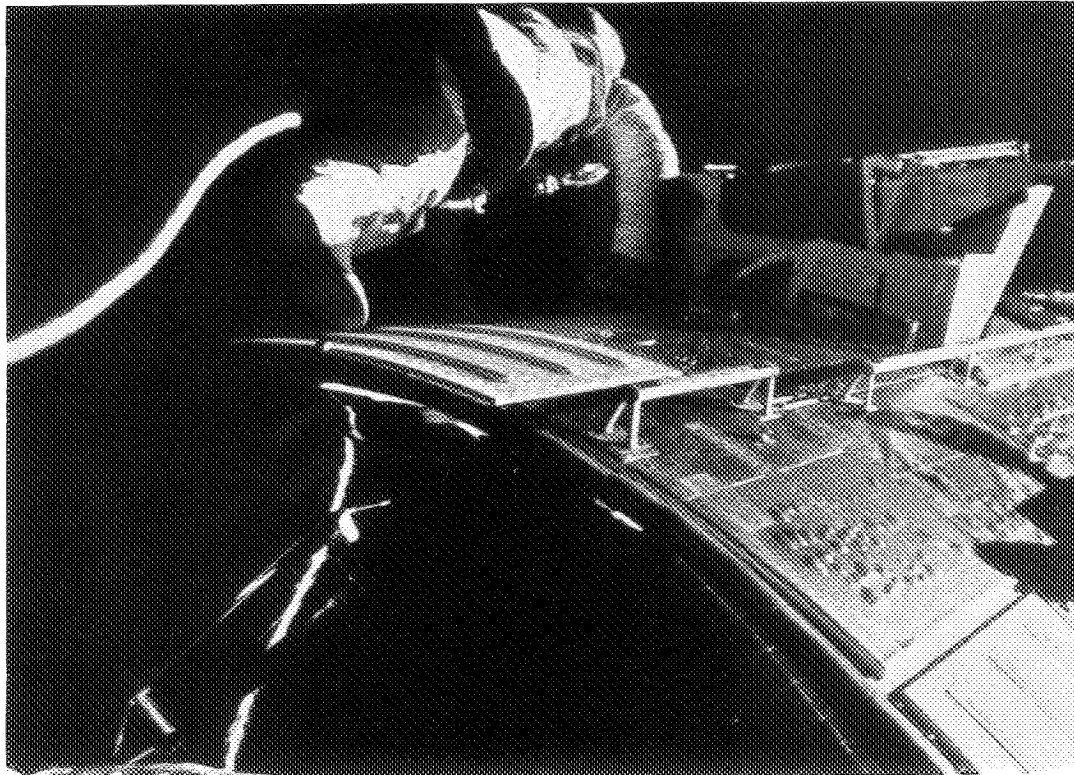


Fig. 1—View of bubbles on Apollo 15 service module

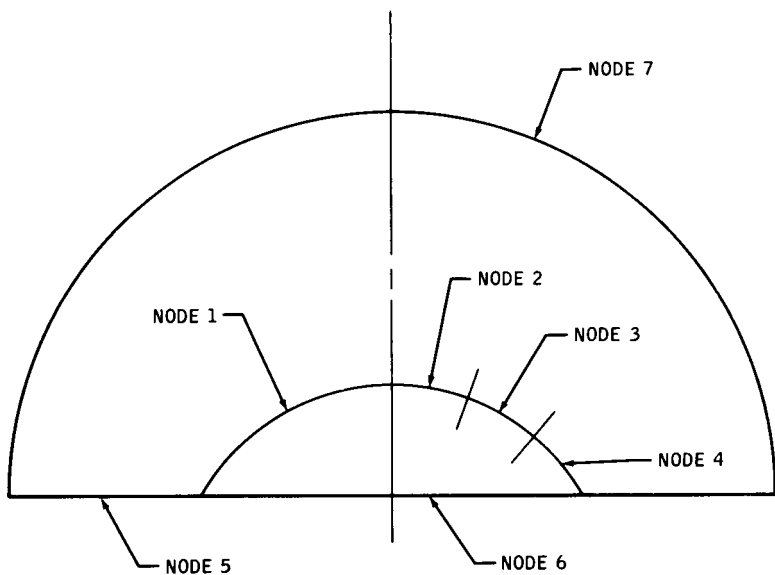


Fig. 2—Analytical model cross section

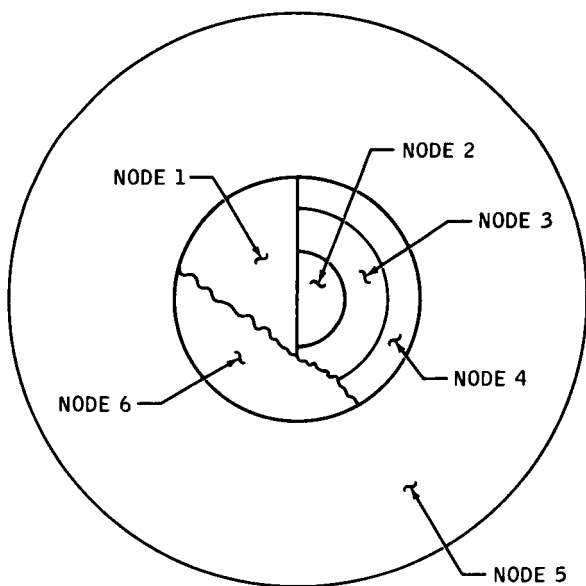


Fig. 3—Analytical model plan view

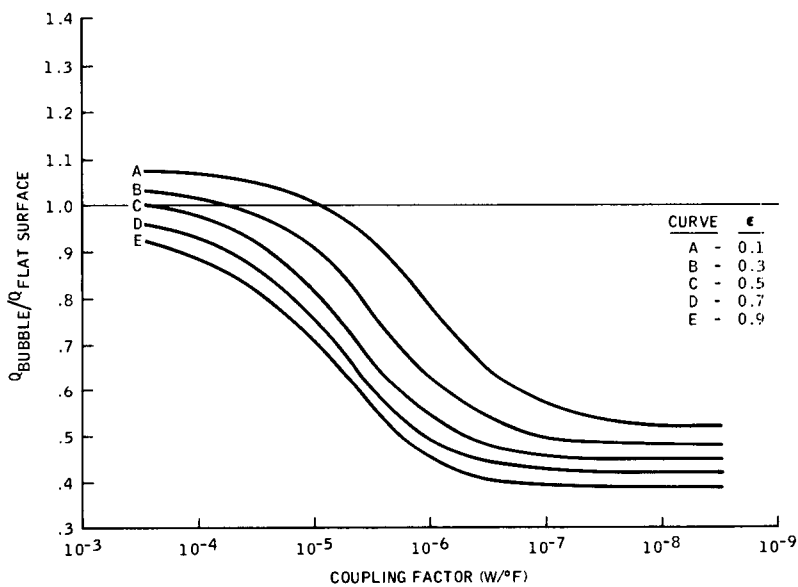


Fig. 4—Net Q ratio for 1380-W/m^2 heat load

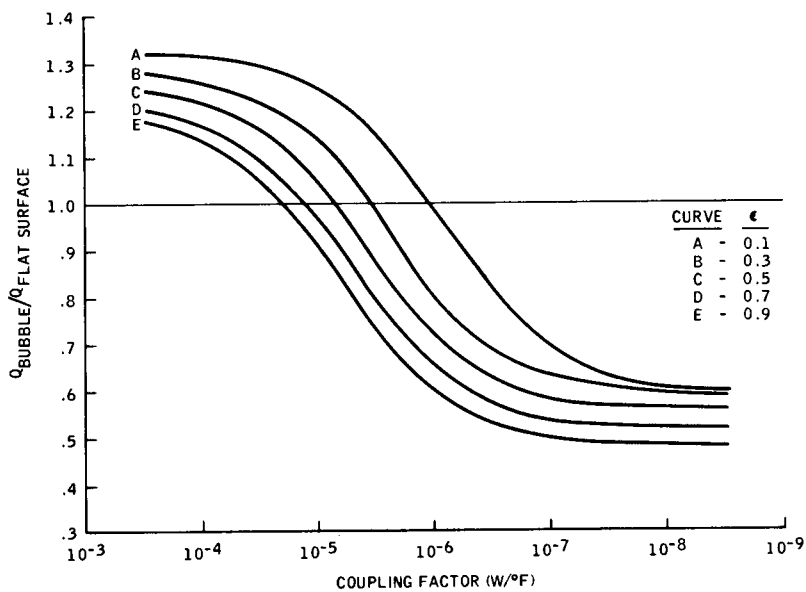


Fig. 5—Net Q ratio for zero heat load

SPACE SIMULATION AND RATE DEPENDENT RADIATION TESTING

H. E. Pollard and D. C. Briggs, *Philco-Ford Corporation, Palo Alto, California*

ABSTRACT

An environmental test facility is described which allows in-situ measurements for evaluation of near real time synergistic effects of combined space environments.

INTRODUCTION

The major objective of radiation testing in the Aerospace industry is to determine the effects of the orbital environment upon specific spacecraft components. Much of the radiation effects work that is done in the field of semiconductor damage research makes use of particle accelerators. The nature of these machines and the inherent high cost of operation makes it necessary to expose the experimental samples to particle flux rates from 100 to 5000 times higher than the rate encountered in typical space environments. This makes it difficult to establish radiation rate dependence or to examine the combined effects of the total environment such as temperature, vacuum, and radiation at the same time.

The combined environments test facility presented in this paper is specifically designed for performing combined environments materials testing, in-situ measurements, and annealing tests in a continuous vacuum environment. The test facility described combines exposure to hard vacuum, solar simulation, thermal cycling, and low level beta spectral irradiation. Primary emphasis has been placed on accomplishing in-situ measurements without interrupting the test conditions. The test chamber is designed to obtain engineering performance data on material properties which can be directly related to spacecraft missions.

The test facility has been designed to simulate near real time testing, allowing for accurate evaluation of the synergistic effects of the combined space environment. One extremely significant test parameter not usually simulated is the radiation spectrum. The facility described employs a beta source which is a mixture of Strontium-90 in secular equilibrium with its short half-life daughter Yttrium-90. This combination of isotopes generates a range of electron energies from 0 to 2 Mev (after encapsulation), with a spectrum which appears to closely match the

space electron spectrum at various altitudes. The intensity, or irradiation rate, can be tailored to specific conditions to simulate or accelerate space effects by varying the mass of the isotope or the distance between the sample and the source.

The combination of beta source, excellent solar simulation, hard clean vacuum, and accurate temperature control provides a maintenance free, long term, low cost test facility which accurately simulates space environments and is adaptable to a wide spectrum of space component testing. This facility has been effectively used for solar cell testing on two Government programs with outstanding results.

Radiation Facility

The radiation facility consists of several irradiation chambers as illustrated in Figure 1. Each test setup includes an irradiation chamber, vacuum system, beta source, and temperature control electronics. Various solar simulation and ultraviolet sources are available for each test chamber. All ancillary control electronics and the data acquisition system are located adjacent to the test equipment, but separated from the radiation environment by a shielded wall as shown.

Radioisotope Source -- The isotope selected was Strontium-90 because of its spectral characteristics which, with its short half-life daughter, Yttrium-90, provides a close approximation of the trapped electron spectrum. The Strontium-90 provides a large flux of low energy beta up to 0.546 Mev. Yttrium-90, in secular equilibrium with the Strontium-90, produces high energy beta up to 2.284 Mev. The combined spectrum, outside the encapsulated isotope, is presented in Figure 2 with a comparison curve of the near synchronous spectrum. Strontium-90 is also ideally suited for this application because of its long term stability (a half-life of 19.9 years).

The chemical form of the isotope selected was Strontium-Titanate, SrTiO_3 , which has a specific activity of approximately 32 curies/gram to produce the smallest obtainable volume and to minimize self-shielding. To further minimize self-shielding, the source was packaged in an 0.080 inch diameter stainless steel (No. 304) tube with a wall thickness of less than 0.004 inch thick. The resulting 6 curie source has an active length of one inch. The active SrTiO_3 of a one curie source was diluted with inactive SrTiO_3 to produce the same one inch active length. It was necessary to increase the length of an 8.5 curie source to 1.5 inches.

The source is mounted to a movable rod to allow withdrawal of the source from the irradiation zone into a lead shielded canister. This canister also houses the isotope during storage and transportation. The unit is vacuum tight to permit isotope location

and positioning while under vacuum. The isotope and canister are shown in Figure 3.

Vacuum System -- The vacuum system includes the irradiation chamber, vacuum pumps, and operational electronics. A typical chamber test configuration is shown in Figure 4. The principal chamber is a 22 inch cube made of aluminum to minimize bremsstrahlung. This chamber mates with an ion pumped vacuum system (Varian Associates VI-260). One face of the chamber has a 15 inch diameter Corning 7940 optical grade fused silica window. The opposite face holds the sample mounting plate with its associated temperature control and instrumentation feedthroughs. The radioisotope with canister mounts to a third side. Additional ports are available on the chamber for ultraviolet lamp insertion if required. Numerous smaller ports are located just below the chamber-vacuum system interface for location of the residual gas analyzer sensing head, vacuum pumps, and system instrumentation. The entire chamber, exclusive of ports, is shielded by 1/4 inch thick lead to reduce the radiation level in the area adjacent to the chamber. The large fused silica window is used to permit illumination of the test samples for space simulation and data acquisition.

The pumping system is a 500 liter/sec ion pump which provides contamination free, long term, stable operating characteristics. Roughing is provided by three cryogenic adsorption pumps and a titanium sublimation pump. The ion pump is connected to an emergency power generator to provide continuous vacuum in the event of a commercial power failure. This safety feature is essential in maintaining test integrity for long term testing.

Illumination Source -- A Spectrolab X-25 solar simulator with close spectral match filtering simulates the solar spectrum from 0.25 to 2.7μ over a 13 inch diameter uniform plane at one air mass zero solar constant (140 mw/cm^2). The large fused silica window has specially polished, flat, parallel surfaces to prevent distortion of beam uniformity. The transmission characteristics of fused quartz were necessary to eliminate spectral distortion and absorption of the illumination. The possibility of radiation damage of the window is evaluated throughout the test. A small fused silica window is located opposite the large window, shielded from the radiation source, through which the light exiting the small window can be monitored for degradation. The solar simulator is standardized before data acquisition by checking uniformity, total intensity, and four portions of the spectral content. The spectral information is used to monitor the decrease in the short wavelength radiation resulting from degradation of the simulator lamp and optics. Figure 1 illustrates the location of the simulator calibration system which is also used for illumination intensity standardization.

When data measurements are not being made during solar cell testing, a quartz-iodine lamp is used to provide illumination to

operate the solar cells through a resistive load. A 1μ filter is used to remove the infrared portion of the lamp spectrum when low temperature test conditions must be maintained. When additional ultraviolet radiation is required, a conventional A-H6 high pressure mercury arc lamp can be employed either outside the large window or inserted directly into the chamber, allowing very high exposure rates.

Residual Gas Analyzer -- The degradation products evolved from material under test can be determined, and an objective measure of the cleanliness of the system can be measured by use of the residual gas analyzer (RGA). Ports are available for locating the head of a Granville-Phillips Model 750 RGA into the chamber. This analyzer is of the quadrupole type, discriminating by mass of ionized particles up to 750. Partial pressure measurements of the gas evolved or relative quantities can be obtained to assist in the degradation analysis and to determine possible contamination products.

Sample Mounting -- The samples are located on temperature controlled blocks positioned so the center of the surface of each block is normal to the radiation source. The temperature of each block is controlled by the use of cartridge heaters and conventional thermal controllers. One block has been connected to a LN_2 reservoir for low temperature control. The blocks controlled above $40^\circ F$ are attached to a refrigerated water cooled heat sink. For the long term testing it was necessary to significantly derate the heaters and employ redundant cooling supplies. In the event of a power failure, the low temperature must be maintained by connecting its controller to the emergency generator.

The uniformity of the beta flux over the test surfaces has been determined using thermoluminescent dosimeters (TLD). The TLD's used successfully are 30 mg of LiF sealed in small plastic packets and attached to the test surface using double-backed tape. Relative isofluence contour lines are then constructed for each sample station. The total activity of the samples has been determined calorimetrically and agrees well with other dosimetry measurements. Correlation of test data from several solar cell experiments have confirmed the uniformity of the flux over the test plane.

Data Acquisition

Solar cell performance is determined by measuring the electrical performance characteristics of each cell using a semi-automatic data acquisition system. Accurate data is obtained using a four-wire connection to each cell, two leads for current measurement and two for voltage measurement. A switching unit automatically selects the cell to be tested. The simulator intensity is constantly monitored while data is taken to compensate for lamp fluctuations. The frequency of data acquisition is selected

based upon the rate of change of measured values, but frequently enough for statistically significant regression and correlation analyses of the results.

TEST RESULTS

The radiation test facility has been used successfully for two Government contracts appertaining to lithium doped solar cell development and evaluation. As an illustration of the typical application of the requirement for rate dependent testing, samples of solar cells which were under long term test were exposed to a pulsed neutron irradiation. Following this irradiation, the samples were returned to the test chamber for continuous low level beta exposure. The variation in damage recovery rate for various types of samples is presented in Figure 5. The exposure to the combined environments and the in-situ measurement have allowed detailed data from which the damage and recovery mechanisms may be studied.

CONCLUSIONS

The results of the studies presented on the irradiation of lithium doped silicon solar cells demonstrate the type of information which can be obtained when irradiating samples at near real rates. Subtle changes resulting from rate effects and continuous monitoring of the radiation effects can be clearly resolved in low rate testing that might normally be obscured in accelerated testing. The combined effects of temperature, solar electromagnetic radiation, and electron radiation upon the material properties of thin films can be determined and a history of the products evolved recorded. The complex problems of determining and isolating synergistic effects is simplified by the large statistical number of samples and frequent collection of accurate data.

The combined environments testing of electronic components can provide details as to lifetime operation of subsystems under simulated space conditions.

REFERENCES

1. "Engineering Experimental Program on the Effects of Near-Space Radiation on Lithium-Doped Solar Cells, WDL-TR4213, Philco-Ford Corporation, Palo Alto, Calif., 1 June 1970.
2. Evaluation of the Effect of Space Radiation on Lithium P-on-N Solar Cells, Report No. TR-DAL875 (First Irradiation Run Report), Philco-Ford Corporation, SRS Division, Palo Alto, Calif., August 1968.
3. D. L. Reynard and D. B. Orvis, Beta Irradiation of Lithium-Doped Solar Cells, Conference Record of the Seventh Photovoltaic Specialists Conference, IEEE, Pasadena, Calif., 19-21 November 1968.

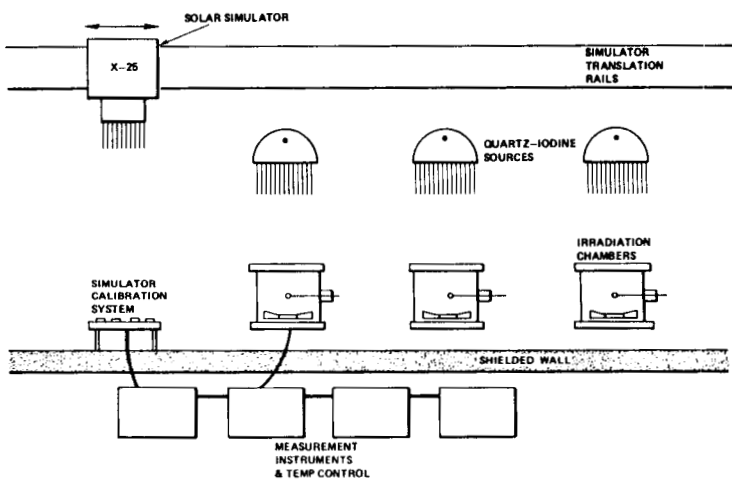


FIGURE 1 PHILCO-FORD RADIATION FACILITY

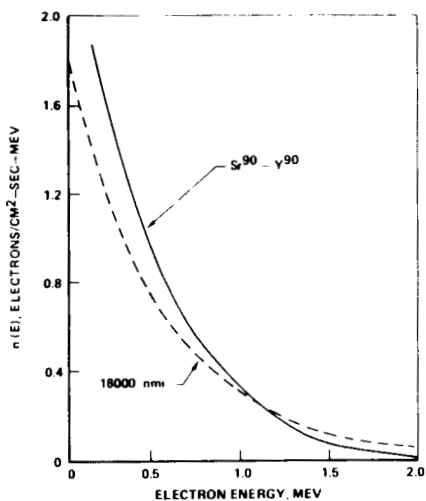


Figure 2 Isotope Characteristics

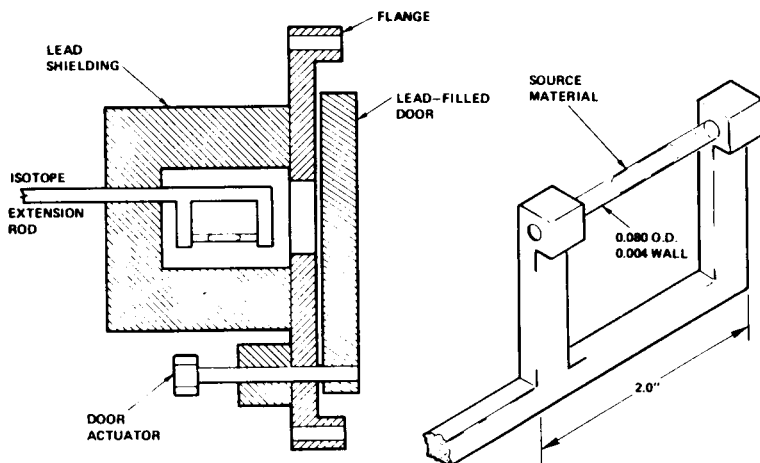


FIGURE 3 ISOTOPE ROD AND CANISTER

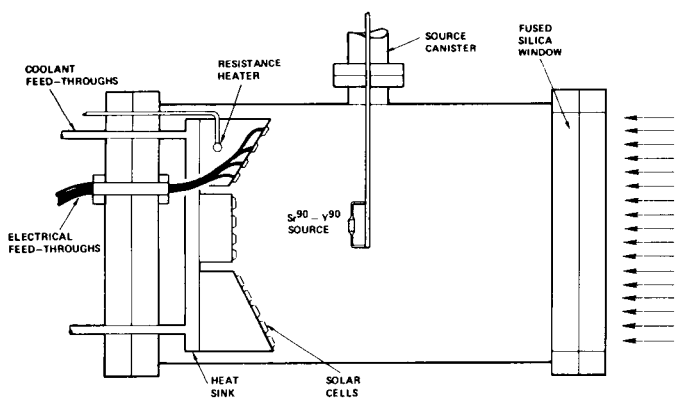


FIGURE 4 CHAMBER DESIGN

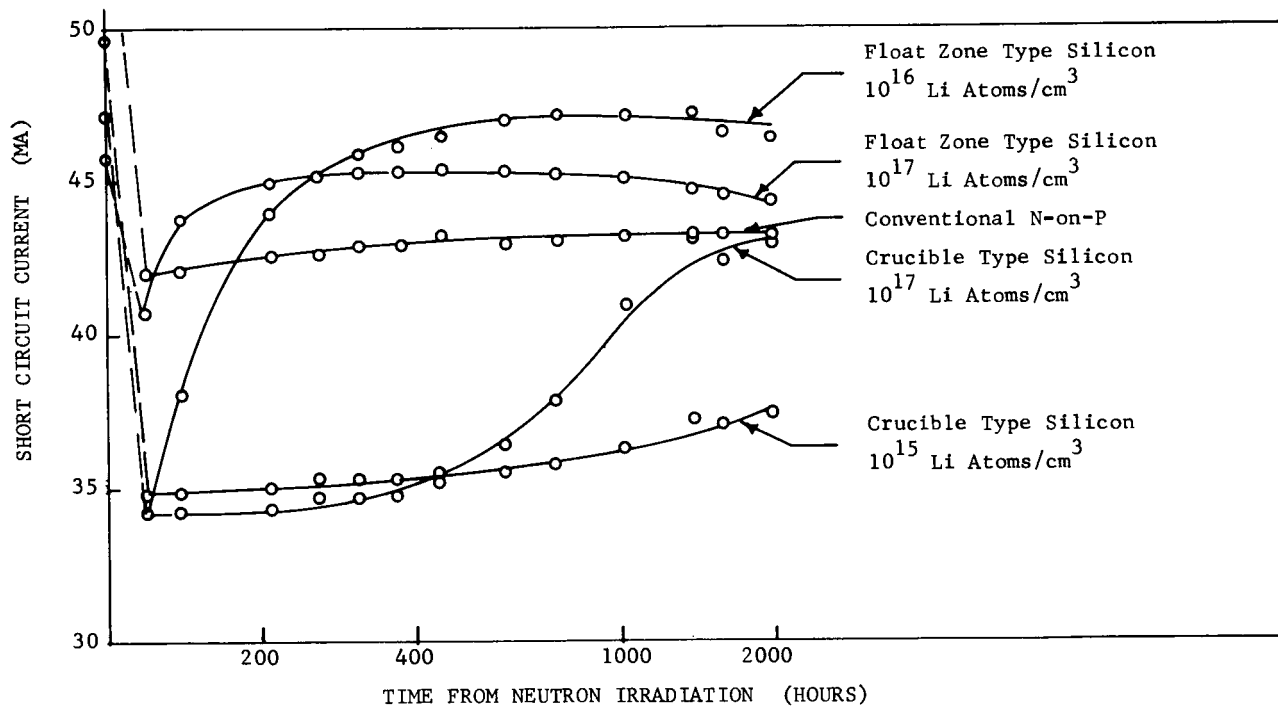


FIGURE 5 RECOVERY OF NEUTRON IRRADIATED SILICON SOLAR CELLS AT 110°F DURING CONTINUOUS BETA IRRADIATION

ENVIRONMENTAL SIMULATION TESTING OF SOLAR CELL CONTAMINATION BY HYDRAZINE

W. Walding Moore, Jr., *Marshall Space Flight Center, Huntsville, Alabama*

ABSTRACT

It is known that spacecraft attitude or reaction control system thrusters are sources of fuel contaminants due to the valve blow-by process. This occurs particularly in the common pulsed mode of thruster operation. This paper deals primarily with test results for thermal/vacuum and radiation environment simulation of this type of contamination. Solar cell performance degradation, as measured by short circuit current, is presented in correlation with the variations used in environmental parameters.

INTRODUCTION

For several years, tests of an operational nature have been performed for rocket engines in a vacuum environment. In certain of the more recent tests [1-4], the vacuum chambers have been additionally instrumented to measure optical contamination effects of the engine firings. As representation in one reaction control system engine test at Manned Spacecraft Center in 1966, the test article was viewed vertically downward from a chamber window 6.096 m (20 feet) away. The engine was operated in a pulsed mode for actuations varying from 5 seconds to 50 milliseconds. Under these conditions, there are no plume or thermal insulation ablation problems. As recorded by the instrumentation motion camera, the chamber window was gradually covered with an opaque, non-uniform deposit. The appearance of the contaminants as they physisorbed indicated the deposit composition was principally unburned propellant fractions rather than combustion by-products. This concept is supported by typical performance data of rocket engines which specify nominal valve opening and closing times on the order of milliseconds. During these periods propellants can continue to flow, as well as during valve blow-by and trapped volumes events. In addition,

at least one investigation [4] has reported a compositional analysis of contaminant deposits indicating the presence of normal engine fuels. Because of this information and the ever present need of spacecraft missions to be sure of their power resources, testing has been performed to measure the effects of rocket engine propellant components on actual output power of solar cell units.

Test Method and Procedure

The test method exposes a pair of calibrated (to balloon primary at 50.63 mA/130.72 mW/cm² and 50.65 mA/133.37 mW/cm²) solar cell units and a quartz crystal microbalance to a source of simulated vents of rocket engine fuel components. In addition to performance and normal environmental parameters monitoring, the test articles can be exposed to near ultraviolet irradiation as well as the necessary visible radiation to drive the solar cells.

The test procedure for the effort to date has concentrated on vents of the Aerozine-50 fuel component, hydrazine. Because of safety considerations, the actual samples were of a 64 percent water solution of hydrazine. Thus the test procedure was structured to compare effects on power performance of both water and the sample solution vents in the one- to two-milliliter range. During all testing events, the parameters monitored were solar cell short circuit current (and associated voltage), chamber pressure, quartz crystal microbalance beat frequency, solar cell temperature, and quartz crystal microbalance temperature. In addition, a test panel of selected optical elements was exposed to the vents for determination of spectral region optical degradation during the vents.

Figure 1 gives a view of the test chamber, particularly showing the functional setup of the feed-throughs ring. By referring to the schematic diagram given in Figure 2, the functions of the individual parts of the system on the photograph can be identified. Likewise, the details of the chamber interior setup as given in Figure 3 may be identified by referring to Figure 2.

Data Discussion and Analysis

Test results for the primary goal of this effort are representatively presented in Figures 5 and 7. These figures show

two selected runs as chronological plots of solar cell power (using voltage produced in short circuit connection as indicator), quartz crystal microbalance beat frequency, test chamber pressure, solar cells temperature, and quartz crystal microbalance temperature. The salient features of the graphs can be reviewed by utilizing Figures 6 and 8 which present in table form the significant events of the test runs. Figure 4 is the conversion graph used in Figure 7 for determining beat frequency from output voltage.

Analysis of Figure 5, and particularly Figure 7, shows that the quartz crystal microbalance mass detection is much more sensitive than even the most sensitive "power" function monitor. This would seem to be due to the integrating factor of even a few square centimeters area of solar cell surface. The physical appearance of the sorbed deposits was that of nonhomogeneous aggregates. On a qualitative basis it was observed that measurements of low wavelength visible region optical property change were more sensitive than the solar cell output.

Conclusions

Small vents of hydrazine/water solutions do produce contamination of sensors and optical surfaces by nonhomogeneous deposits. Deposits produced without ultraviolet irradiation as surface activation energy were nonstable white mist in form, probably mostly water vapor. Deposits produced with ultraviolet irradiation were a nonhomogeneous distribution of brownish liquid, probably an amorphous polymer derivative of the hydrazine. These deposits, by contrast, were significantly stable with respect to re-evolvement from the surfaces. Finally, although further measurements of other rocket fuel components are needed, it would seem the probability of significant solar cell functional degradation by fuels deposition in orbit is small.

Acknowledgments

Appreciation is gratefully expressed to Mr. Dewey F. Newman for significant contributions to the physical setup and operation of test instrumentation.

References

1. Moses, J.; Miller, E.; Miller, J.; and Zoller, L.: Contamination of Optical Surfaces by Solid Rocket Exhausts. NASA TN-P&VE-P-67-2, May 22, 1967.
2. Sodek, B. A.; and Chow, C. Y.: Reaction Control System Rocket Engine Space Plume Flow Fields. Brown Engineering Report RL-SSL-039, April 1968.
3. Borson, N.: Rocket Plumes as Contamination Sources. Optical Contamination in Space Symposium, Aspen, Colorado, August 14, 1969.
4. Arnett, G. M., Technical Coordinator: Lunar Excursion Module RCS Engine Vacuum Chamber Contamination Study. NASA TM X-53859, July 8, 1969.

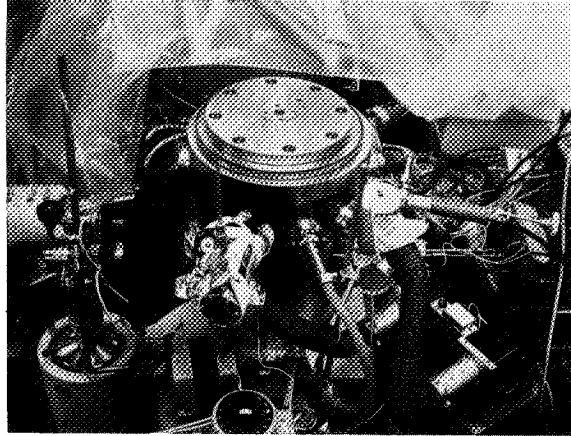


Fig. 1. Exterior view of environmental test chamber setup.

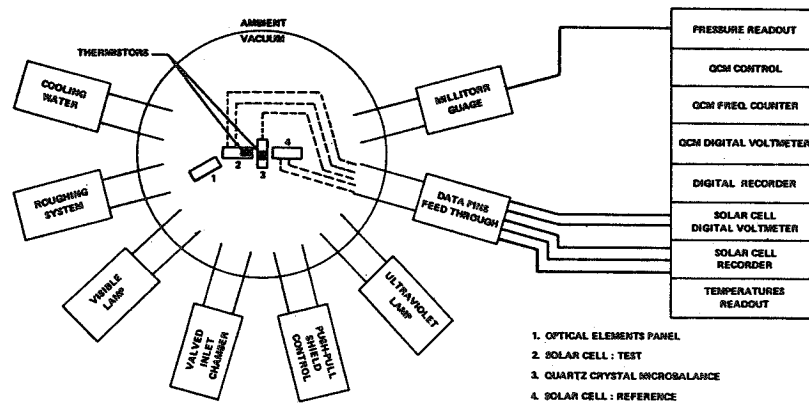


Fig. 2. Schematic of test articles and data acquisition units layout.

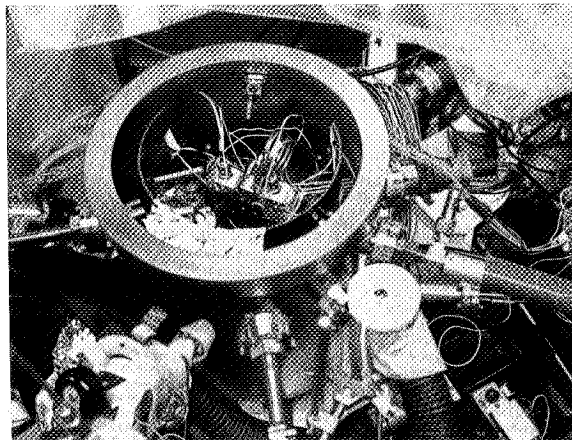


Fig. 3. Interior view of environmental test chamber setup.

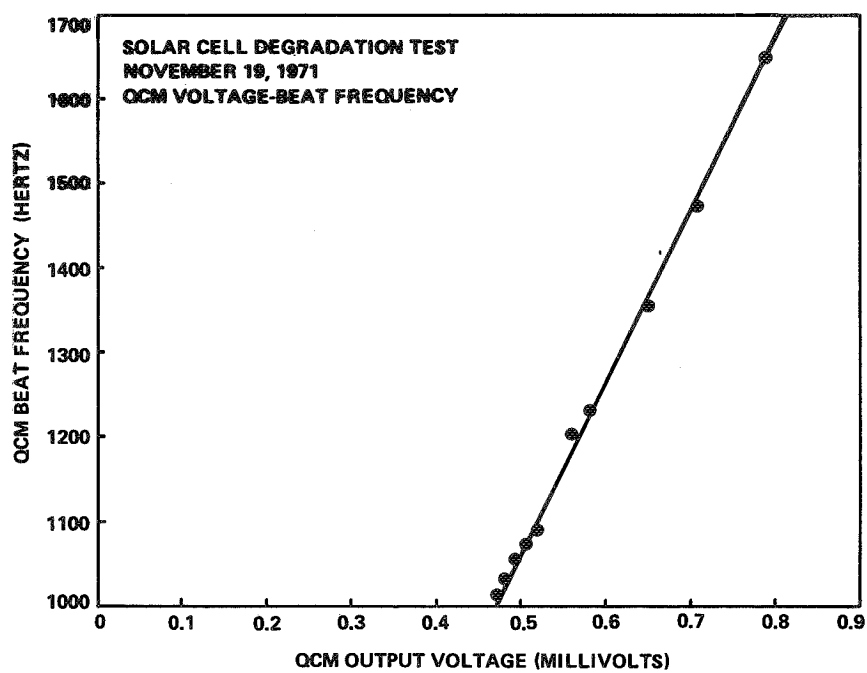


Fig. 4. Conversion chart for output voltage to beat frequency of quartz crystal microbalance.

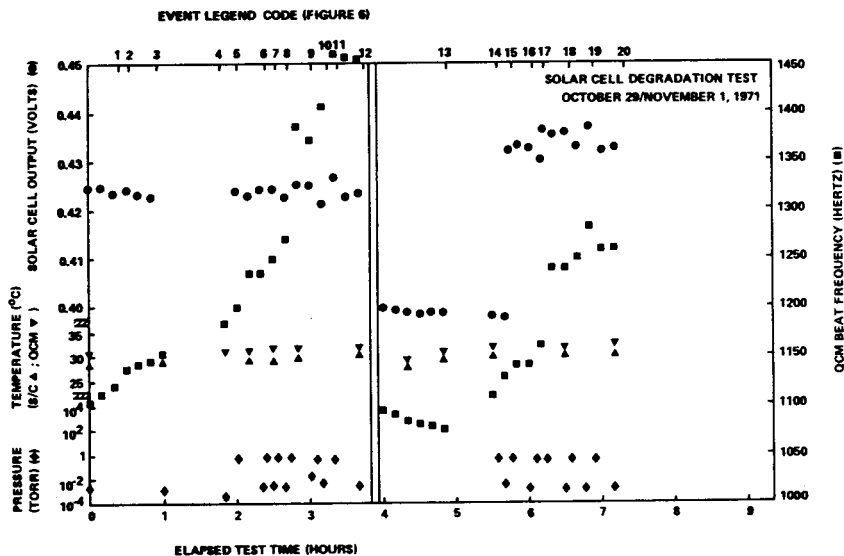


Fig. 5. Chronological plot of measured test parameters.

SOLAR CELL DEGRADATION TEST EVENT LEGEND TABLE	
Event Number	Event Description
1	Open sorption pump; close mechanical pump; 10/29/71
2	Close sorption pump; contaminated from previous run and not functioning
3	Accidentally moved light source
4	Sorption pump replaced with new unit; re-open pump valve
5	Vent 1; laboratory air at room T/P; 750 μ pressure peak
6	Vent 2; laboratory air at room T/P; 750 μ pressure peak
7	Vent 3; 0.5 ml H_2O plus laboratory air
8	Vent 4; 2.0 ml H_2O plus laboratory air
9	Vent 5; 0.5 ml hydrazine/ H_2O (64% mixture) plus laboratory air
10	Vent 6; 2.0 ml hydrazine/ H_2O (64% mixture) plus laboratory air
11	Turned on heater tape to clean vents chamber
12	Shut down; part I of test
13	Open sorption pump; 11/1/71
14-20	Repeat steps 1-10

Fig. 6. Table of events occurring during Figure 5 period.

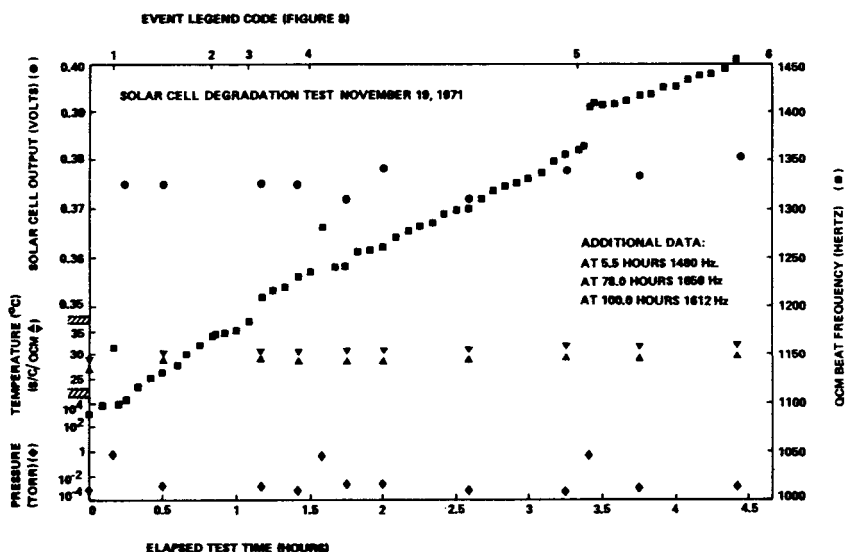


Fig. 7. Chronological plot of measured test parameters.

SOLAR CELL DEGRADATION TEST EVENT LEGEND TABLE	
Event Number	Event Description
1	Sorption pump open; vent 2-ml sample of water plus laboratory air; peak pressure 750μ ; no UV
2	Close samples inlet chamber valve; continue monitor
3	Turn ultraviolet source on; continue monitor
4	End monitor of vent of 2 ml water; vent 1 ml of hydrazine/water mixture plus laboratory air; peak pressure 750μ ; with ultraviolet irradiation
5	Close samples inlet chamber valve; vent 2 ml of hydrazine/water mixture plus laboratory air; peak pressure 750μ ; with ultraviolet irradiation
6	Close samples inlet chamber valve; continue monitor

Fig. 8. Table of events occurring during Figure 7 period.

A CONTAMINATION EXPERIMENT INVESTIGATING THE FAILURE OF THE NIMBUS IV FILTER WEDGE SPECTROMETER

Raymond Kruger, *Goddard Space Flight Center, Greenbelt, Maryland*

ABSTRACT

A ground test is described wherein a quartz crystal microbalance was used in defining the quantity and direction of a contaminant thereby confirming the cause of the failure of an experiment in orbit.

INTRODUCTION

As a result of a failure in the Filter Wedge Spectrometer experiment (FWS) on the Nimbus IV* spacecraft shortly after its launch on April 8, 1970, a review was initiated to determine the cause of this failure. The review (Reference 1) concluded that the failure was most probably due to the accretion of water on the 176K detector surface. Also, tests were recommended to verify this conclusion. This report is an account of a test conducted in accordance with the recommendation. In this test, the quartz crystal microbalance (QCM) was the instrument which provided the major portion of the data used in the analysis.

Summary of Results

Measurements made by the QCM indicate that by the time of FWS turn-on, a thickness equivalent to 0.28 mm of water had accreted on the detector. It is estimated that the flux impinging on the detector should have decreased to a value equal to the desorption flux commensurate with the vapor pressure of water at the detector temperature in about three days. Furthermore, the thickness of the ice layer on the detector would be expected to have decreased to essentially zero in about nine days; such decrease was not noted in orbit in two months at which time another failure made the experiment inoperative.

Background

The FWS on Nimbus IV was designed to measure radiance of the earth as a function of wavelength in the 1.2 to 2.4 and 3.2 and 6.4 μm regions

* Nimbus IV satellite had a period of 107.124 min. with a perigee 1103 km and an apogee of 1113 km.

for meterological purposes. Figure 1 is a photograph of the FWS. At instrument turn-on during orbit five it was found that the 1.2 to $2.4\mu\text{m}$ band was degraded and the 3.2 to $6.4\mu\text{m}$ band was greatly obscured. The existence of what appeared to be ice absorption bands in this and the shorter wavelength region and the occurrence of icing during ground testing caused Dr. W. A. Hovis (FWS principal investigator) to conclude that the failure was due to ice forming on the cold (176K) detector surface.

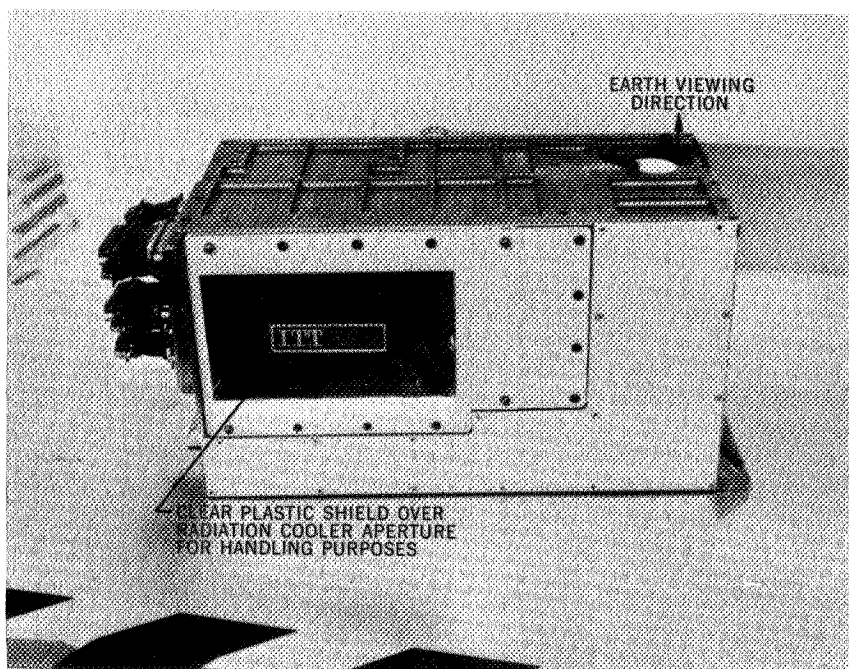


Figure 1. Filter Wedge Spectrometer

The attainment of this low temperature is achieved through the use of a radiation cooler. This is a passive device in which the design is such as to minimize thermal inputs to what is referred to as a "cold patch" (on which the detector is mounted) and to maximize thermal losses from the patch. Figure 2 is a sketch showing the radiation cooler.

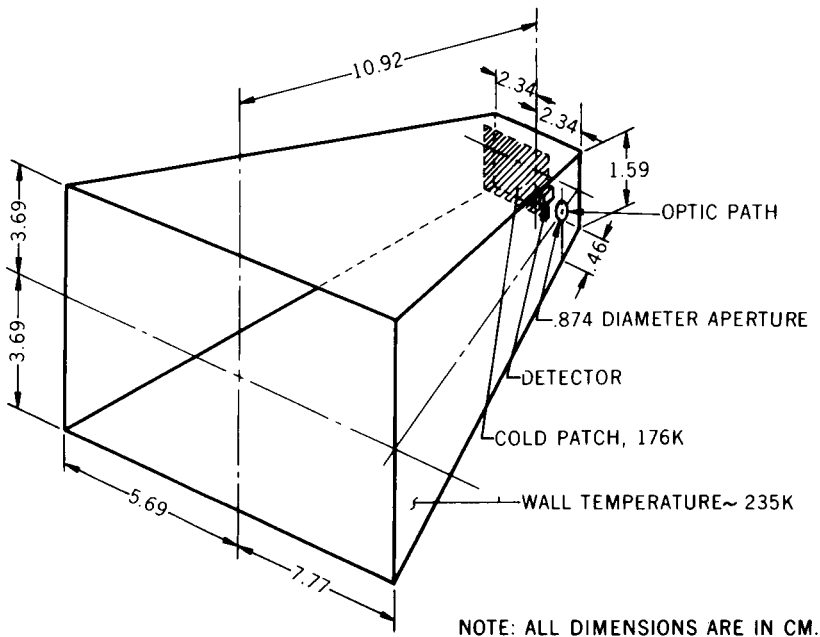


Figure 2. Radiation Cooler

While a high degree of assurance existed as to the nature of the contaminant, a major question existed as to the source of what would have to be a large quantity of water. This report deals with one test conducted to investigate the source of contamination and to define the quantities involved.

Test Equipment and Plan

The test was designed to subject a FWS similar to the one in orbit to a pump-down and cool-down history as close to the flight time-history as practicable. The FWS was instrumented with QCM, and two pressure gages; a thermocouple pressure gage (Hastings model DV6M) and a GE hot filament gage (model 22GT103) were both mounted to a surrogate rear panel of the FWS (Figure 3).

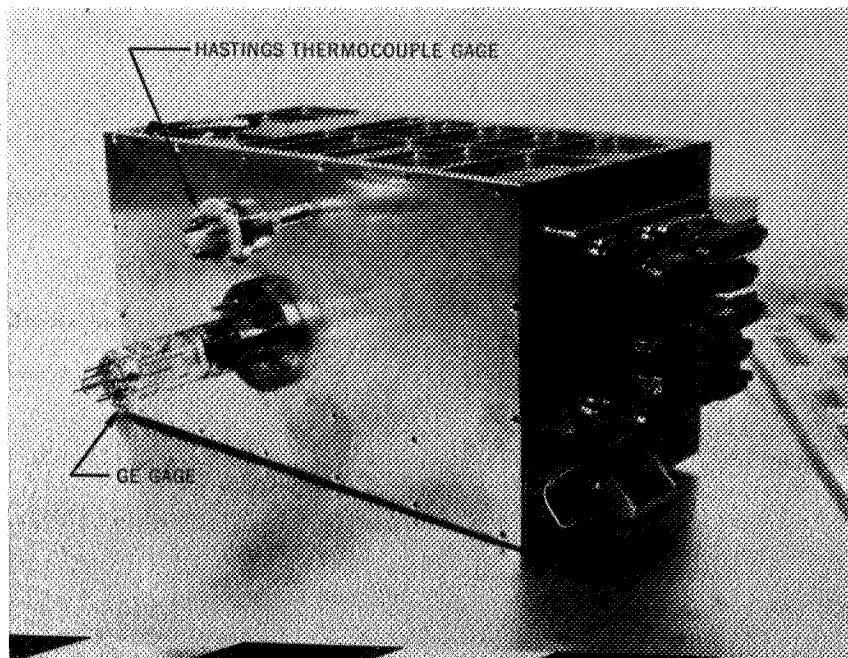


Figure 3. Rear View of FWS with Surrogate Rear Panel

The QCM was built in-house for this test. It consisted of two pairs of 10 MHz crystals mounted to a liquid nitrogen (LN_2) cooled block. The QCM was placed so that the active crystal of one pair was slightly inside the aperture facing into the radiation cooler and the active crystal of the second pair mounted outside the radiation cooler facing fluxes moving toward the radiation cooler from outside (Figure 4).

The unit was encased in the fiberglass cover and superinsulation, as in the orbital configuration, and placed on a temperature controlled plate within the $0.6 \text{ m} \times 0.9 \text{ m}$ LN_2 cooled thermal shroud of the vacuum facility (Figure 5) of NASA GSFC Space Simulation Research Section. The facility was completely cryogenically pumped using LN_2 cooled sorption pumps for roughing and a Linde Co. SHe-8 liquid helium cooled cryosorption pump for high vacuum pumping. The LN_2 cooled shroud also acted as a pump for condensables such as water.

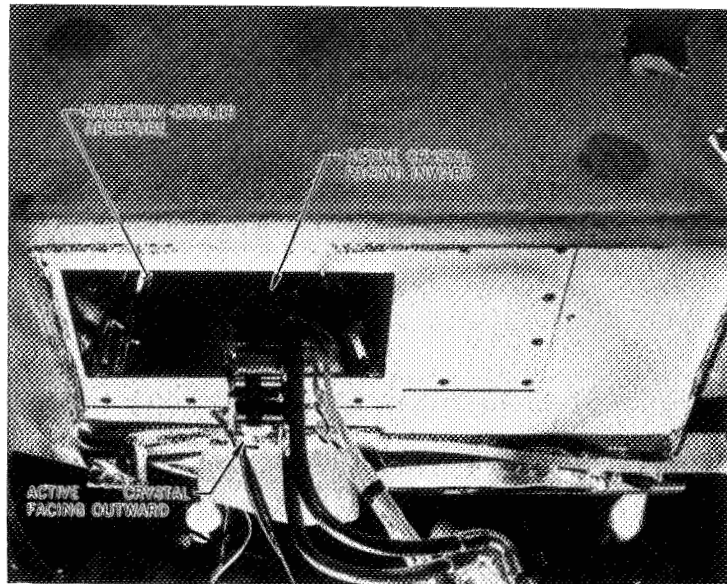


Figure 4. View Showing Quartz Crystal Microbalance

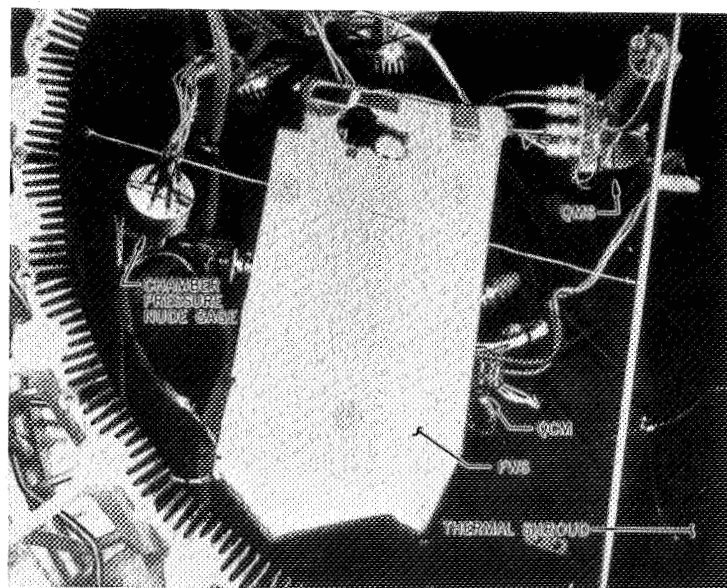


Figure 5. Test Configuration

A nude ion gage was also mounted within the test volume as well as a Bayard-Alpert type of gage mounted on the chamber pressure wall.

A quadrupole mass spectrometer (QMS) was included as part of the instrumentation but failed during pump-down.

The operational plan was to follow the launch pressure and temperature profiles as well as the facility permitted. Table I below indicates the pertinent occurrences during the launch phase.

Table I

<u>Time</u>	<u>Event</u>
t = 0	Launch
t + 4 min	Shroud eject
t + 58 min	Adapter separation (FWS views space)
t + 8 hr 32 min	FWS turn-on

Test History

The test was started at 0600 on 10/13/70 with the opening of the roughing pumps to the vacuum system. At the time of FWS turn-on, it was found that the instrument exhibited a degradation similar to that in orbit showing severe absorption characteristics in certain of the ice bands in the infrared portion of the spectrum. Table II below gives a chronology of test events.

Table II

<u>Time</u> <u>EDT</u>	<u>Decimal</u> <u>Hours</u>	<u>Event</u>
10/13/70		
0600	6.00	Open valves from roughing pumps to chamber
0620	6.33	Open SHE-8 pump valve. Chamber gage indicates 1.9 N/m^2 ; FWS gage indicates 2.9 N/m^2
0645	6.75	LN_2 to shrouds. B-A indicates $5 \times 10^{-2} \text{ N/m}^2$; FWS gage indicates 5.3 N/m^2
0715	7.25	All shroud temperatures $< 155\text{K}$
0730	7.50	LN_2 to QCM; all shroud temperature $< 90\text{K}$

0800	8.00	All shroud temperatures < 87K; nude gage indicates 4.8×10^{-3} N/m ²
1430	14.50	FWS turn on. (t + 8 hr 30 min).
1510	15.17	QMS found shorted inside chamber.
10/14/70		
2030	44.50	Post analysis indicates LN ₂ solenoid stuck closed at this time and shroud began to warm.
11/15/70		
0430	52.50	Shroud temperatures ≈ 180 K
0445	52.75	Action to clear LN solenoid
0630	54.50	Shroud temperatures < 87K
1930	67.50	Nude gage indicates 1.9×10^{-2} N/m ²
2055	68.92	Test aborted; last liquid helium fill of SHe-8 pump apparently was unsuccessful and pump stopped operating. Continuing difficulties with LN ₂ solenoids make continuing test unpractical.

Test Results and Analysis

The analysis may be divided into a number of portions and is so treated below. First, the relationship between the flux issuing from the hole in the radiation cooler wall is established. Second, the desorption flux from the detector, Φ_p , is developed from the temperature history of the detector. The third, fourth, and fifth sections deal with methods for determining the incident flux onto the detector surface.

1. Determination of Flux Relationships

In order to estimate the quantity of material issuing from the 0.874 cm diameter hole in the radiation cooler wall onto the detector, an analogy was formed between molecular flux and radiation heat transfer. In doing this, one may consider this problem as one in radiant heat transfer using configuration factors where the configuration factor is defined as "the fraction of energy directly incident on one surface, from another surface assumed to be emitting energy diffusely" (Reference 2). Then, one may write:

$$\Phi_h A_h F_{h \rightarrow d} = \Phi_d A_d$$

or:

$$\Phi_d = \Phi_h \frac{A_h F_{h \rightarrow d}}{A_d} \quad (1)$$

where

Φ_h = flux leaving the hole, molecules \cdot cm $^{-2}$ \cdot s $^{-1}$

Φ_d = flux arriving at the detector, molecules \cdot cm $^{-2}$ \cdot s $^{-1}$

A_h = area of the hole, taken as 0.65 cm 2

A_d = area of the detector, taken as 0.0056 cm 2

$F_{h \rightarrow d}$ = configuration factor, hole to detector

Using the configuration factor relationship

$$A_d F_{d \rightarrow h} = A_h F_{h \rightarrow d} \quad (2)$$

where:

$F_{d \rightarrow h}$ = configuration factor, detector to hole

and substituting equation (1) in equation (2) and rewriting, one obtains:

$$\Phi_d = \Phi_h F_{d \rightarrow h} \quad (3)$$

One may then, knowing $F_{d \rightarrow h}$, find Φ_d based on Φ_h which, in turn, may be determined either from pressure and temperature measurements within the FWS with assumptions as to the molecular weight of the material comprising the flux. One may also use the QCM to define the flux through the cooler aperture and, by applying passage probabilities, refer this back to Φ_h .

Using the CONFAC II computer program (Reference 3), the value for $F_{d \rightarrow h}$ was determined to be 0.62.

2. Determination of Desorption Flux from Detector

In order to estimate the thickness of the contaminant deposited on the surface of the detector, it is necessary to determine the time at which accretion began. This, in turn, requires a knowledge of the desorption flux. An estimate of the time of onset of accretion may be arrived

at by comparing the flux (which is assumed to be practically all water) impinging of the detector to the desorption flux corresponding to the vapor pressure of water at the temperature of the detector. One may then postulate that accretion began when the flux impinging on the detector became greater than the desorption flux.

Since detector temperature during this test could not be measured until experiment turn-on, the detector temperature was assumed to follow a cool-down curve similar to that measured during the test at the General Electric Co. (GE) on January 24, 2970 as presented in Reference 1. However, with the relatively thermally massive shroud used in the GSFC test as compared with the GE space target, one may not assume that cool-down of the detector directly followed the GE profile. The GSFC shroud is made of sections of extruded aluminum with a wedge or "fir-tree" cross section as seen in Figure 5. In the GSFC test, 33 minutes elapsed between the time LN_2 was admitted to the shroud and the time all temperatures measured on the GSFC shroud were below 155K; 15 more minutes elapsed before all shroud temperatures fell below 90K. For purposes of this study, the detector is assumed to follow the temperature profile as found in the GE test with $T=0$ occurring at 0.55 hours after LN_2 was admitted.

The vapor pressure corresponding to the detector temperature was determined using the Antoine form equation from Reference 4 as:

$$P_v = 133.32 \left\{ \exp \left[24.666 - \frac{6430}{T + 5} \right] \right\} \quad (4)$$

where:

P_v = water vapor pressure, $\text{N}\cdot\text{m}^{-2}$

T = detector temperature, degrees Kelvin

The flux, Φ_{P_v} , which corresponds to the vapor pressure of water at the detector temperature is found from equation 1.3 of Reference 5 as

$$\Phi_{P_v} = 2.635 \times 10^{20} \frac{P_v}{(M T)^{1/2}} \quad (5)$$

where:

M = molecular weight, $\text{g}\cdot\text{mole}^{-1}$. (The flux is considered to be water with a molecular weight of 18.)

This relationship of desorption flux versus time is plotted in Figure 6 as Φ_{d, p_v} with time considered as zero at 0.55 hr (33 min) after LN_2 was admitted to the shroud. This then corresponds to a time of 0718 (or 7.30 hours). Because of the uncertainties involved in establishing T-O and assuming that the cool-down curve of this test is similar to that in the GE test, it seems reasonable to estimate that the time error may be as large as 15 minutes.

The flux arriving at the detector may be derived in a number of ways; three methods are discussed below.

3. Flux Incident Upon Detector Based on Broad Limits; Also The Ambient Flux as Measured by the QCM.

The simplest way to estimate the flux arriving at the detector is to assume that it is due to a pressure lying somewhere between that measured within the FWS and that measured in the open test volume. This leaves a rather broad region of uncertainty since the two are very far apart. The flux due to the internal FWS pressure is discussed later in this report and is shown as $\Phi_{d, g}$ in Figure 6. The flux in the "ambient" may be determined by either the QCM facing away from the radiation cooler or the nude ion gage mounted in the test volume. The nude gage, of course, does not indicate the composition of the ambient molecules. However, one expects that in this chamber the major constituents would be similar to air and so the points on Figure 6 designated as Φ_b are those as determined from the nude ion gage readings assuming the gas to have a molecular weight of 29 and a temperature of 86K (since most arrive after bouncing from the LN_2 shroud).

Data from the QCM mounted so as to face away from the radiation cooler aperture indicates values of $0.05 \text{ Hz}\cdot\text{s}^{-1}$ and $0.03 \text{ Hz}\cdot\text{s}^{-1}$ at 0807 and 0819 respectively. Using a sensitivity of $2.3 \times 10^8 \text{ Hz}\cdot\text{cm}^2\cdot\text{g}^{-1}$ and a molecule weight of $3 \times 10^{-23} \text{ g}$ per molecule for water, the frequency changes correspond to fluxes of 7.2×10^{12} and $4.3 \times 10^{12} \text{ molecules}\cdot\text{cm}^{-2}\cdot\text{s}^{-1}$ respectively. This is some four orders of magnitude lower than that evidenced by the nude gage readings near that time period and confirms that the flux measured by the nude ion gage is mainly due to "noncondensables." Large variations in the mass and temperature of the molecules measured by the nude gage do not change this conclusion significantly.

4. Flux Incident Upon Detector Based on FWS Pressure Measurements

A second method for establishing the flux at the detector is to assume it to be due to the flux through the hole as determined by the GE pressure gage and that as shown above, essentially no accretion results

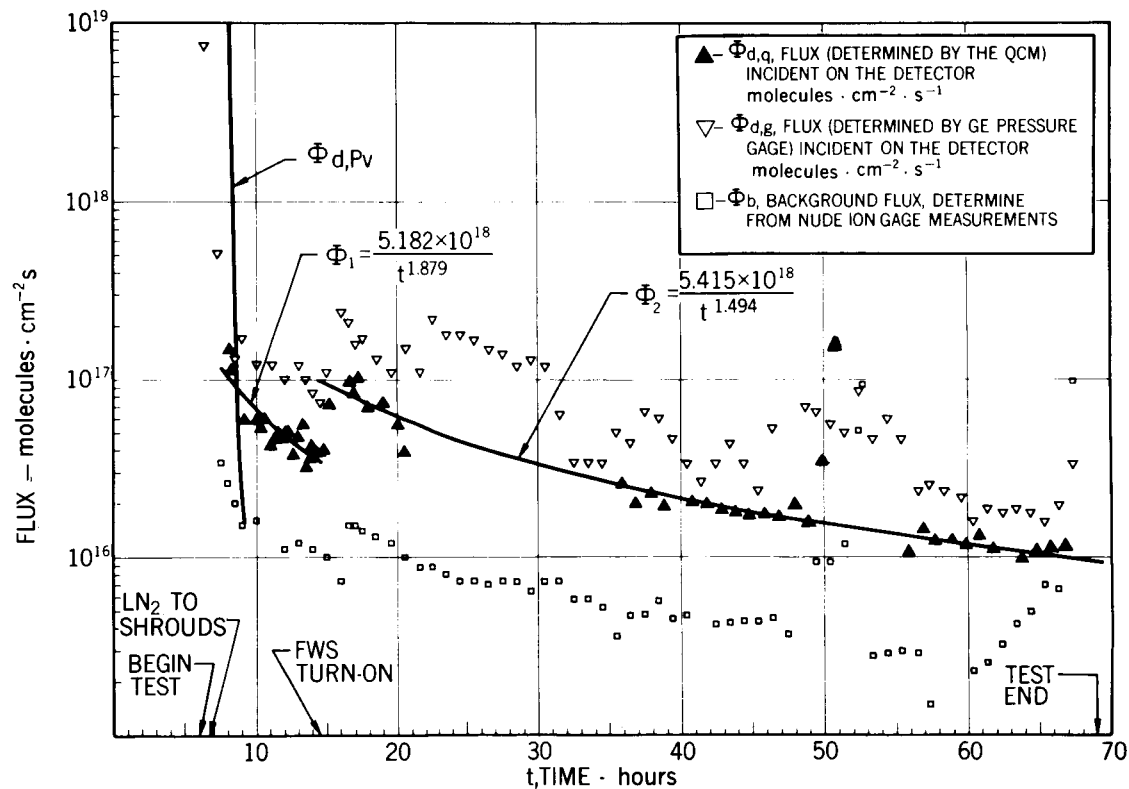


Figure 6. Flux Determination vs Time

from fluxes entering through the radiation cooler aperture. Then, one may define a value for the flux arriving at the detector as:

$$\Phi_{d, g} = \Phi_h \frac{F_{d-h}}{G} \quad (6)$$

where:

$\Phi_{d, g}$ = flux onto the detector based on pressure determined by the gage in the FWS, $\text{molecules} \cdot \text{cm}^{-2} \cdot \text{s}^{-1}$

Φ_h = flux issuing from the hole corresponding to the measured pressure at the average temperature of the FWS (286K) and assuming water to be the gas with a molecular weight of 18.

F_{d-h} = configuration factor, 0.62

G = gage factor for water, 0.9 (Reference 6)

or

$$\Phi_{d, g} = P_g (3.37 \times 10^{20})$$

where

P_g = internal FWS pressure as measured by the GE gage in terms of nitrogen, $\text{N} \cdot \text{m}^{-2}$.

The data points corresponding to $\Phi_{d, g}$ are shown in Figure 6.

5. Flux Incident Upon Detector Based on QCM Measurements

A third method to determine the flux incident on the detector, and the one used in this analysis, and the time of onset of accretion again assumes that essentially no condensable flux reaches the detector from the outside of the radiation cooler and that the QCM facing inward measures that net flux (corrected for areas) which issues from the hole in the optic path and does not condense on the cold patch.

In this approach, the plane in which the cold patch lies is assumed to divide the hole into two portions, one on the radiation cooler aperture side which is designated FHOLE and the other between the patch and the rear of the cooler which is designated RHOLE. The assumption is then made that all molecules leaving FHOLE and RHOLE in a rearward direction are eventually trapped on the cold patch and are, therefore, not measured by the QCM.*

* No attempt is made to describe flux distribution across the radiation cooler aperture.

Of those molecules leaving FHOLE in a forward direction, CONFAC II results indicate that 11% leave through the aperture directly and are, therefore, measured by the QCM ; 23% travel rearward and are, therefore, trapped. This leaves 66% which leave FHOLE and strike the walls of the cooler. Figure 7 depicts these relationships. Using the assumption that all bounces result in a diffuse distribution and also that the probability of passage may be computed as though the pyramidal shaped cooler was a frustum of a right cone of length 10.16 cm, a smaller radius of 1.78 cm, and a larger radius of 5.59 cm, an effective conductance may be defined*.

From Figure 3(a) of Reference 7, which is a graph of total transmission probability versus length-to-inlet ratio with wall half-angle as a variable parameter, the total passage probability is found as 79%. The direct transmission probability (those molecules which go from entrance to exit without a bounce) is found from Figure 4(a) of Reference 7 to be approximately 9%. Therefore, the flux from the hole which reaches the wall has a probability of about 70% of passing through the aperture.

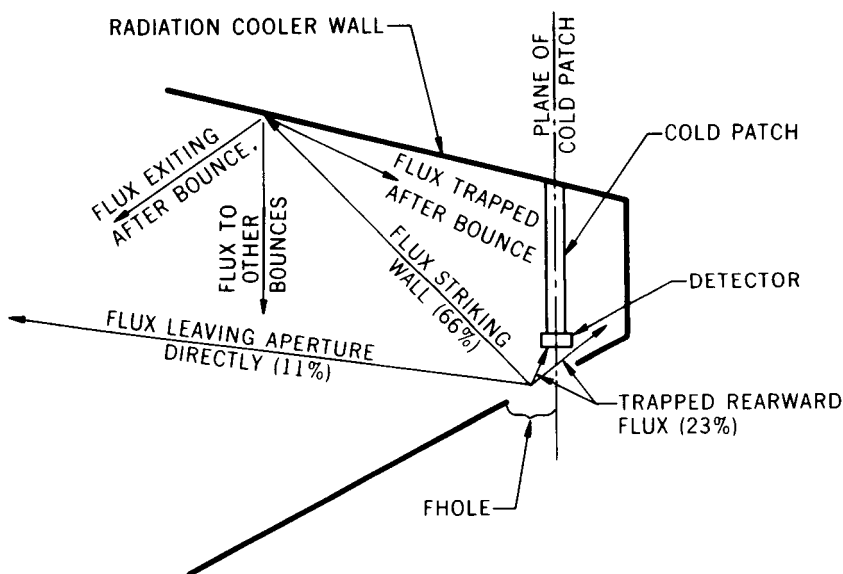


Figure 7. Schematic Representation of Fluxes from FHOLE

* The effective radii are determined using areas equivalent to the radiation cooler dimensions. The use of perimeters (another method) does not materially effect the value of the probability of passage in this particular case. A radiation analogous approach is also applicable in this case but this more sophisticated method was not utilized in view of the other sources of error. For instance, the supposition of diffuse molecular reflection from the radiation cooler walls may not be entirely valid in view of the highly polished surface.

70% of the 66% which strike the wall is added to the 11% which is directly transmitted to arrive at a figure of 57% as the percentage of molecules leaving FHOLE which exit the aperture.

Figure 8 shows the similar relationships for RHOLE. Only those molecules leaving RHOLE through the slot between the patch and the radiation cooler wall can exit the cooler aperture. Again from CONFAC II, 47% of those molecules leaving RHOLE exit the slot. Also, 10% of those leaving RHOLE exit the slot to the aperture directly; therefore, 37% strike the wall. Applying the 70% wall passage probability factor, the 10% may be added to 70% of 37% to arrive at a total of 36% for those particles leaving RHOLE which reach the aperture to exit.

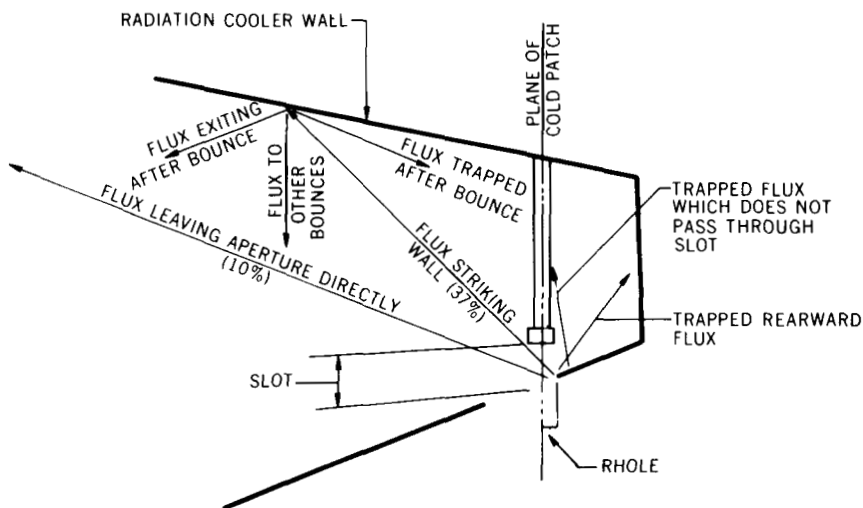


Figure 8. Schematic Representation of Fluxes from RHOLE

Summarizing then, 57% of the particles from FHOLE and 36% of those from RHOLE exit through the aperture. Since the flux through the entire hole is assumed uniform, these figures may be area weighted; the average value of the percentage of flux which originated at the hole and left through the aperture, is then found to be 50%.

Thus, using this third method, $\Phi_{d,q}$, the flux leaving the hole and impinging on the detector may be determined as:

$$\Phi_{d,q} = \Delta f \cdot S \cdot \left(\frac{A_c}{A_h} \right) \cdot \rho \cdot \frac{F_{d \rightarrow h}}{C} \quad (8)$$

where:

Δf = change in QCM beat frequency, $\text{Hz} \cdot \text{s}^{-1}$

S = QCM sensitivity, $4.3 \times 10^{-9} \text{ g} \cdot \text{Hz}^{-1} \cdot \text{cm}^{-2}$

A_c = area of cooler in QCM plane, 90.1 cm^2

A_h = area of hole, 0.65 cm^2

ρ = molecular density for water, $3.33 \times 10^{22} \text{ molecules} \cdot \text{g}^{-1}$

$F_{d \rightarrow h}$ = configuration factor, 0.62

C = passage probability, 0.50

or, rewriting:

$$\Phi_{d,q} = \Delta f (2.48 \times 10^{16}) \quad (9)$$

Figure 6 contains a plot of values of $\Phi_{d,q}$ based on data taken during the test. In order to conduct the analysis, least squares fit curves of the form $\Phi = a/(t^b)$ were defined (Φ is flux, t is time, and "a" the coefficient and "b" the exponent to be determined). This was done in two segments, the first covering the period from 8.12 hours (the first Δf determination after the test was begun) until FWS turn-on and the second covering the period after FWS turn-on. The data around the spike near 50 hours was omitted since this represented an unrealistic anomaly (see Table II). The values for "a" and "b" were found to be 5.182×10^{18} and 1.879 respectively before FWS turn-on and 5.415×10^{18} and 1.494 respectively after turn-on. These equations (shown plotted on Figure 6 as the functions Φ_1 and Φ_2) were computed only for the QCM derived data, that is, using the points designated as $\Phi_{d,q}$.

Conclusions

Referring to Figure 6, a number of conclusions can be drawn. First, the intersection of the curve labeled $\Phi_{d,pv}$ with Φ_1 would determine the onset of accretion since at that time the flux leaving the detector, a function of its temperature, would equal the flux arriving.*

*Small accretions which result in small, basically stable thicknesses due to phenomena such as Van der Waal forces have not been treated in this report; only the major phenomena, e.g. condensation, are considered. Also, a sticking coefficient of 1.0 is assumed throughout.

This crossing occurs at 8.7 hours. As noted earlier, this could be in error by 15 minutes; however, even this would not significantly affect the calculated accretion rates.

By integrating the incoming flux from 8.7 hours to 14.5 hours and subtracting from it the desorbed flux due to vapor pressure (with the flux considered to be 1.5×10^{16} molecules \cdot cm $^{-2}$ \cdot s $^{-1}$ with the detector in the test at 177K), a net accumulation of 8.34×10^{20} molecules \cdot cm $^{-2}$ is found. Defining the density of water as 3×10^{22} molecules \cdot cm $^{-3}$ and dividing this into the net accumulated number of molecules per square centimeter (8.34×10^{20}), the result indicates that an equivalent of 0.28 mm water existed on the detector at the time of FWS turn-on. As a frost, this could be in the order of 2 mm and is sufficient to cause a severe degradation.

Continuing, the curve of ϕ_2 crosses the line corresponding to 1.5×10^{16} molecules \cdot cm $^{-2}$ \cdot s $^{-1}$ (the flux due to the vapor pressure of water at 177K) at 51.5 hours. After this point, the desorption flux would be greater than that arriving and so the deposit thickness should decrease. At about 167 hours, the amount accreted before 14.5 hours plus the integrated flux arriving between 14.5 and 167 hours is approximately equal to the amount which would have been desorbed due to vapor pressure. From that time forward, no significant thickness would be expected to exist on the detector. The test did not continue long enough to note such an effect however, if the same calculation is carried out using a detector temperature of 176K (flight FWS detector temperature) the point of essentially zero thickness is found to occur at 215 hours. The recovery of the FWS which would be expected at this time was not seen during the two months, roughly 1500 hours, of instrument operation in orbit. It therefore appears that another phenomenon was operative in the orbital case which prevented the water from subliming from the detector. A hypothesis was suggested (Reference 1) which supposed the existence of a small quantity of material other than water essentially as a film over the water. If this material had a significantly lower vapor pressure than water at the detector temperature, one could surmise that this acted as an impervious membrane over the water and prevented its sublimation. This test neither proved nor disproved the hypothesis.

It is interesting to note that $\phi_{d, g}$ is almost always greater than $\phi_{d, q}$ by less than one-half a decade. Also, $\phi_{d, g}$ indicates relatively large fluctuations in places where $\phi_{d, q}$ does not. A bias error would result from errors in assumptions. For instance, if $\phi_{d, q}$ were computed assuming the gas to have a molecular weight of 29 (such as for air) rather than 18 (for water), the two sets of data would be in better agreement. The existence of the fluctuations in $\phi_{d, g}$ and not in $\phi_{d, q}$ indicates pressure being evolved within the FWS which would not condense on the QCM. There

is therefore evidence that materials other than "condensables" were being evolved and that these evolutions occurred in what might be termed "bursts."

In summary, the test of the FWS utilized the QCM to confirm the hypothesis that the orbital degradation of the FWS was due to the accretion of material from the internal portion of the experiment onto the detector. The condensed quantity was sufficient to cause severe degradation. Overall then, the QCM formed a practical way of separating the "condensables" from the "non-condensables" and permitted a quantitative evaluation of the deposition thickness of the condensables.

REFERENCES

1. "Report of the Findings of the Radiation Cooler Task Group," NASA/GSFC Report DIRS#02273, August 26, 1970.
2. J. A. Wiebelt, Engineering Radiation Heat Transfer, Holt, Rinehart, Winston, New York, 1966.
3. K. A. Toupe, A General Computer Program for the Determination of Radiant-Interchange Configuration and Form Factors - CONFAC II, North American Aviation, Inc. Rpt. SID 65-1043-2, Oct. 1965.
4. Final Report of the Goddard Summer Workshop Program in Simulation of the Space Environment, GSFC X-320-62-193, June 15 to Sept. 15, 1962.
5. D. J. Santeler, et al, Vacuum Technology and Space Simulation, NASA SP-105, 1966.
6. Flaen and Ownby, J. Vac Sci & Tech, Vol. 8, No. 5. Sept/Oct. 1971.
7. Richley and Reynolds, Numerical Solutions of Free-Molecule Flow in Converging and Diverging Tubes and Slots, NASA TN D-2330, June 1964.

CONTAMINANT REMOVAL FROM OPTICAL SURFACES

Theodore Baurer, Harold W. Goldstein, and Irwin M. Pikus, *General Electric Space Division*

ABSTRACT

Preliminary experiments (Ref. 1) had indicated that ultrasonic excitation is a potentially useful technique for removing both hydrocarbon and silicone oils previously deposited as contaminants on certain optical surfaces. This method has now been improved by the addition of a stream of inert gas (dry nitrogen) blown across the affected surface simultaneously with application of the ultrasonic impulses. Experiments are described in which the transmission of optical flats was measured, using the technique of Reference 1, both before and after contamination (in varying degree) with both types of oil, and after subsequent attempts at contaminant removal by several competing methods. In other experiments, the reflectance of surfaces coated by vapor deposition with 1000A of aluminum substrate plus a 250A overcoating of magnesium fluoride, was measured using a Jarrell-Ash Seya-Namioka Series 78-650 Spectrograph operating in the vacuum ultraviolet as a reflectometer, both before and after contamination and after attempted contaminant removal. For both types of contaminant and both types of surface, at all depths of oil deposited, the combined technique of ultrasonics plus blowing (with house nitrogen at 3 standard cc/sec over a 5 sq cm surface area) provided virtually complete decontamination in a reasonable time. Ultrasonics alone was less effective, and heating (to a maximum of 50°C, matching the temperature induced by the ultrasonic technique) was still less so. Blowing alone had no discernible effect.

Ref. 1 - H. W. Goldstein, I. M. Pikus, and T. Baurer, "A Contamination Control System," Paper No. 71-462, AIAA 6th Thermophysics Conference, Tullahoma, Tennessee, April 1971.

EFFECTS OF SURFACE CONTAMINATION ON THE INFRARED EMISSIVITY AND VISIBLE-LIGHT SCATTERING OF HIGHLY REFLECTIVE SURFACES AT CRYOGENIC TEMPERATURES

Walter Viehmann and Alfred G. Eubanks, *Goddard Space Flight Center, Greenbelt, Maryland*

ABSTRACT

A technique is described for the simultaneous *in situ* measurement of film thickness, refractive index, total normal emissivity, visible-light scattering, and reflectance of contaminant films on a highly reflective liquid-nitrogen cooled, stainless steel substrate. Emissivities and scattering data are obtained for films of water, carbon dioxide, silicone oil, and a number of aromatic and aliphatic hydrocarbons as a function of film thickness between zero and $20\text{ }\mu\text{m}$. Of the contaminants investigated, water has by far the greatest effect on emissivity, followed by silicone oil, aliphatic hydrocarbons, aromatic hydrocarbons, and carbon dioxide. The emissivity increases more rapidly with film thickness between zero and $2.5\text{ }\mu\text{m}$ than at thicknesses greater than $2.5\text{ }\mu\text{m}$. Scattering of visible light changes very little below $2\text{-}\mu\text{m}$ thickness but increases rapidly with thickness beyond 2 to $3\text{ }\mu\text{m}$. The effect of contaminant films on passive radiation coolers is discussed.

INTRODUCTION

Infrared radiometers to be flown in a variety of satellite programs require cooled photodetectors operating in the 80- to 120-K temperature range. These temperatures are achieved by passive radiation cooling, i.e., by means of a "black patch" in radiative equilibrium with space. As a result of orbital, volume, and spacecraft-interface constraints, it becomes generally necessary to shield the patch against radiative energy inputs from the earth, the sun, and the spacecraft. The configuration of a typical cooler that has evolved under these constraints is illustrated in Figure 1. This design is usually referred to as a shielded two-stage cooler. The shield is at spacecraft temperature; the second, or detector, stage is at the photodetector operating temperature, and the first stage is at an intermediate temperature, typically 160 to 180K. The internal cone surfaces are highly reflective specular surfaces having low emittance and absorptance in both the infrared and solar spectral regions

in order to minimize earth and solar radiation absorption, as well as radiation transfer between stages.

Degradation of the optical properties of these surfaces is of great concern since a temperature rise in the detector stage will result. For instance, doubling the emissivity of the first-stage cone from 0.02 (which is typical of evaporated aluminum or gold) to 0.04 will cause an increase in the temperature of the detector stage by 5 to 10K, depending on the particular cooler design (Reference 1). An increase of the nonspecular, or diffuse, component of the solar reflectivity will have a similarly detrimental effect.

Inasmuch as the first-stage cone is at low temperature, optical degradation as a result of condensation of contaminants (e.g., from such polymer outgassing products as low molecular weight solvents, water, and oils) is considered likely.

Quantitative data on the effect of contaminants on the infrared emissivity and visible-light scattering of specular surfaces at cryogenic temperatures are few. Caren, Gilcrest, and Zierman (Reference 2) measured the total hemispherical absorptance of water-vapor and carbon-dioxide deposits on polished aluminum and black-painted aluminum at 77 K for room-temperature blackbody radiation as a function of thickness. Cunningham and Young (Reference 3) investigated the effects of carbon-dioxide condensation on polished copper and a black substrate.

In the present investigation, we have extended our measurements to thin films of model compounds that can be considered typical for outgassing products of satellites, satellite systems, and experiment packages.*

EXPERIMENTAL TECHNIQUES AND MEASUREMENT PRINCIPLES

Instrumentation

The experimental apparatus is designed such that film thickness, emittance, and scattering can be measured simultaneously during deposition of the contaminant film. A schematic diagram of the apparatus is shown in Figure 2. A polished stainless-steel substrate in the form of a hollow block of 8 cm x 6.6 cm x 3 cm (3 in. x 2.6 in. x 1 in.) external dimensions is located inside an evacuated bell jar and is cooled to 77 K by flowing liquid nitrogen. A He-Ne laser beam ($\lambda = 632.8$ nm), modulated at 500 Hz by means of a chopper, is split into two components by a beam splitter and directed onto the substrate at incident angles θ_1 and θ_2 . The intensities of the reflected beams are measured by silicon photodiodes, as is the intensity of scattered light at various angles θ_s . The reflected

*J. C. Goldsmith, and E. R. Nelson, "Molecular Contamination in Environmental Testing at Goddard Space Flight Center," paper no. 2 presented at the ASTM/IES/AIAA Fifth Space Simulation Conference, Gaithersburg, Maryland, 1970.

beams are polarized perpendicularly to the plane of incidence by means of the polarizers P. The signals from the diodes are fed to lock-in amplifiers, and the amplifier outputs are recorded by xy-recorders as a function of time while the films are being deposited. The total normal emittance of the films is measured by means of a thermopile, the output of which is amplified by a millimicrovoltmeter, and is also recorded as a function of time.

The pumping system consisted of a liquid-nitrogen trapped 10-cm (4-in.) diffusion pump backed by a mechanical pump. Pressures lower than 1×10^{-6} Torr could be routinely obtained. Formation of the films was achieved by introducing the various liquids or gases into the chamber through a controlled-leak valve. All films were grown under partial pressures less than or equal to 2×10^{-5} Torr, as measured by an ionization gauge connected to the base ring of the bell jar.

Film Thickness and Refractive Index

The measurement of film thickness is based on the occurrence of optical interference in transparent films.* Interference effects are observed in the reflected light as a result of the optical-path difference between the light reflected at the vacuum-film interface and that reflected at the film-substrate interface. This principle is illustrated in Figure 3. The optical-path difference Δ between the two reflected beams is determined by the angle of incidence θ_i , the thickness d , and the refractive index n of the film. If phase-shift corrections at the vacuum-film and film-substrate interfaces are neglected, the path difference is given by (Reference 4)

$$\Delta = 2d \sqrt{n^2 - \sin^2 \theta_i}. \quad (1a)$$

If this difference is $N\lambda$ and N is an integral number, the two beams will be in phase, resulting in constructive interference (reflectivity maxima), and if N is half integral, the two reflected beams will be 180 deg out of phase, resulting in destructive interference (reflectivity minima).

Since reflectivity minima can be more accurately determined than maxima, film thicknesses are obtained from the relation

$$d = \frac{N\lambda}{2\sqrt{n^2 - \sin^2 \theta_i}}, \quad (1b)$$

where $N = \frac{1}{2}, \frac{3}{2}, \frac{5}{2}, \dots$ is the order of successive interference minima.

*For an example of a recent review of optical-thickness measurements, see Reference 4.

For accurate determination of d , the index of refraction of the film is required. Therefore, two simultaneous reflectivity measurements are made under two incident angles $\theta_1 = 30$ deg and $\theta_2 = 72$ deg, as was mentioned previously. From the number of minima N_1 and N_2 recorded at these angles for a given film thickness d , the index of refraction is determined from the relation

$$\frac{N_1 \lambda}{\sqrt{n^2 - \sin^2 \theta_1}} = \frac{N_2 \lambda}{\sqrt{n^2 - \sin^2 \theta_2}}. \quad (1c)$$

Emissivity

The difficulty of obtaining accurate emissivity values by radiometric methods is generally recognized (Reference 5), and certain precautions have to be taken to avoid serious errors in the results, particularly for low-emissivity values. In this work, we have chosen a comparison method; i.e., all values are measured relative to a blackbody of the same temperature as the sample. In order to create such a blackbody, the substrate was kept at 77 K and coated with a film of "frosty" ice of about 0.1-mm thickness. For this thickness, the emittance becomes independent of thickness, and e_n was taken to be 0.98, a value generally given in the literature for frosty ice (Reference 6).

The distance between thermopile and sample (substrate) is such that the latter fills the 60-deg field of view of the detector completely. If the detector, in thermal equilibrium with its surroundings, is set at zero signal output and a blackbody is then placed in its field of view, the resulting signal is (Reference 5)

$$S_{BB} = k(W_1 - \delta W), \quad (2a)$$

where k is a calibration constant, W_1 is the flux contributed by the blackbody, and δW is the fraction of the ambient flux W obscured by the blackbody. Similarly, for a nonblack sample of emissivity e_n , the signal becomes

$$S_s = k(e_n W_1 - \delta W + W_2), \quad (2b)$$

where $W_2 = R \delta W$ is the fraction of the ambient flux reflected by the sample. The ratio of the two signals thus becomes

$$\frac{S_s}{S_{BB}} = \frac{e_n W_1 + (R - 1) \delta W}{W_1 - \delta W}. \quad (2c)$$

Since the detector, having a field of view of 60 deg, admits only radiation within ± 30 deg of the normal, R can be approximated by $1 - e_n$, and the ratio becomes truly equal to e_n . However, because our sample and

blackbody are at 77 K and ambient temperature is 300 K, W_1 and $e_n W_1$ are small compared with δW and $(R - 1) \delta W$, and the ratio S_s / S_{BB} becomes equal to $1 - R = e_n$ for 300-K blackbody radiation emanating from the surrounding bell jar.

RESULTS AND DISCUSSION

Infrared Emissivity Versus Film Thickness

Table 1 lists the compounds that were investigated and their indexes of refraction at $\lambda = 632.8$ nm as determined by the two-angle interference method described above. With these values, film thicknesses obtained from reflectance measurements in units of effective quarter wavelength were converted to physical thicknesses by use of Equation 1b.

Table 1

Compounds investigated and their indexes of refraction at $\lambda = 632.8$ nm and $T = 77$ K

Material	Index of Refraction ($\lambda = 632.8$ nm)
Water	1.42
Acetone	1.36
Ethanol	1.36
Methanol	1.32
2-Propanol	1.33
Toluene	1.53
Silicone oil (DC-200)	1.36
Benzene	1.49
Trichloroethylene	1.48
Carbon dioxide	1.30

Infrared absorption spectra of water, typical aliphatic hydrocarbons, silicone oil, and aromatic hydrocarbons are shown in Figure 4 (reproduced from commercial literature*). These spectra were measured at room temperature with a standard sample thickness of $10\mu\text{m}$, except for those marked with an asterisk, which were measured "between salts," i.e., with an unspecified thickness smaller than $10\mu\text{m}$. Qualitatively,

*"26 Frequently Used Spectra for the Infrared Spectroscopist," Sadtler Research Laboratories, Inc., Philadelphia, Pa.

therefore, it is apparent that water, aliphatic hydrocarbons, and silicone oil are strong absorbers of 300-K blackbody radiation. Absorption of aromatic hydrocarbons is weaker, and carbon dioxide (not shown in Figure 4) absorbs rather weakly only in the 4- to 5- μm band.*

Figure 5 shows the total normal emissivity of the various contamination layers on polished stainless steel as a function of film thickness at 77 K.

In the early stages of film growth, i.e., between zero and approximately 2.5- μm thickness, emissivity increases rapidly with thickness. For carbon dioxide and benzene, e_n decreases slightly beyond 2.5 μm and goes through a minimum at about 4.5 μm before increasing further at a much slower rate with thickness. Maxima and minima in the emissivity-vs-thickness curves are also observed more or less clearly in the other compounds. Since the separation between successive maxima or minima is about 4 to 5 μm , it seemed proper to interpret them as being due to interference effects in the reflection of the 300-K blackbody radiation, an altogether reasonable assumption in view of the discrete band structure of the infrared absorption of these compounds. In order to support this interpretation, monochromatic emissivity measurements were performed on a limited number of materials by placing an interference filter with a peak transmission wavelength of 10.8 μm and a bandwidth of 0.8 μm in front of the thermopile. The results are shown in Figure 6. Compounds that have little or no absorption in this spectral region show the interference maxima and minima very clearly. For ice, which is a strong absorber, only the first two minima can be observed.

From the point of view of contamination, it is important to note that ice has by far the greatest effect on the emissivity of a reflecting surface, particularly since water is believed to represent a significant fraction of the total weight loss caused by outgassing of polymeric materials. Also, multilayer insulation, which is frequently used for thermal-control blankets in general and in radiation-cooler construction in particular, outgasses copious amounts of water, with typical rates ranging from 10^{-6} Torr-liter-cm $^{-2}$ -s $^{-1}$ initially to 10^{-9} Torr-liter-cm $^{-2}$ -s $^{-1}$ after 15 hours in vacuum.**

At sufficiently large film thicknesses, i.e., for films of several micrometers thickness, the emissivities of the various compounds fall into relative ranges, which one might expect on the basis of their infrared absorption spectra. Aliphatic hydrocarbons and silicone oils have significantly higher emissivities than the less-absorbing aromatic hydrocarbons, and carbon dioxide has the lowest emissivity of the materials

*B. E. Wood, A. M. Smith, B. A. Seiber, and J. A. Roux, "Spectral Absolute Reflectance Measurements of CO $_2$ Frosts in the 0.5 to 12.0 Micron Region," paper no. 41 presented at the ASTM/IES/AIAA Fifth Space Simulation Conference, Gaithersburg, Maryland, 1970.

**A. P. M. Glassford, in an unpublished report by the Lockheed Missile and Space Company, Palo Alto, Calif., NASA-Marshall Space Flight Center Contract No. NAS 9-20758.

investigated. It is important, however, to point out that for film thicknesses less than $2\text{ }\mu\text{m}$, or roughly a quarter wavelength of 300-K blackbody radiation, no such straightforward relative ordering on the basis of absorption alone can be made. For this thickness range, emissivities are to a large degree determined by reflection losses, i.e., by the real part of the index of refraction around $10\text{-}\mu\text{m}$ wavelength. For instance, acetone, which is a relatively weak absorber in the infrared, has the same emissivity below $1\text{-}\mu\text{m}$ thickness as methanol and considerably higher emissivity than propanol and silicone oil, all of which absorb strongly in the infrared.

As was pointed out earlier, an increase in emissivity of the first-stage cone surfaces by about 0.02 results in significant degradation of performance for most radiant-cooler designs. It is apparent from Figure 5 that films of approximately 200-nm thickness of water or of about 1000 nm of carbon dioxide are sufficient to cause such an increase on a highly reflective surface. Values for the critical film thickness for organic contaminants fall in the 300- to 800-nm range, depending on their absorption coefficients and indexes of refraction in the $10\text{ }\mu\text{m}$ region of infrared radiation.

Reflectivity and Scattering in the Visible Range

Scattering measurements were made with an incident angle of $\theta_i = -72^\circ$ and a scattering angle of $\theta_s = -60^\circ$ (backscattering) into a solid angle of 10° . All intensities were normalized relative to that obtained with a perfectly diffuse sample of magnesium oxide in place of the substrate. A typical recording of reflected intensity and scattered intensity as functions of film thickness is shown in Figure 7. Maxima of reflected intensity occur when the effective film thickness

$$d_{\text{eff}} = d \sqrt{n^2 - \sin^2 \theta_i}$$

is an even number of quarter-wave multiples, and minima when the effective thickness is an odd number of quarter-wave multiples. The intensities of successive reflectance maxima and minima decrease due to absorption in the film. It is possible, in principle, to determine the complex index of refraction $n^* = n(1 + ik)$ (where k is the extinction coefficient) of the film from these reflectivity measurements by use of the proper Fresnel formulae (Reference 7) and by fitting measured reflectance data to computed curves. However, this is generally not done in practice, because the effects of scattering are difficult to take into account quantitatively. It has been shown experimentally by Hass and his coworkers (Reference 8) that scattering centers at the film surface affect the reflectance maxima very little and the reflectance minima very strongly. At reflectance minima, or effective odd quarter-wave thicknesses, the standing wave in the film has a loop at the surface that is strongly affected by absorbing

layers or scattering centers; hence, the reflectance at minima changes more rapidly than at maxima, for which the electric field has a node at the surface of the film. Accordingly, interference minima of reflectance are accompanied by scattering maxima, and reflectance maxima by minima of scattered intensity.

In the early stages of film growth (i.e., between zero and about 10 quarter-wave thicknesses), the amplitudes of the scattering maxima increase very little with film thickness, as in Region I in Figure 7. In this region, scattering is largely directional and is concentrated in a cone around the reflected beam. Backscattering is quite small compared to forward scattering.* Beyond a film thickness of about $2\mu\text{m}$, the amplitudes of scattering maxima increase rapidly with thickness (Region II). During this period of growth, the angular distribution of scattering intensity changes from that characteristic of the substrate to that characteristic of the film, albeit still far from Lambertian. The films become hazy and visible to the naked eye during this period of growth, which extends to about 5 to $7\mu\text{m}$ in most cases. Upon further increase in thickness, scattering maxima and minima increase at about the same rate (Region III). Eventually, the films become sufficiently diffuse to obscure interference effects in reflectance as well as scattering. Visually, they attain a frosty appearance. Interference maxima and minima of both reflectance and scattering wash out (Region IV) and finally converge into thickness-independent values characteristic of the diffusely scattering surface (Region V).

A somewhat puzzling feature of the scattering measurements is the occurrence of modulation of the scattering amplitude as a function of film thickness. This modulation was consistently observed in the course of these investigations. If one realizes, however, that an interference condition in the form of Equation 1a exists not only for the reflected beam, with $\theta = \theta_i$, but also for the scattered light, with $\theta = \theta_s \neq \theta_i$ (see Figure 3), and that the total hemispherical scattering intensity as a function of optical thickness is governed by θ_i and the angular intensity at an angle θ_s is governed by θ_s , it becomes apparent that the observed scattering amplitude is the "beat signal" resulting from the difference in optical path difference, $\Delta' = \Delta_i \pm \Delta_s$, between the specularly reflected beam (Δ_i) and the scattered beam (Δ_s). The resulting amplitude modulation of (angular) scattered intensity becomes particularly pronounced when this difference is deliberately made large. Figure 8 shows the amplitude modulation observed with $\theta_i = 5^\circ$ and two different scattering angles of -52° and $+10^\circ$, respectively. A very pronounced modulation is seen for the scattering angle of -52° . For a viewing angle of 10° , on the

*The angular dependence of scattered intensity as a function of film thickness shall be the subject of future investigations.

other hand, the interference conditions for the total hemispherical scattering and angular scattering are sufficiently close to wash out any resulting modulation, since the solid angle of the detector is comparable to the difference in angle between the reflected beam and the scattered beam.

Figure 9 shows the results of the scattering measurements for the various compounds investigated. The above mentioned modulation effects are not shown. Each material is characterized by two curves: an upper curve for scattering maxima, which occur at odd multiples of effective quarter-wave thicknesses, and a lower curve for scattering minima, occurring at even multiples of quarter-wave thicknesses. The former is a measure of the surface scattering, and the latter of volume scattering and absorption in the films. For most compounds, surface scattering is significantly higher than volume scattering and absorption losses for thicknesses below about $20\mu\text{m}$. Exceptions to this are benzene and carbon dioxide, which take on a frosty appearance from the beginning of film growth. Interference effects in films of benzene and carbon dioxide can be observed only for thicknesses below 7 and $10\mu\text{m}$, respectively. In films of acetone and methanol, on the other hand, interference can be seen at thicknesses well beyond $20\mu\text{m}$.

The clean stainless steel substrate has a relative scattering factor of 1 percent of that for magnesium oxide. Except for benzene, films of 1.0- to $1.5\text{-}\mu\text{m}$ thickness will approximately double this value. Only beyond a thickness of about $2\mu\text{m}$ does the scattering of typical films increase significantly. For thin films, therefore, the relative increase in scattering is small compared to changes in infrared emissivity.

SUMMARY AND CONCLUSIONS

Infrared emittance and visible-light scattering of highly reflective substrates are strongly affected by the deposition of contaminant layers. Emissivity increases most noticeably between zero and approximately $2.5\text{-}\mu\text{m}$ thickness of the contaminant film as a result of reflection and absorption losses in the surface coating. In this thickness range, emissivity increase per unit film thickness is highest for water, followed in order by aliphatic hydrocarbons, silicone oil, aromatic hydrocarbons, and carbon dioxide. Scattering of visible light changes very little below about $2\text{-}\mu\text{m}$ thickness but increases rapidly with thickness beyond 2 to $3\mu\text{m}$. Shielded two-stage passive radiation coolers will be significantly degraded by the deposition of infrared absorbing contaminants of between 200- and 500-nm thickness.

Goddard Space Flight Center
National Aeronautics and Space Administration
Greenbelt, Maryland, July 21, 1971
821-21-78-01-51

REFERENCES

1. Annable, R. V., "Radiant Cooling," *Applied Optics* 9(1): 185-193, 1970.
2. Caren, P. R., Gilcrest, A. S., and Zierman, C. A., in *Advances in Cryogenic Engineering*, Plenum Publishing Corp., New York, 1964, Vol. 9, pp. 457-463.
3. Cunningham, T. M., and Young, R. L., in *Advances in Cryogenic Engineering*, Plenum Publishing Corp., New York, 1963, Vol. 8, pp. 85-92.
4. Pliskin, W. A., and Zanin, S. J., in *Handbook of Thin Film Technology*, L. I. Maissel and R. Glang, ed., McGraw-Hill Book Co., New York, 1970, Chapter 11.
5. Drummeter, L. F., and Hass, G., in *Physics of Thin Films*, G. Hass and R. E. Thun, ed., Academic Press, Inc., New York, 1964, Vol. 2, pp. 325-327.
6. Hudson, R. D., Jr., in *Infrared System Engineering*, John Wiley and Sons, New York, 1969, p. 44.
7. Heavens, O. S., in *Physics of Thin Films*, G. Hass and R. E. Thun, ed., Academic Press, Inc., New York, 1964, Vol. 2, p. 205.
8. Hass, G., and Hunter, W. R., "Laboratory Experiments to Study Surface Contamination and Degradation of Optical Coatings and Materials in Simulated Space Environments," *Applied Optics* 9: 2101, 1970.

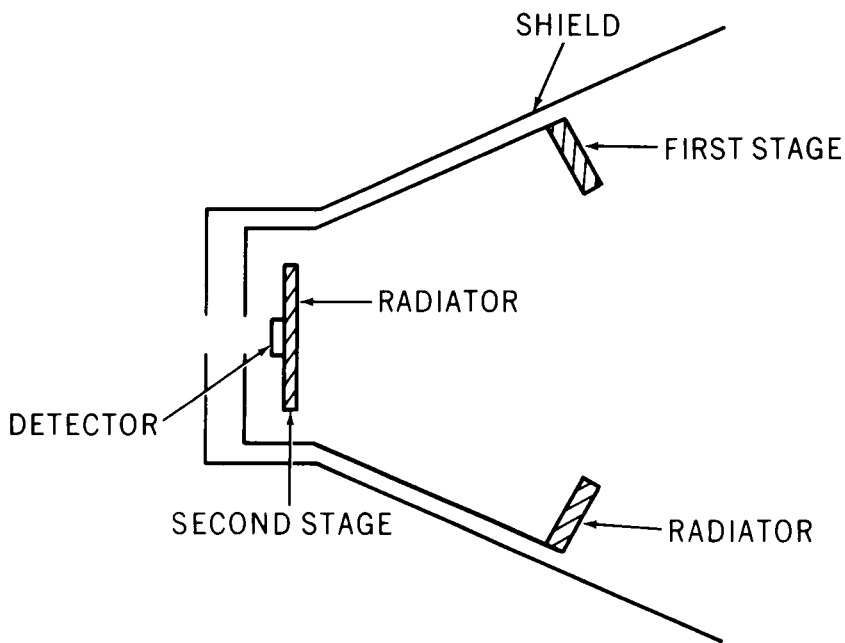


Figure 1—Schematic diagram of a shielded two-stage radiant cooler.

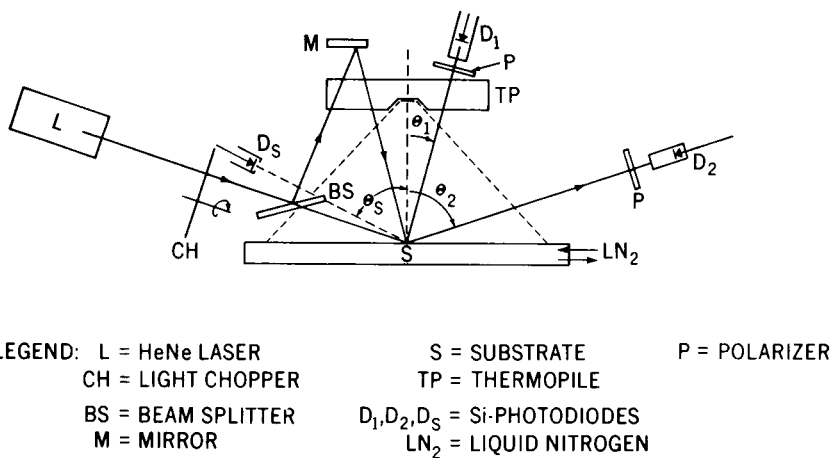


Figure 2—Schematic diagram of experimental setup for optical measurements of contaminant film.

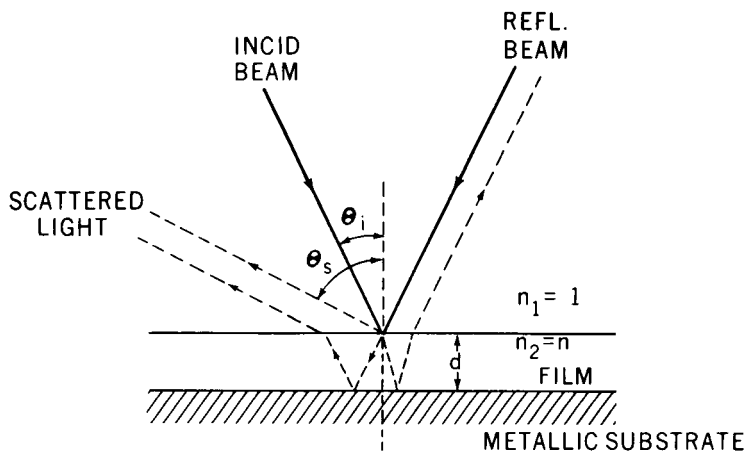


Figure 3—Schematic diagram of reflection and scattering from a transparent film on a metallic substrate.

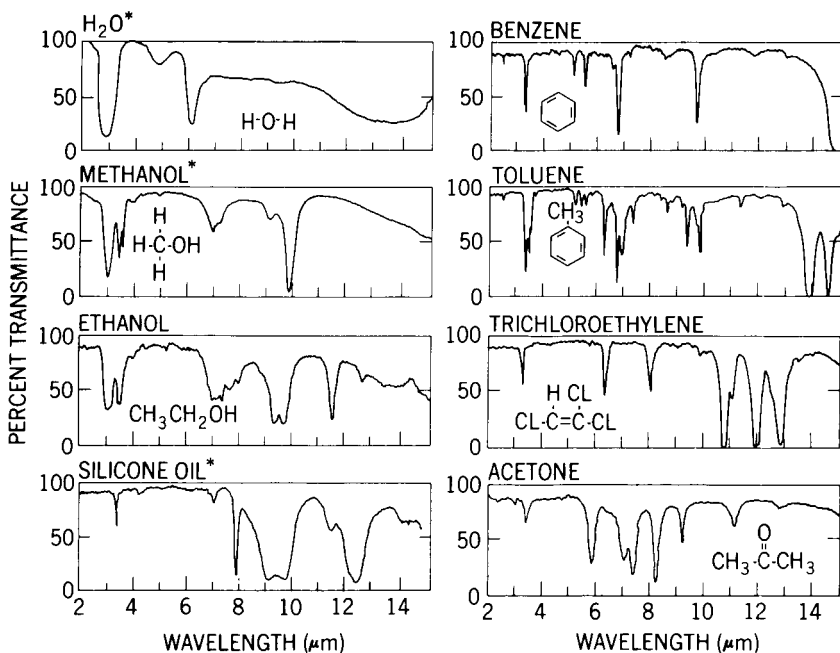


Figure 4—Infrared absorption spectra of water and some organic compounds. Measurements were made at room temperature with a sample of $10\text{-}\mu\text{m}$ thickness, except for those marked with an asterisk, which were made with a sample of unspecified thickness smaller than $10\text{-}\mu\text{m}$.

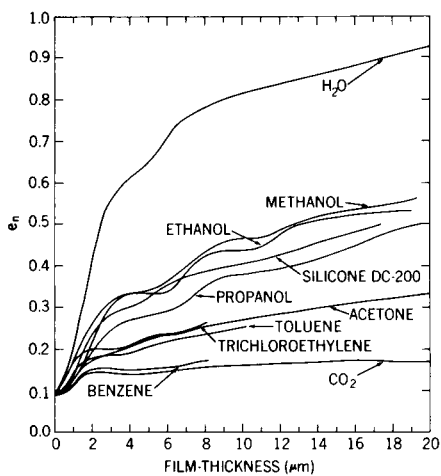


Figure 5—Emissivity as a function of film thickness on polished stainless steel at 77 K.

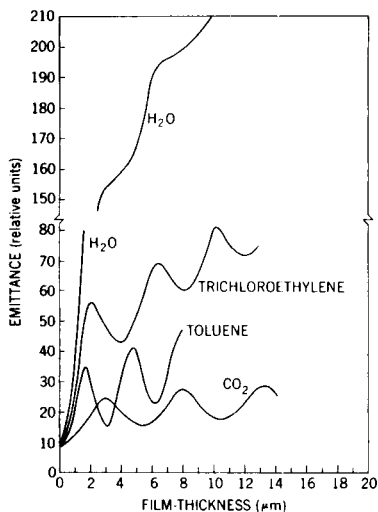


Figure 6—Emissivity as a function of film thickness at $10.8 \pm 0.5 \mu\text{m}$.

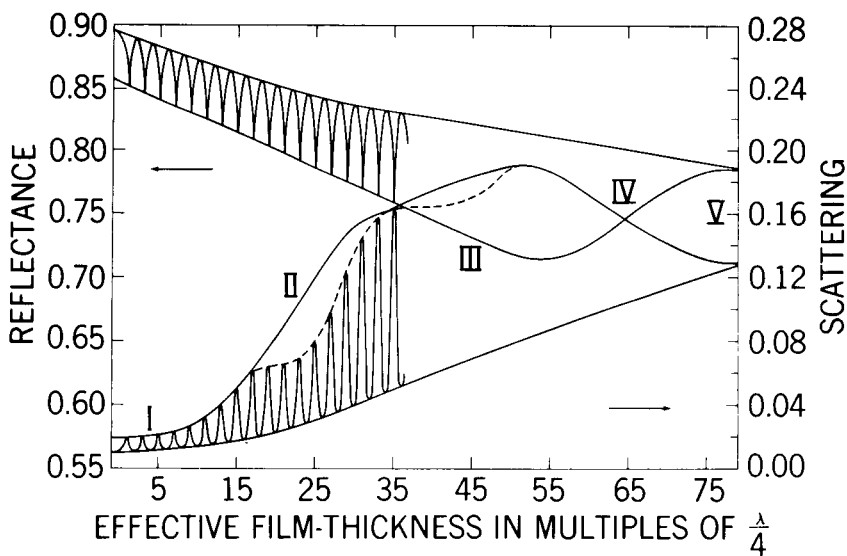


Figure 7—Reflected intensity and scattered intensity as a function of film thickness.

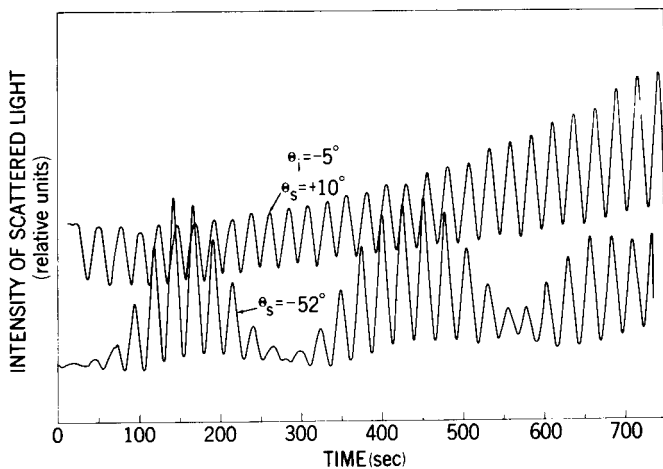


Figure 8—Modulation of scattering amplitude for two different relative angles of scattering.

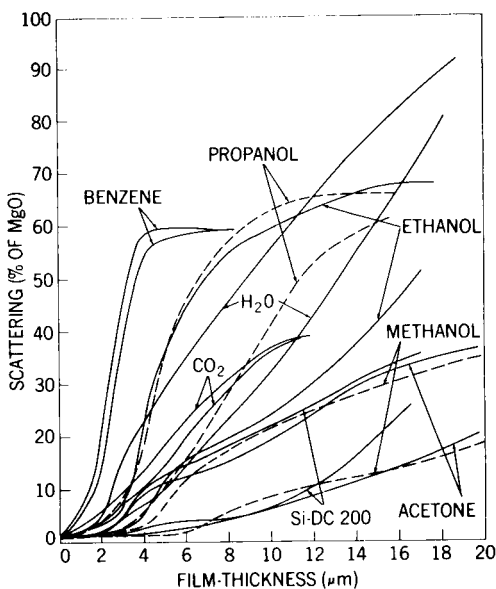


Figure 9—Scattering factor of contaminant films as a function of thickness at 632.8nm, measured with an incident angle of -72 deg and a scattering angle of -60 deg. The upper curves are for odd-numbered multiples of $\lambda/4$, and the lower curves are for even-numbered multiples of $\lambda/4$.

AN INSTRUMENT FOR REAL-TIME DETECTION OF CONTAMINATION IN SPACE ENVIRONMENTAL TEST CHAMBERS

Robert G. Richmond (*NASA*) and Henry N. Harmon (*Boeing Company*),
NASA Manned Spacecraft Center, Houston, Texas

ABSTRACT

A new instrument for the in situ vacuum detection of surface reflectance changes at 1216 Å has been designed. By using successive reflections, this instrument is more sensitive as an indicator of reflectance changes than similar instruments having only a single reflection. The selection of each component of the instrument and its operational performance is discussed.

INTRODUCTION

As space-vehicle designs and experiments become more complex and as spacecraft mission durations increase, many stringent cleanliness requirements have been imposed on the space-environmental testing and simulation facilities. The backstreaming of vacuum-pump oils, and the outgassing of paints, of epoxies, and of the test article can constitute significant sources of molecular contamination. In some instances, the vehicle experiments and systems are relatively insensitive to molecular contamination; however, many spacecraft contain components and systems that are ultrasensitive to any type of contamination. For example, from the viewpoint of the experimenter, the Apollo telescope mount, which was tested recently in the NASA Manned Spacecraft Center (MSC) Space Environment Simulation Laboratory, contains several experiments having optics that can be degraded by fractional molecular layers of some contaminants. The degradation can be compounded by bombardment of the contaminant layer by ultraviolet radiation. From a facility viewpoint, the solar simulator optics also are susceptible to contamination after prolonged periods of exposure. Cleaning and resurfacing of the optics is an expensive and time-consuming task.

Both the viewpoint of the experimenter and of the facility personnel lead to the same general requirement, that is, both

passive and active (in situ, real time) systems of contamination monitoring are required to measure the effect of contamination on the most sensitive test-article components, to identify the contaminant and its source, and to eliminate the contaminant or minimize the contaminant-source strength.

A new instrument to measure the effect of molecular contamination has been designed at the MSC. The instrument detects changes in the reflection of 1216 Å radiation from first-surface mirrors. This ultraviolet region has been extremely valuable in the measurement of thin films (hence, molecular contamination) because of absorption and transmission properties of deposited materials at these wavelengths.

BACKGROUND AND DEFINITIONS

The term contaminate as used in this report is defined as "to make unfit for full beneficial use by the introduction of undesirable elements." The term "unfit for full beneficial use" implies that, although an individual component may not be damaged catastrophically by molecular contamination, the resultant effect may be significant performance degradation. For example, a monolayer of a contaminant on an ultraviolet-wavelength optical system might represent only a 5-percent degradation in terms of reflectance or resolution of the system, but that small degradation could decrease significantly the scientific objectives of the experiment. No standards or criteria have been established for the term "unfit." What is unfit for one experimenter's application may be acceptable for another application. Then it becomes apparent that a sound philosophical approach to the problem of high-vacuum contamination measurement and control is required. Although in the past little effort has been made to correlate data or to standardize techniques, the increased complexities and sensitivities of the test article and of the space-simulation facility require serious consideration to be given to standardization of contamination criteria and measurement techniques. The Manned Spacecraft Center's approach to the problem is summarized in reference 1.

Contamination in space-environment chambers may be considered twofold: particulate and molecular. Particulate contamination, such as lint and dust, generally is of less concern to the experimenter than molecular contamination because particulate usually can be removed easily and completely. Also, particulate contamination usually affects only an extremely small fraction of a test-article surface area (ref. 2).

Molecular contamination is a serious problem in thermal-vacuum testing. Molecular contamination is defined as contamination that migrates and deposits in the test volume as individual molecules, rather than the relatively massive molecular conglomerates and polymers that are referred to as particulates. Molecular contamination may result from evaporation, sublimation, chemical decomposition, or desorption (ref. 2).

Because some of the techniques used in the measurement of molecular contamination have resulted from instrumentation developed to monitor thin-film deposition rates and film thicknesses, this measurement can be considered a relatively new science. Studies of the microstructure of vacuum-deposited thin films, particularly in relation to nucleation and growth, have been made by many investigators (refs. 3 to 7). However, the actual application of thin-film measurement principles and techniques to unknown high-vacuum contaminants has been limited. Each investigator has taken the molecular contamination measurements as required for his particular measurement.

DESCRIPTION OF THE INSTRUMENT

The instrument was designed and developed as part of a continuing research and development program in the MSC Space Environment Test Division. The instrument was designed specifically to detect the presence of small quantities of contaminants that are deposited on the mirrors and degrade the reflectivity of mirrors at a wavelength of 1216 Å. The instrument monitors the output energy of a lamp (source) as the energy is reflected off three mirrors in succession. The change in reflection is a change in the picoameter-measured output of two detectors.

The instrument consists of a hydrogen lamp, a magnesium fluoride (MgF_2) lens, three first-surface mirrors, two nitrous oxide (NO)-filled ionization chambers, and a one-piece aluminum optical bench to house and align the components (Figs. 1 to 3). The bench and component temperatures are stabilized and maintained by a thermal-control system that uses an attached strip heater and a thermocouple.

The optical bench was milled as a single solid piece from 6.25-cm-thick aluminum plate to avoid discontinuities in the heat distribution and to provide a means to simplify and optimize alignment of the optical elements. Machine tolerances applicable to optical reference surfaces were held to 0.025 mm or less. It was concluded that if the critical dimension tolerances were held, a permanently aligned system would result and few, if any, adjustments would be required. The conclusion was validated when the instrument was assembled without alignment and found to be aligned.

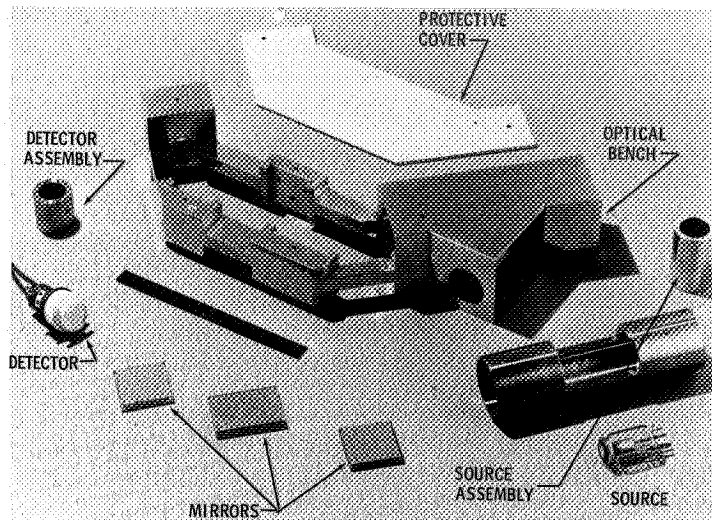


Fig. 1—Multiple bounce reflectance measurement optical bench (exploded view with components)

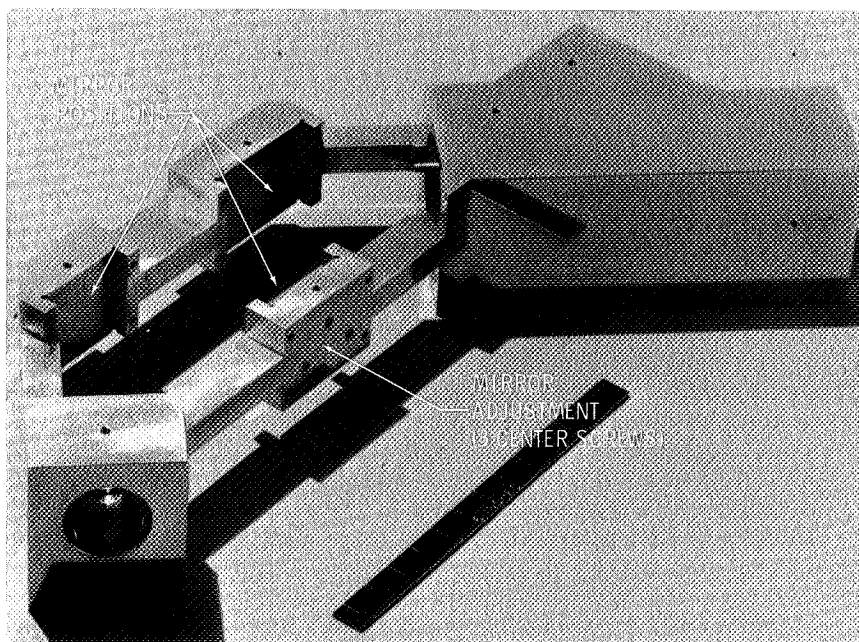


Fig. 2—Multiple bounce reflectance measurement optical bench

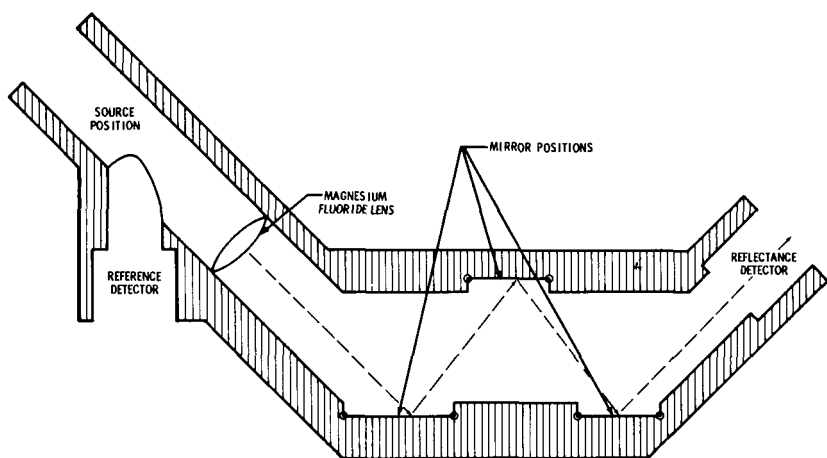


Fig. 3—Multiple bounce reflectance measurement optical bench (cutaway view)

sufficiently to operate without fine adjustments. Adjustment of the central optical path can be made, if required, by means of three screws mounted behind one of the mirrors (Fig. 2).

The small external surface emissivity (less than 0.1) and the physical continuity and high thermal conductivity of the bench provided the qualities that prevent the temperature difference between any two parts on the body from exceeding 1.5°K or that prevent the mirror temperatures from falling more than 4.5°K below the bench temperature under thermal-vacuum conditions. The thermal stability is essential because the optical alinement could change significantly if large thermal gradients developed and because the condensate on the mirror surfaces are dependent on the mirror surface temperature. Mirror surface temperature was computed as a function of the optical bench temperature. Only radiative heat transfer was assumed so that a 4.5°K operating difference is conservative with respect to the monitored temperature. The optical misalinement caused by differential expansion was essentially zero because of the small thermal gradient across the bench. The source and both detectors were mounted inside the optical bench; therefore, the temperatures are essentially constant with respect to bench temperature. The constant temperature was significant because detector output varies with temperature (Fig. 4).

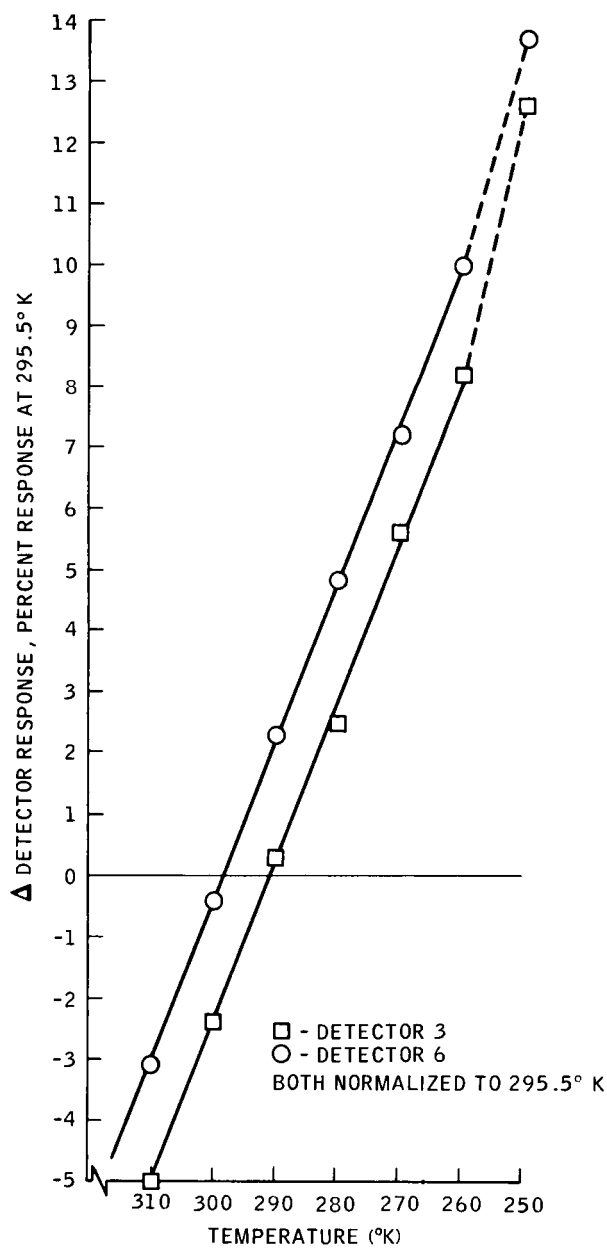


Fig. 4—Typical detector response as a function of temperature

The rate at which a contaminant deposits on the mirrors is a function of the molecular flux density, the directions from which it comes, the temperature, the orientation of the mirrors, and the blockage by the optical bench. Three mirrors were used, and the total view of the environment was greater than that of a single mirror with no blockage.

For maximum response to a single contaminating source, the instrument should be oriented so that the normal to the two-mirror side makes an angle of 26° with the source axis. This angle provides a view equivalent to 0.9 times that which would result if the mirrors were normal to the contamination source and completely unblocked.

The source used in the instrument is a dc glow discharge lamp that is 35 mm long and 22 mm in diameter. The lamp is filled with hydrogen gas at a pressure of 8 torr. The clear aperture of 8 mm is covered with a 1-mm-thick MgF_2 window. The lamp fires at 600 V and operates nominally at 350 Vdc at 1.0 mA or less.

The detectors were NO-filled ionization chambers with windows of MgF_2 and apertures of 0.53 mm. The ionization chambers were operated at 50 Vdc in the saturation region with unity gain. The output was measured with a picoameter. Coaxial

cables, with a leakage of less than 10^{-13} A, are used both outside and inside the vacuum chamber. The combination of window transmittance and NO response to the 1216 Å radiation defines a maximum sensitivity between 1120 and 1340 Å.

The output of the source is collected by a 3.75-cm MgF_2 lens with a focal length of 7.6 cm. The source is mounted 10.10 cm from the lens on the optical axis. The source-to-lens distance produces a convergent beam of energy that is imaged at the entrance aperture of the detector, 30.5 cm away, and yields a 1000-percent increase in detector output over that without the lens. The alinement of the source, the lens, and the detectors was fixed permanently by precision stainless-steel fixtures inside the optical bench.

The mirrors were prepared by depositing 250 Å of MgF_2 over aluminum (refs. 8 and 9) on a prepared quartz optical flat. The reflectance of these mirrors is approximately 80 percent (ref. 8) at 1216 Å.

THEORETICAL CONSIDERATIONS

Assuming that all mirrors are contaminated equally, the output of the detectors may be expressed as

$$E_{1n} = I_n G_1 D_1 \quad (1)$$

$$E_{2n} = I_n G_2 D_2 R_n^3 \quad (2)$$

where E_{1n} = the recorded output of the first detector for the n th measurement

E_{2n} = the output for the second detector

I_n = the output of the energy source W/μ

G_1 = a geometric factor relating the aperture of the first detector to the source output at the source

G_2 = the geometric factor for the second detector, including the remaining optical system

D_1 = the sensitivity response ($A/W/\mu$) of the first detector and the data recording system (assumed constant within small limits)

D_2 = the sensitivity response for the second detector in the system (assumed constant within small limits)

R_n^3 = the cumulative reflectivity of the three system mirrors during the n th measurement

$$R_n^3 = R_{1n} \times R_{2n} \times R_{3n} \quad (3)$$

where $R_1 = R_2 = R_3$.

If the power to the source is adjusted for each measurement so that $E_{11} = E_{12} = \dots = E_{1n}$, then, I_n remains constant and

$$E_{2n} = I_n G_2 D_2 R_n^3 = K_2 R_n^3 \quad (4)$$

The change ΔE in the output of E_2 produced by a small change ΔR in R_n is $3KR_n^2 \Delta R$, and the percent change in E_2 produced by a change in R_1 occurring between measurement 1 and n is

$$\frac{E_{2n}}{E_{2-1}} = \frac{3R_1^2 \Delta R_{1-n}}{R_1^3} = \frac{3\Delta R_{1-n}}{R_1} \quad (5)$$

Therefore, in the stipulated assumption, the minimum detectable reflectance change is one third that of a single-mirror system. Or

$$\frac{E_{2n}}{E_{2-1}} = \frac{n\Delta R_{1-n}}{R_1} \quad (6)$$

for n mirrors.

DATA-ACQUISITION SYSTEM

Because the key requirements in developing a new instrument for the measurement of molecular contamination are accuracy and precision of measurement, a significant effort was made to develop a flexible and reliable data-acquisition system (Fig. 5).

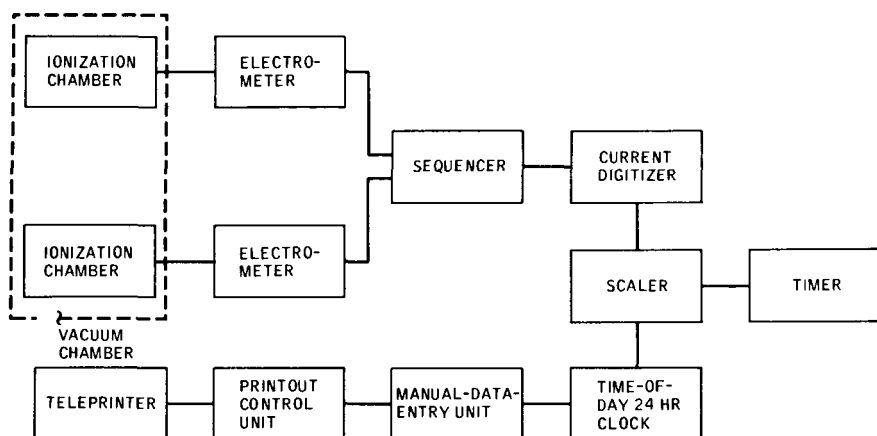


Fig. 5—System block diagram

During instrument operation, the currents from the NO ionization chambers are quite small, 10^{-9} to 10^{-11} A. Output from the ionization chambers is amplified by a picoameter with a current-output capability. A sequencer was used to step from one measurement to the next and to supply the signal current from the picoameter to a current digitizer where the signal is converted to a frequency (pulses/sec). The pulses are simply counted; the total time-integrated count is a direct measurement of the detector output. A time-of-day 24-hour clock and a six-digit manual-data-entry unit provide the exact time and date of the measurement.

At the end of a counting cycle, the data are typed on a teleprinter by means of a printout control unit. Punched paper tape and typed hard copies are available simultaneously. Most of the electronics are off-the-shelf nuclear instrumentation modules (NIM) and are available from several manufacturers. Each module is plugged into a bin power supply, and the necessary wiring connections are made. Extreme flexibility in pulse counting systems is provided by NIM.

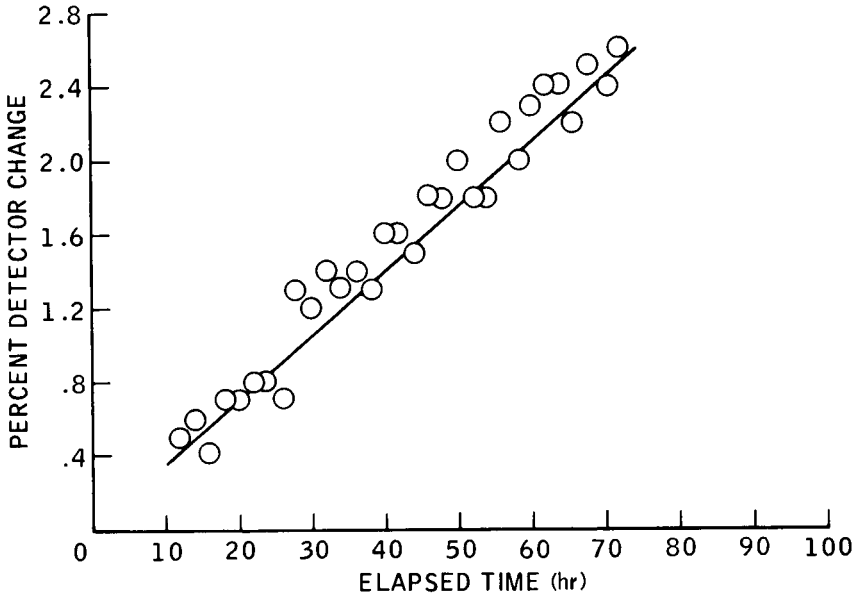
The NIM approach was taken in the design of the data-acquisition system because flexible time integration of the picoameter output was provided. Minor meter fluctuations are "averaged out" by integration. In this particular instance, an integration (pulse counting) time of 10 sec proved to be optimum. In data reduction, the measurements are ratioed so that absolute accuracy is not as pertinent as precision (the short-term reproducibility). By use of this technique, the precision of the measurement was often 0.1 percent or better.

INSTRUMENT COMPONENT TESTS

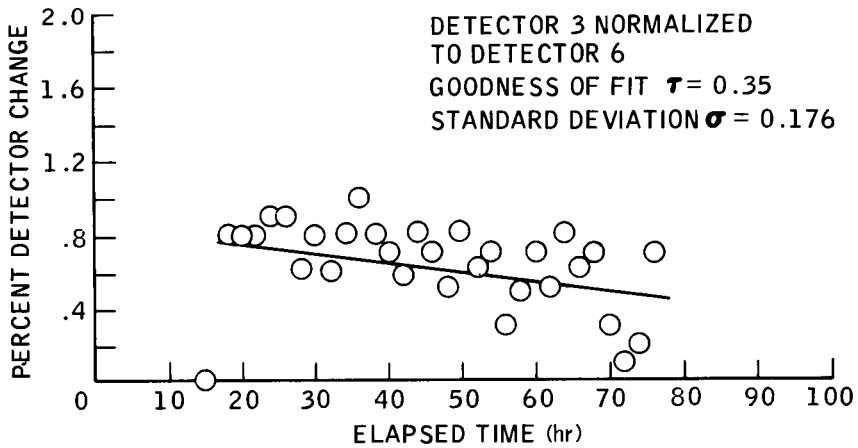
In September 1971, a test using six sources and six detectors under controlled conditions was performed to determine the stability of each component. The six detectors were arranged symmetrically around the axis of a standard hydrogen discharge lamp. The detector outputs were integrated over 10-sec intervals and monitored constantly.

The source power consumption was monitored and adjusted to remain constant. Two of the detectors malfunctioned because of faulty cables inside the chamber. The remaining detectors were evaluated over a 75-hr period of continuous operation, and the drift in every instance was in the direction of increasing signal. The percent change in output of four operational detectors normalized to the original output of detector 6 is shown in Figures 6(a), 6(b), and 6(c). The graphs give an indication of the

DETECTOR 2 NORMALIZED
TO DETECTOR 6
GOODNESS OF FIT $r = 0.975$
STANDARD DEVIATION $\sigma = 0.136$

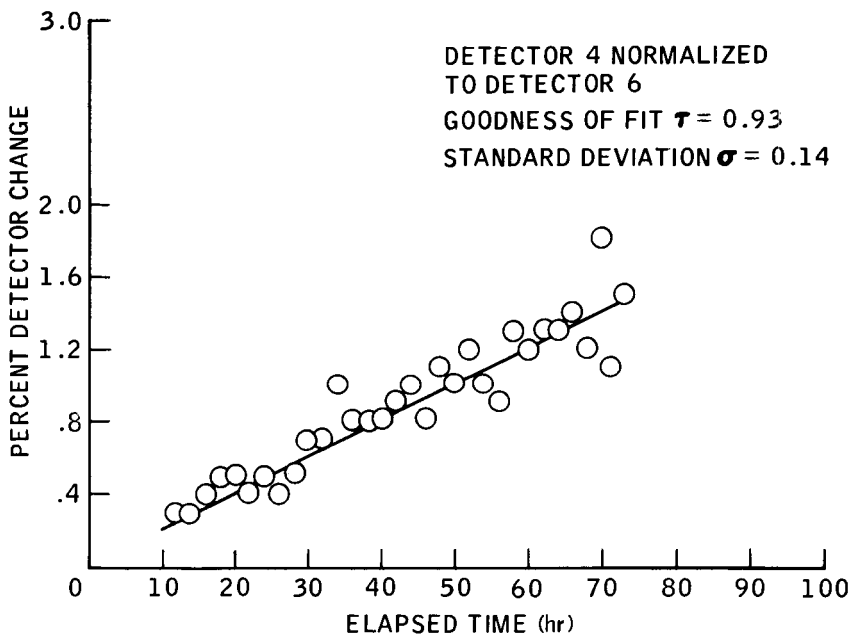


(a) Detector 2



(b) Detector 3

Fig. 6—Detector drift as a function of time for detector



(c) Detector 4

Fig. 6—Concluded

linear change of detector response with respect to time and the constant relationship between detectors. The standard deviation and the closeness of fit are shown on each figure. In the ideal operation of the instrument, the source output is adjusted until the control detector 6 has an output equal to that established before mirror deterioration. This is an effective normalization of the two detectors minus reflectance changes. Short-term changes in sensitivity response and changes in reflectivity then will be the principle variables of the output. The uncertainty associated with an apparent reflectivity change caused by detector response change and drift was determined to be less than 0.5 percent based on these considerations and experimental data.

Thermal response of the detectors was measured. After the chamber had been evacuated to a pressure of 2×10^{-5} torr and the cold walls stabilized at 100°K , one source was ignited and the detectors were stabilized thermally at 310°K . The

source temperature then was maintained at 295° K, and the temperature of the detectors was allowed to decrease to 245° K. A typical plot depicting the percent change in detector response as a function of temperature is shown in Figure 4.

INSTRUMENT TESTS

Several tests were conducted to evaluate the instrument under conditions that might occur during actual operation in a space-simulation (thermal-vacuum) chamber. The tests were conducted in a small, 225-liter vacuum chamber equipped with liquid nitrogen (LN₂) cold shrouds and a LN₂ baffled diffusion pump.

The instrument was placed in the test chamber, evacuated to a pressure of 2×10^{-4} torr, and the output of the instrument was measured as a function of time for 24 hr. The drift observed was effectively zero. The chamber then was backfilled slowly with ambient air, and the response of the instrument was monitored until the pressure in the chamber was 760 torr. A plot of the instrument response as a function of chamber pressure is shown in Figure 7.

The test setup that had been used for the previous test was not disturbed, and the chamber was again evacuated to a pressure of 2×10^{-4} torr. The chamber-wall temperature was lowered to 100° K, and reflectance measurements were taken until the instrument stabilized. The chamber then was warmed and backfilled with dry nitrogen (N₂), and the instrument output again was plotted as a function of chamber pressure. These data are indicative that the instrument can be operated usefully to chamber pressures of approximately 760 torr if the chamber is backfilled with N₂. The results of this test were predictable from a comparison of the absorption coefficients of nitrogen and ambient (moist) air.

The final test in this series was designed to establish a figure of merit for the instrument capability to detect the presence of a contamination source. A small container specifically designed to generate a known molecular evaporation rate of diffusion pump oil was used. The evaporation rate of DC 705 diffusion pump oil as a function of temperature was calculated. The calculations had been verified experimentally in previously conducted calibration experiments. The instrument was mounted in the test chamber so that the axis of the opening in the container made an angle of approximately 26° with the normals to the two mirrors on the same side. The chamber was pumped down to a

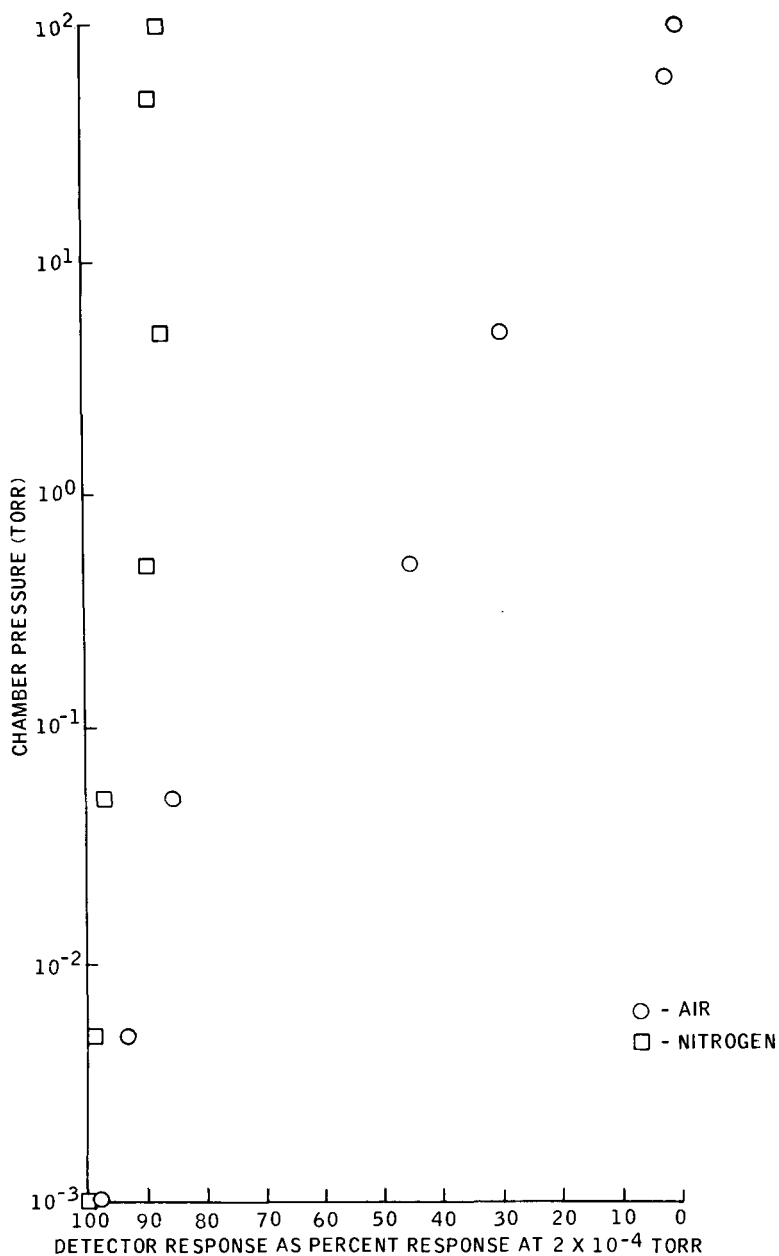


Fig. 7—Typical detector response as a function of chamber pressure

pressure of 2×10^{-4} torr, and the instrument was stabilized. The temperature of the container was elevated, and the response of the instrument was recorded. The instrument response as a function of time at a known evaporation rate is shown in Figure 8. The effective decrease in mirror reflectance calculated to produce the results in Figure 8 is comparable to that reported for similar mirrors (ref. 10).

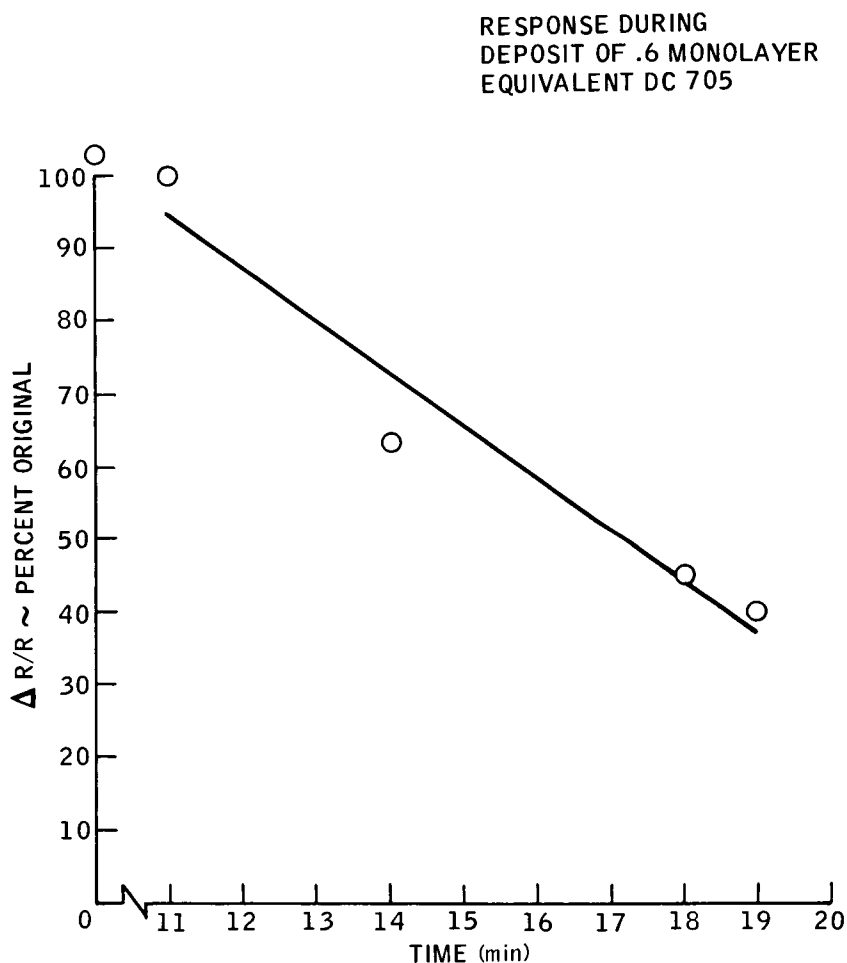


Fig. 8—Instrument response as a function of time for a known deposition rate

SYSTEM UNCERTAINTY

An estimate was made of the ability of the system to detect changes in the reflectance of the instrument mirrors. The data-acquisition system as calibrated with a standard picoameter source was found to have a precision of 0.1 percent on each scale used up to 1 picoampere.

The effect of the total change in one detector response during a test where the sources and detectors are used for 75 hr was less than 1.5 percent as determined by the experimental data. By carefully selecting and matching the detectors and correcting for detector drift as a function of time and temperature, this source of uncertainty can be reduced to less than 0.3 percent. The source produces no measurable effect on the system uncertainty because it was adjusted to produce a fixed response in the direct-beam detector and is averaged over 10 sec. The uncertainty produced by a change of 60° K of the bench temperature was determined, from the experimental data, to be 0.2 percent.

The total uncertainty of the three-mirror system was less than 0.45 percent. This means that a change of approximately 0.15 percent per mirror in mirror reflectance can be detected, if an assumption is made that the three mirrors are contaminated equally.

CONCLUSIONS

Multiple reflectance is an extremely sensitive technique for the detection of molecular contamination in space-simulation chambers. To maximize the sensitivity of the multiple reflectance technique, the selection and control of optical surfaces, detectors, sources, and bench configurations are required. Detector drift as a function of time and temperature must be measured. A method of time integration of detector outputs to average the signal is recommended. The measured sensitivity of the instrument and system was a 0.15-percent change in mirror reflectance.

Actual molecular-contamination measurements used with the system in a large space-simulation chamber are not available at this time. The measurements will be reported as they become available.

REFERENCES

1. Visentine, J. T. et al. Preparation, Verification, and Operational Control of a Large Space Environment Simulation Chamber for Contamination Sensitive Tests. To be presented at the 6th IES-AIAA-ASTM Space Simulation Conference, 1972.
2. Wolff, C. M.; and Ritter, M. L., Contamination Measurement in Space Environment Simulation Chambers. NBS Special Publication (SP)-336, Oct. 1970, pp. 25-49.
3. Green, A. K.; Dancy, J.; and Bauer, E., Growth of fcc Metals on Lead Sulfide. J. Vac. Sci. Tech., vol. 8, no. 1, 1971, pp. 165-170.
4. Reith, T. M.; and Peressini, P. P., Co-Deposited Aluminum Alloy Films. J. Vac. Sci. Tech., vol. 8, no. 1, July/Feb. 1971, p. 159.
5. Lins, S. J., Thickness Determination of Thick Films with Multiple-Beam Interferometry. Trans. Eight Vacuum Symp. and 2nd Inter. Congress, Amer. Vac. Soc., October 1961, pp. 846-851.
6. Miller, R. F.; and Hoffman, R. W., Nucleation Studies Using Electron Transparent NaCl Substrates, J. Vac. Sci. Tech., vol. 6, no. 1, Jan./Feb. 1969, pp. 65-68.
7. Walker, G. A., Structural Investigation of Thin Films. J. Vac. Sci. Tech., vol. 7, no. 4, July/Aug. 1970, pp. 465-473.
8. Hunter, W. R.; Osantowski, J. F.; and Hass, G., Reflectance of Aluminum Overcoated with MgF_2 and LiF in the Wavelength Region from 1600 Å to 300 Å at Various Angles of Incidence. Applied Optics, vol. 10, no. 3, March 1971, pp. 540-544.
9. Hass, G.; and Tousey, R., Reflecting Coatings for the Extreme Ultraviolet. J. Optical Soc. Amer., vol. 49, no. 6, 1959, p. 593.
10. Hass, G.; and Hunter, W. R., Laboratory Experiments to Study Surface Contamination and Degradation of Optical Coatings and Materials in Simulated Space Environments. Applied Optics, vol. 9, no. 9, Sept. 1970, pp. 2101-2110.

THE USE OF A QUARTZ CRYSTAL MICRO-BALANCE AND AN OPTICAL REFLECTOMETER TO DETERMINE CONTAMINANT MATERIAL OPTICAL CONSTANTS

D. A. Wallace and R. L. Chuan, *Atlantic Research*

ABSTRACT

Potential optical degradation of spacecraft optical elements by various vehicle contaminant materials can be predicted once the optical constants in the complex index of refraction are known for those materials. A technique using interference phenomena on the coated mirror of a reflectometer in conjunction with in-situ material thickness measurement with a quartz crystal microbalance has been employed to determine the optical constants of Silastic 140 at 1216 Å wavelength as a typical high loss material.

The reflectometer uses an aluminum coated mirror overcoated with magnesium fluoride of known thickness. Deposition of contaminant material of measured thickness produces a multilayer reflecting composite. Maxwell's equations yield the reflectance change with contaminant layer thickness at a given wavelength. Experimental determination of the reflectance change with QCM measured thickness can thus be used to determine which set of optical constants produce the resultant interference reflectance change.

For the material tested, Silastic 140, the complex index of refraction was determined to be $N = 0.9 - i 1.0$ at 1216 Å.

A SPACE SIMULATION TEST CHAMBER DEVELOPMENT FOR THE INVESTIGATION OF RADIOMETRIC PROPERTIES OF MATERIALS

D. L. Enlow, *Environmental Sciences Laboratory, Re-Entry and Environmental Systems Division, General Electric Company, Philadelphia, Pennsylvania*

ABSTRACT

A thermal vacuum space simulation facility was required to perform studies on the thermal radiation properties of selected materials. This paper will discuss the design, fabrication, and preliminary utilization of such a facility. The requirements for the measurements were that comparisons could be made for bulk material temperature and effective radiation temperatures under simulated solar and earthshine radiation conditions. The scope of such development was such that the facility could accommodate small ($<8''$) specimen and be operable on a minimum turn around time at low cost to attain repeatable space simulated conditions. A test chamber was designed to provide high pumping speed, low pressure (10^{-8} torr), low photon level radiation background (via high emissivity coated-finned cryopanel), internal heat sources for rapid warm-up, and rotary and linear motion of the irradiated material specimen. The radiation detection system consists of two wide-band infrared photoconductive detectors, their cryogenic coolers (LHe, LH), a cryogenic-cooled blackbody source (LN_2), and a cryogenic-cooled optical radiation modulator. The detectors were mated to their respective coolers which are in turn mated to the vacuum instrument ring in a unique mounting configuration. The integration of the space simulation, low thermal background and radiation measurement requirements with all the system components demanded that techniques be refined and new ones developed for the various mounting, aligning and operational procedures.

INTRODUCTION

The thermal profile of a material in a non-equilibrium case in a space environment is a very difficult analytical problem to solve. The major parameters controlling this profile are the material absorption coefficient for incident radiation $\alpha(x)$, depth of adsorption $d(x)$, conductivity, $k(x,y,z)$, and emission of the front surface $\epsilon(x,T)$. These factors

are, in general, not known in total functional dependent form; therefore, an experimental approach to evaluating this profile as well as the surface emission was chosen. Information of this type is required to better characterize the thermal and optical properties of materials that are used on missile and space programs. The maintenance of thermal balance is of prime necessity for the reliability required for such programs. The problems encountered on this measurements program consisted of the following: integration of the vacuum system with the cryogenic and optical components; alignment of optics and detectors for cryogenic operation, and minimization of electronic noise. This paper will deal primarily with the design, fabrication, and operational considerations of the measurement system. The approach taken is shown in a flow diagram (Figure 1).

I. Experimental Requirements

A. Space Simulation

To investigate the thermal-radiative properties of materials, the degree of a space vacuum simulation requires that the pressure be reduced to below a value where thermal conduction of a gas is very small compared to the radiant heat transfer. The vacuum level required is also a function of test sample, its relationship to the vacuum system walls, and its temperature. Since this work will be done for samples whose temperatures are in a range of 250 to 400°K, a pressure of 10^{-5} to 10^{-6} torr will be adequate to assure the gas molecule mean free path is much greater than the distance of the sample to the vacuum walls. The other considerations are that the pumping speed is sufficiently high and gas independent to assure no out-gassing effect and effective removal of all gases since the optical system utilizes liquid hydrogen (and liquid helium) cooled components. The natural approach to meeting these requirements is to use cryopanel.

Thermal absorption in the infrared is a major requirement for radiation-thermal property measurements. That is, cold black (highly absorbing) chamber walls are a necessity. The radiant emitted intensity from all other sources other than from specimen should be very small (i.e. less than 1 in a 100). In addition the condensable gases must be removed to prevent their cryodeposition on the liquid hydrogen and helium components. The cold black walls must completely surround the sample to avoid any unwanted thermal loading.

The solar radiation simulation requirement is that the source have only an approximately spectral similarity and that it provide adequate thermal loading for small specimens. That is, $.14 \text{ watt/cm}^2$ thermal input energy should be incident on the surface under investigation. In addition to the solar thermal requirements, a thermal source simulating the radiation from the earth must be provided. This is most important for thermal

measurements simulating a space-night environment where a major radiation source on a totally passive spaceborne body is from the earth. This may be approximated by a highly emissive 300°K flat plate (for small samples). Although this will not give the exact spectral emittance, the total radiant intensity will be very nearly that required (with a few percent).

B. Thermal Control

To measure the effective radiometric temperature of a body, it must be initially in a known state of thermal equilibrium. A body placed in a cold black environment will radiate according to the Stefan-Boltzmann Law $W = \sigma \epsilon T^4$, where W is the radiant emittance of a body whose emissivity is ϵ at a temperature T , σ is the Stefan-Boltzmann constant. The sample therefore is required to radiate outward only in specified directions and attain starting temperatures via direct conduction or input radiation. Conductive heating should be regulatable to within $\pm 1^\circ\text{K}$ over a 250°K to 500°K temperature range and not contribute a spurious bias during radiation monitoring.

The background temperature must be held to below 100°K to insure minimal error during the radiation measurements. Looking at the Stefan-Boltzmann Law it is seen that when measuring a 300°K body a background of 100°K adds 1.25% error assuming only graybody radiators.

C. Sensors

To make the required bulk temperature measurement thermocouple and platinum resistance thermometer should be used to measure the in-depth sample temperature as these devices have been routinely used with accuracies of $\pm .5^\circ\text{K}$.

The radiometric temperature measurement for the temperature range and space background conditions must be measured with long wavelength infrared detectors. Since the radiating properties of most materials are temperature dependent, these measurements must be done by two detectors each sensitive to a different spectral band. These detectors must be sensitive to small radiation changes of the order of 10^{-10} watts/cm² of sample area in order to accurately correlate bulk to radiative temperature. These detectors must possess stability of sensitivity to allow for long term and repetitive testing.

II. Experimental Apparatus

The above discussed requirements were incorporated in the design, procurement, fabrication, and integration of the following subsystems: a) infrared measurement test chamber; b) support vacuum system; c) infrared detectors and support components; d) reflective optical train. Each of these will be discussed individually in this section.

A. Infrared Measurement Chamber

This chamber, as shown in Figure 2, is a Stainless Steel 304 18" x 18" bell jar mounted on a 8 port 6" feedthrough ring. All gaskets were replaced with Viton A to minimize O-ring out-gassed constituents. The entire interior chambers were cleaned with spectroscopic grade methyl alcohol to remove remaining oils as the optics and detectors utilized in this chamber are cryogenically cooled and as such are highly vulnerable to polymeric and other contaminants¹. The vacuum level is maintained by a vacuum pumping system (see Section B) and cryogenic panelling. The panelling used was HVEC Model High-E which has been found to be excellent providing 7.81 square feet of exposed area for every 1 square foot of projected area. With this panel painted with 3M black velvet an emissivity of greater than .95 has been attained over a spectral band of 2 to 25 microns². Over four square feet of this type was used corresponding to a 250,000 liters per second pumping capability for condensables above liquid nitrogen (approximately 100°K at the panel surface) temperatures³. In all other location HVEC "D" Type panel was heliarc welded to stainless steel 304 sheet which was in turn sprayed with 3M black velvet. All panels and shrouds were vacuum baked at 200°C and 10^{-3} torr for 36 hours to assure the paint was fully outgassed. Each set of panelling is fed with an individual liquid nitrogen line each monitored by single probe level controllers. In this way better overall thermal stability is maintained. One push-pull feedthrough (metal bellows) is used to place the thermal controlled specimen in the focal plane. The other is used to move a second blackbody (calibrated radiation source) into the optical train to enable full calibration of the detectors and optics in-situ. Historically, in-situ calibration of optical components of this type generated difficulties in alignment and known optical components, spectral reflectivities and transmissives. The primary cryogenic coolable blackbody is attached (thermally isolated) to the earthshine simulator support mount. This radiation source, Electro-Optical Industries Model LT-1522CC, provides a calibrated (controllable to $\pm 1^\circ\text{K}$) radiation source over a temperature range of 100°K to 500°K. The cryogenic chopper allows the detectors to alternatively look at the specimen or the blackbody, thus providing calibration reference points throughout the measurement duration. The solar radiation is a 75 watt Xenon arc lamp which is focusable down to a one-half centimeter spot. This radiation enters the vacuum system through a quartz window and is reflected to the sample by a gold aluminum mirror.

The major optical constituent of the measurement facility are the infrared detectors. These detectors are photoconductive in nature (as opposed to thermal detectors, i.e. thermocouples) that is, they actually count photons hitting their sensitive surface. These photons generate charge carriers and

in effect change the resistance of the detector. It is this resistance change that is monitored in a constant voltage bias source. The reason for low background temperatures (less than 100°K) for photodetectors is obvious as the thermal excitation inherent in the detector (doped Germanium) crystal lattice vibrations for temperatures above 100°K is adequate to excite an abundance of charge carriers. Thus the incoming photons would have a reduced effect and an erroneous signal level would be measured. To effectively operate these detectors the background and all the optical train is cryogenically cooled. The Ge:Hg detector is mated to Air Products liquid hydrogen refrigerator AC-2-110, and the Ge:Cu detector is mated to a LT-3-110 liquid helium transfer system. Most IR detectors are mounted to an attached dewar and as such must be operated in an end-looking mode outside any vacuum system. The approach taken here is a highly useful and operationally simplified one. The hydrogen cooler uses the Joule-Thompson cooling principle of isenthalpic expansion of high pressure gases. Both nitrogen and hydrogen gases are used, with LN_2 being produced first to cool the hydrogen gas below its inversion point so that when it expands through an orifice it will liquify. Countercurrent heat exchange techniques are used to minimize gas consumption and thermal load. The liquid helium transfer system merely transfers LHe to the cryotip which is the mating point for the detector. The temperature of the tip is regulated by a balancing of a heat tape and liquid flow to maintain temperatures from 2°K to 300°K with a stability of $\pm 0.01^{\circ}\text{K}$ (in the liquid phase). Mating flanges and connecting double viton O-ring tubes (SS304) were designed, fabricated, and attached to the feedthrough ring and the detector/cryotip assembly was attached. This arrangement allows the detectors to operate in any orientation and eliminates intermediate vacuum interface optics.

The earthshine simulator consists of three heater disks sandwiched between aluminum 6061 disks. Each disk is controlled by a variac and the upper plate temperature is monitored by copper-constantan thermocouple. The top plate is coated with 3M black velvet.

B. Vacuum System

The vacuum system (Figure 3) consists of the test chamber and pumping system. The test chamber, discussed in A., is polished on the inside to reduce its emissivity, completely internally shrouded by LN_2 panelling, and made elevated by an electric hoist to permit easy access. Only the thermocouple, electrical, cryogenic, and mechanical connections with support assemblies contiguous with the bell jar are directly attached. This requires stainless steel flexlines for the cryogenic transfer. The detectors/cryotips, optical cryogenic lines, and all other electrical lines are connected on the feedthrough ring.

The pumping system consists of a 6" HVEC diffusion pump (1700 l/sec), a Welch Mechanical Pump (15cfm), and an optically dense LN₂ baffle. The diffusion pumped system (using DC705 oil) provides a clean baseline vacuum environment (10^{-6} to 10^{-7} torr). A point of conjecture - concern over the inherent "unclean" operation of diffusion pump systems is seemingly unfounded⁴. Actually the lowest ultimate system pressure (and cleanliness) was attained by an oil diffusion pumped system. The diffusion pump can be cooled via a closed cycle refrigerator eliminating the need for open-ended water facilities. The pressure is measured with a Bayard-Alpert type ionization tube connecting a Granville-Phillips Model 236 Controller. This controller has automatic range switching and will follow a system down or up in pressure unattended via solid state switching circuit.

C. Optical System Assembly and Component Configuration

A detailed view of the optical assembly is shown in Figures 4 and 5. This design was developed under constraints of low thermal background operation, alignment and spectral stability for ambient to cryogenic temperature ranges and high sensitivity to radiation in the mid to far infrared region. Reflective metal optics were selected because they have been shown to be athermal and possess wide spectral bandwidth. A review of all possible metals was performed with Aluminum 6061 being selected as having the best thermal expansion and workability properties. All of optics, mounts, and support platforms were made of Al6061. The mirrors were gold coated over a Kanigan (electroless nickel) sandwich layer to insure very high reflective in the infrared. The optical mirrors are arranged in such a manner as to split in half the incident radiation after it is reflected from mirror #4 and direct each signal to a detector. Mirrors M₂ and M₄ are off axis spherical mirrors with a focal length such that the aperture at the detector defines the same equal area seen at the specimen. This system can look at spots of 1/2 to 2 mm in diameter.

The mirror mounts are attached to a plate that is LN₂ cooled and isolated from the rest of vacuum system. From the aperture of detector outward only LN₂ cooled black surfaces are viewed outside of the incident signal. This was accomplished by adding Al6061 sheeting, aperture stops, and tedious alignment procedures. To align this system initial ambient conditions were performed using a lmm spot lamp suspended at the end of a plumb line center directly over M₁. This procedure was repeated for the cooled vacuum case by mounting the lamp internally and replacing the detectors with visible optics viewports with the exact detector location marked on the optics. Visible inspection was thus accomplished with no apparent compensation for infrared radiation required since the reflective properties of the mirrors are nearly non-varying over this spectral range.

Two detectors were used: 1) Raytheon OKN1227 Ge:Hg; 2) Raytheon OKN154 Ge:Cu. Both of these detectors had a D^* (500, 900, 1) (300°K background) of at least $1.0 \times 10^{10} \text{ cmHz}^{1/2}/\text{watt}$. This is a figure of merit for the detectivity normalized to unit area and bandwidth. It can be simply considered a measure of the signal-to-noise ratio. These units can respond to radiation in the 10-12 watt levels in times shorter than a few microseconds and as such provide excellent tools for the measurements. Associated with the operation of these detectors are specific electronics support equipment. These electronics were selected to measure microvolt signals from a high impedance source. These considerations will not be discussed in this paper.

III. Experimental Procedures

The experimental techniques consist of the following procedures: 1) sample placement; 2) in-situ detector calibration; 3) broadband emissivity measurements; 4) parametric correlation measurements of in-depth platinum resistance thermometer and broadband emittance.

The samples, typically 1" to 4" in diameter and less than 2" thick, are placed in an electrically heated annular ceramic glove that encapsulates the sample except for the front surface. This configuration can maintain the bulk temperature at a uniform initial value which is measured by in-depth platinum resistance thermometers and various copper-chromel thermocouples. The electrical connection are all made through Deutsch DM series feedthroughs.

The in-situ detector calibration is performed by pumping the chamber down to at least 10^{-7} torr cooling down the walls, ceiling, optical mirrors, chopper, and lower platform to LN_2 temperature; cooling the detectors down to the operating temperature, use both blackbodies set at 300°K to 500°K ; and modulating the signal with the chopper at 100-200 Hertz. The electronics for the detectors utilize cooled J-FET pre-amplifiers and phase sensitive lock-in amplifiers for maximum sensitivity (lowest noise). Overall gain of the system is of the order of 10^4 with the responsivity of the detectors is 10^5 volts/watt. A 300°K specimen emits $3.2 \times 10^{-3} \text{ watts/cm}^2$ however considering the intercepted solid angle of the detector area, reflection losses, and spectral dependence only 10^{-8} watts is incident on the detector. Therefore, this signal will produce a 10 volt output at the lock-in amplifier (Keithley System 84). The overall precision is estimated to be 2% of the output voltage or $\pm 1^\circ\text{K}$. The signal-to-noise ratio is always in excess of 100 since the amplifier is narrow band and tuned. This calibration takes 4 hours from ambient conditions.

Next, the broadband emissivity is measured in the two spectral bands of the detectors (5 to 15 microns and 14 to 26 microns). This is done by conductively regulating the surface

temperature of the specimens for various temperature values (250°K to 400°K). Thus the validity of using broadband emissivity is determined. In general for most mid to high emissivity non-metals, the spectral dependence is minimal.

After the emissivity values are determined, a correlation between the in-depth temperature and the broadband irradiance from the sample surface is performed. This correlation is to be done as a function of conductive and radiative thermal inputs by varying the heater current, solar and earthshine input. Then the radiometric reading will be converted to effective surface temperatures by applying the Stefan-Boltzmann Law.

The facility described in this paper represents a novel approach to measuring some of the thermal and optical properties of materials in such a way to allow a smaller experimental bias error than other surface temperature measurement techniques.

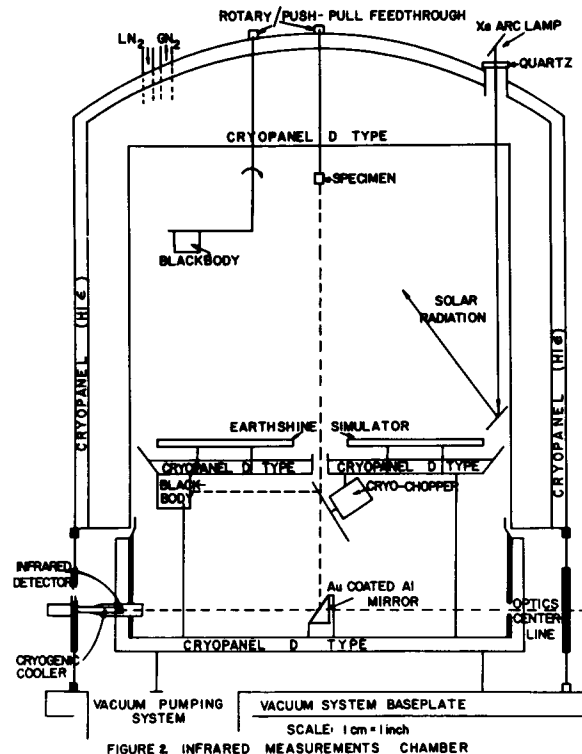
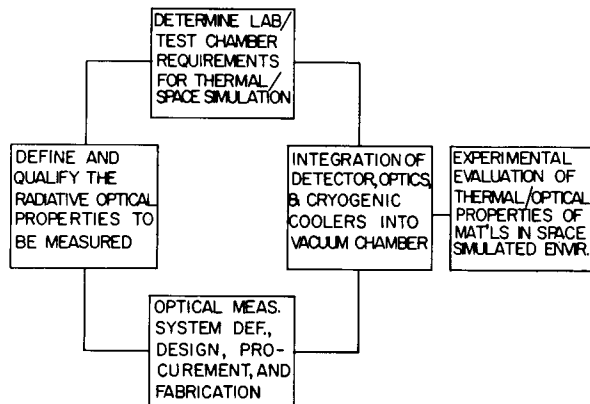
ACKNOWLEDGEMENT

The Author would like to thank Dr. E. L. G. Odell for his assistance on the optical system design; F. Pancoast for design, fabrication and check-out of the vacuum-cryogenic systems, and B. Schein for graphic layouts.

REFERENCES

1. D. Enlow, Space Simulation (National Bureau of Standards SP #336, 1970), pp 51-78.
2. J. Bernstein and D. L. Stierwatt, "Infrared Spectral Emittance of Five Black Coatings", Naval Weapons Center China Lake, 1970.
3. P. A. Redhead, J. P. Hobson, E. V. Kornelsen, The Physical Basis of Ultrahigh Vacuum (Chapman & Hall, London, 1968).
4. D. J. Santeler, Trans. 17th Vac. Symp. AVS H-1 (1970).

FIG. 1 APPROACH TO THERMAL/OPTICAL PROPERTIES INVESTIGATION :
FLOW DIAGRAM



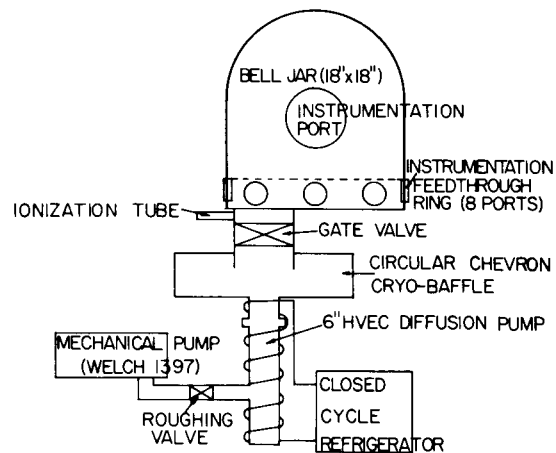
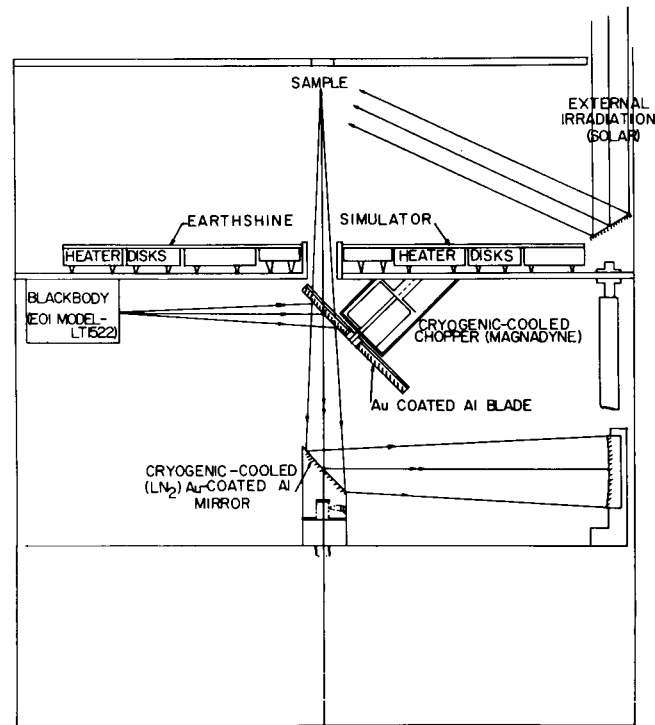


FIG. 3 VACUUM SYSTEM



SCALE -2 to 1

FIG. 4 LOWER OPTICAL SYSTEM ASSEMBLY (PARTIAL, SIDE VIEW)

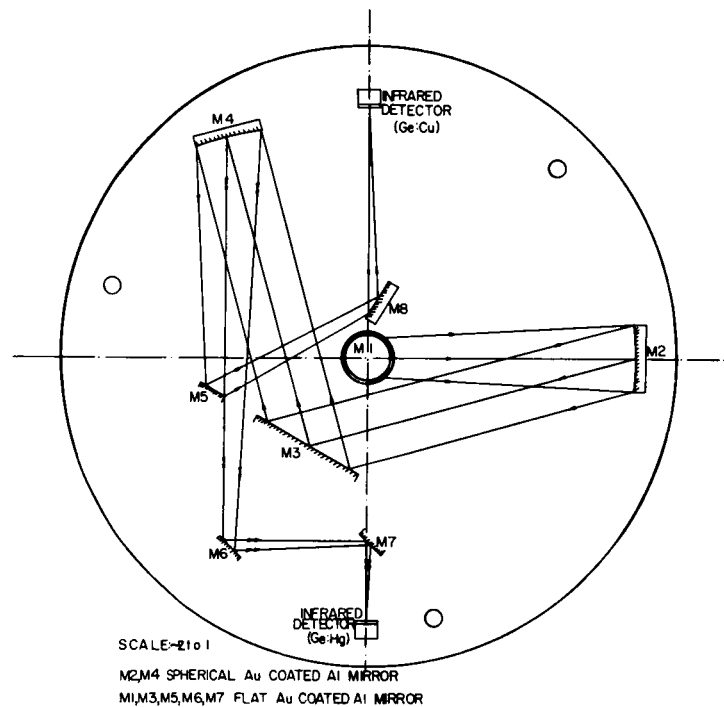


FIG.5 OPTICS CONFIGURATION AND RAY TRACING

THERMAL VACUUM CHAMBER SHROUD PERFORMANCE WITH GASEOUS NITROGEN COOLING

R. A. Farmer, *Martin Marietta Corporation, Denver, Colorado*

ABSTRACT

This report presents the results of a series of calculations of shroud surface temperature for various flow rates of gaseous nitrogen through the liquid nitrogen shrouds of the large thermal vacuum chamber at the Denver Division of the Martin Marietta Corporation. Conditions imposed provide conservative bounds for Mars surface simulation inside the chamber during thermal testing of an appropriate test object. It is shown that the shroud surfaces seen by the object can be held within an acceptable temperature range by providing a reasonable flow of gaseous nitrogen to the shrouds at a reasonable pressure, and that no change to the present shroud system need be made which would affect its suitability for liquid nitrogen cooling.

INTRODUCTION

Shroud temperatures in the large thermal vacuum chamber in the Space Simulation Laboratory at the Denver Division of the Martin Marietta Corporation were analyzed for gaseous nitrogen (GN_2) cooling. The purpose was to obtain representative numbers for GN_2 flow rate and pressure drop under specified wall temperatures and various types of Mars surface simulation. This data was to be used in preparing a specification for competitive procurement of process equipment that would be needed for GN_2 cooling.

PERFORMANCE ANALYSIS

Design Criteria

The large thermal vacuum chamber is illustrated in Figure 1. The chamber is 29' in diameter and 65' high. It can attain a pressure of 10^{-9} torr when clean, dry and empty; and it has a liquid nitrogen shroud system and solar simulation system installed. It will be used for thermal testing of various test articles under conditions of Mars surface simulation. This will not be a condition of cold black outer space, but will be a new application for this chamber.

The criteria used in the analysis consisted of a wall temp-

erature specification and a set of design heat loads. The wall specification required that temperatures to which the test article was subjected in the chamber should not vary more than 10°F from the median temperature. This is equivalent to permitting a 20°F temperature range for the inside walls of the shrouds. No attempt was made to specify a "weighted" temperature variation or range, because it would change with test article orientation (time of Martian day). Furthermore, it would differ from point to point on any three-dimensional test article. Therefore, actual permissible shroud temperature variation was specified. Figure 2 further illustrates the point. Even though the shroud represented in Figure 2b would be a better shroud than that illustrated in Figure 2a, both would meet the requirements of the specification if $T_2 - T_1$ is equal to or less than 20°F in both.

An estimate of the heat loads to be handled by the shrouds during simulated hot and cold extreme Martian days was furnished by others (1). These are broken down into components for the "worst" time of each day, when heat loads are greatest. Heat exchange between the shrouds and the water cooled collimating mirror is neglected, and the shroud in the chamber lid is uncooled.

The nominal shroud temperatures, or Martin sky temperatures, were -135°F and -250°F for hot and cold days, respectively. Actual shroud temperatures were variable with time, but always higher, to compensate for convective chilling of the thin atmosphere over the test article. This method of compensation was assumed to apply to operation of the chamber during test. The design loads would change if some device such as a transparent membrane were used to isolate the atmosphere from the shrouds.

The external loads indicated in Figure 3 and listed in Table 1 are over-estimated because the values shown apply to heat leakage into the chamber at the nominal shroud temperatures. This introduces an element of conservatism into the calculations.

Radioisotope Thermoelectric Generator (RTG) and ground simulator loads were increased from the actual loads so that they could be taken as applied uniformly over the bottom shroud and lower 34 feet of the side shrouds. Thus, the resulting heat flux at any location was equal to or greater than that actually applied in test. This is not conservative, since maximum calculated wall temperatures actually occur on the walls. They just do not occur in as large areas as indicated by this calculation. Less heat was carried away by the shroud walls, however, as shown by the difference between the sum of the design heat loads and the actual total heat load in each part of Table 1.

Use of Table 1 leads easily, with the aid of Figure 4, to Table 2, in which the heat load on each shroud is listed. The worst case for each shroud can be extracted from this table, but in practice it was found necessary to calculate all cases including nighttime heat loads.

Calculational Procedure

In order to obtain the desired data, it was found more con-

TABLE 1 DESIGN HEAT LOADS (Btu/hr)

HOT EXTREME, 6 PM		
LOAD/LOCATION	BOTTOM	SIDES
External	12,300	42,700
Vehicle RTG	2,000	9,000
Ground simulator	7,980	125,500
Solar	51,500	0
	<u>73,780</u>	<u>177,200</u>
Sum	250,980	
Actual total	174,000	

COLD EXTREME, 6 PM		
LOAD/LOCATION	BOTTOM	SIDES
External	16,800	63,200
Vehicle RTG	2,000	9,000
Ground simulator	2,180	21,000
Solar	38,000	0
	<u>58,980</u>	<u>93,200</u>
Sum	152,180	
Actual total	131,000	

TABLE 2 DESIGN HEAT LOADS (Btu/hr)
BY SHROUD

LOCATION/EXTREME	HOT 6 PM	COLD 6 PM
Old bottom External	12,300	16,800
RTG and GS	0	0
Solar	0	0
New bottom External	0	0
RTG and GS	9,980	4,180
Solar	51,500	38,000
2 ft side External	1,530	2,260
RTG and GS	0	0
8 ft side External	6,870	9,600
RTG and GS	0	0
11 ft side External	8,400	13,000
RTG and GS	0	0
34 ft side External	25,900	38,340
RTG and GS	134,500	30,000
	250,980	152,180

venient to choose GN_2 flow rates and calculate resulting temperatures and pressure drops, iterating if necessary to get desired temperatures on each shroud. This procedure leads to a determination of the most efficient distribution of the GN_2 flow rate which is the sum of all flows through the shrouds. In operation this distribution would have to be reproduced by manual adjustment of the shroud inlet valves in order to reproduce the calculated temperature range and pressure drop.

The calculation of shroud wall temperatures depended on knowledge of design heat load, shroud construction details, and material. Radial temperature gradients, across tube walls and plates, were neglected. Transients in shroud wall temperature, or shroud heat content, and gas property temperature dependence were also neglected.

Gas temperature was calculated by keeping track of total heat transferred to the gas up to a given point:

$$T_G - (T_G)_{\text{in}} = \frac{Q}{WC_p}$$

where W was GN_2 flow rate, typically in lb/hr. The film temperature difference ΔT_f between the gas and tube wall was given by local heat flux at the tube wall divided by the heat transfer coefficient, which was calculated by use of the equation:

$$\text{Nu} = 0.023 \text{ Re}^{0.8} \text{ Pr}^{0.4}$$

$$\frac{hd}{K} = 0.023 \left(\frac{\rho V d}{\mu} \right)^{0.8} \left(\frac{\mu C_p}{K} \right)^{0.4}$$

All shrouds were made of parallel tubes spanned by thin plates. Temperatures on the plates would be slightly higher than on the tube walls, so a mean wall temperature difference ΔT_w was calculated. The temperature distribution over a plate would be parabolic, and the mean of the plate temperature over the tube wall temperature could be expressed in terms of the gradient at the tube wall. The gradient was calculated by:

$$A = KA \left. \frac{dT}{dx} \right|_{\text{wall}}$$

A mean temperature across tube and plate may then be calculated by simple geometry, resulting in ΔT_w . The local wall temperature then became:

$$T_w = T_G + \Delta T_f + \Delta T_w$$

In the results, T_w is given in terms of inlet gas temperature:

$$T_w - (T_G)_{\text{in}} = \frac{Q}{WC_p} + \Delta T_f + \Delta T_w$$

Pressure drops were calculated by means of the equation:

$$\Delta p = 4f \frac{L}{d} \frac{\rho v^2}{2g}$$

where L was an equivalent length including the effects of valves, bends, and transitions, and f was taken for smooth tubes and calculated from:

$$f = \frac{0.046}{R^{0.2}}$$

For Reynolds numbers larger than 200,000, the value for f was taken from an experimental data curve⁽²⁾.

All momentum changes were neglected. A rise in temperature and a drop in pressure would each cause an increase in momentum as the gas expanded. However, percentage changes in temperature, and especially in pressure, were small.

An 80 psia system was assumed. At lower pressures, slightly smaller GN₂ flow rates would have given comparable temperature ranges, because of an enhanced heat transfer coefficient, but the gas velocities would be higher, and there would be higher pressure drops.

Results

Sample temperature results are best presented on a map of the inside of the chamber. 10 of the 12 shrouds that would be cooled by GN₂ are shown in Figure 5, a bird's-eye view of the open chamber. The heavy line emphasizes the boundary between the bottom and sides. Figure 5 carries abbreviated designations for the 10 shrouds seen by the test article.

Table 3 lists shroud wall temperatures, for hot 6 PM, at the inlet and outlet of each shroud when the GN₂ flow rate of 25,000 lb/hr is fairly efficiently distributed. The GN₂ flow to the two shrouds not seen by the test article is included in the 25,000 lb/hr, and was determined by the requirement that heat leak to the inside shrouds should be negligible. Figure 6 maps the temperatures of Table 3. Recalling that uniform conservative loads were imposed on each shroud, one can use linear interpolation with position on each shroud to get an approximate temperature at any location between extremes. It is evident that 25,000 lb/hr of GN₂ cooling can reduce the shroud wall temperatures to a 36°F range under hot extreme 6 PM conditions. Figure 7 shows the temperatures under nighttime conditions for the hot extreme with the same flow conditions. The range has increased to 37°F because the minimum inlet temperature has dropped while some outlet temperatures have remained constant. This is about twice the wall specification, especially if some allowance is made for the practical difficulties of distributing GN₂ flow by manual valve adjustment. Figure 8 shows shroud wall temperatures for hot 6 PM when 52,000 lb/hr of GN₂ are supplied. The range has decreased to 18°F. The range slightly increases at hot nighttime for the

TABLE 3 SHROUD TEMPERATURES FOR 25,000 lb/hr AT HOT 6 PM

SHROUD	W	$\frac{Q}{WC_p}$	ΔT_f	ΔT_W	$T_W - (T_G)_{in}$
NB in	4100	0	9.6	0.8	10.4
out		57.0	9.6	0.8	67.4
					38.9*
2 ft	170	0	3.8	0.1	3.9
		34.2	3.8	0.1	38.1
8 ft -90	480	0	12.0	0.3	12.3
		25.0	12.0	0.3	37.3
8 ft -270	480	0	12.0	0.3	12.3
		25.0	12.0	0.3	37.3
11 ft -90	590	0	9.8	0.3	10.1
		28.2	9.8	0.3	38.3
11 ft -270	590	0	9.8	0.3	10.1
		28.2	9.8	0.3	38.3
34 ft -0	3300	0	6.1	0.7	6.8
		32.1	6.1	0.7	38.9
34 ft -180	3300	0	6.1	0.7	6.8
		32.1	6.1	0.7	38.9
34 ft -90	6000	0	6.3	0.7	7.0
		32.7	6.3	0.7	39.7
34 ft chevron	4600	18.0 [†]	2.6	0.8	21.4
		36.0	2.6	0.8	39.4
<p>*Inlet and outlet are in the same plate, so $T_W - (T_G)_{in} = \frac{1}{2} \frac{Q}{WC_p} + \Delta T_f + \Delta T_W$ everywhere.</p> <p>[†]This assumes only inner fins are seen, and GN₂ heats up linearly.</p>					

reason given above.

Cold 6 PM and nighttime conditions were investigated just as thoroughly, and it was found that these conditions gave narrower temperature ranges than hot conditions. However, this was true only if the GN_2 flow was redistributed.

Higher GN_2 flow rates were treated in equal detail to obtain enough data to draw the temperature range curve in Figure 9.

In all cases the 34-foot chevron shroud caused the largest pressure drop when the GN_2 flow was efficiently distributed. It was the only shroud with 0.75 in. tubes (all others had 1 in. tubes). It also had two passes and additional piping. The values calculated for Δp permitted the construction of the pressure drop curve in Figure 9.

Sonic velocity was not approached in any case, so the neglect of Mach number effects was valid. Also, erosion of tube walls by the gas should be negligible.

Sources of Significant Errors

There are several uncertainties in the calculations. The significant ones are listed.

- 1) The validity of the temperature calculations depended upon the validity of the design loads. Since the design loads were furnished by others, no estimate of their accuracy was made;
- 2) Errors in the temperature might occur due to inaccurate prediction of ΔT_f , and due in turn to inaccuracies in the Colburn equation. The limit of that error, in T_w , would be of the order of a percent;
- 3) Pressure drop predictions depend on accurate values for the friction factor f . An error of a few percent in f can be expected, and this would cause a few percent error in pressure drop values. A much more significant source of uncertainty in practice, however, would be caused by variations in flow distributions between shrouds.

The following errors or assumptions can be definitely pinned down as giving conservative results:

- 4) The assumption of external heat loads for nominal shroud temperature gave higher heat loads for all shrouds except for 34-foot chevron and new bottom, which in turn caused outlet temperatures to be overestimated by an amount variable with time, but of the order of 10 percent;

- 5) Neglect of momentum changes caused an over-estimation of ΔT_f , and hence of T_w , of the order of a percent;
- 6) The assumption of direct viewing of the 34-foot chevron is correct for a point on the chamber centerline; but caused an overestimation of wall temperatures seen by a large object, by some small undetermined amount.

The following errors or assumptions had an unconservative influence on the results:

- 7) The tubes may not be smooth throughout as assumed. Burrs left in joints during construction, for example, would raise the pressure drop;
- 8) Neglect of momentum changes caused an underestimation of the pressure drop by as much as 10 percent. This occurred, however, only at the lower flow rates, where Δp is very small, or at the very high flow rates;
- 9) The assumption of direct viewing of the new bottom shroud caused an underestimation, of undetermined amount, of the wall temperature seen by the test article;
- 10) The fine structure of temperature variation on the walls, such as on the plates between tubes, was replaced by mean values. This reduced the range of T_w values calculated, although this is probably not a significant error.

Items 1, 2, 4, 5, 6, and 9 undoubtedly combine to give conservative results on wall temperature so that the curve in Figure 9 can be achieved in practice. Items 3, 7, and 8 might make the pressure drop curve in Figure 9 unconservative by more than 10 percent.

CONCLUSIONS

The results of the analysis to determine thermal vacuum chamber shroud performance with gaseous nitrogen cooling led to the following conclusions:

- 1) The present shrouds are adequate for GN_2 cooling at 80 psia;
- 2) The GN_2 flow rate of 25,000 lb/hr is sufficient to keep shroud wall temperatures within a 40°F range under the worst conditions of design load. Higher flow rates would narrow the range that could be achieved. 52,000 lb/hr will keep shroud temperatures within the 20°F range of the wall specification.

- 3) A narrower wall temperature range can be achieved during cold extreme simulation, at a given GN_2 flow rate, provided the flow is redistributed. Thus, cold and hot extreme simulations should be regarded as separate tests;
- 4) Pressure drop through the system would not be expected to exceed 10 psi at GN_2 flow rates up to 150,000 lb/hr;
- 5) A lower pressure system could be used, but pressure drops would be higher;
- 6) In any case, the cooling gas must be carefully and accurately metered between 12 different shrouds so that the correct amount will flow through each shroud. In practical operation, this will probably mean "tuning" the chamber at 6 PM conditions before starting the test. Thereafter, no changes should be needed except in inlet gas temperature.

REFERENCES

1. VER-28, "Mars Surface Thermal Simulation", Martin Marietta Corporation, Denver Division, 26 January 1970.
2. Schlichting, H.; Boundary Layer Theory, McGraw-Hill, New York, 1960, page 504.

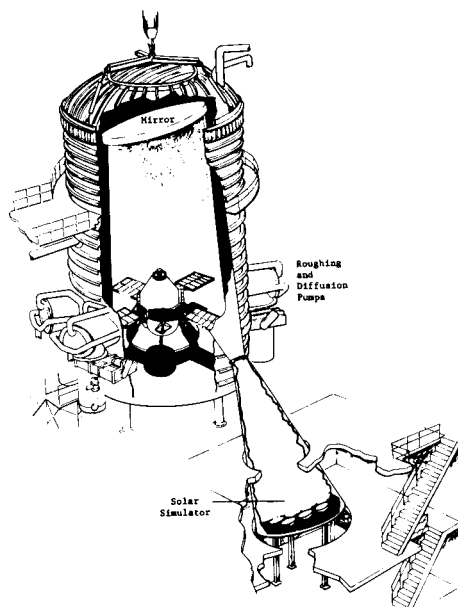


Figure 1 Large Thermal Vacuum Chamber

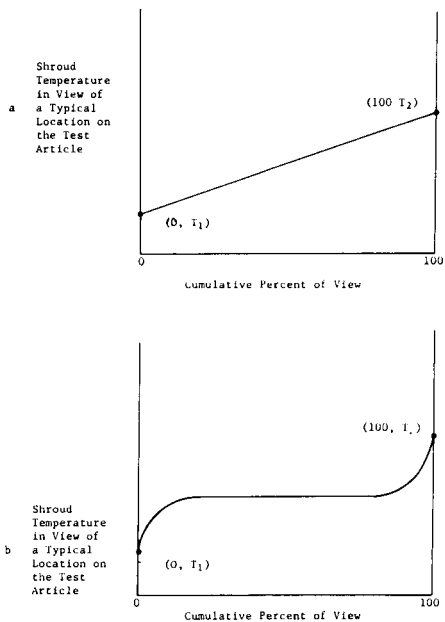


Figure 2 Typical Shroud Temperature Distributions

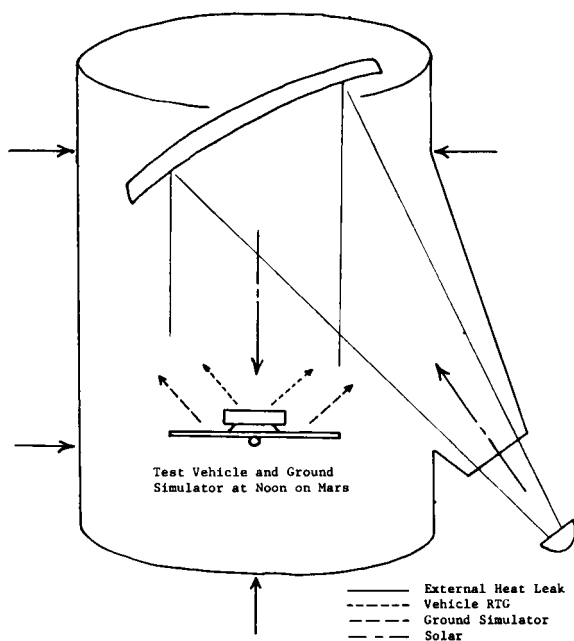


Figure 3 Design Heat Loads

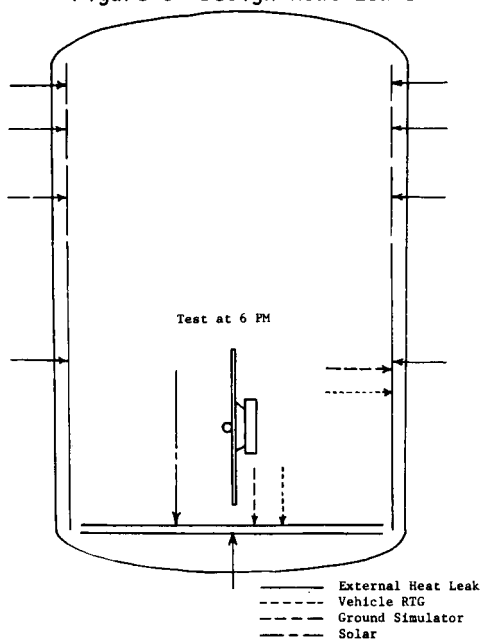
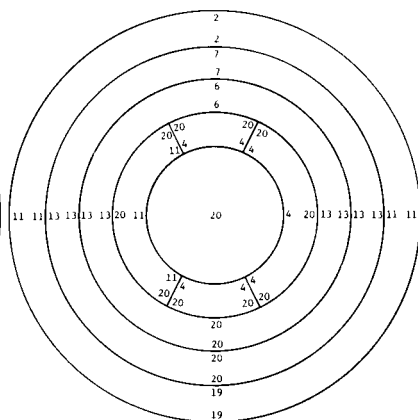
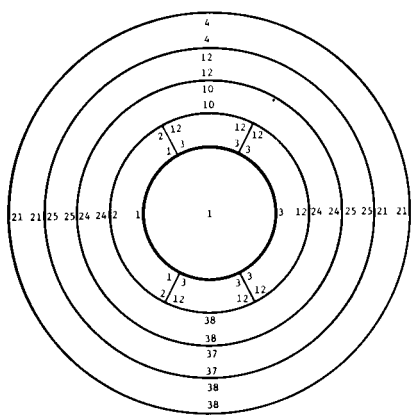
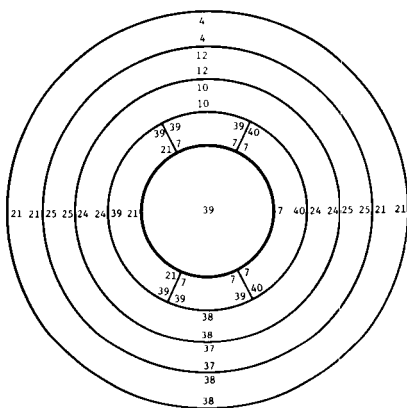
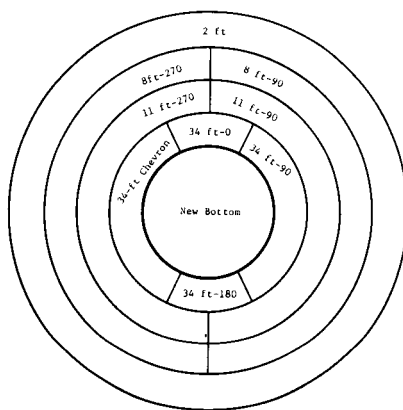


Figure 4 Design Heat Loads by Shroud



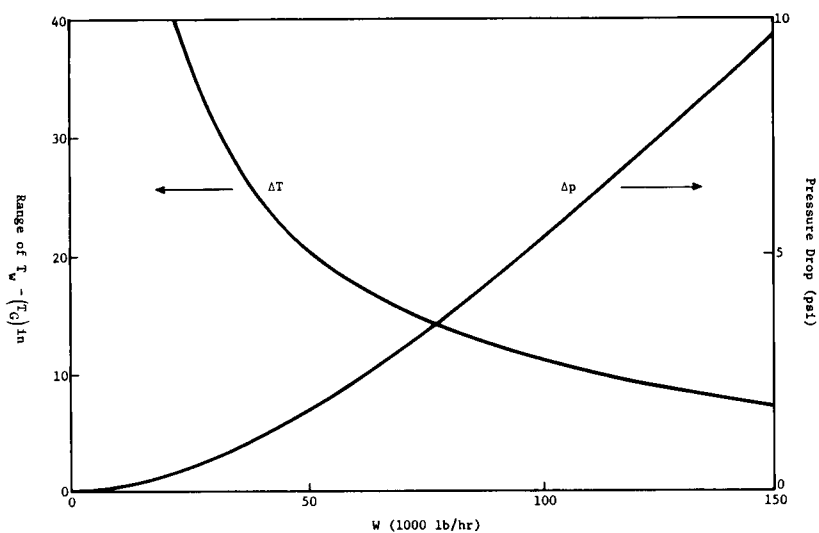


Figure 9 Minimum Variation in Wall Temperatures at Worst Conditions and Corresponding Pressure Drops Versus GN_2 Flow Rate in an 80 psia Shroud System

ADVANTAGES OF CRYOPUMPING WITH LIQUID HYDROGEN INSTEAD OF HELIUM REFRIGERATORS

J. W. Anderson and J. E. Tueller, *Lockheed Missiles and Space Company, Inc., Sunnyvale, California*

ABSTRACT

Open loop hydrogen vaporizers have some distinctive advantages over helium refrigerators when used in selective pumping schemes or 20° cryopanel cooling in thermal vacuum testing. The two systems are compared for operational complexity, installation and operating cost and safety requirements. Data from two Lockheed vacuum chambers using helium refrigerators are used to provide comparative data. In general, the use of hydrogen is shown to be attractive in the larger systems even when extra safety precautions are taken. The emotional resistance to the use of hydrogen because of safety requirements is considered great. However, the experience gained in the handling of large quantities of cryogenics, particularly hydrogen and liquefied natural gases, should be considered in the design of open loop hydrogen cooling systems.

INTRODUCTION

General use of a cryopanel to produce low pressures by reducing the energy level of the gases present is easily associated with the vapor pressure of the gases present. Figure 1 shows the most common fluids encountered in space thermal-vacuum environment simulation. Note that a 20°K panel could probably result in pressures in the 10^{-6} to 10^{-8} torr range for most gases except helium and hydrogen with an operational margin to allow for pumping reduction due to radiation shields and surface/gas coefficients.

The use of low temperature surfaces (cryopanel) to assist in vacuum chamber pumping systems has been widely accepted. This paper proposes that in some cases an open loop hydrogen evaporator can be used advantageously instead of the closed loop helium refrigerator. Cryopumping is usually adopted to avoid backstreaming contamination from diffusion pumps or to handle high mass flows at low pressures. The most attractive feature of the open loop hydrogen system is the inherent reliability related to the simple design.

System Reliability

The expense of thermal vacuum testing of spacecraft is so great that the operation of the facility must be highly reliable. The last two years of operation for two of Lockheed's thermal vacuum chambers provides an experience base for assessing the problems of costs of pumping failure during spacecraft testing in a large chamber. Each of these environment simulation chambers use helium refrigerators to maintain panels within the chamber at 20°K for the primary pumping at low pressures less than 10^{-4} torr. Approximately 70% of test interruptions sufficient to cause opening the chamber have been due to vehicle equipment malfunction. Of the remaining 30% at least 1/3 of the interruptions were due to the helium refrigerator. Any improvement in the reliability of the helium refrigerators, or their replacement by more reliable systems, would be to the advantage of vehicle testing. It is to the credit of the equipment manufacturers that helium refrigerators have improved by orders of magnitude in the last decade and we can assume that their inherent reliability will increase and their operation will become more simple. The comparisons here, though, are made on recent use experience and the manufacturers' recommendations for periodic maintenance and repair that places a definite limit on their operational reliability.

Studies at Lockheed for the use of an alternate system using a hydrogen cooled cryopanel are encouraged because of the inherent simplicity of a hydrogen system. Preliminary designs to date have considered the simple elements required, consisting of a storage tank, temperature sensing control valve, vacuum jacketed transfer lines, and vent gas burner. Each of the components needed have been used sufficiently to establish extremely high reliability factors. Their limits are presently related to the reliability of available electrical power. Since the power requirements are very low (less than 150 watts), the system could easily be connected to facility emergency power.

A systems reliability can also be related to operational complexity. The hydrogen system proposed is extremely simple to operate. Characteristics discussed later support the contention that a hydrogen unit would be easier to operate and increase reliability.

Safety Considerations

Safety was the most restrictive factor in the evaluation of the open loop hydrogen system. Features of the system proposed include:

- Hydrogen storage tank in open area 150 feet from inhabited buildings.

- A single continuous hydrogen circuit from storage vessel through test chamber to burner.
- Flow meters on inlet and exit lines with integrated signals for sensing large flow differences -- large leaks.
- Flow controls that limit initial cooling of the panel.
- Interlocking control valves and vent gas ignition power.

The high flammability of hydrogen has promoted several studies on flame propagation, pool boiling rates, ignition energy requirements, and percentages of hydrogen in air-hydrogen mixtures that are flammable. Reference 1 presents data to support the recommendation that quantities of 5000 lbs may be stored within 150 ft. of an inhabited building. Basic storage considers the tank pad to be surrounded by a crushed rock bed sufficient to absorb all the hydrogen within the storage vessel in case of tank or line failure.

Leakage of hydrogen within the building can best be minimized by keeping all valves, meters, or controls outside the building. Figure 2 shows a single circuit from the storage vessel to the burner. Additional safety could be purchased by routing the hydrogen lines inside a tube filled with dry nitrogen at a pressure exceeding the hydrogen line pressure.

Large hydrogen leaks can be detected by the use of dual flow meters cross-coupled to signal a leaking condition if the vent gas flow is less than the flow through the control valve. The sensitivity and accuracy of this unit is related to the flow rate requirements. Cost comparisons for a particular system may show the design should only have one flow rate, no modulation. Such a one point design would simplify the controls but would use an excess of hydrogen during minimum load periods.

Another source of leaks is from thermal distortion of the cryopanel during rapid cooling at the beginning of operation. This can be minimized, without complicating the system, by limiting flow to the maximum quantity required for normal operation. Even with this limitation, the cryopanel would cool to operating temperatures more quickly than the helium refrigerators could come on the line.

Electrical heating elements used as igniters in the vent gas burners should be redundant and interlocked with the shut off valve. This would insure that all hydrogen vent gases would be burned. The wide range of flammability in air, and the low ignition energy required, reference 2, allows a long life design of the igniter coils. In fact, proper placement of the igniter coils will allow burner ingested air to cool the igniter during hydrogen burning.

The use of hydrogen for cryopumping in environmental chambers has been proposed many times. Most of the objections-related to safety have been due to lack of knowledge or experi-

ence. At present, many of those experienced in the handling of liquid hydrogen and liquid oxygen have less worry of accidents from hydrogen source.

Cost Comparisons

General cost comparisons have been made in support of facilities planning. Considering the potential problems with diffusion pump backstreaming, it is quite likely that cryopanel will continue to be attractive elements of selective pumping systems. Cost elements of two sizes of helium refrigeration units installed and operating for two years or more are listed in Table 1. Cost estimates of an open loop hydrogen system are also included. The latter is based on a design study being used for planning a facility similar in size to one using the 1200 watt helium refrigerator. Table 1 indicates the cost advantage for the hydrogen unit would occur for the larger sizes. This is true for costs that can be projected directly. The price of equipment failure during spacecraft testing is more difficult to assess.

Consider that each pumping system failure significant enough to require bringing one of the large chambers to ambient conditions consumes approximately one full day. Manhour losses will include the basic facility crew plus a larger number of spacecraft support personnel. Direct cost for a single facility failure during a major test will exceed \$20,000. Add this cost potential, and possible critical schedule problems, to helium refrigerator costs and it becomes more important to explore the feasibility of using liquid hydrogen.

REFERENCES

1. M. G. Zabetakis, A. L. Furno, and G. H. Martindill, "Explosion Hazards of Liquid Hydrogen," *Advances in Cryogenic Engineering* Volume 6, 1960.
2. G. B. Yates and A. R. Perl, "Spark Ignition Parameters of Cryogenic Hydrogen in Oxygen and Nitrogen Mixtures," *Advances in Cryogenic Engineering*, Volume 10, 1964.

TABLE 1
Systems Characteristics and Costs

	<u>Helium Refrigerators</u>		<u>Liquid Hydrogen</u>
Capacity @20°F	70 watts	1200 watts	1200 watts
Power Required	11 KW	125 KW	Negligible
Cooling Water	4 gpm	30 gpm	-----
Helium Losses	.01 lbs/hr	.6 lbs/hr	-----
Startup Period	30 min	30 min	30 min
Cost Equipment	\$20,000	\$110,000	\$36,000
Installation	10,000	30,000	12,000
Operating Costs (50 days per year)	\$ 3,310	\$ 14,850	\$19,125
Total Annual Cost	\$ 7,060	\$ 32,350	\$25,125
Operational Complexity	Moderate	Moderate	Low
Maintenance Complexity	Moderate	Moderate	Low
Reliability	Good	Good	Excellent

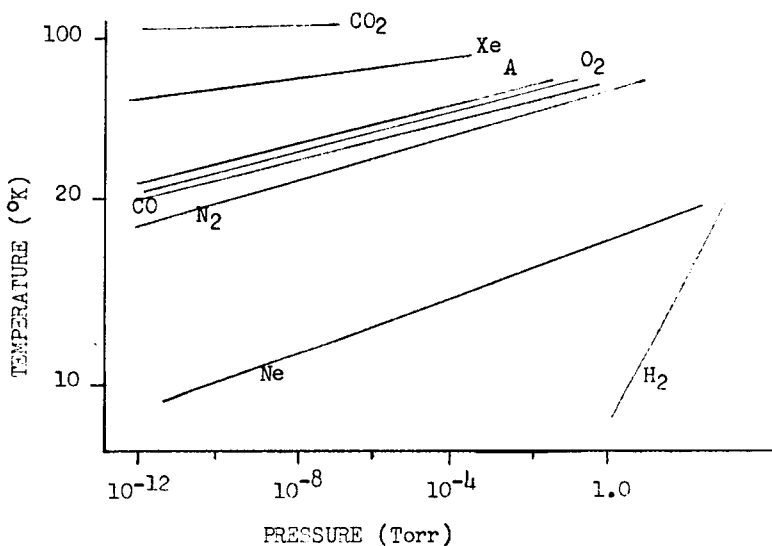


Fig. 1 Vapor Pressure vs Temperature for Gases in Air

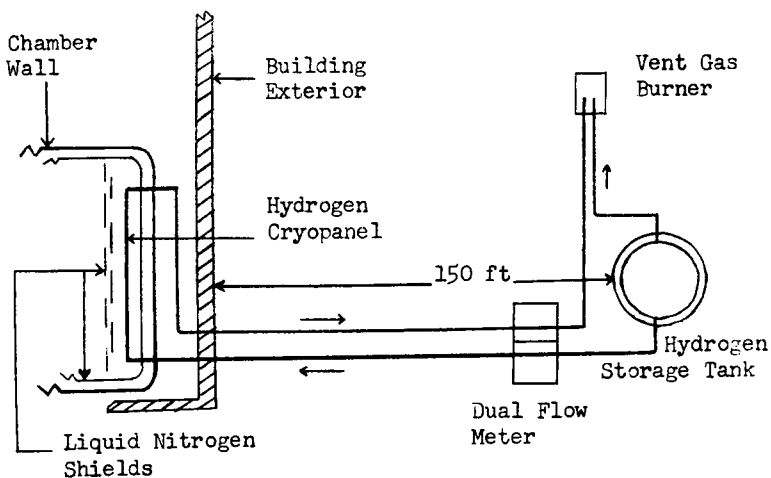


Fig. 2 Open Loop Hydrogen System Schematic

DEVELOPMENT OF A CARBON CLOTH HEAT POST MODULE FOR THERMAL VACUUM TESTING OF A SPINNING SPACECRAFT

M. B. Levine & L. A. Nelson, *Hughes Aircraft Company, El Segundo, California*

ABSTRACT

Development of a high temperature, high power density, isothermal, rapid transient infrared thermal module is described.

The investigation of various alternative approaches is discussed as well as the rationale leading to the choice of a carbon cloth concept.

Evolution of module design configurations and a summary of the development test results are included along with a detailed description of the final design which incorporated a black plate emitter radiantly heated by the carbon cloth.

The final module configuration successfully met design criteria during a 200-hour thermal vacuum performance test at 1000°F operating temperature without contaminating a solar cell array.

INTRODUCTION

A development program was initiated in response to a requirement for a modular infrared source easily configured in an array for simulating incident solar energy on a spinning spacecraft during thermal vacuum testing. Incident radiant energy from the highly concentrated source directed radially towards the spacecraft would integrate over the spacecraft surface at a spin rate commensurate with typical orbital spin speeds of spin-stabilized spacecraft.

The modular approach evolved as a result of the requirement to provide zone control within the array configuration to compensate for view angle and edge effects inherent in boundary thermal conditioning systems. Seasonal variations of orbital sun angle would be simulated by controlling the intensity of radiant energy from the heat post array. Eclipse phases would be simulated by terminating power to the module for the duration of the eclipse.

CRITERIA

The thermal module was to exhibit the following performance

characteristics:

1. Long term maximum operating temperature capability of 1000°F.
2. Power dissipation level of 3000 watts/ft².
3. Known and consistent surface emissivity.
4. Rapid heat-up and cool-down transients for realistic simulation of orbital eclipse environment.
5. Low residual thermal flux from the module for minimum thermal backloading to the spacecraft during simulated eclipse.
6. Isothermal within 2 percent (20°F maximum temperature gradient at 1000°F maximum operating temperature).
7. Low inherent contamination properties to preclude degradation of solar cells or other critical spacecraft surfaces.
8. Discrete and well defined heater area with minimal edge effects.
9. High efficiency with low energy dissipation towards the chamber LN₂ shrouds to preclude undefined reflections from impinging on the spacecraft.

ALTERNATIVES

A number of alternate concepts for providing thermal energy to the spacecraft were evaluated, however, only the carbon cloth-flat plate module exhibited the capability of satisfying the full spectrum of exacting requirements. A brief discussion of alternatives is included to illustrate the inherent mismatch of performance characteristics.

1. Infrared Lamps - Various types of infrared lamps have been utilized successfully for thermal boundary conditioning in a vacuum environment. Tubular quartz-envelope tungsten-filament lamp and reflector arrays provide an efficient reliable high intensity source of thermal energy and exhibit rapid heat-up and cool-down transients. Thermal flux intensity characteristics within the test plane or test volume can be defined and maintained using fairly rigorous but familiar mapping and monitoring techniques. A lamp array can be most effectively used for setting boundary conditions using surface temperatures of the specimen to control intensity.

Spectral distribution mismatch between the sun and the quartz lamps makes true solar simulation impossible. Changes in the lamp spectrum with changes in power makes

it difficult to define absorbed flux for spacecraft surfaces even if incident flux is known. As measured lamp array electrical power cannot be accurately related to incident flux, radiometers must be used to monitor incident flux. Geometric constraints due to the close proximity of the module to the spacecraft would make it impossible to mount radiometers where representative incident flux could be measured.

2. Flat Plate with Bonded Calrod Type Heaters - A flat plate with calrod type heaters bonded to the rear presents virtually a diametrically opposed set of characteristics. Source parameters of this system such as surface geometry, emissivity, and temperature can be readily defined and high temperature-high power density plates are commercially available. The calrod plate, however, exhibits a number of serious deficiencies which must be subjected to a performance tradeoff. Variations in calrod tube spacing, plate thickness, plate material thermal conductivity, bonding techniques, and differential thermal expansion coefficients contribute to performance criteria mismatch.

A calrod plate was tested in a vacuum environment. Empirical data verified earlier analysis which indicated a thin stainless steel (or nickel alloy) plate would exhibit excessive temperature gradients. A thicker plate or one with closer calrod spacing would preclude acceptable eclipse simulation due to high thermal mass. A plate material with a suitable high thermal conductivity such as copper would have optimized the transient versus gradient situation, however, copper jacketed heater elements were not commercially available, at least within a reasonable time period. Probability of achieving successful long term high temperature performance in vacuum with a brazed heater assembly constructed of dissimilar materials of different coefficients of thermal expansion was unknown. Additional problems were indicated when the prototype calrod plate failed at the termination fittings, apparently due to the lack of a mechanism to dissipate heat in a non-convective environment. Compressed schedules did not include provisions for a long leadtime development program.

3. Resistance Panel Heater - An apparently simple solution presented itself in the form of a resistance heater panel close coupled for direct radiation to the spacecraft. A fine mesh carbon cloth panel clamped between two bus bars appeared to offer significant advantages over typical metallic wire screens with respect to panel temperature uniformity, rapid cooldown transients, high temperature dimensional stability, low contamination probability, and

consistence of emissivity measurement. Cloth characteristics such as surface area, temperature, and power dissipation level could be easily defined.

A very cursory functional test conducted in vacuum indicated concept feasibility but additionally pointed out the need for development of a mechanism for accurate direct temperature measurement. The major investigation of this concept consisted of emissivity measurements of the carbon cloth. The results of the calorimetric hemispherical emittance measurements are documented in Table 1 below:

TABLE 1
Total Hemispherical Emittance - Carbon Cloth

<u>Temperature (°F)</u>	<u>ϵ_H (Total)</u>
600	.69; .66
800	.66
1000	.61; .60
1200	.58

After completion of the emittance measurement tests, the carbon cloth temperature was raised to incandescence (approximately 1600°F). At this condition it became apparent that the current carrying strands of the cloth were visibly hotter than the contra-woven strands.

The resistance panel concept was deemed unfeasible as a result of apparent temperature non-uniformity and the uncertainties introduced by either measuring the temperature of the cloth by optical methods or by attaching thermocouples directly to the current carrying carbon cloth.

4. Carbon Cloth - Flat Plate Heater - A more viable concept was evolved by combining the advantages of a flat black plate with the carbon cloth resistance heater panel. Energy would be radiated to the spacecraft directly from the black plate which was radiantly heated by the carbon cloth panel. High thermal conductivity of a copper plate would minimize thermal gradients and the properties of the surface could be readily defined. Temperature of the plate could be monitored by direct thermocouple methods.

A high temperature, high emissivity vacuum compatible paint was chosen for the radiant surface. Emissivity measurements of the Sperex VHT type SP-102 black paint are tabulated in Table 2 below:

TABLE 2

Total Hemispherical Emittance - Sperex VHT (SP-102) Paint

<u>Temperature (°F)</u>	<u>ϵ_H (Total)</u>
600	.86
900	.84
1100	.81
1200	.79
1400	.75

MODULE DEVELOPMENT

Development of the basic carbon cloth-flat plate module was initiated for the purpose of demonstrating feasibility of the concept and optimizing a detailed hardware configuration which would most effectively meet the thermal requirements.

A simple feasibility test was conducted while a test fixture was being fabricated for subsequent configuration optimization studies. In this first test, a 12 x 12 x 0.015 inch thick stainless steel sheet painted on both sides with Sperex VHT (black) was suspended 1.0 inch in front of and parallel to an 11 x 11 inch square carbon cloth heater panel and a test was conducted in vacuum. The basic concept proved feasible, however, this configuration exhibited a temperature gradient measured from the center to the edges of the plate of 235°F at a maximum plate temperature of 875°F and an operating power level of 5.75 KW.

A copper plate (.063 inches thick) was substituted for the steel plate for the second experiment. This configuration yielded a maximum thermal gradient of 125°F at a maximum operating temperature of 910°F and a power level of 7.7 KW. Post test observation revealed that the Sperex had peeled off the bare copper and subsequent copper plates were nickel plated and lightly grit blasted prior to painting to alleviate this problem.

The third test configuration included a gold plated stainless steel reflector added to the rear of the module to provide higher efficiency. The .063 inch copper plate was nickel plated prior to application of the Sperex. A maximum thermal gradient of 80°F was achieved at 4.4 KW and 980°F maximum operating temperature.

Test configuration number four included gold plated stainless steel reflector strips along the edges of the module which would provide more uniform heating at the edges of the plate, but deleted the rear reflector. The thermal gradient was reduced to 61°F at a maximum temperature of 972°F and a power level of 6.5 KW.

The fifth test was conducted with the fourth configuration with the addition of a rear reflector, however, this time the chamber shrouds were conditioned with LN₂ and a windowless Hy-cal radiometer was installed 24" from the plate to monitor thermal flux at a simulated specimen position. The power level dropped to 3.1 KW to achieve a maximum plate temperature of 985°F with a thermal gradient of 150°F and a radiometer reading of 146 watts/ft².

The results of the fifth test indicated that additional energy was required at the edges of the copper plate in an LN_2 environment. It seemed logical to add a second layer of carbon cloth behind the first around the edges of the panel to provide the additional edge energy. This was accomplished by folding back two opposite edges of a slightly larger cloth panel and sewing the folds with carbon thread. The double thickness at the bus bar interfaces was implemented by rolling the cloth around quartz tubes and repositioning the bus bars closer together behind the cloth to provide a 1.5 inch roll back. This configuration was operated at a power level of 3.1 KW and a maximum temperature of 999°F . The thermal gradient was reduced to 32°F , however, in this case the edges of the plate were warmer than the center. The radiometer measured 165 watts/ft^2 of incident energy.

The reversal of gradient brought about by the double layers of cloth at the plate edges was encouraging, but as this configuration was more difficult to fabricate, an alternative was tried. The next configuration (test number 7) substituted a copper pan in lieu of the flat plate. The sides of the pan were designed to act as heating fins to provide additional energy to the edges of the radiator. This configuration yielded a 54°F (hotter edge) thermal gradient at a maximum temperature of 1037°F and an operating power level of 3.2 KW. The radiometer measured a flux of 175 watts/ft^2 .

Since the pan was apparently successful in raising edge temperatures, it was decided to test the pan with the flat cloth panel. This configuration (Test number 8) achieved a lower gradient of 40°F with the edges cooler than the center at a maximum temperature of 1017°F and a power level of 3.1 KW. Incident energy at the radiometer was 172 watts/ft^2 .

Results of the last three tests indicated a combination of copper pan with the fold and roll concept might achieve the desired results. A number of tests were subsequently conducted with a 1.0 inch deep pan edge and various fold-back and roll-back dimensions to optimize the design. The final configuration was implemented with a roll dimension of .62 inches and a fold dimension of .25 inches. A sketch of the production module in Figure 1 illustrates this configuration. Table 3 summarizes the results of all configuration development tests.

The two sets of values given in Table 3 for test number 13 are indicative of equilibrium conditions at the start and completion of a 200-hour life test. The test was conducted to subject the final prototype configuration to a typical life cycle and to determine if outgassing from the module paint would degrade the performance of a solar cell array.

A pre-test four-hour 1100°F vacuum bakeout of an untested module was conducted prior to installation of the solar cell array. During the life test the temperature of the plate was maintained at approximately 1000°F with the solar cells near 70°F .

Pre and post life test performance curves of the solar cell array indicated no measurable contamination from the module. An eclipse simulation which was conducted prior to the life test indicated acceptable module heat-up and cool-down transients.

Figures 2 and 3 show the transient responses as measured by a Hy-cal radiometer.

BY-PRODUCT TECHNOLOGY

A number of interesting implementation techniques were evolved during the development program.

1. Thermocouples - Initial investigations were conducted with high temperature glass insulated chromel constantan thermocouples. The initial procedure of mechanically staking the thermocouple bead into a drilled hole in the copper plate was subsequently replaced by a method which provided more consistent data. Both the chromel and the constantan wires were individually staked into small diameter holes located approximately .10 inches apart, thereby providing a couple within the copper plate itself. This method was eventually improved with electron beam welding techniques where each wire was welded into the hole, resulting in extremely reliable and consistent data generation.

Thermocouple shorting problems were encountered early during the program due to fraying of the fiberglass insulation. This condition was apparently due to the high temperature glass binder volatilizing at operating temperatures, notwithstanding published data indicating high temperature capability of the wire. Stainless steel sheathed-ceramic insulated thermocouples were used on production modules to preclude thermal data anomalies and probability of solar cell contamination by the binder material.

2. Sperex VHT Black Paint (Type SP-102) - As indicated before, paint bond integrity was unacceptable when applied directly to the bare copper. Subsequent applications on nickel plating (grit blasted to improve long term bond reliability) resulted in extremely reliable and consistent surface treatment. Tests have shown no paint degradation after short duration (~ 1 minute) excursions as high as 1800°F .

CONCLUSION

The development program was considered successful in that a module meeting all the design requirements was evolved. Production modules were subsequently assembled into a heat post array and performance tested. The heat post structure consisted of a thick finned LN_2 cooled channel configured around the rear and edges of the modules, thereby precluding stray undefined radiant energy from perturbing the orbital simulation. This post has been operated successfully during a number of long duration space

simulation tests with no measurable decrease of performance.

TABLE 3
MODULE DEVELOPMENT TEST PROGRAM

TEST NO.	TEST CONFIGURATION	VACUUM CHAMBER SHROUD TEMP.	POWER LEVEL (KW)	MAX. OPERATING TEMP. (°F)	MAX. TEMP. GRADIENT (°F)	RADIO-METER MEASUREMENT (Watts/Ft ²)
1	.015 Stainless plate, flat cloth panel	Ambient	5.75	875	235	N/A
2	.063 copper plate, flat cloth panel	Ambient	7.7	910	125	N/A
3	.063 copper plate, flat cloth panel, rear reflector	Ambient	4.4	980	80	N/A
4	.063 copper plate, flat cloth panel, edge reflectors	Ambient	6.5	972	61	N/A
5	.063 copper plate, flat cloth panel, rear & edge reflectors	LN ₂	3.1	985	150	146
6	.063 copper plate, rear & edge reflectors, carbon cloth fold-back and roll-back	LN ₂	3.1	999	32	165
7	.063 copper pan, rear & edge reflectors, carbon cloth fold-back & roll-back	LN ₂	3.2	1037	54	175
8	.063 copper pan, flat cloth panel, rear and edge reflectors	LN ₂	3.1	1017	40	172
9	.063 copper pan, rear & edge reflectors, carbon cloth fold-back & roll-back	LN ₂	3.1	1034	32	176
10	.063 copper pan, rear & edge reflectors, carbon cloth fold-back & roll-back	LN ₂	3.2	1046	25	156

Continued --

TABLE 3 - CONTINUED

TEST NO.	TEST CONFIGURATION	VACUUM CHAMBER SHROUD TEMP.	POWER LEVEL (KW)	MAX. OPERATING TEMP. (°F)	MAX. TEMP. GRADIENT (°F)	RADIO-METER MEASUREMENT (Watts/Ft ²)
11	.063 copper pan, rear & edge reflectors, carbon cloth fold-back and roll-back	LN ₂	3.1	1043	27	157
12	.063 copper pan, rear & edge reflectors, carbon cloth fold-back & roll-back	LN ₂	3.3	1064	26	N/A
13	.063 copper pan, rear & edge reflectors, carbon cloth fold-back & roll-back	LN ₂	2.8 3.0	994 991	18 20	N/A N/A

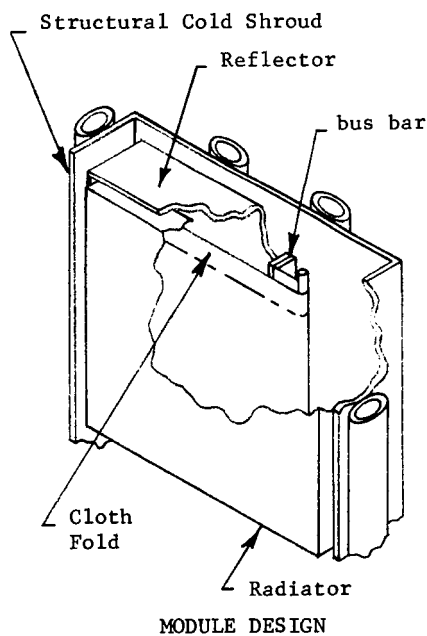


FIG. 1

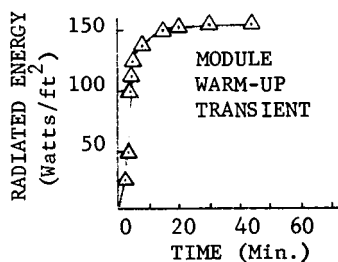


FIG. 2

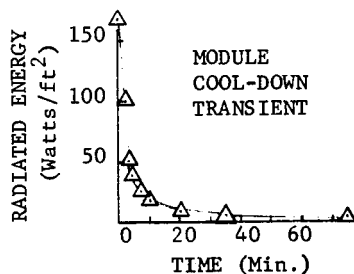


FIG. 3

THE DESIGN AND OPERATION OF A PLANET EMITTED AND ALBEDO RADIATION SIMULATOR

George E. Sweet,* John T. Taylor,[†] Ira H. A. Abbott[‡], NASA Langley Research Center, Hampton, Virginia

ABSTRACT

This paper describes the development of a new simulator that provides a dynamic simulation of planetary albedo and planet emitted thermal radiation. This simulator was designed for model tests of advanced thermal control concepts, the development of new space hardware, and for the flight qualification of small payloads. The simulation of this energy is particularly important for spacecraft employing white thermal control coatings where the secondary radiation may be up to 68% of the total energy absorbed. The simulator described is designed to be used in an existing vacuum chamber equipped with liquid nitrogen cold walls and a solar simulator. The simulator consists of two major components: a gimbaled model support system and an array of quartz infrared lamps. New power supply controls were developed to make independent changes in albedo and planet emitted radiation. During simulator calibration it was found that cold-wall reflections and thermal emissions from cold-wall penetrations and diffusion pump ports may cause serious errors. The errors induced by this energy are discussed and the steps necessary to minimize them described. Tests of the Langley planet emitted and albedo simulator show that it will satisfactorily simulate the secondary radiation on a 0.92-meter spherical body in near-earth orbits. Calculations indicate that other shapes can be accommodated without structural modifications. Problems of thermal lag on short orbits (about 36 min) can be corrected by use of newly developed controls.

*Aerospace Technologist - Mission Environmental Effects Section, Environmental Effects Branch, Space Technology Division.

[†]Aerospace Technologist - Models and Equipment Section, Equipment Engineering Branch, Facilities and Engineering Division.

[‡]Electrical Engineering Technician - Electrical Equipment Section, Equipment Engineering Branch, Facilities and Engineering Division.

SYMBOLS

A	area, meters ²
d	distance, m meter
E	irradiance, W/m ² watts per meters ²
K	geometry constant, per meters ²
L	radiance, watts per steradian - meters ²
M	length of lamp, meter
p	number of lamp arrays
q	number of lamps per array
R	distance between lamp axis and a unit area
W	lamp diameter, meter
α, β	coordinates on a unit sphere, degrees
α_s	solar absorptance, dimensionless
ϵ	low temperature, dimensionless emittance
γ	orbit angle, degrees
ϕ	defines extremities of lamps, degrees
ρ	inclination of an area element from tube axis, degrees
θ_c, λ	defines location of area element on a spherical satellite, degrees
ω	solid angle, steradian

Subscripts

a	albedo
e	earth

INTRODUCTION

Calculations indicate that planet albedo and thermal emission may account for as much as 68% of the total thermal energy absorbed by a white spherical satellite in low earth orbit. Simulation of the thermal balance of a spacecraft in the vicinity of a planet is incomplete without this large quantity of energy. If the spacecraft spins or moves relative to the planet and sun, a dynamic type of simulation is required to match the continually changing angles of incidence and intensities. For many spacecraft where temperature of the electronics and materials can be controlled within broad limits, theoretical analysis made in conjunction with simple thermal tests are adequate. When a flight experiment is dependent on an accurate knowledge of temperature or precisely controlled temperatures, however, accurate simulations are necessary to validate the analytical models. (See Ref. 1.) The present simulator was designed to validate the thermal analysis of advanced thermal control systems for orbiting telescopes and to test and calibrate temperature measuring systems for air-density experiments.

References 2, 3, and 4 describe design criteria for planet heat simulators for general spacecraft and model testing. In practice, however, planet heat simulation has been accomplished for specific missions by contouring arrays of lamps around a specific spacecraft (Ref. 5), or by applying thermal blankets as described in Reference 1. The present paper describes a hemispherical array of quartz lamps that is suitable for testing short-length cylindrical or spherical models. The control system described makes use of precomputed orbit parameters to generate analog signals for the test article motion, simulator motion, and lamp intensity.

This paper describes the analysis and engineering design of model support gimbals and a radiation simulator that closely simulates albedo and planet emitted energy to a space vehicle in any orbit. Included are descriptions of the effects of chamber anomalies on simulator performance and of the performance of the simulator for full-scale and model-scale orbit periods.

SECONDARY RADIATION

Basic Concepts

Secondary radiation consists of albedo and earth-emitted radiation. The albedo of a planet is the fraction of the total incident solar radiation that is reflected into space as a result of scattering in the atmosphere and reflection from clouds and the surface. Practically all of the reflected radiation from earth is in the wavelength range from 0.29 μm to 5 μm .

A portion of the incident solar radiation is absorbed as heat by the earth and its atmosphere, and then emitted as infrared radiation (wavelengths greater than 4 μm). This emission and the radiation flux resulting from albedo comprise the total

outgoing radiation. These radiations are uncollimated and bathe most of a spacecraft surface. (See Refs. 6 and 7.)

Environmental Simulation

When facilities for simulating the radiation environment on spacecraft became necessary, attention was first directed to techniques for simulating the sun. Radiation from other sources was assumed to be of secondary importance. This secondary radiation is normally assumed diffuse and is uncollimated. (See Fig. 1.) Although weaker, secondary sources irradiate larger surface areas than the sun and may provide more total energy per orbit. Table I compares the component parts of the thermal radiation absorbed by orbiting spheres at 185 and 1111 km altitudes. The table shows that earth emitted radiation absorbed

TABLE I.- COMPONENT PARTS OF THE THERMAL RADIATION ABSORBED BY A SPHERE AS A FUNCTION OF ORBIT ALTITUDE

(a) 185 km (100 n.mi.)

Component	Aluminized sphere $\alpha_s = 0.13$ $\epsilon = 0.04$	Black sphere $\alpha_s = 1.0$ $\epsilon = 1.0$	White sphere $\alpha_s = 0.22$ $\epsilon = 0.87$
Solar	0.67	0.55	0.31
Albedo	0.23	0.19	0.11
Earth emitted	0.10	0.26	0.58

(b) 1111 km (600 n.mi.)

Component	Aluminized sphere	Black sphere	White sphere
Solar	0.77	0.67	0.43
Albedo	0.16	0.14	0.09
Earth emitted	0.07	0.19	0.48

by an aluminum sphere is indeed small, 7 to 10%. Because of unacceptably high temperatures, aluminum surfaces are often coated with white thermal control coatings. The earth-emitted energy absorbed by a white sphere is between 48 and 58% and the total secondary radiation is between 57 and 69%. Figures 2 through 4 compare the effect of solar and solar-planet heating

on the quasi-steady-state temperatures at four points on non-conducting spheres. Even though the fraction of earth radiation absorbed by an aluminum sphere is small, Figure 2 shows that it has a significant effect on temperatures when in the earth's shadow. (See Fig. 2.) Figure 4 shows that secondary radiation has a significant effect on the temperatures of a white sphere at all orbit positions.

DESCRIPTION OF PLANET EMITTED AND ALBEDO RADIATION SIMULATOR

Design Assumptions

The following assumptions were used in development of the planet radiator. (See Ref. 6.): 1. The planet emission is diffuse. 2. The planet reflectance is isotropic and diffuse. 3. The planet's reflectance is independent of wavelength, that is, the spectral distribution of reflected radiation is equivalent to that of the incident radiation. In addition, an average albedo, independent of azimuth θ_c , is assumed. (See Fig. 5.) As a result, the irradiance at point $\theta_c = 0^\circ$ on a satellite will be too low and at $\theta_c = 180^\circ$ too high. Figure 6 shows that maximum error would occur at two spots when the orbit position ν is near 60° . Temperature errors would depend upon optical properties and spin rate. For a black nonspinning sphere ($\alpha_s/\epsilon = 1$), the quasi-steady-state temperature error would be several tenths of a degree Kelvin on the sun side and several degrees Kelvin on the dark side. Reference 8 shows, however, that the albedo is nonisotropic and that uncertainties in these variations are greater than differences shown in Figure 6. The present simulator was designed so that these anomalies could be simulated, if desired.

Simulator Concept

Quartz infrared lamps were chosen to simulate both the albedo and planet emitted radiation. Several lamp arrays, each with its own power supply, would surround most of the test article. The power supplies would be individually adjusted to simulate near planet and horizon radiation as shown in Figure 1. Figure 7 shows the arrangement of the lamps and other equipment for simulation of ecliptic and polar orbits. The satellite motion about the earth is simulated by rotating the lamp bank around a fixed model. One revolution of the lamp bank represents one orbit. Figure 8 correlates the planet radiator position with orbit position for an ecliptic orbit. At position A the planet radiator is at its brightest to simulate maximum albedo. As the satellite moves toward B the lamp power is reduced and the lamp bank rotated to simulate the change in intensity and direction of the albedo flux. As the satellite enters the shadow of the planet, the solar simulator shutter (Fig. 7(a)) is actuated and the lamp power held constant to simulate the planet emitted radiation.

Figure 7(b) shows that to simulate a polar orbit it is only necessary to change the axis of rotation of the lamp bank and dispense with the shutter.

Radiation Source Design Criteria

Representative earth-albedo irradiances to be simulated are shown for a spherical satellite in Figure 9. (See Ref. 9.) The power to each of five lamp arrays is independently controlled so that the sum of their heats approximate the desired irradiance distribution. The heat contribution of a single heat tube to an arbitrarily oriented unit area ΔA , as derived in the appendix, is

$$E_{\Delta A} = \frac{E}{2\pi^2 MR} \left[\phi_2 + \frac{\sin(2\phi_2 + \rho)}{2} - \phi_1 - \frac{\sin(2\phi_1 + \rho)}{2} \right] \quad (1)$$

or $E_{\Delta A} = E/2\pi^2 K_o$, where $K_o = 1/MR$ times the bracketed term and where E is the power supplied to one lamp.

Because the quartz lamps radiate primarily in the infrared, the lamp power to simulate the albedo radiation must be adjusted in proportion to the average α_s/ϵ ratio of the test article. The irradiance to be simulated at the model surface is then $E_e + \alpha_s/\epsilon E_a$, where E_e and E_a are the earth and albedo irradiances to be simulated.

For p circular arrays of q lamps per array, the irradiance at a model surface that is oriented at an angle λ with respect to the earth's surface is

$$\left(E_e + \frac{\alpha_s}{\epsilon} E_a \right) \lambda = \frac{1}{2\pi^2} \left[E_1(K_1 + K_2 \dots K_q)_1 + E_2(K_1 + K_2 \dots K_q)_2 + E_p(K_1 + K_2 \dots K_q)_p \right] \quad (2)$$

Because there are p unknown heater powers, E , the irradiance at p model surface locations must be specified. The irradiances at these locations are exactly satisfied. At intermediate locations, however, the irradiance may differ greatly from that desired. When the irradiances were outside desired limits, 5%, a new set of model surface locations, p , were chosen and the calculation repeated until the desired limits were attained.

Because the lamps are not point sources, the irradiance at model surfaces does not follow the distance square law. Calculations show that the average irradiances at model surface elements decreased to about 85% when moved from 40 cm to 60 cm

from the lamp arrays. The average temperatures, however, would be $1 - (0.85)^{1/4}$ or about 4% low. Thus encouraged, calculations were made for a cylinder with a length-to-diameter ratio of 2 for several orbit conditions. The results indicated that it was feasible to test short-length cylinders or portions of long cylinders with the same simulator geometry.

DESIGN AND CONSTRUCTION

The major components of the simulator are: a radiation source, model support system, and radiation and model motion controls.

Radiation Source

Figure 10 is a photograph showing the lamp bank arrangement. Each ring of lamps is controlled from a separate power supply. Sliprings are provided so that the lamp banks can continuously rotate about the test article. Additional sliprings are available for controlling groups of lamps in a given circle if necessary. The lamp bank is rotated by a dc pulse-controlled stepping motor designed for vacuum operation. Bearings and gears were cleaned and dry-film lubricated. Elliptical orbits are simulated by continuously varying the pulse rate to this motor. The lamp assembly is supported by a curved rail shown in Figure 10. This rail allows the lamp rotational axis to be changed from the vertical (an ecliptic orbit simulation) to the horizontal (a polar orbit simulation) as shown in Figure 7. Any orbit inclination can be simulated by intermediate positions.

Model Support System

The model support system consists of gimbals for pitch and yaw. The pitch gimbal supports a third axis for spinning the test article. The gimbal hubs are hollow to accommodate power and data wires. Pitch and yaw motors are commercially available 115-V 60-Hz single-phase hysteresis motors wired for $\pm 180^\circ$ gimbal rotation. These motors, when cleaned and relubricated with a dry-film lubricant, are operable in a vacuum at temperatures as low as 77 K.

Figure 11 is a photograph showing the spin axis drive supporting a balloon model. This spin axis assembly replaces the radiometer support shown in Fig. 10. This spin motor is a dc pulse-controlled stepping motor that was specially designed for vacuum operation. The bearings and gears were also dry-film lubricated. The 18-channel slipring assembly also shown in Figure 10 employs advanced technology brush materials for low noise operation (less than 0.025 MV peak to peak at 1.4 ma and 0.005 MV peak to peak at 0.5 ma in a vacuum at temperatures between 120 and 400 K.

Control System

The control system for the planet radiation simulator is divided into three major groups: model position control, orbit motor controls, and lamp bank power supply system.

The model position and spin motors are described in the previous section. Yaw and pitch are indicated by precision potentiometers, cleaned and lubricated for vacuum use, and read on a digital voltmeter. The system is accurate to about $\pm 1^\circ$. Model spin rate is determined by measuring the pulse rate from the spin axis motor controller.

The orbit position (lamp bank position) is controlled by the pulse motor described in the previous section. The orbit position indicator is slaved to the lamp bank rotation by a servosystem with an accuracy of about $\pm 1^\circ$.

The power to each circular lamp array is independently controlled by predetermined power-position data. Figure 12 shows a block diagram of the feedback power control system. This features a Hall-effect power feedback and power measuring system and specially developed range and zero shift controls. Each power supply uses a voltage set point (power level) compared to a millivolt feedback signal from the Hall-effect device to determine the output power. The set point voltage is determined by the curve drawn on the data track cylinder shown in Figure 12. This curve is traced by a servo-driven pointer tied to a potentiometer. The data track cylinder, along with the orbit position indicator, is slaved to the rotation of the lamp bank.

Special range and zero shift controls have been developed to modify the set point data. The zero shift control allows the zero (power) set point to be moved over the entire span without changing the shape of the curves. The range controls independently change the effective slope of the curves from 30 W/cm to 140 W/cm with a maximum output of 3500 watts. The output power, detected by the Hall-effect transducer, is displayed in watts.

These controls enable the experimenter to introduce step changes in either the albedo (range) or planet emitted heat (zero shift) at any time during a test. In addition, it will allow simulations for several different orbit altitudes to be made without reconstructing the set point curves. In essence, the radiation controls for the planet radiator have been developed into an analog computer.

PLANET RADIATOR PERFORMANCE TESTS

The purpose of these tests was to evaluate the performance of the planet radiator. All tests were conducted at the Langley Research Center in the 244-cm-diameter by 457-cm-long vacuum chamber at a pressure less than 1×10^{-5} torr. Figure 10 shows a photograph of the radiation simulator and test instrumentation in the chamber. Figure 13 shows the arrangement of the apparatus. A survey of the chamber radiation was made to determine background effects. To isolate the effects of background radiation,

the tests were made without rotating the simulator. A servo transmitter driven by a stepping motor was used to simulate rotation of the lamp banks. Thus the power levels on each lamp bank were controlled as though the simulator were rotating.

INSTRUMENTATION

The irradiance that would occur at the surface of a 0.92-meter-diameter sphere was measured with 15 miniature LRC radiometers (Ref. 10) spaced 10° apart (Fig. 10). Measurements made under transient irradiances were also detected with blackened differential thermopiles. Measurements for both devices correspond within $\pm 5\%$.

Chamber Background Radiation

Reference 11 presents analytical results showing that the effect of penetrations and other anomalies in vacuum chamber cold walls can have serious effects on spacecraft temperatures. As a result, chamber background radiation, planet radiator off, was measured as viewed from the surface of a 0.92-meter-diameter sphere. The increase in radiation level for $\lambda > 90^\circ$ (Fig. 14) is because a front liquid nitrogen liner was not available. The large radiations from the left sidewall are from openings leading to the diffusion pumps. Although these radiations are small, relative to solar radiation, they can have serious effects on the temperatures of spacecraft surfaces that normally view deep space. For example, an energy of 2 W/m^2 such as from a blackened liquid nitrogen wall will result in a spacecraft temperature of about 78 K, while a 38-watt-per-square-meter energy as shown in Figure 14 will result in a temperature of about 160 K. A liquid nitrogen liner is being installed at the front of the chamber and a new high absorbent liner, $\alpha_s = 0.99$, at the rear. Also liquid nitrogen liners are being installed to shield the radiation from diffusion pump openings and covers installed over numerous cold-wall penetrations.

Test Procedure

The planet radiation survey equipment was oriented toward the bottom of the chamber because the background radiation was lowest there, as shown in Figure 14.

Quasi-steady-state radiation measurements were taken for each lamp bank as a function of power levels to show the energy profile on a 0.92-m-diameter model. These and calculated results were used to determine lamp power levels that correspond to the energy distribution on a black satellite in a circular orbit of 185 km. Long orbit tests, approximated by quasi-steady-state conditions, and short orbit tests, scale orbit periods of about 36 min, were made to check the overall performance of the radiator.

RESULTS AND DISCUSSIONS

Initial power settings were determined from calculations discussed in Radiation Source Design Criteria. These calculations were inadequate because they did not include the effects of structural heating, reflections, or chamber background radiation. Additional tests were made to determine radiation distribution of each lamp circle on a 0.92-m-diameter sphere. Figure 15 presents results of these tests. By using superpositioning techniques, more accurate settings were possible and the technicians found it easy to obtain the optimum radiation distribution by iteration. Figure 16 presents a comparison of these results with desired distribution for a black sphere at 185 km. Note that the high measured radiation at $\lambda = 140^\circ$ is partly due to the chamber background.

The tests also have shown that background radiation should be known and if excessive, corrected. The performance tests show that the Langley albedo and planet emitter radiation simulator will simulate the secondary heat on an orbiting body in a satisfactory manner.

The above tests were representative of full-scale orbits of greater than 120 minutes. Thermally scaled models often require shorter orbital periods. Tests were made for a 36-minute orbit to determine the radiator performance under dynamic rather than essentially static conditions. Figure 17 presents a comparison of the irradiances at two locations on a sphere for a 36-minute orbit. The power levels indicated by the long time orbits were found to be too low to use on shorter orbital periods. Also, the data for $\lambda = 10^\circ$ show a thermal lag of 3° to 4° . Due to a greater effect of structural heating during the long orbit tests, the power supply settings should be checked under actual orbital time periods. The differences shown between the long-term and short-term orbit tests are easy to compensate for by use of the zero shift and range controls in the case of differences in minimum and maximum power, and by shifting the graph on the control cylinder in the case of the thermal lag.

CONCLUSIONS

Results from the development of a planet heat simulator indicate the following conclusions: (1) The Langley planet emitted and albedo simulator will satisfactorily simulate the secondary radiation on a 0.92-meter spherical body in near-earth orbits. Calculations indicate that other shapes can be accommodated without structural modifications. Problems of thermal lag on short orbits (about 36 min) can be corrected by use of newly developed controls. (2) Measurements of chamber background radiation indicate that the radiation from ports and openings could have significant temperature effects on test articles.

REFERENCES

1. Caruso, P., Jr.; Dan, C., Jr.; Young, E.; and Mengers, D.: The Orbiting Astronomical Observatory Program. NASA TN D-5794, Aug. 1970.
2. Kelley, L. R.: The Design of an Albedo and Planetary Emission Simulator. Paper presented at International Symposium on Solar Radiation Simulation (Los Angeles, Calif.) Jan. 1965.
3. Fitz, C. Dudley: Effectiveness of Albedo and Earth Radiation Simulation Paper presented at International Symposium on Solar Radiation Simulation (Los Angeles, Calif.) Jan. 1965.
4. Clark, L. G.; and Laband, K. A.: Orbital Station Temperature Control. Astronautics, Vol. 7, No. 9 (Sept. 1962), 40-41.
5. Bachtel, F. D.; and Loose, J. D.: Design and Control of an Orbital Heating Simulator. Preprint 71-432, Am. Inst. Aeron and Astronaut, Apr. 1971.
6. Anon.: Earth Albedo and Emitted Radiation. NASA SP-8067, 1971.
7. Katzoff, S.: The Electromagnetic-Radiation Environment of a Satellite, Part I. Range of Thermal to X-Radiation. NASA TN D-1360, Sept. 1962.
8. Raschke, Ehrhard: The Radiation Balance of the Earth-Atmosphere System From Radiation Measurements of the Nimbus II Meteorological Satellite. NASA TN D-4589, July 1968.
9. Stevenson, J. A.; and Grafton, J. C.: Radiation Heat Transfer Analysis for Space Vehicles. ASD Tech. Rep. 61-119, Part I, U.S. Air Force, Dec. 1961.
10. Sweet, George E.; and Miller, Howard B.: A Radiometer for use in Thermal Studies of Spacecraft. NASA TN D-4925, 1968.
11. Rosenberg, Morton Jacob: Theoretical Analysis as Applied to Space Chamber Environmental Anomalies. Proceedings of the Institute of Environmental Sciences, Chicago, Illinois, 1965.

APPENDIX

ENERGY RADIATED FROM A TUBULAR LAMP HEATER TO A SMALL FLAT PLATE

The total hemispherical energy, ΔE , radiated from a small black area on a lamp filament is

$$\Delta E = \int_0^{\pi/2} \int_0^{2\pi} L \sin \alpha \, d\alpha \, d\beta$$

Assuming a diffuse emission $L = L_n \cos \theta$. The angles α and β describe an area element on a unit hemisphere as shown in Figure 18.

Integrating

$$\Delta E = \pi L_n$$

the radiance, L_n , normal to the emitting surface is then

$$L_n = \frac{\Delta E}{\pi}$$

The radiated power ΔE can also be determined from filament dimensions and total power for a tubular filament of length M , diameter W , and total energy emission E , the energy emitted per unit heater area

$$\Delta E = \frac{E}{M} \frac{1}{\pi W}$$

combining, the irradiance becomes

$$L_n = \frac{E}{\pi^2 MW} \quad (A-1)$$

The energy incident to a unit receiving area, ΔA , located at a distance R from the heating tube and inclined at an angle ρ with respect to the tube axis as shown in Figure 19, is

$$dE_{\Delta A} = L_n W \, dm \, \omega \cos \phi \quad (A-2)$$

where ω , the solid angle subtended by ΔA is,

$$\omega = \frac{\cos(\phi + \rho)}{d^2} (\Delta A = 1) \quad (A-3)$$

The distance d and m expressed in terms of angles referenced to a tube normal passing through ΔA are

$$d = \frac{R}{\cos \phi}$$

$$m = R \tan \phi$$

$$dm = R \sec^2 \phi \, d\phi$$

Substituting the above and Equations (A-1) and (A-3) into Equation (A-2), the energy incident at ΔA is

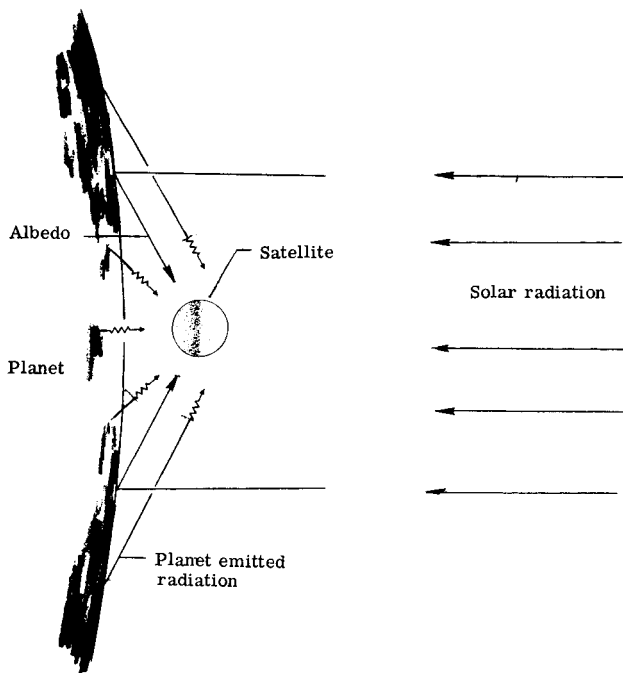
$$dE_{\Delta A} = \frac{E}{2\pi MR} \cos \phi \cos(\phi + \rho) \, d\phi$$

and

$$E_{\Delta A} = \frac{E}{2\pi MR} \int_{\phi_1}^{\phi_2} (\cos^2 \phi \cos \rho + \frac{1}{2} \sin 2\phi \sin \rho) \, d\phi$$

performing the integration

$$E_{\Delta A} = \frac{E}{2\pi MR} \left[\phi_2 + \frac{\sin(2\phi_2 + \rho)}{2} - \phi_1 - \frac{\sin(2\phi_1 + \rho)}{2} \right] \quad (A-4)$$



(a) Orbital heat sources.

Fig. 1 - Thermal radiation on spacecraft.

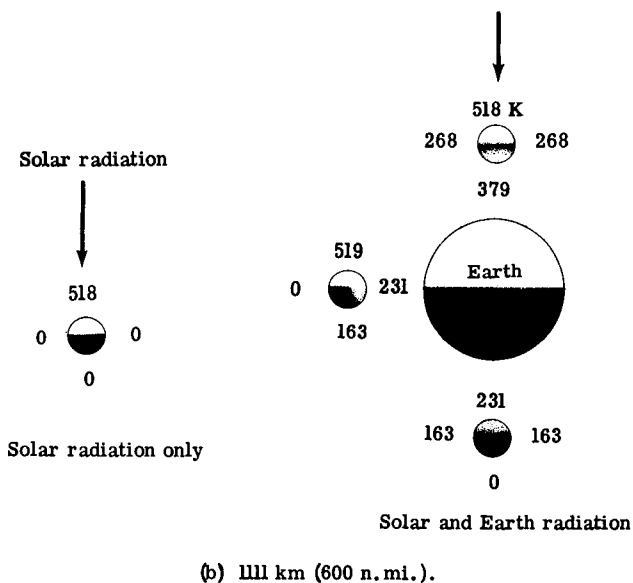
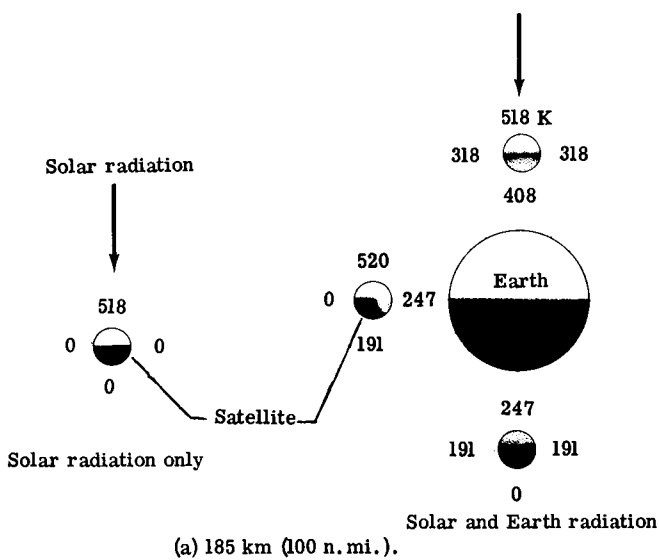
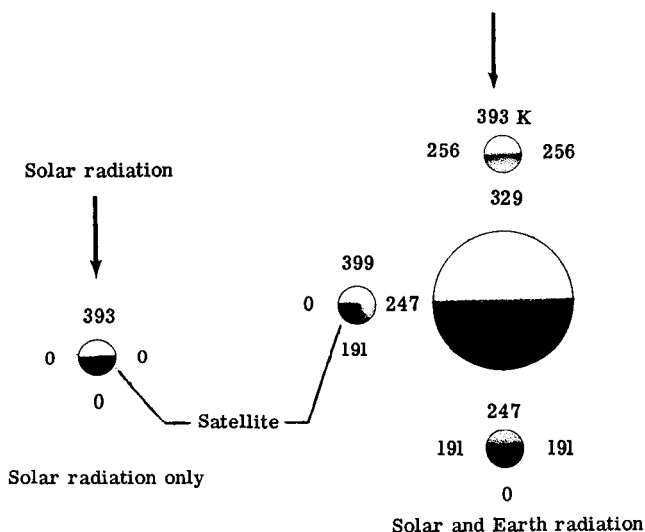
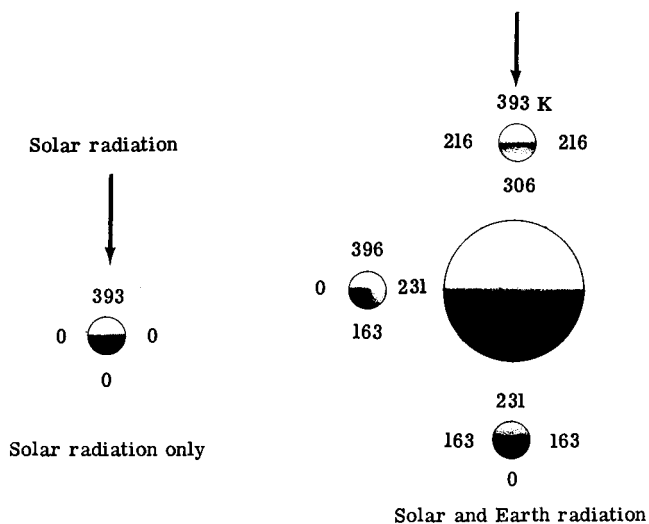


Fig. 2 - Comparison of solar and solar-earth heated aluminum spheres ($\alpha_s = 0.13$, $\epsilon = 0.04$).



(a) 185 km (100 n.mi.).



(b) 1111 km (600 n.mi.).

Fig. 3 - Comparison of solar and solar-earth heated black spheres ($\alpha_s = 1$, $\epsilon = 1$).

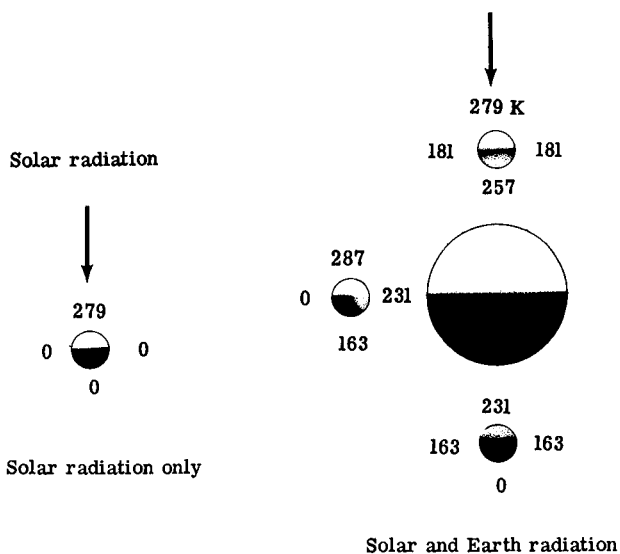
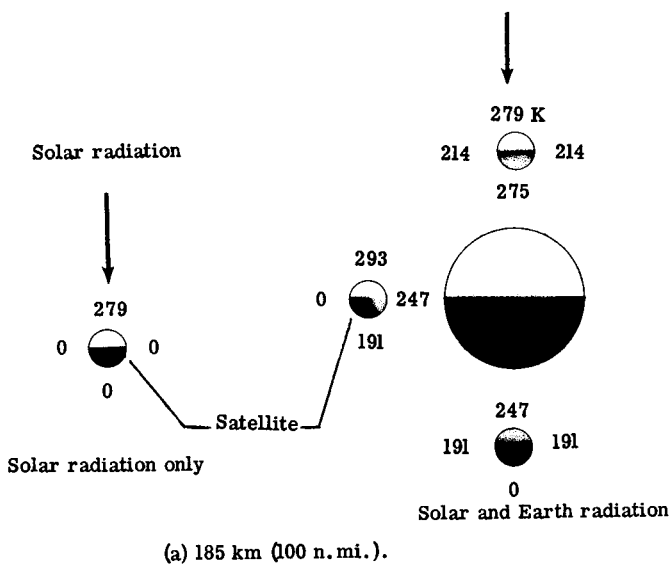


Fig. 4 - Comparison of solar and solar-earth heated white spheres ($\alpha_s = 0.22$, $\epsilon = 0.87$).

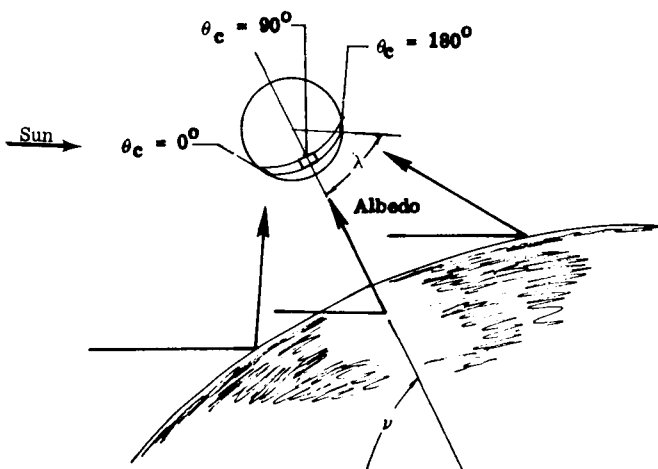


Fig. 5 - Notation used to show dependency of albedo intensity at a unit area flat plate on location as defined by θ_c and λ .

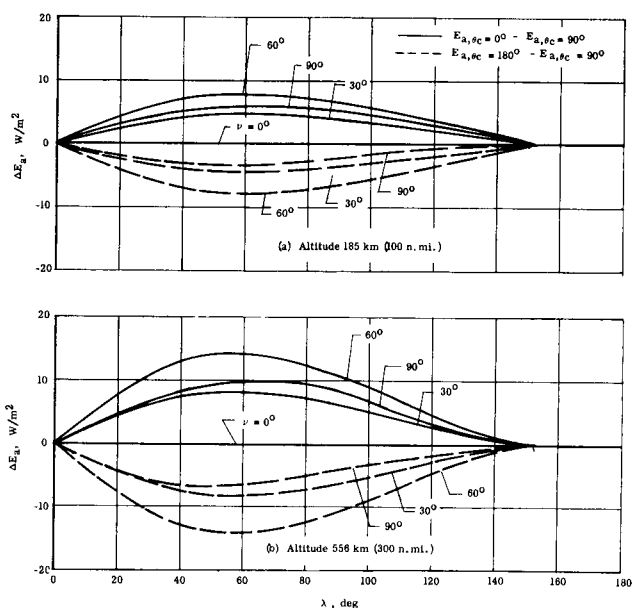


Fig. 6 - Error resulting from the assumption of an average albedo ($\theta_c = 90^\circ$) as a function of orbit position and location on a satellite.

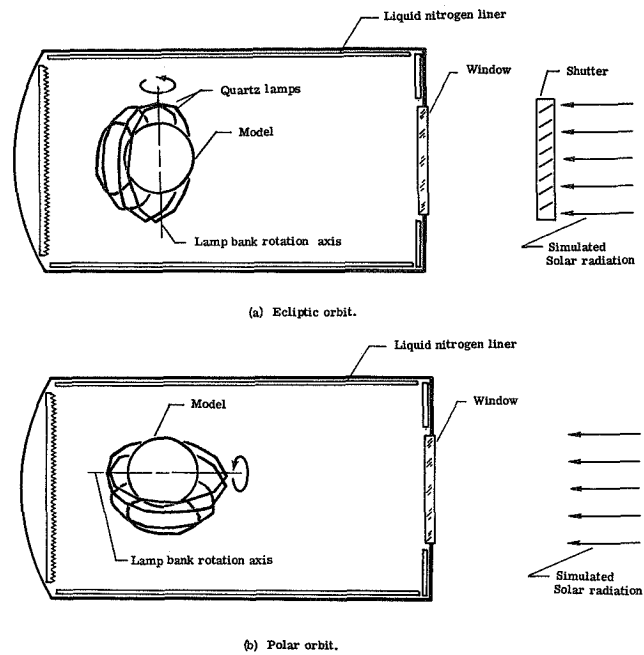


Fig. 7 - Concept of simulator showing ecliptic and polar orbits.

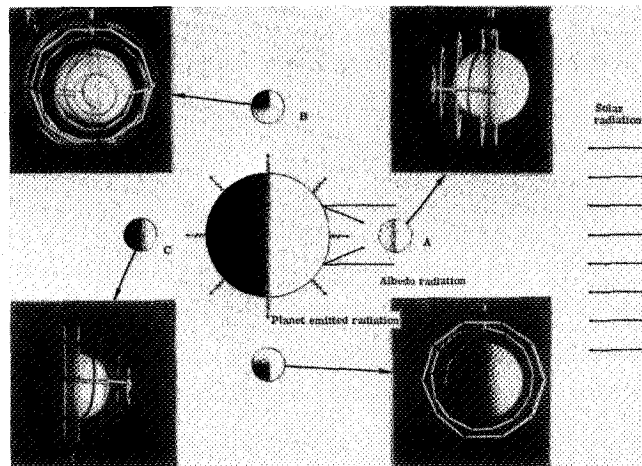


Fig. 8 - Correlation of orbital with simulated planet heating.

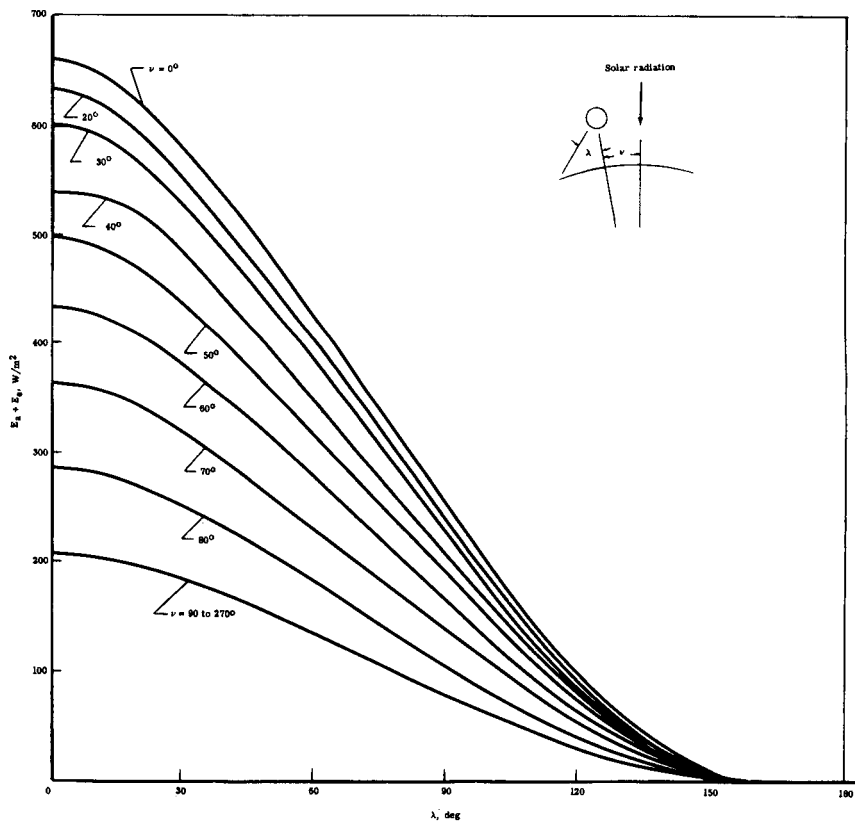


Fig. 9 - Earth-albedo irradiance for a spherical satellite at 185 km (ref. 9).

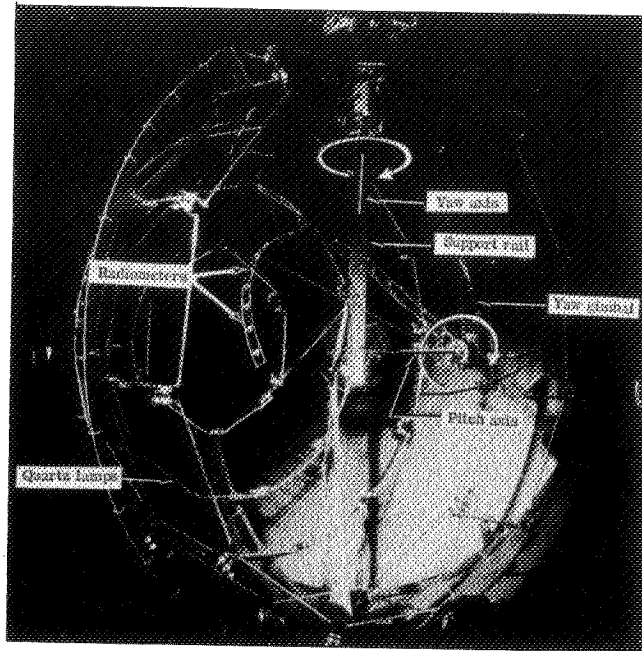


Fig. 10 - Radiation simulator in test chamber for performance test.

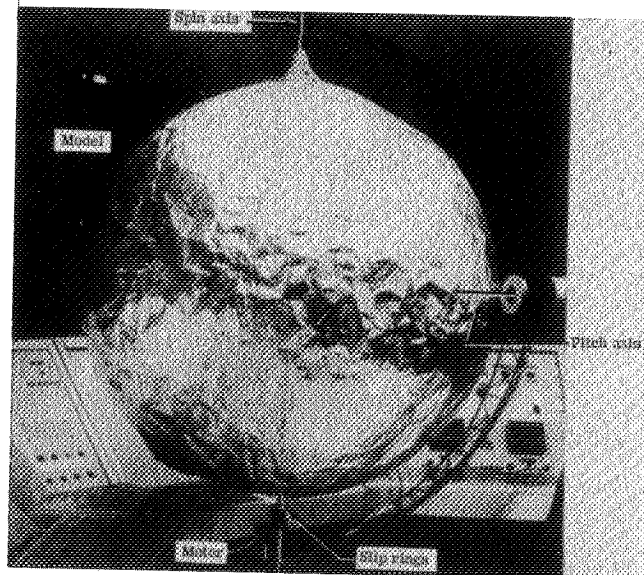


Fig. 11 - Spin axis gimbal supporting balloon model.

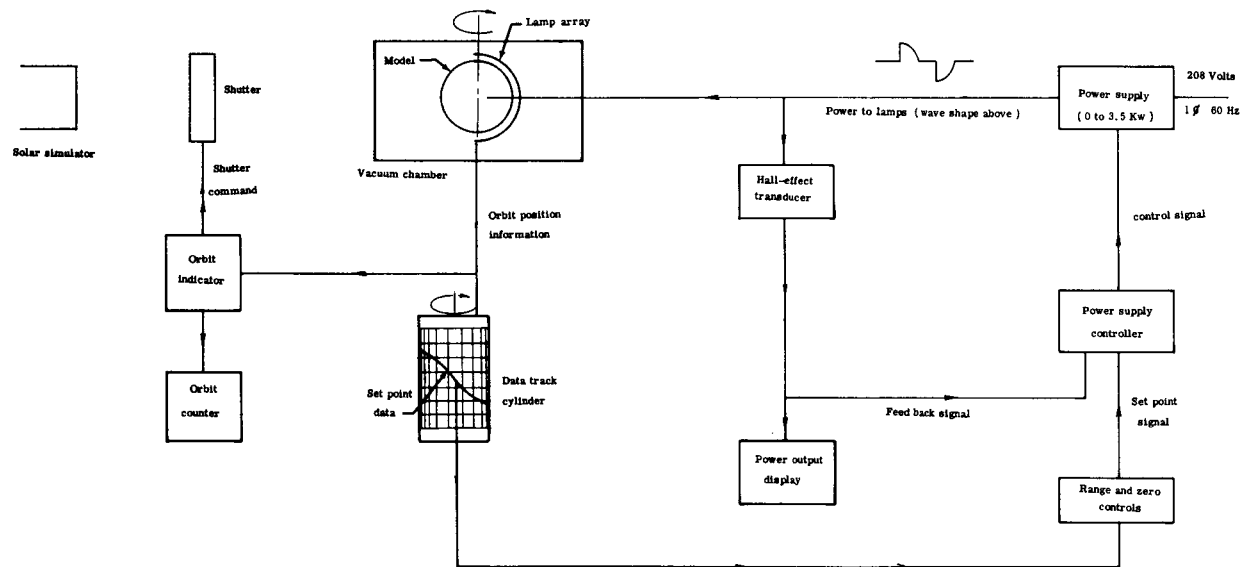


Fig. 12 - Lamp power system block diagram.

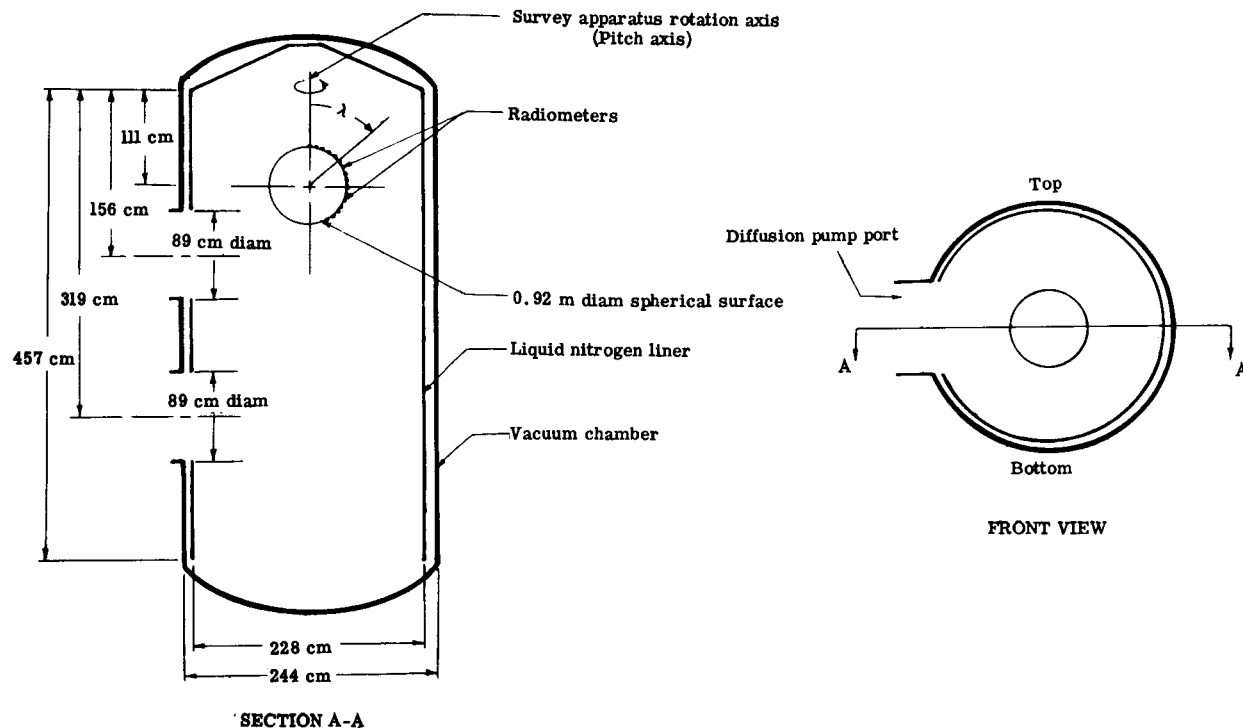


Fig. 13 - Arrangement of apparatus in vacuum chamber.

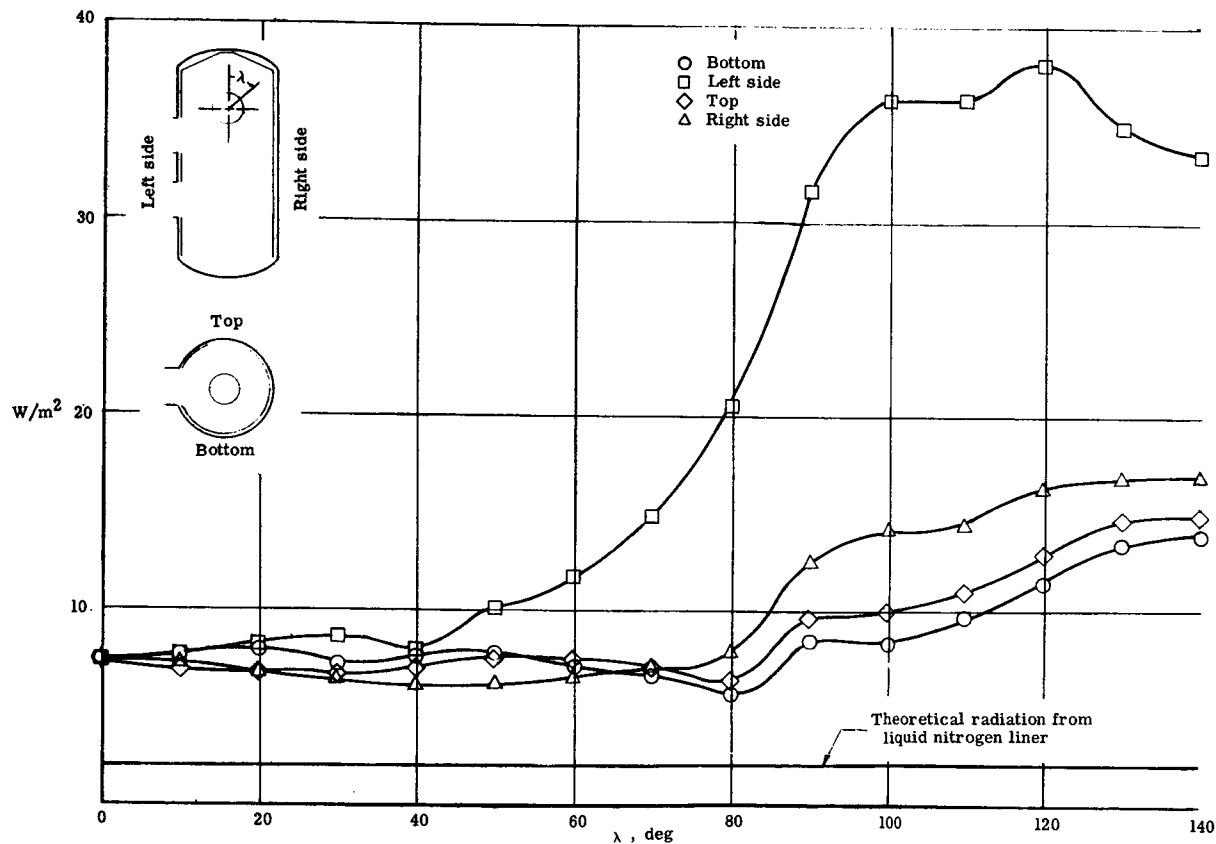


Fig. 14 — Background radiation in the 8 ft by 15 ft vacuum chamber.

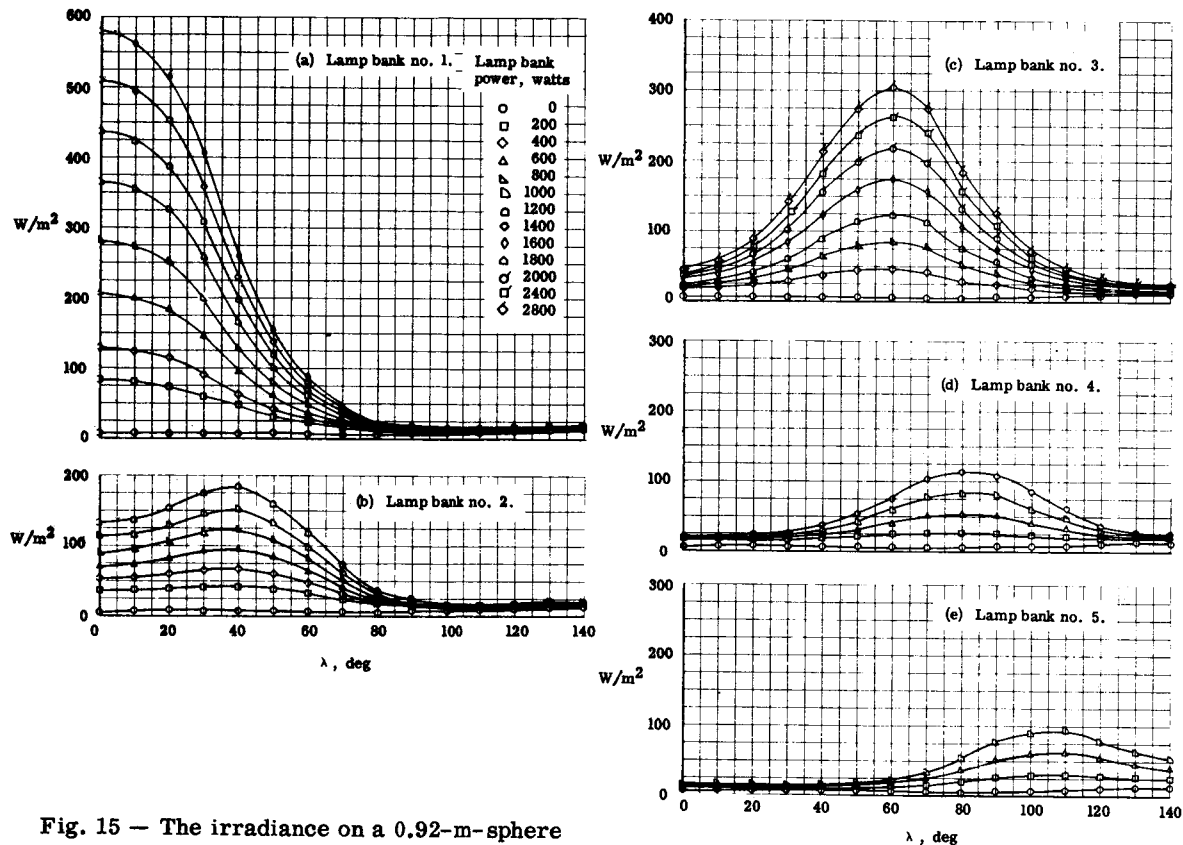


Fig. 15 — The irradiance on a 0.92-m-sphere produced by each lamp bank.

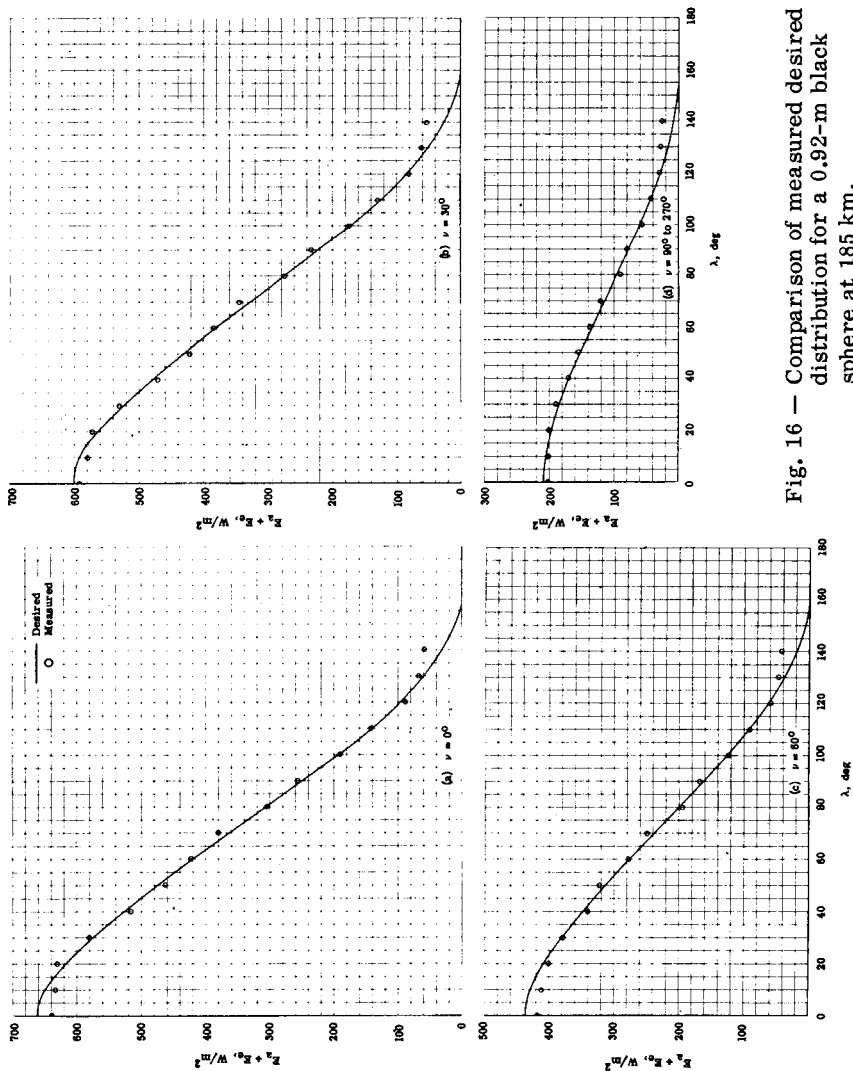


Fig. 16 — Comparison of measured desired distribution for a 0.92-m black sphere at 185 km.

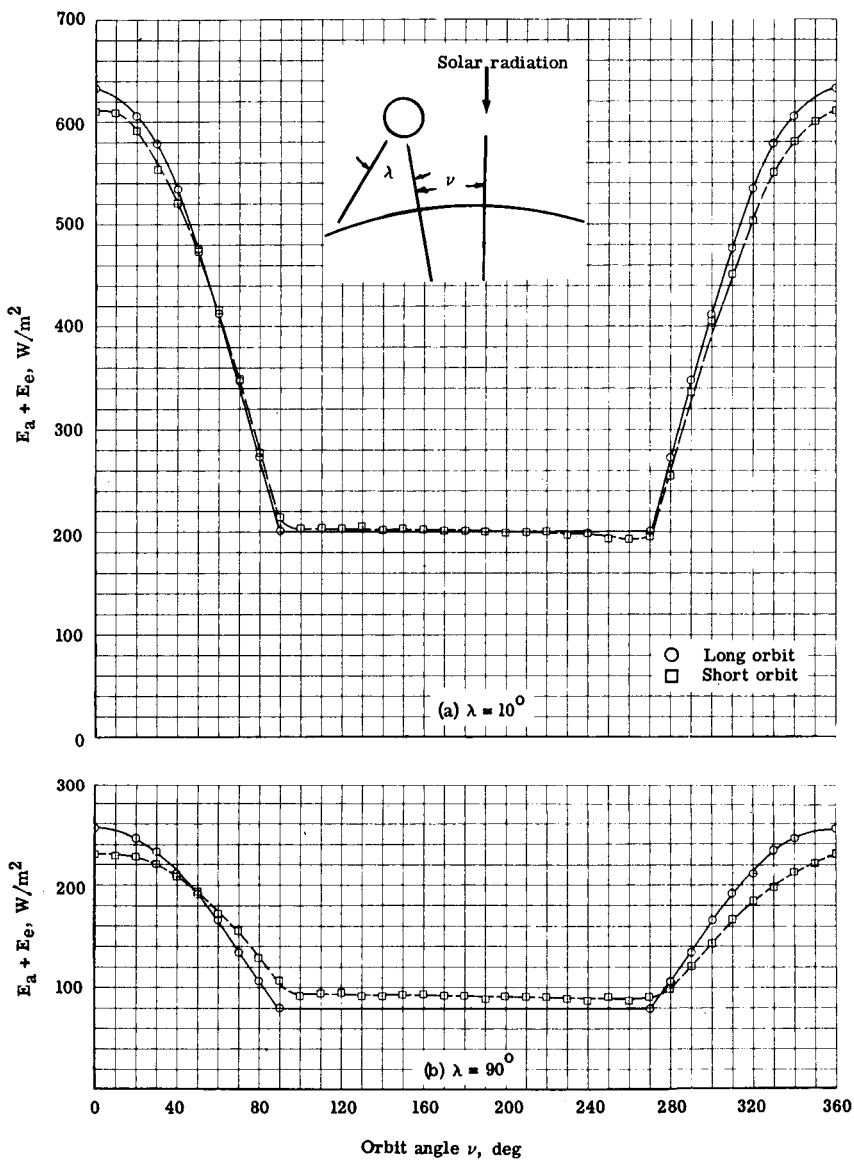


Fig. 17 - Comparison of measured and calculated with desired distribution for a 370-km altitude.

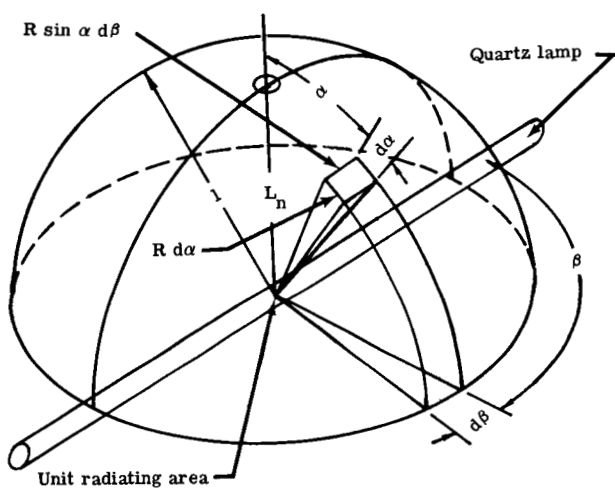


Fig. 18 - Area element of a unit hemisphere.

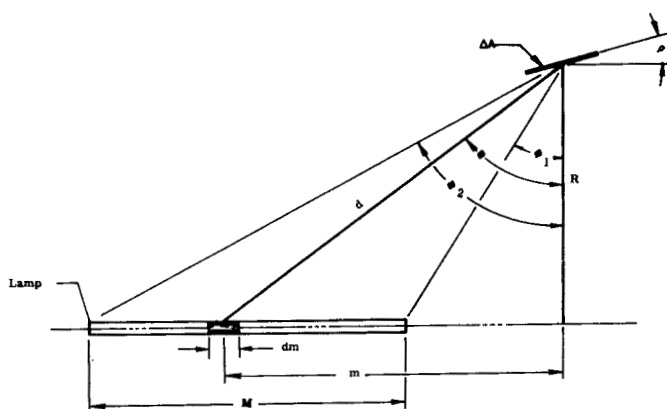


Fig. 19 - Notation used to describe the geometry between a unit area and a lamp segment.

SPACECRAFT THERMAL VACUUM TESTING

B. F. Elam and L. D. Lancaster, *Martin Marietta Corp., Denver, Colorado*

ABSTRACT

An approach for developing a general thermal vacuum test program philosophy is discussed. Guidelines are established that will assist the project engineer in relating the risk associated with flying any spacecraft to its general thermal vacuum test program. Computerized techniques can be used to help ascertain these guidelines. These guidelines relate the risk to the level of test (component, subsystem, etc), as well as to the type of test (development, qualification, etc). The interrelationship between the test program and the analytical effort is also discussed. The Skylab Apollo Telescope Mount (ATM) general thermal vacuum test program, including test schedules, instrumentation, and test results are also shown.

INTRODUCTION

The human risk associated with a manned spacecraft and the economic risk of any spacecraft are of paramount importance to the aerospace project engineer, much more so than for ground operated hardware. These risks must be minimized to as low a level as practical because of the sizeable amount of resources invested, both in terms of lives for manned spacecraft and in terms of dollars for all spacecraft. The amount of resources at stake for each mission at this point in the space program tends to become greater as space technology is expanded. The Skylab program exemplifies this point, where both astronaut lives and significant costs are at stake. Therefore, return on ground test program investments need to be maximized to the fullest extent possible. Assuring maximum return is the responsibility of the project engineer; thus, the question that he must answer is how to get the most from the project dollar and yet maintain an acceptable level of risk.

Design of a thermal control system is a critical aspect of any spacecraft development, demanding the utmost from analytical techniques as well as from the thermal vacuum test program. The overall thermal design depends on the accurate

prediction of flight temperatures as well as the distribution and flow of thermal energy during the thermally critical phases of the spacecraft mission, by means of both analysis and test. Any spacecraft is subjected to the severe, and sometimes extreme, thermal environment of space. There are many uncertainties associated with the definition of the space environment, as well as with the heat transfer parameters, approximations in the analytical model, and inaccuracies due to the computational techniques. These uncertainties, along with others, contribute to the overall risk of any space vehicle. In many situations, the only way in which these uncertainties can be minimized is through thermal vacuum testing.

The dollars reserved for the overall thermal design must be some function of the risk involved with flying the spacecraft. A well balanced analytical and test program must be outlined early in the conceptual phase of the project to minimize the risk and the monetary expenditures. It is the purpose of this paper to provide some insight to the overall thermal design philosophy with emphasis being placed on an approach for developing a thermal vacuum test program. This approach can be computerized to simplify its use.

DESIGN CRITERIA FOR THERMAL VACUUM TEST PROGRAM DEFINITION

Space vehicle failures can be diminished by subjecting the components, subsystems, systems, or total spacecraft to environmental conditions that are expected to be encountered during the mission. Figure 1 illustrates failures due to environmental testing of 64 spacecraft as summarized in reference 1. The largest percentage of failures for both the prototype and flight vehicles were due to temperature and thermal vacuum conditions, thus pointing out the importance of thermal testing. Most spacecraft projects have some type of thermal vacuum test program; the degree of testing varies from project to project. The quantity and quality of the test program, and the resulting cost, should be related to the risk involved. A typical relationship between the risk and the test costs is shown in Figure 2. With additional experience gained by flying more spacecraft, and with an increase in technological developments, the curve should inflect toward the origin. However, each new spacecraft becomes more advanced and in many cases physically larger, demanding more from the thermal vacuum test program. This has a tendency to offset, to a certain extent, the savings accruing from an increase in knowledge. It is the primary objective of this paper to provide guidelines by which a project engineer can assess the risk associated with successfully flying a spacecraft to its general thermal vacuum test program. The project engineer can then determine the test costs relating it to the risk involved.

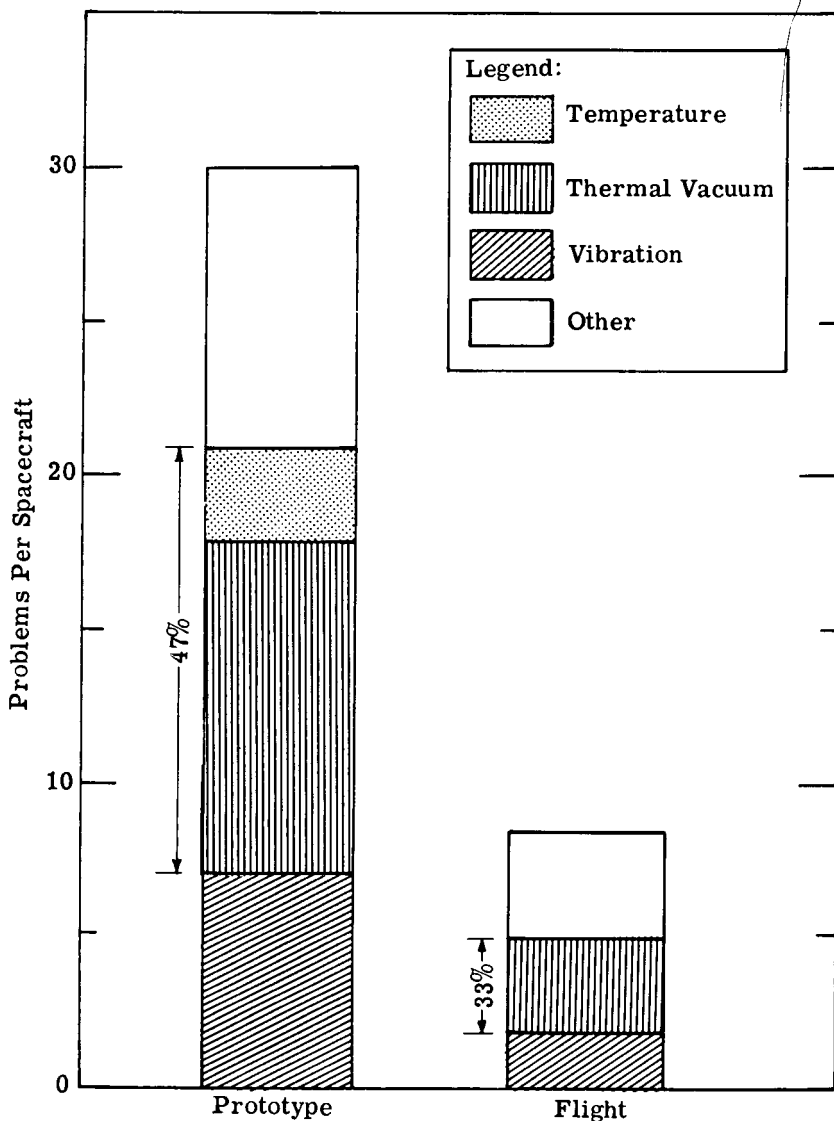


Fig. 1--Spacecraft test problems by environment

Before a specific spacecraft thermal vacuum test program philosophy can be defined, numerous design criteria must be weighed against the risk associated with the mission. These criteria will vary from spacecraft to spacecraft; definition of these requires careful consideration and consultation

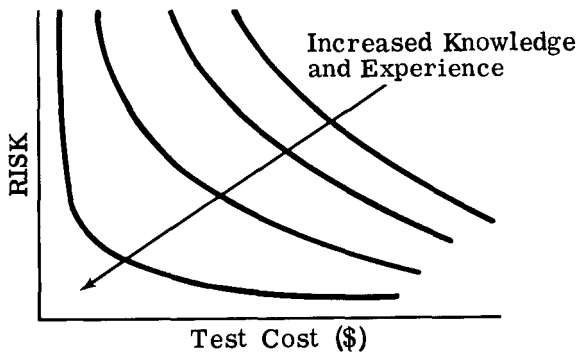


Fig. 2--Risk versus test costs

from all the members of the thermal design team. Table 1 lists some of the design criteria that should be considered, all of which are common to most spacecraft. A complete list will have to be tailored to the particular spacecraft program of interest.

Table 1. Risk criteria matrix

Criteria	Risk Number										Weighting Factor	Score
	1	2	3	4	5	6	7	8	9	10		
Manned/Unmanned			■								1.0	3.0
Mission Objectives									■		0.9	8.1
Environments					■						0.9	4.5
Active/Passive System							■				0.8	5.6
Redundancy									■		0.8	6.4
Thermal Design Complexity						■					0.7	4.2
Required Thermal Tolerances								■			0.6	4.8
Design Constraints							■				0.6	4.2
Analytical Complexity									■		0.5	4.5
Schedule Requirements		■									0.5	1.0
Spacecraft Size									■		0.4	3.6
Off-the-Shelf Hardware				■							0.4	1.6
Instrumentation			■								0.2	0.6
Average Weighted Score												6.3

Table 1 also is a working matrix for associating the criteria to the risk involved. A risk number of 1 to 10 (the range of which is arbitrary) is assigned for each applicable criterion, with 1 being the lowest and 10 being the highest

risk number. The assigned risk number should be based on the importance the criterion has to the total risk of the resources invested. A weighting factor can be applied to each of the criterion, the value of which reflects the significance of one criterion relative to all the other criteria. For this example, the weighting factor is normalized to 1.0 for the maximum value, with a minimum value of 0.1 and increments of 0.1. Weighting factors can be determined in numerous ways by general agreement among the thermal engineers or by employing mathematical techniques, such as regression analysis. Application of mathematical techniques would require compiling pertinent information from previous spacecraft thermal vacuum test experience. The criteria score is obtained by multiplying the risk number by the weighting factor.

A risk criteria matrix can be generated at the component, subsystem, system, or spacecraft level. For instance, to determine the risk associated with a particular subsystem, a risk criteria matrix for each component within that subsystem would be generated. The resulting average weighted score would be an indication of the risk involved with that subsystem. The task of recording and comparing the risk criteria matrices can be accomplished by utilizing digital computers.

Since the first spacecraft were unmanned and relatively inexpensive, the economic risks taken were small in proportion to contemporary unmanned spacecraft. An additional element of risk has been added to the contemporary space program with the advent of manned space vehicles. Figure 3 represents an approximate spacecraft risk distribution for today's space program. It can be seen that the distribution

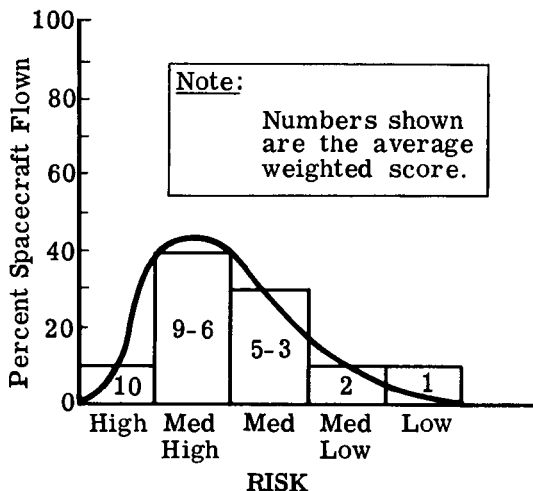


Fig. 3--Spacecraft risk distribution

is skewed to the left. With the development of advanced spacecraft, such as the shuttle vehicle, and as more experience is gained with each additional spacecraft flown, the distribution curve should shift to the right.

It is desirable to relate the weighted score to the risk. Since it is estimated that 10 percent of the spacecraft flown have a high risk, the corresponding weighted score is 10. Figure 3 illustrates the relationship of the weighted scores to the risk. The risk designation for the various levels will aid in the decision-making process of defining a general thermal vacuum test program philosophy.

THERMAL VACUUM TEST PROGRAM PHILOSOPHY

Since it is evident that the risks discussed in the preceding section can be diminished by thermal vacuum testing, it is mandatory to establish the best possible test program as early as possible. To accomplish this goal, an overall thermal design philosophy must be developed that obtains the maximum return on test cost investment and defines the test/analytical interrelationship. The thermal design philosophy should assure accurate predictions of temperatures and thermal energy distributions through the critical phases of the mission. These accurate predictions are obtained through the proper mixing of the two ingredients that support each other--analytical techniques and testing. Thus, the thermal vacuum test program philosophy is a vital part that makes up the overall thermal design philosophy.

General Test Program Approach

The thermal vacuum test program philosophy should be based on a failure pattern concept. As shown in Figure 4 (reference 1), experience suggests that spacecraft failures fall into three phases: infant mortalities, random failures, and wearout failures. The objective of thermal vacuum testing should be to minimize the failures under simulated flight conditions until some random rate is reached, as well as to verify the numerical techniques used in the analysis. In accomplishing this end, it is imperative in planning and executing any thermal vacuum test that all of the boundary conditions to be simulated are clearly defined and assurance made that the facility data acquisition system will record the actual boundary conditions. If these boundary conditions are not clearly defined or accurately recorded, the particular test will not provide meaningful data.

A general thermal vacuum test program could consist of up to three types of thermal tests:

Development Tests--This type of test is accomplished to completely determine the feasibility of the thermal design, verify math model techniques, or determine special heat transfer parameters (contact resistance, thermal conductivity, etc).

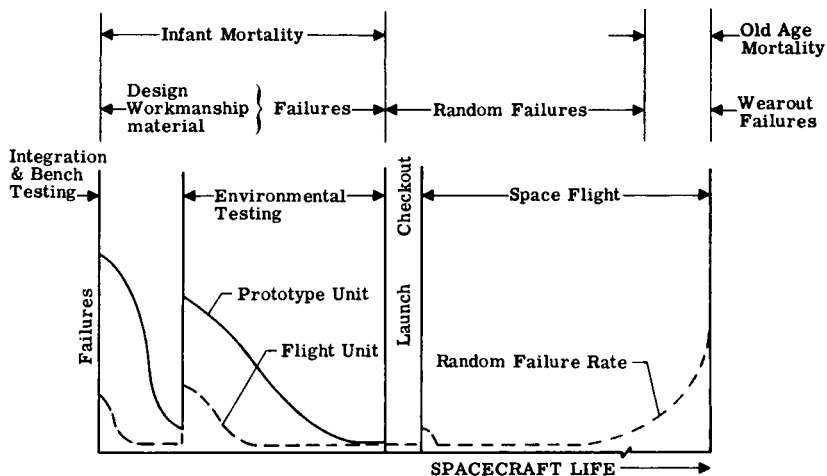


Fig. 4--Failure pattern

Qualification Tests--This type of test is to demonstrate the thermal design adequacy under simulated flight conditions that represent the most severe anticipated; these are usually assumed to be 3σ values. These test data are also applicable to verification of the analytical model techniques.

Acceptance Tests--This type of test is to verify that no defects in material or workmanship exist in the flight hardware. These tests are conducted at more nominal simulated flight conditions, sometimes defined as 2σ values (reference 1).

The three types of test defined above can be accomplished at various levels--

- 1) Component level,
- 2) Subsystem level,
- 3) System level,
- 4) Total spacecraft level.

Thermal design test data should be obtained at the lowest level of testing deemed possible for the particular spacecraft of interest, depending on the state of the art of the design. A model that might be used to relate the risk, level of test, and the type of test is shown in Figure 5. Some of the levels shown in Figure 5 can be eliminated from the test program by associating them with both the type of test and the risk involved.

It should be remembered that an approach for assessing the risk involved in flying a particular spacecraft was presented in the previous section. Figure 5 presents how the risk determined by this approach could be related to the type and level of testing by the project engineer.

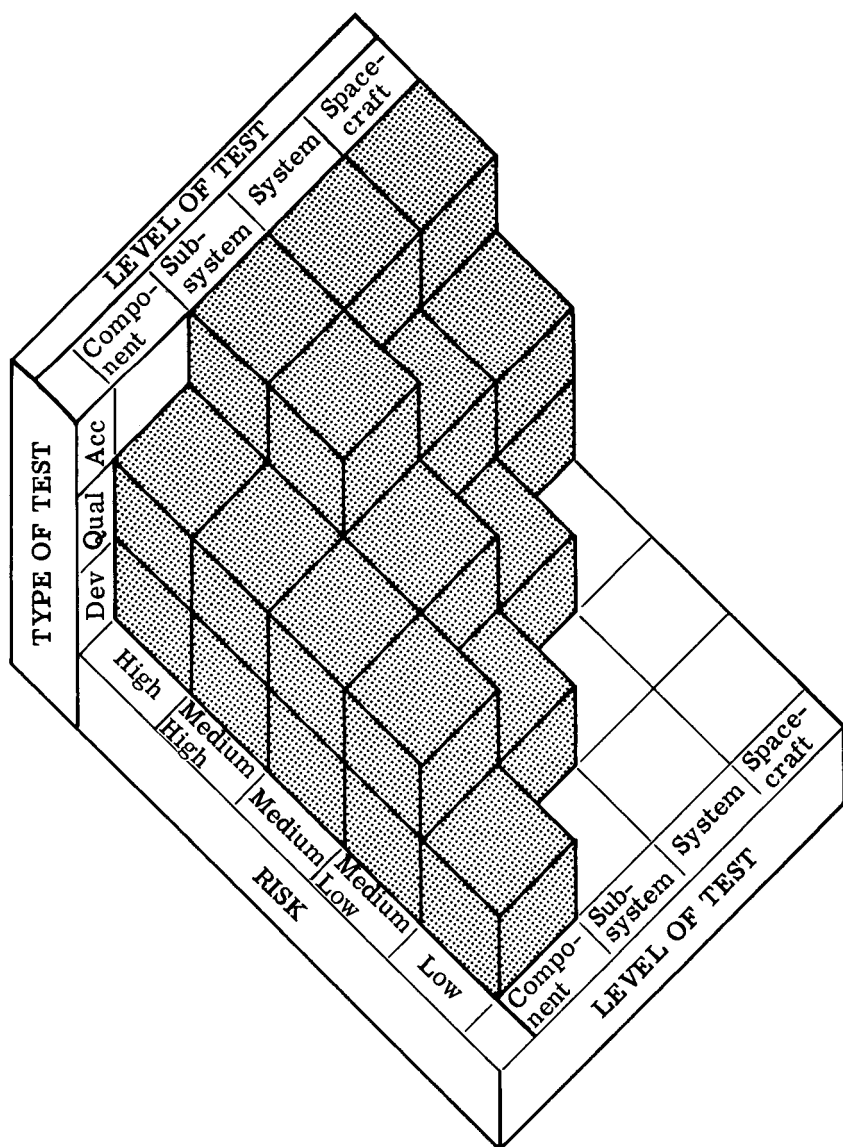


Fig. 5--Risk related thermal vacuum test program model

Initially, all of the discrete solid blocks could be envisioned to make up one total solid block. The project engineer then could tailor the model to represent his particular spacecraft by removing the smaller blocks that are not applicable. This

might result in a model such as the one shown in the figure. This would be done with the direct collaboration of the project thermal organization, as well as other discipline representatives, as applicable. This shaping of a particular spacecraft thermal vacuum test program model would be an iterative process, and could change with time, since initial test and analytical results could increase confidence levels and thus decrease risk. Other factors, such as total test dollars available and the depth (quantity and quality) of testing, would also influence the model shape. Instrumentation also could affect the model shape; sensitivity/error studies performed to assess the variance of the thermal parameters inherent in each test are also important. Indeed, lack of adequate instrumentation for meaningful testing would eliminate some of the discrete solid blocks and sensitivity/error studies could indicate there is no need for certain tests. All significant factors must be considered in the formulation of a model such as the one shown in Figure 5. Once this is accomplished, however, the project engineer has a very useful tool for establishing a general thermal vacuum test plan.

Test and Analytical Interrelationship

After determining how various tests relate to the risk associated with his spacecraft, the project engineer must ascertain the spacecraft test and analytical interrelationship to complete his thermal vacuum test program philosophy and thus establish an overall thermal design philosophy. The project engineer must understand how test and analysis flow together and complement each other, since this must occur to optimize the maximum return on the investments made in each.

In the development and evaluation of spacecraft thermal designs, analytical or math models are used with the computer to determine temperatures and thermal energy distribution. These results are determined primarily with two computer programs--

- 1) The thermal radiation analyzer (reference 2). This program calculates natural incident (solar, albedo, etc) and absorbed environments, as well as radiation interchange factors.

- 2) The thermal analyzer (reference 3). This program calculates spacecraft temperatures and heat flux distributions.

Another useful computer program for use in determining sensitivity/error temperature estimates for a spacecraft is described in reference 4. These estimates can be used, as mentioned previously, to understand the need for testing and to aid in establishing test environmental levels.

The validity of the results obtained from the math models depend on the accuracy of input data such as thermophysical properties, electrical power levels, conductance, etc. Testing is often the only method that can be used to determine

uncertainties in these parameters. The level or type of testing used will vary from one program to another, but the lowest level to obtain these uncertainties should be chosen.

Prior to thermal vacuum testing above the component level, the analytical or math model can be used to define the test runs, duration, simulated environment conditions, and the predicted thermal data. After testing, the test data can be used to correlate the math model predictions, verify the analytical techniques, and update the model for more accurate predictions for subsequent testing and flight. By following this process, very accurate analytical models are available for mission support and evaluation. It is also interesting to note that a risk related analytical model could be fashioned using the same procedure described previously for testing. This risk would be directly associated with the confidence in the analytical model results, and would be updated during the program schedule, just as mentioned for the risk related test model.

Figure 6 presents a flow diagram of a typical spacecraft test program related to the analytical effort. From the above discussion, it is evident that there is a very definite and close relationship between thermal vacuum testing and the analytical models. This flow of information between the two must be clearly defined by the project engineer for maximum results. As an example of how this can be achieved, the next section presents this relationship for a specific spacecraft, and discusses the test results that can be achieved.

ATM THERMAL VACUUM TEST PROGRAM

The Apollo Telescope Mount (ATM) is one of five modules that compose the Skylab, an earth orbiting space station, scheduled to be launched by the National Aeronautics and Space Administration in 1973. The objective of Skylab is to expand the knowledge of manned earth orbital operations and to accomplish scientific investigations. The ATM is an unmanned scientific platform, designed to observe, monitor and record the structure and behavior of the sun outside the earth's atmosphere with the aid of eight solar experiments. High resolution observations of the solar disk will provide data in the visible, ultraviolet, and X-ray regions of the electromagnetic spectrum. Observations of the sun are recorded on the film that is retrieved during extravehicular activities throughout the eight-month mission.

The ATM is the largest unmanned spacecraft developed to date. Figure 7 illustrates an exploded view of the ATM, excluding four X-shaped solar arrays. The central element is an 135-inch-long, 86-inch-diameter cylindrical canister that houses the eight solar experiments, a fine pointing control system and several supporting electronic components. The canister is supported, via a gimbal system, by an octagonal rack truss structure 9 by 13 feet. The rack also provides

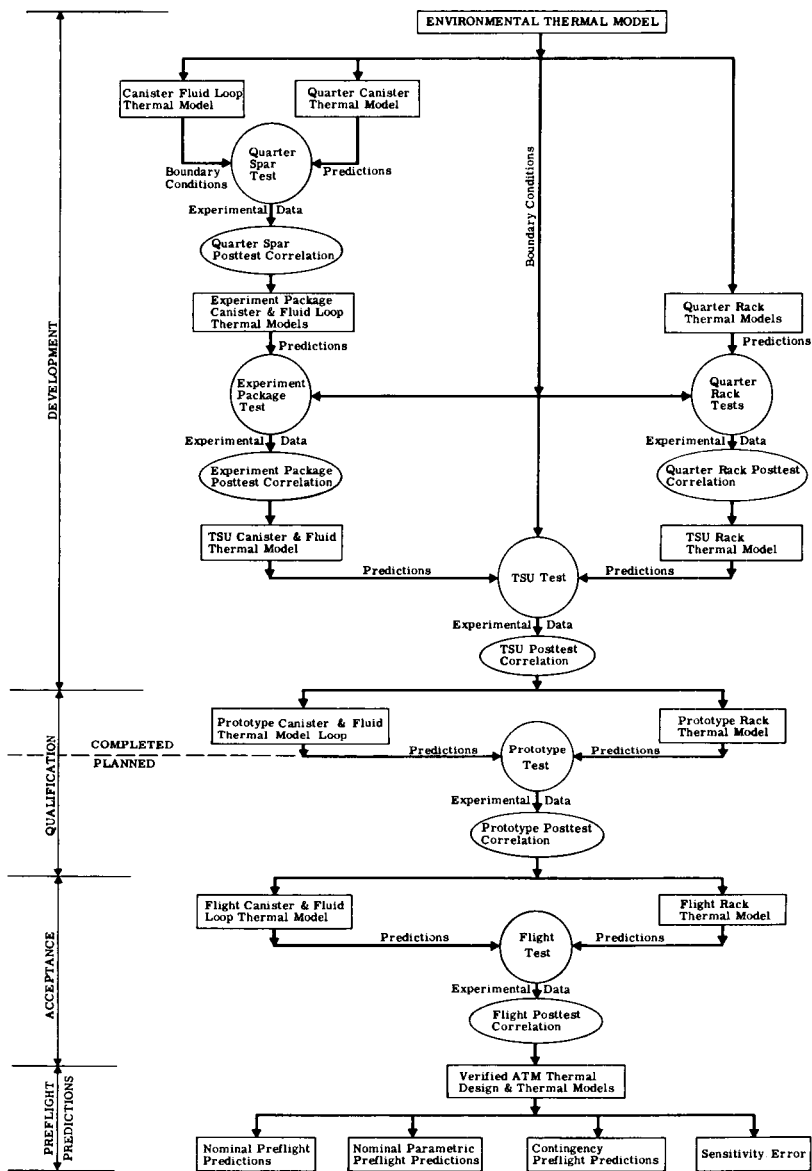


Fig. 6--ATM test/analytical flow diagram

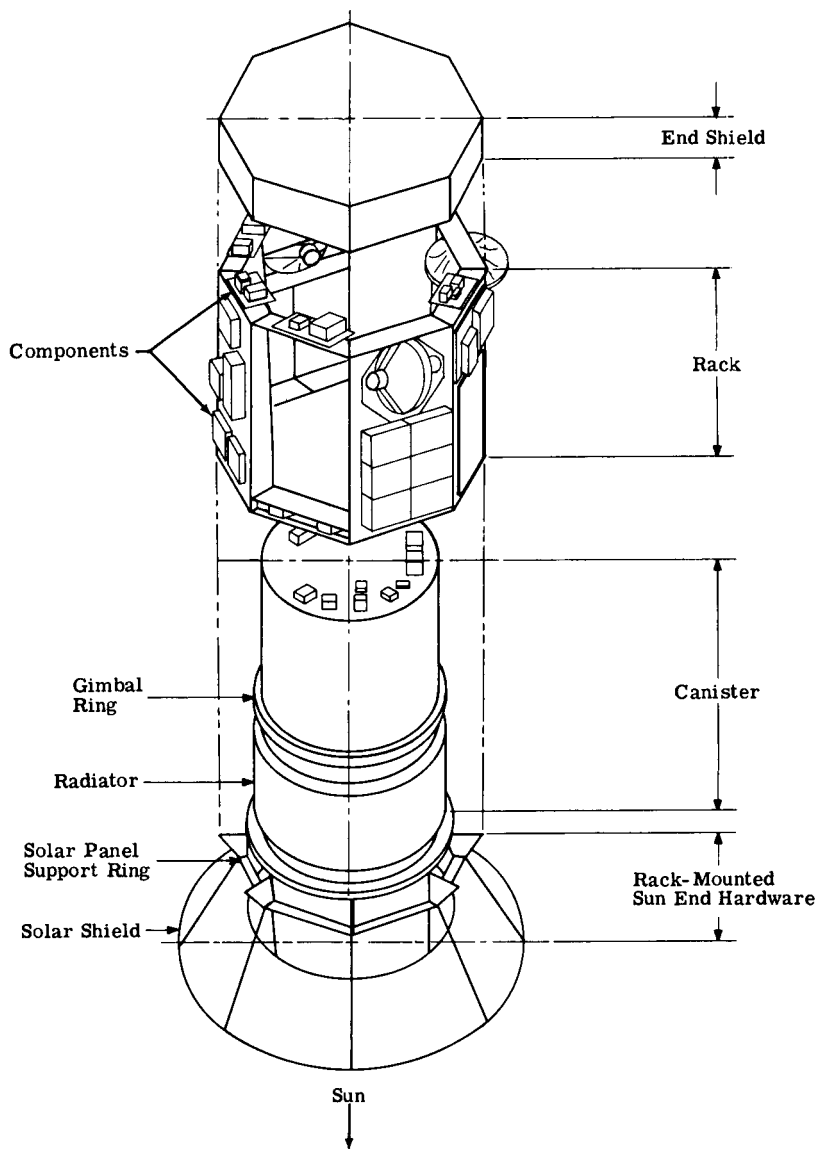


Fig. 7--ATM spacecraft

support for 122 components that compose the electrical, attitude pointing and control, telemetry, caution and warning, command, and experiment supporting electrical systems. A shield is mounted on the rack for protection from the relatively cold external environment. Mounted on the opposite end of the rack, is a conical solar shield and its supporting structure. The conical solar shield prevents the sun's rays from impinging directly on the externally rack-mounted components and on the canister radiator.

Thermal control of the ATM is achieved by passive, semipassive, and active means. The canister thermal control is accomplished with an active fluid loop, complemented by multilayer insulation and thermal paints. This system provides relatively coarse thermal control; thus, six of the eight experiments employ semipassive techniques for fine thermal tuning. These six experiments employ standoff, strip, or blanket electrical resistance heaters, in conjunction with multilayer insulation, and thermal control coatings. The other two experiments rely completely on passive techniques, primarily gold coating.

Thermal control of the rack-mounted components is achieved through passive and semipassive means. The rack thermal design is cold biased, with electrical resistance heaters provided as an integral part of certain components, heaters mounted externally on some components, and with still other heaters mounted in critical locations on the rack structure. Multilayer insulation, low thermal conductance materials, and thermal control paints are judiciously used, along with optimum location of the components relative to the natural environment and individual power dissipations.

General Test Program

Reference 1 defines the rather extensive general test program for the ATM spacecraft. This test program is currently being executed at the systems qualification level on the prototype vehicle. Since the prototype unit is a backup flight unit, the system qualification thermal vacuum test will be conducted so that overstress conditions will not be imposed on the systems.

A detailed discussion of the ATM general test program is beyond the scope of this paper; therefore, only the salient features relative to the thermal vacuum tests will be presented. The test program for the ATM encompasses test activities associated with design, development, manufacturing processes, qualification, acceptance, integrated system tests, orbital flight, prelaunch, and activation. The general test philosophy establishes that all ATM tests are to be performed at the highest hardware generation level practical. Qualification was accomplished by similarity where practical, and supplemented with testing when similarity was not considered adequate. Acceptance tests were conducted at origin of manufacture to

reduce duplicate testing and resources at the integration or assembly site.

Development tests are designed to verify the feasibility of the design approach and provide confidence in the ability of the hardware to pass qualification tests. Development hardware was representative of flight hardware, but included laboratory modules, breadboards, and engineering models, as well as special test units.

Extensive development tests were conducted on the parts and materials, components, and systems levels. Development tests were conducted on a few selected subsystems.

Qualification tests were designed to demonstrate the capability of the ATM hardware to meet the established design criteria. Test articles used for qualification were, for the most part, flight configurations and were manufactured by the same processes and to the same requirements as the flight hardware. Subsystem qualification was satisfied by the results of component and system qualification tests.

The flight article will be subjected to essentially the same tests as the prototype unit. However, upon successful completion of all environmental tests, the flight ATM will be subjected to a final mission simulation sequence test at ambient conditions before being shipped to the Kennedy Space Center.

Figure 8 presents the most significant ATM thermal vacuum tests. In all, there are six tests, four development, one qualification and one acceptance. Two specific objectives of these tests are: (1) provide test data for verification of the analytical techniques used to construct the thermal math models; and (2) obtain experience which can be applied to subsequent thermal vacuum tests as well as to the flight. The quarter spar development test provided preliminary verification of the canister thermal control concept on a full-scale basis. Only one quadrant of the canister was simulated using thermal mechanical units (TMUs) to thermally simulate the experiments.

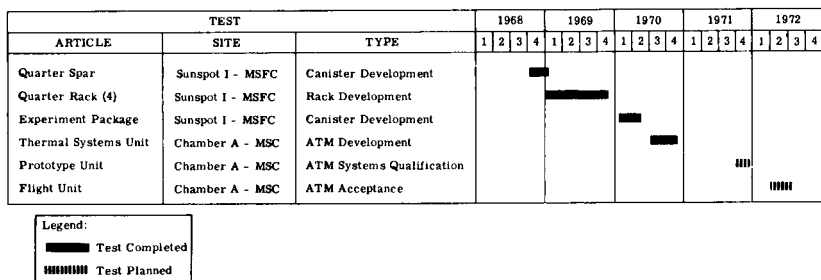


Fig. 8--ATM thermal vacuum test program

A full-scale quarter rack development test provided preliminary experimental verification of the thermal control concept (applied to individual rack mounted components) before the more complex thermal systems unit (TSU) test. One quadrant of the ATM rack structural assembly was simulated. Components peculiar to each of the four rack quadrants were provided separately and mounted on the quarter rack test assembly to simulate each of the four quadrants. TMUs of all rack components were provided.

The experiment package thermal unit provided preliminary verification of the canister thermal control design concepts. The test article consisted of full-scale flight structural hardware, certain electronic boxes, and an active coolant loop, while the experiments and most of the black boxes were simulated by TMUs.

The thermal systems unit test was the first full-scale ATM thermal vacuum test. The general objective of the test was to verify the capability of the thermal control systems to maintain ATM temperatures within the required design ranges during the predicted minimum and maximum thermal environments. The experiment package test article was mated to a flight rack structure with the component TMUs from the quarter rack test articles.

The prototype thermal vacuum test will simulate the extremes of thermal environments to be encountered by the ATM during flight. The prototype backs up the flight unit; therefore, all hardware is flight configured. The general objective of the prototype test is to qualify the systems in a thermal vacuum condition.

The flight ATM will be subjected to the same thermal vacuum conditions as those imposed on the prototype ATM. The flight thermal vacuum test is an environmental acceptance test.

As was mentioned in the previous section, the analytical activities should support and complement the thermal test program. The analytical effort provided information on the types and levels of environmental simulation, layout of the instrumentation, number and time duration of the test runs, and predictions to monitor the various tests. Figure 6 depicts the test/analytical flow for the ATM thermal design. It can be seen from this figure that the thermal math models experience a development, qualification, and acceptance process parallel with the spacecraft. This increases the level of confidence for the math models at each phase of the project. Test predictions, such as reference 6, are generated with the various analytical models before each test. The test data collected are correlated with these predictions, and model modifications are made wherever it is deemed necessary. Caution should be taken in that the experimental data are subject to errors and, therefore, erroneous data must be eliminated before posttest correlation is undertaken.

It is apparent that the initial thermal math models should

be relatively small and simple. However, as the thermal design and test program advances, the math models become somewhat larger and more complicated. This is true for the ATM spacecraft through the TSU thermal vacuum test, at which time the math models are reduced in size and simplified in logic in preparation for the flight vehicle testing and mission evaluation and support. The large math models of the ATM TSU are dictated by the quantity of instrumentation required during the development test. Table 2 tabulates the 1728 instruments employed on the TSU test article. This is in contrast to the prototype and flight units, where there are 256 transducers.

Table 2. ATM TSU instrumentation matrix

		Temperature	Pressure	Percent Quantity	Electrical Power	Heat Flux		Discrete
						Hy-Cal	Calorimeter	
Canister	TCS	49	11	1	5	32	192	18
	Internal	57	5	NA	NA	NA	NA	NA
	Components	87	NA	NA	4	NA	NA	NA
	Miscellaneous	14	NA	NA	NA	8	NA	NA
	Experiments							
	GSFC	23	NA	NA	2	NA	NA	NA
	HAO	24	NA	NA	2	NA	NA	NA
	Hα-1	34	NA	NA	2	NA	NA	NA
	HCO-A	47	NA	NA	2	NA	NA	NA
	Hα-2	33	NA	NA	2	NA	NA	NA
Rack	NRL-B	52	NA	NA	2	NA	NA	NA
	AS&E	30	NA	NA	2	NA	NA	NA
	NRL-A	23	NA	NA	2	NA	NA	NA
	Structure	160	NA	NA	NA	15	55	NA
	Components	528	NA	NA	33	11	125	36
	Total	1161	16	1	58	66	372	54
	Note: This gives a total of 1728 instruments.							

Test Results

The most significant results of the two recently completed ATM thermal vacuum tests, experiment package and TSU, will be discussed in this subsection. References 7 and 8 discuss in depth the results of these tests. Table 3 lists the modifications made to the ATM as a result of the thermal vacuum tests. The most important of these was revealed during the experiment package test. The canister fluid loop was found to be unstable under all test conditions, resulting in the cold plate fluid inlet temperature to be out-of-tolerance. However, this instability was not of serious enough magnitude that the experiment package test could not be completed. Upon completion of the test, a breadboard of the canister fluid system was developed and tests conducted at ambient conditions, except for the radiator panels that were enclosed in a cold

gaseous nitrogen chamber. The breadboard design modification consisted primarily of relocating the modulating flow control valve from the diverting position to the mixing position downstream of the radiator and heater bypass loops. Even though the individual components had been qualified, the fluid loop developed instabilities when the components were integrated into the system. Thus, the design anomaly discovered during the experiment package test highlighted the importance of system testing for certain conditions. The other modifications made to the ATM consisted of various changes ranging from lowering the acceptable temperature limit to adding a 10-watt heater to the rack structure.

Table 3. ATM design modifications resulting from thermal tests

COMPONENT	PROBLEM	MODIFICATION
Acquisition Sun Sensor	Temperature Out-of-Tolerance	1. Sun pedestal area exposed to sun painted black and all other areas insulated. 2. Requalified from -40° F to -58° F.
Acquisition Sun Sensor Electronics (Primary)	Temperature Out-of-Tolerance	Isolated from pedestal with low conductance mounts and fully insulated.
Acquisition Sun Sensor Electronics (Secondary)	Temperature Out-of-Tolerance	Isolated from pedestal with low conductance mounts and fully insulated.
Signal Conditioning Rack 2	Temperature Out-of-Tolerance	Temperature limit lowered to -22° F based on qualification test.
Signal Conditioning Rack 3	Temperature Out-of-Tolerance	Temperature limit lowered to -22° F based on qualification test.
Remote Analog Submultiplexer 1	Temperature Out-of-Tolerance	1. Added insulation to sides, bottom and a portion of the top. 2. Isolated from rack with low conductance mounts.
Remote Analog Submultiplexer 2	Temperature Out-of-Tolerance	Add 10-watt heater to structure near component.
Tape Recorder (Primary)	Temperature Out-of-Tolerance	1. Reconfigured thermal cover insulation pattern. 2. Isolated from rack with low conductance mounts. 3. Insulated sides and bottom of unit.
Tape Recorder (Secondary)	Temperature Out-of-Tolerance	1. Reconfigured thermal cover insulation pattern. 2. Isolated from rack with low conductance mounts. 3. Insulated sides and bottom of unit.
Canister Fluid TCS	System Instability	Relocated valve from diverting to mixing position.

Figure 9 illustrates the temperature range experienced by one of the eight solar experiments, the GSFC (S056). As was pointed out previously, it is very important to interpret the data in the proper manner. The temperature experienced by the GSFC solar shield ring mount and mirror case exceeded their lower limits. This was due, however, to a limitation of the TSU development article rather than a design problem.

During posttest correlation, all of the data must be carefully reviewed to identify erroneous measurements and test associated anomalies. Figure 10 shows a sampling of TSU test data correlated to the predicted data both for pretest and post-test conditions. It can be observed from the pretest curve that the predictions for some measurements were about 90° F; whereas, the test data indicated the measurements were in the range of 60 to 65° F. A heater was assumed to be on in the pretest predictions, but, in fact, was off during the test, thus

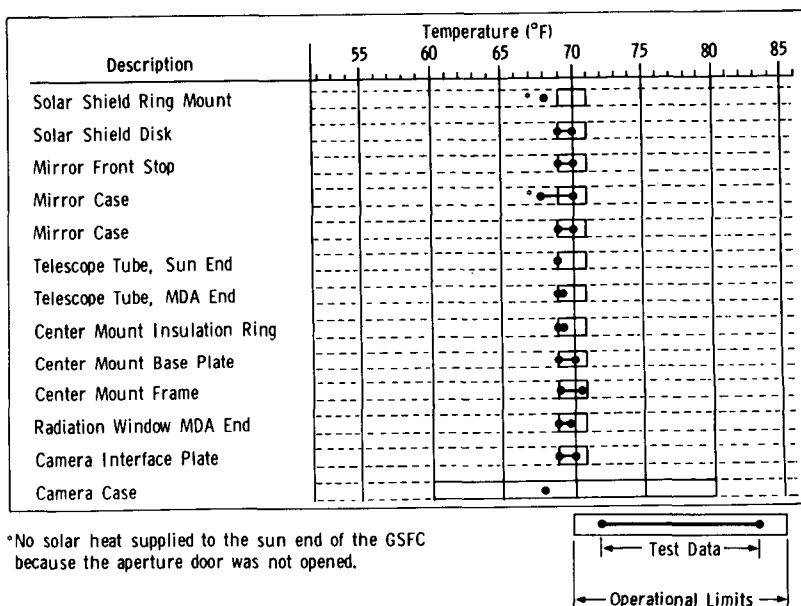


Fig. 9--ATM GSFC (S056) experiment temperatures

lowering the temperatures. The model results agreed more favorably with the test data, as seen in Figure 10 (posttest), after all of the erroneous data had been eliminated, all of the test anomalies taken into account, and all of the necessary modifications made to the math models.

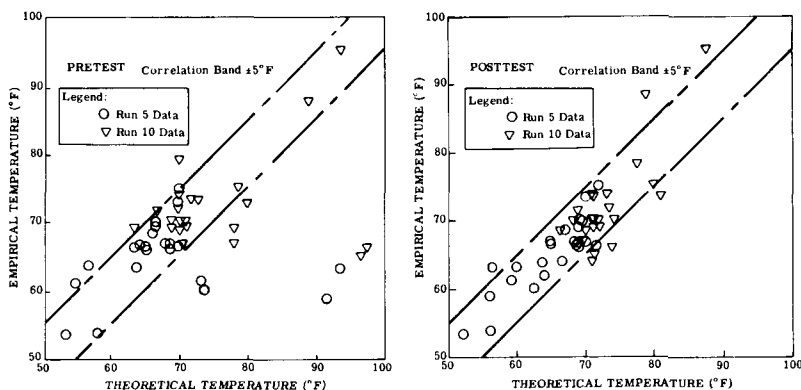


Fig. 10--ATM empirical/theoretical temperature comparison

Since the ATM thermal math models will be used during the Skylab mission for troubleshooting purposes, as well as evaluation and assessment, a certain level of confidence must be established for the analytical tools. Figure 11 compares

the histograms of the ATM canister math model for TSU pretest model correlation to posttest correlation. The thermal data are presented for a cold transient test with the experiments in the nondata-taking mode of operation. It can be seen in Figure 11 that the mean temperature difference between predicted and test data has been improved from -1.5°F for pretest to -0.4°F for posttest. Assuming a normal distribution, the standard deviation has also been improved from 3.0 to 2.7°F .

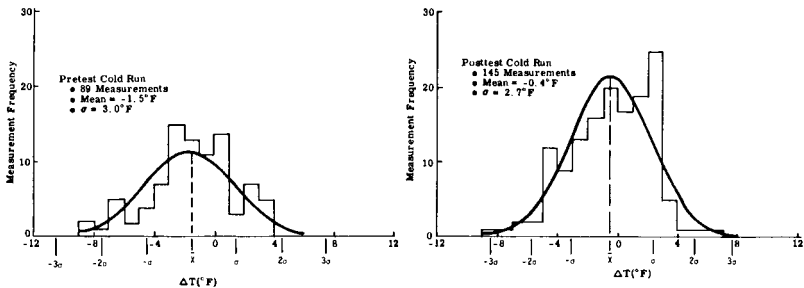


Fig. 11--ATM model/test temperature difference distribution

It is not possible to apply a normal distribution to the data collected during the hot transient test with the experiments in the data-taking mode. This is due, in large part, to an anomaly that occurred with the data acquisition process. The anomaly resulted in not being able to accurately determine the electrical power dissipated within the experiments. Thus, without knowing all of the boundary conditions the data correlation was hindered. If a normal distribution is assumed for the hot case data, however, the mean is $+2.2^{\circ}\text{F}$ and the standard deviation is 3.1°F .

CONCLUSIONS

1. Various design criteria exist that influence the risk associated with any spacecraft mission.
2. From these design criteria, guidelines can be established that relate this risk to the type and level of thermal vacuum tests for the spacecraft of interest. Thus, a general thermal vacuum test philosophy can be developed by using a logical, sequential decision-making process. Compilation and study of past and future general thermal vacuum test program results can enhance the decision-making process by the project engineer. Computerized techniques can be used to simplify the decision-making procedure.
3. A balanced or optimum test/analytical program relationship is essential to obtain maximum return on total program investment.

4. The ATM thermal vacuum test results indicate that excellent data correlation with analytical models can be achieved for a complex spacecraft. Certain design modifications were made as a result of the testing.
5. Sensitivity/error studies are very valuable in determining the need for testing, as well as establishing the environmental conditions to be simulated.
6. As spacecraft grow larger, it is desirable to advance the art of thermal scale modeling since this will be the only economically feasible means of thermal vacuum testing the entire spacecraft.

ACKNOWLEDGEMENTS

The authors gratefully acknowledge the contributions of Mr. Roger Martin of Martin Marietta Corporation who correlated the ATM test data. The ATM thermal data correlation presented was accomplished under NASA Contract NAS8-24000 from Marshall Space Flight Center, Huntsville, Alabama.

REFERENCES

1. New, N. C. and A. R. Timmons, Effectiveness of Environment Simulation Testing for Spacecraft, NASA TN D-4009: June 1967, Goddard Space Flight Center, Greenbelt, Maryland.
2. Holmstead, Gary M. and R. E. Paulson, Martin Marietta Thermal Radiation Analyzer Program (MTRAP), M-70-22: Sep. 1970, Martin Marietta Corporation, Denver, Colorado.
3. Connor, Robert J. et al., Martin Improved Thermal Analysis System (MITAS), MDS-SPLPD-71-FD328: July 1971, Martin Marietta Corporation, Denver, Colorado.
4. Goble, R. G., Steady-State Temperature Sensitivity and Error Analysis (SANDEA), TM-0444-71-38: July 1971, Martin Marietta Corporation, Denver, Colorado.
5. Skylab Program General Test Plan for Apollo Telescope Mount Project, 50M02410, Revision E, Astrionics Laboratory, Marshall Space Flight Center, Huntsville, Alabama.
6. Apollo Telescope Mount Prototype Thermal Vacuum Test Predictions, ED-2002-1362: 17 September 1971, Martin Marietta Corporation, Denver, Colorado.
7. Apollo Telescope Mount Experiment Package Test - Final Report, ED-2002-1116-2: 15 December 1970, Martin Marietta Corporation, Denver, Colorado.
8. Apollo Telescope Mount Thermal Systems Unit Test Thermal Evaluation - Final Report, ED-2002-1174-2: 31 January 1971, Martin Marietta Corporation, Denver, Colorado.

SOME CONTAMINATION PROBLEMS IN THE EUROPEAN TD SATELLITE

J. Dauphin, G. Schamle, A. Zwaal, *Materials Section, Quality & Reliability Division, ESTEC - Noordwijk, The Netherlands*

ABSTRACT

The European satellite TD contains two Stellar U.V. telescopes which are extremely sensitive to chemical contamination of their optical surfaces. It is important for the success of this project that contamination be reduced as well on the ground during the integration and test phases, as in space during the operational life.

The first method used to reach this target was a careful selection of the materials used all over the satellite hardware. Materials were selected by using the Micro-VCM technique and the paper describes some typical cases of materials evaluation. Also needed to ensure the success, was a constant monitoring of the cleanliness of the satellite during the integration and test phases, and in particular during long duration thermal vacuum-tests. This was effected with the help of U.V. and I.R. spectroscopy techniques using suitable sensors.

This approach to the contamination problems contributed towards assuring that the sensitive TD optical system would, at all times, remain at a high level of cleanliness.

1. INTRODUCTION

The European satellite TD is a special project* run by the European Space Research Organisation (ESRO). It is the heaviest (466 kg) and most complex satellite ever built by Europe. Our purpose here is not to describe it or its planned mission, this was done elsewhere (1) we can only say that its design and manufacture raised many difficult technical problems which were, or hopefully will be, solved satisfactorily at the launch date, foreseen at the end of February 1972. The present contribution is devoted to one of the technical problems raised by this project, i.e. the "contamination problem". Under the word "contamination" we understand here any foreign material deposit on a sensitive satellite surface (e.g. a telescope mirror) which could jeopardize the performances of this surface. In the TD satellite contamination is really a critical problem, since the main purpose of the spacecraft is UV astronomy; two among the seven on-board

* A project which is not supported by all the ESRO member states.

experiments are particularly vulnerable, these are S2/68 and S59.

S2/68 is a stellar UV astronomy experiment jointly set up and managed by the Liege University (Belgium) and the Royal Observatory, Edinburgh (UK). The purpose of this experiment is to provide a map of the sky including stars down to magnitude 9 and giving for each a distribution of the light intensity in the UV from 1300 to 3000 Å, with a resolution of 30 to 40 Å. The corresponding equipment is a large telescope of which the main mirror (diameter 291 mm), made of vacuum deposited aluminium coated with magnesium difluoride, is the critical element.

The S59 experiment, set up and managed by the Space Research Laboratory of Utrecht (The Netherlands) is also a stellar telescope. S59 has a smaller size than S2/68 (principal mirror dimensions 220 mm square) but includes a scanning mechanism.

This experiment is intended to allow high resolution (1Å) spectrometry of stellar sources in three spectral zones 100 Å wide around 2085, 2520 and 2800 Å.

S2/68 is contained in a closed tube insulated from the rest of the satellite, whereas S59 is mounted wide open in the experiment compartment of TD.

S59 as well as S2/68 have very close tolerances concerning the change of reflectivity of their active surfaces.

2. CHARACTERISTIC OF THE CONTAMINATION PHENOMENA

2.1. Nature of deposits

An optical surface may become contaminated by different continuous or discontinuous solid or liquid deposits. The discontinuous contaminants are liable to increase light scattering which lowers the optical efficiency of the instrument. The most common case is a deposit of solid atmospheric dust. In this circumstance cleaning is rather easy, even "in-place" and can be done by blowing out the dust with a dry clean gas or by vacuum cleaning. Side phenomena may however enhance the adherence of certain dust particles to the surface (static charges, combined deposit of dust and grease, corrosion of the substrate, etc....).

A solid or liquid layer can be formed due to the condensation on a relatively cold surface of a gaseous atmospheric borne contaminant; the layer is continuous (film) or discontinuous according to the condition of the condensation phenomena. This type of condensation is also possible in a vacuum environment, it is even enhanced due to the evaporation of many materials which would not vaporize efficiently under normal atmospheric pressure. Contaminants deposited under vacuum can re-evaporate at a rate defined by the absolute temperature

of the substrate, the layer may however be stabilized by secondary phenomena like a polymerisation or a reaction with the substrate: high temperature, radiation and catalytic effects play a role in these circumstances. Vacuum deposited contaminants increase the light scattering, when discontinuous, and the light absorption in certain ranges of wavelength depending on the exact chemical nature of the contaminant. On top of this one observes interference effects with continuous films having a thickness comparable to the wavelength of interest. Absorption in the contaminant can be increased by the presence on the optical surface of a transparent film intentionally deposited to protect it or render it more efficient. (2) Cleaning of a vacuum contaminated surface is a tricky problem: if there is no attack of the substrate or polymerisation in the contaminant, solvent methods can be used. The only efficient method to remove a polymerized film seems to be an oxidation by atomic oxygen. (3) It is anyway frequently impractical to clean out contaminated optical surfaces after integration of the experiment in a spacecraft since they become inaccessible to the above methods.

2.2 Location of deposits

Dust will be collected primarily by horizontal surface, this is particularly troublesome for TD since the two telescopes are looking upwards during most integration and test phases. However, they are usually protected by a cover.

Condensed contaminants build up on the surfaces until an equilibrium is reached between condensation and re-evaporation. In the atmosphere any surface can be contaminated depending on its temperature. In a vacuum the orientation of the surface versus the contamination source is a determining factor: gas molecules are travelling along straight lines and only surfaces having a direct view to the contamination source can capture them. The efficiency and duration of this capture depend on a surface property; the "sticking coefficient" and on absolute temperature. A contaminated surface always becomes a secondary source of contamination due to re-evaporation.

Some order of magnitude should be kept in mind, i.e. the dimensions of a typical contaminant molecule are approximately: area 100 \AA^2 , thickness 5 \AA , molecular weight 300. A "monolayer" has a superficial weight of $5 \cdot 10^{-8} \text{ g/cm}^2$. The evaporation or re-evaporation rate of such a contaminant is proportional to $\frac{P}{\sqrt{T}}$, where P is the saturated vapour pressure in torr at absolute temperature T.

2.3 Tolerances of TD optics

The experimenter of S2/68 stated that "as little as 25 Å of condensate uniformly distributed over the U.V. reflecting surfaces could substantially degrade the reflectivity and hence impair the efficiency of the experiment": This is 5 monolayers or $2.5 \cdot 10^{-7} \text{g/cm}^2$. The contamination criterion finally adopted by the experimenter is that at the time of the launch, the optical efficiency should not be lower than 60% of the calibration value : this corresponds to the loss of one stellar magnitude and renders the experiment not worth flying. Since there are five optical surfaces in the optical path, supposing that the contamination deposits equally on them, no more than 10% degradation of each can be tolerated. For smaller degradations, i.e. a loss of two percent for each surface and 10% total, the telescope has to be recalibrated. It is unfortunately nearly impossible to correlate a priori a percent reflectance degradation to an apparent thickness of a given contaminant : only an experiment can give this relation. Calculation of the effect of a dust contaminant is also an intractable problem. Decisions were taken here to rely on the American experience on OAO and to consider that the satellite should be exposed only to class 100,000 or better clean room ambiance. No contamination criterion was evolved for S59 but it is deemed that the levels required for S2/68 will ensure a satisfactory performance.

3. MATERIALS SELECTION POLICY

3.1 The Micro-VCM Screening

The screening method employed for TD materials is the "Micro-VCM" test (VCM = volatile condensable material). It was developed by Jet Propulsion Laboratory and is also applied by Goddard Space Flight Center and since the beginning of 1970 by an ESTEC contractor, INTA-Madrid (4, 5). This test is intended to provide an accelerated means of determination of the total weight-loss of materials and of their contamination ability in a space environment.

3.1.1 Apparatus

The apparatus consists of an insert in a common type of vacuum system suitably chosen to allow for the geometrical volume of the insert and for the necessary feed-throughs. The required clean high vacuum of 10^{-6} torr is attained within one hour for an empty system.

The heatable copper inserts allow 24 samples to be placed in the sample chambers of 16 mm diameter and 8 mm depth.

The sample chambers look via a 6,4 mm hole at condensor inserts which can be cooled. The condensor inserts are equipped with suitable fixtures to hold condensor discs i.e. standard 25 mm salt flats for infrared spectrophotometry.

3.1.2 Operating parameters

The prepared samples of about 200 mg are exposed to vacuum at 125°C for 24 hours in front of condensor discs maintained at +25°C. The samples are weighed before and after the vacuum test. A 24 hours conditioning at 20°C in air (65% R.H.) is applied to the samples before the vacuum test and a 24 hours conditioning at 20°C in a dessicator to the samples after the vacuum test.

The condensor discs are weighed immediately before and after the vacuum test. From these four weight measurements, made with a micro-balance, the total weightloss (% WL) and the condensable weightloss (% VCM) can be calculated. Furthermore a qualitative analysis of the condensed materials is obtained from the condensor discs by infrared spectrophotometry.

3.1.3 Acceptance limits

Materials are qualified for vacuum environment if the total weightloss is below 1,0% and if, at the same time, the condensable weightloss is below 0,1%. These limits are generally accepted by NASA-GSFC and ESTEC.

3.1.4 Remarks

- a) Condensable materials should ideally be absent, but 0,1% can be tolerated, however a simple calculation shows how high this 0,1% limit is:
One kilogram of material loosing 0,1% condensable materials can cover 100 m² with a layer of 10⁻⁶g/cm⁻² (20 monolayers or 100 Å layer).
- b) Post curing of materials at elevated temperatures under atmospheric conditions or under vacuum may reduce the weightloss percentages, but does not always lead to the required results.

3.2 Some specific examples

3.2.1 Black Thermal control paint

The interior parts and optical baffles of the two telescopes must be matt black in order that stray light be minimum. Two paints were proposed initially by the designers:

"CAT-A-LAC" 463 - 3 - 8 (Finch Paints - USA)
CELLON DOCKER 2 SL 5459 (Cellon Docker - UK)

The first one was used on many American spacecrafts (6), the second one on the ESRO II satellite, Micro-VCM tests were run* on these two paints with the following results:

- 2SL 5459 cured 7 days at room temperature
Total weight loss WL = 6,91%
Vacuum condensable material VCM = 0.20%
- Cat-a-lac 463-3-8 with different curing processes
 - 24h/25°C + 72h/65°C WL = 4,50% VCM = 0.12%
 - 24h/25°C + 48h/120°C WL = 1.18% VCM = 0.21%
 - 24h/25°C + 1h/65°C + 47h/175°C WL = 0.35% VCM = 0.17%
 - 24h/25°C + 48h/65°C (under vacuum) WL = 0.55%
VCM = 0.22%

In both cases, the cure schedules envisaged give a product out of specification, particularly noticed is the rather high VCM which could not be reduced and which is extremely dangerous for a paint having a direct view to the telescope mirrors.

At the time this decision had to be taken, no other suitable candidate except "Black Velvet" 401 C 10 (Minnesota - USA) was known**. Micro-VCM results published by JPL (7) showed that VCM could be quite low with proper cure (VCM \sim 0.03%) with, however, a high total weight loss arising from trapped solvents.

It was decided to change to Black Velvet paint which already had been experienced in flight. This paint gave no difference in optical properties ($\alpha_s = 0.97$

$\epsilon_H = 0.84$ for 401 C 10 versus $\alpha_s = 0.96$ $\epsilon_H = 0.85$ for Cat-a-lac). The application procedure is, however, more difficult for Black Velvet and the mechanical properties of it are inferior (tendency to give dust). These points were corrected later by a careful application procedure and a cure schedule applied which allows to obtain the following values : $0.62 < WL < 1.32$ $0 < VCM < 0.05$.

3.2.2 Titanium Bolts Lubricant

All over the structure of TD spacecraft titanium bolts are used with titanium nuts, this gives rise to difficulties since titanium freezes when sliding on itself. A lubricant is needed in order that the bolts can be tightened with the permitted torque.

All proposed lubricants gave an enormous contamination risk: three greases were tested, and all of them were found to have an unacceptably high VCM,

* We are indebted here to the Materials Branch in Goddard Space Flight Centre for their running our VCM Tests before ESTEC/INTA equipment was in operation.

** There exist now some encouraging results on Chemglaze Z306 (Hughson - USA) and Glassofix 802/1240/8 (Glasurit-Germany). Black anodize with inorganic dyes is also worth considering.

Molykote D (Molykote-Germany) WL = 36,6% VCM = 5.0%
 Lithelen (Leybold - Germany) WL = 8.1% VCM = 3.1%
 R. Fett (Leybold - Germany) WL = 8.4 to 17%
 VCM = 3.7 to 4.7%

Molybdenum disulphide burnished on the bolts was good on an outgassing point of view but generated an amount of black dust.

Finally, a tailored lubricant was made for the purpose using F6-1100 (Dow Corning - USA) space grade silicone fluid and suspending in it MS_2 powder (4:10 weight ratio). The Dow Corning fluid is submitted to micro-VCM test by the manufacturer and claimed to have WL = 0.04% VCM = 0.02%.

The smallest possible quantity of this lubricant is to be used to avoid it creeping out of the intended location.

3.2.3 Attach for Multilayer Insulation

A large part of the TD satellite structure is covered with multilayer insulation materials. At many locations, this blanket is attached by the way of Velcro tape (Hartwell Corp. - USA) which provide a very convenient demountable system. The two parts of Velcro tape, hook and pile, have to be bonded to the blanket and the manufacturer proposed a rubber solvent-type adhesive "Velcro No. 45" for this use. It was feared that such an adhesive could be a high outgasser. Samples were submitted to the micro-VCM test with the following results:

Velcro tape V 12.1 (801-100) Hook } WL = 1.47% VCM = 0.01%
 + V 12.2 (100) Pile }

Assembly of above tape on Mylar foil } WL = 1.97% VCM = 0.06%
 with Velcro No. 45 adhesive }

Self adhesive Velcro tape
 V12.1 (80) 63 SA 0145A hook + } WL = 2.89% VCM = 0.10%
 V12.63 SA 0145A pile }

From the above it is seen that the assembly has a low VCM. Considering that most of the outgassing was water this Velcro system (excluding self-adhesive type) was considered tolerable for use on the TD satellite.

3.2.4 Thermal Coupling

Individual parts of the TD structure as well as black boxes have to be thermally coupled at their attachment points. Thermal contact between metal surfaces is extremely difficult to make reliably and reproducibly under vacuum conditions, for this reason a compliant compound is normally used at the joint interface. In the case of TD, a room temperature vulcanizing silicone rubber RTV 11 (General Electric - USA) was initially chosen. As with most RTV silicones, RTV 11 is a rather

high outgasser and has a dangerous VCM which cannot be reduced significantly by a high temperature cure:

RTV 11 + 0.5% Thermolite 12 cured at room temp. WL = 1.73%
VCM = 0.20%

" " cured at 150°C 1 hour
WL = 1.51%
VCM = 0.21%

RTV 11 + 0.1% Thermolite 12 cured at room temp. WL = 1.55%
VCM = 0.26%

" " cured at 150°C 1 hour
WL = 1.19%
VCM = 0.16%

Two possible replacements were proposed for this material: "Space Grade" RTV silicone DC93.500 and Compound C6.1102 (both from Dow-Corning - USA). The table hereunder allows comparison of the relevant parameters:

Material	Outgassing		Thermal Conductivity Kcal/m°C sec	Adhesion to substrate
	WL%	VCM%		
RTV 11	See above		0.7 10^{-4}	high
DC 93 500	0.14	0.01	0.35 10^{-4}	medium
C6 - 1102	<0.06	<0.02	1.0 10^{-4}	low
requested	<1.00	<0.10	as high as poss.	as low as poss.

The compound C6-1102 was finally chosen. It was, however, underlined that working with such a product, which can ooze out of joints and give rise to "greasy marks", necessitates a particularly strong control on the application procedure and the quantity used.

3.2.5 Cadmium Plating

A number of cadmium plated connectors were used in the P1 prototype of TD-spacecraft (not in the flight model), this raised two problems: -

- Whiskers (long single crystals of about 2 microns in diameter) can grow on cadmium surfaces, especially when exposed to vacuum and elevated temperatures. These whiskers may cause short circuits between electrical contacts (8).
- Cadmium vapour may condens on critical places in the spacecraft and the cadmium vapour may give problems with the titanium sublimation pumps of the HBF-3 thermal-vacuum test chamber.

A number of samples, pure cadmium, cadmium plated steel, passivated cadmium plated steel, and connector shields were observed for whisker growth during three weeks in

vacuum at +40°C and during several months at normal atmospheric conditions. The result was negative, it is however known that such whiskers may grow in some cases.

Evaporation tests on the same samples as above indicated that below +150°C the evaporation rates were about 0.1% of the theoretical value, because of a protective layer of cadmium-oxide.

It seems then that the exclusion of cadmium from space hardware could be reviewed provided a suitable protection against possible whiskers growth be applied.

4. CONTAMINATION MONITORING DURING INTEGRATION AND TESTS

4.1 Monitoring Philosophy

As shown above, every effort was made during the design and subsystem assembly phases to trace the possible sources of contamination among the materials used : some changes in processes or in the materials themselves were decided in order that contamination be as low as possible. It was then required that the low contamination target should be verified on the assembled satellite models during integration and tests. It was also interesting to assess that the environment during integration (clean room) and tests (test building, vacuum chambers) was clean enough not to contaminate the satellite and to degrade the performances of the optics.

Two methods were basically used which are described hereunder:

Infrared spectroscopy and ultra-violet spectroscopy. The contamination "sensors" have been designed to be small, easy to handle and transportable : for Infra-red analysis, we used standard sodium chloride discs, for U.V. analysis, either small quartz windows or small mirrors made of vacuum deposited aluminium protected with magnesium fluoride (similar to the big telescope optic). These "sensors", placed at controlled locations inside and outside, accompanied the satellite during integration and tests. In addition, Infra-red type sensors were also used during thermal vacuum qualification of the experiments and to monitor the vacuum chambers used for tests. In some cases, wipes were also taken at different location on the satellite and in the big heat balance facility of ESTEC (HBF3) in order to permit a more sensitive I.R. analysis.

It can be roughly said that the "mirror" detectors are intended to assess the performance degradation of the optical parts in the satellite whereas the sodium chloride and quartz window give us information on the chemical nature and quantity of contaminant and therefore, an indication on it's possible origin. To be sensitive, both types of windows should be kept cold during vacuum exposure; unfortunately,

this was not always the case.

4.2 U.V. Monitoring

Degradation control, of the S2/68 optics was carried out by two groups. The experimenters have their own sensors in the telescope near the primary mirror and in the spectrometer box. They use 1 cm Kanigen flats for the primary mirrors and glass flats for the spectrophotometer box (these sensors were coated at the same time as the telescope mirrors by G.S.F.C.). ESTEC sensors consist of \varnothing 18 mm mirrors, coated with 1000 Å Aluminium 99.999% and 1050 Å Magnesium fluoride, and Tetrasil quartz plates \varnothing 18 mm.

Some sensors were located in the hatches of the optical experiments, others on special holders near the satellite or experiments during integration and tests. Monitoring of the prototypes permitted the location of possible contamination and corrective action prevented it from occurring during flight model tests.

The hatch sensors were changed on an infrequent basis, depending upon activities with the optical experiments. The other sensors were changed every week. The following measurements were carried out: reflection measurements at 1216, 1300 and 1600 Å on the mirror monitors and transmission measurements in the wavelength range of 0,2 to 3,5 μ on the quartz plates.

For vacuum U.V. reflection measurements the light source is a MC PHERSON model 630 HINTERREGGER type, discharge lamp operated in closed version with a LiF window (discharge in hydrogen at a pressure of 2 to 3 mm). The monochromator is a one meter normal incidence vacuum grating type with a 600 lines per mm grating blazed for 1500 Å. A reflectometer (Fig. 1) was attached to the exit slit of the monochromator (angle of incidence 70°).

In the reflectometer a fluorescence screen of sodium salicylate on a rotatable mount intercepts either the incident beam or the reflected beam and directs the light to a photomultiplier. The ratio of the two signals to the photomultiplier gives the reflectivity. To avoid errors due to stray light a chopper (400 Hz) is placed before the entrance slit and the signal of the photomultiplier is amplified with a lock-in amplifier. To keep the contamination level as low as possible, a liquid nitrogen cooled baffle is used between monochromator and diffusion pump and a liquid nitrogen cooled trap is mounted in the roughing line. Vacuum during measurements is in the 10^{-5} Torr range.

Although all precautions were taken to make the monitoring successful, the results obtained were not significant enough. Some blank sensors kept in the laboratory changed randomly

in reflectance by about 2 to 3%, this makes the interpretation of the results with this type of sensors doubtful. Some contaminated mirrors were tentatively cleaned in a ion pumped system and showed a decrease in reflectance, this could be caused by the glow discharge during pumpdown, which could modify the contaminant layer. Some other sensors showed an increase in reflection at 1600 Å which could not be explained because there was only a small decrease at 1216 Å. The quartz monitors showed only in three cases a transmission loss and the mirrors which were in the same test did show also reflection losses: when the quartz showed a transmission loss at 2500 Å of nearly 20% the reflection of the mirror decreased by 40% at 1600 Å.

No absorption band was detected only a loss of transmission of about 5% in the range from 700 nm to 3500 nm, 8 to 10% the range of 350 nm to 700 nm and 10 to 20% in the range 200 - 350 nm.

It seems that the mirror monitors are not stable enough to permit accurate statements on the contamination level. Mg F₂ or LiF windows and transmission measurements in the vacuum U.V. range could provide better results.

4.3. Infrared contamination monitoring

This technique is based on the normal chemical analyses with an infrared spectrophotometer for the range 2,5 - 15 micron wavelength.

Two principal methods of contamination monitoring were used:-

- a) A "direct" method with sodium chloride discs or metal foils: these "sensors" were in or near the spacecraft during integration or tests and could be analysed directly without any further treatment either by transmission or by ATR.
- b) A method by "wipes" with precleaned lens tissues (SS2478) taken at different critical places on the spacecraft and heat balance vacuum chambers, in order to permit detection of contaminants on extremely clean surfaces. Wipes are also used to check any desired place after the tests where there is a visible contamination due to an accident in the spacecraft or in the test facility. After a wipe the lens tissue is washed with a few cm³ carbon tetrachloride (spectral grade) and the solvent is evaporated on 1 cm² of a sodiumchloride disc which is analysed with the infrared spectrophotometer. For contamination levels above 10⁻⁷ gram.cm⁻² the efficiency of the wipe is about 90%; the amount wiped from surfaces with a contamination level below 10⁻⁷ g.cm⁻² is doubtful.

The detection limits for the different methods can be seen in Table 1 for methyl silicones (a volatile product given off by most of the silicones materials used in spacecraft).

TABLE 1

IR -Detection limits for methyl silicones at 12,5 μ wavelength.

Method	Detection limit g.cm ⁻²
Direct method with sodiumchloride disc	2,5 x 10 ⁻⁷
ATR 7 method on 5,4 cm ² metal foil	3 x 10 ⁻⁸
Wipe method on 100 cm ² area	2,5 x 10 ⁻⁹

The ATR-7 method (7 fold attenuated total reflection) is about 20 times more sensitive as the direct disc method, however higher amplification factors are needed and the base-line is not flat so that scale expansion becomes difficult.

Nearly all the IR-spectra obtained indicated mixtures of several components which makes it difficult to find the origin of the contaminations. The Micro-VCM tests (see 3.1) provide infrared spectra of the volatile products given off by the materials tested so that we can use these spectra as standard in our contamination monitoring tests.

Good agreement between contamination levels obtained from weight measurements and calculations from the infrared spectra were obtained by dividing the contaminations in three groups: hydrocarbon equivalent (band at 3,4 μ) ester equivalent (band at 5,8 μ) and methyl silicones equivalent (band at 12,5 μ). The sensitivities for the hydrocarbons and esters were 2 x 10⁻⁶ g.cm⁻² for 1% Absorption and 1,3 x 10⁻⁶ g.cm⁻² for the methyl silicones (see Fig. 2).

A typical contamination spectrum appears on Fig. 3. An example of the contamination levels detected on TD spacecraft is given in Table 2.

TABLE 2

Contamination levels on TD-A2 spacecraft/HBF-3 test facility after thermal vacuum tests.

	CONTAMINATION LEVEL g.cm ⁻²			TOTAL
	hydrocarbon eq.	ester eq.	methyl silicones	
Wipe 600 cm ² -X hood	4,5 x 10 ⁻⁹ (63%)	1,1 x 10 ⁻⁹ (16%)	1,5 x 10 ⁻⁹ (21%)	7,1 x 10 ⁻⁹
Wipe 200 cm ² -X blanket	7,9 x 10 ⁻⁸ (53%)	2,5 x 10 ⁻⁸ (16%)	4,7 x 10 ⁻⁸ (31%)	1,5 x 10 ⁻⁷
Wipe 800 cm ² -mylar blanket	2,0 x 10 ⁻⁷ (13%)	5 x 10 ⁻⁸ (3%)	1,3 x 10 ⁻⁶ (84%)	1,5 x 10 ⁻⁶
NaCl-disc on HBF-3 shroud	2,9 x 10 ⁻⁶ (47%)	1,4 x 10 ⁻⁶ (23%)	1,9 x 10 ⁻⁶ (30%)	6,2 x 10 ⁻⁶
" " " " "	2,4 x 10 ⁻⁵ (40%)	3,3 x 10 ⁻⁵ (56%)	3 x 10 ⁻⁶ (4%)	6,0 x 10 ⁻⁵

5. CONCLUSION

The fight against contamination of the TD satellite was undertaken on two fronts. First, a selection of the materials and processes used for the hardware manufacture with the purpose of screening out possible contaminant sources; second careful monitoring of the contamination deposits during integration and tests.

TD was the first occasion in Europe where contamination was so critical a problem. It was then used as a test bench to set up and refine contamination detection methods. Most of this was done by trial and error since even in the United States no generally recognised policy or method exists. There is, anyway, still plenty of room for improvement of the techniques used.

We are not 100% sure that TD will be undisturbed by contamination in orbit, but we are very confident in that our effort has reduced this problem to a more tolerable level. Also the know-how evolved on this project can now be applied to other spacecraft realisations with a better efficiency and a better chance to obtain a really "clean" vehicle.

The present session of the Space Simulation Conference is proof of contamination being a major disturbance. It should be considered carefully at the beginning of the design phase in any advanced scientific or application spacecraft project. It also shows that the problem can be solved when a convenient approach is decided upon and then applied.

REFERENCES

1. B. TILGNER -ELDO/ESRO Scientific & Techn. Rev. 3 (December 1971).
2. G. HASS & W.R. HUNTER - Appl. Optics 9 2101 (1970).
3. J.R. HOLLAHAN, G.L. CARLTON & R.B. GILLETTE - Boeing Co. report D1-82-0935 (November 1969).
4. A. ZWAAL, J. DAUPHIN & A. ALONSO ROLDAN - ESRO TN 110 (ESTEC) (February 1971).
5. ESRO Specification PSS09-QRM02-T (October 1971).
6. J.B. RITTENHOUSE & J.B. SINGLETARY - Space Materials Handbook - NASA SP 3051 (1969).
7. R.F. MURACA & J.S. WHITTICK - Stanford Research Institute- J.P.L. Contract no. 950745 under NAS 7-100- Final report (September 1967).
8. C.L. CARPENTER & D.N. LETSON - L.M.S.C. - Materials & Process Engineering Bull. No. 1011 (Febr. 1966).

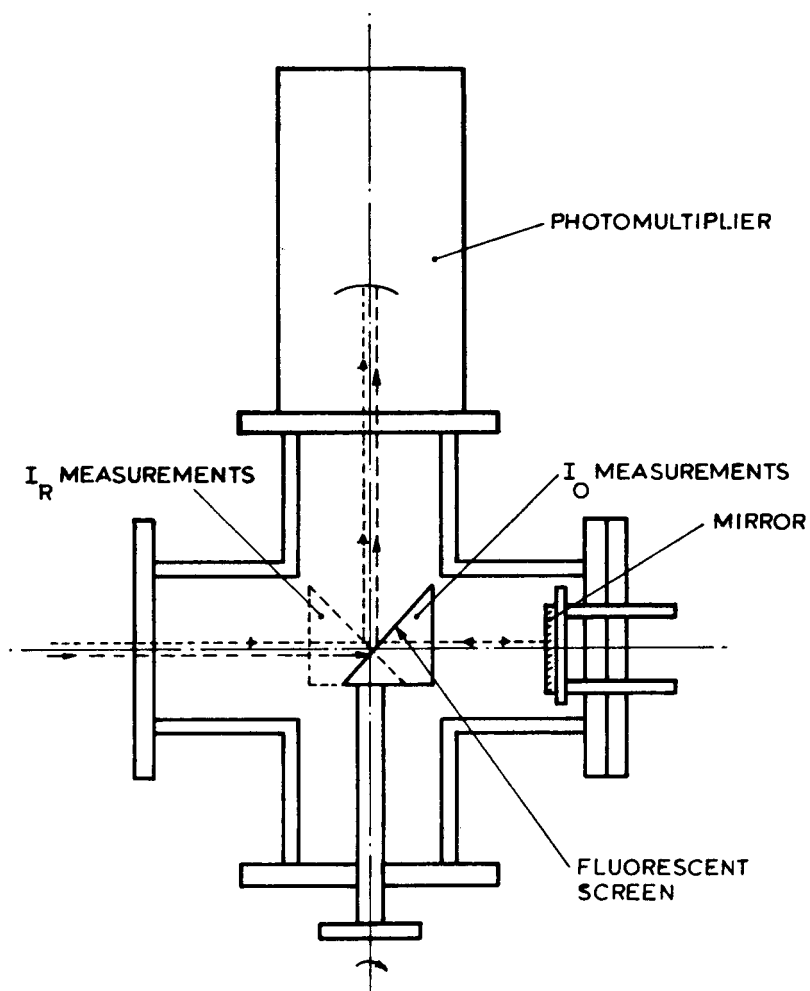


FIG.1 REFLECTOMETER

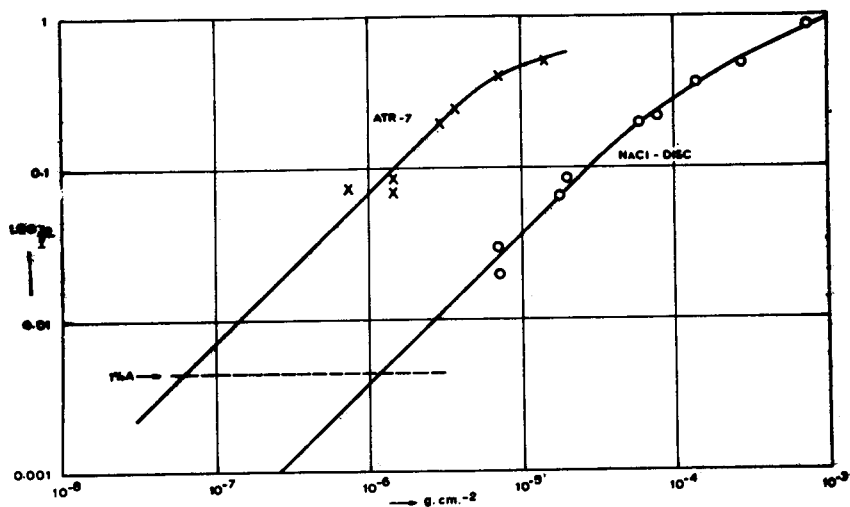


FIG. 2. INFRARED DETECTION OF METHYL SILICONES WITH ATR - 7 AND NACI DISC.
11/4/79-48



FIG. 3. INFRARED SPECTRUM OF 7x10⁻⁶ GRAM SILICONES (TD - SOLAR ARRAY - HBF: 3 TEST)

MARTIAN GRAVITY SIMULATOR FOR FULL-SCALE VIKING LANDING TESTS

Ulysse J. Blanchard and Sandy M. Stubbs, *NASA Langley Research Center, Hampton, Virginia*

ABSTRACT

The feasibility of an elastic shock cord suspension system for conducting landing-impact investigations of a full-scale prototype Mars lander under simulated Martian gravity on Earth has been evaluated experimentally. A full-size model of an early version of the Viking lander has been used to assess the adequacy of the full-scale simulator. Results of landing tests at Mars gravity correlate with results obtained during free-body Earth-gravity landings of the model. Impact accelerations, landing-gear forces and strokes, and behavior experienced during landings were in good agreement and the simulator lift system functioned satisfactorily. These results establish that a simple inexpensive elastic cord suspension system with associated vehicle launching equipment is a practical method for conducting full-scale landing investigations of prototype Mars lander spacecraft. This system would also be applicable for the development of similar spacecraft for landing on the Moon or other planetary objects having a gravity less than Earth.

INTRODUCTION

The development of a spacecraft for landing on the Moon, Mars, or other planets, requires full-scale testing to qualify the landing-gear structure and the primary body structure of the vehicle for the most severe loading conditions the spacecraft is expected to encounter. In order to maintain dynamic similarity during impact testing of the full-scale vehicle, it is necessary that the expected gravitational field be simulated. The effect of structural elasticity on the landing stability and loads may also be evaluated in the simulated planet gravity environment. Several methods can be used to simulate reduced gravitational force for prototype studies on Earth (Refs. 1-5). These include servo-cable lift systems, gimbaled lift engine, controlled elevator descent, or inclined-plane technique.

This paper reports the results of an experimental study to develop and evaluate an elastic shock cord suspension system and

associated vehicle launch equipment for conducting landing impact tests under simulated Martian gravity. A full-scale simulator using principles investigated with small pilot models, Reference 6, has been assembled and operated at Langley Research Center. The landing forces and dynamics of a "Viking" type vehicle were investigated. A full-size dynamic test model was designed and constructed such that its mass and inertia values could be varied; that is, full prototype or 3/8 prototype mass and inertia values could be obtained in a balanced condition about the center of gravity. This permitted testing the vehicle at simulated Mars gravity using the shock cord lift system and unrestrained free-body testing of the vehicle at Earth gravity, respectively. Results from the simulator landings were validated by comparison with results from the free-body landings at similar initial conditions.

DESCRIPTION OF MODELS

A full-scale variable mass dynamic test model of an early version of the Viking Mars lander spacecraft was used in the investigation and is shown in Figure 1. Pertinent dimensions of the model are shown in Figure 2. The model was designed and fabricated such that it could be tested as a free-body model with Earth-gravity acting (Fig. 1(a)) or as a tethered model with simulated Mars-gravity acting (Fig. 1(b)). To compensate for the Mars- to Earth-gravity ratio of 3/8 the model was tested at 3/8 prototype mass and inertia in free-body tests and with full prototype mass and inertia using the reduced gravity simulator. The free-body model was used as the control for evaluating the simulator.

Center Body - The test-model dimensions and characteristics (Fig. 2) are representative of an early engineering version of the Mars lander. The lander body is represented by a stiff boilerplate structure to which are attached three inverted tripod landing-gear legs. The center body is constructed primarily of welded aluminum plate and tubing. Ballast was attached to the center body in order to achieve the required mass properties. Two outrigger trusses mounted on the sides of the model near legs 2 and 3 (see Figs. 1 and 2) provided attachment points for the shock cord lift system during simulator tests. The attachment points were located on the transverse axis (Y-axis) equal distances from the center of gravity; thus, the lift forces had no effect on the stability of the vehicle.

Landing Gear - Each of the three landing-gear legs consists of a telescoping main shock-absorber strut and a hinged bipod truss which has no shock-absorbing capability. At the apex of the tripod is a crushable footpad with some shock-absorbing capability. The landing-gear assemblies are machined, high-strength, aluminum alloys with aluminum bronze used for the main strut piston and

bearing in order to minimize friction. Details of the landing-gear main strut are shown in Figure 3. Landing loads imposed on the telescoping strut were attenuated by crushing internal aluminum honeycomb elements. The cylindrical elements were designed to crush in compression (accordianlike failure) at four approximately constant force levels as illustrated by the dynamic force-stroke graph shown in Figure 3. The axial loads in the main strut are governed by these elements and were nominally 2, 3, 4, and 8 kips. The thin-wall annular cylinders were fabricated of alternate sheets of flat aluminum foil and corrugated aluminum foil wound around a mandrel and adhesively bonded.

Details of the landing-gear footpad are shown in Figure 4. It has a solid backup structure and a crushable honeycomb sole which assists in attenuating landing loads. The footpad is connected to the struts by a universal joint allowing two degrees of freedom (rotation) about a point defined by intersecting center lines of the main strut and bipod members. The graph shows the approximate axial static crush force-stroke curve for the standard expanded aluminum honeycomb sole of the footpad.

Scaling - Scale relationships for providing dynamic similarity of the two test models are shown in Table I. Since it was desirable to use the same body structure, landing gear, and shock-absorber

TABLE I.- SCALE RELATIONSHIPS FOR TESTING FULL-SCALE VIKING MODEL AT EARTH GRAVITY AND AT SIMULATED MARS GRAVITY

[Geometric model scale, $\lambda = 1$; Gravitational ratio, (Earth gravity/Mars gravity), $\beta = 8/3$]

Quantity	Mars prototype	Earth-gravity (free body) Model scale factor ($\beta = 8/3$)	Mars-gravity (simulator) Model scale factor ($\beta = 1$)
Length	l	l	l
Force	F	F	F
Acceleration	a	$8/3 a$	a
Area	A	A	A
Stress	σ	σ	σ
Mass	m	$3/8 m$	m
Velocity	V	$\sqrt{8/3} V$	V
Time	t	$\sqrt{3/8} t$	t
Inertia	I	$3/8 I$	I

elements for both models, the geometric scale factor (λ) was 1 for both. Likewise, the forces were the same for both models. Accelerations were the same for model and prototype in the Mars-gravity simulation test. For the Earth-gravity (free-body) model, the accelerations vary as β , the gravitational ratio; thus, accelerations experienced by the free-body model were $8/3$ times those which would occur on Mars (prototype) or on the Mars-gravity simulator. With these three scale relationships fixed, other pertinent scale relationships follow from laws of physics for dynamically scaled models. For the purpose of comparing Mars-gravity tests with Earth-gravity tests, the gravitational ratio (β) is the only factor that determines the variation between the two test methods. By using these chosen scale relationships the only physical differences in the two models were the masses and inertias (Figs. 1 and 2).

APPARATUS AND PROCEDURE

Photographs of the apparatus and test sites used to conduct the investigation are shown in Figure 5. The investigation was conducted by launching the model as a free body with Earth-gravity acting (Fig. 5(a)) and as a shock-cord-supported body which simulated Mars-gravity conditions (Fig. 5(b)).

Free-body Test - A sketch of the free-body apparatus is shown in Figure 6(a). A four-bar pendulum mounted on a crane was used to launch the model in a given direction and with controlled attitude and velocity components. The pendulum was released from a predetermined height to produce the desired horizontal velocity. The model was released at the lowest point of the swing, and the predetermined free-fall height gave the desired vertical velocity at impact. The model was launched at the desired landing attitude by adjustments in the pendulum-to-model interface fixture.

Simulator Test - A sketch of the Mars-gravity simulation apparatus is shown in Figure 6(b). An elastic suspension system using $3/4$ -inch-diameter shock cord was used to produce an upward force countering part of the Earth's gravitational force. Two shock cords, each 100 feet in length, were attached to the vehicle by outrigger trusses mounted in the horizontal plane of the vehicle center of gravity. The two shock cords weighed a total of 40 pounds. The shock cords extended upward to a cable which was run through a sheave attached to the overhead trolley. The sheave was a low friction ball-bearing type and freely swiveled on a ball-bearing swivel. This suspension system allowed the vehicle to pitch, roll, and yaw simultaneously, restricted only by the friction of the sheave. The shock cords were attached to the vehicle through force transducers which were used to monitor the shock cord forces before and during landing.

The vehicle was supported from the overhead trolley by a support cable which was used to hold the vehicle at the drop

height required to produce the needed vertical velocity at impact (Fig. 6(b)). The support cable was attached to the vehicle with an explosive bolt connection. Several attachment points were provided so the force of the support cable would always pass through the vehicle c.g. for the various pitch attitudes tested.

The trolley was mounted on an overhead track which is installed on the existing structure of the Lunar Landing Facility. The track is approximately 200 feet above the landing surface and allows horizontal motion of the entire reduced-gravity system. The trolley is lightweight (21 lbm) and low friction so it would follow vertically above the model.

The procedure used to conduct a landing test was as follows: The vehicle was placed on the landing surface and the shock cords were stretched in tension (about 100% elongation) by power-driven winch and cable systems mounted on the model until the proper force ($5/8$ of the model weight) was registered by the force transducers. This in effect gives a gravitational force of $3/8$ of the vehicle weight. The model was then lifted and attached to the support cable. In the raised or pre-drop position (Fig. 6(b)), the force in the shock cord was slightly less than that required for Mars-gravity simulation. When the model was released by firing of the explosive connector bolt, the force produced by the shock cord increased as the model fell and at impact was correct for Mars-gravity simulation. The change in shock-cord force due to changes in elongation during impact was about 3% of nominal.

The desired horizontal velocity was obtained by use of a falling mass to accelerate the model and trolley. A tow cable was attached to the model so that its force acted in the plane of the vehicle c.g. This cable ran from the model, over a sheave and down to a falling mass (see Fig. 6(b)). Another tow cable ran from the trolley over a sheave and down to the same falling mass. With the model held at the correct drop height needed for the desired vertical velocity and all tow cables taut, the model was pulled back with a release cable to the prelaunch position raising the falling mass so that the drop height of the falling mass was sufficient to produce the desired horizontal velocity of model and trolley. The model was held in the prelaunch position shown in Figure 6(b) by the cable attached to a release mechanism. When the release mechanism was triggered, the model and trolley moved forward accelerated by the falling mass. The contact of the mass with the ground triggered a microswitch which fired the explosive bolt connections and allowed the model to drop and attain the desired vertical velocity. The model tow cable was also disconnected from the model by explosive bolts when the falling mass hit the ground. The trolley tow cable did not disconnect but did become slack when the falling mass hit the ground. The trolley tow cable was of sufficiently low mass to have a negligible effect on the motions of the trolley.

Test Parameters - Landing tests were made at both Earth gravity and Mars gravity on flat and sloped landing surfaces using

relatively stiff and massive wooden frame platforms. The platform was positioned relative to the launch direction of the model in such a manner as to provide positive (uphill), negative (downhill) and cross-slope landings. Surfaces of smooth plywood or very coarse grit material were installed on the platforms in order to obtain landing-gear footpad sliding coefficient of friction values of about 0.4 and 0.7, respectively. Some landings were made onto 6-inch-deep containers filled with compacted roadbed soil material. Nominal model attitude setup conditions were 0° , 5° , and 10° pitch attitude; 0° roll attitude; and 0° yaw attitude. Nominal vertical impact velocity for the free-body (Earth-gravity) tests was 37.6 ft/sec and nominal horizontal velocity was 9.8 ft/sec, which were scaled values of prototype or simulator test (Mars-gravity) velocities of 23 ft/sec and 6 ft/sec, respectively (see Table I). It was intended that both Earth-gravity and Mars-gravity models be tested at identical landing conditions so that direct comparison or results could be made. It was difficult to obtain identical runs for the two model tests, particularly in the case of landing attitudes, but most landings had generally small differences in test conditions. A total of 21 landings were made with eight each of the two test methods used for comparison purposes.

Instrumentation - Normal acceleration was measured at the vehicle center of gravity using a rigidly mounted piezoresistive strain-gage accelerometer. Main strut stroke was measured on each landing gear using rotary potentiometers. Strain gages were attached to all three struts of each landing gear and were calibrated to measure axial force. The signals from the accelerometer, potentiometers, and strain gages were transmitted through trailing cables to the signal conditioning equipment and recorded on frequency modulated magnetic-tape recorders. The limiting flat frequency response for the accelerometer and potentiometers and associated recording equipment was 1000 Hz. The limiting response for the force measurements was 5000 Hz. Acceleration and stroke data were then passed through a 240-Hz low-pass filter and the force data through 880-Hz filters. Motion pictures were used to determine model landing attitudes, velocities, and motions. The above instrumentation was common to both free-body and simulator tests.

RESULTS AND DISCUSSION

The data obtained in the investigation are presented herein as full-scale values at Mars gravity; that is, for comparison purposes, the data from the free-body (Earth-gravity) tests have been converted to full-scale Mars-gravity values using the scale factors shown in Table I.

Simulator Lift Force - In order to simulate a reduced gravity with the simulator described in this paper, a constant upward or lift force should be applied to the vehicle to oppose a portion

of the force of Earth's gravity. Figure 7 illustrates a typical landing time history of the shock cord forces compared with the force levels needed for Mars-gravity simulation. The acceleration trace is used as a reference to indicate the time of initial contact and subsequent impacts. During the impacts or stopping of the model, a surge was initiated in the shock cord due to its inertia which caused force oscillations. This surge and accompanying force oscillations continued until after the landing was completed. The total maximum and minimum lift-force values experienced during the time of main impacts for eight simulator landings are shown in Figure 8. The force values, the sum of readings taken from the two shock cords, are plotted in terms of percent of nominal lift force (700 lbf) for each landing test. The average lift force on the model during the main impacts, the tick marks on Figure 8, was within $\pm 5\%$ of nominal for all the landings except test number one. During five of eight landings, the average force was within $\pm 2\frac{1}{2}\%$ of nominal.

Landing-Gear Forces - Comparisons of landing-gear force time histories for the free-body (Earth-gravity) and simulator (Mars-gravity) tests are shown in Figure 9. These are force pulses experienced during a landing-impact sequence depicted by the sketches A, B, and C. The leading landing-gear leg initially contacted an uphill slope which caused the model to rotate, resulting in a second impact on the trailing pair of legs. During this second impact the leading gear impacted again. The sample forces shown are for the leading leg (leg 1) and one of the trailing leg main struts (leg 2), containing the crushable honeycomb elements, and one of the rigid bipod struts of the trailing leg. The characteristics of the force time histories are very similar for the two types of tests. There is a difference in time, however, between the free-body and simulator tests for the impact of the trailing legs (event B). This difference in time can be attributed to the difference in pitch attitude of the model at initial contact for the two tests.

A computer analysis was exercised and verified by using the experimental landings made during the present investigation. The correct initial contact attitudes for each, the free body and simulator landing shown in Figure 9, were used as inputs for computer runs and the results are shown in Figure 10. The almost identical agreement in event times between experiment and computer for the two test methods are indicative of the agreement achievable with identical experimental conditions. Overall, the time histories show good agreement between all the free-body and simulator tests.

Data showing the correlation of the main strut forces during free-body and simulator tests are presented in Figure 11. The average force measured in all the legs during the crushing of each of the four honeycomb elements is plotted against a line (solid) indicating exact agreement. The agreement is very good between free-body and simulator tests and most of the data fall within the 10% scatter bands indicated by the dashed lines.

Accelerations and Strokes - Time histories of vehicle normal accelerations and landing-gear strokes resulting from the landing shown in Figure 9 are presented in Figure 12 for the free-body and simulator tests. The characteristics of the acceleration and stroke curves are similar and the maximum values are in good agreement for the two test methods. Again, the difference in time between the free-body and simulator case for second impact (event B) is evident.

Data showing the correlation of maximum normal center-of-gravity acceleration for the free-body and simulator landings are presented in Figure 13. All the normal acceleration data obtained are shown plotted against a line indicating exact correlation. The data indicate that good agreement was obtained between the simulator and free-body test methods. Some of the discrepancy occurs because the landing conditions for the simulator landings were not identical to those for the free-body tests. Asymmetric touchdowns and scatter in landing attitudes that occurred for most simulator landings can be attributed in part to wind-induced oscillations of the model in its prelaunch position. In the case of free-body landings, very symmetric landing attitudes were achieved due to the absence of external forces during the free fall and also because of an existing wind screen.

Data showing the correlation of maximum landing-gear strokes for the free-body and simulator landings are presented in Figure 14. All of the stroke data obtained from the main struts for each landing-gear leg are shown plotted against a line indicating exact correlation. In general, the data fit the correlation line but considerable scatter is noted in this comparison. The stroke of the struts is much more sensitive to differences in landing attitudes between the two tests, free-body and simulator, than the other comparison data discussed.

Motions - Based on the time-history results and motion-picture studies, the basic motions and behavior of the vehicle were quite similar during free-body and simulator landing tests. Motion-picture film sequences of the operation of the two test techniques and comparisons of similar landings, free-body and simulator, are illustrative of behavior similarity.

The apparatus used in this investigation for simulating Mars gravity gave almost complete freedom of model angular motion in pitch, roll, and yaw. The overhead track allowed the vehicle to move freely fore and aft. The vehicle moved vertically with small changes in gravity force. Small lateral motions were slightly restrained by the lateral component of force from the shock cord when the vehicle moved away from the center line of the overhead track. Thus, the simulator had five degrees of freedom with some slight limitations in the sixth degree.

During early tests on the simulator, ground winds were observed to cause vehicle attitude oscillations while at the prelaunch position and also to affect horizontal velocity because of the long elastic shock cords and model area exposed to steady

winds or gusts. Flexibility of the support and launch system (cables) could also cause some vehicle oscillations during launch. The dispersion of the vehicle velocity and attitude at initial contact from the preset or desired values is shown in Figure 15. The errors in vertical and horizontal velocity, pitch, roll, and yaw attitude of the vehicle at touchdown are plotted for each of the eight simulator-test landings. During the eight landings, velocity errors of up to 1-1/2 feet per second were experienced. Headwinds in excess of 10 miles per hour caused significant reductions in launch horizontal velocity as noted for test number 4 (Fig. 15). This was subsequently compensated for by adjusting the size of the falling mass or its drop height. Vertical velocity was relatively unaffected by wind and was primarily dependent upon estimation of the proper model drop height to achieve desired contact velocity taking into consideration the varying force of the shock-cord system during the drop time. Errors in pitch attitude of $3\text{-}1/2^\circ$, in roll attitude of $6\text{-}1/2^\circ$, and in yaw attitude of 4° were also experienced. The unusually large error in roll attitude for test numbers 1 and 2 was due to the lack of vehicle directional alinement and damping when conducting tests with only vertical velocity (release and tow cables, Fig. 6(b), were not attached). Attitude errors could be minimized by testing at low wind velocities. Wind observations and the data show that during the last three landings (tests 6, 7, and 8), when the lowest wind velocity existed, the dispersion was generally minimum for all the parameters shown in Figure 15. It appears that landing velocities (vertical and horizontal) within $\pm 1/2$ foot per second of nominal and landing attitudes (pitch, roll, and yaw) within $\pm 2^\circ$ of nominal can be achieved with increased experience and selectivity of operating conditions for the simulator.

CONCLUSIONS

A full-scale dynamic model investigation has been conducted in order to develop and evaluate a full-scale reduced-gravity simulator. Based on the results presented, the following conclusions can be made: 1. A simple and inexpensive elastic cord lift system with associated launching apparatus is a practical method for conducting landing-impact tests of a prototype Viking spacecraft at simulated Mars gravity. 2. Simulator lift force within 5% of that necessary to meet reduced-gravity requirements can be achieved. 3. The simulator provides five degrees of freedom of motion for the vehicle and slight limitation in the sixth degree. 4. The simulator can be easily adapted for investigations of other planetary landers. 5. Best results (accuracy) can be achieved by conducting landings at wind velocities under 10 miles per hour.

REFERENCES

1. O'Bryan, Thomas C.; and Hewes, Donald E.: Operational Features of the Langley Lunar Landing Research Facility. NASA TN D-3828, 1967.
2. Bellman, Donald R.; and Matranga, Gene J.: Design and Operational Characteristics of a Lunar-Landing Research Vehicle. NASA TN D-3023, 1965.
3. Carden, Huey D.; Herr, Robert W.; and Brooks, George W.: Technique for the Simulation of Lunar and Planetary Gravitational Fields Including Pilot Model Studies. NASA TN D-2415, 1964.
4. Hewes, Donald E.; and Spady, Amos A., Jr.: Evaluation of a Gravity-Simulation Technique for Studies of Man's Self-Loocomotion in Lunar Environment. NASA TN D-2176, 1964.
5. Blanchard, Ulysse J.: Model Investigation of Technique for Conducting Full-Scale Landing-Impact Tests at Simulated Lunar Gravity. NASA TN D-2586, 1965.
6. Stubbs, Sandy M.: Investigation of Technique for Conducting Landing-Impact Tests at Simulated Planetary Gravity. NASA TN D-6459, 1971.

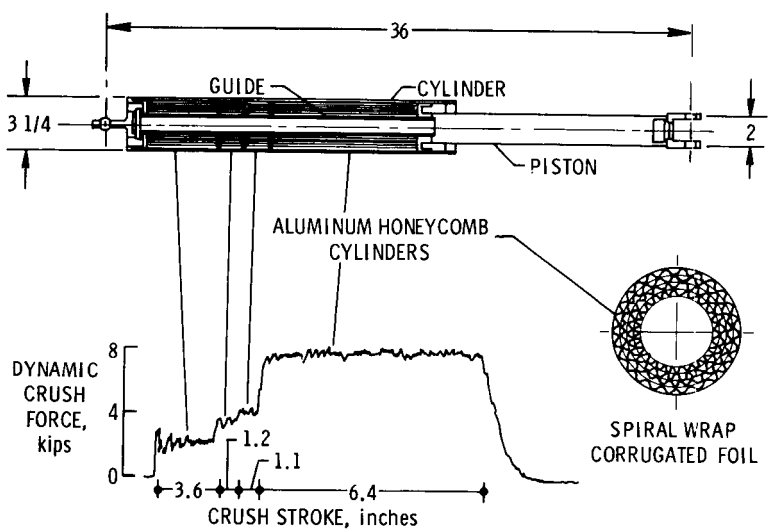


Fig. 3 - Main shock absorber strut.

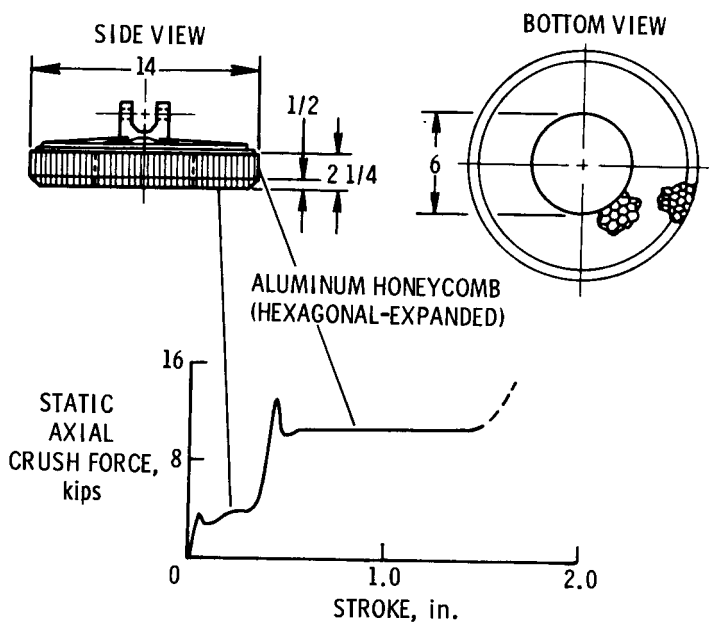
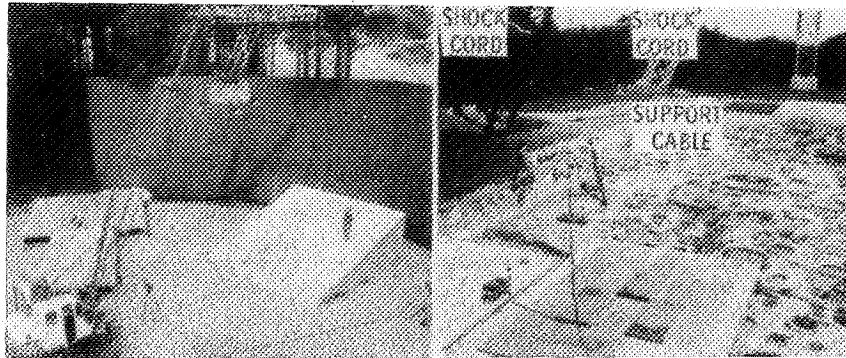


Fig. 4 - Crushable footpad.



(a) Earth-gravity (free-body) tests.(b) Mars-gravity (simulator) tests.

Fig. 5 - Test sites.

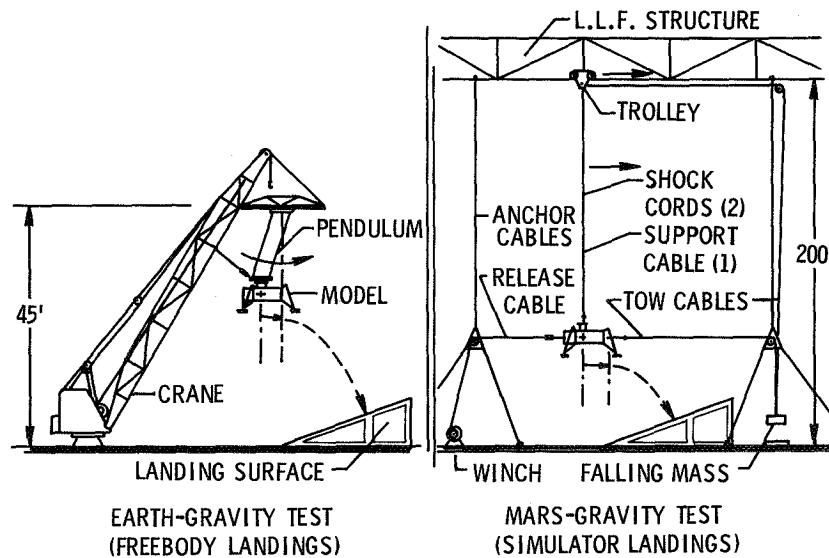


Fig. 6 - Test apparatus.

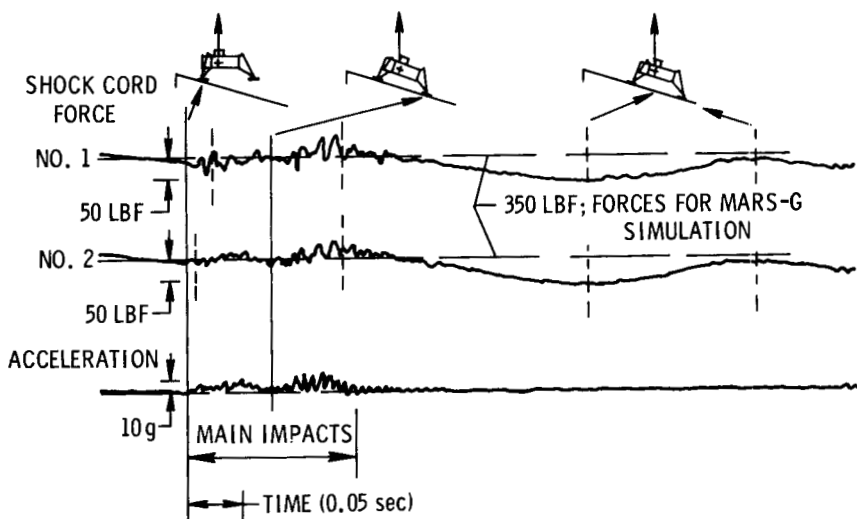


Fig. 7 - Shock cord lift force.

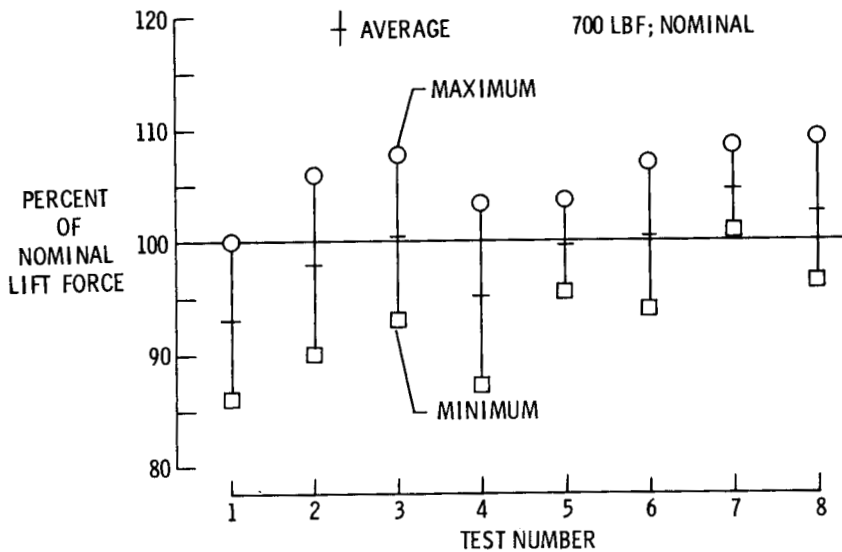


Fig. 8 - Performance of shock cord during impacts.

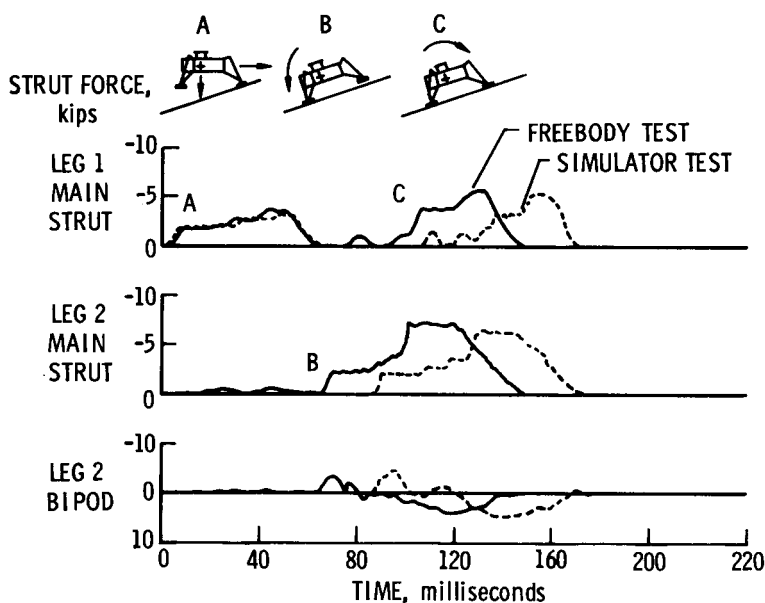


Fig. 9 - Typical landing-gear force time histories.

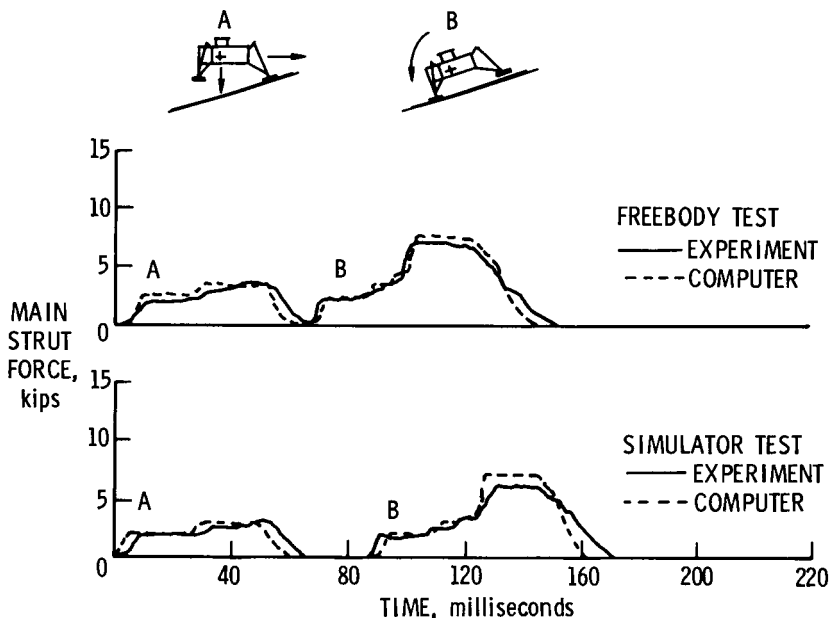


Fig. 10 - Comparison of experimental and computer time histories.

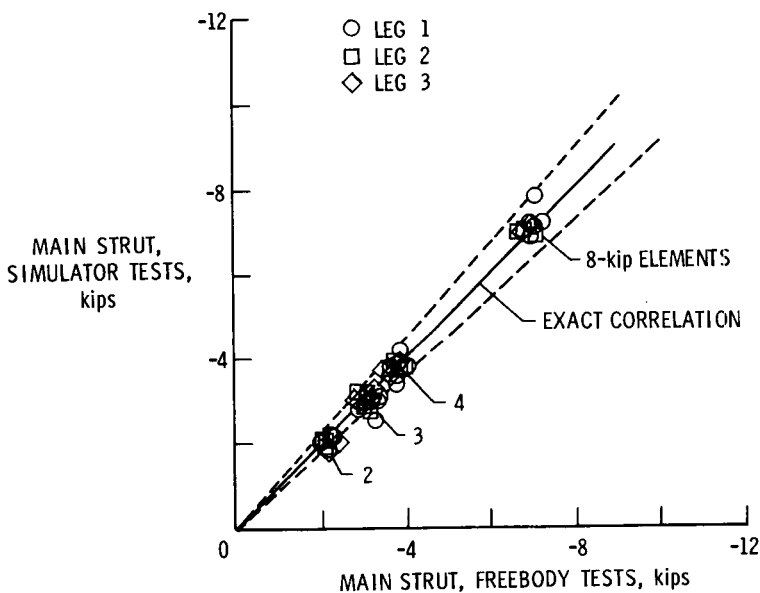


Fig. 11 - Shock absorber force during landing impacts.

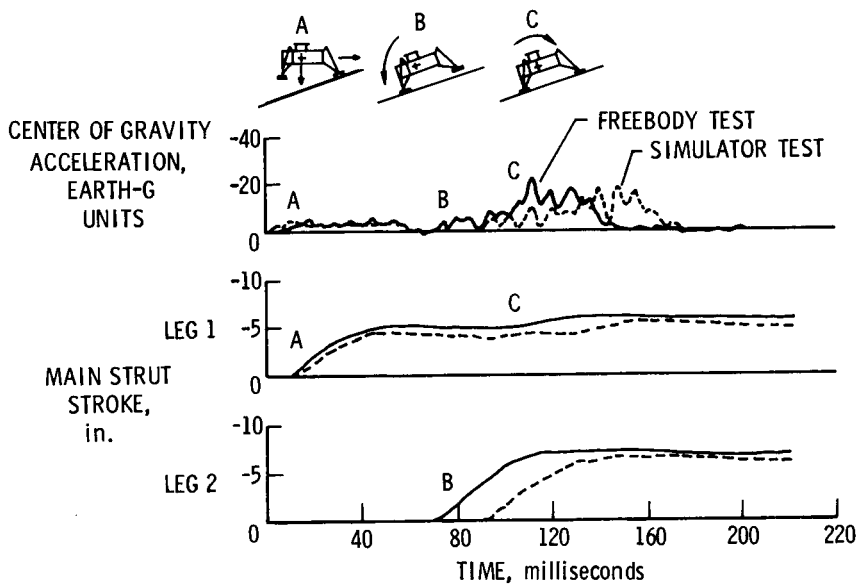


Fig. 12 - Typical acceleration and stroke time histories.

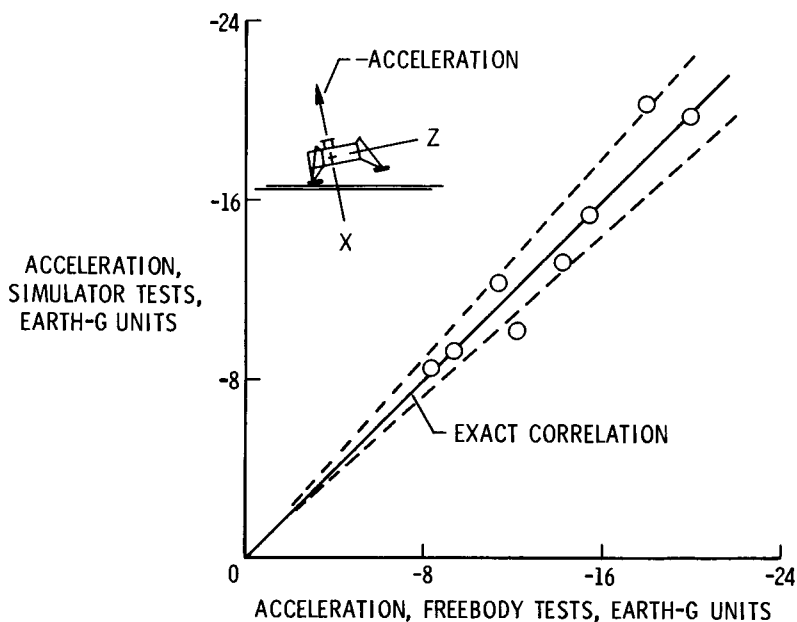


Fig. 13 - Maximum center-of-gravity accelerations.

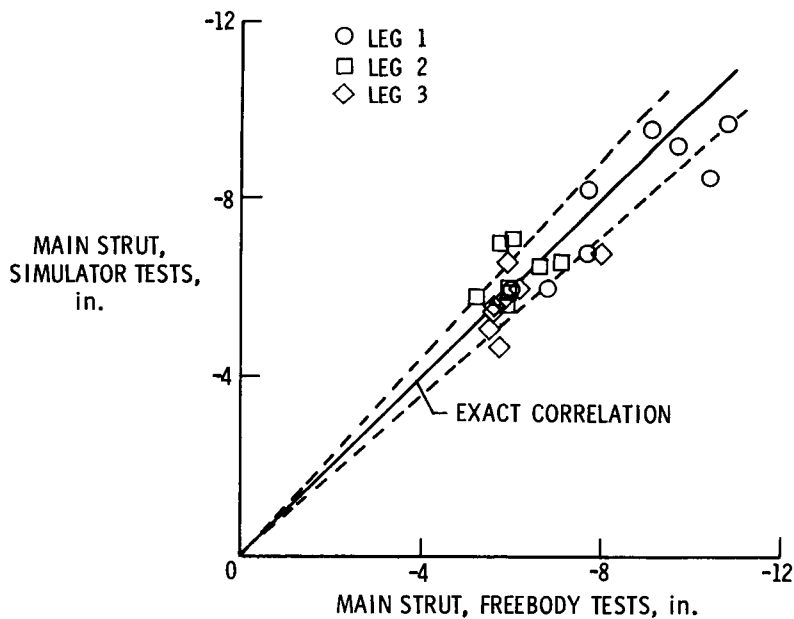


Fig. 14 - Maximum landing-gear strokes.

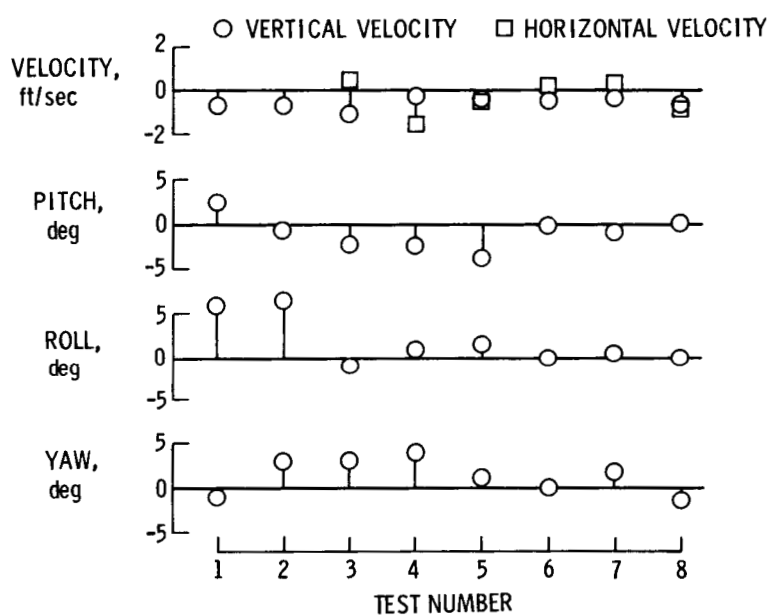


Fig. 15 - Initial landing condition dispersion during simulator tests.

**UTILIZATION OF AEROSPACE AND MILITARY TECHNOLOGY
IN SOLVING MAN'S TERRESTRIAL PROBLEMS**

Malcolm Lillywhite, *Martin Marietta Corporation, Denver, Colorado*

ABSTRACT

The utilization of aerospace and military technology in terrestrial environmental problems, in the outset, appears to be a natural and desirable technology transfer for the industries involved, and the nation as a whole. This paper discusses the subtle advantages and disadvantages of employing existing sophisticated technologies to new problems such as those associated with environmental modifications and pollution.

Particular emphasis is placed on the "new user's" requirements, technological overkill and the transfer system necessary to effectively apply the existing technological asset to solving new problems. Benefit/cost analysis techniques are used to determine which technologies may be economically most effectively used.

**SIMULATION OF WIND EFFECTS ON BUILDINGS
BY MEANS OF WIND TUNNELS**

J. E. Cermak, *Fluid Mechanics Program, Colorado State University,
Ft. Collins, Colorado*

ABSTRACT

Wind effects on earth-bound buildings include stressing of the primary frame, swaying of the structure at its natural frequency, fluxuating loading of cladding panels and glass lights, and adverse environmental conditions at street level. These effects are determined by the distribution of turbulence and mean wind which are related in a complex way to geometry of the building and surrounding structures, topography and local climatological factors.

The development of special meteorological wind tunnels in the last 10 years has made simulation of natural wind characteristics possible in the Laboratory. Because of this capability wind effects on buildings can be simulated and design information obtained from measurements on the small-scale building models submerged in a thick turbulent boundary layer. Studies of wind effects on buildings by this technique include the World Trade Center Towers in New York, the Bank of America, World Headquarters Building in San Francisco, the Standard Oil (INDIANA) Building in Chicago and many others.

AEROSPACE TECHNOLOGY FOR MEDICINE AND BIOLOGY

Jerry V. Mayeux, *Martin Marietta Corporation, Denver, Colorado*

ABSTRACT

This paper discusses examples of aerospace technology which are being applied to research in the medical and biological fields. Problem areas in medicine and biology which could benefit from application of aerospace technology are also being identified for lab. diagnosis (i.e., image enhancement technology and clean room technology applied to surgical rooms).

WATER CONSERVATION THROUGH ADVANCED TECHNOLOGY

J. F. Baxter and L. O. Williams, *Martin Marietta Corporation*

ABSTRACT

United States water use practices were developed in an era of low population density and environment of copious water supply. These practices are too wasteful in current circumstances. Application of recent technology can greatly reduce the consumption of water without compromise of amenities. This technology and its potential impact will be discussed.

**APPLICATION OF THERMODYNAMIC MODELING
TECHNIQUES TO ENVIRONMENTAL POLLUTION**

L. D. Lancaster and B. F. Elam, *Martin Marietta Corporation*

ABSTRACT

This paper presents an existing technique of solving the Fourier Diffusion Equation that can be directly applied to the environmental pollution problem. This technique has been computerized and is now extensively used in the aerospace industry for thermodynamic studies. Also discussed is how physical systems can be represented by math modeling to determine environmental pollution diffusion characteristics. An application of this technique to a fluid system is illustrated. The interrelationship between scaled model testing and the analytical technique is presented.

TECHNOLOGY OF PLANETARY EXTREME ENVIRONMENT SIMULATION

M. E. Wakefield, L. E. Apodaca, C. A. Hall, *Martin Marietta Corporation, Denver, Colorado*

ABSTRACT

FOUR TEST CHAMBER SYSTEMS HAVE BEEN DEVELOPED TO SIMULATE THE EXTREME ATMOSPHERIC ENVIRONS OF THE PLANETS VENUS AND JUPITER TO ASSURE SATISFACTORY PERFORMANCE OF SCIENTIFIC ENTRY PROBES AND THEIR EXPERIMENTS.

INTRODUCTION

As interest in the exploration of other planets in our solar system is increased, it becomes important to establish testing capabilities that will assure success of the space probes developed. The probes and their scientific experiments will be required to survive extreme environments while operating properly during insertion into planetary descent or landing trajectories. The environments of some planets do not fall within the category of simulation covered in this paper. Among these are Mercury, Mars, and Pluto. On the other hand, the environments of Venus, Jupiter, Saturn, Uranus, and Neptune are considered "extreme." Of these planets, the ones most likely to be subject to early interplanetary probe exploration are Venus and Jupiter. Most of the activities covered by this paper concern atmospheric simulation for testing entry probes that will travel to these two planets.

As a planetary probe enters the atmosphere of a planet and descends toward the surface, it is exposed to a variety of environmental factors. Among these are atmospheric temperature and pressure; temperature due to aeroheating; acceleration, shock, and vibrational forces; and impingement of a variety of atmospheric gaseous constituents. Simulation of the environmental factors influencing a probe during the descent portion of the mission forms the basis for the facilities described. The approach taken to date is to provide simulation of the atmospheric pressure, temperature, and gaseous commodities expected and to provide separate testing (corrected analytically as necessary) to assure the probes' compatibility with vibration. The effect of aeroheating during descent is generally duplicated by increasing the temperature above the anticipated environmental temperature to assure equivalent heat transfer into the probe. The pressure and temperature combination is increased at a controlled rate, chosen to match the profile predicted for the de-

scent of a probe.

For a knowledge of these conditions, we must rely heavily on the research performed in evaluating the expected planetary environments. It is somewhat paradoxical that, to evaluate the environment of another planet using an actual probe, a good knowledge of what to expect is necessary to properly design the probe. The early Venus experiments of the USA and the USSR have provided invaluable data for the development of advanced probe designs. Unfortunately, since we have no firsthand data for the Jupiter environment, the parameters used for atmospheric simulation must be developed from data obtained in other ways.

Four facilities for simulation of extreme environments are in use or being built at our Denver installation. These facilities provide a logical evolution of increased test technology through development of techniques and hardware systems. Coined names that have been developed to describe these facilities are Micro-Mini, Mini, Midi, and Maxi Atmospheric Simulation Chambers. The Maxi is the most versatile of the chambers from an environmental simulation standpoint and is a fairly sophisticated facility capable of testing a complete interplanetary probe.

The capabilities of each chamber are described in this paper, along with a description of a variety of tests that have been performed in these chambers.

MICRO-MINI ATMOSPHERIC SIMULATION CHAMBER

When the prospect of entering the field of planetary exploration first presented itself, a number of small component tests were performed to determine if such extreme environments were tolerable to existing hardware items. To perform some of this early testing, a test chamber was assembled and identified as the Micro-Mini Atmospheric Simulation Chamber. This chamber is composed of standard high-pressure carbon steel pipe fittings. When assembled, a test chamber of approximately 36.6 in.³ (600 cc) volume is formed. This chamber is capable of a hydrostatic working pressure of 12,000 psig (8300 N/cm²) at ambient temperature conditions. Instrumentation and pressurization ports are provided through the chamber ends. Figure 1 is an illustration of this chamber.

The chamber is used for the testing of small components. Several electrical feedthroughs have been exposed to high pressure, then checked for leakage and continuity. Typical electronic components (resistors, capacitors, and transistors) have been exposed to the high-pressure environment while their operation was monitored. Most degradation occurred in the transistors, all of which were severely damaged. All of the sapphire windows (which are discussed in further detail in a later section of this paper) were first tested in the chamber to verify structural and seal suitability at high-pressure before being placed in another chamber and subjected to simulated Venusian conditions.

MINI ATMOSPHERIC SIMULATION CHAMBER

The second step in the evolution of test chambers for planetary extreme environments is the Mini Atmospheric Simulation Chamber (Figure 2). To date, this chamber has successfully performed the majority of our extreme environment tests. The chamber is capable of providing a temperature from -40°F (-40°C) at near-vacuum conditions to 1000°F (540°C) at a pressure of 1845 psia (1272 N/cm^2). It is capable of following the temperature/pressure versus time profile predicted for a Venusian entry probe, or may be adjusted to provide steady-state operation with a minimum of monitoring.

The chamber configuration is cylindrical with a welded closure on one end and a flanged entry closure on the other end. It is constructed of ASTM A-106 Grade B carbon steel and has a wall thickness of 1.32 inches (3.35 cm). The interior dimensions of the chamber body are 10 inches (25 cm) in diameter and 33 inches (84 cm) in length with a usable volume of approximately 1.5 cubic feet (43 liters). The internal surfaces of the chamber are nickel-plated for corrosion resistance. The removable mating cap for the flanged entry closure is drilled and fitted for the following feedthrough ports--eight electrical feedthroughs, two 1/2-inch (1.3-cm) diameter pressure ports, and one 1 1/4-inch (3.2-cm) diameter general-purpose port. Test specimens are suspended from the mating cap for insertion into the chamber. A conventional high-pressure seal ring and clamp are used to connect the chamber cap to the chamber body. The chamber is mounted vertically in an insulated shell assembly with the flanged entry closure in the top position. A hoist is provided to handle movement of the mating cap and placement of the chamber into or out of the insulation assembly.

Insulated Shell Assembly

The insulated shell assembly for the chamber is composed of a top half and a bottom half of a hollow cylindrical body. The annular halves of the assembly are filled with expanded mica insulation, which in turn is sealed with a layer of thermal cement at the mating surfaces of the annular halves.

The chamber nests within the hollow core of the bottom annular half of the insulated shell assembly. Woven asbestos rope is used for a thermal seal when the removable top annular half of the assembly is mated to the bottom annular half. A nitrogen purge port is located in the bottom annular half of the assembly for oxidation control and for cooldown of the heated chamber. The outer wall temperature of the assembly is less than 150°F (66°C) when the chamber within is at a stabilized temperature of 800°F (430°C).

Pressurization and Vacuum System

The pressurization and vacuum system for the chamber con-

sists of two independent gas flow circuits and a vacuum circuit (Fig 3). Although nitrogen and carbon dioxide are being utilized in the pressurization system for simulation of Venusian descent conditions, the capability exists for introducing other commodities into the system.

The pressurization and vacuum system is capable of providing pressure from 0.5 psia (0.4 N/cm^2) or less through 3700 psia (2600 N/cm^2) (at ambient temperature conditions) to the chamber. Each independent gas flow circuit in the pressurization system can pressurize the chamber at a rate from 0.1 psi/minute ($0.001 \text{ N/cm}^2/\text{s}$) to 150 psi/minute ($1.72 \text{ N/cm}^2/\text{s}$). The pressure regulation at any given stabilized positive pressure is ± 5 psi (3 N/cm^2) and is automatic.

The carbon dioxide gas flow circuit is heat-traced throughout and is maintained at 150°F (66°C) during test to prevent liquefaction of carbon dioxide in the pressurization lines.

Heating and Cooling System

Heat to the chamber is supplied by band heaters externally positioned around the barrel section that provide a total power of 24 kilowatts. These external band heaters are capable of heating the chamber at a rate of approximately $550^\circ\text{F}/\text{hour}$ (305°C). Supplemental gas heaters are available for mounting within the chamber. At present, the six of these internal heaters being used have a total output of 6300 watts. The external heaters and internal heaters are manually controlled by variable-voltage transformers. Two magnetic circuit breakers and two automatic temperature controllers are used to control the chamber heater system and for overtemperature shutdown of the heater systems. The temperature controller is capable of automatically regulating the temperature of the chamber to $\pm 5.0^\circ\text{F}$ ($\pm 2.8^\circ\text{C}$) of any given stable set point.

When the chamber must be cooled prior to the initiation of a test or following completion of a test, cold nitrogen is injected into the interior and exterior of the chamber. The cooling rate of the chamber from ambient temperature to the desired temperature is approximately 35°F (19°C) per hour. The cooling rate of the chamber from terminal test temperature to ambient temperature is approximately 100°F (55°C) per hour.

Instrumentation System

Information generated from tests conducted within the chamber can be recorded by several different systems. Two of the recording systems are direct visual readout methods that allow the tests to be monitored while in progress. The information recorded by these systems requires manual data reduction. The other systems allow the test information to be recorded and reduced by a digital computer.

TESTS CONDUCTED IN THE MINI ATMOSPHERIC SIMULATION CHAMBER

To date, several types of tests requiring extreme environmental simulation have been performed in this chamber. The following test descriptions represent only a small portion of a logical test matrix that will ultimately guide the design of the components and systems prepared for planetary exploration. As such, the described tests were chosen on the basis of probable general interest and are not intended to indicate that any precise design criteria have been developed as a result of these preliminary tests.

Silicate Phase Stability

Samples of magnesium minerals (forsterite, enstatite, periclase, and magnesite) were crushed and spread in a thin layer on individual stainless steel trays. Possible precursors or reaction products of the minerals were mixed with silicon dioxide and added to selected samples before the samples were spread on the trays. The sample trays, as well as 0.3 cubic inches (5 cc) of water, were sealed within the chamber. The chamber was simultaneously pressurized to 90 earth atmospheres of carbon dioxide, 2 earth atmospheres of nitrogen, and 1 earth atmosphere of oxygen. The chamber was heated to 800°F (430°C) and held at the conditions for four days. It was allowed to cool, was depressurized, and small portions of the samples were removed for X-ray diffraction studies. The chamber was immediately resealed and again heated and pressurized to the experimental operating conditions. This cycle was repeated in an attempt to follow the kinetics of the reactions. Total exposure time at temperature and pressure amounted to approximately 20 days. In a second series of tests wollastonite and calcite were subjected to the same test sequence as the magnesium minerals.

The results of the tests are currently being evaluated for the effect of the data on the design of experiments for future Venus probes.

Venus Probe Circuits

Several different electronic circuit modules representing off-the-shelf components were mounted and instrumented in the chamber, and an operational data baseline obtained prior to test. The chamber was pressurized to 3000 psig (2000 N/cm²) in 500 psig (300 N/cm²) increments. At each increment, data were obtained from the electronic circuit modules. The chamber was depressurized in the same steps with data again being obtained. The pressurization and depressurization cycle was repeated for a second time to verify the data obtained from the first cycle.

High pressure caused two of the electronic circuit modules to fail during the test. Pertinent data were obtained to verify the design of the remaining electronic circuit modules.

Sapphire Window

Several different designs of sapphire windows have been placed in the chamber and tested for structural adequacy. These sapphire windows represent candidate designs for use as observation ports on Venus probes. For each test the chamber was heated and pressurized to obtain a carbon dioxide temperature of 800°F (430°C) and pressure of 1970 psig (1360 N/cm²). These environmental conditions were maintained for a period of several hours while the sapphire windows were checked for leakage.

The first design of a sapphire window proved to be a failure, but careful redesign, with emphasis on the thermal transient resistance of the sapphire seal, resulted in several suitable window configurations.

Cavity Flow Test

The objective of this test was to simulate a probe descent to the surface of Venus and measure heat transfer coefficients that would exist in an observation port of the probe. A carbon steel nozzle with the gas passage machined to simulate the outer skin of a planetary probe was constructed. A cavity was provided in the nozzle gas passage to simulate an observation port in a planetary probe and was instrumented with heat transfer coefficient gages and 0.0010-inch (0.0025-cm) diameter Cr/Al thermocouples. The nozzle was placed in the chamber, which was heated to 880°F (470°C) and pressurized with carbon dioxide to 1175 psig (810 N/cm²). After a stabilization period, the chamber was quickly vented through the test nozzle. The flow of the hot carbon dioxide past the heat transfer coefficient gages simulated the conditions that would be seen in a probe descent to the Venusian surface, and provided data useful for future probe design.

Cloud Particle Sensor Test

A cloud particle sensor was recently tested in the chamber. The objective of the test was to determine if the sensor could survive and operate in a simulated Venusian atmosphere. The sensor is designed to count particles in the micron- through millimeter-size range that are present in the atmosphere by virtue of shadowing a laser beam. The sensor identifies the particles' size and counts them when the particles pass through the laser beam. A portion of the sensor was mounted on the interior of the chamber top, while the sensor instrumentation package was mounted on the exterior of the chamber top and was protected from the chamber heat by insulation and a water coolant plate. This simulated the pressure and temperature protection afforded by an actual probe. The chamber was heated and pressurized to a simulated Venusian carbon dioxide atmosphere of 850°F (450°C) and pressure of 1358 psig (936 N/cm²). During the test, coarse dust, fine sand particles, and bursts of carbon dioxide gas were

injected through the laser beam several different times to determine the sensor's performance. Other operational data for the sensor were also obtained during the test.

The test conducted in the chamber for the cloud particle sensor was successful and obtained pertinent data for the inventor.

Venus Probe Insulation Tests

Several types of insulation being considered for use on a Venus probe configuration that would have insulation external to the pressure shells have been tested in the chamber. The insulation was wrapped to a desired thickness around an aluminum bar of known mass instrumented with several thermocouples. Other thermocouples were embedded in the insulation and also placed on the exterior of the insulation. The insulation sample was placed in the chamber and cooled with cold nitrogen gas. When the aluminum bar and the surrounding chamber environment were stable at -40°F (-40°C), the chamber was evacuated to approximately 0.5 psia (0.3 N/cm^2). Carbon dioxide pressure and temperature were increased manually following the precise conditions currently predicted to act on a probe from initial contact with the Venusian atmosphere through contact with the surface of the planet. By measuring the temperature increase in the aluminum bar and the temperature profile through the insulating material, and using the results of more conventional steady-state insulation tests, information relative to the efficient design of an insulation system for transient use has been generated.

MIDI ATMOSPHERIC SIMULATION CHAMBER

As the third step in the chamber evolution, the Midi chamber (Fig 4) represents the first vessel large enough to test a full-size probe pressure shell. The chamber system is based on a vessel previously used as a solid-propellant rocket motor case. The inside chamber dimensions are 39 inches (100 cm) in diameter and 96 inches (244 cm) long. A 36-inch (91-cm) long tapered nozzle forms a removable closure at one end of the chamber. The chamber barrel section is constructed of 250,000 psi ($172,370 \text{ N/cm}^2$) maraging steel. The nozzle closure is constructed of 4130 and 4340 steels heat-treated to 180,000 psi ($124,100 \text{ N/cm}^2$). The two halves of this chamber are mated in a tongue-and-groove fashion and secured with 88 1.25-inch (3.18-cm) diameter bolts. The two halves are sealed by an O-ring. The chamber is installed in a vertical position with the nozzle section acting as the base for the barrel section. The chamber is rated at a 3000-psi (2068-N/cm^2) operating pressure.

The chamber is a hydrostatic facility only. Its primary intended function is ambient temperature external pressure testing of candidate spherical pressure shells for planetary atmospheric entry.

TESTS CONDUCTED IN THE MIDI ATMOSPHERIC SIMULATION CHAMBER

Test specimens to date are 20-inch (51-cm) diameter hemispheres, candidates for the pressure shell of a planetary probe. Specimens are instrumented with 12 strain gages applied at adjacent points across the thickness of a dome, and with a displacement measuring device fixed to the apex of a dome. The open side of the hemisphere is sealed to a thick plate using an O-ring. Before filling the chamber with water, the volume within a dome is evacuated to help assure a seal. After filling the chamber with water, and after applying moderate pressure, the vacuum is released. From this time through failure of the dome, caution is taken to assure no pressure or buckling resistance is present inside the dome. Pressure in the chamber is increased to provide an external pressure test of the candidate hemisphere to operating pressure or to failure, whichever is desired. Figure 5 shows a candidate hemisphere that failed at 1700 psi (1200 N/cm²).

MAXI ATMOSPHERIC SIMULATION CHAMBER

By far the most extensive undertaking to date is the development of a chamber and its associated support hardware known as the Maxi. The activation of this chamber in the near future will provide a facility that can provide adequate testing to assure that a probe destined for planetary entry is capable of surviving the anticipated environment. In this chamber, probes may be tested independently of any external support equipment, relying solely on their internal power and telemetry links. This provides a rigorous test of the probe's ability to function properly during descent through a planetary environment. The design of this chamber is completed and design of the supporting systems near completion. A summary of its pressure, temperature, and gas capabilities appears in Table 1. Although these are the conditions for which it has been specifically designed, considerable design margin exists in all areas to significantly modify the operational characteristics without appreciably altering the facility. A sketch of the chamber appears in Figure 6. This configuration is the result of a lengthy evolution in size, shape, and material, as well as the location and function of equipment attached to the ports. The basic vessel consists of two halves joined in the center by a conventional bolted flange to allow access to the lower half for test specimen mounting and servicing. The flange requires 24 studs, each 5.5 inches in diameter and 36 inches long, and uses a lens-type seal. This flange configuration was selected after carefully evaluating several other candidate closures of a more quickly operable nature.

The interior size of the chamber is 68 inches (173 cm) high and 56 inches (142 cm) in diameter. Within this volume 4.0 inches (10 cm) of insulation is installed to protect the vessel from the high-temperature gases. All of the ports are 6 inches (15 cm) in diameter except the lower port, which is 10 inches

(25 cm) in diameter.

The basic vessel materials are SA 387 and SA 336 that contain 2.25% chrome and 1.0% molybdenum. The use of a high chromium content steel was necessitated by the hydrogen gas requirement for Jupiter simulations, and the ability of hydrogen to cause embrittlement in most steels. The materials selected represent the result of a detailed study of hydrogen embrittlement effects, confirmed by consultation with the Battelle Memorial Institute of Columbus, Ohio.

The chamber is designed to maintain the temperature distribution of the gas in the chamber uniform to within 10°F (6°C). This necessitated the installation of a recirculation system that could thoroughly mix the gases during transient and steady-state conditions. A unique solution that combined the recirculation system with the gas heater used to heat the incoming gases was developed. A sketch of the combination heater and recirculation system appears in Figure 7. The unit consists of a concentric gas flow duct projecting vertically downward at the bottom of the chamber. A blower located at the bottom receives gas from the center of the duct and returns it to the chamber through the duct annulus. The heating element that imparts thermal energy into the gases is located in the annulus. This arrangement allows maintenance of the blower or heater without disturbing the main vessel or its insulation. Circulation ducts arranged within the main vessel distribute the gases to and from the heater as necessary to provide the proper temperature distribution. In this way a maximum usable space is maintained within the chamber for test item and associated hardware location.

Insulation

To protect the vessel structure from the extreme temperatures expected, internal insulation for the chamber and its attachments was provided. One of the most significant problems during design of the chamber system was the insulation type and its effectiveness with the variety of gases specified. From the insulation data available, it was determined that carbon dioxide should require minimum insulation. It was also determined that hydrogen with its very small molecule and a thermal conductivity approximately an order of magnitude higher than that of carbon dioxide would require the most insulation. No data, however, were available to evaluate the insulating materials at the combinations of high temperature and high pressure we expected to experience. To be certain of our values for insulation conductivity, it was decided to conduct some simplified insulation tests at the required conditions. The results of the testing considerably altered our proposed insulation design. Figure 8 is a graph of the general insulation characteristics determined as a function of temperature, pressure, and gas commodity. As will be noted, carbon dioxide represents the most significant conductivity problem. Although the gas

characteristics that dictate this behavior are not completely understood, it appears that a form of free convection may occur that forces mixing of the gas through the insulation at a rate making the contribution either of the still gas conductivity or the insulation fiber conductivity relatively insignificant. One of the factors that lead to this conclusion is the large difference in conductivity data obtained as a function of test fixture orientation. It was determined that tests using a vertical test plate yielded significantly higher conductivity data than tests using a horizontal test plate. Additional work is planned to further define these phenomena.

SUMMARY

Use of the four described chamber facilities has allowed a beginning to be made in the evaluation of materials, components, and systems that must eventually be designed for compatibility with the extreme environments of other planets. As the field of tests performed broadens, the results compiled will form a valuable guideline for designers of the space probes and of the experiments that must be incorporated in these probes. Finally, the qualification of complete flight assemblies will provide ultimate assurance of the success of space probes sent to other planets of our solar system.

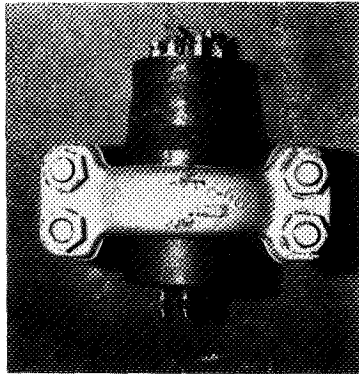


Fig. 1-Micro-Mini Atmospheric Simulation Chamber

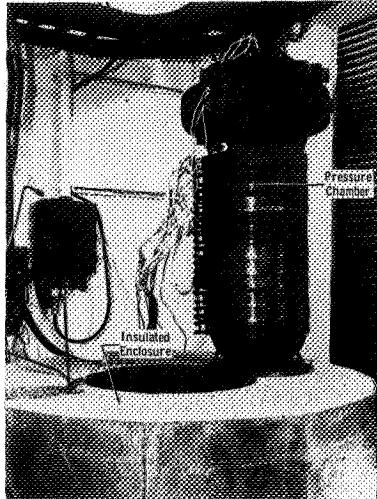


Fig. 2-Mini Atmospheric Simulation Chamber

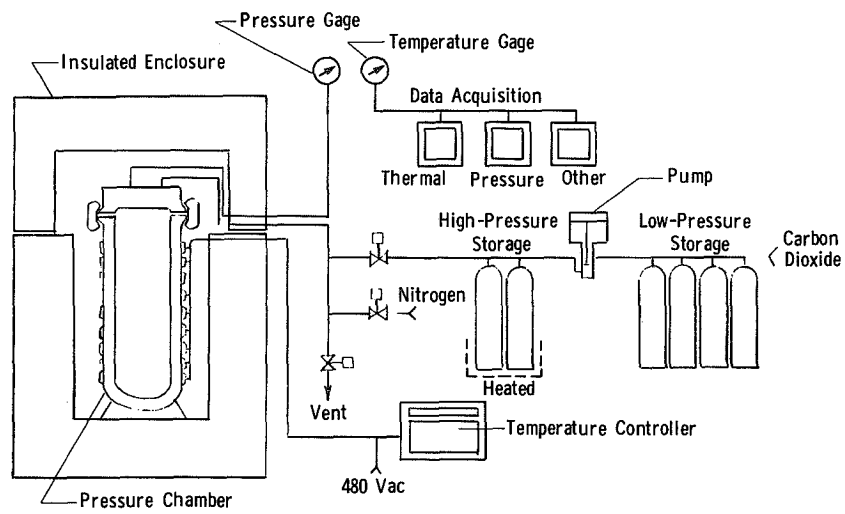


Fig. 3-Mini Atmospheric Simulation Chamber System

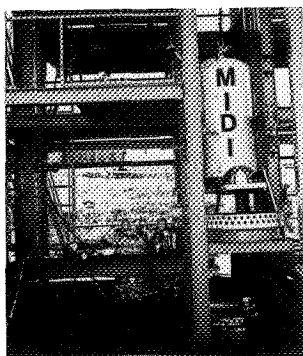


Fig. 4-Midi Atmospheric Simulation Chamber

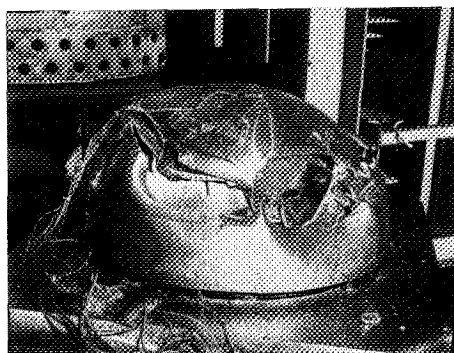


Fig. 5-Midi Atmospheric Simulation Chamber Test Specimen

Table 1-General Capabilities of Maxi Atmospheric Simulation Chamber and Support System

VENUS ATMOSPHERE			
175 Earth Atmospheres			
1000°F			
Descent Profile in 45 Minutes or More			
Constituents:			
(By Volume)	CO ₂	90 to	100%
	N ₂	3 to	10%
	A	3 to	7%
	H ₂ O	0 to	1%
JUPITER ATMOSPHERE			
400 Earth Atmospheres			
1500°F			
Descent Profile in 60 Minutes or More			
Constituents			
(By Volume)	H ₂	50 to	95%
	He	5 to	45%
	NH ₃	3 to	7%
	CH ₄	3 to	7%
	H ₂ O	0 to	1%

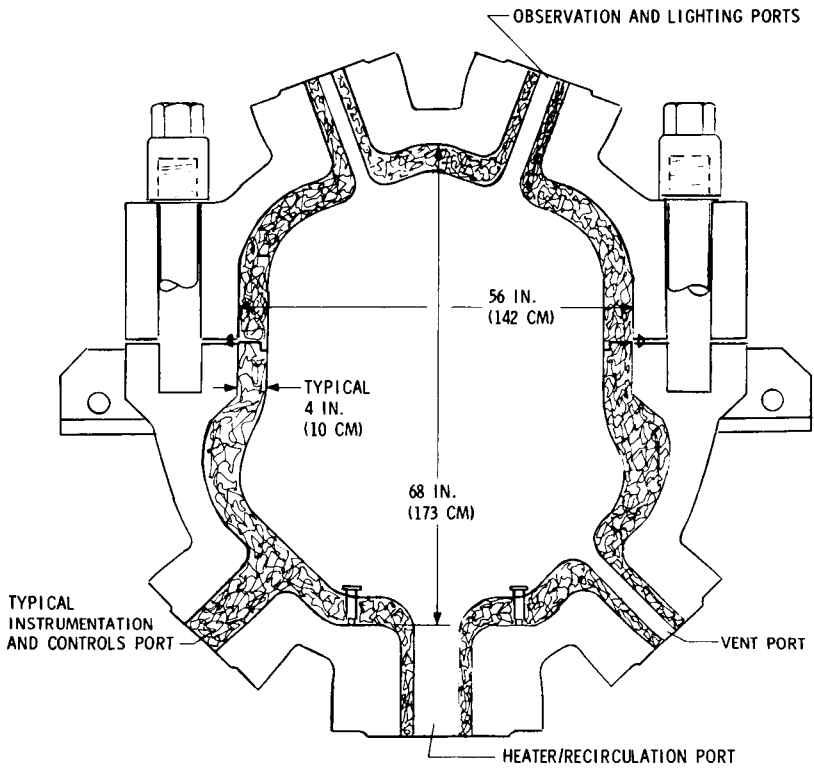


Fig. 6-Maxi Atmosphere Simulation Chamber

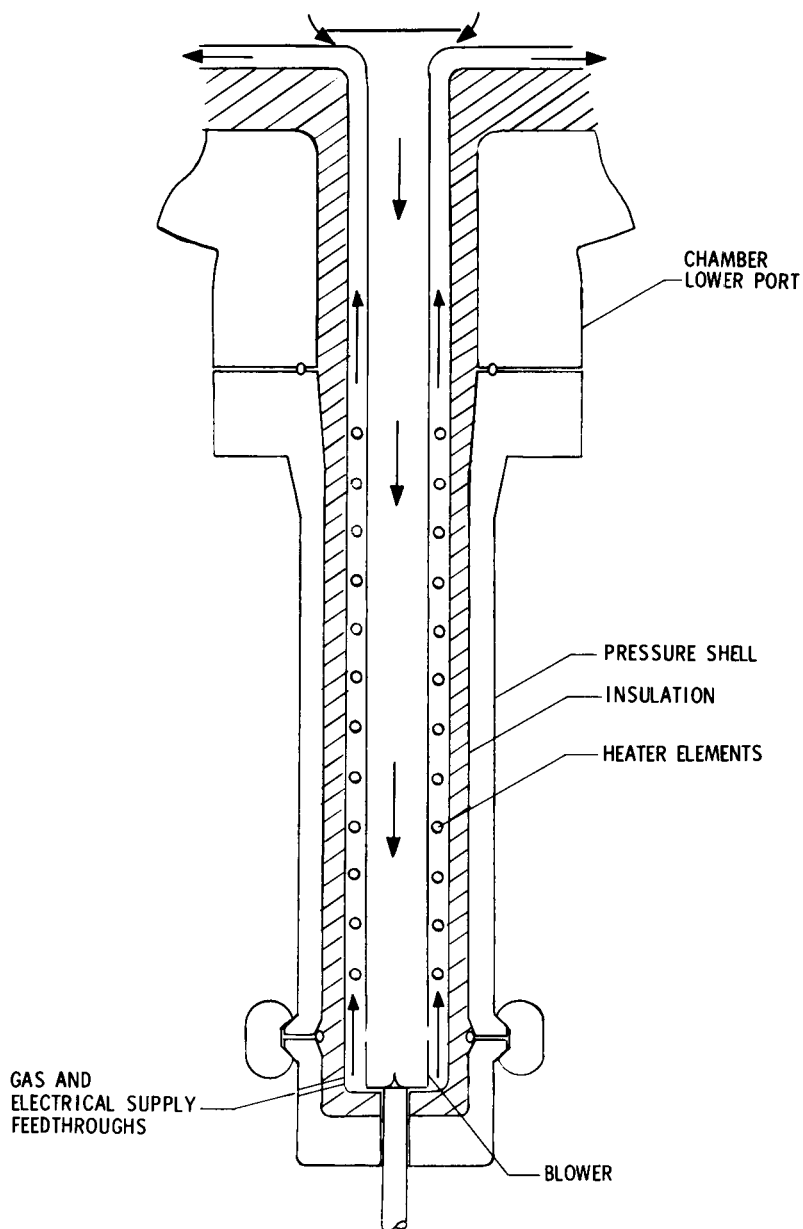


Fig. 7-Heater/Recirculation System

Existing Data

(1) Typical Fibrous Insulation, 0 to 450, CO₂, Vertical & Horizontal

Generated Data

(2) Typical Fibrous Insulation, 3000 psi, CO₂, Horizontal

(3) Typical Fibrous Insulation, 3000 psi, Helium Vertical

(4) Typical Fibrous Insulation, 3000 psi, CO₂, Vertical

(5) Typical Castable Refractory 3000 psi, CO₂, Vertical

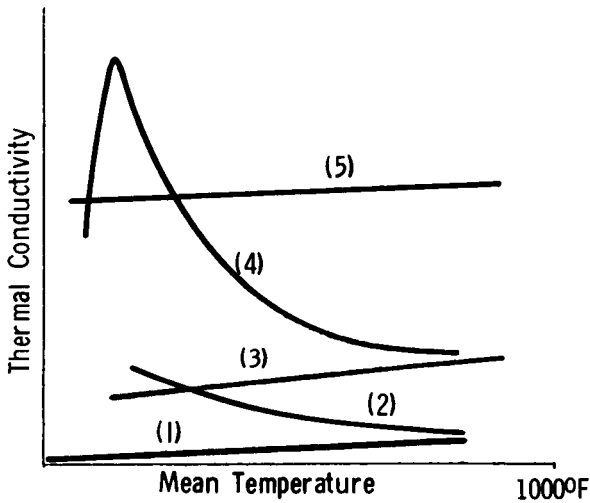


Fig. 8-Typical Insulation Characteristics at Elevated Temperature and Pressure

**DETERMINATION OF TRACE IMPURITIES OR COMPONENT POLLUTANTS
IN AMBIENT GAS SAMPLES USING A COMBINATION OF GAS CHROMAT-
OGRAPHIC AND INFRARED TECHNIQUES**

Jack Smith, *Martin Marietta Corporation*

ABSTRACT

Most pollutants (impurities or components) found in the PPM range in various atmospheric media may be identified and quantitated with combination methods that utilize gas chromatographic and infrared equipment and techniques. The use of such an analytical measurement regime, which was developed to study vacuum effects, is applied to atmospheric pollution problems.

OPERATING CHARACTERISTICS OF THE AIR FORCE FLIGHT DYNAMICS LABORATORY 50 MEGAWATT HYPERSONIC TEST LEG

J. C. Beachler and W. A. Kachel, *AF Flight Dynamics Laboratory, Wright-Patterson Air Force Base, Ohio*

ABSTRACT

A 50 megawatt hypersonic arc wind tunnel with up to 5.0 foot diameter test sections has been developed for thermostructural tests of lifting entry vehicles.

INTRODUCTION

Recent requirements for lifting reentry systems have placed strong emphasis on economical thermal protection techniques. The 50 MW Facility's Hypersonic Test Leg (HTL) was developed by AFFDL to extend the nation's ground test capability for lifting entry vehicle thermal protection systems.

The facility was designed to permit thermostructural evaluation of full scale system components in a hyperthermal environment for test durations corresponding to real time flight profiles.

Facility Description

The 50 MW HTL is an arc heated continuous wind tunnel which produces hypersonic test flows up to 5.0 ft in diameter with centerline stagnation temperatures up to 10,000°R.

The test circuit shown in Figure 1 consists of the 50 MW high voltage arc heater, a hypersonic nozzle, test cabin with model injection system, hypersonic diffuser, heat exchangers, and a 5-stage vacuum system of steam ejectors and mechanical pumps.

The high pressure high voltage arc heater shown in Figure 2 heats up to 7 lbm/sec of high pressure air to centerline stagnation enthalpies (H_0) of 6400 Btu/lbm at 125 atmospheres pressure and can use up to 52 megawatts of electrical power. This air is expanded from the heater throat through an axisymmetric divergent nozzle to a hypersonic exit Mach number. Conical nozzles of 2.0, 3.5, and 5.0 ft exit diameter are presently available.

The test section is of the free jet type with the optional geometries shown in Figure 3. A hydraulic servo-controlled model injection system can maneuver models through the pitch and roll range indicated. Various pneumatic, electronic, and optical probes for flow diagnostics are also located in the test section.

The test flow is slowed by a water cooled hypersonic diffuser and then cooled through a three stage heat exchanger prior to entering the vacuum pumping system.

The vacuum system consists of a 1,000,000 cubic feet per minute two-stage steam ejector and three stages of mechanical pumps. It can exhaust 10 pounds of air per second at 1 mm Hg inlet pressure. Typical tunnel instrumentation used during facility performance tests is shown in Figure 4.

Arc Heater Characteristics

The arc heater employs two water cooled tubular copper electrodes in coaxial-tandem arrangement as shown in Figure 2. The air is heated with a direct current arc which is vortex stabilized along the axis of the electrodes. The arc attachment points are rotated and stabilized longitudinally by the air vortex and electromagnetic coils.

Operating characteristics of the $N=4^1$ heater with various throat sizes from .900 to 2.00 inch diameter are described in References 2 and 3. However, the initial test requirements for the HTL required an untried heater configuration using a 1.5 inch diameter throat with a 72 inch front electrode.

Tests were conducted to determine the operating range of the heater with 1.5 inch throat, 72 inch front electrode, and without front spin coil during the tunnel shakedown operation. A typical operating characteristic is shown in Figure 5. The heater operating map in terms of stagnation pressure and energy balance enthalpy is shown in Figure 6.

Facility Performance

The operating range of the facility with this heater, a 3.5 foot exit diameter conical nozzle, and the 1,000,000 cfm exhaust system was explored during shakedown tests in late 1970.

The DC power to the arc heater was determined by monitoring the operating voltage and current. The air mass flow rate was measured with a subsonic venturi located upstream of the heater and the heater stagnation pressure was measured at the rear of the rear electrode on the centerline as recommended in References

¹Heater scale factor described in Reference 1.

1-4. The flow rates and temperature rise of the heater coolant water were used to calculate efficiency and heat balance enthalpy:

$$H_{O_{HB}} = [EI - (\dot{w}C_p \Delta T)_{H_2O}] / \dot{w}_{air} + H_{air \text{ initial}}$$

The heat balance or bulk enthalpy is an average measurement and is normally less than the test flow centerline value due to the use of highly cooled nozzle and front electrode walls and the centrifuging action of the arc stabilizing vortex which tends to concentrate the hot, less dense plasma near the centerline of the heater. However, since an accurate direct measuring enthalpy probe was not available for local test flow measurements, the data in Figures 5 and 6 are presented using the heat balance values of H_O . A summary of facility performance as determined during the shakedown tests with the 3.5 foot nozzle is shown in terms of arc heater stagnation pressure and heat balance enthalpy in Figure 6.

Typical radial profiles of impact pressure (P_{t2}) and heat transfer rate (\dot{q}) taken with steady state water cooled probes are shown in Figures 7 and 8 from Reference 5. The centerline H_O estimated for laminar heating is 3800 Btu/lbm which is about 1.25 times the heat balance value. This "peaking ratio" is typical over most of the heater operating range. Figure 9 shows the projected facility test range with the 2.0, 3.5, and 5.0 foot diameter conical nozzles in terms of $\dot{q}\sqrt{R}$ and impact pressure. These heating rates are based on test flow centerline H_O using a peaking ratio of 1.25.

The pressure and temperature measurements shown in Figure 4 were taken during facility shakedown operation to evaluate diffuser pressure recovery, heat exchanger performance, and vacuum pumping system characteristics.

The HTL diffusers are of similar geometry to those described in Reference 4. They consist of an inlet collector cone, a straight cylindrical throat, and a divergent conical subsonic exit section. Since the primary reduction in flow velocity occurs through boundary layer growth and an attendant oblique shock system in the cylindrical throat, the throat area and length are the critical design parameters. A throat-area to nozzle-exit-area ratio of 1.20 with a throat length to diameter ratio of 12-15 has given a good compromise between diffuser recovery and model blockage limits in the AFFDL hypersonic facilities.

The heat exchanger is a water cooled transverse tube bank type designed for the low Reynolds number range of the hypersonic facility.

All test leg components performed satisfactorily during these shakedown runs. Reference 4 gives a detailed description of similar arc tunnel components and their expected capabilities. Diffuser pressure recoveries up to 50% of test section impact pressure and heat exchangers which remove up to 90% of the total stream energy are typical.

Summary and Future Plans

The AFFDL 50 MW Facility's Hypersonic Test Leg is operational with both the 2.0 and 3.5 foot nozzles. Shakedown tests have demonstrated the adequacy of the steam ejector pumping system and the heat exchanger over the range of the N-4 arc heater with a 1.5 inch throat and 72 inch front electrode.

Pressure and heat transfer surveys have demonstrated that the test flows are steady and axisymmetric. Runs up to 20 minutes duration have been routinely accomplished.

The 50 MW HTL has been used in performing thermostructural tests on high temperature panel and leading edge models of lifting entry systems concepts for the AFFDL Structures Division since late 1970 (Reference 6).

Future plans include checkout of the facility over the full projected test range with the 3.5, 5.0 and 6.5 foot nozzles, increasing arc heater pressure to 150 atmospheres, and increasing the heater power supply capacity.

REFERENCES

1. R.C. Eschenbach and G.M. Skinner, "Development of Stable High Power, High Pressure Arc Air Heaters for a Hypersonic Wind Tunnel", WADD-TR-61-100, July 1961.
2. R.T. Smith and J.L. Folck, "Operating Characteristics of a Multi-Megawatt Arc Heater Used with the Air Force Flight Dynamics Laboratory 50 Megawatt Facility," AFFDL-TR-69-6, April 1969.
3. J.C. Beachler, "Operating Characteristics of the Air Force Flight Dynamics Laboratory Reentry Nose Tip (RENT) Facility", National Bureau of Standards Special Publication 336, Paper No. 55, September 1970.
4. J.C. Beachler, "Design and Shakedown Operation of the Air Force Flight Dynamics Laboratory's 2 Ft (4 Megawatt) Electro-Gasdynamic Facility", FDM-TM-68-3, July 1968.
5. E.G. Brown-Edwards, "Calibration of the 3.5 Foot Nozzle-- Summary of Preliminary Calibration Data", FXE Test Report HTN3-1, June 1971.
6. L.F. Scuderi, "Analysis of the Tantalum Panel Tests Series I", FXE-TM-71-14, August 1971.

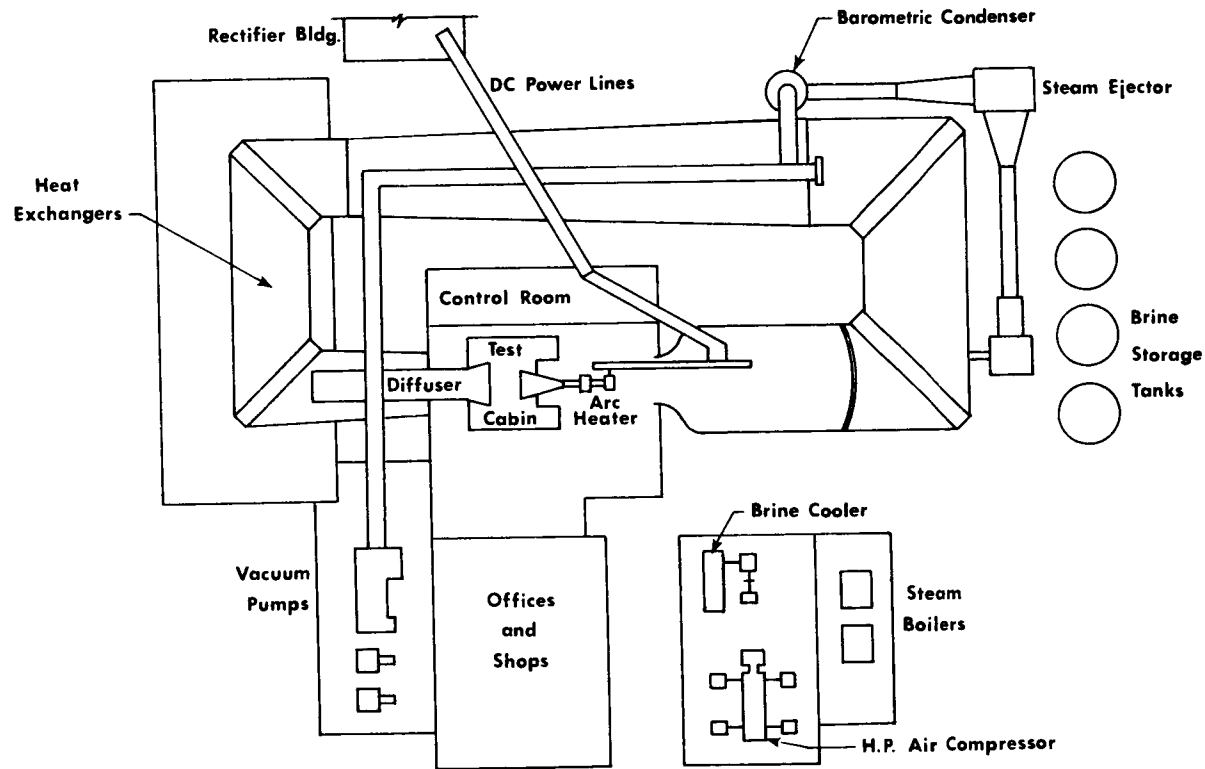


FIGURE 1. 50 MW HYPERSONIC TEST LEG SCHEMATIC

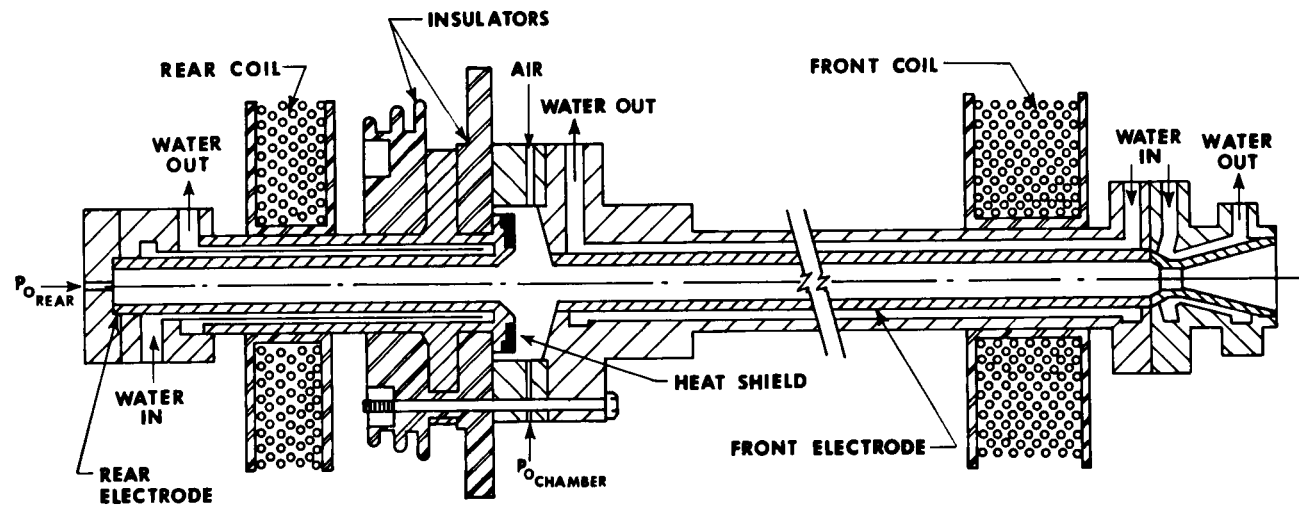


FIGURE 2. ARC HEATER SCHEMATIC

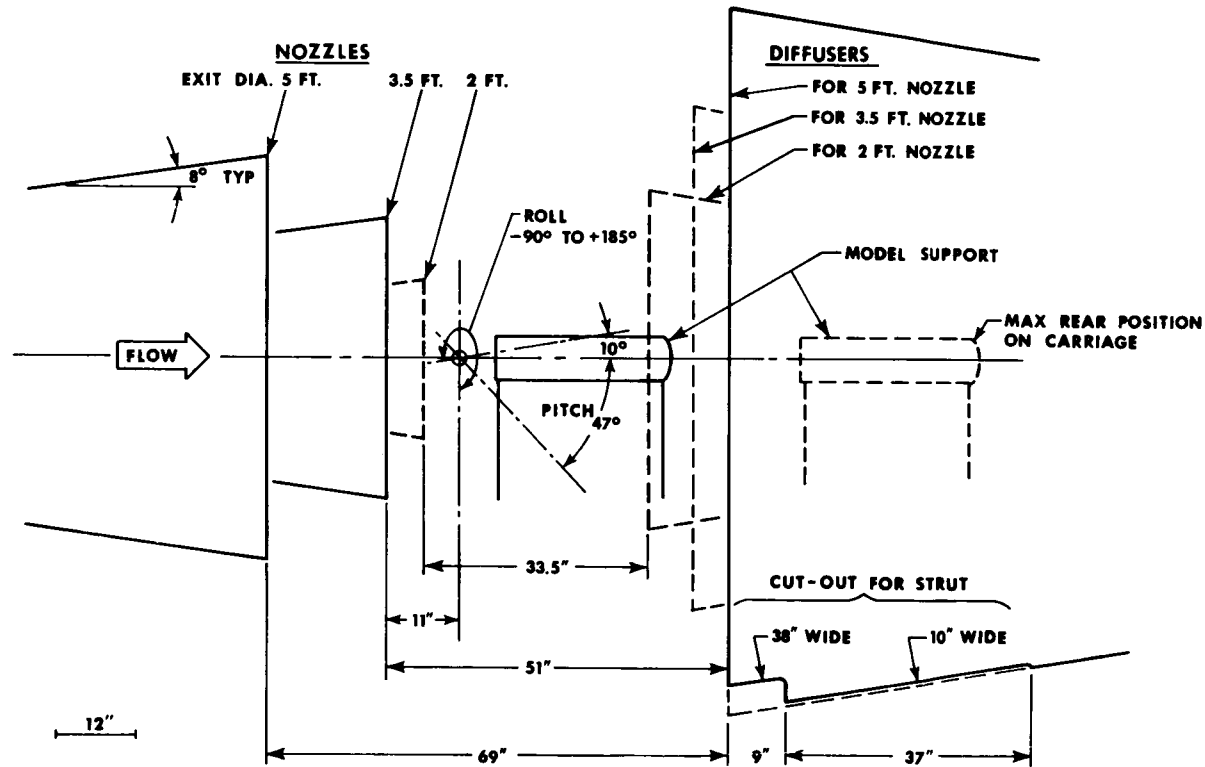


FIGURE 3. TEST SECTION GEOMETRY, HYPERSONIC TEST LEG

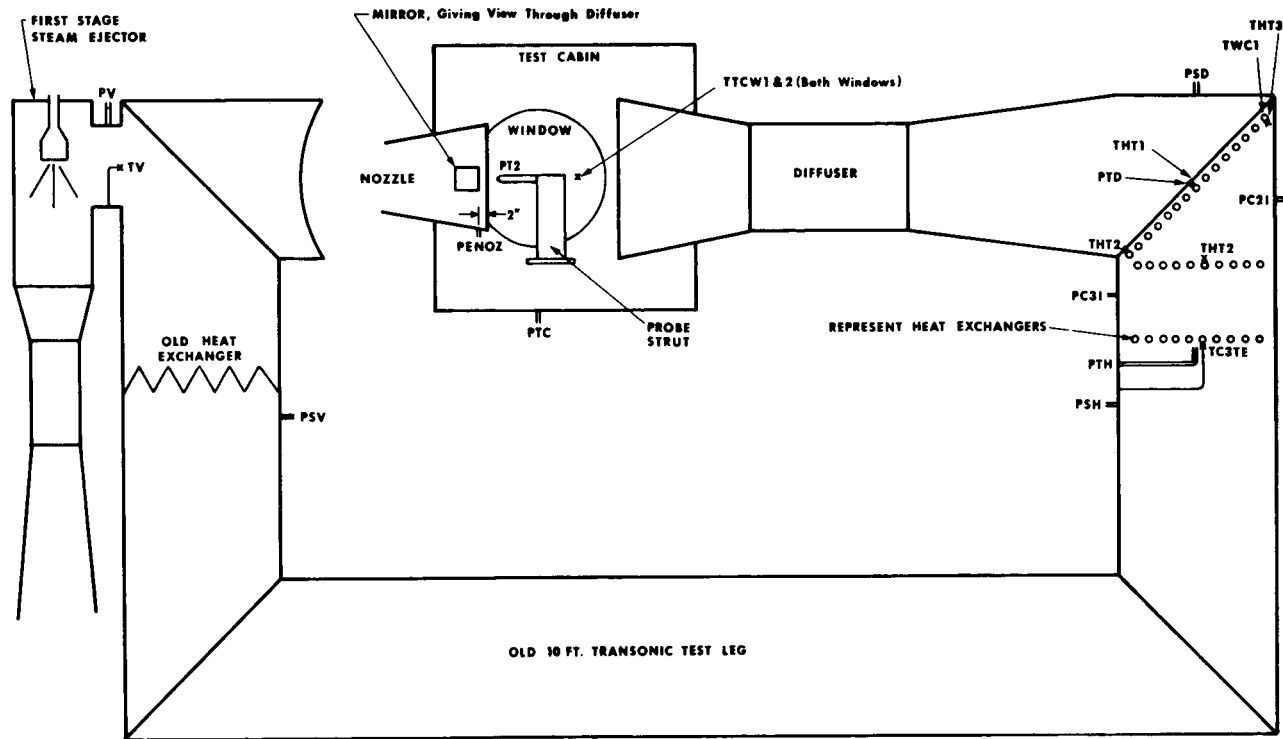


FIGURE 4. SCHEMATIC OF TEST LEG INSTRUMENTATION

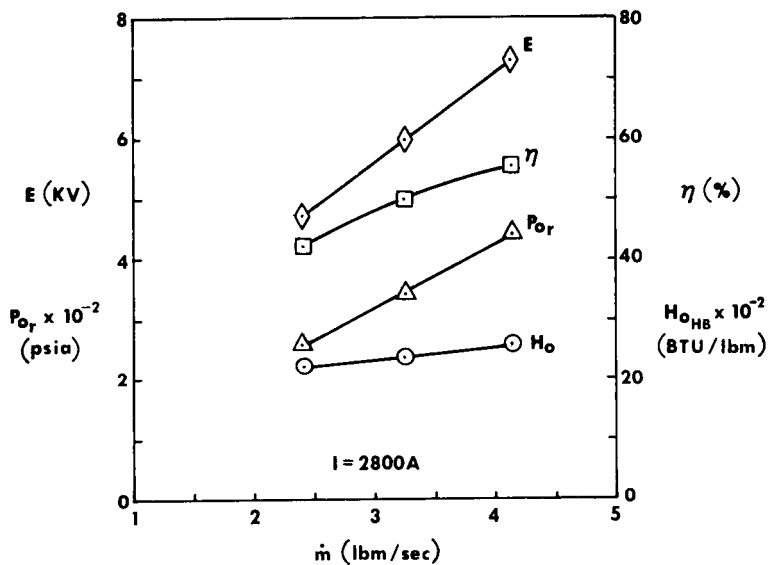


FIG. 5 N=4 OPERATING CHARACTERISTICS
 $d^*=1.50$, 72 INCH FRONT ELECTRODE

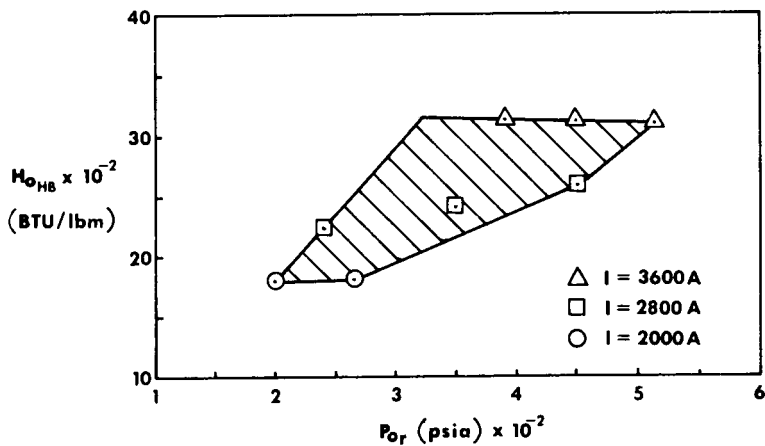


FIG. 6 N=4 ARC HEATER OPERATING RANGE
 $d^*=1.50$, 72 INCH FRONT ELECTRODE

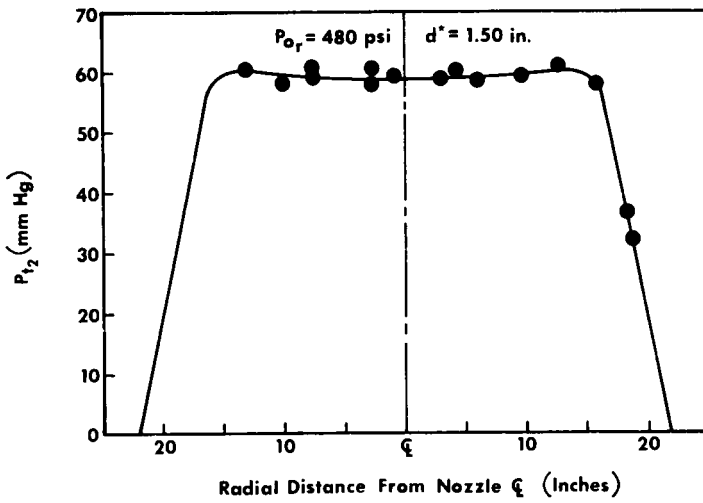


FIG. 7 IMPACT PRESSURE PROFILE OF 3.5 FT. NOZZLE (REF. 5)

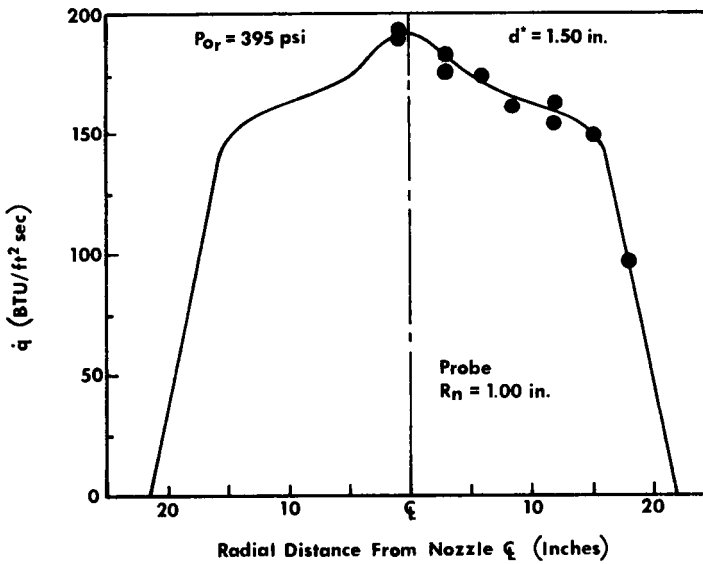


FIG. 8 HEAT FLUX PROFILE OF 3.5 FT. NOZZLE (REF. 5)

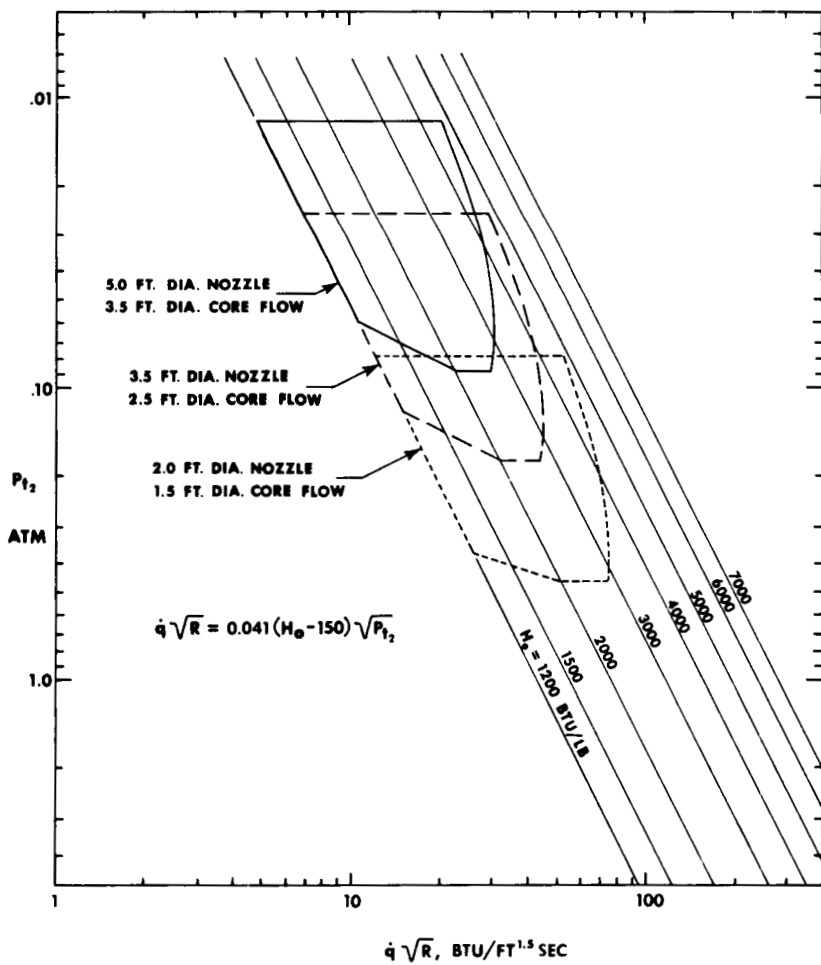


FIGURE 9. PROJECTED STAGNATION POINT HEATING CAPABILITY OF THE HTL

MOLECULAR BEAM SIMULATION OF PLANETARY ATMOSPHERIC ENTRY - SOME RECENT RESULTS

J. B. French and N. M. Reid, *Institute for Aerospace Studies, University of Toronto*; A. O. Nier and J. L. Hayden, *School of Physics and Astronomy, University of Minnesota*

ABSTRACT

Progress is reported in the development of molecular beam techniques to simulate entry into planetary atmospheres. Molecular beam sources for producing fast beams containing CO_2 and atomic oxygen are discussed. Results pertinent to the design and calibration of a mass spectrometer ion source for measurement of the Martian atmosphere during the free molecule portion of the entry trajectory are also presented. The shortcomings and advantages of this simulation technique are discussed, and it is demonstrated that even with certain inadequacies much information useful to the ion source design was obtained. Particularly, it is shown that an open cavity configuration retains sensitivity to atomic oxygen, provides reasonable signal enhancement from the stagnation effect, is not highly sensitive to pitch and yaw effects, and presents no unforeseen problems in measuring CO_2 or atomic oxygen. Hence the simulation techniques used are shown to provide invaluable assistance in designing, developing, and (potentially) in testing and calibrating the required flight instrument.

INTRODUCTION

At the Fourth IES-AIAA-ASTM Space Simulation Conference in 1970, a review was presented on the simulation of flight through planetary upper atmospheres using molecular beam techniques¹. This paper covers subsequent developments in the simulation technique and results obtained as a result of a collaborative program between the Universities of Minnesota and Toronto, specifically aimed at providing initial information for the design of the ion source region of a mass spectrometer. This spectrometer is to

Acknowledgement:—This work was performed for the Martin Marietta Corporation under Contracts RCL-20170 and RCL-207000 as part of the Viking Project. We wish to acknowledge the encouragement and support provided by Martin Marietta personnel, particularly W. S. Chamberlin, and by R. J. Duckett, Viking Project Office, NASA Langley. The financial support of the Canadian Defence Research Board and National Research Council in providing funds for facility development is also gratefully acknowledged.

provide quantitative atmospheric compositional information during the free-molecular phase of entry into the Martian atmosphere of the Viking entry vehicle. The ion source is in the form of a partially stagnating cavity mounted on the front face of the entry vehicle heat shield, and in this form the ions are sampled from a bimodal molecular population in the source - the incoming undisturbed atmospheric molecules which have not as yet collided with the vehicle, and the reflected molecules which have a density and composition dependent on surface reflection processes in the source cavity. Complications exist in interpreting the contributions to instrument response of both parts of this population as discussed below; nevertheless this semi-stagnating configuration is of great interest because it offers sensitivity to reactive species such as atomic oxygen, it provides reasonable signal enhancement from the stagnation effect, it need not be highly sensitive to pitch and yaw effects, it presents no unforeseen problems in interpretation and calibration for gases such as the dominant CO_2 of the Martian atmosphere, and it minimizes errors due to outgassing or filament chemistry. How these conclusions were reached is covered in this paper in order to discuss the utility of the simulation techniques used.

FORMULATION OF SIMULATION REQUIREMENTS

Most mass spectrometers flown on rockets or satellites to date have been statically calibrated, that is, the instrument response determined for known densities of gases in the ion source under completely thermalized conditions. Due to the high vehicle speeds, the reactive nature of atmospheric species, and sometimes gauge conditioning and time response problems, difficulties in interpreting flight data arise. It was therefore felt necessary to study the ion source region in a dynamic simulation approximating insofar as possible the Martian entry condition. Exposing the ion source region to a high speed high Mach number molecular beam in a molecular sink cavity would provide the closest available approximation to the flight condition.

In flight, the atmospheric CO_2 molecules will be impacting at the 4.5 km/sec Martian entry velocity in a highly ordered Mach 15 stream, with an energy of about 3.8eV per CO_2 molecule. Since the ion extraction fields strengths are of comparable magnitude to this in the ion formation region, it would be expected that ion collection efficiencies for ions formed from these energetic neutrals would be very different than for a randomized gas, and that pitch and yaw, which would introduce velocity components transverse to the ion extraction direction, would influence ion collection from the incident molecules crossing the ion formation region. Further, pitch and yaw influence the source geometry presented to the flow and hence affect the density of the reflected cloud of molecules in the ion formation region. Thus it is necessary to use a molecular beam possessing as nearly as possible the flight velocity and Mach number, and it is also necessary to be able to pitch and yaw the

ion source in this beam. The lateral extent of the beam need only be large enough to fully illuminate the ion source region, since all other molecules rebounding from the heat shield do not influence the signal.

The density of the reflected molecules of each species is influenced not only by the source geometry but also very much by the accommodation or adjustment toward a distribution of reflected velocities corresponding to wall temperature. The accommodation process is complex and is a strong function of the gas molecule-surface molecule mass ratio, incident velocity and angle. Hence it is influenced by adsorbed gases or contamination in the source region, so that ideally the source should be in the same clean and identifiable state as it will be after its journey to Mars. This is a very difficult simulation requirement to meet, but it obviously would be assisted by a molecular sink capability around the test region to prevent contamination by outgassing or reflected molecules, and by proper bake-out and surface preparation techniques.

Besides the kinetic energy accommodation there is the important question of the physical chemistry of complex or reactive molecules such as CO_2 or atomic oxygen. Because of the primary mission emphasis on the possibility of life forms, it is desired to be able to identify traces of O_2 or O in the presence of large amounts of CO_2 .

Thus the beam simulation must involve both atomic oxygen and CO_2 . As it is neither practical nor advantageous to have O_2 , O and CO_2 all in the same beam the recombination coefficient of atomic oxygen in the source was therefore studied separately from the behaviour of CO_2 . It is important to study the behaviour of CO_2 , that is, to learn if the "cracking pattern" or ratio of the parent 44 peak to the daughter 28, 16 and 12 peaks characterizing CO_2 in the mass spectrogram is affected by the high impact energies involved, because this would confuse the identification of atomic oxygen or nitrogen in the atmosphere.

To summarize simulation requirements, the molecular beam should be of the correct velocity, Mach number, capable of containing the expected species, uniform in intensity profile and of adequate width. The beam intensity should ideally match the expected fluxes over the operational flight altitude range of the instrument, for operational testing, but for development work it is only necessary to provide sufficient intensity for adequate signal-to-noise ratios. The test chamber should ideally be an ultra-clean molecular sink system to match the entry situation and eliminate spurious facility background effects, although it is practical within limits to take unavoidable facility background signals into account. Finally, all these beam and system parameters must be separately measured and calibrated so that the test instrument can be subjected to known conditions.

The next sections cover the beam production and diagnosis methods used, and present typical results obtained so that the utility and shortcomings of the simulation techniques used can be discussed.

SIMULATION AND MEASUREMENT TECHNIQUES

The central facility used in these series of tests was the improved version of the high energy nozzle source molecular beam developed at UTIAS.

The primary simulation requirement is that the kinetic energy of the beam molecules (i.e., their velocity relative to the test instrument) be the same as in flight. It has been found that velocities of this magnitude can be produced by combining a high stagnation temperature in the gas source with a seeding technique in which a low molecular weight carrier gas, such as helium or hydrogen is used to dilute the desired atmospheric mixture of gases. If this gas mixture is expanded in a free jet having an extreme pressure ratio, about 95% of the complete conversion of temperature energy in the source into directed motion in the beam is achieved. Thus energies corresponding to tens of thousands of °K can be achieved using relatively low temperature electrically heated sources. The price paid is that the final beam contains carrier gas, but free molecular effusion after skimming (beam collimation), and scattering during skimming, reduces carrier dilution to less than 50%. It has been demonstrated during the program that the presence of this carrier gas does not affect the simulation.

A complete discussion of the technique involved may be found in Refs. 1 and 2. In summary, a high pressure gas (1 atmosphere) is expanded through an orifice (of the order of 0.004" dia.) into a vacuum chamber (10^{-3} torr) producing a hypersonic free jet (Mach No. 10-20). A sharp-edged hollow cone or skimmer defines a beam from the core of the free jet, which passes through a second collimator (as indicated in Fig. 1) which collimates a flat profiled beam from the gross beam emanating from the skimmer. The molecular beam may be considered as emanating from a point source, with a uniform intensity over the small divergence angle utilized. In the series of tests to be described, beam intensity (molecules/cm²/sec) was maximized by minimizing the distance between the beam source and the test instrument (approx. 125 cm). This resulted in a beam diameter of about 1.5 cm at the test instrument plane, with a half angle divergence of about 0.5°.

The overall layout of the test facility arranged for the project is shown schematically in Fig. 1, together with approximate operating vacuum levels. Basically, the beam passed across the interaction chamber where instruments diagnosed its properties, and impinged on the test instrument mounted on a bellows assembly on the far wall. The beam fully illuminated the instrument entry cavity, which was less than 1.5 cm in diameter. The test instrument was mounted on a specially designed bellows-articulated flange. The flange was designed so that pins could be inserted to define either a vertical or horizontal axis of rotation, each axis passing through the center of the ionization region so that no translation occurred upon rotation. A pin detente assembly allowed quick settings at 5° increments between

0° and 25°.

The beam mixtures used heavy dilution by helium (> 95%) to lower the mean molecular weight in the source and hence increase the beam velocities up to 3.4 km/sec. For all the beams except the atomic oxygen, the source used was a zirconium oxide tube with an orifice in one end, resistively heated by an external spiral molybdenum ribbon heater (Fig. 2). This source proved to be much more resistant to oxidation produced by thermally dissociated CO₂, and thus allowed higher CO₂ velocities than the previous hot tungsten source. The upper velocity was limited by the softening temperature of the zirconium oxide (about 1800°C) and by the fact that helium had to be used as a beam diluent rather than hydrogen in order to circumvent the strong reaction $H_2 + CO_2 \rightarrow H_2O + CO$. Using argon and hydrogen, beam velocities to 4.1 km/sec were achieved.

The atomic oxygen beam was produced by a 60 watt microwave discharge in a quartz source tube (Fig. 3). This source, originally developed by one of us (Ref. 3) utilizes a coaxial microwave discharge geometry which can be placed very close to the beam formation orifice, greatly reducing recombination losses. In order to produce a significant dissociation of O₂ in the 90% He, 5% Ar, 5% O₂ mixture, a low source pressure (20 torr) had to be used, lowering mean beam velocities and Mach numbers to about 1 km/sec and Mach 5 (Ref. 2). It was found that the addition of trace amounts of water vapour to the gas mixture markedly increase atomic oxygen production and beam stability.

Essentially two independent parameters were measured in the course of beam specification, the in-flight density of each component of the beam and the beam velocity. The derived parameter of component fluxes was then obtainable.

As shown in Fig. 1 the beam, after collimation in the collimation chamber, passes into the main test chamber which can be isolated from the molecular beam formation apparatus using a gate valve. The in-flight beam composition was then measured by allowing the beam to pass axially through a Model 270-950 Extra-nuclear quadrupole mass spectrometer (QMS) fitted with a coaxial high intensity ion source. The defining aperture for beam diameter was the entrance to the quadrupole mass spectrometer ion source and was made large enough so that the beam diameter at the test instrument plane was in the order of 1.5 cm. To obtain this diameter at the test plane necessitated the "opening up" of the aperture in the quadrupole ion source lens system and therefore a compromise had to be made between beam diameter at the test plane and lens system performance. However, it was found that a 1.5 cm diameter beam could be obtained without appreciable degradation of the ion lens system performance. Mass spectra were obtained using 75 eV electrons, and by dynamic calibration to be described in a later section, beam compositions and in-flight densities of the species in the beam were obtained.

The standard QMS was modified by the addition of a 5/8" length to the quadrupole rods to which the AC potential only was

supplied. This was done so that the instrument could be operated in a "delayed DC ramp mode" which has been shown to give flat-topped peaks and hence improved accuracy by Brubaker (Ref. 4). This effect was observed with this instrument and all mass spectra were taken in this mode, however the main advantage of this mode of operation appeared to be in the reduction of high-mass discrimination which was apparent when the instrument was operated in the normal mode.* An off-axis electron multiplier was used to collect the ion signal which was amplified and displayed by conventional means.

Both the beam monitoring quadrupole mass spectrometer (hereafter referred to as QMS) and the test mass spectrometer (referred to as 4Bl) were statically calibrated by generating known densities of calibrating gases in the test chamber by a dynamic leak system of fairly standard design in which input and output conductances were known. The reference standard was an MKS Baratron measuring pressure ahead of the input conductance.

It should be noted that a difficulty exists in converting the sensitivity of the QMS to a static gas into a sensitivity for a high collimated beam passing through it. An equivalent density of beam produces a larger ion signal because of the enhanced collection of ions created from neutrals already "aimed" in the right direction with energies of 1eV or so. This factor was studied by replacing the Baratron leak system with a beam of known number flow, cross-sectional area, and velocity (hence in-flight density). Uncertainties in beam profile placed wider confidence on this calibration than desirable, but a strong beaming enhancement was observed. This work and a more detailed discussion of the beam/QMS operation will be reported elsewhere in more detail. However, using the best QMS sensitivity calibration and the measured beam velocities, the beam intensities typically available at the test instrument were:

He	6.4×10^{15} molecules/cm ² sec
Ar	8.9×10^{14}
CO ₂	1.65×10^{14}
O ₂	2.04×10^{15}
O	1.0×10^{15}

The CO₂ corresponds to a Martian atmospheric pressure of 2×10^{-8} millibars, which is equivalent to an altitude somewhere in the range 120 to 180 km.

The beam mean velocity together with the small spread of molecular velocities about the mean velocity (from which the beam Mach number or speed ratio can be derived) was measured by the metastable time-of-flight technique. The basis of this method has been well documented elsewhere (Ref. 5) and a detailed description will not be given here. Essentially it involves "tagging" beam molecules by means of long-lived electronic excitation and performing a time-of-flight analysis over a known flight base terminated by an electron multiplier (Bendix M306).

* The help provided by W. S. Chamberlin of Martin Marietta in setting up the "delayed DC ramp" is gratefully acknowledged.

Excitation is introduced by a repetitively-pulsed electron beam which provides an essentially ideal and readily-selected shutter function. Because of the low excitation rates typical in this system, despite a high-perveance electron gun operating at high repetition rates (up to 2 kHz), storage of detector counts in a 512-channel analyzer is required to permit statistical smoothing. There are fundamental limitations to the technique, however, due to absence of suitable electronic states in some gases, or low cross-sections for excitations in others, and still further problems associated with molecular scattering (i.e. "recoil") as a necessary consequence of the exciting collision. Considering the gases of interest in the current program, hydrogen and helium are both unsuitable for the highly-directional beams used due to the scattering problem. The momentum imparted by the colliding electron is sufficient to scatter the metastable particle outside the acceptance angle of the detector. Both atomic oxygen and molecular oxygen possess long-lived states but none are sufficiently energetic to produce an Auger electron at the detector. Carbon monoxide, while it possesses a long-lived state of adequate energy, and is sufficiently heavy to alleviate the recoil problem, has an excitation cross-section of inadequate magnitude. Carbon dioxide possesses no known long-lived metastable states and furthermore dissociates under electron impact. Argon, however, is acceptable on all counts, and has the highest overall efficiency of any gas studied by this technique. The procedure adopted, therefore, was to add Argon to all gas mixtures as a "trace" gas for velocity analysis. In all cases this was desirable since argon added further insight into the mass spectrometer performance.

A typical beam time-of-flight distribution is shown in Fig. 4.*

To compare instrument responses and deduce the true behaviour under Martian entry conditions, it is necessary to "flag" the beam (intercept it in front of either instrument) so that the local facility background pressure (which of course would not exist during entry) can be subtracted. Additionally, a large stagnation plate could be inserted to seal off the front of the cavity mounting the test instrument, with a small orifice in the beam flux, thus providing signals corresponding to "ideal" stagnation (stagnation produced in a large cavity with a small orifice normal to the flow) for reference purposes when various source geometries were tested. The operating modes are:

<u>Condition</u>	<u>Significance</u>
A All flags and stagnation plate removed, beam on	Beam signal plus background
B 4Bl flag inserted, beam on	Local background when beam on
C 4Bl flag in, stagnation plate in, beam on	100% stagnation

* The help provided by Prof. R. H. Prince, York University, in obtaining these velocity measurements is gratefully acknowledged.

D	4Bl flag out, stagnation plate in, beam on	Check on A, B, C
E	Stagnation plate in, beam off	Signal at 4Bl due to 4Bl out-gas as well as facility residual gases
F	Beam on, flagged at QMS	Facility background at QMS when beam on
G	Beam off, stagnation plate out	Facility residual gases

and the derived parameters become:

A - B "Martian entry" signal

$\frac{A - B}{C - E}$ Fraction of ideal stagnation achieved by test ion source cavity, properly corrected for local backgrounds

B - B + C Should equal D

A - F Provides QMS with properly corrected in-flight beam signal

RESULTS

From the many exploratory measurements made, the following results are presented as representative of the information which can be deduced from this type of simulation.

Effect of Vehicle Entry Velocity

Figure 5 shows the relative stagnation, that is, the actual density measured for each gas in a typical source cavity compared to the density an ideal cavity with small inlet aperture would achieve. The actual geometry for these runs approximated an open cylinder 1/4" diameter by 3/16" depth facing into the flow. In spite of the scatter, it is apparent that the dominant trend is a decrease in stagnation toward beam velocities approaching the entry velocity. This is as would be predicted from current accommodation coefficient theories (Ref. 6), which generally predict lower accommodation at higher incident velocities, hence faster moving reflected molecules and therefore lower mean reflected densities. The importance of correct velocity simulation is indicated by these results, particularly for calibration work.

Response of Test Mass Spectrometer to High Velocity CO₂

A primary concern in these exploratory studies of the semi-open ion source was that CO₂ might behave anomalously because of the high impact energies, which could presumably result in highly vibrationally excited reflected CO₂ molecules. The vibrational

temperature affects the ratio of the parent CO_2^+ mass 44 ions to the daughter 28, 16 and 12 ions, higher temperatures assisting the break up into fragment ions upon impact of the ionizing electron. This is illustrated in Fig. 6 showing for the QMS ion source the decrease in parent and increase in fragment 12 peak with source temperature. However, the results presented in Fig. 7 show that to the highest beam velocities attained these fears are unfounded, from two pieces of evidence. Comparison of the solid curves shows that the parent-daughter ratio remains constant. The dashed curve shows that the 44 ion signal remains proportional to the incident CO_2 flux. The corollary conclusion is that the one or two high velocity impacts with the source wall are inefficient in transforming kinetic energy into vibrational energy, and Oman has produced theoretical calculations which support this (Ref. 7). This result is important in allowing the utilization of the semi open source configuration for this mission, since a strong parent-daughter variation in the dominant CO_2 would have made it very difficult to identify nitrogen or atomic oxygen in the atmosphere.

Results with Atomic Oxygen-Selection of Source Material

Here the basic aim was to study various candidate source materials - gold, aluminum, stainless steel - to see if the recombination coefficient, which governs the density of reflected atomic oxygen, was affected. For this work, a slender flag in the form of a wire, as shown in Fig. 8, was added so that it could exactly shadow the ionizing electron beam from the incident molecular beam. In this configuration the only signal due to atomic oxygen had to come from reflected atomic oxygen. A typical test result is shown in Fig. 9, where the signal due to reflected atomic oxygen O_r equals the total atomic O signal O_t less the signal due to the incident beam density O_i . The results may be summarized by saying that within the experimental error there was no appreciable loss by recombination on any of the sources, atomic oxygen producing much the same stagnation ratios as the other gases. This result, which contradicts recombination coefficient data obtained at thermal energies (Ref. 8) may be explained by the high impact velocities (1 km/sec) which favours reflection rather than adsorption and subsequent recombination on the surface.

Angle of Attack and Source Geometry Effects

In these studies the purpose was to study the trade-off between enhanced stagnation signal and sensitivity to pitch or yaw which occurs as the open cup forming the ion source is made deeper. Typical results are shown in Figs. 10 and 11. Increased sensitivity to pitch or yaw is observed for the deeper cups, this being expected since incident molecules on the average strike closer to the entry and hence have a higher immediate escape

probability for the tilted deep cups. The relative stagnation in Fig. 11 is plotted against a curve which is simply the clausius conductance factor for tubes of length-to-diameter ratio approximating the sources used. This model assumes in effect that the incident molecules reflect from the base plane with a random or cosine distribution, and agreement is surprisingly good.

Other Qualitative Results

During the course of this work many effects were noted and some suspect data discarded because of contamination of the test instruments with facility residual gases which contained organic molecules, water vapour, etc., and because of unexpected coupling between the instruments and the stray magnetic fields of the electron multiplier used. This experience reinforces the idea that an ultra clean molecular sink chamber provides the best simulation of reality and that such a facility will be necessary for work on the operational characteristics of the test instrument such as its own outgassing characteristics, or its quantitative calibration.

CONCLUSIONS

Conclusions concerning the ion sources tested:

1. Up to the velocities tested, CO_2 neither dissociates nor changes its fragmentation pattern appreciably.
2. A shallow cylindrical volume (3/16" deep and 1/4" in diameter) appears to be a satisfactory compromise as the ionizing region of the mass spectrometer. A deep cylinder gives a more favourable stagnation factor but a larger sensitivity to angle-of-attack. The shallow geometry is also recommended because it would undoubtedly minimize the effect of source outgassing and filament chemistry although these effects were not studied in this preliminary investigation.
3. Tests made with the atomic oxygen beam at 1.02 km/sec showed no appreciable loss of atomic oxygen in the source cavities made of stainless steel, gold, or aluminum, under the conditions of these tests in which all the surfaces may have been contaminated to an unknown degree.

Conclusions concerning the simulation techniques used:

1. The main shortcomings of the simulation used were the unavailability of an ultra clean molecular sink test chamber and the inability with the present beam sources to reach full entry velocity, particularly with atomic oxygen. At present, the molecular beam is being installed in the large molecular sink space simulator at UTIAS, and new sources promising higher velocities are being tested, so these shortcomings should be overcome in future work.
2. Even at the present stage of development, the simulation techniques used were invaluable in assessing factors to be considered in the initial design specification of the prototype flight instrument, and greatly increased the confidence that the

basic design was a good choice.

3. The importance of correct kinetic energy simulation has been demonstrated. Specifically, future calibration (at various angles-of-attack) of any flight instrument must be done in the full dynamic simulation afforded by the molecular beam. Of course, this conclusion applies to any other atmospheric mass spectrometers, such as in earth orbit, unless a fully stagnating geometry is used which completely relaxes the sampled population to the cavity ambient conditions before ionization. This choice however eliminates the possibility of studying reactive species and often introduces spurious sources effects.

4. The capability of providing insight into the potentially complicated behaviour of CO_2 and atomic oxygen has been demonstrated. As atmospheric sampling techniques became increasingly more sophisticated and as missions evolve to other planets possessing atmospheres containing hydrocarbons, ammonia, etc., it will become increasingly necessary to utilize fully molecular beam dynamic simulation techniques because of the potentially complex interactions of these species with the test instrument.

REFERENCES

1. French, J. B. "Planetary Atmospheric Simulation Using Molecular Beams", IES/AIAA/ASTM 4th Space Simulation Conference, Los Angeles, Calif., 1969, AIAA Paper No. 69-1031. Also published in CASI Transactions, Vol. 3, No. 2, p. 77, 1970.
2. French, J. B. "Continuum Source Molecular Beams", AIAA J., Vol. 3, p. 993, 1965.
3. Reid, N. M. "A Study of Reactions of Free Nitrogen Atoms by Mass Spectrometry", Ph.D. Thesis, Univ. of St. Andrews, 1968 - The microwave discharge cavity used was a modified version of Model No. 210L available from Electro-Medical Supplies Ltd., London, England.
4. Brubaker, W. M. "Final Report Quadrupole Mass Spectrometer", prepared for NASA under Contract NASW-1736, ES-4103, 1969.
5. Locke, J. W.
French, J. B. "Critical Evaluation of the Metastable Time-of-Flight Technique for Obtaining Molecular Velocity Distributions", J. Vac. Sci. Technol., Vol. 7, No. 1, p. 46, 1970.
6. Goodman, F. O. "The Theory of the Scattering of Gas Atoms by Solid Surfaces", Surface Sci., Vol. 26, p. 327, 1971.

7. Oman, R. A. Rarefied Gas Dynamics, Suppl. 4 (Proc. 5th Inter. Symp. on Rarefied Gas Dynamics, Oxford, England, 1966) (Academic Press, New York, 1967), Vol. 1, p. 83.
8. Wood, B. J. Final Report, Contract NASr-49 (30), June, 1950.
Baker, B. R.
Wise, H.

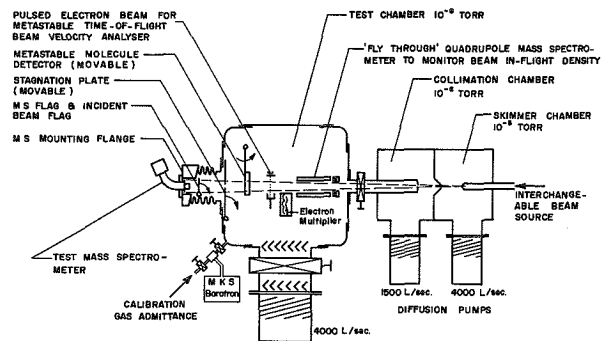


FIG. 1 SCHEMATIC OF FACILITY ARRANGEMENT FOR ENTRY SIMULATION TESTS

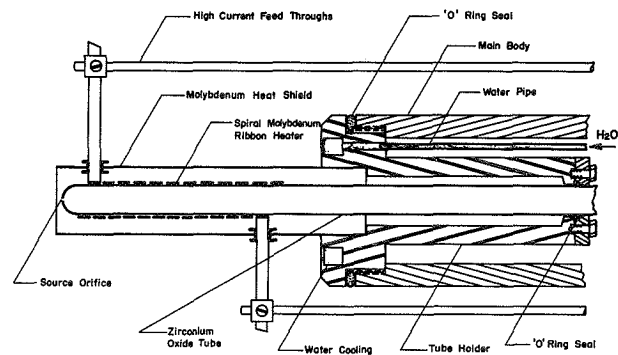


FIG. 2 RESISTIVELY HEATED SOURCE FOR MOLECULAR BEAM

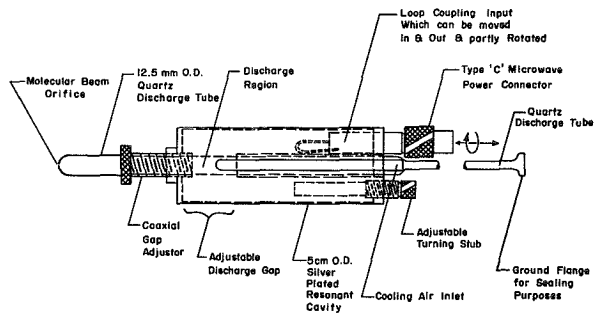


FIG. 3 MICROWAVE DISCHARGE ATOMIC OXYGEN SOURCE

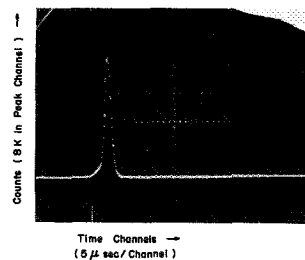


FIG. 4 TIME - OF - FLIGHT DISTRIBUTION RESULT

Measurement of Argon Velocity in
1% CO₂, 1% Ar, 98% He Beam
with Parameters: $P_0 = 19.4$ psia
 $T_0 = 958^\circ\text{K}$

Electron Beam Pulse Amplitude = 28 v
Pulse Width = .5 μsec .
Current = 5×10^{-6} amp.

Flight Base = 18.5 cm
Beam Velocity = 2.76 km/sec
Mach Number = 13.4

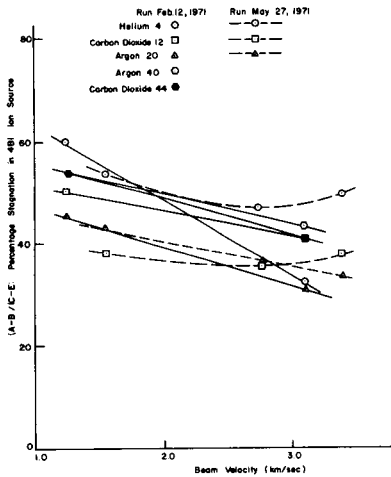


FIG. 5 PERCENTAGE STAGNATION VERSUS BEAM VELOCITY PLOT

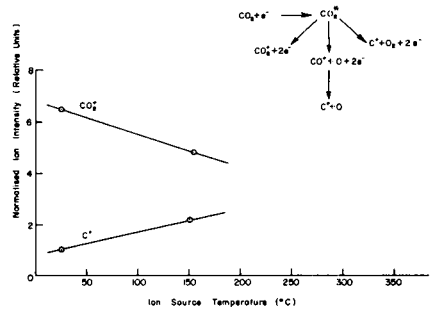


FIG. 6 CO_x CRACKING PATTERN VERSUS TEMPERATURE - STATIC RESULTS

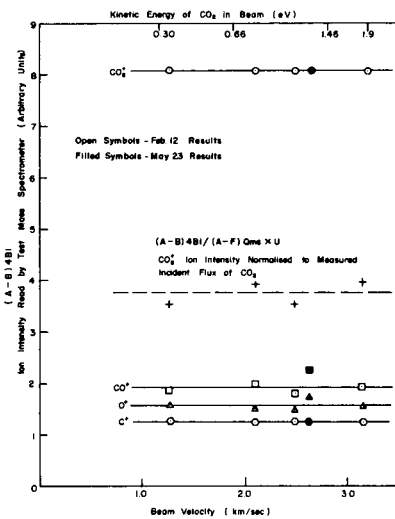


FIG. 7 CO_x CRACKING PATTERN FOUND AT 481 NORMALISED TO 44° PEAK

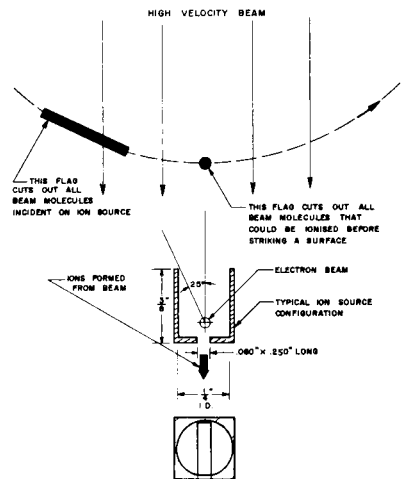


FIG. 8 TYPICAL ION SOURCE CONFIGURATION WITH RESPECT TO THE INCIDENT BEAM

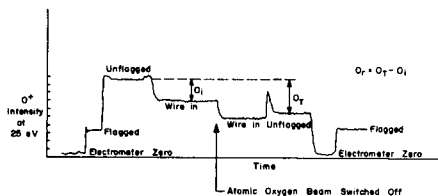


FIG 9 TYPICAL 48: RESPONSE DURING ATOMIC OXYGEN RUN

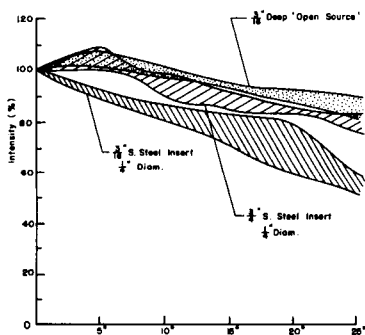


FIG 10 EFFECT OF PITCH FOR VARIOUS SOURCE GEOMETRIES :-
THE SPREAD IN EACH BAND COVERS THE VARIOUS
MASS PEAKS 4, 20, 40, 44.

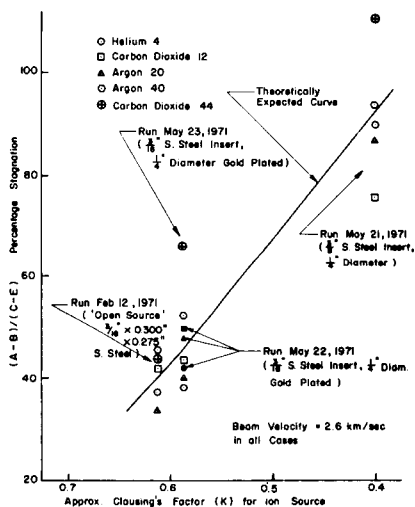


FIG 11 STAGNATION PERCENTAGE AS A FUNCTION OF
SOURCE GEOMETRY

SUPERALLOY MATERIAL TESTS IN A PLASMA ARC TUNNEL*

*D. W. Land, McDonnell Douglas Research Laboratories, McDonnell
Douglas Corporation, St. Louis, Missouri 63166*

ABSTRACT

Seven superalloy models were tested in the McDonnell Douglas Research Laboratories (MDRL) Plasma Arc Tunnel (PAT) facility at the peak heating condition existing on the space shuttle orbiter lower surface during a low cross-range entry. The models were 3 x 3 in. flat surfaces nominally 0.01 to 0.02 in. thick, held in a water cooled wedge holder at a 60 deg angle-of-attack. Five test models were recycled 25 times for 10 min periods (two were recycled 50 times) in a Mach 4.6 test stream with the model leading edge temperature maintained at 2200°F (2000°F in one case).

INTRODUCTION

The concept of a reusable space shuttle vehicle requires knowledge of high temperature material performance and material degradation with reuse. Several candidate metallic materials are being considered for use on the space shuttle in regions where the reentry heating is moderate (maximum temperatures less than 2200°F). Among these materials are the nickel-base alloys dispersed with thoria (TD-NiCr) to improve their high temperature properties.

Earlier tests of TD-NiCr have shown these materials to be highly resistant to oxidation in static or slowly moving air¹. More recent tests in high flow rate combustion gases² and arc-heated air³ have produced much higher oxidation rates and significantly larger mass loss than would be predicted from static oxidation tests.

* This work was performed under contract NAS3-14666-H for NASA Lewis Research Center

The conditions maintained on the model leading edge for these tests included a surface pressure of 10 Torr and an equilibrium temperature of 2200°F. These conditions correspond to those which occur on the orbiter lower surface at the peak heating point (approximately 300 sec into the entry) of the low cross-range entry vehicle proposed by NASA Manned Space Flight Center⁴. The pitch angle during this entry is 60 deg with a total entry time of 800 sec. Proposed high cross-range vehicles may incur higher peak heating upon entry and have entry times from 400,000 ft as long as 2200 sec.

This paper describes the McDonnell Douglas Research Laboratories (MDRL) Plasma Arc Tunnel (PAT) facility, the test model, calibration tests, and model tests. Furthermore, an analysis of the optical and thermocouple model temperature measurements is presented. Additional test results such as model weight changes and temperature distributions are discussed.

Facility Description

The McDonnell Douglas PAT facility consists of a Hüls type arc heater, model actuator, 6 ft diam water-cooled vacuum tank, power, air and water supplies, and associated instrumentation. The arc heater is dc powered with tandem, water-cooled, cylindrical hollow electrodes. The electrode material used was OFHC copper with 20% Cu - 80% Ag alloy inserts in the arc attachment regions. Model contamination resulting from electrode erosion was small (less than 0.008% by weight when ratioed to the air mass flow rate).

Figure 1 shows the facility simulation capabilities for flat-face splash test models. The capabilities in terms of conditions existing downstream of an attached shock on a wedge holder at 5 through 60 deg angle-of-attack are shown in Fig. 2. The two solid symbols indicate the test conditions for this program. To operate at these low air enthalpy levels, an air injection system was installed in the heater downstream of the arc attachment point. This system provided a secondary means of controlling the test stream enthalpy level. Primary regulation of the enthalpy level is obtained through the arc heater current and primary gas flow control. Dry, filtered air is supplied to the arc heater at pressures up to 3600 psi.

Wedge Holder

Several items were considered in the design of the wedge holder for these material tests. One

requirement was testing 3 x 3 in. models so that two tensile specimens could be cut from each model after the thermal tests. This model size required a large holder surface area to remove any edge effects on the test model. Models larger than the Mach cone diameter experience edge effects resulting from bow shock-jet boundary interactions. The maximum model radius at a given axial position is determined as follows:

$$R_{\max} = R_{\text{ex}} - \delta - x \tan \sin^{-1} \left(\frac{1}{M} \right).$$

The boundary layer displacement thickness which essentially reduces the effective nozzle exit radius can be expressed as:

$$\frac{\delta}{s} = C \left(\frac{\rho_r \text{ vs }}{\mu_r} \right)^{-0.3}.$$

Based upon the following predicted arc heater parameters for these tests: 1.0 atm arc chamber pressure, 2500 Btu/lb enthalpy, 1.0 in. diam throat, and a 15 deg half-angle conical nozzle, the boundary layer displacement thickness was 0.66 in. at the 8.0 in. exit diameter. Thus, the test stream diameter at the nozzle exit was typically 6.68 in., and was the limiting factor in the holder design.

The outside dimensions of the wedge holder were 4 x 4 in. with a 3.06 x 3.06 in. cavity, 1.0 in. deep to accept the model and backside insulation. The holder and model geometric centers were concentric, and were located on the nozzle centerline during testing. Model retention was provided by four pins at the midpoint of each side. This allowed the model to expand freely in all directions, and at the same time provided minimal thermal losses because of the small contact area.

A pointed set screw in each quadrant of the model holder perpendicular to the model surface provided fine adjustment of the model surface height relative to the holder when it became apparent how sensitive the model temperature was to this variable. The small contact area of the screws with the model did not create large thermal losses.

The air space in the cavity behind the model was filled with loosely packed Fiberfrax. The type (DS-5R 1064 Lo-Con Blanket) used contained no organic binders and was chemically and thermally stable at 2300°F. Its thermal conductivity was low (2.3 Btu in./hr ft²°F

at 2200°F) thereby providing adequate thermal insulation in addition to protecting the model backface from oxidation.

Model Design

The final model configuration was based upon a design developed in MDRL. One of the major difficulties of testing metallics at elevated temperatures is distortion. Several designs were considered, including those shown in Fig. 3.

The model configuration actually used for this program was basically a flat plate nominally 3 x 3 in. with a 0.09 in. 90 deg radius along each edge. At the midpoint of each edge, a 0.25 in. square tab having a 0.052 in. diam hole extended from the radius to accept the retention pins described previously. This final model configuration caused minimum surface distortion during model test cycles.

Each model tested in this program was fabricated from sheets of material furnished by NASA Lewis Research Center. During fabrication it was necessary to polish the edge radius region prior to bending to prevent stress cracks from developing and subsequent fracture of the material. Polishing was particularly necessary when bends were parallel to the grain, especially in the less ductile materials such as TD-NiCrAlY.

Heat Flux and Pressure Calibrations

Measurements were made of the surface heat flux and pressure distributions which existed when the model surface was maintained at temperatures of 2000 and 2200°F, 0.5 in. downstream of the model leading edge. These quantities were determined by first testing a representative model (TD-NiCr) until the proper equilibrium temperature levels were attained. Having established the arc heater operating conditions, the model was then replaced by flat plates containing transient heat flux sensors and pressure ports as shown in Fig. 4. The average values obtained from several runs with the appropriate arc heater operating conditions are plotted in Fig. 5 for the 2200°F test point. Also shown are predicted centerline distributions calculated by computer programs modified for plasma testing. The complete heat flux and pressure distributions are shown in Fig. 6a for the two NASA test points of 2000 and 2200°F. Both the heating and pressure distributions show good lateral uniformity. A comparison of equilibrium temperatures based on radiation alone for the two lateral points along the model

leading edge shows that a variation in the heating rate of 1.9 Btu/ft²sec can result in a temperature difference of 30°F. For these tests, the lateral model temperatures at the leading edge were to be maintained within $\pm 20^\circ\text{F}$. Although the lateral heat flux distribution as measured could affect the lateral temperatures by as much as $+ 15^\circ\text{F}$, it was possible to maintain the models within the $\pm 20^\circ\text{F}$ temperature requirement by adjusting the model surface position with the pointed support screws in each quadrant. The surface pressure distribution in Fig. 6b was identical for both test points. The axial heating and pressure variation is indicative of laminar flow at the model surface.

Difficulties in interpretation can be encountered when measuring the heating rate distribution in a plasma test stream. Since each surface may exhibit different catalytic effects in a dissociated non-equilibrium stream, the heat flux measured by a calorimeter is not necessarily identical to that of the model surface. However, no great deviation between the heat flux measured by the copper sensors and that experienced by the nickel base test models was expected. This conclusion was based upon data by R. B. Pope⁵ which shows the catalytic reaction rate constants to be approximately the same for copper and nickel when exposed to a high temperature non-equilibrium air stream.

The calorimeter plate contained five OFHC copper sensors each 0.125 in. in diameter and length. The average sensor temperature as a function of time was measured using a 30 gauge chromel-alumel thermocouple peened into small holes in the sensor base. The cold wall heat flux at each sensor position was calculated from the following relationship:

$$q_{cw} = \frac{mc_p}{A} \frac{\Delta T}{\Delta t}.$$

Thermal errors were minimized by mounting each copper sensor in a centering transit support and then sealing the surface with Sauereisen #8 cement.

Model surface pressures were measured at five 0.030 in. diam ports at the locations shown in Fig. 6b. The ports were connected to 0-1 psid transducers using 1/8 in. o.d. copper tubing. The response time of the system was approximately 2 sec.

Test Procedure

A typical test cycle was begun by starting the arc heater and stabilizing it at the predetermined condition. The model was then indexed into the test stream. Model backface temperatures were continuously monitored at four positions where Pt-Pt 10% Rh thermocouples had been attached by tack welding. Each thermocouple output was displayed (one signal at a time) for the arc heater operators, who maintained the leading edge within $\pm 20^{\circ}\text{F}$ of the desired temperature through small arc current adjustments. During the first few cycles of most models tested, small adjustments of the model surface were necessary to balance the heating on the model and remain within $\pm 20^{\circ}\text{F}$ at the leading edge.

Surface temperatures were measured with an optical pyrometer (Infrared Industries TD-9H) having an operating wavelength of $0.8\text{ }\mu\text{m}$. A point 1 in. downstream of the model leading edge and on the axial centerline was normally monitored continuously. At the midpoint of each test cycle (approximately 300 sec) a temperature measurement was obtained at 13 positions on the model surface. Some difficulties were encountered in attempting to interpret these data because of arc radiance. This is discussed in more detail in the next section.

After 600 sec in the stream, the model was removed and cooled to 400°F (150 sec elapsed time). The model was then indexed back into the test stream. This procedure was repeated until the required number of cycles had been completed. The test conditions for each model are listed below.

<u>Material</u>	<u>Leading Edge Temperature ($^{\circ}\text{F}$)</u>	<u>Surface Pressure (Torr)</u>	<u>Stream Enthalpy (Btu/lb)</u>	<u>Number of 600 sec Cycles</u>
TD-NiCr	2200	9.6	2850	25
TD-NiCrAlY	2200	9.6	2850	25
DS-NiCr	2200	9.6	2850	25
Haynes-188	2000	9.6	2450	25
TD-NiCr	2200	9.6	2850	50
DS-NiCr	2200	9.6	2850	50
TD-NiCrAl	2200	9.6	2850	25

Spectrographic Measurements

In similar superalloy test programs³, the total emittances of the various alloys were determined from

a comparison of radiometric and thermocouple temperature measurements. This was done by equating the material backface thermocouple temperature to the optically determined surface temperature and the surface emittance obtained from the expression

$$\epsilon_{\text{surface}} = \frac{\epsilon_{\text{Rad}}}{\epsilon_{\text{window}}} .$$

A similar method was attempted during this program; however, difficulties were encountered as illustrated by the following tabulation of various alloy emittances. These values were obtained from material in the "as received" condition, and at room temperature (75°F).

<u>Model No. and Material</u>	<u>Emittance at $\lambda = 0.8 \mu\text{m}$</u>	<u>Total Emittance $0.2 < \lambda < \mu\text{m}$</u>
Haynes-188	0.528	0.145
TD-NiCr	0.610	0.168
DS-NiCr	0.520	0.124
MDC-TD-NiCr	0.650	0.145

These values show the material dependency on wavelength, therefore any emittance values determined with the TD-9H would be at $\lambda = 0.8 \mu\text{m}$. Another error, resulting from the low material emittances, was the reflection of arc radiance at the model being detected by the pyrometer.

The following describes the technique for measuring reflected arc energy to determine its effect on the surface temperatures and emittance measurements. The test set-up is shown in Fig. 7. The optical axis of the monochromator entrance was approximately 6 in. downstream of the nozzle exit plane and intersected the nozzle centerline at a right angle. Two detectors were used to cover the required spectral bandwidth; a photomultiplier tube ($0.2 \mu\text{m}$ to $0.6 \mu\text{m}$) and a 2 mm x 10 mm lead sulfide cell ($0.5 \mu\text{m}$ to $2.9 \mu\text{m}$). Two types of measurements were made of the radiant background flux. The plasma radiance downstream of the nozzle was measured with the aperture adjusted so that only a narrow volume of the plasma was viewed by the detector.

Another set of radiance measurements was made of the flux emitted by the plasma in the region of the arc electrodes located upstream of the nozzle throat. This was accomplished by inserting a water-cooled aluminized copper mirror (3 x 3 in. x 1/4 in.) into the test stream at the intersection of the monochromator

optical axis and the test stream centerline. The mirror was positioned at a 45 deg angle-of-attack so the flux generated in the arc heater electrode region was focused onto the spectrometer entrance slit. A thin coating of magnesium fluoride was deposited over the aluminum coating for protective purposes.

The data from the spectral scan made at the arc heater operating condition which produced a model temperature of 2200°F are presented in Fig. 8. Results from the two types of measurements indicate the radiance of the expanded test stream to be insignificant when compared with that emanating from the arc heater electrode region. Superimposed on the arc radiance curve of Fig. 8 are several blackbody radiance curves to indicate the relative magnitude of the arc radiance. It is apparent that the arc radiance will be a significant source of blackbody flux near $\lambda = 0.8 \mu\text{m}$. How this radiance affects the pyrometer temperatures and emittance determination is illustrated in the following example calculations.

The apparent radiance of the test model surface as measured by the pyrometer is the sum of that emitted by the model surface plus the arc radiance reflected at the model surface. Thus, the radiosity observed by the pyrometer can be expressed as:

$$W_a = \epsilon W_b + rG.$$

If $r = 1 - \alpha$, and $\alpha = \epsilon$ then, $W_a = \epsilon W_b + (1 - \epsilon)G$.

Using the spectrographic measurement of arc heater radiance at a wavelength of $0.8 \mu\text{m}$ as obtained from Fig. 8, it can be shown that the effect of a large change in model emittance is insignificant on the apparent temperature observed by the pyrometer.

With $G = 0.22 \text{ W cm}^{-2} \text{ sr}^{-1} \mu\text{m}^{-1}$, and

$$W_b = 0.19 \text{ W cm}^{-2} \text{ sr}^{-1} \mu\text{m}^{-1} \text{ at } 2200^\circ\text{F},$$

$$W_a = 0.217 \text{ which corresponds to a blackbody temperature of } 2227^\circ\text{F}.$$

$$\begin{aligned} \text{For } \epsilon &= 0.9, \\ W_a &= 0.193, \end{aligned}$$

which corresponds to a blackbody temperature of 2200°F. Since the arc heater radiance at the operating condition for this test program is comparable to the blackbody radiance at 2200°F, the pyrometer is quite insensitive to model emittance change. As a result, it is impossible to determine material emittance from the backface thermocouple outputs and pyrometer measure-

ments since the accuracy of the pyrometer is $\pm 1\%$ full scale or $\pm 25^\circ\text{F}$.

Test Results

Table 1 contains representative thermocouple and surface temperatures for 25 test cycles on a DS-NiCr model. Figure 9 identifies the thermocouple and pyrometer observation positions on the model. From the values of thermocouple Nos. 2 and 4 it is apparent that the leading edge region was kept within the required $2200 \pm 20^\circ\text{F}$ temperature limits. Also, the temperatures obtained at the 13 locations on the model surface with the pyrometer are indicative of the oxide layer development.

In the early test cycles the surface temperatures exceeded the corresponding backface temperatures. This was caused by an initial high surface reflectance of the model, since each model was tested in the "as received" condition without any pre-test oxidation. Gradually diminished surface temperatures with increased test time are indicated by successive pyrometer scans of the surface. This trend of decreasing surface temperatures was exhibited by the other models tested, with time to stabilization being roughly 10 cycles of 10 min each. The surface temperatures in Table 1 were based on a post-test calibration of the pyrometer, and an additional correction was applied to account for the window transmission.

The surface temperature measurements were taken with the pyrometer emittance control set at 1.0 since the material emittance was not known. Therefore, the values do not represent true surface temperatures. However, the data do exhibit the general behavior of all models tested, and can be utilized in determining a relative temperature distribution over the model surface. This distribution was obtained for each model tested, and verified the uniformity of the heating. The fact that the observed temperatures exceeded the values indicated by the backface thermocouples was evidence for the existence of an additional source of radiation, the arc heater.

Figure 10 shows a typical centerline temperature profile for a model surface at 60 deg angle-of-attack. Heat losses to the holder occur at the model edges so that the curve cannot be extrapolated to a high temperature ($> 2200^\circ\text{F}$) at the model leading edge. The temperature distribution agrees well with the centerline heat flux profile shown in Fig. 5.

A typical temperature history illustrating the model material response is plotted in Fig. 11. The

data for the curves were obtained during the 25th cycle of NASA test model No. 5 (TD-NiCr). The final equilibrium temperature of 2200°F was attained in approximately 100 sec which was typical for all tests. This response occurred while the arc heater parameters and stream conditions remained constant at the predetermined values. The symbols represent data from the two leading edge thermocouples and show the variation between thermocouples to be less than 20°F with the absolute measurement on each thermocouple being 2200°F \pm 12°F. At the cycle termination (600 sec) when the model was removed from the air stream the temperatures decreased abruptly to approximately 1500°F in 10 sec by radiation cooling. The total time required for cooling the model to 400°F or less required 2 to 3 min. The temperature variation of 20°F between the two thermocouples was typical of all model test cycles except the two TD-NiCrAl models. During these tests it was impossible to maintain this differential. Model No. 2 was, therefore, cycled maintaining thermocouple No. 4 at 2200°F \pm 20°F. Model No. 7 was cycled maintaining the average of thermocouples Nos. 2 and 4 at 2200°F \pm 20°F.

Table 2 contains pre- and post-test measurements of thickness and weight changes for the seven alloys tested. Figure 9 shows the locations where thickness measurements were made. These thickness values do not indicate the amount of virgin material remaining since there is an initial thickness of oxide on the surface. In general, the trend indicated by the centerline thickness changes is that of a uniform oxide layer growth. The total material weight changes follow the predicted behavior of Goldstein⁴, wherein the total model weight increases during approximately the first 300 min of testing and then a weight loss begins to occur.

An inconsistency appears in the weight changes of models Nos. 3 and 6 which were DS-NiCr materials with heating times of 250 and 500 min respectively. This may have resulted from problems encountered in removing the tack welded thermocouples for post-test measurements. The No. 4 model (Haynes-188) which is a cobalt rather than a nickel base alloy showed the largest material loss even though tested at a lower temperature (2000°F). Model Nos. 2 and 7 which contained small percentages of aluminum showed the greatest weight increases. Previously reported results³ attribute this to the formation of a stable aluminum oxide layer (Al_2O_3) which retards the volatilization of chromium oxides (Cr_2O_3) thereby reducing the internal chromium loss in the metal. The initial weight increase of the test models is the result of physisorbed

oxygen combining to form nickel and chromium oxides on the material surfaces. This initial weight gain is a net value since chromium loss is occurring simultaneously.

Concluding Remarks

1. The material distortion which occurred when testing 3 x 3 in. models at temperatures of 2000 and 2200°F was reduced to acceptable limits by rolling an edge radius on the models. The edge radius was typically five to seven times the model thickness.

2. Model backface oxidation was minimized by filling the model holder cavity with loosely packed layers of Fiberfrax.

3. Emittance measurements of several test materials indicate that in the "as received" condition the models do not approximate greybody behavior. Measurements made after 250 min at 2200°F on a TD-NiCrAlY model show that the emittance at $\lambda = 0.8 \mu\text{m}$ is slightly higher than that measured over the range $0.2 \leq \lambda \leq 27 \mu\text{m}$.

4. Material degradation as determined from thickness and weight loss measurements was not evident from these tests, because of finite surface oxide layers which were included in the measurements.

5. A spectrographic survey of the arc heater radiance indicates that in situ emittance measurements will contain sizable errors, unless techniques are used to eliminate arc radiance. The error was greatest early in the test when the model surface reflectance was relatively high since the models were tested in the "as received" condition without pre-test oxidation of the surface.

6. The greatest weight loss was experienced by the Haynes-188 model which is a cobalt base material, even though it was tested at a less severe condition of 2000°F for 250 min. It was noticed that the oxide growth was very rapid during the early heating cycles for the Haynes-188 material compared to the other materials tested in this program.

7. The least weight loss occurred for the two models containing aluminum. This was attributed to the protective alumina oxide layer which reduces the volatilization of chromium at the surface. The weight loss would have been even less had not some spalling of the oxide layer occurred in the leading edge region.

Acknowledgement

It is my pleasure to acknowledge the suggestions of Dr. H. B. Probst, NASA Lewis Research Center in the preparation of this paper and for allowing data from NASA contract NAS 3-14666-H to be used. The assistance of Messrs. W. A. Rinehart and R. R. Williams of the McDonnell Douglas Research Laboratories in the preparation of this paper was also greatly appreciated.

Nomenclature

- A - calorimeter sensing area, ft²
- C - constant, 0.49 for air
- c_p - temperature averaged heat capacity of copper, Btu/lb°F
- ex - nozzle exit value
- G - arc heater radiance
- m - mass of each calorimeter sensor, lb
- M - Mach number
- q - heat transfer rate, Btu/ft²sec
- r - evaluated at Eckert's reference temperature
- R - radius
- s - surface distance along nozzle wall
- $\frac{\Delta T}{\Delta t}$ - calorimeter sensor temperature rise rate, °F/sec
- v - free stream gas velocity
- W_a - apparent radiance as observed by pyrometer
- W_b - blackbody radiance at model temperatures
- x - axial distance from nozzle exit
- α - absorptance
- δ - boundary displacement thickness
- ε - emittance
- ρ - air density
- μ - dynamic viscosity

References

1. E. A. Gulbransen and K. F. Andrew, "Oxidation Studies on the Nickel-Chromium and Nickel-Chromium Aluminum Heater Alloys," J. of the Electrochem. Soc., 106, 941 (1959).
2. J. R. Johnston and R. L. Ashbrooke, "Oxidation and Thermal Fatigue Crackings of Nickel and Cobalt-Base Alloys in a High Velocity Gas Stream," NASA TN D-5376 (August 1969).
3. F. J. Centolenz, "Hypervelocity Oxidation Tests of Thoria Dispersed Nickel Chromium Alloys," NASA TM X-62,015 (11 February 1971).

4. H. E. Goldstein, "An Analytical Model for Hypersonic Ablation of Thoria Dispersed Nickel Chromium Alloy," AIAA Paper No. 71-34, presented at the AIAA 9th Aerospace Sciences Meeting, New York, 25-27 January 1971.
5. R. B. Pope, "Stagnation Point Convective Heat Transfer in Frozen Boundary Layers," AIAA Paper No. 68-15, presented at the AIAA 6th Aerospace Sciences Meeting, New York, 22-24 January 1968.

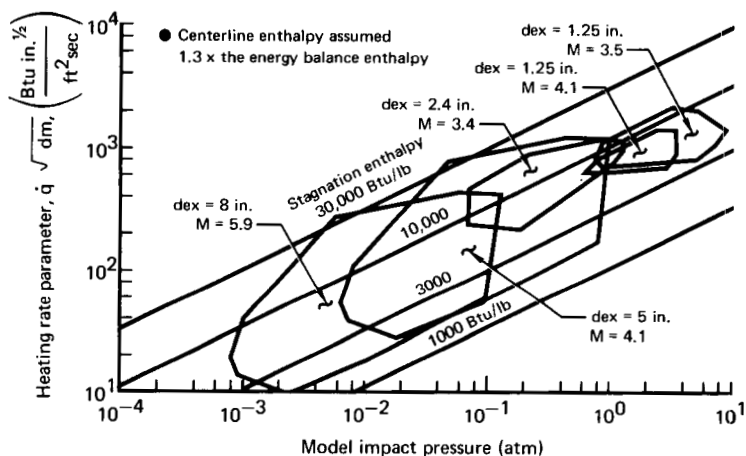


Fig. 1 PAT facility splash testing capability

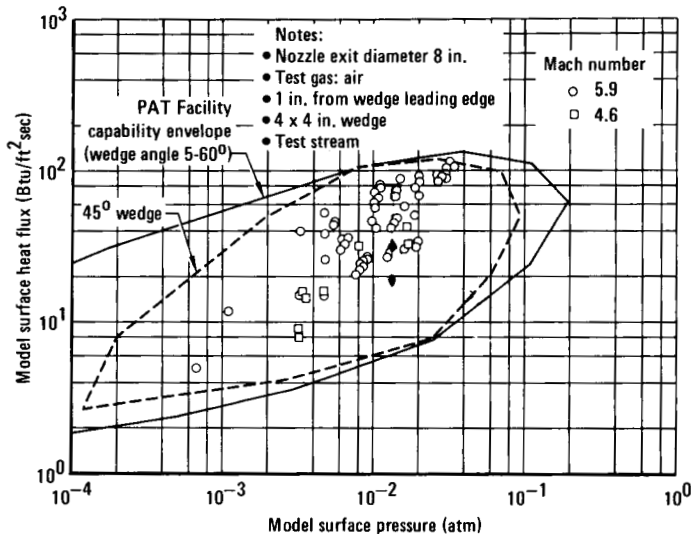


Fig. 2 PAT facility wedge testing capability

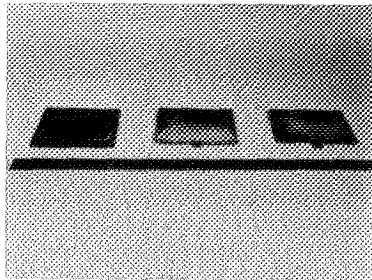


Fig. 3 Trial model configurations with the final design in center

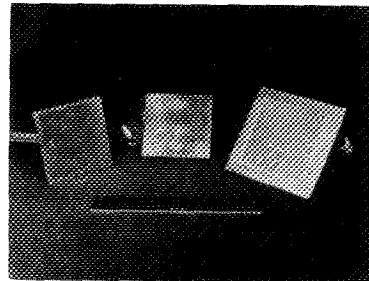


Fig. 4 Calibration plates and typical model in holder

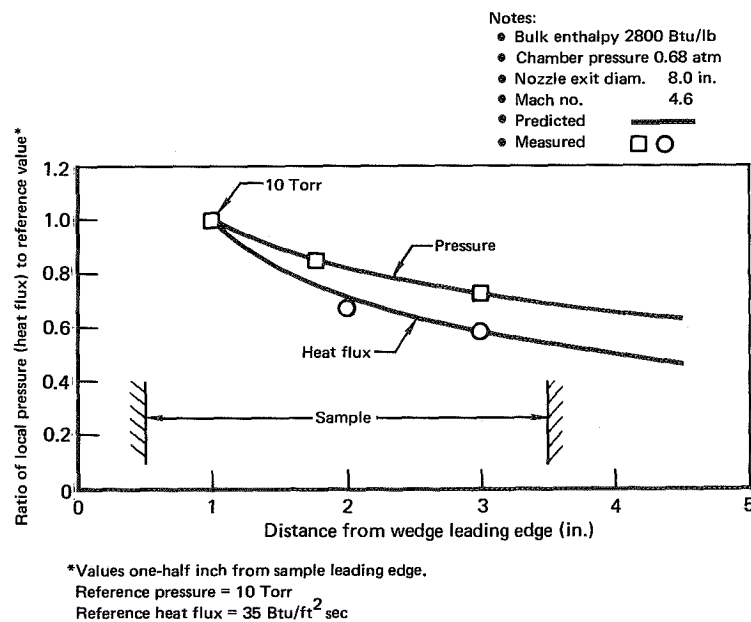
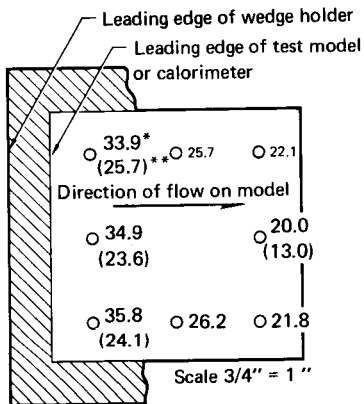


Fig. 5 Heat flux and pressure distributions along 60 deg wedge surface centerline



*Heat flux in $\text{Btu/ft}^2 \text{ sec}$ with model temperature at 2200°F

**Heat flux in $\text{Btu/ft}^2 \text{ sec}$ with model temperature at 2000°F

Fig. 6a Cold wall heat flux with model at 60 deg angle-of-attack

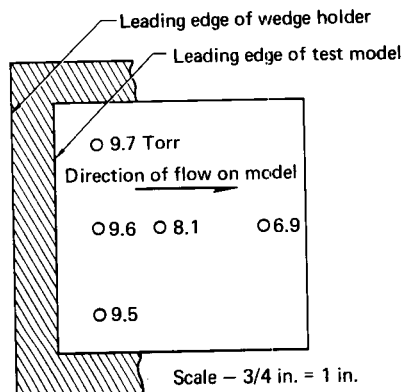


Fig. 6b Surface pressure with model at 60 deg angle-of-attack

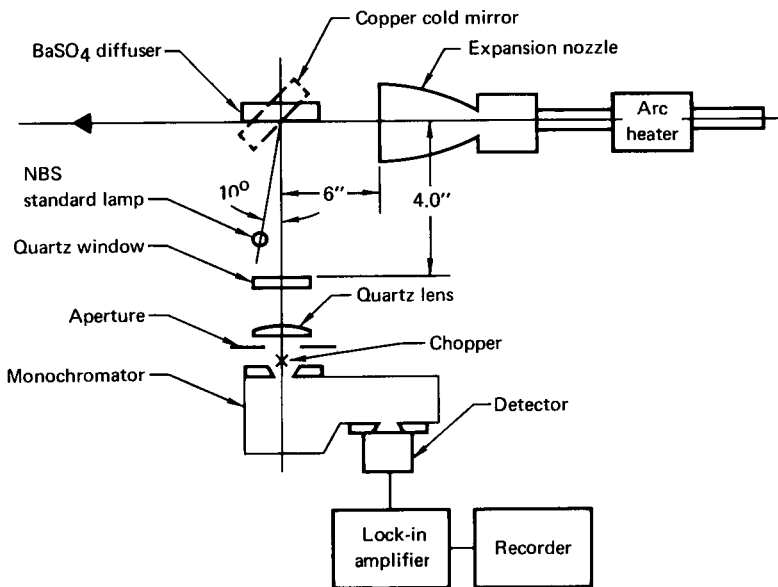


Fig. 7 Test arrangement for arc radiance measurements

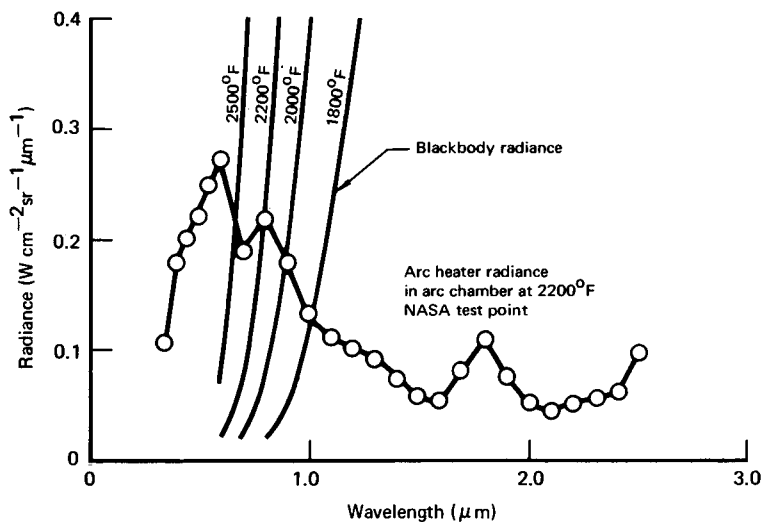
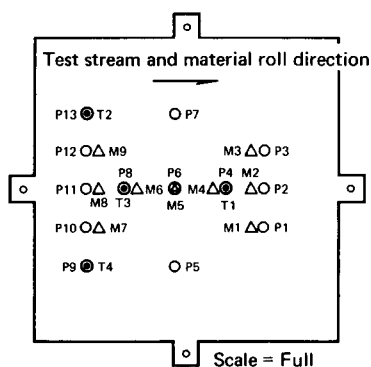


Fig. 8 Background radiant flux from the PAT arc heater



- Pt/Pt 10% Rh thermocouples (4)
- Optical pyrometer readings (13)
- △ Thickness measurements before and after tests (9)

Fig. 9 Model temperature and thickness measurement locations

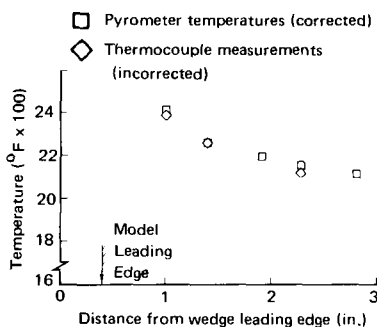


Fig. 10 Typical model response 0.5 in. from leading edge

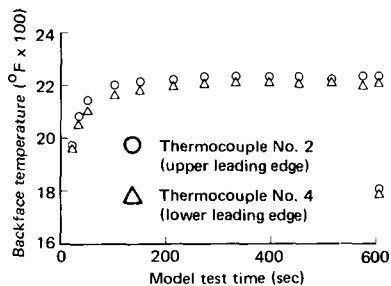


Fig. 11 Model temperature response 0.5 in. from leading edge

Table 1 Model No. 3 (DS-NiCr) surface* and backface temperatures (°F) at midpoint of test cycle

Pyrometer sighting position (see Fig. 11)	Test cycle					
	2	5	10	15	20	25
1	1985	1911	1845	1850	1845	1835
2	1995	1911	1858	1850	1820	1835
3	2015	1925	1902	1890	1858	1870
4(1)**	2025	1960	1913	1921	1870	1915
5	2140	2092	2092	2052	1980	2050
6	2086	2048	2005	2030	1980	2005
7	2231	2120	2072	1992	2088	2090
8(3)**	2250	2155	2140	2130	2140	2090
9(4)**	2290	2275	2250	2130	2185	2185
10	2296	2291	2238	2238	2220	2200
11	2306	2275	2230	2238	2220	2215
12	2306	2278	2258	2243	2220	2215
13(2)**	2306	2270	2258	2255	2221	2185

Back face thermocouple position						
1	1963	1909	1875	1899	1916	1917
2	2195	2218	2204	2218	2211	2205
3	2109	2100	2271	2097	2101	2101
4	2191	2227	2215	2206	2199	2189

*Temperature as measured by the pyrometer with the emittance control set on 1.0

**Thermocouple number that corresponds to this pyrometer sighting position

Table 2 Model physical characteristics

Thickness (in.) at position (see Fig. 11)	Test model						
	1 (TD-NiCr)	2 (TD-NiCrAlY)	3 (DS-NiCr)	4 (Haynes 188)	5 (TD-NiCr)	6 (DS-NiCr)	7 (TD-NiCrAl)
<u>M1</u> Pre post change	0.0127 0.0135 +0.0008	0.0140 0.0150 +0.0010	0.0120 0.0125 +0.0005	0.0168 0.0180 +0.0012	0.0115 0.0110 -0.0005	0.0115 0.0125 +0.0010	0.0163 0.0170 +0.0007
<u>M2</u> Pre post change	0.0126 0.0132 +0.0006	0.0140 0.0150 +0.0010	0.0120 0.0130 +0.0010	0.0168 0.0180 +0.0012	0.0115 0.0110 -0.0005	0.0115 0.0120 +0.0005	0.0163 0.0170 +0.0007
<u>M3</u> Pre post change	0.0132 0.0135 +0.0003	0.0140 0.0150 +0.0010	0.0120 0.0125 +0.0005	0.0168 0.0180 +0.0012	0.0115 0.0110 -0.0005	0.0115 0.0125 +0.0010	0.0163 0.0173 +0.0010
<u>M4</u> Pre post change	0.0125 0.0135 +0.0010	0.0140 0.0150 +0.0010	0.0120 0.0125 +0.0005	0.0168 0.0180 +0.0012	0.0115 0.0112 -0.0003	0.0115 0.0120 +0.0005	0.0162 0.0170 +0.0008
<u>M5</u> Pre post change	0.0125 0.0130 +0.0005	0.0142 0.0150 +0.0008	0.0120 0.0130 +0.0010	0.0168 0.0180 +0.0012	0.0115 0.0120 +0.0005	0.0115 0.0125 +0.0010	0.0161 0.0170 +0.0009
<u>M6</u> Pre post change	0.0124 0.0134 +0.0010	0.0145 0.0155 +0.0010	0.0120 0.0130 +0.0010	0.0168 0.0180 +0.0012	0.0115 0.0120 +0.0005	0.0115 0.0125 +0.0010	0.0157 0.0161 +0.0004
<u>M7</u> Pre post change	0.0127 0.0135 +0.0008	0.0145 0.0155 +0.0010	0.0120 0.0125 +0.0005	0.0168 0.0180 +0.0012	0.0115 0.0110 +0.0005	0.0115 0.0120 +0.0005	0.0162 0.0170 +0.0008
<u>M8</u> Pre post change	0.0126 0.0140 +0.0014	0.0145 0.0155 +0.0010	0.0120 0.0125 +0.0005	0.0168 0.0180 +0.0012	0.0115 0.0112 -0.0003	0.0115 0.0125 +0.0010	0.0162 0.0173 +0.0011
<u>M9</u> Pre post change	0.0126 0.0138 +0.0012	0.0145 0.0155 +0.0010	0.0120 0.0130 +0.0010	0.0168 0.0182 +0.0014	0.0115 0.0110 -0.0005	0.0120 0.0128 +0.0008	0.0163 0.0175 +0.0012
Model weights (grams)							
Pre post change	15.787 15.790 +0.003	17.261 17.312 +0.051	14.918 14.906 -0.012	23.316 23.225 -0.091	14.231 14.224 -0.007	14.844 14.852 +0.008	19.352 19.371 +0.019

ABLATIVE MATERIALS EVALUATION FOR HIGH PERFORMANCE LIFTING ENTRY VEHICLES*

Don L. David and K. R. Carnahan, *Convair Division of General Dynamics*;
Richard N. Mueller, *Wright-Patterson Air Force Base*

ABSTRACT

An ablative materials evaluation program was conducted to support the design of a lower surface thermal protection system for high performance lifting entry vehicles. A total of twenty elastomeric and carbon-phenolic materials were evaluated.

Preliminary screening of materials was accomplished using results of a plasma-arc test program. Test models were two-inch diameter cylinders, having in-depth temperature instrumentation. All models were exposed to stagnation heating on the front face until the temperature reached 600°F at a depth of 0.75 inches. Evaluation criteria included surface recession, depth of degradation, char integrity, and insulative characteristics. Ablation response was correlated with analytic techniques, and predictions of performance under flight conditions were made.

Five materials were selected and tested in a plasma-arc tunnel using a 30 degree half-angle wedge model configuration. Good simulation of flight conditions was obtained for cold-wall heating rate and surface pressure. It was not possible to obtain the correct stream enthalpy; however, this was felt to be the least significant parameter. Use of the wedge configuration allowed evaluation of surface recession characteristics under realistic surface shear conditions. Two materials were selected for use in the design of test articles simulating the first 72 inches of the Air Force Dynamics Laboratory FDL-5A basepoint vehicle; the model will be tested in the 50 MW arc heater at Wright-Patterson.

*Work conducted under contract to AFFDL, No. F33615-70-C-1304.

DEVELOPMENT OF A SILICONE ABLATOR FOR HIGH-HEAT-FLUX AND HIGH-SHEAR-RATE CONDITIONS

Richard A. Campbell, James A. Ramseyer, *Technical Service & Development*; Arnold Huntress, *Aerospace Materials Development*, Dow Corning Corporation, Midland, Michigan.

ABSTRACT

A development program was instituted to develop a silicone material which would give suitable ablative protection in the high heat flux, high-shear environments encountered in severe reentry applications such as nosecones for ballistic vehicles, protection of leading edges or other critical areas of a vehicle. In addition, the ease of handling, low application cost and room temperature cure would make such a silicone material a definite candidate material for the fabrication of liners and nozzles for the large rockets so necessary for the launch of these vehicles.

This paper traces the development work of this product from the selection of suitable polymers through the choice of the best fillers and the finalization of filler loadings which culminated in the production of a final, salable product.

INTRODUCTION

Since the introduction of commercial silicone products over twenty-five years ago, they have been used consistently in environments too severe for other materials. Their usage in the aerospace industry has been due to their serviceability in extremes of temperature (-130° to 550° F.), thermal stability, aging characteristics in oxygen and ozone, resistance to such harsh chemicals as Skydrol* hydraulic fluid, and their electrical and thermal insulating properties.

The thermal insulative nature of silicones is two-fold: first, they can afford protection to delicate components due to low thermal conductivity; and secondly, they can supply ablative protection when conditions demand it.

Silicone ablative materials have been used for years in applications involving heat shields for manned space vehicles, protective coatings for high-speed missiles and rockets, ablative sealants for engine compartments of commercial aircraft as well as protection of ground support equipment for land and ship-launched missiles and rockets.

These ablative applications for silicones have traditionally been of short duration and in low to moderate heat flux ranges (less than 200 BTU/ft.² sec.) and low shear rates. Silicone ablatives had traditionally been limited to these "mild" ablative conditions because of the lack of char strength and stability at the higher heat fluxes

* Trademark of The Monsanto Corporation

and shear rates. Materials such as phenolic laminates, castable carbons, and silicon carbides have been used for these more severe applications, including the high-heat flux, high-shear environment involved in re-entry applications such as nose cones of ballistic missiles and protection of leading edges of vehicles. Other uses include rocket liners and nozzles.

In early 1966, we began the development of a silicone to withstand these severe ablative environments. We evaluated many refractory materials to find a suitable filler which would lend stability to a char in high shear, high flux environments. Of all materials listed, see Table I; silicon carbide looked the most promising.

We used a common two-component, heat curable dimethylpolysiloxane sealant, Dow Corning® 93-022 aerospace sealant, as a base, compounded with various levels of silicon carbide. Materials such as quartz fibers, sugar, and fibrous potassium titanate, which had been shown to be good fillers, were then added. Formulations are included in Table II. After suitable curing, samples of these formulations were submitted for ablative screening in our ablative test laboratory. The test selected for this screening was Dow Corning Ablative Test Condition No. 3. This test uses a Linde Jet Piercing Torch fueled with kerosene and oxygen to provide an ablative environment of about 760 BTU/ft.² sec. with a gas stream velocity of Mach 3 (See appendix.). Because the penetration rate measured on a sample run until burn through includes both virgin material and char and since the samples varied in initial thickness, the Performance Indices* reported for the burn-through test were used only for rough screening of the materials. In the twenty-second test, however, the initial thickness has no influence and the penetration rate of only virgin material is being measured. Thus, this 20-second test gives a more valid comparison of ablative performance.

The results of this screening, Table III, indicated that silicon carbide alone, Formulation No. 6, is not a good ablative filler in this silicone base. Formulation No. 5 shows that quartz fibers performed quite well but when silicon carbide was added, as in formulation No. 4, the performance index was increased by 50%.

Since both Performance Indices for formulations No. 8 and No. 9 were lower than for the No. 4 formulation, an optimum ratio of silicon carbide to quartz fibers appeared to exist.

At this time, other work had demonstrated that a definite relationship existed between the number of phenyl molecules included in a standard dimethyl silicone chain and the ablation performance of rubbers made from polymers containing such a formulation. Figure 3 shows that an optimum amount of phenyl contained in the silicone polymer lowers the penetration rate in the Linde Torch Test.

Using this knowledge, we decided to test one of these optimized phenyl-containing polymers in an ablative formulation utilizing silicon carbide. For comparative purposes we also tested four phenolic-based materials (Table IV). These materials were tested with the Linde torch using the same 760 BTU/ft.² sec. test. The results contained in Table V show that formulation No. 13 had the best

$$\text{* Performance Index} = \frac{100}{\text{Sp. Gr.} \times \text{Penetration rate (mils/second)}}$$

ablative performance. This formulation was better than the best phenolic tested. It also appeared from this test that the optimum silicon carbide/quartz fiber concentrations had been bracketed.

The handling properties of the materials in Table IV decreased as filler loadings increased but the No. 13 formulation was very manageable.

At this point in our study, a report from the Air Force Materials Laboratory* described several rocket engines and the Linde Torch. The maximum heat flux produced by any of these engines was 1085 BTU/ft.² sec. at a velocity of about Mach 2.5. Since this closely resembled our Ablative Test Conditions No. 51 and 52 (see appendix), we decided to test these latest materials in the high heat flux environments. Test Conditions No. 51 and No. 52 have heat fluxes of about 1045 and 1550 BTU/ft.² sec. respectively. The results of these two tests are contained on Tables VI and VII. The 1045 BTU/ft.² sec. test shows that formulation 14 outperformed the other formulations with the exception of the phenolic-quartz fiber laminate which was marginally better. The severe 1550 BTU/ft.² sec. test contained in Table VII was too severe and the erosion was by means of mechanical removal rather than ablation. Although measurements were not made on the pressures involved in the 1550 BTU/ft.² sec. flame, they were noticed to be several times stronger than in the other tests.

These tests of the combination of the phenyl-methyl silicone-based sealant and silicon carbide showed that in some of the higher heat fluxes that the silicone materials can perform better than competitive materials. This work suggested more investigation could be done in lowering the quartz fiber content. This adjustment would also improve the flow and handling properties of the sealant. The next formulations tested, see Table VIII, contained lower levels of quartz fibers and also various mixtures of quartz fibers and quartz powders and the effects of these changes on the base viscosity. These materials were tested in test conditions No. 3 and No. 51 (710 and 1045 BTU/ft.² sec.). The results of these tests are given on Tables IX and IV. Since we were looking, in this test, for a low viscosity ablator, the only materials evaluated at the higher heat flux, 1045 BTU/ft.² sec., were those formulations having the lowest viscosities. Of these, the formulation No. 20 performed the best. All the materials tested had significant longer burn-through times than the competitive material tested which was a trowelable butadieneacrylonitrile rubber.

One of the formulations in this last test, Formulation 20, was tested by several contractors as a high shear, high heat flux ablator. Although the material performed well, it had several disadvantages: high specific gravity (1.75) and high thermal conductivity ($4.1 \frac{\text{BTU-in}}{\text{Ft.}^2\text{°F hr.}}$). To correct these shortcomings, we decided to try lowering the silicon carbide levels and finding an alternate fibrous material. Since it is known that the fibers contribute much to the strength of the char we felt that by switching to a higher melting fiber we could increase the melt viscosity in the filler decomposition level of the char and thereby increase its strength and shear resistance. Since carbon fibers are thermally stable to 6600° F, while the quartz fibers melt at 3000° F, we decided to incorporate them.

The results of testing, see Table XI, shows that the substitution of carbon fibers

* AFML TR-65-4 by D. L. Schmidt

for the quartz fibers did not significantly decrease the penetration rate or increase the performance index of the formulation 20-type material at the lower two parts level. However, the addition of the carbon fibers did allow us to drastically decrease the amount of silicon carbide necessary in the formulation and still get excellent ablative results. As can be seen in figures No. 4 and No. 5, the levels of five parts silicon carbide and four parts carbon fibers were the best in ablative performance. A further series of tests were run to investigate the influence of carbon fibers from different manufacturers. Figure 6 shows the results of these tests with the fibers from supplier No. 4 out-performing the others tested.

These latest tests demonstrated to us an optimum formulation, number 32, which had a lower specific gravity, 1.46, and a low thermal conductivity, 2.42 BTU-in/ft.²-degrees F-hour.

We now felt that we had a formulation which could be competitive in the high shear, high heat flux ablative environments.

We took this information and ran a complete bank of ablative tests on it including tests with oxygen/acetylene torches and the Linde Jet Piercing torch. A sample of the tests run with the oxygen-acetylene torch is the proposed ASTM test at 702 BTU/ft.² sec., see Table XII. This test simulates a high, subsonic velocity ablative application, (See ASTM E285-65T). In this test No. 32 formulation was compared to Dow Corning 93-072 aerospace sealant which is currently being used on high-speed missiles as an exterior ablative coating. The shear rates in this test are not severe enough to take advantage of the char strength of the high shear ablator.

Finally, using the Linde torch test, this final formulation was tested against nine commonly used plastic materials listed below.

- 1) trowelable butadiene acrylonitrile (BAN) rubber
- 2) heat and pressure vulcanized BAN rubber
- 3) a phenolic silica
- 4) a phenolic-refrasil
- 5) a phenolic asbestos
- 6) a silica-filled phenolic asbestos
- 7) a phenolic with long fiber asbestos
- 8) phenolic with magnesium hydroxide fibers
- 9) phenolic-carbon powder (castable carbon)

These results are listed in Table XIII. You will notice that in this test the silicone material out-performed all other materials tested.

CONCLUSION

Our testing, just described, was concluded with the commercialization of a silicone ablative which, besides being an excellent ablative in the high heat-flux, high shear rates applications, has features not available in most plastic ablaters. It is:

- 1) elastic
- 2) curable at room temperature
- 3) lower density
- 4) lower thermal conductivity
- 5) easy to apply
- 6) easy to mold
- 7) easy to trowel

- 8) low cost
 - . . . low cost per unit volume
 - . . . lower application cost
- 9) adheres well to a variety of substrates

The production number assigned to the formulation No. 32 is Dow Corning® 93-104 ablative material.

APPENDIX

Linde Torch Test - This test utilizes a small kerosene-oxygen fueled device, originally designed to drill blast holes in taconite ore for strip mining. It was originally known as the Linde FSJRF-3 Jet Piercing Torch and has been modified for our use as a high heat flux, high shear force, supersonic testing device. The modification of this torch involves addition of flow meters, pressure gauges, safety controls, ignition systems and the normal sample conveying devices. This modification has been thoroughly discussed in an earlier paper.* Figure 1 is a schematic of the system used for this torch. Figure 2 shows the sample configuration and location used during the standard test, condition 3, and the two other tests, conditions 51 and 52. This torch consumes approximately 1,000 cubic feet per hour of gaseous oxygen and 6 to 7 gallons per hour of kerosene. It creates, on a relatively inexpensive laboratory scale, very severe chemical combustion conditions. We commonly use this device to evaluate materials which will be exposed to the direct impingement of chemical rocket exhausts. Some studies on re-entry materials for high heat flux use (500 to 1,000 BTU/ft² sec.) have also been run on this device although obviously results obtained with a chemical combustion system may vary considerably from plasma test results.

* Boyd, G. C. and Hoffman, K. R., "Simulated Rocket Environments for Material Screening", Proceedings, Society of Plastics Engineers National Meeting, Philadelphia, Pa., January 1962.

LINDE TORCH FLOW SHEET

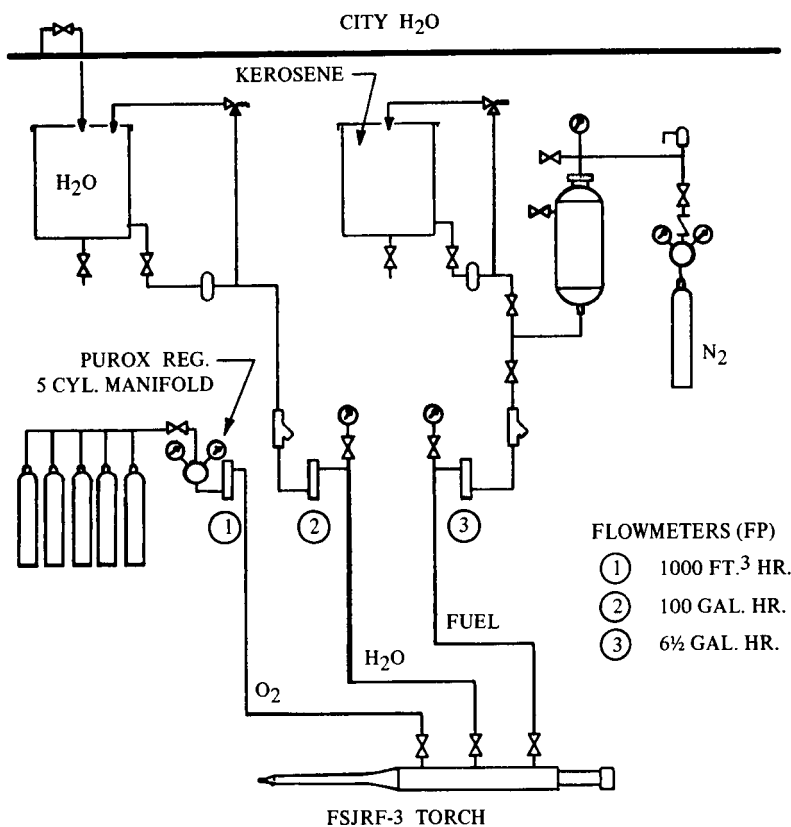
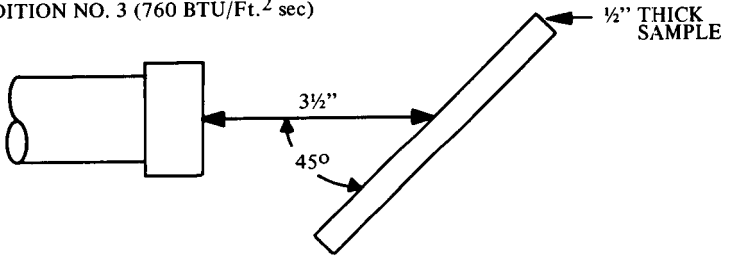


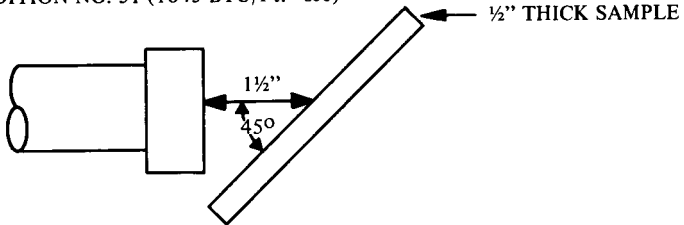
Fig. 1

LINDE TORCH TESTS

CONDITION NO. 3 (760 BTU/Ft.² sec)



CONDITION NO. 51 (1045 BTU/Ft.² sec)



CONDITION NO. 52 (1550 BTU/Ft.² sec)

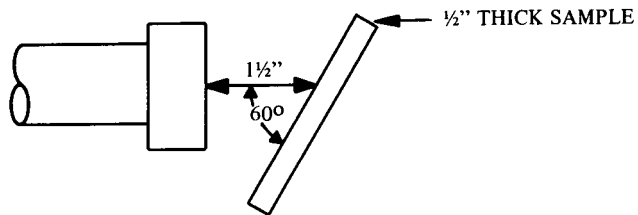


Figure 2

EFFECT OF PHENYL CONTENT ON SILICONE ELASTOMER
ABLATIVE PERFORMANCE (LINDE TORCH TEST)

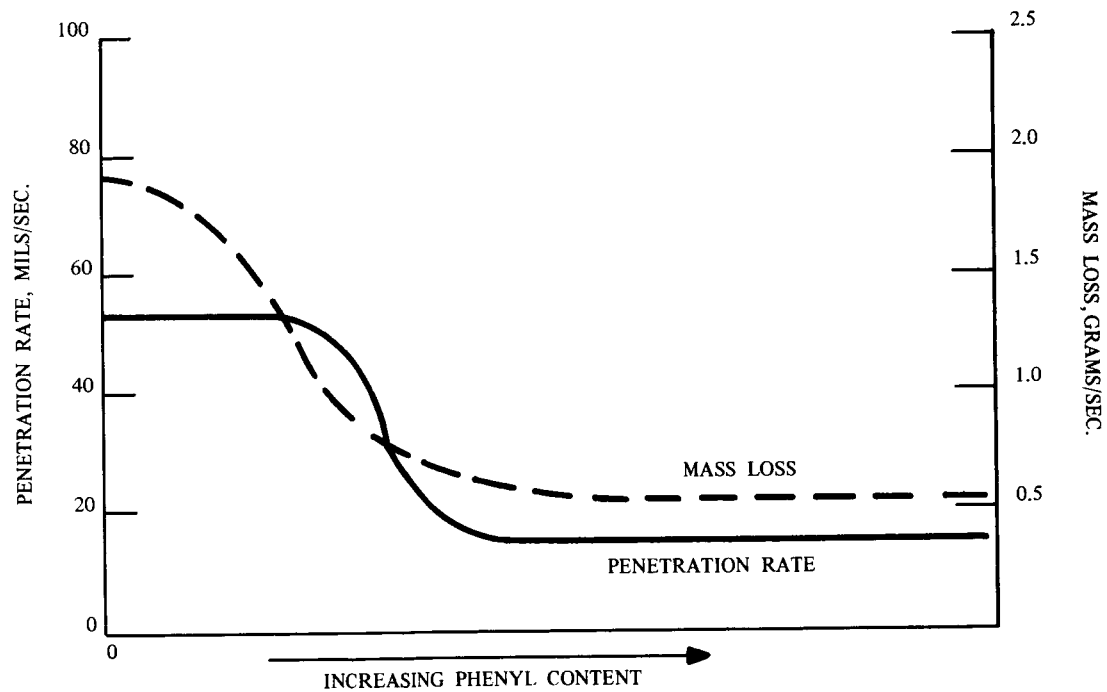


Fig. 3

ABLATIVE PERFORMANCE VS. SILICON CARBIDE CONTENT
 LINDE TORCH 760 BTU/Ft²-Sec, MACH 3

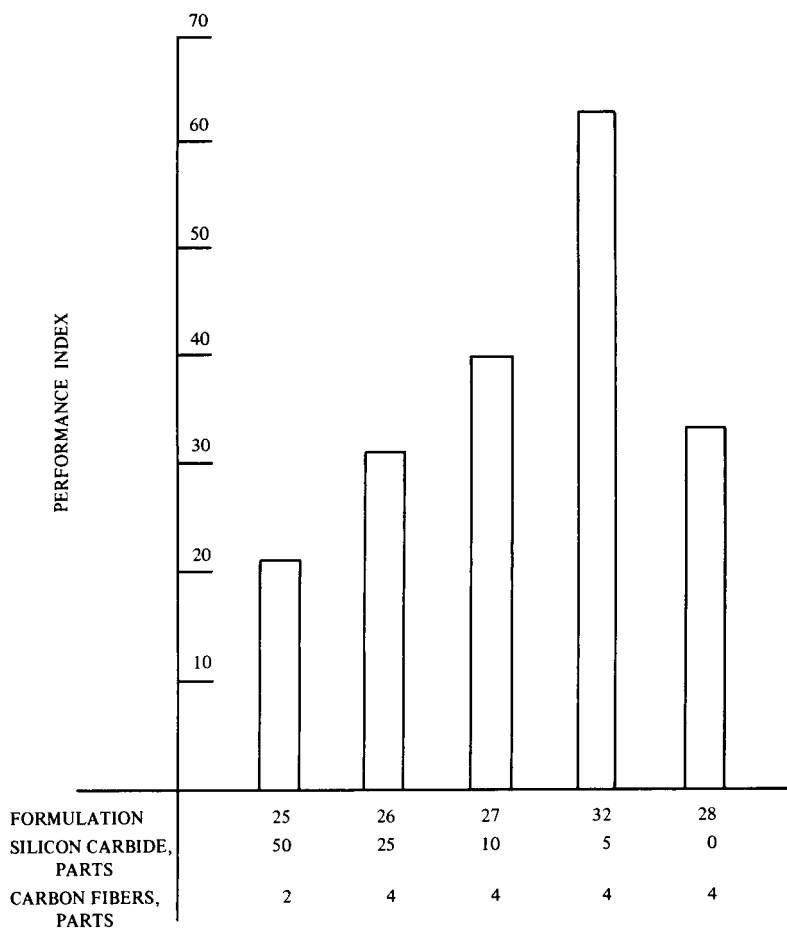


Fig. 4

ABLATIVE PERFORMANCE VS. CARBON FIBER CONTENT
LINDE TORCH 760 BTU/Ft²-Sec, MACH 3

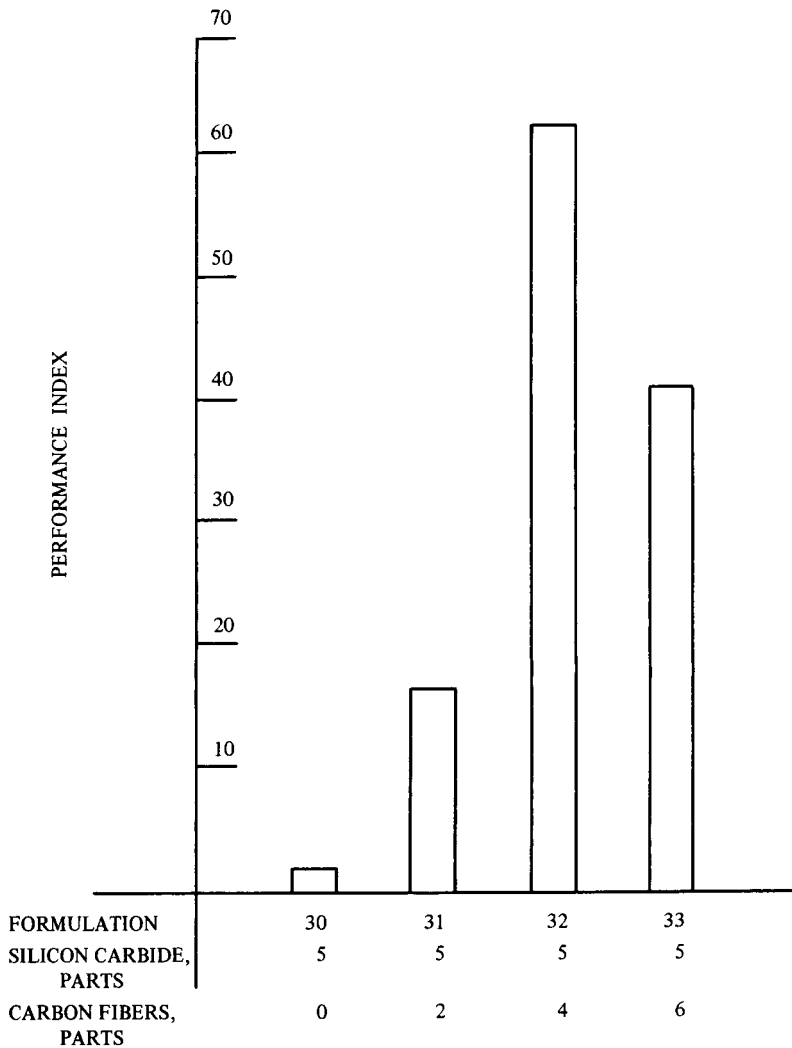


Fig. 5

ABLATIVE PERFORMANCE BY FIBER SUPPLIERS

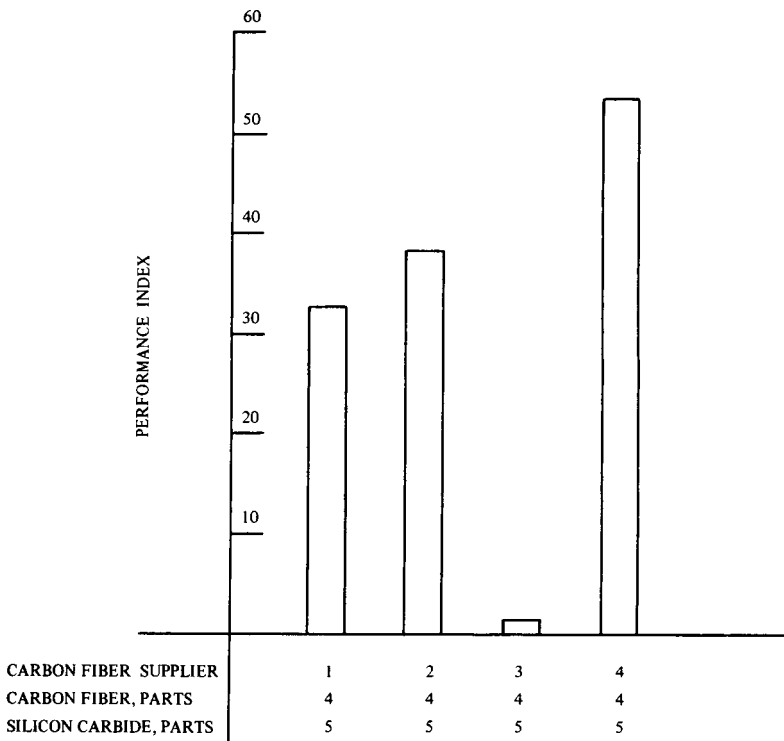


Fig. 6

TABLE I
REFRACTORY MATERIALS EVALUATED

Al ₂ O ₃	ZrB ₂
B ₄ C	ZrC
BN	ZrSiO ₄
MoC	WB
NbC	WC
TiB	SiC
TiC	

TABLE II

EVALUATION OF SILICON CARBIDE AS ABLATIVE FILLER
IN TYPICAL SEALANT

FORMU- LATION	PARTS DOW CORNING 93-022 BASE	PARTS DOW CORNING 93-022 CURING AGENT	PARTS SILICON CARBIDE	PARTS QUARTZ FIBERS	PARTS SUGAR	PARTS POTASSIUM TITANATE
1	100	10	40	20	20	10
2	100	10	40	20	—	10
3	100	10	40	20	—	—
4	100	10	50	15	—	—
5	100	10	—	15	—	—
6	100	10	50	—	—	—
7	100	10	—	20	—	10
8	100	10	100	10	—	—
9	100	10	100	15	—	—

TABLE III

LINDE TORCH ABLATIVE PERFORMANCE
 TEST CONDITION NO. 3
 760 BTU/Ft²-Sec, MACH 3

FORMULATION	SPECIFIC GRAVITY	20-SECOND TEST			BURN-THROUGH TEST		
		INITIAL THICKNESS, INCHES	PENETRATION RATE, INCHES/SEC.	PERFORMANCE INDEX	INITIAL THICKNESS, INCHES	PENETRATION RATE, INCHES/SEC.	PERFORMANCE INDEX
1	1.36	—	—	—	0.550	0.00764	9.7
2	1.34	0.513	0.00954	7.8	0.519	0.00514	14.5
3	1.35	0.517	0.00805	9.2	0.532	0.00304	24.4
4	1.32	0.532	0.00630	12.0	0.516	0.00355	21.4
5	1.09	0.538	0.01075	8.5	0.553	0.00666	10.0
6	1.36	0.537	0.05370	1.4	0.518	0.05760	1.3
7	1.10	0.563	0.01130	8.0	0.535	0.00622	14.6
8	1.53	0.523	0.00844	7.8	0.519	0.00335	19.5
9	1.54	0.475	0.00775	8.4	0.481	0.00306	21.2

TABLE IV

FORMULATIONS OF ABLATIVE FILLERS IN PHENYL-CONTAINING
SILICONE SEALANT

FORMU- LATION	PARTS BASE MATERIAL	PARTS CURING AGENT	PARTS SILICON CARBIDE	PARTS QUARTZ FIBERS	OTHER
10	100	10	—	—	
11	100	10	15	—	
12	100	10	30	50	
13	100	10	15	50	
14	100	10	7.5	25	
15	—	—	—	—	60% Phenolic 40% Asbestos with some Quartz Fibers
16	—	—	—	—	26% Phenolic 74% Random Quartz Fibers
17	—	—	—	—	29% Phenolic 71% ½" Squares of Silica
18	—	—	—	—	Phenolic/Quartz Laminate 39% Phenolic 61% Quartz Fiber Fabric

TABLE V

LINDE TORCH ABLATIVE PERFORMANCE
HEAT FLUX 760 BTU/Ft²-Sec, MACH 3

FORMULATION	SPECIFIC GRAVITY	INITIAL THICKNESS INCHES	PENETRATION RATE INCHES/SEC	TEST DURATION, SECONDS TO BURN THROUGH	PERFORMANCE INDEX
10	1.45	0.521	0.00983	57	7.1
11	1.48	0.530	0.00482	110	14.0
12	1.60	0.548	0.00390	140	16.0
13	1.76	0.558	0.00178	313	32.0
14	1.78	0.544	0.00185	294	30.4
15	1.36	0.551	0.0120	46	6.1
16	1.73	0.571	0.0204	28	2.8
17	1.80	0.547	0.00250	219	22.2
18	1.71	0.550	0.0157	35	3.7

TABLE VI

LINDE TORCH ABLATIVE PERFORMANCE

TEST CONDITION NO. 51

HEAT FLUX 1045 BTU/Ft²-Sec

FORMULATION	SPECIFIC GRAVITY	INITIAL THICKNESS INCHES	PENETRATION RATE INCHES/SEC	TEST DURATION SEC TO BURN THROUGH	PERFORMANCE INDEX
10	1.45	0.545	0.01190	46	5.8
12	1.60	0.548	0.00400	137	15.6
13	1.76	0.555	0.00433	127	13.1
14	1.78	0.560	0.00284	197	19.8
18	1.71	0.549	0.00276	199	21.2

TABLE VII

LINDE TORCH ABLATIVE PERFORMANCE
 TEST CONDITION NO. 52
 HEAT FLUX 1550 BTU/Ft²-Sec

FORMULATION	SPECIFIC GRAVITY	INITIAL THICKNESS INCHES	PENETRATION RATE INCH/SEC	TEST DURATION, SECONDS TO BURN THROUGH	PERFORMANCE INDEX
10	1.45	0.499	0.0238	21	3.9
12	1.60	0.552	0.0204	27	3.1
13	1.76	0.563	0.0310	18	1.8
14	1.78	0.568	0.0242	23.5	2.3
15	1.36	0.550	0.0458	12	1.6
16	1.73	0.571	0.0204	28	2.83
18	1.71	0.550	0.0157	35	3.7

TABLE VIII

INVESTIGATION OF LOWER QUARTZ CONTENT AND VISCOSITY

FORMULATION	PARTS PHENYL- CONTAINING BASE	PARTS CURING AGENT	PARTS SILICON CARBIDE	PARTS QUARTZ FIBERS	VISCOSITY, POISE
10	100	10	—	—	500
19	100	10	50	—	700
20	100	10	50	2	700
21	100	10	50	8.5	—
22	100	10	50	15	5,000
23	100	10	50	5	950
24	— TROWELLABLE BUTADIENE ACRYLONITRILE RUBBER —				

TABLE IX

LINDE TORCH ABLATIVE PERFORMANCE
TEST CONDITION NO. 3
HEAT FLUX 760 BTU/Ft²-Sec, MACH 3

FORMULATION	INITIAL THICKNESS, INCHES	PENETRATION RATE, INCHES/SEC.	TEST DURATION, SECONDS TO BURN THROUGH
10	0.531	0.00916	58
19	0.514	0.00547	94
20	0.514	0.00400	128
21	0.524	0.00499	105
22	0.535	0.00594	90
23	0.535	0.00272	203
24	0.524	0.0194	27

TABLE X

LINDE TORCH ABLATIVE PERFORMANCE
 TEST CONDITION 51
 HEAT FLUX 1045 BTU/Ft²Sec - VELOCITY MACH 3

FORMULATION	INITIAL THICKNESS INCHES	PENETRATION RATE, INCH/SEC	TEST DURATION SECONDS TO BURN THROUGH
10	0.526	0.01170	45
19	0.535	0.00524	102
20	0.550	0.00314	175
23	0.547	0.00828	66
24	0.530	0.0321	16.5

TABLE XI

FORMULATION	PARTS PHENYL- CONTAINING SILICONE BASE	PARTS CURING AGENT	PARTS CARBON FIBERS	PARTS SILICON CARBIDE	SPECIFIC GRAVITY	PENETRATION RATE, INCHES/SEC	TEST DURATION, SECONDS TO BURN THROUGH	PERFORMANCE INDEX
20	100	10	2*	50	1.73	0.00288	195	20.1
25	100	10	2	50	1.74	0.00218	273	20.6
26	100	10	4	25	1.59	0.00204	292	31.0
27	100	10	4	10	1.51	0.00165	337	39.9
28	100	10	4	—	1.44	0.00194	289	35.8
29	100	10	6	10	1.38	0.00174	330	41.7
30	100	10	—	5	1.37	0.0584	9.6	1.2
31	100	10	2	5	1.37	0.00452	122	16.2
32	100	10	4	5	1.38	0.00117	497	62.0
33	100	10	6	5	1.34	0.00173	349	41.8
34	100	10	4	5	1.36	0.00132	439	55.7
35	100	10	4	5	1.39	0.00175	520	41.2

* QUARTZ FIBERS INSTEAD OF CARBON FIBERS

TABLE XII

OXYGEN/ACETYLENE TORCH ABLATIVE PERFORMANCE
 ASTM E 285-65T, 702 BTU/Ft²Sec-HIGH VELOCITY-SUBSONIC

MATERIAL	SPECIFIC GRAVITY	INITIAL THICKNESS, INCHES	PENETRATION RATE, INCHES/SEC	ΔT °C	TEST DURATION, SECONDS	PERFORMANCE INDEX
FORMULATION NO. 32	1.46	0.255	0.00510	595	50	13.5
DOW CORNING 93-072 AEROSPACE SEALANT	1.12	0.271	0.00657	475	40	13.8

TABLE XIII
LINDE TORCH ABLATIVE PERFORMANCE
TEST CONDITION NO. 3
760 BTU/Ft²-Sec

MATERIAL	SPECIFIC GRAVITY	INITIAL THICKNESS, INCHES	PENETRATION RATE, INCH/SEC.	TEST DURATION, SEC. TO BURN THROUGH	PERFORMANCE INDEX
FORMULATION NO. 32	1.46	0.530	0.00198	267	35
CASTABLE CARBON PHENOLIC/CARBON	1.82	0.515	0.00542	95	10.1
PHENOLIC/ MAGNESIUM HYDROXIDE	1.85	0.527	0.00659	80	8.4
PHENOLIC/ ASBESTOS	1.78	0.614	0.01095	56	5.2
PHENOLIC/LONG, FIBER ASBESTOS	1.84	0.600	0.01132	53	4.8
PHENOLIC/ SILICA ASBESTOS	1.81	0.512	0.01067	48	5.2
TROWELLABLE BUTADIENE- ACRYLO-NITRILE	1.30	0.524	0.0194	27	3.9
HEAT & PRESSURE VULCANIZED BAN RUBBER	1.27	0.470	0.0289	16.8	2.7
PHENOLIC/SILICA	1.80	0.547	0.00250	219	22.2
PHENOLIC/ QUARTZ FIBER	1.71	0.555	0.00190	293	30.8
PHENOLIC/ ASBESTOS	1.36	0.551	0.0120	46	6.1

AN EVALUATION OF FLIGHT DATA FOR THE APOLLO THERMAL PROTECTION SYSTEM

E. P. Bartlett, *Aerotherm Division of Acurex Corporation, Mountain View, California*; D. M. Curry, *NASA Manned Spacecraft Center, Houston, Texas*

ABSTRACT

A study has been conducted to correlate Apollo ablation and thermal response flight data using advanced state-of-the-art analytical procedures. The agreement between flight data and predictions is consistently excellent for in-depth temperature distributions, char density profiles, and surface ablation, thus validating the analytical procedures.

INTRODUCTION

Several early Apollo flights were heavily instrumented with thermocouples, char sensors, and calorimeters. Also, detailed chemical analyses of cores cut from recovered heat shields were performed. These data are compared to predictions generated with advanced state-of-the-art analytical procedures. The basic calculational approach consists of one-dimensional charring ablation solutions considering char density buildup in depth due to coking and equilibrium chemistry at the surface. Thus surface ablation prediction is based on detailed chemical considerations rather than empirically derived relationships. The surface convective heating boundary condition is represented by heat- and mass-transfer coefficients. These were provided by correlations of solutions for the laminar/turbulent nonsimilar chemically reacting boundary layer over an ablating Apollo heat shield. These correlations are also presented in the paper. The methods and results presented in this paper are described in detail in Reference 1.

PREDICTION METHODOLOGY

Prediction of the ablation and thermal response behavior of the Apollo heat shield material requires inviscid flow field information, convective and radiative heating rates, and modeling of material surface and internal response mechanisms. The methods employed to represent these phenomena are described in the following subsections.

Inviscid Flow Field

A need for detailed inviscid flow field information was

circumvented in the present study. Radiation heating calculations were based upon extension¹ of a simple flow field correlation presented by Page et al.² Boundary-layer solutions generated to obtain convective heating rates required only surface pressure distributions and streamline spreading factors. The pressure distributions were obtained from correlations of wind tunnel and flight data developed at NASA/MSC.³ In order to obtain an independent evaluation of Apollo pressure distribution data, a code developed by Abbett and Fort⁴ was modified¹ for application to Apollo geometry. A comparison of results generated with this code with zero-incidence pressure distribution data is presented in Figure 1. The agreement is seen to be satisfactory. Streamline spreading factors were calculated using the method of Hearne et al.⁵ which employs thin shock layer and Newtonian crossflow pressure distribution approximations.

Radiative Heating

A small study was also conducted to obtain an independent evaluation of radiation flux levels and distribution factors employed by NASA/MSC.⁶ Solutions for radiant intensity generated with the RAD code⁷ are compared in Figure 2 to superorbital Apollo data and results generated with the NASA/MSC procedure. The RAD code considers in moderate detail⁷ the spectral distribution of line as well as continuum radiation. The agreement is judged satisfactory, especially in view of the fact that radiant heating is a relatively small contribution to total integrated heating to the Apollo heat shield.

Convective Heating

Convective heating rate levels and distributions were determined through correlations of solutions generated with the BLIMP nonsimilar chemically-reacting laminar/turbulent boundary layer code.⁸ After validating the NASA/MSC convective heating factors³ (which are based on wind-tunnel laminar heating data), the local heat flux at a position around the body was obtained by correcting these factors for turbulent flow, for flight conditions, and for mass addition. This approach is described in the following subsections.

Validation of Wind-Tunnel Correlations--Laminar pitch-plane boundary layer solutions were generated for wind tunnel test conditions for various degrees of incidence. A typical result is shown in Figure 3 for $\alpha = 33^\circ$. Solutions are shown for assumed planar flow, for an assumed effective axisymmetric body, and using the small crossflow approximation to the three-dimensional boundary layer equations.⁹ Comparison with the latter theoretical model is seen to be excellent. (It should be noted that the comparison of heating rates is on an absolute basis since both prediction and data are normalized by the same value.) Direct comparison of another prediction (for $\alpha = 25^\circ$) with the appropriate

NASA/MSC convective heating factors is made in Figure 4. The present results confirm the validity of the NASA/MSC factors for laminar, nonablating wind-tunnel distributions in the pitch plane (i.e., $\lambda = 90^\circ$ and 270°); values at positions off the pitch plane can be assumed to be given by the NASA/MSC factors. The influence of flight conditions, turbulent flow, and ablation are discussed below.

Stagnation Point Flight Predictions--A matrix of air boundary-layer solutions was generated to encompass the range of flight conditions typically encountered in orbital or superorbital manned reentry (stagnation pressures PT_2 of 0.0001 to 1.0 atmosphere and edge total enthalpies H_e from 26,000 to 1500 Btu/lb). The results for a wall temperature T_w of $2000^\circ R$ are presented in Figure 5 in the form of $\rho_e U_e C'_{H_{os}} / PT_2^{1/2}$ where $\rho_e U_e C'_{H_o}$ is a heat transfer coefficient defined by

$$\rho_e U_e C'_{H_o} = q_{w_o} / (H_e - h_w) \quad (1)$$

with the subscripts o and s referring to the nonablation case and the stagnation point, respectively. Here h_w is the enthalpy of the gas at the wall. An effective nose radius of 13.0 feet was used in these calculations. The variation of $\rho_e U_e C'_{H_{os}} / PT_2^{1/2}$ with PT_2 and H_e is primarily due to chemistry effects. In order to illustrate this, curves of percent dissociation and ionization are also shown in Figure 5. Solutions generated at other wall temperatures suggest negligible effect except at high temperatures (e.g., $\rho_e U_e C'_{H_{os}}$ is reduced by 4 percent at $T_w = 6000^\circ R$).¹

Laminar Nonsimilar Flight Predictions--Laminar air convective heating distributions were calculated around the leeward and windward pitch plane rays at several angles of attack and flight conditions with the result that flight conditions are seen to have little effect on the distribution given the same pressure distribution. Thus, the wind-tunnel-derived convective heating factors can be applied directly to flight for nonablating laminar flow as long as the normalizing flux is obtained from Figure 5 and as long as the pressure distribution does not vary substantially from wind tunnel to flight.

Turbulent Nonsimilar Flight Predictions--Turbulent air boundary layer solutions were also generated with the BLIMP code for several flight conditions. The $\rho_e U_e C'_{H_o}$ for turbulent flow normalized by the local laminar values are presented in Figure 6. Solutions for various flight conditions are seen to correlate for the windward and the leeward sides when the distance is measured from the point of transition. In these solutions transition was assumed to occur at laminar momentum thickness Reynolds numbers Re_θ of 200.

Stagnation-Point Mass-Transfer Correlations--A matrix of unequal diffusion BLIMP solutions was generated over a wide range of flight conditions for the stagnation-point (zero incidence)

boundary layer over ablating Apollo heat-shield material while satisfying surface equilibrium and a steady-state surface energy balance. Surface ablation rate \dot{m}_w and surface temperature T_w as well as convective heating rate q_w are calculated during the course of the solution with this approach. Flight conditions considered cover the range of H_e of 26,000 to 5000 Btu/lb and P_{T_2} of 1.0 to 0.0001 atm. Various incident radiation heating rates were assigned in these problems: these fluxes were considered to pass unattenuated through the boundary layer but to enter into the surface energy balance. Solutions were also generated for several flight conditions for assigned T_w and assigned pyrolysis gas rates \dot{m}_g . Both moderate and high \dot{m}_g were considered. The composition of the pyrolysis gas was considered to be a function of T_w consistent with the coking model to be discussed later. Although energy balances were not satisfied in these latter solutions, a surface equilibrium requirement was retained; hence, char recession rates \dot{m}_c and convective heating rates were calculated during the course of these solutions as well. In all, a total of 72 boundary-layer solutions was generated, and all of these were considered in the heat- and mass-transfer correlations presented below.

Mass transfer coefficients were calculated from the boundary-layer solution data according to the approach described in Ref. 10 and evaluated in Ref. 11, namely

$$\rho_e U_e C_M = \sum_k |\tilde{j}_{k_w}| / \sum_k |\tilde{Z}_{k_w}^* - \tilde{Z}_{k_e}^*| \quad (2)$$

where \tilde{j}_k is the diffusive mass flux of element k , \tilde{Z}_k^* is a pseudo elemental mass fraction defined¹¹ so as to represent diffusive as well as convective processes, and the subscripts w and e refer to the wall and boundary-layer edge, respectively. The $\rho_e U_e C_M$ were then seen to correlate within two percent as

$$C_M / C_{H_O}^i = 2\lambda_M B_O^i (e^{2\lambda_M B_O^i} - 1) \quad (3)$$

$$\text{where} \quad B_O^i \equiv \dot{m} / \rho_e U_e C_{H_O}^i = (\dot{m}_g + \dot{m}_c) / \rho_e U_e C_{H_O}^i \quad (4)$$

$$\text{and} \quad \lambda_M = 0.141 \mathcal{M}_{rat}^2 - 0.820 \mathcal{M}_{rat} + 1.861 \quad (5)$$

where $\mathcal{M}_{rat} \equiv \mathcal{M}_w / \mathcal{M}_e$. The resulting correlation is shown graphically in Figure 7.

Heat-transfer coefficients were calculated from the boundary-layer solution data as

$$\rho_e U_e C_H^i = q_w / (H_e - h_w) \quad (6)$$

The $\rho_e U_e C_H^i$ correlate within three percent as

$$C'_H/C'_{H_0} = \max\{[1.0 - \max\{\lambda_H(B'_O - 0.125), 0\}], 0.27\} \quad (7)$$

with $\lambda_H = 0.417$ for $m_{rat} \leq 1.0$ and

$$\lambda_H = 0.224(m_{rat} - 1)^2 + 0.134(m_{rat} - 1) + 0.417 \quad (8)$$

for $m_{rat} > 1.0$. The resulting correlation is shown graphically in Figure 8.

Nonsimilar Mass-Transfer Correlations--Several solutions were also generated for laminar and turbulent boundary layers around the windward and leeward pitch plane rays of Apollo at 25° incidence including Apollo material ablation. In all cases char removal rates were determined by surface equilibrium considerations while various T_w and \dot{m}_0 distributions were assigned. The stagnation point C'_H/C'_{H_0} correlation was seen to apply for turbulent as well as laminar nonsimilar flow within 10 percent. The stagnation point C'_M/C'_{H_0} correlation yielded somewhat higher errors (up to 20 percent over some portions of the body under the more severe laminar conditions) but the larger errors were restricted to positions past the toroid on the windward side where the $\rho_e U_e C'_{H_0}$ itself is an order of magnitude lower than values in the stagnation region. Thus, it appears to be adequate to apply the stagnation point blowing corrections to all positions on the body for turbulent as well as laminar flow.

Material Response Mechanisms

The Apollo heat shield employs a low density ablation material bonded to a primary structure. The ablation material is Avcoat 5026-39/HC-GP, an epoxy novolac resin with phenolic microballoons and silica fiber reinforcement in a fiberglass honeycomb matrix. Although the epoxy-honeycomb combination maintains its cellular appearance after fabrication, the virgin material is treated theoretically as a continuum with uniform thermal and mechanical properties. Upon being subjected to sufficiently high heating, the Avcoat material decomposes chemically forming a pyrolysis gas and a char residue. The fully-developed char is principally carbon and silica, while the pyrolysis gas as initially evolved is in a highly nonequilibrium state, containing substantial excess carbon. There is considerable experimental evidence that under certain conditions the pyrolysis gas cokes out carbon which then deposits on the char. Also, chemical reactions between the carbon and silica in the char can take place. There are several competing mechanisms which interact to control the surface ablation response. These include carbon oxidation, redeposition of silica on the surface due to reaction of silica-carbon reaction products with oxygen in the boundary layer, and liquid-layer runoff of silica. The situation is further complicated by the chemical state of the pyrolysis gas which can be oxidizing, reducing, or inert relative to the char material in the vicinity of the surface.

Models for material decomposition, char layer behavior, and surface ablation selected for use in the present study are discussed in the following subsections.

Material Decomposition--The Avcoat material is considered to decompose into a char containing carbon and ash (assumed to be pure silica) and a pyrolysis gas containing species in the H, C, N and O elemental system in accordance with an Arrhenius rate law. Details of this model are presented in Ref. 1. The fraction of elemental carbon in the pyrolysis gas is above that typically required for equilibrium with the char thus creating a potential for coking.

Char Layer Model--Detailed chemical, physical and visual (microscopic) observations of cores of recovered Apollo heat shield material performed by Avco Corporation¹² were studied in an attempt to establish a consistent char layer model. It was observed that substantial carbon buildup due to coking occurs over the temperature range 1250° to 2000°K. It was also observed that significant excess ash exists in the char layer suggesting that silica-carbon reactions may not proceed extensively. Therefore, a simple coking model neglecting silica-carbon reactions was adopted. The results of the flight predictions have demonstrated the adequacy of this model. The coking model is accomplished simply by varying the mass fraction of carbon in the pyrolysis gas with temperature and pressure as shown in Figure 9. At high temperatures ($> 2000^{\circ}\text{K}$), the pyrolysis gas is assumed to be in equilibrium with carbon. At low temperatures ($< 1250^{\circ}\text{K}$), the fraction of carbon in the pyrolysis gas \tilde{K}_{Cg} is at the level attained in the initial decomposition process (i.e., higher than the local equilibrium value, thereby constituting a potential for coking). The complex nonequilibrium coking regime is represented by a linear decrease of \tilde{K}_{Cg} with temperature as shown in Figure 9. Within this temperature range, pyrolysis gas moving through the char to a region of higher temperature deposits carbon since $d\tilde{K}_{\text{Cg}}/dT$ is negative.

Surface Thermochemical Ablation Model--A review of ground test data for the Apollo heat shield material conducted previously¹³ indicated that little surface recession occurs at low T_w ($< 1200^{\circ}\text{K}$ or so), that a carbon ablation model works well at high T_w ($> 2000^{\circ}\text{K}$), and that ablation increases up to the carbon ablation level in the intermediate T_w range. It was also observed that in the absence of coking, zero recession is predicted for high \dot{m}_g if the pyrolysis gas is assumed to equilibrate with the char and boundary layer gases at the wall. (This occurs since excess carbon in the pyrolysis gas consumes oxygen which diffuses to the wall.) This observation suggests that the present coking model coupled with an assumption of pyrolysis gas equilibrium at the surface should yield at least qualitatively the observed ablation behavior over the entire T_w range. The resulting normalized ablation rates, $B_C^* = \dot{m}_C / (\rho_e U_e C_M)$, calculated with the EST program,¹⁴ are presented in Figure 10. (The dips in B_C^* at high T_w are due to preferential diffusion of hydrogen into the boundary layer.) It can be seen

that the B_C^I is indeed zero at low T_w for $B_C^I \equiv \dot{m}_g / \rho_e U_e C_M > 0.6$ and rises to carbon oxidation values at $T_w \geq 2000^\circ\text{K}$. This model was tentatively selected as adequate for the flight data study. As with the coking model, the success of the initial flight predictions suggests that the model is adequate.

Validation of Thermal Properties Model--In order to perform in-depth charring ablation solutions it is also necessary to specify thermal properties of the char and pyrolysis gas. Virgin plastic and char specific heat data were taken from Ref. 15. Virgin and char emissivities were taken as 0.65 consistent with Refs. 16 and 17. The thermal conductivity of the virgin plastic is based on laboratory data presented in Ref. 12. Char conductivity was also investigated in Ref. 12 and seen to be highly dependent upon the maximum temperature to which the char has previously been exposed, variations of an order of magnitude and more being evidenced at a given temperature for a range of "prechar" temperatures. A variation of char conductivity with temperature was selected from these data consistent with the prechar temperature effect (but not including prechar temperature as a parameter) such as to best match flight thermocouple data. These effective thermal conductivity data were determined by "driver temperature" one-dimensional conduction solutions performed with the CMA program.¹⁸ In this approach a thermocouple response near the heated surface is employed as an assigned surface temperature. A typical calculation is presented in Figure 11. The thermal properties are tabulated in detail in Ref. 1.

Summary of Flight Prediction Procedure

The flight prediction procedure employs the one-dimensional charring ablation code CMA modified to include coking.¹⁸ This code uses as its surface boundary condition the thermochemical ablation results of Figure 10 (generated a priori with the EST code¹⁴), the convective heating correlations described above, and assigned pressure and radiation heating rate taken from the NASA/ MSC design procedures.^{3,6}

FLIGHT PREDICTIONS

The computational technique described above was applied to a series of orbital and superorbital velocity unmanned Apollo flights. A total of seven flight predictions were performed for flight AS-202 (orbital), AS-501 (Apollo 4, superorbital), and AS-502 (Apollo 6, superorbital). The specific body points which were considered are identified in Table 1, together with a brief summary of the basic heating environment, the instrumentation which provided useful information, and the primary purpose for the selection of the body point. Selected flight prediction results are presented in the following subsections. The results of all predictions are presented in Ref. 1. All predictions presented herein and in Ref. 1 are first-try calculations. That is, the analytical

procedure described above was developed and the solutions presented below were generated with no changes in analytical methods, material properties, or the like.

In-Depth and Surface Temperatures

Typical temperature predictions for laminar and laminar/turbulent flows are presented in Figures 12 and 13, respectively. Transition in the latter case was assumed to occur in accordance with a blowing-dependent Re_{ocr} criteria developed during the course of the study.* The agreement is seen to be excellent for the in-depth thermocouples, but agreement with the "surface temperatures" predicted with the consumable thermocouples¹⁹ is seen to be poor. It is believed from these results that the consumable thermocouples do not yield an accurate representation of surface temperature since all other data comparisons are accurate and self-consistent.

Ablation Depth and Char Penetration

Predictions for the progression of the incipient char (0.02 char), fully developed char (0.98 char), and surface recession are compared to char sensor data and final char penetration and surface recession data for two cases in Figure 14. The bands in the measured data represent discrepancies as reported by different sources. The agreement is seen to be within the range of uncertainty of the measured data.

Char Density

Carbon density profiles predicted to occur for two typical flights are compared to profiles reconstructed in the laboratory¹² in Figure 15. The laboratory post-flight evaluations indicated a buildup of excess ash in the char layer. This excess ash was often seen to be equivalent to the amount of silica corresponding to the ablated depth.¹ If this is the case it would suggest that the silica does not react substantially with the carbon or flow away. (Alternatively, it has been suggested¹² that the excess ash may be the result of unburned carbon in the chemical analysis.) Comparisons are made for both interpretations in Figure 15. The agreement is seen to be excellent for the former interpretation (i.e., that the excess ash is silica). This result is also consistent with the material response and coking models which were employed in that silica-carbon reactions were ignored in depth and at the surface.

Convective Heat Transfer

The Apollo aft heat shield was instrumented with wafer calo-

* Re_{ocr} is nominally seen to decrease from 160 to 100 as the blowing rate $B_g + B_c$ is increased from 0 to 10. Details of this correlation are presented in Ref. 1.

rimeters while the conical afterbody employed asymptotic calorimeters. The wafer calorimeters consist of stacked graphite wafers designed to allow removal of single wafers by aerodynamic forces as the surrounding heat shield ablates. Thermocouples imbedded in the wafers measure temperature histories from which net heating rates (convection plus incident radiation) can be calculated given material properties and estimates of conduction and re-radiation losses. They did not function properly after surface recession started, but did supply fairly smooth temperature responses early in the trajectory. The asymptotic calorimeters, on the other hand, typically performed well throughout the entire reentry mission.

Reduced wafer calorimeter data for flight AS-502 are presented in Figure 16 as net heating rate (convection plus incident radiation) and compared to laminar and turbulent net heating rate predictions. Early time laminar heating is seen to be overpredicted somewhat; however, transitional and turbulent heating is predicted accurately as far as the calorimeter data go.

Asymptotic calorimeter measurements reported for flight AS-501 at a position near body point 710 are compared to the body point 710 predictions in Figure 17. The predictions are seen to agree well with the data until a trajectory time of nominally 450 seconds, where the measured heating rates indicate that transition to turbulent flow probably occurs. The Re_θ at this point is in substantial agreement with the transition criteria which had been developed from other flight data.

SUMMARY

A method has been presented for predicting the performance of the Apollo heat shield. It employs correlations for pressure distributions, radiative heating distributions, and convective heating distributions. Some of these correlations were developed during the study, others were validated. A simple self-consistent model for material decomposition, char layer coking, and surface ablation was also developed. This method was applied to a wide variety of Apollo flight data with excellent success.

ACKNOWLEDGEMENTS

The authors wish to acknowledge the important contributions of W.E. Nicolet, M.J. Abbett, and C.B. Moyer of Aerotherm Corporation in the incident radiation and inviscid flow studies and the development of the char layer model, respectively. This work was supported by NASA Manned Spacecraft Center under Contract NAS9-9494.

REFERENCES

1. Bartlett, E.P., Abbett, M.J., Nicolet, W.E., and Moyer, C.B.: Improved Heat-Shield Design Procedures for Manned Entry Systems, Aerotherm Corp., Mtn. View, Ca., Rep. 70-15, Part II, June 1970.

2. Page, W.A., et al.: Radiative Transport in Inviscid Nonadiabatic Stagnation-Region Shock Layers. AIAA Paper 68-784, June 1968.
3. Nelson, M.L.: Determination of Factors at Heat Shield Body Point Locations. TRW Systems Group, Houston, Texas, TRW IOC 68. 3302.13-4, March 1968.
4. Abbett, M.J. and Fort, R.: Three-Dimensional Inviscid Flow About Supersonic Blunt Cones at Angle of Attack, Part III: Coupled Subsonic and Supersonic Programs for Inviscid Three-Dimensional Flow. General Applied Science Laboratories, Inc., Westbury, New York (Sandia Rep. SC-CR-68-3728, Sept. 1968).
5. Hearne, L.F., Chin, J.H. and Woodruff, L.W.: Study of Aerothermodynamic Phenomena Associated with Reentry of Manned Spacecraft. Lockheed Missiles & Space Co., Sunnyvale, Calif. Rep. Y-78-66-1, May 1966.
6. Ried, R.C., Jr., NASA Manned Spacecraft Center, Private Communication.
7. Nicolet, W.E.: A Nongrey Radiation Transport Model Suitable for Use in Ablation-Product Contaminated Boundary Layers. NASA CR-92473, Aerotherm Corp. Mtn. View, Calif. Oct. 15, 1968.
8. Aerotherm Corp., Mtn. View, Calif. User's Manual, Boundary Layer Integral Matrix Procedure, Version C (BLIMPC). Rep. UM-70-20, June 1970.
9. Cooke, J.C. and Hall, M.G.: Boundary Layers in Three Dimensions. Progress in Aeronautical Sciences: Boundary Layer Problems, edited by D. Küchemann and A. Ferri, Vol. II, Pergamon Press, New York, 1962, pp. 221-285.
10. Kendall, R.M., Rindal, R.A., and Bartlett, E.P.: A Multicomponent Boundary Layer Chemically Coupled to an Ablating Surface. AIAA Jour., Vol. 5, No. 6, June 1967, pp. 1063-1071.
11. Grose, R.D. and Bartlett, E.P.: An Evaluation of a Transfer Coefficient Approach for Unequal Diffusion Coefficients, AIAA Jour., Vol. 8, No. 6, June 1970, pp. 1146-1148.
12. Ihnat, M.E.: Evaluation of the Thermophysical Properties of the Apollo Heat Shield. Space Systems Div., Avco Missiles, Space & Electronics Group, Lowell, Mass., Rep. AVSSD-0375-67-RR, Vol. I & II, Aug. 1967.
13. Bartlett, E.P., Anderson, L.W., and Curry, D.M.: An Evaluation of Ablation Mechanisms for the Apollo Heat Shield Material. Jour. of Space. & Rockets, Vol. 8, No. 5, May 1971, pp. 463-469.
14. Aerotherm Corp., Mtn. View, Calif. User's Manual, Aerotherm Equilibrium Surface Thermochemistry Computer Program, Version 4 (EST4). Rep. No. UM-70-18, June 1970.
15. Curry, D.M. and Stephens, E.W.: Apollo Ablator Thermal Performance at Superorbital Entry Velocities. NASA TN D-5969, Sept. 1970.
16. Pope, R.B.: Measurements of the Total Surface Emittance of Charring Ablators, AIAA Jour., Vol. 5, No. 12, Dec. 1967, pp. 2285-2287.
17. Wilson, R.G. and Spitzer, C.R.: Visible and Near-Infrared Emittance of Ablation Chars and Carbon. AIAA Jour., Vol. 6, No. 4, April 1968, pp. 665-671.

18. Aerotherm Corp., Mtn. View, Calif.: User's Manual, Aerotherm Charring Material Thermal Response and Ablation Program with Coking (CMAc). Rep. No. UM-70-19, June 1970.
19. Moen, W.K.: Apollo Heat Shield Thermal Gradient Thermocouple. Space Division, North American Aviation, Inc., Downey, Calif., Rep. TDR 67-108, Sept. 1967.

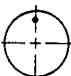


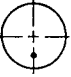
Case	Flight	Body Point	Location	Description of Thermal Environment	Instrumentation Yielding Good Data	Purpose of Calculation
1	202	705 (Z71,Y0)		Relatively nonsevere convective heating - negligible radiation heating - little recession	6 thermocouples Char sensor Core analysis performed	Test of stagnation-point convective heating model
2	502	705		Severe convective heating - little radiation heating - moderate recession	4 thermocouples Char sensor Wafer calorimeter Core analysis performed	Test of surface ablation as well as convective heating models.
3	501	705		Severe convective and radiation heating - relatively high recession	4 thermocouples Char sensor Wafer calorimeter Core analysis performed	Test of radiation heating as well as surface ablation and convective heating models
4	202	Z0,Y33		Relatively nonsevere convective heating - negligible radiation heating - no recession	3 thermocouples Core analysis performed	Test of convective heating model for position off the pitch plane
5	501	710		Mild convective heating - negligible radiation heating - no recession	3 thermocouples Asymptotic calorimeter	Test of convective heating model for position on conical afterbody
6	502	707		Severe convective heating - mild radiation heating - moderate recession	4 thermocouples Char sensor Wafer calorimeter Core analysis performed	Test of transition and turbulent heating model as well as surface ablation
7	501	707		Severe convective heating - mild radiation heating - moderate recession	4 thermocouples Char sensor Wafer calorimeter Core analysis performed	Second test of transition and turbulent heating model

Table 1 - Summary of Apollo flights and body points for which flight predictions were made

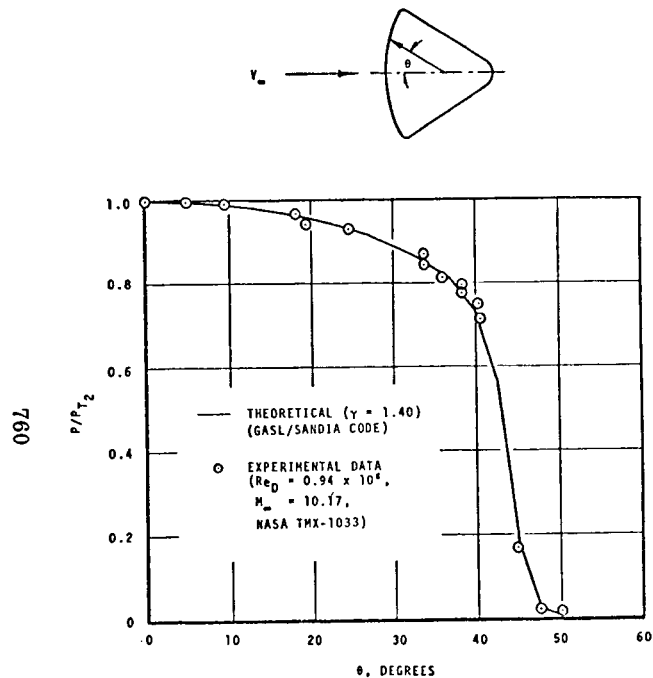


Fig. 1 - Predicted and measured wind-tunnel pressure distributions about Apollo at zero incidence

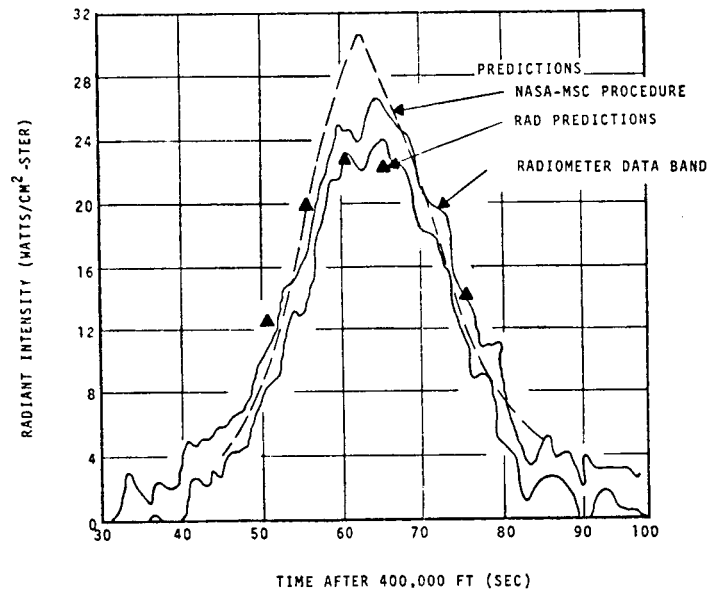


Fig. 2 - Predicted and measured radiation intensities for Apollo flight AS 501, body point 705

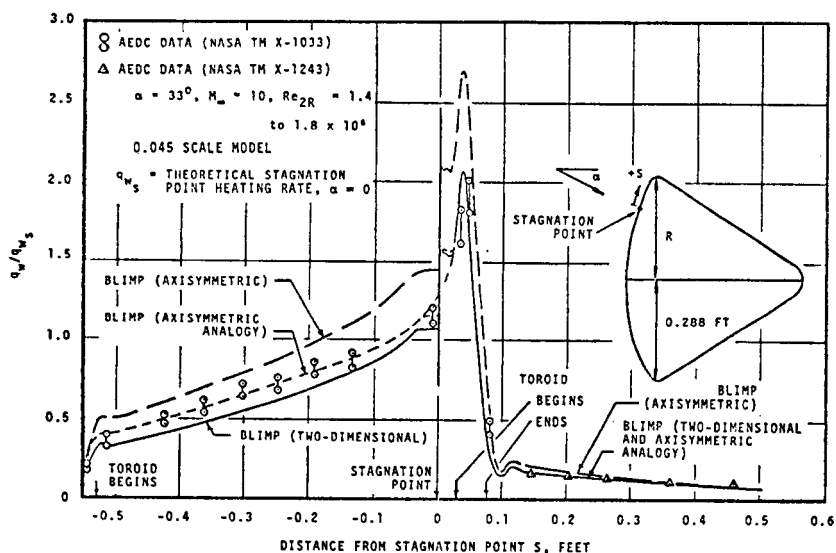


Fig. 3 - Predicted and measured wind tunnel convective heating distributions for Apollo at 33° incidence

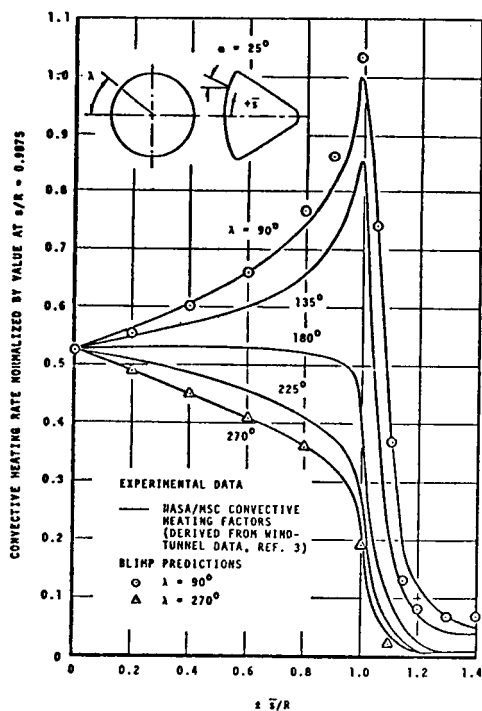


Fig. 4 - Comparison of predictions with NASA/MSC heating factors for Apollo at 25° incidence

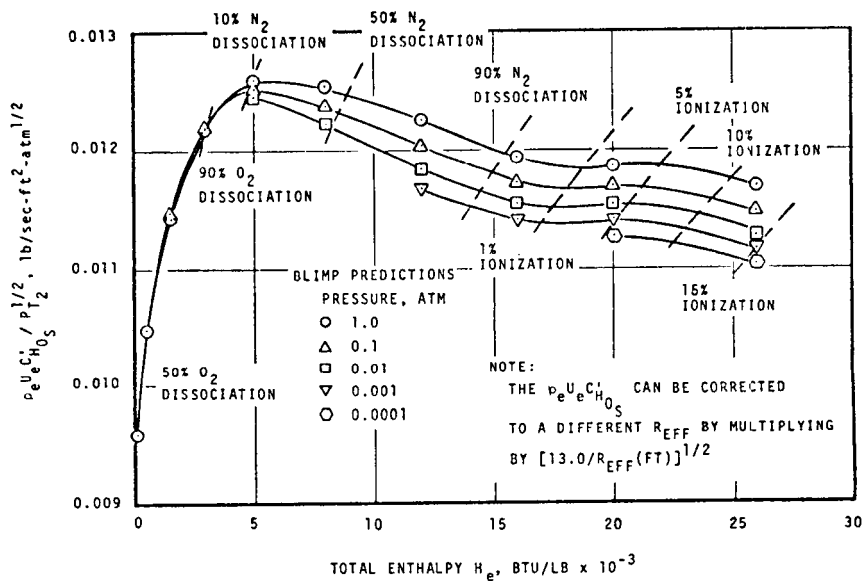
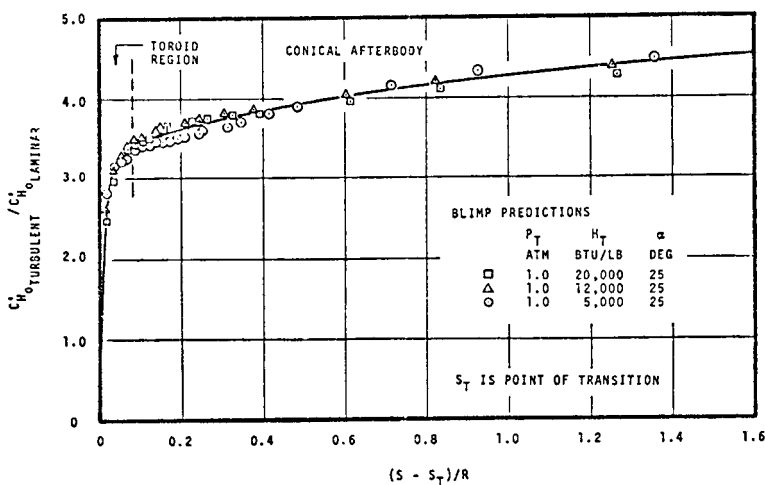
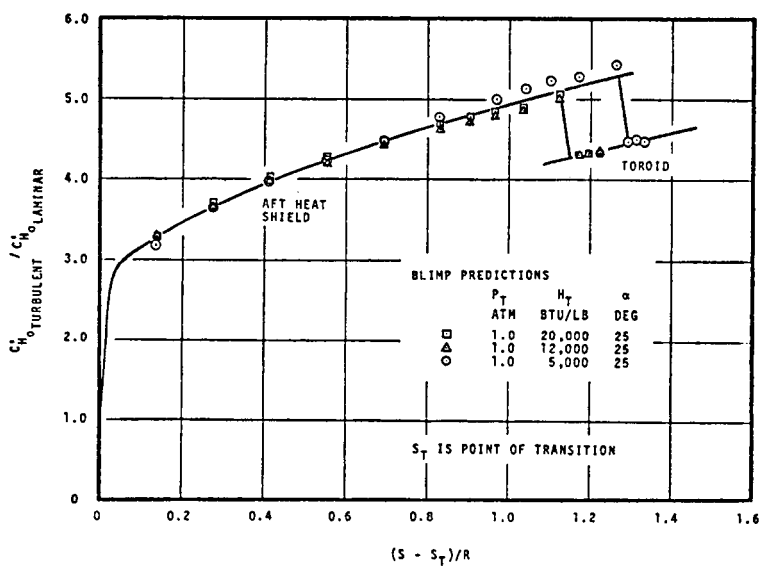


Fig. 5 - Predictions for nonablating heat-transfer coefficient to axisymmetric stagnation point: $R_{eff} = 13.0 \text{ ft}$, $T_w = 2000^\circ\text{R}$



a. Windward Side

Fig. 6 - Correlation of predicted turbulent to laminar nonablating heat transfer coefficients for Apollo at incidence



b. Leeward side

Fig. 6.- Concluded

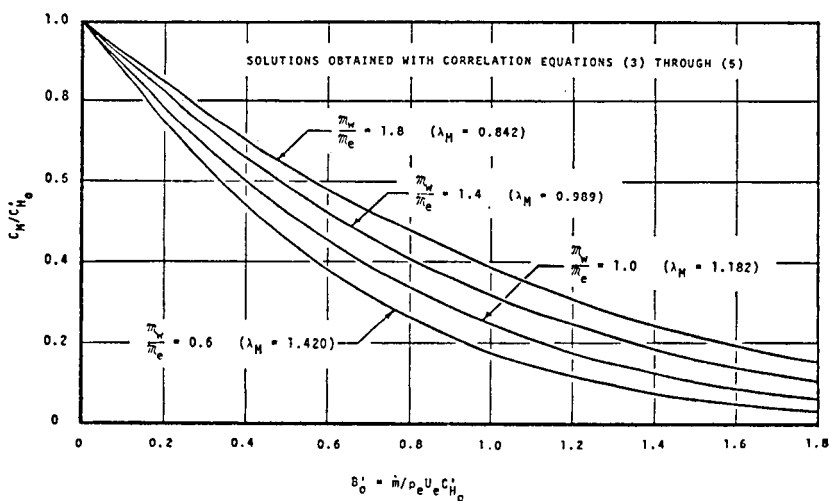


Fig. 7 - Mass-transfer coefficient blowing correction for Apollo material ablation

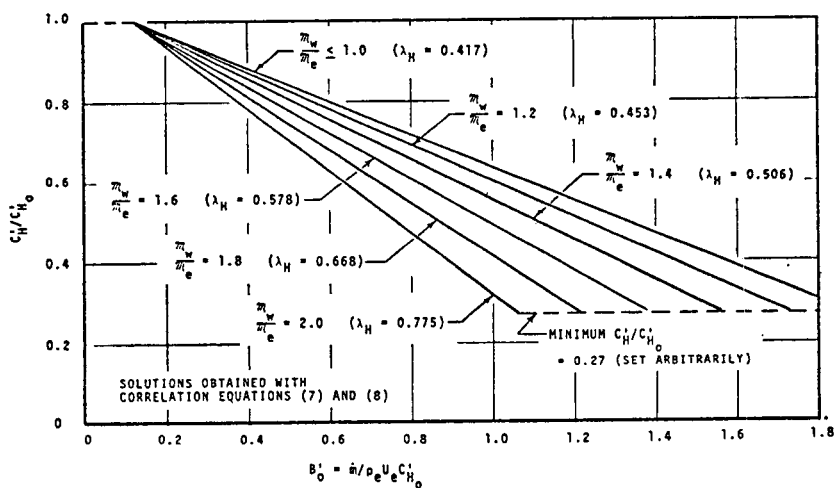


Fig. 8 - Heat-transfer coefficient blowing correction for Apollo material ablation

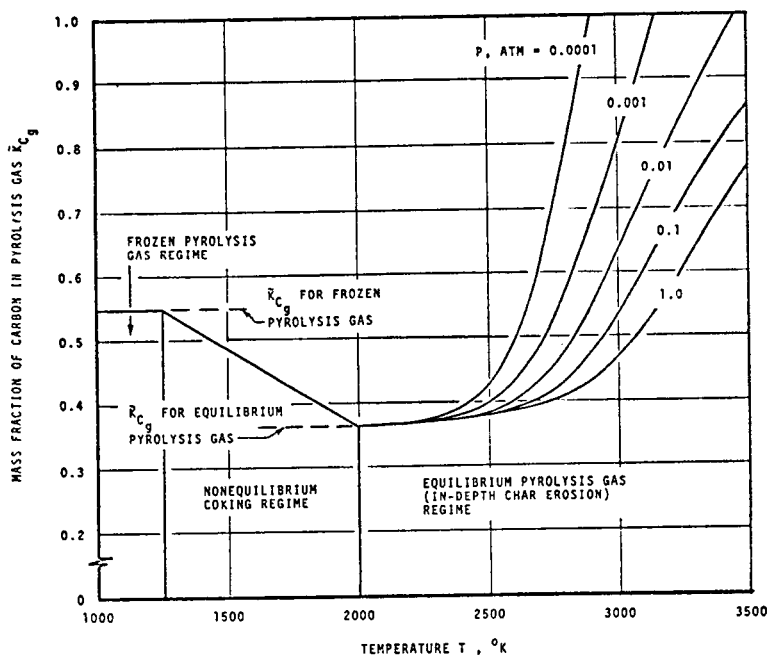


Fig. 9 - Pyrolysis-gas carbon mass fraction for the Apollo material including coking

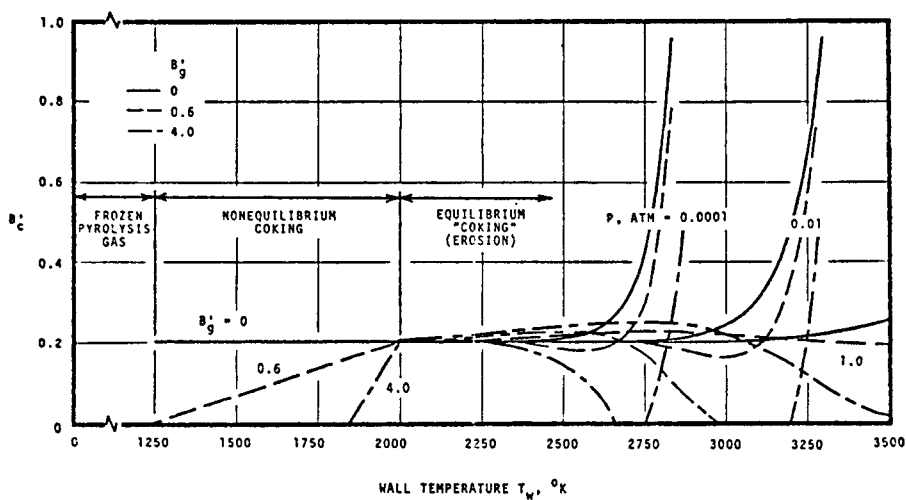


Fig. 10 - Normalized char recession rates for the Apollo material including coking and reactive pyrolysis gas

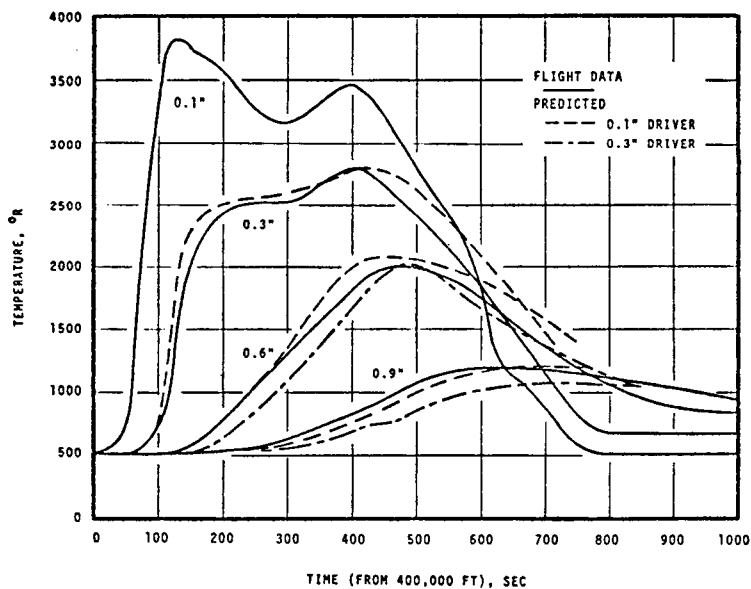


Fig. 11 - Driver temperature calculations for Apollo flight AS 502, body point 705

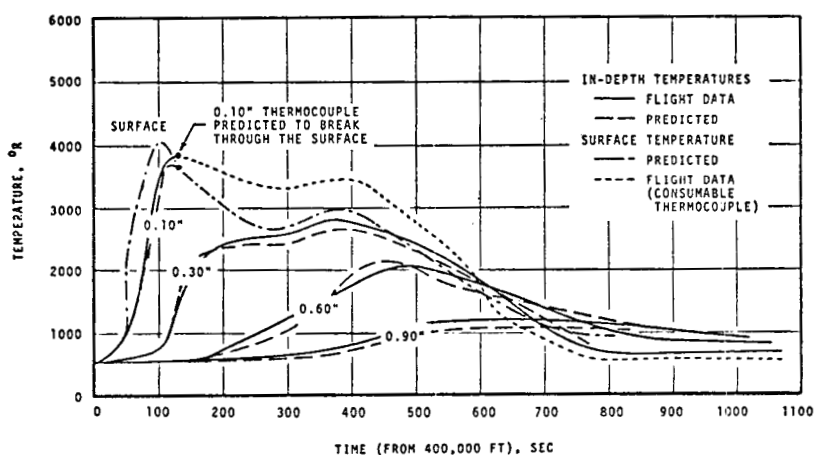


Fig. 12 - Comparison of predicted temperatures with thermocouple response for Apollo flight AS 502, body point 705.

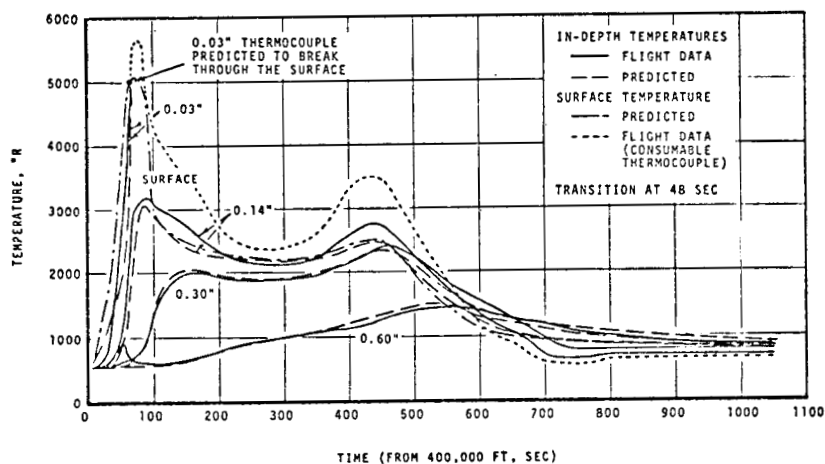
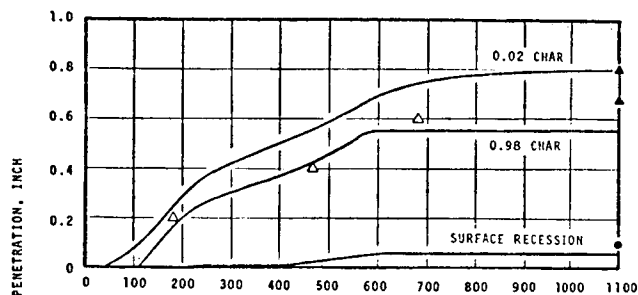
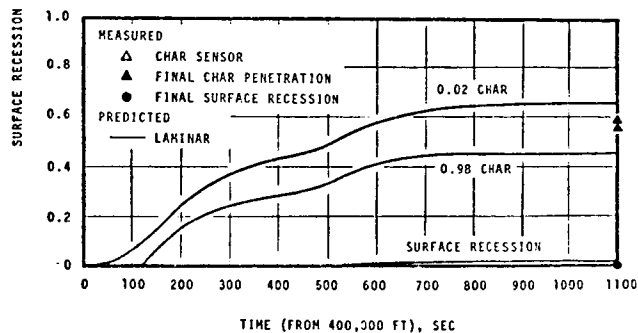


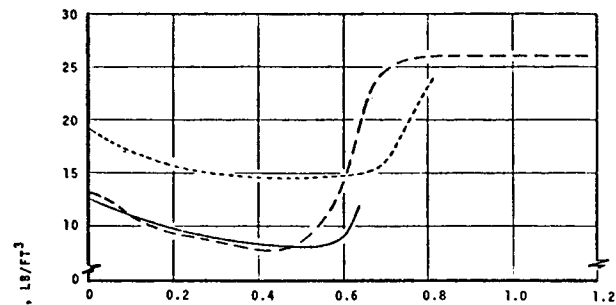
Fig. 13 - Comparison of predicted temperatures with thermocouple response for Apollo flight AS 501, body point 707



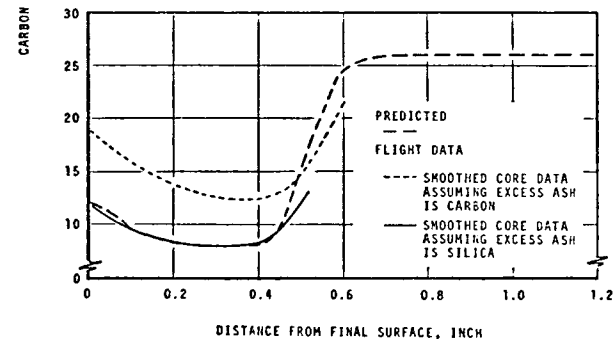
a. Body point Z71, Y0



b. Body point Z0, Y33



a. Body point Z71, Y0



b. Body point Z0, Y33

Fig. 14 - Predicted and measured surface recession and char penetration for Apollo flight AS 202

Fig. 15 - Predicted and measured carbon density profiles for Apollo flight AS 202

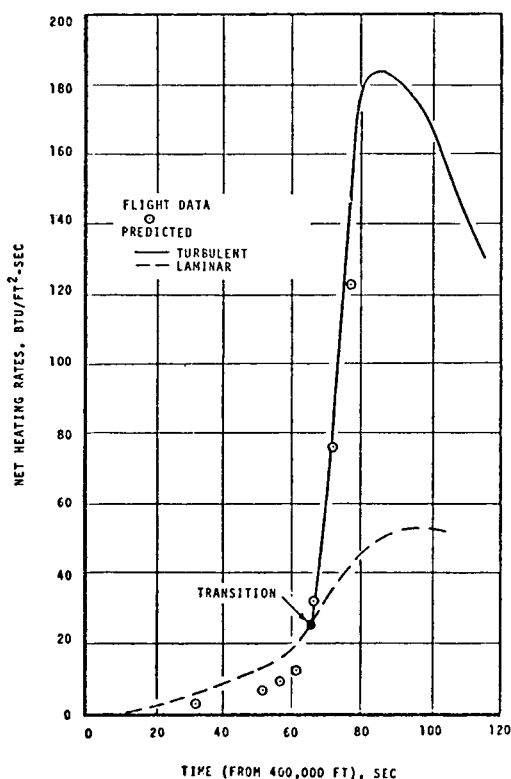


Fig. 16 - Comparison of predicted net heating rates with wafer calorimeter data for Apollo flight AS 502, body point 707

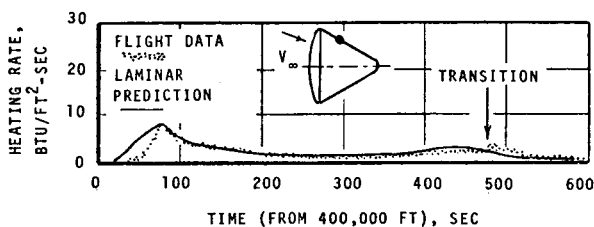


Fig. 17 - Comparison of predicted heating rates with asymptotic calorimeter data for Apollo flight AS 501, body point 710

SPACECRAFT APPLICATIONS OF QUADRUPOLE MASS SPECTROMETRY

Matthew P. Thekaekara, NASA, Goddard Space Flight Center, Greenbelt, Md.

ABSTRACT

Techniques of mass spectrometry are reviewed and the theory of the quadrupole mass spectrometer (QMS) is discussed. The QMS is shown to have several advantages over older types of mass spectrometers. The QMS has been flown on a large number of rockets and several satellites. The design and construction of the instrument have shown great improvements during the last two decades. More sophisticated versions of the QMS are proposed for future satellites. Special emphasis is placed on problems of contamination which are likely to be encountered on a large and complex satellite like the Advanced Technology Satellite ATS-G. The development of a QMS to detect and forestall such contamination is discussed.

MASS SPECTROMETRY

A mass spectrometer is an instrument to determine the mass of an ionized atom or molecule and its relative abundance. It differs from the mass spectrograph in that the separated beams of ions are measured electrically. In a mass spectrograph the beam forms a very sharp image on a photographic plate; this permits a higher degree of accuracy in the determination of atomic mass as is required in the study of isotopes and nuclear interactions.

Mass spectrometers are on the whole more compact and versatile instruments, more sophisticated in the techniques they use for the separation and deflection of ion beams. They fall into two general types, magnetic and non-magnetic. The magnetic type uses the focussing properties of a magnetic field to bring ions of the same specific charge, e/m , to a single focus, regardless of their initial velocity and direction. A more useful method of distinguishing the different types of mass spectrometers is according to their basic principles of mass separation and analysis. The main types are the following: magnetic sector, time-of-flight, radio-frequency, cyclotron resonance and quadrupole mass spectrometer. The magnetic sector mass spectrometer consists of a uniform magnetic field over a certain region or sector. Ions are shot into this

region; they trace a curved path, the radius of curvature being a function of the specific charge. The principle of the magnetic sector was employed in the original Aston's mass spectrograph and in the later more elaborate versions used for research in isotope ratios and packing fraction.

The time-of-flight instruments depend on the time required for an ion to traverse a specific distance between the ion source and the detector. Since the time of flight is inversely proportional to the velocity and the velocity acquired by singly charged ions falling through a given potential is a function of the mass, the mass can be determined from the time of flight. The time of flight instrument is effectively a velocity selector; by employing pulsed ion sources and detectors or by subjecting the ions to an RF field, all ions except those with a specific velocity are prevented from reaching the detector.

In the radio frequency mass spectrometer ions are accelerated by a radio frequency field and then subjected to a DC potential barrier. Only ions with a particular value of initial velocity acquire sufficient energy in the RF field to overcome the DC barrier; these ions reach the collector and all others are stopped. The Bennet tube in single stage or multiple stages is one of the most widely used forms of the radio frequency mass spectrometer.

The cyclotron resonance type of mass spectrometers is based on the principle of the cyclotron which is used to accelerate ions to high energies. A well known instrument which employs this principle is the omegatron. An RF field is applied to increase progressively the velocity of the ions and to make them spiral out to a collector. The mass spectrum is obtained by changing either the magnetic field or the RF field.

THE QUADRUPOLE MASS SPECTROMETER

Compared to these four types of instruments, the quadrupole mass spectrometer is a more complex instrument. It was developed by W. Paul and his coworkers in the University of Bonn, Germany, in 1953 to 1958.^{1,2} The mathematical theory has been discussed by Paul, Reinhard and Zahn.³ Since the original discovery, the instrument has received considerable development in its design and operation, mainly in the United States. A very detailed account of the design and construction of the quadrupole mass spectrometer along with a discussion of the underlying theory is available in an unpublished report prepared for the Office of Naval Research in 1961 by M. Mosharrafa and H. H. Oskam.⁴ The principle on which the instrument operates is that the motion of an ion subjected to a quadrupole RF and dc electric field is governed by a well-known differential equation developed by E. Mathieu in 1868.⁵ The Mathieu equation was derived to describe the motion of a stretched membrane with an elliptical boundary. Over the years the equation and its solutions have been found to have applications in many fields of physics

and engineering and a vast amount of mathematical literature has grown around this topic. A comprehensive treatise on the theory and applications of Mathieu functions, was published by N. W. McLachlan in 1947, and since has been reprinted several times.⁶ The book lists over 200 references, brings together all that was known at the time about the equation and its solutions, fills in the gaps through the author's original research and discusses the applications in such varied fields as loud speakers, RF modulation, oscillations of membranes and plates, electromagnetic wave guides, scattering of sonic and electromagnetic waves, etc. Another useful reference is "Mass Spectrometry" by R. Jayaram⁷; it gives a description of different types of mass spectrometers, including also the quadrupole, and reviews the applications of non-magnetic mass spectrometers to upper atmosphere research.

The quadrupole mass spectrometer is shown schematically in Figure 1. It consists of three parts, the ion source which produces positive ions from ambient atoms and molecules, the quadrupole analyzer which selects ions of a given specific charge and guides them along the axis of the analyzer while allowing all other ions to impinge on the poles, and a collector assembly or ion detector which measures the ion current. The ion source and the collector are common to all types of mass spectrometers; what distinguishes the quadrupole mass spectrometer is the analyser section. It consists of four circular rods arranged symmetrically

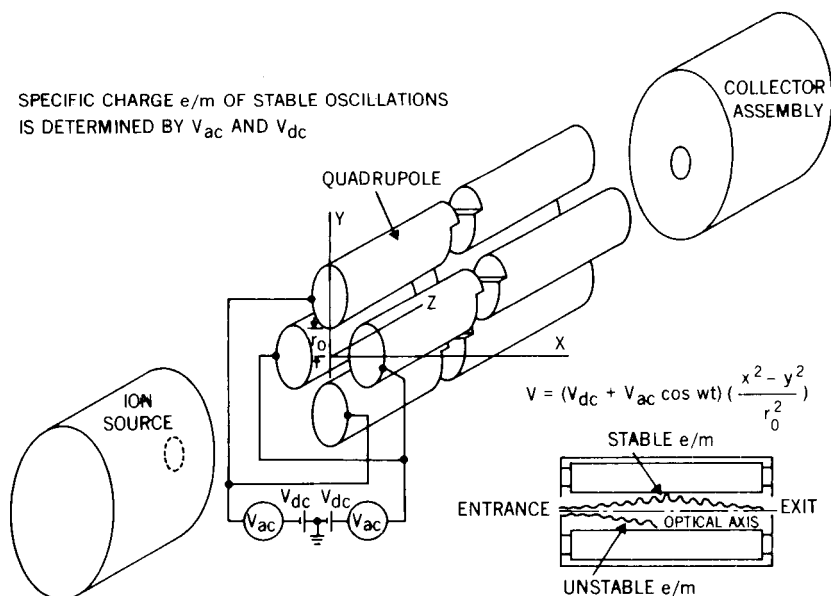


Figure 1. Quadrupole Mass Spectrometer Shown Schematically.

about the z-axis as shown in Figure 1. Opposite rods are connected electrically and the two pairs are subjected to radio frequency (V_{ac}) and direct current (V_{dc}) voltages. Scanning different masses is accomplished by varying either the RF frequency or more commonly by changing the RF and dc voltages, keeping, however, their ratio constant.

THEORY OF THE QMS

The potential at a given point (x, y) in the space between the four rods is given by

$$V = (V_{dc} + V_{ac} \cos \omega t) \frac{x^2 - y^2}{r_0^2} \quad (1)$$

where V_{dc} is the dc voltage, V_{ac} is the amplitude and $\omega/2\pi$ the frequency of the RF voltage, r_0 is the distance of any of the four rods from the axis. Strictly speaking this potential function is valid only when the field forming electrodes have hyperbolic surfaces, but it has been shown⁸ that a very good approximation to equation (1) is obtained also when the rods are cylinders.

The component E_x of the electric field along the x-axis is $-\partial V/\partial x$, and the x-component of force $E_x e$ on an ion of charge e is $m\ddot{x}$. Thus from equation (1) the equation of motion along the x-axis is obtained as:

$$m \ddot{x} + 2e (V_{dc} + V_{ac} \cos \omega t) \frac{x}{r_0^2} = 0. \quad (2)$$

Similarly for the other two components,

$$m \ddot{y} - 2e (V_{dc} + V_{ac} \cos \omega t) \frac{y}{r_0^2} = 0, \quad (3)$$

and

$$m \ddot{z} = 0. \quad (4)$$

The last equation leads to $\dot{z} = \text{constant}$; in other words, the axial injection velocity of the ion is unaffected by the RF and dc fields of the quadrupole. The peculiar dependence of the force on $x \cos \omega t$ in equation (2) and $y \cos \omega t$ in equation (3) makes the direct integration of these equations impossible.

The positive sign for the dc field in equation (2) and the negative sign in equation (3) show that a positively charged ion is focussed in the

x-direction but defocussed in the y-direction by the dc field. However, the ac field dominates the motion, since, as will be shown later V_{ac} is larger than V_{dc} . The combination of the two fields produces the mass filter effect of the quadrupole.

It is convenient to introduce two dimensionless quantities a and q defined by

$$a = \frac{8e}{mr_0^2\omega^2} V_{dc} \text{ and } q = \frac{4e}{mr_0^2\omega^2} V_{ac}, \quad (5)$$

and to change the independent variable from t to γ , where

$$\gamma = \frac{\omega t}{2}. \quad (6)$$

Making these substitutions, equations (2) and (3) are transformed to

$$\frac{d^2x}{d\gamma^2} + (a + 2q \cos 2\gamma) x = 0, \quad (7)$$

and

$$\frac{d^2y}{d\gamma^2} - (a + 2q \cos 2\gamma) y = 0. \quad (8)$$

Equations (7) and (8) are "Mathieu type equations." The behavior of the ions is determined by the properties of the solutions to these equations.

The Mathieu equation is a linear, second order differential equation; in its canonical form it is

$$\frac{d^2v}{dz^2} + (a - 2q \cos 2z) v = 0. \quad (9)$$

The motion of the charged particle in the x-direction is obtained, by changing q in equation (9) to $-q$, that is, by changing the phase by $\pm\pi/2$; and the motion in the y-direction is obtained by changing a in equation (9) to $-a$. Equation (9) has stable solutions only for certain ranges of values of a and q . In the case of the quadrupole mass spectrometer we are interested only in those stable solutions for which q is < 1 and > 0 . Whether the trajectory is stable or unstable, that is, whether the amplitude of the oscillation remains bounded or tends to infinity, is independent of the initial conditions of injection of the ion, and is determined solely

by the values of a and q . The a - q plane is divided into regions of stability and instability, as shown in Figure 2. Ignore for the present the dashed line a'_0 and straight line a/q . For $0 < q < 1$, the boundaries of the stability region in solutions to the canonical equation (9) are the lines b_1 and a_0 . The equations to these lines are (approximately) for b_1 ,

$$a = 1 - q - \frac{1}{8} q^2 + \frac{1}{64} q^3 - \frac{1}{1536} q^4 \quad (10)$$

and for a_0 ,

$$a = -\frac{1}{2} q^2 + \frac{7}{128} q^4 - \frac{29}{2304} q^6. \quad (11)$$

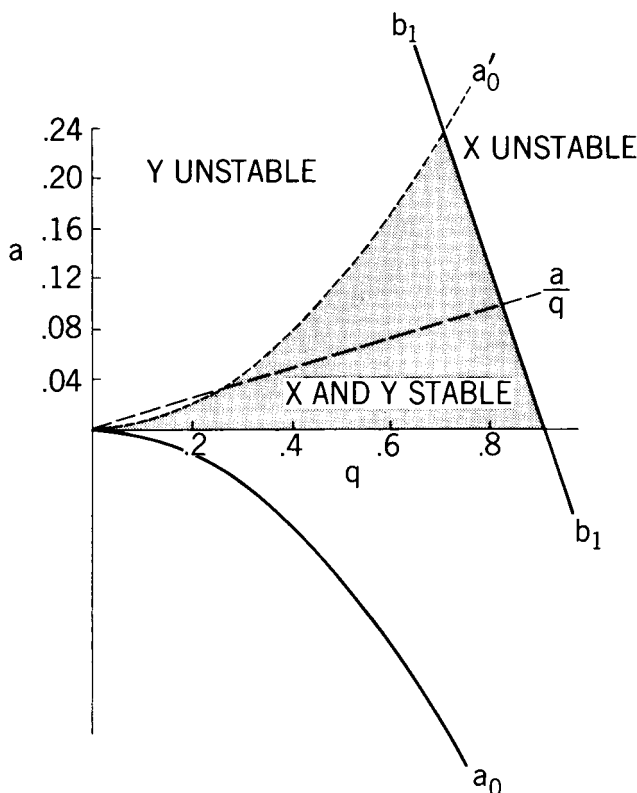


Figure 2. Stability diagram for the QMS. Ions for which values of a and q are bounded by the curves b_1 and a_0 and the q -axis execute stable oscillations in the x - and y -directions.

In the mass spectrometer case we are dealing with two Mathieu equations simultaneously, describing the motion of the charged particle in the x- and y-directions. The requirement is thus that solutions to both equations (7) and (8) be stable simultaneously.

Apart from the phase shift the difference between these equations (7) and (8) and equation (9) is that a in equation (8) is negative. The phase shift of π has no influence on the stability of the solution.

Referring to Figure 2, equation (7) for the x-direction motion has $a > 0$, and hence the stable solutions to this equation are confined to the upper half of the figure. Equation (8) for motion in the y-direction has $a < 0$, and hence the stable solutions of this equation are confined to the lower half of the figure. We can now determine the regions where both solutions are stable by just folding the plane about the q -axis. Thus the dashed curve a'_0 is obtained.

We distinguish four regions in the upper half of figure 2, $a > 0$, $q > 0$: (1) to top right of curve b_1 , x solutions unstable, y solutions stable; (2) to top left of curve a'_0 , x solution stable, y solutions unstable; (3) to top of both curves a'_0 and b_1 both x and y solutions unstable; (4) region bounded by the q -axis and curves a'_0 and b_1 , both x and y solutions stable.

We conclude that if the parameters V_{dc} , V_{ac} , m , r_0 and ω for a specific mass m are such that the operating point lies within the region (4), the motion of the particle is stable; the amplitude of the oscillation in x- or y-direction will not tend to ∞ as the particle traverses the quadrupole field. This is the principle of mass filtering on which the quadrupole mass spectrometer operates.

From equation (5), $a/q = 2 V_{ac} / V_{dc}$. A straight line through the origin represented by the equation $a = px$ (where p is twice the ratio of RF to dc voltage) is the locus of operating points of all masses from 0 to ∞ . Different masses can be scanned by increasing both RF and dc voltages, keeping however their ratio constant. By increasing the slope of the line, the line can be made to approach the vertex of region 4, thus reducing the range of masses with stable oscillations. Thus increasing the ratio of RF to dc voltages increases the resolution of the spectrometer. Resolution is defined as $m/\Delta m$, where Δm is the half-width of the transmission peak or the mass difference between two adjacent ionic species which can be distinguished according to the Rayleigh criterion.⁹ It has been shown that for a resolution greater than 70, only the portion of the stability diagram bounded by $0.69 < q < 0.71$ and $0.23 < a < 0.24$ is of interest.

The general solution of the Mathieu equation for the stability region may now be given in terms of t and ω of equation (2) rather than a and q .

$$x(\omega t) = A \sum_r C_{2r} \cos (r + \beta/2) \omega t + B \sum_r C_{2r} \sin (r + \beta/2) \omega t \quad (12)$$

Here the constants A and B contain the initial conditions x , dx/dt at the point of injection; C_{2r} and β depend only on a and q and is independent of the initial conditions; $0 < \beta < 1$. There is a similar expression for $y(\omega t)$. Thus the paths of all ions of the same mass differ only in the constants A and B, corresponding to their differences in initial conditions. They all have the same frequency spectrum of vibration, with $\omega_0 = \beta\omega/2$.

Ions of different mass have different values of C_{2r} and β since they have different operating points in the stability diagram. The frequency spectra of their motion and especially the fundamental frequency $\omega_0 = \beta\omega/2$, are different.

In order that an ion which satisfies the condition for stable oscillation may traverse the entire length of the quadrupole and reach the collector, it is also essential that at no point along the path the amplitude exceeds or equals the distance r_0 of the electrodes from the field axis. In other words, the maximum values of x and y should be less than r_0 . The maximum amplitude depends not only on the operating point (a , q) but also on the initial conditions.

From equation (2)

$$|x_{\max}| = (A^2 + B^2)^{1/2} \sum_r |C_{2r}|$$

In spite of the fact that the solution for $x(\omega t)$ is not exactly periodic, after only a few vibrations, the actual vibration amplitude very closely approaches x_{\max} . A and B can be evaluated in terms of the initial conditions. It has been shown¹⁰ that the maximum amplitude of oscillation is greater than the initial displacement of the ion from the quadrupole axis for all phases of high frequency voltage at the instant the ion enters the field except at $\gamma_0 = \pi/2$, where they could be equal. As a result only a certain portion of the total cross section can be utilized for the injection of ions.

SPACECRAFT APPLICATIONS

For use on board rockets and satellites the quadrupole mass spectrometer offers several advantages, compared to magnetic type instruments or other non-magnetic spectrometers. Since no magnetic field is required, weight, size and cost can be reduced, and there is no risk of stray fields to interfere with other experiments on board. The transmission ratios are higher than in other types of instruments and may be as high as 100 per cent. Since the quadrupole operates on the principle of resonance rather than stable orbits there are no severe restrictions on the axial momentum of the injected ions. The upper limit is imposed by the number of RF periods for which the ion must remain the quadrupole

field for mass selection. Radial momentum requirements also are not too highly restrictive. The resolution at any selected mass may be varied electronically by adjusting the ratio of RF to dc voltages. The ionic mass to be filtered through the quadrupole can be changed by changing either both the voltages or the frequency of the RF voltage. Thus it is possible to observe one selected mass for any length of time until sufficient numbers of pulses are counted or jump from peak to peak at selected mass numbers or scan the entire mass spectrum. This feature of mass selection and scanning is unique to the quadrupole. Unlike many other types of mass spectrometers, the quadrupole has no grids or slits; and thus has few surfaces which are exposed to contamination and can cause spurious peaks in the output. Of special significance for use on satellites is that the quadrupole mass spectrometer is relatively compact and light-weight, with low power requirements, has no moving parts, is fully automatic, has long life-expectancy, can be remotely controlled and can transmit data by telemetry.

Measurements with mass spectrometers mounted on rockets and satellites have been conducted by numerous investigators. In the early years of upper atmosphere research with rockets, the instrument most commonly used was the Bennet tube. Johnson and Meadows¹¹ seem to have been the first to make mass spectrometric analysis of the upper atmosphere; the data, however, were considered preliminary, due to two major sources of error, contamination due to the vehicle and the negative potential acquired by it in the ascent stage. The initial difficulties were overcome in later rocket flights. The instrumentation was highly improved. A large mass of data on the composition of the upper atmosphere and on the changes with time of day and latitude, was obtained. Reference 7 should be consulted for a review of these early measurements. Several groups of experimenters both in the United States and USSR helped to develop this area of research. The magnetic sector and time-of-flight types of mass spectrometers were also flown on some of the rockets. V. G. Istomin¹² reported results of measurements made with a radio frequency mass spectrometer on board a satellite, Sputnik III.

The development of the quadrupole mass spectrometer as a major tool for research on board rockets and satellites has taken place in the years 1959 to the present. Many different groups of experimenters have been engaged in this effort and each has profited a great deal from the experiences of others. Among the major research teams which have helped in the development of the quadrupole mass spectrometer and obtained valuable results from it are those of the Department of Aeronautical and Astronautical Engineering, University of Michigan, Ann Arbor, Michigan (Schaefer and Nichols^{13, 14}, also Leite et al^{15, 16}, of the same Department); Geophysics Research Directorate, AFCRL, Bedford, Mass. (Narcisi et al^{17, 18, 19, 20}) Space and Earth Sciences Directorate, NASA, Goddard Space Flight Center, Greenbelt, Md. (Reber et al^{21, 22}), Department of Electrical Engineering, University of Michigan (Carignan and

Pinkus²³), the Department of Physics, University of Pittsburgh (Donohue et al²⁴), and outside the United States, the Physics Institute of the University of Bonn in Germany where the quadrupole mass spectrometer was first developed (U. von Zahn et al²⁵). References 13 through 25 cited here deal mainly with the results obtained from the mass spectrometric measurements. Several of them also contain descriptions of the instrumentation, and special features of design and construction which were introduced to meet the specific objectives of the experiment or to correct for defects observed in earlier flights. Practically all the work discussed in these papers was done under the sponsorship of NASA or the Air Force. In the design and construction of the instrument several industrial laboratories cooperated with the government and the universities, among which are Bell and Howell²⁶, Perkin-Elmer, General Electric, etc. More complete descriptions of the instrumentation are to be found in the numerous contractor's reports, user's manuals and other documents generated in connection with each of the experiments.

The mass filter part of the spectrometer has remained essentially the same in all the flight instruments. The four rods arranged parallel to each other with RF and dc voltages impressed on them do not permit any substantial modification. Considerable improvements have been effected over the years in the ion source and collector assembly. As an example of the state-of-the-art in quadrupole mass spectrometer, the instrument which was flown on OGO-6 by Reber et al might be cited. The primary objective was to study the behavior of the concentrations of the major constituents (N_2 , O_2 , O, He and H_2) of the Earth's neutral atmosphere during varying solar activity and magnetic disturbances, and during diurnal, seasonal and latitude variations. A second objective was to obtain accurate measurements of the concentration of trace constituents of the Earth's neutral atmosphere. The instrumentation consisted of the quadrupole (rods of length 15 cm, radius 0.58 cm), an enclosed dual filament electron bombardment ion source, an electron multiplier, supporting electronics, and a break off device to expose the evacuated mass spectrometer to the atmosphere once in orbit. The analyzer was operated in three configurations, (a) fixed-tuned sequentially to masses of special interest, in skipping and sweeping sequences, (b) variably tuned over 6 selected mass ranges to measure trace constituents, and (c) fixed-tuned to certain masses of special interest for indefinite periods. The quadrupole on OGO-6 was launched in June 1969 and collected data for two years in the altitude range 400 to 1100 km.

Most of the quadrupole flights have been on rockets (Narcisi, Schaefer, Donohue, Reber, von Zahn); a few on satellites of the Air Force, or the OGO 2, 4 and 6, and AE 17 of NASA (Narcisi, Leite, Reber). Plans for future quadrupole flights, some in advanced stage of testing and spacecraft integration, others in rather preliminary stages, include the Atmospheric Explorer C, the German AEROS, the Skylab and the ATS-G.

MSM FOR SPACECRAFT CONTAMINATION STUDIES

The rest of this paper will be concerned with the experiment which is proposed for ATS-G. A major difference between this experiment and the quadrupole mass spectrometers flown hitherto on satellites and rockets is that the scope and objective is more in the field of engineering than of physics. All earlier QMS's were interested in the upper atmosphere, Sun-Earth relations, problems of aeronomy, meteorology and geophysics. Here the objective is to study the atmosphere or "cloud" generated by the satellite. In earlier flights the QMS had an orifice in the direction of the velocity vector or it was deployed to a distance away from the rocket.

The ATS-G will be at a synchronous altitude of about 38,000 km, where the atmosphere of the Earth vanishes to the low particle density of the solar ecliptic plane and the effluents of the satellite are of major importance.

Basic data on the proposed experiment are given in Figure 3. The ATS-G shown on top left has an earth-viewing module of size about 1.5 meter cube, a dish antenna of diameter over 9 m and large solar panels at either end of a 16 m boom. The MSM will be located on either the N or S face of the EVM, facing in a direction at right-angles to the velocity vector of the satellite.

The MSM can be operated in a scanning mode or the stepping mode. In the scanning mode, the d.c. voltage sweeps through a given range, thus focussing ions of different masses in succession on the detector. In the stepping mode, the MSM is set to step successively through a certain number of values of mass number, remain at each value for a sufficiently long time to give a measure of ambient ions of that mass. This mode of operation increases the sensitivity of the MSM by three decades. The MSM can also be operated with a cold cathode source. In this mode of operation, no heated filament is required for the production of ions, thus reducing the power input and heat dissipation and also avoiding any interference of the light from the filament with any of the other experiments on-board such as the star-tracker. However, the cold cathode source requires a magnet, and the problem of possible interference with the magnetometer at the hub of the antenna should not be ignored. It may well be that the distance of about 8 m between MSM magnet and the magnetometer makes the problem of vanishing significance.

Spacecraft project offices have long considered the necessity of monitoring the contamination on-board satellites.

A proposal to install mass spectrometer monitors on satellites was made in 1966 to NASA Headquarters by the QMS experimenters of OGO-4. This proposal was studied by the NASA Contamination Review Board and was unanimously recommended for flight. Many types of spacecraft were considered as suitable vehicles for the experiment, the Earth Resources Technology Satellite, the Mariner-Mars Probe, the Mariner Mercury Venus Probe, the Viking Orbiter, the Skylab and satellites of the

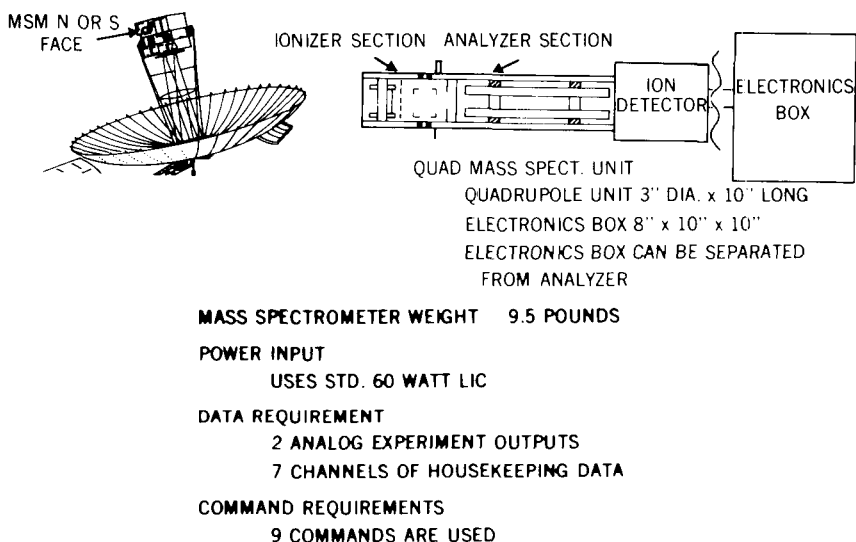


Figure 3. Proposed QMS for Advanced Technology Satellite ATS-G.

Nimbus series. While the problem was considered to be one that called for an urgent solution, no definite decisions were taken to implement the contamination monitor program.

Contamination to a greater or less extent had been observed by many experimenters from the beginning of the space program. V. G. Istomin¹² reported that a Bennet type mass spectrometer detected water vapor in the vicinity of Sputnik III. The amount of water vapor which was quite high in the first revolution decreased to one-sixth in the third revolution and became still less in subsequent revolutions. In the first revolution, the ion current due to H_2O , mass 18, was 230 times the ion current due to 0, mass 16.

From the rate of decrease with respect to time of the amount of H_2O , Istomin concluded that this was a contaminant and not a natural constituent of the atmosphere. The decrease was rapid probably because it was a small satellite with few outgassing materials. J. W. Townsend commenting on Istomin's report observed that he and his colleagues had obtained similar mass spectra.

The persistence of water vapor over a long period of time was reported by Hinton, Leite and Mason.¹⁵ Their data were based on quadrupole mass spectrometers flown on OGO 2 and 4. At the beginning of the satellite life, the amount of water vapor generated by the satellite increased the local density of H_2O to about 10^5 times the ambient H_2O density at the OGO altitude. Three months later, the ratio was about 10^3 and six months later, about 10^2 . That even after six months the satellite was outgassing water vapor was a surprising conclusion.

Contamination of surfaces by outgassing on OGO 6 was reported by McKeown and Corbin.²⁷ The detectors were quartz crystal microbalances which can measure the total amount of material deposited on a given surface without, however, an accurate identification of species. The primary source of outgassing on the satellite was the solar panels baking out in the sun. The change in mass of the crystal was considerably greater when the solar panels were in view than when the crystal was directed away from the solar panels. The mass deposited on the crystal reached a maximum when the satellite was 5 months in orbit and amount to $9.6 \mu\text{g}/\text{cm}^2$ for an aluminum coated crystal and $5.2 \mu\text{g}/\text{cm}^2$ for a gold coated crystal. From the desorption activation energy of the accreted mass, the authors conclude that the outgassing contamination from the panels was most probably epoxy assembly materials of the panels and diffusion pump oil adsorbed during prelaunch tests. While this identification of species may be open to further study, the fact that effluents from the solar panels reached the spacecraft and gave it a thin film coating cannot be questioned. Under these circumstances, a mass spectrometer may have identified the material in question.

Several examples might be given from past experience of satellites of contamination and consequent degradation or failure of on-board experiments. The effect is obvious, the cause is a matter of conjecture and educated guess. An example which has received a great deal of attention in NASA Centers and contracting laboratories is the failure of the filter wedge spectrometer (FWS) on Nimbus IV. The FWS was designed to measure radiance of the earth in the wavelength bands 1.2 to $2.4 \mu\text{m}$ and 3.2 to $6.4 \mu\text{m}$. The spacecraft was launched on April 8, 1970. When the FWS was turned on in orbit 5, it was found that the 1.2 to $2.4 \mu\text{m}$ band was degraded and the 3.2 to $6.4 \mu\text{m}$ band was totally obscured. The presence of ice absorption bands in the 1.2 to $2.4 \mu\text{m}$ range showed clearly that an ice cap had been formed over the low temperature (176K) detector by the condensation of water vapor. This was recognized to be a generic problem common to the upcoming generation of radiation coolers; and hence a Radiation Cooler Task Group was formed under the chairmanship of H. E. LaGow,²⁸ Director of Systems Reliability G.S.F.C., to investigate the FWS failure. The formation of the ice cap could readily be explained; but why it did not sublime shortly afterwards was puzzling. One hypothesis which has been advanced is that other foreign materials of low volatility such as oils, adhesives or plasticizers condensed over the ice cap, thus effectively sealing it off.

A major recommendation of the Radiation Cooler Task Group was a flight test to define the gas environment in the vicinity of a spacecraft. Experiments to determine the atomic and ionic species in space and their relative abundances have been flown on several satellites, but in general, they were so designed as to avoid as completely as possible any interference from the effluents of the satellites. When such interference occurred, they were ignored because they were of no value to the experimenter.

An experiment specifically designed to monitor the contamination due to the outgassing materials on the satellite is highly desirable for the upcoming generation of radiation coolers which will operate at lower temperatures than the one on Nimbus IV.

Though such an experiment would be considered useful for many types of satellites, it would seem uniquely necessary for the ATS-G satellite. There are three radiation coolers on-board the ATS-G, two for the MET package Sounder-Imager and one for the CO₂ laser. These two are among the major experiments onboard. There are also large optical surfaces, one of 20 cm diameter, probably another of 40 cm diameter, which are vulnerable to contamination. The shape and size of the spacecraft is another major consideration. The 9 m dish antenna with its 48 radial ribs and copper coated dacron mesh presents a large area to the earth viewing module at a distance of 7 m. There are also the two large semi-cylindrical solar panels at either end of the boom. Both the solar panels and the antenna can give rise to effluents in the process of baking out. They can also reflect towards the EVM the outgassing particles of the EVM itself.

The EVM is a major source of outgassing. It is a large body with many components and compartments, layers of insulation, polymeric materials, and other sources of vapor. It may be expected to persist in evolving significant quantities of material which may contaminate sensitive experiments. Many hypotheses exist as to how these may leave the surface and then return to some other area where they form a contaminating substance. These include such considerations as molecule-molecule interactions and electrostatic attractions.

Another area of concern for all satellites and especially for the ATS is the exhaust from the thruster engines themselves. The engines are fired periodically to maintain the position and attitude of the spacecraft. The effects of the thruster exhausts have been discussed by W. C. Lyon²⁹ and by Mayer, Taylor and Schieler.³⁰ As Lyon has shown, in addition to the collimated primary beam which moves away from the spacecraft along the axis of the thruster, there are uncollimated ions and neutrals which travel obliquely and impinge on the spacecraft. Mayer, Taylor and Schieler have shown the possibility of contamination from pre-ignition products of restartable thruster engines. It is also well known that most propulsion nozzles do not fully expand the fuel within the thruster and considerable expansion takes place outside the nozzle. The gases due to the delayed expansion do not travel away from the spacecraft along the thruster axis, but radially in all directions from the point where the expansion takes place. These gases constitute a major source of contamination for the north and south faces of the EVM where the hydrazine thrusters are located.

The quadrupole mass spectrometers which are being proposed for the Skylab have scope and objectives similar to that of ATS-G. In the vicinity of an orbiting laboratory where humans live and work the kind of

information about molecular flux by species and quantity which a QMS can give is of considerable importance.

The history of science and technology have shown repeatedly that practical applications of great value have resulted from seemingly futile speculations of basic physics. There seems to be as little in common between differential equations for a stretched membrane and the out-gassing of a satellite as between Maxwell equations and color television or between Lorentz transformation and nuclear power stations. The spacecraft applications of quadrupole mass spectrometry are entering a new field where the results may prove even more valuable than in the past.

REFERENCES

1. W. Paul and H. Steinwedel, "A New Mass Spectrometer Without a Magnetic Field," *Z. Naturforsch.*, Vol. 8A, p. 448, 1953.
2. W. Paul and M. Raether, "The Electrical Mass Filter," *Z. Physik*, Vol. 140, p. 262, 1955.
3. W. Paul, H. P. Reinhard, and U. Von Zahn, "The Electric Mass Filter as a Mass Spectrometer and Isotope Separator" (In German), *Z. Physik*, Vol. 152(2) pp. 143-182, 1958; also available in English as Astia AD230932.
4. M. Mosharrafa, and H. J. Oskam, "Design and Construction of a Mass Spectrometer for the Study of Basic Properties in Plasma Physics," Technical Report No. 2, University of Minnesota, July 1971 (also available as AD 274 249).
5. É. Mathieu, "Mémoire sur le Mouvement Vibratoire d'une Membrane de Forme Elliptique," *J. de Math. Pures et Appliquées*, (J. de Liouville) Vol. 13, p. 137, 1868.
6. N. W. McLachlan, "Theory and Application of Mathieu Functions," Dover Publications, Inc., New York, 1964 xii + 394 pp.
7. R. Jayaram, "Mass Spectrometry, Theory and Applications" Plenum Press, New York, 1966, xiii + 225 pp.
8. I. E. Dayton, F. C. Shoemaker and R. F. Mosely, "Measurement of Two-Dimensional Fields, Part II: Study of a Quadrupole Magnet, *Rev. Sc. Inst.* Vol. 21, No. 5, pp. 485-489, May 1954.
9. F. A. Jenkins and H. E. White, "Fundamentals of Optics" McGraw-Hill Book Company, Inc. 1957, p. 300.

10. E. Fisher, "The Three-Dimensional Stabilization of Charge Carriers in a H. F. Electric Quadrupole Field," *Z. Physik*, Vol. 156, 1959, p. 1.
11. C. Y. Johnson and E. B. Meadows, "First Investigation of Ambient Positive Ion Composition to 219 Kilometers by Rocket-Borne Spectrometer," *J. Geophys. Res.* Vol. 60, 1955, p. 193.
12. V. G. Istomin, "Investigations of the Ion Composition of the Earth's Atmosphere With Rockets and Satellites," *Annals of the IGY*, Vol. 12, Part I, Pergamon Press, 1960.
13. E. J. Schaefer and M. H. Nichols, "Upper Air Neutral Composition Measurements by a Mass Spectrometer," *J. Geophys. Res.* Vol. 69, No. 21, Nov. 1964, pp. 4649-4660.
14. E. J. Schaefer and M. H. Nichols, "Neutral Composition Obtained from a Rocket-Borne Mass Spectrometer," *Space Res.* Vol. 4, 1964, pp. 205-234.
15. B. B. Hinton, R. J. Leite and C. J. Mason, "Comparison of Water Vapor Measurement from Two Similar Spacecraft," *EOS, Trans. Am. Geophys. Union*, Vol. 50, No. 4, April 1969, p. 267.
16. B. B. Hinton, R. J. Leite and C. J. Mason, "Representative Neutral Atomic Oxygen Density Results from the OGO IV Neutral and Ion Mass Spectrometer Experiment," *EOS, Trans. Am. Geophys. Union*, Vol. 50, No. 4, April 1969, p. 267.
17. R. S. Narcisi and A. D. Baily, "Mass Spectrometric Measurements of Positive Ions at Altitudes from 64 to 112 kilometers," *J. Geophys. Res.* Vol. 70, No. 15, Aug. 1965, pp. 3687-3700.
18. R. S. Narcisi, "Ion Composition of the Mesosphere," *Space Research*, Vol. 7 (R. L. Rose-Smith, ed.) North-Holland, Amsterdam, 1967, pp. 186-196.
19. R. S. Narcisi, "Processes Associated with Metal Ion Layers in the E. Region of the Ionosphere," *Space Research*, Vol. 8, (A. P. Mitra, L. G. Jacchia and W. S. Newman, eds.), North-Holland, Amsterdam, 1968, pp. 360-369.
20. R. S. Narcisi, et al., "Mass Spectrometric Measurements of Negative Ions in the D- and Lower E-Regions," *J. Atmos. and Terrestrial Physics*, Vol. 33, No. 8, Aug. 1971, pp. 1147-1159.

21. C. A. Reber, D. N. Harpold, R. Horowitz and A. E. Hedin, "Horizontal Distribution of Helium in the Earth's Upper Atmosphere," J. Geophys. Res. Vol. 76, No. 7, March 1971, pp. 1845-1848.
22. C. A. Reber and A. E. Hedin, "The Distribution of Neutral Gases in the Northern Fall Polar Atmosphere," see also D. N. Harpold and R. Horowitz, "Minor Gases Measured with the OGO-VI Neutral Mass Spectrometer," EOS, Trans. Ann. Geophys. Union, Vol. 52, No. 4, April 1971, pp. 293, 294.
23. G. R. Carignan and W. H. Pinkus, "OGO-F-04 Experiment Description," Technical Note 08041-3-T, University of Michigan, Ann Arbor, Michigan, Oct. 1968.
24. E. C. Zipf, W. L. Borst and T. M. Donohue, "A Mass Spectrometer Observation of NO in an Auroral Arc," J. Geophys. Res. Vol. 75, No. 31, Nov. 1970, pp. 6371-6376).
25. U. von Zahn and G. Schoneppe, "Neutral Composition of Polar Thermosphere," see also D. Offerman and U. von Zahn, "First Results Obtained from Rocket-Borne Neutral Gas Spectrometer Employing a Helium Cooled Ion Source," EOS Trans. Am. Geophys. Union, Vol. 52, No. 4, April 1971, p. 292.
26. W. M. Brubaker, "Mass Spectrometer System for Exploring the Upper Atmosphere," CEC Recordings, Vol. 17, No. 4, Oct. 1963, pp. 19-21.
27. D. McKeown and W. E. Corbin, Jr., "Space Measurements of the Contamination of Surfaces by OGO-6 Outgassing and their Cleaning by Sputtering and Deabsorption," ASTM/IES/AIAA Space Simulation Conference, 14-16 September, 1960, Space Simulation, NBS Special Publication, 336, pp. 113-123.
28. Herman E. LaGow, Chairman, "Report of the Findings of the Radiation Cooler Task Group," DIRS 02273-I-2-TR-239-032-215, September 11, 1970, Goddard Space Flight Center, Greenbelt, Maryland 1970.
29. Warren C. Lyon, "Thruster Exhaust Effects on Spacecrafts," AIAA 8th Electric Propulsion Conference, Stanford, Calif., Aug. 31 - September 2, 1970.
30. S. W. Meyer, D. Taylor, and L. Schieler, "Preignition Products from Propellants at Simulated High Altitude Conditions," Combustion Science and Technology, Vol. I., No. 2, pp. 119-129, 1969.

INTEGRATED REAL TIME CONTAMINATION MONITOR— RESIDUAL GAS ANALYZER MODULE

Thomas R. Edwards, *NASA, Marshall Space Flight Center*

ABSTRACT

The residual gas analyzer of the Integrated Real Time Contamination Monitor is being developed for evaluating the effects of both ground based and space flight contamination environment.

The mass range is 0 to 300 atomic mass units with an intensity range of 10^6 operating between 10^{-4} torr and 10^{-10} torr. The ionization source is a cold cathode magnetron discharge type. The residual gas analyzer is a quadrupole with hyperbolic rods and two overlapping mass ranges. The power budget is approximately 25 watts maximum with a scan time in the neighborhood of a minute. The size is 40 CM long by 7.5 CM in diameter. An electron multiplier detector is mounted off axis to achieve an enhanced signal to noise ratio. All electronics are integral to the unit with the exception of D.C. power supplies.

The RGA data will be fed to a computer for interpretation. Smoothing, normalization, peakpicking, background elimination and mass number calculation will be performed automatically. The spectra will then be interpreted in terms of a reference library using regression techniques with a non-negativity constraint and F-level testing.

The resulting analysis will be formatted to indicate the Qualitative and Quantitative Chemical Composition of the contamination environment complimenting the output from the optical module.

DIRECTIONAL MOLECULAR FLOW ANALYSIS AND LEAK DETECTION WITH A ROTATABLE GAS ANALYZER IN A LARGE SPACE SIMULA- TION CHAMBER

Horst K. F. Ehlers, *NASA Manned Spacecraft Center, Houston, Texas*

ABSTRACT

Thermal vacuum testing of spacecraft in large chambers requires the establishment of certain gas pressure levels and molecular flow conditions simulating the space environment. A system has been developed and applied at the NASA Manned Spacecraft Center for measuring and analyzing directional molecular flows in a large thermal vacuum chamber in order to verify molecular environment and identify characteristic and abnormal test article and chamber conditions.

INTRODUCTION

In April 1968, the Space Environment Simulation Laboratory at the NASA Manned Spacecraft Center (MSC) began to supplement the "standard" ionization gages with a system of pairs of ionization gages mounted in fixed opposing directions in order to measure directional molecular flow in various locations and orientations in the large space environment simulation chambers. This system proved to be a valuable diagnostic tool for verifying required test conditions as well as for detecting abnormal test article and chamber conditions in real time during various spacecraft tests totaling 1941 hours of test time (1). Since then, measurement techniques and instrumentation have been significantly improved. Provision for the capability to rotate the ionization gage pairs (resulting in reduced systematic measurement error and extended angular range of directional measurement) and the addition of a gas analyzer are the two major improvements. This directional gas flow measurement (DGFM) system has been in use during tests in Chamber A for over 1200 operating hours. This paper describes this new system and some of the results obtained with it.

SYSTEM DESCRIPTION

The DGFM system consists of two similar subsystems with rotating platforms located on opposite sides of the chamber (Fig. 1). Each platform can be rotated about two mutually perpendicular axes to permit the instruments to scan any direction (Fig. 2). Platform rotational directions are defined in spherical (azimuth and elevation) coordinates.

Each platform includes two pairs of tubulated Bayard-Alpert ionization gages that point in opposite directions. In addition, platform 1 has one tubulated quadrupole head that is co-aligned with the ionization gages.

The tubulated ionization gages and quadrupole function as directional molecular flow sensors. The geometrical relationships of sensing elements and tubulations are presented in Figure 3. The actual dimensions of the tubulations have been determined by the availability of "standard" equipment, and no attempt has been made at optimization. The gage tubulations are made of metal to reduce wall temperature differences. Ionization gage temperatures are measured to permit correction of gage readings for thermal effects. The quadrupole tubulation temperature is maintained at 150° C by electrical heaters to reduce memory effect. Ionization gage controls provide for automatic pressure range switching to permit uninterrupted optimum pressure measurement during rapidly changing chamber pressure conditions.

All data are automatically recorded. The quadrupole has a scanning range that is continuously variable within the range from 1 to 750 amu. The instrument sensitivity is increased through an electron multiplier integrated into the quadrupole head. The quadrupole head and preamplifier, which are mounted on platform 1, are connected with the outside controls by a cable 17 meters long.

OPERATIONAL MODES

The DGFM subsystem 1 has been operated during testing in the following three modes:

1. Calibration - The quadrupole is directed toward a mass marker gas source at a known location from which gas is released at a fixed rate for in situ directional and mass calibration of the quadrupole.

2. Fixed direction gas analysis scans - The quadrupole is directed toward specific objects such as the spacecraft, infrared (IR) heater, albedo simulator, solar simulator, or cold wall to measure the mass spectrum of directional molecular flow as a function of time. This technique is particularly useful in cases involving rapidly changing outgassing processes.

3. Directional scanning - The DGFM platform is rotated in either of two automatic scan modes:

- a. Horizontal (azimuth) scanning at a fixed elevation angle.
- b. Vertical (elevation) scanning at a fixed azimuth angle.

During these scans, the ionization gages measure the variations in total pressure resulting from the directional molecular flow patterns in the chamber. Simultaneously, the quadrupole gas analyzer provides information on the molecular composition of the flow. The operating mode of the quadrupole is set to monitor partial pressures using either single mass peaks or groups of mass peaks.

The DGFM subsystem 2 is used to supplement and verify the DGFM subsystem 1 data. The normal operational mode is directional scanning. The existence of two DGFM subsystems in the chamber significantly increases the possibility of locating leaks below the chamber floor, behind liquid nitrogen (LN₂) shrouds, and around other structures.

RESULTS AND DISCUSSION

The results described in the following paragraphs concern specific events that occurred during the thermal vacuum testing of spacecraft 2TV-2 (Apollo command and service module) in MSC space environment simulation Chamber A in the spring of 1971 and are illustrative of the capabilities of the DGFM system.

Analysis of Test Events with the DGFM Platforms in Fixed Directions

The directional molecular flow field in a large thermal vacuum chamber is a function of the following variables:

1. The geometry of the chamber, test article, and special test equipment
2. Outgassing of chamber, test article, and special test equipment surfaces
3. Leakage from the chamber and test article
4. Special test events

The DGFM system was used during certain time periods of the 2TV-2 test with DGFM platform 1 in a fixed position to analyze the variations in molecular flow resulting from some of these prime causes. Events such as the start of solar simulation, power-up of IR heater arrays, and turning on of chamber lights caused significant changes in the mass spectra recorded by the quadrupole. Figure 4 depicts the changes in the major peak (m/e 69) of a spacecraft outgassing spectrum observed

during a portion of the test with the quadrupole on DGFM platform 1 viewing the test article. Analysis with respect to chamber events occurring during this time period showed the following observations:

1. The molecular flow from the spacecraft to DGFM platform 1 was at a minimum when the IR heater array that was used to simulate the lunar orbit thermal conditions was in position, surrounding the side of the spacecraft toward DGFM platform 1 (Fig. 1). This was expected because the array almost completely blocked the view of the spacecraft from this DGFM platform.

2. The molecular flow to DGFM platform 1 was at a maximum whenever the IR heater array was retracted and positioned above the spacecraft during simulation of the lunar orbit "night side" conditions. Under these conditions, the DGFM platform had an unobstructed view of the spacecraft.

3. Turning on of chamber lights after a long period of deactivation resulted in release of spacecraft outgassing products previously condensed on the cold lamps.

Chamber Molecular Flow Characteristics

Correct interpretation of the DGFM system data for recognition of off-normal test article or chamber conditions requires (a) positive identification of molecular flow originating from the test article or ground support equipment and (b) comparison with results of baseline measurements in the clean, empty, and tight chamber. Accordingly, such measurements have been periodically recorded in Chamber A for the mass range of 1 to 750 amu. Recent testing in the empty Chamber A provided quadrupole data showing no measurable molecular flow involving masses larger than 40 amu (typical of most contaminants) with the LN_2 shroud below 100°K . Detection of masses larger than

40 amu during testing of spacecraft 2TV-2 under similar thermal vacuum conditions therefore indicated directional molecular flow originating from the spacecraft. Such results are useful in appraising spacecraft degassing rates to meet specified contamination limits.

Another result of baseline measurements in Chamber A is the identification of certain "sources" for relatively high molecular flow that are indicated in specific directional, single-peak curves in the form of maxima (see A in Fig. 5). Data analysis reveals that these maxima (or the minima in between) are the result of the particular chamber design and appear during all tests on properly adjusted DGFM instruments. Figure 6 shows the chamber area in the vicinity of DGFM platform 1, including LN_2

cold shroud and helium cryopanel to illustrate this point. The areas between and behind the front LN_2 panels are areas of relative low gas density for gases pumped by the helium cryopanel (but not pumped by the LN_2 panels) reflected in the m/e 28

single-peak curve minima when the instrument is directed toward these areas and maxima in other directions (see A in Fig. 5).

The total pressure curve in Figure 5 follows the same pattern, as do the curves for m/e 14, m/e 16, m/e 32, and m/e 40 (not shown). In contrast, the quadrupole m/e 18 single-peak curve does not have these maxima. These results are important for correct interpretation and identification of molecular flow originating from (and returning to) the test article.

Comparison with baseline measurements shows that the major curve maxima (see B in Fig. 5) are caused by molecules originating from spacecraft 2TV-2 since these maxima are relatively higher than when the chamber is empty.

Chamber Leak Checking

The DGFM system has been a very useful and economical tool for locating and identifying chamber leaks in several tests. Leak checking is relatively simple and fast, and requires only one DGFM subsystem when the leak is in the direct field of view of the instrument.

The direction of the leak from the DGFM platform is found by horizontal and vertical scanning with the instruments until maximum output is indicated. This includes cases in which the leak is located behind a side solar simulator collimator. Figure 7 illustrates the change of DGFM platform 2 ionization gage output caused by the appearance of an air-argon leak in the feedthrough of the side solar simulator module 42.

Presence of this leak was indicated immediately by the sudden rise in chamber pressure and the shift of the major curve maximum from the direction of the spacecraft and IR heater array to the direction of the leak. Thus, the general location of the leak was defined quickly and the quadrupole identified the leak as an air-argon leak. The exact location of this leak was then determined within a few minutes by applying conventional helium tracer leak detection techniques to this localized area, permitting quick repair and recovery of test conditions.

The availability of two DGFM platforms in different locations within the chamber is valuable in situations in which leaks in chamber walls, penetrations, and pipes behind LN_2 shrouds need to be

located. Instruments on the two platforms are directed toward openings between LN_2 shroud segments, from which the molecules emerge into the test volume, from different angles and distances. Additional information provided by the quadrupole as to the identity of the leaking gas helps in deducing the specific location of the leak.

Figures 8 and 9 show an example of identification and location of an in-chamber leak of Freon TF from a pipe below the chamber floor. This identification was made possible by using DGFM subsystem 1 and applying gas analysis (Fig. 8), vertical m/e 101 single-peak scanning (Fig. 9(a)), and horizontal m/e 101 single-peak scanning (Fig. 9(b)). In addition, directional scanning with DGFM-2 platform was used.

The Spacecraft as a Molecular Source

The DGFM system also has been used to identify and locate molecular sources and to detect and analyze abnormal conditions on the spacecraft. Spacecraft rotation, in cases in which the test setup has provided this capability, can simplify and improve the identification of molecular flows originating from the spacecraft. Figure 10 shows an example of DGFM-quadrupole recordings during spacecraft rotation and directional peak group scanning. The peak group in this case consists of peaks m/e 16, m/e 17, and m/e 18. The height of these maxima varies, depending on the spacecraft orientation with respect to the quadrupole. Similar data have been recorded for other peak groups. To simplify data reduction, peak height maxima for some masses are plotted as functions of spacecraft orientation (Fig. 11). While peak height for m/e 32 does not change much, significant variation characterizes m/e 18, m/e 28, and the total pressure reading. The result suggests varying degassing of the spacecraft surface at the recorded rate and not the presence of a local leak.

CONCLUSIONS

The measurements with the DGFM-quadrupole system show that this system is able to perform the intended task of measuring and analyzing directional molecular flows in a large space environment simulation chamber. Characteristic as well as abnormal test article and chamber conditions such as leaks and outgassing processes were identified during spacecraft tests. The quick location and identification of in-chamber leaks saved costly spacecraft testing time and proved the system to be a valuable tool for monitoring test conditions. The results indicate

that the system performs this function within a pressure range from ultra-high vacuum into the high 10^{-4} torr range. Present gage configuration permits directional location of leaks that are in the direct field of view of the sensors with an error of less than $\pm 2^\circ$, sufficient for most applications. Development of computerized quadrupole data analysis and recording is in progress and should improve real-time application of the system. The basic technique may be applicable to locate leaks and measure directional molecular flow on spacecraft in space as well as in space simulation chambers.

ACKNOWLEDGMENTS

The author wishes to express his appreciation to the Brown and Root-Northrop Space Environment Simulation Laboratory Department for designing the rotatable mounts and fabricating and operating the system. The author is also grateful to Mr. Paul Gauthier of the Boeing Company for helpful discussions and for providing assistance with the graphics.

REFERENCE

1. Ehlers, H. K. F.: Pressure Measurements and Gas-Flow Analysis in Chambers A and B during Thermal Vacuum Tests of Spacecraft 2TV-1 and LTA-8. J. Spacecraft and Rockets, vol. 7, no. 4, Apr. 1970, pp. 480-482.

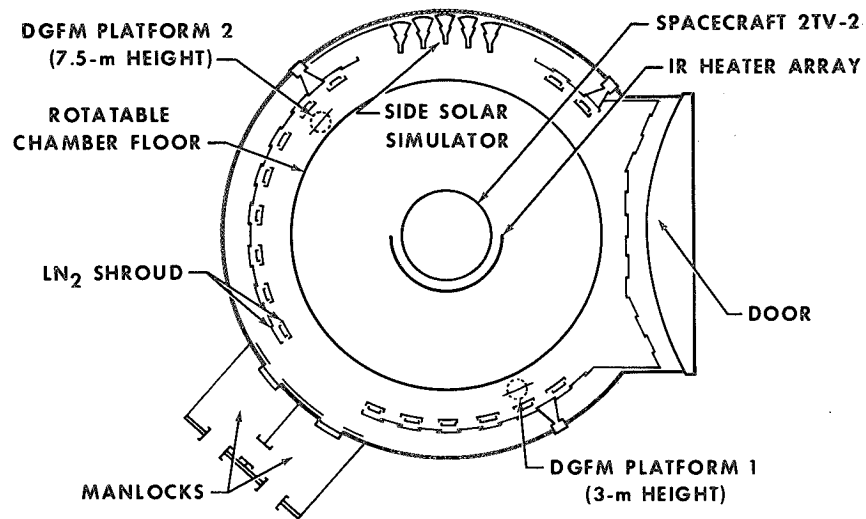


Fig. 1—Chamber A

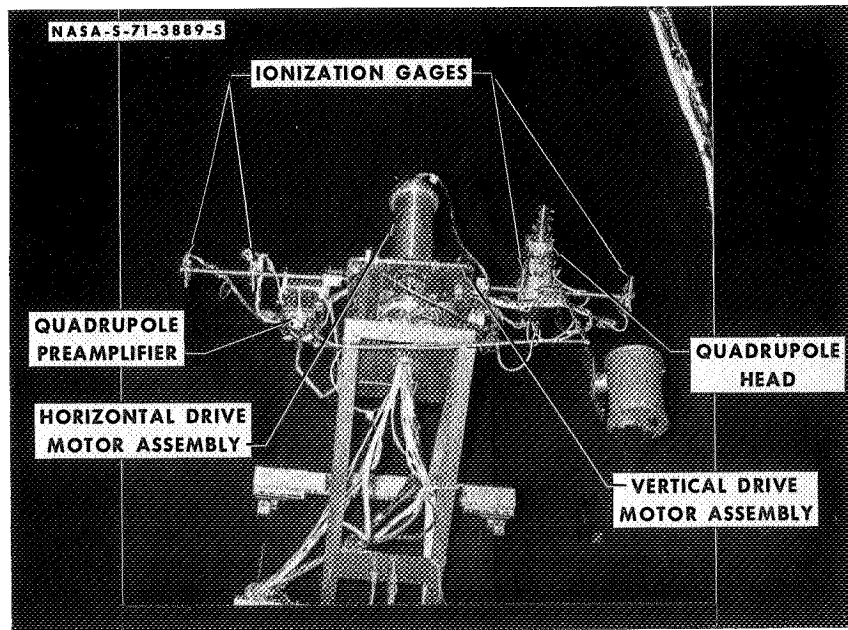


Fig. 2—The DGFM platform 1 in Chamber A

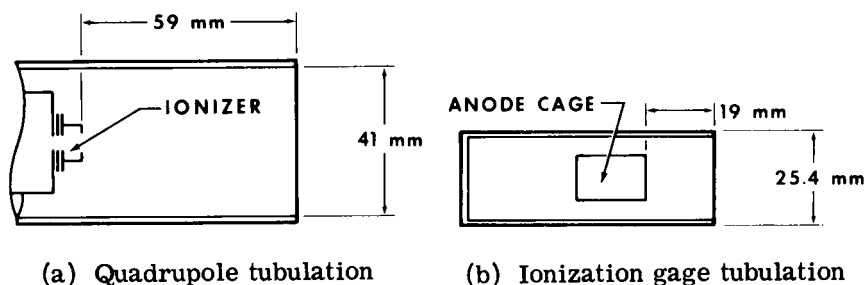


Fig. 3—Gage tubulations

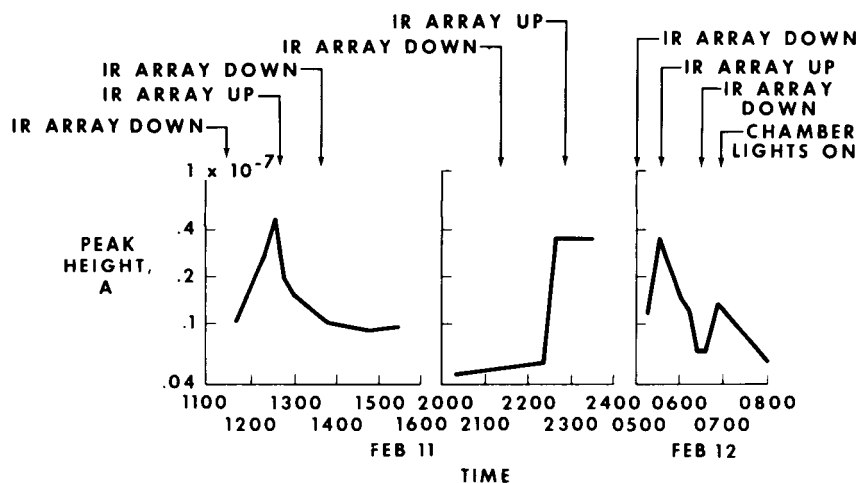


Fig. 4—Plot of m/e 69 peak height as a function of time (DGFM platform 1 fixed in direction toward test article)

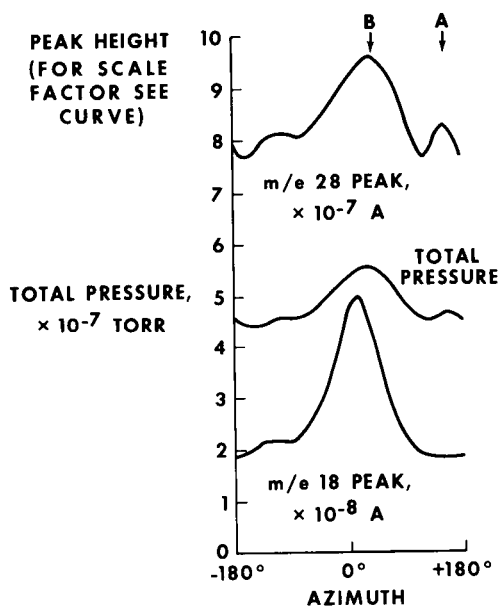


Fig. 5—The DGFM platform 1 horizontal scanning

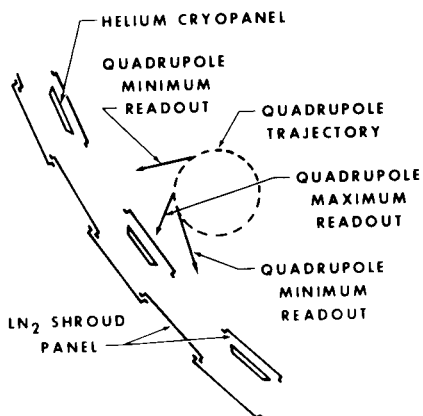


Fig. 6—Location of DGFM platform in Chamber A

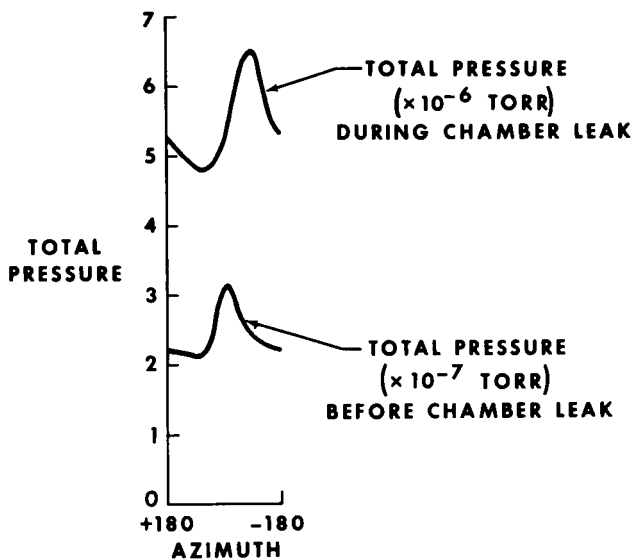


Fig. 7—The DGFM platform 2 horizontal scanning

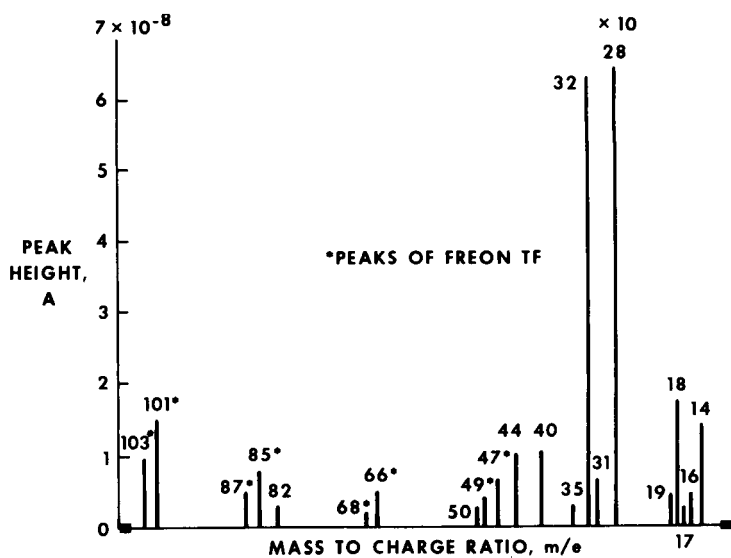
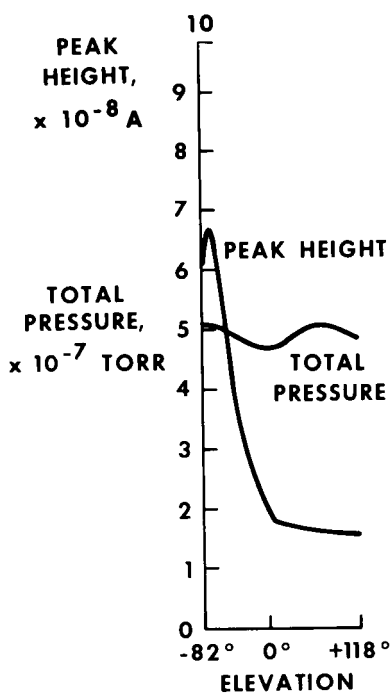
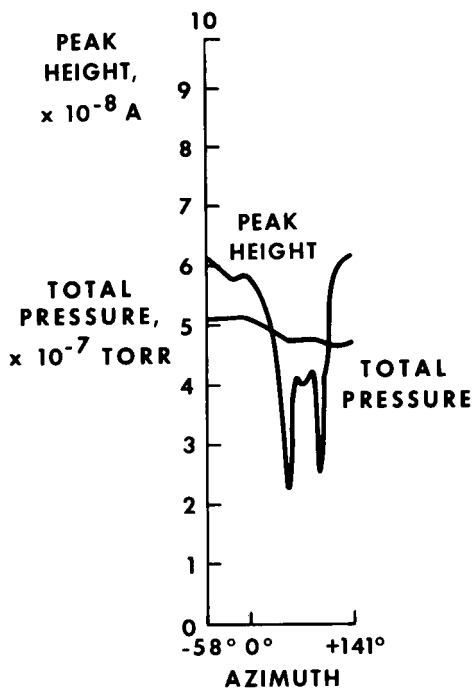


Fig. 8—Quadrupole mass spectrum with platform 1 in fixed direction (total pressure: 5×10^{-7} torr)



(a) Vertical scanning



(b) Horizontal scanning

Fig. 9—The DGFM platform 1 directional scanning, m/e 101 peak and total pressure

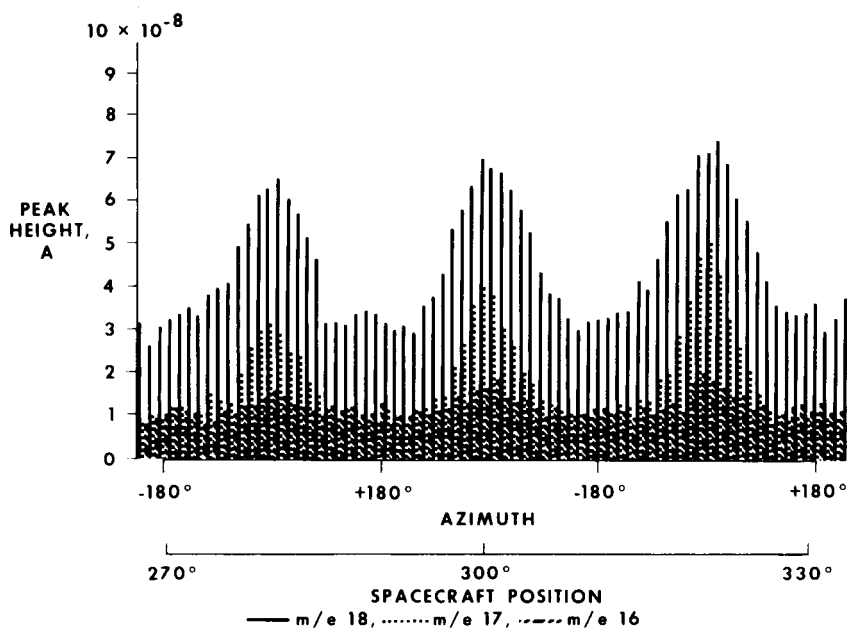


Fig. 10—Horizontal scanning of peak group, m/e 16, m/e 17, m/e 18

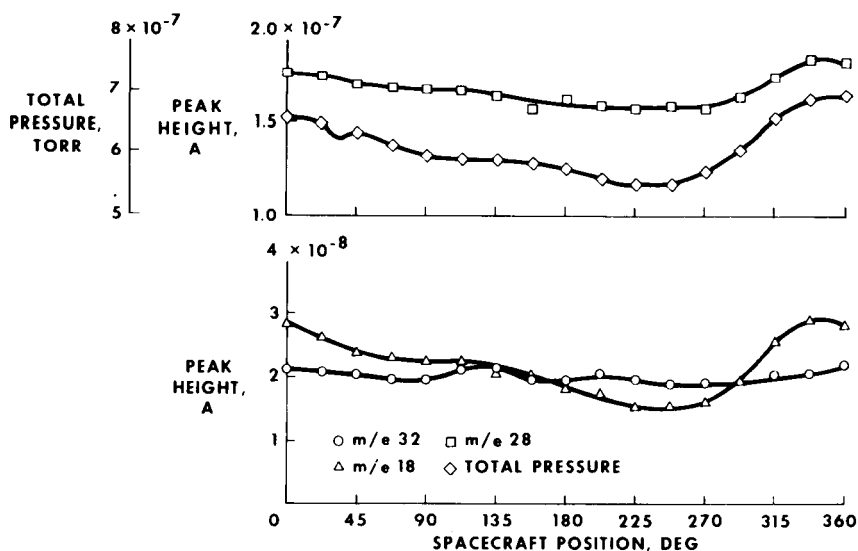


Fig. 11—Peak height as a function of spacecraft orientation

RESIDUAL GAS ANALYZER CALIBRATION

R. H. Lilienkamp, *McDonnell Aircraft Company, St. Louis, Missouri*

ABSTRACT

To obtain significant data from the Residual Gas Analyzer (RGA), the instrument must be calibrated for each gas expected among the residual gases in the vacuum system being monitored. This calibration must include both the cracking patterns of the gases and the sensitivity of the RGA to each of the gases. Most calibrations are made with pure gases. This paper deals with a new technique which employs known gas mixtures to calibrate the RGA.

The mass spectra from the RGA are recorded for each gas mixture. This mass spectra data and the mixture composition data each form a matrix. From these two matrices the calibration matrix may be computed. The matrix mathematics requires the number of calibration gas mixtures be equal to or greater than the number of gases included in the calibration.

This technique was evaluated using a mathematical model of an RGA to generate the mass spectra. This model included shot noise errors in the mass spectra. Errors in the gas concentrations were also included in the evaluation. The effects of these errors were studied by varying their magnitudes and comparing the resulting calibrations.

Several methods of evaluating an actual calibration are presented. The effects of the number of gases in the calibration, the composition of the calibration mixture, and the number of mixtures used are discussed.

INTRODUCTION

The Residual Gas Analyzer (RGA) has the capability to determine the composition of the residual gas in a Space Simulator. In general, the full potential of the instrument is not utilized because of the difficulties encountered in analyzing the data and in obtaining an accurate calibration. A method of calibration has been developed which uses known mixtures of gases to obtain a calibration which includes both the cracking patterns and sensitivity for each gas included in the calibration.

In this method mass spectra are recorded for each gas mixture along with the mixture composition. From these data the calibration matrix is computed. The method should be well suited for computerized RGA's which can collect and analyze the data.

The method is evaluated using a mathematical model of a RGA to generate mass spectra. With this model the effects of various factors were examined.

THEORY

The operation of a Residual Gas Analyzer (RGA) can be expressed by the matrix equation

$$\begin{bmatrix} A \end{bmatrix} \times \begin{bmatrix} P \end{bmatrix} = \begin{bmatrix} H \end{bmatrix} \quad (1)$$

where the matrix A is a $n \times m$ rectangular matrix in which m is the number of gases included in the calibration and n is the number of peaks possible in the spectra produced by these m gases. This matrix contains both the cracking pattern data and the gas sensitivity data for the particular RGA. The matrix P is a $m \times 1$ column matrix of the gas concentrations and the matrix H is a $n \times 1$ column matrix of the corresponding mass spectra, i.e., peak height. The problem is to obtain the matrix A from experimental observations of the P and H matrices.

For a group of o observations equation (1) can be written as

$$\begin{bmatrix} A \end{bmatrix} \times \begin{bmatrix} P \end{bmatrix} = \begin{bmatrix} H \end{bmatrix} \quad (2)$$

where the matrix P is now a $m \times o$ rectangular matrix and the matrix H is $n \times o$ rectangular matrix. Post multiply both sides of equation (2) by the transpose of matrix P to obtain

$$\begin{bmatrix} A \end{bmatrix} \times \begin{bmatrix} R \end{bmatrix} = \begin{bmatrix} S \end{bmatrix} \quad (3)$$

where

$$\begin{bmatrix} R \end{bmatrix} = \begin{bmatrix} P \end{bmatrix} \times \begin{bmatrix} P \end{bmatrix}^t \quad (4)$$

and

$$\begin{bmatrix} S \end{bmatrix} = \begin{bmatrix} H \end{bmatrix} \times \begin{bmatrix} P \end{bmatrix}^t \quad (5)$$

Matrix R is a $m \times m$ square matrix and matrix S is a $n \times m$ rectangular matrix. If matrix R is nonsingular, matrix A may be obtained by post multiplying both sides of equation (3) by the inverse of R, giving

$$\begin{bmatrix} A \end{bmatrix} = \begin{bmatrix} S \end{bmatrix} \times \begin{bmatrix} R \end{bmatrix}^{-1} \quad (6)$$

THE MODEL

To evaluate the technique developed in the preceding section, a computer simulation of a Residual Gas Analyzer similar to that previously reported¹ was used to generate mass spectra. Published cracking patterns and sensitivities² were used in this model. Shot noise effects were simulated by adding errors, which were random both in direction and magnitude, to the spectra. These errors were proportional to the square root of the peak height.

Random errors were also introduced into the gas concentration data used to generate the mass spectra. Both type of errors were varied to evaluate their importance in obtaining a good calibration matrix.

The eight gases (hydrogen, methane, water vapor, carbon monoxide, nitrogen, oxygen, propane and carbon dioxide) used in a previous study¹ were also used for this study. Mixtures containing oxygen and one of the fuels (hydrogen, methane, carbon monoxide and propane) were not allowed since these mixtures would be too hazardous to use in actual calibrations.

CALIBRATION EVALUATION

The values of shot noise and concentration errors were varied and a calibration matrix was obtained for each combination of errors; since the actual calibration matrix was known, comparisons could be made. However in an actual calibration some other method of evaluation is required; three possible techniques were evaluated. The first method used the concentration data and the calculated calibration matrix to compute mass spectra which were compared to the observed mass spectra. The second approach used the observed mass spectra and the calculated calibration matrix to compute the gas concentrations using Multiple Regression Analysis. The computed concentrations were compared to the known concentrations. The third and simplest technique was to determine the most negative number in the calibration matrix. Since there should be no negative numbers in this matrix this is a direct measure of the error.

The results obtained using these three methods of evaluation are presented in Tables 1 through 3, for eight observations, and in Tables 4 through 6, for nine observations. The data given in Table 1 and 2 show these techniques to be of little value when the number of observations is equal to the number of gases. The top row of Table 3 shows a direct correlation between shot noise and the error in the calibration matrix. Similarly the first column of data shows a direct relationship between concentration errors and the error in the calibration matrix. With shot noise and concentration errors present, a tenfold increase in both is required to produce a tenfold increase in the error of the calibration matrix.

The data presented in Tables 4, 5, and 6 follow the pattern established in Table 3. For the remainder of the work described in this paper the most negative number technique will be used for evaluation of calibration matrices.

TABLE 1
CALIBRATION EVALUATION

Standard Error of Peak Heights

8 Gas Mixtures

Concentration Error — %	Shot Noise — %			
	0	.001	.01	.1
0	9.59289×10^{-3}	8.10309×10^{-3}	7.18161×10^{-3}	9.26369×10^{-3}
0.001	9.13482×10^{-3}	1.18801×10^{-2}	9.06995×10^{-3}	7.96502×10^{-3}
0.01	1.00701×10^{-2}	8.23473×10^{-3}	9.89649×10^{-3}	9.13569×10^{-3}
0.1	1.09452×10^{-2}	1.01589×10^{-2}	9.06592×10^{-3}	1.07064×10^{-2}
1.0	0.010501	0.008344	7.93876×10^{-3}	9.94591×10^{-3}

**TABLE 2
CALIBRATION EVALUATION**

Standard Error of Pressures

8 Gas Mixtures

Concentration Error – %	Shot Noise – %			
	0	.001	.01	.1
0	2.4056×10^{-7}	2.17532×10^{-7}	2.85737×10^{-7}	2.34598×10^{-7}
0.001	2.15933×10^{-7}	$2.3724E \times 10^{-7}$	2.75059×10^{-7}	1.84077×10^{-7}
0.01	2.09998×10^{-7}	2.11088×10^{-7}	2.49035×10^{-7}	2.17039×10^{-7}
0.1	2.69472×10^{-7}	2.37373×10^{-7}	2.9557×10^{-7}	2.37394×10^{-7}
1.0	3.03546×10^{-7}	2.24468×10^{-7}	2.28232×10^{-7}	2.03606×10^{-7}

**TABLE 3
CALIBRATION EVALUATION**

Most Negative Numbers in Calibration Matrices

8 Gas Mixtures

Concentration Error – %	Shot Noise – %			
	0	.001	.01	.1
0	-1.46484×10^{-3}	-7.31396	-73.1362	-731.347
0.001	-7.1759	-12.3579	-78.1797	-736.392
0.01	-71.7603	-66.5978	-123.579	-781.801
0.1	-717.601	-712.438	-665.963	-1235.88
1.0	-7176.01	-7170.84	-7124.25	-6658.37

**TABLE 4
CALIBRATION EVALUATION**

Standard Error of Peak Heights

9 Gas Mixtures

Concentration Error – %	Shot Noise – %			
	0	.001	.01	.1
0	3.69547×10^{-5}	3.16715	31.6715	316.715
.001	1.75105	3.52399	31.6127	316.612
.01	17.5105	17.603	35.2394	316.12
.1	175.105	174.94	176.03	352.341
1	1751.05	1750.86	1749.42	1760.38

TABLE 5
CALIBRATION EVALUATION

Standard Error of Pressures

9 Gas Mixtures

Concentration Error – %	Shot Noise – %			
	0	.001	.01	.1
0	8.62281×10^{-8}	1.49081×10^{-4}	1.4817×10^{-3}	1.39016×10^{-2}
.001	8.65869×10^{-5}	2.06257×10^{-4}	1.52631×10^{-3}	.013942
.01	8.65786×10^{-4}	9.48656×10^{-4}	2.05227×10^{-3}	1.43238×10^{-2}
.1	8.65473×10^{-3}	8.72962×10^{-3}	9.47336×10^{-3}	1.94834×10^{-2}
1	8.62399×10^{-2}	8.63128×10^{-2}	.086969	9.33982×10^{-2}

TABLE 6
CHOICE OF CALIBRATION MIXTURES

Most Negative Numbers in Calibration Matrices

9 Gas Mixtures

Concentration Error – %	Shot Noise – %			
	0	.001	.01	.1
0	-2.86102×10^{-6}	–1.63115	–16.3114	–163.114
.001	–.298454	–1.89319	–16.5734	–163.376
.01	–2.98455	–4.25159	–18.9311	–165.726
.1	–29.8455	–29.8711	–42.5077	–189.228
1	–298.455	–298.479	–298.695	–424.252

NUMBER OF GAS MIXTURES

For this method to work, the inverse of the R matrix must be obtained and thus the R matrix must be nonsingular. The R matrix is the product of the P matrix by the transpose of the P matrix. The P matrix is a $m \times o$ matrix, the R matrix is always a $m \times m$ matrix. If the number of observations (i.e., number of different gas mixtures) is less than the number of gases included in the calibration, the P matrix is of the order m and rank o . The transpose of P and the R matrix also are of the order m and the rank o . Thus the R matrix is singular. If the number of observations is equal to or greater than the number of the gases then the rank of the three matrices is m and the R matrix is nonsingular. The effect of the number of gas mixtures from 8 to 24 on the most negative number in the calibration matrix is shown in Figure 1. By increasing the number of gas mixtures from 8 to 10 the most negative number is reduced by an order of magnitude. Further increases in the number of gas mixtures do not appear to follow a predictable pattern.

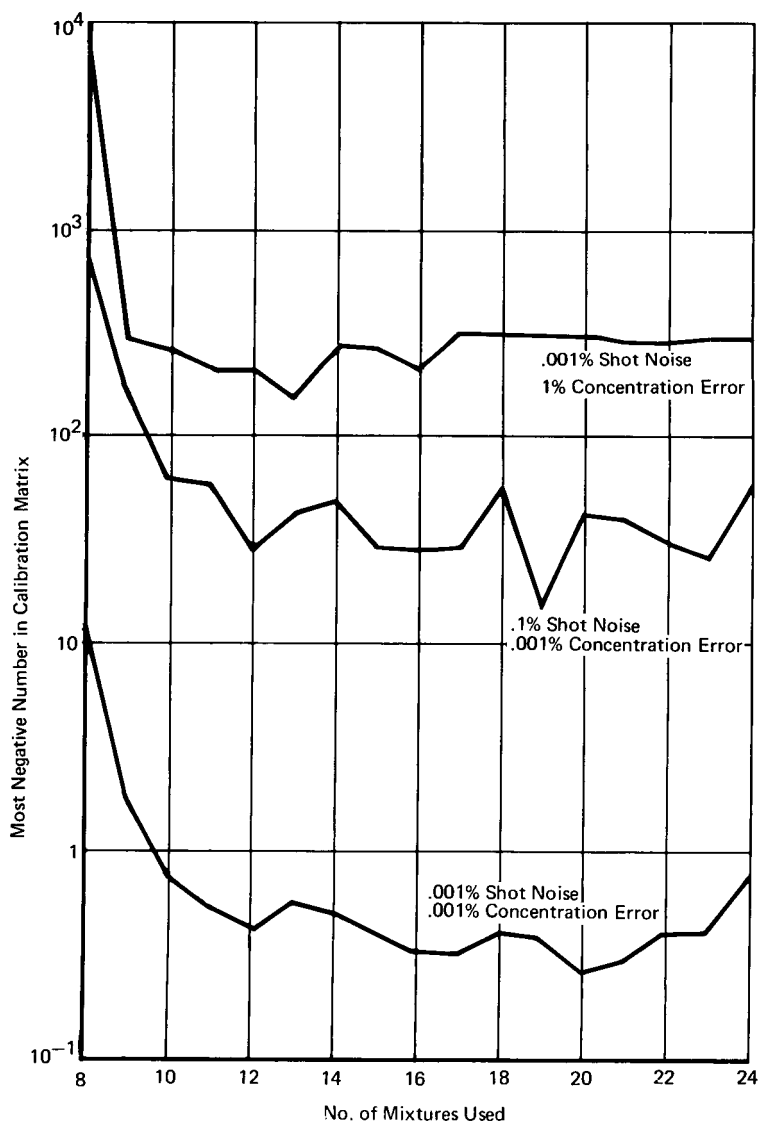


FIGURE 1
NUMBER OF GAS MIXTURES
(8 GASES IN CALIBRATION)

The location of the most negative number in the calibration matrix generally changed as additional gas mixtures were added to the computation. The locations also were different for the various combinations of shot noise and concentration errors.

Several of the factors which could influence the results were investigated. The first of these was the effect of the number of gas mixtures used on the inverse of the R matrix. The product of R by its inverse should give an identity matrix. However round-off errors in the computations result in very small numbers, rather than zero, in many of the elements off the main diagonal. For eight gas mixtures the errors in the identity matrix ranged from 10^{-9} to 10^{-8} . For nine gas mixtures these errors were reduced to 10^{-13} to 10^{-11} . The addition of more gas mixtures did not produce any further significant reduction in the errors.

The second factor investigated was the choice of gas mixtures. The results presented in Table 3 were obtained from the eight gas mixtures given in Table 7. A new set of eight gas mixtures given in Table 8 was selected. This selection excludes gas mixtures in which one of the gases has important peaks overlapping minor peaks of the other gas. The results using this set of eight gas mixtures are presented in Table 9. Comparing these results with those of Table 3 show that the second set of mixtures is a better choice and that choice of gas mixtures will influence the magnitude of the most negative number if the calibration matrix.

TABLE 7
CALIBRATION EVALUATION

Original Set of Eight Mixtures

Mixture	H ₂	CH ₄	H ₂ O	CO	N ₂	O ₂	C ₃ H ₈	CO ₂
1	39	61						
2	46							54
3		57	43					
4			47			53		
5				57	43			
6				49			51	
7					38	62		
8							45	55

TABLE 8
CALIBRATION EVALUATION

Set of Eight Mixtures Selected to Exclude Mixtures in Which One of the Gases has Important Peaks Overlapping Minor Peaks of the Other Gas.

Mixture	H ₂	CH ₄	H ₂ O	CO	N ₂	O ₂	C ₃ H ₈	CO ₂
1	46							54
2			47			53		
3				57	43			
4						39		61
5		39			61			
6		38					62	
7	50						50	
8			58	42				

TABLE 9
CALIBRATION EVALUATION

Most Negative Numbers in Calibration Matrices for Mixtures in Table 8.

Concentration Error — %	Shot Noise — %			
	0	.001	.01	.1
0	-7.27177×10^{-5}	-1.5824	-15.824	-158.24
0.001	-3.34907	-3.17703	-15.4329	-157.848
0.01	-33.4908	-33.3188	-31.7716	-154.322
0.1	-334.908	-334.737	-333.199	-317.824
1.0	-3349.08	-3348.92	-3347.48	-3333.07

See Table 3 for Comparison

NUMBER OF GASES

The number of gases included in the calibration was increased from the original eight to ten by the addition of ethane and argon with an increase in the number of peaks to 27. The most negative numbers in the calibration matrices obtained are presented in Figure 2. Seven of the starting ten mixtures were identical to mixtures used in original eight mixtures of eight gases. The results are similar to those of Figure 1, however the most negative numbers in the matrix generally have larger magnitudes than those in Figure 1.

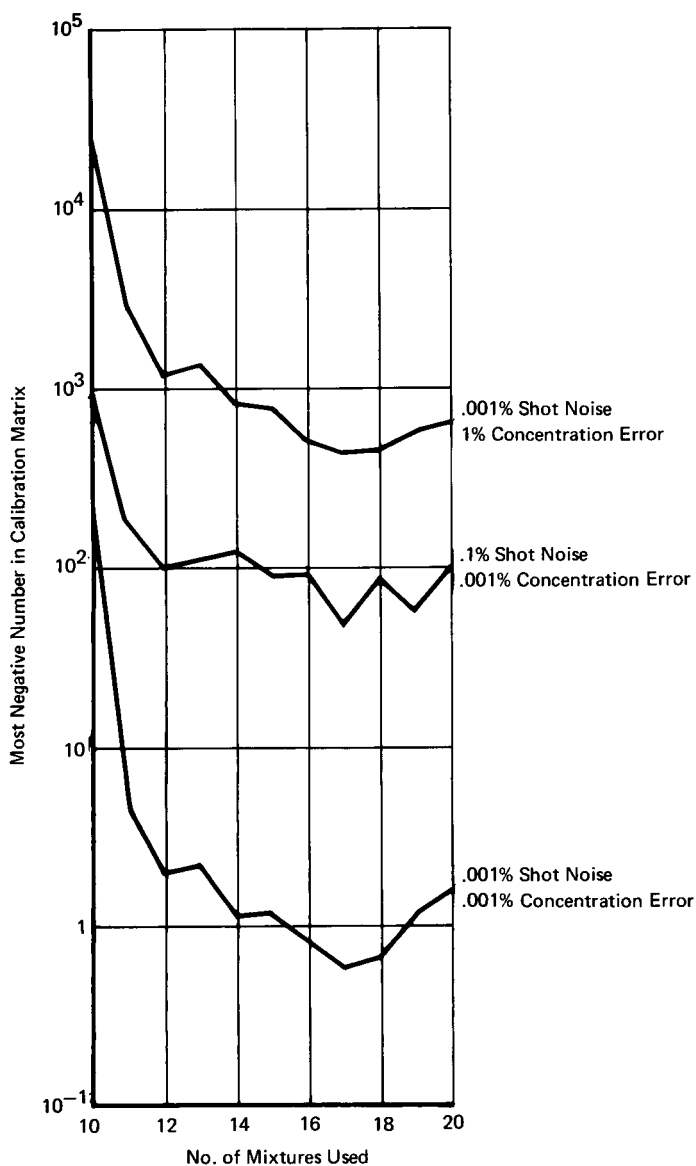


FIGURE 2
NUMBER OF GASES
(10 GASES IN CALIBRATION)

The number of gases was reduced to six by deleting water vapor and oxygen from the original eight. The results obtained from six to fifteen calibration mixtures are presented in Figure 3. These results differ from those presented in the previous two figures in that no great improvement is shown by the addition of one or two mixtures over the minimum required.

GAS CONCENTRATIONS

It has been previously suggested that calibration mixtures contain 50 percent concentrations of gases to minimize the calibration errors³. To test this suggestion the first twelve calibration mixtures of the eight gases were modified so that the concentration of the first gas in each mixture was varied from 10% to 90% with the second gas making up the difference. The results are presented in Figure 4. The curves are not quite symmetrical and the minimum occurs at about 60% for this particular group of gas mixtures. From these results the 50% mixtures appear to be a good target value for calibration mixtures.

CONCLUSIONS

A method of calibrating Residual Gas Analyzers using known gas mixtures has been developed based on sound mathematical principals. The method has been demonstrated using simulated RGA data containing errors caused by shot noise and errors in composition of the mixtures. A simple method of evaluation has been developed.

It has been shown that the number of calibration mixtures must be equal to or greater than the number of gas species included in the calibration, and that the addition of one or two mixtures can produce a significant improvement in the calibration.

It has been shown that the choice of mixtures used in the calibration can affect the quality of the calibration and that mixtures in which one of the gases has major peaks at the same mass-to-charge ratio as the other gas has minor peaks should be avoided.

It has been shown that the mixtures containing approximately 50% of each gas produced the best calibration.

REFERENCES

1. R. H. Lilienkamp, "Methods of Determining Residual Gas Composition for Residual Gas Analyzer Data," U.S. Dept. of Commerce NBS Special Publication 336 "Space Simulation" edited by J. C. Richmond, U.S. Govt. Printing Office, Washington, D.C., 1970. pp. 161-164.
2. A. Cornu and R. Massot, "Compilation of Mass Spectral Data," Hayden and Sons Ltd., London, England, 1966.
3. R. H. Lilienkamp, H. F. McKinney and D. I. Fiste, "A Computerized Mass Spectrometer System," AIAA Paper No. 69-1016.

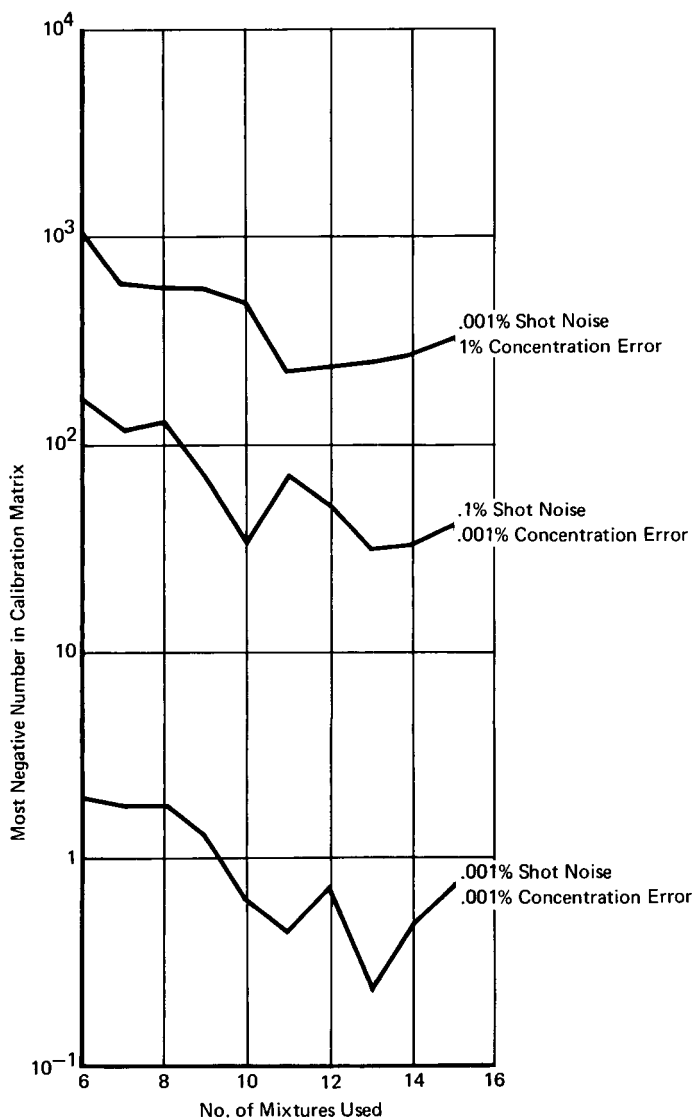


FIGURE 3
NUMBER OF GASES
(6 GASES IN CALIBRATION)

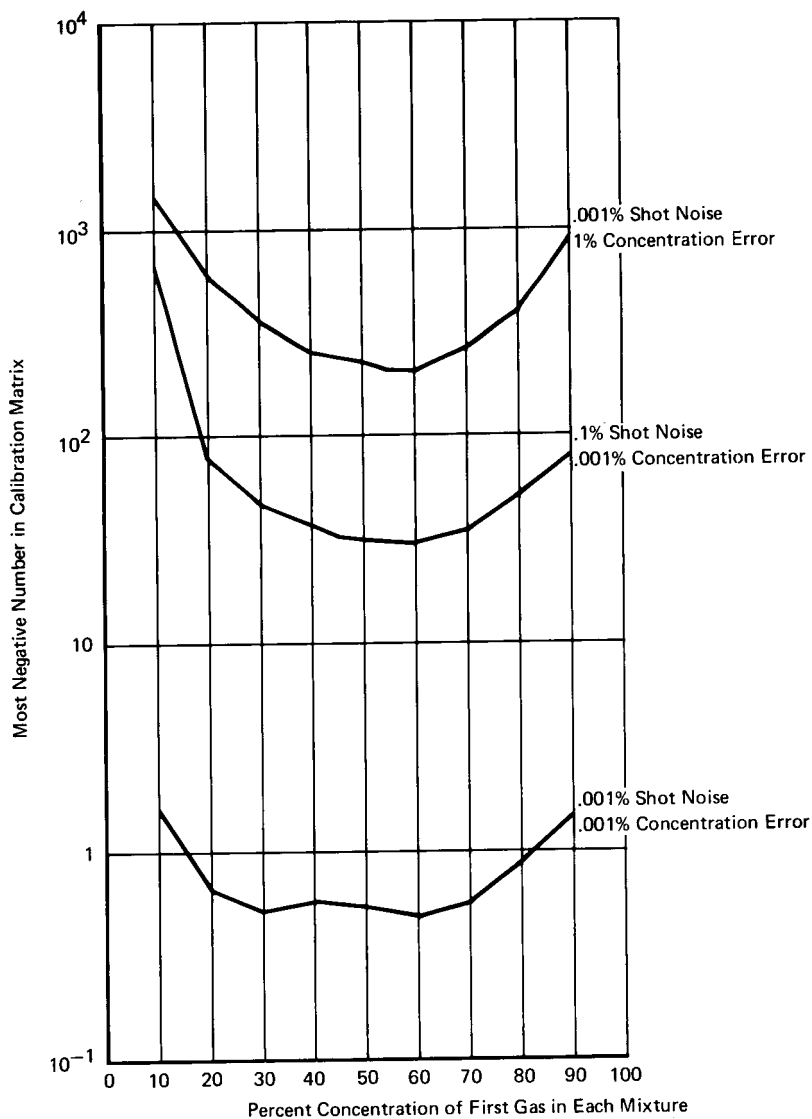


FIGURE 4
GAS CONCENTRATION

A COMPARISON OF QUARTZ CRYSTAL MICROBALANCE MEASUREMENTS WITH MASS SPECTROMETER DETERMINATIONS

Raymond Kruger, John J. Scialdone, and Harold Shapiro, *NASA, Goddard Space Flight Center, Greenbelt, Maryland*

ABSTRACT

An experimental program has been undertaken in which mass accretion rates, as determined by a liquid nitrogen cooled quartz crystal microbalance, were compared with the mass flux rates, as determined by both a cycloidal type and a quadrupole type residual gas analyzer for five simple materials. The data indicate a high degree of correlation between these instruments insofar as the shape of the curves. There are large variations however among the absolute values. These differences are probably due in the main to uncertainties in the sensitivities of the residual gas analyzers to materials tested.

INTRODUCTION

The quartz crystal microbalance (QCM) is basically a mass measuring device. It can be used to measure mass flux by determining the mass difference due to accretion over a known time interval. Knowing the temperature and molecular weight of the particles impinging on and adhering to the QCM, one may convert the flux measurements to pressure.

The residual gas analyzer (RGA), such as either of the two used in this study, is basically a number density sensitive device. Assuming a known temperature for the molecule, this then can be used as a pressure measuring device. The pressure measurement may be translated into a mass flux measurement of the instrument identified molecular species.

Therefore, by applying the factors involving the temperature and molecular weight of the material under study, the data from the RGA should therefore be directly comparable with the QCM data. Furthermore, if the RGA data are left in terms of pressure, they should bear a relation to the QCM mass flux data which is a function of the square root of the molecular weight of the material.

This experimental program was undertaken to test these hypotheses.

Theory

The theory behind operation of an RGA is well explained in a number of sources (References 1 and 2). Two types of instrument were used in this investigation. One was a Consolidated Engineering Corp. Model 21-614 cycloidal focusing mass spectrometer. In this instrument, ions are formed by the impact of electrons upon a representative molecular density in an ionizer section. These ions are accelerated, focused, and then dispersed. The dispersion of the ions is a function of the mass-to-charge ratio (m/e) and is caused by crossed magnetic and electrostatic fields. Varying the electrostatic field, E , while maintaining a constant ratio of E to the accelerating potential, causes a scanning of the ions of the various m/e ratios past a slit to a detector. The value of the ion current, measured through an electron multiplier, is a function of the number of impacting ions and in this way one may establish a relationship between the ion current (nominally, a partial pressure) and the particular value of m/e corresponding to the magnitude of E at that time.

The second instrument was of the quadrupole type and was manufactured for Goddard Space Flight Center in 1965 by Bell and Howell Co., Pasadena, Cal. In this type of instrument, ions are formed from the ambient molecules as in the case of the cycloidal RGA. Separation of the ions of varying m/e ratios however is accomplished in an electric field consisting of a direct current and a radio frequency field. The ions follow paths described by the Mathieu equation. Only ions with the proper m/e ratio (as selected by the strength and frequency of the electric fields created by the four rods) pass through the field of the detector. Here again, an electron multiplier is used to amplify the ion current.

Both of these devices basically measure number density, n . Assuming the temperature, T , to be constant for all the molecules, the RGA can be considered to measure pressure, P , as

$$P = nkT \quad (1)$$

where k is the Boltzman constant.

The theory of the quartz crystal microbalance, too, is well defined in the literature (References 3, 4 and 5). The instrument is basically a quartz crystal oscillating in the shear mode. The shear mode resonant frequency of the quartz crystal is given by

$$f = \frac{c}{2t} = \frac{N}{t} \quad (2)$$

where c is the velocity of the transverse wave in the direction of thickness t . Differentiating this expression with respect to the thickness and assuming that accumulation of mass dm on the crystal of area A and crystal density ρ is equivalent to a change of crystal thickness dt , i.e., $dt = dm/\rho A$, one obtains

$$df = -\frac{1}{N\rho A} f^2 dm = -\frac{f}{t\rho A} dm = -C_f \frac{dm}{A} \quad (\text{Hz} \cdot \text{g}^{-1}). \quad (3)$$

The mass sensitivity, C_f , is $2.22 \times 10^8 \text{ Hz} \cdot \text{cm}^2 \cdot \text{g}^{-1}$ for a crystal of thickness $t = 1.7 \times 10^{-2} \text{ cm}$, density, $\rho = 2.65 \text{ g} \cdot \text{cm}^{-3}$ and resonant frequency, $f = 10 \times 10^6 \text{ Hz}$.

The change of frequency with time, \dot{f} , resulting from the accretion of mass per unit time, \dot{m} , will be

$$\dot{f} = -C_f \frac{\dot{m}}{A} = -C_f \nu \frac{M}{N_0} = C_f \phi \quad (\text{Hz} \cdot \text{s}^{-1}) \quad (4)$$

where M is the molar mass, $\text{g} \cdot \text{mole}^{-1}$, of the gas, N_0 is Avogadro's number, ν is the molecular flux and ϕ , the mass accretion rate. The rate of mass accretion can be expressed as a function of the gas pressure P ($\text{N} \cdot \text{m}^{-2}$), the gas temperature T (degrees K) and the molar mass, M . Therefore, one may write:

$$\phi = \frac{PM}{4RT} \left(\frac{8RT}{\pi M} \right)^{1/2} = \frac{5.83 \times 10^2}{133} \sqrt{\frac{M}{T}} P \quad (\text{g} \cdot \text{cm}^{-2} \cdot \text{s}^{-1}). \quad (5)$$

where: R = gas constant

The frequency change in this form will be

$$\dot{f} = -C_f(\phi) = -C_f \left(4.38 \times 10^{-4} \sqrt{\frac{M}{T}} \right) P \gamma = -k_f P. \quad (6)$$

A coefficient γ has been introduced to account for the actual amount of the impinging mass flux which is retained by the crystal. The coefficient is the condensation or the sticking coefficient depending on whether the molecules condense on molecules of the same species or on a different substrate. For condensation on the same material, the coefficient will be a function of the gas, gas temperature, and crystal temperature. For cryogenic crystal temperature and gas temperature less than 300K, the

coefficient varies from about 0.1 to 1.0 for common gases. Of the materials used in this study, the value for water was found to be 0.9 at 77K (Reference 10). The values for the other materials were not available.

The quartz oscillator can be used as a pressure indicator when the constant $K_f = c_f \gamma \cdot 4.38 \times 10^{-4} \sqrt{M/T}$ ($\text{Hz} \cdot \text{s}^{-1} \cdot \text{N}^{-1} \cdot \text{m}^2$) is evaluated for each gas. It is also apparent that the condensation coefficient could be evaluated if one compares the mass flux measured by the quartz oscillator to the impinging flux since

$$\gamma = \frac{\phi}{\phi_i} = \frac{\dot{f}/c_f}{\phi_i} = \frac{\dot{f}/c_f}{4.38 \times 10^{-4} \sqrt{M/T} P_i} \quad (7)$$

where the subscript i indicates the impinging flux. In regard to the response of the quartz oscillator as a function of the mass accretion, substitution of $f = f - \Delta f$ in equation (3), and disregarding high order values of Δf one obtains

$$\frac{df}{dm} = -\frac{1}{N\rho A} f (f - 2\Delta f) = -\frac{c_f}{Af^2} f (f - 2\Delta f). \quad (8)$$

This indicates that the frequency shift is not linearly related to the change of mass accretion. The deviation from linearity is given by

$$D = \frac{f_i^2 - f_i (f_i - 2\Delta f)}{f_i^2}. \quad (9)$$

It can be shown that linearity is maintained if one measures the period change ($1/f$) instead of frequency change. In this report, since the data was recorded in terms of frequency, the correction indicated by equation (9) has been applied assuming that the crystals have a natural frequency of 1×10^7 Hz. The flux accretion was then, from equation (8) found to be

$$\frac{\Delta M}{A \Delta t} = \phi_M = \frac{N\rho \left(\frac{f_2 - f_1}{\Delta t} \right)}{(f_0 + f_1) [(f_0 + f_1) - 2(f_2 - f_1)]} (\text{g} \cdot \text{cm}^{-2} \cdot \text{s}^{-1}) \quad (10)$$

where:

ρ = density of quartz, $\text{g} \cdot \text{cm}^{-3}$

Δt = time interval over which the measurements were made, 100 s

f_1 = initial beat frequency, Hz

f_2 = final beat frequency, Hz

f_0 = estimated natural, unloaded frequency, Hz.

Assuming both the two RGA's and the QCM to have a response which is linear with number density and accreted flux respectively, one would expect that by comparing one with the other, the data should fit a first degree equation. Curves of the form $y = mx + b$ and $y = ax^d$ were fitted to the data. Least square solutions as found in References 6 and 7 were applied to the data. These also permitted an evaluation of the goodness of fit in the form of a correlation coefficient, r , which may range from zero, indicating no correlations, to ± 1 , indicating perfect correlation.

In addition, the RGA flux readings may be converted into pressure by the equation

$$P = G \left(\frac{M}{T} \right)^{-1/2} \phi \quad (11)$$

where

G = a coefficient which includes units conversion ($.228 \times 10^{-4}$),

Assuming the gases coming to either of the RGA's or to the QCM to be at room temperature (298K), the equation then becomes:

$$P = 3.93 \times 10^4 (M)^{-1/2} \phi \quad (12)$$

where: $G\sqrt{T} = 3.93 \times 10^4$

For any given M , we then have a first degree equation between P and ϕ and one should be able to compare P as found by the RGA with ϕ as found by the QCM.

For the remainder of this report, the subscript RGA will refer to values obtained by either of the two residual gas analyzers, subscript C will indicate the cycloidal RGA and subscript Q the quadrupole RGA. The

subscript M will refer to measurements made by the quartz crystal microbalance. Also, ϕ will be used to indicate flux in $\text{g} \cdot \text{cm}^{-2} \text{ s}^{-1}$ and P will be used to indicate pressure in $\text{N} \cdot \text{m}^{-2}$.

Test Configuration

Figure 1 shows the chamber in which this investigation was conducted. The 36 cm (14 inch) glass bell jar which completes the system is removed so that the QCM may be seen. The system is pumped via two elbows by two 15 cm liquid nitrogen (LN_2) trapped oil diffusion pumps. The relative location of the various instruments can be seen. The RGA's have been previously described.

Figure 2 is a photograph of the QCM configuration. The system basically consisted of an LN_2 cooled mounting block on which were mounted two mounting rings. To these rings were attached the quartz crystals. The crystals were edge mounted using a polyurethane adhesive (Dupont L-100 urethane with Dupont MOCA polymerizing agent using tetrahydrofuran as a vehicle).

The crystals used were 1.27 cm in diameter, AT cut at $39^\circ 49'$, and 1.7×10^{-2} cm thick to have a natural frequency of 10 MHz. Only the active crystal can be seen in Figure 2. The reference crystal is mounted similarly to a mounting ring and is between the active crystal and the mounting block. The reference crystal and the rear of the active crystal are vented to the chamber by means of a groove milled into the mounting ring. The groove is made with a right angle in it so that, when cooled by the LN_2 , it forms an effective baffle to contaminants. The beat frequency of the two crystals was read on a Hewlett-Packard 3735A frequency counter at ten second intervals over a period of 100 seconds (to insure stability of the readings).

The Bell and Howell quadrupole RGA output was read on a Mark 280 Brush recorder and the CEC 21-613 cycloidal RGA on a Leeds and Northrup Speedo-Max G recorder.

Test Procedure

The general test procedure was to close the leak valve and fill the sample holder (see Figure 1) which was a copper tube about 15 cm long and 0.6 cm in diameter with a few cubic centimeters of the sample liquid. The sample holder was then attached to the inlet system via a flexible plastic hose. The holder was then immersed in LN_2 to solidify the liquid and achieve a very low vapor pressure. The inlet system was then roughed out with an auxiliary mechanical roughing pump. After roughing, the valve to the roughing line was closed and the leak valve was opened to the previously evacuated chamber. The leak valve was then closed and LN_2 admitted to the QCM.

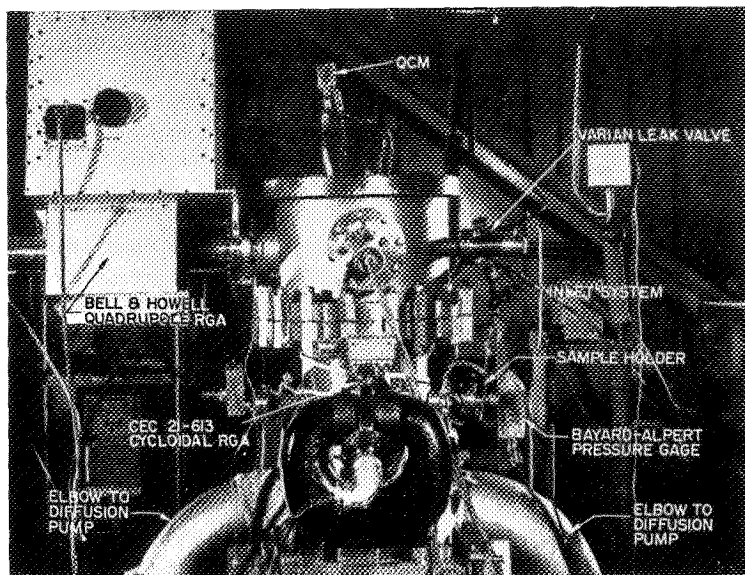


Figure 1. Test Configuration

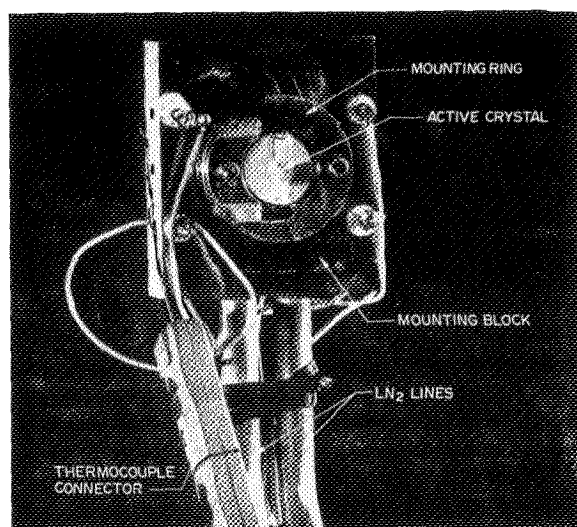


Figure 2. QCM Configuration

After reaching a steady state as noted by the Bayard-Alpert ionization gage, the RGA's, and a steady, slow accretion rate as noted on the QCM (usually in the order of $1/2 \text{ Hz} \cdot \text{s}^{-1}$), background measurements were made. The condensable component, as measured with the RGA, was substantially all water. Pressure, as measured by the ionization gage was typically about $1.5 \times 10^{-5} \text{ N} \cdot \text{m}^{-2}$ of which water formed about 76%, nitrogen 18%, oxygen 4%, and carbon dioxide 2%. The leak valve was then opened until the pressure, as measured on the ionization gage, roughly doubled. Stability was again established and the instrument readings recorded. This doubling procedure was continued until the accretion rate increased so rapidly as to cause the change in frequency over the period of the test to exceed 50 KHz or the RGA outputs to become saturated.

At the completion of the test, the LN_2 supply to the QCM was stopped and the crystals allowed to warm up releasing the accreted mass before the next material was admitted. In most cases, the chamber was opened between runs.

The five materials used in this investigation were:

1. Water, H_2O , molecular weight = 18.
2. Ethanol, $\text{CH}_3\text{CH}_2\text{OH}$, molecular weight = 46
3. Benzene, C_6H_6 , molecular weight = 78
4. Xylene, C_8H_{10} , molecular weight = 106
5. Carbon Tetrachloride, CCl_4 , molecular weight = 152

Data Reduction

The basic test data took three forms: QCM data was recorded as a beat frequency (Hz) at given time intervals, the cycloidal RGA data was read from a chart and was recorded as divisions, and the quadrupole data was read from a chart as amperes.

Using equation (10), the QCM data was interpreted as the mass flux of that material impinging on and sticking to the QCM ($\text{g} \cdot \text{cm}^{-2} \cdot \text{s}^{-1}$). Except in the case of water, the background flux was subtracted from each reading. This leaves a net ϕ_M which is due to the test material only. Since the condensable background is mostly water, this subtraction was not performed on the water data.

In order to utilize the RGA data, it was necessary to conduct a calibration of the RGA's against the ionization gage using nitrogen as the medium. The ionization gage was, in turn, calibrated in a small in-house calibration facility which uses a Baratron pressure gage as a working standard on the high pressure side of a two stage orifice system. The system is basically calibrated with a McCloud gage.

Given a calibration of the RGA for nitrogen, a major difficulty arose in the calibration for the materials undergoing test. For water

and benzene the sensitivities from Reference 8 were used; the sensitivities for the other materials were taken from Reference 9. These, however, are given with respect to n-butane and therefore the sensitivity for n-butane with respect to nitrogen must be accounted for. This value was taken from Reference 8.

Another difficulty arises from the fact that the sensitivities found in Reference 9 are the result of the works of a number of laboratories. Each laboratory report is denoted by a serial number in Reference 9. It is found that results by different laboratories for the same material vary considerably. For instance, the sensitivity for xylene (taken as 1,2-dimethylbenzene) are found in ser. no. 178 as 0.87 and 0.91. Data from ser. no. 307, another laboratory, is found to be 1.41, different by almost a factor of two. In this investigation, prime reliance was placed in the data from Reference 8 since this was from the manufacturer of one of the RGA's being used. Other sensitivities were taken as the average of source found in Reference 9 excluding any data which was significantly different from the other sources.

Table I below shows the sensitivities used and the sources.

Table I
RGA Sensitivity Values

Material	Sensitivity with Respect to:	
	n-Butane, S_B	Nitrogen, S_N
n-Butane	-	0.85 (Reference 8)
Water	-	1.3 (Reference 8)
Ethanol	0.63 (Reference 9, ser. nos. 364, 1620, and 1646)	1.3 *
Benzene	-	0.63 (Reference 8)
Xylene	0.89 (Reference 9, ser. no. 178)	0.96 *
Carbon Tetrachloride	0.38 (Reference 9, ser. no. 603)	2.2 *

$$*S_N = \frac{S_N \text{ for n-Butane}}{S_B}$$

Tests run to determine the sensitivity of the RGA's for nitrogen C_{RGA} , indicated that the sensitivity of the cycloidal RGA was 2.39×10^{-8} ($N \cdot m^{-2} \cdot Division^{-1}$) and the quadrupole RGA was 1.45×10^6 ($N \cdot m^{-2} \cdot Ampere^{-1}$). These figures were corrected by the gage calibration, C_1 , found to be 0.89. The typical calculation was then of the form

$$P_{\text{RGA}} = (\text{Instrument Divisions or Amperes}) (C_{\text{RGA}}) (C_1) (S_N) \quad (13)$$

and then the flux, ϕ_{RGA} , equals

$$\phi_{\text{RGA}} = P_{\text{RGA}} \left[4.38 \times 10^{-4} \left(\frac{M}{T} \right)^{1/2} \right]. \quad (14)$$

Data Analysis

Using the relationships established in the previous section, values were obtained for ϕ_M , ϕ_C , and ϕ_Q . Since these are also related to the pressure as a function of the square root of the molecular weight, relationships of ϕ_M with P_C and P_Q were also established.

As noted earlier, it was expected that the two instruments would be linearly related. Curves of the form $y = mx + b$ and $y = ax^d$ were fitted to the data; the exponential form was tried to investigate the variation from a first degree equation. Table II presents the equations for the various substances. The correlation coefficients in all cases were greater than 0.998.

Table II
RGA Pressure as a Function of Quartz Crystal
Microbalance Measured Flux

Material	$P_{\text{RGA}} = m\phi_M + b$	$P_{\text{RGA}} = a\phi_M^d$
Water:	$P_T = 9263 \phi^*$ $P_C = 5670 \phi_M + 1.72 \times 10^{-5}$ $P_Q = 5130 \phi_M + 6.80 \times 10^{-6}$	$P_C = 3640 \phi_M^{0.970}$ $P_Q = 3480 \phi_M^{0.976}$
Ethanol:	$P_T = 5794 \phi^*$ $P_C = 4700 \phi_M + 1.08 \times 10^{-5}$ $P_Q = 7469 \phi_M + 4.05 \times 10^{-6}$	$P_C = 4130 \phi_M^{0.989}$ $P_Q = 5370 \phi_M^{0.980}$
Benzene:	$P_T = 4450 \phi^*$ $P_C = 3000 \phi_M - 3.04 \times 10^{-7}$ $P_Q = 3230 \phi_M - 3.45 \times 10^{-6}$	$P_C = 3430 \phi_M^{1.008}$ $P_Q = 3600 \phi_M^{1.010}$
Xylene:	$P_T = 3817 \phi^*$ $P_C = 3420 \phi_M - 1.53 \times 10^{-7}$ $P_Q = 4410 \phi_M + 1.34 \times 10^{-6}$	$P_C = 3470 \phi_M^{1.001}$ $P_Q = 3530 \phi_M^{0.986}$
Carbon Tetrachloride:	$P_T = 3167 \phi^*$ $P_C = 1460 \phi_M - 1.16 \times 10^{-6}$ $P_Q = 2250 \phi_M - 4.29 \times 10^{-6}$	$P_C = 2540 \phi_M^{1.034}$ $P_Q = 3180 \phi_M^{1.024}$

* P_T is what one would expect assuming an ideal case, e.g., condensation coefficient equals 1.0 and RGA sensitivities being perfect.

Figure 3 shows both equation forms plotted against the actual data points for water. The curves are rather typical of the data in that the power curve fit appears to the eye to be the better one. The line with a slope of 1, the ideal case, is placed in the figure as a reference. Figures 4 and 5 are plots of the data obtained with the RGA's, ϕ_C and ϕ_Q , against ϕ_M for all five materials. In all cases the slopes are near the expected value of 1.0 but their distance from the expected line varies with both instrument and material.

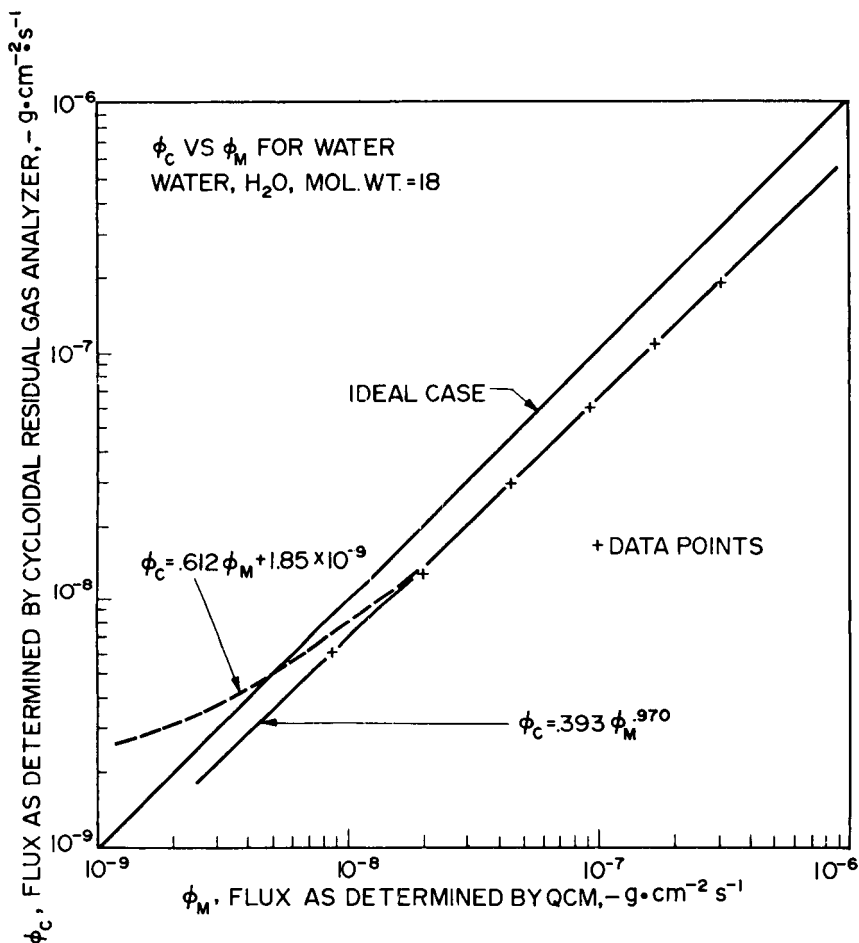


Figure 3

If this data is replotted as P_{RGA} vs ϕ_M for all materials, one would expect a family of curves with a slope of 1.0 and the position of the curve dependent on the molecular weight. This type of presentation is contained in Figures 6 and 7. In these figures the curves plotted are of the form $y = ax^d$. The materials and their molecular weights are shown

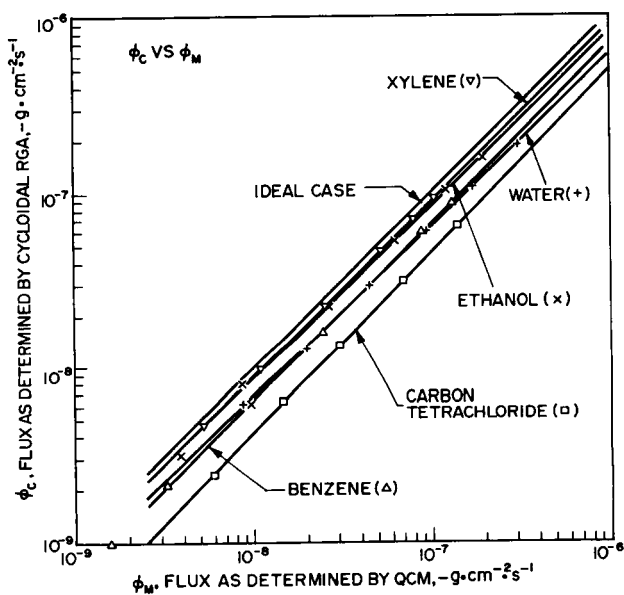


Figure 4

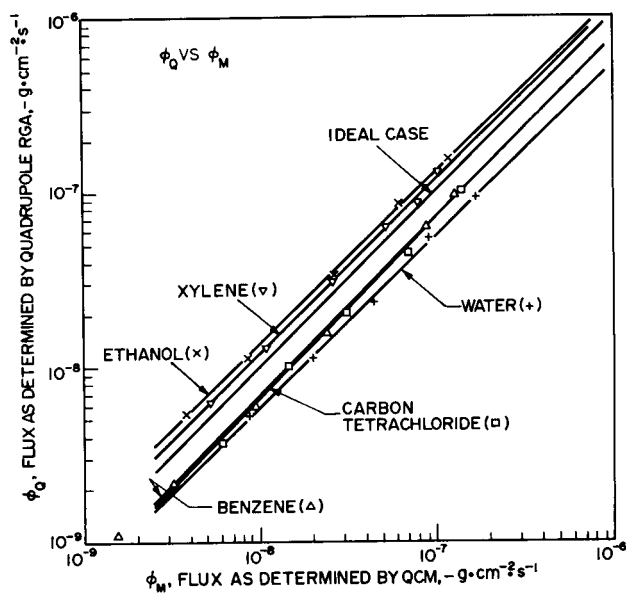


Figure 5

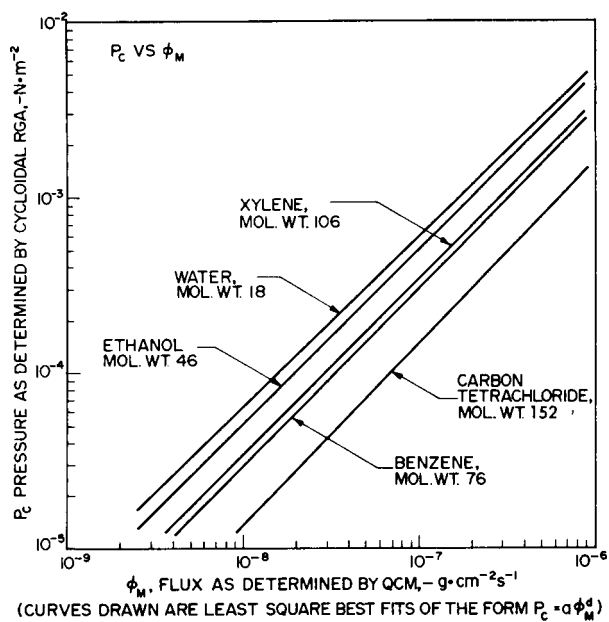


Figure 6

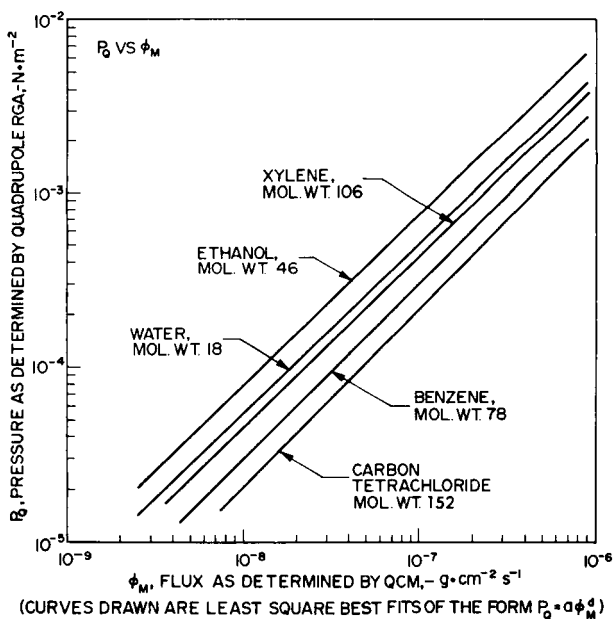


Figure 7

on the figures. It can be seen that they do not vary monotonically with molecular weight. For instance, in Figure 6 xylene and benzene seem to be out of sequence and in Figure 7 water and ethanol are also out of sequence.

A more readily apparent presentation is to be seen in Figures 8 and 9. In these, the coefficient of ϕ_M (a or m as the case may be) is plotted against M, the molecular weight. In addition, a line is drawn which expresses the expected theoretical result. This value is derived simply by assuming the linear relationship and writing pressure as a function of flux (see equation 12). The value a, or m, then is set as

$$a, \text{ or } m, = 39,300 (M)^{-1/2}. \quad (15)$$

In Figure 8, which is based on the form $P = a\phi^d$, water seems to be furthest from the expected value; in Figure 9, based on the form $P = m\phi + b$, there is significantly more scatter, with water and carbon tetrachloride being furthest from the expected value.

It is interesting to note that in the cases of water and benzene, the data from the two RGA's virtually lie one atop the other in Figures 8 and 9. (It might be noted that in these two cases the sensitivities were taken from Reference 8.) The other cases, except for ethanol on Figure 8, show a significant scatter. Two major questions arise. First, why do the points for the same material differ from each other for the two different RGA's, and second, why do they not lie on the predicted line?

In partial answer to the first, one can hypothesize that the two instruments do not have equal sensitivities for all materials. This would not be at all unexpected in view of the varying sensitivities reported by different investigators using rather similar analyzers. One would, however expect closer correlation between the way the analyzers act upon water and ethanol or upon benzene and xylene because these materials have certain chemical similarities as opposed to the fact that they seem to act the same way between water and benzene - chemically quite dissimilar.

As to the second question, we may again strongly suspect erroneous values for the assumed sensitivities. Figures 4 and 5 show that the major problem does not lie in the assumption of a condensation coefficient of 1.0 inasmuch as the data often indicates a coefficient greater than 10, an impossibility. The differences in instrument position might account for different fluxes at these locations but this should not be a function of the material.

Summary of Conclusions

First, the data supports the hypothesis that the QCM and RGA both act in a linear manner in the range of pressures investigated. Second, a

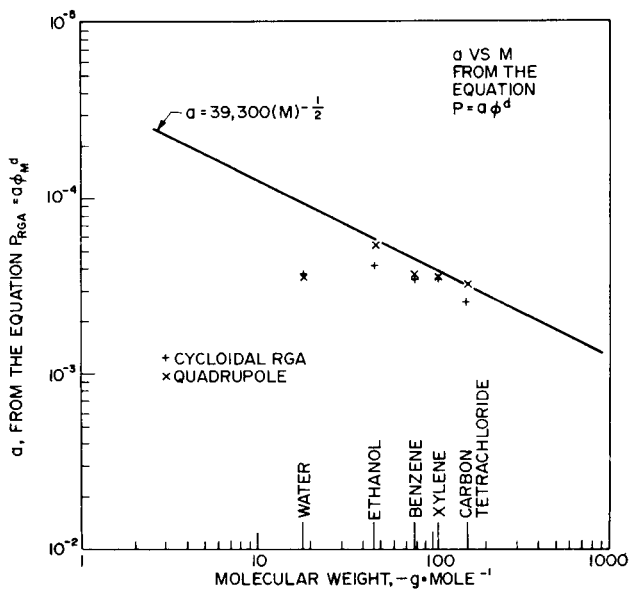


Figure 8

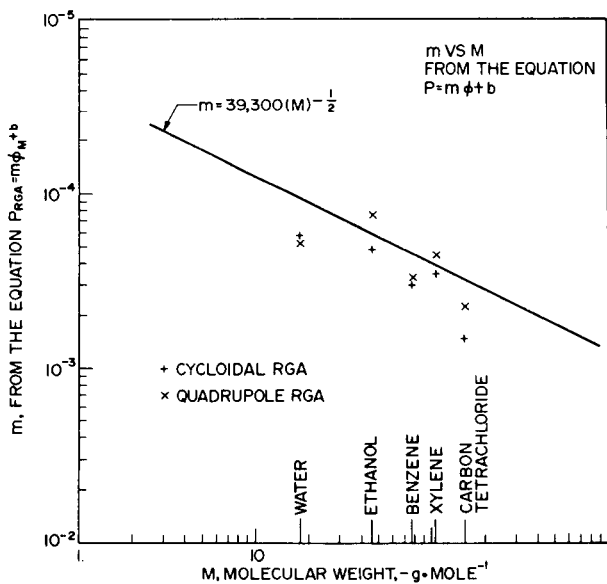


Figure 9

great uncertainty exists in the literature values of sensitivities for the RGA and this is reflected back as differences between fluxes measured by the QCM and fluxes, or pressures, measured by the RGA's. Water, traditionally a difficult substance to investigate, again appears to have the greatest uncertainties associated with the data. Third, while the data shown in Figures 8 and 9 do not follow the predictions, the general trend is there and, with proper sensitivities, would probably fit the predictions quite closely.

As a last item, the use of a QCM at cryogenic temperatures appears to be a viable method for obtaining sensitivities for mass spectrometers. If the condensation coefficients are known, this method should be quite accurate and would permit in-situ calibration of an RGA.

REFERENCES

1. D. A. Redhead, J. P. Hobson, and E. V. Kornelsen, "The Physical Basis of Ultra-high Vacuum," Chapman and Hall, Ltd., 1968.
2. R. Jayaram, "Mass Spectrometry-Theory and Applications," Plenum Press, 1966.
3. K. H. Behrndt, "Long Term Operations of Crystal Oscillators in Thin Film Deposition," Journal of Vacuum Science and Technology, vol. 8, no. 5, Sept.-Oct. 1971, pp. 622-626.
4. G. Doring, G. Marx, and G. Sauerbrey, "Adsorption von Öldämpfen auf reinen Metalloberflächen," Vacuum Technik, vol. 15, no. 10, 1966, pp. 245-249.
5. W. W. Youngblood, "High Vacuum Calibration of a Cryogenic Quartz Crystal - An Atmospheric Density Gage," Proceedings American Vacuum Society, vol. 8, no. 1, Jan.-Feb. 1971, pp. 294-298.
6. J. E. Freund, "Mathematical Statistics," Prentice-Hall, 1962.*
7. K. A. Brownlee, "Statistical Methodology in Science and Engineering," John Wiley and Sons, 1965.*
8. Consolidated Electromagnetics Operation and Maintenance Manual for the 21-613 Residual Gas Analyzer, Pasadena, Cal., 1962.
9. American Petroleum Institute Project #44 (Compilations of Mass Spectral Data).
10. E. S. Wang, et al., "General Cryopumping Study," AEDC TN 61-114, Oct. 1961.

*These references were obtained from the Hewlett-Packard Calculator Model 9100A Program Library, Program numbers 09100-70803 and 09100-70811.

A VACUUM THERMOGRAVIMETRIC METHOD FOR OUTGASSING EVALUATIONS OF SILICONE-COATED FIBERGLASS CLOTH

L. B. Jensen, G. B. McCauley and M. Honma, *Lockheed Palo Alto Research Laboratories, Palo Alto, California*, and A. E. Hultquist, *Lockheed Missiles & Space Company, Inc., Sunnyvale, California*

ABSTRACT

A novel method for evaluating outgassing characteristics of space-sensitive materials has been devised by modifying a thermogravimetric balance so that a continual weight loss trace is obtained as a function of time at constant temperature and nearly constant pressure. In addition the apparatus is capable of collecting room temperature condensibles during the outgassing run. A series of silicone-coated glass cloth samples have been evaluated by this method. The major advantage of the technique is that data presentation is developed in the form of a continuous trace. This data can then be utilized to develop the kinetics of weight loss. The technique has been shown to be a useful and valid one for indicating small differences between materials under vacuum and elevated temperature conditions.

INTRODUCTION

Thermogravimetry has been highly developed as a technique for determining loss or gain in weight as a function of temperature. It has been shown to be useful to 1200°C and higher with a wide range of sample sizes, generally from 1-300 mg. Sensitivities of the order of a few micrograms are attainable. The basic unit consists of a programmer, furnace, amplifier, recorder, a cell containing the sample supported on a spring balance and a transducer to detect weight changes.

However, the standard thermogravimetric analysis (TGA) apparatus is not too suitable for evaluation of materials for use in space applications, i.e. under conditions of high vacuum and elevated temperature together with collection of volatile condensable materials (VCM).

A modified thermogravimetric analysis system developed by Stanford Research Institute enabled determination of weight loss and total VCM for potential space use materials such as polymers (Refs. 1, 2, 3). This procedure utilized a standard TGA apparatus, but the sample chamber was replaced by a high vacuum bell jar chamber. Mechanical and oil diffusion pumps were employed to give a pressure of the order of 10^{-6} torr. The system was set up to evaluate 24 samples simultaneously. It was developed in both a micro version utilizing samples of 100-200 mg, and a macro

version employing samples of the order of 4-10 g. The basic sample system consists of 2 copper block heater units, each accommodating 12 samples, and a common cooling unit for the VCM collectors. Samples are inserted into separate bored-out cavities in the blocks and covered with copper discs sealed with Teflon O-rings. Heating elements are made of Xactglo wire silver-soldered in place. VCM collector plates are located adjacent to each sample compartment with a relatively large exit port for each compartment situated such that effluents impinge directly on the room temperature collection plate. Thus with this system it is possible to screen a large number of samples, obtaining total weight loss (or gain) and total VCM for each sample.

The system to be described provides for all the advantages of the SRI system plus providing for a continuous time-weight loss output and an improved VCM collection plate. The system is a macro type, employing samples of 250 mg to 12 g. At present the unit is a single sample system, although it could be modified to accept multiple samples by use of multiple balance-transducer-recorder systems. A major use of the Lockheed vacuum TGA unit has been the evaluation of silicone-coated fiberglass materials. This work is described following. The technique has been very useful in demonstrating the potential utility of these coated fiberglass cloths as space materials.

EXPERIMENTAL PROGRAM

Materials

The materials used to evaluate the vacuum TGA procedure are silicone-coated glass cloth samples. The fiberglass cloth is a standard 0.002 ins. thick material. The black and white silicones are the same Dow-Corning 432 stock with different pigmentation. The white is based on titanium oxide pigmentation and the black is a cobalt oxide-based material. The coatings are calcined on the fiberglass and cured at 480°F for 16 hours.

TGA Equipment

The basic TGA unit is the Thermo-Grav number 4-4430 manufactured by the American Instrument Company. Used with this procedure, the furnace and sample tube were removed. A standard Pyrex resin reaction kettle replaced the sample tube. Heating was accomplished by use of a heating mantle. Vacuum connection was made through the cover of the kettle to a high speed oil diffusion pump backed up by a standard mechanical pump. The water cooled collector plate is situated at the top of the vessel and consists of gold plated copper foil. A forthcoming paper will describe the system in detail.

Experimental Procedure

A weighed and measured silicone-coated glass cloth sample is

inserted into the sample chamber. Samples are suspended from a glass rod by means of a wire hook or crucible hanger; this insures uniform heating from all sides. The chamber is then closed and pre-evacuated, first with the mechanical pump and then with the diffusion pump down to 10^{-5} to 10^{-6} torr. Samples of between 250 mg and 12 g can be accommodated. Samples as large as 4 ins. in diameter have been employed, but they must be within the 12 g maximum weight limit. Heating is then initiated and the run started. The sample temperature is monitored by means of a thermocouple placed below the sample and fed to a digital read-out in the TGA unit. Provisions are also provided for thermocouple readings on a Leeds and Northrup potentiometer recorder. The VCM collector plate temperature is also monitored by means of a thermocouple connected to a potentiometer. The recorder in the TGA unit is utilized to obtain the weight loss/time plot. Its range is 0-260 mg weight loss. The recorder can be reset to zero by transducer adjustment to allow several multiples of the 260 mg range.

At the end of the run period (usually 24 hrs., but sometimes up to 100 hrs.), heating power is shut down, the sample cooled and the chamber brought up to atmospheric pressure. Sample weight is then determined along with the weight of VCM.

Materials Conditioning

Some samples were pre-conditioned prior to the TGA analysis to cut down on the amount of volatiles emitted. This "space conditioning" treatment was generally carried out at 400-425°F at 10^{-3} torr pressure for 100 hrs. Other samples were evaluated "as received".

EXPERIMENTAL RESULTS

A number of runs have been carried out to evaluate silicone-coated materials in the vacuum TGA system. Both black and white coated materials have been employed, some coated on only one side and others coated on both sides. Typical data obtained for a given run is shown in Table 1. Basically information is taken on pressure and the temperature of sample and collector. The recorder plots the temperature/weight loss curve. Total weight loss and total VCM weights are determined by weighing before and after the run.

From this information the sample weight loss is computed together with the total room temperature volatile condensable materials. Weight loss is also calculated as a function of unit area. Data for black coated samples is shown in Table 2 and that for white-coated materials in Table 3.

Vacuum-Thermal Effects

Typical weight loss/time TGA curves for black coated materials are shown in Figure 1. Figure 1 shows two curves for one

Time Min.	Pressure torr $\times 10^{-4}$	Sample Temp. °F	Collector Temp. °F	Remarks
0	0.5	77	59	Start, after pump down
5	1.0	99	59	
10	1.3	163	63	
15	0.9	221	68	
20	0.9	246	72	
25	0.52	257	73	
85	0.09	257	73	
208	0.05	257	73	
340	0.04	259	73	
1415	0.02	259	73	
1475	0.02	259	73	OFF
Wt. Loss = $0.0957/11.5636 \times 100 = 0.83\%$ Wt. Loss/Unit Area = $0.0957/461 \times 100 = 0.21 \text{ mg/cm}^2$ Collector Wt. Gain = $0.0308/11.5636 \times 100 = 0.26\%$ Conditions - 260°F, 24 hrs., 10^{-4} torr				

Table 1 Typical Run Data for Vacuum
TGA - TGA No. 106

TGA No.	No. Sides Coated	Sample Conditioning	Vacuum-TGA Conditions			Wt. Loss %	RT- VCM %	Wt. Loss mg/cm ²
			Temp °F	Pressure torr	Time hrs.			
20	1	As Received	100	10 ⁻⁴	50	0.099	*	
27	1	As Received	150	10 ⁻⁴ -10 ⁻⁵	30	0.14	0.010	
25	1	As Received	300	10 ⁻⁴ -10 ⁻⁵	96	0.65	0.026	
23	1	As Received	400	10 ⁻⁴	96	1.70	0.057	
106	1	As Received	260	10 ⁻⁴ -10 ⁻⁵	24	0.83	0.26	0.21
105	1	As Received	400	10 ⁻⁴	24	1.50	0.58	0.38
107	1	Space Conditioned**	260	10 ⁻⁵ -10 ⁻⁶	24	0.42	0.19	0.10
111	1	Space Conditioned**	400	10 ⁻⁵ -10 ⁻⁶	100	1.01	0.36	
122	1	As Received	260	10 ⁻⁵ -10 ⁻⁶	24	0.66	0.099	0.19
123	1	Space Conditioned**	260	10 ⁻⁵ -10 ⁻⁶	24	0.72	0.076	0.21
117	2	As Received	400	10 ⁻⁵ -10 ⁻⁶	100	2.26	0.63	0.78
163	2	As Received	260	10 ⁻⁶	24	0.63	0.19	0.21
* VCM Not Collected								
** Corresponds to 400-425°F, 10 ⁻³ torr, 100 hrs.								

Table 2 Vacuum Thermogravimetric Analysis of Black Silicone Treated Glass Cloth

TGA No.	No. Sides Coated	Sample Conditioning	Vacuum-TGA-Conditions			Wt. Loss %	RT- VCM %	Wt. Loss mg/cm ²
			Temp. °F	Pressure torr	Time hrs.			
98	1	(As Received	260	10 ⁻⁵	24	0.70	0.61	
96	1	(As Received	400	10 ⁻⁴	24	1.18	*	
92	1	(400°F, 10 ⁻⁴ torr, (24 hrs.	260	10 ⁻⁵	24	0.17	**	
150	2	(Space Treated***	260	10 ⁻⁶	24	0.23	0.08	0.09
151	2	(Space Treated***	260	10 ⁻⁶	24	0.30	0.03	0.12
162	2	(As Received	260	10 ⁻⁶	24	0.27	0.06	0.56
150A	2	(As Received	400	10 ⁻⁶	100	1.89	*	0.76
151A	2	(Space Treated***	260	10 ⁻⁶	24	0.30	0.027	0.76
* VCM Not Collected ** Collection Contaminated *** Corresponds to 400-425°F, 10 ⁻³ torr, 100 hrs.								

Table 3 Vacuum Thermogravimetric Analysis of White Silicone Coated Glass Cloth

side coated and for a material coated on both sides. The curves have been replotted on a log time scale so as to show the complete curve for a 24 hr. run. Normally the overnight portion of the curve is not recorded. Indications are that in most cases, all volatiles are lost within a 24 hour period, and the curve stabilizes at that point. This is true for the 260°F temperature. Runs were also carried out at 400°F, and in this case, a significant increase in volatiles is observed. Runs on black samples at 100 and 150°F yield an expected reduction in volatiles.

The curve for sample 163 in Figure 1 would appear to yield a lower weight loss for a two side-coated specimen than for sample 106 (1 side coated). However, specimen 106 had nearly twice the area of 163, so that actually the two side-coated material had a higher weight loss per unit area.

Typical curves for white coated materials are shown in Figure 2. These cannot be compared directly with the curves for the black materials since surface areas differ in all cases.

From the information in Tables 2 and 3, it is seen that percent weight loss increases with temperature, with time, and probably to some extent with pressure decrease. The latter is not too evident since variation in pressure was nominal. In general weight losses under comparable conditions are higher for the black coatings than for the white for the 260°F runs; however, limited information indicates that the reverse may be true at 400°F.

Space Conditioning Effects

Some of the samples in Tables 2 and 3 were subjected to a preconditioning treatment prior to the TGA run. This consisted of heating the samples at 400-425°F under a vacuum of 10^{-3} torr for 100 hrs. This reduced weight loss figures in all except one case (No. 151). There is no immediate explanation for this exception.

Room Temperature Volatile Condensable Materials (VCM)

The percentage of VCM obtained is also shown in Tables 2 and 3. This amount is generally less for the white-coated materials than for the black. In all cases the space conditioning treatment reduced this figure for both black and white coatings. From the black coatings data, it appears the VCM also increases with time and temperature. All VCM materials were examined by infrared absorption spectroscopy. These analyses showed the condensed materials to be essentially silicone oil; this probably represents unpolymerized coating material.

Weight Loss-Time Effects

Data is shown in Table 4 for the five runs represented by the curves in Figures 1 and 2. Each curve has been broken down into a series of time segments where the weight loss rate was

TGA No.	-Sample-	Area cm ²	Time Interval min.	Wt. Loss/Time Interval		
				mg	mg/min	mg/cm ² /min x10 ⁻⁵
106	Black-1 Side-AR	461	2	0	0	0
			14	25	1.79	388
			12	8	0.67	145
			32	7	0.22	47.8
			144	12	0.083	18
			136	5	0.037	8
			1075	12	0.012	2.6
			60	2	0.033	7.2
107	Black-1 Side-SC	433			Avg.	10.45
			4	0	0	0
			12	9	0.75	17.4
			34	2	0.059	13.7
			100	1	0.01	2.3
			1030	0	0	0
			148	0	0	0
			62	2	0.032	7.4
163	Black-2 Sides-AR	232			Avg.	2.32
			3	0	0	0
			13	11	0.85	366
			18	5	0.28	121
			25	4	0.16	68.8
			106	8	0.075	32.3
			1050	11	0.010	4.3
			228	0	0	0
150	White-2 Sides-AR	155			Avg.	11.68
			3	0	0	0
			10	10	1.0	646
			13	2	0.15	96.9
			24	1	0.042	27.2
			170	3	0.018	11.6
			1035	3	0.002	1.3
			110	1	0.009	5.8
151	White-2 Sides-SC	194			Avg.	10.60
			3	0	0	0
			5	13	2.60	1345
			8	2	0.25	129
			74	1	0.014	7.2
			1020	8	0.008	4.1
			300	0	0	0

AR - As Received; SC - Space Conditioned

Table 4 Calculation of Weight Loss as a Function of Time

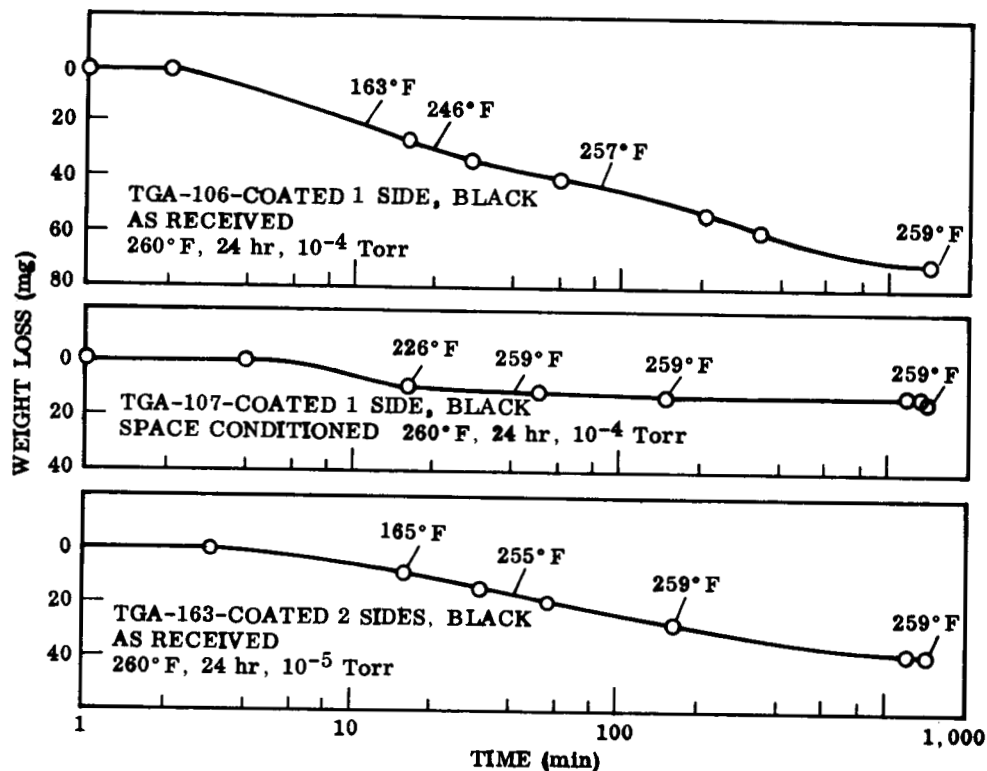


Figure 1 - Vacuum-TGA Curves for Single and Double Side Black Silicone-Coated Fiberglass Samples

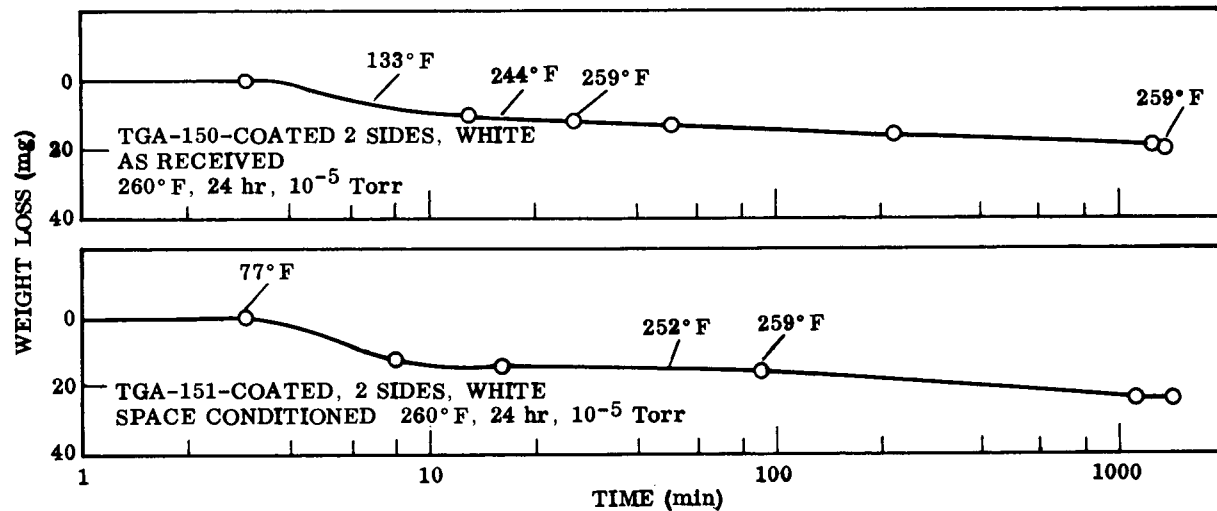


Figure 2 - Vacuum-TGA Curves for Two White Silicone-Coated Fiberglass Samples

approximately linear. Data was taken from the original traces, and not from the log-based curves in Figures 1, 2 and 3. The weight loss was then calculated for each segment in mg/min and mg/cm²/min. The average weight loss rate is also shown. In all cases the largest rates occur within the first 30 - 45 min. of the run. The effects of the space conditioning treatment are also evident from this data (Runs 107 and 151). It is more effective with the black material than the white. This would seem to correlate with the observation that weight losses and VCM run at higher levels for the black as opposed to the white materials. The data in Table 4 indicates an average weight loss rate for both black and white coatings in the as received condition of 10-12 mg/cm²/min. Space conditioning reduces this figure to about 25% of the original for the black material and about 80% for the white.

CONCLUSIONS

The vacuum TGA technique described has been shown to be a valid and useful technique for evaluating the thermal behavior of silicone materials. It provides for obtaining a continuous trace of weight loss/time behavior at constant pressure and temperature. It also provides for determination of room temperature volatile condensable materials.

The space conditioning treatment effectively reduces both the weight loss and VCM figures for both black and white coatings. However, it is more effective with the black coating than with the white. It appears that the white coating is more thermally stable than is the black.

Most of the weight loss for both materials occurs during the first 30-45 mins. of the run. Average rates are about the same for both materials in the as-received condition. Weight loss and VCM increase, as would be expected, with time and temperature. There is also probably a pressure effect, with weight loss and VCM increasing with pressure decrease.

REFERENCES

1. Muraca, R. F. and Whittick, J. S., "Polymers for Spacecraft Applications", Stanford Research Institute, Menlo Park, Cal., Sept. 15, 1967.
2. Harrington, R. and Maxwell, H., "Polymers for Spacecraft Hardware: Test Equipment Design", Stanford Research Institute, Menlo Park, Cal., Dec. 9, 1966.
3. Fisher, A. and Mermelstein, B., "GSFC Micro-Volatile Condensable Materials System for Polymer Outgassing Studies", Goddard Space Flight Center, Greenbelt, Md., Oct. 1969.

PREDICTION OF THE MECHANICAL PROPERTIES OF A FILLED ELASTOMER IN VACUUM

Gerald L. Gregory, *NASA Langley Research Center, Hampton, Virginia*

ABSTRACT

Research has shown that the mechanical properties of many nonmetallic spacecraft materials change during exposure to the space environment. Therefore, there is a need to predict the behavior of these materials to determine if the mechanical properties remain within design limits during space missions. This paper describes an experimental program to predict the mechanical behavior of a filled elastomer during exposure to vacuum. Constant force creep measurements were made at three stress levels on samples of an ammonium perchlorate filled butadiene-acrylic acid copolymer in vacuum (10^{-7} torr) and in the atmosphere (air, 50% relative humidity) at a temperature of 28° C. The creep compliance of the samples decreased as much as 50% after 14 days of vacuum exposure. Shift factors were developed which, when applied to the atmospheric compliance measurements, predicted the behavior in vacuum. The experimental results led to the following conclusions: (1) shift factors can be applied to predict compliance behavior in vacuum from measurements in air, and (2) the shift factors are independent of stress but increase in magnitude with increasing vacuum exposure.

INTRODUCTION

With the continuation of the space program, there has been an increasing requirement to measure the engineering properties of spacecraft materials in simulated space environments. In many cases, the selection of a spacecraft material is based on the performance — as determined from measurements of key engineering properties — of the material in simulated space environments. In developing criteria for the selection of spacecraft materials, much emphasis is placed on in situ testing of these key engineering properties rather than inferring engineering property changes from such peripheral measurements as weight loss, differential thermal analysis (DTA), and thermogravimetric analysis (TGA). Due to the large number of materials and the many anticipated mission environments that must be considered to

design a spacecraft, in situ testing of spacecraft materials is fast becoming an enormous task. To better meet this task, there is a need to develop test techniques which can be used to predict environmental effects on materials.

The purpose of this paper is to present the results of a recently completed experimental program in which the compliance behavior in vacuum of a filled elastomer was successfully predicted from air compliance measurements. The predictive technique employed is similar in concept to the well-known time-temperature superposition technique, and consists of experimentally determining for the material a set of vacuum effect shift factors which, when applied to air compliance measurements, predicts the vacuum compliance behavior of the material. Predicted results are confirmed by in situ vacuum test results.

THEORY

Numerous applications of shifting techniques have been used in mechanical property testing of polymeric materials to determine mechanical behavior (Refs. 1,2) (aging effects, corrosion effects, etc.) in earth-type environments and more recently in space environments (Ref. 3). One well-known shift technique is time-temperature superposition (Refs. 3,4) in which the modulus or compliance of a material is measured as a function of time at various temperatures. Then by a horizontal translation of the isothermal data along the time axis (superposition), the isothermal curves are generated into a single curve (master curve) at a reference temperature. Figure 1 illustrates the shifting technique in which each isothermal curve is shifted to form the master curve. Associated with the master curve is a shift factor-temperature curve which defines at each temperature the number of log time cycles each isothermal curve was shifted to form the master curve.

Analytically, the horizontal shift employed in Figure 1 is represented as

$$J_{T_0}(t) = J_T \left(\frac{t}{a_t} \right) \quad (1)$$

or in terms of log time

$$J_{T_0}(\log t) = J_T(\log t - \log a_T) \quad (2)$$

where:

- J_{T_0} = compliance at reference temperature
- J_T = compliance at temperature T
- t = loading time

$\log a_T = \log \text{shift factor} - \text{number of log time cycles}$
a given curve was shifted to form the master
curve

Following the example set by time-temperature superpositioning and numerous experimental verifications of the technique, shifting techniques have been developed for various environments, such as stress (Ref. 5) and humidity (Ref. 6), and for the present investigation for length of vacuum exposure. The shift equation for vacuum testing and for constant temperature is

$$J_{V_0} (\log t) = J_V (\log t - \log a_V) \quad (3)$$

where:

J_{V_0} = compliance at reference vacuum exposure V_0
 J_V = compliance after vacuum exposure V ; that is, after material has been exposed to the vacuum for time period V
 t = loading time
 $\log a_V$ = log vacuum shift factor

Implicit in Equation (3) are the assumptions:

- (1) no new deformation mechanisms are introduced as the result of vacuum exposure; that is, since in this investigation the reference environment was 50% r.h. air, then it is assumed that the deformation mechanisms are identical in air and vacuum;
- (2) vacuum affects only the rate of response of the material.

EXPERIMENTAL PROGRAM

The purpose of the experimental program was: (1) to validate the shift technique (Eq. (3)) for the vacuum environment, (2) to determine if vacuum effect shift factors are stress independent, and (3) to predict compliances in vacuum from air measurements using Equation (3). To accomplish these purposes, samples (Fig. 2) of an ammonium perchlorate filled butadiene-acrylic acid copolymer (a composite solid propellant trade name TPH 3105) (Ref. 7) were creep tested in vacuum and in 50% r.h. air. A total of 138 samples were tested of which 66 were tested in vacuum. All creep measurements were made at $28^\circ \text{C} \pm 0.3^\circ \text{C}$ and all test samples were preconditioned for a minimum of 35 days at $28^\circ \text{C} \pm 0.3^\circ \text{C}$ and in 50% r.h. $\pm 2\%$ air. Vacuum samples were creep tested to failure after being exposed to vacuum for 2, 7, and 14 days. Samples were stored in vacuum in an unstressed condition for the stated exposure periods and then creep tested in situ. Vacuum environments ranged from 5×10^{-6} torr (1.7×10^{-2} Nt/m²) after 2 hours of exposure to 5×10^{-8} torr after 14 days of vacuum. The vacuum effect shift factors were

determined from 51 psi (3.5×10^5 Nt/m²) and 61 psi stress level measurements. Predicted compliances for 56 psi stress were confirmed by in situ measurements.

The experimental apparatus is shown in Figure 3. The sample storage table located in the center of the chamber is designed to store 24 test samples along its periphery. The test apparatus is constructed primarily of stainless steel and aluminum. The stainless-steel vacuum chamber is liquid nitrogen trapped and diffusion pumped. Details of the vacuum chamber are given in Reference 8. The storage table is a 30-inch (0.76 m) diameter gear which can be rotated from outside the vacuum chamber using a magnetic feed through. Creep measurements are conducted in situ using the loading frame on top of the chamber and a vertical loading bar connecting the loading frame to the test sample and test weight. The loading bar, test sample, and test weight are self-aligning insuring a uniaxial tensile loading. With the loading bar in the down position and the test weight resting on the loading platform, the storage table is free to rotate. Activation of the loading frame motor lifts the test sample which in turn lifts the test weight, thus starting the creep measurement.

A creep measurement is conducted by rotating a sample into the test position under the loading bar. Approximately 30 seconds after the test sample is loaded, the elongation of the sample is recorded by photographing the bench marks (Fig. 2) on the test sample with a 70-mm sequence camera. The camera viewed the test sample through a feed-through window located in the chamber door (see Fig. 4) and was programmed to photograph the test sample at predetermined intervals. Sample elongation was recorded up to sample failure and failure time was automatically recorded. During the creep measurements, the sample temperature was maintained at $28^\circ \text{C} \pm 0.3^\circ \text{C}$ by resistance heaters in the vacuum chamber.

Creep measurements were made on samples of TPH 3105 at three stress levels (51, 56, 61 psi) and for four environmental exposures (50% r.h. air and 2, 7, and 14 days of vacuum). For air creep measurements, the vacuum chamber was left at atmospheric pressure and a humidity solution used to maintain the chamber humidity at 50% r.h. Table I shows the number of samples tested in each environment.

The test material, TPH 3105, is an 82% ammonium perchlorate filled butadiene-acrylic acid copolymer having a cured density of 1.617 gm/cc. Test samples were individually cast and prepared from the same mix of propellant. The gage length for the elongation measurements was taken to be the center 1-inch (2.54 cm) length of the sample which has a diameter of 0.5 inch (1.27 cm). To grip the test material for testing, circular washers were attached, perpendicular to the axis of the sample, to the sample with epoxy. Further details of the test sample geometry are given in Reference 9.

DATA REDUCTION

From the camera records, the length strain as a function of loading time was calculated for each sample tested. The calculation involved subtracting the initial gage length of the sample from the elongation at any loading time and then dividing the resulting quantity by the initial gage length. The compliance-loading time behavior of each sample was then calculated by dividing the strain at any loading time by the applied stress (test weight/sample area). The accuracy of these calculated compliances ranged from 4.3% to 12.8% of the indicated value, with the larger errors occurring at the shorter loading times (smaller strains) and lower stresses.

As shown in the literature (Ref. 10) and as observed by the author, large sample-to-sample variations were found in the measured mechanical properties. Therefore, the mean of the compliance was calculated for each sample group and plotted against loading time. This gave a satisfactory description of the compliance-loading time behavior until one of the samples in the group failed. The compliance-loading time curve had a discontinuity at the loading time where the first and each subsequent sample of the group failed. Further analysis of the data indicated that this discontinuous behavior could be minimized and the compliance-loading time behavior extended to the average failure time of the sample group, if the compliance at each loading time was calculated by taking the mean of the compliances of only those samples (of the sample group) which failed within the 90% confidence interval of the average (mean) failure time of the sample group. The compliance results presented in this paper were obtained by the 90% confidence interval approach. It is noted that prior to the first sample failure of a sample group, the compliance-loading time behavior as determined by the 90% confidence interval approach is approximately the same as that obtained by taking the mean of the compliances of all samples in the sample group.

DISCUSSION OF RESULTS

Vacuum Effect Shift Factors

The compliance-loading time behaviors for TPH 3105 at the 51-psi stress level are shown in Figure 5. The results for four environmental exposures (one air, three vacuum) are shown. In each environment, compliance generally increased with increased loading time, thus indicating the creep of the material under the applied force. For example, in 50% r.h. air, compliance after 60 seconds of loading was 5.60×10^{-4} (psi)⁻¹ and increased to 12.7×10^{-4} (psi)⁻¹ after approximately 2100 seconds or 35 minutes (at sample failure). Increasing the vacuum exposure time resulted in lower compliances at virtually all loading times. For instance, at 200 seconds into the loading, compliances were approximately 6.62×10^{-4} , 5.87×10^{-4} , 4.48×10^{-4} ,

and 4.12×10^{-4} (psi)⁻¹ for air, 2, 7, and 14 days of vacuum exposure, respectively. Reductions as large as 50% occurred after approximately 14 days of vacuum exposure.

To obtain the vacuum effect shift factors, Equation (3) is applied to the data of Figure 5 using the 50% r.h. air results as the reference environment. For example, the vacuum effect shift factor for the 2-day vacuum exposed samples was obtained by horizontally shifting, to the left, the 2-day vacuum compliance curve until the area (as visually determined) between the vacuum curve and air curve was minimal (i.e., the two curves approximately coincided). The vacuum effect shift factor ($\log a_v$) is the number of log time cycles the vacuum curve was shifted or for this case +0.20. Performing similar shifts for the 7-day and 14-day exposures of Figure 5 results in a single "master" compliance - log time curve (at 51 psi and for 50% r.h. air) and two additional vacuum effect shift factors. This master curve is shown in Figure 6 and the associated shift factors in Figure 9.

The measured compliance-loading time behaviors for TPH 3105 at the 61-psi stress level are shown in Figure 7. The master curve obtained by applying the shift technique to the 61-psi data (Fig. 7) is shown in Figure 8 and the corresponding shift factors in Figure 9. As shown in Figure 9, the vacuum effect shift factors are independent of the stress level and increase with increasing vacuum exposure time. The shift factor variations at a given exposure time are believed to represent the errors associated with performing the shift of the experimental measurements. Thus, the average shift factor (Fig. 9) at a given exposure time will be used in the prediction analysis of the next section. It should be mentioned at this point that an attempt was made to shift the master curves of Figures 6 and 8 into a single master curve with a stress shift factor. The curves would not shift thus requiring that air compliances measurements be made at the stress level at which the vacuum prediction is to be made.

Predicted Compliance Behavior

Having determine the vacuum effect shift factors from the 51-psi and 61-psi results, Equation (3) can now be used to predict the vacuum compliance behavior of TPH 3105 at 28° C and 56 psi stress. The only experimental measurements needed to perform the prediction are compliance-loading time measurements at 28° C and in 50% r.h. air and at 56 psi stress. Figure 10 shows these measurements along with the predicted compliances for vacuum exposure times of 2, 7, and 14 days at the 56-psi stress level. The predicted behaviors were obtained from Equation (3) using the average vacuum effect shift factors of Figure 9 and the experimental measurements of Figure 10. Figure 11 shows a comparison between the predicted results and in situ vacuum measurements at 56 psf stress. Four features of the comparison should be noted:

(1) In general, the agreement between predicted and experimental results is good; the maximum error at any loading time and vacuum exposure time is approximately 15%.

(2) The compliance-shift technique gives no information as to vacuum effects on failure time.

(3) The overall comparison of predicted and experimental results appear to be worst at the shortest exposure times; however, at this exposure time the magnitude of the shift factor and the probable uncertainty in this magnitude are approximately the same.

(4) To obtain predicted results at the early loading times for the vacuum samples requires that the reference compliance measurements (50% r.h. air) be made at loading times less than 30 seconds after load application. These measurements were not made in this investigation.

In summary, the compliance shift technique does appear to satisfactorily predict the vacuum behavior of TPH 3105 for exposure times up to 14 days and for the stress levels considered. Predicted results are well within 15% of the experimental compliance values. Best agreement between predicted and experimental results occurred at the longer exposure times where it was probable that any errors in determining the vacuum effect shift factors were small compared to the absolute value of the shift factor. In addition for this material and for the stress range considered, shift factors are independent of the stress level of the experiment; a more general statement concerning the stress independency of the shift factors is not valid at this time. One obvious shortcoming of the compliance shift prediction is that it gives no information as to the vacuum effects on failure time and, in fact, predicts compliance values past sample failure.

CONCLUSIONS

1. The compliance shift technique does work for TPH 3105, a filled elastomer, and shift factors can be applied to predict compliance behavior in vacuum from measurements in air.

2. The vacuum effect shift factors appear independent of stress and increase in magnitude with increasing vacuum exposure; whereas, the master air compliance curves are dependent on the stress level.

REFERENCES

1. Seitz, J. T. and Balazs, C. F.: Application of Time-Temperature Superposition Principle to Long Term Engineering Properties of Plastic Materials. Polymer Engineering and Science, April 1968, pp. 151-159.

2. American Society for Testing and Materials: Recommended Practices for Testing Long-Time Creep and Stress

Relaxation of Plastics Under Tension or Compression Loads at Various Temperatures. 1968 Book of ASTM Standards, ASTM D 674-56.

3. Greenwood, L. R. and Ward, T. C.: Prediction of Long-Term Vacuum Effects on Mechanical Properties of a Heat Shield Material. 1971 Proceedings of Institute of Environmental Sciences, pp. 435-439.

4. Tobolsky, Arthur V.: Properties and Structure of Polymers. John Wiley and Sons, Inc., 1960.

5. Bree, H. W.; Schwarzl, F. R.; and Struik, L. O. E.: Mechanical Properties of Highly Filled Elastomers. Central Laboratory T. N. O., DELEFT, Report CL/65/58, 1965.

6. Fishman, Norman and Rinde, James A.: Development of Dilatational Equation-of-State. Bulletin of Third Meeting ICRPG Working Group on Mechanical Behavior, CPIA Publication 61V, October 1964, pp. 267-289.

7. Brownell, Robert M.: Determination of Crosslink Densities and Percentages of Sol in TPH 3105 Propellant Specimens Aged in Vacuum and Under 50 Percent Relative Humidity. Thiokol Chemical Corp., Elkton Division, Contract NAS1-9397, NASA CR-111775, 1970.

8. Bradford, James M., Jr.: Operating Parameters of the Omegatron Mass Spectrometer in Ultrahigh Vacuum. NASA TN D-3129, 1965.

9. Saylak, D.: True Stress-Strain Properties for Filled and Unfilled Polymers and Elastomers as Functions of Strain Rate and Temperature. Applied Polymer Symposia, No. 1, pp. 247-260, 1965.

10. Bills, K. W., Jr.; Sampson, R. C.; and Steele, R. D.: Solid Propellant Cumulative Damage Program. Aerojet General Corporation, Contract FO-4611-67-C-D102, AFRPL-TR-68-131, October 1968.

TABLE I. DESCRIPTION OF SAMPLE GROUPS

Stress, psi	Environment	Number of samples
51	Air, 50% r.h.	42
51	Vacuum, 2 days	10
51	Vacuum, 7 days	7
51	Vacuum, 14 days	6
56	Air, 50% r.h.	20
56	Vacuum, 2 days	8
56	Vacuum, 7 days	7
56	Vacuum, 14 days	7
61	Air, 50% r.h.	10
61	Vacuum, 2 days	8
61	Vacuum, 7 days	7
61	Vacuum, 14 days	6

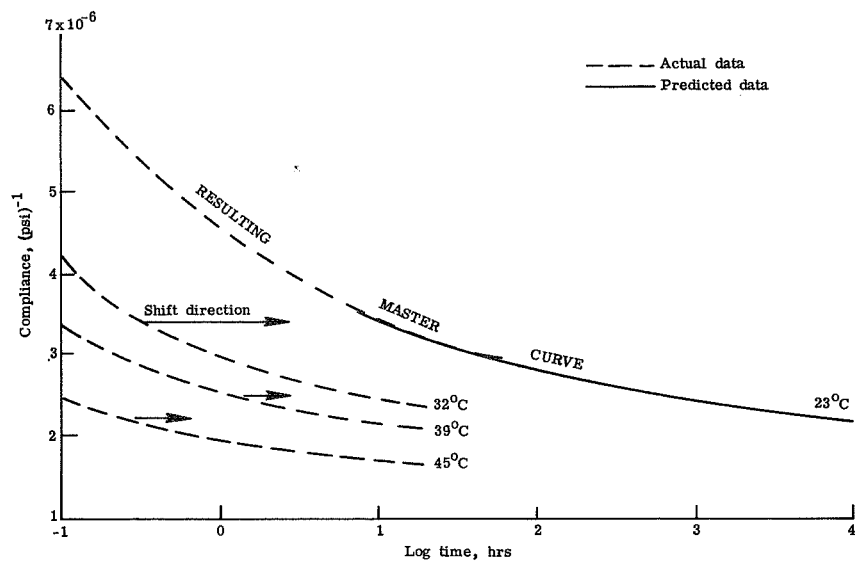


Figure 1.- Time-temperature superposition applied to polyethylene.

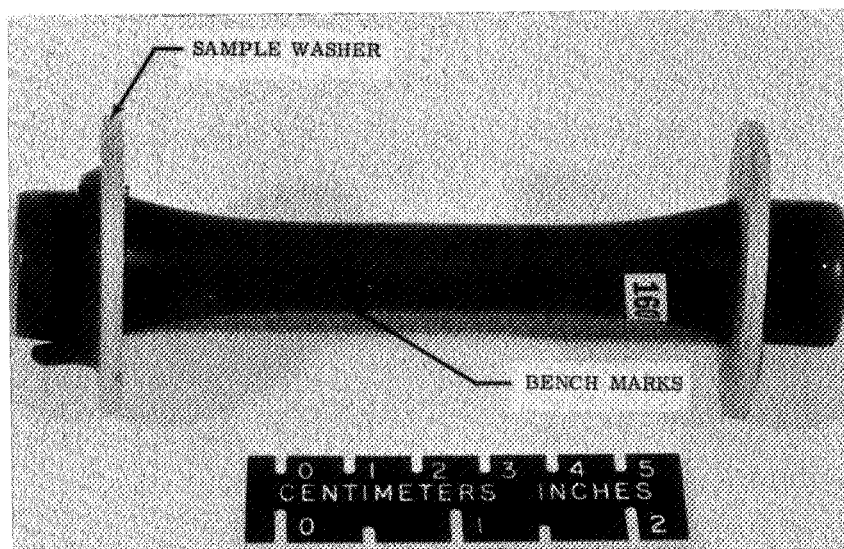


Figure 2.- Photograph of test sample.

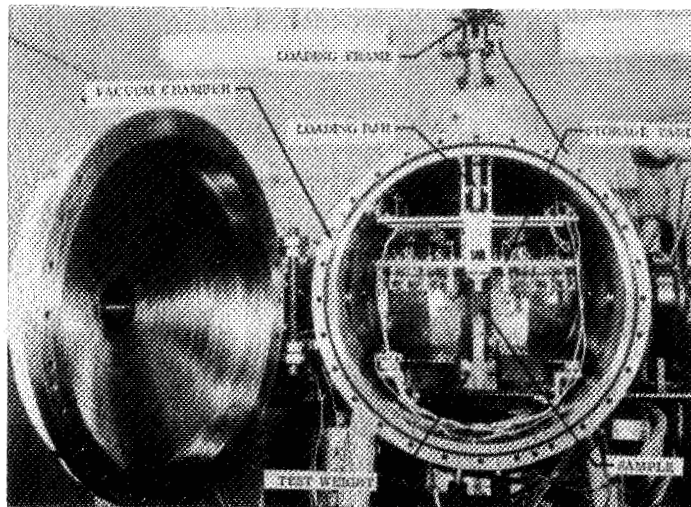


Figure 3.- Photograph of test apparatus.

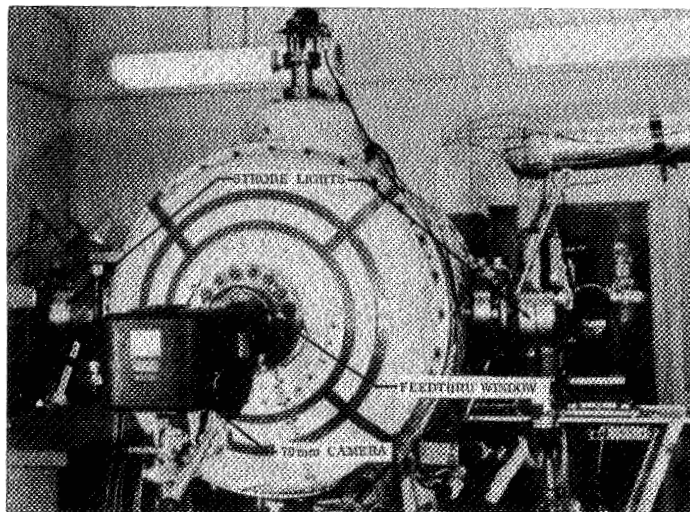


Figure 4.- Test camera location.

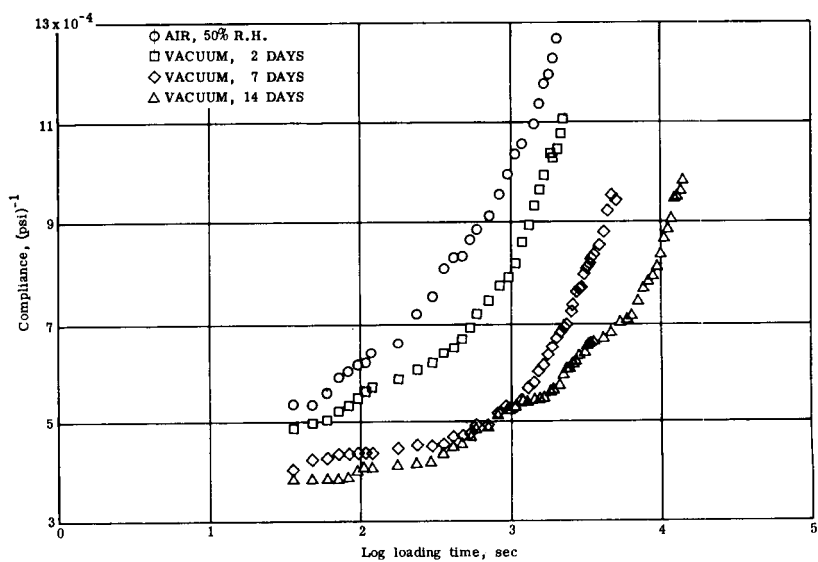


Figure 5.- Compliance results for TPH 3105, 28°C and 51 psi stress.

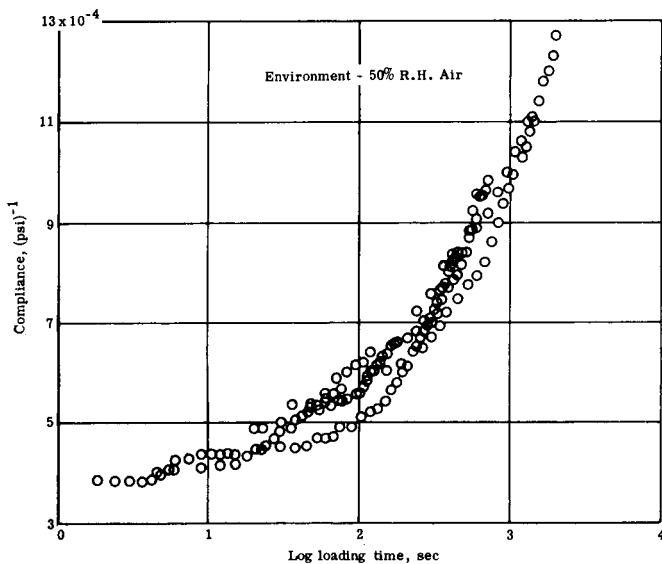


Figure 6.- Compliance master curve for TPH 3105, 28°C and 51 psi stress.

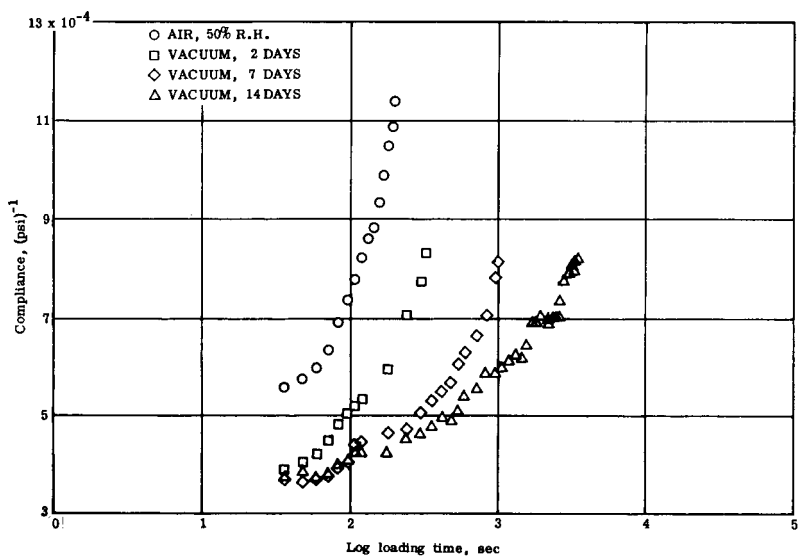


Figure 7.- Compliance results for TPH 3105, 28°C and 61 psi stress.

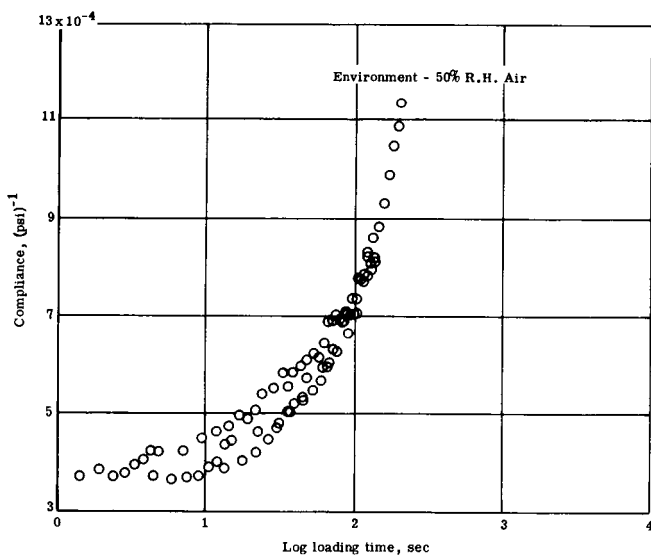


Figure 8.- Compliance master curve for TPH 3105, 28°C and 61 psi stress.

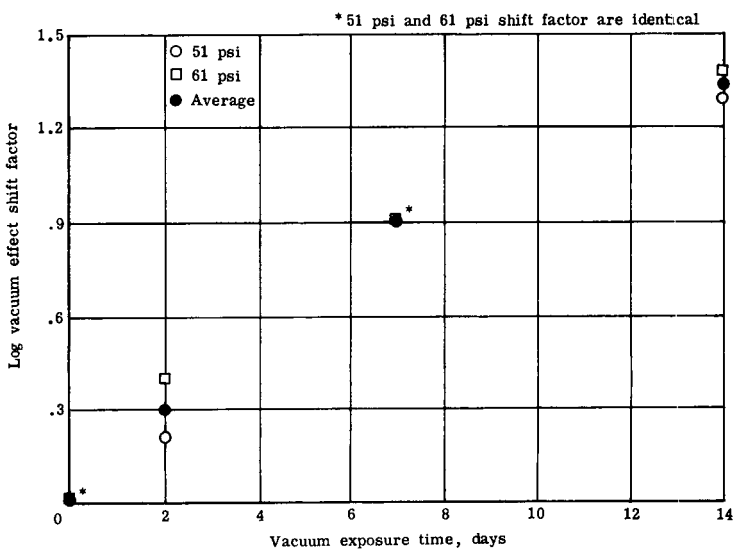


Figure 9.- Vacuum effect shift factors for TPH 3105, 28°C.

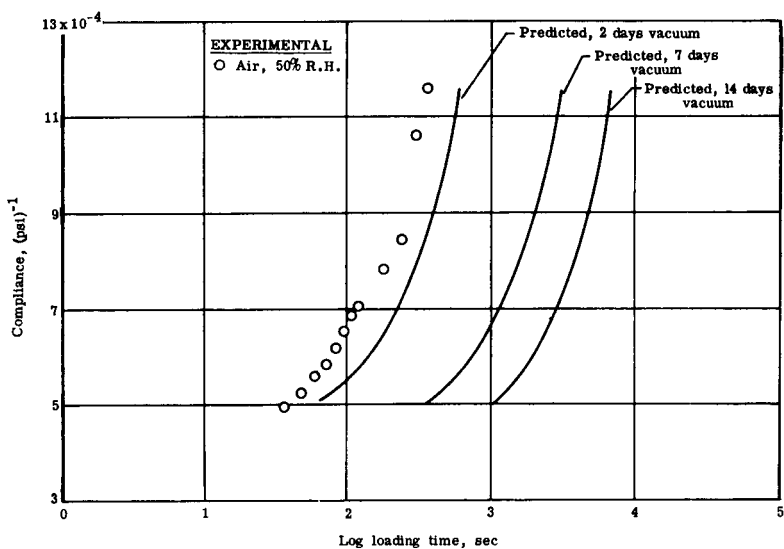


Figure 10.- Predicted compliance results for TPH 3105, 28°C and 56 psi stress.

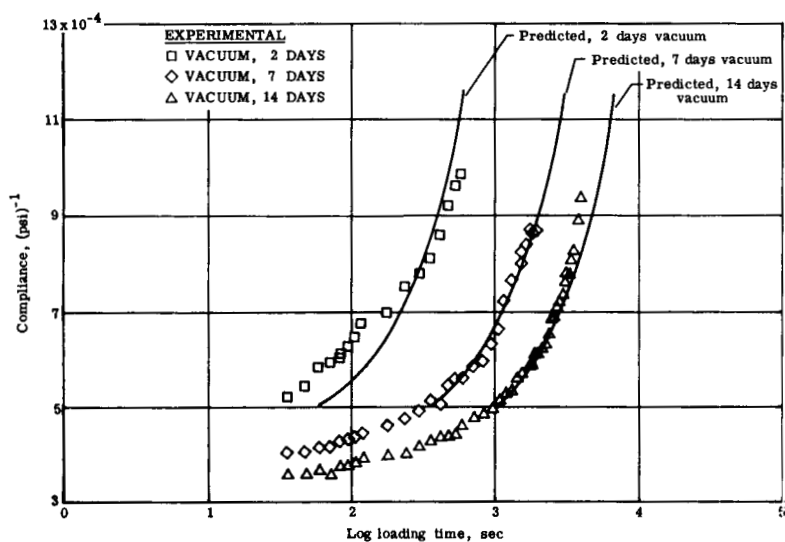


Figure 11.- Comparison of predicted and in situ vacuum compliances for TPH 3105, 28°C and 56 psi stress.

ACCELERATED TESTING OF A FILLED ELASTOMER IN VACUUM

Morris L. Evans and Thomas C. Ward, *Virginia Polytechnic Institute and State University, Blacksburg, Va.*; Gerald L. Gregory, *NASA, Langley Research Center, Hampton, Va.*

ABSTRACT

A program has been conducted to evaluate an in situ dynamic modulus measurement on a solid propellant exposed to vacuum environment. The prediction of long-term vacuum exposure effects was examined.

INTRODUCTION

It has recently become apparent that polymeric-based materials may undergo significant mechanical property changes when exposed to vacuum environments [1]. In space flight, vacuum environments may be applied to a material for relatively long (years) periods. Catastrophic consequences may be projected for severe alterations in, for example, the modulus of a solid propellant during space vacuum exposure. In view of the number of candidate materials to be screened for vacuum exposure effects and the required length of vacuum exposure, the need for a predictive (or accelerated) testing capability is also apparent.

Few methods exist to reliably perform in situ tests on the mechanical properties of polymeric samples when in vacuum environments [2]. In addition, accelerated testing procedures are far from well founded when vacuum induced changes are involved.

Propellant binders are generally viscoelastic materials; the filler-binder composite must be tested in a way which reflects this behavior. The torsion pendulum [3] provides a relatively simple way in which the shear modulus of a material may be analyzed in terms of its elastic (storage) and viscous (loss) components.

The purpose of the present investigation was to evaluate a torsion pendulum instrument designed for testing the dynamic mechanical properties of materials in vacuum. The evaluation was to focus on two points:

- (1) Were vacuum induced changes detected over test periods of several days and what were they?
- (2) Could any induced changes be used to predict long-term vacuum effects on mechanical properties?

The sample temperature during vacuum exposure, the length of vacuum exposure, and the relative humidity conditioning of the materials prior to vacuum exposure were considered the important variables in this investigation.

Propellant TPH 3105 was chosen for investigation. It is representative of a large class of inorganic salt filled elastomeric composites used as rocket fuels.

EXPERIMENTAL

Materials

The TPH 3105 propellant had a butadiene-acrylic acid copolymer binder which was cross-linked with trispropyleneimine (MAPO) and cured in air for 64 hours at 135° F. The filler-oxidizer was ammonium perchlorate with the following size distribution (based on wt % of final composite):

Passes through 200 μ sieve 54.4%
Passes through 20 μ sieve 24.6%

Sample Preparation and Preconditioning

Starting with a block of propellant, a thin wall stainless steel borer was used to core out cylindrical rod shaped samples which averaged about 0.8 cm diameter. The rods were then cut to about a 7-cm length. An epoxy resin was used to glue aluminum mounting disks to the sample ends. The disks were aligned parallel to one another and perpendicular to and centered on the long axis of the sample.

Each sample was preconditioned at a designated relative humidity and at room temperature for a minimum of 2 weeks. The proper relative humidity atmospheres were achieved by water-glycerin solutions placed in the bottom of airtight desiccators. Prepared samples were placed on shelves above the solutions.

Test Apparatus

The torsion pendulum constructed for testing moduli of solid materials in vacuum is shown in Figure 1. During a run, a bell jar surrounded the entire apparatus, sitting on the illustrated feedthrough collar. The torsion pendulum was designed to apply an oscillating shear torque to one end of a cylindrical test sample while holding the other end fixed. To achieve this the sample, A, was attached between a freely oscillating inertia wheel, B, and a lower shaft, C, which could be locked into a fixed position. A wire, D, lever arm, E, and weight pan, F, were used to counterbalance the inertia wheel and prevent any tensile stresses in the sample. The oscillatory motion was initiated via a rotary feedthrough, G, operating on a lever, H, attached to the lower shaft, C.

In operation, the oscillating inertia wheel was restricted only by the sample which damped out any applied motion. A linear variable differential transformer attached to the pendulum provided an analog signal for amplification and recording. Figure 2 shows the recorder trace of a typical run on the torsion pendulum apparatus.

The temperature of the entire apparatus was raised or lowered to roughly a few degrees below the desired sample temperature by blowing air and dry ice vapor into an insulated box which completely enclosed the bell jar and feedthrough collar. Once approximate temperature control was established, the resistance heating coils, J, seen in Figure 1, were used to fine control the sample temperature. A dummy sample (propellant with a bead thermistor placed in its center) was mounted in the apparatus so as to have the same thermal environment as the real sample. The thermistor's resistance was used to indicate temperature and to activate a proportional controller whose output controlled the heating coils. Temperature control of $\pm 0.2^\circ \text{C}$ or better was achieved for all runs.

The pumping station was of conventional design; a 6-inch oil diffusion pump was backed up by a standard mechanical forepump. A liquid nitrogen trap protected the bell jar from pump oil contamination. Pressures of 5×10^{-5} torr, measured by a calibrated ionization gage and controller, could be achieved in 30 minutes with this system.

Test Procedure

On removing a sample from the proper preconditioning desiccator, the time required to mount the samples and align all of the complimentary components of the torsion pendulum was approximately 1 hour. After this, an additional half hour was needed to pump the system down to the test pressure, and achieve temperature control. The zero of vacuum exposure time was noted when 1×10^{-5} torr was reached. A data point was taken at this time.

Intervals of 15 to 30 minutes separated the data points on the first day of a test run. Several hours typically intervened between points on the following 3 days of a run.

Preconditioning environments of 25%, 50%, or 75% relative humidity were applied to the various propellant samples. Test runs were made at 5°C or 25°C or 45°C .

DATA REDUCTION

The formulas used for the calculations are essentially the same as those used by Nielsen [4] and others [5]:

$$G' = \frac{w^2 I}{b} \quad (1)$$

$$b = \frac{\pi r^4}{2L} \quad (2)$$

$$G'' = \frac{G'}{\pi} \ln \left(\frac{A_2}{A_1} \right) \quad (3)$$

w = frequency of output, radians/sec
 I = moment of inertia of wheel, gr cm²
 r = sample radius, cm
 L = sample length, cm
 A_1 = amplitude of wave "n"
 A_2 = amplitude of wave "n - 1" (see Fig. 2)
 b = shape factor, cm³
 G' = storage modulus, dynes/cm²
 G'' = loss modulus, dynes/cm²

Equations (1) - (3) are applicable when $G'' < G'$ as was found to be true for TPH 3105. These equations also presume that the material under analysis is linearly viscoelastic.

Test for Linearity

A sample of TPH 3105 at 25° C was subjected to a number of shear strains up to 5.25×10^{-3} radian per cm length, approximately twice the strain level used in the standard testing procedure. In all cases, the calculated moduli were identical and independent of strain. This constitutes sufficient proof of linear viscoelastic response.

Accuracy of the Data

The accuracy of the torsion pendulum instrument was checked by comparison of its results obtained on a composite elastomer with results of the National Bureau of Standards on the same material. Briefly, the moduli obtained in the subject work were within 4% of the NBS values. This indicates that the torsion pendulum equipment was functioning properly and that the calculation procedure was correct.

Precision of the Data

The precision (reproducibility) of the torsion pendulum data obtained on TPH 3105 was very good. Duplicate runs were made on four samples at 45° C and two samples at 25° C. The mean modulus values were calculated at each temperature. The range (spread) of the moduli data was found to be less than 0.436% of the mean value at both temperatures.

There was little uncertainty associated with the sample dimensions, and no visible or viscoelastic signs of dewetting of the filler-binder interface were found. In addition, there was no apparent color change at any stage of the preparation or testing of TPH 3105.

RESULTS

The effects of vacuum exposure on the moduli of 50% relative humidity preconditioned TPH 3105 are shown in the isotherms

plotted in Figures 3 through 6. Pressure-time histories for these runs showed that vacuum environments of 5×10^{-5} torr or less were applied to the samples during testing.

Storage Modulus Results

This discussion is confined to those samples preconditioned at 50% relative humidity. Figure 3 shows that G' increased with increasing vacuum exposure. The resulting 5°C , 25°C , and 45°C isotherms are very similar in shape. In the initial stages of vacuum exposure, it appears that a linear relationship exists between $\log G'$ and the logarithm of vacuum exposure time. During the final 3.5 or so days of the test (3×10^5 seconds), however, these variables are nonlinearly correlated. Figure 4 contains a replot (25°C isotherm only) of the data from the curved region appearing in Figure 3. The linear scale used in Figure 4 makes it clearer that G' asymptotically approached a limiting value during the test run. This limiting value represented an increase in G' of 23%, 37%, and 31% at 5°C , 25°C , and 45°C , respectively.

Loss Modulus Results

Only the data from samples preconditioned at 50% relative humidity are discussed in this section. Figure 5 shows that the TPH 3105 loss modulus behavior in vacuum environments paralleled that of the storage modulus. The 25°C isotherm shown in Figure 6 suggests the same asymptotic characteristic for G'' as was observed in the storage modulus case. The asymptotes approached by G'' gave rise to 36%, 56%, and 54% increases in the loss modulus at 5°C , 25°C , and 45°C , respectively.

Results of Varying Sample Preconditioning

Different preconditioning environments clearly altered the TPH 3105 propellant's viscoelastic properties. This is most clearly shown by a comparison of the moduli of differently preconditioned samples just prior to vacuum exposure (essentially the ordinate intercept of plots like those in Figs. 3 and 5). Figures 7 and 8 show that at 25°C the initial (pre-vacuum exposure) loss and storage moduli were increased by 32.4% and 46.0%, respectively, when the preconditioning relative humidity was lowered from 75% to 25%. Figures 9 and 10 present the initial modulus-R.H. relationship in linearized form.

Pressures of about 5×10^{-5} torr and a temperature of 25°C were applied to the three differently preconditioned samples for 4 days. Figures 7 and 8 show the modulus changes resulting from this exposure.

DISCUSSION OF RESULTS

Moisture Content and Mechanical Properties

Considering the strong influence of preconditioning relative humidity on initial G' and G'' values and also the preconditioning induced vertical shifts in the vacuum exposure isotherms of Figures 7 and 8, the moisture content history apparently plays a large role in determining the mechanical behavior of a TPH 3105 sample. Many examples can be found in the general polymer science literature to document the strong influence of varying amounts of water on the moduli of solid polymeric materials. In most cases [6] an assumption that the water functions as a plasticizer is sufficient to account for mechanical property alterations. This is not always the case, however, particularly when the polymer in question is filled with an inorganic salt [7].

For homogeneous polymeric materials, the loss and storage moduli usually are observed to change in opposite directions when environmental parameters are altered [6]. The elastic component, G' , is a measure of the energy stored in the material during one cycle in the dynamic test. Conversely, G'' measures the dissipation of energy per cycle and is manifested as the damping effect in the torsion pendulum type of test [6]. In the present results on vacuum exposed TPH 3105, both G' and G'' increased simultaneously. The propellant was becoming, at the same time, more resistant to strain (the elastic component) and to rate of strain (the viscous component). There are several possible explanations consistent with this behavior:

- (1) An alteration of the binder microstructure (see refs. [8], [9], [10]) might have been involved. This is thought to be caused by partial dissolution of the ammonium perchlorate into the binder. This consequently raises the internal viscosity of the binder's polymeric network and, hence, the contribution of G'' .

- (2) The binder-filler interface might have been altered both geometrically and with respect to intermolecular forces. The internal resistance to flow as measured by G'' would thus be modified.

- (3) There might be competing mechanisms of some kind initiated by the vacuum exposure. One of these might influence G' and the other G'' .

Inspection of Figure 7 suggests that the three storage moduli represented there converged toward a common isotherm at the longer vacuum exposures. This trend was not observed for the loss modulus according to Figure 8. Only for G' were the effects of varying preconditionings lessened by the vacuum environment. This evidence supports explanation (3) above because it implies that multiple mechanisms were involved in the changes in TPH 3105.

Temperature and Mechanical Properties

The isochronal temperature dependence of G' and G'' as represented in Figures 3 and 5 is rather typical for a filled elastomer somewhat above its glass transition temperature. Thus, the decreasing G' with increasing temperature is indicative of the glass-rubber region of viscoelastic response. The corresponding decrease in G'' occurred because the propellant was heated beyond its point of maximum damping ability at the glass transition temperature.

In terms of vacuum exposure effects, Figures 3 and 5 show that temperature changes merely shifted the isotherms vertically along the log modulus axis. The relative rate of change as measured by the slopes of these isotherms appears unaffected by temperature. This temperature independence suggests that explanation (2) in the discussion above must be considered. It seems somewhat improbable that two competing mechanisms as required in explanation (3) would both be independent of temperature over a 40°C range.

Accelerated Testing Discussion

For polymeric based materials, accelerated testing has been based on the time-temperature superposition principle (tTSP) [17], [12]. Basically, tTSP depends on the unimechanistic acceleration of molecular relaxations with increasing temperature in order to predict long-time mechanical properties. In practice, modulus isotherms taken over short-time periods are shifted along the time axis relative to a reference isotherm in order to produce a "master curve" extending over much longer times. The development of a rationale for the isotherm shifts by William, Landel, and Ferry [13] provided major impetus to the practice of tTSP.

The time dependent mechanical properties of filled polymer systems, specifically elastomer-inorganic salt composites, have also been successfully analyzed by the tTSP [14], [15]. It appears that as long as the polymeric binder dominates the material's stress-strain behavior, then tTSP is valid. Unfortunately, this validity is based on criteria other than long-time testing to confirm predicted moduli.

Drawing analogies with the tTSP, work has been done in which variables other than temperature have been used to accelerate mechanical property changes. These analyses depend on an empirical shifting of curves along a time axis to produce master curves much as was done with the isotherms in tTSP. Constant relative humidity [16] and high vacuum exposure [17] are two of the environmental conditions that have been used in superposition-type accelerated testing of polymeric materials. In both cases, it was possible to obtain smooth master curves extending over long periods of time from short-time experiments under controlled conditions.

The data on TPH 3105 were found to be nonsuperimposable; they could not be used to construct a master curve of the tTSP

type. Similarly, attempts to superimpose the data using the preconditioning R.H. as the independent variable instead of temperature were not successful. A variety of linear, logarithmic and semilogarithmic plots were made in these unsuccessful efforts to expand the time scale of vacuum exposure.

In lieu of superposition methods, an analytic technique was applied to accelerate testing of TPH 3105. Equation (4) was used to represent the data shown in Figures 3-6.

$$\log G = I + n(B-3) + d \cdot \tanh\left(\frac{B-B_c}{B}\right) \quad (4)$$

where G can be either the storage or the loss modulus, I is \log of G at 1000 seconds of vacuum exposure, B is the \log of the vacuum exposure time expressed in seconds, n is the slope of the linear line segment extending from $B = 3$ to some exposure time $B = B_c$, and d is a constant equal to zero if $B < B_c$ and equal to 0.405 if $B > B_c$. This equation was not chosen from theoretical considerations but because it was found to provide an adequate representation of the data. Constants of the equation were empirically adjusted for each isotherm and preconditioning in order to obtain an accurate fit to the data over the entire test period. The agreement between moduli calculated using Equation (4) and the actual experimentally determined moduli was quite good; they were within 0.020 log unit of each other over most of the 4-day vacuum exposure. Using Equation (4) the predicted storage and loss modulus of TPH 3105, preconditioned at 50% relative humidity and exposed to 10^{-5} torr for 12 months at 25°C , shows an 86% and 108% increase (as compared to the pre-vacuum values), respectively. These predicted values have not been experimentally confirmed by real time testing.

The following conclusions were drawn from the results of this investigation:

1. The torsion pendulum was a sensitive and accurate instrument for monitoring the complex modulus of polymeric materials during vacuum exposures of about 5×10^{-5} torr.
2. The storage modulus of TPH 3105 increased about 37% and the loss modulus increased about 56% on exposure of the material to vacuum of approximately 1×10^{-5} torr for 4 days at 25°C . Tests at 5°C and 45°C produced smaller changes.
3. The TPH 3105 propellant's mechanical properties were very sensitive to preconditioning relative humidities.
4. Accelerated testing of vacuum induced changes in moduli of TPH 3105 could not be done using time-temperature superposition concepts. However, moduli predictions were made based on analytical extrapolations of trends in the data. Predicted results have not been experimentally confirmed.

REFERENCES

1. Greenwood, L. R.: The Effect of Vacuum on the Mechanical Properties of a Solid Rocket Propellant During Space Storage. Ph. D. Thesis, Virginia Polytechnic Institute, 1967.
2. Mugler, J. P., Jr.; Greenwood, L. R.; Lassiter, W. S.; and Comparin, R. A.: In Situ Vacuum Testing - A Must for Certain Elastomeric Materials. J. Spacecraft and Rockets, Vol. 6, No. 2, Feb. 1969, pp. 219-221.
3. Gillham, J. K.: Torsion Braid Analysis. Listed in Encyclopedia of Polymer Science and Technology, Vol. 14, pp. 77-78. John Wiley and Sons.
4. Nielsen, L. E.: A Recording Torsion Pendulum for the Measurement of the Dynamical Mechanical Properties of Plastics and Polymers. Review of Scientific Instruments, Vol. 33, No. 9, Sept. 1951.
5. Ferry, J. D.: Viscoelastic Properties of Polymers. Second ed., John Wiley and Sons, Inc., 1970.
6. McCrum, N. G.; Read, B. E.; and Williams, G.: Anelastic and Dielectric Effects in Polymeric Solids. John Wiley and Sons, Inc., 1967.
7. Ward, T. C.; and Tobolsky, A. V.: A Viscoelastic Study of Ionomers. J. Appl. Polym. Sci., Vol. 11, p. 2403, 1967.
8. Landel, R. F.; and Moser, B. G.: The Effects of Moisture on the Dynamic Mechanical Properties of Ammonium Perchlorate - Polyurethane Propellants. JPL-TR-32-389 (contract NAS 7-100), 1963.
9. Colodny, P. C.; and Ketchum, G. F.: Humidity and Temperature Effects on the Creep Behavior of Solid Propellants. Bulletin of 4th Meeting of the Interagency Chemical Rocket Propulsion Group, Oct. 1965, pp. 135-139.
10. Oberth, A. E.; and Bruenner, R. S.: The Cause of Moisture Embrittlement in Solid Propellants. Presented to the Interagency Chemical Rocket Propulsion Group, 1966, AFSC-66-951.
11. Tobolsky, A. V.: Properties and Structure of Polymers. John Wiley and Sons, Inc., 1960.
12. Fesko, D. G.; and Tschoegl, N. W.: Time-Temperature Superposition in Thermorheologically Complex Materials. J. Polymer Sci., part C, No. 35, pp. 51-69, 1971.

13. Williams, M. F.; Landel, R. F.; and Ferry, J. D.: The Temperature Dependence of Relaxation Mechanisms in Amorphous Polymers and Other Glass-Forming Liquids. J. Amer. Chem. Soc., Vol. 77, pp. 3701-3707, 1955.

14. Martin, D. L.: The Effect of Filler Concentration on the Viscoelastic Response of a Composite Solid Propellant. RK-TR-64-2 (AD-433612), 1964.

15. Schwarzl, F. R.: On Mechanical Properties of Unfilled and Filled Elastomers. From the Mechanics and Chemistry of Solid Propellants, ed. by Eringen, A. C.; Liebowitz, H.; Koh, S. L.; and Crowley, J. M.; Pergamon Press, pp. 503-539, 1965.

16. Quistwater, J. M. R.; and Dunell, B. A.: Dynamic Mechanical Properties of Nylon 66 and the Plasticizing Effect of Water Vapor on Nylon. J. of Appl. Polymer Sci., Vol. 1, pp. 267-271, 1959.

17. Greenwood, L. R.; and Ward, T. C.: Prediction of Long-Term Vacuum Effects on Mechanical Properties of a Heat Shield Material. Proc. Institute Environmental Sciences, April 1971, pp. 435-439.

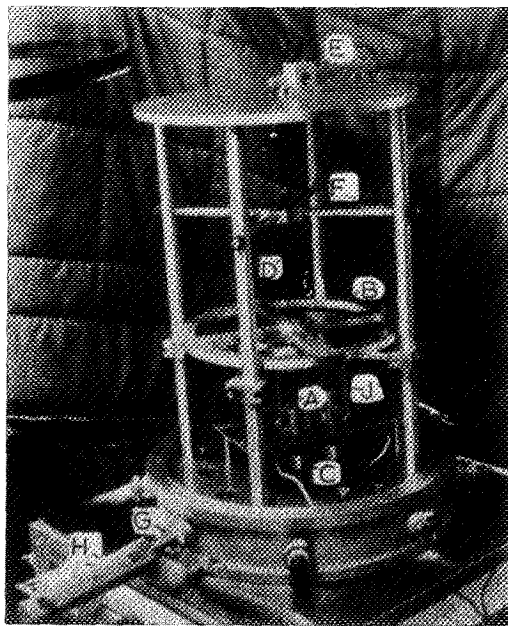


Figure 1. - The torsion pendulum.

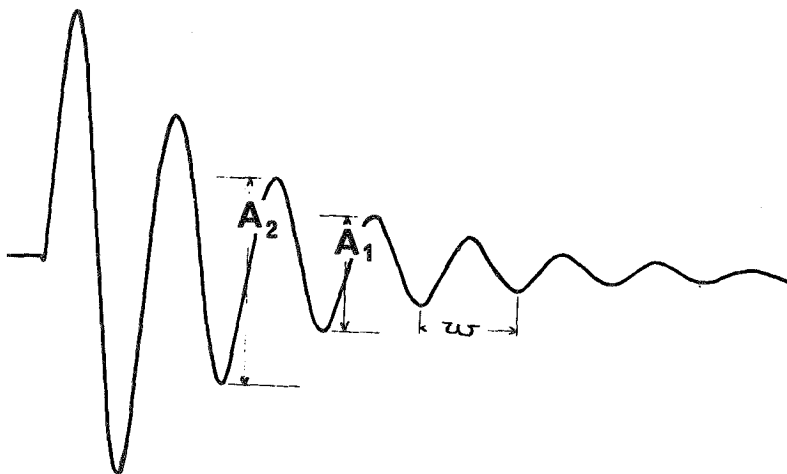


Figure 2. - Typical data trace from the torsion pendulum.

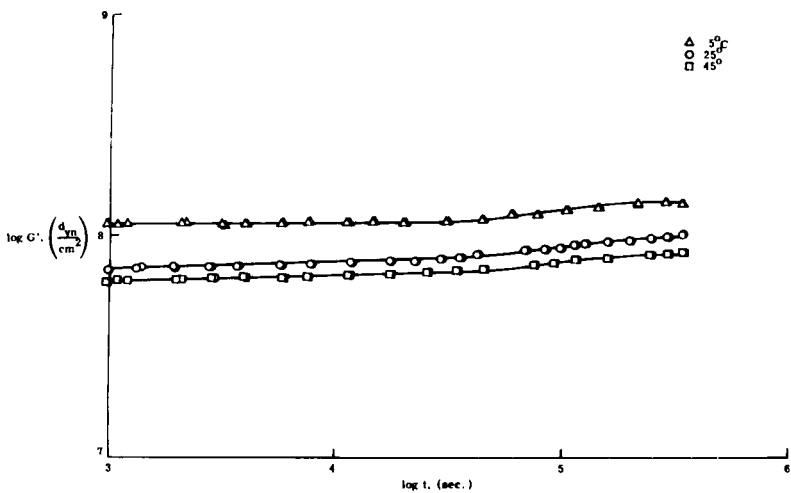


Figure 3. - Vacuum effects on the storage modulus.

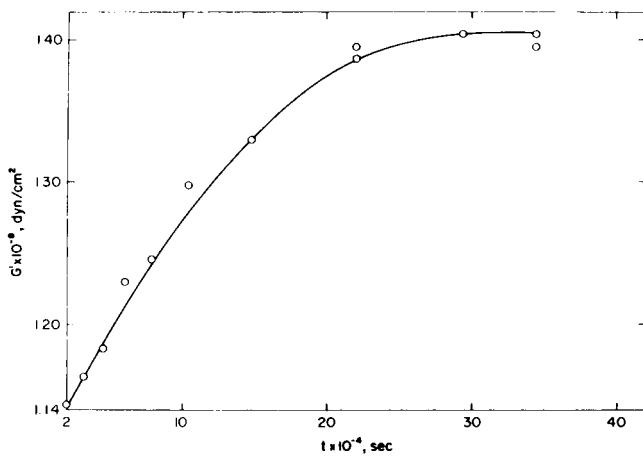


Figure 4. - Limiting behavior of the storage modulus.

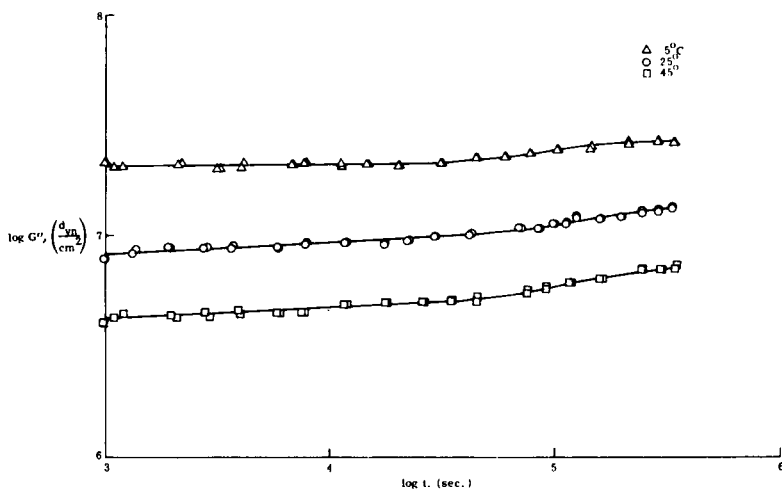


Figure 5. - Vacuum effects on the loss modulus.

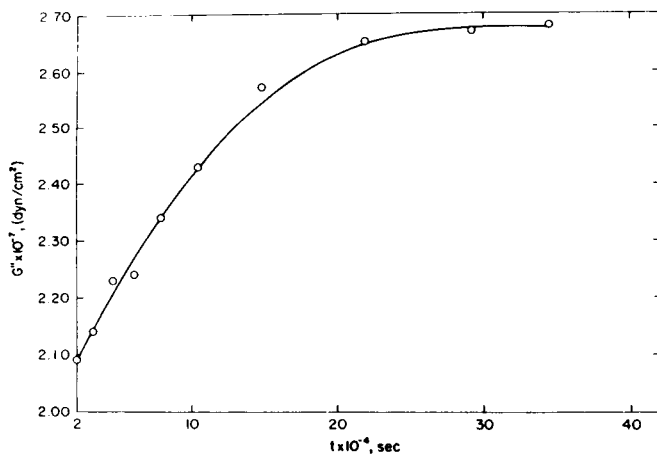


Figure 6. - Limiting behavior of the loss modulus.

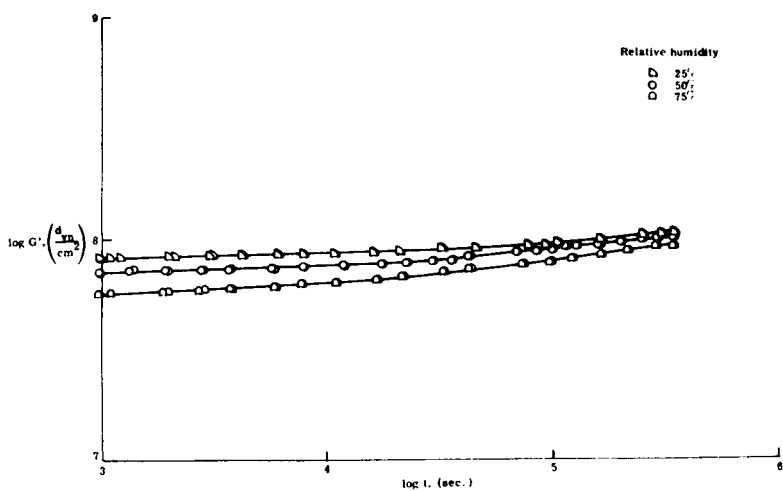


Figure 7. - Preconditioning and vacuum effects on G' .

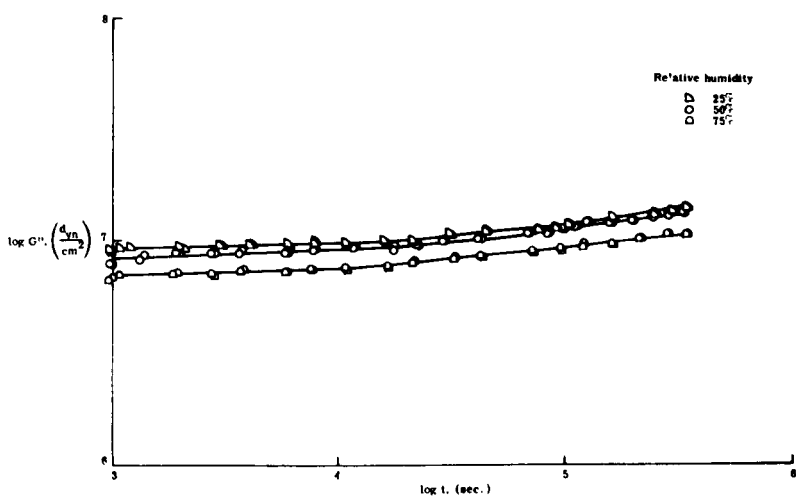


Figure 8. - Preconditioning and vacuum effects on G'' .

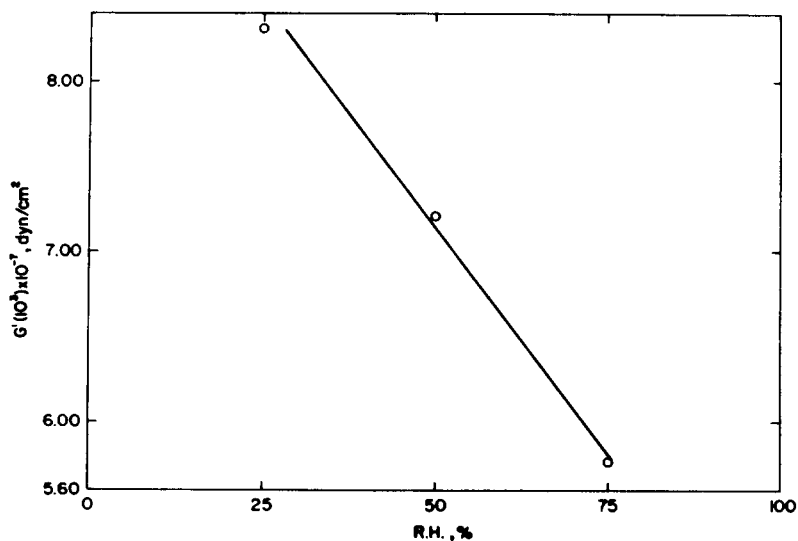


Figure 9. - Preconditioning effects on the initial storage modulus. Plot is a 25° C isotherm.

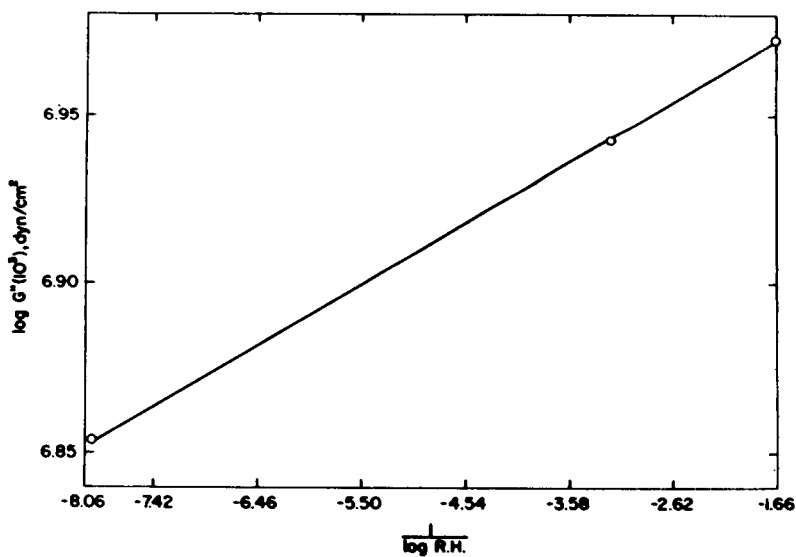


Figure 10. - Preconditioning effects on the initial loss modulus. Plot is a 25° C isotherm.

CHANGES IN SOME PHYSICAL PROPERTIES INDUCED BY VACUUM HEAT TREATMENT

A. E. Hultquist, *Lockheed Missiles and Space Company, Inc.*
Sunnyvale, California

SUMMARY

A proposed method for reducing or eliminating outgassing of materials is to heat treat them in vacuum prior to use. This may be performed on the raw material prior to manufacturing and installation or after fabrication of parts. Processing of a fabricated part can be performed only on relatively small parts and on assemblies containing no components which are affected by the required temperatures and pressures. Processing conditions of temperature and time are dependent on the particular application and the materials involved. Silicone-coated Fiberglass cloth was vacuum-heat treated for 100 hrs at $400 \pm 25^\circ\text{F}$ at pressures of 10^{-3} torr or less. The materials were tested in terms of tensile strength and tear properties in both the smooth and several creased configurations. Data obtained on one side silicone coated Fiberglass showed large reductions in these properties as a result of the vacuum-heat treatment. The problem was alleviated by coating both sides of the Fiberglass.

INTRODUCTION

The inclusion of outgassing characteristics as one of the criteria for selection of materials for use in spacecraft structures and components has become common in recent years. Materials which outgas under space conditions can adversely affect other materials or components within the spacecraft or lose their own critical properties, or both.

The most commonly-used test for screening materials has been the thermogravimetric procedure developed by Stanford Research Institute and the Jet Propulsion Laboratory (1). This procedure determines total weight loss and total volatile condensable materials. The latter are collected on cooled plates adjacent to each sample chamber; they can be subjected to appropriate analysis for identification if desired. The system is run under high vacuum and under either programmed or constant temperature conditions. Although the technique is useful as a general materials screening test, it merely suggests elimination of materials with unsatisfactory outgassing behavior; as such it

does not satisfy all design engineering needs. Substitution of one material for another due to outgassing characteristics is not always desirable or even feasible. Other properties required by a particular design may be of greater engineering importance than the outgassing properties, or economic factors may be very unfavorable.

An alternate to material substitution is to precondition the material by exposure to vacuum and heat prior to or after manufacture. Such pre-treatment or "space conditioning" serves to remove a major percentage of volatile materials present. This technique has been employed by Lockheed Missiles & Space Company.

It has been found that outgassing behavior is improved, but some material properties may be significantly changed during the vacuum heat treatment. This problem and test efforts to resolve it for one class of materials are described in this paper.

TEST PROGRAM

The materials test program to be described was concerned with one class of materials, silicone-coated Fiberglass; materials were used coated on one side and on both sides. Tensile strength determinations were used as the primary evaluation test. All samples were pre-conditioned in the same manner, heated at $400 \pm 25^\circ\text{F}$ for 100 hrs at 10^{-3} torr pressure. All samples were also tested in an identical manner. The major variable was the method of sample preparation. Both creased and uncreased samples were tested; direction of creasing was also varied with creases made both parallel to and perpendicular to the direction of pull during tensile testing. A tensile strength value of at least 15 lbs/ins. is required for the coated Fiberglass material.

Materials

Pertinent data for silicone-coated Fiberglass materials is shown in Table 1.

Table 1

Materials Description

Material Designation	Fiberglass Cloth		Silicone Coating	
	Number	Thickness Ins.	Number of Sides Coated	Coating Thickness Ins.
A	108	0.002	0	0
B	108	0.002	1	0.003
C	108	0.002	2	0.0015 each side
D	116	0.004	2	0.0025 each side

Sample Preparation

Creased samples were prepared by passing a 4.5 lb. roller once along the fold. Samples were prepared with creases both parallel and perpendicular to direction of tensile pull. Materials coated on one side only could be folded either Fiberglass/Fiberglass or silicone/silicone. Both types of folds were used. In addition uncoated 108 Fiberglass cloth was tested in the same manner to determine if the heat cure of the silicone during manufacture of the cloth was responsible for the poor performance of the material.

The Problem

During initial efforts to utilize material B (Table 1), it was noted by manufacturing personnel that the tendency to tear was much greater after vacuum heat treating compared with the material as received from the vendor. It was also noted that the tearing occurred primarily along lines formed when the material had been creased. As a result of these observations, a series of laboratory tests were initiated to verify this behavior and to evaluate alternate material configurations.

Test Results

Uncoated 108 Fiberglass cloth (Material A): Test results for the uncoated Fiberglass are shown in Table 2.

Table 2

Tensile Strength of 108 Fiberglass Cloth
(Material A)
All values in lbs/inch

Condition	A With Weave	B Against Weave	C Creased Parallel To Pull - 1 Pass		D Creased Perpendicular To Pull - 1 Pass	
			With Weave	Against Weave	With Weave	Against Weave
As Received	61.2 (Avg. of 3)	50.0	61.9	51.0	63.0	45.1
Heated to 350°F for 2 hours to simulate vendor curing method	85.6 (Avg. of 5)	54.5 (avg. of 5)	80.0	70.0	44.6	33.0

Although the tensile strength values are slightly lower with heat treated material, particularly when pulled perpendicular to the crease, the material is still very strong. No difference would be observed in the handling characteristics.

Silicone-Coated 108 Fiberglass, One Side (Material B): The test results observed for the one side coated 108 Fiberglass are given in Table 3.

Table 3

Tensile Strengths of One Side Silicone-Coated
108 Fiberglass Cloth
(Material B)
All values in lbs/inch

	A	B	C	D	E	F
Condition	Uncreased	Creased Length- wise Method 1	Creased Length- wise Method 2	Creased Cross- wise Method 1	Creased Cross- wise Method 2	Creased Cross- wise Method 2
As Received	91	76	69	16	6.0	1.0
After Vacuum Heat- Treatment	61	55	52	39	0.3	0.2

Method 1 - Silicone/Silicone Crease

Method 2 - Fiberglass/Fiberglass Crease

These results indicate that if the material is not creased, the vacuum heat treatment does not significantly degrade the strength of the cloth. However, if the material has been creased such that Fiberglass is against Fiberglass, catastrophic degradation of the vacuum-heat treated material results. While the as-received material did suffer rather large decreases in strength, they were not quite as disastrous as those observed for the vacuum-heat treated samples. However, all values in columns E and F are lower than engineering requirements.

Silicone Coated, Two Sides, 108 Fiberglass (Material D) and Silicone Coated, Two Sides, 116 Fiberglass Cloth (Material C): Strength values for these materials are found in Table 4.

Table 4

Tensile Strength of Two Side
Silicone Coated Fiberglass Cloth
(Materials C & D)

All values in lbs/inch

Condition	Uncreased		Creased Perpendicular to Pull			
			Side A		Side B	
	Material		Material		Material	
	C	D	C	D	C	D
As Received	85	85	43	95	50	82
After Vacuum Heat Treatment	-	32	59	22	40	21

These results show that - (1) The increased total thickness reduces the creasing effect, and (2) Vacuum heat treating reduces the strength of the material. However, it is also evident that all values are well above the 15 lbs/ins. strength which is required. No ripping or tearing was encountered in handling either of these materials during manufacturing.

CONCLUSIONS

The treatment of marginal materials, with respect to out-gassing properties, by heating them in a vacuum may change other physical properties. These changes may have an impact on subsequent manufacturing operations and behavior of the material in service.

In all cases, careful evaluation of possible changes in physical properties should be investigated in order to avoid material failures during manufacturing, testing or final use.

The reported study indicates definite effects of the vacuum heat treatment on silicone-coated Fiberglass materials. Effects on uncoated material were minimal. Degradation was greatest for the single side-coated material, and especially when creased with Fiberglass against Fiberglass. In all cases, for treated materials, creasing reduced strength values.

References

1. Muraca, R. F. and Whittick, J. S., "Polymers for Spacecraft Applications", Stanford Research Institute, Menlo Park, California, Sept. 15, 1967

THERMAL TESTING TECHNIQUES FOR SPACE SHUTTLE THERMAL PROTECTION SYSTEM PANELS*

B. G. Cox, *McDonnell Aircraft Company, St. Louis, Mo.*

ABSTRACT

An experimental system was developed at the McDonnell Aircraft Company, McDonnell Douglas Corporation, for evaluation of the effects of aerodynamic heating and cooling, vacuum, and pressure loading on candidate insulation packages proposed for use on the Space Shuttle. The system includes a number of design features which facilitate rapid recycle times. This is necessary to efficiently conduct extensive thermal cycling tests on these insulation packages to determine their reuse capabilities. The heart of the system is a 26-inch x 26-inch graphite element radiant heater. A susceptor plate functions as a uniform-temperature intermediate radiating surface. The susceptor also forms the lid of an inert atmosphere enclosure which separates the heater from the oxidizing test atmosphere. In some tests the plate properly simulates the heating from an actual flight heat-shield panel. Although other materials were used at lower required test temperatures, 2500°F was routinely achieved using a coated columbium susceptor plate. Since vibration and acoustic testing were to be performed in conjunction with the thermal cycling, we designed special specimen holders that were easily removable for alternate mounting in the desired test apparatus. This allowed rapid turnaround time between various tests without any damage incurred from specimen handling. One of the specimen holders would accept up to five insulation packages at a time. This increased the number of candidate insulations which could be screened in a given time.

In the first 6 months of operation nearly 300 thermal cycles, including 200 cycles using the coated columbium susceptor plate, have shown no significant problems in the system.

INTRODUCTION

The advent of the Space Shuttle program, and the accompanying requirements for multiple re-use capabilities has pointed up the need for accelerated testing techniques. The extensive launch-reentry conditions to which a shuttle vehicle will be subjected required new developments in the field of thermal protection systems (TPS). Along with these development programs came the need for realistic means of proving out such systems within a reasonable time span and at a reasonable cost.

*This paper is related to work performed under NASA Contracts NAS8-26115 and NAS9-11221.

With the awarding of contracts by NASA to develop Shuttle Thermal Protection Systems, the McDonnell Aircraft Company Engineering Laboratories devised a test apparatus capable of simulating the effects of aerodynamic heating and cooling, vacuum, and loading due to differential pressure. This apparatus is presently being used for the extensive thermal cycling required to evaluate re-use capabilities of candidate insulation packages proposed for use on the Space Shuttle.

Design Constraints The design of the test apparatus was based on the anticipated environments the TPS panels would encounter at various stations on the Shuttle vehicle. These environments were projected from the Shuttle specifications outlined by NASA and from the McDonnell Douglas Astronautics Company engineering concepts of the final vehicle design. The basic design ground rules for the test apparatus were:

1. The test apparatus must reproduce, as the maximum temperature thermal profile, the curve shown in Figure 1. This thermal profile was developed from a wide range of temperature-time histories possible from the flight characteristics and entry trajectories of the Shuttle vehicle.

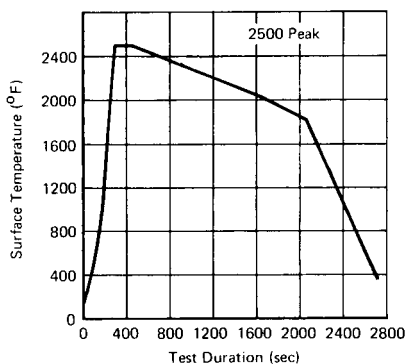


FIGURE 1 COMPOSITE TEMPERATURE-TIME CURVE FOR TESTING HIGH TEMPERATURE INSULATIONS

2. The apparatus had to produce at least 100 thermal cycles without mechanical failure or preventive maintenance.

3. The testing had to be accomplished in a reasonable time span. Since a large number of insulations and concepts were to be examined, the test system required a quick turn around capability.

4. An oxidizing atmosphere must be supplied to the test specimen during the heating cycle.

5. Acoustic and vibration testing was to be performed separately from the thermal tests. This was realistic since the peak sound pressures and temperatures along the mold lines were out of phase with each other.

6. Maximum specimen size for the insulation screening was to be no larger than 20-inches x 20-inches.

7. Differential pressure loading would be required on some of the insulation concepts proposed for use on the surface of the vehicle. This loading would be done during and/or after thermal cycling of the specimen.

The system which was put into operation in December 1970, included all the features outlined above.

SYSTEM COMPONENT DESCRIPTIONS:

Graphite Element Heater The heater of the test system is a modified version of a graphite element radiant heater developed under NASA Langley Research Center Contract NAS1-8921. The design of this heater utilized knowledge gained through government funded and in-house development programs over a three and one-half year period.

The graphite heater was chosen over more conventional tungsten-filament quartz lamps as a radiant energy source because our analysis indicated that for a large number of thermal cycles both time and money would be saved. With the heat flux requirements of these tests, the quartz lamps would be operating near their upper limits, and therefore would require frequent replacement; the graphite heater would be operating well within its nominal performance envelope. Life tests had shown the graphite elements would last well over 100 thermal cycles.

The graphite heater (Figure 2) has a heated area of approximately 26-inches x 26-inches provided by an array of 12 two-pass, hairpin-type graphite elements. Each element is machined from a single piece of artificial graphite having an average grain size of about .008-inch. At both ends of the element, where electrical connection is made or where expansion take-up blocks attach, the strips are thickened to avoid excessive heat load to the end blocks.

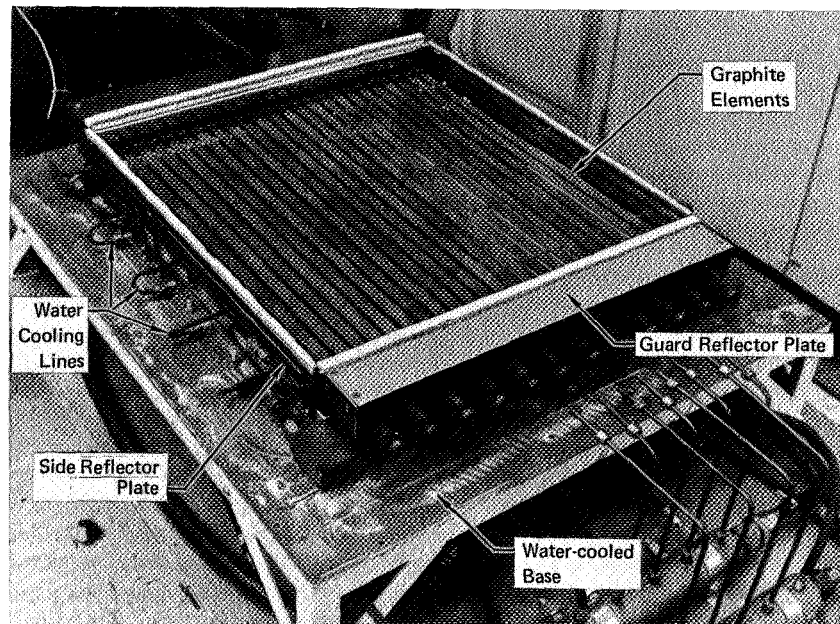


FIGURE 2 GRAPHITE ELEMENT RADIANT HEATER

Electrode End Block Assembly The electrode end block assembly (Figure 3) conducts the electrical power to the element through water-cooled brass blocks. A brass clamp bar holds the element firmly against the electrode block thereby providing good electrical contact. The required electrical insulation is provided by a ceramic spacer between the electrode block and a common brass water manifold. This manifold provides cooling water to all 24 electrodes. The electrode blocks are attached to the split ends of each element so the two segments of the element are connected in series.

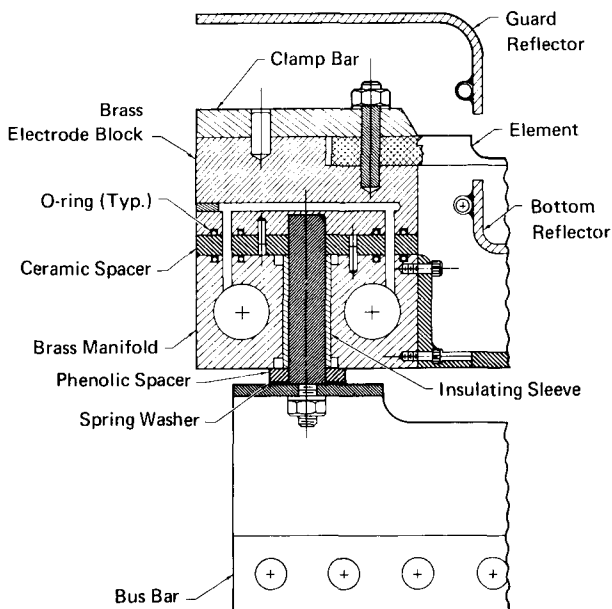


FIGURE 3 ELECTRODE END BLOCK ASSEMBLY

Expansion End Block Assembly The expansion end block assembly (Figure 4) supports the ends of the elements and provides a tension force on the elements. The tension force prevents excessive sag of the elements and compensates for their expansion. A ceramic spacer again provides electrical isolation from a cooling water manifold common to all expansion end block assemblies.

Reflectors Chrome-plated, water-cooled copper plates are mounted below and along the sides of the heater elements. These reflectors reflect incident heat flux, increasing both the uniformity of the heat flux to the specimen and the heater efficiency.

Heater Electrical Power Power is supplied to the heater by a standard 480 volt ignitron power controller. The output of the power controller is connected through 4:1 stepdown transformers to the electrode end block assemblies in a series-parallel

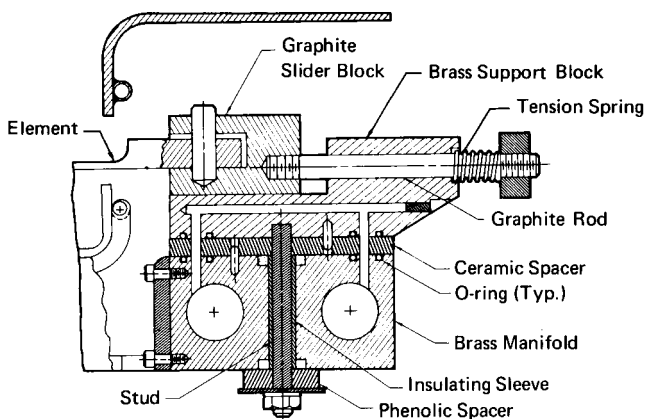


FIGURE 4 EXPANSION END BLOCK ASSEMBLY

arrangement which utilizes available power sources as efficiently as possible. The arrangement selected provides six parallel circuits, each of which has two 2-segment elements connected in series.

A function generator used in conjunction with the closed-loop temperature feedback system of the power controller provides the means of programming the desired temperature-time profile for any test series. Several temperature-time profiles were stored on spare function generator drums, so programs could be readily changed as the test dictated.

Inert Atmosphere Enclosure Graphite heater elements must be operated in an oxygen free atmosphere to prevent oxidation. Therefore, the heater assembly is mounted inside a water-cooled, gaseous-nitrogen-purged enclosure. A water-cooled plate coil forms the base of the enclosure and acts as the structural backbone of the heater assembly. A flanged, water-cooled spool, also formed from a plate coil, is mounted on the base plate. The lid of the enclosure is a chrome plated, water-cooled copper sheet containing a 21.5-inch square "window" centered over the heated area of the heater elements. A metallic plate, designated a susceptor plate, is mounted in this window with the space between the water-cooled copper and the susceptor plate sealed with a high temperature felted insulation. The inert atmosphere enclosure with the susceptor plate installed is shown in Figure 5.

Susceptor Plate The susceptor plate functions as a uniform intermediate radiating surface while separating the graphite heater from the oxidizing test atmosphere. In some tests the plate properly simulates the heating from an actual flight heatshield panel. The maximum operating temperatures for a test series determined the type of material used for the susceptor plate. Inconel 601 was used for maximum temperatures up to 1800°F, with a D-14 columbium plate coated with Sylvania Coating R-512-E being used for test temperatures up to 2500°F.

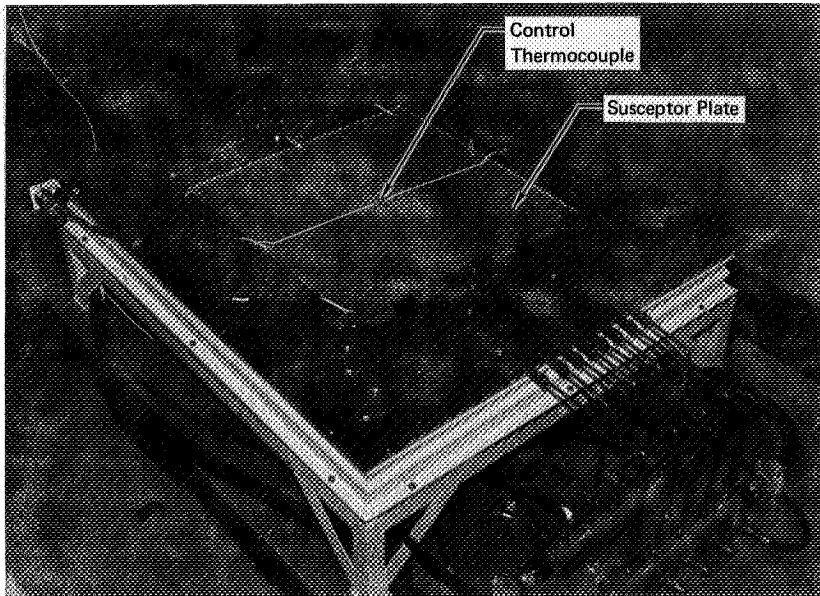


FIGURE 5 HEATER ASSEMBLY - VIEW OF INERT ATMOSPHERE ENCLOSURE WITH SUSCEPTOR PLATE INSTALLED

Oxidizing Atmosphere Water-cooled, air spray bars mounted along two opposite edges of the susceptor plate supplied an oxidizing atmosphere across the heated surface of the test specimens. These spray bars are simply twin passage copper tubes with water flowing through one passage and air through the other. Orifices in the air tube are spaced along the length of the susceptor plate, providing a constant flow of air across the entire heated surface of the specimen.

Universal Specimen Holder Support Assembly A water-cooled frame and plate coil assembly (Figure 6) supported either of two types of specimen holders above the heater. The frame is constructed from 1-inch square tube stock thus providing its own cooling water passages. A water-cooled plate coil is hinged from one of the cross members of the frame. The hinge permits 180° rotation of the plate to allow one type of specimen holder to be bolted to it. Rotating the plate back over the heater positions the specimens over the center of the heated area. The other type of specimen holder has two support poles bolted to the back plate. These poles rest in notched brackets attached to the support frame to suspend the specimens above the heater. Both of the support methods allow for quick removal or installation of the specimens above the heater.

Universal Specimen Holders Two types of fixtures are used to hold insulation specimens above the heater during testing. One has the capability of loading the specimen with differential pressure and was used primarily for candidate TPS panels proposed for use on the mold line of the vehicle. The other fixture was

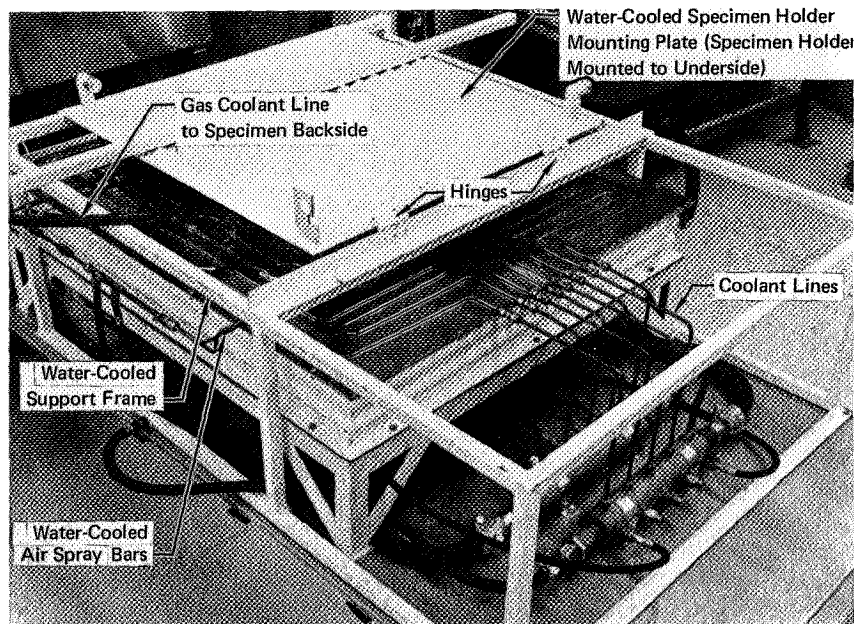


FIGURE 6 HEATER ASSEMBLY - VIEW OF SPECIMEN HOLDER SUPPORT ASSEMBLY

designed to hold metal-foil-encased fibrous or felted insulation packages for use primarily behind the metallic heat-shield surface panels of the vehicle. These specimen holders were designated "universal" because they could be detached from the thermal testing facility and installed in the vibration or acoustic test facility without removing the test specimens from the holder. This eliminated handling of the specimens during transfer between facilities thereby reducing the probability of damage.

The specimen holder designed for metal-foil-encased specimens (Figure 7), was a stainless steel frame with web-reinforced flanges. The re-inforcing was necessary to increase the stiffness for the vibration and acoustic testing. Foil packaged specimens (Figure 8) were mounted in the holder by tabs extending from each end of the specimen. The tabs were clamped between bars located along opposite sides of the specimen holder flange. These clamping bars had a spacer which could be placed so that either a 1.5-inch or 2-inch thick specimen could be accommodated while maintaining the surfaces to be heated at the same distance from the heat source. The clamps were arranged so that five 4-inch x 20-inch specimens, one 20-inch x 20-inch specimen, or a combination of intermediate size specimens could be mounted. This allowed the initial screening process to be performed on as many as five materials at one time, reducing the total test time. Five foil packaged specimens are shown mounted in the specimen holder shown in Figure 9. This specimen holder was the one attached to the hinged plate coil shown in Figure 6.

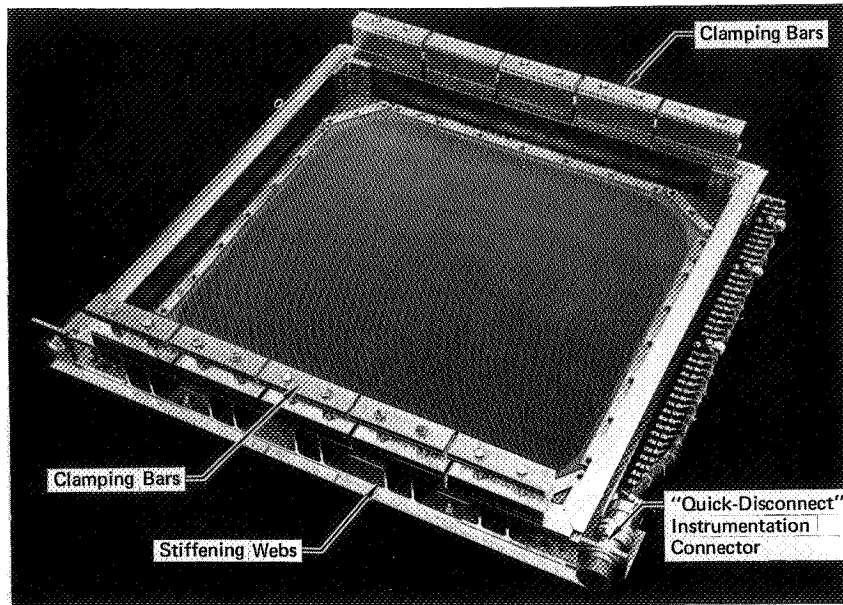


FIGURE 7 SPECIMEN HOLDER FOR METAL-FOIL-ENCASED SPECIMENS

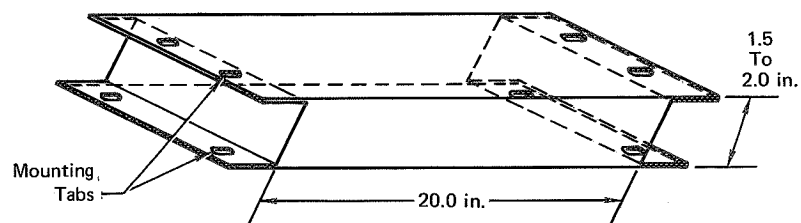


FIGURE 8 TYPICAL FOIL-ENCASED HIGH-TEMPERATURE INSULATION SPECIMEN

The "differential-pressure" specimen holder was designed with a cavity behind the specimen. This cavity could be pressurized or evacuated to load the specimen by differential pressure and was designed primarily to test 12-inch x 20-inch reusable surface insulation (RSI) specimens. It is shown in Figure 10 with a specimen clamped in place. An additional feature of this holder was a Schaevitz Engineering Linear Variable Differential Transformer (LVDT) deflection measuring device mounted to the back plate. A ceramic rod was attached to the core of the transformer and rested on the back side of the specimen. The output of the LVDT was



FIGURE 9 FIVE FOIL ENCASED SPECIMENS MOUNTED
IN SPECIMEN HOLDER

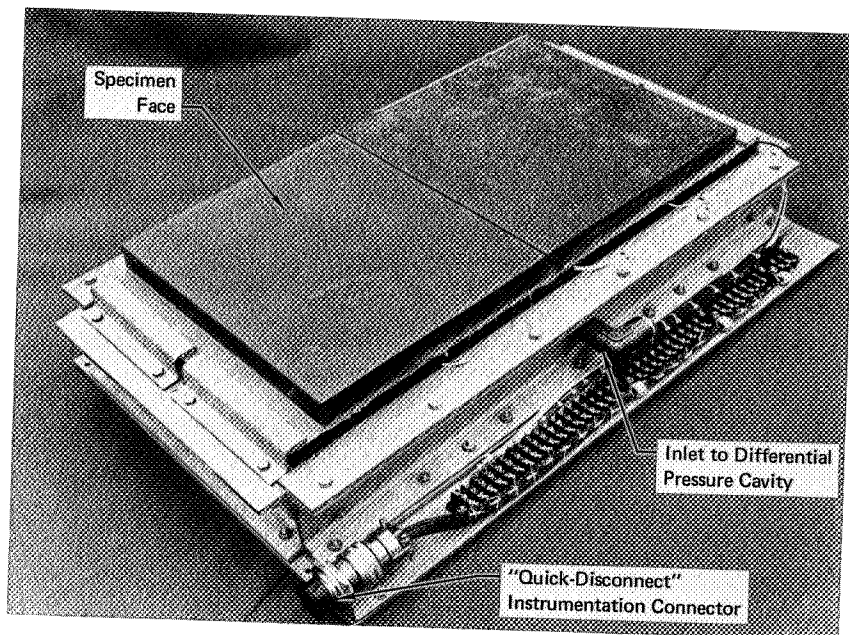


FIGURE 10 SURFACE INSULATION TEST SPECIMEN ATTACHED
TO "DIFFERENTIAL-PRESSURE" SPECIMEN HOLDER

recorded during thermal cycling and/or pressure loadings to give an indication of panel deflections. The weight and thickness of the specimen holder precluded mounting it on the hinged plate coil; this fixture simply rested on notched brackets.

Differential-Pressure Loading System A manually operated pressure/vacuum gas system was utilized to subject specimens to the air pressure loads they might experience in flight. A schematic of this system is shown in Figure 11. The piping was arranged in the manner shown, with the idea of automating the system in the future. To provide a lower (negative) pressure in the cavity, the vent valve and manual pressure equalizing valve were closed and the bypass control valve and vacuum shutoff valves were opened. Then by controlling the bypass valve position the cavity could be evacuated to obtain the desired differential pressure. To provide a higher (positive) pressure in the cavity, the procedure was the same except the vacuum shutoff valves were closed and the pressure shutoff valves opened.

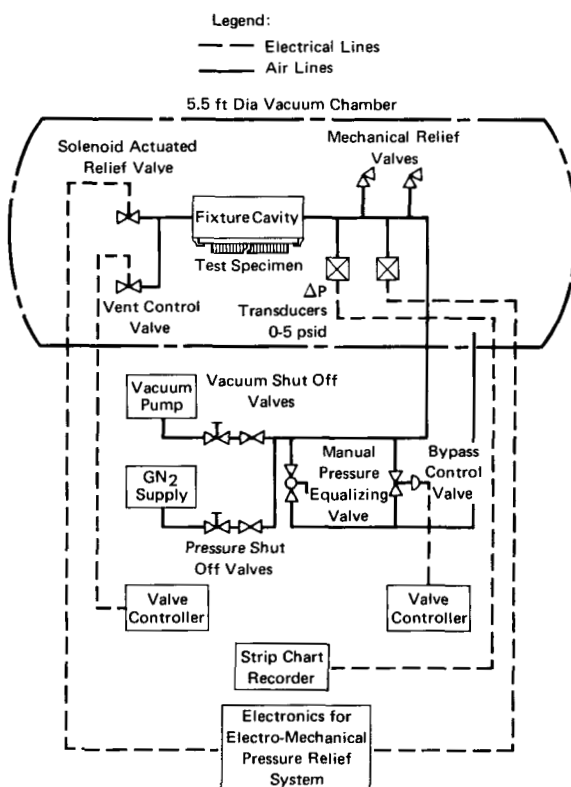


FIGURE 11 DIFFERENTIAL-PRESSURE LOADING SYSTEM

Reduced Pressure Environment The reduced pressure environment is provided by one of the 5.5-foot diameter vacuum chambers (Figure 12) located in the McDonnell Aircraft Company Space Systems Laboratories. The heater test assembly was mounted on a working platform attached to the inside of the door (Figure 13). The door can be rolled away from the chamber to provide access to the experiment. The chamber's 200 cfm mechanical pump was used during these tests. The electrical power, instrumentation, cooling water, and gas supplies are introduced through vacuum pass-throughs on the chamber door. All external instrumentation, water, and gas connectors are of the quick disconnect and/or self-sealing type so that these lines can be quickly disconnected at the conclusion of a test. The electrical power lead connectors are of the push-pull type, again for easy disconnect.

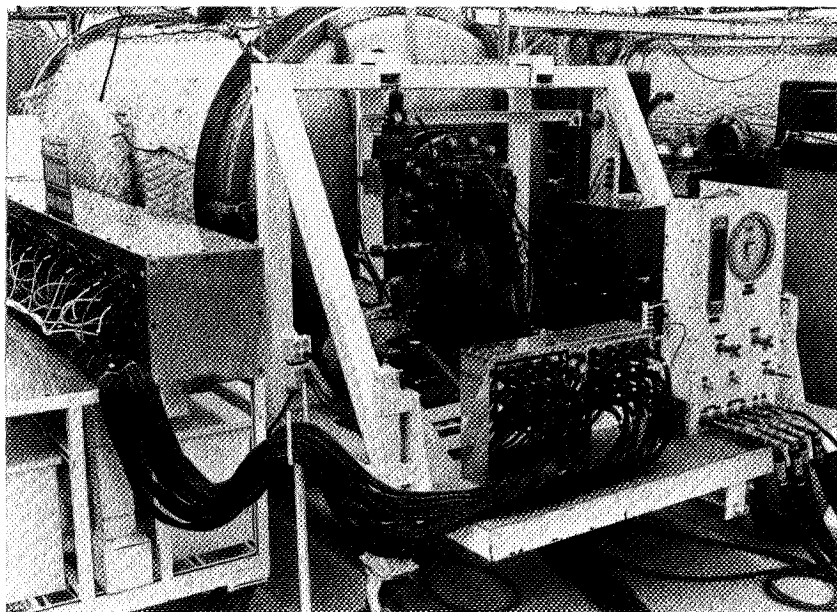
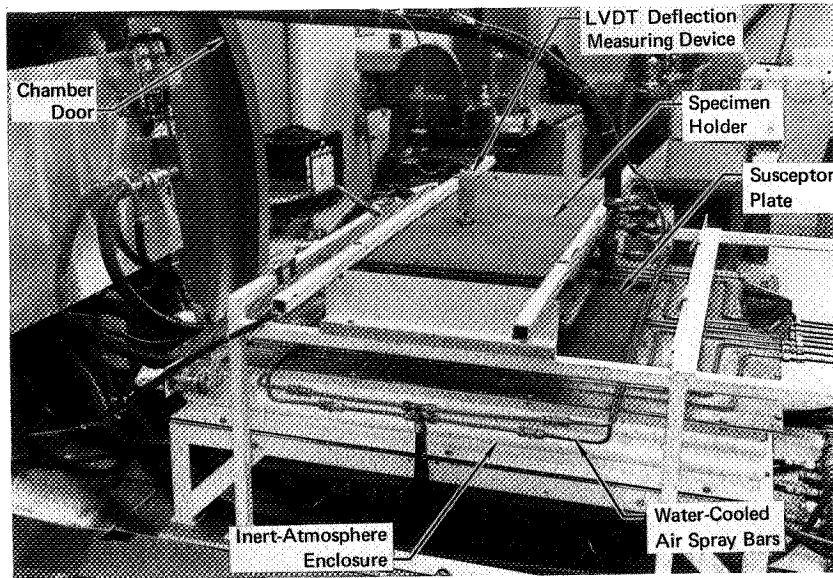


FIGURE 12 VACUUM CHAMBER FOR REDUCED PRESSURE ENVIRONMENT TESTING

Specimen Instrumentation Specimen instrumentation consisted primarily of thermocouple temperature sensors strategically located to provide the data required to determine thermal characteristics. The characteristics of interest were not only of an absolute nature, but also of a relative nature, so that changes in the insulation properties due to the extended test environments might be detected. The primary goal was to come up with the insulation type and density that would provide the necessary thermal shielding and/or structural properties over the life of the vehicle at the lowest possible density-thermal conductivity product. Instrumentation terminal strips and quick disconnect connectors were mounted on each specimen holder, so the instrumentation leads to the specimens did not have to be disconnected when the holder was transferred to the vibration/acoustic test facility.



**FIGURE 13 DIFFERENTIAL PRESSURE TEST SETUP MOUNTED ON
DOOR OF 5.5-FOOT DIAMETER VACUUM CHAMBER**

Data Acquisition and Processing During the thermal cycles, the thermocouple outputs, deflection gauge output, and real time are recorded on magnetic tape after being conditioned by a Hewlett Packard "Dymec" digital data acquisition system. All the data were recorded in absolute millivolts. At the end of a block of thermal cycles, the tape reel was processed through a Scientific Control Corporation 670-2 Computer, where the data is converted to appropriate engineering units and recorded on another magnetic tape. From this tape, the data can be tabulated, or plots similar to the samples shown in Figures 14, 15 and 16 can be obtained by feeding the tape into a Cal-Comp 565 digital plotter.

The thermocouple data from several thermal cycles are compared and if significant degradation has occurred in the insulation package it is readily apparent. Usually, the temperature data from every fifth or tenth cycle is plotted. If one shows a change during that block of tests, the intervening test data can be retrieved to determine the actual time of failure. All the data is stored on master tapes for future reference.

System Operation A test program for candidate insulation packages or an RSI panel consisted of a combination of environmental conditions including thermal, vibration, acoustic, and pressure loading. For instance the specimens might be subjected to five thermal cycles, five vibration, five thermal, and five acoustic in one complete series. If no failures had occurred, the sequence would be repeated until a predetermined number of cycles had been completed or a specimen failure occurred. Each cycle was designed to simulate one flight of the vehicle.

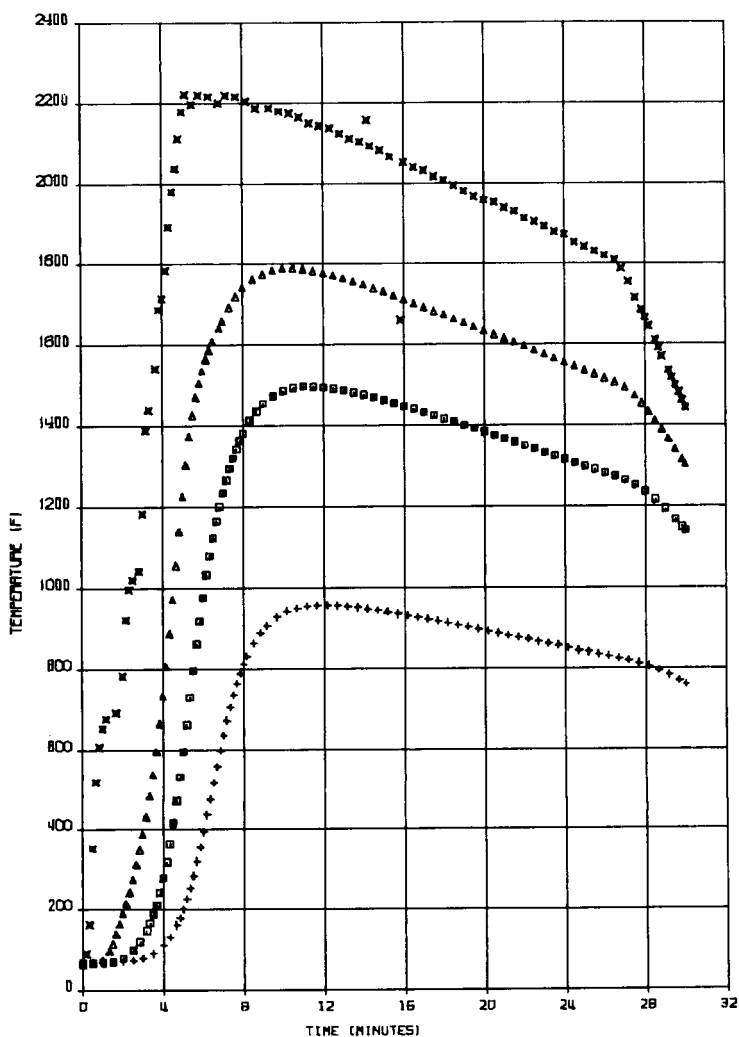


FIGURE 14 TYPICAL TEMPERATURE-TIME DATA PRODUCED BY CAL-COMP PLOTTER FOR HIGH TEMPERATURE INSULATION TEST PROGRAM

Specimen: XV-3
 Insulation: Refrasil A-100
 Packaging: 4 Mil Inconel 601
 Cumulative Cycles:
 15 Vibration
 15 Acoustic
 30 Thermal

Legend:
 X Susceptor Plate Temperature
 Δ Specimen Hot Face Temperature
 □ Specimen Center Temperature
 + Specimen Back Face Temperature

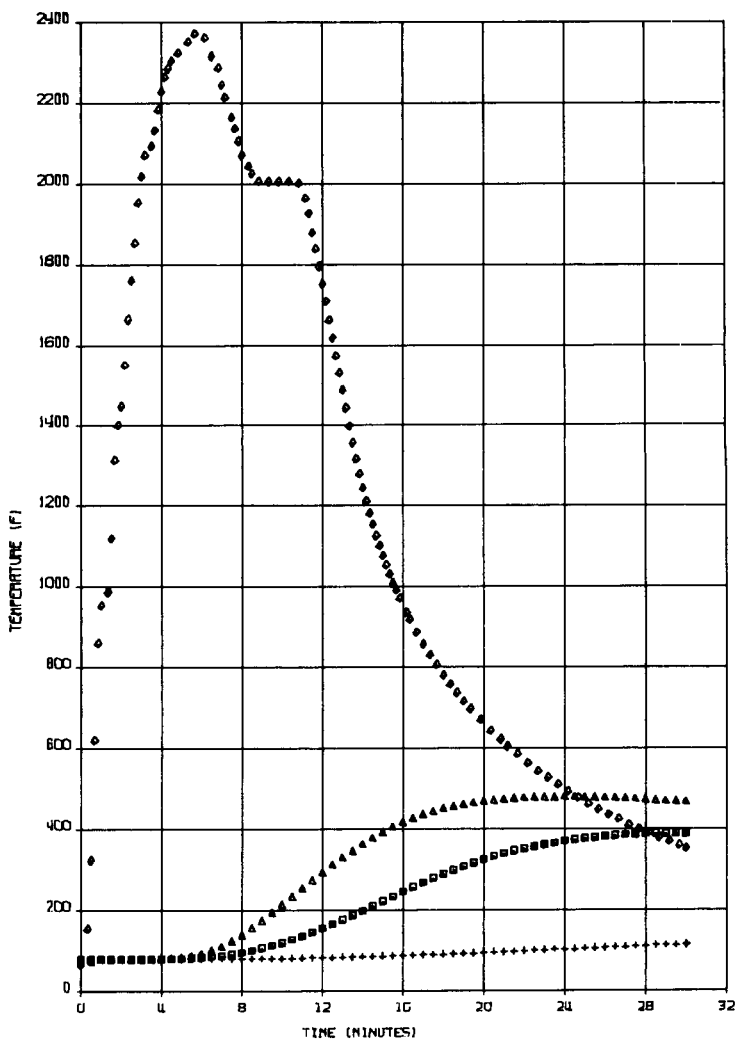
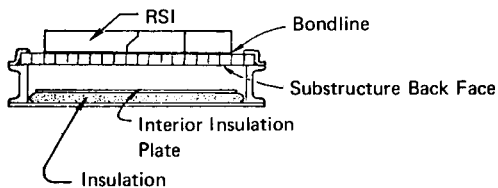


FIGURE 15 TYPICAL TEMPERATURE-TIME DATA PRODUCED BY CAL-COMP PLOTTER FOR REUSABLE SURFACE INSULATION TEST PROGRAM

Legend:

- ◇ Susceptor Plate Temperature
- △ Specimen Hot Face Temperature
- Specimen Center Temperature
- + Specimen Back Face Temperature



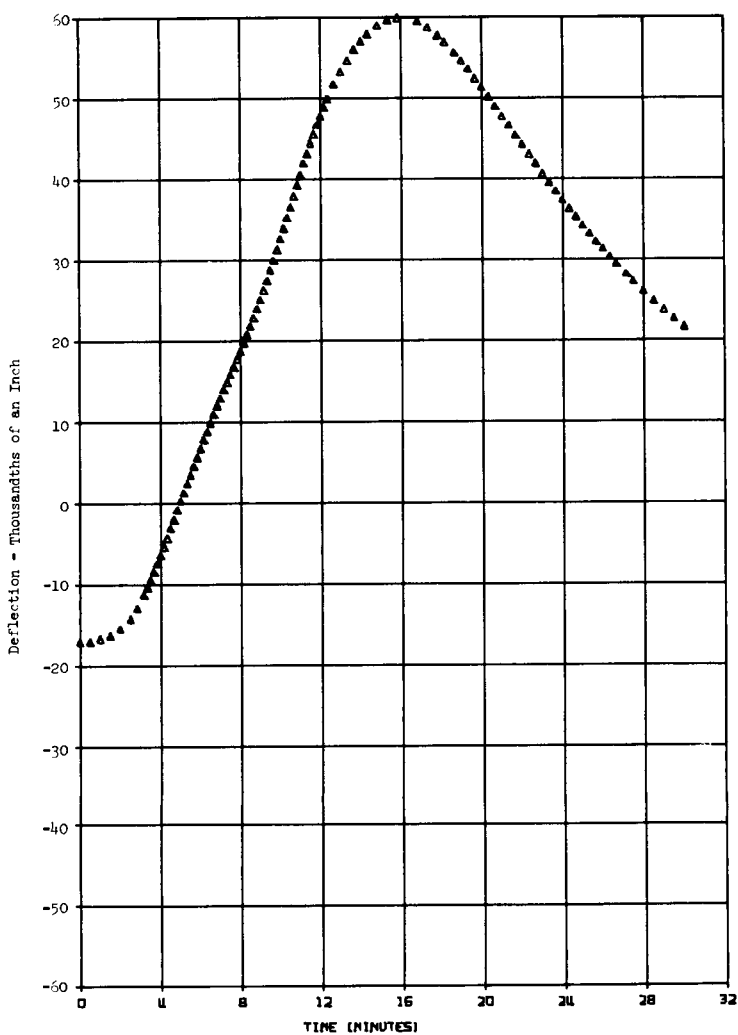
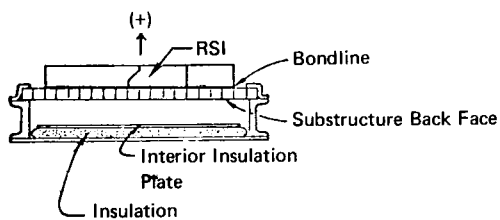


FIGURE 16 TYPICAL DEFLECTION-TIME DATA PRODUCED BY CAL-COMP PLOTTER FOR REUSABLE SURFACE INSULATION TEST PROGRAM



A typical set of thermal cycles on a foil package test specimen of the type shown in Figure 8 is as follows:

The specimen has three thermocouples embedded in the insulation. One is near the heated surface, one near the back side, or cold face, and one about halfway between the two. The specimen is clamped into the specimen holder in one of the five available locations. Four other specimens would be mounted also, if available. A log is kept of the type of insulation, packaging material, specimen thickness, and any other pertinent data. Any spaces between adjacent specimens is packed with Johns-Manville Dynaflex insulation. The fixture is then bolted to the hinged plate coil fixture support. The plate coil is rotated about the hinges until the surface of the specimens to be heated is about one inch from the susceptor plate.

Instrumentation quick-disconnects are connected and layers of protective insulation are placed around the outer edges of the specimens and overlap onto the water-cooled plate framing the susceptor plate. This prevents stray radiation from heating the sides of the specimens and/or escaping into the surrounding areas. It also enhances the temperature uniformity of the susceptor plate by preventing free radiation from localized areas.

The setup is then moved into the vacuum chamber and the chamber pressure reduced to the pressure required for that test (usually about 10 torr). While the chamber is pumping down, all water lines, instrumentation cables, power leads, etc., are connected. When the desired chamber pressure is reached, heater enclosure purge gas and spray bar air are turned on. These gas loads are set to maintain the desired chamber pressure.

After a suitable time has elapsed to allow for purging of the heater enclosure, usually less than 10 minutes, the thermal cycle is initiated. This is accomplished by activating a function generator which has been programmed to generate a predetermined thermal profile. The control thermocouple in the feedback loop is located at the center of the susceptor plate, which in this case simulates the metallic heatshield panel of the flight vehicle.

At the conclusion of the thermal cycle, the function generator is reset, and cooling air introduced to the backside of the specimen while the spray bar air flow is increased. When the specimen thermocouples indicate all specimens are cool, the procedure is repeated until the desired number of thermal cycles are completed. When the last cycle is completed the chamber is backfilled, opened, and the specimens are removed and inspected for visible damage. They are then transferred to the vibration/acoustic test facility.

Future Apparatus Refinements These are some of the areas where system refinements could be made:

1. Automation of the pressure loading system, so that pressure-time profiles can be programmed.
2. Increase the cooling capability after a thermal cycle has been completed. By decreasing the time required to remove the stored heat in the test specimens, the recycle time would be decreased.
3. Materials capable of withstanding higher temperature could be utilized as susceptor plates.

4. The ultimate refinement lies in developing an oxidation resistant graphite so the heater can be operated without the susceptor plate in oxidizing atmospheres. Without the limitations imposed by the susceptor plate the 26-inch x 26-inch graphite heater has the capability of producing cold wall heat fluxes of over 200 Btu/Ft²-sec.

Concluding Remarks In the first 6 months of operation, nearly 300 thermal cycles, including 200 cycles using a coated columbium susceptor plate, have shown no significant problems in the system. It is economically encouraging that the coated columbium is standing up so well, since it is the most expensive single item in the material cost. The graphite elements have been replaced only as preventive maintenance. Some elements were in service over 150 cycles before being replaced. In the 6 month period, no element failures occurred.

STADAN AND DATA RELAY SATELLITE SIMULATION (EMPHASIS ON THE SCHEDULER)

B. Kerne and N. Shusterman, *Operations Research, Inc.*; P. Pease, *Goddard Space Flight Center, Greenbelt, Maryland*

ABSTRACT

A set of computer programs has been developed which can be used to simulate the operation of NASA's Satellite Tracking and Data Acquisition Network (STADAN). The simulation consists of two major modules, a Computerized Algorithmic Satellite Scheduler (CASS) and a Generalized Evaluation Model Simulator (GEMS). CASS generates in-view time intervals of satellites over ground stations, and using these "candidate passes," produces a schedule of service times for specific satellites to be serviced by specific ground stations in an attempt to fulfill certain inputted service requirements. GEMS then examines how well STADAN fulfills this schedule in terms of the availability and dependability of different (inputted) complements of equipment at the ground stations. The simulation was recently modified to allow for the introduction of one or more tracking and data relay satellites, which can serve as orbital receiving and command stations.

INTRODUCTION

The Satellite Tracking and Data Acquisition Network (STADAN) has been used by NASA to collect data from, send commands to, and track a wide variety of Earth orbiting unmanned spacecraft. The network is global, constituting about 14 stations, ranging in latitude from Fairbanks, Alaska (64.6°N) to Canberra, Australia (35.4°S). STADAN has been servicing (on the average) 30-35 satellites for the past several years. The complexities of STADAN encompass both technical, organizational and political factors, all of which make it difficult to change STADAN in a short time frame. Thus, advanced planning for the deployment of equipment, location of stations, maintenance, etc., must be sufficiently thorough so as to provide a high measure of confidence that the

network will be able to provide adequate service to what are at this time, only projected requirements for the future. The high costs associated with STADAN include both capital investment and operational expenses, dictating that cost effectiveness be used as criteria for the network deployment.

This paper describes a highly simulative, modular set of computer models (CASS and GEMS) that provides a tool for the analysis of the combined network, and which has been used in its separate sub-models, to provide insight into the solution of many problems anticipated during the next decade of operations.

ADVANCED PLANNING FOR STADAN

The costs associated with the operation of STADAN and the importance of its mission are sufficiently large to require a comprehensive and detailed planning operation to assure that STADAN will continue to provide adequate services on a cost-effectiveness basis. The evaluation of potential designs for an advanced STADAN requires detailed analyses of operational effectiveness and cost. The Computerized Algorithmic Satellite Scheduler (CASS) is intended to provide inputs to such analyses. By considering the satellite demand and station resources, CASS is intended to develop a schedule which is representative of the real-world schedule that would be derived to satisfy the demand. Further, CASS is computerized so that many combinations of scheduling concepts, station resources and satellite demands can be considered in a relatively short period of time.

The schedules developed by CASS can be used to establish anticipated utilization rates for the stations and their communication links. However, the effect of equipment malfunction and certain scheduled anomalies, e.g., scheduling three satellites simultaneously at one station having enough equipment to service only two, cannot be evaluated by CASS. The CASS schedule is used as an input to a model of the network, using the GEMS simulation. GEMS simulates station operations and generates measures of effectiveness on a station/network basis.

Thus, the combination of CASS and GEMS provides a powerful tool for the evaluation of STADAN effectiveness, which may be used to conduct detailed analyses of proposed modifications to the STADAN.

TRACKING AND DATA RELAY SATELLITE SYSTEM

The Tracking and Data Relay Satellite System (TDRSS) concept is presently under study. A possible TDRSS configuration would be composed of one or more spacecraft in a geostationary orbit over the equator. A set of Data Relay Satellites properly placed is expected to provide data relay, tracking, and command and control of user spacecraft on a near-continuous basis. Advanced planning for the TDRSS clearly impacts on the future STADAN. Which ground stations are no longer needed due to the availability of service from the TDRSS? What is the effectiveness of different combinations of ground stations and 1, 2 or 3 satellite TDRSS's? What is the "best" beamwidth for the relay satellite? These questions must be answered. As an aid in addressing these questions, the ability to include the TDRSS concept in the simulation has recently been added to the CASS/GEMS combination.

CASS

CASS is intended to provide schedules that are statistically similar to the current schedules used by STADAN. Thus, the average performance of the network, as scheduled by CASS, is expected to be comparable to the actual average performance of STADAN. These schedules will provide valid inputs to the cost-effectiveness analysis of the network.

Significant CASS capabilities are listed below:

1. Accepts as input, orbital parameters for up to 99 spacecraft
2. Considers the use of up to 30 ground stations at arbitrary locations, and up to 3 data relay satellites
3. Assigns the major equipments, i.e., antennas at each ground station
4. Considers a number of required items for each spacecraft such as:
 - (a) Link type, e.g., command, telemetry
 - (b) Primary and secondary stations
 - (c) Minimum acceptable pass length
 - (d) Intrapass and interpass requirements.

5. Accepts priority ratings for satellites
6. Utilizes a variable algorithm to generate a schedule for the network which is representative of a typical STADAN schedule
7. Develops a statistical summary of the schedule
8. Formats the schedule so that it is acceptable by GEMS.

CASS has been designed on a modular basis, and consists of three basic modules, each of which may be used independently, or in combination with other modules. The basic modules are the Candidate Pass Generator, (CPG), Requirements Tape Generator (RTG), Scheduler. The relationships among these modules, and the flow of information through them are depicted in Figure 1.

Candidate Pass Generator

The Candidate Pass Generator computes the in-view and out-of-view times for all spacecraft, at each ground station and Data Relay Satellite (DRS) of interest. It accomplishes this as follows: The position of each user spacecraft as a function of time (where time is incremented by specified intervals) is computed based on the Brower general perturbations method. These generated positions are used in conjunction with the ground station locations and data relay satellite longitude and altitude to calculate the vectors between the stations (including DRS) and user spacecraft. The vectors are then tested against range and visibility criteria (i.e., outside the specified antenna beamwidth, behind the earth, or beyond a specified maximum range).

Inputs which describe the spacecraft orbits consist of all the orbital parameters, i.e., semi-major axis, eccentricity, inclination, mean anomaly, argument of perigee and right ascension of the ascending node. These parameters, and epoch times, used with a mathematical model, completely define the position of a spacecraft, as a function of time. Inputs which describe the ground station include the station latitude, longitude, elevation, and the minimum allowable elevation angle. DRS parameters include longitude, orbital altitude, and antenna beamwidths. Control information for the program include the time domain of interest, minimum view time, maximum slant range and the time interval at which the computations are made.

The output of the Candidate Pass Generator is a tape that is ordered by time out-of-view (TOV), and is random in spacecraft and station. A standard sort routine orders the candidate passes by spacecraft, and time-in-view (TIV). This tape mainly serves as input to the Scheduler. However, it can also be used by

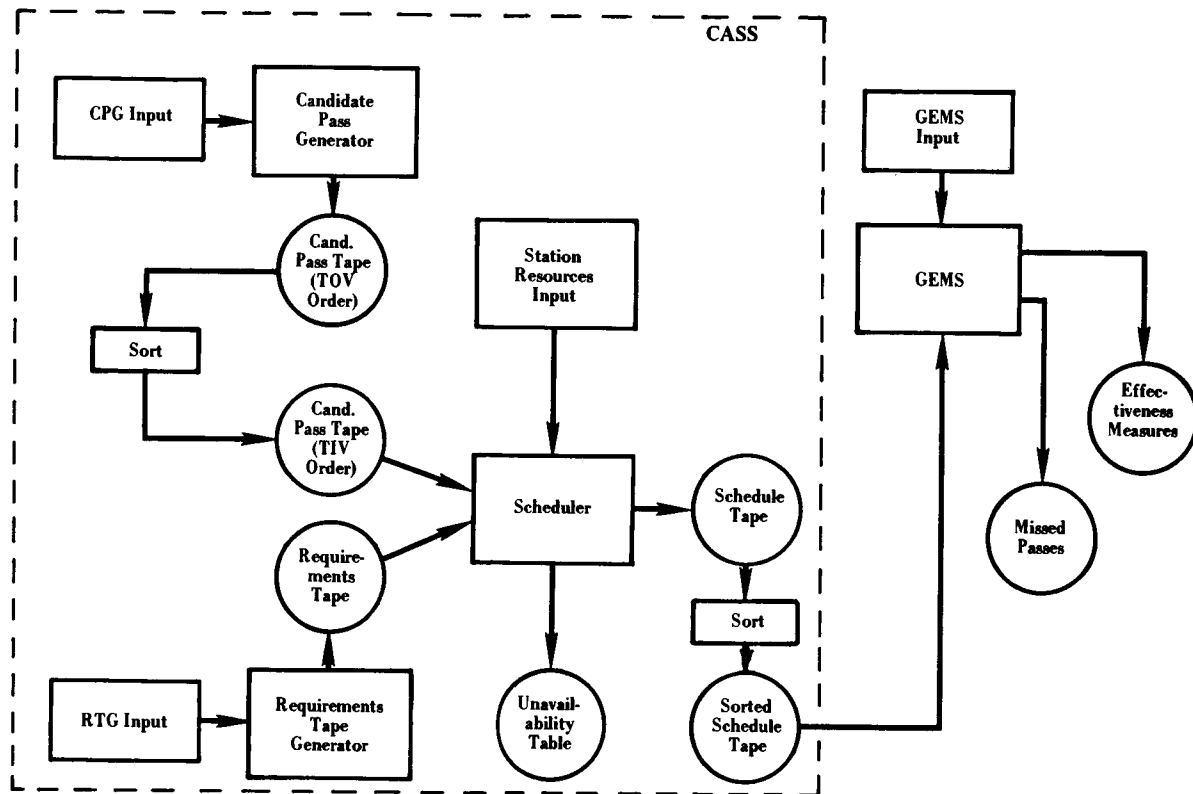


Fig. 1—CASS information flow

a statistics routine to compute such items as histograms of gap duration and pass duration by satellite, coverage in minutes as a function of satellite and station, and percentage of time domain of interest that each user satellite is in view of at least one station.

Requirements Tape Generator

The Requirements Tape Generator accepts scheduling requirements and priorities as inputs, orders these requirements as a function of the priorities, and produces a priority ordered scheduling requirements tape. The requirement defining items which serve as inputs should be based on existing or proposed operation plans. They include such items as user satellite requiring service, stations (including DRS) required to provide the service, link type required (e.g., command, telemetry, VHF band, S-band), time domain in which service is required, "interpass" requirement (i.e., the required relationship among the passes to be scheduled), and "intrapass" requirement (i.e., the required relationship of each individual pass to be scheduled to the original candidate pass of which it is a subset). Three levels of priorities are permitted—user satellite, link type and interpass type. Thus the inputs must include a list of the satellites requiring service in order of importance and for each of these satellites, a list of their required link types and interpass types in order of importance. The program then uses these priorities to generate the ordered requirements tape which is the second source of generated input for the Scheduler.

Scheduler

The Scheduler attempts to fill the input requirements from the selected candidate passes, in consonance with the station resources, i.e., equipments. The resources considered by the Scheduler are limited to type and quantity of antennas (in the case of ground stations), and number of S-band antennas and VHF band channel capacity (in the case of a DRS). The scheduling is done on a first come, first serve basis. That is, the first requirement on the requirement tape will be filled, if possible, first. Then the second requirement will be considered, and so on. Thus, the order established by the Requirement Tape Generator is the order in which passes will be scheduled. In general, if the requirements are consistent with the candidate passes and station resources, then the first several requirements will probably be filled satisfactorily. However, as the station resources become committed to the spacecraft in accordance with the requirements,

eventually it will become impossible to satisfy some of the requirements. For example, if two spacecraft (e.g., Nimbus, OAO) each require a dish at a particular station (Alaska) and the times-in-view overlap, and only one dish is available, then it is clear that only the first requirement considered can be filled. The Scheduler processes each requirement in order, until all the requirements have either been filled or found to be impossible to fill.

A few examples of the types of requirements that the Scheduler can fulfill will help to illustrate its versatility. Any of 6 link types may be required: Command, telemetry, dish, range and range rate, and telemetry and command (either simultaneously, or command interspersed within a telemetry pass). A requirement may call for S-band DRS command link service when available and selected ground stations command link service when DRS is not available. It can further call for passes of at least 5 minutes and at most 20 minutes duration to be scheduled at least 60 minutes and at most 75 minutes apart. With respect to DRS VHF band service, the Scheduler can handle either coded or frequency division multiplex accessing.

The Scheduler produces a tape that contains for each assigned pass, the spacecraft ID number, station ID number, and start and finish times for the pass, which may be different from the actual TIV and TOV. That is, the Scheduler may assign only a portion of the period of visibility. This tape is in the order in which the requirements were filled. To be used with GEMS, the tape must be sorted by station and pass start time. However, the resulting schedule may be examined, without GEMS, in detail, or statistically to evaluate the scheduling process. A detailed printout of the treatment of each requirement is provided for analysis. Included in this printout are (for each requirement) a listing of all the passes assigned, a textual description of the requirement, the number of passes assigned in attempting to fulfill the requirement and a statement as to whether the requirement was fulfilled.

GEMS

GEMS simulates the behavior of a STADAN ground station under the demand specified by the Scheduler output. GEMS is capable of generating statistics on the proportion of scheduled time that is fulfilled, and also indicates the causes of lost data. These causes may include "shortages" (for the scheduled demand) of equipment, spares, repair facilities: excessive prepass time; or equipment failure and repair characteristics. In addition, GEMS can develop separate statistical outputs for many "classes"

of user, within the same station. For example, if a ground station is simultaneously supporting both low orbiting satellites (class 1) and a synchronous satellite (class 2), then it is possible to segregate the demand and good data acquired for each class of user as well as for the station as a whole.

The Monte Carlo technique used in GEMS results in a specific pattern of pseudo-random numbers that are used to control the stochastic events with GEMS. Thus a single run of GEMS for a week may result in a "typical" set of random numbers, or may result in a "rare-event" that has a significant effect on the results. For example, the failure of an antenna drive may occur with an exponential distribution and a mean time before failure (MTBF) of 4 months. However, there is still a finite probability that it will fail in 1 day's operation. (The probability of 10 heads in a row is $(.5)^{10}$; nevertheless, it sometimes happens.) On the other hand, it is expected that on the average an MTBF of about 4 months will be experienced. If in the 1-week run (a single sample) this antenna drive failure is "experienced," the station effectiveness may be seriously degraded. The average results desired cannot be achieved in a short run time.

The law of large numbers indicates that as the number of samples is increased, the "sample mean" can be expected to approach the population mean, i.e., expected average results. Thus, to achieve statistical significance the 1-week schedule must be re-run many times, and the random number sequence varied on each run.

The number of runs are controlled in two ways. First, upper and lower limits are controlled by card inputs. In addition, the output statistics of each run are accumulated and tested for convergence to a steady state value, within a specified "error." When convergence is achieved, the runs are terminated. Printed output includes the statistics for each run, the cumulative statistics, and the number of runs needed to reach convergence.

GEMS begins each run with all equipments up and available, and a full complement of spares. In actual operation, at the start of any schedule interval, some equipments are failed or in repair, spares are depleted, etc., and some equipments are in use. These factors are relatively insignificant for a long run, but for a short run (1 week), the computed effectiveness will be too high due to the favorable disposition of resources at the start of the run.

GEMS therefore permits the input of "initial" conditions prior to the start of a run. Two modes are provided. In the first, initial conditions are entered on cards, and the runs start with the same initial conditions each time. This necessitates the

preparation of a great deal of input data, and is necessary if multiple runs are not used. In any case, this mode is sometimes desirable to force specific initial conditions.

The alternative mode does not require additional input data. The first run begins with all resources available. At the end of the run, the conditions associated with all station resources are retained, and used as initial conditions for the next run. In this way, the simulation is self-initializing. Although the first run will generate somewhat atypical results, the accumulated statistics are unaffected.

SOME INTERESTING RESULTS

Many computer runs exercising one or more modules have been made over the last year. To illustrate the types of information capable of being derived from such runs, two of these will be briefly described. In the first case, single and dual DRS systems' visibility with regard to a typical mix of 42 user satellites was investigated using the Candidate Pass Generator.

It was found that a minimum of 61% visibility is achieved by a single DRS on all user satellites with orbits completely within a 25.08° DRS beamwidth. This number jumps to about 97% when dual DRS are considered. Of these, the satellites with near polar orbits (i.e., inclination angles close to 90°) are afforded the greatest percentage coverage. In fact, such satellites may remain visible for periods of time greater than one orbit. For a nearly circular orbiting satellite at altitude R (from center of the Earth) at least one complete orbit will be visible from a single DRS (see Figure 2) if the inclination angle α of the orbit satisfies $(R_c + R \cos \alpha) \tan \varphi \leq R \sin \alpha$.

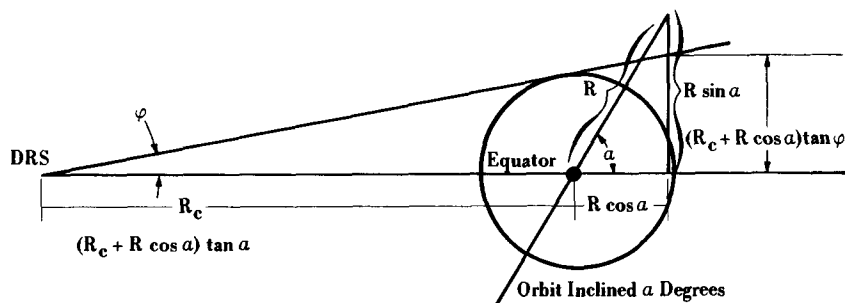


Fig. 2—Geometry for full orbit visibility from DRS

where

R_C = distance from the center of the Earth to the DRS

$$\phi = \sin^{-1} \frac{R_e}{R_C}$$

R_e = radius of Earth.

Although three quarters of the user satellites considered can be fully serviced by a single DRS, only 35% of the total telemetry time required can be handled by the DRS. This is due to the fact that a single DRS (or even dual DRS) can only provide a small percentage of the service required by highly elliptical satellites and these satellites account for a large percentage of the required telemetry time. For the same reason, only a small increase (about 5%) in the percentage telemetry coverage by DRS is achieved by supplying DRS service to satellites whose requirements can only partially be fulfilled by DRS, in addition to those users whose requirements can be completely filled.

The second run of interest involved the exercise of the Scheduler. Of course the Candidate Pass Generator and the Requirements Tape Generator had to be run to generate inputs. A mix of 35 satellites, 14 ground stations and a single DRS was considered. The Scheduler attempted to satisfy 35 requirements, one with respect to each satellite. Each requirement called for telemetry passes with simultaneous command links for 2 minutes at the beginning and end of each pass. The minimum and maximum duration of the passes and the interval between passes were functions of the user satellite. The Scheduler was able to fulfill all but 7 of the requirements. However, these 7 requirements were nearly fulfilled in the sense that only a few required passes could not be assigned. Of the 3,568 passes assigned (equivalent to 45890 minutes) 1,840 passes (23488 minutes) were scheduled for the DRS.

SAS ATTITUDE SUPPORT SYSTEM*

J. L. Snyder[†]; G. F. Meyers^{††}

ABSTRACT

The unique attitude determination, prediction, and control requirements of the Small Astronomy Satellite-1 are satisfied by the SAS Attitude Support System software.

INTRODUCTION

The Small Astronomy Satellite-1 (SAS-1) is the first of a series of earth-orbiting Explorer satellites designed to survey the celestial sphere from above the earth's atmosphere and search for sources radiating in the X-ray, gamma-ray, ultraviolet, visible, and infrared spectral regions inside and outside our galaxy.

Attitude determination for SAS-1 involves decoding telemetry readouts from the spacecraft to ascertain satellite orientation with respect to some known reference system. Accurate knowledge of attitude is necessary both to control the satellite orientation and to aid in the analysis of experiment data.

SAS-1 is a dual-spin stabilized spacecraft. X-ray experiment sensors are mounted in the rotating plane of the satellite. As the spacecraft rotates, the sensors sweep a 10-degree-wide annulus of the celestial sphere perpendicular to the satellite's spin axis. Thus, in order for the sensors to cover the entire celestial sphere, the spin-axis orientation has to be changed systematically by magnetically torquing the spin axis to various predetermined attitudes.

A unique ground control system was designed and implemented at the Goddard Space Flight Center (GSFC) to support SAS-1 and meet the stringent mission requirements established by the SAS Project Office

* Work for this paper was funded under Contract Number NAS5-11790 within the Computation Division, NASA Goddard Space Flight Center.

[†] Computer Sciences Corporation, Silver Spring, Maryland

^{††} Computations Division, NASA/GSFC, Greenbelt, Maryland

and the SAS-1 experimenter, American Science and Engineering. This paper describes the important and novel features of this ground support system, with special emphasis on the SAS Attitude Support System software used to control the orientation of the spacecraft. The paper concludes with a summary of the operational experience acquired when the SAS Attitude Support System was used for the SAS-1 mission and a discussion of the performance of the software subsystems relative to the mission requirements.

SAS PROFILE

MISSION OBJECTIVES

Spacecraft SAS-1 was launched from the San Marco platform off the coast of Kenya, Africa in the early morning of December 12, 1970. After injection, the satellite achieved its nominal circular orbit with a radius of 300 nautical miles, an inclination of 2.9 degrees, and an orbital period of 95 minutes. A yo-yo despin from 180 rpm to 5 rpm was followed by a despin by ground command to the spacecraft nominal 1/12 rpm using an onboard magnetic spin-despin subsystem. Deployment of the yo-yo caused four spring-loaded solar paddles to lock into position, making SAS-1 operational.

The primary objective of the SAS-1 spacecraft is to detect and measure X-ray sources throughout the celestial sphere. Specifically, the mission studies the position, strength, spectral composition, time variation, and correlation with optical and radio sources, of known X-ray sources and of new sources discovered by the spacecraft instruments. This process includes searching for temporal variations of several percentages in X-ray source intensity, over periods of minutes to months, and determining the spectral distribution in the energy range from 2 to 20 kev for all sources detected.

Effective performance of these studies requires a near equatorial orbit that bypasses the South Atlantic anomaly where the radiation belts extend far into the earth's atmosphere. This 300 nautical mile orbit prevents deterioration of the satellite's operation by maintaining a minimum X-ray background count which could otherwise adversely affect data obtained by several types of experiment sensors used in satellite astronomy.

SPACECRAFT CONFIGURATION

The basic structure of SAS consists of an experimenter's instrument package mounted on top of a control package (see Figure 1). The instrument package houses all the sensors and electronics in a dual-module structure covered by a thermal shroud, with provisions for sensor-viewing ports.

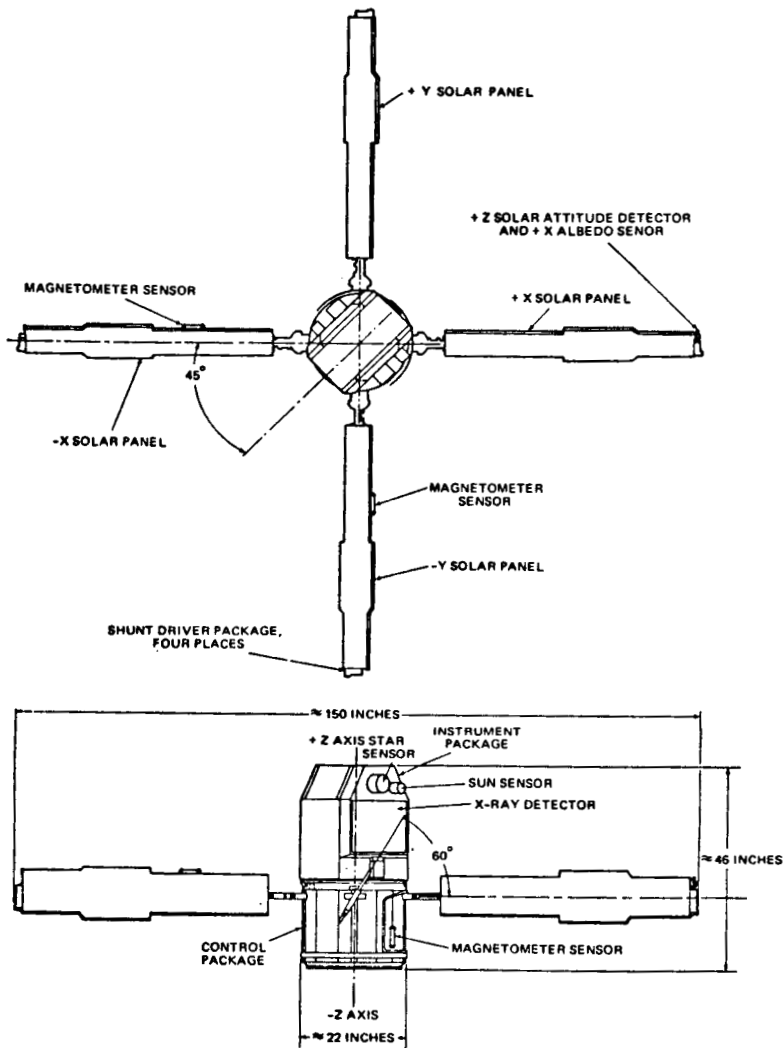


Figure 1. Small Astronomy Satellite-1 Configuration

The control package is a cylinder 22 inches in diameter, consisting of an outer shell and an inner deck. A nutation damper and electronics books are mounted on the underside of the deck, while the transmitter, stabilization rotor, tape recorder, and batteries are supported by the top of the deck. The upper end of the cylinder interfaces with a transition ring that supports the instrument package. Four hinge assemblies, attached to the cylinder exterior, support the solar paddles. These paddles are folded down against the cylinder during launch. Upon deployment, they are perpendicular to the cylinder surface and canted 30 degrees from the spin or Z-axis.

The satellite's nominal spin rate of $1/12$ rpm is not sufficient to keep the spin-axis drift rate below the maximum allowable rate of 5 degrees per day. Therefore, a high-speed rotor was included in the attitude subsystem to provide adequate momentum for good gyro-stabilization. The rotor system consists of a 10-inch diameter flywheel driven at a constant 2000 rpm by an alternating hysteresis synchronous motor. Additional stability is achieved by an onboard nutation damper which dissipates energy associated with spin-axis nutation. Spin rate control of the spacecraft is accomplished using signals from the X- and Y-axis vector magnetometers mounted on two solar panels to form an orthogonal triad with the Z-axis magnetometer mounted on the outer shell parallel to the spin axis. These signals are amplified and applied in quadrature to direct current amplifiers that supply power to the X- and Y-axis torquing coils. In the best case, where the spin axis is perpendicular to the geomagnetic field, the rate change is 0.005 rpm per minute.

ATTITUDE MISSION REQUIREMENTS

Three types of onboard attitude sensors are used to determine spacecraft attitude: an Adcole Digital Solar Attitude Detector (DSAD), three induction magnetometers manufactured by the Schonstedt Instrument Company, and two American Science and Engineering star sensors.

The DSAD, mounted in the rotating plane of the satellite, determines the time at which the sun line crosses the sensor and the angle between the sun and the +Z-axis of the spacecraft to an accuracy of 0.5 degrees. The DSAD is positioned on the control section of the satellite at -135 degrees from the spacecraft +X-axis and furnishes sun information once for each spin revolution of the satellite.

Nominally, the three magnetometers are mounted orthogonally on the spacecraft and aligned to the spacecraft coordinate system. The +Z-magnetometer is mounted parallel to the spin axis on the control section of the spacecraft at approximately -45 degrees from the +X-satellite axis. Both the X- and Y-magnetometers are mounted on the top edges of the solar paddles, with the X located on the -X solar paddle,

and the Y located on the -Y. The three magnetometers are sampled sequentially once every 49.152 seconds and each is time tagged. The individual readings are 0.768 seconds apart. The measuring accuracy of this particular system under operating conditions is ± 3.5 millioersteds, which is expected to produce attitude accuracies to better than 5 degrees.

Each of the star sensors consists of a lens that focuses starlight through an N-shaped reticle onto a sensitive photomultiplier. The signal produced by the detector is amplified, integrated into a pulse, digitized, and inserted into the telemetry stream. Because the sensor is mounted with the reticle parallel to the spin axis, the vertical slits generate star azimuth data as they sweep a path across the celestial sphere during spacecraft rotation. The oblique slit in the reticle can provide star elevation information to a one arc-minute resolution. Both sensors are mounted in the rotating plane of the satellite in the experiment section. One is mounted at -45 degrees to the spacecraft X-axis and the other at 135 degrees.

To reorient the spin axis, a coil wound parallel to the satellite's X-Y plane is energized to produce a dipole along the spacecraft spin axis of approximately $\pm 10,000$ or $\pm 50,000$ pole-centimeters (p-cm). This dipole reacts with the earth's magnetic field to produce a torque normal to the Z-axis, causing the satellite to precess. With the 50,000 p-cm coil setting, the precession rate is about 1.7 degrees per minute. SAS-1 also carries a programmable timer that allows the torquing coil to be turned on and off once within 60 minutes after the timer is activated over a tracking station. The timing increment is 2.5 minutes.

With only a nominal six-month prime spacecraft lifetime for detecting and mapping X-ray sources, SAS-1 must scan the celestial sphere and special regions of interest quickly. Consequently, the attitude of SAS is changed daily to a new spin axis orientation specified in a monthly schedule furnished by the experimenter. Rapid reorientation of the satellite is also necessary to meet special event coverages required by the experimenter. Special events are X-ray source occurrences of unusual interest which, being of short duration, have to be brought into the field-of-view of the experiment sensors quickly in order to perform ground and sounding rocket coordinated observations. Within two orbits after notification of such an event, the spin axis has to be magnetically torquing into position for the coverage.

ATTITUDE GROUND SUPPORT SYSTEM

GROUND SUPPORT HARDWARE

The prime tracking station for normal mission operations of the SAS-1 satellite is Quito, Ecuador. Because only one tracking station

was scheduled, an onboard GSFC closed-loop tape recorder is used to store data over the entire orbit. Data is recorded at the rate of one kilobit per second and played back over the station at 30 times the recording rate using a VHF downlink.

During each station acquisition, Quito receives approximately 3.5 minutes of real-time data, followed by the tape recorder dump in about the same amount of time. After the dump, real-time data is again received until the end of the pass. Real-time segments of data are sent directly to GSFC. Selected playback passes are also sent to GSFC immediately following the completion of the pass. All SAS-1 data is passed by way of a 2400 bps Data Transmission System from Quito to the XDS 930 computer in the Multi-Satellite Operations Control Center at GSFC. There the attitude-related information is stripped from the telemetry stream, reformatted, and simultaneously written on a seven-track backup magnetic tape and sent by way of 2400 bps Attitude Data Link to an IBM System 360 Model 95 (360/95) computer through an IBM 2703 Transmission Control Unit. Using the Binary Synchronous Communications feature in the transparent mode, the 2703 receives the attitude data in a half-duplex mode and passes it to a Telemetry Data Handling Program which is resident on the 360/95. This program receives all attitude data, and stacks it in the appropriate satellite-dependent data set on a private IBM 2314 disk pack. From there, or from the backup Control Center Attitude Tape, the data is processed by the Attitude Support System software.

Throughout the SAS Attitude Support System, extensive use is made of interactive graphics capabilities on IBM 2250 and 2260 display units. These capabilities provide the operator with a means to input run control parameters, to monitor results, and to implement decisions on-line.

Figure 2 illustrates the SAS-1 ground support system.

ATTITUDE SUPPORT SOFTWARE SYSTEM

The SAS Attitude Support System consists of FORTRAN, PL/I, and Assembler Language programs operating on the 360/95. In support of the SAS-1 mission, the basic functions of the system are to monitor the status of onboard attitude related hardware, to determine the spacecraft attitude accurate to the limits of onboard sensors, and to calculate the magnetic control commands necessary to accomplish desired spin-axis reorientations.

The system consists of five subsystems: the Telemetry Processor Subsystem, the Bias Determination Subsystem, the Sun/Mag Attitude Determination Subsystem, the Star Attitude Determination Subsystem, and the Attitude Prediction/Control Subsystem. In general, the subsystems are serially executed in the order listed, with each subsystem

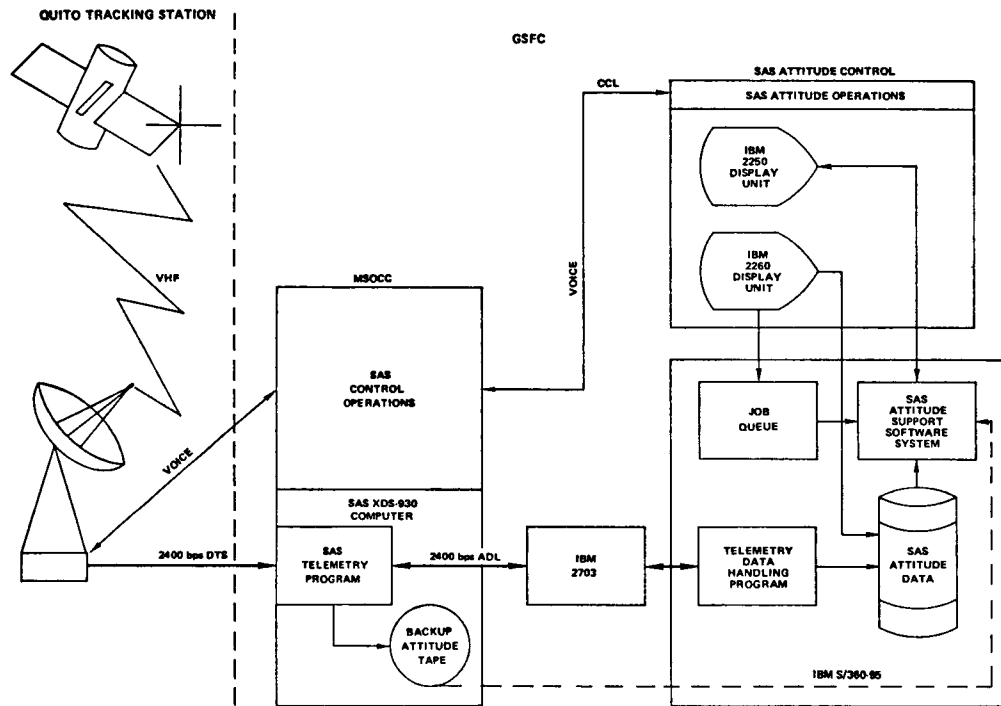


Figure 2. Attitude Ground Support System

providing data to one or more of the following subsystems. Figure 3 illustrates the basic software flow and indicates the data sets used for communication between subsystems.

The Telemetry Processor Subsystem reads the data set generated by the Telemetry Data Handling Program and sorts, screens, calibrates, and converts the data to engineering units. Attitude-related hardware parameters, sun sensor and magnetometer readings, and star sensor readings are written into three separate sequential disk data sets.

The Bias Determination Subsystem calculates the magnetometer bias and misalignment angles using magnetometer readings from the data set generated by the Telemetry Processor Subsystem. Since these parameters should not change over short periods of time, this subsystem is usually run "off-line" (as indicated in the figure).

The Sun/Mag Attitude Determination Subsystem calculates the spacecraft attitude using the sun sensor and magnetometer readings from the data set generated by the Telemetry Processor Subsystem and the correction factors provided by the Bias Determination Subsystem. Spin-axis orientations obtained from these readings are accurate to within three degrees of arc.

The Star Attitude Determination Subsystem calculates the spacecraft attitude using the star sensor readings from the data set generated by the Telemetry Processor Subsystem and the attitude determined by the Sun/Mag Attitude Determination Subsystem. Spin-axis orientations obtained from these readings are accurate to within one-half degree of arc.

The Attitude Prediction/Control Subsystem predicts the spacecraft attitude, using the attitude determined by either the Sun/Mag or the Star Attitude Determination Subsystem, and calculates the control commands necessary to accomplish desired spin-axis reorientations.

MISSION SUPPORT-OPERATIONS

Normal daily attitude operations begin with the first station acquisition after 6 a.m. GSFC local time. Data from this station pass is used to determine the attitude of SAS-1 in order to calculate the commands required for the next reorientation. Both segments of real-time data are sent immediately to GSFC; playback data is sent during a 50- to 60-minute period following the pass. As the data is being received at the 360/95 by the Telemetry Data Handling Program, the raw attitude data is being monitored on an IBM 2260 Display Unit.

IBM Graphics Terminal System (GTS) is a program for graphics devices which allows the user to edit card-image data sets on IBM 2314 disk packs, submit jobs into the job stream queue, and execute jobs

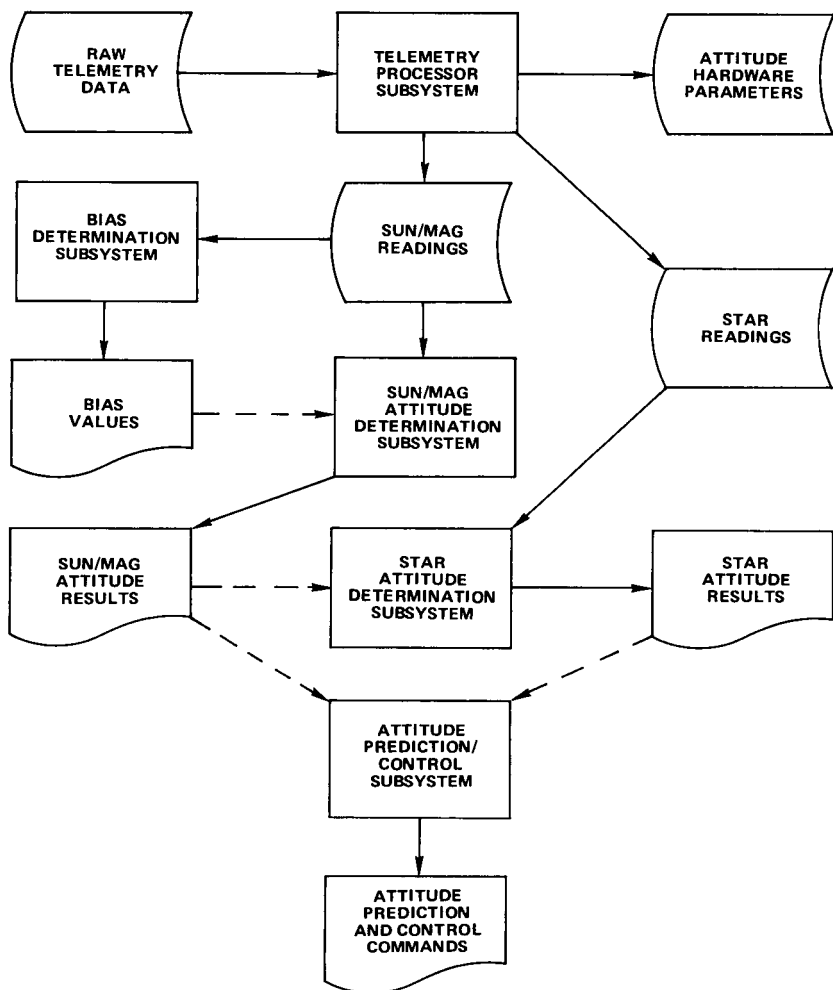


Figure 3. SAS Attitude Support System Software Flow

attached to the master GTS program. Attached jobs use the core and initiator assigned to GTS and begin execution immediately upon submittal. This feature of GTS is frequently used for SAS-1 to determine where to begin processing within the attitude telemetry data set and to view the data qualitatively to determine if there are large segments of unusable data. When sufficient playback data has been received, the Telemetry Processor, Sun/Mag Attitude Determination, and Star Attitude Determination Subsystems are submitted to the job queue via GTS. The computed attitude is then used as input to the Attitude Prediction/Control Subsystem which determines the complete set of commands needed to accomplish the daily maneuver.

The series of magnetic torquing commands is delivered directly to the Multi-Satellite Operations Control Center. Here the commands are encoded and communicated to Quito for execution.

These commands are implemented on successive orbits until the desired attitude is achieved. On selected intermediate playback passes, the latest attitude is calculated using sun and magnetometer data and compared to the predicted attitude. Should they differ significantly, the computed attitude is input to the Attitude Prediction/Control Subsystem and the remainder of the commands are regenerated. The command sequence is then resumed. Under normal conditions a maximum of three torques are sent without attitude verification.

After all of the commands are implemented, the attitude is determined using star data. If this attitude is more than 2.5 degrees in arc distance from the desired attitude, new commands are generated to move within the desired limits and the attitude is recalculated. Once at the desired attitude, three consecutive playback passes are sent to GSFC for "quick-look" processing. The attitude of the spacecraft is calculated from star data on the first of these three orbits and furnished to the experimenter on a daily basis. For the remainder of the 24-hour period, this attitude is held unless the spacecraft drifts more than five degrees. In that event, commands are established to bring the spin axis within the 2.5-degree tolerances. Once the desired attitude is reached, a prediction run is made to predict the spin-axis drift for the remainder of the 24-hour period. The resultant attitude is then used to generate tentative commands for the next day's maneuver. These commands are used in the event that computer failures delay obtaining attitudes at the beginning of the next day's reorientation period.

With the occurrence of special events, which can occur anytime during the 24-hour period, the experiment notifies the SAS attitude control center of the location of the X-ray source. Within two orbits after notification of such an event, the commands must be initiated to begin maneuvering the spin axis into position to view the desired source. Once the

new attitude is achieved, the spin axis is not allowed to drift more than 2.5 degrees. If this occurs, the spacecraft is maneuvered back into position.

ATTITUDE SUPPORT ANALYSIS

BIAS DETERMINATION

Experience with previous satellites has shown that spin-axis attitudes obtained from induction magnetometer readings are subject to several types of instrument error (Reference 1). These systematic errors include sensor mounting errors and sensor biases. Once these errors have been determined, it is possible to correct for them and improve the accuracy of the attitude determination process. Random noise arising from the coarseness of the instruments or of the telemetry will be filtered out by a differential correction process.

Nominally, the three magnetometers on SAS-1 are mounted so that one is parallel to the geometrical symmetry axis and the other two are perpendicular to the symmetry axis forming a right-handed orthogonal triad. Three cases may be considered as examples of possible mounting error. A systematic error occurs if the individual magnetometers are mounted improperly. In this case, the triad is no longer orthogonal and cannot measure the geomagnetic field vector correctly. A second type of instrument error can occur even if the magnetometers are mounted correctly. This error arises when the spin axis does not coincide with the symmetry axis. Then the triad, as a unit, is coherently misaligned to the spin axis. A third source of error results if the triad, as an orthogonal unit, is mounted so that it is misaligned to the symmetry axis.

In addition to the errors due to non-orthogonality and misalignment, the magnetometers register a residual bias due to residual spacecraft magnetism and sensor bias. This bias is linearly superimposed on the magnetometer's measurement of the geomagnetic field.

Some of these errors may develop after launch; therefore, it is necessary to be able to determine them in flight. A method for determining residual bias was developed which is also capable of determining the alignment and the orthogonality of the magnetometer triad.

Since a correct measurement of the geomagnetic field strength is impossible with a non-orthogonal triad, the model cannot depend on such a measurement. Complications caused by non-orthogonality are avoided by treating each magnetometer separately. If each is then referenced to the same inertial coordinate system, the angles between the three sensors can be determined. A magnetometer measurement is described mathematically as the dot product of the magnetic field vector with a unit vector along the direction defined in the same coordinate system. A suitable

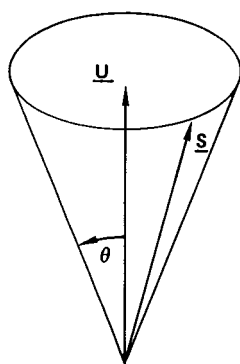
system is an inertial spherical coordinate system with the spin axis as the Z-axis. Due to the stringent requirements concerning a low drift rate and small nutation amplitude for SAS-1, the assumption of the spin axis being inertially fixed is easily fulfilled. In order to describe the magnetometer's reading, the geomagnetic field must be known in the spin-inertial system. Mathematical models provide geomagnetic field vectors in geocentric inertial coordinates. These are transformed to the spin-inertial system using a recently determined attitude from star sensor data.

A least-squares solution is applied to the readings of each magnetometer to determine simultaneously the sensor's position in spacecraft coordinates and the associated residual bias. At the completion of the least-squares solution for each of the three magnetometers, their directions are known in the same coordinate system. Dot products taken among the triad yield the cosines of the angles between pairs of magnetometers. With these angles it is possible to determine whether the triad is orthogonal or not. If not, it may be possible to determine the type of non-orthogonality and correct for it. (One type of non-orthogonality would be that arising from improper deployment of the solar paddles.)

SUN/MAG ATTITUDE DETERMINATION

Attitude determination using sun sensor and magnetometer readings is a two-step process. First, the spin-axis orientation is calculated from direct and indirect sensor measurements of the angle between the satellite spin axis and known directions in space. Then the readings are used to calculate the spin rate and rotational orientation of the spacecraft, based upon the spin-axis orientation.

The SAS-1 sun sensor and magnetometer triad are used to determine the angles between the spin axis and the sun line and between the spin axis and the local magnetic field direction respectively. The sun line and local magnetic field direction are assumed to be well known from ephemeris and physical models. Once the magnetometer readings have been corrected for local bias and misalignment and the sun sensor readings have been corrected for misalignment, a single angle measurement θ from either sensor locates the spin axis on a cone with generating angle θ about the associated known direction line (see Figure 4). With three or more perfect measurements, all conical loci for the spin axis intersect in a common line whose spatial orientation unambiguously defines the spin-axis attitude. Of course, because of angle measurement errors, an exact common intersection of the locus cones is never obtained in practice (see Figure 5). Thus the problem does not admit a deterministic solution. To make use of all available data, it is natural to seek an



CONICAL LOCUS FOR \underline{S}
 \underline{S} = UNIT SPIN AXIS
 \underline{U} = UNIT CONE AXIS
 θ = CONE ANGLE

Figure 4. Single Cone Locus

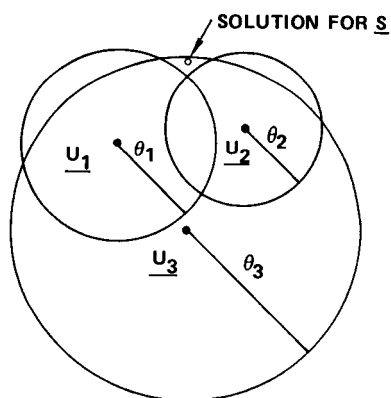


Figure 5. Top View of Multiple Cone Intersections

approximate "best intersection" of all cones, in some least squares sense, as defining the attitude solution.

The attitude may be defined in terms of right ascension (α) and declination (δ) rotation angles in the geocentric inertial system (Figure 6). Since this type of geometrical problem is inherently nonlinear and difficult to solve in such a form, linearizing about an a priori attitude state estimate (α_0, δ_0) is necessary. The solution is then developed as a linear differential correction ($\Delta\alpha, \Delta\delta$) to this estimate. Letting the updated attitude $\alpha_0 + \Delta\alpha, \delta_0 + \Delta\delta$ take the role of α_0, δ_0 , the process can be repeated iteratively until convergence; i.e., until the corrections fall below some preassigned tolerance level.

In order for the attitude (α, δ) to lie closest to n locus cones at once, the criterion adopted is that the n equations of conditions:

$$\cos \theta_i = \hat{U}_i \cdot \hat{S} = (U_x)_i \cos \alpha \cos \delta + (U_y)_i \sin \alpha \cos \delta + (U_z)_i \sin \delta \quad (i = 1, \dots, n)$$

should be simultaneously satisfied in the sense of weighted least squares of residuals in the $\cos \theta_i$. (U_x, U_y, U_z) are the direction cosines of the i th locus cone axis U_i in geocentric inertial coordinates, and $\cos \alpha \cos \delta$, $\sin \alpha \cos \delta$, and $\sin \delta$ are the direction cosines of the spin axis \hat{S} . Linearizing the solution to this problem in the usual manner about an initial attitude state estimate (α_0, δ_0) gives rise to the differential correction equation (Reference 2):

$$\begin{bmatrix} \Delta \alpha \\ \Delta \delta \end{bmatrix} = \left[H^T K^{-1} H \right]^{-1} H^T K^{-1} \begin{bmatrix} \rho_1 \\ \vdots \\ \rho_n \end{bmatrix}$$

H is an $n \times 2$ matrix of partial derivatives of the observables $\cos \theta_i$ with respect to the attitude state variables α, δ , evaluated at the estimated state α_0, δ_0 . The weighting matrix K is the $n \times n$ diagonal covariance matrix of errors in the observables. Each residual ρ_i is defined as the difference between an observed $\cos \theta_i$ and the corresponding value obtained using α_0, δ_0 . Thus:

$$\rho_i = \cos \theta_i - ((U_x)_i \cos \alpha_0 \cos \delta_0 + (U_y)_i \sin \alpha_0 \cos \delta_0 + (U_z)_i \sin \delta_0)$$

These two equations are the differential corrections to the initially estimated state (α_0, δ_0).

α = RT. ASCENSION
 δ = DECLINATION
 X, Y, Z = GEOCENTRIC
 INERTIAL
 COORDINATE
 AXES

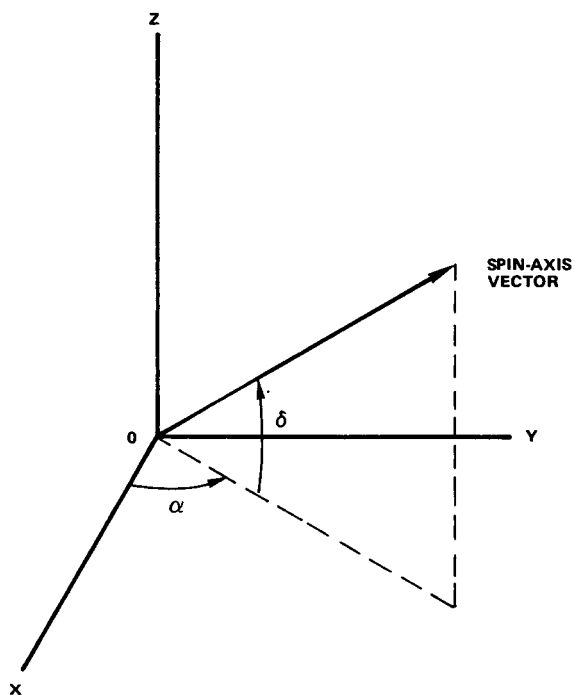


Figure 6. Spin Axis Attitude Parameters

Spacecraft spin rate may be calculated from magnetometer data alone if the spacecraft attitude and the geomagnetic field vector are known in inertial coordinates.

The total apparent motion of the geomagnetic field in the spacecraft coordinate system (spin system) $\Delta\gamma$ is given below (see Figure 7), where X_1 and Y_1 are the X and Y magnetometer readings at time t_1 , and X_2 and Y_2 have a similar meaning.

$$\Delta\gamma = \tan^{-1} \left(\frac{Y_1}{X_1} \right) - \tan^{-1} \left(\frac{Y_2}{X_2} \right)$$

Part of this apparent motion is due to spacecraft spin and part is due to the change in the geomagnetic field arising from the change in spacecraft orbital position from time t_1 to time t_2 . To calculate the apparent motion due to the latter cause, a spin inertial coordinate system is defined. The Z-axis of this system is parallel to the spacecraft Z-axis, but the system is inertially fixed. Using Goldstein's (Reference 3) convention, the following angles of rotation may be used, where α and δ are the right ascension and declination of the spacecraft spin-axis:

$$\phi = \alpha + \frac{\pi}{2}$$

$$\theta = \frac{\pi}{2} - \delta$$

$$\psi = 0.0$$

The third rotation angle, ψ , is arbitrary and is chosen for convenience to be zero. The geomagnetic field vector in inertial coordinates

$\begin{pmatrix} X_I \\ Y_I \\ Z_I \end{pmatrix}$ is transformed to spin inertial coordinates, using Goldstein's

matrix A:

$$\begin{pmatrix} X_S \\ Y_S \\ Z_S \end{pmatrix} = A \begin{pmatrix} X_I \\ Y_I \\ Z_I \end{pmatrix}$$

The angular change is given by the following equation, where X_{S1} and Y_{S1} are at time t_1 , and X_{S2} and Y_{S2} are at time t_2 :

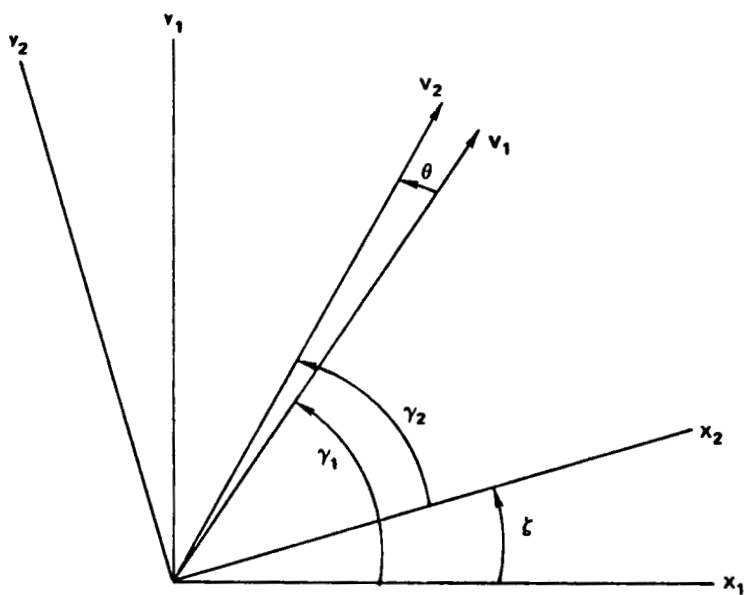


Figure 7. Magnetometer Spin Rate

$$\theta = \tan^{-1} \left(\frac{Y_{S2}}{X_{S2}} \right) - \tan^{-1} \left(\frac{Y_{S1}}{X_{S1}} \right)$$

The spin rate is given by the following equation:

$$\omega = \frac{\Delta\gamma + \theta}{t_2 - t_1}$$

Using the spin-inertial system defined above, the angle between the spin-inertial system and the spin system (σ), which determines the rotational orientation, is given by the following equation, where all the values are as previously defined:

$$\sigma = \tan^{-1} \left(\frac{Y_1}{X_1} \right) - \tan^{-1} \left(\frac{Y_{S1}}{X_{S1}} \right)$$

STAR ATTITUDE DETERMINATION

Spacecraft attitude can be refined for SAS-1 using star sensor data. As the satellite spins, stars transit the slit system of the star sensors and generate a stream of pulses (see Figure 8), the amplitudes of which are a function of the magnitude of the star. The time difference between pulses from the same star through different slits in the sensor reticle provides information about the spin rate and the elevation of the star with respect to the body-fixed spacecraft coordinate system. The spin-axis determination process of the program involves using a pattern recognition system to identify the stars which caused the observed pulses. This recognition system compares the processed telemetry pulses to a system-resident catalog of known star positions. The star catalog is edited on the basis of the less accurate sun/magnetometer attitude.

The first step in reducing star data is to translate the telemetry data frames into events that make up the star pulse stream. The next step is to determine the spacecraft spin rate using event frequencies. The program searches the distribution of time differences between possible pairs of pulses for a peak. In theory, the peak then corresponds to the true spin rate.

Next, the events, or star pulses, are grouped into "triplets." A triplet is a group of three pulses that represents the transit of a single star across the three slits of the star reticle (Figure 9). Since the middle slit is not parallel to the outer slits, the time differences within a

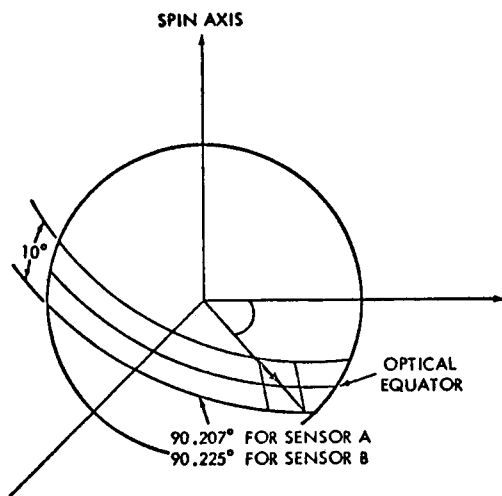


Figure 8. SAS-A Scanner Field-of-View on Celestial Sphere

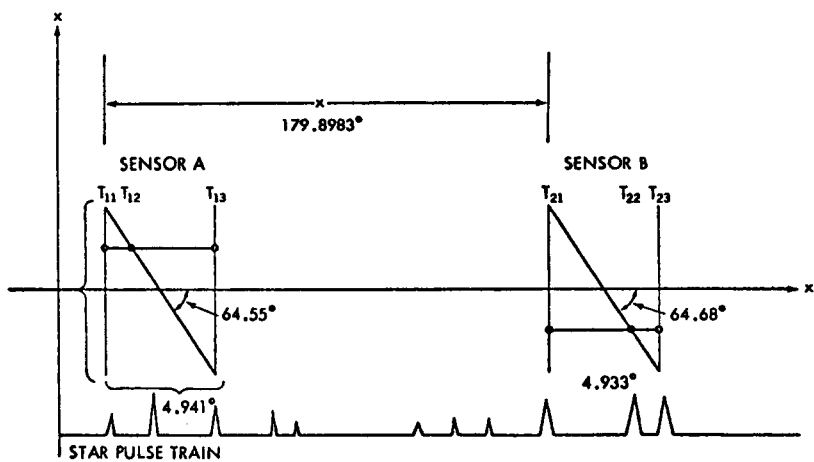


Figure 9. Slit Geometry of the SAS-A Star Sensor

triplet can be used to determine the star elevation from the plane normal to the spin axis. The time associated with the transit of the first slit is converted to an azimuthal angle.

Once the triplets with their azimuth and elevation have been determined, the process of star identification is performed. The star identification process for the case in which no stars have been previously matched with transits is based on matching angular separations of stars in the catalog to angular separations between triplets. Once the stars have been identified with triplets, the spin-axis orientation is determined using a least squares fit to the observed elevation angles.

ATTITUDE PREDICTION/CONTROL

SAS-1 attitude motion is caused primarily by the following disturbance torques: magnetic, aerodynamic, solar, and geopotential. Magnetic torque is the result of either the spacecraft residual moment or the magnetic attitude control coil. Mathematical models are used to calculate values for disturbance torques, given the spacecraft orbital position and attitude.

The spin axis vector is assumed to be along the total angular momentum vector, \bar{H} , of the spacecraft. By integrating the motion of \bar{H} under these torques, the attitude of the spacecraft is predicted as a function of time for a given set of initial conditions. Thus:

$$\bar{H}(t) = \bar{H}_0 + \int_{t_0}^t \bar{T}(\tau) d\tau = \bar{H}_0 + \Delta\bar{H}$$

where \bar{T} is the sum of disturbance torques. The radial component of \bar{H} is considered to contribute to a spin rate change only while the normal component causes precession. The total angular momentum is the sum of the momentums resulting from the spinning spacecraft and the momentum wheel. Simpson's Rule is used to evaluate the integral.

The magnitude of the magnetic torque varies directly with the magnitude of the satellite magnetic moment and the earth's magnetic field vector. In general, this torque is a major cause of attitude motion. However, if a satellite has an onboard magnetic moment that generates a magnetic torque that is small relative to the total torque, or if the orbit is of such a nature as to avoid the earth's magnetic field, then the magnetic torque will produce little or no change in attitude.

The aerodynamic torque is predominantly a function of the density of the ambient atmosphere, the satellite surface, and the satellite surface coefficients of normal and tangential momentum transfer. In general, the magnitude of this torque decreases rapidly as the altitude increases.

However, since most existing attitude prediction programs do not include modules to compute this torque, little is known about its long range effect on attitude.

The direct solar radiation pressure torque is basically a function of satellite surface parameters, which include coefficients of diffusivity and reflectivity, and the surface area exposed to incident solar radiation. The magnitude of this torque varies directly with the square of the ratio of the earth-sun to the satellite-sun distances; however, this ratio is usually (very) close to one so that this variation may be ignored. In general, the direct solar radiation pressure torque is only significant for satellites whose area-to-mass ratio is large ($A/M > 10$ with A and M expressed in cgs units).

The magnitude of the geopotential torque is inversely proportional to the square of the distance from the center of the earth to the satellite center of mass and is a function of the satellite mass and moments of inertia. Thus the magnitude of the geopotential torque decreases with the distance from earth. On a spin-stabilized satellite this magnitude varies directly with the sine of twice the angle between the spin axis and the satellite position vector. Hence, the magnitude may be periodic over an orbit. The geopotential torque generally has a perturbative effect on attitude, although for satellites with high enough perigee, it too may be negligible.

The primary function of the Attitude Prediction/Control Subsystem is to calculate commands that are used to accomplish desired spin-axis reorientations. For one station pass, the command consists of a time to turn the coil on, a time to turn it off, and a setting for the magnetic attitude control coil. Each minute of "on-time" with a setting of either plus or minus 50,000 cm will result in spin-axis motion averaging 1.7 degrees of arc/min. Due to the low inclination of the SAS-1 orbit, spin axis motion induced by magnetic torque is primarily in the direction of right ascension. Declination motion is significantly less than motion parallel to the equatorial plane. Thus, if the desired spin-axis reorientation consists primarily of declination motion, a series of maneuvers may be required, resulting in a "zig-zag" motion to the final spin-axis orientation (Figure 10). The attitude control problem is basically one of finding the best set of commands to either directly or indirectly reach the final spin-axis orientation. This problem is solved by optimizing on the subsystem's magnetic torque model. Inspection of the present and desired attitudes indicates whether a direct or zig-zag maneuver is required. For a direct maneuver, the subsystem will compute the command which will result in a final attitude closest to the desired attitude. For a zig-zag maneuver, the subsystem will compute the command which

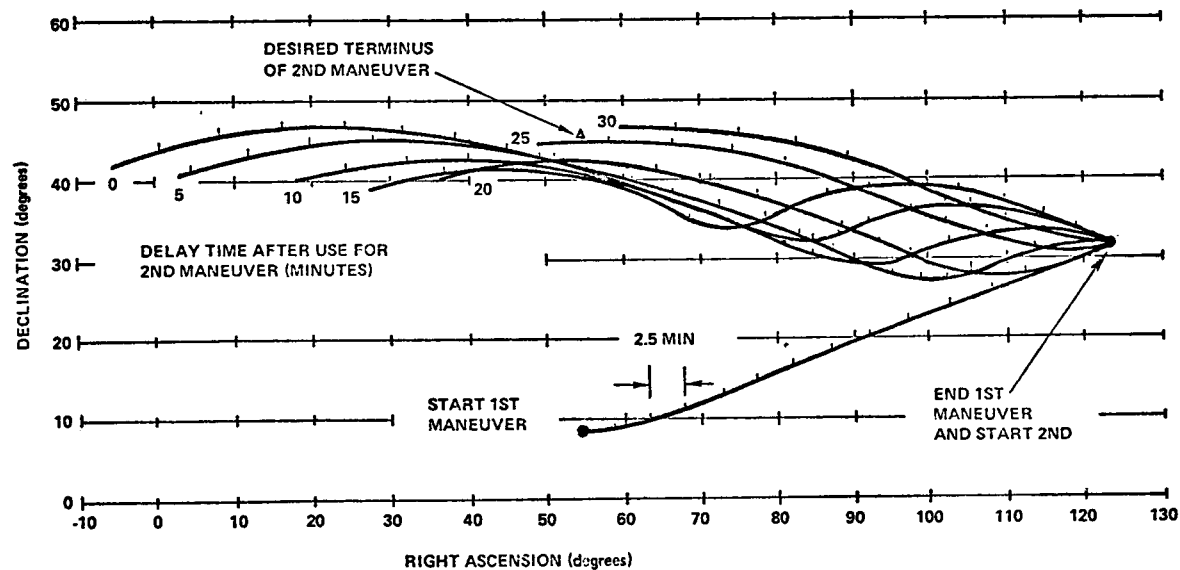


Figure 10. SAS-1 Declination Maneuver Sequence

produces the largest change in declination in the direction of the desired attitude. If this command is implemented, the resulting intermediate attitude becomes the present attitude and the entire process is repeated.

CONCLUSIONS

The SAS Attitude Support System was designed and implemented at GSFC by Computer Sciences Corporation. The software has operated according to design specifications in support of the SAS-1 mission since the day of launch.

The Sun/Mag Attitude Determination Subsystem provides attitudes which are sufficiently accurate to be input to the Attitude Prediction/Control Subsystem for the calculation of control commands. Daily spin axis reorientations and coverage of special events which satisfy mission objectives are performed using these commands. The Star Attitude Determination Subsystem provides very accurate attitudes which are normally used for the evaluation and analysis of experiment data.

The Bias Determination Subsystem was developed to ensure adequate support with magnetometer data alone. Although the SAS spacecraft proved to be magnetically clean with properly aligned magnetometers and all attitude sensors have performed well, this subsystem represents an advance in the analytical methods used to determine systematic sensor bias.

The direct data link with the spacecraft control center and the extensive use of interactive graphics within the SAS Attitude Support System result in a significant operational advantage for near real-time attitude support.

REFERENCES

1. Ferrenteno, A. B., "Attitude Processing for the Satellite AE-B," IBM Federal Systems Division Technical Memorandum, Gaithersburg, Md., December 1966.
2. Schlegel, L. B., "Cones: An Iterative Differential Technique for Attitude Determination of a Spinning Satellite," IBM Federal Systems Division Technical Memorandum, Gaithersburg, Md., May 1967.
3. Goldstein, H., Classical Mechanics, Addison-Wesley Publishing Co., Inc., Reading, Mass., 1965.

TECHNIQUES ASSOCIATED WITH THERMAL-VACUUM TESTING OF THE OAO-C HEAT PIPES

James P. Marshburn, *NASA, Goddard Space Flight Center, Greenbelt, Md.*

ABSTRACT

The OAO-C spacecraft has three circular heat pipes, located in the space between the spacecraft structural tube and the experiment tube, which pipes are designed to isothermalize the structure. Each pipe, experimental in nature, is of a different design. Two are used to transport high-heat loads and the third is for low-heat loads. The mechanical problems associated with testing the two high-heat load pipes are discussed in this paper. One of these pipes was tested three times before being accepted. The first test resulted in the discovery of non-condensable hydrogen gas, which prevented the pipe from functioning properly. The second test was a repeat of the first, to see if all the gas had been removed. The third test was to see if any changes had occurred to the pipe as a result of saddle modifications. Saddle modifications were necessary because the epoxy binding agent between the saddles and the pipe had decomposed during the testing.

The test problems discussed deal with the specially designed heat-removal devices, the mobile tilt table, the table position indicator, and the heat input mechanisms, all of which were necessary to conduct a high-heat load, thermal-vacuum test. The final results showed that the techniques used were adequate for thermal-vacuum testing of heat pipes.

INTRODUCTION

The three OAO-C heat pipes, illustrated in Figures

1 and 2, were designed and built for two purposes -- (1) to isothermalize the spacecraft structure and (2) to fly as an experiment. All three pipes were made of 6061-T6 seamless aluminum tubing, and the working fluid in each is anhydrous ammonia with a specified purity of 99.995% with less than 50 ppm of H_2O . The two high-heat transport pipes were designed (1) to operate for 12,000 hours or more (Ref. 2); (2) to carry the spacecraft heat load of 500 watt-inches along the entire pipe with a maximum delta temperature (ΔT) of $1.6^\circ C$; (3) to carry an auxiliary heater load of 4,400 watt-inches with a maximum ΔT of $6.7^\circ C$; and (4) to carry 7,000 watt-inches in a 1-G field, with the evaporator elevated $3/4"$ (or 0.92 degree) above the condensers, at a maximum ΔT of $11.1^\circ C$. The low-heat pipe was designed to meet the requirements of (1) and (2) above. Satisfactory performance of these conditions in the temperature range of $-40^\circ C$ to $+30^\circ C$ must also be demonstrated (Ref. 1).

Each pipe forms a torus 46.9 inches in diameter, with a nominal four-inch gap. The wall thickness is 0.035 inches, and the pipe O.D. is 0.500 inch. Only the hollow artery and the spiral artery pipes were thermal-vacuum tested. Since test problems for both pipes are similar, only the problems associated with the testing of the spiral artery pipe are discussed.

Test Setup

In order to meet the four basic requirements in the $-40^\circ C$ to $+30^\circ C$ temperature range, it was necessary to utilize a vacuum-rated tilt table (Figure 3), a variable-control heat-removal device, and vacuum-rated heaters.

The 52-inch by 52-inch aluminum tilt table was elevated by an encased (sealed) slo-syn vacuum-rated motor (Figure 3, lower center), with a heater. The heater was thermostatically controlled to keep the motor at $+20^\circ C$ throughout the test. In order to determine the tilt position, a vacuum-rated linear potentiometer was calibrated and used to monitor the table position throughout the test. The overall table levelness was $\pm 1/32"$ with a $\pm 1/64"$ positioning accuracy.

The heat removal system consisted of two auxiliary Conrad cooling units or condensers, the tubes of which

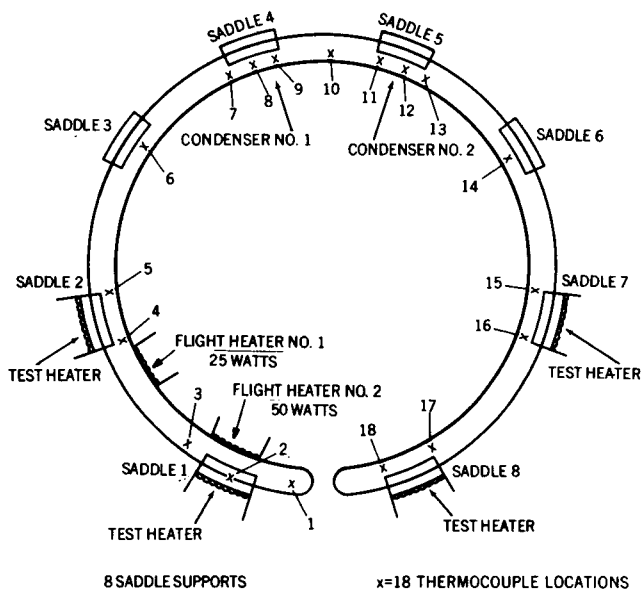


Fig. 1-Heat Pipe Test Setup

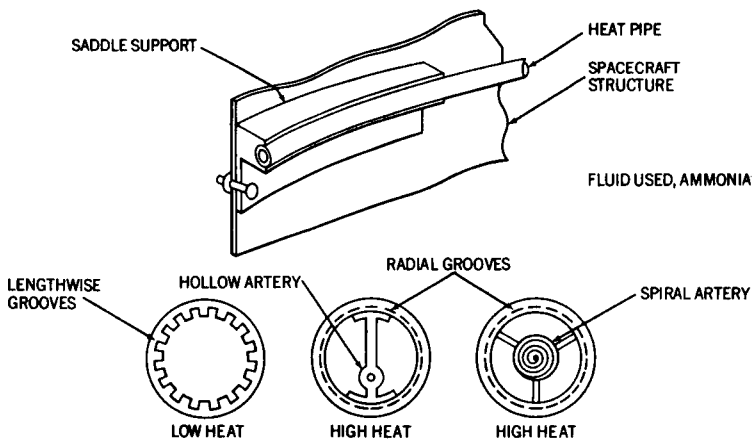


Fig. 2-Three Types of Heat Pipes
Used on OAO-C

are shown in Figures 3 and 4, upper right and left. The Conrad units were capable of temperature control between -65°C and $+50^{\circ}\text{C}$ with an accuracy of $\pm 2^{\circ}\text{C}$. This accuracy is essential since heat pipes function differently at different thermal levels.

Four vacuum-rated heaters (capable of 100 watts output each) were mounted on saddles on the outer circumference of the pipe, equidistant from the gap in the pipe, and two flight heaters are permanently mounted on the inner circumference, both on one side of the gap, as shown in Figure 4. Thermocouple locations are also shown in Figure 4.

Since the heaters had a different absorptivity/emissivity (α/ϵ) value than the aluminum tube, they were first coated and bonded to the pipes with Kapton tape and then wrapped with aluminum foil tape. The Kapton tape proved to be necessary in the first heat pipe test, because the aluminum tape showed signs of burning. The Kapton tape was able to withstand the heater temperatures, and prevented the aluminum foil tape from burning.

Thermal Data Retrieval

After functionally achieving a workable test setup, it was essential to have a flexible data retrieval system. Several methods were used during the heat pipe tests. The first method utilized an independent thermistor system, with twisted shielded pairs, but due to solenoid switching in the test complex, the twisted pairs picked up noise spikes which falsely indicated changes of ± 3 to 5°C . The second method utilized a programmed time-sharing computer system with thermocouples. This method successfully avoided the noise spikes, but increased the data retrieval time per channel from approximately 20 seconds to 90 seconds. However, pipe average temperatures and delta temperatures (ΔT 's) were easily calculated with the computer system, whereas the former system required hand calculations. In a later heat pipe test, the computer system in conjunction with a Brown recorder was used very successfully. The computer was used to calculate ΔT 's and average pipe temperatures, while the Brown recorder was used to monitor the thermal trends. A slight modification of this system was used in a fourth test. This consisted of using a

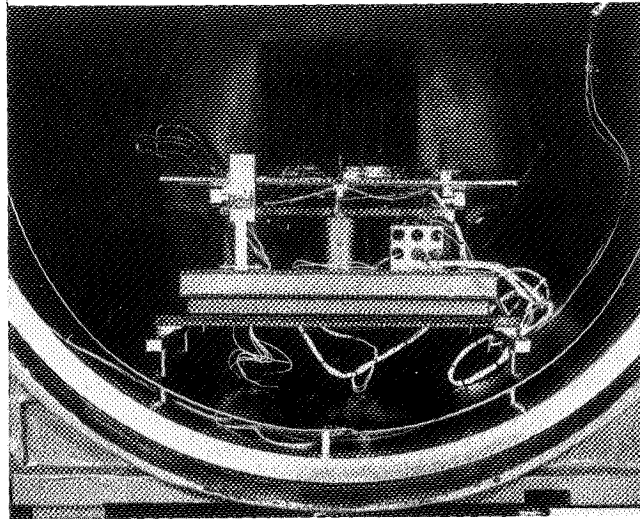


Fig. 3-Mobile Tilt Table and Heat Pipe
in Thermal Vacuum Chamber

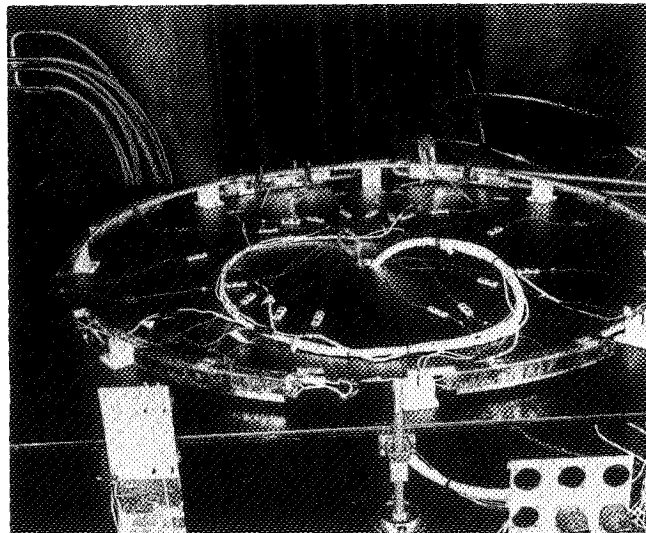


Fig. 4-Heat Pipe on Tilt Table

Doric Thermocouple Thermometer system, which retrieves data faster than the time-sharing computer system, and can average up to 36 data channels at the push of a button. The only drawback to this latter system was the lack of a print out data system.

Test Results

The spiral artery pipe was tested three times. The first test indicated an excessive amount of non-condensable gas within the heat pipe, which prevented the pipe from functioning properly; the gas blocked the condenser (heat removal) areas of the pipe. This caused the pipe to overheat; i.e., it exceeded its upper acceptance limit of +54°C. It was shown by test methods that the blockage was due to gas and not excess fluid. This was first accomplished by showing that the blocked area could be diminished by increasing the internal vapor pressure; and, second, by tilting the pipe beyond its capillary pull limit (evaporator $1\frac{1}{2}$ inches higher than the condenser), and waiting for blockage to reoccur (Ref. 3). This problem was resolved by opening the pipe, removing all the gas, and recharging the pipe. When the gas was removed hydrogen gas was discovered, which apparently was introduced when the pipe was originally charged and sealed. The charging procedure required the utmost care, since the inclusion of any water vapor could lead again to the generation of hydrogen gas. After the pipe was recharged, a second test was conducted. This one was very successful. Data was taken under three basic thermal conditions, as follows: (1) vacuum with chamber walls at -40°C and condensers at -55°C; (2) vacuum with chamber walls at 0°C and condensers at 0°C; (3) vacuum with chamber walls at +20°C and condensers at +20°C. In each test, data was recorded at five different pipe tilt positions, with the condensers below the evaporators, at 0, $\frac{1}{4}$, $\frac{1}{2}$, $\frac{3}{4}$, and 1-inch tilts. This corresponds to the condensers being below the evaporators at tilts of 0.30, 0.61, 0.92, and 1.22 degrees. The test results showed that the pipe functioned very well in all three cases (Ref. 4). Data showed that the pipe functioned better at the $\frac{1}{4}$ -inch (0.30-degree) tilt position than in the level position for 65% of the test cases.

The first test condition (chamber walls at -40°C,

condensers at -55°C) represents the most extreme condition under which the pipe had to function. Results show, Table 1, that the tube would experience burnout when both flight heaters were ON (75 watts total) and the pipe was tilted $3/4$ inch or 0.92 degree. Raising the condenser temperature to -40°C allowed the pipe to function without burning out even at a 1-inch, 1.22 -degree tilt. This demonstrates the affect of the condenser on the pipe. Table 2 lists the test data with the four saddle heaters under test condition one. The 80 watt/saddle case was unattainable.

In the second test condition (chamber walls at 0°C , condensers at 0°C) the largest gradient recorded for the flight heaters occurred at a 1-inch (1.22 -degree) tilt, and was recorded as 1.8°C (Table 3). The limit recorded by using the four saddle heaters (based upon ΔT 's only) occurred with 70 watts/saddle at a tilt of $1/2$ inch (0.61 degree). (See Table 4.)

In the third test condition (chamber walls at $+20^{\circ}\text{C}$, condensers at $+20^{\circ}\text{C}$) the highest flight heater ΔT (2.1°C), as shown in Table 5, was recorded at a 1-inch (1.22 -degree) tilt position. The largest gradient with the saddle heaters occurred for 200 watts (50 watts/saddle heater) at a tilt of $1/2$ inch (0.61 degree). See Table 6.

Upon removing the pipe from the test chamber it was noted that the bonding agent used to bond the saddles to the pipe had crumbled in some areas. Therefore mechanical clamps were manufactured, and the pipe was tested for a third time, with results similar to those of the second test.

In summary, the pipe has proven itself capable of handling high heat loads with small ΔT 's, even with tilts of 1 inch (1.22 degrees). It has also been shown that the test setup and the equipment used was adequate for thermal-vacuum testing of these heat pipes.

TABLE 1 - TEST DATA WITH FLIGHT HEATERS

<u>Chamber Walls at -40°C</u>		<u>Conrad at -55°C</u>	
<u>Power</u>	<u>Pipe Tilt</u>	<u>Pipe</u>	
<u>Watts</u>	<u>Inches</u>	<u>Average</u>	<u>ΔT</u>
		<u>Temperature</u>	
25 ¹	0	-42.0°C	0.4°C
50 ¹	0	-37.0	1.0
75 ²	0	-32.0	1.0
25	1/4	-40.0	0.4
50	1/4	-35.5	1.0
75	1/4	-29.5	1.0
25	1/2	-41.0	0.4
50	1/2	-35.0	1.3
75	1/2	-29.0	1.0
25	3/4	-41.5	1.0
50	3/4	-37.0	1.0
75	3/4	-	* ³
<u>Chamber Walls at -40°C</u>		<u>Conrad at -40°C</u>	
50	1/2	-24.5°C	1.2°C
50	3/4	-24.0	1.1
75	3/4	-18.0	1.6
25	1	-27.5	0.5
50	1	-23.5	3.0
75	1	-16.0	3.0

¹One heater ON.

²Both heaters ON.

³Burnout pipe was allowed to reprime and burnout reoccurred under the same test conditions.

TABLE 2 - TEST DATA WITH FOUR SADDLE HEATERS

<u>Chamber Walls at -40°C</u>		<u>Conrad at -55°C</u>	
<u>Power/ Saddle Watts</u>	<u>Pipe Tilt Inches</u>	<u>Pipe Average Temperature</u>	<u>ΔT</u>
50	0	-17.0°C	4.5°C
70	0	-11.5	4.5
80	0	- 4.0	4.0
10	1/4	-39.7	0.7
30	1/4	-26.8	3.8
50	1/4	-16.4	4.0
70	1/4	- 6.0	4.0
80	1/4	0.5	4.5
10	1/2	-40.0	2.3
30	1/2	-27.5	2.5
50	1/2	-16.0	3.5
70	1/2	- 5.0	4.5
80	1/2	- 3.0	7.0
10	3/4	-40.0	1.5
30	3/4	-29.0	3.0
50	3/4	-14.0	4.0
70	3/4	- 3.0	14.0*

* ΔT was increasing rapidly when all power was turned off.

TABLE 3 - TEST DATA WITH FLIGHT HEATERS

Chamber Walls at 0°CConrad at 0°C

<u>Power</u>	<u>Pipe Tilt</u>	<u>Pipe</u>	
<u>Watts</u>	<u>Inches</u>	<u>Average</u>	<u>ΔT</u>
		<u>Temperature</u>	
25	0	9.0°C	1.0°C
50	0	14.0	1.0
75	0	20.1	1.0
25	1/4	8.5	0.5
50	1/4	14.0	0.5
75	1/4	19.0	0.5
25	1/2	9.0	0.5
50	1/2	14.5	1.0
75	1/2	20.2	0.9
25	3/4	10.0	0.1
50	3/4	14.8	0.6
75	3/4	21.0	1.2
25	1	9.6	0.4
50	1	15.0	1.2
75	1	21.1	1.8

TABLE 4 - TEST DATA WITH FOUR SADDLE HEATERS

<u>Chamber Walls at 0°C</u>		<u>Conrad at 0°C</u>	
<u>Power/ Saddle</u>	<u>Pipe Tilt</u>	<u>Pipe Average</u>	
<u>Watts</u>	<u>Inches</u>	<u>Temperature</u>	<u>ΔT</u>
10	0	7.5°C	2.0°C
30	0	17.5	2.0
50	0	26.5	3.0
70	0	41.0	4.0
80	0	46.0	5.0
10	1/4	7.0	1.0
30	1/4	18.0	2.0
50	1/4	29.0	3.0
70	1/4	40.0	6.0
80	1/4	46.5	7.0
10	1/2	8.5	1.0
30	1/2	18.5	2.0
50	1/2	28.0	3.5
70	1/2	44.0	19.0
10	3/4	10.5	2.0
30	3/4	22.0	2.5
50	3/4	33.5	5.2
70	3/4	44.0	19.5
10	1	11.0	1.2
30	1	23.0	3.5
50	1	33.5	22.0 ¹
70	1	-	B ²

¹Possible burnout started before all power was turned off.

²Burnout.

TABLE 5 - TEST DATA WITH FLIGHT HEATERS

Chamber Walls at +20°C Conrad at +20°C

<u>Power</u>	<u>Pipe Tilt</u>	<u>Pipe</u>	
<u>Watts</u>	<u>Inches</u>	<u>Average</u>	<u>ΔT</u>
		<u>Temperature</u>	
25	0	28.0°C	0.7°C
50	0	32.0	0.7
75	0	37.1	0.9
25	1/4	27.2	0.5
50	1/4	31.6	0.9
75	1/4	37.3	0.7
25	1/2	28.0	0.6
50	1/2	32.4	0.8
75	1/2	37.1	0.9
25	3/4	28.0	0.4
50	3/4	32.7	1.0
75	3/4	38.3	1.5
25	1	28.0	0.9
50	1	32.0	1.9
75	1	36.9	2.1

TABLE 6 - TEST DATA WITH FOUR SADDLE HEATERS

<u>Chamber Walls at +20°C</u>		<u>Conrad at +20°C</u>	
<u>Power/ Saddle Watts</u>	<u>Pipe Tilt Inches</u>	<u>Pipe Average Temperature</u>	<u>ΔT</u>
10	0	28.4°C	0.9°C
10	1/4	28.5	1.2
10	1/2	28.5	1.4
10	3/4	28.6	2.1
10	1	28.6	6.0
30	0	39.0	1.8
30	1/4	39.0	2.1
30	1/2	41.6	2.4
30	3/4	41.7	3.7
30	1	41.5	6.6
50	0	50.4	3.2
50	1/4	51.5	3.7
50	1/2	-	*

*Terminated power because the upper limit +54°C was reached.

References

1. Goddard Specification, OB-A-0086-C, "OAO-C Heat Pipe," September 18, 1970.
2. Ollendorf, S., and Stipandic, E., "Heat Pipes for Spacecraft Temperature Control: Their Usefulness and Limitations," 6th Aerospace Mechanical Conference, Ames Research Center, September 9-10, 1971.
3. "Results of Thermal-vacuum Testing of the Grumman OAO-C Structural Heat Pipe," NASA Internal Memo, J. P. Marshburn, November 10, 1971, to R. McIntosh.
4. "Test of the Redesigned Level-6 Spiral-artery Heat Pipe Under Thermal Vacuum Conditions," NASA Internal Memo, J. P. Marshburn, December 20, 1971, to R. McIntosh.

RADIATION SCALES ON WHICH STANDARD VALUES OF THE SOLAR CONSTANT AND SOLAR SPECTRAL IRRADIANCE ARE BASED

Matthew P. Thekaekara, *Goddard Space Flight Center, Greenbelt, Maryland*

ABSTRACT

Standard values of the solar constant and solar spectral irradiance which have been recently proposed are based on measurements made by several independent observers. In the calibration of their instruments they have used different radiation scales. The question of radiation scales is critically examined. There are two radiation scales which are of fundamental validity and there are several calibration standards and radiation scales which have been set up for practical convenience. The interrelation between these scales is examined. It is shown that within the limits of accuracy of irradiance measurements in general and solar irradiance measurements in particular, the proposed standard values of the solar constant and solar spectrum should be considered to be on radiation scales of fundamental validity, those based on absolute electrical units and on the thermodynamic Kelvin temperature scale.

INTRODUCTION

Standards values of the solar constant and solar spectrum have recently been proposed under the sponsorship of the Institute of Environmental Sciences and these values are now going through the normal route of review and approval, with a view to their being issued as an engineering standard by ASTM¹. These values are based on the measurements made independently by several observers using different instruments and methods of data collection and analysis. For instrument calibration each observer used a reference scale of radiation which for him was sufficiently reliable and practicable and not all scales were the same. Hence a question naturally arises, on what scale are the proposed standards. Though the original publications from which the standards are derived have dealt with the question briefly, a further clarification seems to be called for in view of more recent discussions and certain experimental results.

As is well known the scale with reference to which energy measurements are reported is one of the major problems in all measurement of

energy. Internationally accepted standards exist for fundamental units like length, mass and time and for many of the derived units like volt, ampere and watt. For total and spectral radiant flux, however, different standards and scales exist and intercomparisons between them show that they are not in perfect agreement.

STANDARD SCALES OF RADIOMETRY

Two scales are of fundamental validity, the absolute electrical units scale (AEUS) and the thermodynamic Kelvin temperature scale (TKTS). These scales are of fundamental validity because they can be derived from the fundamental units of length, mass and time by the use of well established laws of physics. On the AEUS energy in watts is defined in terms of the electrical units, ampere and volt. On the TKTS the quantity first defined is the temperature from laws of thermodynamics, and energy is defined in terms of temperature using either the Stefan-Boltzmann equation for total energy or the Planck equation for spectral energy. Any self-checking instrument of total irradiance, or absolute radiometer as it is sometimes called, should give total irradiance on the AEUS, provided all the necessary correction factors are properly applied. Best known among such instruments are the compensated water flow calorimeter which established the original Smithsonian scale² and the compensated strip pyrhelimeter³ of K. J. Ångström on which the Ångström scale is based. Of more recent development are the wire-wound cone radiometer of Goddard Space Flight Center^{4,5}, three models of cavity radiometer developed by Jet Propulsion Laboratory, Temperature Control Flux Monitor⁶ (TCFM), Total Radiation Absolute Radiometer⁷ (TRAR) and the Active Cavity Radiometer⁸ (ACR), the radiometers developed at National Bureau of Standards by J. Geist, the Institut Royal Météorologique of Belgium by R. Dogniaux, at the National Physical Laboratory of U.K. by E. J. Gillham. The provision that all the necessary corrections be properly applied is extremely difficult to achieve in practice. Hence it is that the original Smithsonian scale had to be revised three times, in 1913, 1932 and 1954. Comparisons between the Smithsonian scale of 1913 and the original K. J. Ångström scale showed a difference of 3.5 percent with the sun as source and a difference of 2.8 percent with laboratory sources (Ref. 9, p. 380).

The international pyrhelimetric scale IPS 56 was established in 1956 as a compromise between the Smithsonian 1913 scale (S13S) and the Ångström pyrhelimetric scale (APS)⁹. Readings on APS have to be multiplied by 1.015 and those on S13S by 0.98 to give IPS56. Comparisons between IPS56 and the JPL cavity radiometric scale have been made both at JPL and the Eppler Laboratory. The JPL measurements⁸ showed that readings on TRAR or ACR scale have to be multiplied by 0.978 to give IPS56. The Eppler comparisons were made between six JPL, TRAR type radiometers and the set of Ångström radiometers which maintain

IPS56 at Eppley. The correction factors supplied by JPL were used for the JPL radiometers. The results do not confirm the JPL findings of 2.2% difference between IPS56 and the scale of the cavity radiometers; the difference if any, according to Eppley, is less than 1%¹⁰.

The JPL radiometers are presumably on the AEUS; so also is the GSFC wirewound cone radiometer. Comparisons between the values of the solar constant obtained from the GSFC cone and the JPL TCFM, (both on AEUS), the Leningrad actinometer, and the Eppley normal incident pyr heliometer (both on IPS56) do not show any systematic difference between IPS56 and AEUS¹¹.

If the AEUS is difficult to realize in practice, the thermodynamic Kelvin temperature scale (TKTS) presents even greater difficulties. Hence it is that the gold point blackbody has been measured with reference to the TKTS and the international practical temperature scale IPTS has been defined. The temperature of the melting point of gold has been redefined in 1927, 1948 and more recently, in 1968. Thus, we have the IPTS 27, IPTS 48 and IPTS 68. The temperature of the melting point of gold was 1336.15K on IPTS 48, and it is 1337.58K on IPTS 68¹².

Thus, we have two scales of basic validity, that of electrical units AEUS and that of Kelvin temperature, TKTS, both related to fundamental units of length, mass and time through well-known physical laws, but both inconvenient for practical applications. There are two other scales IPS56 and IPTS 68 which are presumed to be identical with AEUS and TKTS respectively. IPS56 is maintained by a set of standard Ångström pyr heliometers in Sweden and the IPTS 68 by a gold point blackbody.

The gold point blackbody has been used to establish calibration standards of spectral radiance and irradiance. If the temperature of the blackbody is known (on TKTS), the application of the Planck's equation gives its radiance at any given wavelength. Calibration standards such as the quartz-iodine 1000W lamp have been issued by the National Bureau of Standards based on this principle¹³.

It has been assumed by some authors that the standard lamps issued by NBS (such standards are now issued by Eppley) are on IPTS 48. This assumption seems to have been justified by the fact that the older standards of spectral irradiance (tungsten strip lamps) were referred to a gold point blackbody before IPTS 68 was defined and that the spectral irradiance standards (coiled coil quartz iodine lamps) were referred to the spectral radiance standards. But a careful study of the relevant literature¹³ and discussions with the persons who were responsible for setting up these standards show that this assumption is not justified. As an example, a recent publication¹⁴ of Labs and Neckel might be cited. The authors assume that the values of the solar constant proposed by Stair and Ellis¹⁵, Arvesen et al.¹⁶ and McNutt and Riley¹⁷ are on IPTS 48, and hence, they raise the values by 0.7 percent to adjust them to IPTS 68. The validity of this procedure is open to question. In setting up the NBS standards of spectral irradiance, three methods were used¹⁸

to adjust the values obtained by spectrometer comparison between the standards of radiance and irradiance: filter radiometric comparison with the ribbon lamps, luminous efficacy of the CIE standard observer, use of a cavity detector calibrated with reference to the NBS carbon-filament standard of total radiation. More recent evaluations made at the NBS¹⁹ show that errors due to these three methods at $0.655\ \mu\text{m}$ are +0.84% from ribbon lamp, -0.9% from CIE observer and +0.4% from standard of total radiation. The sum of these three divided by 3 yields an error of 0.1%. (The correction from the CIE observer is due to the revision of the platinum point by -4.4°K^{20}).

Further, it should be recalled that Stair and Ellis used the NBS standard lamp only for the range 0.31 to $0.55\ \mu\text{m}$; the Johnson curve was adopted for the rest of the spectral range. Arvesen used the NBS spectral irradiance standard for the range 0.25 to $2.5\ \mu\text{m}$. But the value which Labs and Neckel quote for Arvesen is not 139.0 derived by Arvesen, but 135.5 derived by Duncan²¹ who applied what was then believed to be the corrections needed for the spectral irradiance standard. With these corrections, the value is presumably on the TKTS. The Hy-Cal value of McNutt and Riley should also be considered to be on the TKTS since in the calibration of the Hy-Cal with reference to the blackbody cavity the corrections needed for making the IPTS 48 agree with the TKTS had already been made.

The accuracy of the spectral irradiance tables of the NBS 1000W lamps (QM type lamps) has been the topic of extensive investigations in several laboratories. The QM type lamps like the earlier 200W QL type lamps described by Stair, Schneider and Jackson¹³, were established as calibration standards by reference to the tungsten strip lamps (spectral radiance standards). The spectral radiance of the strip lamps was determined by comparison with a blackbody. Thus, the primary standard is a blackbody. Hence arises the question, what was the melting point of gold assumed for computing the Planck functions of the blackbody? The melting point of gold on IPTS 68 is $1337.58\text{K}^{22,23}$. The NBS standards of reference were established several years earlier at a time when the accepted value for the melting point of gold was 1336.15K as defined by the International temperature scale of 1948 (ITS 48). However, the NBS text on ITS 48 recognized that significant differences existed between ITS 48 and the more fundamental TKTS. Various corrections were applied to make temperatures measured on ITS 48 to agree as closely as experimentally possible with TKTS. Thus, the reference for the spectral irradiance standards is a blackbody of which the temperatures are defined on the TKTS.

However, it should be noted that the values used by Stair et al. for the radiation constants¹³ were $c_1 = 4.9918 \times 10^{-15}\ \text{erg cm}$ and $c_2 = 1.4380\ \text{cm}^\circ\text{K}$. The values currently accepted²⁴ are $c_1 = 4.9926 \times 10^{-15}\ \text{erg cm}$ and $c_2 = 1.4388\ \text{cm}^\circ\text{K}$. The errors due to these differences are significantly less than the experimental errors in the measurement of spectral irradiance.

As an illustration of the possible experimental errors may be mentioned the corrections made to Arvesen's solar spectral curve by Duncan. The reason is that "preliminary results from the current work with spectral radiance and irradiance standard lamps at the NBS indicate that the new values of spectral energy are lower in all wavelength regions with about a 6% difference at 250 nm, a 2.5% difference at 650 nm and a 3.5% difference at 850 nm."²¹ Though this work of reevaluation of standards had been begun at NBS about five years ago, no report has yet been officially published. A round robin of spectral irradiance measurements made at four major U.S. laboratories, NBS, Redstone Arsenal, Eppler Laboratory and Optronics, Inc. on the same set of lamps showed that the maximum values of the differences between two labs varied between 3 and 5 percent²⁵.

SCALES FOR SOLAR IRRADIANCE MEASUREMENT

This discussion on the energy scales and their interrelations permits us to examine more closely on which scale the standard values^{1,26,27} of the solar constant and solar spectral irradiance are quoted.

The values of the solar constant are based on the absolute electrical units for Willson⁸, Plamondon⁶ and Kruger and Thekaekara (GSFC cone radiometer)⁵, on IPS 56 for the GSFC Ångströms, Eppler-JPL, Denver balloon and Leningrad balloon, and presumably on the thermodynamic Kelvin temperature scale (TKTS) for GSFC Hy-Cal. The differences between these scales is not sufficiently well known to permit the reduction of all values to the same scale. Further, such reduction is not justified since the measurement uncertainties are considerably greater than any difference in scales.

The spectral irradiance curve is based mainly on the GSFC NASA 711 results; modifications were introduced on the basis of the Eppler-JPL data. For the NASA 711 curve, the reference standard was the NBS quartz iodine lamp. As discussed earlier, it is presumably on the TKTS. The Eppler-JPL measurements were made with a radiometer calibrated with reference to IPS 56 and a series of filters of which the transmittance curves are known. The IPS 56 is presumed to agree with the absolute electrical units scale (AEUS) as far as experimental accuracy permits. Comparison between the GSFC NASA 711 data and Eppler JPL data show that in the range of wavelength greater than 0.7 μm , both give practically the same value for the energy of the sun. There are minor differences in the range 0.3 to 0.7 μm . Hence a weighted average of the two sets of values were taken to give the standard curve. The area under the curve is 135.3 mW cm^{-2} , the same as obtained from the total irradiance instruments. The weighted average of the four GSFC total irradiance instruments was 135.1 mW cm^{-2} and the area under the spectral curve obtained from the five GSFC spectral irradiance instruments was 135.2 mW cm^{-2} . These differences are well within the degree of inaccuracy in the different radiometric scales, TKTS, AEUS, IPS 56, IPTS 68, NBS lamps, etc.

If IPS 56 is in error by +2.2% as found by Willson⁸, the solar constant should be scaled down from 135.3 to 132.3 which almost everyone would agree is too low a value. And further, the Eppley measurements do not show this difference between IPS 56 and AEUS. If the spectral measurements of NBS to which Duncan refers are correct, the standard solar spectral irradiance curve will need considerable modification, especially in the range near 0.3 μm . But the GSFC NASA 711 values (on the scale of the NBS lamps) have been confirmed by the MUSE data of Heath²⁸ (IPS 56). The Eppley-JPL filter data (also on IPS 56) give values which are higher by 2 to 8% (not lower) than the GSFC data.

It is certain that considerably more experimental work needs to be done to determine the relationships between the different scales. But on the basis of evidence available at present there seems to be no clearly established systematic difference between the two scales of fundamental validity, AEUS and TKTS, and the other more practical scales which have been established to conform to these fundamental scales. The values of the solar constant and solar spectral irradiance which have been proposed should be assumed to be on the absolute electrical units scale (AEUS) or the thermodynamic Kelvin temperature scale (TKTS).

REFERENCES

1. M. P. Thekaekara, Proposed Standard Values of the Solar Constant and Solar Spectrum, *J. Environmental Sc.*, Vol. 13, no. 4, Sept.-Oct. 1970, pp. 6-9.
2. C. G. Abbott, *The Sun and the Welfare of Man*, Smithsonian Scientific Series, Vol. II, p. 88.
3. A. Ångström, Das Ångströmsche Kompensations pyrheliometer und die pyrheliometrische Skala, *Met. Z.* 31, 369 (1914).
4. C. L. Korb, J. D. Rancourt and M. P. Thekaekara, Conical Radiation Detectors, GSFC Summer Workshop Report, X-100-65-407, pp. B-1 to B-21, GSFC 1965.
5. M. P. Thekaekara, ed., *The Solar Constant and the Solar Spectrum Measured from a Research Aircraft*, NASA TR R-351, NASA, October 1970, see R. Kruger and M. P. Thekaekara, The Cone Radiometer, pp. 21-28.
6. J. A. Plamondon, The Mariner Mars 1969 Temperature Control Flux Monitor, JPL Space Program Summary, 37-59, Vol. III, pp. 162-168, JPL, Pasadena, Calif., October 1969.
7. J. M. Kendall, Sr., The JPL Standard Total Radiation Absolute Radiometer, Technical Report 32-1263, Jet Propulsion Laboratory, Pasadena, Calif., May 15, 1968.
8. R. C. Willson, Active Cavity Radiometric Scale, International Pyrheliometric Scale and Solar Constant, *J. Geophys. Research*, Vol. 76, No. 19, 1971, pp. 4325-4340.

9. Anon: IGY Instruction Manual, Part VI, Radiation Instruments and Measurements, Pergamon Press, London, 1957, pp. 378-380.
10. A. J. Drummond, private communication.
11. See Ref. 5, pp. 65 and 71.
12. W. Thomas, W. Zander, H. Wagenbreth, J. Otto, Bericht über die Tätigkeit der PTB in Jahre 1966, Abt. 3, No. 134, Braunschweig, 1967.
13. R. Stair, W. E. Schneider and J. K. Jackson, A New Standard of Spectral Irradiance, *App. Optics*, Vol. 2, No. 11, November 1963, pp. 1151-1154.
14. D. Labs and H. Neckel, The Solar Constant, *Solar Physics*, Vol. 19, 3-15 (1971).
15. R. Stair and H. T. Ellis, The Solar Constant Based on New Spectral Irradiance Data from 3100 to 5300 Ångströms, *J. App. Meteorology*, Vol. 7, No. 8, August 1968, pp. 635-644.
16. J. C. Arvesen, R. N. Griffin and B. D. Pearson, Determination of Extraterrestrial Solar Spectral Irradiance from a Research Aircraft, *App. Optics*, Vol. 8, No. 11, November 1969, pp. 2215-2232.
17. See Ref. 5, pp. 28-30.
18. See Ref. 13, p. 1153.
19. H. Kostkowski, private communication.
20. T. J. Quinn and T. R. D. Chandler, A New Determination of the Freezing Point of Platinum, *Metrologia*, Vol. 7, No. 3, July 1971, pp. 132-133.
21. C. H. Duncan, Radiation Scales and the Solar Constant, *Proc. 4th Space Simulation Conf.*, Am. Inst. of Aer. and Astro., Los Angeles, Calif., September 1969. Also available as GSFC X-713-69-382.
22. R. P. Benedict, The International Practical Temperature Scale of 1968, *Leeds Northrup Technical Journal*, IVa. 6, p. 2, 1969.
23. Anon, International Practical Scale of 1968, Foreword by C. R. Barber, *Metrologia* Vol. 5, p. 35, 1969.
24. B. N. Taylor, W. H. Parker and D. N. Langenberg, Determination of e/h , Using Macroscopic Quantum Phase Coherence in Superconductors: Implications for Quantum Electrodynamics and the Fundamental Physical Constants, *Rev. Modern Physics*, Vol. 41, no. 3, July 1969, pp. 375-496; see table p. 478.
25. H. J. Kostkowski, *Proceedings, IES Solar Simulation Committee Meeting*, NASA Langley Research Center, November 21, 1969.
26. Anon: Solar Electromagnetic Spectrum, NASA Space Vehicles Design Criteria NASA SP 8005, NASA, Washington, D.C., May 1971.
27. M. P. Thekaekara and A. J. Drummond, Standard Values for the Solar Constant and its Spectral Components, *Nature, Physical Sciences*, Vol. 229, No. 1, January 4, 1971, pp. 6-9.
28. D. F. Heath, Observations on the Intensity and Variability of the Near Ultraviolet Solar Flux from Nimbus III Satellite, *J. Atmos. Sc.* Vol. 26, No. 5, p. 2: 1157-1160, September 1969.

**PROPOSED SPECIFICATION FOR THE SOLAR CONSTANT AND AIR
MASS ZERO SOLAR SPECTRAL IRRADIANCE**

IES Solar Radiation Committee and ASTM Space Simulation Committee E-21

FOREWORD

This Specification for the Solar Constant and Air Mass Zero Solar Spectral Irradiance resulted from a joint effort between the Institute of Environmental Sciences Solar Radiation Committee and the American Society for Testing and Materials Committee E-21 on Space Simulation. It was the subject of a colloquium session held at the 17th Annual Meeting of the Institute of Environmental Sciences at Los Angeles, California, 26-30 April, 1971. The material upon which this specification is based is now in the process of being published by the IES as a case bound book which will be titled "The Solar Constant and Solar Spectrum."

Members of the two committees and other interested persons have contributed to this specification by offering comments and suggestions. The task originated in the East Sub-Committee of the IES Solar Radiation Committee and was assigned to a sub-committee section which consisted of the following individuals:

Dr. Matthew P. Thekaekara,
Chairman - NASA/Goddard Space Flight Center
Dr. Andrew G. Drummond - Eppley Laboratory
Dr. P. Rupert Gast - Air Force Cambridge Research
Laboratories
Eric G. Laue - Jet Propulsion Laboratory
Dr. David G. Murcray - University of Denver
Richard C. Willson - Jet Propulsion Laboratory

The document is planned for eventual publication by ASTM in the Book of Standards. The present reproduction of this document is the draft as approved by the IES Solar Radiation Committee. The document now has to be voted on by ASTM and may be revised before it appears in the ASTM Book of Standards.

It is printed in this proceedings to give it a wider distribution among those who may find it useful in their work.

Charles H. Duncan
Chairman, IES Solar Radiation
Committee

1. SCOPE

1.1 This specification defines the solar constant and the zero air mass solar spectral irradiance for use in thermal analysis, thermal balance testing, and other tests of spacecraft and spacecraft components and materials.

1.2 This specification is based upon data from experimental measurements made from high altitude aircraft, balloons, spacecraft, and the Earth's surface. The stated accuracies are based on the estimated accuracies of the measurements, calibrations, and radiometric scales.

2. DEFINITIONS OF TERMS

2.1 Air Mass (Optical Air Mass). The ratio of the path length or radiation through the atmosphere (l_m) at any given angle, Z° , to the sea level path length toward the zenith (l_z)

$$AM = \frac{l_m}{l_z} \cong \sec Z^\circ, \text{ for } Z^\circ \leq 62^\circ.$$

Symbol: AM1 (Air Mass One), AM2 (Air Mass Two).

2.2 Air Mass Zero. The absence of atmospheric attenuation of the solar irradiance at one astronomical unit from the Sun. Symbol: AM0.

2.3 Astronomical Unit. A unit of length defined as the mean distance between the Earth and the Sun, 149,597,890 \pm 500 Km. Symbol: AU.

2.4 Irradiance at a Point on a Surface. Quotient of the radiant flux incident on an element of the surface containing the point, by the area of that element. Symbol: E; Unit: Watt per square meter, $W \cdot m^{-2}$.

2.5 Irradiance, Spectral. The irradiance per unit wavelength interval at a specific wavelength, or as a function of wavelength. Symbol: E_λ . Unit: $W \cdot m^{-2} \cdot \mu m^{-1}$.

2.6 Integrated Irradiance. Spectral irradiance integrated over a specific wavelength interval from λ_1 to λ_2 .

Symbol: $E_{\lambda_1 - \lambda_2} = \int_{\lambda_1}^{\lambda_2} E_{\lambda} d\lambda$ Unit: $W \cdot m^{-2}$

2.7 Additional definitions will be found in E349.

3. SOLAR CONSTANT

The solar constant, based on the average of the values shown in Table 1, is:

$$1353 \text{ W} \cdot \text{m}^{-2} \text{ . Estimated Error: } \pm 21 \text{ W} \cdot \text{m}^{-2} \text{ .}$$

Table 2 summarizes the results in different units and Table 3 presents the total solar irradiance at various planetary distances from the Sun.

4. SOLAR SPECTRAL IRRADIANCE (AIR MASS ZERO)

The zero air mass solar spectral irradiance is based on data from the NASA 711 research aircraft experiments^(1,2,3) (see Table 4) with additions and revisions based on other recent measurements⁽¹⁶⁾. Previously compiled solar spectral irradiances were based on ground based measurements^(17 to 25) and some measurements from rockets⁽²⁶⁾. Spectral irradiance data from the NASA Ames Research Center⁽²⁷⁾ were not included because of calibration uncertainties. Further discussion on the methods of calculation and historical information can be found in References 3, 16 and 28 to 31.

Table 5 presents the solar spectral irradiance in tabular form for the range 0.12 to 1000 μm . The first column gives the wavelength (λ) in μm ; the second gives the spectral irradiance (E_{λ}) at λ in $W \cdot m^{-2} \cdot \mu\text{m}^{-1}$; the third gives the total irradiance for the range 0 to λ ($E_{0-\lambda}$) in $W \cdot m^{-2}$; and the fourth gives the percentage of the solar constant associated with wavelengths shorter than λ , ($D_{0-\lambda}$).

Table 6 presents an abridged version of Table 5. Figure 1 plots the Standard Solar Spectral Irradiance.

The irradiance in the range 0 to 0.12 μm (nearly $0.006 \text{ W} \cdot \text{m}^{-2}$) is based on Hinteregger's results⁽³²⁾. In the 0.14 to 0.20 μm range, the values are based on Naval Research Laboratory data^(17, 26) that have been adjusted downward because of data by Heath⁽³³⁾ and Parkinson and Reeves⁽³⁴⁾. In the range 0.20 to 0.30 μm , the values of the Goddard Space Flight Center curve have been retained because of confirming Nimbus satellite data⁽³³⁾. The Epply-JPL data were used for revision in

Table 1
SOLAR CONSTANT

Platform	Detector	Year	Solar Constant $\text{W} \cdot \text{m}^{-2}$	Reference
NASA 711 Aircraft	Hy-Cal Pyrheliometer	1967	1358	1, 2, 3
NASA 711 Aircraft	Ångström 7635	1967	1349	1, 2, 3
NASA 711 Aircraft	Ångström 6618	1967	1343	1, 2, 3
NASA 711 Aircraft	Cone Radiometer	1967	1358	1, 2, 3
Soviet Balloon	U. of Leningrad Actinometer	1961- 1968	1353	4, 5
U. of Denver Balloon	Eppley Pyrheliometer	1969	1338	6, 7
Eppley-JPL High Altitude Aircraft	Eppley Pyrheliometer	1966- 1968	1360	8-13
Mariner VI & VIII Spacecraft	Cavity Radiometer	1969	1353	14
JPL Balloon	Cavity Radiometer	1968- 1969	1368	15
Average Estimated Error			1353 ±21	

the range 0.3 to $0.7 \mu\text{m}$ ⁽⁹⁻¹³⁾. The 20 to $1000 \mu\text{m}$ range^(9-13, 16) irradiances were computed from the combined data on the brightness temperature of the Sun from many different authors as quoted by Shimabukoro and Stacey⁽³⁵⁾.

Table 2

THE SOLAR CONSTANT
(Conversion Factors)

Solar Constant = $1353 \text{ W} \cdot \text{m}^{-2}$ ($\pm 21 \text{ W} \cdot \text{m}^{-2}$) [preferred unit]

$$= 0.1353 \text{ W} \cdot \text{cm}^{-2}$$

$$= 135.3 \text{ mW} \cdot \text{cm}^{-2}$$

$$= 1.353 \times 10^6 \text{ erg} \cdot \text{cm}^{-2} \cdot \text{sec}^{-1}$$

$$= 125.7 \text{ W} \cdot \text{ft}^{-2}$$

$$= 1.940 \text{ cal} \cdot \text{cm}^{-2} \cdot \text{min}^{-1} \text{ } (\pm 0.03 \text{ cal} \cdot \text{cm}^{-2} \cdot \text{min}^{-1})$$

$$= 0.0323 \text{ cal} \cdot \text{cm}^{-2} \cdot \text{sec}^{-1}$$

$$= 429.2 \text{ Btu} \cdot \text{ft}^{-2} \cdot \text{hr}^{-1}$$

$$= 0.119 \text{ Btu} \cdot \text{ft}^{-2} \cdot \text{sec}^{-1}$$

$$= 1.937 \text{ Langleys} \cdot \text{min}^{-1}$$

The calorie is the thermochemical calorie-gram and is defined as 4.1840 absolute joules. The Btu is the thermochemical British thermal unit and is defined by the relationship: $1 \text{ Btu (thermochemical)} / (^{\circ}\text{F} \times \text{lb}) = 1 \text{ cal} \cdot \text{g (thermochemical)} / (^{\circ}\text{C} \times \text{g})$.

The Langley, however, is defined in terms of the older thermal unit the calorie \cdot gm (mean), i.e., $1 \text{ Langley} = 1 \text{ cal} \cdot \text{g (mean)} \cdot \text{cm}^{-2}$; $1 \text{ cal} \cdot \text{g (mean)} = 4.19002 \text{ joules}$.

Table 3

SOLAR IRRADIANCE AT THE PLANETS

Planet	Solar Irradiance $\text{W} \cdot \text{m}^{-2}$		
	Mean	Perihelion	Aphelion
Mercury	9029.0	14309.0	6211.0
Venus	2586.0	2621.0	2551.0
Earth	1353.0	1399.0	1309.0
Mars	583.0	709.0	487.0
Jupiter	50.0	55.2	45.5
Saturn	14.9	16.6	13.4
Uranus	3.68	4.07	3.34
Neptune	1.496	1.500	1.493
Pluto	0.870	1.556	.555

Table 4

SPECTRAL IRRADIANCE INSTRUMENTS ON BOARD THE NASA 711 GALILEO RESEARCH AIRCRAFT,
 USED FOR OBTAINING THE GSFC CURVE OF SOLAR SPECTRAL IRRADIANCE
 (References 1, 2, 3)

Instrument	Energy Detector	Type of Instrument	Aircraft Window Material	Wavelength Range (μm)
Perkin-Elmer Monochromator	1P28 Tube, Thermocouple	LiF Prism	Sapphire	0.3 - 0.7
		LiF Prism	Sapphire	0.7 - 4
Leiss Monochromator	EMI 9558QA, PbS Cell	Quartz Double Prism	Dynasil Quartz Dynasil Quartz	0.3 - 0.7 0.7 - 1.6
Filter Radiometer	Phototube	Dielectric Thin Films	Dynasil Quartz	0.3 - 1.2
P-4 Interferometer	1P28 or R136 PbS Cell	Soleil Prism	Infrasil Quartz	0.3 - 0.7
		Soleil Prism	Infrasil Quartz	0.7 - 2.5
I-4 Interferometer	Thermistor Bolometer	Michelson Mirror	Irtran 4	2.6 - 15

Table 5

SOLAR SPECTRAL IRRADIANCE - PROPOSED STANDARD CURVE

 λ - Wavelength in micrometers E_{λ} - Solar spectral irradiance averaged over small bandwidth centered at λ , in $\text{W}\cdot\text{m}^{-2}\cdot\mu\text{m}^{-1}$ $E_{0-\lambda}$ - Integrated solar irradiance in the wavelength range 0 to λ , in $\text{W}\cdot\text{m}^{-2}$ $D_{0-\lambda}$ - Percentage of solar constant associated with wavelengths shorter than λ .Solar constant - $1353 \text{ W}\cdot\text{m}^{-2}$

Note: Lines indicate change in wavelength interval of integration.

λ	E_{λ}	$E_{0-\lambda}$	$D_{0-\lambda}$	λ	E_{λ}	$E_{0-\lambda}$	$D_{0-\lambda}$	λ	E_{λ}	$E_{0-\lambda}$	$D_{0-\lambda}$
.120	.100	.0059992	.00044	.525	1052	352.591	26.059	1.78	202	1221.23	90.261
.140	.830	.0072999	.00053	.530	1042	361.026	26.742	1.75	188	1230.78	91.967
.150	.07	.00708	.00057	.535	1018	378.976	27.418	1.80	159	1239.25	91.933
.160	.23	.00930	.00069	.540	1783	379.479	28.084	1.85	142	1246.78	92.149
.170	.63	.01360	.00100	.545	1754	380.021	28.737	1.90	126	1253.40	92.644
.180	1.25	.02300	.00169	.550	1725	397.519	29.380	1.95	114	1259.40	93.088
.190	2.71	.04200	.00316	.555	1720	406.131	30.017	2.00	103	1264.90	93.483
.200	10.7	.21905	.00811	.560	1695	414.669	30.668	2.10	90	1274.55	94.202
.210	22.9	.27785	.02053	.565	1705	423.169	31.276	2.20	79	1283.00	94.826
.220	57.5	.67905	.05024	.570	1712	431.711	31.907	2.30	69	1290.40	95.373
.225	64.9	.90585	.07720	.575	1719	440.289	32.561	2.4	62.0	1296.95	95.850
.230	66.7	1.31485	.09771	.580	1715	448.874	33.176	2.5	55.0	1302.00	96.290
.235	59.3	1.62985	.1204	.585	1712	457.441	33.809	2.6	48.0	1307.95	96.670
.240	63.0	1.93580	.1430	.590	1708	465.971	34.439	2.7	43.0	1312.50	97.003
.245	72.3	2.27305	.1680	.595	1682	474.426	35.068	2.8	39.0	1316.60	97.310
.250	78.4	2.63060	.1944	.600	1666	482.796	35.683	2.9	35.0	1320.30	97.568
.255	104	3.06660	.2266	.605	1647	491.079	36.295	3.0	31.0	1323.60	97.827
.260	138	3.65100	.2698	.610	1635	499.284	36.902	3.1	26.0	1326.45	98.083
.265	165	4.43910	.3280	.620	1602	515.469	38.098	3.2	22.6	1328.88	98.219
.270	232	5.48160	.4051	.630	1570	531.329	39.276	3.3	19.2	1330.47	98.374
.275	284	6.5716	.4857	.64	1544	546.899	40.421	3.4	16.6	1332.76	98.547
.280	222	7.6366	.5644	.65	1511	562.174	41.550	3.5	14.6	1334.32	98.628
.285	315	8.9791	.6636	.66	1485	577.159	42.657	3.6	13.5	1335.73	98.728
.290	402	10.9716	.8109	.67	1456	591.060	43.744	3.7	12.3	1337.02	98.842
.295	584	13.3666	1.0788	.68	1427	606.284	44.818	3.8	11.1	1338.19	98.956
.300	514	16.3816	1.2107	.69	1402	620.429	45.885	3.9	10.3	1339.26	99.074
.305	603	19.1741	1.4171	.70	1369	634.284	46.879	4.0	9.5	1340.25	99.159
.310	689	22.4041	1.6558	.71	1344	647.049	47.882	4.1	8.7	1341.16	99.1252
.315	764	26.0366	1.9243	.72	1314	661.139	48.864	4.2	7.8	1341.98	99.1661
.320	830	30.0216	2.2188	.73	1298	674.159	49.826	4.3	7.1	1342.73	99.2412
.325	975	34.5341	2.552	.74	1260	686.989	50.769	4.4	6.50	1343.441	99.291587
.330	1055	39.6191	2.928	.75	1235	699.384	51.691	4.5	5.98	1344.0341	99.337331
.335	1081	44.9691	3.323	.76	1211	711.614	52.595	4.6	5.30	1344.5941	99.378721
.340	1074	50.3566	3.721	.77	1185	723.594	53.480	4.7	4.80	1345.0991	99.416049
.345	1069	55.7441	4.117	.78	1159	735.314	54.346	4.8	4.50	1345.5641	99.450413
.350	1093	61.1191	4.517	.79	1134	746.779	55.194	4.9	4.10	1345.9941	99.482159
.355	1083	66.5591	4.919	.80	1109	757.994	56.023	5.0	3.83	1346.3906	99.511589
.360	1068	71.9366	5.316	.81	1085	768.966	56.834	6.0	1.75	1346.1806	99.717708
.365	1132	77.4366	5.723	.82	1060	779.694	57.627	7.0	.99	1350.5506	99.818965
.370	1161	83.2191	6.150	.83	1036	790.174	58.401	8.0	.68	1351.3456	99.877723
.375	1157	89.0641	6.582	.84	1013	800.419	59.158	9.0	.380	1351.8356	99.913939
.380	1128	94.7666	7.003	.85	990	810.434	59.899	10.0	.250	1352.1586	99.937221
.385	1098	100.3616	7.413	.86	968	820.224	60.622	11.0	.170	1352.3606	99.952742
.390	1098	105.7916	7.819	.87	947	829.799	61.330	12.0	.120	1352.5056	99.963459
.395	1109	111.5091	8.241	.88	926	839.164	62.022	13.0	.087	1352.6091	99.971108
.400	1429	118.0541	8.725	.89	908	848.334	62.700	14.0	.055	1352.6881	99.976356
.405	1644	125.7366	9.293	.90	891	857.329	63.365	15.0	.049	1352.7721	99.980149
.410	1751	134.2241	9.920	.91	880	866.184	64.019	16.0	.038	1352.7756	99.983414
.415	1774	143.0366	10.571	.92	869	874.929	64.665	17.0	.031	1352.8101	99.985964
.420	1747	151.8391	11.222	.93	858	883.564	65.304	18.0	.024	1352.8376	99.987997
.425	1693	160.4391	11.858	.94	847	892.08	65.934	19.0	.02000	1352.8596	99.989623
.430	1639	168.7691	12.473	.95	837	900.58	66.556	20.0	.01600	1352.8776	99.990953
.435	1663	177.0241	13.083	.96	828	908.79	67.168	25.0	.00610	1352.9328	99.995037
.440	1810	185.7666	13.725	.97	803	916.90	67.768	30.0	.00300	1352.9556	99.996718
.445	1822	195.0366	14.415	.98	785	924.84	68.355	35.0	.00160	1352.9671	99.997560
.450	2006	204.8566	15.140	.99	767	932.60	68.928	40.0	.00094	1352.9734	99.998317
.455	2057	215.0141	15.891	1.00	748	940.18	69.488	50.0	.00038	1352.9803	99.998825
.460	2066	225.3216	16.653	1.05	688	975.58	72.135	60.0	.00019	1352.9829	99.999236
.465	2048	235.6666	17.413	1.10	583	1007.10	74.435	80.0	.00007	1352.9855	99.999820
.470	2033	245.8091	18.167	1.15	535	1035.30	76.519	100.0	.00003	1352.9865	99.999902
.475	2044	256.001	18.921	1.20	485	1068.88	78.404	100.0	.00000	1353.0000	01.000000
.480	2074	266.2396	19.681	1.25	438	1083.88	80.109				
.485	1976	276.421	20.430	1.30	397	1104.75	81.652				
.490	1950	286.236	21.155	1.35	358	1123.63	83.047				
.495	1968	296.811	21.878	1.40	337	1143.00	84.331				
.500	1942	306.766	22.599	1.45	312	1167.23	85.530				
.505	1920	315.421	23.312	1.50	288	1172.23	86.639				
.510	1882	324.926	24.015	1.55	267	1186.10	87.665				
.515	1833	334.214	24.701	1.60	245	1196.90	88.611				
.520	1833	343.379	25.379	1.65	223	1210.60	89.475				

Table 6

SOLAR SPECTRAL IRRADIANCE -
PROPOSED STANDARD CURVE ABRIDGED VERSION

- λ - WAVELENGTH IN μm
- E_{λ} - SOLAR SPECTRAL IRRADIANCE AVERAGED OVER SMALL BANDWIDTH
CENTERED AT λ , IN $\text{W}\cdot\text{m}^{-2}\cdot\mu\text{m}^{-1}$
- $D_{0-\lambda}$ - PERCENTAGE OF THE SOLAR CONSTANT ASSOCIATED WITH WAVELENGTHS
SHORTER THAN λ

SOLAR CONSTANT - $1353 \text{ W}\cdot\text{m}^{-2}$

λ	E_{λ}	$D_{0-\lambda}$	λ	E_{λ}	$D_{0-\lambda}$	λ	E_{λ}	$D_{0-\lambda}$
0.12	.1	4×10^{-4}	0.43	1639	12.47	0.90	891	63.37
0.14	.03	5×10^{-4}	0.44	1810	13.73	1.00	748	69.49
0.16	.23	7×10^{-4}	0.45	2006	15.14	1.2	485	78.40
0.18	1.25	1.7×10^{-3}	0.46	2066	16.65	1.4	337	84.33
0.20	10.7	8.1×10^{-3}	0.47	2033	18.17	1.6	245	88.61
0.22	57.5	0.05	0.48	2074	19.68	1.8	159	91.59
0.23	66.7	0.10	0.49	1950	21.15	2.0	103	93.49
0.24	63.0	0.14	0.50	1942	22.60	2.2	79	94.83
0.25	70.9	0.19	0.51	1882	24.01	2.4	62	95.86
0.26	130	0.27	0.52	1833	25.38	2.6	48	96.67
0.27	232	0.41	0.53	1842	26.74	2.8	39	97.31
0.28	222	0.56	0.54	1783	28.08	3.0	31	97.83
0.29	482	0.81	0.55	1725	29.38	3.2	22.6	98.22
0.30	514	1.21	0.56	1695	30.65	3.4	16.6	98.50
0.31	689	1.66	0.57	1712	31.91	3.6	13.5	98.72
0.32	830	2.22	0.58	1715	33.18	3.8	11.1	98.91
0.33	1059	2.93	0.59	1700	34.44	4.0	9.5	99.06
0.34	1074	3.72	0.60	1666	35.68	4.5	5.9	99.34
0.35	1093	4.52	0.62	1602	38.10	5.0	3.8	99.51
0.36	1068	5.32	0.64	1544	40.42	6.0	1.8	99.72
0.37	1181	6.15	0.66	1486	42.66	7.0	1.0	99.82
0.38	1120	7.00	0.68	1427	44.81	8.0	.6	99.88
0.39	1098	7.82	0.70	1369	46.88	10.0	.25	99.94
0.40	1429	8.73	0.72	1314	48.86	15.0	4.9×10^{-2}	99.98
0.41	1751	9.92	0.75	1235	51.69	20.0	1.6×10^{-2}	99.99
0.42	1747	11.22	0.80	1109	56.02	50.0	3.8×10^{-4}	100.00

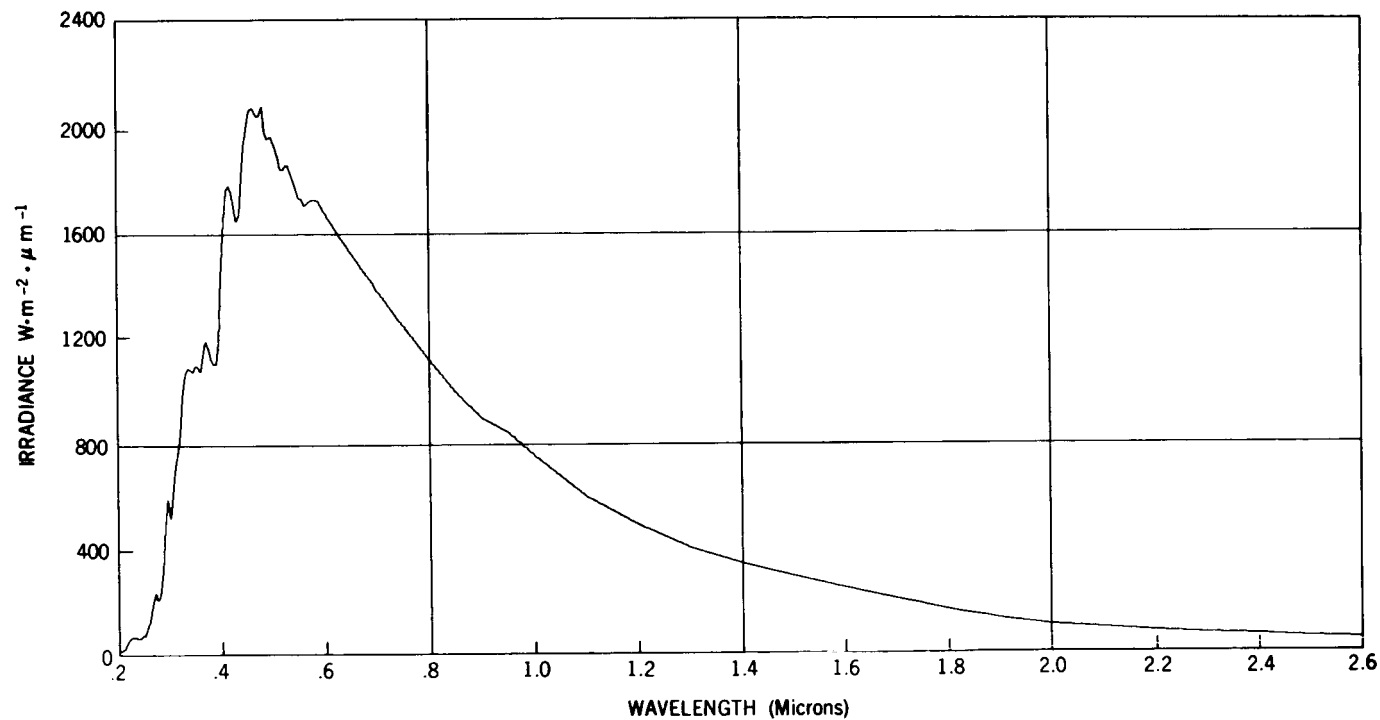


Figure 1. Solar Spectral Irradiance.

REFERENCES

1. Thekaekara, M. P.; Kruger, R.; and Duncan, C. H.: Solar Irradiance Measurements from a Research Aircraft. *Applied Optics*, vol. 8, no. 8, Aug. 1969, pp. 1713-1732.
2. Thekaekara, M. P.; et al.: The Solar Constant and the Solar Spectrum Measured from a Research Aircraft at 38,000 Feet. NASA, Goddard Space Flight Center, Report X-322-68-304 (Greenbelt, Maryland), Aug. 1968. (Also available as NASA TMX-63324.)
3. Thekaekara, M. P., ed.: The Solar Constant and the Solar Spectrum Measured from a Research Aircraft. NASA TR R-351 (Washington, D.C.), Oct. 1970.
4. Kondratyev, K. Ya.; and Nikolsky, G. A.: Solar Radiation and Solar Activity. *Quarterly J. Royal Meteorological Society*, vol. 96, no. 3, July 1970, pp. 509-522.
5. Kondratyev, K. Ya.; Nikolsky, G. A.; Badinov, J. Ya.; and Andreev, S. D.: Direct Solar Radiation up to 30 km and Stratification of Attenuation Components in the Stratosphere. *Applied Optics*, vol. 6, no. 2, Feb. 1967, pp. 197-207.
6. Murcray, D. G.: Balloon Borne Measurements of the Solar Constant. University of Denver Report AFCRL-69-0070 (Denver, Colorado), Jan. 1969.
7. Murcray, D. G.; Kyle T. G.; Kosters, J. J.; and Gast, P. R.: The Measurement of the Solar Constant from High Altitude Balloons. University of Colorado, Report AFCRL-68-0452 (Denver, Colorado), Aug. 1968.
8. Drummond, A. J.; Hickey, J. R.; Scholes, W. J.; and Laue, E. G.: New Value of the Solar Constant of Radiation. *Nature*, vol. 218, no. 5138, April 20, 1968, pp. 259-261.
9. Drummond, A. J.; and Hickey, J. R.: The Eppley-JPL Solar Constant Measurement Program. *Solar Energy*, vol. 12, no. 2, Dec. 1968, pp. 217-232.
10. Laue, E. G.; and Drummond, A. J.: Solar Constant: First Direct Measurements. *Science*, vol. 161, no. 3844, Aug. 1968, pp. 888-891.

11. Drummond, A. J.; Hickey, J. R.; Scholes, W. J.; and Laue, E. G.: The Eppley-JPL Solar Constant Measurement Experiment. Proceedings International Astronautical Federation 17th Congress, Madrid, vol. 2, 1966, pp. 227-235 (Gordon and Breach, New York, 1967).
12. Drummond, A. J.; Hickey, J. R.; Scholes, W. J.; and Laue, E. G.: Multichannel Radiometer Measurement of Solar Irradiance, J. of Spacecraft and Rockets, vol. 4, no. 9, Sept. 1967, pp. 1200-1206.
13. Drummond, A. J.; Hickey, J. R.; Scholes, W. J.; and Laue, E. G.: The Calibration of Multichannel Radiometers for Application in Spacecraft and Space Simulation Programs. Proceedings International Astronautical Federation 18th Congress, Belgrade, vol. 2, 1967, pp. 407-422 (Pergamon Press, New York, 1968).
14. Plamondon, J. A.: The Mariner Mars 1969 Temperature Control Flux Monitor. Jet Propulsion Laboratory Space Programs Summary 37-59, vol. 3, Oct. 1969, pp. 162-168.
15. Willson, R. C.: New Radiometric Techniques and Solar Constant Measurements, paper presented at the 1971 International Solar Energy Society Conference, May 10-14, 1971, Goddard Space Flight Center, Greenbelt, Maryland, "Summaries and Abstracts," p. IV-8. Willson, R. C.: Active Cavity Radiometric Scale, International Pyrheliometric Scale and Solar Constant. J. Geophys. Research, vol. 76, no. 19, 1971, pp. 4325-4340.
16. Thekaekara, M. P.; and Drummond, A. J.: Standard Values for the Solar Constant and its Spectral Components. Nature, Physical Sciences, vol. 229, no. 1, Jan. 4, 1971, pp. 6-9.
17. Johnson, F. S.: The Solar Constant. J. Meteorology, vol. 11, no. 6, Dec. 1954, pp. 431-439.
18. Moon, P.: Proposed Standard Solar Radiation Curves for Engineering Use. J. Franklin Inst., vol. 230, Nov. 1940, pp. 583-617.
19. Aldrich, L. B.; and Abbot, C. G.: Smithsonian Pyrheliometry and the Standard Scale of Solar Radiation. Smithsonian Miscellaneous Collections, vol. 110, no. 5, Publ. No. 3920, Smithsonian Institution, Washington, D.C., April 15, 1948.
20. Aldrich, L. B.; and Hoover, W. H.: The Solar Constant, Science vol. 116, no. 3024, Dec. 12, 1952, p. 3.

21. Dunkelman, L.; and Scolnik, R.: Solar Spectral Irradiance and Vertical Attenuation in the Visible and Ultraviolet. *Opt. Soc. Amer. J.*, vol. 49, no. 4, April 1959, pp. 356-367.
22. Allen, C. W.: Solar Radiation. *Quart. J. Roy. Meteorol. Soc.*, vol. 84, no. 362, Oct. 1958, pp. 307-318.
23. Nicolet, M.: Sur le Problème de la Constante Solaire. *Ann. d'Astrophysique*, vol. 14, no. 3, July-Sept., 1951, pp. 249-265.
24. Labs, D.; and Neckel, H.: The Radiation of the Solar Photosphere from 200 Å to 100 μ . *Zeitschrift für Astrophysik*, vol. 69, 1968, pp. 1-73.
25. Makarova, E. A.: A Photometric Investigation of the Energy Distribution in the Continuous Solar Spectrum in Absolute Units. *Soviet Astronomy-AJ*, vol. 1, no. 4, April 1957, pp. 531-546.
26. Detwiler, C. R.; Garrett, D. L.; Purcell, J. D.; and Tousey, R.: The Intensity Distribution in the Ultraviolet Solar Spectrum. *Ann. de Geophysique*, vol. 17, no. 3, July-Sept. 1961, pp. 9-18.
27. Arvesen, J. C.; Griffin, R. N.; and Pearson, B. D., Jr.: Determination of Extraterrestrial Solar Spectral Irradiance from a Research Aircraft. *Applied Optics*, vol. 8, no. 11, November 1969, pp. 2215-2232.
28. Thekaekara, M. P.: Proposed Standard Values of the Solar Constant and the Solar Spectrum. *J. Environmental Sci.*, vol. 13, no. 4, Sept.-Oct. 1970, pp. 6-9.
29. Thekaekara, M. P.: The Solar Constant and Spectral Distribution of Solar Radiant Flux, *Solar Energy*, vol. 9, no. 1, Jan.-Mar. 1965, pp. 7-20.
30. Thekaekara, M. P.: Survey of the Literature on the Solar Constant and the Spectral Distribution of Solar Radiant Flux, NASA SP-74, National Aeronautics and Space Administration, Washington, D. C., 1965. (Also available as NASA-N65-22362).
31. Duncan, C. H.: Radiation Scales and the Solar Constant, Proceedings, 4th Space Simulation Conference, American Institute of Aeronautics and Astronautics, Los Angeles, Calif., 1969. Also available as GSFC document #X-713-69-382.

32. Hinteregger, H. E.: The Extreme Ultraviolet Solar Spectrum and Its Variation During a Solar Cycle. *Ann. Geophysique*, vol. 26, no. 2, 1970, pp. 547-554.
33. Heath, D. F.: Observations on the Intensity and Variability of the Near Ultraviolet Solar Flux from the Nimbus III Satellite. *J. Atmospheric Sciences*, vol. 26, no. 5, pt. 2, Sept. 1969, pp. 1157-1160.
34. Parkinson, W. H.; and Reeves, E. M.: Measurements in the Solar Spectrum Between 1400 Å and 1875 Å with a Rocket Borne Spectrometer. *Solar Physics*, vol. 1, 1969, pp. 342-347.
35. Shimabukoro, F. J.; and Stacey, J. M.: Brightness Temperature of the Quiet Sun at Centimeter and Millimeter Wavelengths. *Astrophys. J.*, vol. 152, no. 6, June 1968, pp. 777-782.

RECOMMENDED PRACTICE FOR SOLAR SIMULATION FOR THERMAL BALANCE TESTING OF SPACECRAFT

IES Solar Radiation Committee and ASTM Space Simulation Committee E-21

FOREWORD

This Recommended Practice for Solar Simulation for Thermal Balance Testing of Spacecraft resulted from a joint effort between the Institute of Environmental Sciences Solar Radiation Committee and the American Society for Testing and Materials Committee E-21 on Space Simulation. It was the subject for a Workshop and Panel Discussion at the Fifth ASTM-IES-AIAA Space Simulation Conference held at The National Bureau of Standards in Gaithersburg, Maryland, 14-16 September, 1970. It was also the subject for a colloquium session held at the 17th Annual Meeting of the Institute of Environmental Sciences at Los Angeles, California, 26-30 April, 1971.

Members of the two committees and many other interested persons have contributed to this recommended practice by offering comments and suggestions. The individuals who accepted the responsibility for writing this document were:

Eugene N. Borson	- The Aerospace Corporation
John A. Castle	- Spectrolab, Division of Textron, Inc.
Charles H. Duncan	- NASA/Goddard Space Flight Center
John S. Griffith	- Jet Propulsion Laboratory
Raymond W. Haney	- Brown, Root - Northrop
Eric G. Laue	- Jet Propulsion Laboratory
Albert R. Lunde	- Boeing Company
Donald Male	- Arnold Engineering Development Center
Anthony F. Matel	- Hughes Aircraft Company
Roy McIntosh, Jr.	- NASA/Goddard Space Flight Center
Leonard E. Nielsen	- TRW Systems
David H. Orbock	- Brown, Root - Northrop
Benson T. Replogle	- Brown, Root - Northrop
James J. Webb	- NASA/Goddard Space Flight Center

This document is planned for eventual publication by ASTM in the Book of Standards. The present reproduction of this document is the draft as approved by the IES Solar Radiation

Committee. The document now has to be voted on by ASTM and may be revised before it appears in the ASTM Book of Standards.

It is printed in this proceeding to give it a wider distribution among those who may find it useful in their work.

Charles H. Duncan
Chairman, IES Solar Radiation
Committee

1. SCOPE

1.1 Purpose

The primary purpose of this recommended practice is to provide guidance for making adequate thermal balance tests of spacecraft and components where solar simulation has been determined to be the applicable method. Careful adherence to this document should ensure the adequate simulation of the radiation environment of space for thermal tests of space vehicles.

A corollary purpose is to provide the proper test environment for systems integration tests of space vehicles. An accurate space simulation test for thermal balance generally will provide a good environment for operating all electrical and mechanical systems in their various mission modes to determine interferences within the complete system. Although adherence to this practice will provide the correct thermal environment for this type of test, there is no discussion of the extensive electronic equipment and procedures required to support systems integration testing.

1.2 Non-applicability

This practice is not applicable to or else provides incomplete coverage of the following types of tests:

1. Launch phase or atmospheric reentry of space vehicles.
2. Landers on planet surfaces.
3. Degradation of thermal coatings.
4. Increased friction in space of mechanical devices, sometimes called "cold welding."
5. Sun sensors.
6. Man in space.

7. Energy conversion devices.
8. Tests of components for leaks, outgassing, radiation damage, or bulk thermal properties.

1.3 Range of Application

The extreme diversification of spacecraft, design philosophies and analytical effort makes the preparation of a brief, concise document impossible. Because of this, various spacecraft parameters are classified and related to the important characteristic of space simulators in a chart in Section 5.6.

The ultimate result of the thermal balance test is to prove the thermal design to the satisfaction of the thermal designers. Flexibility must be provided to them to trade off additional analytical effort for simulator shortcomings. The combination of a comprehensive thermal analytical model, modern computers, and a competent team of analysts greatly reduces the requirements for accuracy of space simulation.

1.4 Utility

This recommended practice will be useful during space vehicle test phases from development through flight acceptance test. It should provide guidance for space simulation testing early in the design phase of thermal control models of subsystems and spacecraft. Flight spacecraft frequently are tested before launch. Occasionally, tests are made in a space chamber after a sister spacecraft is launched as an aid in analyzing anomalies that occur in space.

2. SUMMARY

Thermal balance testing of spacecraft can be performed in many ways. The specific methods depend upon such items as the spacecraft design, the characteristics of the available simulator, the mission requirements, cost, and schedule. Therefore, it is not desirable or possible to include all thermal balance tests in one test method.

This Recommended Practice defines terms, discusses test requirements and instrumentation, and reviews general procedures, safety, and maintenance. The test, instrumentation, and thermal engineers must provide the detail test method that will satisfy their particular requirements and be fully aware of the effects of the necessary deviations from the ideal.

3. DEFINITIONS, SYMBOLS, UNITS, AND CONSTANTS

3.1 This section contains the recommended definitions, symbols, units and constants for use in solar simulation for thermal balance testing of spacecraft. The International System of Units (SI) and International and American National Standards have been adhered to as much as possible. ASTM E 349-68T, Tentative Definitions of Terms Relating to Space Simulation is also used. The source of each definition originated in this Recommended Practice is referenced.

3.2 Definitions

- (1) Absorptance, n. ratio of the absorbed radiant or luminous flux to the incident flux. Symbol: α_e , α_v , α .
- (1) Absorptivity of an Absorbing Material, n. internal absorptance of a layer of the material such that the path of the radiation is of unit length.
- (2) Air-Mass-One, the equivalent atmospheric attenuation of the electromagnetic spectrum to modify the solar irradiance as measured at one astronomical unit from the sun outside the sensible atmosphere to that received at sea level, when the sun is in the zenith position.
- (2) Air-Mass-Zero, the absence of atmospheric attenuation of the solar irradiance at one astronomical unit from the sun.
Symbol: AMO
- (2) Albedo. The ratio of the amount of electromagnetic radiation reflected by a body to the amount incident upon it.
- (2) Apparent Source. The apparent source is defined as the minimum area of the final elements of the solar optical system from which issues 95% or more of the energy that strikes an arbitrary point on the test specimen.
- (2) Astronomical Unit. A unit of length defined as the mean distance from the Earth to the Sun, 149,597,890 \pm 500 km. Symbol: AU
- (1) Blackbody (USA), Planckian Radiator, n. Thermal radiator which absorbs completely all incident radiation, whatever the wavelength, the direction of incidence or the polarization. This radiator has, for any wavelength, the maximum spectral concentration of radiant exitance at a given temperature.

- (2) Collimate. To render parallel, as rays of light.

- (2) Collimation Angle. In solar simulation the term "collimation angle" has from practice been used to denote the angular non-parallelism of the solar beam, i.e., the decollimation angle. In general, a collimated solar simulator uses an optical component to image at infinity an apparent source (pseudo sun) of finite size. The angle subtended by the apparent source to the final optical component referred to as the collimator, is defined as the solar subtense angle and establishes the nominal angle of decollimation. A primary property of the "collimated" system is the near constancy of the angular subtense angle as viewed from any point in the test volume. The solar subtense angle is therefore a measure of the nonparallelism of the beam. To avoid confusion between various scientific fields, the use of solar subtense angle in lieu of collimation angle or decollimation angle is encouraged. See Solar Subtense Angle.

- (2) Collimator. An optical device which renders rays of light parallel.

- (2) Decollimation Angle. Not recommended. See Collimation Angle.

- (1) Diffuse Reflector. A body that reflects radiant energy in such a manner that the reflected energy may be treated as if it were being emitted (radiated) in accordance with Lambert's law. The radiant intensity reflected in any direction from a unit area of such a reflector varies as the cosine of the angle between the normal to the surface and the direction of the reflected radiant energy.

- (2) Dispersion Function. The dispersion function, $\frac{X}{\lambda}$, is a measure of the separation of wavelengths from each other at the exit slit of the monochromator, where X is the distance in the slit plane and λ is wavelength. The dispersion function is, in general, different for each monochromator design and is usually available from the manufacturer.

- (2) Divergence Angle. See Solar Beam Angle.

- (1) Electromagnetic Spectrum. The ordered array of known electromagnetic radiations, extending from the shortest wavelengths, gamma rays, through X-rays, ultra-violet radiation, visible radiation, infrared and including microwave and all other wavelengths of radio energy.

- (1) Emissivity of a Thermal Radiator, *n.* Ratio of the thermal radiant exitance of the radiator to that of a full radiator at the same temperature. Symbol: ϵ , $\epsilon = M_{e, th} / M_e$ ($\epsilon = 1$). NOTE: Formerly "Pouvoir emissif" (Fr.).
- (2) Emittance (ϵ). The ratio of the radiant exitance of a specimen to that emitted by a black body radiator at the same temperature, identically viewed. Generally refers to a specific sample or measurement of a specific sample. Total hemispherical emittance is the energy emitted over the hemisphere above the emitting element for all wavelengths. Normal emittance refers to the emittance normal to the surface to the emitting body.
- (1) Exitance at a Point on a Surface (Radiant Exitance), *n.* Quotient of the radiant flux leaving an element of the surface containing the point, by the area of that element. Symbol: M . Unit: watt per square meter, $W \cdot m^{-2}$.
- (2) Field Angle. See Solar Beam Subtense Angle. Not recommended.
- (2) Flight Model. An operational flight capable spacecraft that is usually subjected to Acceptance Tests.
- (1) Flux. (Radiant, particulate, etc.). For electromagnetic radiation, the quantity of radiant energy flowing per unit time. For particles and photons, the number of particles or photons flowing per unit time.
- (1) Gray Body. A body for which the spectral emittance and absorptance is constant and independent of wavelength. The term also is used to describe bodies whose spectral emittance and absorptance is constant within a given wavelength band of interest.
- (2) Incident Angle. The angle at which a ray of energy impinges upon a surface, usually measured between the direction of propagation of the energy and a perpendicular to the surface at the point of impingement, or incidence.
- (1) Infrared Radiation. See Electromagnetic Spectrum.
- (2) Insolation. Direct solar irradiance received at a surface. (Contracted from incoming solar radiation.)
- (1) Integrating (Ulbrecht) Sphere, *n.* Part of an integrating photometer. A sphere which is coated internally with a white diffusing paint as nonselective as possible, and which is provided with an

associated equipment for making a photometric measurement at a point of the inner surface of the sphere. A screen placed inside the sphere prevents the point under observation from receiving any radiation directly from the source.

(2) Intensity. See Radiant Intensity.

(1) Irradiance at a Point on a Surface, n. Quotient of the radiant flux incident on an element of the surface containing the point, by the area of that element. Symbol: E_e , E ; $E_e = d\Phi_e/dA$; Unit: watt per square meter, $W \cdot m^{-2}$.

(2) Irradiance, Mean Total. The average total irradiance over the test volume. Defined by the following equation. Symbol: \bar{E}

$$\bar{E} = \frac{\int_v E(r, \theta, z) dV}{\int_v dV}$$

where $\bar{E}(r, \theta, z)$ is the total irradiance as a function of position.

(2) Irradiance, Spectral. The irradiance at a specific wavelength over a narrow bandwidth, or as a function of wavelength. Symbol: E_λ or $E(\lambda)$.

(2) Irradiance, Temporal. The stability of irradiance is the temporal variation of individual irradiances from the mean irradiance. The temporal variations should be measured over time intervals equal to the thermal time constants of the components.

The temporal stability of total irradiance can be defined as:

$$E_t = \pm 100 \left(\frac{\Delta E_t(\min) + \Delta E_t(\max)}{2\bar{E}} \right)$$

(2) Irradiance, Total. The integration over all wavelengths of the spectral irradiance.

(2) Irradiance, Uniformity of. Uniformity of total irradiance can be defined as:

$$E_u = \pm 100 \frac{E_{(\min)} + E_{(\max)}}{2\bar{E}}$$

where E_u is the uniformity of the irradiance within the test volume, expressed as a percent of the mean irradiance. $E_{(\min)}$ is the smallest value obtained for irradiance within the test volume; and, $E_{(\max)}$ is the largest value obtained for irradiance within the test volume. Uniformity of irradiance values must always be specified together with the largest linear dimension of the detector used.

- (2) Lambert's Law. The radiant intensity (flux per unit solid angle) emitted in any direction from a unit radiating surface varies as the cosine of the angle between the normal to the surface and the direction of the radiation. Also called Lambert's cosine law.

Lambert's law is not obeyed exactly by most real surfaces, but an ideal black body emits according to this law. This law is also satisfied (by definition) by the distribution of radiation from a perfectly diffuse radiator and by the radiation reflected by a perfectly diffuse reflector. In accordance with Lambert's law, an incandescent spherical black body when viewed from a distance appears to be a uniformly illuminated disk. This law does not take into account any effects that may alter the radiation after it leaves the source.

- (2) Maximum Test Plane Divergence Angle. The angle between the extreme ray from the apparent source and the test plane. This applies principally to direct projection beams where it is equivalent to one-half the projection cone angle. See Figure 3-1.
- (2) Natural Bandwidth. The width at half height of a radiation source emission peak. It is independent of instrument spectral bandwidth, being an intrinsic property of the radiation source.
- (2) Penumbra. See Umbra.
- (2) Planck's Law. Law giving the spectral concentration of radiant exitance of a full radiator as a function of wavelength and temperature. For the total radiation emitted (unpolarized):

$$M(\lambda, T) = c_1 \lambda^{-5} (e^{c_2/\lambda T} - 1)^{-1}$$

where M is in watts per square meter, λ is the wavelength in meters, T is the absolute temperature in Kelvin, and the constants are:

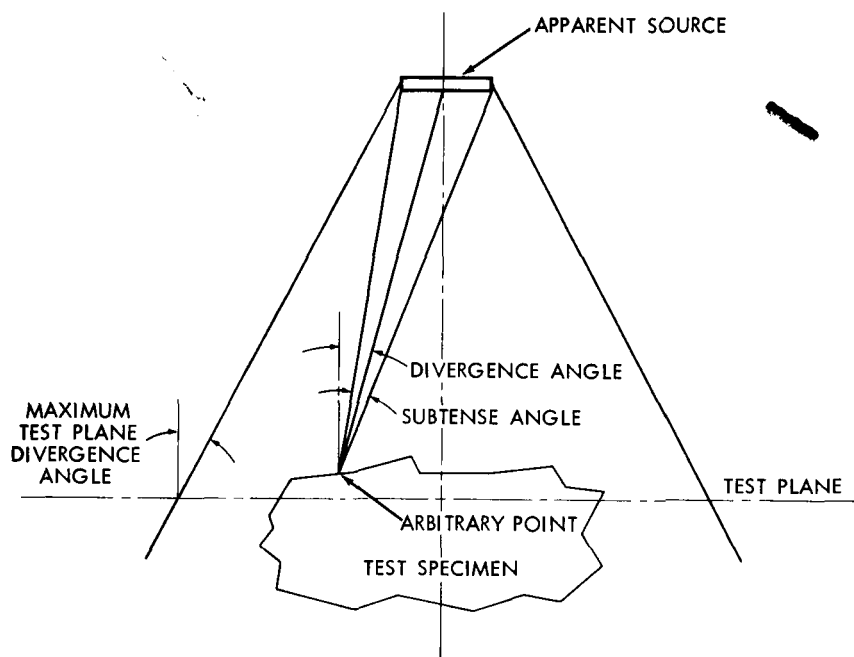


Figure 3.1. Solar Subtense and Divergence Angles.

$$c_1 = w h c^2 = 3.741844 \times 10^{-16} \text{ W m}^{-2}$$

$$c_2 = \frac{h c}{k} = 1.438833 \times 10^{-2} \text{ m K}$$

where h = Planck's Constant
 c = Velocity of light in vacuum
 k = Boltzmann Constant

Note: It is recommended that the constant c_1 is always used with the meaning noted above. The numerical constants applicable to other aspects of the radiation emitted are shown below. They should be designated c_1 multiplied by an appropriate factor.

$$\pi h c^2 = \frac{c_1}{2} \text{ (for the exitance of the polarized radiation)}$$

$$2 h c^2 = \frac{c_1}{\pi} \text{ (for the radiance of the non-polarized radiation)}$$

$$hc^2 = \frac{c_1}{2\pi} \text{ (for the radiance of the polarized radiation)}$$

$$3hc = \text{(for the energy per unit volume of the nonpolarized radiation)}$$

- (2) Prototype Model. A spacecraft or subsystem that is used for development or qualification test. This is an accurate reproduction of actual space hardware, and is identical or nearly to the flight model.
- (2) Pyranometer. An instrument which measures the combined solar irradiance and diffuse sky irradiance. The pyranometer consists of a recorder and a radiation sensing element which is mounted so that it views the entire sky.
- (2) Pyreheliometer. An instrument which measures the direct solar irradiance, consisting in a casing which is closed except for a small aperture through which the direct solar rays enter, and a recorder unit.
- (2) Angstrom Compensation Pyreheliometer. An instrument developed by K. Angstrom for the measurement of direct solar irradiation. The radiation receiver station consists of two identical manganin strips whose temperatures are measured by attached thermocouples. One of the strips is shaded, whereas the other is exposed to sunlight. An electrical heating current is passed through the shaded strip so as to raise its temperature to that of the exposed strip. The electric power required to accomplish this is a measure of the solar irradiance.
- (1) Radiance (in a given direction, at a point on the surface of a source or receptor, or at a point in the path of a beam), n. - quotient of the radiant flux leaving, arriving at, or passing through an element or surface at this point, and propagated in directions defined by an elementary cone containing the given direction by the product of the solid angle of the cone and the area of the orthogonal projection of the element of surface on a plane perpendicular to the given direction.

Symbol: L_e , L ; $L_e = d^2 \Phi / (d\omega dA \cos \theta)$; Unit: watt per steradian and per square meter, $W \cdot sr^{-1} m^{-2}$.

- (1) Radiant Flux: Radiant power, n. - power emitted, transferred, or received as radiation: Unit: watt (W). Symbol: Φ .

- (1) Radiant Flux (Surface) Density at a Point of a Surface, n. - quotient of the radiant flux at an element of the surface containing the point, by the area of that element. (See also Irradiance and Radiant Exitance.) Unit: watt per square meter, $\text{W}\cdot\text{m}^{-2}$.
- (1) Radiant Intensity of a Source, in a Given Direction, n. - quotient of the radiant flux leaving the source propagated in an element of solid angle containing the given direction, by the element of solid angle. Symbol: I ; (Unit: watt per steradian, $\text{W}\cdot\text{sr}^{-1}$).

Note: For a source which is not a point source: The quotient of the radiant flux received at an elementary surface by the solid angle which this surface subtends at any point of the source, when this quotient is taken to the limit as the distance between the surface and the source is increased.

- (1) Radiation - Monochromatic. Radiation at a single wavelength. By extension, radiation of a very small range of frequencies or wavelengths. Use of the adjective "spectral." When certain properties, such as absorptance or transmittance, etc., are considered for monochromatic radiation, and they are functions of wavelength (or frequency or wave number, etc.), the term may be preceded by the adjective, spectral, and/or by the property symbol followed by the subscript λ ; example: spectral transmittance τ_{λ} .
- (1) Radiometer. Instrument for measuring irradiance in energy or power units.
- (1) Radiometry. Measurement of the quantities associated with irradiance.
- (1) Reflection, n. - Return of radiation by a surface without change frequency of the monochromatic components of which the radiation is composed.
- (1) Reflection - Diffuse. Reflection in which, on the microscopic scale, there is no specular reflection.
- (1) Reflection - Mixed. Partly specular and partly diffuse reflected.
- (1) Regular (Specular) Reflection, n. - Reflection without diffusion in accordance with the laws of optical reflection.
- (2) Resolution. Resolution is a qualitative term relating to the fidelity of reproduction of the natural band (both in height and

width). An emission peak is said to be completely resolved when the observed band is practically identical to the natural band. Figure 2 shows the relationship between resolution (observed peak height/true peak height) and the ratio of spectral bandwidth to natural bandwidth. Note that when this ratio is small, the deviation from true peak height is small, the fraction being 99.6% at a ratio of 0.1.

- (1) Reflectance. Ratio of the reflected radiant or luminous flux to the incident flux. Symbol: ρ .
- (1) Reflectivity. Reflectance of a layer of material of such a thickness that there is no change of reflectance with increased thickness.
- (2) Slit Width. The physical width of a monochromator slit opening. In general, all slits should be equal in width at all times. The exit defines the wavelength bandwidth directed to the detector. The energy incident upon the detector varies as the square of the slit width.
- (2) Solar Absorptance. The ratio of the absorbed solar flux to be incident solar flux. Symbol: a_s .

$$\alpha = \frac{\int_0^{\infty} \alpha(\lambda) E(\lambda) d\lambda}{\int_0^{\infty} E(\lambda) d\lambda}$$

- (2) Solar Beam Divergence Angle. The angle measured from a line extending from the center of the apparent source to an arbitrary point in the test volume and to a line parallel to the principal axis of the solar beam. (Figure 3-1.)
- (2) Solar Beam Incident Angle. The angle measured from a line extending from the center of the apparent source to an arbitrary point on the test specimen and the surface normal at that point.
- (2) Solar Beam Subtense Angle. The solar beam subtense angle is that angle subtended by the maximum dimension of the apparent source at an arbitrary point on the test specimen. (See Figure 3-1.) Note: The terms "collimation angle" and "field angle" are sometimes used for "subtense angle." The term "subtense angle" is preferred.

- (2) Solar Constant. The total solar irradiance at normal incidence on a surface in free space at the Earth's mean distance from the Sun (one AU). Note: Current accepted value of $1353 \pm 21 \text{ W/m}^2$ and is subject to change.
- (2) Space Environment Simulation. A laboratory duplication of one or more of the effects of the space environmental parameters on a spacecraft, components, or materials.

The natural environmental parameters include vacuum-pressure, particulate radiation, electromagnetic radiation and meteoroid radiation.

Induced environmental parameters include vibration, shock and acceleration.

The effects can include: Thermal balance, heat transfer, material property change, operational/mechanical subsystem problem and subsystem functional testing .

- (2) Spectra, Line. The spontaneous emission of electromagnetic radiation from the bound electrons as they jump from high to low energy levels in an atom.

This radiation is essentially at a single frequency determined by the jump in energy. Each different jump in energy level, therefore, has its own frequency and the net radiation is referred to as the line spectra. Since these line spectra are characteristic of the atom, they can be used for identification purposes.

- (2) Spectropyrheliometer. An instrument which measures the spectral distribution of direct solar irradiance.
- (1) Spectroradiometer. An instrument for measuring the spectral concentration of radiant energy or radiant power. Also called "spectrometer."
- (2) Spectrum, Continuous. 1. A spectrum in which wavelengths, wave numbers, and frequencies are represented by the continuum of real numbers or a portion rather than by a discrete sequence of numbers. See Spectra, Line 2. For electromagnetic radiation, a spectrum that exhibits no detailed structure and represents a gradual variation of intensity o with wavelength from one end to the other, as the spectrum from an incandescent solid.

- (2) Spectral Filter. An optical component which is spectrally selective. Any optical component that rejects radiation in spectral regions in order to shape the resulting spectral distribution.
- (2) Stefan-Boltzmann Law. The relation between the radiant exitance of a blackbody radiator and its temperature.

$$M = \sigma T^4$$

where the constant of proportionality (σ) is called the Stefan-Boltzmann constant and has a value of

$$\sigma = 5.66961 \times 10^{-8} \text{ W m}^{-2} \text{ K}^{-4}$$

- (2) Subtense Angle. See Solar Beam Subtense angle.
- (2) Test Volume, Simulator. The total volume within the space environmental chamber which can simulate the desired effects.
- (2) Test Volume, Spacecraft. The volume occupied by the spacecraft within the space simulation chamber throughout the duration of the test. Unless otherwise specified, test volume is meant to mean spacecraft.
- (2) Thermal Analytical Model. A mathematical model of the thermal characteristics of a spacecraft that is usually solved using a computer.
- (2) Thermal Balance Test. A test or series of tests conducted upon a spacecraft or model to determine the temperatures in **space** under normal or extreme operating conditions. Both **transient** and equilibrium conditions can be simulated.
- (1) Thermal Radiator. Source emitting by thermal radiation.
- (2) Thermopile. A transducer for converting thermal energy **di-**rectly into electrical energy, composed of pairs of **thermocoup-**les which are connected either in series or in parallel.
- (1) Transmission. Passage of radiation through a **medium** without change of frequency of the monochromatic components of which the radiation is composed.
- (1) Transmittance (τ). Ratio of the transmitted radiant flux to the incident flux.

- (1) Ultraviolet Radiation. See Electromagnetic Spectrum.
- (2) Umbra. The darkest part of a shadow in which light is completely cut off by an intervening object. A lighter part surrounding the umbra, in which the light is only partly cut off, is called pen umbra.

- (1) Visible Radiation. See Electromagnetic spectrum.

Note:

- (1) Terms defined in E349-68T.

- (2) New Terms.

3.3 Commonly Used Constants

The values of the physical constants presented below are taken from References 3.3 and 3.4. The constants are subject to change and the latest available supplied by the National Bureau of Standards should be used.

Symbol	Constant	Value	
c	Velocity of light in vacuum	2.997	$925 \cdot 10^8 \text{ m} \cdot \text{s}^{-1}$
h	Planck constant	6.626	$196 \cdot 10^{-34} \text{ J} \cdot \text{s}$
c_1	First Radiation Constant	3.741	$844 \cdot 10^{-16} \text{ W} \cdot \text{M}^{-2}$
C_2	Second Radiation constant	1.438	$833 \cdot 10^{-2} \text{ m} \cdot \text{k}$
b	Wien displacement constant	$2.89978 \text{ m} \cdot \text{k}$	
c	Stefan-Boltzmann constant	$5.66961 \text{ w} \cdot \text{m}^{-2} \cdot \text{k}^{-4}$	

References

- 3.1 Metric Practice Guide (A Guide to the Use of SI-the International System of Units) ASTM E380-70
- 3.2 International Organization for Standardization, ISO Recommendation R1000, "Rules for the Use of Units of the International System of Units and a Selection of the decimal multiples and Sub-multiples of the SI units," American National Standards Institute, 1969

TABLE OF COMMONLY USED SYMBOLS

Symbol	Quantity	Definition Equation or Value	Units	Abbreviation
Q	Radiant Energy, work, quantity of heat		joule	J
\dot{q}	Radiant Flux	$\dot{q} = dQ/dt$	watt (joule/second)	W, JS ⁻¹
E	Irradiance (Receiver) Flux Density	$E = d\dot{q}/dA$	watt per square meter	W m ⁻²
M	Radiant Exitance (Source)	$M = d\dot{q}/dA$	watt per square meter	W m ⁻²
I	Radiant Intensity (Source)	$I = d\dot{q}/d\omega$ ω = solid angle through which flux from source is radiated	watt per steradian	W sr ⁻¹
L	Radiance	$L = \frac{dI}{(dA \cos \theta)}$ θ = angle between line of sight and normal to surface dA	watt per steradian per square meter	W sr ⁻¹ m ⁻²
T	Transmittance	$\tau = \frac{\dot{q}_{\text{Transmitted}}}{\dot{q}_{\text{Incident}}}$	none	
$\tau(\lambda)$	Spectral Transmittance	$\tau(\lambda) = \frac{\dot{q}(\lambda)_{\text{Transmitted}}}{\dot{q}(\lambda)_{\text{Incident}}}$	none	
ρ	Reflectance (total)	$\rho = \frac{\dot{q}_{\text{Reflected}}}{\dot{q}_{\text{Incident}}}$	none	
ϵ_H	Emittance (total hemispherical)	$\epsilon_H = \frac{M_{\text{Specimen}}}{M_{\text{Black Body}}}$		
α	Absorptance	$\alpha = \frac{\dot{q}_{\text{Absorbed}}}{\dot{q}_{\text{Incident}}}$	none	
α_s	Solar Absorptance	$\alpha_s = \frac{\text{Solar Irradiance Absorbed}}{\text{Solar Irradiance Incident}}$	none	

- 3.3 Chapter 2. NBS Applied Mathematics Series 55, Handbook of Mathematical Functions, Ninth Printing, February 1971, Superintendent of Documents, U.S. Government Printing Office, Washington, D.C. 20402
- 3.4 Taylor, B. N., Parker, W. H., & Langenberg, D. N., Reviews of Modern Physics, Vol. 41, p. 375, 1969
- 3.5 American National Standard USAS Y10.18-1967, "Letter Symbols for Illuminating Engineering," American Society of Mechanical Engineers
- 3.6 American National Standard, USAS 27.1-1967, "Standard Nomenclature and Definitions for Illuminating Engineering, Illuminating Engineering Society
- 3.7 Tentative Definitions of Terms Relating to Space Simulation, ASTM E349-68T
- 3.8 American National Standard ANSI Y 10.19-1969, "Letter Symbols for Units Used in Science and Technology"

4. GENERAL CONSIDERATIONS

The use of solar simulation for thermal balance testing of spacecraft imposes a number of specific technical requirements and methods. The general considerations covered here relate more to the philosophical bases of the various thermal balance tests rather than to their specific implementation.

A space program can be said to have its own unique characteristics and problems and the same can be said for each test facility. The characteristics of both the facility and the test item must be considered in the definition of the thermal balance tests. First, however, one must establish the purpose of the test and determine what must be proved or verified. Second, one may devise an excellent test program assuming no monetary, schedule, or facility limitations. Finally, one may recognize the restraints and establish a set of meaningful compromises.

This section is separated into four parts:

- (1) Purposes or reasons for performing thermal balance tests. Each test rationale is related to a specific model of the spacecraft; that is, the thermal control model, the qualification model, or prototype, and the acceptance, or flight model. On each of these the test is performed for a slightly different reason.

- (2) Ideal thermal balance test program. This is the one that would be performed if there were no restraints, such as cost, schedule, and facility limitations. This ideal test is also described in terms of thermal control model, prototype model, and flight model spacecraft.
- (3) Tradeoff considerations that should be examined before establishing the final test program; and typical test configurations.
- (4) Definition and content of the selected program.

4.1 Purpose of Thermal Balance Testing

The severity of the space thermal environment demands a thorough verification of the thermal design of the spacecraft and its subsystems. In order to do this, a number of spacecraft models are tested within a given program. Usually these include a thermal model, a prototype, and one or more flight models. In each of these test exposures there are specific, but slightly different reasons, for performing the test.

4.1.1 Thermal Control Model

The purpose of the thermal balance test of the thermal model is to obtain empirical data relative to the spacecraft thermal properties. This data is in the form of temperature measurements provided by temperature transducers distributed over the spacecraft. In some cases, as many as several hundred locations are monitored. During the test exposure various spacecraft operational modes may be simulated as well as external thermal inputs from solar, earth and lunar simulators. The test item normally has dummy electronic assemblies which provide a simulation of the mass and thermal dissipation of the actual units. Both passive and active thermal control techniques are tested in this manner. The data derived from the thermal control model test may be used to refine the mathematical model, if one exists, or may be used directly by the thermal analyst to assess the adequacy of the thermal design.

4.1.2 Prototype Model (Qualification Test)

The configuration of the spacecraft used for qualification testing is closely representative of that of the flight vehicle. The thermal balance test performed on this model gives the opportunity, once again, to verify the thermal design and also to evaluate any changes which were made due to thermal model test results. The test method here includes exposure of the spacecraft to as realistic a space environment as possible and also perhaps to some unrealistic, but readily definable thermal environments. The accurate simulation of the space environment allows a determination

of in-space operating temperatures. The thermal inputs which do not simulate space conditions may be used in some cases to determine the spacecraft thermal response. Perhaps the most important aspect of the qualification test is the verification of spacecraft functional operation while all components are at, or near, their in-space thermal conditions (both transient and steady state).

4.1.3 Flight Model (Acceptance Test)

The thermal balance test on a flight spacecraft provides assurance of satisfactory operation in space. The purpose of the test is to show up any deficiencies, either functional or thermal, that may only be recognizable under thermal-vacuum conditions. Frequently, this is the final check of the thermal systems, and of spacecraft functional performance, before launch.

4.2 The Ideal Thermal Balance Test Program

It is desirable to outline a test program that will satisfy all test objectives, and provide the highest possible confidence in the reliability of the spacecraft. This idealistic planning may be done without considering many of the normal restraints such as cost, schedule, and facility limitations. However, when the restraints are imposed, the compromises, as discussed in part 4.3, tend to highlight those areas where deviations from this ideal have been made. The method of implementation and the test results will be different for each model of the spacecraft, since the test exposure is specifically arranged to satisfy the desired objectives.

4.2.1 Thermal Control Model Test

The design of the ideal thermal control model spacecraft test includes two test concepts. One of these test concepts involves the accurate simulation of all significant characteristics of the space environment, the orbital conditions, and the precise control of spacecraft operational modes. Since this concept leads to test results which match the response that would be obtained under real space flight conditions, an analytical (mathematical) thermal model may not be necessary.

A second test concept involves a known deviation from accurate simulation of all significant characteristics. A prime purpose of this test is frequently the verification of the thermal analytical model. It is often the case that arbitrary test conditions may be more accurately controlled and more reproducibly established than can the true space environment be simulated. These known thermal inputs may then be inserted as forcing functions for a computer run of the analytical model, thus providing a basis for the prediction of in-chamber temperatures. The success of these predictions establishes the validity of the analytical model. The

arbitrary test condition exposures need not replace an accurate orbital simulation, but often are performed in addition to it. The ideal thermal control model test conditions should have no unknown thermal inputs. Among the things that should be known are the differences between the solar simulator and the real in-space sun, thermal radiative emission and reflection from chamber walls (even at LN₂ temperatures).

4.2.2 Prototype (Qualification) Model Test

The prototype spacecraft is normally used for qualification tests. Typically it is near flight configuration, with all subsystems capable of performing their normal functions. The ideal qualification test will include some test exposures that are identical to those used on the thermal control model. This provides a further verification of the thermal design, and particularly of any parts of the thermal subsystem that were modified as a result of thermal control model testing. The most significant result of the qualification spacecraft test exposure is proof of the functional performance of all spacecraft subsystems, in addition to the thermal subsystem. In order to achieve this end, and to demonstrate system design margins, an environment is produced which thermally stresses all systems more severely than they will be stressed by the anticipated space conditions. In conjunction with the thermal stresses, functional design margins are also verified by operation at high and low bus voltages and at various input signal threshold conditions.

4.2.3 Flight Model (Acceptance) Test

The final thermal balance test is performed on flight spacecraft prior to launch. The ideal test is one in which the simulated conditions are representative of all of those which will be experienced in flight. The extreme case hot, cold, and transient conditions should be simulated as well as nominal operations. Again, the functional design margin, as represented by bus voltage and control signal tolerances is demonstrated concurrently with the verification of the thermal design. Ideally, this would be a long duration test, and would include numerous temperature cycles from hot to cold extremes. This technique has a relatively high probability of exposing infant mortalities and marginal operations due to component parameter drift.

4.3 Tradeoff Considerations

It is not usually possible to have as complete and rigorous a test program as the one described in Paragraph 4.2. Among the restraints to be considered are the costs, in terms of money and schedule, and as detailed in section 5, the characteristics and limitations of the existing test facilities, as well as the nature of the spacecraft and its mission parameters.

4.3.1 Cost and Schedule

The cost per hour to operate a major environmental test facility must enter into each decision about the duration of test exposures. The more desirable long duration tests are much more costly. Costs include not only the environmental test facilities personnel and materials, but also the supporting spacecraft personnel and data reduction activities.

On flight spacecraft the space simulation test comes very late in the integration sequence. At this time in a space program there is usually a considerable schedule urgency in order to meet a launch date commitment. These cost and schedule factors must be examined in terms of reliability as well as spacecraft requirements. For example, there are specific technical factors in addition to the subjective view that a longer test is a better test. The thermal time constant of the spacecraft, that is the time required to reach an equilibrium condition under a given set of thermal inputs, establishes a minimum duration for thermal design verification. For qualification and acceptance spacecraft, this may be further extended by the minimum length of time required to perform a complete spacecraft functional test.

4.3.2 Facilities

The test facility itself, provides the major influence on test trade-offs and configuration. The size of the available chamber, the method of loading it (that is top, bottom, side, etc.) and the direction of incidence of the solar simulator beam, are all important factors. Among other things, these tend to determine the basic geometry of the support fixture. The fixture design is also influenced by spacecraft orbital characteristics such as spin rate and sun angles, and by thermal influences, including conduction errors into and out of the fixturing and shadowing from various sources. The solar simulator characteristics must be thoroughly understood in order to allow proper test evaluation. Major factors are spectrum, total beam irradiance, uniformity of irradiance in the total test volume, solar beam divergence angle, and temporal variations. These factors, together with recommended tradeoffs are discussed in 5.2 and 5.5.

4.3.3 Spacecraft and Mission Parameters

Each spacecraft and each mission present unique characteristics which must be considered in the design of the test exposure. For attitude-stabilized planet-orbiting spacecraft, the orientation with respect to sun and planet has considerable thermal influence. The altitude of the orbit determines the amount of albedo and earth emission that must be simulated or accounted for. The structure of the spacecraft also has an affect in the amount of self shadowing by appendages and solar paddles. Along

this same line there may be extraneous heat sources. An example is the use of nuclear generators for power sources on deep space missions. There are some spacecraft, or spacecraft subsystems, in which the test item surface temperature is so high (for example several hundred degrees F) that it may not be necessary to use a liquid nitrogen temperature cold wall in the chamber. All of these things are considered in the tradeoffs which lead to the optimum test design. 5.3 and 5.4 cover the subject in more detail.

4.4 Final Test Definition

The final test plan should be evaluated in terms of test adequacy after careful consideration of the objectives and facility capabilities. In the case of the thermal control model test, the evaluation consists of assessing the fidelity of the space simulation and the completeness and accuracy of the instrumentation. The qualification and acceptance tests pose a somewhat more complex problem since all subsystems must be tested. A matrix of test objectives, facility characteristics, and spacecraft and mission parameters may be prepared to assist in the final test definition. For a complete systems integration test, this matrix is very complex and certainly is beyond the scope of this recommended practice. However, a matrix is provided in section 5.6 for the thermal balance testing phase only.

The final test definition is a pyramid formed by the many materials tests, subsystem tests, and supporting analysis which all provide confidence in meeting the overall objectives.

Several examples of test facility configurations are given to illustrate special conditions which may influence the test design.

- (a) Variable Solar Flux Vector. Most spacecraft do not maintain a constant orientation with respect to the sun. The change in attitude may occur at the orbital period, seasonally, during spacecraft maneuvers, or at other times depending upon the mission profile. The simulation of different solar flux angles may be accomplished by physically moving the spacecraft to the desired position within the stationary solar beam. In some instances, especially with spin-stabilized spacecraft, the mechanical complexity of producing a variable-spin axis, handling fixture precludes this approach. An equally effective test method employs a movable mirror to redirect the solar beam to the desired angle. Tests have been successfully performed in this manner using plane mirrors up to 100 square feet in area. The use of a remotely positionable mirror frame may permit the simulation of summer, equinox and winter incident angles on a spinning, geo-synchronous spacecraft without returning the chamber to atmospheric pressure.

- (b) **Stationary Test of Spinning Spacecraft.** It is sometimes necessary to perform a stationary test on a spacecraft that is designed to spin in orbit. An example of this is provided by a communications satellite on which the transponders must be connected to the test equipment by waveguides or coaxial cables, which preclude the use of sliprings. This thermal balance test may be accomplished by a circumferential tungsten lamp array.
- (c) **Combined Solar Sources.** A combination of tungsten or infrared sources may have to be used in conjunction with a spectrally accurate source if the high quality source does not irradiate a large enough area. Whenever this technique is employed it is essential to consider all of the effects of the differences between the sources in spectrum, subtense angle and divergence angle. These aspects are discussed more thoroughly in 5.1 and 6.5.2.1.

5. THERMAL CHARACTERISTICS AND TEST REQUIREMENTS

5.1 Thermal Sensitivity of Spacecraft

An ideal thermal balance test of a spacecraft would simulate precisely the thermal and radiation environment of space. No solar simulator, vacuum chamber, and cold shroud perfectly simulate space. Furthermore, some spacecraft are more sensitive to errors in simulation than others. The factors that make spacecraft more sensitive are discussed in this section and are specified in section 5.3.

5.1.1 Materials of the Spacecraft

The materials used on any spacecraft surface that has a view of the solar simulator or chamber shroud should have the same thermal response during test as in space. The most important properties are the surface absorptance (α) and thermal emittance (ϵ) and their ratio, (α/ϵ).

The absorptance, α , of a surface determines how much of the incident irradiance is absorbed. The remainder is reflected. The absorptance is defined as:

$$\alpha = \frac{\int_0^{\infty} \alpha(\lambda) E(\lambda) d\lambda}{\int_0^{\infty} E(\lambda) d\lambda} \quad (5.1)$$

Where $a(\lambda)$ is the spectral absorptance of the material.

$E(\lambda)$ is the spectral irradiance (amount of flux as a function of wavelength) of the source.

λ is the wavelength.

Since $E(\lambda)$ for a solar simulator will, in general, be different than for the Sun, a will be different. Some materials show a lesser change than others and the former are more desirable from a simulation standpoint. It should be noted that material properties might vary from sample to sample depending on quality control.

In general, different thermal coatings will be used on a spacecraft to achieve a desirable temperature range. A typical high a/ϵ material is gold plating. It absorbs relatively well in the ultraviolet and visible range (where the solar irradiance is strong) and has a low emittance. As a result, a gold plated component will stay warm. Second surface mirrors have the opposite effect since they have a low a/ϵ .

If a spacecraft were coated with only one material, an adjustment of the simulator irradiance could be used to match the absorbed simulated solar irradiance to that of the Sun's irradiance. With a variety of surfaces, this isn't possible in most cases. There have been cases where special thermal coatings have been applied to the specimen to correct for a poor solar simulator spectral irradiance. If this isn't done and the mismatch is severe, the thermal analyst will have difficulty reconciling the data.

The emittance, ϵ , of a thermal coating is the ratio of the thermal energy radiated due to its own temperature to that emitted by a black body radiator. The emittance of a specific sample seldom causes simulation problems because this property is a function of the material temperature and varies only slowly with temperature. However, with a certain set of circumstances (low emittance of a small component at low temperature) the thermal conductance of the residual gas in the chamber may become relatively high compared to the emission from the surface. In most cases a pressure of 1×10^{-5} torr is low enough. However, an isolated (insulated) aluminized component at low temperature (i.e., at 100 K, $\epsilon = 0.02$) requires a pressure of 1×10^{-7} torr if the conductive heat transfer is to be kept at 1% of the emission (Fig. 4-11, Ref. 5.1).

5.1.2 Construction of Spacecraft

Spacecraft are extremely diverse in their geometrical complexity and variety. Some are of closed design, being little more than enclosed cubes, cylinders, spheres, octahedrons, etc. Others have appendages, cavities, solar panels, antenna arrays, etc.

Geometrical complexity makes a spacecraft sensitive to solar simulation that has a large divergence angle and subtense angle. The shadows cast by antennae, solar panels, etc., are misplaced when there is a divergence angle. A too-large subtense angle will cause the shadows to be fuzzy. Surfaces aligned parallel or nearly parallel to the Sun's rays may receive appreciable side lighting when there should be little or none. There may be appreciable error even with simple closed construction such as a sphere when irradiated by a diverging beam through a small window. In this case the point of tangency of the rays is too far forward (closer to the solar source) and the "sides" of the test object will be too cold.

5.1.3 Type of Thermal Control System

A spacecraft with an active thermal control system can offset some of the spacecraft's thermal sensitivity compared to a passive thermal control system. Internal electrical heaters with thermostats can be used successfully if the electrical requirements aren't high. Polished aluminum louvers that open up to expose high emittance surfaces have been used. If the spacecraft thermal designers can reduce the number of thermal coatings or use more spectrally flat surfaces, this will reduce the sensitivity and simplify the space simulation requirements.

5.1.4 Spacecraft Motion Relative to the Sun

Spacecraft may operate during the mission with one axis directed at the Sun, or slowly or rapidly rotating with respect to the Sun. In planetary orbits, the albedo and thermal emission from the planet may provide a significant and varying thermal input. It is generally necessary to rotate the test specimen in the space chamber to simulate rotation relative to the Sun (exceptions are the use of a "cage" of IR lamps, thermal blankets, etc.). If the rotation is fast enough, it reduces the thermal sensitivity to non-uniform solar beam irradiance, at least in a plane normal to the axis of rotation. If the rotation is very slow, there may be no benefit. In fact, it may make analysis more difficult because of the changing thermal inputs to various surface nodes as they sweep through regions of changing irradiance.

5.1.5 Thermal Analytical Model

"An adequate Thermal Analytical model in essence simplifies the requirement for fidelity of the solar simulation test. A prime objective of the solar simulation test is the verification of this analytical model. The class of simulator is quite flexible as long as it permits this verification. Temperatures for other aspects or missions, variations in space thermal inputs, and electrical power dissipations, etc., can be predicted with a high degree of assurance if the mathematical model has been found adequate."

5.2 Solar Simulator Characteristics Which Affect Thermal Response of Spacecraft or Test Specimen

The characteristics of a solar simulator which can affect the thermal response of a spacecraft or test specimen are discussed in sections 5.2.1 through 5.2.9. The thermal design engineer and the simulator operator will determine the effect each characteristic may have upon the test requirements and specify the proper requirements for each characteristic.

5.2.1 Test Volume Dimensions

The test volume includes, as a minimum, all the space occupied by the spacecraft or test specimen for the duration of the test. When motion of the spacecraft or test specimen occurs during the test, all portions of the test volume which are occupied during such motion must be included in the test volume.

5.2.2 Mean Total Irradiance

The mean total irradiance (\bar{E}) within the test volume is:

$$\bar{E} = \frac{\int_v E(r, \theta, z) dV}{\int_v dV} \quad (5.2)$$

where \bar{E} is the mean total irradiance within the test volume, $E(r, \theta, z)$ is the irradiance at a position within the test volume, and $\int_v dV$ is the volume integral of the test volume.

Irradiance must be determined by use of a detector with finite dimensions. The dimensions of such detectors are discussed in Section 6. However, the largest linear dimension of such detectors may not exceed the linear dimensions of the smallest part of the spacecraft or test specimen which exhibits a different thermal response than its immediate surroundings. The mean total irradiance must be equal to the test requirements for the duration of the test.

5.2.3 Uniformity of Total Irradiance Throughout Test Volume

The uniformity of total irradiance throughout the test volume is a measure of the deviations of individual irradiances from the mean value of total irradiance for all positions within the test volume. The procedures developed within this field are such that the most uniformly irradiated systems will have a low number value for uniformity. In accordance with this practice uniformity of irradiation is defined as shown in equation 5.3.

$$E_u = \pm 100 \left(\frac{\Delta E_{(\min)} + \Delta E_{(\max)}}{2\bar{E}} \right) \quad (5.3)$$

where E_u is the uniformity of the irradiance within the test volume, expressed as a percent of the mean irradiance. $\Delta E_{(\min)}$ is the mean irradiation minus the smallest value obtained for irradiance within the test volume; and, $\Delta E_{(\max)}$ is the largest value obtained for irradiance within the test volume minus the mean irradiance. A perfect system would have a value of uniformity of total irradiance of zero.

Uniformity of irradiance values must always be specified together with the largest linear dimension of the detector used. Measurements of the irradiance should be made at a sufficient number of positions within the test volume to ensure, within a stated degree of certainty, that the extreme values of ΔE are included. Iso-irradiance plots are desirable for most tests. These plots should show one percent deviations from the mean irradiance for Class A systems; two percent deviations from the mean irradiance for Class B systems; and, five percent deviations from the mean irradiance for Class C systems.

5.2.4 Temporal Stability of Irradiance Throughout Test Volume

The temporal stability of the irradiance throughout the test volume for the duration of the test can be defined similarly to the Uniformity of Irradiance. The stability of irradiance is the temporal variation of individual irradiances from the mean irradiance. The temporal variations should be measured over time intervals equal to the thermal time constants of the components. In practice, one position in each portion of the test volume which is irradiated by different sources of radiant flux or different optical systems must be monitored. For each position monitored a maximum and minimum value of irradiance will be obtained. An equation of the form of 5.3 can then be used to determine the stability of irradiance during the test.

$$E_t = \pm 100 \left(\frac{\Delta E_t(\min) + \Delta E_t(\max)}{2\bar{E}} \right) \quad (5.4)$$

5.2.5 Solar Beam Divergence Angle

The solar beam divergence angle is a measure of the non-parallelism of the irradiance in the test volume. It is defined in Section 3. The divergence angle is the most important simulator characteristic from the standpoint of spacecraft construction. Actually, the subtense, divergence and maximum divergence angle (see Section 3) are quite different and have different effects on a spacecraft. Use of the single column "Solar Beam Divergence Angle" in Table 5.3 is an attempt to simplify matters by considering the most important aspects of these characteristics.

Direct projection systems generally have much larger divergence angle than well-collimated systems. Projection systems frequently have divergence angle of 3° or more at the edge of the test plane. On the other hand, solar simulators with large internal collimating mirrors may have divergence angles of less than 1/8 of a degree throughout the test volume. With a system such as this a traverse of the beam perpendicular to the solar axis will show that the apparent source moves with (follows) the traverse. The apparent source always maintains a line of sight to any point in the test volume very nearly parallel to the solar axis.

Table 5.3 in Section 5.6 contains a section, "Construction-Depth of Irradiated Components," dealing with the depth of the test object (dimension of the test object parallel to the solar axis). A simple relationship exists between irradiance and depth with a direct projection system. The irradiance decreases inversely proportional to the base area of the cone of rays defined by twice the maximum divergence angle. Divergence angle Classes A, B, and C in Table 5.2 are for use with direct projection systems.

No simple relationship exists between the irradiance and the very small divergence angles of a well-collimated system. Here, the divergence angle is generally a result of spherical or other aberrations of the optics. Divergence angle Classes 2A through 5A are to be used with these systems. In particular, the "Depth of Irradiated Components" section of Table 5.3 requires actual measured values of irradiance change with depth.

5.2.6 Spectrum

The spectrum of a solar simulator is determined from spectral irradiance measurements. The wavelength interval for such measurements should include all wavelengths which are pertinent to the test. In general, the wavelength interval from 250 nm to 2500 nm will be sufficient. The actual interval to be used will depend upon the materials of the spacecraft or test specimen which is tested. In some cases the interval beyond 2500 nm is very important. The simulator operator and thermal analyst should determine if this wavelength region is important for each test performed and obtain spectral data over the wavelength region required.

The irradiance per measured wavelength interval (bandwidth), E_λ , is compared to the currently accepted values for the air mass zero solar irradiance (AMOSI) for the same bandwidth. This yields a ratio of solar simulator irradiance (SSI) to air mass zero solar irradiance as:

$$\text{Ratio} = \frac{E_\lambda (\text{SSI})}{E_\lambda (\text{AMOSI})} \quad (5.5)$$

Table 5.1A and B lists the requirements for Class A and Class B spectrum in terms of the ratio of SSI to AMOSI for bandwidths within these intervals. The table divides the spectrum into four large wavelength

Table 5.1A & B

SPECTRAL IRRADIANCE TOLERANCES FOR CLASS A AND CLASS B SOLAR SIMULATION

Wavelength Interval	Measurement Bandwidth	Number of Bands	AMOSI per Interval	Ratio per Bandwidth
Table 5.1A. CLASS A				
250-400 nm	10 nm	15	11.5 mW cm ⁻²	0.60-1.40
400-700 nm	10 nm	30	51.6 mW cm ⁻²	0.80-1.20
700-1000 nm	50 nm	6	30.6 mW cm ⁻²	0.60-1.40
1000-2500 nm	100 nm	15	36.3 mW cm ⁻²	0.60-1.40
Total		66	130.0 mW cm ⁻²	
Two-thirds of bandwidths in each interval must fall within ratio tolerances indicated				

Table 5.1B. CLASS B				
250-400 nm	50 nm	3	11.5 mW cm ⁻²	0.35-1.65
400-700 nm	100 nm	3	51.6 mW cm ⁻²	0.50-1.50
700-1000 nm	150 nm	2	30.6 mW cm ⁻²	0.35-1.65
1000-2500 nm	500 nm	3	36.3 mW cm ⁻²	0.20-1.80
Total		11	130.0 mW cm ⁻²	
Eight of the bandwidths must fall within ratio tolerances indicated				

intervals in the column titled "Wavelength Interval." These intervals should be used for tests in which all of the materials of the spacecraft or test specimen exhibit a linear absorptance as a function of wavelength; i.e., when the absorptance of the material of the spacecraft or test specimen has a constant value throughout the indicated wavelength interval or varies linearly over the wavelength interval. Then, only four determinations of spectral irradiance need be made, one determination for each wavelength interval. The values obtained are then compared directly to the values in the column titled "AMOSI per Interval" by use of equation 5.5. A ratio for each interval is thus obtained. This ratio is then compared to the tolerances shown in the column titled "Ratio per Bandwidth."

When the spacecraft or test specimen is composed of materials which have absorptances which vary strongly within the wavelength intervals or have absorption peaks or other non-linearities, a more detailed spectral comparison is necessary. In these cases, each wavelength interval must be divided into an additional number of bands which are indicated in the column titled "Number of Bands." The number of bands is such that resolution of 10 nm is obtained from 250 nm to 700 nm, 50 nm is obtained from 700 nm to 1000 nm, and 100 nm is obtained from 1000 nm to 2500 nm. These measurement bandwidths are indicated in the column titled "Measurement Bandwidth." The ratio of the solar simulator irradiance to the air mass zero solar irradiance for each of the bands within each wavelength interval is then obtained using equation 5.5. These values are compared to the values for AMOSI per band which are given in the standard air mass zero solar spectral irradiance table. The ratio for each band within a wavelength interval is then compared to the ratio indicated in the column of Table 5.1 titled "Ratio per Bandwidth." When the ratio tolerances per bandwidth coincide with the tolerances shown in Table 5.1 for Class A solar simulation for two-thirds of the bands within each wavelength interval, the spectral correlation of the SSI to AMOSI is sufficient to classify the spectrum as class A. Similarly, for Class B, 8 of the 11 bandwidths must fall within the ratio per bandwidth indicated.

Uniformity and temporal stability of spectral irradiance can be determined in a manner discussed in Section 5.2.3 and 5.2.4, the only difference being that each bandwidth of irradiance pertinent to the test must be compared using a wavelength dependent form of equations (5.3) and (5.4). These characteristics may be important for some tests and should be considered by the thermal design engineer in such cases.

5.2.7 Reflected Irradiance

The radiant flux incident upon a spacecraft or test specimen which does not originate from the first pass of radiant flux through the optical system is termed reflected irradiance. This may be flux reflected from the spacecraft or test specimen back to the collimator and then back to the spacecraft. It can also originate from reflections of the irradiance

flux upon the surface at the side or beyond the spacecraft or test specimen which is then reflected back onto the spacecraft. The quantity and direction of reflected irradiance should be determined after the spacecraft or test specimen is mounted into position in the test chamber. Care must be exercised in these measurements to ensure that the presence of the detector within the test volume has a negligible effect.

5.2.8 Radiation Environment Temperature

The thermal-radiant exitance of the surfaces which surround the spacecraft or test specimen must be determined. The uniformity of the radiant exitance as well as the direction of each surface which departs significantly from the mean must also be determined. This energy may be expressed in terms of the equivalent temperature of a black body that would supply the same radiant exitance, or:

$$\epsilon \sigma T_a^4 = 1.0 \sigma T_e^4 \quad (5.6)$$

where T_e is the black body or equivalent temperature and T_a is the actual shroud temperature. Since most shrouds have a black surface (with high absorptance and emittance) to minimize reflectance of the solar beam, the actual temperature measured will be close to the equivalent black body temperature. However, if a low emittance shroud is used, a higher actual temperature may then be used. This T_a can be obtained from the relation:

$$T_a = T_e \epsilon^{-1/4} \quad (5.7)$$

where T_e is the Radiation Environment Temperature given in Table 5.2.

5.2.9 Chamber Pressure

The pressure level within the test volume should be monitored with gages placed such that the pressure levels at the spacecraft or test specimen may be determined. Gages shall be used in accordance with ASTM Method E296, Recommended Practices for Ionization Gage Application to Space Simulators.

5.3 Characterization of Spacecraft or Test Specimen

The designs of spacecraft have been very diversified to accomplish a wide variety of missions. Mission requirements and state-of-the-art dictate a multitude of design approaches including

1. Spinning, tumbling, slowly rotating, or stabilized spacecraft.

Table 5.2

CLASSIFICATION OF SOLAR SIMULATOR CHARACTERISTICS

Test Volume Characteristic	Class A	Class B	Class C	See Section
1-Uniformity of Irradiance, E_u	3%	5%	>5%	5.2.1, 5.2.2, 5.2.3
2-Stability of Irradiance, E_t	1%	3%	>3%	5.2.4
3-Solar Beam Divergence Angle*	<2°	<4°	>4°	5.2.5
4-Spectrum	Table 5.1A	Table 5.1B	All others	5.2.6,
5-Reflected Irradiance	<2% of incident	<5% of incident	>5% of incident	5.2.7
6-Radiation Environment Temperature	<20K	≤100K	>100K	5.2.8
7-Chamber Pressure	10 ⁻⁶ Torr	10 ⁻⁵ Torr	<10 ⁻⁴ Torr	5.2.9
*For highly collimated beams, additional classes are necessary:				
	Class 5A	Class 4A	Class 3A	Class 2A
Solar Beam Divergence Angle	0.125°	0.25°	0.5°	1°
Change in E with depth (%/m)	0.3	0.5	1	2
				5.2.5
				5.2.5

2. Variation in shapes, sizes, appendages.
3. Variations in thermal design, passive and active, flat or spectrally sensitive coatings, conductive or insulating surfaces.
4. Terminal conditions—distance from the Sun, planetary radiation.

An attempt to classify spacecraft by listing all combinations of the above would yield a list unmanageably large. Therefore, the important spacecraft factors above are taken individually, where possible, and each compared to the space simulator characteristics that is most closely related to it. The spacecraft characteristics below are listed vertically in Table 5.3. The simulator characteristics from Section 5.5 are listed horizontally on the chart. To obtain the final classifications of the simulator, add all of the classifications required for the various spacecraft characteristics.

Frequently, thermal balance tests and systems tests are run in a space chamber simultaneously. A combined test may change the environmental requirements. One example of a thermal balance test is one that is run in a space chamber with mocked-up structure and components equipped with resistors to simulate the true components' electrical dissipation. These test items are generally called "thermal control models" or TCMs. A systems integration test would not be possible on a TCM.

A systems integration test is one that is run with all spacecraft flight systems installed and operating so that possible interactions between the systems can be studied. A systems integration test can be run at ambient laboratory conditions. However, running this type of test in a space chamber is generally preferred because the space temperatures and pressure conditions are more accurately simulated and electronic and mechanical failures may occur under these conditions that wouldn't occur at ambient conditions.

Another important factor affecting the simulator-spacecraft relationship is the existence or lack of a thermal analytical model. (See also Section 5.4.) The notations on Table 5.3 assume there is no analytical model to correct temperature errors. This not only yields a simulation with accurate temperatures but provides for a good systems integration test. Ordinarily, an analytical model could not correct the performance of electronic and mechanical systems subjected to erroneous temperatures, especially if temperature limits are exceeded. The existence of an analytical model reduces the simulator requirements for a purely thermal balance test but is of little assistance in a systems integration test.

5.3.1 Spacecraft Rotation

Spacecraft rotation relative to the Sun is an important variable. Rotation is also important for orbiting spacecraft if the spacecraft surfaces are exposed to high irradiance of planetary albedo and thermal emission.

Table 5.3A

SPACECRAFT CHARACTERISTICS		SOLAR SIMULATOR CHARACTERISTICS					
		UNIFORMITY OF IRRADIANCE	STABILITY OF IRRADIANCE	DIVERGENCE ANGLE	SPECTRUM	REFLECTED IRRADIANCE	ENVIRONMENT TEMPERATURE CHAMBER PRESSURE
ROTATION							
RANDOM TUMBLING		C	B	C	C	C	
FAST SINGLE AXIS ROTATION		B	A	A	A	B	
NO ROTATION OR SLOW ROTATION							
• HIGH CONDUCTIVITY STRUCTURE		B	A		B	C	
• LOW CONDUCTIVITY STRUCTURE		A	A		A	B	

Table 5.3B

SPACECRAFT CHARACTERISTICS		SOLAR SIMULATOR CHARACTERISTICS					
		UNIFORMITY OF IRRADIANCE	STABILITY OF IRRADIANCE	DIVERGENCE ANGLE	SPECTRUM	REFLECTED IRRADIANCE	ENVIRONMENT TEMPERATURE CHAMBER PRESSURE
CONSTRUCTION							
INCIDENT ANGLE*							
• PLANAR SURFACE, INCIDENT ANGLE = 0°				C	C	C	
• INCIDENT ANGLE < 20°				B	C	B	
• INCIDENT ANGLE 20° TO 35°				A	B	B	
• INCIDENT ANGLE 35° TO 55°				2A	A	A	
• INCIDENT ANGLE 55° TO 70°				3A	A	A	
• INCIDENT ANGLE 70° TO 80°				4A	A	A	
• INCIDENT ANGLE 80° TO 85°				5A	A	A	
° STATIONARY OR SLOWLY ROTATING SPACECRAFT							

Table 5.3C

TEST REQUIREMENTS							
SOLAR SIMULATOR CHARACTERISTICS							
SPACECRAFT CHARACTERISTICS	UNIFORMITY OF IRRADIANCE	STABILITY OF IRRADIANCE	DIVERGENCE ANGLE	SPECTRUM	REFLECTED IRRADIANCE	ENVIRONMENT TEMPERATURE	CHAMBER PRESSURE
CONSTRUCTION DEPTH OF IRRADIATED COMPONENTS ^{1,2} <ul style="list-style-type: none">• DEPTH < 5% OF BEAM DIA.• DEPTH 5% TO 10% OF BEAM DIA.• DEPTH 10% TO 15% OF BEAM DIA.• DEPTH < 1m• DEPTH < 2m• DEPTH < 4m• DEPTH < 8m			C B A 2A 3A 4A 5A				
NOTES: 1. STATIONARY OR SLOWLY ROTATING SPACECRAFT 2. USE MAXIMUM TEST PLANE DIVERGENCE ANGLES FOR DIRECT PROJECTION SYSTEMS, MEASURED CHANGE IN IRRADIANCE WITH DEPTH FOR WELL-COLLIMATED SYSTEMS							

Table 5.3D

TEST REQUIREMENTS								
		SOLAR SIMULATOR CHARACTERISTICS						
SPACECRAFT CHARACTERISTICS		UNIFORMITY OF IRRADIANCE	STABILITY OF IRRADIANCE	DIVERGENCE ANGLE	SPECTRUM	REFLECTED IRRADIANCE	ENVIRONMENT TEMPERATURE	CHAMBER PRESSURE
CONSTRUCTION								
SHADOWING APPENDAGES *				C B A 2A 3A 4A 5A				
<ul style="list-style-type: none">• $D < 0.2L$• $0.2L < D < 0.4L$• $0.4L < D < 0.7L$• $0.7L < D < 1.4L$• $1.4L < D < 3L$• $3L < D < 6L$• $6L < D < 12L$								
*STATIONARY OR SLOWLY ROTATING SPACECRAFT								

SOURCE

L

D

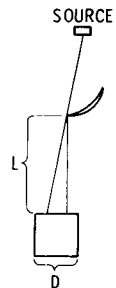


Table 5.3E

TEST REQUIREMENTS							
SPACECRAFT CHARACTERISTICS				SOLAR SIMULATOR CHARACTERISTICS			
	UNIFORMITY OF IRRADIANCE	STABILITY OF IRRADIANCE	DIVERGENCE ANGLE	SPECTRUM	REFLECTED IRRADIANCE	ENVIRONMENT TEMPERATURE	CHAMBER PRESSURE
SPECTRAL SENSITIVITY • ONE COATING OR ALL FLAT COATINGS • $\Delta\alpha_i/\alpha_i \leq -0.04^\circ$ • HAS BOTH UV AND IR PREFERENTIAL ABSORBERS				C B A			
* USE OF ELECTRIC HEATERS ASSUMED							

Table 5.3F

TEST REQUIREMENTS							
SPACECRAFT CHARACTERISTICS				SOLAR SIMULATOR CHARACTERISTICS			
	UNIFORMITY OF IRRADIANCE	STABILITY OF IRRADIANCE	DIVERGENCE ANGLE	SPECTRUM	REFLECTED IRRADIANCE	ENVIRONMENT TEMPERATURE	CHAMBER PRESSURE
PRESSURE SENSITIVITY (TEST COMPONENT 1 METER DIA.) • $\epsilon_m \sim 1, T \geq 300^\circ\text{K}$ • $\epsilon_m \geq 0.2, T \geq 300^\circ\text{K}$ • $\epsilon_m \geq 0.03, T \geq 250^\circ\text{K}$						C B A	

Non-uniformities of irradiance in a test chamber will cause errors in thermal input. Highly conductive spacecraft surfaces will minimize these errors.

Categories listed on Table 5.3 include:

1. Random tumbling of the spacecraft at a rate that is fast compared to the thermal time constant of the surface materials.
2. Single axis rotation that is fast compared to the thermal time constant of the surface materials. This motion will tend to average out non-uniform irradiance except at the intersections of the rotational axis and the spacecraft surface.
3. Non-rotating spacecraft, those rotating around the line-of-sight to the sun, or rotation that is slow compared to the thermal time constant of the surface materials.

5.3.2 Spacecraft Construction

The spacecraft geometry is an important factor in its sensitivity to solar simulation inaccuracies.

5.3.2.1 Incident Angle

Surfaces with small incident angles are less sensitive to solar beam divergence angle. (See 5.2.5.)

1. A planar or two dimensional surface, irradiated at normal incidence. This type of test article is ordinarily insensitive to solar subtense and divergence angle. An example is a solar panel irradiated at normal (zero) incidence to the solar beam axis.
2. A surface incident angle $< 20^\circ$.
3. A surface incident angle between 20 and 35° .
4. A surface incident angle between 35 and 55° .
5. A surface incident angle between 55 and 70° .
6. A surface incident angle between 70 and 80° .
7. A surface incident angle between 80 and 85° .

5.3.2.2 Depth of Irradiated Components

A diverging beam solar simulator will provide lower irradiance to test surfaces that are farther from the source. The maximum divergence angle is the half angle of the cone of rays. This angle is used on Table 5.3 for diverging beams. Actual measured change in irradiance with depth in the test volume must be used with simulators using collimating mirrors as the final optical element.

1. For diverging beams
 - a. The extreme limits of the projection of all irradiated surfaces on the solar beam axis are less than 5% of the solar beam diameter.
 - b. 5 to 10%.
 - c. 10 to 15%.
2. For simulators with collimating mirrors
 - a. Depth < 1 m.
 - b. Depth < 2 m.
 - c. Depth < 4 m.
 - d. Depth < 8 m.

5.3.2.3 Shadowing Appendages

Shadows cast on a surface from an appendage, such as a solar panel, will not be properly simulated if the subtense and divergence angles of the beam are greater than those of the sun. A large subtense angle casts a large penumbra but otherwise, the shadow is properly located. High thermal conductance spacecraft skin reduces the error. A large divergence angle casts a shadow displaced from the correct position. For simplification, only divergence angle is considered.

Table 5.3 uses simplified geometrical criteria between D, the distance between an appendage and the test component shadowed, and L, the dimension of the component shadowed perpendicular to the shadow line. These criteria are subject to the following qualifications:

1. The projection of the shadow-edge solar ray onto the test plane is perpendicular to the shadow line. If not, D should be multiplied by the sine of this angle.

$$2. \quad \frac{\Delta l}{L} \approx \frac{\Delta a}{A} \quad (5.8)$$

where

Δl = displacement of shadow, distance normal to shadow line

L = characteristic dimension, e.g., diameter of test component shadowed normal to the shadow line.

Δa = change in area shadowed due to shadow displacement Δl

A = area of the shadowed component projected on the test plane

This expression merely insures that the percentage error in the area shadowed is proportional to the percentage error in the shadow line displacement. For components of circular cross section or of unusual shapes, a correction for the area shadowed may be necessary.

The chart classifications, subject to these qualifications, are:

1. $D < 0.2 L$
2. $0.2 L < D < 0.4 L$
3. $0.4 L < D < 0.7 L$
4. $0.7 L < D < 1.4 L$
5. $1.4 L < D < 3 L$
6. $3 L < D < 6 L$
7. $6 L < D < 12 L$

5.3.3 Spectral Sensitivity (see Section 5.1.1)

1. Irradiated surfaces are of one type of coating or of several spectrally flat coatings.
2. $\Delta a_i / a_i \geq -0.04$. Per definitions in 5.5.3.2 the minus sign will produce overheating of a component in a space chamber. Electrical heaters can be used to remedy underheating.
3. A variety of coatings, some that preferentially absorb at UV and some at IR wavelengths.

5.3.4 Pressure Sensitivity

The residual gas pressure must be kept low enough so that the thermal conductance is negligible compared to radiative heat transfer. The criterion used is that the conductive heat transfer is 1% or less of the radiative heat transfer. Spacecraft components at low temperatures and low emittance have low radiative emission. In these cases the ratio of conduction to emission tends to get larger requiring a lower chamber pressure to maintain a 0.01 ratio. For $\epsilon_m D_m \leq 1.0$ (ϵ_m is emittance, D_m is component characteristic dimension in meters) and an 80 K cold shroud the categories below and pressures given in Section 5.6 are valid⁽¹⁾. For intermediate values, radiation increases as $\epsilon_m T^4$, conduction as pressure to the first power.

1. $\epsilon_m \sim 1$, $T \geq 300^\circ\text{K}$
2. $\epsilon_m \geq 0.2$, $T \geq 300^\circ\text{K}$
3. $\epsilon_m \geq 0.03$, $T \geq 250^\circ\text{K}$

5.4 Types of Spacecraft or Test Specimen Tests

5.4.1 Thermal Tests to Verify Thermodynamic Analytical Models

These tests of spacecraft or test specimens can tolerate a less perfect simulation because the variations in simulator performance from conditions extant in space can be added to the analytical model as variables. Spacecraft or test specimens for which an adequate thermal analytical model has been developed can, in general, receive an adequate test with any class of solar simulator characteristics specified in 5.5.1.

5.4.2 Thermal Tests to Verify Thermal Balance when an Inadequate Thermodynamic Model Exists

In contrast to an adequate thermodynamic model of Section 5.4.1, most spacecraft testing is done when the analytical model is not complete in all respects. A complete model covers the thermodynamics of all errors of simulation, all inputs and outputs for various missions and modes, shadows, view factors, reflections and multiple interreflections of packages both internal and external, radiation and conductive heat transfer, steady-state and transient. With a spacecraft of even moderate complexity, this is a monumental task. Thus, the category, inadequate thermodynamic model, covers most spacecraft.

The category obviously can't be quantified. A thermal analyst that is familiar with both the performance of the space simulator and the space mission can do a great deal to adapt the analytical model to the simulator deficiencies.

5.4.3 Test to Verify Thermal Balance when no Thermodynamic Model Exists

If no model exists, several or all of the following factors would normally be present: short schedule, low budget, simple and easy mission, few innovations, experienced spacecraft designers. If the design and mission are simple and the thermal analysts are experienced, an unsophisticated simulator might suffice. However, for complicated designs without an analytical model, the ultimate in simulator characteristics would generally be required as shown on the chart in Section 5.6. Also, the very important system integration test normally conducted prior to flight should be done under conditions as similar to space as possible (see Para. 5.3).

5.5 Solar Simulator Requirements for Spacecraft or Test Specimen Tests

5.5.1 Classification of Solar Simulators

The classification of solar simulators can be accomplished in many ways. The approach taken here is to identify each of the parameters which characterize solar simulators generally and identify three classes for each parameter. Class A represents the state-of-the-art for simulators, except for divergence angle where additional classes 2A, 3A, 4A, and 5A are defined. Classes B and C are provided to accommodate those simulators of less sophistication. In most cases the B and C classes designated on Table 5.3 will give adequate simulation. However, discretion on the part of the thermal design engineer must be exercised in the interpretation of results.

This approach is taken to give more flexibility of operation for solar simulation tests in order to allow the thermal design engineer to specify those parameters which are most important to the success of his test at the expense of others which are less important. For example, if spectrum were not an important parameter to the thermal design engineer but the irradiance level to be provided required the full rated capacity of the system, then the simulator operator could remove any spectral filters or other means used to provide good spectrum and thereby increase the maximum irradiance capability of the simulator. Another example: if divergence angle were extremely important but irradiance level were not, the simulator operator, for some types of systems, could provide an improved divergence angle at the expense of irradiance. Other trade-offs can also be made between the parameters listed in Table 5.2. It also follows that any solar simulator with performance characteristics which exceed or equal the class specifications for each of the seven items is a simulator with performance at that class.

5.5.3 Methods to Reduce Spectral Sensitivity of Spacecraft or Test Specimen

5.5.3.1 Method I - Effective Absorptances of Surface Materials

If an analytical thermal model has been developed for the spacecraft or test specimen, the effective absorptance of each surface material as a function of the simulator spectrum can be calculated and applied to the thermal analytical model. This will yield a series of test equilibrium temperatures which will be different from those obtained in orbit unless the simulator spectrum correlates closely with the solar spectrum. However, if the thermal balance test equilibrium temperatures agree with those predicted by the thermal analytical model, a high degree of confidence in the accuracy of the model is obtained.

5.5.3.2 Use of Different Surface Materials During Test

Section 5.1.1 describes the affects on simulation of surface materials of different thermal properties. The thermal designer may be able to desensitize the spacecraft to simulation errors by a proper choice of surface materials. However, he is generally constrained by the space environment and the mission objectives to use durable coatings with a variety of thermal responses. A possible alternative is to use one set of thermal coatings for space simulation test and another set for flight.

A suggested criterion for thermal balance testing where no analytical model is used is:

$$\left| \frac{\Delta \alpha_1}{\alpha_1} \right|, \left| \frac{\Delta \alpha_2}{\alpha_2} \right|, \dots, \left| \frac{\Delta \alpha_n}{\alpha_n} \right| \text{ are all } \leq 0.04, \quad (5.9)$$

where a is as defined as in 5.1.1 and Δa is the difference in a between space and simulated conditions ($\Delta a = a_s - a_{ss}$ where subscript s refers to the Sun and ss to the solar simulator). Numerical subscripts refer to different surface coatings. This is generally difficult to achieve except with a spectrally accurate solar simulator.

If electrical heat is applied to the test item where the absorptance in the simulated sun is too low, the positive tolerance given above can be increased.

5.5.4 Methods of Reducing Uniformity Requirements of Test

5.5.4.1 Spacecraft Spinning During Test

For certain space missions, spacecraft will be spun or tumbled to simplify thermal control or stabilization. These motions make the

spacecraft less sensitive to solar beam non-uniformity as noted in Section 5.3.1. However, if the space mission requires that the spacecraft be stabilized or slowly rotating, it generally isn't possible to spin it in the simulator without seriously compromising the test results. If the space mission allows the thermal designer the option of spinning or not, his choice of spinning will, of course, desensitize the spacecraft during simulation. Rapid rotation will tend to compensate for poor uniformity unless the uniformity gradients are primarily between planes perpendicular to the axis of rotation.

5.5.4.2 High Thermal Conductivity Structures

Some spacecraft designs use high conductivity skins, heat pipes, and internal connections with high conductivity to equalize the temperatures in space. Furthermore, if the design is not weight limited, extra conduction can be provided to desensitize the spacecraft during simulation.

5.5.4.3 Active Thermal System

Spacecraft designs sometimes use active thermal systems such as automatic louvers, electrical heaters, thermal switches, etc. for variations in thermal balance during a mission. These and extra heaters may be used to improve simulation. By reducing the solar irradiance to the value that provides the correct heat input to the components which have a positive Δa , the deficiency in absorptance of the other components can be made up by electrically supplied heat.

5.5.5 Methods to Reduce Subtense and Divergence Angle Requirements of Test

A large subtense angle causes fuzzy shadows to be cast. This effect is generally minor for thermal balance testing except with very low conductivity or insulating skins. If an irradiated surface is approximately parallel to the solar beam axis, some of the rays strike the surface at a steeper angle. These minor effects can be ignored or easily taken into consideration during analysis of the data.

A large divergence angle is a more serious matter. This will displace a point at the edge of a shadow cast by an appendage in proportion to the sine of the angle between the projection of the solar ray on the test plane and the shadow line. All surfaces that are not perpendicular to the solar axis are not properly irradiated depending on their angle to this axis and depth of the test volume.

5.5.5.1 Shadow Panels

The location of shadows can be improved by moving the shadow-casting component closer to the item shadowed. The component can

frequently be removed from the test altogether and a dummy panel installed close to the item shadowed. This panel should be temperature controlled so as to provide the proper emission to the test article. Although this will help reduce gross errors in shadow location, care must be taken to avoid substantial view factor changes for adjacent surfaces.

5.5.5.2 Spinning Spacecraft

This will reduce test requirement (see 5.3.1).

5.6 Test Requirements Chart (Table 5.3)

The chart in this section should be used as a guide by spacecraft designers and others interested in space simulation. It is not intended as a standard or as a substitute for data analysis, analytical modelling or any of the functions performed by the thermal designers. Wide latitude and flexibility is needed by those responsible for the spacecraft thermal performance. This chart and the text of Section 5 should be used with that objective in mind.

To use the chart enter from the left with each spacecraft characteristic, one at a time. Where a letter appears, that simulator class from Table 5.2 will be adequate for that spacecraft characteristic. If different letters are found in a column for that simulator characteristic, the higher quality (lower letter) must be used.

Reference

- 5.1 J. S. Griffith, "Test Requirements," pp 4-16, 4-17, Handbook of Solar Simulation for Thermal Vacuum Testing, IES, Mount Prospect, Ill., 1968.

6. INSTRUMENTATION

6.1 Introduction

This section is intended to describe the techniques used to measure the parameters involved in space simulation testing. This includes the measurement of solar simulator total and spectral irradiance in air and in vacuum, the reference scale to be used, uniformity in plane and volume, solar beam divergence angle, and vacuum gages. It should be recognized that the methods and techniques discussed are not meant to be all-inclusive, but rather to represent the best approach to be used based on a combination of accuracy, ease of adaptation to most systems, and commercial availability.

6.2 Total Irradiance Standard Detector

6.2.1 Scope

This section covers the detector used by a laboratory as its primary working standard from which other detectors are calibrated and used to set irradiance levels.

6.2.2 Reference Scale

It is recommended that the current International Pyrheliometric Scale, (1956 as of this writing) be used as the reference. This scale is embodied in a group of electrical-compensation type instruments maintained by the World Meteorological Organization (WMO) at Davos, Switzerland. Intercomparisons, against these standards, of regional and national primary working standard pyrheliometers are conducted there at approximately five year intervals. The establishment of this scale is discussed in references 6.1, 6.2, and 6.3.

Each laboratory or facility would have at least one reference pyrheliometer capable of $\pm 0.5\%$ reproducibility with its calibration directly traceable to the current WMO scale. This instrument would be periodically (perhaps twice a year) intercompared with one of the primary pyrheliometers which preserve the IPS scale in the U.S. (These pyrheliometers are maintained by the Eppley Laboratory, Newport, Rhode Island.) The intercomparisons would take place at any high mountain site (2000 m or more altitude) with the sun as source. This reference instrument would then be used to calibrate the detectors normally employed in simulator operations.

While total irradiance standards, traceable to NBS standards, are commercially available to calibrate detectors, it is felt that the IPS (1956) scale offers an easier way for every user to re-calibrate his reference detector periodically against a common primary standard.

The reader is warned that the field of radiometry is undergoing strenuous development. On an international basis several countries are actively investigating the use of cone and cavity type radiometers as reference standards. Improved thermal detection capabilities, and precision read-out instruments have spurred the rapid development of the so-called absolute radiometers. The development, inter-comparison and subsequent adoption of an absolute radiometer as an international reference probably will not occur for many years. Reference 6.4 will provide the reader with a more complete description of this type of radiometer.

6.3 Measurement of Total Irradiance in Air

6.3.1 Scope

This section covers a general method for measuring the total irradiance of a solar simulator in air, prior to pumppdown or the mounting of

any payload in the vacuum chamber. These measurements are made to characterize the solar beam only, and thus require the use of a view limited detector.

6.3.1.2 Detectors

Detectors can be divided into two general types: thermal and photoelectric. The photoelectric types are characterized by a relatively rapid response and a high signal level. However, they suffer from narrow spectral response which varies with wavelength. Before this type of detector can be used for solar simulation measurements, it is necessary to establish that spectral variation in the beam is negligible compared to the desired accuracy limits.

Thermal type detectors are usually characterized by relatively slow time constants and low signal levels, and may be made to be stable with respect to environmental temperature over a limited range. Thermal types are uniformly sensitive over a wide spectral range.

The thermal type detector is recommended for use in simulator operation. It should possess the following characteristics:

- a. It should be spectrally flat over the spectral range 250 to 2500 nanometers (or greater).
- b. It must be capable of withstanding flux densities of one solar constant (1353 Wm^{-2}), or higher if tests require it.
- c. It should be capable of resolving 0.01 solar constants (14 Wm^{-2}) and exhibit repeatability of 0.01 s.c. or better.
- d. It must have its field of view limited so as to prevent the measurement of spurious radiation such as from scattered, reflected, and emitted radiation. However, it cannot be limited to less than the subtense angle of the beam or false readings will result. In addition, a field of view of approximately five degrees is necessary for calibration against the primary working standard.
- e. Either the detector or the solar source must be equipped with a shutter mechanism or shield so that tare or zero readings can be made. The use of an electrical meter zero (such as a shorting plug in a voltmeter) is important but not sufficient. This simply zeros the voltmeter, not the entire measuring system. Also, a knowledge of the detector's time constant is obviously essential in determining the shutter open and close time. Some of the newer thermopiles have time constants of one second or less, while older types may be as slow as 30 seconds or longer.

- f. The detector should be maintained within its specified temperature limits by whatever means recommended by the manufacturer.
- g. The detector must either have a window cover (normally quartz) or suitable view limiting and baffle in order to minimize the effects of convective air currents.

6.3.1.3 Calibration

It is assumed that the operator has at his facility at least one reference pyrheliometer used as his primary working standard (see Section 6.2). All other detectors are calibrated against this reference. This is done out of doors on a clear day with natural sunlight as the source and the detectors set for normal incidence. Since the reference pyrheliometer has a field of view of approximately 5 degrees, all other detectors must be equipped with diaphragms limiting them to about the same angle for this calibration.

6.3.1.4 Location

The detector must be mounted at the measurement location in the simulated solar beam. Sampling at several locations may be necessary to determine the mean irradiance.

In some systems, particularly the module type, it may be advisable to sample the total beam at random positions and apply statistical analysis to determine the mean.

A single point measurement may be used if the value is correlated to uniformity of irradiance measurements made by relative irradiance detectors. The detector is mounted in a known position with regard to the uniformity scan and a correlation is then made between this position and the rest of the test volume.

6.3.1.5 Readout Devices

For accurate measurement of irradiance levels, a voltmeter capable of resolving the anticipated signal to 0.1% with an accuracy of 0.25% of full scale can be used.

6.3.1.6 Other Considerations

Since most of the thermal transducers operate in the millivolt region, it is necessary to verify the calibration of the readout equipment using test voltage sources having impedance characteristics similar to the transducers'. Evaluation of the level and effect of spurious noise upon the readout system performance should be done.

Parameters which require consideration in the application of thermal type radiometers are:

- a. Disposition of energy intercepted by detector and case. For example, verify that reflected radiation does not cause an increase of heat input to the heat sink of the detector;
- b. Verify when operating above the calibrated range that internal temperature differentials are small so that thermal conduction is large compared to convection and radiation;
- c. Spectral differences between the calibration source and the unknown require consideration, particularly if optics are used in the detector. Any neutral density attenuators used must be truly neutral with respect to the spectrum of the standard and the unknown sources.
- d. The effect of stray electrically induced signals in the detector cables must be evaluated.

6.4 Measurement of Spectral Irradiance in the 250 to 2500 nm Wavelength Range

6.4.1 Scope

This section covers a general method of performing measurements of the spectral irradiance of radiation sources in the 250 to 2500 nm wavelength range. The method employs conventional spectrophotometric equipment (i.e., monochromator, detectors, etc.) to perform measurements, relative to a source of known spectral irradiance. A detailed, high resolution measurement of the continuous spectrum can be obtained by this method.

6.4.2 Summary of Method

A spectral measurement of irradiance versus wavelength is made on the standard source to determine the measurement system transfer function $X(\lambda)$. Spectral measurements of the unknown source (solar simulator beam) are then made in an identical manner as used for the standard source. The spectral irradiance of the solar simulator beam may then be determined by correction of the measurement by the transfer function of the instrument system.

$$\text{Transfer Function } X(\lambda) = \frac{M \text{ std. } (\lambda)}{E \text{ std. } (\lambda)} \frac{\text{Measurement of Standard}}{\text{Known Spectral Irradiance of Standard}} \quad (1)$$

$$\text{Solar Simulator } E_{ss}(\lambda) = \frac{M_{ss}(\lambda)}{X(\lambda)} = \frac{M_{ss}(\lambda)}{M_{std.}(\lambda)} E_{std.}(\lambda) \quad (2)$$

6.4.3 Apparatus

6.4.3.1 System

Instrumentation required for the measurement consists of a monochromator, diffusing entrance optics, a standard source of special irradiance, detectors, amplifier and auxiliary equipment. A complete system incorporating the necessary instrumentation is shown in Figure 6.1. The monochromator is free to translate along an optical bench in such a way as to view either the unknown or reference sources, which are separated by a radiation shield. This configuration is shown primarily for purposes of illustration and any technique such as a rotating mirror which allows unobstructed alternate viewing of sources can be used.

6.4.3.2 Monochromator

An extremely wide variation of spectral irradiance can exist for the standard source and the test source over the spectral range 250 to 2500 nm. In conjunction with the wide dynamic range of the monochromator/detector transfer function places a stringent requirement on minimizing the stray light from the monochromator. Use of a double prism/grating monochromator is mandatory. Precise correlation between wavelength and instrument readout is necessary.

6.4.3.3 Diffusing Optics

Diffusing entrance optics for the monochromator are necessary because the optical properties of the reference and unknown sources vary greatly in spatial distribution. The transfer function of the spectral measurement system varies with this spatial distribution. However, both these difficulties are minimized by using the diffusing technique. This can best be accomplished through the use of a diffusing sphere or diffusing plate which is alternately irradiated by the unknown and reference sources. For a sphere coating, MgO offers good reflectance from about 250 to 1600 nm. MgO is prepared by burning magnesium ribbon in air. ASTM E-259-66, Recommended Practice for Preparation of Reference White Reflectance Standards, contains additional information on the preparation of smoked MgO. At wavelengths longer than 1600 nm the reflectance falls off fairly rapidly, but can still be useful up to 2500 nm with a sacrifice in efficiency. MgCO₃ in block or plate form has a high diffuse reflectance through most of the solar spectral region. The efficiency of a flatplate diffuser is about 10 times that of the integrating sphere. The improved diffusing characteristics of integrating spheres may be necessary for precise measurements.

6.4.3.4 Standard of Spectral Irradiance

The most significant advance in spectroradiometry in recent years has been the establishment of a Standard of Spectral Irradiance by the National Bureau of Standards (ref. 6.7). This standard is a 1000 W coiled tungsten filament enclosed in a 3/8 inch x 3 inch quartz envelope containing a small amount of iodine.* The standard is issued from several commercial sources. A calibration traceable to the NBS Standard is furnished over the wavelength range 250 to 2500 nm for each standard that is issued. The calibration is expressed in terms of energy per unit area and unit bandwidth ($\text{W}/\text{m}^2\text{-nm}$) incident on a surface 50 cm distant when 8.30 amperes (AC or DC) is passing through the lamp. The stability of the lamp is extremely good with less than 1 percent expected degradation after 50 hours of careful use. However, several working standards should be calibrated by the user for routine measurements. The uncertainty in the calibration is 3 percent for the visible and infrared, increasing to 8 percent in the ultraviolet.

6.4.3.5 Detectors

In order to cover the full spectral range from 250 to 2500 nm, at least two photoelectric detectors are required. Phototubes and thermopiles are, in general, too insensitive to be useful. A high-sensitivity, low-noise, photomultiplier, such as the RCA 1P-28 or EMI 6256B, is used to cover the ultraviolet and visible spectral region. A PbS detector is used to cover the 600 nm to 2500 nm region.

6.4.3.6 Signal Processing

Signal levels from the detectors are typically in the microamp and microvolt region. Low noise, wide dynamic range amplifiers employing synchronous or phase lock detection must be used to process these low level signals. Although the signals may be read out on laboratory voltmeters on a point by point (wavelength by wavelength) basis, the large number of data points required for a complete scan usually leads to the use of an automatic data handling readout such as an analog strip chart or digital data recording system. Since computations are typically necessary to reduce raw data to calibrated spectral irradiance, the digital data handling technique is preferred.

6.4.3.7 Screen Attenuators

In many measurements, a large difference in the irradiance between the standard source and the unknown source may exist. This irradiance

*Designation: General Electric DXW-1000

ratio between the two sources can range up to several orders of magnitude and will usually vary considerably with wavelength. Unless the more intense source is attenuated by a known amount, so that the energy falling on the detector is roughly equivalent for both the standard and the unknown source, difficult linearity and dynamic range requirements will be imposed upon the detector-amplifier system. The use of neutral density screens has proven most satisfactory in attenuating radiant flux by a repeatable amount. The transmittance of these screens can be determined in conventional spectrometers whose linearity can be conveniently checked by samples with precisely known concentrations of absorbing agents. Some spectroradiometers provide such attenuation through a pre-programmed technique.

6.4.4 Operational Considerations

6.4.4.1 Monochromator Calibration

The calibration of wavelength as a function of wavelength-drive position is accomplished by observing spectra from low-pressure arc lamps such as mercury, sodium, neon, cesium, potassium, etc. The wavelengths of major spectral lines are precisely known for these sources and may be found in references such as the American Institute of Physics Handbook (ref. 6.8). The calibration should be performed by scanning in the same direction (i.e., long λ to short λ) as during actual measurement to minimize the problem of backlash in the wavelength drive.

6.4.4.2 Optimization of Scan Parameters

The optimum choice of slit width, amplification, system response time, scan rate, etc., is dependent upon the capabilities of the system and the end use of the data. As an example, a requirement of near-perfect resolution of the spectral bands of a high-pressure arc lamp necessitates as a first consideration that the spectral bandwidth be considerably less than the natural bandwidth. This, in turn, requires increased amplification and increased system response time (increased integration interval or time constant) to achieve a reasonable signal-to-noise ratio. The scan rate must then be slow enough so that resolution is not limited by the response time of the system. A scan rate of 1/10 spectral bandwidth per system response time is recommended for precise work.

In general, the end use of spectral irradiance measurements does not require near-perfect resolution of spectral peaks, and tradeoffs can be accomplished between decreased resolution (increased slit width) and increased signal level and rate of scan. Since resolution (spectral bandwidth) is proportional to the square of slit width, a considerable increase in signal can be gained by a relatively small decrease in resolution. With decreased resolution and higher signal the system response time for the

same signal-to-noise ratio can be reduced and the rate of scan can be proportionately increased. For general work a scan rate of from 1/5 to 1 spectral band-width per system response time may be acceptable. In practice, the operator usually varies the scan parameters according to the presence or absence of band structure in the spectrum being measured. A high resolution, slow scan is employed within spectral regions containing significant band structure, while a low resolution, rapid scan is used where band structure is absent.

For measurements of solar simulator spectral irradiance to test for compliance with simulator clarification as discussed in Section 5, the slit width (spectral bandwidth) must be compatible with Table 5.1.

6.4.5 Operational Procedures

6.4.5.1 Preliminary Measurement

It is desirable to obtain a preliminary indication of the relative intensity levels of the unknown and standard sources as a function of wavelength. This is accomplished by performing for each source a relatively rapid scan over the entire spectral range of interest. It is desirable for these preliminary scans that only amplification be varied to maintain adequate signal level and for slit width, scan rate and system response time to remain constant. If, however, at the extremes of the spectral range it becomes necessary to vary one or more of these parameters, the values must be the same for both the unknown and reference sources.

6.4.5.2 Selection of Scan Parameters

The entire spectral range is divided into sub-regions, each covering an order of magnitude or less change in signal level from either the unknown or standard source. A table with format similar to Table 6.1 should be constructed to aid in establishing the scan parameters to be used in the final measurements.

A screen attenuator is selected for each of the above spectral regions to bring the signal levels of the unknown and standard sources to approximately the same value. The scan parameters are selected based upon the information obtained in the preliminary scan and the criteria discussed in paragraph 6.4.4.2. It may be necessary to repeat certain spectral regions to establish natural bandwidths and to check final selections of scan parameters in regions of band structure.

6.4.5.3 Final Measurements

Alternate measurements are performed on the unknown and standard sources within each of the selected wavelength regions using the scan parameters determined above. It is desirable to keep the time interval

between measurement of the unknown source and measurement of the standard source as short as possible to minimize errors due to amplifier drift and sensitivity change. The spectral irradiance of the unknown source within each wave-length region can be determined by equation 6.4.2 (2) from the measured ratio of signal levels, knowledge of the transmittance of the attenuator screen, and the calibration of the standard source.

6.4.5.4 Data Reduction and Presentation

There are many methods of data acquisition ranging from the time consuming point by point hand recording of meter readings into a chart format to the completely automated system which provides raw data (detector output vs wavelength) into an appropriately programmed computer. Nevertheless, the basic computation techniques are embodied in the equations in 6.4.2 and the subsequent discussion concerning the use of gain changes, slit width or screen attenuation. The series of sketches (Fig. 6.3-6.6) in this section attempt to indicate in analog form the various processes which are utilized to transform the raw data into a normalized spectral irradiance. It must be emphasized that these are merely sketches and in no manner to be considered quantitative. The semifinished data usually can be presented in a tabular format similar to Table 6.2. It must be emphasized that the final normalization relates to the area under the resultant curve and that the indicated spectral irradiance value is valid only at a specific wavelength. Though by custom the plotted data are presented as a smooth curve while the true representation would be a small rectangle at each datapoint. While tabular data are most useful for subsequent computation, spectral irradiance divergences are most readily apparent when plotted. It is recommended that both formats be provided the user.

6.5 Total Irradiance Monitoring During Testing

6.5.1 Scope

This section covers the monitoring of the total irradiance during a thermal vacuum-solar simulation test. Total irradiance here refers to the total incident energy from all sources. IR energy from internal solar simulator optics, some vacuum gages, and the chamber view ports must be added to that from the solar beam. Also, the chamber LN_2 shrouds contribute some emitted and reflected energy. Reflections of the spacecraft can also add to the total energy balance. The total energy which arrives on the surface over the 2π steradian view angle can be as much as 10% greater than the solar simulation component.

Additional components of radiation often creates differences between predicted and measured temperatures during test.

6.5.2 Detectors

Three types of detectors can be used to monitor the total irradiance during a test. The first type recommended is the same thermopile detector discussed in Section 6.3.2, but with certain modifications. This detector must now be capable of operating in a vacuum of 10^{-4} torr or less as well as in air. This requires that the window cover be removed during vacuum operation to prevent it from emitting IR radiation to the detector surface. Note that the sensitivity of the radiometer under vacuum is different than in the atmosphere and in addition the removal of the window requires a change in the radiometer calibration factor. Furthermore, the detector must be maintained within its specified temperature limits. This may require the use of fluid or thermo-electric temperature control.

A second type of detector that could be used is a flat or v-grooved metal plate coated with a material of well known absorptivity and emissivity. Generally, the back side is insulated to eliminate uncertainties of reflected beam energy, etc. The plate (of arbitrary dimensions) is hung in the beam and its temperature carefully monitored with thermocouples. A calibration of temperature vs beam energy is made and thereafter used to determine the energy over the 2π view angle. This type of detector is not as accurate as the thermopile type because the measurement depends on an accurate knowledge of the properties of the coating and also on the fourth power of temperature. Since the temperature may not be known to better than 0.5 K, it is easy to see that overall accuracies of $\pm 5\%$ are considered good. On the other hand, the thermopile type can be accurate to $\pm 2\%$ or better. One advantage of the plate is that it does not require any means for temperature control. Thus, a facility which restricts the use of fluids under vacuum conditions would still be able to monitor beam irradiance using this type of detector.

A third type of detector may be called an electrically calibrated radiometer. In general these radiometers contain cavities of known dimensions and optical properties. Calibration is obtained by substitution of electrical power for radiant energy.

For thermal balance testing with solar simulation sources widely differing in spectral irradiance from solar, i.e., tungsten lamps, a more meaningful term than incident irradiance is the absorbed irradiance. Absorbed flux radiometers may be used as detectors rather than the total irradiance radiometer for calibration of such facilities.

6.5.3 Recording Devices

For beam monitoring during tests, a good strip or digital recorder should be used so that a continuous record of irradiance can be kept.

6.6 Spectral Irradiance Monitoring

6.6.1 Scope

This section covers the monitoring of the spectral content of the simulator beam. Users must be aware that the spectrum changes with time due to degradation of the optical components and variations in power supply output. The instrumentation requirements vary considerably as to the basic optical system. It has been found that the modular systems require careful checking of the spectral properties of the beam, particularly after a source or optical element has been changed. Experience has shown that the pseudo-random element replacement which occurs in an integrating system causes only a minor change in the spectral irradiance. Apparently, after a few hundred hours of operation the system has spectrally degraded to a constant level. Naturally, if the primary collimating mirror of the integrating system is recoated a spectral change should be anticipated and verified.

6.6.2 Procedure

The spectral distribution should be measured often enough to monitor significant changes in spectral distribution. The frequency of measurement will vary with the type of lamps, power levels, spacecraft spectral sensitivity, etc. The spectrum of a solar simulator should be monitored periodically in order to keep a record of spectral change with time. A double prism monochromator of the type described in Section 6.4.3 should be used, viewing the beam through a fused silica port. Should it be necessary to measure from inside the vacuum chamber, filter radiometer instruments are available that operate in a vacuum environment.

However, great care must be used in calibrating this type of radiometer to insure that the air to vacuum correlation is known. A properly calibrated filter radiometer after correlation with monochromator measurements, provides a rapid, economical method of verifying spectral irradiance stability.

6.7 Uniformity

6.7.1 Scope

This section discusses the methods for determining the uniformity of the solar simulation system. It should be noted that the area of the detector utilized for these tests must be commensurate with the size of the minimum thermally independent portion of the test article. Although it is possible to utilize a group of the same type of thermopile detectors as mentioned in Section 6.3, the slow time constant of most thermopiles places severe restrictions upon the scan rates and thus makes uniformity testing a tedious process. Where spectral nonuniformity is observed the use of the spectrally neutral thermopile type detectors is mandatory. In

describing the uniformity of a solar beam some form of statistical analysis is recommended.

6.7.2 Plane

In general, uniformity in a test plane should be measured with a 2 x 2 cm (or smaller) solar cell mounted on a mechanical carriage device which moves it in the area of the beam. This size solar cell is recommended because it is commercially available. Any larger sampling area would require multiple cell connections (which demand careful calibration). The cell should be loaded with a low resistance (usually 1 ohm or less) in order to approximate the short-circuit current (which varies linearly with irradiance). Monitoring of the cell temperature is recommended for irradiance levels above 1350 W m^{-2} to insure that it remains within the manufacturer's specified limits.

6.7.3 Volume

Volume uniformity is measured by making plane uniformity scans at different depth locations in the test volume. Then the variation of irradiance between planes must be determined to relate the planar data to the entire volume.

6.7.4 Data Reduction and Presentation

Since any temporal change in total irradiance during the uniformity measurements will give erroneous results it is necessary to monitor the beam at a fixed location during all uniformity scans. With the use of modern digital instruments it is possible to ratio two signals automatically and thus it is possible to express uniformity deviations as a percent variation. This technique is immediately applicable to the integrating type solar simulation systems. Modular systems having individual power regulation require special consideration to prevent the uniformity data from being masked by temporal changes. For the modular systems, scanning using multiple detectors is the preferred technique.

For large area solar simulators the uniformity scan data may be collected from multiple detectors mounted on a scanning beam or arm. In this case the sensitivity and zero calibration of each detector must be known and the ratioing measurement to a stationary reference detector must be accomplished. Scanning time is therefore greatly reduced, however, digital data acquisition, conversion, and computation facilities are necessary in order to handle the data output.

Data presentation may be analog or digital and chart, table or even CRT display in format. However, some technique of displaying the variation in uniformity is preferred. Isoplots of irradiance in various planes

throughout a volume are a typical display technique. Both analog and tabular data have proven to be equally useful.

6.7.5 Spacecraft/Solar Simulator Interaction

After uniformity scans have been completed and the test object mounted in position, spot checks should be made prior to pumpdown. These are performed by manually measuring the total irradiance of the simulator beam at different locations near the test object. The irradiance at these locations is frequently changed by reflections and re-reflections from spacecraft components to each other and their interactions with the chamber.

6.8 Solar Beam Angles

This section covers the measurement of the divergence angle, maximum divergence angle, subtense angle, and apparent source. (See Section 3 and Fig. 3.1 for definitions.) Though these angles may be computed from knowledge of the optical design, for reasons cited in Section 6.8.2, these characteristics should be measured by an accurate optical angle measuring instrument such as a theodolite.

6.8.1 Maximum Divergence Angle

This angle is of particular interest with direct projection systems. It can be measured with a theodolite or other optical angle measuring instruments. However, with a direct projection system it probably is simpler to observe the pattern of illumination at the test plane. With these data, and knowing the distance from the test plane to the apparent source and the diameter of the apparent source, it is easy to calculate this angle.

6.8.2 Divergence Angles, Subtense Angle, Apparent Source

The theodolite is set up at any arbitrary point in the test volume by carefully aligning its reference axis parallel to the axis of the solar beam. Then a minimum of four sightings are taken on the extreme edges of the apparent source and the angles recorded. For instance, with a vertical solar beam, the sightings might be to the north, east, south, and the west edges of the apparent source. From these values the subtense and divergence angles can be computed for this point in the test volume. As an example, the subtense angle, north-south, is the difference in those angles, similarly for the east-west measurements. The divergence angle, north-south, is the difference between the bisector of the angles measured and the true vertical (for the example chosen).

The method given above assumes the apparent source is nearly circular, sharply defined, and of symmetrical radiant intensity about the

center. If the apparent source is not circular, measurements of best and worst cases should be made. For example, with direct projection through two small windows, sightings along the long dimension of the two windows to the outside edges of each source should be made. The smaller angle across the apparent source should also be measured.

If the outline of the apparent source is not sharply defined, the minimum area from which issues 95% or more of the total energy should be used. Infrared emission from window frames, etc., should be included in the total energy.

If the radiant intensity is not symmetrical about the center of the apparent source, the principal measurement affected will be the divergence angle. In this event, a point must be selected in the apparent source that represents the mean value of the radiant energy. The divergence angle in the test volume is the difference between the direction to this point and a line parallel to the solar axis.

After completing the angle measurements at one point in the test volume, the theodolite is moved to other points and the measurements repeated. A test volume is chosen for illustrative purposes that has a well-collimated beam and is a right circular cylinder aligned vertically. In the principal test plane the beam should be measured with the theodolite at the center, at radial distances representing $1/3$, $2/3$, and $3/3$ of the beam dimension at 0° , 90° , 180° , and 270° , and at the edge of the beam at 45° , 135° , 225° , and 315° . These test points are representative only. Different points providing equivalent coverage may be chosen for different installations. The top and bottom planes of the test volume cylinder should be tested at the beam edges at 0° , 90° , 180° , 270° orientations each. If these latter values are not predictable or as expected, more readings should be taken.

These measurements normally will have variations throughout the test volume. The worst cases of subtense and divergence angle should be used and quoted for the system. However, all measurements should be carefully preserved because individual test items frequently can be positioned within the nominal test volume to take advantage of the best portions of the beam.

6.9 Vacuum Gages

6.9.1 Vacuum gages shall be used in accordance with ASTM E296-70, Recommended Practices for "Ionization Gage Application to Space Simulators."

6.9.2 Vacuum gages shall be calibrated in accordance with ASTM E297-70, "Standard Methods for Calibrating Ionization Vacuum Gages Tubes."

Table 6.1

SCAN PARAMETERS FOR FINAL MEASUREMENTS

Wavelength Region	Attenuator Screen Transmittance		Slit Width	Amplification	Response Time	Scan Rate
	Unknown	Standard				

COMPUTATION SHEET, TYPICAL

$$E_{ssn} \lambda = \frac{\sum E_{ssn}}{\sum E_{ssn}(\lambda)} \times E_{ssn}(\lambda)$$

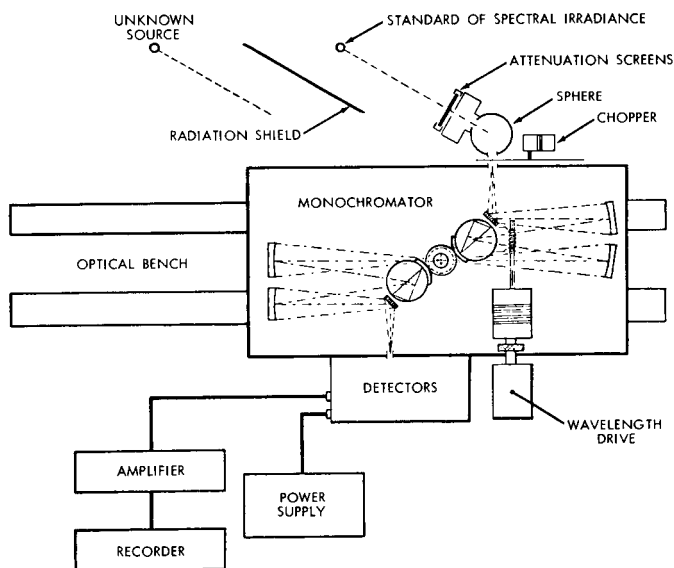


Figure 6.1. Diagram of System for Measurement of Spectral Irradiance.

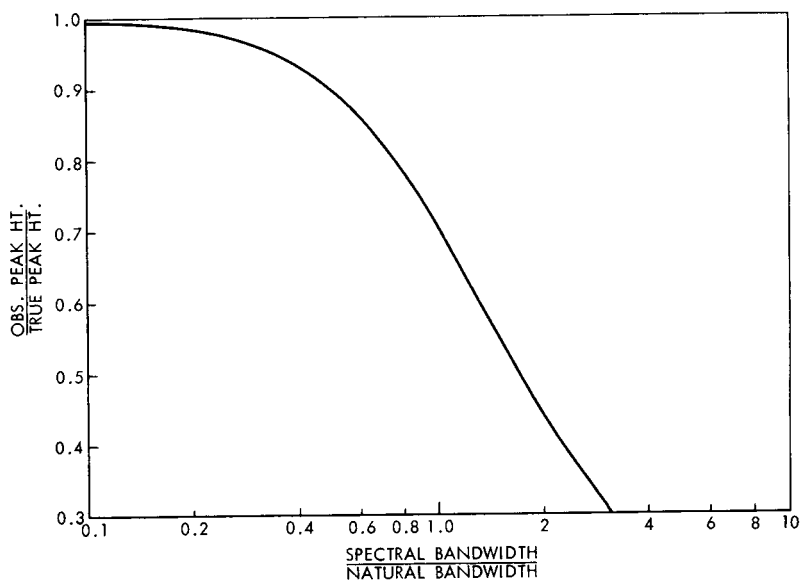


Figure 6.2. Relationship of Peak Height to Spectral Bandwidth/Natural Bandwidth Ratio.

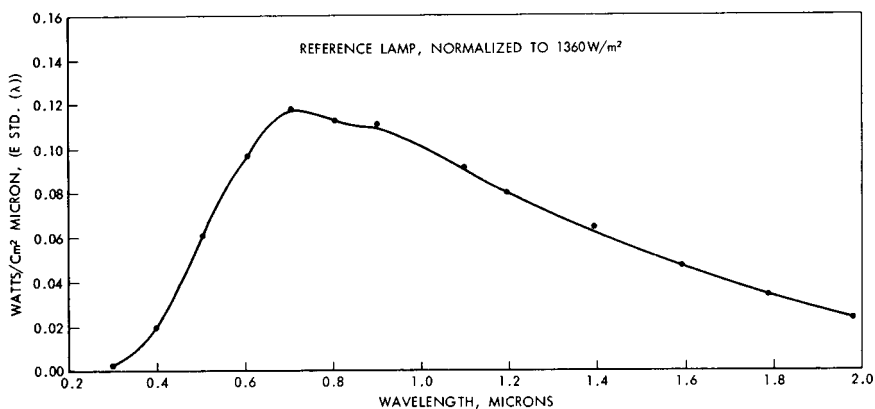


Figure 6.3. Reference Spectral Irradiance.

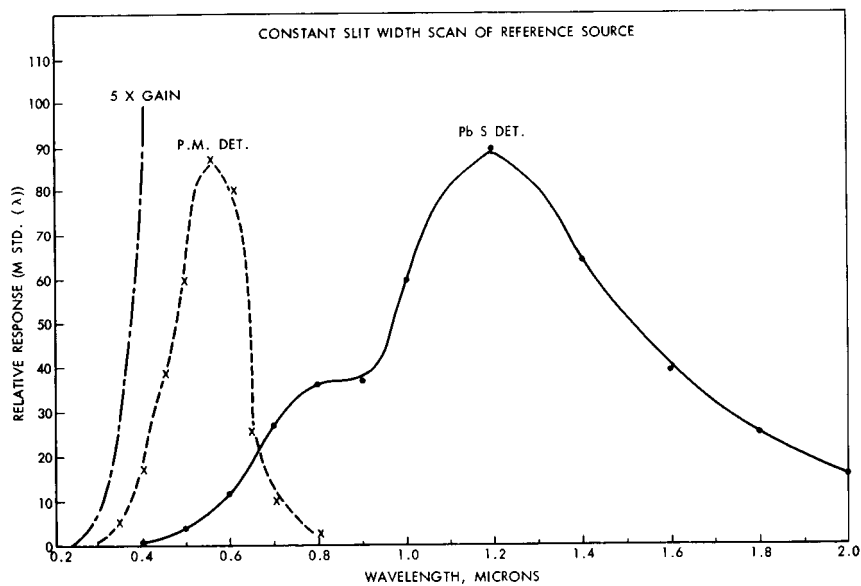


Figure 6.4. Reference Source Measurements.

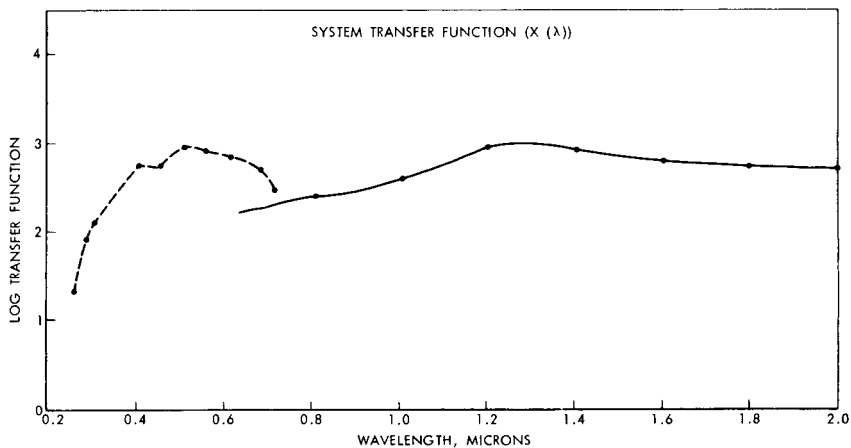


Figure 6.5. System Transfer Function.

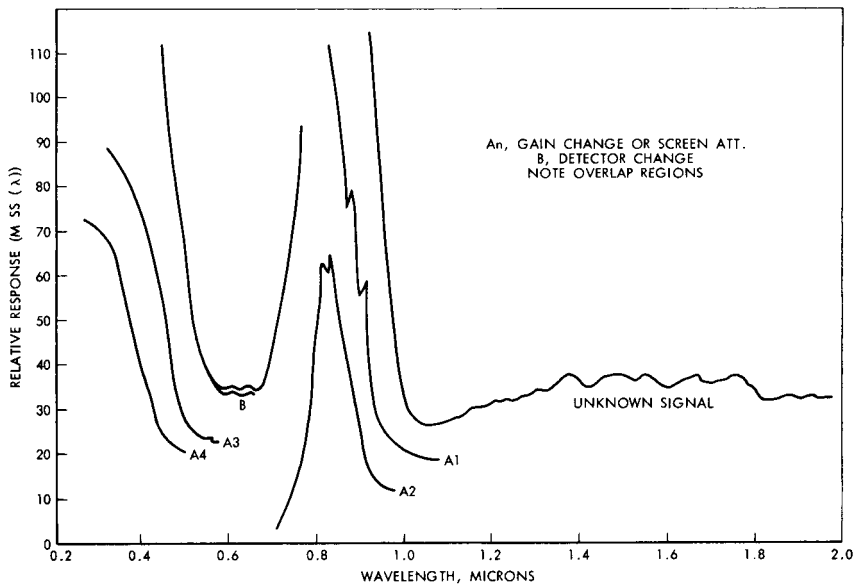


Figure 6.6. Unknown Source Measurements.

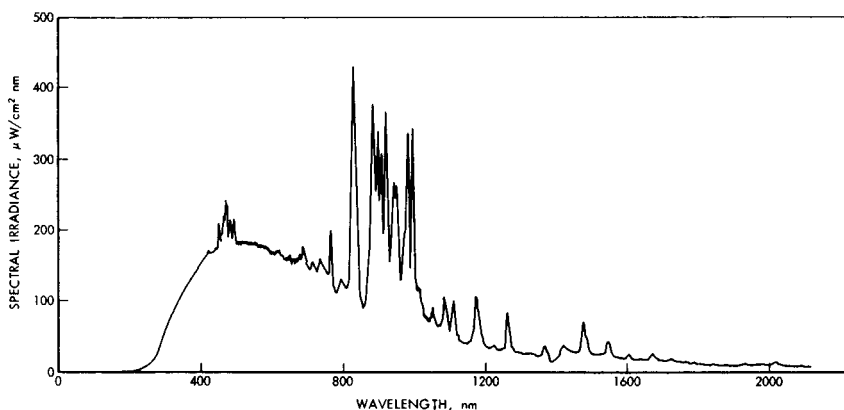


Figure 6.7. Example of Spectral Irradiance Measurement - Xenon Arc Lamp.

REFERENCES

- 6.1 A. J. Drummond and J. R. Hickey, Solar Energy, II, 1, 1967.
- 6.2 A. J. Drummond, "The Absolute Calibration of Thermal Radiation Detectors," ISA Preprint PG-1-PHYMMID-67, September, 1967.
- 6.3 Annals of the International Geophysical Year, (Pergamon Press, London, 1958), Vol. V, Part VI, p. 378.
- 6.4 J. M. Kendall, Sr., and C. M. Berdahl, "Two Blackbody Radiometers of High Accuracy," Applied Optics, Vol. 8, p. 1082, May, 1970.
- 6.5 A. Ångström, Tellus, 13, 3, 1961.
- 6.6 Thermal Radiation Heat Transfer, NASA, SP-164, Vol I & II, 1969.
- 6.7 R. Stair, W. E. Schneider and J. J. Jackson, "A New Standard of Spectral Irradiance," Applied Optics, 2, pp. 1151-1154, November, 1963.
- 6.8 American Institute of Physics Handbook, McGraw-Hill, 1963, Vol 2.

7. OPERATIONS AND MAINTENANCE

7.1 Introduction

7.1.1 Applicability of this Section

This section will discuss primarily the operation and maintenance of large space simulation chambers with cryogenically cooled shrouds, pumping systems capable of 10^{-4} torr or less, and high caliber solar simulators with A and B characteristics listed in Section 5.0. The operations described will be thermal balance testing or systems testing integration. Many of the recommendations apply to smaller and/or less sophisticated chambers, of course.

The subject matter will include chamber operation before, during and after the test, procedures and documents, maintenance and calibration, and cleanliness and contamination.

7.1.2 Related Topics in this Recommended Practice

Certain topics that are closely related to this subject matter can be found in other sections of this recommended practice:

<u>Topic</u>	<u>Sections</u>
Instrumentation Calibration	6.0
Safety	8.0
Test Requirements	5.0
Types of Tests and General Considerations	4.0

7.2 The Space Simulator Operations Organization

A great deal of flexibility exists in setting up an organization for operating a space simulator. The size and complexity of the facility and the test objectives will determine the degree of specialization and departmentalization required to operate the following systems and functions.

- a. Chamber Vacuum System
- b. Chamber Cryogenic System
- c. Chamber Solar Simulator
- d. Chamber Instrumentation

- e. Test Item Instrumentation Readout Equipment
- f. Building Utilities and Physical Plant Water, Electrical Systems and Heavy Equipment, Gas Ventilation and Air Conditioning
- g. Test Planning, Coordination, and Report Writing

The last item, test planning, deserves special consideration. There is generally a need for test planners who are able to relate the customer requirements to the facility. This group should be organizationally separate from both the customer and the chamber operating group, at least at the group engineer level, to make possible an objective outlook to the test. The test planner needs an intimate knowledge of the chamber and its performance but also familiarity with the customer's concerns such as thermal design, test item function and purpose, etc.

7.3 Procedures and Documentation

7.3.1 Introduction

All procedures and facility performance that are routine should be documented and the documents used. The safety of the personnel, facility, and test item are very dependent on proper procedures. It is generally impossible for even experienced engineers and technicians to remember all procedures and in their proper order. Documents are very valuable in training new personnel, refreshing the memories of experienced personnel, and upgrading. Perhaps most important of all, the responsible engineers who prepare the procedures and the supervisors who approve them are more likely to give careful thought to the best way to carry out their responsibilities.

Procedures and performance documents are also valuable to other groups such as the customer, safety department, and service departments.

7.3.2 Facility Operations Manual

It is desirable to file all procedures in a single loose-leaf manual, if possible, so that a single source will be available. A typical list of topics for this manual is as follows:

INDEX OF PROCEDURES

- 1.0 Emergency
- 2.0 Operations
- 3.0 Maintenance

- 4.0 Administration
- 5.0 Training
- 6.0 Safety
- 7.0 Calibration
- 8.0 Schematic Diagrams
- 9.0 Special Equipment
- 10.0 Valves and Interlocks
- 11.0 Test Item Handling
- 12.0 Operational Instrumentation

An example of the further breakdown of each topic is that for "2.0 Operations:"

2.0 OPERATING PROCEDURES

INDEX

- 2.1 To Close and Open Chamber Door
- 2.2 Chamber Pre-Evacuation
- 2.3 To Evacuate Chamber
- 2.4 To Fill the LN₂ Storage Tank
- 2.5 To Chill to Warm the Contamination Plates
- 2.6 Temperature Control of Shroud System
- 2.7 Mirror Temperature Control
- 2.8 Backfill Sequence Using GN₂ , Contamination Plate
- 2.9 To Backfill Chamber Using Facility Filtered Air
- 2.10 Hourly Inspection Tour Check List
- 2.11 Priming and Securing LN₂ Pumps
- 2.12 Solar Simulator Pre-Operation Inspection Check List
- 2.13 Solar Hood Purge Procedure
- 2.14 Lamp Operating Procedure
- 2.15 Vacuum System Conditioning with Chamber at Atmosphere
- 2.16 Pre-Operation Emergency Equipment Check List
- 2.17 To Secure Facility

A detailed consideration of these topics is beyond the scope of this recommended practice. Since similar documents are available at most space simulation facilities, personal contacts should be made to obtain copies, if needed.

Certain special areas of concern for solar simulation are discussed in Paragraph 7.5 below.

7.3.3 Facility Performance

The performance of the various systems of the space simulator should be described in one or more documents for the use of customers and operations personnel.

- 7.3.3.1 Vacuum System - effective pumping speed, method of trapping all pumping ports, pumpdown and chilldown time, ultimate pressure.
- 7.3.3.2 Contaminant measurement systems - contaminant levels during pumpdown, test, shutdown and with the chamber open. Particulate contaminant levels in the room just outside the chamber door should be noted.
- 7.3.3.3 Cryogenic system - reflecting and emission from the cold wall with the solar beam on and off.
- 7.3.3.4 Solar simulation system - Solar simulation data that should be provided are:
 - a. Total irradiance,
 - b. Uniformity of irradiance,
 - c. Spectral irradiance,
 - d. Solar beam subtense angle,
 - e. Divergence angle of the solar beam, and
 - f. Maximum usable beam diameter and depth.

The uniformity of irradiance must relate local irradiance with position throughout the test volume, usually in the form of an iso-irradiance plot (lines of constant irradiance relative to beam position in the test volume). The usable beam diameter is apparent from this plot. The iso-irradiance lines may be expressed in percent of one solar constant. Measurements of irradiance should be made as described in Section 6.2. It is important that chamber reference points be identified on the iso-irradiance plot. The spectral energy distribution measured should be compared to the solar spectrum, and tabulated similar to the example contained in Table 7-1.

Table 7-1

SPECTRAL ENERGY DISTRIBUTION

Band No.	Bandwidth nm	Matched Data	Normalized Matched Data W.R.T. 1.0 Solar Constant (W/M^2)	Reference NRL Spectral Solar Irradiance (W/M^2)	% Deviation
1	250-350			62.8	
2	350-400			61.4	
3	400-450			95.9	
4	450-500			106.1	
5	500-600			191.3	
6	600-700			161.9	
7	700-800			127.0	
8	800-900			100.5	
9	900-1000			81.0	
10	1000-1200			121.5	
11	1200-1500			111.7	
12	1500-1800			61.8	
13	1800-2200			44.3	
14	2200-2500			19.1	

7.3.4 Special Instruction Manuals

Because of the great amount of detail in complex systems it is desirable to have special operating, maintenance, and instruction manuals for the solar simulator, computer data systems, etc.

7.3.5 Daily Space Simulator Log

7.3.6 Test Plan and Test Reporting

Special documents that vary with each test include test plans and a final report. (See Paragraph 7.2.1 describing the test planning group.) Results of meetings with the customer, special test item procedures, preliminary and final test plans should be written and distributed. The final test report should contain a copy of the final test plan.

7.4 Calibration

7.4.1 Test Equipment Calibration

Individual items of test equipment are generally maintained in calibration by a standard lab or test equipment group in the company. If not, a routine maintenance and calibration system must be set up. Some test equipment calibrations unique to space simulation is described in Section 6.0.

7.4.2 Solar Simulator Calibration

The solar data in Paragraph 7.3.3.4 are needed by the customers and operators of the facility. Periodic calibration is necessary of the first two items, total irradiance and uniformity of total and spectral irradiance.

Calibration frequency of the solar simulator is primarily dependent on the number of operating hours accumulated on the system and the type of simulator. It is usually established by past performance of the system and covers an operating time span in which the system performance does not change. Initially, the solar simulator would normally be given an acceptance test and a thorough calibration. Then it is suggested that a calibration be performed at least twice for each test, once before the test and again after the test is completed. This is due to the fact that the scanner used to calibrate the solar beam in the test volume must be removed to allow for installation of the test article. However, some facilities have retractable scanners mounted in the space chamber such that they can be deployed during the test and the uniformity of irradiance measured any number of times during the test. Two points of concern with respect to this method are: a. the uniformity of irradiance is not measured exactly in the test volume at the test article position, and b. further inaccuracies in thermal sink simulation occur due to the scanner mechanism acting as a thermal source unless it is properly shielded.

A secondary consideration is the time the simulator was in a standby condition. For example, if the simulator has been inoperative for several weeks, it is usually good test procedure to spot check the last

calibration to insure there has not been any significant change in the performance such as misalignment or optical degradation. However, it may be a test requirement that a specific calibration schedule be established in order to support, for example, a long term component degradation test.

The calibration may require only a few hours or as much as one or two days to complete, depending on the solar simulator size. However, alignment and refurbishment of the optics, and lamp changes could last several weeks, again depending on the type of system and lead time for procurement and/or replacement of parts.

After a number of solar calibrations have been performed the changes in performance can be assessed as a function of operating time, calendar time, lamp operating power, etc. It is generally possible then to reduce the frequency of calibration. Obviously, good and complete records of the solar simulator system, individual lamps and other components must be kept.

The solar simulator continuous operational time is a function of the life of the source or lamp and the reflective surface degradation rate. The lamp light output or energy output will drop off with time due to contamination deposits on the inside of the lamp. Further requirements for increased power input to the lamp results in optical degradation of the reflective surfaces. It should be pointed out that for off-axis or mixer type systems, spare sources may be in the system. As the original source approaches its expected life, the spare can be started. Replacement of the used sources could then be accomplished one at a time enabling the simulator to operate continuously. The effects on the system performance would not be noticed during the replacement. For on-axis systems, the source can also be exchanged for other pre-aligned sources during test. The results, however, would require that the source be turned off during the exchange for a period of approximately one hour. This is not expected to cause any significant change in the test results.

The approximate actual lamp lifetimes to be expected can be taken as the manufacturer's warranted lifetime, derated to provide the desired margin against failure. However, actual operating experience will provide the best guide since lamp life will vary considerably between different installations.

7.4.3 Heat Sink - Space Chamber

Other sources of energy must be considered in the final temperature equilibrium measurements. For example, the LN_2 shroud is painted black and cooled to absorb most of the energy striking it. Solar simulation optics, test article support structure, view ports, condition of the black paint on LN_2 shrouds all contribute to the effective heat sink of the chamber. Two methods can be used to determine the chamber cold sink properties. The first is by the use of radiometers strategically placed in the chamber at critical locations and operating irradiances measured

during an actual simulated test condition. This would require the measurements to be made with the solar simulator on and off to obtain the net effective heat sink. The other method consists of determining the nature and location of all energy sources within the space environment with respect to the test article, and include this in the final thermal analysis of the test results. Total reflected and emitted radiation arriving at the test vehicle for several classes of cold sinks, exclusive of the solar simulator, is shown in Table 5-2.

7.5 Operating The Facility

7.5.1 Test Item Considerations

Generally, the test item is designed, built, handled, and system tested by others. The space simulator operations is a service function to the spacecraft (test item) group. However, certain aspects of the spacecraft handling, fabrication, and system test are of direct concern to and involve the simulator group. A test planner who aggressively performs this liaison function will generally insure an on-time test completion that meets all of the objectives.

7.5.1.1 Spacecraft Design and Fabrication

Simulator personnel should become involved with the earliest stages of spacecraft design, especially if the designers are inexperienced. The simulator group's principal interest is in the materials of construction and component pre-conditioning. Self-contamination of a spacecraft and of the facility is quite common because of vacuum outgassing of improper materials. Space qualified material lists and components are available and should be used. A preconditioning vacuum treatment of non-qualified materials should be performed at temperatures above their expected operating temperatures. A conditioning chamber equipped with a full LN₂ cold wall, heating means, and a pumping system capable of pressures below 5×10^{-5} torr during outgassing should be used. The minimum time and temperature required can be determined from the following formula (Ref. 7-1).

$$\log t_s - \log t_b = 0.219 \Delta E_c \left(\frac{1}{T_s} - \frac{1}{T_b} \right) - 1$$

where

t_s = time the spacecraft component will be under vacuum in the simulator, hours

t_b = time of bakeout conditioning, hours

T_s = anticipated temperature of component in the simulator, K

T_b = temperature of bakeout, K

ΔE_c = critical absorption energy, cal (g mol)⁻¹

$$= 4.58 (16.2 + \log t_s) T_s .$$

7.5.1.2 Test Fixtures, Thermal Isolation, Instrumentation

The method of mounting the spacecraft to meet the test objectives should be worked out jointly by spacecraft and simulator personnel.

7.5.1.3 Test Objectives

The simulator group must keep foremost in mind the customer's test objectives. Operating procedures may have to be modified to satisfy the test.

7.5.1.4 Spacecraft Handling

While this is primarily the responsibility of the spacecraft crew, the entire operation must be carefully planned with simulator personnel to insure proper equipment is available including building cranes, installation equipment, spacecraft preparation area, fixtures, etc.

7.6 Contamination

7.6.1 Particulate Contamination of the Spacecraft

Operators of many of the newer facilities are fortunate to have clean room design features incorporated into the building construction. Spacecraft groups generally desire, if not demand, class 100,000 to 10,000 clean rooms, or better. It is generally uneconomical to change a standard building into a clean room. Several alternate schemes should be considered.

7.6.1.1 Air Conditioned Space Simulator

Frequently the space simulator can be air conditioned with highly filtered air. Large ports or doors at the top and bottom of a chamber will permit pumping air in at the top to provide a downward flow. Excess open areas at the bottom should be sealed off to maintain a positive pressure and avoid entry of dust from the outside. Although the air velocity

will seldom approach that of a laminar flow room, surprisingly low particulate levels can be achieved.

In some cases it is possible to bring the spacecraft in its shipping container right into the air conditioned space chamber. First, the container is cleaned, then the spacecraft is removed and mounted in the chamber for test preparation.

7.6.1.2 Portable Clean Room

One or more portable laminar flow rooms may be installed adjacent the chamber, especially if a side-opening door is available. The chamber door opening is sealed to the clean room. Test preparation, component storage, etc., can be carried out in the portable clean room.

7.6.2 Contamination Under Vacuum

7.6.2.1 Introduction

Many sources of contamination exist in the simulated space environment. These contaminants cause optical degradation of the solar simulator mirrors as well as coating the space chamber and the spacecraft. Outgassing and migration of the molecules throughout the space chamber eventually reach the solar simulator mirrors. High solar irradiance on the mirrors and the concentration of UV energy can cause major reflectance degradation of the mirrors. Then, in order to maintain a constant irradiance level in the test volume, it requires an increase in input power to the system. Measurement of the degradation rate and correction of the irradiance in the test volume can be accomplished by continuously monitoring the solar beam irradiance within the space environment.

The most uncontrolled source of contamination that causes mirror degradation is the spacecraft. Other sources of contamination include mechanical pumps, oil diffusion pumps, residue from previous tests, and atmospheric exposure. Basic chamber contamination should be measured prior to test. Then, during the test of the spacecraft, the total contamination can be determined and a comparison of the chamber background should indicate the spacecraft contamination. These measurements may be taken by means of a mass spectrometer, witness plates, quartz crystal microbalances, or other similar devices. This information provides a history for determining the causes of mirror degradation and corrective action to prevent recurrence in the future.

7.6.2.2 Contaminants from the Spacecraft

Most residues obtained during and after space simulation tests show that the contaminants are outgassed materials from the spacecraft, and/or its cabling and fixtures. Selection of proper materials during the

design stage and pre-conditioning (see Paragraph 7.5.1.1) will eliminate or greatly reduce this problem.

If these precautions have not been taken, it may be necessary to consider a bake-out phase in the test sequence. This could eliminate or at least reduce the degradation of the solar simulator. The bakeout phase should remove most of the contaminants from the spacecraft and test fixtures. Prior to the thermal vacuum test the test articles are baked at a maximum allowable temperature until a pressure of no more than twice the anticipated chamber pressure during the test is reached. If this is not feasible, the bakeout may be discontinued after achieving a pressure of 1×10^{-5} torr or less for a period of four hours. The test article is placed within a semi-enclosure inside the space chamber. The test article temperature is brought up slowly and the chamber pressure monitored. The test article is heated by infrared panels or similar devices located within the enclosure. The enclosure is kept at a low temperature to trap and condense the contaminants as they are liberated.

7.6.2.3 Contamination From The Facility During Test

In addition to contamination from the spacecraft, contaminants can come from a large variety of sources within the space chamber and its associated equipment. Examples are backstreaming diffusion and mechanical pump oil, cleaning detergents, volatiles in shroud paint, wiring, organic seals.

It is probably true that most contamination comes from the test item. However, this shouldn't be used as a shield for mediocre chamber operations. Some spacecraft are clean but have devices unusually sensitive to the chamber contaminants.

Measuring low levels of high molecular weight contaminants is difficult; it is expensive in equipment and personnel. Less sophisticated measurement techniques generally show no contamination. Furthermore, if the contaminant levels were known accurately, there is very little information available on the damage a particular compound does to a particular spacecraft surface.

The fact that measurements are difficult or show negative results (with gross methods) doesn't mean that there is no problem.

The reputation of oil diffusion pumped chambers is so poor in some quarters that some customers will not use them. Large facilities have even been converted from oil diffusion to other pumping means. Most of the poor reputation is due to faulty operating techniques.

Under these conditions the responsible simulator operator will redouble his efforts to avoid contamination even though he has no effective measurements and damage data.

It is probably a good assumption that most space chambers have walls that contain contaminants that will outgas or evaporate and then migrate to the spacecraft. Most large space chambers have extensive cold shroud

systems to simulate the radiation field of space. These are excellent pumps for contaminants from the spacecraft, the room temperature pressure vessel, seals, diffusion and fore pumps, etc. Most of the test item contamination from such chambers occurs after pumpdown before the shrouds are cooled or during warmup of the shrouds. Thus, one of the most important operating rules is to minimize the time of vacuum operation with uncooled shrouds. Also, a clean gas purge as described below is very helpful during these periods.

A test chamber that has no cold shrouds requires a much higher degree of cleanliness. A high temperature vacuum bakeout prior to test is essential if the walls could have become contaminated from the previous test item, oil pumps, organic seals, etc.

A valuable accessory to the chamber cold shrouds is a contamination plate—a separate LN cooled plate that can be rapidly chilled during pumpdown and kept cold continuously through shroud warmup at the end of the test. It should be one square meter or larger for large chambers. It should be mounted so as to minimize the radiative transfer to the spacecraft, i.e., edge toward the spacecraft.

Effect of Pressure

At atmospheric pressure the migration of contaminants is minimal. There is little danger from contaminant migration until the mean free path (distance between molecular collisions) increases to 1/10 the distance from the wall to the test item. This is equivalent to 5×10^{-5} torr for a one meter distance. If the shrouds are still warm when this pressure is reached during pumpdown, relatively large quantities of gas are being outgassed, some of which will migrate and stick to the spacecraft. Thus, the cooling of the cold shrouds should be started before this pressure is reached and a purge should be used as explained below.

Chamber Purge

During pumpdown and warmup, when the cold shrouds are not completely cooled, it is desirable to maintain a clean gas purge in the chamber. The shrouds, if cooled to 100 K or below, act as very efficient pumps for vacuum condensable material. Without a purge or adequately cooled shrouds, the large variety of contaminants in most chambers are free to outgas, and reflect off the warm walls. Depending on the contaminants, concentration, and spacecraft surface temperature, there is a certain probability that these molecules will stick to the spacecraft. An even worse situation occurs during warmup. Then the evaporation from the shroud is greater because most of the contaminants generated during the test were frozen onto the shroud. They are released in the vicinity of the spacecraft as the shrouds warm up. Thus, the purge is needed during pumpdown - cooldown and for warmup, as well.

A number of factors must be considered in the design of a purge system. The technical limit on the amount of purge gas is the danger of chilling the spacecraft. Except for this, it would be desirable to start a high purge rate before the shrouds start to warm up.

It is a good procedure to turn on the purge when pumpdown is started at a rate equal to the nominal mass flow rate at the bottoming-out pressure of the first stage pumps. Normally, the diffusion pump speed is 100 to 1000 times larger than the roughing pump speed. As soon as the diffusion pumps start pumping the purge flow rate can be increased to maintain 0.5 to 1.0×10^{-3} torr. When this pressure is reached, the contamination plate should be cooled, followed by the cold shrouds.

The purge gas should be injected into the chamber on the opposite side of the chamber from the pumping ports. That is, the purge gas should surround and sweep across the test item on its way to the pumping ports. Also, the injection of gas should be through a diffuser, e.g., a porous metal. Otherwise, under some conditions of flow and low pressure, high velocities will result with possible damage to test specimen or equipment. A diffused, low velocity flow originating near the spacecraft and moving outward from the spacecraft is the ideal. As the shroud temperature drops, the purge flow should be reduced to avoid chilling the spacecraft.

Mechanical Roughing and Forepump

Mechanical pumps are frequently high contaminant sources because of their relatively high oil vapor pressures at operating temperatures. Also, the tendency of some pumps to become contaminated with water vapor accentuates the backstreaming. Even rotary lobe blowers and turbomolecular pumps are contaminant sources. (Ref. 7.2.)

Some of the precautions that should be taken are as follows:

- a. As the chamber is roughed down, close the roughing valve when the pressure drop in one minute declines to 20% of the chamber pressure. For example, if pumpdown from 50 to 40 microns requires less than a minute, but it requires a minute or more to reduce the pressure from 40 to 32 microns, close the roughing valve at 32 microns. Backstreaming rapidly increases as the bottoming-out pressure approaches.
- b. Use a purge as described above.
- c. Use effective traps in the roughing line and diffusion pump forelines. These may be high conductance sorption traps or cold traps. In either case, the design must be adequate for effective trapping from viscous flow to molecular flow conditions.

- d. Use gas ballast in the first stage mechanical pumps to avoid water contamination of the oil.

7.7 Maintenance

Maintenance of the solar simulator is a continuous function during thermal vacuum testing of the spacecraft and is included here to illustrate typical problems associated with the operation of the solar simulator. The two major problems are lamp life and optical degradation. The continuous operating life of the solar simulator is primarily limited by the life of the lamp. The average lamp will degrade approximately 29 percent over its life span. This means that the input power to the lamp will increase by 20 percent in order to maintain a constant output irradiance level. As the lamp envelope darkens it absorbs more of the UV portion of the spectrum and causes additional heating of the lamp which results in a spectral shift towards the infrared in the solar simulator spectral energy distribution performance.

In order to insure continuous reliable system performance the replacement lamps and refurbished optical reflective surfaces require rigid procurement specification and acceptance tests. A good example of this is the Joint Industry/Government Standard Drawing-Spectrolab number 015978 revision B. This drawing provides for a standard configuration that is compatible for most solar simulators using the 20/30 KW xenon compact arc lamp. Similar drawings and specifications can be established for any size lamp.

There are several causes for spectral energy distribution shifts. One cause is normal optical degradation. This is caused by the irradiance level on the mirror surface, the type of reflective surface/substrate composition, and the environment to which the mirrors are exposed. Additional degradation is caused by the high level of UV energy from the lamps which is detrimental to optics and materials.

The lamps may vary in spectral output. Darkening of the envelope will shift the spectral distribution. To overcome this degradation, the power must be increased which also shifts the spectrum.

Section 11 of Ref. 7-3 contains more suggestions for solar simulator maintenance.

REFERENCES

- 7.1 Griffith, J. S., Some Tests for Increase in Friction of Mechanisms of the Mariner Mars 1969 Spacecraft in the JPL Molsink Space Simulation Chamber, AIAA Paper 69-996, AIAA/ASTM/IES 4th Space Simulation Conference, 1969 (JPL TR 32-1446).

7.2 Langdon, W. M. and Ivanuski, V. R., Backstreaming from Oil Diffusion Pumps, IIT Research Institute Report No. IITRI-C6030-10.

7.3 Handbook of Solar Simulation for Thermal Vacuum Testing, IES, 1968.

8. SAFETY CONSIDERATIONS

8.1 Purpose

The purpose of this section is to recommend procedures which will help to assure the safety of persons (including casual observers) associated with the use, operation, and maintenance of solar simulators.

8.2 Scope

Potential hazards are discussed in terms of what they are, damage or consequences, and exposure rates and times (where applicable). The hazards have been categorized with respect to mechanical, chemical, electrical, radiation, thermal, and miscellaneous hazards, for simplicity. The preventions, protection, and care of the hazards are also discussed. Also, only those hazards and injuries which are peculiar to solar simulation are included.

8.3 General Instructions

Whenever a solar simulator, laser, or similar equipment is being operated, suitable warning signs should be clearly displayed at all entrances to the work area. A complete list of safety procedures appropriate to the facility should be clearly and prominently displayed.

There is no substitute for education. Every person who may be operating in the work area should be informed of the hazards involved, safety precautions to be taken, and supervisory or medical personnel to be contacted in case of accidents. All operational personnel should be required to observe appropriate safety measures at all times. Accidents all too often occur because someone thought he "couldn't be bothered this time." If experienced personnel do not observe rules of safety, then new employees and/or visitors will probably not do so either.

Most large industrial facilities and government installations employ medical and safety personnel. The expertise of these departments should be utilized. Local, state, or federal safety requirements differ and the safety officer or industrial hygienist is in the best position to be informed regarding these standards, which should include periodic checkups. Cooperation between operational and safety personnel should be supported and encouraged whenever possible.

8.4 Safety Consciousness

The keys to an effective safety program are awareness of the hazards—both special and ordinary—common sense, and safe working habits. A man who is aware of the hazards of a particular job (without being panicked by them) is less apt to be hurt than one who thinks "safety is for sissies" and safety procedures unimportant or designed for people who don't know as much as he does. Awareness and common sense together make for safety consciousness, the opposite of the feeling, "it can't happen to me." A few rules to help your own safety consciousness are:

1. Read the Safety Handbook, and also learn all the special hazards and necessary safety precautions related to the equipment or material you work with.
2. Become familiar both with the equipment you must use and the material or item you are working on.
3. Be alert for any unsafe conditions in your work area and correct them or bring them to the attention of your supervisors or safety representative.
4. Learn the proper exit route in case of fire or other danger.
5. Learn where first aid kits, fire extinguishers, and other safety equipment are located.
6. Use the Buddy System described as follows: The "buddy system," long established for hazardous situations in industry and elsewhere, is designed to provide immediate help in case of accident and, in most cases, will help to avoid serious accidents. Its prime purpose is to insure that no man works alone on a dangerous job; there is always a "buddy" to help in case of danger or accident.

8.5 First Aid

A knowledge of first aid on the part of as many persons as possible is an essential part of any safety program. All personnel involved in potentially hazardous operations should be acquainted with the basic principles of first aid; indeed it would be desirable for all personnel to have such knowledge. In addition, it is essential that certain key personnel in each operation have a thorough grounding in first aid techniques, particularly those related to the special hazards of their own jobs. Appropriate first aid texts are referenced in Section 8.7.

8.6 Discussion of Hazards

8.6.1 Mechanical Hazards

8.6.1.1 Description of Mechanical Hazards

Mechanical hazards involve those hazards which could produce physical injury to personnel or equipment.

8.6.1.2 Types of Mechanical Hazards

Mechanical hazards can be caused by exploding high pressure lamps, implosion of vacuum windows, falls, ruptures or high pressure systems, structural hazards, lifting and handling, rotating machinery, etc.

8.6.1.2.1 Exploding High Pressure Lamps

A compact arc lamp, when in use, is at a high internal pressure. The 20 & 30 KW lamps carry approximately 3 atm cold and 10 to 15 atm when hot. Pressures in small lamps are considerably higher. The lamp is subject to failure at any time and the damage to both equipment and personnel can be extreme. Proper shielding and safety precautions must be considered to protect personnel when observing and handling these high pressure lamps. Recent tests indicate that the smaller lamps (up to 5 KW) are in many cases more dangerous than larger lamps (20 KW to 30 KW). If depressurization of lamps (see Section 8.7.5) is not possible, they must be kept in their protective covers until the last possible moment. Safety glasses are an absolute must whenever lamps are being handled. The presence of a safety cover around a lamp should not build one into a sense of over-confidence. PROTECTIVE CLOTHING, SUITABLE FOR HANDLING THESE LAMPS, IS A MUST.

8.6.1.2.2 Implosion of Vacuum Windows

Due to excessive expansion (from heating of vacuum window by the solar beam), improper cushioning, impact, etc., glass view windows, solar entrance ports or bell jars might implode. Any vacuum implosion can impart considerable velocity to pieces of material involved. These may receive sufficient energy to pass through the center of the implosion and continue out the other side as an outward bound projectile. Such projectiles can pass through glass windows and injure anyone nearby. Adequate provision for window expansion and keeping window surfaces clean of contaminants will minimize the hazards. Screens or shields around all glass ports are a must to protect observers and operators from injury.

8.6.2 Chemical Hazards

8.6.2.1 Description of Chemical Hazards

A chemical hazard is any hazard which has the capacity to produce personal injury or illness through indigestion, inhalation or absorption through any body surface. Many of the chemicals, solvents and metals used in solar simulation testing have known toxic properties and standard handbooks on toxic materials can be contacted for easy reference. Accidents involving toxic materials are often of the kind that can leave the victim blinded or disfigured for life.

8.6.2.2 Type of Chemical Hazards

Toxic materials associated with Solar-Vacuum Simulation testing are ozone, mercury, cadmium, and carbon arc fumes. Nontoxic, but suffocating gases, include nitrogen. Gases heavier than air will accumulate near the floor and low areas, while gases lighter than air, such as N_2 will accumulate near the ceiling or elevated areas. Areas where gases accumulate should be recognized as hazardous and the proper ventilation provided.

8.6.2.2.1 Ozone

Ozone is produced by exposing oxygen in the air to ultraviolet light. It is a strongly oxidizing gas which attacks metal and rubber rapidly. The effects of ozone on man are mainly on the respiration system. Air concentrations of ozone in excess of a few tenths of a part per million (ppm) cause discomfort to exposed individuals in the form of a headache, dryness of throat and mucous membranes of nose and eyes, following exposure of short duration. The industrial limit for an 8-hour exposure is set at 0.1 ppm.

Ozone is detectable by smell; however, it is a subtle hazard in that personnel working in an area where ozone is being introduced have a tendency to miss early detection of the gas. Personnel entering an ozone contaminated area from a different environment with a "fresh nose" have much greater sensitivity and can smell the health hazard.

If personnel smell ozone or think they do, contact the safety officer and leave the area. The safety officer should measure the ozone concentration in the area and determine if a hazard exists.

8.6.2.2.2 Mercury

Many types of high pressure short arc lamps utilize mercury in combination with other gases. If the mercury enters the laboratory environment through lamp explosions or other means a definite safety hazard

exists. Suitable mercury detectors should be installed in locations where the possibility of mercury contamination exists. Although a metal, mercury evaporates at ordinary room temperature, and its volatility is rapidly augmented by relatively small temperature increases. An exploding Hg lamp is particularly bad because the entire content is released as vapor and so a considerable quantity may be inhaled in one or two breaths by someone nearby. If a lamp explosion spillage should occur, the area involved should be sprinkled generously with sulfur powder. Allow the sulfur to remain for at least one hour so that it can react with the mercury. Then scrape the contaminated sulfur and dispose of it in a sealed container. Good "housekeeping" practices are very important in the control of mercury both in the simulator and the adjoining areas. While liquid mercury can be absorbed through the skin, its effect on the body is unclear. Therefore, skin contact should be avoided whenever possible and protective clothing should be worn. Symptoms of mercury poisoning are not immediately detectable and may not show up until much later in life. Some symptoms are chronic nervousness, restlessness, and shaky handwriting. Acute symptoms can be bloody discharges, abdominal pains, and worse.

8.6.2.2.3 Cadmium

Cadmium is used as a protective plating on iron and steel articles, as an ingredient in many solders, and frequently as a pigment in yellow, orange, and red paints. Welding, soldering, or any high temperature heating of cadmium or cadmium-plated parts can produce toxic fumes.

8.6.2.2.4 Toxic Fumes

Toxic fumes are produced in the burning of carbon arcs. Adequate ventilation in the form of a hood or open system exhausting to the outside of the building must be provided.

8.6.2.2.5 Nitrogen

Nitrogen is commonly used to purge simulators of oxygen to minimize the production of ozone and to backfill chambers to minimize condensation of moisture on cold surfaces. The hazard connected with GN_2 is that pure nitrogen will cause rapid anoxia. Complete deprivation of oxygen for 5 minutes can cause death. Anoxia usually sneaks up on a person and he is not aware of anything wrong until he is on the verge of collapse. Thus, it is extremely important to prevent conditions from existing where anoxia may occur. Adequate ventilation should precede entering simulators or facilities where N_2 is used. Oxygen concentration monitors must be employed when backfilling large chambers with GN_2 to ensure that a safe level of oxygen ($>18\%$) exists before personnel enter the facility.

8.6.3 Electrical Hazards

8.6.3.1 Description of Electrical Hazards

Solar Simulators require large amounts of electrical power and use this power in many diverse circuits. The circuits range from high voltage incoming supply lines rated at many kilowatts, to control circuits operating at small fractions of a watt but still using dangerous voltages.

8.6.3.2 Types of Electrical Hazards

There are several types of electrical hazards which should be considered. These include dangers from high voltage, high current, improper insulation, grounding, etc. A good healthy respect for these hazards will both improve the operation of the system as well as protect the personnel. Before installing a new system or modifying an existing one, the local, state, and federal codes should be studied to insure operation and maintenance of a safety system. Several of the more important hazards are listed below.

8.6.3.2.1 High Voltage

Voltages of 75 kilovolts or more are used to ignite the various types of short arc lamps used in solar simulators. This voltage is produced by step-up transformers and can be lethal if not handled properly. Lead lengths should be kept as short as possible and personnel should not touch and must be well clear of any part of the circuit during ignition.

8.6.3.2.2 Open Circuit Voltages

Voltages in the ranges of 75-400 volts are available as open circuit power supply voltages prior to the ignition of the lamps or carbon arcs. These voltages can again be lethal if they interact with the body. Heavy insulation should be used on all power supply leads and no terminals should be left exposed. Maintenance personnel should be aware that these power supplies use large capacitors which can retain large charges long after the power has been turned off. These capacitors should always be discharged before any maintenance is attempted.

8.6.3.2.3 High Current

The high powered lamps used for solar simulation require from fifty to several hundred amperes. It is important, therefore, that adequately-size cables be used to transmit this high current. With this much current, even small contact resistances can result in the formation of considerable heat. Good ventilation is important, particularly where cables must be run through small crevices. Alignment tools must be electrically insulated.

8.6.4 Radiation

8.6.4.1 Discussion of Radiation Hazards

One of the most serious hazards associated with the operation of short arc lamps and carbon arcs such as those used in solar simulators, is the intense optical radiation which they emit. This radiation has wavelengths which range from $0.2\text{ }\mu\text{m}$ in the ultraviolet to about $2.5\text{ }\mu\text{m}$ in the infrared. The most physiologically damaging wavelengths, however, lie in ultraviolet and visible regions. Several types of potential hazards are discussed in the following paragraphs and suggestions are made for preventing or minimizing the danger to personnel.

8.6.4.2 Types of Radiation Hazards

8.6.4.2.1 Erythema

Erythema is a condition which closely resembles sunburn and affects exposed skin surfaces. This condition can be caused by exposure to ultraviolet energy emitted from almost every type of light source used in solar simulation. It is a particularly important problem when working with mercury, mercury-xenon, xenon, and carbon arc sources. The wavelengths which do the most damage lie below approximately $0.32\text{ }\mu\text{m}$. Like sunburn, erythema is not immediately detected by the victim, but it appears a matter of hours later.

The table below indicates the relative effectiveness as referenced to $\lambda = 0.297\text{ }\mu\text{m}$ of various wavelengths in producing erythema:

<u>Wavelength - μm</u>	<u>Relative Effectiveness</u>
0.240	0.95
0.250	0.90
0.260	0.65
0.270	0.15
0.280	0.05
0.290	0.30
0.297	1.00
0.300	0.96
0.310	0.10

Depending on the irradiance associated with the lamp which is being used, an exposure of only a few minutes is sufficient to produce a very painful and possibly severe case of erythema.

Fortunately, the prevention of this hazard is relatively simple. Erythema cannot occur if the skin is not exposed. Therefore, this hazard can be avoided by covering all skin areas with a heavy cloth material. When this cannot be done, a good commercial suntan preparation or an industrial skin creme shall be applied to all exposed skin surfaces. This includes face, neck, hands, etc. These precautions apply both to operational personnel and visitors.

8.6.4.2.2 Conjunctivitis

Conjunctivitis is an inflammation of the mucous membranes which cover the eye. This condition is caused by exposure of the eye to ultraviolet energy with wavelengths below $0.320\mu\text{m}$. These wavelengths correspond roughly to those wavelengths mentioned for erythema. However, the effectiveness of the various wavelengths is somewhat different. This danger is, again, not easily detected at the time of exposure. After a few hours, the victim experiences a feeling likened to having hot sand under the eyelids. This sensation can be extremely painful and last for many hours or days. If the condition does not disappear within a few hours, a qualified physician should be consulted.

In order to eliminate or at least minimize this danger, all personnel who may have an opportunity to view either the direct or reflected (stray) radiation from high intensity arc lamps should be required to wear dark sunglasses or goggles. The sunglasses or goggles should preferably be made of glass and should provide dark side shields to prevent light from entering the side of the eye. These precautions should be observed by operational and visiting or occasional personnel.

8.6.4.2.3 Retinal Burns

A third type of hazard involves the possibility of severe burns to the retinas of the eyes. The damage caused by such burns are particularly dangerous and may be irreversible. The eye is an excellent optical imaging system and good vision depends upon the ability of the eye to image energy on the retina. Images so produced are transduced into heat by absorption in the pigment structure of the retina and the pigmented choroid which lies immediately behind the retina.

If sufficient heat is produced, a burn may result. Unfortunately, such burns often occur in the area of the fovea centrales which is responsible for acute central vision. In such cases, the victim may experience a severe loss of visual acuity which may seriously impair his ability to read or perform other tasks requiring high visual resolution.

The threshold exposure required to produce such burns is a function of several factors, including length of exposure, radiance, and size of the light source, irradiance at the eye, transmission of the various ocular components of the eye, retinal image area, etc. For this reason, there is no widespread agreement as to what should constitute a threshold exposure value. However, it should be noted that permanent retinal damage has been caused by viewing solar eclipses, atomic fireballs, laser beams, and arc lamps. Because of this potential danger, special and conscious care should be taken by ALL personnel to avoid viewing the arc of any discharge or arc lamp. Dark glasses or goggles should be worn by ALL personnel when exposed to the radiation of any of these lamps. If anyone does accidentally view the arc and the after image lasts for more than a few minutes, he should consult a physician.

8.6.4.2.4 Lasers

Many laboratories have adopted the practice of using small gas continuous wave (cw) lasers for aligning optical systems including solar simulators. The total output power of these lasers is generally one milliwatt or less. The laser is a particularly useful tool for optical alignment because of its excellent collimation and high intensity. These advantages may also be disadvantageous in terms of personnel safety. The problems involved are much the same as those outlined above for retinal burns. The energy from a laser is concentrated into a very narrow beam with relatively high energy density, easily capable of damaging the delicate eye components. This is true for direct as well as reflected laser radiation.

Special goggles are available for some lasers which reject most of the energy at certain laser wavelengths. These goggles transmit well in other regions of the visible spectrum so that operating personnel will not be hampered by the dark goggles which would otherwise be required. If these special goggles are not available, then operational and visiting personnel should wear dark goggles with at least a No. 7 shade. All personnel should avoid viewing the beam directly. If anyone does accidentally view the beam directly, and the after images linger for more than a few minutes, a competent physician should be consulted.

8.6.5 Thermal

8.6.5.1 Description of Thermal Hazards

While the fire hazard for solar simulators is not high, the complex electrical apparatus and high solar energies do present fire and personnel burn problems. The high currents required to operate the light sources can produce excessively high temperatures if high contact resistances are encountered. Lenses or reflective surfaces which absorb

an excessive amount of energy will also become extremely hot. Excessively cold temperatures also pose a hazard when using cryogenic fluids.

8.6.5.2 Type of Thermal Hazards

The types of thermal hazards encountered could be fire due to faulty power supply or excessive contact resistance, personnel burns due to handling hot components (including the light source), and the implosion of ports due to increased absorption of the "solar entrance" window. The use of LN_2 to make GN_2 or to produce a "simulated space environment" is also a potential hazard.

8.6.5.2.1 Excessive Heating of Vacuum Windows

Due to excessive expansion or a change in physical properties, a number of solar simulator windows have recently imploded. Adequate provision for window expansion and keeping window surfaces clean of contaminants will minimize these hazards. Screens or shields around ALL glass ports is a must to protect observers and operators from injury.

8.6.5.2.2 Liquid Nitrogen

Liquid nitrogen (LN_2) is also commonly used near solar simulator systems both as a cooling medium for simulator components and as the thermal fluid for simulating the temperature conditions of extraterrestrial space. The principal hazard of LN_2 is its extremely low temperature (77°K) (-320°F); however, it also can cause explosions if contained and allowed to warm up in a closed volume. The low temperature of LN_2 will cause burns (frost bite) when it comes in contact with the skin. Therefore, body, head, and face protection must be worn. Insulated gloves (asbestos or heavy leather) should be worn but these must be loose fitting to enable quick removal should LN_2 get down inside the glove. Clothing should be of such a nature as to prevent LN_2 from collecting anywhere on it (e.g., cuffless trousers). Personnel working with LN_2 must be made thoroughly familiar with its properties and proper handling techniques.

8.6.6 Miscellaneous Hazards

8.6.6.1 Discarding of High Pressure Lamps

Before discarding high pressure lamps, the pressure should be relieved by drilling the lamp near the neck using a special lamp holding fixture. This fixture will protect the operator in case of lamp explosion. Lamps containing mercury must never be deposited in trash containers but should be returned to the manufacturer or disposed of by the plant

safety officer. Before drilling the lamps, condense the Xenon by placing the bulb in contact with LN_2 (a plastic or styrofoam dish will do).

8.6.6.2 Emergency Lighting

Emergency lighting should be available in cases of power failure to allow personnel to evacuate the area. In large vacuum chambers, especially, this could pose a problem.

8.6.6.3 Emergency Alarms

Power disrupt switches and alarms should be placed in strategic locations within and without facilities to allow persons to stop an operation if it is detrimental to personnel working in the area and to hear emergency signals. Vacuum disrupt switches inside large facilities are a necessity.

8.7 References

- 8.7.1 Trainor, D. C., "A Handbook of Industrial Toxicology," Angus and Robertson, Sydney (1966).
- 8.7.2 Stolinger, H. E., "A Review of Research and Industrial Experience, 1954-1964," Arch. Environ. Health (Vol. 10, May, 1965.)
- 8.7.3 Sax, I., "Dangerous Properties of Industrial Materials," Reinhold Publishing Corp., New York (1961).
- 8.7.4 Brobeck, Wm., "Particle Accelerator Safety Manual," U.S. Department of Health, Education, and Welfare (1968).
- 8.7.5 Argoud, M. J., "Safety Equipment for Handling the 20 KW and 5 KW Arc Lamps," JPL TM 33-429 (1969).
- 8.7.6 Griffith, J. S., et al., "Handbook of Solar Simulation for Thermal Vacuum Testing," IES (1968).
- 8.7.7 American Red Cross, "First Aid Textbook," Doubleday & Company, Inc., 4th Edition, December (1969).

Page intentionally left blank

MECHANISMS FOR THE ADHESION OF SILVER TO GLOW DISCHARGE SENSITIZED PERFLUORINATED ETHYLENE PROPYLENE (FEP)

John B. Schutt, William H. Gilchrist, Robert N. Sheehy, and Frank N. Paczkowski, *NASA, Goddard Space Flight Center*

ABSTRACT

Details are given for the deposition of silver onto FEP for a batch coater capable of handling 864 square inches at a time. Process variables are not presented for other vacuum coat-ers because they must be worked out on an individual basis. The effectiveness of the glow discharge is shown to be optimum when the FEP faces the anode. Using solid state theory based upon the work function difference, and the heuristic assumption that the surface of FEP is populated with fluoride ions, it is argued that an anode sensitized surface develops states receptive to electron transfer from silver, whereas a cathode sensitized surface is polarized only, and as a result cannot permanently trap charge. Thermodynamic arguments given show that an order of magnitude of 10^9 electrons are transferred into states to a depth of 10 nm.

INTRODUCTION

The laboratory investigation of the radiation stability of polyimide films and perfluorinated ethylene propylene (hereafter referred to as FEP) under predicted perihelion conditions for HELIOS disqualifies polyimide as a primary thermal control surface and demonstrates that FEP may perform creditably for a quiet "Helios". In order to give perspective to the above comments, we relate the context from which they were derived: Each material is tested beginning from the virgin state under simulated dynamic conditions by exposing to the photon and particulate environments at sample temperatures corresponding to the terminal or disqualification solar absorptances. The approximation inherent to this type of testing resides in the assumption that the slope of the change of solar absorptance with time, from the initial value at elevated temperatures, is a close approximation to the slope at the terminal value. In this viewpoint there somehow resides a hope that data may be scaled, particularly in time, such that the initial time scale is maintained: Physically speaking we may say that the processes leading to perihelion degradation are the same for all times both mechanically and cooperatively. So be it with polymeric films.

Turning our attention to the silver-FEP composite, we immediately recognize that environmental stability can be influenced by the interface, and the junction potential arising between the silver and FEP. Accordingly,

for peace of mind, it would be desirable to be able to neglect the contributions of ultraviolet photons, proton, and electron induced junction polarization currents upon dynamic increases in solar absorptances. For freedom from a concern of this nature, the application of a metal with a work function as close to the work function of FEP as that of silver requires considerable finesse, otherwise spurious quantum states will be introduced, and verified after environmental testing as the accelerated increases in solar absorptance. The interposing of FEP into the conventional glow discharge and its accompanying electrical environment, to perform a more complex function than "plasma cleaning", determines a process characteristic of coater and one which must be carried out conformally from application to application.

In an effort to recapitulate remarks recorded above, and to justify in some measure usage of the conveying words "finesse", and "conformally", a discussion utilizing the concept of entropy is offered.

Interposing FEP in the conventional gas discharge for plasma cleaning only must be characterized by

$$\Delta S_{0,c} = 0,$$

where S as usual is the symbol for entropy and the subscripts reading left to right reference initial and cleaned conditions. Experience has demonstrated that the adhesion of silver to FEP under these conditions is a short lived interaction. Well demonstrated, too, is the satisfactory adhesion of silver to FEP treated by a sodium base. Equally well demonstrated is the occurrence of ultraviolet solarization of silverized FEP prepared by this process. The effect of the sodium on surface reduction treatment is therefore such that

$$\Delta S_{0,R} > 0,$$

where R symbolizes the entropy after treatment by this process. In other words, quantum states have been introduced whose energies, $\{\epsilon_{iR}\}$ (i referring to a state and $\{\}$ the set of states) obey

$$(\text{Boltzmann's constant} \times T) = kT \ll \{\epsilon_i\} \leq h\nu_{\max} = hc/\lambda_{\min}$$

with T indicated at the test temperature and ν_{\max} at the maximum ultraviolet frequency or minimum ultraviolet wavelength (c is the velocity of light in vacuo). With finesse, therefore, we obtain the adhesion of silver to FEP where

$$\Delta S_{0,Ag}^I > 0 \quad (\text{sensitizing process}) \quad (1)$$

but

$$\Delta S_{0,Ag}^{II} < 0 \quad (\text{deposition process}) \quad (2)$$

such that

$$\Delta S_{0, Ag} = \Delta S_{0, Ag}^I + \Delta S_{0, Ag}^{II} \approx +0 \quad (3)$$

with

$$|\Delta S_{0, Ag}^I| \sim |\Delta S_{0, Ag}^{II}| \sim 0(kT). \quad (4)$$

That is to say, the entropy changes as developed in the environment provided by the glow discharge and metallizing processes must be carried out reversibly, giving a net zero entropy change for the processes, when considered in relationship to the sensitivity of conventional optical measurement techniques.

$\Delta S_{0, Ag}^I$ will then have a finite relaxation time. It is in this spirit that the term "finesse" was judged appropriate. It follows now that "conformally" refers to the repeatability or the confidence limits within which the constraint (4) can be held to from application to application.

In the following section a detailed description of the mechanics of silver deposition onto FEP is given as worked out by two of us (W. H. G., R. N. S.) along with a presentation of potential, electric field and charge distributions extended to include the case with forward biasing. A section is then included encompassing some solid state theory for adhesion mechanisms. An extension of the thermodynamic concepts initiated in this section is also included. In closing, a summary of the concepts and ideas is presented as an aid to other facilities involved in producing silvered FEP.

Procedure for the Noncontinuous Application of Silver to FEP

As is mentioned in the previous section, the preparation of the surface of FEP for the reception of silver is a process requiring optimization with respect to the variables of glow discharge treatment and deposition processes for a given coater. The particular coater receiving attention in this paper can accept for treating and coating plastic sheets dimensioned to 24 inches by 36 inches. Figure 1 shows schematically the electrode circuitry and placement, dielectric and ground under actual operating conditions. Discharge treatment and silver deposition are carried out in practice with the anodes and silver containing boat positioned at the bottom of the chamber. Optimization of environmental stability versus adhesion occurs when a glow charge applied to the surface of the FEP — initially at room temperature — biases it during treatment slightly above ground. During application of the electric field, the pressure is held in the neighborhood of 20 microns, while the field is maintained at the FEP-ambient interface for a duration of 60 seconds. Under these conditions, the applied field results from a potential difference of 4000 volts between anode and cathode separated by a distance of four feet. Upon completion of the treatment by the electric field, the surrounding pressure is lowered to 5×10^{-6} microns. Immediately thereafter, the silver film is deposited to a thickness of about 1000 Å in about one (1) minute. The deposition of silver must be carried out in haste, once field treatment has been completed, otherwise the particulate forces governing the adhesive bond will relax between the treatment and deposition phases

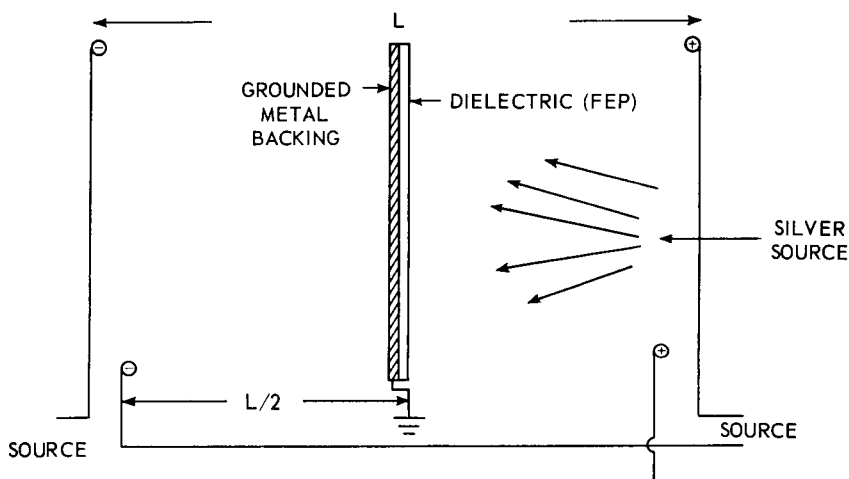


Figure 1. Schematic Representation of Relative Position of Electrodes and Supported Plastic Film in Coater

of the process to produce a bond subject to failure upon aging or upon thermal stressing.

The remainder of this section is concerned with pictorial representations for potential, field and charge distributions according to the relationships between components given in Figure 1, but employing plane parallel electrodes instead of the system of rods shown in the schematic. This tact is followed in anticipation of the following section on solid state mechanisms.

Below in Figure 2, a conventional drawing representing the glow discharge phenomenon is reproduced for reference.⁽¹⁾ The drawing is self-explanatory and complete in its terminology. It should be pointed out, however, that the glow discharge in the conventional coater may or may not contain a positive column. Its presence is not relevant for the purpose of surface sensitizing FEP, but rather is necessary for cleaning in a zero field by positive and negative ion bombardment.

Because the side of the dielectric facing the anode is maintained at zero or ground potential (by virtue of its being mounted to a grounded metal support), the exposed surface of the FEP film facing the anode must be at a potential (cf. Figure 3(a)) above ground, thereby keeping it in the Faraday dark space (cf. Figure 1), and hence in an electric field (cf. Figure 3(b)). Bearing this in mind, the ambient charge distribution bathing the surface is positive (Figure 3(c)) and not neutral. Polarization in the field compensates by creating a negative surface when the negative cloud surrounding the fluoride ion drifts towards the anode with the counter movement of positive carbon ions in the direction of the

(1) Llewellyn-Jones, "The Glow Discharge and an Introduction to Plasma Physics", Methuen and Co, London (1966).

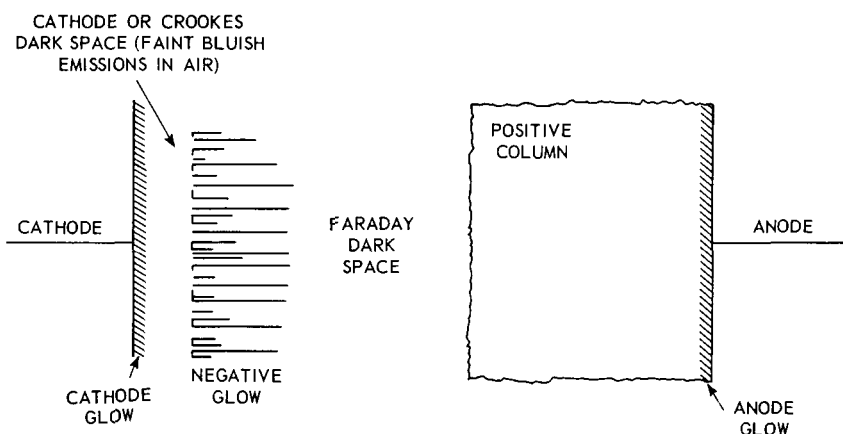


Figure 2. Conventional Representation of Glow Discharge Between Plane Parallel Electrodes

cathode. The net effect of the field on the FEP is to electrostrict the surface in the positive sense without causing dielectric breakdown.

For completeness, consider the case where the dielectric is positioned to face the cathode (cf. Figure 4). All remarks just given may then be read in the opposite sense. The surface is now under negative electrostriction or compression with the drift of electrons inward. Mechanically speaking therefore, experience teaches that to adhere silver to FEP, the surface of the film is most receptive to bond formation whenever it is under tension, assuming of course that the chemical composition and natural band structure have not been altered appreciably. Under these conditions, changes in internal energy are 0 (kT) implying that $\Delta S \cong 0(kT)$. We conclude from this reasoning that the tension will relax in a finite time, provided the deposition of silver is not allowed to interrupt the relaxation process.

Solid State Mechanism

Having ended the last section with the observation that the adhesion of silver to FEP may be attained by simply establishing states derived from tension or compression across the surface layer(s) of FEP prior to deposition, we are now at liberty to inquire into the function of pre-stressing in bond formation.

First, however, we present a heuristic argument to establish the polarity of the surface of FEP, otherwise undue ambiguity will arise in relating, for example, the direction of flow of negative charge with respect to the surface with regard to its expansion or compression. The unrelenting hydrophobic nature of FEP implies a high degree of charge compensation with negative ions comprising the surface population. If this were not the case, carbon ions in valence states of plus two and three would exist in the surface for compensation by the fluoride ions, necessitating an outward drift of negative charge into unoccupied carbon states. Empty states in the surface are active and may ionize water as

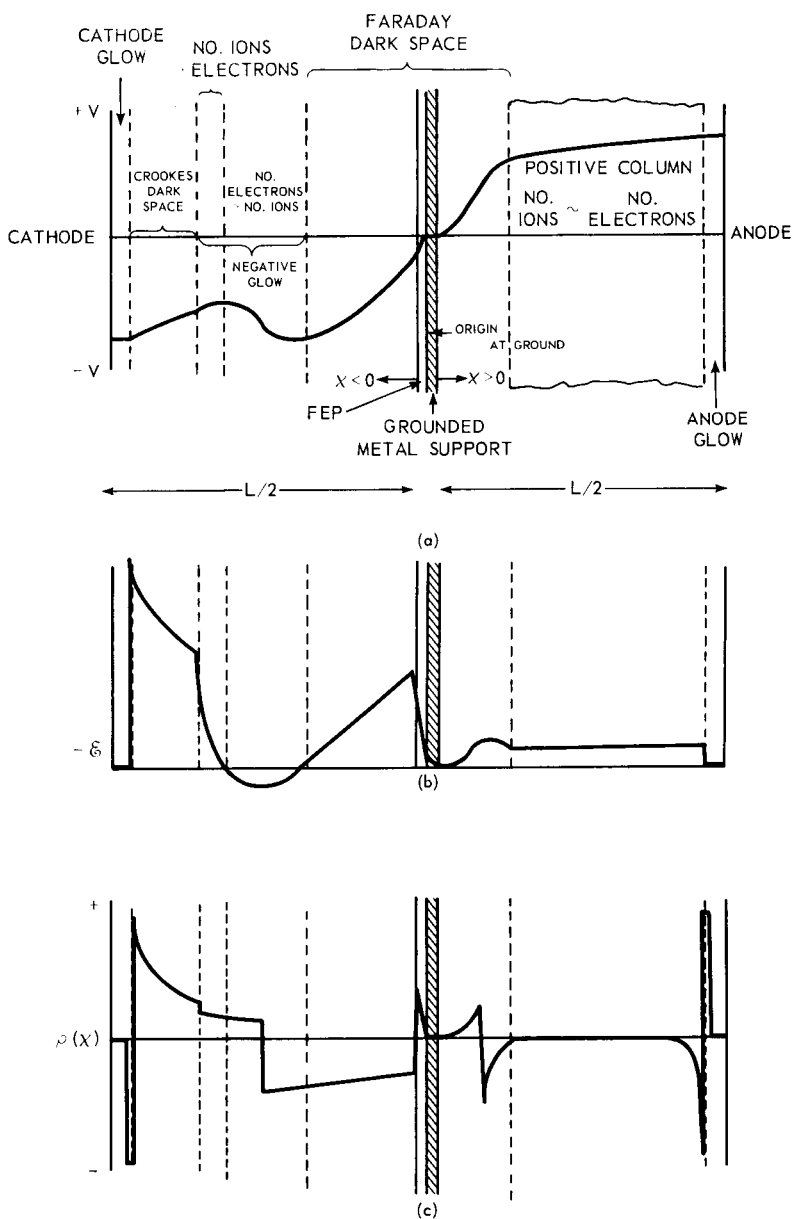


Figure 3. (a) Schematic of Potential Distribution with Forward Biased Junction According to Figures 1 and 2, (b) and (c) Are Successive Differentiations After (a) for the Field (E) and Charge Distributions (ρ), Respectively.

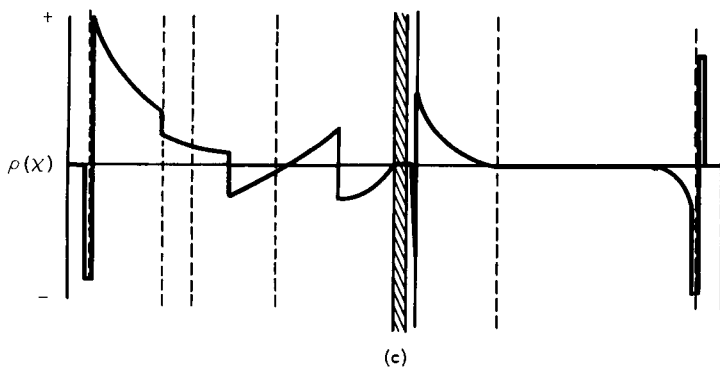
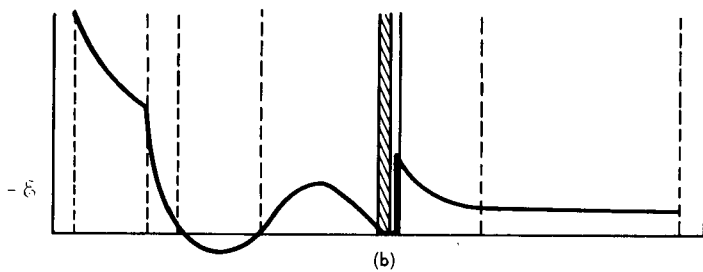
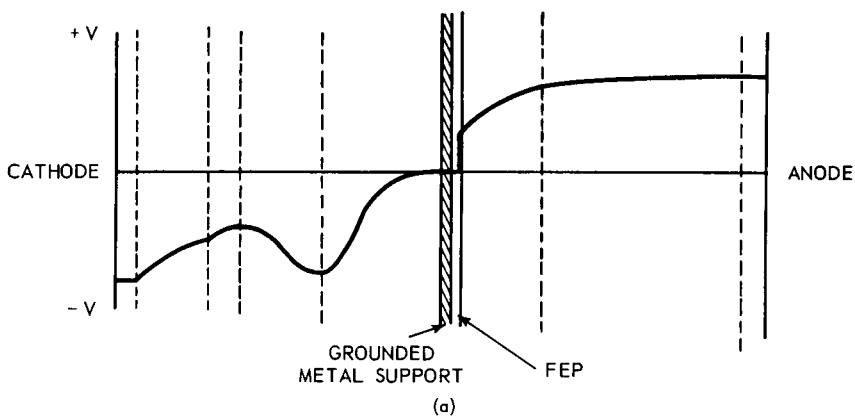


Figure 4. Schematic of Potential Distribution with Reverse Biased Junction: (a) Potential Distribution, (b) Field Distribution (E), (c) Charge Distribution

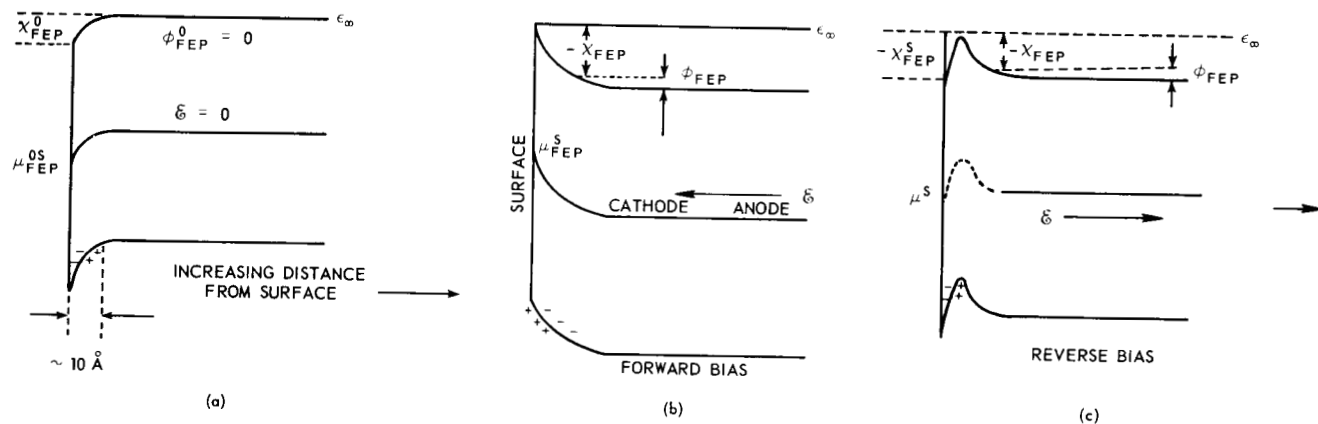
do silicon and aluminum. On the other hand, fluoride ions positioned in the surface with a neon electronic configuration, do not possess surface states low enough in energy to permit chemical reactions with the ambient environment. Charge compensation, therefore, occurs by the inward drift of electrons. Our reference surface must, consequently, be slightly negative. Facing the anode as in Figure 1, the surface of FEP is under tension and is under a reverse bias with respect to the application of silver. The situation discussed first, however, is the case with forward bias because it is conceptually more straightforward.

From a thermodynamic viewpoint bonding takes place because the Fermi energies (electronic chemical potentials) for FEP and silver can be made to equilibrate somehow at the interface, once the activation energy for charge introduction into the surface of FEP has been overcome by the field of the glow discharge. This drift of electrons from silver to FEP occurs before the curvature in the surface potential reassumes its initial value.

Figure 5 gives a band scheme for charge distributions in the first couple of atomic layers comprising the surface. The surface (Figure 5 (a)) is unperturbed and represented by nearly vertically juxtaposed positive and negative charge to emphasize the highly charge compensated positioning of fluoride and carbon ions. This surface arrangement gives rise to a surface potential $-\chi_{\text{FEP}}^0$ relative to infinity. The application of a positive field (forward bias) creates an internal potential, ϕ_{FEP} , (cf. Figure 5(b)), the magnitude of which is critical for lowering the work function of FEP sufficiently to permit the formation of a junction or adhesive bond with silver. An estimate of the bond strength (not bond lifetime) can be gotten from the work function difference between the two materials. In the case of silver, the value 4.7 e.v.⁽²⁾ is used here, but for FEP, a simple heuristic calculation is offered. From transmission measurements the Fermi energy for intrinsic FEP can be estimated to be about 3 e.v. For χ_{FEP} we use the electron affinity for fluoride which is about 3 e.v. to give a work function of 6 e.v. Subtracting these values the result is 1.3 e.v.: this number is then a lower bound for ϕ_{FEP} . The resultant polarization stabilized silver-FEP bond is shown in Figure 6.

Under the reverse bias condition, electrons are made to polarize in a direction opposite to that predicted by work functions. In this case, therefore, the surface goes under tension when facing the anode. This means that fluoride and carbon ions flow in opposite directions giving rise to possible decoupling of electronic states donated to the FEP network by these ions. What results is, of course, interband states splitting from both conduction and valence bands separated by some sort of resonance energy, which in this case must be much greater than kT . The peaking or accentuated curvature of these bands is given in Figure 5(c), and the actual splitting is shown in Figure 7. The importance of grounding the rear surface is now transparent: it assures surface state formation only and prevents narrow band formation throughout the bulk of the material.

(2)Burford, W. B., Verner, H. G., "Semiconductor Junctions and Devices", McGraw-Hill, New York (1965), p. 260.



ϵ_{∞} = REFERENCE ENERGY OF SURFACE RELATIVE TO INFINITY
 χ^0 = SURFACE POTENTIAL, INTRINSIC, $-\chi$ = SURFACE POTENTIAL INDUCED
 ϕ = INNER POTENTIAL INDUCED BY FORWARD BIASING

Figure 5. Surface Charge Distributions (a) Intrinsic, (b) Under Forward Biasing, (c) Under Reverse Biasing

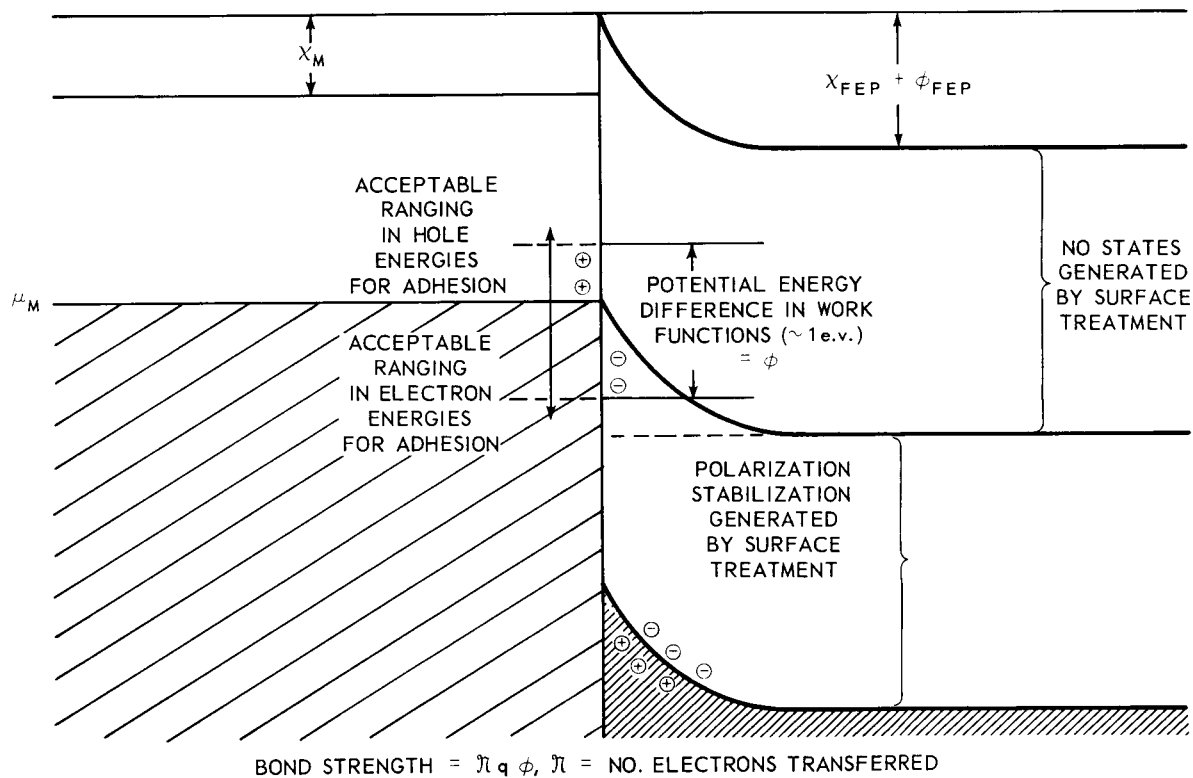


Figure 6. Band Representation of Ideal Silver-FEP Junction Formed Under Forward Bias and Polarization Stabilized

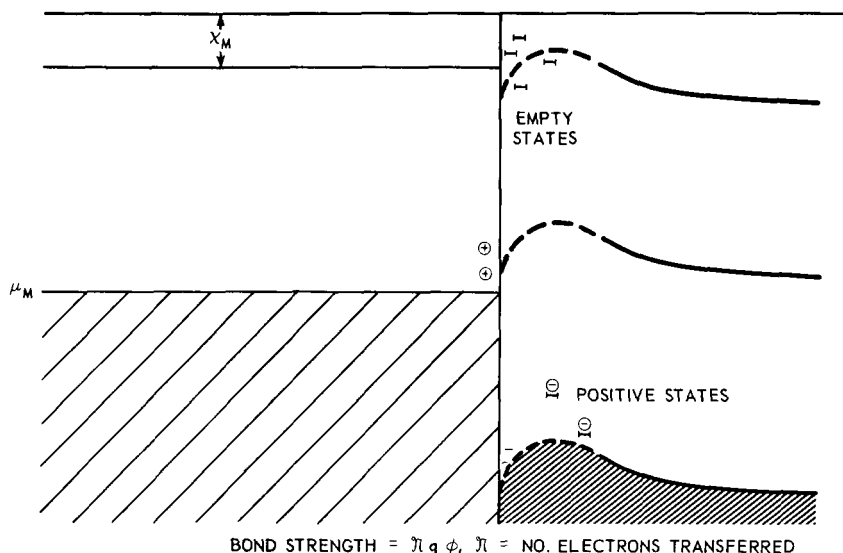


Figure 7. Band Representation of Silver-FEP Junction Formed Under Reverse Biasing Showing Permanent Bond Resulting From Created States

In the interest of conciseness we shall now address ourselves to a summary of the above remarks based on some simple thermodynamic relationships. Beginning with the per particle energy balance required for any system of charges in equilibrium, that is,

$$\mu_M^S = \mu_{FEP}^S,$$

where μ is a chemical potential (the subscript M refers to a metal), we can write the chemical potential at the surface of FEP immediately after treatment by the glow discharge (cf. Figure 5(a), (b) in the form

$$\begin{aligned} \mu_{FEP}^S &= \mu_{FEP}^0 - q \phi_{FEP} \\ &= \mu_{FEP}^0 - q(\phi_{FEP}^0 + \chi_{FEP} + \Delta V). \end{aligned}$$

In Figure 5(a) $\phi_{FEP}^0 = 0$, that is the inner potential was assumed to be zero and if

$$\mu_{FEP}^{0S} = \phi_{FEP}^0 - q \chi_{FEP}$$

then

$$\mu_{FEP}^S = \mu_{FEP}^{0S} - q \Delta V,$$

but

$$\begin{aligned}\mu_M^S &= \mu_{FEP}^S \\ &= \mu_{FEP}^{0S} - q \Delta V\end{aligned}$$

or

$$\mu_M^S - \mu_{FEP}^{0S} = -q \Delta V,$$

that is, the surface energy of a charge in the surface of FEP is just increased by an amount $-q\Delta V$ where ΔV is the potential of this surface above or below ground depending upon the direction of bias resulting from the surface sensitization technique. The free energy change occurring in formation of the junction is

$$\mathcal{N}(\mu_M^S - \mu_{FEP}^{0S}) = -\mathcal{N} q \Delta V = \Delta G$$

with \mathcal{N} representing the equilibrium number of electrons removed from the metal and trapped in the potential ΔV .

But

$$\Delta G = -T \Delta S + v \Delta P - \iint \mathcal{D} d \mathcal{E} d v,$$

by our hypothesis for stability $\Delta S \sim 0$, and $\Delta P \sim 0$, so that

$$\Delta G = - \iint \mathcal{D} \mathcal{E} d v = -\mathcal{N} q \Delta V$$

with \mathcal{D} and v representing the Maxwell's displacement current and v volume. Write

$$v = v_0 + \left(\frac{d v}{d \mathcal{E}} \right) \Delta \mathcal{E} = v_0 + \kappa \Delta \mathcal{E}$$

with $\kappa < 0$ according to Figure 5(b), (c). Substituting for dv and letting $\mathcal{D} = \epsilon \mathcal{E}$ (ϵ is the static dielectric constant) and integrating

$$\mathcal{N} q \Delta V = - \frac{v_0}{2} \epsilon \mathcal{E}^2 - \frac{\epsilon \kappa}{6} \mathcal{E}^3$$

for the forward bias case and

$$\mathcal{N} q \Delta V = - \frac{v_0}{2} \epsilon \mathcal{E}^2 + \frac{\epsilon \kappa}{6} \mathcal{E}^3$$

when a reverse bias is applied.

In other words, the direction of the field resulting from the glow discharge effects the state of stress at the vacuum interface of FEP. Therefore, $\hbar q \Delta V$ must represent the bond strength between the two materials. Pull-tests have been made for 2 and 5 mil FEP giving magnitudes of 2-3 psi.⁽³⁾ Using 3 psi for the bond strength and equating to $\hbar q \Delta V$ with $q \Delta V$ equal to about 1 e.v., a simple calculation for a 1 nm (10 \AA) junction gives about 10^9 electrons per centimeter squared. Every order of magnitude increase in the junction depth lowers \hbar by the same ratio. Increasing the work function differences by using, e.g., aluminum, will increase ΔV and therefore bond strength.

Conclusions

Although this paper has been derived from the weaving together of observations relating the glow discharge processing variables optimized in forming the silver-FEP composite, and not from experiments in basic physics, it is felt that the physical concepts and explanations would not be significantly variant from those already put forward if the latter had been carried out. Information collected over some months of application experimentation and occasional discussions have established that the surface of FEP must be sensitized with considerable care in order to preserve its natural ultraviolet and particulate stabilities, while at the same time allowing for the establishing of a metal-insulator bond with long-lived surface interactions. Although adhesion may appear stable toward thermal cycling tests prior to lamination onto a rigid surface, the lamination mode remains critical because of the extraordinary thermal expansion coefficient of FEP. Mindful of these factors, a work function difference of about 1 e.v. leaves little margin for variations in bond energy per electron transferred. 10^9 electrons is probably an upper bound, but for the estimated difference in work function, a substantial number of electrons must be involved in bond formation. Experimentally established and theoretically argued is the requirement of reverse bias for providing maximum bond strength through the creation of surface states. In the case of forward bias, it is argued that bonding is not permanent because a junction would be formed based on a polarization potential, and as a result be subject to relaxation.

A thermodynamic argument is used to demonstrate the necessity for max. $\Delta S \sim 0$ (kT), otherwise excess states would appear in the gap and be detected as degradation or a downgrading in environmental stability. The stability requirement emphasizes need for reproducible processing under carefully monitored conditions by a glow discharge.

(3) Private communication from Drs. Park and Seidenberg of the Materials Engineering Branch.